





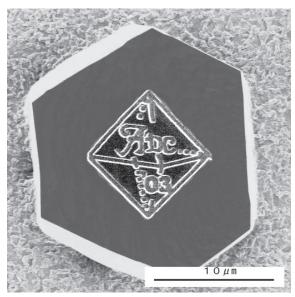




Proceedings of the Seventh Applied Diamond Conference/Third Frontier Carbon Technology Joint Conference (ADC/FCT 2003)







Since its founding, NASA has been dedicated to the advancement of aeronautics and space science. The NASA Scientific and Technical Information (STI) Program Office plays a key part in helping NASA maintain this important role.

The NASA STI Program Office is operated by Langley Research Center, the Lead Center for NASA's scientific and technical information. The NASA STI Program Office provides access to the NASA STI Database, the largest collection of aeronautical and space science STI in the world. The Program Office is also NASA's institutional mechanism for disseminating the results of its research and development activities. These results are published by NASA in the NASA STI Report Series, which includes the following report types:

- TECHNICAL PUBLICATION. Reports of completed research or a major significant phase of research that present the results of NASA programs and include extensive data or theoretical analysis. Includes compilations of significant scientific and technical data and information deemed to be of continuing reference value. NASA's counterpart of peerreviewed formal professional papers but has less stringent limitations on manuscript length and extent of graphic presentations.
- TECHNICAL MEMORANDUM. Scientific and technical findings that are preliminary or of specialized interest, e.g., quick release reports, working papers, and bibliographies that contain minimal annotation. Does not contain extensive analysis.
- CONTRACTOR REPORT. Scientific and technical findings by NASA-sponsored contractors and grantees.

- CONFERENCE PUBLICATION. Collected papers from scientific and technical conferences, symposia, seminars, or other meetings sponsored or cosponsored by NASA.
- SPECIAL PUBLICATION. Scientific, technical, or historical information from NASA programs, projects, and missions, often concerned with subjects having substantial public interest.
- TECHNICAL TRANSLATION. Englishlanguage translations of foreign scientific and technical material pertinent to NASA's mission.

Specialized services that complement the STI Program Office's diverse offerings include creating custom thesauri, building customized databases, organizing and publishing research results . . . even providing videos.

For more information about the NASA STI Program Office, see the following:

- Access the NASA STI Program Home Page at http://www.sti.nasa.gov
- E-mail your question via the Internet to help@sti.nasa.gov
- Fax your question to the NASA Access Help Desk at 301–621–0134
- Telephone the NASA Access Help Desk at 301–621–0390
- Write to:

NASA Access Help Desk NASA Center for AeroSpace Information 7121 Standard Drive Hanover, MD 21076









Proceedings of the Seventh Applied Diamond Conference/Third Frontier Carbon Technology Joint Conference (ADC/FCT 2003)

M. Murakawa, K. Miyoshi, Y. Koga, L. Schäfer, and Y. Tzeng, editors

Proceedings of a conference held at Epochal Tsukuba International Conference Center cosponsored by the Nippon Institute of Technology,
National Institute of Advanced Industrial Science and Technology,
Japan New Diamond Forum,
Auburn University, and
NASA Glenn Research Center
Tsukuba, Japan
August 18–21, 2003

National Aeronautics and Space Administration

Glenn Research Center

About the cover

CVD diamond process:

All diamond (111) flats as large as 20 µm were grown in air with the oxyacetylene torch (combustion synthesis).

High-speed, nano machining process of logos carved on CVD diamond:

The nano machining of the ADC conference logo was conducted using the focused ion beam with a beam diameter of approximately 20 nm at an accelerating voltage of 40 keV for a machining time of 2 minutes. All the nanomachining of the NIT, JNC, NASA, and AIST logos shown herein were conducted using the focused ion beam with a beam diameter of approximately 30 nm at an accelerating voltage of 40 keV for a machining time of 2 minutes with each logo.

Nanomachining process of ADC logo carved on CVD diamond:

The nanomachining of the conference logo "ADC" was conducted using the focused ion beam with a beam diameter of approximately 20 nm for a machining time of 30 minutes.

Note that all CVD and nanomachining processes were performed at the Nippon Institute of Technology.

Contents were reproduced from author-provided presentation materials.

Trade names or manufacturers' names are used in this report for identification only. This usage does not constitute an official endorsement, either expressed or implied, by the National Aeronautics and Space Administration.

The Propulsion and Power Program at NASA Glenn Research Center sponsored this work.

Available from

NASA Center for Aerospace Information 7121 Standard Drive Hanover, MD 21076 National Technical Information Service 5285 Port Royal Road Springfield, VA 22100

FOREWORD

The Applied Diamond Conference was established in 1991. During its first stage, emphasis was put on promoting practical applications and discussing the sciences and technologies associated with diamond and related superhard materials. In its second stage, advances in novel carbon materials and nanostructures such as fullerenes and nanotubes were explored. Momentum grew when the diamond and frontier carbon technology community convinced the Japanese government (then the Ministry of International Trade and Ministry) to sponsor the diamond and frontier carbon technology project (known as the Industrial Science and Technology Frontier Program). As a result, the International Conference on Frontier Carbon Technology (FCT) was established and the two conferences were held jointly at the Fifth Applied Diamond Conference (ADC/FCT '99) in Tsukuba, Japan, in 1999. The Industrial Science and Technology Frontier Program is being continued in a more focused way, this year emphasizing nanotubes and their commercialization.

These are the Proceedings of the Seventh Applied Diamond Conference/Third Frontier Carbon Technology Joint Conference hosted and supported by the Nippon Institute of Technology and the National Institute of Advanced Industrial Science and Technology from August 18 to 21, 2003, in Tsukuba, Japan. The conference received 177 papers from 18 countries: 77 from Japan, 24 from China (including 7 from Hong Kong), 17 from the United States, 14 from Russia, 11 from Germany, 10 from the United Kingdom, 4 from France, 4 from Singapore, 3 from Ukraine, 3 from South Korea, 2 from Brazil, 2 from Taiwan, and 1 each from Armenia, Canada, India, Italy, Sweden, and Switzerland.

We thank all the sponsors, invited speakers, contributors, attendees, committee members, and session chairs who have made this conference a success.

M. Murakawa Organizing Committee, Chairperson

Y. Koga Organizing Committee, Co-chairperson Program Committee, Co-chairperson K. Miyoshi Program Committee, Chairperson Organizing Committee, Co-chairperson

L. Shäfer Program Committee, Co-chairperson

Y. Tzeng Program Committee, Co-chairperson

PROCEEDINGS OF THE SEVENTH APPLIED DIAMOND CONFERENCE/THIRD FRONTIER CARBON TECHNOLOGY JOINT CONFERENCE (ADC/FCT 2003)

ORGANIZING COMMITTEE

M. Murakawa, Chairperson

Nippon Institute of Technology, Japan

Y. Koga, Co-chairperson

National Institute of AIST, Japan

T. Ando

National Institute of Materials Science, Japan

P. Chalker

The University of Liverpool, United Kingdom

P.J. Doering

Apollo Diamond, Inc., United States

A. Hiraki

Kochi University of Technology, Japan

T. Ito

Osaka University, Japan

H. Kawarada

Waseda University, Japan

K. Kobashi

Kobe Steel, Ltd., Japan

J. Meneve

VITO-Flemish Institute of Technology

Research, Belgium

K. Nakajima

Tokyo Institute of Technology, Japan

K. Prassides

University of Sussex, United Kingdom

A. Sawabe

Aoyama Gakuin University, Japan

H. Shinohara

Nagoya University, Japan

Z. Sitar

North Carolina State University, United States

K. Miyoshi, Co-chairperson

NASA Glenn Research Center, United States

P.B. Abel

NASA Glenn Research Center, United States

J.E. Butler

Naval Research Laboratory, United States

D.S. Dandy

Colorado State University, United States

O. Fukunaga

Ace-Tech, Inc., Japan

T. Imai

Sumitomo Electric Co., Japan

H. Kanda

National Institute of Materials Science, Japan

M. Kitabatake

Matsushita Elect. Indu. Co., Ltd., Japan

K. Komaki

New Diamond Forum, Japan

S. Miyake

Nippon Institute of Technology, Japan

H. Ohkushi

National Institute of Advanced Industrial

Science and Technology, Japan

V. Ralchenko

General Physics Institute, Russia

L. Schäfer

Fraunhofer IST, Braunschweig, Germany

R. Silva

University of Surrey, United Kingdom

J.K. Sutter

NASA Glenn Research Center, United States

A. Tanaka

National Institute of Advanced Industrial

Science and Technology, Japan

Y. Tzeng

Auburn University, United States

B. Williams

Cree Research, United States

M. Yoshikawa

Institute of Technologists, Japan

S. Yugo

The University of Electro-Communications, Japan

PROGRAM COMMITTEE

K. Miyoshi, Chairperson

NASA Glenn Research Center, United States

Y. Koga, Co-chairperson

National Institute of Advanced Industrial

Science and Technology, Japan

L. Schäfer, Co-chairperson

Fraunhofer IST, Braunschweig, Germany

Y. Tzeng, Co-chairperson

Auburn University, United States

P.B. Abel

NASA Glenn Research Center, United States

T. Ando

National Institute of Materials Science, Japan

P.J. Doering

Apollo Diamond, Inc., United States

A. Hatta

Kochi University of Technology, Japan

H. Hirai

University of Tsukuba, Japan

K. Komaki

New Diamond Forum, Japan

T. Kumagai

Nanocoat TS, Ltd., Japan

T. Nakamura

National Institute of Advanced Industrial Science

and Technology, Japan

Y. Nitta

Asahi Diamond Industrial Co., Ltd., Japan

N. Ohtake

Tokyo Institute of Technology, Japan

A. Sawabe

Aoyama Gakuin University, Japan

A. Sudoh

Showa Denko K.K., Japan

H. Sumiya

Sumitomo Electric Industries, Ltd., Japan

J.K. Sutter

NASA Glenn Research Center, United States

S. Takeuchi

Nippon Institute of Technology, Japan

T. Taniguchi

National Institute of Materials Science, Japan

S. Watanabe

Nippon Institute of Technology, Japan

T. Yamada

Tohoku University, Japan

PAST CONFERENCE CHAIRPERSONS

A. Feldman

National Institute of Standards and

Technology, United States

M. Yoshikawa

Institute of Technologists, Japan

Y. Tzeng

Auburn University, United States

INTERNATIONAL ADVISORS

J.C. Angus O. Fukunaga

Case Western Reserve University, United States Ace-Tech., Inc., Japan

A. Grill A. Hiraki

International Business Machines, United States Kochi University of Technology, Japan

V.I. Konov

Russian Academy of Science, Russia

LOCAL ARRANGEMENTS COMMITTEE

T. Nakamura, Co-Chairperson S. Takeuchi, Chairperson

Nippon Institute of Technology, Japan National Institute of Advanced Industrial

Science and Technology, Japan

M. Gamo-Nishitani A. Hirata

Toyo University, Japan Tokyo Institute of Technology, Japan

M. Ishihara M. Jin

National Institute of Advanced Industrial Nippon Institute of Technology, Japan

Science and Technology, Japan

H. Miyazawa H. Noguchi

Nippon Institute of Technology, Japan Nippon Institute of Technology, Japan

T. Ohana

National Institute of Advanced Industrial

Science and Technology, Japan

A. Tanji

Nippon Institute of Technology, Japan

S. Watanabe

Nippon Institute of Technology, Japan

PUBLICATION COMMITTEE

K. Joyce L.C. Feher

InDyne, Inc., at NASA Glenn Research InDyne, Inc., at NASA Glenn Research

Center, United States Center, United States

K. Soboslay P. Hutka

InDyne, Inc., at NASA Glenn Research InDyne, Inc., at NASA Glenn Research

Center, United States Center, United States

TABLE OF CONTENTS

FOREWORD	iii
ORGANIZING COMMITTEE	v
1. NANOTUBE	
DEVELOPMENT OF CNT BASED FIELD EMISSION X-RAY SOURCE AND IMAGING SYSTEM FOR BIOMEDICAL AND INDUSTRIAL APPLICATIONS Otto Zhou, University of North Carolina, United States	3
CATALYSTS TO CONTROL THE GROWTH AND STRUCTURE OF SINGLE-WALL CARBON NANOTUBES Masako Yudasaka, NEC, Japan	4
A NOVEL CATALYTIC SYNTHESIS OF CARBON NANOTUBES IN ALCOHOL LIQUID Kiyoharu Nakagawa and Toshihiro Ando, National Institute for Materials Science, Japan; and Mikka Nishitani-Gamo, Toyo University, Japan	5
DESIGNING CARBON-BASED NANOTECHNOLOGY ON A SUPERCOMPUTER David Tománek, Michigan State University, United States	10
ULTRA-FAST DYNAMICS IN ELECTRONICALLY EXCITED NANOTUBES: TIME-DEPENDENT DENSITY FUNCTIONAL APPROACH Yoshiyuki Miyamoto, NEC Corp., Japan; Angel Rubio, International Physics Center, Spain; and David Tománek, Michigan State University, United States	11
HYDRATION PROPERTIES OF CARBON NANOTUBES AND THEIR EFFECTS ON ELECTRICAL AND BIO-SENSOR APPLICATIONS Y. Tzeng, T.S. Huang, and Y.C. Chen, Auburn University, United States; and Y.K. Liu, National Tsing-Hua University, Republic of China	12
CARBON NANOTUBE ELECTRODE ARRAYS FOR ENHANCED CHEMICAL AND BIOLOGICAL SENSING Jie Han, NASA Ames Center for Nanotechnology, United States	17
GROWTH AND CHARACTERISATION OF MULTIWALL CARBON NANOTUBES/ FIBRES FOR FIELD EMISSION APPLICATIONS W.I. Milne, K.B.K. Teo, R. Lacerda, M. Chhowalla, and G.A.J. Amaratunga, Cambridge University Engineering Department, United Kingdom; D.G. Hasko and S-B. Lee, Cavendish Laboratory, University of Cambridge, United Kingdom; and P. Legagneux and D. Pribat, Thales Research and Technology, Domaine de Corbeville, France	
THE LARGE-SCALE PRODUCTION OF NANOFIBERS, MWNTs, SWNTs AND THEIR PRACTICAL APPLICATIONS M. Endo, T. Hayashi, Y.A. Kim, and T. Yanagisawa, Shinshu University, Japan; and M.S. Dresselhaus, Massachusetts Institute of Technology, United States	10
GISAXS STUDY OF THE ALIGNMENT OF ORIENTED CARBON NANOTUBES GROWN ON PLAIN SiO2/Si(100) SUBSTRATES BY A CATALYTICALLY ENHANCED CVD PROCESS F. Normand and C.S. Cojocaru, CNRS, France; Mane Mane, University Yaound Cameroon, France; and O. Jean and T.H. Metzger, ESRF, France	

CONTROLLED SYNTHESIS OF CARBON NANOTUBES BY ARC IN WATER WITH REDUCED PRESSURE Noriaki Sano, Masakazu Naito, Kenji Iimura, Satoshi Matsuda, Tatsuo Kanki, and Takeyuki Kikuc Himeji Institute of Technology, Japan; Manish Chhowalla, Rutgers University, United States; and Haolan Wang and Gehan A.J. Amaratunga, University of Cambridge, United Kingdom	
LARGE-SCALE SYNTHESIS OF SINGLE-WALLED CARBON NANOHORNS USING THE ARC IN LIQUID METHOD Haolan Wang and G.A.J. Amaratunga, University of Cambridge, United Kingdom; S. Jia, Xi'an Jiaotong University, China; N. Sano, Himeji Institute of Technology, Japan; and	
M. Chhowalla, Rutgers University, United States FORMATION OF CARBON NANOTUBES BY CATALYSIS OF TRANSITION METALS OBTAINED FROM MOLECULAR PRECURSORS Hermann Sachdev and Dominik Tince, University of Saarland, Germany; and	
Michael Knorr, Université de Franche-Comté, France	
NOVEL CARBON NANOSTRUCTURES: NANOPIPETTES AND NANO NOZZLES G. Bhimarasetti, R.C. Mani, and M.K. Sunkara, University of Louisville, United States; and K. Rajan and X. Li, Rensselaer Polytechnic Institute, United States	34
WELL-ALIGNED CARBON NANOTUBES FROM METHANE/NITROGEN PLASMA W.K. Wong, C.S. Lee, and S.T. Lee, City University of Hong Kong, China	40
SONOCHEMICAL SYNTHESIS OF CARBON NANOTUBES AND NANOONIONS UNDER AMBIENT CONDITIONS USING A SINW TEMPLATE C.P. Li, X.H. Sun, N.B. Wong, and C.S. Lee, City University of Hong Kong, China; B.K. Teo, University of Illinois, United States; and S.T. Lee, City University of Hong Kong, China	41
SYNTHESIS OF NANOGRAPHITE-RIBBON Mutsumasa Kyotani, Frontier Carbon Technology Laboratory, Japan Fine Ceramics Center; Chiharu Yamaguchi and Hisaji Matsui, Osaka Gas Co., Japan; and Yoshinori Koga, Research Center for Advanced Carbon Materials, Japan	42
ABOUT THE INFLUENCE OF BIOAKTIVITE CARBON MATERIALS NANOCLUSTERS STRUCTURES ON EFFECTIVITY OF ECOSYSTEM SORPTION-CATALYTIC PURIFYING FROM OIL PRODUCTS Shvets Dmitriy, Institute for Sorption and Problems of Endoecology, Ukraine	45
KINETICS OF CARBON NANOTUBE FOREST GROWTH BY CHEMICAL VAPOR DEPOSITION O.A. Louchev, T. Laude, Y. Sato, and H. Kanda, National Institute for Materials Science, Japan	
CARBON NANOTUBE NUCLEATION FROM GRAPHITIC NANOFRAGMENTS Oleg A. Louchev, National Institute for Materials Science, Japan; and James R. Hester Australian Nuclear Science and Technology Organization, Australia	52
KINETICS STUDY OF Cd ²⁺ IONS IN SODIUM SULFATE SOLUTION AT CARBON NANOTUBE ELECTRODE C.G. Hu, W.L. Wang, K.J. Liao, H. Wang, and X.H. Xian, Chongqing University, China	53

TEMPERATURE
B.O. Boskovic, Morgan Group Technology Ltd., United Kingdom; V. Stolojan, D.A. Zeze,
R.D. Forrest, and S.R.P. Silva, University of Surrey, United Kingdom; and S. Haq,
BAE SYSTEMS, United Kingdom
ON DULL W MODULITIE OF CUREDITARD 2D DOLVMEDC OF CARDON MANOCLUCTED
ON BULK MODULUS OF SUPERHARD 3D POLYMERS OF CARBON NANOCLUSTER M. Popov, Max Planck Inst. fur Chemie, Hochdruck Mineralphysik, Germany; and Y. Koga,
National Institute of Advanced Industrial Science and Technology, Japan64
1 varional institute of Advanced industrial Science and Technology, Japan
INTERACTION BETWEEN CATALYST METALS AND STONE-WALES DEFECTS IN CARBON NANOTUBES
F.Y. Meng and L.G. Zhou, The Hong Kong Polytechnic University, China, and
Chinese Academy of Sciences, China; San-Qiang Shi, The Hong Kong Polytechnic
University, China; and Rui Yang, Chinese Academy of Sciences, China
FRICTIONAL PROPERTIES OF CARBON NANOTUBE REINFORCED POLYMER MATRIX COMPOSITES
Kazuki Enomoto, Toshiyuki Yasuhara, Shintaro Kitakata, Hiroya Murakami, and
Naoto Ohtake, Tokyo Institute of Technology, Japan70
SOLID LUBRICANT PROPERTIES OF CATALYTICALLY GROWN CARBON NANOTUBES Atsushi Hirata and Nobuaki Yoshioka, Tokyo Institute of Technology, Japan
Atsustit filiata and Nobuaki Fositioka, Tokyo filstitute of Technology, Japan
STUDY ON TEMPLATE PORE ACTING ON THE FABRICATED ARRAYS OF
NANOMATERIALS
Y.B. Zhu, W.L. Wang, K.J. Liao, C.G. Hu, and Q. Feng, Chongqing University, China80
AGE CONTROL OF A DRADENT THERMAN GONDAGTH WITH OF NAMED BARTIST FOR
MEASUREMENT OF APPARENT THERMAL CONDUCTIVITY OF NANO PARTICLES
Efim Litovsky and Jacob Kleiman, Integrity Testing Laboratory Inc., Canada; and Yoshinori Koga, National Institute of Advanced Science and Technology, Japan
Toshmori Roga, National Institute of Advanced Science and Technology, Japan
CHARACTERISTICS OF CARBON NANOTUBE ELECTRON FIELD EMISSION
DEVICES PREPARED BY LTCC PROCESS
Tsong-Yen Tsai, Nyan-Hwa Tai, and I-Nan Lin, National Tsing-Hua University,
Republic of China
CARBON NANO-MATERIALS FOR VACUUM ELECTRONICS
A.N. Obraztsov, A.P. Volkov, Al.A. Zakhidov, A.A. Zolotukhin, A.O. Ustinov, and
D.A. Lyshenko, Moscow State University, Russia
· · · · · · · · · · · · · · · · · · ·
ELECTROCHEMICAL OXIDATION OF PHENOL AT CARBON NANOTUBE ELECTRODE
C.G. Hu, W.L. Wang, K.J. Liao, X.H. Xian, Q. Feng, and G.B. Liu, Chongqing
University, China90
CHARACTERIZATION AND FIELD EMISSION PROPERTIES OF SWNTs AND MWNTs
Sigen Wang, Qing Zhang, S.F. Yoon, J. Ahn, D.J. Yang, Q. Wang, J.Q. Li, Q. Zhou,
J.Z. Tian, Nanyang Technological University, Singapore
7 7 6 7 6 1
SPATIALLY RESOLVED ANALYSIS OF THE ELECTRONIC PROPERTIES OF
WS ₂ -COATED CARBON NANOTUBES USING EELs IN A TEM
V. Stolojan, M.J. Goringe, and S.R.P. Silva, University of Surrey, United Kingdom; and R.L.D.
Whitby, D.R.M. Walton, W.K. Hsu, and H.W. Kroto, University of Sussex, United Kingdom96
STUDY ON GAS SENSITIVITY OF CARBON NANOTUBE FILMS
W.L. Wang, Y. Ma, K.J. Liao, Z.H. Wu, G.B. Liu, and B.Y. Wan, Chongqing University, China101

ON THE CALCULATION OF THE FIGURE OF MERIT FOR CARBON NANOTUBES BASED DEVICES A. Vaseashta, Marshall University, United States
2. DIAMOND EPITAXY AND DIAMOND SENSORS
EXCITONIC EMISSION FROM HIGH QUALITY HOMOEPITAXIAL DIAMOND FILMS Hideyuki Watanabe, National Institute of Advanced Industrial Science and Technology, Japan, and Japan Science and Technology Corporation, Japan; Shokichi Kanno, Ibaraki University, Japan, and Japan Science and Technology Corporation, Japan; and Hideyo Okushi, National Institute of Advanced Industrial Science and Technology, Japan, and Japan Science and Technology Corporation, Japan
LARGE AREA DEPOSITION OF HETEROEPITAXIAL DIAMOND THIN FILMS ON ION-IRRADIATED IRIDIUM A. Sawabe, J. Kuwabara, H. Okamura and T. Yamada, Aoyama Gakuin University, Japan; K. Suzuki, Toplas Engineering Co. Ltd., Japan
APPLICATIONS OF SINGLE CRYSTAL CVD DIAMOND Daniel J. Twitchen, Geoffrey A. Scarsbrook, Andrew J. Whitehead, Chris Wort, and Steve E. Coe, Element Six Ltd., United Kingdom; and Jan Isberg, Uppsala University, Sweden
ELECTRICAL PROPERTIES OF DIAMOND <i>PN</i> -JUNCTION DEVICES S. Koizumi, M. Katagiri, K. Watanabe, and H. Kanda, National Institute for Materials Science, Japan
DIAMOND LED UTILIZING FREE EXCITON RECOMBINATION EMISSION Kenji Horiuchi, Aki Kawamura, Yuichiro Okajima, Takuhiro Ide, and Takefumi Ishikura, Tokyo Gas Co., Ltd., Japan
DIAMOND MICRO-OPTICS M. Karlsson, H. Högström, and F. Nikolajeff, The Ångström Laboratory, Uppsala University, Sweden
DIAMOND MICRODOSIMETERS AND MICRODETECTORS C. Manfredotti, E. Vittone, F. Fizzotti, A. Lo Giudice, C. Paolini, and D. Olivero, University of Torino, Italy; and INFM, National Institute for Matter Physics, UdR To-University, Italy
ELECTROCHEMICAL ADVANCED OXIDATION PROCESS FOR WATER TREATMENT APPLICATIONS Matthias Fryda, Thorsten Matth, and Shane Mulcahy, CONDIAS GmbH, Germany; and Lothar Scher, Markus Ger, and Inga Tter, Fraunhofer IST, Germany
HIGH-DENSITY ELECTRON EMISSION FROM ION-IMPLANTED DIAMOND Tadashi Sakai, Tomio Ono, Mariko Suzuki, and Naoshi Sakuma, Japan Fine Ceramics Center, Joint Research Consortium of Frontier Carbon Technology, Japan, and Toshiba Corporation, Japan; Hiroaki Yoshida, Japan Fine Ceramics Center, Joint Research Consortium of Frontier Carbon Technology, Japan; and Masataka Hasegawa, Hideyo Okushi, and Yoshinori Koga, Research Center for Advanced Carbon Materials
ULTRAVIOLET SENSORS USING HIGHLY-ORIENTED DIAMOND FILMS Kazushi Hayashi, Takeshi Tachibana, Yoshihiro Yokota, and Koji Kobashi, Kobe Steel, Ltd., Japan; Jocelyn Achard and Alix Gicquel, Université Paris-Nord, France; Charles Olivero and Marie-Claude Castex, Université Paris-Nord, France; and Alexey Treshchalov, University of

BI-STABLE THERMAL MICROACTUATORS BASED ON CVD DIAMOND R. Müller, P. Schmid, A. Munding, F.J. Hernandez-Gullien, and E. Kohn, University of Ulm, Germany	136
CAPACITANCE-VOLTAGE-FREQUENCY CHARACTERISTICS OF NI/DIAMOND SCHOTTKY DIODES ON OXIDIZED BORON-DOPED HOMOEPITAXIAL DIAMOND FILM Y.G. Chen, M. Ogura, and H. Okushi, Diamond Research Center, National Institute of Advanced Industrial Science and Technology, Japan; and CREST, Japan Science and Technology Corporation, Japan.	141
HOLE MOBILITY IN BORON-DOPED HOMOEPITAXIAL CVD DIAMOND THIN FILMS Kunio Tsukioka and Hisashi Ogawa, Tamagawa University, Japan; and Hideyo Okushi, National Institute of Advanced Industrial Science and Technology, Japan	147
ELECTRICAL EFFECT OF VACUUM-EVAPORATED \(\alpha\)-NPD ON OXYGEN-TERMINATED BORON-DOPED CHEMICAL-VAPOR-DEPOSITED HOMOEPITAXIAL DIAMOND FILMS Min-seung Chun, Tokuyuki Teraji, and Toshimichi Ito, Osaka University, Japan	152
PREPARATION OF DIAMOND COATED ELECTRODES AND THE APPLICATION TO WASTEWATER TREATMENT X.C. He, X.Q. Yang, H.S. Shen, R.B. Li, Y.L. Wang, and J.P. Jia, Shanghai Jiao Tong University, Shanghai	153
FIELD EMISSION PROPERTIES OF DIAMOND PARTICLES: ELECTRON INJECTION INTO THE CONDUCTION BAND BY TUNNELING AT THIN INSULATING INTERFACE LAYER Akihiko Watanabe, Osaka University, and Makoto Kitabatake, Osaka University, Japan, and Matsushita Electric Industrial Co., Ltd., Japan.	154
EXPERIMENTAL COMPARISON OF DIAMOND COATED ELECTRODE WITH RELATED MATERIALS IN ATMOSPHERIC BIPOLAR CORONA DISCHARGE Tetsuya Akitsu and Kayoko Iwamura, University of Yamanashi, Japan; Akimitsu Hatta, Kochi University of Technology, Japan; Shuji Takaishi, YGK Corporation, Japan	155
MICROWAVE POWER PERFORMANCE OF DIAMOND SURFACE-CHANNEL FETs USING HIGH-QUALITY HOMOEPITAXIAL LAYERS M. Kasu, University of Ulm, Germany, and NTT Corporation, Japan; M. Kubovic, A. Aleksov, I. Kallfass, and U. Spitzberg, University of Ulm, Germany; N. Kobayashi and T. Makimoto, NTT Corporation, Japan; and H. Schumacher and E. Kohn, University of Ulm, Germany	159
CHARACTERIZATION OF THE CONTACT LAYER FORMED BY AR ION IMPLANTATION INTO HOMOEPITAXIAL DIAMOND FILM H. Yoshida, Japan Fine Ceramics Center, Joint Research Consortium of Frontier Carbon Technology, Japan; M. Suzuki, N. Sakuma, and T. Sakai, Toshiba Corporation, Japan; and M. Ogura, K. Yamamoto H. Okushi, Research Center for Advanced Carbon Materials, Japan	163
ELECTRICAL PROPERTIES OF DOPED AND UNDOPED HOMOEPITAXIAL DIAMOND LAYERS GROWN BY MICROWAVE PLASMA CVD Suzuki Mariko, Hiroaki Yoshida, Naoshi Sakuma, Tomio Ono, and Tadashi Sakai, Toshiba Corporation, Japan; and Masahiko Ogura and Hideyo Okushi, National Institute of Advanced Industrial Science and Technology, Japan	164

OPTICAL AND ELECTRIC PROPERTIES OF (111)-ORIENTED DIAMOND HOMOEPITAXIAL LAYER	
M. Kasu, NTT Corporation, Japan, and University of Ulm, Germany; A. Aleksov, N. Teofilov, and M. Kubovic, University of Ulm, Germany; Y. Taniyasu, NTT Corporation, Japan; R. Sauer,	
and E. Kohn, University of Ulm, Germany; and T. Makimoto and N. Kobayashi, NTT Corporation, Japan	.165
3. PROPERTIES AND APPLICATIONS OF DIAMOND	
CHARACTERIZATION AND APPLICATIONS OF SINGLE CRYSTAL CVD DIAMOND Patrick J. Doering, Apollo Diamond, Inc., United States.	.173
DIAMOND FIELD EFFECT TRANSISTORS FOR MICROWAVE DEVICES AND BIOSENSING APPLICATIONS	
H. Kawarada, H. Umezawa, S. Miyamoto, H. Matsudaira, and K-S. Song, Waseda University, Japan	.174
DIAMOND ELECTROCHEMISTRY	
John Foord, James McEvoy, Arnab Chatterjee, and Richard Compton, University of Oxford, United Kingdom; and Frank Marken, University of Loughborough, United Kingdom	.178
SCANNING PROBE MICROSCOPY OF CARBON-NANOPARTICLE-BASED EMITTERS V.D. Frolov, A.V. Karabutov, V.I. Konov, and S.M. Pimenov, General Physics Institute, Russia; P. Ya. Detkov, and V.V. Ovsyakov, Russian Federal Nuclear Center—Institute of	
Technical Physics, Russia; and E.N. Loubnin, Institute of Physical Chemistry, Russia	.179
FABRICATION OF 3–D SHAPED MICRO BODY STRUCTURES OF DIAMOND BY USE OF FOCUSED ION BEAM	
Masao Murakawa, Hiroyuki Noguchi, and Sadao Takeuchi, Nippon Institute of Technology, Japan	.185
TRIBOLOGICAL BEHAVIOR OF CVD DIAMOND TOOLS E. Uhlmann and M. Brücher, Technical University of Berlin, Germany	.191
EVALUATION OF MECHANICAL PROPERTIES OF HIGH-TOUGHNESS MULTILAYERED DIAMOND FILMS	
S. Takeuchi, M. Kojima, and M. Murakawa, Nippon Institute of Technology, Japan	.197
PROCESSING OF DIAMONDS BY SHORT PULSE LASERS H. Miyazawa and S. Takeuchi, Nippon Institute of Technology, Japan; and K. Shihoyama HOYA Photonics Corp., Japan	.201
A SYSTEM MADE OF DIAMOND FOR ASSEMBLING MICROELEMENTS Yuichi Nakazato, Akiyoshi Sekine, Goro Sekine, Hajime Miyazawa, and Sadao Takeuchi, Nippon Institute of Technology, Japan	.207
MICROCUTTING OF DURALUMIN USING FOCUSED-ION-BEAM-PROCESSED PROFILE	
CUTTING DIAMOND BITES Hiroyuki Noguchi, Sadao Takeuchi, and Masao Murakawa, Nippon Institute of Technology, Japan	.213
FORMATION OF FLAT POLYCRYSTALLINE DIAMOND SURFACE BY ION BEAM ETCHING Takatoshi Yamada, Tohoku University, Japan; and Atsuhito Sawabe, Aoyama Gakuin	210

DIAMOND AS AN ELECTRODE	
Kiyoshi Suzuki, Nippon Institute of Technology, Japan; Manabu Iwai, Toyama Prefectural	
University, Japan; Anurag Sharma, Nippon Institute of Technology, Japan; Tetsutaro Uematsu, Toyama Prefectural University, Japan; Kazuo Shoda, Nippon Institute of Technology, Japan;	
and Masanori Kunieda, Tokyo University of Agriculture and Technology, Japan	.222
WEAR BEHAVIOR OF THIN CVD DIAMOND FILMS DURING THE INTERRUPTED CUT	
Eckart Uhlmann and Rouven Kott, Technical University Berlin—Institute for Machine Tools	220
and Factory Management, Germany	.228
NEW DIAMOND COATED CARBIDE DENTAL BUR IN OPERATION	
Htet Sein and Waqar Ahmed, Manchester Metropolitan University, United Kingdom;	
Mark Jackson, Tennessee Technological University, United States; and Ricardo Polini,	22.4
Universita' di Roma "Tor Vergata," Via Della Ricerca Scientifica, Italy	234
AURORA PLD GROWTH OF CaF ₂ THIN FILM AND APPLICATION TO IMPROVED	
CaF ₂ /DIAMOND MISINTERFACE FORMATION	
Shigeto Honda, Shinsuke Komatsu, and Takeshi Kobayashi, Osaka University, Japan	.244
THERMODYNAMICALLY PREDICTED C-H-O PHASE DIAGRAM	
Takahiro Tsutsumoto and Akira Yamamoto, Western Industrial Research Institute	
of Hiroshima, Japan	.250
PIEZORESISTIVE PROPERTY OF CVD DIAMOND FILMS	
Akira Yamamoto and Takahiro Tsutsumoto, Western Industrial Research Institute of	
Hiroshima Prefecture, Japan.	255
COANDING TURNET INCLUDE OCCORN CTURIES OF HADDOCENATED AND	
SCANNING TUNNELING MICROSCOPY STUDIES OF HYDROGENATED AND OXYGENATED CVD DIAMOND (100) SURFACES	
J. Nakamura, T. Teraji, and T. Ito, Osaka University, Japan	259
THEORETICAL ANALYSIS ON PIEZORESISTIVE EFFECT OF DIAMOND FILMS BY CHEMICAL VAPOR DEPOSITION	
K.J. Liao, W.L. Wang, C.Y. Kong, S.X. Wang, Q. Feng, and Y. Ma, Chongqing	
University, China	.260
IDENTIFICATION OF THE CHEMICAL STATE OF CARRON ATOMS ON	
IDENTIFICATION OF THE CHEMICAL STATE OF CARBON ATOMS ON NANODIAMOND POUDER SURFACES	
A.P. Dementjev and K.I. Maslakov, RRC Kurchatov Institute, Russia	.266
CHEMICAL MODIFICATION OF DIAMOND POWDER USING PHOTOLYSIS OF PERFLUOROAZOOCTANE	
T. Nakamura, M. Ishihara, T. Ohana, and Y. Koga, National Institute of Advanced	
Industrial Science and Technology, Japan	.271
OVER A TWO VERDER CITE ON POLYMORY AND THE REAL MONE BY A CAMPE A CE	
OXIDATION EFFECTS ON POLYCRYSTALLINE DIAMOND FILM SURFACE Jingqi Li, Qing Zhang, S.F. Yoon, and J. Ahn, Nanyang Technological University,	
SingaporeSingapore	.275
CHEMICAL REACTIONS OF C-ATOMS WITH NANODIAMOND AND DIAMOND SURFACES	270
A.P. Dementjev and K.I. Maslakov, RRC Kurchatov Institute, Russia	.219
ELECTRON EMISSION FROM NANO-STRUCTURED DIAMOND FILMS DEPOSITED ON	
ION IMPLANTED SI SUBSTRATES	261
Changzhi Gu, State Key Laboratory of Surface Physics, Institute of Physics, China	284

CHARGE-BASED DEEP LEVEL TRANSIENT SPECTROSCOPY OF DEFECTS IN ELECTRON-IRRADIATED AND ANNEALED CVD DIAMONDS	
V.I. Polyakov, A.I. Rukovishnikov, and N.M. Rossukanyi, Institute of Radio Engineering and Electronics, Russia; and V.G. Ralchenko and I.I. Vlasov, General Physical Institute, Russia	285
HYDROGEN IMPLANTED CVD BORON DOPED MONOCRYSTALLINE DIAMOND D. Ballutaud, F. Jomard, and E. Rzepka, Centre National de la Recherche Scientifique,	
France; and A. Boutry-Forveille, Université deVersailles-Saint-Quentin, France	291
DIELECTRIC LOSSES IN CVD DIAMONDS AT FREQUENCIES 1 kHz–200 GHz AND TEMPERATURES 70–800 K B.M. Garin and M.P. Parkhomenko, Institute of Radio Engineering and Electronics of Russian Academy of Sciences, Russia; V.V. Parshin and S.E. Myasnikova, Institute of Applied Physics of Russian Academy of Sciences, Russia; R. Heidinger and I. Danilov, Institute for Materials Research I, Germany; J. Molla, Association Euratom—CIEMAT, Spain; V.G. Ralchenko, Natural Science Centre of General Physics Institute of Russian Academy of Sciences, Russia; and V.N. Derkach and S.I. Tarapov, Institute of Radiophysics and Electronics NAS of Ukraine, Ukraine	297
EXCIMER LASER ANNEALING OF DIAMONDS IMPLANTED WITH LIGHT IONS S.M. Pimenov, V.V. Kononenko, T.V. Kononenko, and V.I. Konov, General Physics Institute, Russia; P. Fischer, V. Romano, and H.P. Weber, University of Bern, Switzerland; A.V. Khomich, Institute of Radio Engineering and Electronics, Russia; and R.A. Khmelnitskiy, P.N. Lebedev Physical Institute, Russia.	
MEASUREMENTS OF THERMAL CONDUCTIVITY OF UNDOPED AND BORON-DOPED CVD DIAMOND BY TRANSIENT GRATING AND LASER FLASH TECHNIQUES V.G. Ralchenko and A.V. Vlasov, Russian Academy of Sciences, Russia; E.V. Ivakin and A.V. Sukhadolau, Academy of Sciences of Belarus, Belarus; and A.V. Khomich, Institute of Radio Engineering and Electronics, Russia.	309
X-RAY THREE-BEAM DIFFRACTION BY DIAMOND SINGLE CRYSTALS V.N. Tkach, V.N. Bakul Institute for Superhard Materials of the National Academy of Sciences of Ukraine, Ukraine; and I.M. Fodchuk and M.D. Borcha, Yu. Fedkovich Chernovtsy State University, Ukraine	315
MOLECULAR DYNAMICS SIMULATION OF BORON IMPLANTED INTO DIAMOND Rongbin Li, Yongbin Dai, Xiaojun Hu, Heshen Sheng, and Xianchang He, Shanghai Jiaotong University, China	320
4. DIAMONDLIKE CARBON AND CUBIC BORON NITRIDE	
TRIBOLOGICAL PROPERTIES OF GRAPHITE LIKE AND DIAMOND LIKE CARBON COATINGS	
D.G. Teer, Teer Coatings Ltd., United Kingdom	323
ELECTRONIC POWER SYSTEM APPLICATION OF DIAMOND-LIKE CARBON FILMS Richard L.C. Wu and H. Kosai, K Systems Corporation, United States; S. Fries-Carr and J. Weimer, Wright-Patterson AFB, United States; M. Freeman, DARPA TACTICAL Technology, United States; and G.E. Schwarze, NASA Glenn Research Center, United States	324
APPLICATION OF DIAMOND LIKE CARBON FILMS TO GAS BARRIER FOR HYDROGEN FUEL CELL TECHNOLOGY Akimitsu Hatta, Haruka Matsuhisa, Tetsuya Kaneko, and Michio Watamori, Kochi University of Technology, Japan; Yoshinori Koga, National Institute of Advanced Industrial Science and Technology, Japan; and Hironobu Inagaki and Kenzo Fukuda,	
The Institute of Applied Energy Jones	228

CUBIC BORON NITRIDE AND BORON BASED TOOL COATINGS—MECHANICAL AND TRIBOLOGICAL PROPERTIES Martin Keunecke and Klaus Bewilogua, Fraunhofer-Institute for Surface Engineering and Thin Film, Germany	329
FROM MOLECULES TO MATERIALS: HARD AND SOFT BORON NITRIDE PHASES OF TECHNOLOGICAL IMPORTANCE	
Hermann Sachdev, Universität des Saarlandes, Saarbrücken, Germany	330
INTRINSIC ABSORPTION-EDGE SPECTRUM AND INDIRECT EXCITON RELATED LUMINESCENCE OF CUBIC BORON NITRIDE Kenji Watanabe, Takashi Taniguchi, Isao Sakaguchi, and Hisao Kanda, National Institute for Materials Science, Japan	331
DLC FILM GROWTH ON THE SURFACE OF MONOCRYSTALLINE Si AND α -AL $_2$ O $_3$ WITH THE USAGE OF ION SOURCE	
Zh. Panosyan, S. Voskanyan, Y. Yengibaryan, and A. Stepanyan, State Engineering University of Armenia, Armenia	334
PREPARATION AND PROPERTIES OF DIAMOND-LIKE CARBON FILMS FROM CH ₄ , C ₂ H ₄ , AND C ₂ H ₂ WITH PLASMA SOURCE ION IMPLANTATION K. Baba and R. Hatada, Industrial Technology Center of Nagasaki, Japan; and S. Miyagawa,	
National Institute of Advanced Industrial Science and Technology, Japan	340
IDENTIFICATION OF CHEMICAL BONDS ON UPPER LAYERS OF DLC USING AUGER SPECTROSCOPY AND XPS A.P. Dementjev and K.I. Maslakov, RRC Kurchatov Institute, Russia; Kensuke Uemura, ITAC Ltd. Company, Japan; and I.Sh. Trakhtenberg, A.P. Rubshtein, S.A. Plotnikov, A.B. Vladimirov, and V.A. Yugov, Metal Physics Institute Ural Branch RAS, Russia	345
DIAMOND-LIKE CARBON FILMS DEPOSITED BY PLASMA-BASED ION IMPLANTATION METHOD Masatou Ishihara, Takako Nakamura, Akihiro Tanaka, and Yoshinori Koga, National Institute of Advanced Industrial Science and Technology, Japan; and Masahiro Suzuki, Toshiya Watanabe, and Osamu Tsuda, Japan Fine Ceramics Center, Joint Research Consortium of Frontier Carbon Technology, Japan	350
SYNTHESIS OF CARBON MATERIALS USING ABNORMAL DC GLOW DISCHARGE PLASMA CVD Hiromichi Yoshikawa, Japan Fine Ceramics Center, Joint Research Consortium of Frontier Carbon Technology, Japan; and Yoshinori Koga, National Institute of Advanced Industrial Science and Technology, Japan	351
DEPOSITION OF BC/TA-C MULTILAYER THIN FILMS BY LASER ABLATION Manabu Taniwaki and Masahiro Suzuki, Japan Fine Ceramics Center, Joint Research Consortium of Frontier Carbon Technology, Japan; Masatou Ishihara and Yoshinori Koga, National Institute of Advanced Industrial Science and Technology, Japan; and Fumio Kokai, Mie University, Japan	352
SEMICONDUCTING TETRAHEDRAL CARBONS TRANSFORMED TO SEMIMETAL NANOCOMPOSITE MATERIALS BY ION IMPLANTATION O. Kutsay, I. Bello, Y. Lifshitz, W.Y. Luk, C.W. Lam, S.T. Lee, and X.M. Meng, City	
University of Hong Kong, China.	353

NANO-GRAPHITE DEPOSITION BY ELECTRON CYCLOTRON RESONANCE PLASMA SPUTTERING METHOD	
T. Ohana, T. Nakamura, A. Tanaka, and Y. Koga, National Institute of Advanced Industrial Science and Technology, Japan; and K. Tsugawa, Japan Fine Ceramics Center, Joint Research	
Consortium of Frontier Carbon Technology, Japan	ļ
CN _X FILMS PREPARED ALTERNATIVE IRRADIATION OF ¹² C ⁺ AND ¹⁴ N ⁺ ION BEAMS Kazuhiro Yamamoto and Yoshinori Koga, National Institute of Advanced Industrial Science and Technology, Japan; and Toshiya Watanabe and Koichiro Wazumi, Japan Fine Ceramics Center, Joint Research Consortium of Frontier Carbon Technology, Japan)
CALCULATION OF THE ELECTRONIC STRUCTURE OF SiCN CRYSTAL BY LAPW METHOD	
X.L. Zhu, X.B. Niu, Y. Liao, L. Yu, Q.X. Yu, G.Z. Wang, and R.C. Fang, University of Science and Technology of China, China	,
SYNTHESIS OF B-C-N FILMS BY ELECTRON BEAM EXCITED PLASMA-ASSISTED rf MAGNETRON SPUTTERING	
Takeshi Hasegawa, Japan Fine Ceramics Center, Joint Research Consortium of Frontier Carbon Technology, Japan; and Kazuhiro Yamamoto and Yozo Kakudate, National	
Institute of Advanced Industrial Science and Technology, Japan	Ó
FORMATION OF REFRACTORY COATINGS ON CARBON-BASED MATERIALS BY GAS PHASE TRANSPORT REACTIONS N.I. Baklanova, V.N. Kulyukin, and T.M. Zima, Institute of Solid State Chemistry and	
Mechanochemistry of Siberian Branch of Russian Academy of Sciences, Russia	7
DEPOSITION OF CUBIC BORON NITRIDE FILMS BY PLASMA BASED ION IMPLANTATION Osamu Tsuda, Toshiya Watanabe, and Masahiro Suzuki, National Institute of Advanced Industrial Science and Technology, Japan	2
NUCLEATION MECHANISM OF CUBIC BORON NITRIDE IN VAPOR PHASE DEPOSITION Hangsheng Yang, Chihiro Iwamoto, and Toyonobu Yoshida, University of Tokyo, Japan378	}
A NANOINDENTATION STUDY OF THICK CUBIC BORON NITRIDE FILMS PREPARED BY CHEMICAL VAPOR DEPOSITION	
C.Y. Chan, W.J. Zhang, K.M. Chan, I. Bello, and S.T. Lee, City University of Hong Kong, China; and S. Matsumoto, National Institute for Materials Science, Japan379)
INFLUENCE OF IMPURITIES ON THE MORPHOLOGY AND THE RAMAN SPECTRA OF CUBIC BORON NITRIDE	
Hermann Sachdev, Universität des Saarlandes, Germany)
PERSISTENCE OF GRAPHITE PHASE IN G-BALL UNDER HIGH PRESSURE SHOWING METALLIC BEHAVIOR Atsuko Nakayama, National Institute of Advanced Industrial Science and Technology,	
Japan; Katsuya Shimizu, and Takehiro Matsuoka, Osaka University, Japan; Fumio Kokai, Mie University, Japan; and Yoshinori Koga and Sumio Iijima, National Institute of Advanced Industrial Science and Technology, Japan	
CUBIC BN SINGLE CRYSTALS AND SINTERED BODIES SYNTHESIZED AT HIGH PRESSURE	
Takashi Taniguchi, National Institute for Materials Sciences, Japan)
CHEMICAL SYNTHESIS OF GRAPHITE-LIKE B/C/N MATERIALS LEADING TO THE SHOCK SYNTHESIS OF THE HETERODIAMOND	
Tamikuni Komatsu Asahi-Kasei Corporation Japan 383	6

5. PROPERTIES AND APPLICATIONS OF DLC

RESONANT RAMAN SPECTRA OF CARBON SYSTEMS J. Robertson and A.C. Ferrari, University of Cambridge, United Kingdom	389
AN OVERVIEW OF DLC COATINGS FOR BIOLOGICAL APPLICATIONS R. Hauert, Swiss Federal Laboratories for Materials Testing and Research, Switzerland	395
CARBON-BASED WEAR COATINGS: PROPERTIES AND APPLICATIONS Kazuhisa Miyoshi, NASA Glenn Research Center, United States	404
TRIBOLOGICAL CHARACTERISTICS OF NOVEL SUPERHARD CARBON COMPACTS FOR SELF-LUBRICATING APPLICATIONS M.Y. Chen and S.T. Korfhagen, Air Force Research Laboratory, MLBT, United States; and O.A. Voronov, Diamond Materials, Inc., United States	406
VARIOUS APPLICATIONS OF DLC INCLUDING FLEXIBLE DLC-COATED RUBBER COMPONENTS	
Hisanori Ohara and Takahiro Nakahigashi, Nippon ITF Inc., Japan	407
DEVELOPMENT OF HARD CARBON FILMS AND CHARACTERIZATION OF THEIR TRIBOLOGICAL PROPERTIES FOR THE FRONTIER CARBON TECHNOLOGY PROJECT Akihiro Tanaka, National Institute of Advanced Industrial Science and Technology, Japan	413
FRICTIONAL BEHAVIOR OF NANO-UNDULATED SURFACE OF DIAMOND-LIKE CARBON FILMS S.J. Park, C.S. Lee, T.Y. Kim, and KR. Lee, Korea Institute of Science and Technology, Korea; and DH. Ko, Yonsei University Seoul, Korea.	419
TRIBOLOGICAL PROPERTIES OF SEGMENT-STRUCTURED DIAMOND-LIKE CARBON FILMS Yuichi Aoki and Naoto Ohtake, Tokyo Institute of Technology, Japan	423
TRIBOLOGICAL PROPERTIES OF a-C:H THIN FILMS FORMED BY THE SIMULTANEOUS APPLICATION OF PULSE AND DC BIAS Toshiya Watanabe, Osama Tsuda, and Masahiro Suzuki, Japan Fine Ceramics Center, Joint Research Consortium of Frontier Carbon Technology, Japan; and Kazuhiro Yamamoto, Yoshinori Koga, and Akihiro Tanaka, Research Center for Advanced Carbon Materials, Japan	
THE TRIBOLOGICAL PROPERTIES OF DLC FILMS DEPOSITED BY HOT FILAMENT PLASMA CVD TECHNIQUE Masahiro Suzuki and Toshiya Watanabe, Japan Fine Ceramics Center, Joint Research Consortium of Frontier Carbon Technology, Japan; and Akihiro Tanaka and Yoshinori Koga, National Institute of Advanced Industrial Science and Technology, Japan	430
TRIBOLOGICAL PROPERTIES OF PULSE-BIASED HYDROGENATED AMORPHOUS CARBON FILMS Koichiro Wazumi and Kenji Fuchigami, Ishikawajima-Harima Heavy Industries Co., Ltd., Japan; and Akihiro Tanaka and Yoshinori Koga, Research Center for Advanced Carbon Materials, Japan.	436
VISCO-ELASTIC PROPERTIES OF REACTOR ON DIAMOND-LIKE CARBON FILMS IN BOUNDARY LUBRICATION T. Saitoh, S. Miyake, and S. Watanabe, Nippon Institute of Technology, Japan; and Y. Yasuda and Y. Okamoto, Nissan Motor Co. Ltd., Japan	440

SOLID LUBRICANT PROPERTIES OF CARBON NANOMATERIALS AND THEIR POLYMERIC COMPOSITE COATINGS M.Y. Chen and S.T. Korfhagen, Air Force Research Laboratory, MLBT, United States; and Z. Bai and S.C. Tan, Wright Materials Research Co., United States	144
TRIBOLOGICAL PROPERTIES OF Ti-DLC FILMS ON VARIOUS POLYMERS T. Hashizume, Oiles Corporation, Japan; S. Miyake and S. Watanabe, Nippon Institute of Technology, Japan; and M. Sato, Oiles Corporation, Japan	445
TRIBOLOGICAL PERFORMANCE OF Cr-CONTAINING DLC FILMS Katsuyuki Kotake, Shojiro Miyake, and Shuichi Watanabe, Nippon Institute of Technology, Japan	147
FLUORINATED AMORPHOUS DIAMOND LIKE CARBON FILMS BY PECVD G.Q. Yu, B.K. Tay, Z. Sun, and S.P. Lau, Nanyang Technological University, Singapore	451
DEPOSITON OF C-F THIN FILMS BY SPUTTERING AND THEIR MICRO-MECHANICAL PROPERTIES	160
M. Wang, S. Watanabe, and S. Miyake, Nippon Institute of Technology, Japan	100
Kyung Hwang Lee, Riichiro Ohta, Hiroyuki Sugimura, Yasushi Inoue, and Osamu Takai, Nagoya University, Japan4	165
ANTI-WEAR CHARACTERISTICS OF CARBON NITRIDE THIN FILMS Shuichi Watanabe, Shojiro Miyake, Mieko Sutoh, and Masao Murakawa, Nippon Institute of Technology, Japan	166
MECHANICAL PROPERTIES OF ta-C FILMS DEPOSITED ON POLYETHYLENE AND METALLIC SUBSTRATES Carlos J.M. Siqueira, Wanderley Veiga, Vladimir P. Poliakov, and Ivo A. Hümmelgen, Federal University of Parana, Brazil; and Gregory G. Kirpilenko, Patinor Coatings Ltd., Russia	471
EFFECT OF TEMPERATURE AND ION BOMBARDMENT ON DLC RELIEF GENERATION AND MODIFICATION	
A.P. Rubshtein, I.Sh. Trakhtenberg, V.A. Yugov, S.A. Plotnikov, Yu.S. Ponosov, and A.B. Vladimirov, Metal Physics Institute Ural Branch RAS, Russia; and Kensuke Uemura, ITAC Ltd., Japan	172
APPLICATION OF DLC COATED DIES TO VARIABLE SHAPE EXTRUSION OF ALUMINUM SQUARE PIPES Naoto Ohtake, Ko-ichi Horita, and Akira Yamagata, Tokyo Institute of Technology, Japan; and Kaoru Hara, Institute of Technologists, Japan	478
THE CHARACTERISTICS OF PHOTO-CVD $\mathrm{SiO_2}$ AND ITS APPLICATION IN GaN MIS PHOTODETECTOR	
Bohr-Ran Huang and Tien-Kun Lin, National Yun-lin University of Science and Technology, Republic of China; and Yan-Kuin Su, Shoou-Jinn Chang, and Yu-Zung Chiou, National Cheng Kung University, Republic of China	184
FABRICATION OF DIAMOND-LIKE CARBON FILM Wataru Ohashi, Hiroaki Yoshimura, Haruka Matsuhisa, Yusuke Aoki, and Akimitsu Hatta, Kochi University of Technology, Japan	490

DIAMOND LIKE CARBON PREPARED BY PULSED LASER DEPOSITION	
Lin Yu, Qihong Wu, Yuan Liao, Qingxuan Yu, Guanzhong Wang, and Rongchuan Fang,	
University of Science and Technology of China, China	491
THE EFFECT OF ANNEALING ON THE FIELD EMISSION PROPERTIES OF AMORPHOUS CN _x FILMS	
J.J. Li, Jilin University, China, and Yanbian University, China; and Z.S. Jin, W.T. Zheng, and X.Y. Lu, Jilin University, China	492
INFLUENCE OF THE DC SUBSTRATE BIAS ON THE FILED EMISSION OF AMORPHOUS CARBON NITRIDE FILMS DEPOSITED ON SILICON TIPS ARRAYS J.J. Li, Jilin University, China, and Yanbian University, China; and Z.S. Jin, W.T. Zheng, and X.Y. Lu, Jilin University, China; and Z.K. Li, Z. Jin, and L. Sun, Yanbian University, China4	493
INVESTIGATION OF STRUCTURE AND FIELD EMISSION CHARACTERISTICS OF DIAMOND-LIKE FILMS PREPARED BY HIGH POWER EXCIME LASER	
H.Y. Peng, National Laboratory of Superhard Materials, China; Z.S. Jin, J.J. Li, and H. Ji, National Laboratory of Superhard Materials, China, and Institute of Optical-Electric Technology of Heilongjiang Province, China; and H. Shen, L.X. Zhao, and J.J. Shen, Institute of Optical-Electric Technology of Heilongjiang, China	494
MULTI-SENSOR DURABILITY CHARACTERIZATION OF THIN DIAMOND-LIKE FILMS N. Gitis, J. Xiao, and M. Vinogradov, Center for Tribology, Inc., United States	495
CALIBRATION OF THE MEASUREMENT OF sp ² -TYPE BONDING IN CARBON USING EELS IN AN ELECTRON MICROSCOPE V. Stolojan, M.J. Goringe, J.H.B. Deane, and S.R.P. Silva, University of Surrey, United Kingdom	500
STUDY OF HIGH TRANSPARENCY DIAMOND LIKE CARBON FILM ON QUARTZ SUBSTRATE GROWTH BY HOT-FILAMENT CHEMICAL VAPOR DEPOSITION	
Niu Xiaobin, Liao Yuan, and Shi Hualiang, University of Science and Technology of China, China	506
NANO NI DOT EFFECT ON THE STRUCTURE OF TETRAHEDRAL AMORPHOUS CARBON FILMS	
Churl-Seung Lee, Tae-Young Kim, and Kwang Ryeol Lee, Korea Institute of Science and Technology, Korea; and Ki Hyun Yoon, Yonsei University, Korea	507
SELECTIVE NANO COPPER DOT FORMATION ON DIAMOND-LIKE CARBON FILM Tae-Young Kim, Churl-Seung Lee, Seung-Cheol Lee, and Kwang-Ryeol Lee, Korea Institute	
of Science and Technology, Korea; and Kyu-Hwan Oh, Seoul National University, Korea	511
THE MICROSTRUCTURE AND PROPERTIES OF TETRAHEDRAL AMORPHOUS CARBON FILMS DEPOSITED BY FILTERED ARC ACCELERATED AT DIFFERENT ENERGETIC GRADES	
Zhu Jiaqi, Han Jiecai, Meng Songhe, and Li Qiang, Harbin Institute of Technology, China; and Zheng Weitao, Jilin University, China	512
6. NOVEL SYNTHESIS AND DEPOSITION PROCESSES	
SYNTHESIS AND SOME PROPERTIES OF POLYHEDRAL GRAPHITE Fumio Kokai, Mie University, Japan	523
THE NOVEL NUCLEATION PROCESS—AN UPDATE: A METHOD IN THE WORKING Shlomo Rotter, UES Inc., Wright-Patterson AFB, United States	524
- ,	-

INTERRELATIONSHIPS AMONG CARBON NANOSTRUCTURES Michael Sternberg, Dieter M. Gruen, and Peter Zapol, Argonne National Laboratory, United States	525
HIGHER DIAMONDOIDS: A NEW CLASS OF 3–D DIAMOND MOLECULES 1 TO 2 nm IN SIZE	
J.E. Dahl, S.G. Liu, R.M.K. Carlson, and W. Qureshi, Molecular Diamond Technologies, Chevron Texaco Technology Ventures, United States	526
CO-DOPING OF DIAMOND WITH BORON AND SULFUR Sally C. Eaton, Alfred B. Anderson, and John C. Angus, Case Western Reserve University, United States	527
FORMATION OF C-N NANOFIBERS IN HIGH ISOSTATIC PRESSURE APPARATUS AND THEIR FIELD EMISSION PROPERTIES V.D. Blank, D.V. Batov, S.G. Buga, B.A. Kulnitskiy, and E.V. Polyakov, Technological Institute for Superhard and Novel Carbon Materials, Russia; Sahn Nahm and Yun-Hi Lee, Korea University, Korea; U. Bangert, A. Gutiérrez-Sosa, A.J. Harvey, and A. Seepujak, UMIST, United Kingdom; and Yang-Doo Lee, Duck-Jung Lee, and Byeong-Kwon Ju, Micro-system Research Center/KIST, Korea	533
INVESTIGATION OF LARGE AREA HFCVD-DIAMOND DEPOSITION PROCESSES BY MULTI-FILAMENT TEMPERATURE MEASUREMENTS Markus Höfer and Lothar Schäfer, Fraunhofer Institute for Surface Engineering and Thin Films, Germany	539
FABRICATION OF VERY-HIGH-ASPECT-RATIO MICROCHANNELS IN CVD DIAMOND BY A MOLDING TECHNIQUE V.G. Ralchenko, General Physics Institute, Russia; and E.I. Givargizov, Institute of Crystallography, Russia.	540
THE GROWTH OF DIAMOND FILMS ON POROUS ANODIC ALUMINA Q.T. Wang, X.B. Niu, L. Yu, B. Xu, Y. Liao, Q.X. Yu, G.Z. Wang, R.C. Fang, University of Science and Technology of China, China	544
SELF NUCLEATION OF DIAMOND ON ZEOLITE BY CHEMICAL VAPOR DEPOSTION METHOD E. Titus, P.K. Tyagi, M.K. Singh, and D.S. Misra, Indian Institute of Technology, India; A.K. Dua and Mainak Roy, Bhabha Atomic Research Centre, India; and P.N. Joshi and M.V. Kasture, National Chemical Laboratory, India	545
ELECTRON PARAMAGNETIC RESONANCE • AN AID IN SOLVING TOPICAL PROBLEMS OF DIAMONDS Tamara Artemevna Nachalna, N.V. Novikov, G.A. Podzyrey, and V.G. Malogolovets, Institute for Superhard Materials of NAS of Ukraine, Ukraine.	546
NANOCRYSTALLINE DIAMOND FILMS DEPOSITED BY MICROWAVE PLASMA CVD IN MIXTURES OF ARGON AND METHANE WITH AND WITHOUT HYDROGEN ADDITIVE Y.K. Liu, Auburn University, United States, and National Tsing-Hua University, Republic of China; Y. Tzeng, Auburn University, United States; and P.L. Tso and I.N. Lin, National Tsing-Hua University, Republic of China.	547
NOVEL DIAMOND CONE ARRAYS: SINGLE CRYSTALLINE AND NANOCRYSTALLINE Y. Wu, W.J. Zhang, C.Y. Chan, X.M. Meng, W.K. Wong, I. Bello, Y. Lifshitz, and S.T. Lee, City University of Hong Kong, China	553

A DC HF CVD PROCESS TO GROW FILMS OF ALIGNED CARBON NANOTUBES— APPLICATIONS TO FIELD EMISSION F. Le Normand, Cojocaru, CNRS, France	554
CO-DOPING OF DIAMOND WITH BORON AND SULFUR Rongbin Li, Xiaojun Hu, Hesheng Shen, and Xianchang He, Shanghai Jiaotong University, China	555
NANOCRYSTALLINE DIAMOND FILM ON LARGE AREA GLASS SUBSTRATE K. Tsugawa, M. Shelby, and H. Yoshikawa, National Institute of Advanced Industrial Science and Technology, Japan; M. Ishikawa, Ibaraki University, Japan; M. Liehr, Applied Films GmbH & Co KG, Germany; and Y. Koga, Research Center for Advanced Carbon Materials, Japan.	556
DIAMOND SYNTHESIS IN TEN MINUTES WITH CLOSED REACTION CHAMBER Kaoru Gyoda, Yuki Tanaka, Kazuhiro Aoki, and Yoshiki Takagi, Teikyo University of Science and Technology, Japan	557
FREQUENCY-DEPENDENCE OF PULSED BIAS-ENHANCED NUCLEATION OF DIAMOND ON (100) SILICON F. Okuzumi and Z. Sitar, North Carolina State University, United States; and S.D. Wolter and J.T. Prater, U.S. Army Research Office, United States	564
ACHIEVEMENT OF 10 ¹⁴ [1/CM ²] SURFACE HOLE CARRIER DENSITY ON DIAMOND FILM BY THE SULFUR HEXAFLURIDE INCORPORATED HYDROGEN PLASMA POST-TREATMENT Go Ota and Takeshi Kobayashi, Osaka University, Japan; and Sung-Hoon Kim, Silla University, Korea	569
CHEMICAL VAPOR DEPOSITION OF DIAMOND FILM AT HIGH GAS PRESSURE BY USING PULSED DISCHARGE PLASMA Mikio Noda, Aichi University of Education, Japan	573
TWO-STAGE BIAS ENHANCED GROWTH OF NANOCRYSTALLINE DIAMOND FILMS Tarun Sharda, Seki Technotron Corporation, Japan; and Tetsuo Soga, Nagoya Institute of Technology, Japan	579
SYNTHESIZE OF NANOSTRUCTURE DIAMOND BY MICROWAVE PLASMA CHEMICAL VAPOR DEPOSITION WITH BIASED ENHANCED NUCLEATION AND HYDROGEN-ARGON PLASMA IRRADIATION Yasuhiko Hayashi, Daisuke Mori, Tetsuo Soga, and Takashi Jimbo, Nagoya Institute of Technology, Japan	585
INFLUENCE OF METALS ON DIAMOND TO GRAPHITE PHASE TRANSFORMATION A.Y Nozhkina, YNDALMAS, Russia	591
DIAMOND SPONTANEOUS CRYSTALLIZATION FROM Mg-Ni-C SYSTEM AT HPHT G.S. Bobrovnitchii, A.S. Osipov, and A.L.D. Skury, North Fluminense State University, Brazil	592
POLYMERIC NITROGEN M.I. Eremets, M. Popov, I.A. Trojan, V. Denisov, P. Dera, and R.J. Hemley, Max Planck Institute für Chemie, Germany; and Carnegie Institute of Washington, United States	597

FORMATION AND ANALYSIS OF DENSE BORON CARBIDE COATINGS WITH A LOW POROSITY FORMED BY ELECTROMAGNETICALLY ACCELERATED PLASMA SPRAYING Junya Kitamura, Japan Fine Ceramics Center; and Shu Usuba, Yozo Kakudate, Hiroyuki Yokoi, Kazuhiro Yamamoto, Akihiro Tanaka, and Shuzo Fujiwara, National Institute of Advanced Industrial Science and Technology, Japan	598
PROPERTIES OF CARBON DEPOSITS FORMED BY PLASMA SPRAYING OF NANODIAMOND Anna Gubarevich and Osamu Odawara, Tokyo Institute of Technology, Japan; and Junya	
Kitamura, Shu Usuba, Hiroyuki Yokoi, Yozo Kakudate, and Akihiro Tanaka, National Institute of Advanced Industrial Science and Technology, Japan	599
THE JOINING OF DIAMOND TO SiC BY ENERGIZATION PULSE SINTERING METHOD Jun Tanabe, Nippon Institute of Technology, Japan	605
MODELING THE DEPOSITION OF CARBON AND NITROGEN ATOM/IONS ON WURTZITE AIN (001) SURFACE R.Q. Zhang, and Dongju Zhang, City University of Hong Kong, China	609
ROOM TEMPERATURE GROWTH OF HOMOGENEOUS ULTRATHIN Co FILMS ON 6H-SiC (0001)- $6\sqrt{3}\times6\sqrt{3}R30^{\circ}$ SURFACE	
Wei Chen, Hai Xu, A.T.S. Wee, and Kian Ping Loh, National University of Singapore, Singapore	610
AUTHOR INDEX	611

NANOTUBE

Development of CNT based field emission x-ray source and imaging system for biomedical and industrial applications

Otto Zhou

Dept. of Physics and Astronomy and Curriculum in Applied and Materials Sciences, University of North Carolina, Chapel Hill, NC 27599

X-ray radiation is widely used for medical and industrial imaging applications. Current x-ray tubes use thermionic cathodes to produce the electron beams which bombard on metal targets to generate x ray. The design has several intrinsic limitations. In this talk we demonstrate that diagnostic x-ray radiation can be generated using a carbon nanotube based field emission cathode. The device can readily produce both continue and pulsed x-ray with a programmable waveform and repetition rate. The x-ray intensity is sufficient to image human extremity. Pulsed x-ray with a repetition rate greater than 100 kHz was readily achieved by programming the gate voltage. The performance of this cold-cathode x-ray tube will be discussed and compared with the conventional thermionic systems. We will also present imaging systems/modalities enabled by the field emission x-ray source.

This work was carried out in collaboration with J.P. Lu, Y. Cheng, J. Zhang, S. Dike at UNC Physics; S. Chang, W. Lin, and Y. Lee at UNC Med School; and Q. Qiu, B. Gao and H. Shimoda at Applied Nanotechnologies, Inc. The work was partially supported by ONR and ANI.

Catalysts to Control the Growth and Structure of Single-Wall Carbon Nanotubes

Masako Yudasaka

JST, NEC, 34 Miyukigaoka, Tsukuba, Japan yudasaka@frl.cl.nec.co.jp

Abstract

In previous reports, we compared the catalytic efficiencies of various metals in producing SWNTs by arc discharge and Nd:YAG laser ablation, and discussed what causes the different catalytic activities (1,2). We suggested that the crystallographic orientation of catalysts might influence the growth of SWNTs and mentioned that it might also control the chirality of SWNTs. It is known that a metal film deposited on a surface with a defined crystallographic face takes a unique orientation. We also reported that Ni deposited on different faces of sapphires took different orientations and had different graphitization effects on carbon (3, 4). These results suggest that SWNT growth on catalysts whose crystallographic orientation is controlled by a well defined surface would enable us to study how the catalysts influence the structures of SWNTs. In our first trial of this, we grew SWNTs on Fe-coated sapphire by chemical vapor deposition and found that the yield and diameter distribution depended on the crystallographic face of the sapphire (5). Further investigation indicated that strong Fe-sapphire interaction resulted in Fe-Al alloy formation, and the sapphire-surface damages were considerably increased by carbon. Degree of these structure changes depended on the crystallographic face and surface states of sapphires. It is likely that these structure changes also occur when another metals and substrate materials were used for SWNT growth. Studies on the carbon-metal-substrate interaction would enable to prepare the SWNT-growth catalysts suitable to grow SWNTs with well-defined structures.

- 1) Yudasaka et al. J. Phys. Chem. B 103, 6224 (1999).
- 2) Yudasaka et al. Appl. Phys. A 74, 377 (2002).
- 3) Yudasaka et al. Carbon, 34763 (1996).
- 4) Yudasaka et al. J. Vac. Sci. Tech. A 16, 2463 (1998).
- 5) Hongo, Yudasaka et al. Chem. Phys. Lett. 361, 349 (2002).

ANOVEL CATALYTIC SYNTHESIS OF CARBON NANOTUBES IN ALCOHOLLIQUID

Kiyoharu NAKAGAWA, Toshihiro ANDO*

National Institute for Materials Science (NIMS), 1-1, Namiki, Tsukuba, Ibaraki 305-0044, Japan *c-diamond@ md.neweb.ne.jp

Mikka NISHITANI-GAMO

Department of Applied Chemistry, Faculty of Engineering, Toyo University, 2100 Kujirai, Kawagoe, Saitama 350-8585, Japan

ABSTRACT

Well-aligned carbon nanotubes arrays were grown on silicon substrates by using a novel catalytic method in organic liquid such as alcohols. Un-equilibrium catalytic deposition gave significantly pure carbon nanotubes with very little soot within a few minutes in mathanol. Scanning electron microscope images indicate that the nanotubes arrays are grown perpendicular to the silicon substrate surface with a significantly high density like a flower arrangement frog. This very fast and dense production of carbon nanotubes can be attributed to the great difference of chemical potential between the substrate surface and reactant liquid.

Keywords: Well-aligned carbon nanotubes, Iron, Alcohol liquid

INTRODUCTION

The quest for artificial methods of carbon nanotubes (CNTs) production is motivated not only by its unique nanotube structures and properties, but also by its synthetic tunability and verity for numerous important applications. The production and utilization of nano-carbon materials such as fullerene and CNT have attracted much recent attention, several techniques have been developed for the synthesizing these materials toward the production of various CNTs in macroscopic quantities and oriented growth, such as catalytic pyrolysis of hydrocarbons to condensed-phase electrolysis and SiC sublimation. In general, these methods can produce nanotubes with yields suitable for limited research use and aligned carbon nanotube arrays stay weakly on substrate. Here, we show that aligned mutiwalled CNTs can be synthesized efficiently in solutions of hydroxyl hydrocarbons and stand firmly on Si substrate. This liquid phase synthetic method can enable great chemical flexibility and synthetic tunability, and the synthesis process is compatible with the existing semiconductor processes and easily adaptable to industrial production levels.

EXPERIMENTAL

The apparatus employed in our experiments is consisted of a glass chamber with outside water-cooling (Fig. 1). A DC electric power supplier was used to apply a controlled current to the substrate. High purity methanol (99.7%) was used as the organic liquid source. Si (100) substrates of low resistively (0.002 1cm) with a size of 10 x 20 x 1 mm³ were placed perpendicularly at the center of the chamber in the liquid and connected with the electric power supplier. The Si (100) substrate was ultrasonically cleaned in acetone and coated by a Fe film of 2.4-30 nm thick in a magnetron sputtering system using low DC electric voltage (0.4 kV, 30 mA) and low Ar pressure (0.6 Torr), and then treated in hydrogen plasma at 500-850 °C for sticking well with substrate surface and producing nucleation sites for CNTs growth. After organic liquid was filled into the chamber, N_2 gas was introduced into the chamber

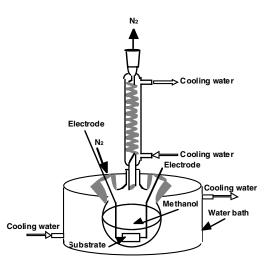


Fig.1 Schematic of the experimental setup chamber used to synthesize CNTs in organic liquids.

for several minutes to blow out the remaining air. Then, the Si substrate was heated to a temperature of 500-1000 °C at the starting stage by applying electrical current through the Si substrate. Numbers of gas babbles was generated continuously from the substrate surface and were flowing up from the substrate surface and dissolved into the relatively cooled liquid top layer. A circulate of the organic liquid in the chamber could rune through heating up from the hot substrate surface and cooling down in the top liquid. The water-cooling chamber was served for controlling the liquid temperature to be a little lower than its boiling point in the chamber and for returning the vapor above the organic liquid surface by the condensation effect. The substrate temperature was detected using an optical pyrometer by focusing on the substrate surface. The electric current applied to the substrate was kept constant during the growth. The detected surface temperature was observed decreasing slowly with the lengthening of the nanotubes on the Si substrate.

RESULTS AND DISCUSSION

A. SEM observations

Methanol and ethanol were used mainly as the liquid source in our experiments. The as-grown CNTs look like a dark black film on the Si substrate. Scanning electron microscope (SEM) images (Fig. 2) show that the sample consists almost entirely of nanotubes. This sample synthesized by using a 2.4 nm Fe film coated Si(100) substrate at the substrate temperature of 930 °C in methanol. Aligned carbon nanotube array grew in orientation normal to the surface of the Si substrate (Fig. 2a). The density of the nanotubes on the substrate surface is very high (>1x10¹¹ cm⁻²) and the substrate surface is covered completely by the roots of nanotubes (Fig. 2b, a crosssectional view of the aligned carbon nanotube film). The CNTs token off from the substrate surface adhere together and look like black blocks (Fig. 2c-e). The roots of CNTs cohere firmly on the substrate surface and when they are token off by tweezers, some roots were broken and remained on the substrate surface. The growth rate of every near-by nanotubes was nearly same and the top ends of the nanotubes stay very closely at a same front of the tube array (Fig. 2f).

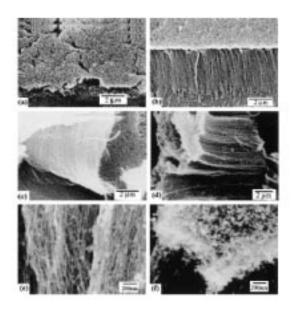


Fig. 2. SEM images of a ligned carbon nanotube arrays formed in methanol on a Si surface. (a) The top-view morphology of the nanotube arrays showing the growth tips of bundles of nanotubes sticking together and leaving some valleys. (b) A cross-sectional view of an edge of the nanotube array showing a ligned and uniform structure. (c) The morphologies of nanotube bundles taken off of the substrate. (d) Side-view of a bundle of nanotube array. (e,f) High-magnification morphology of the lateral side and top ends of the nanotubes in image (d), respectively.

The critical role of the catalytic Fe film was confirmed by the fact that if no Fe film on the Si substrate, there was no growth of CNTs, except of a carbon film. The morphology of CNTs was observed very sensitive to both of the substrate temperature and the thickness of the Fe film on Si substrate. When the thickness of the Fe film on the Si substrate was 3 nm, the density of the synthesized CNTs at the substrate surface was lower than $6x10^{10}$ cm⁻² and all of the grown CNTs lied down on the substrate surface when they were longer than a micrometer (Fig. 3a and b).

B. TEM observations

High-resolution transmission electron microscopy (HRTEM) shows the nanotubes have primarily smooth and uniform hollow mutiwall tube-like structures (Fig. 4). The intershell spacing is 0.34 nm. The diameter of most nanotubes remains nearly the same throughout the whole length of the nanotube and the external diameters of the nanotubes in the sample range from 13 to 26 nm with a distribution peak at 20 nm. The ratio of tube radius to the thickness of tube shells is about 1.2 to 2.1. Some disorder and defects have been seen in the wall fringes and surfaces. This is most likely caused by the reaction of carbon with oxygen related radicals generated by the catalytic

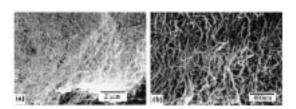


Fig. 3. (a,b) SEM images of the CNTs grown on Si coated by Fe film with a thickness of (a) 3 nm. CNTs formed in (c) methanol and (d) ethanol on the Si surface by using a 3 nm Fe film

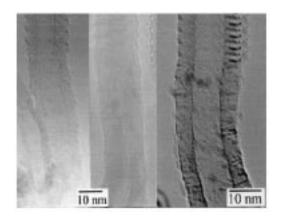


Fig. 4. HRTEM images of some CNTs formed into a shell of several tube walls and a large hollow tube.

heterogeneous process at substrate surface. The top ends of the nanotubes are closed with nearly seamless caps and the catalyst Fe have not been found on the top ends (Fig. 5a). The roots of the nanotubes grown on the substrate surface have a shape of open tube.

Fig. 5b shows a HRTEM image of the CNTs obtained on a Si substrate of 860 °C in ethanol. It clearly shows that the produced nanotubes are mostly mutiwalled hollow tubes. The ratio of tube radius to the thickness of tube shells is between 2.2 to 5.8. The top ends of the nanotubes are also closed with nearly seamless caps.

C. Raman spectra

Raman scattering measurements of the CNTs were performed at room temperature using a confocal micro-Raman sysem in a backscattering geometry. The excitation source was the 514.5 nm line of an argon ion laser with a spot size of 1 mm in diameter and a power of ~50 mW. As the carbon nanotube is a narrow-band-gap material, the light penetration depth of the excitation laser light is rather small. Especially, by using the confocal function, Raman scattering can be gotten from a small surface area with small depth on the sample. The main feature of the Raman spectra for the sample shown in Fig. 2a presented the peak position and shape dependening on the measured location. The first-order Raman G peak from the CNT lateral surface (tube walls) appeared predominately at 1570 cm⁻¹ with a fall width at half maximum (FWHM) of 20 cm⁻¹(Fig. 6a). The G peak reflects one of the two E2g modes of graphite crystal. A 1603 cm⁻¹ peak at the shoulder position was assigned to disorder-induced symmetry breaking by the microscopic nanotube size. 10, 11 The D peak at 1340 cm⁻¹ is high sensitive to the defects and the size effect of graphite structure. A comparable intensity of G and D peaks indicates a considerable density of structural defects in the curved graphene sheets in the CNTs. Fig. 6b shows the Raman scattering from the top caps of CNTs. The G and D peaks are weak and broad, indicating the seamless tips of the CNTs have a structure of high disorder graphite and less symmetry of Raman activation. The graphite E2g peak shifted from 1570 to 1580 cm⁻¹ from the tube wall to the tube caps, suggesting the formation of carbon bonding with high stress in the tube caps.

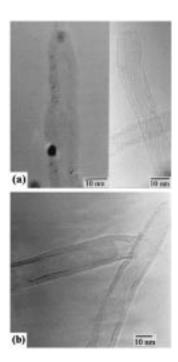


Fig 5. High-magnification images showing seamless ends of nanotubes and no Fe nanoparticles on the top side of the nanotubes for thesamples synthesized (a) in methanol and (b) in ethanol.

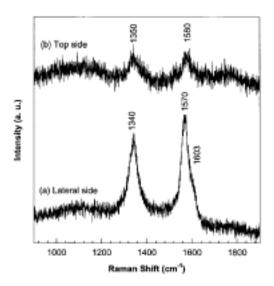


Fig. 6. The Raman spectra from (a) the top side and (b) the lateral side of the aligned CNTs array shown in Figs. 2(a) and 2(b).

D. Growth processes of CNTs in liquid

The thermal absorption and decomposition of methanol on metal catalyst surface has been the interesting subject for many years. 12, 13 The speed of the thermal decomposition and adsorption on the catalyst surface increases as the surface temperature increases. The carbonatoms for the formation of the nanotubes on the hot substrate surface submerged in liquid might be due both surface absorption and the decomposition ofhydroxyl hydrocarbons. The deposition of the precursor was essentially heterogeneous process, which proceeded on the catalyst rather than in the bulk of the liquid. The temperature of the substrate catalyst surface is very high (approximately 1000 °C), and at the same time the temperature of the reactant liquid is very low (<< boiling point). Because the decomposition reaction can proceed only at the hot substrate surface and must not occur in the bulk liquid phase, the byproducts such as a soot or other carbonaceous materials cannot be generated in the bulk liquid phase. The large difference in temperature of the

interface between the substrate catalyst and the liquid phase causes a large gradient of the chemical potential to give very high nucleation density and high growth rate. That also affects the growth direction of the CNTs. In result, only pure aligned CNTs were given at the substrate surface. The fact that the catalyst Fe stays on the substrate surface implies that the growth tip of the nanotubes was at their roots on the substrate surface, where the temperature might be kept relatively high and stable during the experiment. On the substrate surface, hydroxyl hydrocarbon are absorbed and decomposed into carbon atoms and hydrogen gas in the catalyst Fe film. Carbon atoms then diffuse through the catalyst to an outlet, forming CNTs.

Here we describe a very interesting research direction for a variety of production possibilities, such as synthesizing various CNTs and films directly in liquids. This method of CNT synthesis demonstrates several important features. First, the CNTs were formed by a catalytic process in nonequilibrium thermal conditions, and the growth tip of the nanotubes was at their root on the substrate surface, where the temperature could be controlled in organic liquid. Second, the large temperature gradient at the nanotube root perpendicular to the substrate surface may be an important force for the normal orientation of the CNTs because of the liquid surrounding the substrate. Third, our synthetic method is very simple; the phenomena of CNTs formed in a liquid phase may not only induce a large scale synthesis of aligned arrays, but also easily introduces different elements into the liquid source for synthesizing doped CNTs. The produced CNTs are hollow tubes, which are suitable for the fabrication of various nanowires by capillary-induced filling of the CNTs. Finally, the liquid phase synthesis process is entirely compatible with current Si technology and easily adaptable to industrial production levels.

CONCLUSIONS

Synthesizing CNTs in organic liquids has been demonstrated as an artificial and efficient technique. Using methanol and ethanol as the organic liquid source and a Fe film on Si, aligned mutiwalled CNTs were obtained with external diameter ranging from ~13 to 26 nm and lengths up to 20 mm. The alignment and structural properties of the CNTs have been characterized by SEM, TEM, and Raman scattering. Most of the CNTs have the primary smooth and uniform mutiwall tube-like structure with good alignment direction, while some curves and bends of the CNTs identified in the aligned arrays. The top ends of the nanotubes were closed with nearly seamless caps and a relatively higher stress in the caps than in the nanotube walls. By changing the catalyst Fe file thickness, a special kind of coupled CNTs of which the structure of one CNT is left hand rotated and the other right hand rotated. Chains bridge periodically the coupled CNTs. Nanometer sized coupled whirlpools on substrate surface were proposed to be formed at the growth root of the CNTs for the formation of these CNTs with the driving spiral force from the liquid phase. The growth mechanism of CNTs in liquid is proposed to be a catalytic process at the substrate surface in an non-equilibrium thermal condition of organic liquid phase. This vacuum-free and gas-free

process is adaptable to industrial levels, and may find a large field of applications for synthesis of various kinds of nanomaterials and films, especially for producing hollow CNTs and doped materials by using liquid sources.

ACKNOWLEDGMENTS

This work obtained the support from the Core Research for Evolution Science and Technology (CREST) of Japan Science and Technology Cooperation (JST), and a Grant-in Aid for Scientific Research (B) No. 14350429 from the Japan Society for the Promotion of Science (JSPS).

REFERENCES

- 1. "The Science and Technology of Carbon Nanotubes" edited by K. Tanaka, T. Yamabe, and K. Fukui, Elsevier, 1999, pp. 1-191.
- 2. M. Inagaki, "New Carbons -Control of Structure and Functions-", Elsevier Scientific Publications, Amsterdam, New York, 2000, pp. 1-240.
- 3. M. Jose-Yacaman, M. Miki-Yoshida, L. Rendon, and J. G. Santiesteban, Appl. Phys. Lett. 62 (1993) 657.
- 4. S. Amelinckx, X. B. Zhang, D. Bernaerts, X. F. Zhang, V. Ivanov, and J. B. Nagy, Science, 265 (1994) 635.
- Z. W. Pan, S. S. Xie, B. H. Chang, C. Y. Wang, L. Lu, W. Liu, W. Y. Zhou, W. Z. Li, L. X. Qian, Nature, 394 (1998) 299.
- W. K. Hsu, J. P. Hare, M. Terrones, H. W. Kroto, D. R. M. Walton, and P. J. F. Harris, Nature, 377 (1995) 687.
- 7. W. K. Hsu, M. Terrones, J. P. Hare, H. W. Kroto, D. R. M. Walton, and H. Terrones, Chem. Phys. Lett. 262 (1996) 161.
- 8. M. Kusunoki, M. Rokkaku, and T. Suzuki, Appl. Phys. Lett. 71, (1997) 2620.
- 9. H. Takikawa, R. Miyano, M. Yatsuki, and T. Sakakibara, Jpn. J. Appl. Phys. 37 (1998) L187.
- 10. Q. Zhang, S.F. Yoon, J. Ahn, B. Gan, Rusli, M.-B. Yu, J. Phys. Chemi. Solids, 61(2000) 1179
- J. Kastner, T. Pichler, H. Kuzmany, S. Curran, W. Blau, D.N. Weldon, M. Dlelamesiere, S. Draper, H. Zandbergen, Chem. Phys. Lett. 211 (1994) 53.
- 12. W. -H. Hunga and S. L. Bernasek, Surface Science, 346 (1996) 165.
- 13. Tecle S. Rufaela, James D. Batteasa and C. M. Friend, Surface Science, 384 (1997) 156.
- 14. P. M. Ajayan and S. Iijima, Nature, 361 (1993) 333.

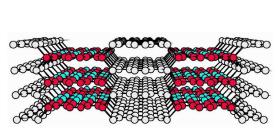
DESIGNING CARBON-BASED NANOTECHNOLOGY ON A SUPERCOMPUTER*

David Tománek

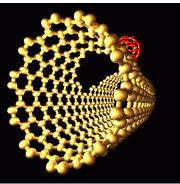
Physics and Astronomy Department, Michigan State University, East Lansing, MI 48824-2320, USA
Email: tomanek@pa.msu.edu Web: http://www.pa.msu.edu/~tomanek

The continuous reduction of device sizes, which is rapidly approaching the atomic level, calls for new approaches to design and test future building blocks of Nanotechnology. Supercomputers are rapidly becoming the most powerful tool to interpret what happens on the nanometer scale. In nanotubes, the large phonon mean-free path, a consequence of atomic-scale perfection and quasi one-dimensional structure, leads to an extremely high thermal conductivity. In nanostructures that form during a hierarchical self-assembly process, even defects may play a different, often helpful role. Utilizing defect engineering, scrolls may be efficiently transformed to multi-wall nanotubes [1], and adjacent nanotubes may fuse to form Y-junctions. Fullerenes may enter nanotubes to form peapods [2] and, once encapsulated, fuse to nanocapsules. The presentation will show, how some of these challenging problems can be most efficiently addressed in simulations on recently available massively parallel supercomputers.

- * Supported in part by NSF-NIRT Grant Number DMR-0103587 and the RIST (Japan) Computational Nanotechnology Program.
- [1] J. Gerard Lavin, Shekhar Subramoney, Rodney S. Ruoff, Savas Berber, and David Tománek, Scrolls and Nested Tubes in Multiwall Carbon Nanotubes, Carbon 40, 1123 (2002).
- [2] Savas Berber, Young-Kyun Kwon, and David Tománek, Microscopic Formation Mechanism of Nanotube Peapods, Phys. Rev. Lett. **88**, 185502 (2002).



Schematic model of carbon foam



Fullerene encapsulation in a defective nanotube

ULTRA-FAST DYNAMICS IN ELECTRONICALLY EXCITED NANOTUBES: TIME-DEPENDENT DENSITY FUNCTIONAL APPROACH

Yoshiyuki Miyamoto

Nanotube Technology Center, Fundamental Res. Labs. NEC Corp. 34 Miyukigaoka, Tsukuba, 305-8501, Japan

Angel Rubio

Dpto, Fisica de Materiales, Facultad de Qiumicas U. Pais Vasco, Centro Mixto CSIC-UPV/EHU Donosita; International Physics Center (DIPC) apdo. 1072, 20018 San Sebastian/Donosita, Spain

David Tomanek

Department of Physics and Astronomy, Michigan State University East Lansing, MI 48824-1116, USA

ABSTRACT

Because of extreme mechanical and electronic performance, carbon nanotube is promising material for application in nano-technology. Currently formed nanotubes are with structural defects and impurities, which may cause degradation of nanotubes. Therefore, influence of defects and impurities on mechanical and electronic properties of nanotube should intensively be investigated. Furthermore, defect-control will be an important technology in future nanotube-applications.

In this talk, we provide our recent first-principles simulations on ultra-fast dynamics in nanotubes triggered by electronic excitation. We first demonstrate that electronic excitation is useful to 'repair' defected nanotube being alternated to heat treatment. Second, we show optical excitation can be a useful tool to detect particular kind of defects in nanotube, i.e. Stone-Wales type defects.

We have performed molecular dynamics (MD) simulations based on of local density approximation (LDA) of the density functional theory (DFT) with use of plane-wave basis set and pseudopotentials. We adopted time-dependent LDA in order to perform MD simulation under electronic-excitation, where the time-dependent Kohn-Sham equation is solved to monitor time-evolution of electron wave functions. The details of this method are shown by Sugino and Miyamoto [Phys. Rev. B59, 2579 (1999)].

Keywords: carbon nanotube, defect, impurity, time-dependent density functional theory, molecular dynamics.

Yoshiyuki Miyamoto Nanotube Technology Center, Fundamental Res. Labs. NEC Corporation 34 Miyukigaoka, Ibaraki, 305-8501, Japan Phone: +81-29-850-1586

Fax: +81-29-850–2647

E-mail: y-miyamoto@ice.jp.nec.com

HYDRATION PROPERTIES OF CARBON NANOTUBES AND THEIR EFFECTS ON ELECTRICAL AND BIO-SENSOR APPLICATIONS

Y. Tzeng^a, T.S. Huang^b, Y.C. Chen^a, and Y.K. Liu^c

^aAlabama Microelectronics Science and Technology Center
Department of Electrical and Computer Engineering

^bDepartment of Nutrition and Food Science
Auburn University, Auburn, Alabama 36849 USA

^cPower Mechanical Engineering,
National Tsing-Hua University
Hsin-Chu, Taiwan, 300 ROC

ABSTRACT

As-grown carbon nanotubes are hydrophobic, i.e., more attractive to non-polar groups than polar substances. Surfaces of hydrophobic carbon nanotubes have been treated by means of electrochemical, thermal, and plasma oxidation processes to convert them to hydrophilic surfaces. Effects of hydration properties of carbon nanotubes on electron field emission characteristics and interactions of carbon nanotubes with polar and non-polar molecules were explored. This paper summarizes our work in this area of research and presents results on the modification of the hydration properties of carbon nanotubes and their applications.

Keywords: nanotubes, hydrophobic, hydrophilic, electrical, biosensor

INTRODUCTION

Carbon nanotubes have been studied extensively and become one of the most promising nanoscale materials (ref. 1). Not only the mechanical strength of carbon nanotubes, but also the electrical transportation properties and electron field emission characteristics make them attractive for a broad range of applications (refs. 2 to 3). Although surfaces of as-grown carbon nanotubes are hydrophobic and water does not wet it easily, it is also known that this hydration property of carbon nanotubes can be modified by oxidation and plasma activation processes (refs. 4 to 7). In this paper, vertically aligned carbon nanotubes were prepared by a thermal chemical vapor deposition process (ref. 8). Various oxidation processes were applied to the surfaces of as-grown hydrophobic carbon nanotubes, of which the hydration properties and their effects on applications were studied (refs. 9 to 10).

EXPERIMENTAL DETAILS

Carbon nanotubes used for this research were grown by a thermal chemical vapor deposition process in a gas mixture of argon and acetylene. Iron catalyst thin films were sputtered onto Silicon substrates by a RF magnetron sputtering process and then oxidized to form nanoparticles before the growth of carbon nanotubes started. The carbon-nanotube growth process was carried out in a vacuum furnace heated to 700°C at a pressure of 75 Torr. The typical growth time was 20 min. Vertically aligned carbon nanotubes with an average length of 20 um were confirmed by means of SEM (See Fig. 1). Modification of the hydration properties of these carbon nanotubes were carried out by subjecting them oxidizing environments including electrochemical anodization in water, heating in ambient air, and a brief exposure to an air plasma.

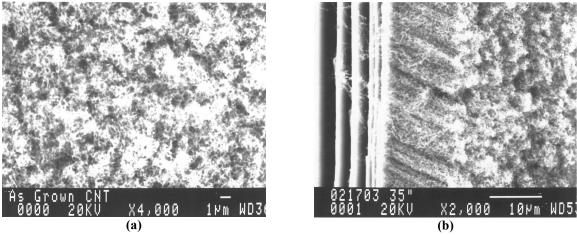


Figure 1. SEM images of vertically aligned carbon nanotubes: (a) top view and (b) side view.

Electron field emission characteristics of the as-grown and oxidized samples were analyzed at room temperature in a vacuum chamber at a base pressure of 10^{-7} Torr. In these measurements carbon nanotubes served as the cathode while a metal anode was placed in parallel to the carbon nanotubes at a desired distance. An electric field up to 9 V/um was applied. The area of the electron field emission site was determined by the collecting area of the anode that was surrounded by an electrical insulator except one flat surface which served as the anode. Immobilization of antibodies and the attachment of bacteria on oxidized and hydrophilic carbon nanotubes were studied.

RESULTS AND DISCUSSION

Electrochemical anodization

A D.I. water drop was placed on the hydrophobic as-grown carbon-nanotube coated silicon substrate. A tungsten wire was inserted into the water drop as an electrode while the carbon nanotubes where the water drop sat served as the counter electrode. The experiment setup was shown in Figure 2. Positive voltage up to 10 volts was applied to the nanotubes with respect to the tungsten wire causing a current to flow through the water drop in the range of microamperes. Water in contact with the electrodes decomposed as bubbles came out around the wire while the water drop gradually reduced in size and the carbon nanotubes became hydrophilic. A SEM image for the electrochemically anodized carbon nanotubes is shown in Figure 3.

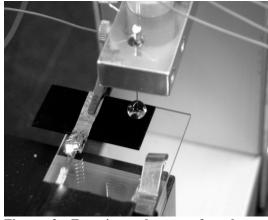


Figure 2. Experimental setup for electrochemical anodization of carbon nanotubes in water.

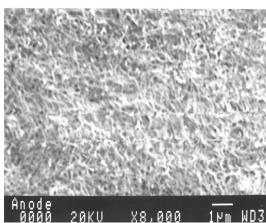


Figure 3. SEM photograph of vertically aligned carbon nanotubes after being subjected to the electrochemical anodization treatment.

Figure 4 shows a water drop on an as-grown hydrophobic carbon-nanotube coated silicon substrate (left) and a water film on the right-hand side of the substrate where carbon nanotubes have been electrochemically anodized to become hydrophilic (right). The photograph clearly shows that water does not wet the as-grown carbon nanotubes while it wets the electrochemically treated carbon nanotubes easily.



Figure 4. A water drop on the as-grown carbon nanotubes (left) and a water film on the electrochemically anodized carbon nanotubes (right).

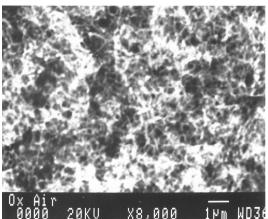


Figure 5. SEM photograph of the thermally oxidized and vertically aligned carbon anodized nanotubes.

Thermal oxidation

Carbon-nanotube coated silicon substrates were placed on a hot plate with the carbon-nanotube coating facing up and heated up to 400°C in air for a few minutes. Both the sidewalls and the tips of carbon nanotubes were oxidized by the ambient air. Figure 5 shows a SEM image of the thermally oxidized carbon nanotubes. The surface morphology of the carbon nanotube coating did not change much from that for the as-grown carbon-nanotube coating; however, the carbon nanotubes became hydrophilic.

Oxidation by a plasma in ambient air

Carbon-nanotube coated silicon substrates were briefly exposed to a microwave plasma in ambient air for one to a few seconds. The upper part of the carbon nanotubes coated on a silicon substrate was exposed to the transient air plasma while the lower part of the carbon nanotubes was masked by the upper part of the carbon nanotubes because of the very high number density of carbon nanotubes. Figure 6 shows the SEM image of the air plasma treated specimen. The air plasma treated carbon nanotubes became hydrophilic allowing a water film to form easily on them when a water drop is applied.

Electron field emission

Electron field emission characteristics of carbon nanotubes after being treated by thermal oxidation and air plasma oxidation were only slightly affected as compared with that for the as-grown carbon nanotubes. The I-E curves for the as-grown, thermally oxidized, and air plasma oxidized carbon nanotubes are shown in Figure 7.

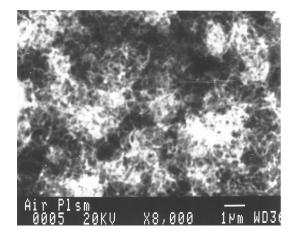


Figure 6. SEM photograph of the air plasma treated vertically aligned carbon nanotubes.

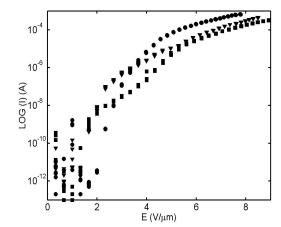


Figure 7. I-E curves of the as-grown (square), thermally oxidized (triangle), and air plasma treated (circle) carbon nanotubes.

Immobilization of antibodies on carbon nanotubes

For biosensor applications, functionalized sensing materials are first coated with immobilized bioreceptors. The bioreceptors recognize the specific analytes and allow them to attach to the bioreceptors and therefore stay on the surfaces of the sensing materials. Shown in Figure 8 are bacteria that were attached to carbon nanotubes that have been oxidized to become hydrophilic and then coated with a specific antibody for the bacteria. *Salmonella typhimurium* bacteria can be seen in Figure 8 to easily attach to carbon nanotubes on which specific antibodies have been immobilized.

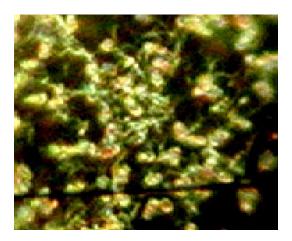


Figure 8. Hydrophilic carbon nanotubes coated with antibody, partially blocked by bovine serum albumin (BSA), and then attached with *Salmonella typhimurium*. Some carbon nanotubes are visible in this photo. Particles like objects attached to carbon nanotubes are *Salmonella typhimurium*. Carbon nanotubes were pre-treated to convert them from being hydrophobic to hydrophilic before the experiment.

CONCLUSION

In summary, electrochemical anodization, thermal oxidation, and air plasma oxidization processes have been shown to convert surfaces of vertically aligned carbon nanotubes from being hydrophobic to hydrophilic. Electron field emission characteristics of carbon nanotubes after being treated by thermal oxidation and air plasma oxidation were only slightly affected as compared with that for the as-grown

carbon nanotubes. Hydrophilic carbon nanotubes have been shown to effectively immobilize antibody which allows specific bacteria to attach to the carbon nanotubes.

REFERENCE

- 1. S. Iijima, "Carbon nanotubes: past, present, and future," Physica B 323 (2002) 1-5.
- 2. Young Joon Yoon and Hong Koo Baik, "Synthesis of carbon nanotubes by chemical vapor deposition for filed emitters," Journal of vacuum science and technology B: Microelectronics and nanometer structures, v19, n 1, Jan 2001, and pp.27-31.
- 3. Sishen Xie, Wenzhi Li, Zhengwei Pan, Baohe Chang, Lianfeng Sun, "Mechanical and physical properties on carbon nanotube," Journal of physics and chemistry of solids, v 61, n 7, Jul 2000, p1153-1158.
- 4. Lin Feng, Shuhong Li, Yingshun Li, Huanjun Li, Lingjuan Zhang, Jin Zhai, Yanlin Song, Biqian Liu, Lei Jiang, and Daoben Zhu, "Super-hydrophobic surfaces: from natural to artificial," Advanced materials, v 14, n 24, Dec 17 2002, p1857-1860.
- 5. Elena V. Basiuk, Vladimir A. Basiuk, Jose-Guadalupe Banuelos, Jose-Manuel Saniger, Valeriy A. Pokrovskiy, Taras. Yu. Gromovoy, Aleksandr V. Mischanchul, and Boris G. Mischanchul, "Interaction of oxidized single-walled carbon nanotubes with vaporous aliphatic amines," Journal of physical chemistry B, v 106, n 7, Feb 21 2002, p1588-1597.
- 6. Qidao Chen, Liming Dai, Mei Gao, Shaoming Huang, and Albert Mau, "Plasma activation of carbon nanotubes for chemical modification," Journal of physical chemistry B, v 105, n 3, Jan 2001, p618-622.
- 7. Joseph N. Barisci, Gordon G. Wallace, and Ray H. Baughman, "Electrochemical studies of single-wall carbon nanotubes in aqueous solutions," Journal of electroanalytical chemistry, v 488, n 2, Jul 2000, p92-98.
- 8. Cheol Jin Lee, Jeunghee Park, "Growth model of bamboolike structured carbon nantubes synthesized using thermal chemical vapor deposition," Journal of physical chemistry B, v 105, n 12, Mar 29 2001, p2365-2368.
- 9. A.Y. Cao, X.F. Zhang, X. Xiao, M.Q. Ding, D.M. Zhuang, C.L. Xu, B.Q. Wei, J. Liang, and D.H. Wu, "Field emission behavior of aligned carbon nanofiber arrays," Material letters, v 51, n 5, Dec 2001, p371-374.
- A.L. Musatov, N.A. Kiselev, D.N. Zakharov, E.F. Kukovitskii, A.I. Zhbanov, K.R. Izrael'yants, E.G. Chirkova, "Field electron emission from nanotube carbon layers grown by CVD process," Applied surface science 183 (2001) 111-119.

CARBON NANOTUBE ELECTRODE ARRAYS FOR ENHANCED CHEMICAL AND BIOLOGICAL SENSING

Jie Han

NASA Ames Center for Nanotechnology <u>jiehan@mail.arc.nasa.gov</u>

Abstract

Applications of carbon nanotubes for ultra-sensitive electrical sensing of chemical and biological species have been a major focus in NASA Ames Center for Nanotechnology. Great progress has been made toward controlled growth and chemical functionalization of vertically aligned carbon nanotube arrays and integration into micro-fabricated chip devices. Carbon nanotube electrode arrays devices have been used for sub-attomole detection of DNA molecules. Interdigitated carbon nanotubes arrays devices have been applied to sub ppb (part per billion) level chemical sensing for many molecules at room temperature. Stability and reliability have also been addressed in our device development. These results show order of magnitude improvement in device performance, size and power consumption as compared to micro devices, promising applications of carbon nanotube electrode arrays for clinical molecular diagnostics, personal medical testing and monitoring, and environmental monitoring.

GROWTH AND CHARACTERISATION OF MULTIWALL CARBON NANOTUBES/FIBRES FOR FIELD EMISSION APPLICATIONS

W.I.Milne, K.B.K.Teo, R.Lacerda, M.Chhowalla and G.A.J.Amaratunga

Cambridge University Engineering Department, Trumpington Street, Cambridge CB2 1PZ, England

D.G.Hasko and S-B.Lee

Microelectronics Centre, Cavendish Laboratory, University of Cambridge, Cambridge CB3 0HE

P.Legagneux and D.Pribat

Thales Research and Technology, Domaine de Corbeville, 91404 Orsay Cedex, France

ABSTRACT

Carbon Nanotubes have generated an increasing amount of interest since their initial observation by Ijima in 1991(1). Recently numerous groups have demonstrated both the lateral and vertical growth of carbon nanotube/fibres (CNTs) with a high degree of control over their alignment, length and diameter using catalytically mediated Plasma Enhanced Chemical Vapour Deposition (PECVD). CNTs have thus emerged as highly promising candidates for use as electron field emitters in such applications as scanning probes, x-ray sources, flat panel displays, microwave amplifiers and parallel e-beam lithography systems. This paper will review the work that we have carried out using such a technique, employing Ni as the catalyst, to produce arrays of multiwall CNTs. The electrical properties of individual tubes will be described and the microscopic characterisation and field emission from such tubes will also be reported.

1) S.Ijima, Nature, 354, 56 (1991)

The corresponding author:

W.I.Milne, Cambridge University Engineering Department, Trumpington Street, Cambridge CB2 1PZ, England, wim@eng.cam.ac.uk, + 1223 766207, +1223 332757

Keywords: Carbon Nanotubes, Field Emission, flat panel displays, electron sources

THE LARGE-SCALE PRODUCTION OF NANOFIBERS, MWNTS, SWNTS AND THEIR PRACTICAL APPLICATIONS

M. Endo*, T. Hayashi, Y. A. Kim and T. Yanagisawa

Faculty of Engineering, Shinshu University, 4-17-1 Wakasato, Nagano-shi 380-8553, Japan

M. S. Dresselhaus

Massachusetts Institute of Technology, Cambridge, Massachusetts 02139-4307, USA

ABSTRACT

The sp²-based fibrous carbons, such as carbon nanofibers, multi-wall carbon nanotubes and single-wall carbon nanotubes, have acted as a vanguard among nanomaterials with a high potential of applications in various fields of nano-technology, due to their extraordinary chemical and physical properties. One obstacle to recent trends toward widespread practical applications of fibrous carbon is considered to be the difficulty of large-scale production of high purity the fibrous carbons at a reasonable cost. In this sense, the catalytic chemical vapor deposition method (or pyrolysis of hydrocarbons) is considered to be the answer for the large-scale production of these fibrous carbons, especially, using a floating reactant method. Through exact control of synthetic conditions, it is possible to tailor the diameter, crystallinity, and the angle of truncated cones with regard to tube axis. In this study, we will report the synthetic method of fibrous carbons including SWNTs, especially the floating reactant method, describe structural characterizations for various fibrous carbons, and finally deal with practical applications for these fibrous carbons such as the filler in advanced nano-composite, electrochemical applications, field emitter etc.

Keywords: Fibrous carbon, CVD method, Large-scale production, Applications.

*Corresponding author (Morinobu Endo) Email: endo@endomoribu.shinshu-u.ac.jp, Tel: +81-26-269-5201, Fax: +81-26-269-5208

INTRODUCTION

The sp²-based fibrous carbons, from carbon nanofibers (CNF), multi-wall carbon nanotube (MWNT) to single-wall carbon nanotube (SWNT), have attracted much attention as fascinating nanomaterials in the recent years not only because of their extraordinary physical and chemical properties but also their versatile potential applications (ref. 1). Among the various synthesis methods for carbon nanotubes, a catalytic thermal chemical vapor deposition (CVD) synthesis method has been considered as a promising method for large-scale production of carbon nanotubes (refs. 2 to 3), especially using a floating reactant method (ref. 4), because this method has been shown to be more controllable and cost efficient as compared with the arc discharge or laser ablation methods (refs. 5 to 7). In terms of

the morphology of carbon nanotubes, it is recognized that carbon nanotubes consist of one or several graphene sheets rolled into concentric cylinders (ref. 8), resulting in extraordinary physical and chemical properties, such as robust mechanical properties caused by their small diameter and low chemical reactivity typical of highly graphitized carbonaceous materials. Recently, a new type of carbon nanotube (cup-stacked type carbon nanotube) was synthesized as a novel functional nanomaterial (ref. 9). One of main features of this carbon nanotube is its stacking morphology of truncated conical graphene layers (cups), which, in turn, exhibit a large portion of open edges on the outer surface and also in the inner hollow core (high chemical reactivity). Simply speaking, it is possible to obtain various fibrous

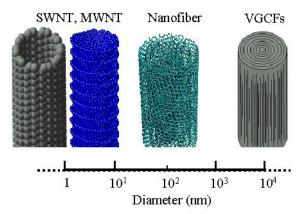


Figure 1. Schematic diagram of fibrous carbons from VGCFs to SWNT

carbons which exhibit a wide range of diameters (from vapor grown carbon fibers (=15µm), carbon nanofibers (50 to 200 nm), multi-wall carbon nanotube (50nm<) to single wall carbon nanotube (3nm<)), different crystallinity (from highly crystalline, semi-crystalline and highly ordered carbon nanotubes) and cup-stacked type morphology, through exact control of synthetic conditions of CVD method (see Fig. 1).

Here, we describe the possible route to large-scale production of fibrous carbons including SWNTs through the floating reactant method, and report the smallest isolated SWNT, and then deal with practical applications of these fibrous carbons as filler in advanced functional nano-composite, conductive filler in electrochemical field, field emitter etc.

LARGE SCALE FABRICATION OF FIBROUS CARBONS

In recent years, much attention has been focused on the growth control of the fibrous carbons. In this

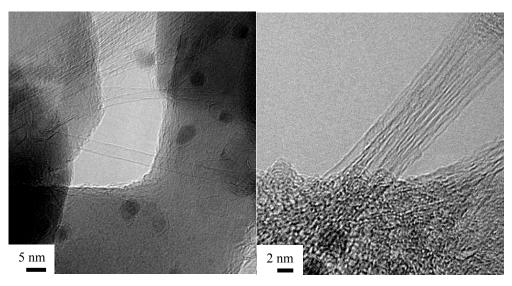


Figure 2. HRTEM images of isolated and bundle-type SWNTs

sense, it is very important to understand the manufacturing parameters for the purpose of obtaining fibrous materials with optimum properties for specific applications. Among these parameters, carrier gas, flow rate and feeding method show major effects on the carbon product that are obtained when a benzene solution containing ferrocene $[Fe(C_5H_5)_2]$ was used as the feedstock. Especially, the development of the floating reactant technique made possible to the large-scale production of CNF and MWNTs (ref. 4). In the synthesis of SWNTs, nano-sized SiO₂ impregnated

with Fe-containing compounds (seeding method) were fed into the reactor (around 1000°C) with benzene as carbon feedstock (floating method), and with hydrogen as the carrier gas (ref. 10). In contrast to current CVD methods, combinational technique allows high yield efficiency of the nanotubes. A detailed TEM and Raman studies revealed that there are large variations in textures (isolated and bundle) and also diameters (see Fig. 2). It is a natural thing that this large variation is due to different environments in a three-dimensional state when considering the floating reactant system. Relatively large density of D band from Raman scattering indicate that CVDbased SWNTs is relatively defective as compared with those of arc-discharge and laser ablation methods (see Fig. 3), which is due to lower tube formation temperature. The most important factor

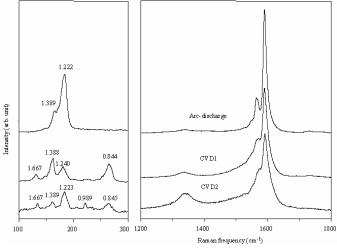


Figure 3. Raman spectra of arc- and CVD-derived SWNTs.

for obtaining high purity SWNTs is the optimization of synthetic conditions through the balance of the carbon density, metal concentration and size in the reaction chamber. This combinational technique will spur the practical large-scale applications of SWNTs at relatively low cost in the field of nano-composite.

THE SMALLEST STANDING SINGLE-WALL CARBON NANOTUBES

The quest for small diameter carbon nanotubes is important for making use of the size-effect that is predicted to lead to different properties from those for larger nanotubes (ref. 9). The SWNTs reported in the present study were produced by a nano-zeolite floating reactant method. The floating reactant method, primarily used to produce vapor grown carbon nanofibers and nanotubes (ref. 4) based on the use of small catalytic particles, is one of the most promising methods for the mass-production of carbon nanotubes, and it is already industrialized by several companies worldwide. The zeolite template method is known for its ability to produce thin nanotubes and SWCNTs as well, but it is hard to produce carbon nanotubes in mass. By combining improved versions of both the floating reactant method and the zeolite template method we obtain a very attractive method for the mass production of thin SWNTs. We have to note here that the zeolite used in the present method is not used as a template for the formation of the SWNT, but rather is used to limit the size and structure of the catalytic particles, which have much to do with controlling the diameter and the growth process of the resulting carbon nanotubes. In the present report, we have used a fine zeolite powder as catalyst support and as floating substrate, and iron as a catalyst to grow small diameter carbon panotubes

Our observation differs from previously reported papers in that our observed small diameter SWNT is not on an amorphous film that disturbs the observation, nor is it located in the central core part of a multi-walled carbon nanotube that is virtually useless. Another important point is that the small diameter SWNTs in the present study were produced in an unconfined system unlike the previously reported papers, which used a template (ref. 11) or the central part of a MWNT (refs. 12 to 13). These distinctions are very important for the advancement of the SWNT

synthesis field and of the related fields of properties measurements and applications to obtain a direct visual proof for the existence of the isolated small diameter SWNT as reported here.

Low magnification observations showed that the sample consisted mainly of two parts: bundles of SWNTs and large hollow spherical carbon particles. We could also find some metal particles remained unwashed. Higher magnification observations showed that the tubes in the bundles were all single-walled nanotubes with diameter around 1 nm, and the particles were made of rather turbostratic carbon layers. The smalldiameter SWNT, as shown in Figure 4, was found isolated from other bundles and could be clearly observed through the use of the energy filter equipped in the TEM. The diameter of the tube was measured to be 0.426 nm, which is the smallest diameter nanotube yet to be produced by the CVD method, and to our knowledge, it is the smallest diameter tube ever to be observed as a freestanding or isolated structure. The tube was unstable under electron beam irradiation during TEM observation in comparison with other thicker SWNTs, and deformed within a minute. even when we were trying to bring the camera into focus, showing a behavior very similar to that of a polymer sample. From the observed diameter, and by comparing with the observed and simulated TEM image of SWCNT model as shown in the inset of Figure 1, we conclude that the nanotube can be assigned the (5, 1) indices which has a diameter of 0.436 nm, although it is hard to be sure about the assignment because of the deformation due to the irradiation effect.

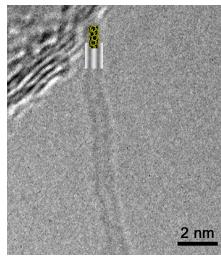


Figure 4. HRTEM image of a small diameter SWNT. Inserted images are the model of (5,1) tube and the TEM simulated image, which is in good agreement with the observation.



Figure 5. Simulated model of the cap of a (5, 1) nanotube. The cap consists of 6 pentagonal rings, just like part of C_{20} molecule, but slightly deformed.

We couldn't find the end of tube because of the sufficiently long length of the tube, and because it is mostly overlapped with either bundles of SWNTs or with carbon particles. But it is worthwhile to note that the diameter of the small tube is well consistent with the diameter of a C₂₀ molecule, and we can imagine that if there exists an end of a (5, 1) tube, it should be like the model shown in Figure 5, which is capped with 6 adjacent pentagonal rings, and can be closed with no difficulty.

There are two major mechanisms for the catalytic growth of carbon nanotubes depending on the position of the catalyst, where the tube growth occurs. As shown in Figure 6, one is the tip-growth mechanism whereby the catalyst particle is

Figure 6. Schematic image of the tip-growth and root-growth models, which the catalytic particles (red balls) are located at the tip and at the root, respectively. The blue balls are the carbon atoms, and the brown base is the simplified model of a zeolite.

at the tip of the tube, and the other is the root-growth mechanism, whereby the catalytic particle is placed at the root of the tube. For the SWNTs in the present study, as shown in Figure 7, catalytic particle can

be found both at the root and at the tip of the tubes. This indicates that two major growth mechanisms coexist in the growth of our small diameter SWNT. Moreover, we can imagine that both growth mechanisms are qualitatively the same just depending on the position of the catalyst particle that plays a role as a carbon feeding source.

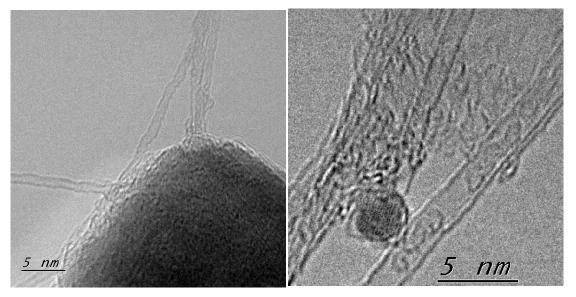
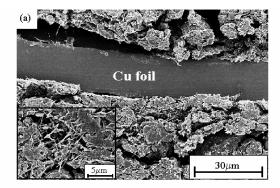


Figure 7. TEM image of the tubes with the catalytic particle (dark contrast indicated by the arrows) at the root of the tubes (Top), and at the tip of the tube (Bottom). This shows that the tube growth in the nano-zeolite floating substrate method occurs both at the root and at the tip of the tube.



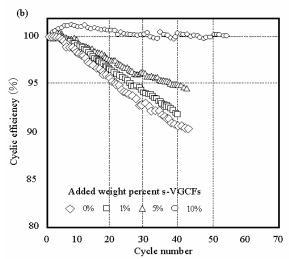


Figure 8. FE-SEM image of synthetic graphite-based electrode containing carbon nanofiber (a) and cyclic efficiency as a function of weight percent of pyrolytic nanofiber (b).

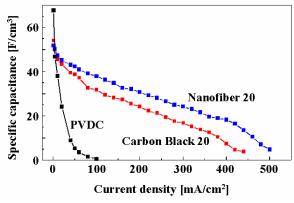


Figure 9. Variation of specific capacitance for two types of electrode containing carbon nanofiber and carbon black,

PRACTICAL APPLICATIONS

High degree of graphitizability, high surface to volume ratio caused by small diameter make these fibrous carbons potentially useful for a number of applications, for example filler in various composites and electrochemical application such as the anode material itself or additive in lithium-ion battery system, and the electrode itself or additive in double layer capacitor, especially at relatively low cost.

Among them, carbon nanofibers showed prominent performance as the additive in the electrode of Li-ion battery system (ref. 6). FE-SEM image of practical electrode containing 10wt% of nanofibers as additive shows homogeneous distribution of fibers in synthetic graphite (Fig 8. (a)). Figure 8 (b) shows the cyclic efficiency of a synthetic graphite (HTT=2900°C) anode as a function of weight percent of nanofiber added. By increasing weight percent of graphitized nanofiber, the cyclic efficiencies of the synthetic graphite anode increase continuously and in particular when 10wt% of the nanofiber was added, the cyclic efficiency was maintained at almost 100% up to 50 cycles. At higher concentrations, the nanofibers interconnect graphite powder particles together to form a continuous conductive network. When applied this fiber as an additive in the electrode of double layer capacitor, improved capacity, especially, at higher current density (Fig. 9), resistance property of electrode has improved through network formation as compared with those of carbon black (ref. 14). This system will be very promising for EV (electric vehicle) and also for fuel cell EV.

The efficient impregnation of Pt nanoparticles (OD < 3nm) on the cup-stacked type carbon nanofiber is carried out through the dispersion of the fibers in H_2PtCl_6 , followed by low temperature annealing. The Pt particle is always homogeneous, and can be controlled selectively on the outer or internal core using the hydrophobic nature of the material (see Fig. 10) (ref. 15). Since the Pt particle activity on the fiber is high, this material could find applications as efficient catalysts and allied biological devices.

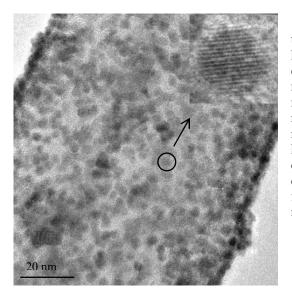


Figure 10. HRTEM image exhibiting high dispersion of Pt nanoparticles on the outer surface of a pristine nanofibers, and the inset shows an enlarged view of an individual Pt cluster $(d_{(11)} = 2.26\text{Å})$

CONCLUSION

The remarkable properties of carbon nanotubes enable them to be used as light-weight structural fibers of ultimately high strength, as conducting and semiconducting component in electronics, as connectors between macroscopic and nanoscopic regimes. Therefore, it is critically important to invent new R&D methods for inexpensive production of high quality carbon nanotubes. In this sense, large-scale synthesis of carbon nanotubes including SWNT through CVD method (pyrolysis of hydrocarbon) is very promising. Finally, future technology developments have to be done to compete with other types of carbon fibers in relation with various applications areas for fibrous carbons, and to substantiate enormous potential of nanotubes in relation with nanotechnology.

REFERENCES

- 1. M.S. Dresselhaus, G. Dresselhaus, and P. C. Eklund, Science of Fullerenes and Carbon Nanotubes, Academic Press, San Diego (1996).
- 2. A. Oberlin, M. Endo, T. Koyama, J. Cryst. Growth 32, 335 (1976).
- 3. M. Endo, K. Takeuchi, S. Igarashi, K. Kobori, M. Shiraishi and H. W. Kroto, J. Phys. Chem. Solids 54, 1841 (1993).
- 4. M. Endo, Chem. Tech. (Leipzig) 18, 568 (1988).
- 5. M. Endo, Y. A. Kim, Y. Fukai, T. Hayashi, M. Terrones, H. Terrones, M. S. Dresselhaus, Appl. Phys. Lett. 79 (10), 1531 (2001).
- 6. M. Endo, Y. A. Kim, T. Hayashi, K. Nishimura, T. Matushita, K. Miyashita and M. S. Dresselhaus, Carbon 39, 1287 (2001).
- 7. M. Endo, Y. A. Kim, S. H. Hong, T. Matushita, T. Takeda, T. Hayashi and M. S. Dresselhaus, Carbon, 39, 2003 (2001).
- 8. S. Iijima, Nature 354, 56 (1991).
- 9. M. Endo, Y. A. Kim, T. Hayashi, Y. Fukai, K. Oshida, M. Terrones, T. Yanagisawa, S. Higaki and M. S. Dresselhaus, Appl. Phys. Lett. 80, 1267 (2002).
- 10. T. Hayashi, Y. A. Kim, T. Matoba, M. Esaka, K. Nishimura, M. Endo and M. S. Dresselhaus, Nanoletters (In press)
- 11. N. Wang, Z.K. Tang, G.D. Li, J.S. Chen, Nature 408, 50 (2000).
- 12. L. C. Qin et al., Nature 408, 50 (2000).
- 13. A. Koshio, M. Yudasaka, S. Iijima, Chem. Phys. Lett. 356, 595 (2002).
- 14. M. Endo, T. Takeda, Y.J. Kim, K. Koshiba, K. Ishii, Carbon Science, 1, 91-97 (2000).
- 15. M. Endo, Y. A. Kim, M. Ezaka, K. Osada, T. Yanagisawa, T. Hayashi, M. Terrones and M. S. Dresselhaus, Nanoletters (In press).

ACKNOWDELGEMENTS

This work was partly supported by the Research for the Future Program of the Japan Society for the Promotion of Science (JSPS), "Nano carbons for advanced energy devices" and also supported by the CLUSTER of Ministry of Education, Culture, Sports, Science and Technology.

GISAXS study of the alignment of oriented carbon nanotubes grown on plain SiO2/Si(100) substrates by a catalytically enhanced CVD process

F. NORMAND, C.S. COJOCARU

CNRS, STRASBOURG, FRANCE

francois.le-normand@ipcms.u-strasbg.fr

MANE MANE

University Yaound CAMEROON

O. JEAN, T.H. METZGER

ESRF, GRENOBLE, FRANCE

Abstract

Despite the importance in the alignment of carbon nanotubes films to provide quite accurate emission centers for field emission, there are to our knowledge no quantitative study of the degree of alignment of CNTs films in the literature. Indeed SEM images provide a valuable qualitative impression of alignment in many reports but i) the images are only qualitative; ii) this is a local probe that can induce some misinterpretation about the true uniformity of the sample. Grazing Incidence Small Angle X-Ray Scattering (GISAXS) is well suited to get important structural information on the alignment and the correlation between nanostructures. In addition, we also investigate the alignment of CNTs by angular measurements of Auger electrons (C KVV transitions sensitive to the p electrons). In both cases the strong 1D anisotropic character of p electrons in oriented CNTs is spectroscopically probed.

We have performed GISAXS experiments to get structural (orientation of the alignment mainly, but also size distribution and density) and correlation information (mutual alignment, presence of defects in the orientation) on nanostructures grown on plain SiO2 (thickness 2-8 nm)/Si(100) substrates after dispersion of a metallic catalytic islands. It is expected to get a sharp GISAXS signal if the nanotubes are perfectly aligned normal to the surface. The degree of the alignment of CNTs was studied according to growth parameters (substrate temperature, NH3 concentration, gas activation parameters, nature of the metal).

CONTROLLED SYTHESIS OF CARBON NANOTUBES BY ARC IN WATER WITH REDUCED PRESSURE

Noriaki Sano, Masakazu Naito, Kenji Iimura, Satoshi Matsuda, Tatsuo Kanki, Takeyuki Kikuchi* Himeji Institute of Technology, Department of Chemical Engineering, *Department of Engineering Science 2167 Shosha, Himeji, 671-2201 Japan sano@mech.eng.himeji-tech.ac.jp, TEL/FAX 81-792-67-4845

Manish Chhowalla[#], Haolan Wang⁺, Gehan A. J. Amaratunga⁺

*Rutgers University, Department of Ceramic and Materials Engineering, NJ 08854-8065 USA *University of Cambridge, Department of Engineering, Trumpington Street, Cambridge CB2 1PZ, UK

ABSTRACT

Synthesis of multi-walled carbon nanotubes (MWCNT) by an arc discharge between two graphite electrodes submerged in water under controlled pressure (from 400-760Torr) is reported. Transmission and scanning electron microscopy investigations of the arc discharge product collected from the bottom of the reactor revealed high concentrations of MWCNTs at all pressures. Dynamic light scattering (DLS) on suspensions containing MWCNTs showed that the mean diameter of the nanotubes increases with decreasing pressure. Raman Spectroscopy analysis reveals that the relative amount of disordered carbon is significantly less in the low pressure samples. Furthermore, the yield of the deposit was found to be independent of the pressure. These results suggest that the physical properties of MWCNTs formed by the submerged arc can be controlled by varying the pressure.

Keywords: carbon nanotube, arc discharge, water, pressure

INTRODUCTION

Since fullerens and carbon nanotubes (CNTs) were discovered (refs 1, 2), many intensive efforts to develop CNTs fabrication methods have been carried out over a decade. By these efforts, several types of methods have been commonly applied to fabricate CNTs, for example, the use of arc discharge in inert gas at reduced pressure (ref. 3), the thermal pyrolysis of organic gases (ref. 4), and plasma chemical deposition (ref. 5). In addition to these conventional methods, the submerged arc discharge in cold liquid was recently proposed (refs. 6 to 8), and has been researched to fabricate nano structural materials. The arc in cold liquid gives ideal environment to quench a high-temperature plasma to form several nano structures from materials evaporated from electrodes. Since MWCNTs were synthesized by arc discharge in liquid nitrogen (ref. 6), the capability to synthesize metal-included CNTs (ref. 7), carbon onions (ref. 8), MWCNTs (ref. 9), and carbon nanohorns (CNHs) (ref. 10) by arc in water or liquid nitrogen have been reported. Furthermore, it was shown that the method using arc discharge in water can produce nano structural materials from not only carbon but also from other materials such as MoS₂ (ref. 11).

It is expected that nano structural products by the submerged arc can be controlled by varying the state of the arc quenching zone (ref. 12). One of the ways to control the quenching rate of the submerged plasma is to change the pressure of the water. Atmospheric pressure had been applied in the all experiments previously reported on the submerged arc system to produce nano materials (refs. 6 to 12). In spite of this condition, it is known that there is an optimized pressure to grow CNTs by the arc in inert gases, which is around 500 torr in He (ref. 13). This discrepancy motivated us to examine the influence of pressure-reduction on the submerged arc system. This article shows some experimental results which shows the effect of pressure-reduction on the CNTs formation by submerged arc in water in the pressure range, 400-760 torr.

EXPERIMENTAL

Experimental set-up is shown in Fig. 1. The direct current (d.c.) submerged arc was generated between graphite electrodes in 100ml de-ionized water in a glass reactor. The diameters of the cathode and the anode were

respectively 12mm and 6mm. The anode was shifted through a Teflon bellows joint, and the cathode was fixed. The arc was initiated by touching these electrodes, and the anode-cathode gap were kept approximately 1mm to keep the arc current 40A with 20V. The pressure of the air above the water was reduced by a rotary pump through a buffer vessel to avoid a sudden pressure elevation caused by the boiling of the water. To minimize the escape of the water from the reactor by its evaporation, a heat exchanger with cooling water was set above the reactor to condense the evaporated water vapor to let it return to the reactor. The pressure in the reactor was estimated from the pressure measured at the buffer vessel. The solid deposit found in the reactor bottom, which is supposed to contain MWCNTs at a high concentration (ref. 9) was collected for analysis.

The collected products were analyzed by transmission electron microscopy (TEM; JEOL2010), scanning electron microscopy (HITACHI, S-900), dynamic light scattering (DLS; MALVERN Inc., ZETASIZER300HSA), and Raman spectroscopy (Renishaw Raman Spectroscopy). To prepare specimen for TEM, the collected deposits were grinded at a mortar, and were sprinkled onto a TEM grid with an amorphous-carbon supporting film. SEM analysis was carried out on as-grown solid deposit. DLS analysis was carried out on the particles suspended in toluene with a controlled temperature at 20 °C. The laser wave-length used in DLS was 633nm. To prepare the suspensions for DSL analysis, the collected deposits were grinded first, and ultrasonicated (150W) for 30 minutes with repeated sets of a 30-second ultrasonification with a 30-second interval. Raman analysis was carried out on as-grown deposits and grinded ones with a laser wave-length 514.5 nm.

RESULTS AND DISCUSSION

1. Formation of MWCNTdeposit

In the typical CNTs formation by arc in gas, a solid deposit grows to a large size at the tip of cathode (refs. 2, 3, 13). However, such cathode deposit did not grow in the submerged arc in water, unlike by the arc in gas. It was thought that the deposit was formed on the cathode tip also in the submerged arc, but the deposit was pealed away from the cathode surface by a pressure caused by the expansion of gas bubbles in water. This consideration is based on an observation that we could find many disk-like deposits of the similar diameters to the anode at the water bottom after the discharge process. These deposits were thought to sink down to the water bottom after being pealed away from the cathode tip. Therefore, the mechanism of CNTs-growth in the submerged arc should be in principle the same as in the arc in gas (ref. 14). The main differences between the

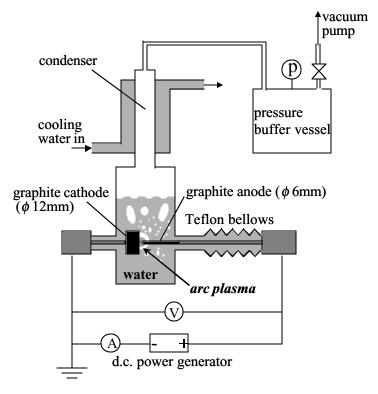


Figure 1. Experimental se-up.

submerged arc and the gas arc are the gas components surrounding the arc spot and the quenching rate to solidify the evaporated carbon to the solid products.

2. Physical analysis of the deposit products 2.2 Microscope observations

Observations by TEM and SEM revealed that MWCNTs were produced in the collected deposit in all pressures examined here. Figure 2 shows typical TEM and SEM images of the MWCNTs produced by the submerged arc at 760 torr. The TEM images of MWCNTs formed at 600, 500, 400 torr were quite similar to Fig. 1. Figure 1 shows the same features observed in the typical MWCNTs formed by the gas arc in 500 torr He as follows: (1) All CNTs are multi-walled; (2) Most MWCNTs are perfectly strait; (3) CNTs edges are caped; (4) Muli-walled caged polyhedral nano particles are also formed as byproducts. SEM image in Fig. 2 shows the CNTs formed by the submerged arc in 760 torr. This SEM image shows the straight structure of the CNTs and coexisting nano particles.

2.3 Dynamic Light Scattering

During these microscopy observations, we were impressed that the diameters of the CNTs produced in the reduced pressure are larger than that by the higher pressure. However, such diameter distribution can not be clearly revealed in microscopy analyses because microscopy observations concentrate selected zones in the sample specimen. Then, other physical analyses by DLS and Raman spectroscopy are considered to be important to analyze the sizes and the structures of our products. We should be careful for that the particle diameter directly estimated by DLS should be larger than the real CNTs diameters because of the long geometry of CNTs. Nevertheless, we expect the DLS results can indicate qualitative trend about the CNTs sizes. Figure 3 shows the DLS results on the deposits formed by the submerged arc in 400, 500, 600, and 760 torr. It is shown that the effective diameters evaluated from DLS increases with the lower pressure.

2.4 Raman spectroscopy

Figure 4 shows Raman spectra of the MWCNTs-contained deposits formed at each pressure. The peaks at 1353 cm⁻¹ and 1582 cm⁻¹ correspond to so-called disorder band (D-band) and graphite band (G-band), which indicate defective graphite and well-crystallined structures, respectively. In these figures, it is noticed that the relative intensity of D-band peak becomes very small when the pressure is reduced down to 500

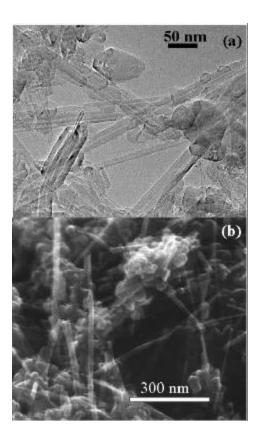


Figure 2. Microscopy observations on collected deposit formed by submerged arc in water at 760 torr: (a) TEM image of MWCNTs with multi-shelled polyhedral particles, (b) SEM image of the same products.

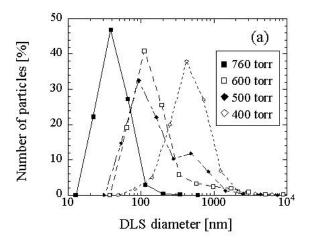


Figure 3 DLS analysis on suspensions in toluene (20 °C) prepared by ultrasonicated MWCNTs-contained deposits formed by the submerged arc in water.

torr. The Raman shift peaks around 2700 cm⁻¹ corresponds to the secondary peaks from the graphite structure. This result indicates that the MWCNTs and nano particles formed under reduced pressure are well crystallined. Raman peaks in a low wave-number range around 100-200 cm⁻¹ are commonly observed to estimate diameters of single walled CNTs (SWCNTs) (ref. 15). However such low-wave number Raman peak may not appear from MWCNTs because the zone-folding effect is not significant for their relatively large diameters (ref. 16). In our products, such low wave-number Raman-peaks were not observed, suggesting that CNTs produced by submerged arc in water under the pressure range 400-760 torr are mostly the typical MWCNTs which have the diameters not showing such low wave-number peaks.

2.5 Production rate

The weight of the deposits collected from water bottom was measured to evaluate the production rate at each pressure. Figure 5 shows the production rates of the deposits and the conversions of the evaporated anode to the deposits. The conversions are defined by the ratio of the weight of the collected deposit to that of weight-drop of the anode during the arc discharge. It is shown in these figures that the both production rates and conversions are not significantly sensitive to the pressure.

3. Pressure effect on CNT growth mechnism

It was expected that the gas density and quenching rate in the submerged arc can be controlled by varying the pressure. In the submerged arc system, the arc plasma is generated in a gas bubble formed by a hot temperature at the arc spot. When the pressure of the reactor system was lowered, the bubble expansion increases. This increased bubble expansion may decrease the quenching rate because of the two reasons: (1) The mean distance between the hot arc spot and the gasliquid interface increases. (2) The thermal conductivity becomes lower when the pressure decreases (ref. 17). This lowered quenching rate may cause the larger MWCNTs because the time to grow MWCNTs can be reserved longer. Also, lowering pressure can decrease the density of the gas components in the plasma zone, which are considered to be H_2 , CO (ref. 7) and water vapor. The lower density of such reactive gases may decrease the probability of the termination of the MWCNTs-growth, causing the higher crystallined structure and the larger CNTs.

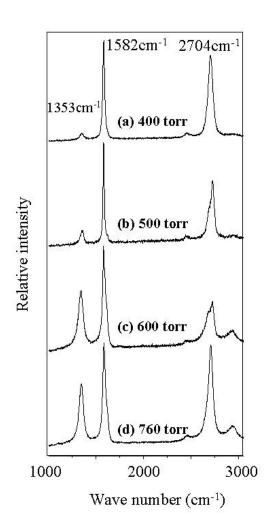


Figure 4. Raman shift on MWCNTs -contained deposits produced by submerged arc in water in various pressures.

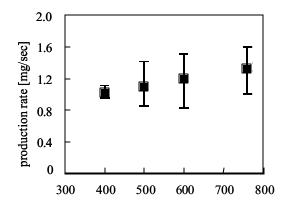


Figure 5. Influence of pressure on production rates.

CONCLUSIONS

MWCNT were formed by d.c. submerged arc in water with graphite electrodes under the pressure range from 400 to 760 torr. The microscopy analyses by TEM and SEM on the deposit collected from water bottom after the discharge process showed that high concentration MWCNTs can be obtained in all these pressures. Dynamic light scattering on these MWCNTs revealed that the MWCNTs sizes increase with the lower pressure. Raman analysis indicated that the defects on these MWCNTs can be reduced by lowering the pressure. On the contrary to these pressure effects on the structures of MWCNTs, the yield of the MWCNTs -contained deposit was almost independent from the pressure. It is important to be noted from these results that the structures and physical properties of MWCNTs formed in the submerged arc can be controlled by varying the pressure. One of the physical reasons of this effect is considered that the reduced pressure enlarges the bubble size around the submerged arc spot so that the quenching rate of the evaporated carbon decreases. In addition, the decrease of the reactivity of gas inside the bubble around the arc spot may cause the larger MWCNTs structure with smaller defects.

ACKNOWLEDGEMENT

Authors are grateful to Dr. A. C. Ferrari for permission to use the Renishaw Raman Spectroscopy at the EDM group of the University of Cambridge (UK), engineering department. Financial support by Grant-in-Aid for Young Scientists (B) of Japan Society for the Promotion of Science (JSPS), Kawanishi-Kinen-Shinmeiwa-Kyoiku Foundation (2002), and Kinki-Chiho-Hatsumei Center (2002) are acknowledged.

REFERENCES

- 1 H. W. Kroto, J. R. Heath, S. C. O'Brien, et al., Nature, 318, 1985, 162.
- 2 S. Iijima, Nature 354, 1991, 56.
- 3 T. W. Ebbesen and P. M. Ajayan Nature 358, 1992, 220.
- 4 M. Endo, T. Takeuchi, S. Igarashi, K. Kobori, M. Shiraishi, H. W. Kroto, J Phys Chem Solids 54, 1993, 1841.
- 5 M. Chhowalla, K. B. K. Teo, C. Ducati, N. L. Rupesinghe, G. A. J. Amaratunga, A. C. Ferrari, D. Roy, J. Robertson, W. I. Milne, J. Appl. Phys. **90**, 2001, 5308.
- 6 M. Ishigami, J. Cumings, A. Zettl, and S. Chen, Chem. Phys. Lett. 319, 2000, 457.
- 7 Y. L. Hsin, K. C. Hwang, F.-R. Chen, and J.-J. Kai, Adv. Mater. 13, 2001, 830.
- 8 N. Sano, H. Wang, M. Chhowalla, I. Alexandrou, and G. A. J. Amaratunga, Nature 414, 2001, 506.
- 9 H.W.Zhu, X.S.Li, B.Jiang, C.L.Xu, Y.F.Zhu, D.H.Wu, X.H.Chen, Chem. Phys. Lett. 366, 2002, 664.
- 10 H. Wang, N. Sano, S. Jia, M. Chhowalla, and G A. J. Amaratunga, Chem. Phys. Lett. submitted.
- 11 N. Sano, H. Wang, M. Chhowalla, I. Alexandrou, G. A. J. Amaratunga, M. Naito, and T. Kanki, Chem. Phys. Lett. **368**, 2003, 331.
- 12 N. Sano, H. Wang, I. Alexandrou, M. Chhowalla, K. B. K. Teo, G. A. J. Amaratunga, and K. Iimura, J. Appl. Phys. 92, 2003, 2783.
- 13 P. J. F. Harris, Carbon Nanotubes and Related Structures, Cambridge University Press, Cambridge, UK, 1999, p. 19.
- 14 E. G. Gamaly and T. W. Ebbesen, Phys. Rev. B, 52, 1995, 2083.
- 15 R. Saito, G. Dresselhaus, and M. S. Dresselhaus, Physical Prop-erties of Carbon Nanotubes, Imperial College Press, London, 1999.
- 16 Y. Saito and S. Bandow, Carbon Nanotube NO KISO ("Fundamentals of carbon nano tubes" in Japanese), CORONA Inc., Tokyo, 1998, p.125.
- 17 R. B. Bird, W. E. Stewart, E. N. Lightfoot, Transport Phenomena, John Wiley and Sons Inc., New York, 1960.

Large-scale synthesis of single-walled carbon nanohorns using the arc in liquid method

Haolan Wang, and G. A. J. Amaratunga

University of Cambridge, Department of Engineering, Trumpington Street, Cambridge CB2 1PZ, UK

S. Jia*, N. Sano#, and M. Chhowalla^

*Xi'an Jiaotong University, Department of Electrical Engineering, Xi'an 710049, PRC #Himeji Institute of Technology, Department of Chemical Engineering, 2167 Shosha, Himeji, 671-2201, Japan ^Rutgers University, Department of Ceramic and Material Engineering, NJ 08854, USA

ABSTRACT

A novel and cost effective method has been developed for large-scale synthesis of single-walled nanohorns (SWNHs). This is the first report of an alternative method to laser ablation for formation of carbon nanohorns. The method is based on igniting an arc discharge between two graphite electrodes submerged in liquid nitrogen. Production rates of up to 17g/hr have been achieved. SEM analysis shows the nanohorns to be aggregated as nanoparticles with sizes in the range of 20~80nm. HRTEM reveals the internal structure of individual nanoparticle is an aggregation of either 'dahlia-like' or 'bud-like' single-walled nanohorns (SWNHs). It was further found that both the yield and morphology of nanohorns changed as a function of arc current density in liquid nitrogen. The yield of nanohorns increases with the increment of current density. Samples produced by higher current density contains more dahlia-like nanohorns than bud-like compared to those produced at lower current.

The carbon arc in liquid nitrogen method holds the potential for controlling the structure of nanohorns as well as for allowing their production in large scale quantities required for applications such a fuel cell electrodes.

Keywords: SWNHs, liquid arc, large scale, current density

FORMATION OF CARBON NANOTUBES BY CATALYSIS OF TRANSITION METALS OBTAINED FROM MOLECULAR PRECURSORS

Hermann Sachdev *a), Dominik Tince a), Michael Knorr b)

a) Institute for Inorganic Chemistry FR 8.11, University of Saarland, P. O. Box 1150, D- 66041 SAARBRUECKEN, Germany; e-mail: h.sachdev@mx.uni-saarland.de; b) Université de Franche-Comté, Faculté des Sciences et des Techniques, La Bouloie - 16 Route de Gray, F-25030 BESANÇON CEDEX, France

Abstract

There is considerable interest to achieve a selective growth of carbon nanotubes from distinct nucleation centers on specific substrates, since they display a huge range for new applications. Transition metals can act as catalysts for the formation of carbon nanotubes. For this reasons, the influence of catalytically active metals supplied in an nanodisperse form regarding the formation of nanostructured carbon from the gas phase was studied. By this novel method, catalytically active transition metal complexes were used to generate nucleation centers on silicon substrates for the formation of carbon nanotubes. A CVD route using methane was used to supply activated carbon species from the gas phase. Since the transition metals used for this investigation are catalyzing dehydrogenation reactions, the effects of the presence of those metals on the morphology of the deposits were studied in correlation with the process parameters (pressure, substrate temperature, precursor concentration). The deposits were characterized with SEM, infrared- and raman spectroscopy.

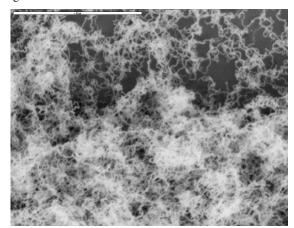


Fig. 1: Carbon Nanotubes obtained from CVD of methane

CARBON NANOTUBES ARRAY GROWN ON SUBSTRATES PATTERNED BY COMBINED LITHOGRAPHIC TECHNIQUES

F. LE NORMAND, COJOCARU, BOUKHARI, LEZEC

CNRS STRASBOURG FRANCE

francois.le-normand@ipcms.u-strasbg.fr

EBBESEN

Universit

Abstract

Field emission is one of the most promising potential applications of carbon nanotubes (CNTs). These nanostructures combine positively a geometrical effect (local exhaltation of the electric field due to a strong curvature radius) and an electronic effect (weak work function) as well as they display strong chemical inertness and thermal conductivity, which open the way to the realization of convenient electrons sources for vacuum electronics such as flat panels and cold cathodes. Field emission measurements obtained on CNTs grown on SiO2/Si(100) substrates by the DC HF CCVD process where a dispersion of metallic catalytic transition metal (Co, Ni) particles was previously performed, showed that the thresholds of emission were strongly dependent on the nature of the material. Therefore they were within the range 1-4 V/µm for CNTs. By contrast they ranged above 10V/mm either for carbon nanofibers or nanocones. However, the current densities were quire variable and often reached a rapid saturation both due to screening of the field by the high density of CNTs and to conductivity limitations of the substrate. Therefore, we used patterned surfaces to grow array of CNTs emitters. Patterned surfaces were obtained by controlled deposition of metallic spots by a combination of lithographics techniques, using either photons, electrons or ion beams. Array of particle islands of Co or Ni were obtained in the range 5-100 nm. Under proper CVD conditions we could grow subsequently one CNT by metallic island if the size of the metallic island did not exceed 60 nm.

NOVEL CARBON NANOSTRUCTURES: NANOPIPETTES AND NANO NOZZLES

G. Bhimarasetti, R.C. Mani, M.K. Sunkara*

Dept. of Chemical Engineering, University of Louisville, Louisville, KY 40292

K. Rajan and X. Li

Dept. of Material Science and Engineering, Rensselaer Polytechnic Institute, Troy, NY 12180

* Corresponding and presenting author: Phone: 502-852-1558. Fax: 502-852-6355. Email: mahendra@louisville.edu

ABSTRACT

We present synthesis of two novel carbon nanostructures in the form of nanopipettes and nanonozzles. The synthesis of both nanopipettes and nanonozzles are highly reproducible. Nanopipettes synthesized using platinum thin film covered, diamond film coated wires at low CH_4/H_2 ratios, are tapered whiskers, having a shell containing helical graphitic sheets and a hollow core 1-20 nm in diameter throughout the length. Carbon nozzles, synthesized using Ga-Mo alloy film covered substrates at high CH_4/H_2 have an inner diameter of about 200nm at the base and 3-4 μm at the end with a constant wall thickness of 30 nm throughout the length. These nozzles were typically filled with Ga at the tip and in some pockets along the length. We hypothesize that the mechanisms involved in the growth of nanopipette and nozzles are quite different than those suggested for the growth of multiwalled carbon nanotubes and other conical structures.

INTRODUCTION

The myriad structural manifestations and their material properties have made carbon nanostructures very interesting not only for potential applications but also for understanding carbon at the atomic scale. Several different nano-sized structures of carbon have been investigated intensely. A few of these include single and multi-walled nano tubes (ref. 1), helical nanotubes (ref. 2), cones (ref. 3), horns (ref. 4), conical crystals (ref. 5, 6) and micro-trees (ref. 7). A potential application of hollow carbon nanostructures is fluid transport at the nano-scale for drug delivery (ref. 8, 9). There are however several issues such as inner diameter of nano-structures, rigidity, ability to produce an ordered arrays, obstructions in the channels, and sufficient volume delivery that limit their application. Most of the published studies on conical structures indicate either solid, tapered whiskers (ref. 10) or short cones with prescribed angles with one end closed (ref. 3). In this paper, we report the synthesis of two more interesting morphologies for carbon nanostructures (nanopipettes and nozzles) with open ends.

EXPERIMENTAL

We performed two types of experiments for growing carbon nanostructures. In the first set of experiments, Platinum thin film covered diamond coated platinum wires were immersed vertically into the microwave plasma in an ASTeX model 5010 Chemical vapor deposition (CVD) reactor. The gas phase composition at was 1-2 % of CH₄/H₂, which was typical of diamond growth. At the end of the deposition experiment, some regions of the platinum wire substrate were coated with a microcrystalline diamond film. In this region, along with diamond crystals, several whiskers that were about 200-700 nm in diameter and 6 µm in length emerged. These whiskers had a pointed tip (in the shape of a pipette), while the base was in the sub-micron regime (Figure 1). They also indicated some minor faceting on their surface. In the second set of experiments, gallium-covered substrates were used in ASTeX 5010 reactor. A known quantity of molybdenum powder was sprinkled on the gallium film. The gas phase composition was 18% CH₄/H₂ plasma at 40 torr pressure, 1100 W microwave power. The duration of these experiments was about one hour. The structures obtained in these experiments were thin walled, cones and tubes without any structural obstructions inside the internal surfaces (Figure 2). These resulting structures were analyzed using a Scanning electron microscope (SEM) and a Transmission electron microscope (TEM) (Figures 1, 2).

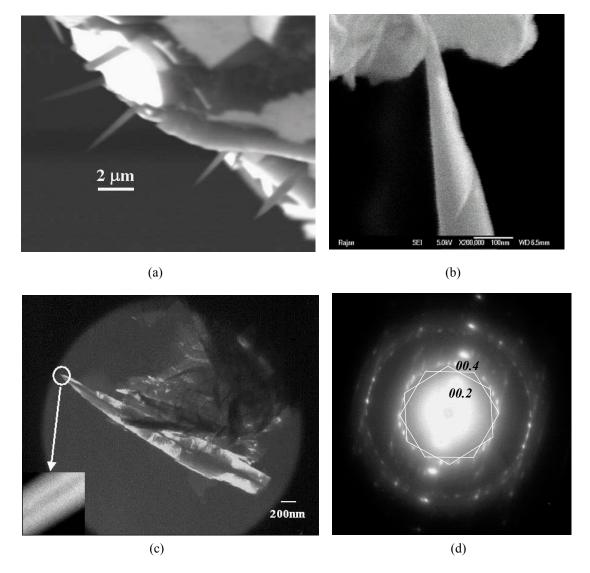


Figure 1. (a-b) SEM image of Nanopipettes growing from the diamond film (c) Dark Field TEM image (inset is the corresponding Energy Filtered TEM (EFTEM) image from $\rm sp^2$ Carbon core loss peak). (d) Diffraction pattern from hollow whiskers, with indexing consistent with helical graphite sheets, outline indicates multiple sets of hexagonal symmetry with helical sheets at an angle $\sim 9^\circ$

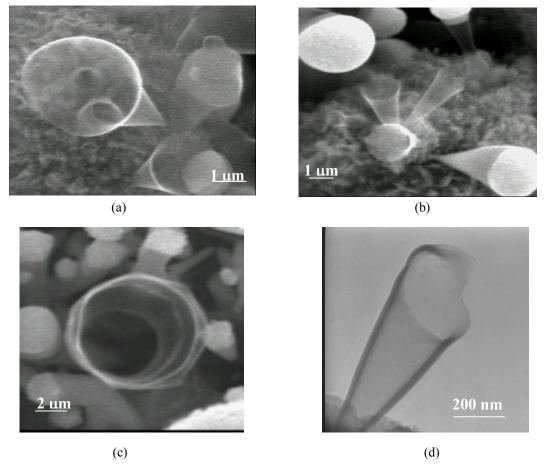


Figure 2. (a-c) SEM micrographs of nano-nozzles, which are transparent to the electron beam in the SEM. Gallium droplets are seen at the tip (b) TEM of a nozzle.

RESULTS AND DISCUSSION

The first set of experiments using carbon deposition onto vertically immersed platinum film covered wires yielded the growth of carbon nanopipettes. The second set of experiments using Mo-Ga alloy film covered flat substrates yielded the growth of carbon nanostructures in the form of nozzles (a form of conical structures that do not correspond to the expected conical angles of graphene sheet).

(a) Structural Characteristics of Carbon Nanopipettes

The dark field image in Figure 1c highlights this hollow structure even further by showing the core along the entire length. At the tip of the whisker, where the thickness permitted a reasonable signal, an energy-filtered image using the sp² core loss peak clearly illuminated the specimen (Figure 1c, inset). The dark region running down the axis of the whisker corresponds to the hollow core, which evidently does not contribute to any signal (in this case inelastically scattered core loss electrons). For details, please see ref. 11. Based on the energy loss images, the walls of the whisker at least in the tip region appeared to be graphitic in nature. Basic basal plane lattice images confirmed this graphitic structure. The details of the structure of the walls of the whisker require further work but our preliminary observations do help provide some insight. Diffraction patterns from thicker regions of the whisker (Figure 1d) however exhibited characteristic features of possible helical morphologies. The pitch angle associated with this type of structure can vary (in the case of region of the whisker sampled shown in Figure 1d, this angle is 9°) giving rise to a more complex morphology. Hence it is suggested that these "nanopipettes" are hollow whiskers possibly made up of helical sheets of graphite. Clearly this is an area of requiring further study, which is presently underway.

(b) Structural Characteristics of Carbon Nano-nozzles

These are typically 100-250 nm at one end, 3-5 μm at the broader end, 30 nm constant wall thickness, 2-4 μm length and open ended. Figure 2a, 2b and 2c shows SEM micrographs of these structures. The conical angles of the observed nozzles vary from 7° to 55° and hence their diameters. These conical angles do not correspond to the conical angles that are expected if the cones are formed by the structural arrangements of pentagonal and hexagonal rings of carbon atoms (ref. 12). In addition, there is a significant variation in the curvature of the cones at the base. A very interesting observation is that these conical structures are transparent to the electron beam of the SEM as shown in Figure 1 (a-c).

(c) Discussion on Possible Growth Mechanisms

Conical structures of graphite have been studied long before the knowledge of carbon nanotubes. Some of the earliest research on one-dimensional nanostructures of graphite described a model for the growth of graphite whiskers (ref. 13). According to this model, a sheet of graphite (consisting of several monolayers) overlaps itself and continues to wind around the whisker axis many times rather than joining opposite edges and forming concentric tubes. This scroll structure gave rise to a simultaneous thickening and growth along the length. In another attempt, while heating silicon carbide crystals, graphite whiskers were obtained (ref. 14). An explanation for these needle-shaped crystals was that a flat graphite sheet rolled into a cone, and each time it wraps around by lifting itself to form a rotation over a small angle. Graphite sheets are known to grow along their edges, thus if subsequent growth takes place, a helical surface will be formed by growth along steps to form a spiral shape (ref. 15). Graphite polyhedral crystals, synthesized from gas phase (ref. 5), had folded and closed graphene planes different from ordinary graphite but similar to Multi-walled carbon nanotubes. There were small angle conical crystals (ref. 6), which were as large as 3 µm and 300 nm in diameter. These conical crystals were not nucleated from fullerenes and fullerene-like structures. Libera et al (ref. 16) also reported hydrothermal synthesis of graphite tubes with higher inner diameters ranging from 70-1300 nm using nickel as a catalyst. They also found that the tubes encapsulated "hydrothermal fluid" and process gases during the growth and there were inner closures inside the tube. The conical structures synthesized in this paper are partially and, in some cases, fully filled with the liquid metal, gallium. Gallium filled nano-tubes have been synthesized and a nano-thermometer based on gallium filled tubes has been demonstrated (ref. 17). None of the above conical crystals had a structure similar to the ones described in this work. Hence, none of the above mechanisms could explain the formation of Nanopipettes and Nano-nozzles.

The temperatures in the center of the plasma could reach as high as 2000 °C. In experiments using platinum, the substrate is placed vertically into the plasma. Hence the plasma tends to discharge at the tip of the platinum wire, making it close to the melting point of Platinum. These high temperatures and the peculiar conical shape made us assume that the growth mode could be due to an evaporating catalyst i.e., a platinum catalyst particle initiates the growth of multi-walled carbon nanotubes. Since the temperatures in the dense zone of the plasma are high enough to evaporate platinum, the catalyst droplet evaporates. As the catalyst droplet evaporates, the outer diameter of the multi-walled shell reduces. This hypothesis could be easily tested using a sequential step experiment by growing for shorter time scales and seeing the catalyst at the tip of the nanostructures.

Hence, in another experiment, platinum thin films (~50 nm) were electrodeposited on platinum wires coated with microcrystalline diamond films. Diamond films acted as a non-reactive stable substrate. The platinum coating on the diamond film melted into droplets when exposed vertically into the plasma. The growth experiments were performed for over a period of one hour or less. These experiments indicated a continuous gradient of nanostructures along the substrate length, probably due to temperature gradients. The region close to the tip of the Pt wire has a conical structure, whose core contains a multi-walled (or single-walled) carbon nanotube (Figure 3a). The nanotube is surrounded by graphite deposit. As we move along the length of the wire, there is a competition between the etching and growth of crystalline phase (sp²) of carbon. Hence the central nanotube remains, while the surrounding graphite material also grows rapidly. Thus, a short distance away from the conical structures, we obtain structures with a higher aspect ratio (shown in Figure 3b) and further away we obtain nanopipettes (Figure 3c). The density of these nanopipettes gradually reduces as we move to the end of the substrate.

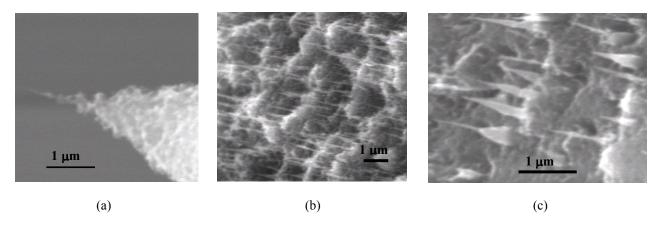


Figure 4. (a) Conical structure with a central nanotube (b) The aspect ratio of the conical structure increases, giving rise to (c) nanopipettes

If the model of an evaporating catalyst were true, then we should not be seeing such a variation of structure discontinuously. The morphology seen in Figure 3a would mean that the rate of evaporation changes abruptly along the length of the whisker, which would be quite impossible. Hence, these experiments clearly indicate that selective etching and growth simultaneously is responsible for the growth of these conical nanopipettes with different aspect ratios along the length of the substrate. Overall, there is an initial open-ended nanotube that grows out. Surrounding this nanotube are helical sheets of graphite coiling around. Due to a continuous coiling around one another, the outer layer appears conical, while the initial nanotube maintains the inner hollow core. Depending on the placement in the plasma, there is a competitive growth and etching of the graphite sheets surrounding the central nanotube. At the top, etching seems to dominate giving rise to a low aspect ratio. While as we move away from the plasma, growth seems to dominate giving rise to high aspect ratio whiskers. Hence, a dual growth/etch mode seems to be more consistent with the experimental observations for the growth of carbon nanopipettes.

The growth of another set of conical structures termed here as nozzles seems to occur with a mechanism aided by the presence of molten gallium. We hypothesize the following growth mechanism for the growth of the nanonozzles. As described in the experimental section these structures, are synthesized on different substrates by spreading a film of gallium and putting molybdenum powder on the gallium film. Gallium and molybdenum form a series of alloys of different compositions at these temperatures (800-1000° C) (ref. 18). During the initial growth process the mixture of gallium and molybdenum forms an alloy and a phase separation occurs, with the excess gallium separating out of the mixture. As the gallium is separating out, it is exposed to the CH₄/H₂ plasma. Upon exposure to the plasma, gallium tends to form spherical droplets. Carbon from the gas phase gets dissolved into gallium and precipitates out, forming an interface of carbon and gallium. As new carbon atoms are being added, gallium also moves upwards, maintaining the interface of gallium and carbon. The interface goes through an unsteady dynamics during the initial phase of growth, forming varying curvatures at the base of the nozzles. Once a certain steady state is attained, the interface set by gallium and carbon decides the conical angle of the nozzle. Due to the non-wettability of gallium with carbon, gallium tends to agglomerate towards the growth front (the tip) and leaving behind a hollow core from the base of the feature. The contact angle of the carbon wall formed with the gallium varies with the temperature. The changing contact angle determines the conical angle of the resulting structure and hence the shape, which varies from cones to tubes. Recently, carbon tubular structures were synthesized by high temperature reduction of gallium oxide using carbon (ref. 17). These structures also exhibited extremely thin walls. These studies produced only straight tubes with internal diameters of few nanometers and containing gallium. Even though, no growth mechanism for these structures was suggested, we hypothesize that the mechanism is similar to the described above except for a 90 ° contact angle of carbon-gallium interface during growth.

The first set of structures, nanopipettes, is currently being tested for drug delivery and sensing applications due to their rigidity and open channel for fluid delivery. The second set of structure, nozzles, is ideal for microfluidic experiments for delivering large amount of fluids. The wall structure of the nozzles is currently being investigated using TEM. Such novel applications in drug delivery, neurological solute detection and field emission based devices are the focus of our current efforts.

In summary, we present synthesis of novel growth morphologies of carbon nanostructures. Both of these conical structures are extremely interesting for use in micro/nano fluidics.

ACKNOWLEDGEMENTS

One of the authors (M.K. Sunkara) greatly appreciates partial financial support from NSF through CAREER grant (CTS 9876251). One of the authors (R.C. Mani) gratefully acknowledges Speed Scientific School at University of Louisville for Grosscurth fellowship. Authors also appreciate Dr. Shashank Sharma at University of Louisville and Dr. Roy Gat at Coating Technology Solutions Inc., MA for helpful discussions during the course of this study.

REFERENCES

- 1. Iijima, S.: Helical Microtubules of Graphitic Carbon, Nature, 354, 6348, Nov 1991, 56-58.
- 2. Amelinckx, S., et al.: A Formation Mechanism for Catalytically grown Helix-shaped Graphite Nanotubes, Science, 265, 5172, Jul 1994, 635-639.
- 3. Krishnan A., et al.: Graphitic Cones and the Nucleation of Curved Carbon Surfaces, Nature (London), 388, July 1997, 451-454.
- 4. Iijima, S. et al.: Nano-aggregates of Single-walled Graphitic Carbon Nano-horns, Chem. Phys. Lett., 309, 3-4, Aug 1999, 165-170.
- 5. Gogotsi, Y. et al.: Graphite polyhedral crystals, Science, 290, 5490, Oct 2000, 317-320.
- 6. Gogotsi, Y.; Dimovski, S.; Libera, J.A., Conical crystals of graphite, Carbon, 40, 12, 2002, 2263-2267.
- 7. Ajayan, P.M. et al.: Growth of carbon micro-trees Carbon deposition under extreme conditions causes tree-like Structures to Spring up, Nature, 404, 6775, Mar 2000, 243.
- 8. Henry S. et al.: Microfabricated Microneedles: A Novel Approach to Transdermal Drug Delivery, J. Pharm. Sci., 87, 8, Aug 1998, 922-925.
- 9. Megaridis C. M. et al.: Attoliter fluid experiments in individual closed-end carbon nanotubes: Liquid film and fluid interface dynamics, Phys. Fluids, 14, 2, Feb 2002, L5-8.
- 10. Tsai C. L., Chen C. F., Wu L. K.: Bias effect on the growth of Carbon Nanotips using Microwave Plasma Chemical Vapor Deposition, Appl. Phys. Lett., 81, 4, Jul 2002, 721-723.
- 11. Mani R. C. et al: Carbon Nanopipettes, Nanoletters (in press), 2003.
- 12. Ge M.; and Sattler K.: Observation of Fullerene Cones, Chem. Phys. Lett. 220, Apr 1994, 192-196.
- 13. Bacon, R.: Growth, Structure, and Properties of Graphite Whiskers, J. Appl. Phys., 31,2, Feb 1960, 283-290.
- 14. Haanstra, H.B.; Verspui, G.; Knippenberg, W.F.: Columnar Growth of Carbon, J. Cryst. Growth, 16, 1, Oct 1972, 71-79.
- 15. Amelinckx, S. et al.: Conical, Helically Wound, Graphite whiskers A limiting Number of the Fullerenes, J. Cryst. Growth, 121, 4, Aug 1992, 543-558.
- Libera J.; and Gogotsi Y.: Hydrothermal Synthesis of Graphite Tubes using Ni Catalyst, Carbon, 39, 2001, 1307-1318.
- 17. Gao Y.; and Bando Y.: Carbon Nanothermometer Containing Gallium, Nature, 415, 2002, 599.
- 18. Bonard J.D.; Siemens R.E.; and Oden L.L.: Phase Relations in the Molybdenum-gallium System, J. less-common metals, 30, 1973, 205-209.

WELL-ALIGNED CARBON NANOTUBES FROM METHANE/NITROGEN PLASMA

W. K. Wong, C. S. Lee, and S. T. Lee*

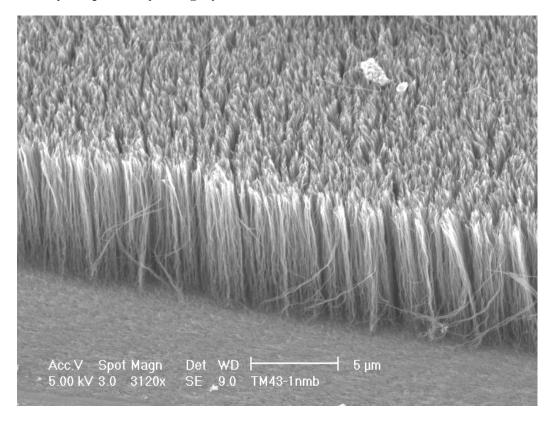
Center of Super-Diamond and Advanced Films (COSDAF) and Department of Physics and Materials Science, City University of Hong Kong, Hong Kong SAR, P.R. China

ABSTRACT

Well-aligned carbon nanotubes (CNTs) were grown by microwave plasma-enhanced chemical vapor deposition using N_2 as the carrier gases and CH_4 as the carbon source. Iron films with different thicknesses on silicon substrates acted as catalysts. The growth and field emission properties of the CNTs were studied as functions of the iron catalyst film thickness and the $CH_4:N_2$ ratio. Scanning Electron Microscopy (SEM) and Atomic Force Microscopy (AFM) were used to study morphologies of the CNT films and the relationship between the iron film thickness and size of the iron clusters formed after the plasma treatment.

Keywords: nanotubes, electron microscopy, Atomic Force Microscopy, microwave plasma-enhanced chemical vapor deposition.

*Corresponding author: apannale@cityu.edu.hk



SONOCHEMICAL SYNTHESIS OF CARBON NANOTUBES AND NANOONIONS UNDER AMBIENT CONDITIONS USING A SINW TEMPLATE

C. P. Li, X. H. Sun¹, N. B Wong¹, C. S. Lee, B. K Teo², S. T. Lee*

Center of Super-Diamond and Advanced Films (COSDAF) & Department of Physics and Materials Science, City University of Hong Kong, China

¹ COSDAF & Department of Biology and Chemistry, City University of Hong Kong, Hong Kong SAR, China

² On leave from Department of Chemistry, University of Illinois, Chicago IL 60607, U.S.A.

Abstract

Under ambient conditions, room-temperature and atmospheric-pressure, carbon nanotubes (CNTs) and carbon nanoonions (CNOs) were synthesized by reacting silicon nanowires (SiNWs) with organic solvents in a laboratory sonicator. As many common organic solvents are applicable and SiNWs can be produced plentifully from the oxide-assisted growth process, this simple method using the mildest growth conditions provides a convenient, inexpensive synthesis of large quantities of CNTs and CNOs. We believe both the local high temperature caused by sonication and the reductive power of the hydrogen-passivated SiNW (oxide-coated SiNW did not work) contribute to the conversion of the organic solvent molecules to graphite sheets which wrap around the SiNWs or Si nanoparticles (SiNP) to form CNTs or CNOs, respectively. With proper tuning (e.g. solvent type and temperature, ultrasonic power, etc), the sonochemical process can be adapted for mass production of either CNTs or CNOs.

Keywords: carbon nanotubes, carbon nanoonions, sonication, sonochemical synthesis

* Corresponding author: apannale@cityu.edu.hk

SYNTHESIS OF NANOGRAPHITE-RIBBON

Mutsumasa Kyotani

FCT Laboratory, Japan Fine Ceramics Center
Tsukuba Central 5-4-B, AIST, Higashi 1-1-1, Tsukuba, Ibaraki 305-8565, JAPAN
Chiharu Yamaguchi and Hisaji Matsui
Department of Research and Development, Osaka Gas Co

Department of Research and Development, Osaka Gas Co. 6-19-9 Torishima, Konohana-ku, Osaka 554-0051, JAPAN

Yoshinori Koga

Research Center for Advanced Carbon Materials Tsukuba Central 5-2, AIST, Higashi1-1-1, Tsukuba, Ibaraki 305-8565, JAPAN

ABSTRACT

Graphitic materials in nanometer size (nanographite) having edges of carbon hexagonal bond network is in very recent years attracting much attention because the theoretical approach has shown that such a nanographite is able to have a special electronic state at the edges, especially the zigzag ones. We have succeeded in synthesizing the nanographite by means of electrochemical reduction following electron beam irradiation for per-fluoro-aromatic pitch and by means of thermal decomposition of hydrocarbon polymers. The structural properties of graphitic materials were investigated using x-ray photo-electron spectroscopy, Raman scattering spectroscopy, x-ray diffraction measurements and electron microscopy. In this work, ribbon-shaped nanographite (nanographite-ribbon) in a thickness of below 10 nm having the edges was obtained. The structure of the nanographite-ribbon will be discussed.

Keywords: open edge graphite, nanographite, ribbon-shaped, π -electron localization, electron microscope,

INTRODUCTION

Recently it is well-known that carbon materials in nanometer size form curved sp² hexagonal bond networks containing pentagonal bonds such as fullerene molecules and carbon nanotubes. In most case, it is characteristic of these nano-size carbons that the edges of hexagonal networks are closed. Therefore, these nano-size carbons hardly take opened edges of the hexagonal networks.

On the other hand, graphite especially in macroscopic size is a flat crystal. In this case the edges of the hexagonal bond networks are opened. A flat graphite crystal in nano-size, however, is considered to be unstable because the edges of the hexagonal networks are able to have dangling bonds (ref. 1 to 2). In very recent years, theoretical studies on the electronic states of graphenes or flat graphite crystals in nano-size (nanographite) have been carried out using a tight-binding band calculation within Hückel approximation (ref. 3 to 5). According to this theory, it is possible that the π electrons localize at the edges of the hexagonal bond networks of the nanographene or the nanographite (ref. 3 to 5). This special electronic state at the edges is expected to bring about useful electronic and magnetic properties. So the nanographite with open edges is becoming known as another new class of carbon materials in nanometer size. However, there are few papers of studies of the synthesis of the nanographites so far (ref. 6).

We have undertaken to prepare electrochemically (ref. 7) and pyrolytically (ref. 8 to 9) carbon materials from aromatic pitch and hydrocarbon polymers as organic precursors, respectively. Nanographites have been obtained from these carbon materials with the treatment of electron beam irradiation. The synthesis and structure of nanographites are described in this paper.

EXPERIMENTAL

The electrochemical carbonization from fluorinated aromatic (naphthalene, anthracene, and quinoline) pitch as a organic precursor was carried out using an apparatus as described in a previous paper (ref. 7). Carbyne structure was contained in the carbon specimens obtained by the electrochemical reduction (ref. 7). The obtained carbon specimens were exposed to an electron beam of 0.01A/m^2 at $800\,^{\circ}\text{C}$ for 1 to 2 hr in vacuum of below 10^{-6} torr, using an electron microscope (ref. 7). We have used a polyacetylene thin film below $100\,\mu$ m in thickness as another organic precursor. The polyacetylene thin film was carbonized by means of pyrolysis under the same conditions as the exposure to an electron beam mentioned above (ref. 9).

Nanostructural properties of the electron-beam irradiated carbons described above were investigated using an x-ray photo-electron spectroscope (XPS) and scanning and transmission electron microscopes (SEM and TEM, respectively).

RESULTS AND DISCUSSION

The XPS spectra of the electron beam irradiated specimens showed an only peak corresponding to carbon/carbon bond energy. Therefore, the electronbeam irradiated specimens are almost pure carbon.

Figure 1 exhibits a high resolution TEM image (HRTEM)of typical nanographites synthesized from fluorinated anthracene pitch, showing ribbon-like shaped graphite in which (002) lattice fringe having 0.34nm in distance can be definitely observed. Two nanographite ribbons are seen in Figure 1, one of them being composed of 16 graphenes 5.60 nm in thickness (central part in Figure 1) and another one of 4 graphenes 1.38nm in thickness (upper left-side in

Figure 1). The nanographite ribbon as shown in Figure 1 was obtained by means of the electrochemical defluorination and then the treatment of electron beam irradiation for all of fluorinated aromatic pitch used in this work. Moreover, the carbon specimens obtained pyrolytically by an electron beam irradiation at 800 °C for polyacetylene thin films also form nanographite ribbons similar to those shown in Figure 1. Figure 2 demonstrates a schematic representation of a nanographite ribbon comprising 5 graphenes. Judging from all of TEM images observed, the nanographite ribbons are below 30nm in width and less than 1 μ m in length.

A bending nanographite ribbon is often observed. Figure 3 shows a HRTEM image of a bending nanographite ribbon synthesized from fluorinated quinolin pitch. The angle of the bending in this Figure is about 135 degree, while a bending angle is not constant and is more than 90 degree.

A branching nanographite ribbon is sometimes seen. In this nanographite ribbon, a layer being composed of less than ten graphene sheets is divided into two ones at some point, which is observed just as Y-junction.

As already mentioned in Introduction section, the nanographite ribbons described above are composed of flat graphene sheets which have open edges of sp² hexagonal carbon networks. Studies

<u>5 nm</u>

Fig.1 HRTEM of nanographite ribbons synthesized from fluorinated anthracene pitch, showing the one 5.60nm in thickness (center part) and another one 1.38nm (upper left-side).

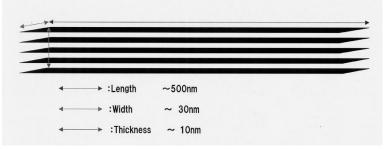


Fig.2 Schematic representation of a nanographite ribbon

on the electronic, magnetic, and chemical properties of the nanographite ribbon are now in progress.

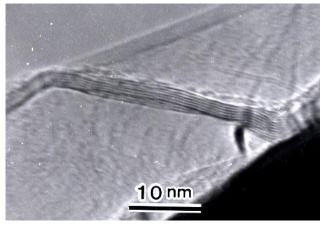


Fig.3 HRTEM of a nanographite ribbon synthesized from fluorineted quinolin pitch, showing bending at an angle of 135 degree.

CONCLUSIONS

Nanographite including nanographite ribbons having open edges of hexagonal carbon bond network is a prospective new carbon materials different from that having closed ones such as fullerens and nanotubes. Nanographite ribbons were synthesized by means of electrochemical carbonization of fluorinated aromatic pitch and then treatment of electron beam irradiation to the carbon. Nanographite ribbons synthesized comprise several to tens flat graphenes having below 30nm in width. Bending and branching nanographite ribbons were sometimes obtained.

REFERENCES

- 1. Krot, H.W.,: Carbon Onions Introduce New Flavour to Fullerene studies, Nature, 359, 1992, p.670.
- 2. Ugarte, D.,: Curling and Closure of Graphitic Networks under Electron-beam Irradiation, Nature, 1992, p707.
- 3. Fujita M., Wakabayashi K., Nakada K., et al.,: Peculiar Localized State at Zigzag Graphite Edge, J.Phys.Soc.Jpn., 65, 1996, p1920.
- 4. Nakada K., Fujita M., Dresselhaus, G.,: Edge State in Graphene Ribbons: Nanometer Size Effect and Edge Shape Dependence, Phys.Rev. B, 54, 1996, p17954.
- 5. Kawai T., Miyamoto Y., Sugino O., et al.,: Graphitic Ribbons without Hydrogen-Termination: Electronic Structure and Stabilities, Phys.Rev. B, 62, 2000, pR16349.
- 6. Li, Y., Xie, S., Zhou, D., et al.,: Nanographite Ribbons Grown from a SiC Arc-Discharge in a Hydrogen Atmosphere, Carbon, 39, 2001, p626.
- 7. Kyotani M., Yamaguchi C., Goto A., et al.,: Structural Properties of Carbon Materials from the Electrochemical Reduction of Fluorinated Naphthalene Pitch, Carbon, 40, 2002,p1583.
- 8. Goto A., Kyotani M., Tsugawa K., et al.,: Nanostructures of Pyrolytic Carbon from a Polyacetylene Film, Carbon, 41, 2003, p131.
- 9. Kyotani M., Goto A., Piao, G., et al.,: Nanostructural Properties of Pyrolytic Carbon from Polyacetylene Thin Film, Synth.Met., in press.

About the influence of bioaktivite carbon materials nanoclusters structures on effectivity of ecosystem sorption-catalytic purifying from oil products

Shvets Dmitriy

Institute for Sorption and Problems of Endoecology, NAS of Ukraine
Mailing address: 13, General Naumov Str., 03164, Kiev-164, Ukraine
dshvetz@ispe.kiev.ua

Abstract

Abstract not available at time of printing.

KINETICS OF CARBON NANOTUBE FOREST GROWTH BY CHEMICAL VAPOR DEPOSITION

O. A. LOUCHEV, T. LAUDE, Y. SATO AND H. KANDA

National Institute for Materials Science, 1-1 Namiki, Tsukuba, Ibaraki 305-0044, Japan

A theoretical study of carbon nanotube (NT) forest growth by chemical vapor deposition is given, including (i) ballistic mode of C species impingement into the NT surface, (ii) C diffusion over NT surface and through the metal nanoparticle and (iii) the temperature drop at the NT tip occurring with increase in NT length. The presence of a metal nanoparticle is shown to shift NT growth from being surface diffusion controlled to being controlled by bulk diffusion through the nanoparticle. For typical growth conditions the growth rate is shown to be controlled simultaneously by surface diffusion over NT surface and bulk diffusion of C through metal nanoparticle. Even in specific cases where NT growth rate is controlled by bulk diffusion through the nanoparticle the initial stage may be controlled by surface diffusion, as revealed by the exponential change in NT length with time. A parametric study of the growth rate of NT forest with metal nanoparticles held at the NT tips as a function of temperature reveals the existence of a maximum near 1050-1100 K, agreeing with reported experiments. A thermal analysis based upon the heat conductance equation shows that with NT forest growth the temperature of the NT tips decreases, leading to growth deceleration and termination, suggesting that the larger the pressure the smaller the forest height that may be grown.

Keywords: growth kinetics, carbon nanotube, forest, diffusion

1. INTRODUCTION

The growth of well aligned C nanotube (NT) forests by chemical vapor deposition (CVD) is an effective technique for NT production studied by several groups trying to optimize the parameters of this process for cold electron emitters and other applications [1-21]. Wherever the catalyst nanoparticles are found in growth experiments, i. e. on the NT tips or on the substrate, the majority of experimental reports refer to a model of carbon filament growth by continuous C diffusion or extrusion through the metal nanoparticle [22-24] ("tip" or "base" growth model). However, NT forests have also successfully been grown by plasma enhanced CVD even without a catalyst [21], suggesting that another kinetical mechanism may be involved in this process. Additionally, Ref. [25] provides an order to magnitude analysis of CVD process of carbon NT forest growth outlining several contradictions which arise in the application of the model [22-24] for a particular experimental study where the Fe catalyst remained at the substrate [14]. Ref. [25] suggests another NT forest growth mechanism within the general framework of the surface diffusion (SD) model [25-28] which may be responsible for CVD growth in many practically important cases. In particular, the involvement of the SD mechanism explains [28] the existence of the exponential time dependence observed in NT growth. In the case of open ended NT growth controlled by SD this exponential stage extends to the moment when the NT length reaches the length of surface diffusion, of order 0.1-1 microns depending on T [28]. However, experimental data related to the growth mediated by metal catalyst particles [23] shows that, when the particle is present, this exponential stage reduces to the order of 10 nanometers and even less, depending on the metal used. In Ref. [25] we suggested that the metal nanoparticles do not play a significant role in feeding NT growth because the carbon flux is mainly provided by SD over the NT surface. In contrast, an early review [23] and other more recent papers, suggest that the growth is controlled by bulk diffusion through the metal particle. In this paper we provide a comprehensive analysis based on an analytical model which includes both surface diffusion over NT surface and bulk diffusion of C through the metal particle. The resulting analytical expressions allow one to distinguish various modes of forest growth and determine growth controlling effects under different operating conditions.

NASA/CP—2003-212319 46 August 18, 2003

2. CARBON NANOTUBE FOREST GROWTH KINETICS

2.1 Ballistic mass transfer

Let us consider parameters for a NT forest grown on a metal catalyst nanoparticle array (see Fig. 1) in order to analyze the transport phenomena in the gas phase involved in growth experiments [14]. In this and many other practical cases where metal particles remain at the substrate, base growth via the diffusion of C through the particles cannot be involved in the latest postnucleation stages of NT forest growth, when the NT length exceeds several microns. This is because, to reach the metal particles remaining on the substrate, chemically active C species should penetrate through the forest. This looks to be impossible in view of the typical mean free path in the gas estimated as:

$$l_g \approx k_B T / \left(\sqrt{2}\sigma P\right) \approx 30 - 50 \,\mu m \,, \tag{1}$$

for operational conditions $P \approx 20$ Torr and T=600-1000 K [18], ($\sigma \approx 10^{-19}$ m²) which appears to be much higher than the intertube distance within the forest, 1 μm (for NT surface density $N=10^8$ cm²). That is, inside the forest ballistic mass transfer takes place in which chemically active carbon species collide only with NTs without collisions with gas species, and without diffusion along the intertube space to the forest bottom.

The ballistic penetration of species into the forest may be characterized by the distribution of the angle factor along the NT surface given by:

$$F_{\text{gas}}(x,l) = \pi^{-1} \iint_{\Omega} (\mathbf{w}, \mathbf{n}) d^{2}\Omega$$
(2)

where Ω is the solid angle within which the gas phase is "seen" from a particular point of the NT surface. The distribution of the angle factor computed numerically and averaged over the NT circumference:

$$\bar{F}_{gas}(x) = \frac{1}{2\pi R} \int_{0}^{2\pi} F_{gas}(x,l)dl , \qquad (3)$$

is given in Fig.2 for the intertube separation $l_{\text{int}}=1~\mu m$ [14] and for typical values of NT radius $R=0.1-0.15~\mu m$. It shows that the impingement rate decays rapidly towards the forest bottom. For a NT forest with NT radius $R=0.1~\mu m$ at a distance of 10 μm from the top the impingement rate decreases by an order of magnitude (from 0.5

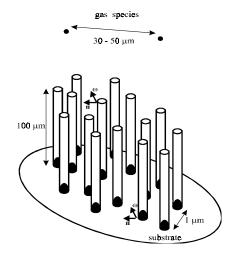


Fig.1 Sketch of carbon NT forest growth.

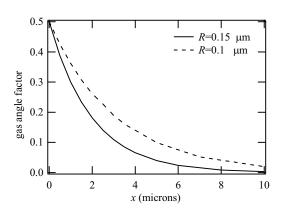


Fig. 2 Angle factor along NT surface from the top.

near the top to 0.02) and for R=0.15 μm this decay is even more significant. These calculations show that majority of species impinge into the NT surface within several microns of the top and do not penetrate to the bottom of a NT forest of several dozens of microns in depth [14]. The distributions given in Fig. 2 may be well approximated by an exponential function, i.e. $0.5\exp(-x/l^*)$ with characteristic decay length $l^*=2-3$ microns.

2.2 Metal nanoparticle mediated tip growth kinetics

Let us now consider NT forest growth for the case when metal particles are held on NT tips. Metal nanoparticles play multifold role in C NT growth: (i) nucleation, (ii) inhibition of NT end closure by pentagons and (iii) the selection mechanism which defines whether metal particles are held on NT tips or remain on the substrate. Nevertheless, the main pathway of C incorporation into NT corresponds to the C flux (i) impinging initially into the NT surface, (ii) diffusing over NT surface to the metal particle where the NT is rooted, and (iii) later diffusing through the particle to the NT edge. In order to reveal the interplay of SD diffusion over the NT surface and bulk diffusion through the metal particle we consider the initial NT growth stage when the NT forest length is much smaller than the ballistic penetration length and the C flux may be assumed to be constant over the NT surface. In this case, the kinetic equation for NT growth, formulated originally for SWNT growth [28], may be used including the number of atomic layers in the NT wall, N, as:

$$dL / dt = \frac{\Omega k Q_c \tau_a \sinh(L / \lambda_D)}{N \left[\sinh(L / \lambda_D) + \left(k \lambda_D / D_s \right) \cosh(L / \lambda_D) \right]}, \quad (4)$$

where Q_c is the carbon flux density onto NT surface, Ω is the area per one C atom in the NT wall, $\lambda_D \approx (D_S \tau_a)^{1/2}$

is the surface diffusion length, $D_S \approx a_0^2 v \exp(-\delta E_D / k_B T)$ is the SD coefficient dependent on the activation energy

of δE_d , $\tau_a \approx v^{-1} \exp(E_a / k_B T)$ is the adsorption time dependent on the adsorption energy E_a , and k is the kinetic constant of atom incorporation into NT wall. This constant is given by:

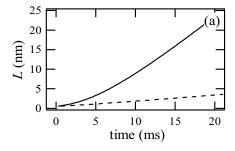
$$k \approx a_0 / \tau_{inc} \qquad , \tag{5}$$

where a_0 is the characteristic growth distance per one atom, and τ_{inc} is the characteristic time, required for the adatom to transfer from the lateral surface onto the NT edge and to incorporate into it. In general, τ_{inc} includes several steps. In the case of MWNTs growing with a metal particle attached to the end the slowest step is obviously defined by C atom diffusion from the edge of the external layer to the edge of the internal layer through the metal layer

with thickness δ corresponding to that of NT wall, $\tau_{inc} \approx \delta^2 / D_b$, giving:

$$k \approx a_0 D_b / \delta^2$$
, (6)
bulk diffusion coefficient with $D_0 = 0.1 - 0.5$ cm²/s and $\delta E_b = 1.4 - 1.6$ eV for

where $D_b \approx D_0 \exp(-\delta E_b / k_B T)$ is the bulk diffusion coefficient with $D_0 = 0.1 - 0.5$ cm²/s and $\delta E_b = 1.4 - 1.6$ eV for practical growth temperatures T=1000-1500 K [29].



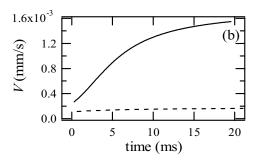


Fig. 3 MWNT length (a) and MWNT growth rate (b) for growth of 10 layer MWNT under control of bulk diffusion through the metal nanoparticle $k\lambda_D/D_S \ll 1$.

In Fig. 3 we show the solution of Eq. (4) for T=1300 K and $Q_c=2\times 10^{-19} \text{ 1/cm}^2\text{s}$ (equivalent to $P_c=10 \text{ Pa}$), calculated for $E_a=1.8$ eV and $\delta E_d=0.13$ eV [26] for two different modes corresponding to MWNT growth consisting of 10 atomic layers at the edge of which a metal particle is attached with diffusion coefficient corresponding to the (i) liquid metal $D_{\rm b}=10^{-5}~{\rm cm^2/s}$ (solid line), and (ii) the solid metal $D_{\rm b}=10^{-6}~{\rm cm^2/s}$ (broken line). For both cases considered in Fig. 3 the values of $\lambda_D = 0.2 \ \mu m$ and $D_s = 1.9 \times 10^{-3} \ cm^2/s$, and the difference in growth behavior is caused only by the kinetic constant of incorporation, Eqs. (5). For MWNT growth with meta nanoparticle $k=1.2 \times 10^{-2}$ m/s (solid line) or $k=1.2\times10^{-3}$ m/s (broken line). Correspondingly, the growth of a MWNT with $k\lambda_D/D_s << 1$ is controlled by C diffusion through the metal particle. The growth modes depicted in Fig. 3 agree well with experimental data [23], which show that the dependence of L on time may be linear or exponential depending on the metal involved in the synthesis. The presence of the exponential dependence in MWNT growth [23], showing that in the initial stage $dL / dt \propto L$, is a clear experimental indication of the involvement of the SD in carbon NT growth.

2.3 Steady-state stage and temperature dependence of the growth rate

let us consider steady state growth of the NT forest, taking into account the exponential decay of the impinging flux along the MWNT surface and also investigating how the MWNT forest growth rate depends on the temperature. We use here a one dimensional quasi-steady-state surface diffusion approximation:

$$D_S d^2 n / dx^2 + Q_C(x) - n / \tau_a = 0, (7)$$

 $D_S d^2 n / dx^2 + Q_C(x) - n / \tau_a = 0,$ (7) where *n* is the surface concentration and $Q_c(x)$ is the C flux distribution along NT surface of defined by:

$$Q_C(x) = Q_C \stackrel{-}{F}_{gas}(x) \approx 0.5 Q_C \exp(-x / l^*),$$
 (8)

For the case when the metal particle is detached from the substrate and remains at the MWNT tip we use the following condition on the NT edge x=0:

$$D_{S}dn / dx = kn \quad , \tag{9}$$

where the kinetic constant k is defined by Eq. (6).

Assuming that the NT length is sufficiently high, i.e. dn/dx=0 at $x \to \infty$ we find an equation for the MWNT forest growth rate with metal nanoparticles on the tips:

$$dL / dt = \frac{0.5\Omega \ Q_c \tau_a k}{N(1 + \lambda_D / l^*)(1 + k\lambda_D / D_s)} \qquad , \tag{10}$$

In Fig. 4 we show the dependence of the dimensionless value of growth rate $VN / (a_0 \Omega Q_C)$ as a function of T for 10-layer MWNT growth with a metal particle at the edge and parameters for diffusion coefficient $D_{\rm b}$, $D_0=0.1~{\rm cm^2/cm^2}$ s and $\delta E_b = 1.4$ eV, corresponding to a solid metal. The ballistic factor is estimated by Eq. (8) with typical values of $l^*=2$, 3 microns, which approximates well the distribution shown in Fig. 2.Both graphics shown in Fig. 4 exhibit a maximum in the growth rate near T=1050 -1100 K agreeing with experimental data [18]. We are not able to compare absolute values of the growth rates because of the unavailability of measurements of real C fluxes impinging into the NT surface in the experimental study [18].

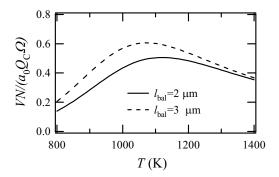


Fig. 4 MWNT growth rate as function of T.

3. THERMAL PHYSICS AND NT GROWTH DECELERATION EFFECT

The growth rate depends on *T* and with increase in NT length the temperature at the tip may change from that of the substrate. The temperature distribution along an individual NT may be considered on the basis of the steady-state heat conductance approximation for thermally thin body:

$$k_S \frac{d^2 T}{dx^2} + \frac{1}{\delta} \left\{ q(x) - \varepsilon \sigma T^4 - h_g (T - T_g) \right\} = 0 \quad , \tag{11}$$

where $k_s = 250-400$ W/m K is the heat conductance, q(x) is the distribution of heat sources including (i) all heat effects ongoing on the NT surface and (ii) local radiative flux from surrounding surfaces (substrate, neighboring NTs), seen from a particular point x, h_g is the heat exchange with atoms of the inert gas proportional to the kinetic

energy difference prior to and after the collision with the NT, $\Delta E_k \approx 3k_B \left(T - T_g\right)/2$, and to the number of

collisions per unit area $Q_g = P_g / (2\pi m_g k_B T)^{1/2}$ for the buffer gas under the pressure P_g , giving:

$$h_{\rm g} \approx 3Q_{\rm g}k_{\rm B}/2\,,\tag{12}$$

Fig. 5 shows the temperature change on the NT tip for different NT lengths L as a function of the ambient gas pressure at $T_{\rm g}$ =300 K. The radiative heating from the substrate and the neighboring NTs as well as from the surrounding cold wall reactor is approximated in Eq. (11) by:

$$q_r(x) \approx \left[1 - 0.5 \exp(-x / l^*)\right] \varepsilon \sigma T_S^4 + 0.5 \exp(-x / l^*) \varepsilon \sigma T_0^4, \tag{13}$$

which is similar to the ballistic impingement function, Eqs. (8), due to the formal equivalency of the ballistic impingement and radiation flux incoming from the same solid angles. The problem is solved for black body approximation with the boundary condition $T=T_s$ at the NT root (x=L). Fig. 5 shows that with increase in the NT length the temperature decreases leading to deceleration of NT growth. Fig. 5 show what the temperature on the NT tip would be if the NT had the length of 10 or 30 microns. In reality, this figure shows that the NT may not reach this length because of the temperature fall on the tip. Many experimental studies on NT forest growth report growth rate deceleration when the NT forest length attains a level well similar to the heat conductance length: growth deceleration is reported in Ref. [18]; another study reports that, during synthesis the growth rate started to decrease for NT forest lengths over 30 microns [17]. Our model suggests that it is caused by the temperature decrease on the upper part of the NTs where we believe growth takes due to the lack of chemically active carbon penetration to the bottom of the forest several dozen microns in depth. A similar effect was recently observed and interpreted as a time dependence anomaly [20].

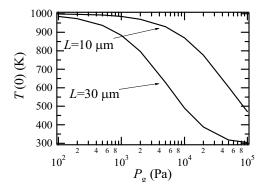


Fig. 5 Dependence of the temperature on the tip of 10 and 30 micron long NTs (10 atomic layers) as a function of $P_{\rm g}$ (He) for $T_{\rm g}$ =300 K.

Fig. 5 suggests that the higher the pressure the smaller the length of the NT forest which may be grown. In particular, Fig. 5 shows that for $P_g = 10^5$ Pa the maximal length of NT forest will be several microns and after that NT growth in the axial direction should stop because the NT tip will be "frozen". However, for NT forest dimensions of several microns C deposition may actually continue, leading to NT radial extension at the bases, where T is kept close to T_s . This result of our model agrees well with the experimental results [12] on NT forest growth performed at atmospheric pressure. Even a moderate temperature change on the NT tip is able to decrease significantly the diffusion time through the nanoparticle body, leading to the precipitation of C on the upper part of the metal nanoparticle, growth termination or a change of growth mode.

4. SUMMARY

The considered model does not take into account several microenergetic parameters, which define chemical kinetics transformation of hydrocarbon species on the surface of the NT and on metal nanoparticle. These parameters including chemisorption of different carbon species on the surface of the NT and metal nanoparticle, and activation energies of dehydrogenation, are not available, preventing a more comprehensive analysis. Determination of these surface chemistry parameters would allow a significantly deeper insight into this subject. The determination of such parameters will also significantly increase the predictive value of this model which even in its present simplified form generally agrees with experimental observations and allows clear interpretation of many effects.

REFERENCES

- [1] W. Z. Li et al., Science 274, 1701 (1996).
- [2] M. Terrones et al., Nature 388, 52 (1997).
- [3] Z. W. Pan et. al, Nature 394, 631 (1998).
- [4] Z. F. Ren et al., Science 282, 1105 (1998).
- [5] Z. P. Huang et al., Appl. Phys. Lett. 73, 3845 (1998).
- [6] Z. W. Pan et al., Chem. Phys. Lett. 299, 97 (1999).
- [7] S. Fa et al., Science 283, 512 (1999).
- [8] J. S. Suh and J. S. Lee, Appl. Phys. Lett. 75, 2047 (1999).
- [9] C. Bower, W. Zhu, S. Jin and O. Zhou, Appl. Phys. Lett. 77, 830 (2000).
- [10] W.-Q. Han et. al, Appl. Phys. Lett. 77, 1807 (200)
- [11] N. Grobert et al., Appl. Phys. A 70, 175-183 (2000).
- [12] H. Ago et al., Appl. Phys. Lett. 77, 79 (2000).
- [13] C. J. Lee and J. Park, Appl. Phys. Lett. 77, 3397 (2000).
- [14] H. Cui, O. Zhou and B. R. Stoner, J. Appl. Phys. 88, 6072 (2000).
- [15] M. Okai, T. Muneyoshi, T. Yaguchi and S. Sasaki, Appl. Phys. Lett. 77, 3468 (2000).
- [16] Y. Y. Wei, G. Eres, V. I. Merculov and D. H. Lowndes, Appl. Phys. Lett. 78 1394 (2001).
- [17] C. J. Lee, S. C. Lyu, Y. R. Cho, J. H. Lee, K. I. Cho, Chem. Phys. Lett. 341, 245 (2001).
- [18] M. Chhowalla et al., J. Appl. Phys. 90, 5308 (2001).
- [19] C. K. Lee and J. Park, J. Phys. Chem. **B** 105, 2365 (2001).
- [20] B. H. J. Jeong et al., Chem. Vap. Deposition 8, 11 (2001).
- [21] A. N. Obraztsov et al., J. Vac. Sci. Technol. B 18, 1059 (2001).
- [22] A. Oberline, M. Endo and T. Koyama, J. Crystal Growth 32, 335 (1976).
- [23] R. T. K. Baker and P. S. Harris, In Chemistry and Physics of Carbon, Eds. P. L. Walker, Jr. and P. A. Thrower, (Deker, New York, 1978) pp.83-161, and refs. therein.
- [24] G. G. Tibbetts, J. Crystal Growth 66, 632 (1984).
- [25] O. A. Louchev, Y. Sato and H. Kanda, Appl. Phys. Lett. 80, 2752 (2002).
- [26] O. A. Louchev, Appl. Phys. Lett. 71, 3522 (1997).
- [27] Y. H. Lee, S. G. Kim and D. Tomanek, *Phys. Rev. Lett.* **78**, 2393 (1997).
- [28] O. A. Louchev, Y. Sato and H. Kanda, Phys. Rev. E 66, 011601 (2002).
- [29] Physical properties. Eds. I. S. Grigoriev and E. Z. Meilikhov (Moscow, Energoatomizdat, 1991) (Fizicheskie vellichini, in Russian).

Carbon nanotube nucleation from graphitic nanofragments

Oleg A. Louchev

Advanced Materials Laboratory, National Institute for Materials Science louchev.oleg@nims.go.jp

James R. Hester

Australian Nuclear Science and Technology Organization,
PMB 1, Menai, NSW 2234, Australia

Abstract

A detailed analysis of nanotube nucleation from graphitic nanofragments by thermal vibration via the interaction with amorphous carbon, fullerene-like and carbonized metal catalyst nanoparticles is given predicting a variety of nanotube chiralities observed experimentally. The issue of kinetic selection between (i) carbon nanosheet wrapping around the metal nanoparticle, (ii) NT growth from the nanoparticle surface by the root mechanism and (iii) metal nanoparticle surface being covered by an amorphous carbon layer is considered. The temperature fall rate and the heat dissipation by the inert gas are shown to play a crucial role in providing conditions for the root mechanism of NT nucleation. At low inert gas pressure the heat dissipation is very slow and the time required for particle cooling and C segregation is comparable with the characteristic time of C impingement into the surface from vapor. Under these conditions nanoparticles will be covered by C impinging from the vapor, and the root mechanism of NT nucleation is inhibited. In this case the nanoparticle provides a template for carbon condensation which can lead to the formation of a graphitic layer and nanoring nuclei wrapped around the nanoparticle. However, at inert gas pressures >0.1 bar the characteristic time for metal-carbon nanoparticle cooling becomes much lower than the characteristic impingement time of C from vapor providing conditions for NT nuclei formation by the kinetic pathway of C segregation from metal particle and root mechanism.

KINETICS STUDY OF Cd²⁺ IONS IN SODIUM SULFATE SOLUTION AT CARBON NANOTUBE ELECTRODE

C. G. Hu¹, W. L. Wang ¹, K. J. Liao ¹, H. Wang ¹, X. H. Xian ²

¹Department of Applied Physics, Chongqing University, Chongqing 400044, P. R. China ²Department of Chemistry, Chongqing University, Chongqing 400030, P. R. China

ABSTRACT

The electrochemical response to Cd²⁺ ions on an electrode of carbon nanotubes functionalized with carboxylic acid group was studied mainly by use of cyclic voltammetry in aqueous sodium sulfate. A well-defined quasi-reversible voltammograms for the Cd²⁺ / Cd redox couple were shown on the carbon nanotube electrode, and the anodic and cathodic peak potentials were –0.67 V and –0.92 V vs. SCE at a scan rate of 50 mVs⁻¹, respectively. Both anodic and cathodic peak currents depended linearly on the square root of the scan rate over the range of 0.05-0.8 Vs⁻¹. Such linearity indicated that the reaction rate was limited by semi-infinite linear diffusion of the analyte to the interfacial reaction zone. The electron-transfer and diffusion coefficients for Cd²⁺ / Cd were evaluated from the dependence of the voltammograms on the potential scan rate and concentration of analyte.

Keywords: carbon nanotubes; cyclic voltammetry; cadmium chloride; electron-transfer rate coefficient; quasi-reversibility

INTRODUCTION

Carbon nanotube (CNT) has attracted the attention of many scientists worldwide. The small dimensions, strength and the remarkable physical properties of these structures make them a very unique material with a whole range of promising applications (ref. 1 to 4). Due to their atomic structure, carbon nanotubes behave electrically as metal or as a semiconductor (ref. 5 to 7). The subtle electronic properties suggest that carbon nanotubes have the ability to promote electron-transfer reactions when used as an electrode in chemical reactions (ref. 8). But as a nanotube is such an unusual macromolecule, it leads to indissolubility. However, chemical reactions might happen on nanotubes when some changes in the structure of nanotubes take place and some active functional groups appear on it, such as hydroxyl and carboxyl (ref. 9 to 11). Our previous investigation has demonstrated (ref. 12), with a high aspect ratio, the modified CNT films have a much larger surface area than conventional electrodes such as glassy carbon (CG) electrode and highly oriented pyrolytic graphite (HOPG) electrode, and it results in a large charge current on CNT electrode. The carboxyl-modified CNT electrode showed high electrochemical activity. An electroanalytical application of this new electrode material was highlighted.

Cadmium is one of industrial toxic element and is widely found in our environment, which usually exists in a form of inorganic compounds. It has been reported that cadmium chloride can cause damage to liver, lung and kidney in human body. Moreover, it induces disorder of energy metabolism and endocrine function by poisoning endocrine gland such as sex gland, thyroid gland and adrenal gland. However, in many cases, a process of physical

NASA/CP—2003-212319 53 August 18, 2003

system invaded by toxic element is electrochemical reaction process. In order to know clearly how cadmium ion acts in physiological system, a reliable electrochemical analysis for trace levels of cadmium chloride is needed.

In this work, we have investigated the behaviors of Cd²⁺ ion in NaSO₄ solution at the carboxyl-modified CNT electrode and a well-defined quasi-reversible voltammograms are shown for the Cd²⁺/Cd redox couple. The equilibrium redox potential of the Cd²⁺/Cd couple was derived from the cyclic voltammograms. The electron-transfer and diffusion coefficients for Cd²⁺/Cd and were evaluated from the dependence of the voltammograms on the potential scan rate and concentration of analyte.

EXPERIMENTAL

All the reagents used were of analytical grade. All solutions were prepared in deionized distilled water and all experiments were carried out at room temperature (ca. 23 2 °C).

Cyclic voltammetric experiments were performed using a Microcomputer-based Electrochemical Analyzer (LK98BII, home made) with a conventional three-electrode cell. The working electrodes were the modified CNT electrod, the auxiliary electrode was a platinum electrode, and a saturated calomel electrode (SCE) was used as the reference electrode.

FTIR spectra (MAGNA-IR 550, USA) was used to characterize the modified CNTs.

Carbon nanotubes were synthesized by hot filament chemical vapor deposition and then were modified by concentrated nitric acid. The details of the fabrication and modification have been reported elsewhere (ref. 12). The only difference is that we prolonged the ultrasonic dispersing time to 10 min and controlled the temperature at 40 °C during the dispersing process.

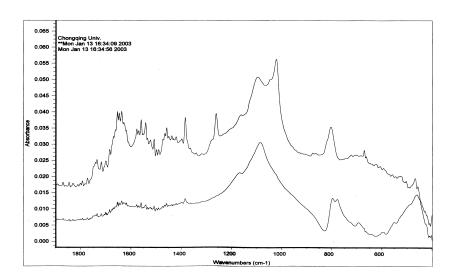


Figure 1. FTIR spectra of the CNTs before (bottom) and after (top) the modification.

The modified CNT electrode was prepared by sonic dispersing the modified CNTs in DMF to give a black solution, then depositing them on the surface of insulated substrate. Ohmic contacts for the planar electrodes were made in the front side of the films with silver paste. The electrodes were mounted with epoxy. Film thickness was

approx. 20 μm and resistivity was about 350 Ω -cm. The apparent geometric area of the working electrode was estimated to be 0.126 cm².

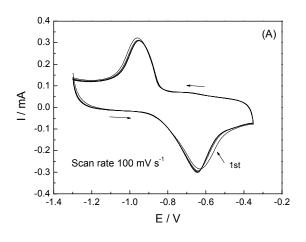
RESULTS AND DISCUSSION

CHARACTERISTICS OF THE ELECTROACTIVE GROUP

The morphology of the modified CNTs is characterized by transmission electron microscopy (TEM) image. The average diameter of the CNTs is about thirty nm from TEM (not shown here). The end of the CNT is opened and there are a few defects on the wall that might be attributed to the treatment with nitric acid. We assume that some functional groups might have been grown on the end and defects sites, which can greatly enhance the solubility and electrochemical activity of the CNTs. In order to study which group appears on the modified CNTs, the FTIR experiment is performed on the solid CNTs with potassium bromide. From figure 1 (top) we can see the appearance of peaks corresponding to the carboxylic acid group: >C=O stretch vibration $v_{>C=O}$, at 1730 cm⁻¹, and the two peaks due to the couple of C-O stretch vibration v_{C-O} and OH bend vibration δ_{OH} , at 1380 cm⁻¹ and at 1260 cm⁻¹, which is in accordance with literature (ref. 13,14).

CYCLIC VOLTAMMETRY

Cyclic voltammetry analysis has been used to characterize CNT electrodes in past few years. Most of these CNT electrodes are formed casting CNTs on traditional electrodes, such as Au, Pt, GC and HOPG electrodes (ref. 13,15,16), as a kind of modified electrode. However, our electrode is pure CNT electrode different from other CNT electrodes.



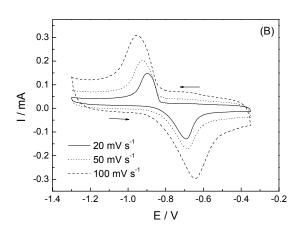


Figure 2. Cyclic voltammograms for five cyclics (A) and different scan rates (B) at the CNT electrode in 2 m mol L⁻¹ CdCl₂ / 0.5 mol L⁻¹ Na₂SO₄.

Figure 2. (A) shows the cyclic volatmograms for our carboxyl modified CNT electrode in 2 m mol L^{-1} CdCl₂ with supporting electrolyte of 0.5 mol L^{-1} Na₂SO₄ at scan rate of 100 mV s⁻¹. From this, we can see that the redox reaction

Cd²⁺+2e Cd, oxidation and reduction peak potentials are at -0.645 V and -0.953 V, respectively. The curves are almost repeatable, which indicates the advantages of the CNT electrode in electroanalysis. Cyclic voltametric behaviors under different scan rates are presented in Figure 2. (B). From the further study, we can obtained that the peak currents are increased linearly with square root of scan rate, only with a small non-zero intercepts. The cathodic peak current is

$$I_{pc} = -0.039 + 1.105 v^{1/2}, \quad r = 0.998,$$
 (1)

where, v is scan rate and r is linear correlation coefficient. This predicts that the cathodic reaction is under control of the diffusion of Cd^{2+} . A similar conclusion can be obtained for anodic reaction process. The voltametric study has shown that the reaction at the CNT electrode may be analyzed by the quasi-reversibility criteria: I_p increases with $v^{1/2}$ but do not completely keep proportionality; ΔE_p is larger than 60/n mV and increases with v.

For Nernstian systems, the peak current can be described as (ref. 17)

$$I_{p} = (2.69 \times 10^{5}) n^{\frac{3}{2}} A D_{j}^{\frac{1}{2}} C_{j}^{*} v^{\frac{1}{2}},$$
 (2)

300

at 25 °C, for A (the effective area of electrode) in cm², D_j (diffusion coefficient of species j) in cm² s⁻¹, C_j^* (bulk concentration of species j) in mol L⁻¹ cm⁻³, v in V s⁻¹ and I_p in amperes. If a small non-zero intercepts in (1) is neglected and we assume that equation (2) still suits the redox species of Cd²⁺/Cd, we can calculate the diffusion coefficient D. But first, we have to calculate the effective area of the CNT electrode A here from the result of our other experiment of Fe³⁺/Fe²⁺ in 1 mol L⁻¹ HClO₄ and diffusion coefficient of Fe³⁺/Fe²⁺ in the same solution (ref. 18). Then the diffusion coefficient of Cd²⁺ in 0.5 mol L⁻¹ Na₂SO₄ is estimated as $D = 3.64 \times 10^{-6}$ cm² s⁻¹.

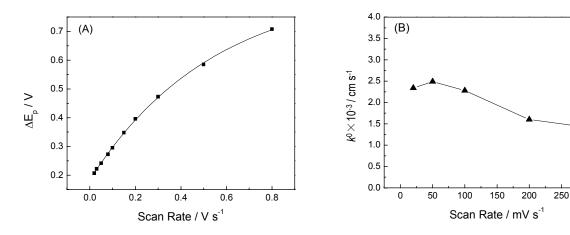


Figure 3. The difference between the anodic and cathodic peaks ΔE_p (A) and kinetic parameters k^0 (B) as a function of scan rate for the CNT electrode in 2 m mol L⁻¹ CdCl₂ / 0.5 mol L⁻¹ Na₂SO₄.

Figure 3. (A) shows that the separation ΔE_p is associated with the rate of electron transfer kinetics at the CNT electrode surface. For quasi-reversible reactions I_p is not proportional to $v^{1/2}$, as is observed by reversible and irreversible reactions, where k_0 can be evaluated directly from this relation. The treatment of systems called quasi-reversible is associated with reactions that show electron transfer kinetic limitations where the reverse reaction has to be considered. The results presented in our experiments have led us to conclude that this is the more suitable treatment for such CNT electrode for the redox systems studied, mainly due to the range of ΔE_p obtained as a function of scan rate.

The evaluation of the papameter k^0 as a function of ΔE_p is performed by using the curve of the dimensionless parameter ψ (ref. 17). The results obey the validity domain for typical values presented in the literature, where ψ is defined by:

$$\psi = \frac{(D_O/D_R)^{\frac{3}{2}} k^0}{[D_O \pi v (nF/RT)]^{\frac{1}{2}}}.$$
 (3)

Some approximations are made, by considering the diffusion coefficient $D_O = D_R$ and ψ becomes independent of the transfer coefficient α . The other parameters used are the Faraday constant F, the scan rate v, the number of electrons evolved in the reaction n, at T=298 K. A table of typical results of ψ dependence on ΔE_p is obtained in reference (ref. 17). This method is very useful in estimating k^0 for quasi-reversible reaction by determining the variation of ΔE_p with v, and from variation of parameter ψ . From equation (3) k^0 is obtained as a function of scan rate as shown in figure 3. (B). There is a maximum of kinetic parameter k^0 at scan rate of 50 mV s⁻¹ and as the scan rate increases, the k^0 decreases and goes to be a constant.

CONCLUSION

The CNTs, treated by concentrated nitric acid and characterized by FTIR spectra, were used as electroanalytical electrode to investigate the electrochemical behaviors of 2 m mol L^{-1} CdCl₂ in 0.5 mol L^{-1} Na₂SO₄. The electrochemical study has shown that redox reactions of Cd²⁺/Cd system at the CNT electrode follow the quasi-reversibility criteria. Both anodic and cathodic peak currents are as a linear function of square root of scan rate, which indicates that the redox processes are controlled by diffusion of the species. The diffusion coefficient has been calculated for cathodic reaction. We also observed that the electron-transfer rate coefficient k^0 for the system is as a function of scan rate and has a maximum at scan rate of 50 mV s⁻¹. From the results, the CNT electrode as an electroanalytical electrode is highlighted.

ACKNOWLEDGMENTS

This work has been financially supported by the Applied Research in Basics Foundation (7327) of Scientific Committee of Chongqing City.

REFERENCE

- 1. Iijima S., Helical microtubules of graphitic carbon, Nature, vol.354, 1991, 56-58
- Kazaoui S., Mianmi N., Jacquemin R., Amphoteric doping of single-wall carbon-nanotube thin films as probed by optical absorption spectroscopy, Phys. Rev. B, vol.60, no.19, 1999, 13339-13342
- 3. Bower C., Zhou O., Nucleation and growth of carbon nanotubes by microwave plasma chemical vapor deposition, Appl. Phys. Lett. vol.77, no.17, 2000, 2767-2769
- 4. Bachtold A., Hadley P., Nakanishi T., Dekker C., Logic Circuits with Carbon Nanotube Transistors, Science, vol. 294, 2001, 1317-1320

- 5. Sun L. F., Xie S. S., Zhou W. Y., et al., Materials: Creating the narrowest carbon nanotubes, Nature, vol. 403, 2000, 384
- 6. Pan Z. W., Xie S. S., Chang B. H., et al., Very long carbon nanotubes, Nature, vol. 394, 1998, 63
- 7. Colbert D. T., Zhang J., McClure S. M., et al., Growth and Sintering of Fullerene Nanotubes, Science, vol.266, 1994, 1218
- 8. Baughman R. H., Cui C., Zakhidov A. A., et al., Carbon Nanotube Actuators, Science. vol. 284, 1999, 1340-1344
- 9. Tsang S. C., Chen Y. K., M. Green L. H., et al., A Simple Method of Opening and Filling Carbon Nanotubes, Nature, vol. 372, 1994, 159
- 10. Hiura H., Ebbesen T. W., Tanigaki K., Opening and Purification of Carbon Nanotubes in High Yields, Adv. Mater, vol. 7, no. 3, 1995, 275-283.
- 11. Liu J., Rinzler A. G., Dai H., et al., Fullerene Pipes, Science, vol. 280, 1998, 1253-1256
- 12. Hu C. G., Wang W. L., Wang S. X., Zhu W., Li Y., Investigation on Electrochemical Properties of Carbon Nanotubes, Diamond and Related Material, 2003, in press
- 13. Luo H. X., Shi Z. J., Li N. Q., et al., Investigation of the Electrochemical and Electrocatalytic Behavior of Single-Wall Carbon Nanotube Film on a Glassy Carbon Electrode, Anal. Chem. vol. 73, 2001, 915-920
- 14. Chen J., Hamon M. A., Chen Y., et al., Solution Properties of Single-Walled Carbon Nanotubes, Science, vol. 282, 1998, 95-98
- 15. Liu C. Y., Bard A. J., Wudl F., Weitz I., Heath J. R., Electrochemical Characterization of Films of Single-Walled Carbon Nanotubes and their Possible Application, Electrochem. Solid State Lett. vol. 2, 2001, 915
- Wang Z. H., Liang Q. L., Wang Y. M., Luo G. A., Carbon nanotube-intercalated graphite electrodes for simultaneous determination of dopamine and serotonin in the presence of ascorbic acid, J. Electroanal. Chem. vol. 540, 2003, 129-134
- 17. Bard A. J., Faulkner L. R., Electrochemical Methods Fundamentals and Applications, John Wiley and Sons, NY, 1980, p.218-231
- 18. Gil A. F., Galicia L., González I., Diffusion coefficients and electrode kinetic parameters of different Fe(III)-sulfate complexes, J. Electroanalyt. Chem. vol. 417, 1996, 129-134

STRUCTURAL ANALYSIS OF CARBON NANOFIBRES SYNTHESISED AT ROOM TEMPERATURE

B. O. Boskovic*, V. Stolojan, D. A. Zeze, R. D. Forrest, and S. R. P. Silva

Advanced Technology Institute, University of Surrey, Guildford, Surrey, GU2 7XH, UK *Present address: Morgan Group Technology Ltd, Bewdley Road, Stourport-on-Severn, Worcestershire, DY13 8QR, UK

S. Haq

Advanced Technology Centre, Sowerby Building, BAE SYSTEMS, FPC 267, PO Box 5, Filton, Bristol, BS34 7OW, UK

ABSTRACT

Structural characteristics of carbon nanofibres synthesised using radio frequency plasma enhanced chemical vapour deposition (PECVD) and radio frequency assisted microwave PECVD at room temperature were determined using transmission electron microscopy and Raman analysis. The material was generated by the catalytic growth of carbon nanofibres at room temperature using an industry standard radio frequency (13.56 MHz) PECVD and custom designed microwave combined radio frequency PECVD. The thermal energy requirements for the growth were substituted by plasma decomposition of methane upon a nickel catalyst. Room temperature synthesis conditions offer the advantage of growing carbon nanofibres and nanotubes on different temperature sensitive substrates, such as organic materials, plastics and other polymers over relatively large areas. Carbon nanofibres grown using radio frequency combined microwave PECVD exhibit branching during the growth thus forming "Y"-shaped junctions. The interconnecting networks formed by the branched carbon nanofibres could be useful for nanoelectronics applications. The characteristic D and G peaks were observed in the Raman spectra and their intensity ratio and peak width were compared. Electron microscopy analysis provides evidence for a "tip" growth model, with the nickel catalyst particle attached to the tip of the nanofibre.

Keywords: Carbon nanofibres, PECVD, Raman spectroscopy.

INTRODUCTION

Carbon nanotubes (CNTs), first reported by Iijima in 1991 (ref. 1), have been synthesized in a carbon arc-discharge and since then other authors have reported the growth of CNTs from an arc-discharge (ref. 2, 3) and other methods have been developed to synthesize nanotubes. CNTs have also been produced by vaporization processes using lasers (ref. 4, 5), electron beams (ref. 6) and solar energy (ref. 7). Catalytic pyrolysis and chemical vapour deposition of hydrocarbons (ref. 8, 9) are now widely used for carbon nanotube growth as simple and efficient methods. In addition to CNTs, similar methods have been used for the synthesis of carbon nanofibres (CNFs), also known as carbon filaments since the early 1950's (ref. 10). CNFs can be grown using catalytic decomposition of hydrocarbons over transition metal particles such as iron, cobalt, nickel, and their alloys at temperatures ranging

NASA/CP—2003-212319 59 August 18, 2003

from 500 to 1000 °C (ref. 11). A microwave plasma enhanced chemical vapour deposition (PECVD) process, used for the preparation of diamond and diamond-like carbon films, has been developed successfully for the growth of CNTs and CNFs (ref. 12 to 17). Recently we have published the first evidence of carbon nanofibres growth at room temperature using radio frequency PECVD (r.f. PECVD) (ref. 18).

Raman spectroscopy is one of the most sensitive methods for studying carbon materials, providing very important information on the microstructure and crystalline ordering of carbon materials (ref. 19). Crystalline perfection can be characterised using Raman spectroscopy, as Raman scattering from perfect crystals is limited to contributions from Raman active zone-centre modes. Raman spectra are very sensitive to changes in translational symmetry and thus are useful for the study of disorder and crystallite formation in carbon materials. The Raman spectrum of carbon nanofibres shows features common to the spectra of any graphite-like material with characteristic G and D peaks or bands at about 1580 cm⁻¹ and 1355 cm⁻¹ respectively (ref. 20). The G and D peaks are attributed to sp² sites only. The G peak is due to the bond stretching of all pairs of sp² atoms in both rings and chains (ref. 21).

EXPERIMENTAL

Two different apparatus were used for PECVD of CNF, one using radio frequency PECVD and the other a radio frequency combined microwave PECVD system. The radio frequency PECVD system used for carbon nanofibre growth was an industrial standard Plasma Technology DP800, widely used for thin film growth in the semiconductor industry. It was operated at a radio frequency of 13.56 MHz and 200W power with a 1000 mTorr process pressure. Methane gas (99.999% purity), with flow rate of 30 sccm, was used for plasma glow discharge and nickel powder was used as a catalyst for CNF growth. Approximately 50 mg of the nickel powder catalyst (4-7 µm in diameter) was dispersed as a uniform thin layer on the top of a graphite, silicon wafer, glass or plastic foil substrate on the lower earthed electrode. Experiments were performed at temperature 30 °C for 15 min durations. The radio frequency assisted microwave PECVD system was custom designed for reactive ion etching and PECVD. Carbon nanofibre growth in radio frequency combined microwave PECVD was performed with 100 W radio wave (13.56 MHz) power and microwave (2.45 GHz) power ranging from 250 to 850 W with methane gas (99.999% purity, 70 sccm flow rate) as the carbon source and nickel powder (4-7 µm in diameter) as the catalyst. Experiments were run for 15 minutes at a process pressure of 12 mTorr. In order to achieve room temperature growth conditions the substrate was placed on a water-cooled sample holder and heated directly by plasma without any other heating source.

The characterisations of the nanofibres were conducted using conventional scanning electron microscopy (SEM) on the Hitachi S 3200 N and the S 4000, and transmission electron microscopy (TEM) on the Philips CM 200, operating in high-resolution mode for bright field imaging equipped with a Gatan Imaging Filter GIF2000. Raman analysis was performed using a Renishaw RM 1000 Raman Microscope.

RESULTS

A TEM image of carbon nanofibre obtained at room temperature using r.f. PECVD with a nickel catalyst particle at the tip is shown in Fig. 1a. Electron microscopy analysis has shown that the average length of the CNF is between 0.5 and 5 μ m with a thickness from 30 to 100 nm. CNF diameter distribution analysis has shown that average diameter is about 50 nm⁽¹⁸⁾. The nanofibres are produced in clumps originating from the surface of the catalyst particles. Catalyst particles were observed on the tip of CNF indicating the tip growth model (ref. 11). Poorly ordered graphene layers are characteristics of all PECVD grown CNF. In a majority of observed CNF graphene layers are parallel to the surface of catalyst particle at the tip and in a cup-stacked arrangement.

Variations in carbon nanofibres produced by radio frequency combined microwave PECVD are much greater compared to carbon nanofibres grown by radio frequency PECVD in terms of diameter and shape. In addition to the well known whisker-like and bi-directional morphologies CNF grown by the radio frequency combined microwave PECVD method have shown branching during the growth, which results the formation of "Y"-shaped junctions. Two CNF "welded" together forming a "Y" junction is shown in Figs. 2a. The image shown is slightly under focused in order to show the contrast between carbon nanofibre edges and channel better.

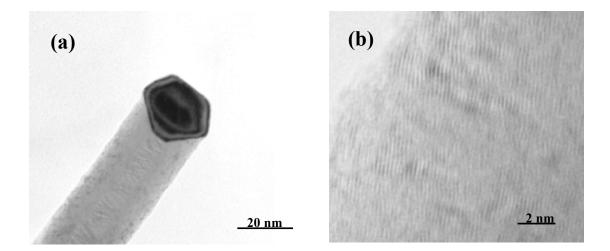


Figure 1. Transmission electron micrograph of carbon nanofibers at room temperature in a r.f. methane plasma on Ni catalyst. (b) Carbon nanofibre graphene planes in a herring-bone or stacked cup structure.

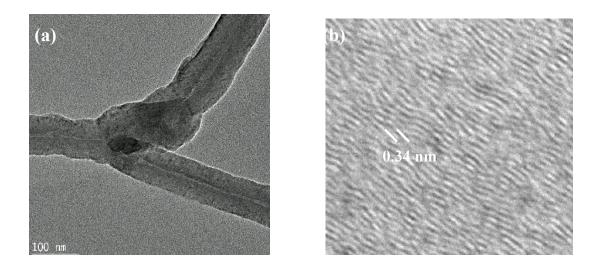
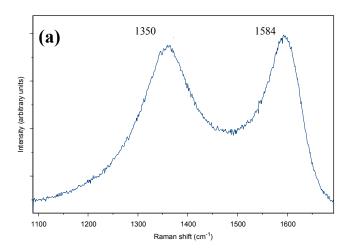


Figure 2. TEM micrograph of CNF produced usinf r.f. supported MW PECVD at P_{MW} =840 W: (a) "Y" junction of welded CNF, (b) structure of CNF with graphene platelets with 0.34 nm distance.

Both samples studied exhibit mainly G and D Raman bands. G-bands at about 1580 cm⁻¹, correspond to the Raman-allowed E_{2g2} mode called the graphite mode. The D-band, at about 1355 cm⁻¹, represents the contribution of disordered graphitic material. Amorphous carbon deposits on the surface of as-grown carbon nanofibres induce the large intensity of the D-band. The Raman spectrum of carbon nanofibres synthesised at room temperature using PECVD have shown broad overlapping G and D peaks indicating imperfectly crystalline graphene layers characteristic of CVD grown carbon nanofibres. Lorentzian peak fitting routines were used to establish peak frequencies and relative intensity ratios. Raman spectra of carbon nanofibres synthesised at room temperature (30 °C) is shown in Figure 3a. The G peak is around 1584 cm⁻¹, and the D peak around 1350 cm⁻¹. The ratio of intensities of the G and D peak is $I_G/I_D = 1.041$. Carbon nanofibres synthesised at a higher microwave power of 840

W have shown overlapping G and D peaks at around 1592 cm⁻¹ and 1356 cm⁻¹, respectively with $I_G/I_D = 1.23$ (Fig. 3b).



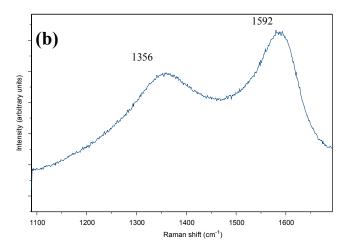


Figure 3. Raman spectra of carbon nanofibres synthesised using (a) r.f. PECVD, P_{RF} =200W CH₄, 30 sccm at T=30 °C, I_G/I_D = 1.041, (b) r.f. combined MW PECVD P_{RF} =100W, T=24 °C, CH₄, 70 sccm at P_{MW} = 840 W, I_G/I_D = 1.232.

CONCLUSION

Carbon nanofibres synthesised at room temperature using two different methods r.f PECVD and microwave combined r.f. PECVD, with nickel powder catalyst and methane as the carbon source, have shown very similar structural properties.

Comparison of Raman spectra shown in Fig. 3 for the two different PECVD methods give very similar degrees of structural perfection. The ratio of G and D peak intensities for microwave PECVD grown CNF ($I_G/I_D=1.232$) is higher compared to this ratio for r.f PECVD grown CNF ($I_G/I_D=1.041$). This could be an indication of the higher degree of crystalline perfection of carbon nanofibres synthesised using microwave combined r.f. PECVD. But, based on the half width Lorentzian peak comparisons, the carbon nanofibres exhibit similar G peak half widths ($w_G=84$).

CNF grown by the radio frequency supported microwave PECVD method have shown the remarkable characteristic of branching during the growth and "Y"-shaped junctions have been formed. The synthesis of connections between two or more CNF is an important step in the development of carbon nanofibre networks by creating interconnections for nanometer scale. These structures could be important from an electrical connectivity point of view or a three dimensional structural integrity.

REFERENCES

- 1. S. Iijima, Nature, 354 (1991) 56.
- 2. T.W. Ebbesen, and P.M. Ajayan, Nature, 358 (1992) 220.
- 3. P.M. Ajayan, and S. Iijima, Nature, 361 (1993) 33.
- 4. A. Thess, R. Lee, P. Nikolaev, H. Dai, P.Petit, J. Robert, C. Xu, Y.H. Lee, S.G. Kim, D.T. Colbert, G. Scuseria, D. Tomanek, J.E. Fisher, and R.E. Smalley, Science, 273 (1996) 483.
- 5. A. M. Rao, E. Richer, S. Bandow, B. Chase, P.C. Eklund, K.A. Williams, S. Fang, K.R. Subbaswamy, M. Menon, A. Thess, R.E. Smalley, G. Dresselhaus, and M.S. Dresselhaus, Science, 275 (1997) 187.
- 6. L.A. Chernozitonskii, Z. Ja, Kosakovskaja, E.A. Federov, and V.I. Panov, Phys. Lett. A, 197 (1995) 40; Z. Ja. Kozavskaja, L.A. Chernozatonskii and E.A. Federov, Nature, 359 (1992) 670.
- 7. D. Laplaze, P. Bernuer, W.R. Maser, G. Flament, and T. Guillard, Carbon, 36 (1998) 681.
- 8. S. Amelinckx et al., Science, 256 (1994) 678; M. Endo, et al., J. Phys. Chem. Solids, 54 (1993) 1841.
- 9. M-J Yacaman, M. Miki-Yoshida, L. Rendon, and J.G. Santiesteban, Appl. Phys. Lett. 62 (1993) 657; A.M. Benito, Y Maiette, E. Munoz, and M.T. Matinez, Carbon, 35 (1998) 681.
- 10. Davis WR, Slawson RJ, Rigby GR, Nature, 171 (1953) 756.
- 11. N. M. Rodriguez, J. Mater Res, 8 (1993) 3233.
- 12. L.C. Qin, D. Zhou, A.R. Krauss, and D.M. Gruen, Appl. Phys. Lett., 72 (1998) 3437.
- 13. S.H. Tsai, C.W. Chao, C.L. Lee, and H.C. Shih, Appl. Phys. Lett., 74 (1999) 3462.
- 14. Y.C. Choi, et al., Appl. Phys. Lett., 76 (2000) 2367.
- 15. C. Bower, W. Zhu, S. Jin, O. Zhou, Appl. Phys. Lett., 77 (2000) 830.
- 16. M. Okai, T. Muneyoshi, T. Yaguchi, and S. Sasaki, Appl. Phys. Lett., 77 (2000) 3468.
- 17. F. Hoshi, at al., Diamond and Rel. Mat. 10 (2001) 254.
- 18. B. O. Boskovic, V. Stolojan, R. U. A. Khan, S. Haq, and S. R. P. Silva, Nature Materials 1 (2002) 165-168.
- 19. T. C. Chen, M. S. Dresselhause, M. Endo, Phys Rev B, 26 (1982) 5867.
- 20. M. Endo et al., J. Mater. Res., 14, (1999) 4474.
- 21. A. C. Ferrari and J. Robertson, Phys. Rev. B, 20 (2000) 14095.

ON BULK MODULUS OF SUPERHARD 3D POLYMERS

OF CARBON NANOCLUSTER

M. Popov

Max Planck Inst. fur Chemie, Hochdruck Mineralphysik, Postfach 3060, 55020 Mainz, Germany.

Y. Koga

Research Center for Advanced Carbon Materials, National Institute of Advanced Industrial Science and Technology (AIST), Tsukuba Central 5, 1-1-1 Higashi, Tsukuba, Ibaraki 305-8565, Japan.

New superhard phase of single wall carbon nanotube (SP-SWNT) has been compared experimentally with 3D polymeric phases of analogous carbon cluster - fullerene C_{60} (both SWNT and C60 composed from curved graphene sheets). Mechanical properties of material composed from the polymerized clusters are determined by properties of the cluster. The 3D carbon nanocluster polymers were studied both in situ under pressure in a shear diamond anvil cell and after pressure release. Information about bulk modulus was derived from the pressure dependence for the phonon mode in high-energy range of the Raman spectra (i.e. the band 1594 cm⁻¹ for SP-SWNT and 1570 cm⁻¹ for 3D polymer of C_{60}). This mode is similar for both materials: it is the bond-stretching mode of pair of carbon sp² atoms, it is building bond for the clusters and in general it does not require the presence of graphitic structure and lies in the range 1500-1630 cm⁻¹.

In present study the Gruneisen parameter for 3D fullerite polymer was estimated experimentally using available experimental and theoretical data for bulk modulus of ultrahard fullerite (540 to 800 GPa depending on structure and synthesis conditions). The reasonable value for the fullerite Gruneisen parameter is the same as for the graphene sheet (1.1). The same value was used for the present estimation of bulk modulus of SP-SWNT (465 GPa). The value is close to diamond and consistent with theoretical calculations 420 GPa (L.A. Chernozatonskii et all. JETP Letters, 74, 467 (2001)). In addition to high bulk modulus SP-SWNT reveals superhard properties: its hardness (62 to 150 GPa) belongs to the range between cubic BN and diamond.

Self-consistency of the experimental data and their correspondence with theoretical calculations gives base for an estimation and prediction of mechanical properties of new carbon nanocluster-based polymeric materials.

Keywords: Single wall carbon nanotube; Superhard phase; Ultrahard fullerite

INTERACTION BETWEEN CATALYST METALS AND STONE-WALES DEFECTS IN CARBON NANOTUBES

F. Y. Meng^{1,2}, L. G. Zhou^{1,2}, San-Qiang Shi^{1,*}

¹Department of Mechanical Engineering, The Hong Kong Polytechnic University,
Hung Hum, Hong Kong
Rui Yang²

²Institute of Metal Research, Chinese Academy of Sciences, 72 Wenhua Road,
Shenyang 110016, China

ABSTRACT

A Stone-Wales (SW) defect is a dipole of 5-7 ring pair in graphite networks. A SW defect has a strong effect on the mechanical properties of carbon nanotubes (CNTs), and is in fact one of most important defective structures in CNTs. Using first-principles methods, we calculated the interaction of SW defects with a series of foreign atoms that had been used as catalysts for the growth of CNTs, including Fe, Ni, Co, Ti, Cu, Al, Mg, and Mo. It was found that the adsorption of most of these foreign atoms at SW defects is energetically preferred when compared with a defect-free structure, and that transition metals generally have a strong attractive interaction with CNTs due to the unfilled 3d shells.

Keywords: Carbon Nanotubes; Stone-Wales Defect; Atomic Adsorption; First-Principles Calculation.

1 INTRODUCTION

CNTs are unique nanostructures with remarkable electronic and mechanical properties. Many potential applications of CNTs rely on the interaction between foreign atoms and carbon atoms in the tubes. One potential application of CNTs is the reinforcement of composite materials, and the performance of a CNT-reinforced composite system depends critically on the interaction and bonding between CNTs and the matrix materials. The metal catalysts play an important role in the growth of CNTs (ref. 1 to 2); however the mechanisms of metal catalysts in the growth of CNTs are still not clearly understood. In the development of nano-electronic devices, the contacts between a metal wire (Cu, Au, Al, or Ti) and a carbon nanotube can change the electronic transport characteristics of the tube (ref. 3 to 4). On the other hand, defects such as non-hexagonal rings, kinks, Y-junctions, impurities and incomplete bonds may be present in CNTs (ref. 5 to 6). It is hoped that the defective structures may affect the interaction between foreign atoms and CNTs, resulting in an increase in the adsorption capacity of some foreign atoms such as hydrogen and lithium, or an improvement of the bonding strength between CNTs and the polymer matrix, or a change in the electronic property of the tubes. Using first-principles methods, we studied the interaction between a SW defect and some foreign atoms such as H, B, C, N, O, F, P, Si, Li and Na (ref. 7). In this paper we report our study of the interactions between a SW defect and other interesting foreign atoms such as Fe, Ni, Co, Ti, Cu, Al, Mg, and Mo.

2 MODELING AND METHODOLOGY

The Stone-Wales defect (ref. 8 to 9) is one of the most important defective structures in CNTs. Thrower pointed out a possible 5-7 ring defect in graphite (ref. 10). Stone and Wales showed that a dipole consisting of a pair of 5-7 rings can be created by rotating a C-C bond in the hexagonal network by 90°. Such a dipole was later called a Stone-Wales (SW) defect. The structure of a SW defect is simple, and it possesses relatively low formation energy. Fig. 1 shows one result of our molecular dynamics simulation on a (20,20) carbon nanotube using a bond-order potential (ref. 11). In this simulation, the initial defect-free structure was annealed at 5000 K for 25ps, and then relaxed to an

NASA/CP—2003-212319 65 August 18, 2003

_

^{*} Corresponding author. Tel.: (852) 2766-7821; fax: (852) 2365-4703; email: mmsqshi@polyu.edu.hk

equilibrium state. It can be seen that the SW defects are the only defects that appear after this annealing process.

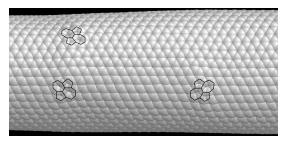


Fig.1. Stone-Wales defects in a (20,20) single-walled CNT generated by annealing at 5000 K.

2.1 Cluster model

The cluster model used in the current calculation consists of 81 atoms, 80 of which are carbon atoms forming a flat graphene sheet, and one a foreign atom. Two types of cluster models are investigated: one in which a SW defect is embedded, and the other is defect-free (Fig.2). In the current calculation, the effect of wall bending and chirality on CNTs has been neglected. For the defect-free model, the foreign atom is placed over the sheet at some symmetrical positions, namely, over a carbon atom, or over a bond, or over the center of a hexagonal ring (Fig.2 (a)). For the cluster model in which a SW defect is embedded, the foreign atom is placed over the center of a heptagon or pentagon ring respectively, or over the center bond (Fig.2 (b)). The binding energy of a foreign atom to a CNT at a distance R from the wall of graphene sheet can be calculated by

$$E_{\text{bin}}(R) = E_{\text{tot}}^{\text{Cluster}}(R) - E_{\text{tot}}^{\text{sheet}} - E_{\text{tot}}^{\text{Im purity}}$$

where $E_{tot}^{Cluster}$ is the total energy of the cluster, including all 81 atoms; E_{tot}^{sheet} is the total energy of the 80 carbon atoms in the graphene sheet only; and $E_{tot}^{Impurity}$ is the total energy of the foreign atom at the free state. By changing the value of R in small steps, we may obtain the function $E_{bin}(R)$.

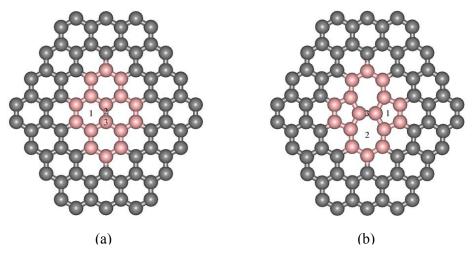


Fig. 2. Model clusters: (a) defect-free cluster, (b) Stone-Wales defect embedded cluster. 1, 2 and 3 in (a) correspond to positions of over-ring, over-bond and over-atom, respectively.

2.2 Methodology

In this study, two methods were adopted in the calculation of total energies. One is the discrete variational method (ref. 12) in which the molecular eigenfuctions are obtained by linear combinations of atom orbitals (LCAO). These orbitals are obtained by numerically solving the Hartree-Fock for a free atom with a set of discrete sample points. The non-local exchange-correlation operator of the

Hartree-Fock equation is approximated by a local exchange-correlation Barth-Hedin potential. The matrix elements of the Hamiltonian and overlap operators are calculated by a three-dimensional Diophantine numerical integration. The chosen convergence criterion is that the difference between two consecutive values of the charge self-consistent integration should be less than 10⁻⁴. Another method is to use a commercial package, HyperChemTM. In this case, an empirical Amber94 force field was chosen for the geometrical optimization and a semi-empirical PM3 method was used for the calculations of single-point energy (ref. 13 to 14). The convergence criterion is that the difference between two consecutive values of charge self-consistent integration should be less than 10⁻³. The models and methodologies were validated by comparing the results of our calculations on the binding energy of a carbon atom within the graphene sheet, as well as on the formation energy of a SW defect against other experimental and theoretical data in the literature (ref. 15 to 16).

3 RESULTS AND DISCUSSION

In an early report (ref. 7), we had investigated the interaction of a SW defect with 10 light foreign atoms; i.e., H, B, C, N, O, F, Si, P, Li, and Na. It was found that, of the 10 foreign atoms studied, the introduction of SW defects would only benefit the adsorption capacity of B, N, F, and Si. In the current study, we selected the following eight metals that have been used as catalysts in the growth of CNTs: Al, Mg, Ti, Fe, Co, Ni, Cu, and Mo. As an example, Fig. 3 shows the binding energy of these foreign atoms at the over-bond position as a function of the distance between the wall of a defect-free graphene sheet and the foreign atoms. Usually, a minimum in the binding energy curve may be found at a distance of a couple of angstroms away from the graphene sheet. We call this minimum the cohesive energy, and it is a key indicator of the absorbing tendency of a foreign atom to CNTs.

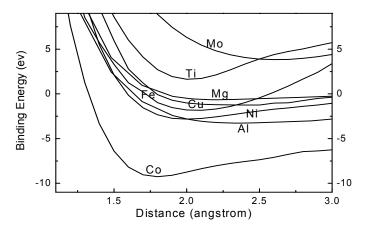


Fig. 3 Binding energies at the over-bond position in a defect-free cluster.

A positive value for cohesive energy indicates that an external force is required for the adsorption of foreign atoms on CNTs, while a negative value implies a spontaneous attraction between the graphene sheet and the foreign atom. It was found that the cohesive energy of these foreign atoms at an over-atom position is mostly higher than that at the other two positions, except for Co. This is reflected in Fig. 4 for a defect-free graphene sheet. Among the eight metal atoms studied, only Mo and Ti always exhibit a positive cohesive energy, which indicates that there was no bonding of these metal atoms to CNT. However, this situation may change if a cluster of Mo or Ti atoms is involved in the interaction.

Ti, Fe, Co, Ni, and Cu are transition metals. From Ti to Cu, the cohesive energy first decreases and then increases as the number of d electrons increases. A minimum is found at Co with a half-filled d band, showing a strong attractive interaction with CNTs. Considering all symmetric positions, one can see that the cohesive energies for Fe, Co, and Ni are relatively low; therefore, these metals may show a strong attractive interaction with CNTs and they are often used as catalysts for the growth of CNTs (ref. 1 to 2).

Al and Cu also have low cohesive energies for some symmetric positions. The low cohesive energy of Al may be due to its single valence electron in the 3p shell, which can result in some degree of hybridization between the Al and C atom. Charge transfer and hybridization between the Al cluster and CNT have been reported in the literature (ref. 3). It was observed (ref. 4) that a chain of Cu atoms could change the electron transport characteristics of a carbon nanotube through nanotube-metal

contact by forming a weak ionic bonding between the copper cluster and tube. The cohesive energy of Cu in our study agrees well with that of reference 4. Mg has a relatively higher binding energy than Fe, Co, Ni and Al, possibly due to the fact that it has no p or d valence electron.

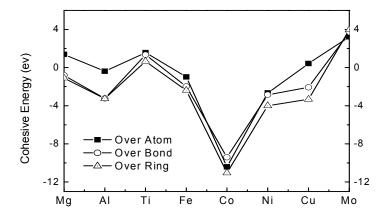


Fig. 4 Cohesive energies at different symmetric positions on a defect-free graphene sheet.

With the introduction of a SW defect in the graphene sheet, a pair of pentagon and heptagon rings has been created. Fig. 5 (a) shows a comparison of the cohesive energy for foreign atoms over the center of pentagonal, hexagonal and heptagonal rings, respectively. Foreign atoms at a heptagon-site possess the lowest cohesive energies. The cohesive energy of a Ti atom at hexagonal and heptagonal rings is close to zero, indicating a weak interaction with the graphene sheet, as compared to all other metals. However, the presence of a heptagon reduces the cohesive energy of Ti to a negative value, which would improve the adhesiveness of Ti to CNT wall. Fig. 5 (b) compares the cohesive energies of eight foreign atoms to a graphene sheet with and without an embedded SW defect. One can see that, in most cases, the SW defect results in the lowest cohesive energies.

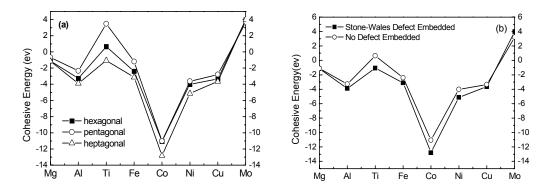


Fig. 5 (a) A comparison of cohesive energy of foreign atoms absorbed at the center of a pentagon, hexagon and heptagon, (b) A comparison of the minimum cohesive energy of foreign atoms to the graphene sheet with and without an embedded Stone-Wales defect.

4 CONCLUSIONS

First-principles methods have been applied to study the interaction of Stone-Wale defects in a carbon nanotube with eight different metal atoms. The results show that:

- (1) The adsorption of these foreign atoms over a heptagon is energetically preferred when compared with other symmetric positions.
- (2) For transition metal atoms, the cohesive energy is mostly negative, indicating a strong attractive interaction and bonding with CNTs due to the unfilled 3d shell.
- (3) Mo has no bonding with CNTs due to large positive cohesive energies at all symmetric positions.

- (4) The cohesive energy of Ti is close to zero, implying a weak interaction with CNTs, while the presence of a SW defect may increase the adsorption capacity of Ti on CNTs.
- (5) SW defects generally reduce the cohesive energy of all metal atoms studied.

ACKNOWLEDGMENT

This work was funded by a research grant from The Hong Kong Polytechnic University (A-PE54).

REFERENCES

- 1. Li, H. Y., Kim, S. G., Tomanek, D.: Catalytic growth of single-wall carbon nanotubes: an ab initio study. Phys. Rev. Lett., vol. 78, no. 12, Mar 1997, 2393
- 2. Lee, G. D., Han, S., Yu, J., et al.: Catalytic decomposition of acetylene on Fe (001): a first-principles study. Phys. Rev. B, vol. 66, no. 8, Aug 2002, 081403 (R)
- 3. Nardelli, M. B., Fattebert, J. L., Bernholc. J.: O (N) real-space method for ab initio quantum transport calculations: application to carbon nanotube-metal contacts. Phys. Rev. B, vol. 64, no. 24, Dec 2001, 245423
- 4. Kong, K., Han, S., Ihm. J.: Development of an energy barrier at the metal-chain-metallic-carbon-nanotube nanocontact. Phys. Rev. B, vol. 60, no. 8, Aug 1999, 6074
- 5. Peter J. F. Harris: Carbon nanotubes and related structures: new materials for the twenty-first century, Cambridge University Press, 1999.
- Ebbesen, T. W., eds.: Carbon nanotubes: preparation and properties, Boca Raton, Fla.: CRC Press, 1997.
- 7. Zhou, L. G., Shi. S. Q.: Adsorption of foreign atoms on Stone-Wales defects in carbon nanotube, Carbon, vol. 41, no. 3, 2003,613
- 8. Nardelli, M. B., Yakobson, B. I., Bernholc, J.: Brittle and ductile behavior in carbon nanotubes, Phys. Rev. Lett., vol. 81, no. 21, Nov 1998, 4656
- 9. Choi, H. J., J. Ihm, Louie, S. G., Cohen, M. L.: Defects, Quasibound States, and Quantum Conductance in Metallic Carbon Nanotubes, Phys. Rev. Lett., vol. 84, no. 13, Mar 2000, 2917.
- Thrower, P. A., in: Walker, P. L. Jr., editor, Chemistry and Physics of Carbon, vol. 5, New York: Dekker, 1969, 262
- Brenner, D. W.: Empirical potential for hydrocarbons for use in simulating the chemical vapor deposition of diamond films. Phys. Rev. B, vol. 42, no. 15, Nov 1990, 9458
- 12. Delley, B., Ellis, D. E., Freeman, A. J., et al.: Binding energy and electronic structure of small copper particles. Phys. Rev. B, vol. 27, no. 4, Apr 1983, 2132
- 13. Cornwell, C. F., Wille, L. T.: Critical strain and catalytic growth of single-walled carbon nanotubes. J. Chem. Phys., vol. 109, no. 2, Aug 1998, 763
- 14. Hyperchem Computational Chemistry, Part 2: Theory and Methods (Release 7 for Windows). Hypercube Inc., Canada, 2002
- 15. Zhang, P., Lammert, P. E., Crespi, V. H.: Plastic deformation of carbon nanotubes. Phys. Rev. Lett., vol. 64, 1998, 5346.
- 16. Hua, X., Cagin, T., Che, J., et al.: QM (DFT) and MD studies on formation mechanisms of C60 fullerenes. Nanotechnology, vol. 11, no. 2, June 2000, 85.

FRICTIONAL PROPERTIES OF CARBON NANOTUBE REINFORCED POLYMER MATRIX COMPOSITES

*Kazuki ENOMOTO, Toshiyuki YASUHARA, Shintaro KITAKATA, Hiroya MURAKAMI and Naoto OHTAKE

Department of Mechanical Sciences and Engineering, Tokyo Institute of Technology 2-12-1, O-okayama, Meguro-ku, Tokyo 152-8552, Japan *e-mail: enomotok@stu.mech.titech.ac.jp, TEL: +81-3-5734-2418, FAX: +81-3-5734-2824

ABSTRACT

Carbon nanotubes (CNTs) are expected to be a new functional material. We fabricated polystyrene (PS) matrix composites filled with multi-walled carbon nanotubes (MWCNTs) and vapor grown carbon fibers (VGCFs). The concentration of the fillers in the composites was varied from 0 to 50 wt%. Specimens were fabricated by injection molding and friction coefficient and wear resistance of the surface of the molded specimens were measured using a ball-on-disk friction tester. In the case of VGCF/PS composites, the friction coefficient decreased with increasing the filler concentration, although the surface roughness increased with the filler concentration. Finally, the friction coefficient decreased from μ =0.45 to μ =0.2 when VGCF concentration was 50wt%. In the case of MWCNT/PS composites, the friction coefficient was almost same as that of bulk polystyrene when the MWCNT concentration was 30wt%. The change in the friction coefficient of CNT/PS composites was discussed in terms of the surface roughness, CNT contact area and Young's modulus. The specific wear rate of CNT/PS composites was also measured. The wear rate of MWCNT was 2.0×10^{-7} mm³/N, that is eight-fold smaller than VGCF/PS composites.

Keywords: carbon nanotube (CNT), vapor grown carbon fiber (VGCF), injection molding, polymer matrix composite, friction coefficient, wear resistance

INTRODUCTION

Carbon nanotube (CNT) (ref. 1) is expected as one of the most important material in the 21st century. CNT has a very detailed diameter as 1/1000 as conventional carbon fibers, but its aspect ratio is almost same as conventional carbon fibers. It also has outstanding properties such as high mechanical strength, high Young's modulus and high electrical conductivity (refs. 2 to 4). By adding CNTs as fillers to plastics and fabricating by injection molding, it is expected that the mechanical and electrical properties of molded composites are improved with small amount of fillers in conparison with the conventional fillers (refs. 5 to 9). Moreover, if CNTs were sticking out from the surface of the molded composites, it is also expected that friction coefficient and wear resistance could improve by reduction of contact area. However, only a few results have been reported on the injection molding of polymer matrix composites filled with CNTs.

The objectives of this study are fabricating CNT/polymer composites to thin plates by injection molding and evaluating friction properties such as friction coefficient and wear resistance. The effects of filler content on these properties were discussed, and the friction mechanisms of the CNT/PS composites were considered.

EXPERIMENTAL

Multi-walled carbon nanotube (MWCNT: Frontier Carbon Technology Project) was used as fillers to the composites in this study, and vapor grown carbon nano fiber (VGNF: Showa Denko K.K.) and vapor grown carbon fiber (VGCF: Showa Denko K.K.) were also used. SEM images of MWCNT and VGCF are shown in Fig.1. These images show that MWCNTs are curly and the dispersion of the diameter of MWCNT seems to be larger than that of VGCF. Conductive carbon black and PitchCF were also used for comparison. Table 1 shows the properties of the carbon fillers used in this study. An injection molding grade polystyrene (PS: STYRON 679) was used as a matrix polymer. Polystyrene (PS) is transparent and colorless non-crystalline polymer and is widely used in injection molding. This grade of polystyrene is especially excellent in fluidity.

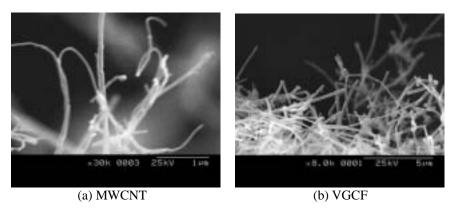


Figure 1. SEM images of MWCNT and VGCF.

Table 1. Properties of MWCNT and other carbon fillers.

	MWCNT	VGNF	VGCF	PitchCF	CB
Diameter [nm]	10~50	80	150	10000	40
Length [µm]	~10	~10	10~20	6000	-
Aspect ratio	~1000	~100	100	600	1

Polystyrene matrix composites were obtained by kneading with a twin screw kneader to distribute fillers in the matrix. The filler content in the composites was varied from 0 to 50 wt%, and after kneading composites for 5 min. at 220°C, they were crushed and were recovered as pellets. Square shape $(30 \times 30 \times 2 \text{ mm}^3)$ specimens were fabricated by injection molding.

The friction and wear tests for the CNT/PS composites were performed with a ball-on-dick friction tester. Normal load is given by contacting steel ball (diameter of 10 mm) to the specimen fixed to the rotational disk (diameter of 50 mm, thickness of 10 mm), and the frictional force is measured by the load cell. The main axis rotation speed is varied from 0 to 700 rpm. In this study, the rotation speed was set to 200 rpm, and the normal load was set to 0.20 N. The friction test was performed at room temperature in the air, and lubricant was not used.

RESULTS AND DISCUSSION

Friction property

Figure 2 shows results of the ball-on-disk friction test. The vertical axises of these graphs are friction coefficient and the horizontal axises are the number of friction. In the case of bulk polystyrene, a friction coefficient of the surface increases slightly with the increase of the number of frictions. In the case of 10wt% MWCNT/PS composite, the friction coefficient increases rapidly in early stages of friction. After that, the friction coefficient decreases to about 0.45 and becomes almost constant. In the case of 30wt% MWCNT/PS composite, the friction coefficient becomes almost constant at about 0.43 from the early stages of friction. In the case of VGNF/PS and VGCF/PS composites, the fluctuation of the friction coefficient shows the similar tendency. When the filler content is 10wt%, the friction coefficient increases with the increase in the number of friction and becomes larger than that of bulk PS. When the filler content is more than 30wt%, the friction coefficient becomes almost constant from the early stages of friction and the coefficient is much smaller than that of bulk PS. In the case of PitchCF/PS, the friction coefficient increased with the increase in a number, and became larger than that of bulk PS.

The relations of the friction coefficient and filler content which were obtained from these results are summarized in Figure 3. In the case of MWCNT/PS composites, the friction coefficient slightly decreases in the range of filler content from 0 to 30wt%, and reduction of the friction coefficient of 30wt% MWCNT/PS composites was 6% in comparison with the case of PS. In the case of VGNF/PS and VGCF/PS composites, the friction coefficient is larger than that of bulk polystyrene when the filler content is 10wt%, but when the filler content is over 30wt%, the friction coefficient decreases with the increase in the filler content. In comparison with the case of bulk PS, the reduction of the friction coefficient of 30wt% VGNF/PS composites was 32% and reduction of the

friction coefficient of 50wt% VGCF/PS composites was 62%. On the other hand, in PitchCF/PS composites, the the friction coefficient increases with the increase in the filler content.

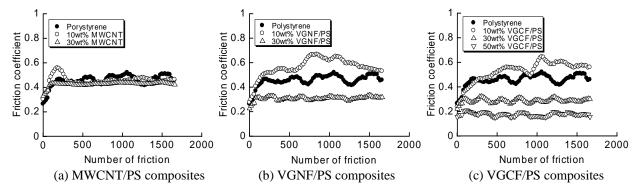


Figure 2. Fricion coefficient of the composites as a function of number of friction.

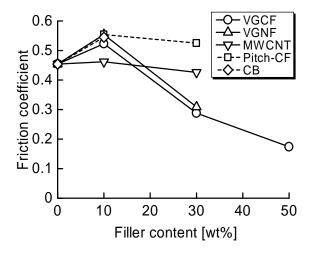


Figure 3. Fricion coefficient of the composites filled with various carbon fillers as a function of filler content.

The factors which affect the friction coefficient can be classfied as follows:

- (A) Increase of the surface roughness derived from the increase of the entropy of the mixing.
- (B) Increase in the area which fillers contact to the ball.
- (C) Reduction of the contact area due to the increase of Young's modulus.

Then, the effect of each factor on the friction coefficient was considered in detail. First, the effect of the surface roughness is discussed. Figure 4 shows the relations between the surface roughness and filler content. The surface roughness increases with the increase of filler content because the number of fillers which appear in the surface of the composites increase with the increase of filler content. Generally, the larger the surface roughness is, the larger the friction coefficient becomes. The relations between the friction coefficient and the surface roughness are shown in Figure 5, when the filler content is 10wt% and 30wt%. When the filler content is 10wt% (Figure 5-a), there is a tendency that the friction coefficient becomes larger if the surface roughness becomes larger, and the correlation coefficient was 0.74. This result shows that the friction coefficient has a high correlation with the surface roughness. Therefore, when the filler content is 10wt%, the increase of the surface roughness by the increase of filler content seems to be a dominant reason why the friction coefficient is larger than that of bulk PS.

Second, the effect of the increase of the area which fillers contact to the ball is discussed. Figure 6 shows SEM images of the surface of the composites which VGCFs were added as the filler. When the filler content increases, the fillers sticking out from the surface of the composites increase, and as the result, the ratio of the contact area to which fillers contact increases. Since the surface of VGCF was graphitized by the heat treatment, it can be assumed that the friction coefficient of VGCF is as small as that of graphite. Therefore, if the ratio of the

contact area between the fillers and the ball increases, the friction coefficient should decrease. The reduction of the friction coefficient by the increase of the area contact area over 30wt% can be explained by the increase of the area to which fillers contact as described above.

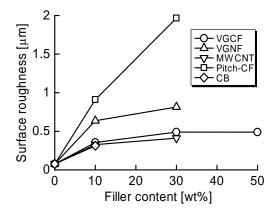


Figure 4. Surface roughness of the composites filled with various carbon fillers as a function of filler content.

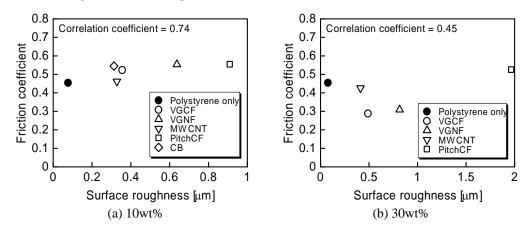


Figure 5. The relations between the friction coefficient and the surface roughness.

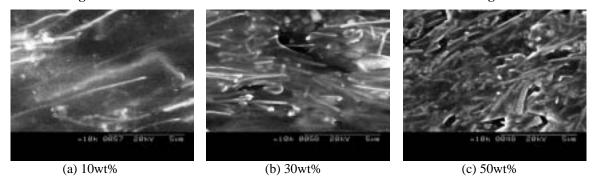


Figure 6. SEM images of the surface of the composites which VGCFs were added as the filler.

Third, the effect of the reduction of the contact area due to the increase of Young's modulus is discussed. In the case of VGCF/PS composites, Young's modulus increases with increasing VGCF content (ref. 10). If Young's modulus increases, the indentation depth by the ball decreases in order that the contact stress decreases, so the energy which is required for digging up gaps of the surface roughness decreases. Therefore, if Young's modulus increases, the friction coefficient decreases.

Figure 7 demonstrates the effects of these factors of CNT/PS composites.

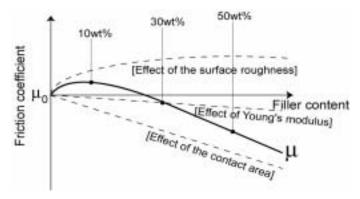


Figure 7. Effects of the factors which affect the friction coefficient of CNT/PS composites.

Wear property

Wear resistance of the composites was evaluated by calculating the specific wear rate derived from the volume of the wear tracks which remained in the surface of the specimen after the ball-on-disk tests. The surface profile of the wear tracks was measured by using a stylus profilometer (SURFTEST SV-600, Mitsutoyo Corp.). The specific wear rate is the wear volume per unit load and unit friction distance, and it is an index of the wear resistance.

In the case of polystyrene and 10wt% CNT/PS composites, circular wear tracks were observed and the profiles of the suraface roughness were also able to be measured by the stylus profilometer. When each specific wear rate was calculated, the specific wear rate of polystyrene was 1.29×10^{-5} mm/N and that of 10wt% VGCF/PS composites was 1.46×10^{-6} mm/N, so it shows the wear resistance of the composites will be improved by adding CNTs. When the filler content more than 30wt%, the circular wear tracks were observed from appearance but they could not be observed from the profiles of the suraface roughness. This is because the depth of the wear tracks seems to be the almost the same order as the surface roughness of the specimens. SEM image of the wear track is shown in Figure 8. The area of the wear track looks like "rollered surface" with a plastic flow of the polymer. Therefore, when the filler content is more than 30wt%, the composite seems to be hardly worn out.

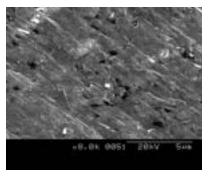


Figure 8. SEM image of the wear track when the VGCF content is 50wt%.

Figure 9 summerizes the relations between the friction coefficient and the specific wear rate obtained from above experiments. In this figure, the composite which exists in the lower left can be considered to as a excellent material in the friction and wear characteristic. The 50wt% VGCF/PS composite is the most excellent in this study. In the case of VGCF/PS and VGNF/PS composites, both of the friction coefficient and the specific wear rate are small, so it is thought that VGCF and VGNF have self-lubricity. In the case of MWCNT/PS composites, on the other hand, it is remarkable that the specific wear rate is very small but the friction coefficient is larger than that of VGCF/PS or VGNF/PS composites, so it is thought that MWCNT does not have self-lubricity.

CONCLUSIONS

We studied injection molding of polystyrene matrix composites filled with carbon nanotubes. Friction properties are evaluated and effects of filler content on the friction properties were discussed. The results are listed

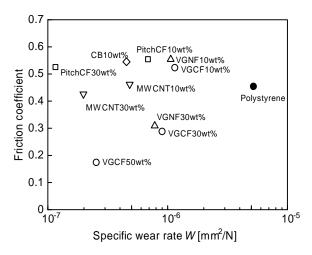


Figure 9. Relations between the friction coefficient and the specific wear rate obtained in this study.

as follows:

- In MWCNT/PS composites, the friction coefficient slightly decreases when the filler content is under 30wt%.
- In VGNF/PS and VGCF/PS composites, the friction coefficient is larger than that of bluk polystyrene when the filler content is 10wt%, but when the filler content is over 30wt%, the friction coefficient decreases with the increase of the filler content.
- The change in the friction coefficient of CNT/PS composites was discussed in terms of the surface roughness, CNT contact area and Young's modulus.
- Wear resistance of the composites are significantly improved by adding CNTs.
- MWCNT/PS composites shows very low wear rate and high frivtion coefficient whereas the VGCF/PS and VGNF/PS composites shows low wear rate and very low friction coefficient

ACKNOWLEDGEMENT

The authors express their gratitude to Frontier Carbon Technology Project and Showa Denko K.K., for providing MWCNT, VGNF and VGCF.

REFERENCES

- (1) Iijima, S., Helical microtubules of graphitic carbon, Nature vol. 354, no. 7, November 1991, p56.
- (2) Treacy, M.M.J, Ebbesen, T.W, and Gibson, J.M, Exveptionally high Young's modulus observed for individual carbon nanotubes, *Nature* vol. 381, no. 20, June 1996, p678.
- (3) Issi, J.P. et al., Electronic properties of carbon nanotubes: experimental results, *Carbon* vol. 33, no. 7, 1995, p941.
- (4) Nygard, J , et al, Electrical transport measurements on single-walled carbon nanotubes, Appl. Phis. A 69, 1999, p297.
- (5) Tibbetts, G.G. and McHugh, J.J., Mechanical properties of vapor-grown carbon fiber composites with thermoplastic matrices, J. Mater. Res., vol. 14, no. 7, July 1999, p2871.
- (6) Carneiro, O.S, et al., Production and assessment of polycarbonate composites reinforced with vapour-grown carbon fibres, Compos. Sci. and Technol., vol. 58, 1998, p401.
- (7) Frank, K.K, et al, Structure and popperties of carbon nanotube reinforced nanocomposites, Proceedings of the 43rd AIAA/ASME/ASCE/AHS/ASC Structures, Structual Dtnamics, and Materials Conference, 2002, p1426.
- (8) Gordeyev, S.A. et al., Transport properties of polymer-vapour grown carbon fibre composites, Physica B, vol. 279, 2000, p33.
- (9) Kymarkis, E., Alexandou, I. and Amaratunga, G.A.J., Single-walled carbon nanotube-polymer composites: electrical, optical and structual investigation, Synthetic Metals, vol.127, 2002, p59.
- (10) Enomoto, K., et al, Injection Molding of Polystyrene Matrix Composites Filled with Vapor Grown Carbon Fiber, JSME Int. J., in press.

SOLID LUBRICANT PROPERTIES OF CATALYTICALLY GROWN CARBON NANOTUBES

Atsushi HIRATA* and Nobuaki YOSHIOKA

Department of Mechanical Sciences and Engineering,
Graduate School of Science and Engineering, Tokyo Institute of Technology
2-12-1 O-okayama, Meguro-ku, Tokyo 152-8552, Japan
*Corresponding author. Tel.: +81-3-5734-2163; fax: +81-3-5734-2893, e-mail: ahirata@ctrl.titech.ac.jp

ABSTRACT

Solid lubricant properties of carbon nanotubes catalytically deposited by microwave plasma CVD using methane and hydrogen gaseous mixture have been investigated by means of ball-on-disk type friction testing. Carbon nonotubes with various crystallinity were deposited by changing microwave power and bias voltage onto silicon substrate. Nickel was used as a catalyst and coated on the substrate by DC sputtering before deposition. SEM and Raman spectroscopy were employed to examine carbon nanotubes. In friction testing, a bearing steel ball slid on the substrate coated with carbon nanotubes or covered with vapor grown carbon fibers used as a reference carbon material. Friction force was measured in air containing water vapor, dry nitrogen and vacuum. As a result, low friction has resulted from the carbon nanotubes with fewer defects, in particular, in water-free atmosphere such as dry nitrogen and vacuum. Cemented carbide substrate has improved the adhesion of carbon nanotubes, and lower friction coefficient below 0.1 was consequently attained.

Keywords: carbon nanotube, vapor grown carbon fiber, solid lubricant, friction, adhesion

INTRODUCTION

Superior mechanical properties of carbon nanotubes (CNTs) are attractive for designing new materials from nanoscale structure. Tribological application is a promising alternative because of weak intermolecular reaction resulted from closed bonding of graphene sheets that form CNTs. One of the approaches to investigate the tribological properties of CNTs is the preparation of carbon nanotube composites using metal (refs. 1 to 3) or resin (ref. 4) matrix. In this method, surface of test pieces for measuring friction is composed of CNTs and matrix materials both of which affect tribological behavior of the composite. CNTs fundamentally should cover all over the sliding region of the test pieces to inherently characterize the tribological properties of CNTs. One of the methods to prepare the surface formed with no other than CNTs is direct coating by chemical vapor deposition (CVD). The present paper describes the solid lubricant properties of CNTs catalytically deposited on silicon and cemented carbide by microwave plasma CVD. Microstructure and adhesion strength of CNTs are discussed to attain solid lubrication.

EXPERIMENTAL

Multi-walled carbon nanotubes were catalytically deposited by microwave plasma CVD with gaseous mixture of methane and hydrogen. Nickel was used as a catalyst for CNTs growth and coated on silicon substrate by DC sputtering before deposition of CNTs. Cemented carbide (WC-Co) was also used as substrate in order to improve adhesion strength of CNTs. CNTs were grown under various microwave power and bias voltage and characterized by scanning electron microscopy (SEM) and Raman spectroscopy. Table 1 lists the deposition conditions of CNTs. The friction testing of CNTs coating were performed with a ball-on-disk type friction testing apparatus using stainless steel (SUS440C) balls of 3/16 inch in diameter. Friction behaviors of CNTs were examined in air at relative humidity of 55% and vacuum at 1.7x10⁻³ Pa at room temperature. Friction conditions were varied within 8.3-12.5 mm/s of sliding speed and 0.11-0.52 N of normal force applied to the steel ball.

Table 1. Deposition conditions.

Methane flow rate	2 cc/min
Hydrogen flow rate	20 cc/min
Pressure	$6.7x10^2 Pa$
Microwave power	300-900 W
Deposition time	10-60 min
Bias voltage	50-200 V
Ni film thickness	5-10 nm

RESULTS AND DISCUSSION

Preliminary friction testing was carried out for CNTs deposited on silicon substrate. CNTs coatings were prepared under different deposition conditions, in addition, vapor grown carbon fibers (VGCFs) of which approximate diameter is 150 nm were used as a reference material. For the testing, twenty milligrams of VGCFs were simply placed on silicon substrate to cover its surface. Figure 1 shows the variation of friction coefficients as a function of sliding distance, coefficients which were measured in air and vacuum. In air, both CNTs and VGCFs exhibit high friction coefficients that were almost the same value for unlubricated silicon. On the contrary to this, friction coefficients for the one CNTs and VGCFs clearly decrease at around 0.2 in vacuum. The other CNTs however show no lubrication property both in air and vacuum. Raman spectra of the CNTs and VGCFs are shown in Fig. 2. The CNTs and VGCFs that show lubrication property in vacuum have a slightly sharp peak at around 1580 cm⁻¹, that is typical for graphite structure. In addition, a broad peak at around 1340 cm⁻¹ appears for the CNTs, that implies the CNTs contain disordered structure of sp² bonding. For the other CNTs that have no effect to reduce friction, the two peaks shift and broaden, which indicates lower crystallinity and much defect included. Thus, we believe that CNTs with highly ordered crystal structure exhibit low friction property, in particular, in vacuum.

Considering practical use of solid lubricant, lower friction coefficients below 0.1 are required. Figure 3 shows the sliding area of the silicon substrate coated with the lubricative CNTs after friction testing in vacuum. It is clearly

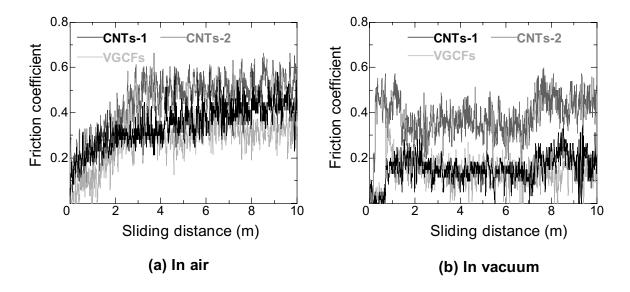


Figure 1. Variation of friction coefficient of CNTs and VGCFs on silicon in air and vacuum.

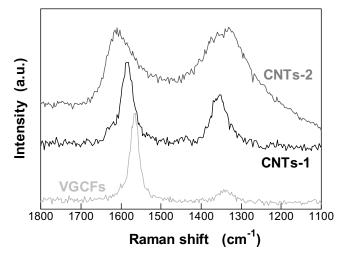


Figure 3. Silicon surface after sliding

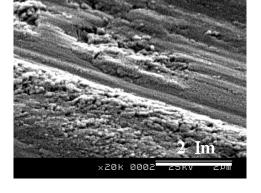
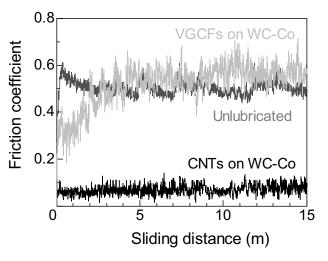


Figure 2. Raman spectra of CNTs and VGCFs.



2 <u>Im</u> ×29к 0021 - 25ку дрш

Figure 4. Variation of friction coefficient of CNTs and VGCFs on WC-Co in vacuum.

Figure 5. CNTs on WC-Co after sliding

observed that most CNTs are removed and the substrate surface is exposed, under which sliding conditions partial direct contact between silicon and steel causes higher friction.

In order to examine the tribological behaviors CNTs more precisely and achieve lower friction of CNTs coating, it is necessary to strengthen the adhesion of CNTs onto substrate surface. Considering micro topography of substrate surface would affect adhesion strength, cemented carbide (WC-Co alloy) was selected as substrate material. Cemented carbide has porous structure as well as a catalyst for CNTs deposition. Figure 4 shows the variation of friction coefficients during sliding between a stainless steel ball and CNTs coated on the cemented carbide sintered using WC of which average particle size is $1.0~\mu m$ and 5~wt.% of cobalt. It is found that friction coefficient is reduced lower than 0.1 and shows relatively stable variation. CNTs on cemented carbide are observed to stay on sliding area even after friction testing as shown in Fig. 5, which indicates improvement of the adhesion strength and would cause low friction.

SUMMARY

Tribological properties of CNTs coating catalytically deposited on silicon and cemented carbide substrates have been investigated by Ball-on-disk type friction testing. As a result, CNTs with fewer defects have displayed low friction property. Moreover, low friction property of CNTs has been exhibited in vacuum. Higher adhesion strength of CNTs has been achieved on cemented carbide substrate and has resulted in reduced friction coefficients below 0.1.

REFERENCES

- 1. Dong, S.R., Tu, J.P., and Zhang, X.B.: An Investigation of the Sliding Wear Behavior of Cu-matrix Composite Reinforced by Carbon Nanotubes. Mater. Sci. Eng. A, vol. 313, no. 1-2, 2001, 83-87.
- 2. Chen, W.X., et al.: Electroless Preparation and Tribological Properties of Ni-P-Cabon Nanotube Composite Coatings under Lubricated Conditions. Surf. Coatings Technol., vol. 160, no. 1, 2002, 68-73.
- 3. Chen, W.X., et al.: Tribological Properties of Ni-P-multi-walled Carbon Nanotubes Electroless Composite Coating. Mater. Lett., vol. 57, no. 7, 2003, 1256-1260.
- 4. Lim, D.-S., An, J.-W., and Lee, H.J.: Effect of Carbon Nanotube Addition on the Tribological Behavior of Carbon/Carbon Composites. Wear, vol. 252, no. 5-6, 2002, 512-517.

STUDY ON TEMPLATE PORE ACTING ON THE FABRICATED ARRAYS OF NANOMATERIALS

Y. B. Zhu^{1,2}, W. L. Wang¹, K. J. Liao¹, C. G. Hu¹ and Q. Feng¹

¹Department of Applied Physics, Chongqing University, 400044, P. R. China ²Department of Physics, Xuzhou Normal University, 221009, P. R. China

ABSTRACT

In this work, the features of template approach are discussed. Then the influences of density and sizes of their pores on the emission of fabricated arrays are theoretically studied. Especially, the emission from the arrays of carbon nanotubes or silicon nanowires was mainly discussed. Their tip electric field, electric field enhancement factor and optimum array density are wholly presented with analytic equations. The theoretical results showed that the field electron emission properties of carbon nanotube or silicon nanowire arrays are closely related to template pore density. When the pore density is near to the optimum array density, the fabricated arrays will have better electron emission and their field enhancement factor may be sharply improved. It was found the length and the radius of pores having different effect on the emission. It was certain that the pore radius played more effective role. A uniformly distributed model about templates and nanomaterial arrays was introduced, and applied into the concrete analysis of some carbon nanotube array samples with satisfactory results.

INTRODUCTION

There are many methods for preparing nanomaterials, however, most of them have the weakness which are attributed to the poor control of final morphology of produced nanostructures, although some special properties are exhibited only with enhanced molecular order. C. R. Martin et al. used a method lately termed "template synthesis" to produce conductive polymers. Then, the method has been used in experiments for many years, and a variety of micro- and nano-materials of a desired morphology were prepared. Various porous templates are employed and the nanostructures are synthesized within the pores. If the templates that are used have cylindrical pores of uniform diameter, monodisperse nanocylinders of the desired material can be obtained within the voids of the template material. The operating parameters define these nanocylinders of being solid (nanorods) or hollow (nanotubes). The nanostructures can still be freed and collected as an ensemble nanoparticles. Alternatively, they can protrude from the surface in an array. Therefore, one is able to prepare monodisperse nanorods and nanotubes of almost any desired geometry with the template approach. In fact, the method has been used to prepare both nanotubes and nanofibrils composed of polymers, metals, semiconductors, carbon, silicon and other materials.

Due to their particular electrical and optical properties, carbon nanotubes and silicon nanowires are highly focused on recently (ref.1-13). Especially, their electron emission properties are attractive (ref.2, 9-13). With high aspect ratio and other special geometrical features, carbon nanotube arrays are thought to be ideal materials for field emitters, and are expected for applications in the electron sources of ultrathin flat-panel field emission display (FED), microsensors and nanoprobes for atomic force microscopy (AFM) or scanning tunneling microscope (STM) etc. (ref.14-17). The silicon wire arrays may have the similar electrical characteristics.

NASA/CP—2003-212319 80 August 18, 2003

Up to now, the approach based on template has been used to fabricate the arrays of carbon nanotubes (CNTs) and silicon nanowires (SiNWs) (ref.2,12). It is an important thing in experiment to develop these arrays with low turn-on voltage, high current density and stable performance. Moreover, the field emission properties of arrays are usually evaluated with their electric field enhancement factor β that could be affected by some features or properties of templates, including the sizes and density of pores and structure in templates. For these reasons, the theoretical understanding of the relationship between the field enhancement and the features of template will be much helpful to finding more efficient ways of fabricating high emitting CNT or SiNW arrays with template synthesis.

Therefore, in the paper, we will theoretically explore the pores of templates acting on the fabricated arrays and their electron emission. This paper contains the following aspects: a model for templates and the fabricated arrays is put forward firstly; in virtue of this model under suitable physical boundary conditions, the correlation between the factor β and density and size of pores is presented and the corresponding equations is evolved; using the theoretic formula to evaluate the field enhancement factors of some CNT array samples. Our theoretical results demonstrated that the pores of template could produce an important effect on the field emission properties. Once the pore density equals to the optimum density, the emission properties of corresponding arrays are much improved. We work out the values of β of some carbon nanotube arrays, which are then compared with the experimental values obtained from the Fowler-Nordheim theory. Our results are found to be satisfactory.

A MODEL FOR TEMPLES AND THE FABRICATED ARRAYS

Template approaches have been successfully practiced to produce carbon nanotube or silicon nanowire arrays. In the synthesis, the choice of template is very important. The two types of nanoporous materials are often used as template in experiments: 'track-etch' polymeric membranes and porous alumina or silica membranes. 'Track-etch' materials generally contain randomly distributed channels of uniformed diameter, and the pore densities approach 10^9 pores cm^{-2} . By anodic oxidation of aluminum in solutions of sulfuric and oxalic acid, alumina membranes with uniform and parallel porous structure can be obtained. The densities of pores in this template are as high as 10^{-11} pores cm^{-2} and the thickness range from 10 to $100\mu m$. Likewise, silica aerobes, aluminosilicates, zeolite, natural scaffolds, and DNA etc. are also well suited for such applications.

Considering the characteristics of these temples ahead, a model for templates and their fabricated arrays here is constructed under following hypotheses. The templates have cylindrical channels or pores with uniform length and radius. These pores are parallel with each other, are evenly distributed (pore density is n), and have no tilt to the surface of the templates. Based on the ideal templates, the fabricated carbon nanotube or silicon nanowire arrays have uniform sizes as well. All nanotubes or nanowires in an array possess same length of l and (outside) radius of r_0 and are parallel with each other. They are also well aligned and arranged vertically toward the substrate. Because of the density and (outside) radius of nanotubes or nanowires being decided by that of pores of their template, here we think the array has totally same density (n) and radius (r_0) with its template. Figure 1 shows the sketch of the ideal templates.



Figure 1. The sketch of ideal templates.

THE OPTIMUM ARRAY DENSITY

For an array of CNTs or SiNWs with uniform size in an external electric field (\vec{E}_0), each nanotube or nanowise can be supposed to lie in a cylindrical equipotential well formed by adjacent nanotubes or nanowires because CNTs and SiNWs can be regarded as conductor. The potential distribution arrays should meet Laplace equation

$$\nabla^2 \varphi = 0 . (1)$$

In consideration of its symmetry in equipotential well and with cylindrical coordinates, equation (1) should become

$$\frac{1}{r}\frac{\partial}{\partial r}\left(r\frac{\partial\varphi}{\partial r}\right) + \frac{\partial^2\varphi}{\partial z^2} = 0. \tag{2}$$

According to the uniformly distributed model, one nanotube (nanowire) of the array locates in its potential well. The nanotube array is a potential volume. Let it be the cathode and its potential zero, namely $\varphi = 0$. The well radius R_0 is decided by the nanotube density n in the array, which is also the pore density, and can be expressed as

$$R_0 = \frac{1}{\sqrt{n}} - r_0 \quad . \tag{3}$$

And the boundary conditions of potential distribution in the well are

$$\begin{cases} \varphi = 0 & r = r_0 \\ \varphi = 0 & r = R_0 \\ \varphi = 0 & z = 0 \\ \varphi = f(r) & z = l \end{cases}$$

$$(4)$$

where $\varphi = f(r)$ is the top boundary function of well, which is to be determined. Owing to the symmetrical potential distribution in the well cylinder, the solution to equation (2) can be obtained through variable separation method

$$\varphi = (A_1 \ell^{kz} + A_2 \ell^{-kz}) [B_1 J_0(kr) + B_2 Y_0(kr)], \tag{5}$$

which gives the potential distribution in the well. Both $J_0(kr)$ and $Y_0(kr)$ in (5) are Bessel functions. Substituting the boundary conditions (4) into equation (5) or letting $z=0, \varphi=0$, $r=r_0, \varphi=0$ and $r=R_0, \varphi=0$ in equation (5), we can get

$$\begin{cases} J_0(kr_0) / Y_0(kr_0) = J_0(kR_0) / Y_0(kR_0), \\ A_1 = -A_2 \end{cases}$$
 (6)

where k is a set of values, $k_1, k_2, k_3, \dots (k_1 < k_2 < k_3 \dots)$. And the general solution of the equation (2) is

$$\varphi = \sum_{i=1}^{\infty} A_i sh(k_i z) [J_0(k_i r) - \frac{J_0(k_i R_0)}{Y_0(k_i R_0)} Y_0(k_i r)] = \sum_{i=1}^{\infty} A_i sh(k_i z) R(k_i r).$$
 (7)

Here,

$$R(k_i r) = J_0(k_i r) - \frac{J_0(k_i R_0)}{Y_0(k_i R_0)} Y_0(k_i r).$$
(8)

To get the coefficient A_i in eq. (7), the top boundary function $\varphi = f(r)$ must be determined beforehand.

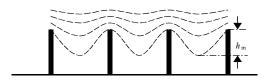


Figure 2. . Simulation of equipotential surface for nanomaterial arrays in electric field

Fig. 2 shows the equipotential surface among the nanotubes or nanowires of the array and $h_{\rm m}$ is the longest distance between the equipotential surface and the top surface of the array. In consideration of the characteristics of the equipotential surface, we choose the top boundary function as

$$\varphi = f(r) = \pm E_0 h_m R(k_1 r) \tag{9}$$

where $r_0 < r < R_0$, $0 < h_m < l$ and the sign '+' or '-' is adopted when the curve $R(k_1 r)$ is convex or concave. Substituting (9) into (7), and getting

$$\begin{cases} A_1 = \pm E_0 h_m / sh(k_1 l) \\ A_2 = A_3 = A_4 = \dots = 0 \end{cases}$$
 (10)

the potential distribution function can be written as

$$\varphi = \pm \frac{E_0 h_m}{sh(k_1 l)} sh(k_1 z) R(k_1 r) \qquad . \tag{11}$$

Bessel functions have the property that

$$\frac{\partial R(k_1 r)}{\partial r} = k_1 \frac{\partial R(k_1 r)}{\partial (k_1 r)} = -k_1 [J_1(k_1 r) - \frac{J_0(k_1 R_0)}{Y_0(k_1 R_0)} Y_1(k_1 r)], \tag{12}$$

so we get the electric field of nanotube or nanowire tips:

$$E_{tip} = -\frac{\partial \varphi}{\partial r}\Big|_{z=l,r=r_0} = \pm E_0 k_1 h_m [J_1(k_1 r_0) - \frac{J_0(k_1 R_0)}{Y_0(k_1 R_0)} Y_1(k_1 r_0)]. \tag{13}$$

The electric field enhancement factor of the array could be defined through its tip's field and the external field E_0 or

$$\beta = \frac{E_{tip}}{E_0} = \pm k_1 h_m [J_1(k_1 r_0) - \frac{J_0(k_1 R_0)}{Y_0(k_1 R_0)} Y_1(k_1 r_0)]. \tag{14}$$

which is usually used to evaluate field emission properties of arrays. The equation (14) shows the relation among the factor β , array sizes and density n. Substituting eq. (3) into eq. (14) and making $\partial \beta/\partial n = 0$, the optimum array density (n_0) can be calculated through

$$\frac{\partial}{\partial n} \left\{ \pm k_1 l \left[J_1(k_1 r_0) - \frac{J_0(k_1(\sqrt{1/n} - r_0))}{Y_0(k_1(\sqrt{1/n} - r_0))} Y_1(k_1 r_0) \right] \right\} \Big|_{n = n_0} = 0$$
 (15)

A curve of $\beta \sim n$ of function (14) for an array (r_0 =0.1, $h_{\rm m}$ =60 μm) is given shown as Fig. 3, in which the maximum value of β corresponds the optimum density of the array.

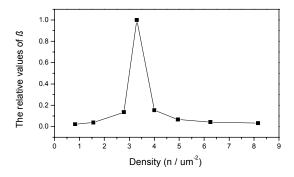
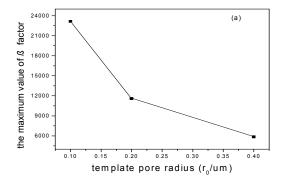


Figure 3. The plots of β -n curves of the array with nanotube radius of 0.1 μ m and length of 60 μ m

TEMPLATE PORE ACTING ON THE FABRICATED ARRAYS

The densities of arrays are always decided by their template pore densities. Therefore, figure 3 also demonstrates the relation between β factor of an array and its template pore density. From the figure, we can draw some valuable conclusions. To a template-synthesized array with a certain length and radius, its electric field enhancement factor may be greatly improved when the chosen template gets a specific, optimum pore density. If the pore density is away from the optimum value, the factor β will decrease obviously. It means emission properties of arrays are closely related to the density of pores and will be superior at the optimum pore density.



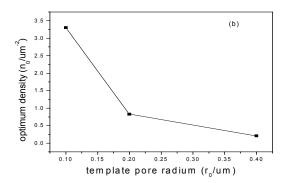


Figure 4. (a) The plots of the maximum values of β factor of CNT arrays changing with their template pore radius, (b) the optimum densities of templates changing with their pore radius.

Through further analyzing our calculation, we give the Fig.4. More information about templates and their fabricated arrays are obtained from Fig.4. That tells the fact: the smaller the pore radius of templates, the bigger the maximum value of the factor β of fabricated arrays, and the denser the corresponding optimum density. It implies that the nanomaterial arrays, which are fabricated on the templates with thinner channels, will have better field emission properties. Here, we use our theoretic equations (14) and (15) to evaluate the electric field enhancement factor β of the CNT array and the optimum pore density of the template in reference [13]. The data used are as below:

$$r_0=0.1\mu m$$
, $l=60\mu m$, $n=5.3\mu m^{-2}$, $R_0=0.334\mu m$, $k_1=13.199$;

and
$$J_1(k_1r_0) - \frac{J_0(k_1R_0)}{Y_0(k_1R_0)} Y_1(k_1r_0) = 1.622$$
 and $h_m = l$.

Tn, the factor β and the optimum pore density n_0 are worked out as 1285, 3.3×10^8 pores cm^{-2} respectively. The calculated value of β agrees with the experimental evaluation in the reference (ref.12).

The equation (14) obviously shows that there is no direct connection between the factor β and thickness of pores of templates. The parameter h_m relate to the thickness (l) of arrays but that does not always equal to that of templates. Moreover, we still find that due to the action of the field screening (ref.18), there is complicated relation between the parameter h_m and the thickness of arrays and these arrays made of the same material with the same radius and density but different thickness should have the same field enhancement factor value.

SUMMARY

To summarize, in this paper, template-based synthesis methods were reviewed and their features were introduced. Template synthesis method is one of important approaches used to fabricate carbon nanotube or silicon nanowire arrays. In synthesis experiments with CVD (chemical vapor deposition), to efficiently improve the field emission properties of the fabricated arrays, suitable length corresponding to the radius and density of the pores on templates should be selected through the control of source gases deposition time to make the arrays achieve a best state. In order to study the influence of the density and radius of pores on nanomaterial arrays, we put forward a uniformly distributed model for templates and nanomaterial arrays, and the tip electric field and the field enhancement factor of the arrays were studied in depth. We reported that pore densities greatly affect the field emission properties of template-based arrays and that there is an optimum pore density corresponding to each fabricated array. Once the optimum densities are achieved, the field enhancement factor and the emission properties of the fabricated arrays will be greatly improved. The effects of radius and length of pores on field emission property are also analyzed. The arrays formed within thin channels are superior on field emission properties to that formed within thick ones, while pore length has little influence on field emission. There should exist a proper ratio between pore radius and density, which plays a very important role in improving emission from arrays. The studies here will enlighten the process of choosing the proper ratio for array syntheses in experiments.

ACKNOWLEDGMENTS

The author acknowledge the financial support provide by Jiangsu education hall (2002, Nature Science Program, serial number: SL02009), and also thank C. Y. Kong, and G. B. Liu for their help and stimulating discussions.

REFERENCES

- 1. Sunkara M. K., Sharma S., and Miranda R. et al.: Bulk synthesis of silicon nanowires using a low-temperature vapor–liquid–solid method, Appl. Phys. Letts., vol. 79, no.10, 2001,1546.
- 2. Li M. K., Wei C. W., and Li H. L. et al.: Synthesis of ordered Si nanowire arrays in porous anodic aluminum oxide templates, Chinese Science Bulletin, vol. 46,no.21,2001, 1793

- 3. Ma X. L., Zhu Y. L., and Zhang Z.: Growth orientation of one-dimensional silicon nanowires prepared by thermal evaporation, Philosophical Magazine Letters, vol.82, no.8, 2002,461.
- 4. Gran A., Han J. and Sinnott S. B.: Interactions of carbon-nanotubele proximal probe tips with diamond and graphite, Phys, Rev. Lett., vol. 81, no.11, 1998, 2260.
- 5.Salvetat J. P., Bonard J. M. and Thomson N. H. et al.: Mechanical properties of carbon nanotubes, Appl. Phys. A, vol. 69, 1999, 255.
- 6. Tan S. J., Verschueren A. R. M. and Dekker C.: Room-temperature transistor based on a single carbon nanotube, Nature, vol.393, 1998, 49.
- 7. Kasumov A., Deblock R. and Kociak M. et al.: Supercurrents through single-welled carbon nanotubes, Science, vol.284, 1999, 1508.
- 8. Benerd J. M., Stockli T. and Maier F. et al.: Field-emission-induced luminescence from carbon nanotubes, Phys. Rev. Lett., vol.81,no.7,1998,1441.
- 9. Bonard J. M., Salvetat J. P. and Stockli T. et al.: Field emission from carbon nanotubes: Perspectives for applications and clues to the emission mechanism, Appl. Phys. A, vol. 69, 1999, 245.
- 10. Saito Y., Hamaguchi K. and Uemura S. et al.: Field emission from multi-walled carbon nanotubes and its application to electron tubes, Appl. Phys. A, vol. 67, 1998, 95.
- 11. Davydov D. N., Sattari P. A. and AlMawlawi D. A. et al.: Field emitters based on porous aluminum oxide templates, J. Appl. Phys., vol.86, no.7, 1999,3983.
- 12. Wang C. W., Li M. K. and Li H. L.: The field emission properties of self oriented regular array of carbon nanotubes on template, Science in China A, vol. 30, no.11, 2000, 1019.
- 13. Fan S., Chapline M. G. and Franklin N. R. et al.: Self-oriented regular arrays of carbon nanotubes and their field emission properties, Science, vol.283, 1999, 512.
- 14. De Heer W. A., Chatelain A., and Ugarte D.: A carbon nanotube field-emission electron source, Science, vol.270, 1995,1179.
- 15. Saito Y., Uemura S., and Hamaguchi K.: Cathode ray tube lighting elements with carbon nanotube field emitters, Jpa. J. Appl. Phys., vol.37, 1998, 346.
- 16. Chang T. H. P. et al.: Scanning microscope controlled field emission microprobe system, J. Vac. Sci. Technol. B, vol. 9, 1991, 438.
- 17. Nagy G., Levy M., and Scarmozzino R. et al.: Carbon nanotube tipped atomic force microscopy for measurement of <100 nm etch morphology on semiconductors, Appl. Phys. Lett., vol.73, 1998, 529.
- 18. Nishizawa M., Mukai K., and Kuwabata S. et al.: Template synthesis of polypyrrole-coated spinel LiMn2O4 nanotubules and their properties as cathode active materials for lithium batteries, J. Electrochem. Soc., vol.144, 1997, 1923.

MEASUREMENT OF APPARENT THERMAL CONDUCTIVITY OF NANO PARTICLES

Efim Litovsky, Jacob Kleiman

Integrity Testing Laboratory Inc. 80 Esna Park Drive, Units 7-9, Markham, Ontario, L3R 2R6, Canada jkleiman@itlinc.com; tel. 905 - 415-2207; fax: 905-415=3633

Yoshinori Koga

National Institute of Advanced Science & Technology 1-1-1-, Higashi, Tsukuba-shi, Ibaraki-ken, 305-8565, Japan

ABSTRACT

A new measurement method based on a proprietary, developed at ITL methodology for measurement of thermal conductivity of thin rods is being developed and used in a project aimed at measurement of thermal conductivity of various types of nano particles including single wall carbon nanotubes (SWCNT).

The thermal conductivity of nano particles can be determined based on mathematical models of apparent thermal conductivity of mixtures of such particles with liquids [1-4]. The different mathematical models take into account the shape of particles, their sizes, volume concentration and orientation f the particles inside the mixture.

Measurement of apparent thermal conductivity of the prepared mixtures will be conducted using standard well-established methods. For reliable and stable results, very good wetting of the particles by the chosen liquid should be provided. A thorough study of wetting behavior of the SWCNT by liquids will be conducted and the most appropriate liquid will be chosen for experiments.

Based on apparent thermal conductivity measurements and the above mathematical models, the thermal conductivity of nano particles of different shapes will be determined in different directions. Special theoretical corrections must be introduced and taken into account in building the model of the nanotubes with the liquid inside them. The introduced corrections will take into account the fact that the substitution of air by liquid will decrease the thermal conductivity (Kn number) behavior of the nanotubes interior [2-3].

References:

- 1. Litovsky E.Ya., Shapiro M., "Gas Pressure and Temperature Dependences of Thermal Conductivity of Porous Ceramic Materials. Part I. Refractories and Ceramics with Porosity Below 30%, J. *American Ceram Soc.* 12, pp. 3425-3439, (1992).
- 2. Litovsky E., Shapiro M. and Shavit A, "Gas Pressure and Temperature Dependences of Thermal Conductivity of Porous Ceramic Materials. Part II. Refractories and Ceramics with Porosity Above 30%", J. *American Ceram. Soc.*, 79/5, 1996 1366-1376.
- 3. Litovsky E., Gambaryan-Roisman T., Shapiro M. and Shavit A, Heat Transfer Mechanisms Governing Thermal Conductivity of Porous Ceramic Materials, *Trends in Heat, Mass & Momentum Transfer, Research Trends*, vol. 3, pp 147-167, 1997.
- 4. E. Litovsky, J. Kleiman, "Relative Influence of Heat Transfer Mechanisms on Apparent Thermal Conductivity of Porous Materials", 26th International Thermal Conductivity Conference, MA, USA, 2001.

Keywords: nanoparticles, carbon nanotubes, thermal conductivity, modelling

Characteristics of Carbon Nanotube Electron Field Emission Devices Prepared by LTCC Process

Tsong-Yen Tsai, Nyan-Hwa Tai

Department of Material Science and Engineering, National Tsing-Hua University, Hsin-Chu Taiwan.

I-Nan Lin

Material Science Center, National Tsing-Hua University, Hsinchu, Taiwan inlin@mx.nthu.edu.tw

Abstract

Carbon nanotubes (CNT) possess marvelous electron field emission properties and have been widely investigated for applications as electron sources in field emission displays (FED). While the high quality carbon nanotubes can be synthesized by several method, including laser ablation, thermal chemical vapor deposition and plasma enhanced chemical vapor deposition techniques, direct growth of CNT on electron field emission devices is still very difficult due to stringent control of synthesizing conditions necessary. Screen-printing of CNT/Ag-paste on glass substrates is an inexpensive and efficient way of making large patterned emitter arrays, but suffered from the packaging and electrical connecting problems. In contrast, low temperature cofirable ceramics (LTCC), which provide mutilayer inter-connection and hermit seal at the same time, are thus suitable for using as substrate materials for electron emitters. In this paper, we shall demonstrate the electron field emitters using CNT printed on LTCC as electron sources.

CARBON NANO-MATERIALS FOR VACUUM ELECTRONICS

A.N. Obraztsov, A.P. Volkov, Al.A. Zakhidov, A.A. Zolotukhin, A.O. Ustinov, D.A. Lyshenko
Department of Physics, Moscow State University
Moscow 119992, Russia

ABSTRACT

A number of vacuum electronic devices, including MW generators and amplifiers, CRT, X-ray tubes etc., utilize electron beams produced by cathode. An essential improvement of the devices may be obtained using field emission cathodes providing intense monoenergetic electron beam and operating at room temperature. Material of these cold cathodes must sustain very strong electric field and residual gas ion bombardment in the vacuum tubes. This requirement limits list of appropriate materials by a few hard metals (like Mo, W), semiconductors (Si) and carbons with diamond and graphite atomic configurations. The carbon materials have strongest interactomic σ - σ bonding but diamond has no free electrons to emit them into vacuum and graphite itself has layered structure with very weak interlayer bonding. Carbon nanotubes seems to be ideal field emitters having strongest graphite-type interatomic bonding, cylindrical configuration of atomic layers, preventing their destruction under strong electric field and highest aspect ratios allowing significant decrease of used voltages.

This report presents our comparative study of field emission from various carbon nano-materials. Carbon nanotubes synthesized by arc-discharge methods, nano-diamond powders and films, and nano-graphitic CVD films were tested for field emission and other properties. The conditions of used CVD process were optimized to obtain most efficient carbon cold cathode material. We propose mechanism of electron emission from carbon nanomaterials based on assumption of heterogeneous sp²-sp³ structure formation. Device applicability of the cold carbon cathodes is demonstrated in prototypes of cathodoluminescent light sources.

Keywords: Nano-carbon, Field emission, Cold cathode, CVD

Preference: oral

<u>The corresponding author</u>: Alexander N. Obraztsov, Department of Physics, Moscow State University, Moscow 119992, Russia. E-mail: <u>obraz@acryst.phys.msu.ru</u>, Fax: +7-095-939-2988, Tel.: +7-095-939-4126

ELECTROCHEMICAL OXIDATION OF PHENOL AT CARBON NANOTUBE ELECTRODE

C. G. Hu¹, W. L. Wang ¹, K. J. Liao ¹, X. H. Xian ², Q. Feng ¹, G. B. Liu¹

¹Department of Applied Physics, Chongqing University, Chongqing 400030, P. R. China ²Department of Chemistry, Chongqing University, Chongqing 400030, P. R. China

ABSTRACT

The carbon nanotubes synthesized by hot-filament chemical vapor deposition were modified by concentrated nitric acid with a little surfactant. The electrochemical oxidation of phenol at the carbon nanotube electrode has been studied in phosphate buffer solution by cyclic voltammetry. The results showed that the direct electron transfer reactions on the carbon nanotube electrode surface could occur in the potential region of water stability, which resulted in the active groups on the carbon nanotubes due to the chemical modification. The well defined and reproductive oxidation peaks at 0.73 V vs. SCE, scan rate 50 mVs⁻¹ were clearly observed at the carbon nanotube electrode, which indicated that the electrode could avoid electrode fouling. The reaction process was controlled by diffusion process. The anodic peak current increased linearly with the concentration of phenol in the range of 1.0×10^{-5} - 1.0×10^{-4} mol L⁻¹ in cyclic voltammetric measurement. The electrochemical oxidation of phenol was also carried out on a fresh polished GC electrode for comparison, which did not have well defined oxidation peak and peak current decayed rapidly down with the every cycle. The mechanism of oxidation was discussed in details.

Keywords: carbon nanotube; electrochemistry; chemical modification; phenol; cyclic voltammetry

INTRODUCTION

With a rapidly growing world population and increasing levels of pollution, the protection of the environment and the preservation of resources have become a major issue for future technological progress. Strategies for ecological protection generally include development of new or improved industrial processes that have no or minor effects on nature, and of processes for the treatment of inevitable waste.

Due to the fact that water is a limited and vital resource, it should not end as inevitable waste after having been used e.g. in industrial processes. Therefore, one of the major research and development tasks in the future is the provision of high quality water in sufficient quantity and at an affordable price. These research and development tasks aim at the treatment of wastewater for reuse. Therefore, electrochemical process used for the recovery or treatment of wastewater from industrial plants plays an important role (ref. 1,2). Oxidative processes have a continuously increasing importance in the reduction of toxic pollutants or at least in their conversion to biocompatible species (ref. 3). Economical and efficient oxidation rates for industrial water recycling are urgent.

A reason for the low reaction rate found with electrochemical oxidation of some aromatic organic compounds (ref. 1-5) is electrode fouling. Fouling is minimized at low concentrations, elevated temperatures and large values of applied overpotentials that increase the rate of anodic discharge of H_2O to generate hydroxyl radicals. Two different

pathways are described in the literature for the anodic oxidation of undesired organics (ref. 4,5): electrochemical conversion and electrochemical combustion. Electrochemical conversion transforms only the toxic non-biocompatible pollutants into biocompatible organics, so that biological treatment is still required after the electrochemical oxidation. Electrochemical combustion yields CO₂ and no further purification is necessary. Experimental results indicate that the accumulation of hydroxyl radicals favors the combustion reaction whose occurrence is related to catalyst pretreatment and experimental conditions used (ref. 4 to 8)

Carbon nanotube (CNT) has attracted the attention of many scientists worldwide. Their small dimensions, strength and the remarkable physical properties of these structures make them a very unique material with a whole range of promising applications (ref. 9 to 12). Depending on their atomic structure, carbon nanotubes behave electrically as metal or as a semiconductor (ref. 13 to 15). The subtle electronic properties suggest that carbon nanotubes have the ability to promote electron-transfer reactions when used as an electrode in chemical reactions (ref. 16). CNTs as an electrode material have been investigated in past few years (ref. 17 to 23). However, most of these electrodes are constructed by casting or intercalating CNTs on the surface of traditional electrodes, such as Pt, Au, GC and graphite electrodes (ref. 20 to 22). In this work, electrochemical oxidation of phenol is conducted at a pure CNT electrode. Phenol is an important pollutant widely found in natural water, which mainly comes from the wastewater of petroleum, plastics, organic chemicals and other industries. Phenol is well known for its ability to foul traditional electrodes and the tarry deposit formed on the electrodes during phenol oxidation. Our experiment results show that CNT electrode has high overpotentials for water electrolysis. This electrochemical window is large enough to produce hydroxyl radicals with high efficiency, which may oxidize organics completely to carbon dioxide. The properties of CNT electrodes might well meet the requirements for an efficient electrochemical wastewater treatment.

EXPERIMENTAL

Carbon nanotubes were synthesized by hot filament chemical vapor deposition. The details of the fabrication have been reported elsewhere (ref. 23). In order to increase solubility of CNTs, we treated CNTs as follow: First, soak the CNTs in 5 M nitric acid, ultrasonically disperse them for 10 minutes at 40 °C and then put them under a infrared lamp oven for 4 hours at 45 °C with strongly dispersing in half hour interval. Second, dilute them with a large amount of water and add a little Triton X-100 surfactant to increase solubility, sonicate them to be a black solution. Third, filter the black solution with 0.2 µm diameter film and collect the nanotubes. Repeat the second and the third steps.

Cyclic voltammetric measurements were performed with a Microcomputer-based Electrochemical Analyzer (LK98BII, home made) with a conventional three-electrode cell. The working electrodes were the CNT electrode and a GC electrode, the auxiliary electrode was a platinum electrode, and a saturated calomel electrode (SCE) was used as the reference electrode. All the reagents were of analytical grade and all solutions were prepared in deionized distilled water. The cyclic voltammetric experiments were carried out at room temperature (about 18 0 C).

The CNT electrode that was prepared by sonicating CNTs in DMF to give a black solution, then depositing them on the surface of insulated substrate. Ohmic contacts for the planar electrodes were made on the front side of the films with silver paste. The electrodes were mounted with epoxy. Film thickness was approx. 20 μ m and resistivity was about 350 Ω ·cm. The geometric area of the working electrode was estimated to be 0.142 cm². The diameter of GC electrode was 8 mm (area, 0.5 cm²) and its surface was polished with 0.5 m alumina on a polishing micro-cloth and rinsed with deionized water.

RESULTS AND DISCUSSION

Figure 1. (a) shows cyclic voltammetric curves for CNT electrode in a solution containing different concentration of phenol in 0.1 M phosphate buffer solution, pH 7, at scan rate 100 mV s⁻¹. Well-defined oxidation peaks appear and the potential position of peak is at 0.74 V when concentration of phenol is 0.1 m mol L⁻¹. Peak current density j, which is defined as current divided by apparent area, increases linearly over the range of $10^{-5} - 10^{-4}$ mol L⁻¹ phenol, while position of peak shifts toward positive potential as the concentration of phenol increases. This result reveals that it is very promising to use CNT electrode for the trace phenol detection. This advantage should be valuable for the electroanalytical application. In order to further know the reaction process, we vary the scan rate; and the anodic peak current density increases linearly as a function of the square root of the scan rate as shown in figure 1. (b). The linear equation is $j_{pa} = -0.54 + 11.26 \text{ v}^{1/2}$, r = 0.999, where j_{pa} is anodic peak current density, v is scan rate and r is correlation coefficient. Such linearity indicates that the reaction rate is limited by semi-infinite linear diffusion of phenol to the interfacial reaction zone.

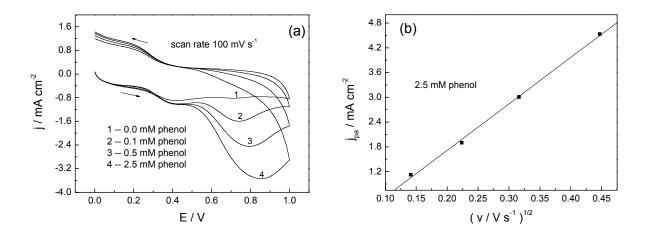


Figure 1. (a) Cyclic voltammograms for different concentrations of phenol and (b) anodic peak current density as a function of scan rate for 2.5 m mol L⁻¹ phenol at CNT electrode in 0.1 mol L⁻¹ phosphate buffer, pH 7.

Figure 2. (a) gives five cyclic curves at CNT electrode for 2.5 m mol L^{-1} phenol in 0.1 mol L^{-1} phosphate buffer, pH 7, scan rate 50 mV s⁻¹. We can see good reproducible curves except first cyclic, which indicates that the CNT electrode could avoid electrode fouling. The possible reason for the CNT electrode antifouling is that the active groups such as carboxyl groups on the CNTs due to the chemical treatment and the CNT electrode has high overpotential in aqueous media. This electrochemical window is large enough to produce hydroxyl radicals with high efficiency, which may oxidize phenol completely to carbon dioxide. We also assume that phenol is combusted to CO_2 and H_2O near the electrode surface (ref. 8):

$$C_6H_5OH + 11 H_2O \rightarrow 6CO_2 + 28H^+ + 28 e^-$$
.

As the oxidation of phenol at the CNT electrode is a completely combustion process, there is no fouling at the surface of the electrode so that cyclic voltammograms show superb repetition for long time potential scan. For the

comparison, the same experiment has been carried out at freshly polished GC electrode and the results are shown in figure 2. (b). From figure 2., we can clearly see that oxidation peak current decreases rapidly as the cyclic number increases. This demonstrates that the fouling has happened on the GC electrode surface, thus the electrode cannot remain its activity.

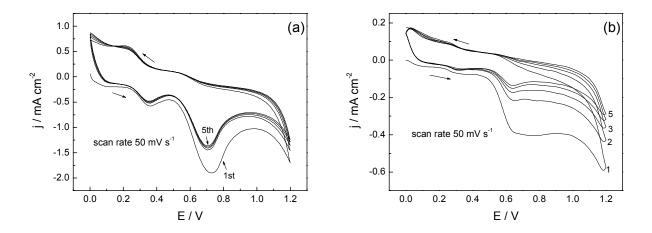


Figure 2. (a) Five cyclic curves at the CNT electrode and (b) at GC electrode for 2.5 m mol L^{-1} phenol, in 0.1 mol L^{-1} phosphate buffer solution, pH 7.

CONCLUSION

The efficient electrochemical oxidation of phenol at the CNT electrode has been shown in this investigation, which has two major applications: one is for electroanalytic application and another is for electrochemical treatment of organics in wastewater. Due to the high overpotentials at the CNT electrode in water media, hydroxyl radicals can be produced with high efficiency, which might oxidize organics completely to carbon dioxide. Therefore, there is little fouling happened on the surface of the electrode, thus the electrode can remain active for long time. This result reveals that it is very promising to use the CNT electrode for the trace phenol detection. Since the complete combustion of phenol has been demonstrated at the CNT electrode, this process could be used by industry as further treatment of aqueous phenolic wastes.

ACKNOWLEDGMENTS

This work has been financially supported by the Applied Research in Basics Foundation (7327) of Scientific Committee of Chongqing City.

REFERENCES

- 1. Rajeshwar K., Ibanez J. G., Swain G. M., Electrochemistry, Photochemistry and the Environment, J. Appl. Electrochem., vol. 24, 1994, 1077
- 2. Iniesta J., Michaud P. A., Panizza M., et al., Electrochemical oxidation of phenol at boron-doped diamond electrode", Electrochimica Acta, vol. 46, 2001, 3573-3578

- 3. Foti G., Gandini D., Comninellis Ch., et al., Oxidation of Organics by Intermediates of Water Discharge on IrO₂ and Synthetic Diamond Anodes, Electrochemical and Solid State Letters, vol. 2, 1999, 228
- 4. Gattrell M., Kirk D. M., A Study of the Oxidation of Phenol at Platinum and Preoxidized Platinum Surfaces, J. Electrochem. Soc. vol. 140, 1993, 1534-1540
- 5. Comninellis Ch., Electrocatalysis in the electrochemical conversion/combustion of organic pollutants for waste water treatment, Electrochem. Acta, vol. 39, 1994, 1857-1862
- 6. Iniesta J., Michaud P. A., Panizza M., et al., "Electrochemical oxidation of phenol at boron-doped diamond electrode", Electrochimica Acta, vol. 46, 2001, 3573-3578
- 7. Grimm J., Bessarabov D., Maier W., et al., "Sol-gel film-preparation of novel electrodes for the eledtrocatalytic oxidation of organic pollutants in water", Desalination, vol. 115, 1998, 295
- 8. Iotov P. I., S Kalcheva. V., Mechanistic approach to the oxidation of phenol at a platinum/gold electrode in an acid medium, J. Electroanalyt. Chem. vol. 442, 1998, 19-26
- 9. Iijima S., Helical microtubules of graphitic carbon, Nature, vol. 354, 1991, 56-58
- 10. Kazaoui S., Mianmi N., Jacquemin R., Amphoteric doping of single-wall carbon-nanotube thin films as probed by optical absorption spectroscopy, Phys. Rev. **B**, vol. 60, no.19, 1999, 13339-13342
- 11.Bower C., Zhou O., Nucleation and growth of carbon nanotubes by microwave plasma chemical vapor deposition, Appl. Phys. Lett. vol. 77, no.17, 2000, 2767-2769
- 12. Bachtold A., P Hadley., Nakanishi T., Dekker C., Logic Circuits with Carbon Nanotube Transistors, Science, vol. 294, 2001, 1317-1320
- 13. Sun L. F., Xie S. S., Zhou W. Y., et al., Materials: Creating the narrowest carbon nanotubes, Nature, vol. 403, 2000, 384
- 14. Pan Z. W., Xie S. S., Chang B. H., et al., Very long carbon nanotubes, Nature, vol. 394, 1998, 63
- 15. Colbert D. Zhang T., J., McClure S. M., et al., Growth and Sintering of Fullerene Nanotubes, Science, vol. 266, 1994, 1218
- 16. Baughman R. H., Cui C., Zakhidov A. A., et al., Carbon Nanotube Actuators, Science, vol. 284, 1999, 1340-1344
- 17. Britto P. J., Santhanam K. S. V., Ajayan P. M., Carbon nanotube electrode for dopamine oxidation, Bioelectrochem. Bioenerg. vol. 41, 1996, 121
- 18. Davis J. J., Coles R. J., Hil H. A. O., Protein electrochemistry at carbon nanotube electrodes, J. Electroanal. Chem. vol. 440, 1997, 279-282
- 19. Campbell J. K., Sun L., Crooks R. M., Electrochemistry Using Single Carbon Nanotubes, J. Am. Chem. Soc. vol. 121, 1999, 3779-3780
- 20 Liu C. Y., Bard A. J., Wudl F., Weitz I., Heath J. R., Electrochemical Characterization of Films of Single-Walled Carbon Nanotubes and their Possible Application, Electrochem. Solid State Lett. vol. 2, 2001, 915
- 21. Luo H. X., Shi Z. J., Li N. Q., et al., Investigation of the Electrochemical and Electrocatalytic Behavior of Single-Wall Carbon Nanotube Film on a Glassy Carbon Electrode, Anal. Chem. vol. 73, 2001, 915-920
- 22. Wang Z. H., Liang Q. L., Wang Y. M., Luo G. A., Carbon nanotube-intercalated graphite electrodes for simultaneous determination of dopamine and serotonin in the presence of ascorbic acid, J. Electroanal. Chem. vol. 540, 2003, 129-134
- 23. Hu C. G., Wang W. L., Wang S. X., Zhu W., Li Y., Investigation on Electrochemical Properties of Carbon Nanotubes, Diamond and Related Material, 2003, in press

CHARACTERIZATION AND FIELD EMISSION PROPERTIES OF SWNTS AND MWNTS

Sigen Wang, Qing Zhang, S. F. Yoon, J. Ahn, D. J. Yang, Q. Wang, J.Q. Li, Q. Zhou, J.Z. Tian

Microelectronics Centre, School of EEE, Nanyang Technological University

esgwang@ntu.edu.sg

Abstract

Carbon nanotubes have been rapidly recognized as one of the most promising electron field emitters ever since the first emission experiments reported in 1995, due to their unique structure and properties such as high aspect ratio, small radius of curvature at their tips, high mechanical strength and high chemical strength. In this paper, single-walled nanotubes (SWNTs) and multi-walled nanotubes (MWNTs) were characterized using scanning electron microscopy, transmission electron microscopy and Raman spectroscopy. Electron field emission from these SWNTs and MWNTs was measured. The experimental results show that the field emission property of MWNTs is better than that of SWNTs. The field emission mechanisms were also discussed.

SPATIALLY RESOLVED ANALYSIS OF THE ELECTRONIC PROPERTIES OF WS₂-COATED CARBON NANOTUBES USING EELS IN A TEM

V. Stolojan*, M.J. Goringe

School of Engineering, University of Surrey, Guildford, GU2 7XH, UK.

S.R.P. Silva

Advanced Technology Institute, University of Surrey, Guildford, GU2 7XH, UK.

R.L.D Whitby, D.R.M. Walton, W.K. Hsu and H.W. Kroto

School of Chemistry, Physics and Environmental Science, University of Sussex, Brighton, BN1 9QJ, UK.

*Corresponding author: tel.: +44 (0)1483 686299, fax: +44 (0)1483 686291, email: V.Stolojan@surrey.ac.uk

ABSTRACT

Using the line focusing properties of the Gatan Imaging Filter (GIF) fitted to a transmission electron microscope (TEM), it is possible to extract electron energy loss (EEL) spectra with sub-nanometre spatial resolution from interfaces, whilst still maintaining parallel illumination. This non-contact technique allows for the investigation of the electronic properties of heterojunctions on a nanometre and sub-nanometre scale.

Here we investigate the dielectric properties of the tungsten disulfide coating of a multi-walled carbon nanotube (MWCNT), by examining the change in the plasmon energy as a function of the coating's thickness. We show that for coating layer thicknesses above 5 monolayers (~3.1 nm), there is a change in the plasmon region of the EEL spectra across the interface that indicates a change in the dielectric properties.

Keywords: EELS, TEM, tungsten disulfide, spatial resolution.

INTRODUCTION

Carbon nanotubes can be used as templates for the production of metal oxide thin layers (ref.1). By pyrolysing H_2S/N_2 over MWCNTs coated with WO₃, the oxide converts to one or more layers of WS₂ (ref. 2 and ref. 3). Thus a heterojunction is created, comprising of metallic and semiconducting phases, at the cylindrical interface between the MWCNT and the WS₂ coating. Electron Energy Loss Spectroscopy (EELS) performed with high spatial resolution in a (Scanning) Transmission Electron Microscope (S)TEM is the only technique capable of investigating the electronic structure across this interface. For a dedicated STEM, this means scanning a sub-nanometre sized probe across the coated MWCNT (perpendicular to the tube's axis of symmetry) and collecting EEL spectra at each of the points (see for example ref. 4). In an average TEM, such as used here, the smallest probe size that can be achieved is of the order of 1-2 nm, but using the line spectroscopy technique (ref. 5 and ref. 6), it is possible to obtain information about the electronic structure with sub-nanometre spatial resolution, whilst at the same time maintaining parallel illumination (as opposed to focusing and scanning a probe across the interface). This is possible because of the line-focusing properties of the magnetic quadrupole lenses in the GIF.

EXPERIMENTAL METHOD

The WS₂ were prepared by pyrolysing WO₃-coated MWCNT at 900°C in the presence of a gaseous H₂S/N₂ mixture (ref. 3). Figure 1 shows a typical image of such a MWCNT, covered with 6 layers of WS₂. The image in Figure 1 is formed with the elastically scattered electrons (i.e. only their momenta have changed when passing through the sample); the much heavier W atoms scatter the electrons to higher angles, hence the much darker fringes in the image correspond to WS₂ layers whilst the lighter fringes correspond to the carbon layers of the MWCNT. Most coated MWCNTs also exhibit an amorphous layer of 1-2 nm thickness. Electron Energy Loss Spectroscopy reveals this layer to be carbon, possibly as a residue of incomplete oxidation.

The electron microscopy sample was prepared by ultrasonically dispersing the powder containing WS₂-coated MWCNT in ethanol, and then placing a few drops of the suspension onto a 3 mm holey carbon Cu support grid.

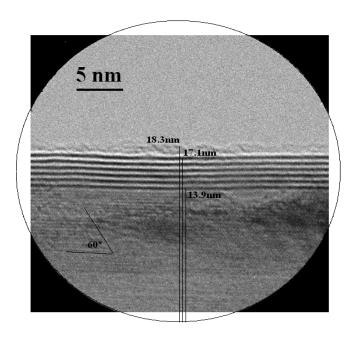


Figure 1. Typical image of the WS₂-coating on a MWCNT, formed with elastically scattered electrons. Also shown is the size of the collector aperture which is mapped into the line spectra in figure 2b. The total thickness of the 6-layered WS₂ coating is ~3.7 nm.

The sample was analysed using a Philips CM200 TEM operated at 200 kV, equipped with a LaB₆ filament and a Gatan Imaging Filter (GIF) electron spectrometre. The GIF is operated most commonly in either energy filtered imaging mode or in spectroscopy mode.

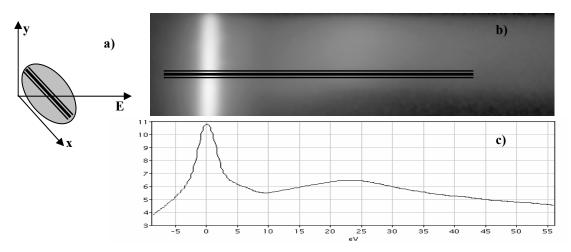


Figure 2. Experimental recording of spatially resolved spectra using parallel illumination. a) The 3D-data set available, with a schematic image of the WS_2 -layer drawn oriented parallel to the X-axis and bordered by the collector aperture; b)Log of the data recorded in the (y,E) plane in Fig. 2a) contains spatial information vertically and energy loss information horizontally. The line shows the position of the layer in Fig. 2a; c) Vertical projection of the data set in b) shows a typical low loss spectrum (in log format) containing the zero energy loss peak and the plasmon peak (\sim 24 eV).

One way to view these operating modes is to look at the dimensionality of the information provided and the way it is recorded (Fig.2a). A GIF provides three orthogonal dimensions (two are the spatial information and one is energy loss information), but only has a two-dimensional detector (the CCD). Thus, an energy filtered image is simply a section (selected by an energy-selecting slit) of the 3D data set parallel to the x-y plane, integrated over a region of energy loss E. On the other hand, a one-dimensional energy loss spectrum is obtained by integrating over one of the spatial dimensions (say x) using the line focusing properties of quadrupole lenses and then using the CCD to integrate the recorded image in the Y direction. We can see that if a linear feature is oriented parallel to the axis integrated by the quadrupoles (X), then the CCD records a 2D data set with one dimension the energy loss spectrum and the other (Y) the spatial dimension across the layers (Figure 2b) (ref. 5). The spatial resolution is determined by the magnification and is limited, in the first instance, by the chromatic aberration of the TEM-GIF system, but it can be usually better than 1nm, below the smallest spot size achievable in an average TEM (ref. 6).

The MWCNTs with varying thickness of the WS_2 -coating were aligned with their axis parallel to the axis over which the quadrupoles of the GIF integrate to within 0.5° , by means of a tilt-rotate holder. In each case, 25 line spectral images (Figure 2b) were collected, aligned, summed and calibrated in energy and position across the nanotube.

RESULTS AND DISCUSSION

Figure 3 shows in detail the plasmon peaks from successive spectra across a MWCNT with a 5-layer WS₂ coating, with the distances measured from the outer surface of the WS₂-coating layer (positive towards the centre of the MWCNT and negative away from it). Previous analyses (ref. 4 and ref. 7 to 10) of the low energy-loss spectra across carbon nanotubes have shown that for nano-objects of finite thickness, such as discussed here, surface and interface excitation effects can couple to bulk excitation modes resulting in the splitting of the modes of excitation. In particular Kociak et al (ref. 9) show that for a thin WS₂ nanotube (note: no carbon), the low loss spectrum splits into a band of peaks between 0 and 15eV and another peak at 22 eV. As the thickness of the coating increases, the 0-15 eV band and the 22 eV peak are expected to merge.

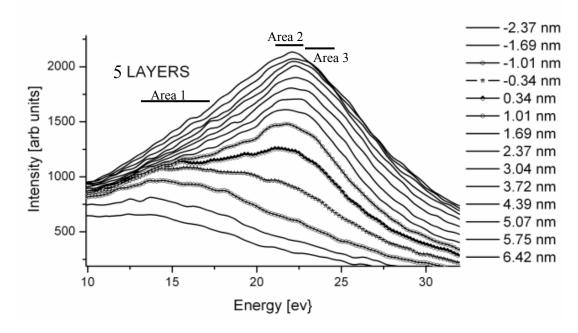


Figure 3. Detail of the plasmon peaks at positions across a 5-layer WS₂-coated MWCNT. The top-most spectrum corresponds to 6.42 nm and then continuously to the lowest spectrum corresponding to -2.37 nm. Distances are measured from the outer WS₂ layer, with positive direction towards the centre of the MWCNT. There is a transition from the bulk plasmon mode (open hexagons 1.01 nm) through to a surface mode (open circles:-1.01 nm) with a small region (~2 nm) where the two modes are combined. Also shown are the windows of integration 1, 2 and 3 centred on three modes of excitation.

Although the case studied here involves carbon nanotubes coated with WS_2 , we attempt to recognise some of the features relevant to pure WS_2 tubes (such as the 22 eV peak – ref. 9). Indeed, in Figure 3 we note that there is an increase in the intensity of the plasmon peak at around 22 eV for the spectra which are 1.69 nm and 1.01 nm from the outside of the WS_2 coated nanotube, roughly at the position of the interface between the coating and the nanotube. In order to analyse this mode, we identify three windows of interest in the spectra in figure 3: 14 to 17eV (centred on 15.5 eV), 21 to 23 eV (centred on 22 eV) and 23 to 25 eV (centred on 24eV) which we will call areas 1, 2 and 3 respectively.

When looking at the change in the intensity of the 22 eV plasmon mode, there is no apparent increase for coating thicknesses up to 4 layers (Figure 4 a-d). However, there is a marked change for 5 layers (and up), showing an increase in the 22 eV peak intensity at the coating.

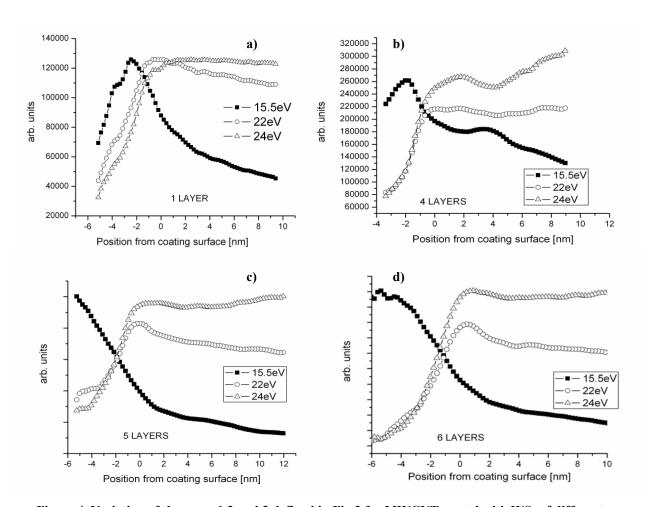


Figure 4. Variation of the areas 1,2 and 3 defined in Fig.3 for MWCNT coated with WS₂ of different thicknesses: a) 1-layer coating; b) 4-layer coating; c) 5-layer coating, showing the presence of a 22eV interfacial mode at the coating; d) 6-layer coating showing a similar behaviour to the 5-layered coating.

The plasmon mode seen at 22 eV for coating layer thicknesses above 5 monolyers, at the position of the interface, suggests that it is due to the WS_2 coating (ref. 9). In the case of the pure WS_2 nanotube, this plasmon mode appears because of the coupling between the plamons on the outer and inner surfaces of the tube. The appearance of this mode in our spectra indicates that one can define an inner surface of the WS_2 coating from a dielectric point of view. At this interface, we expect to have an interfacial plasmon with an energy given as some weighted average of the surface WS_2 and carbon plasmon energies (ref. 11). The surface plasmon for a thick carbon nanotube is bimodal, with peaks at 15 eV and 18 eV (ref. 10), whilst the WS_2 surface plasmon energy is at ~17 eV. The averaged interface plasmon energy is expected to be around 17 eV, which means that the plasmon mode seen at

22 eV in the region of the coating is an effect of the dielectric interface between the WS_2 coating and the MWCNT. It follows that the reason for which this plasmon mode does not appear, for coating thicknesses of 4 monolayers and below, could be the fact that the interface between the MWCNT and the coating is not defined (from the dielectric point of view). This would suggest that in order to establish a heterojunction between the WS_2 coating and the MWCNT template, at least 5 monolayers of WS_2 are needed (i.e. \sim 3.1 nm).

CONCLUSIONS

We have studied the electronic structure across the cylindrical interface between a MWCNT and its WS_2 coating by using the line spectrum imaging technique, performed under parallel illumination in a TEM equipped with a GIF. We have shown that a plasmon mode that is specific to WS_2 cylindrical layers appears for coating thicknesses above 5 monolayers, which indicates that one can define dielectrically the interface between the MWCNT and its coating, if the coating thickness exceeds 3.1 nm. The coupling of the various surface modes of the nano-object (the MWCNT and its coating) is currently being investigated.

ACKNOWLEDGEMENTS

We are grateful to the EPSRC for financial support (multi-disciplinary project grant GR/N36073/01).

REFERENCES

- 1. Ajayan, P.M., et al.: Carbon Nanotubes as Removable Templates for Metal-Oxide Nanocomposites and Nanostrucutres, Nature, 375, 1995, 564.
- 2. Whitby, R.L.D., et al.: Complex WS₂ nanostructures. Chem. Phys. Lett., 359, 2002, 68.
- 3. Whitby, R.L.D., et al.: Tungsten disulphide multi-walled carbon nanotubes, 359, 2002, 121.
- 4. Stephan, O. et al.: Electron Energy-Loss Spectroscopy on Individual Nanotubes, J. of Electron. Spectrosc., 114-116, 2001, 209.
- 5. Bentley, J., and Anderson, I.M.: Spectrum Lines Across Planar Interfaces by Energy Filtered TEM, Proc. Microscopy and Microanalysis '96, San Francisco Press, 1996, 532.
- 6. Walther, T.: Application of Spatially Resolved Electron Energy-Loss Spectroscopy to the Quantitative Analysis of Semiconducting Layer Structures, Inst. Phys. Conf. Ser. No 164, IOP Publishing, 1999, 121.
- 7. Suenaga, K. et al.: Synthesis of Nanoparticles and Nanotubes With Well Separated Layers of Boron Nitride and Carbon, Science, 278, 1997, 653.
- 8. Henrard, L. et al.: Excitations of Plasmons of Anisotropic Nanostructures by Nearby Electrons, J. of Electron. Spectrosc., 114-116, 2001, 219.
- 9. Kociak, M. et al.: Experimental Evidence of Surface-Plasmon Coupling in Anisotropic Hollow Nanoparticles, Phys. Rev. Lett., 87, 2001, 75501-1.
- 10. Stephan, O. et al.: Dielectric Response of Isolated Carbon Nanotubes Investigated by Spatially Resolved Electron Energy Loss Spectroscopy: From Multiwalled to Single-Walled Nanotubes, Phys. Rev. B, 66, 2002, 155422.
- 11. Walls, M.G.: Electron Energy-Loss Spectroscopy of Surfaces and Interfaces, PhD. Thesis, University of Cambridge, 1987, 18-23.0

STUDY ON GAS SENSITIVITY OF CARBON NANOTUBE FILMS

W. L. Wang, Y. Ma, K. J. Liao, Z. H. Wu, G. B. Liu, B. Y. Wan

Department of Applied Physics, Chongqing University, Chongqing 400044 P. R. China

ABSTRACT

The gas sensitivity properties of carbon nanotubes were investigated. The carbon nanotubes in this study were fabricated by hot filament chemical vapor deposition using Ni/Fe catalyst. The sensor samples were treated by chemical etching using H₂SO₄/HNO₃. The experimental results have shown that the electrical resistance of carbon nanotubes was sensitively changed on exposure to gaseous ambient containing ethanol and water vapor. It was found that the gas sensitivity of carbon nanotubes was greatly enhanced after chemical treatment. It was also shown that the response time of nanotube sensor was faster than that of usual sensors.

Keywords: carbon nanotubes, gas sensitivity, chemical treatment, water vapor, ethanol, CVD

INTRODUCTION

Carbon nanotubes are candidates for future nanoelectronic device applications due to their unique structural and electronic properties (ref. 1 to 2). Using carbon nanotubes as miniaturized chemical sensors in one of the most promising applications because of their unusually high aspect ratio, mechanical and chemical stability and good conductance. The small dimensions and high surface area of the carbon nanotubes have special advantages for the sensors, which could be operated at room temperature or high temperature for sensing application (ref. 3 to 4). In this work, the gas sensors of carbon nanotubes were investigated. The experimental results showed that resistance of carbon nanotubes was found to change sensitively on exposure to gaseous ambient.

EXPERIMETAL

Carbon nanotubes in this study were fabricated by hot filament chemical vapor deposition. The Ni/Fe/Si was used as substrates (ref. 5). The catalyst is the mixed films of Ni and Fe. Catalyst thin films on Si were produced by radio frequency sputtering from a Ni-Fe alloy target. The Ni-Fe alloy target with an atomic radio of 1:1, 100mm in diameter, made of metal Ni and Fe of purity 99.99% was used. The film thickness is about 20nm. The Ni/Fe/Si substrates were loaded on a quarts boat. The catalyst films were treated in flowing hydrogen (200sccm, 20 Torr) at 850 °C. Subsequently ammonia (NH₃) was introduced to completely replace the hydrogen, and acetylene (C₂H₂) was added shortly after 1 min to start the nucleation and growth of carbon nanotubes. The flow rate of NH₃ gas is 250 sccm, and C₂H₂ gas is 120 sccm. Growth temperature was maintained at 550 °C, and time is 10 min. The samples obtained were characterized by scanning electron microscopy, transmission electron microscopy and Raman spectroscopy.

Fig. 1. Shows the SEM micrographs of carbon nanotubes. From Fig. 1. it can be known that the carbon nanotubes were grown homogeneously on the substrate, and the diameter of tubes in about 20 nm.

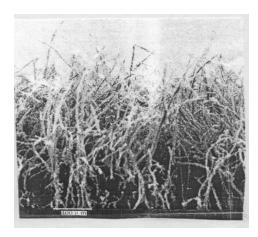


Fig. 1. SEM micrographs of carbon nanotubes

Fig. 2. Shows the Raman spectrum of carbon nanotubes using Ar excitation ($\lambda = 514.5nm$). From Fig. 2, as can be seen that the G-line at 1589 cm⁻¹ which originated from the graphitic sheets, and an extra peak near 1566 cm⁻¹ indicated the general trends of single wall carbon nanotubes (ref. 6).

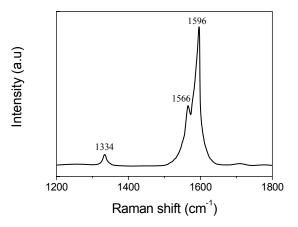


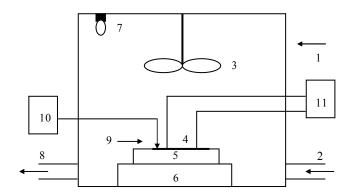
Fig. 2. Raman spectrum of carbon nanotubes

The carbon nanotubes were removed from the substrate in acetone solution using the ultrasonic treatment. The carbon nanotubes films were prepared by dispersing the raw material in ethanol and then by spraying on top of predeposited Au electrodes on quarts plate using an airbrush for gas sensitive measurements.

The experimental set-up for measuring the samples' sensitivity to gas was shown in Fig. 3. The sensor of carbon nanotube films was placed in the chamber (volume 60L). The chamber can be evacuated by a mechanical pump. The fed gas flow was controlled by mass flow meter. The samples were kept at a desired temperature adjusted by the iodine-tungsten lamp heater, and the sample temperature was measured by a Pt-Ph thermocouple. The films resistance was measured by a four-probe contact configuration. The sensitivity of the sensor to gases is defined by (ref. 7).

$$S = (R_{\varphi} - R_0)/R_0 \tag{1}$$

where R_{g} and R_{0} are the resistance of the sensor with and without gas, respectively.



- 1. Glass chamber
- 2. Gas inlet
- 3. Fan
- 4. Film
- Heater
- Firebrick
- 7. Bulb
- 8. Gas outlet
- 9. Thermocouple
- 10. Temperature controller
- 11 Multimeter

Fig. 3. Experimental set-up for monitoring the sensitivity to gas for carbon nanotubes films

RESULTS AND DICCUSSION

To enhance the sensitivity of gas sensors based on carbon nanotubes, the samples were treated by chemical etching using H₂SO₄/HNO₃ mixed solution. The processed samples were rinsed in de-ionized water and annealed at 250 °C in vacuum. Fig. 4 shows the changes of electrical resistance sensitivity for carbon nanotubes with pure ethanol concentration at 295 °C. From Fig. 4, as can be seen that the sensitivity of the films sensors to ethanol gas was increased with increasing gas concentration. The sensitivity was increased from 2.2% to 9.6% when ethanol concentration at air at room temperature increased 50 PPm to 150 PPm.

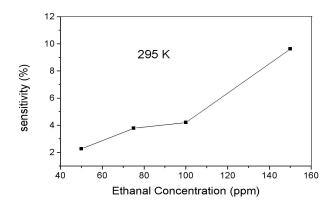


Fig. 4. Change in sensitivity of carbon nanotube films with ethanol gas concentration

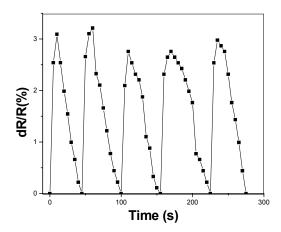


Fig. 5. Relative change in resistance to water vapor for carbon nanotube films without chemical treatment

Fig. 5 and Fig. 6 show the sensitivity of the electrical resistance for carbon nanotube films to water vapor with and without chemical treatment, respectively. It is quite clear that the gas sensitivity was greatly improved by chemical treatment. The relative changes in resistance was about 3.0% without chemical treatment, but reached to 100% after treatment.

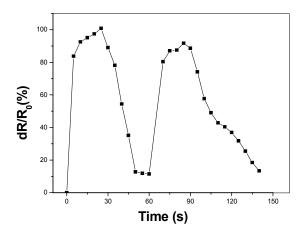


Fig. 6. Relative change in resistance of carbon nanotube films to water vapor with chemical treatment

As mentioned about the results, it was demonstrated that the carbon nanotubes have a good sensitive to gas environment. This is because of extreme high aspect ratios in carbon nanotubes, and further increased the aspect ratios after the treatment owing to opened ends and cut shorter for carbon nanotubes. In gas atmosphere, the charge transfers from adsorbed gas to carbon nanotubes may be occurred, especially in the presence of catalytic particles in carbon nanotubes.

CONCLUSION

The experimental results have shown that there is a good gas sensitive property in carbon nanotubes. Moreover, the gas sensitivity was further enhanced by chemical treatment. Miniaturized chemical sensors based on carbon nanotubes would be one of the most promising applications because of their high aspect ratio, mechanical and chemical stability and good conductance.

ACKNOWLEDGMENTS

This work has been financially supported by the Applied Research in Basics Foundation (7327) of Scientific Committee of Chongqing City.

REFERENCES

- 1. Yoon Y. G, Mazzoni M. S. C, Choi H. J, et al., Structural deformation and intertube conductance of crossed carbon nanotube junctions, Phys. Rev. Lett., Vol. 86, No. 4, 2001,488-691
- 2. Paulson S, Falvo M. R, Snider N, et al., In situ resistance measurements of strained carbon nanotubes, Appl. Phys. Lett., Vol. 75, No. 19, 1999, 2936-2938
- 3. Baughman R. H, Cui, C. X, Zakhidov A. A, et al., Carbon nanotube actuators, Science, Vol. 284, 1999,1340-1344
- 4. Mazzoni M. S. C. Chacham H, Ordejon P, et al., Energetics of the oxidation and opening of a carbon nanotubes, Phys. Rev. B, Vol. 60, No. 4, 1999, 2208-2211
- 5. Lee C. J. Park J, Han S. W, et al., Growth and field emission of carbon nanotubes on sodaline glass at 550 □ using thermal chemical vapor deposition, Chem. Phys. Lett, Vol. 337, 2001, 398-402
- 6. Kim J. M, Choi W. B, Lee N. S, et al., Field emission from carbon nanotubes for displays, Diamond. Relat. Mater, Vol. 9, 2001, 1184-1189
- Dong Y. F, Wang W. L. Liao K. J, Ethanol-sensing characteristics of pure and Pt-activated CdIn₂O₄ films prepared by r.f. reactive sputtering, Sensors and Actuators, B, Vol. 67, 2000, 254-257

On the calculation of the figure of merit for Carbon Nanotubes based devices

A. Vaseashta Marshall University Department of Physics One John Marshall Drive Huntington, WV 25755, USA

The dimensionality of a system has a profound influence on its physical behavior. With advances in technology over the past few decades, it has become possible to fabricate and study reduced-dimensional systems in which electrons are strongly confined in one or more dimensions. In the case of 1-D electron systems, most of the results, such as conductance quantization, have been explained in terms of non-interacting electrons. In contrast to the cases of 2D and 3D systems, the question of what roles electron-electron interactions play in real 1-D systems has been difficult to address, because of the difficulty in obtaining long, relatively disorder free 1-D wires. Since their first discovery and fabrication in 1991, carbon nanotubes (CNTs) have received considerable attention because of the prospect of new fundamental science and many potential applications. Hence, it has been possible to conduct studies of the electrons in 1-D. Carbon nanotubes are of considerable technological importance due to their excellent mechanical, electrical, and chemical characteristics. The potential technological applications include electronics, opto-electronics and biomedical sensors. The applications of carbon nanotubes include quantum wire interconnects, diodes and transistors for computing, capacitors, data storage devices, field emitters, flat panel displays and terahertz oscillators. One of the most remarkable characteristics is the possibility of bandgap engineering by controlling the microstructure. Hence, a pentagon-heptagon defect in the hexagonal network can connect a metallic to a semiconductor nanotube, providing an Angstrom-scale hetero-junction with a device density approximately 10⁴ times greater than present day microelectronics. Also, successfully contacted carbon nanotubes have exhibited a large number of useful quantum electronic and low dimensional transport phenomena, such as true quantum wire behaviors, room temperature field effect transistors, room temperature single electron transistors, Luttinger-liquid behavior, the Aharonov Bohm effect, and Fabry-Perot interference effects. Hence it is evident that CNT can be used for a variety of applications. To use CNT based devices, it is critical to know the relative advantage of using CNTs over other known electronic materials. The figure of merit for CNT based devices is not reported so far. It is the objective of this investigation to calculate the figure of merit and present such results. Such calculations will enable researchers to focus their research for specific device designs where CNT based devices show a marked improvement over conventional semiconductor devices.

DIAMOND EPITAXY AND DIAMOND SENSORS

EXCITONIC EMISSION FROM HIGH QUALITY HOMOEPITAXIAL DIAMOND FILMS

Hideyuki Watanabe 1), 3), Shokichi Kanno 2), 3) and Hideyo Okushi 1), 3)

- National Institute of Advanced Industrial Science and Technology (AIST), AIST Tsukuba Central 5, 1-1, Higashi
 1-Chome, Tsukuba-shi, Ibaraki-ken 305-8565
- 2) Graduate School of Science and Engineering, Ibaraki University, 2-1-1, Bunkyo, Mito, Ibaraki-Ken, 310-8512
- 3) Core Research for Evolutional Science and Technology (CREST), Japan Science and Technology Corporation

ABSTRACT

Recently, deep-ultraviolet (deep-UV) light emitting diodes (LEDs) based on diamond have been proposed using a free-exciton emission from diamond. Presently, it is well known that commercially available LEDs and laser diodes (LDs) are based on direct band-gap semiconductors such as GaAs and other III-V compound semiconductors. On the other hand, diamond is an indirect band-gap semiconductor. In order to realize commercially available deep-UV LEDs and LDs based on the free-excitons of the diamond, therefore, the nature of the indirect free-excitons from the diamond should have some advantages that overcome the handicap of the indirect band-gap.

The excitons in high quality diamond crystal have a high binding energy (80 meV), excitonic emission can be observed even up to room temperature. We have successfully observed the strong deep-UV emission of 235 nm (ie., 5.27 eV) due to free-exciton at room temperature in cathodoluminescence (CL) spectra from homoepitaxial diamond films prepared by microwave plasma assisted chemical vapor deposition (CVD) using CH4 gas system. More recently, under the condition of the very low CH4 concentrations less tahn 0.05%, we have successfully grown homoepitaxial diamond films with atomically flat surface. In these films, we found that the free-exciton emission intensity not only becomes stronger than the previous one, but the excitonic emission intensity increases super-linearly with the electron bean current in the high excitation region above a threshold value at room temperature. The nonlinear effects strongly suggest that application of free-exciton emission of diamond to deep-UV LEDs is very promising.

In this paper, we report detailed behaviors of the nonlinear effects in free-exciton emission of CVD diamond films studied by the CL measurements.

Keywords: exciton, deep ultraviolet, cathodoluminescence, homoepitaxial diamond film, nonlinear effect

LARGE AREA DEPOSITION OF HETEROEPITAXIAL DIAMOND THIN FILMS ON ION-IRRADIATED IRIDIUM

A. Sawabe, J. Kuwabara, H. Okamura and T. Yamada

Aoyama Gakuin University 5-10-1 Fuchinobe, Sagamihara, Kanagawa 229-8558 Japan

K. Suzuki

Toplas Engineering Co. Ltd., 1-9-9 Nishitsutsujigaoka, Chofu, Tokyo 182-0006 Japan

ABSTRACT

Heteroepitaxy of diamond is one of the main topics in diamond research society for scientific and industrial point of view. There have been attempted to fabricate heteroepitaxial diamond thin films on foreign substrate such as cubic boron nitride, nickel, silicon, beta-silicon carbide and platinum. Our research group has started to study on heteroepitaxial growth of diamond on iridium/magnesium oxide (MgO) (001) stacking by using two-step dc plasma chemical vapor deposition method from 1995. Growth area of epitaxial diamond, however, is 3mm in diameter, which is limited by the form and the size of the grid used for pretreatment of ion irradiation.

We have developed another pretreatment technique (planar diode type dc plasma) to enlarge the size of ion irradiation area. After this pretreatment, epitaxial diamond can be grown on whole iridium substrate surface with the size of 10x10x0.5 mm. The obtained epitaxial diamond thin film was transparent to visible light with a relative smooth surface. The growth process and the results of characterization will be presented in detail.

Keywords:

diamond thin film, heteroepitaxy, dc plasma CVD, iridium

Corresponding Author:

Name: Atsuhitto Sawabe

Mailing address Aoyama Gakuin University

5-10-1 Fuchinobe, Sagamihara, Kanagawa 119-8558

Japan

Telephone: +81-42-759-6253 Fax: +81-42-759-6522

e-mail sawabe@ee.aoyama.ac.jp

APPLICATIONS OF SINGLE CRYSTAL CVD DIAMOND

Daniel J. Twitchen, Geoffrey A. Scarsbrook, Andrew J. Whitehead, Chris Wort & Steve. E. Coe Element Six Ltd, King's Ride Park, Ascot, Berkshire SL5 8BP, UK.

Jan Isberg

Division for Electricity Research, Box 539, S-751 21 Uppsala University, Sweden.

ABSTRACT

The desire for electronic devices with higher power throughput, wider frequency bandwidth and higher operational temperatures is driving research and development of new semiconductors. One such area of research is wide band gap materials. Diamond is extreme in this group of materials (which includes SiC, ZnO and GaN), having a direct band gap of 7.5 eV, an indirect gap of 5.5 eV and a room temperature thermal conductivity in excess of 2000 Wm⁻¹K⁻¹. Diamond electronic devices, such as power diodes and high-frequency field effect transistors, are expected to deliver outstanding performance due to the material's excellent intrinsic properties such as high carrier mobilities and high breakdown field. However, the development of diamond electronics has been hampered by several problems including a lack of shallow dopants, heteroepitaxy as a route to large area single crystal growth, low crystal quality and poor consistency of synthetic material.

We will report recent results on the fabrication and characterization of device quality single crystal CVD diamond. These results show, not only that material can be fabricated with performance that matches the very best natural diamond, but also that key properties such as the mobility and lifetime of the carriers, far exceed expectations. It has been lack of material quality that has limited diamond's progress in the past, making it a minority player against SiC and GaN. However, the figures of merit now demonstrated for diamond are so extreme that the material should be re-examined as an ideal material for the most demanding power electronics and switching applications.

Keywords: single crystal diamond, CVD, high power, high frequency, electronics

Reference:

[1] J. Isberg et al., Science, 6 Sept, 297 (2002) p1670.

Corresponding author:

Dr Daniel Twitchen

<u>Daniel.Twitchen@e6.com</u>

Element Six Ltd,

King's Ride Park,

Ascot,

Berkshire SL5 8BP

UK

Tel: + 44 1344 638215 Fax: + 44 1344 638236

ELECTRICAL PROPERTIES OF DIAMOND *PN*-JUNCTION DEVICES (ADC/FCT 2003)

S. Koizumi, M. Katagiri, K. Watanabe and H. Kanda

Advanced Materials Laboratory, National Institute for Materials Science, 1-1 Namiki, Tsukuba 305-0044, Japan

ABSTRACT

n-Type diamond thin films were successfully formed by optimizing the growth condition of chemical vapor deposited diamond under phosphorus doping to obtain better crystalline perfection. The pn –junction made with stacking film of boron doped (p-type) and the phosphorus doped (n-type) layers has shown good rectification characteristics with the ratio of 10^{10} at \pm 10V. The diode characteristics and the behavior of pn –junction interface have been characterized by temperature dependent IV and CV measurements. By forward bias operation, the diode shows ultraviolet light emission at 235 nm that attributes free exciton luminescence. The diode also shows photoelectric response against ultraviolet light with the wavelength shorter than 225 nm that corresponds the bandgap of diamond. It is expected these characteristics of diamond pn –junction will be applied for the next generation opto-electrical devices.

Keywords: n-type doping, pn-junction, electrical properties, light emission

INTRODUCTION

Diamond is a potential material for ultraviolet (UV) devices and high-temperature electronics application because of its large band gap. The formation of pn-junction is very important fundamental technology to realize the diamond solid state devices such as solar-blind deep UV photo-diode, UV-LED and UV laser diode. It has been reported that diamond pn-junction diode can be formed using boron doped and phosphorus doped diamond thin films, and it generates UV light emission at 235 nm (ref. 1). In the present study, the high-temperature electrical properties and light emission characteristics of diamond pn-junction have been investigated.

EXPERIMENTAL

A boron (B)-doped diamond thin film is formed on the heavily B-doped HT-HP diamond {111} surface by microwave plasma CVD using trimethylboron as an impurity source. The thickness of the film is $1 \mu m$ and the boron concentration is 1×10^{17} cm⁻³. The phosphorus (P)-doped film has been deposited on the B-doped film using phosphine as an impurity source with the thickness of 0.5-1 μ m and the phosphorus concentration of $5x10^{18}$ cm⁻³. The electrical properties of both the films are individually characterized by Hall measurements and have been convinced their conduction to be p-type and n-type, respectively for B- and P-doped layers. After the deposition of both the films, the sample was chemically oxidized to remove hydrogen and contaminants which may cause unexpected electrical conduction. The ohmic electrodes were formed for p-type diamond film by depositing Au / Ti film by EB deposition. For the n-type side, the heavily P-doped thin layer has been formed on the surface followed by deposition of Au / Ti cap films. The sample has been processed by reactive ion etching to form mesa structure for the device separation.

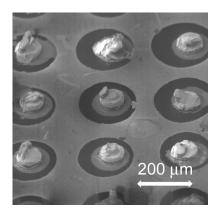


Figure 1. SEM image of a mesa structured sample surface.

RESULTS AND DISCUSSION

The I-V characteristics of the pn structure clearly show the rectification properties as shown in figure 2. The rectification ratio is about 10^{10} at ± 10 V at RT. Even at 600 °C, the diode characteristics can be clearly observed with the rectification ratio of about 10^6 . The ideality factor has been improved from 3.5 at RT to 1.9 at 600 °C with the temperature increase. The improvement is considered to be due to the reduction of charge trapping state density due to thermal excitation of defect energy states in the crystal. The frequency response of the diode has been improved as well with the temperature increase. The built-in potential deduced from capacitance-voltage measurements (not shown here) showed good agreement with the theoretical calculation and it was 4.5 eV at 600 °C, while slight discrepancy has been observed at RT (~5.0 eV). Thus, it is revealed that the present diamond pn-junction rather prefers high-temperature operation.

Figure 3 shows a typical photoresponse spectrum of diamond *pn*-junction. It is clearly observed the rapid increase of photoresponse at 5.5 eV (225 nm) that corresponds to the indirect band-gap of diamond. The discrimination ratio was over 10³ at 5.5 eV. However, it is also observed sub-gap response below 3 eV (2.3 eV) which corresponds to that of substitutional nitrogen exists in HPHT diamond used as a substrate. The photo-carriers generated in the substrate diffuse into *pn*-junction interface and cause the photoresponse. It is basically possible to reduce this response by simply replacing the substrate to type-II diamond. Thus, it is demonstrated that perfect solar-blind UV-photodetector can be obtained by using diamond *pn*-junction diode

CONCLUSION

pn-Junction diode was successfully formed by stacking boron-doped and phosphorus-doped chemical-vapor-deposited diamond thin films. The pn-junction showed better diode characteristics at higher temperature and the ideality factor was 1.9 at 600 °C. The photoresponse of the diode showed a sharp rising edge at diamond band-edge and the feasibility of a solar-blind photodetector has been convinced using diamond pn-junction.

Reference

1. S.Koizumi, K.Watanabe, M.Hasegawa and H.Kanda, "UV light emission from diamond pn junction" Science **292** (2001) 1899.

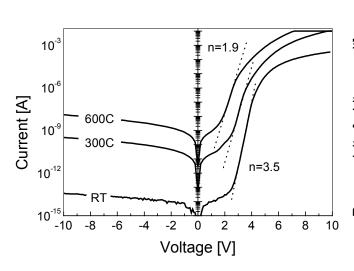


Figure 2. Temperature dependent IV characteristics of diamond *pn*-junction measured in vacuum.

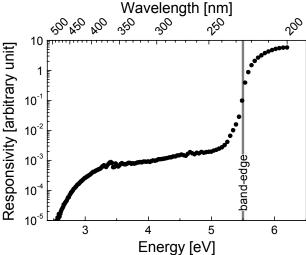


Figure 3. Photoresponse of diamond *pn*-junction in visible (blue) to deep UV region.

DIAMOND LED UTILIZING FREE EXCITON RECOMBINATION EMISSION

Kenji Horiuchi, Aki Kawamura, Yuichiro Okajima, Takuhiro Ide and Takefumi Ishikura

Frontier Research Institute, R&D Planning Department, Tokyo Gas Co., Ltd.
1-7-7 Suehiro-cho, Tsurumi-ku, Yokohama 230-0045 Japan.
ken_hori@tokyo-gas.co.jp
Fax. +81-45-505-8821 Tel. +81-45-505-8813

ABSTRACT

Diamond free exciton (FE) recombination emission located around 235 nm in wavelength is expected to be highly efficient and a good candidate for deep UV LED. We previously reported that an external efficiency (η_{ext}) of 8 x 10⁻⁵ was obtained at room temperature from a pn junction sample composed of a S-doped CVD layer and a B-doped synthesized substrate. But a peak intensity ratio of band-A to that of FE emission ($r_{A/FE}$) was about 100. This undesired behavior seemed to be caused by lattice defects on the mechanically polished p-type substrate.

In order to improve LED characteristics, a B-doped layer was grown on a B-doped substrate by MW-assisted CVD method at the following conditions; C/H atomic ratio 0.05%, B/C atomic ratio 50 ppm, temperature 875 C° and thickness 0.8 μ m. Atomic force microscope analysis showed that the averaged roughness (Ra) of the surface was reduced from 0.48 nm to 0.32 nm. Then S-doped CVD layer growth and device separation by reactive ion etching were done the same way as previous sample. A typical $r_{A/FE}$ of thus fabricated LED's was greatly suppressed to 0.5, which suggested a defect concentration reduction at the junction. Maximum η_{ext} of 2.7 x 10^{-4} and maximum output power of FE emission of 17 μ W was obtained.

Keywords: LED, free exciton, quantum efficiency, pn junction, lattice defects

DIAMOND MICRO-OPTICS

M. Karlsson, H. Högström and F. Nikolajeff

Department of Materials Science, The Ångström Laboratory, Uppsala University P.O. Box 534, SE-751 21 Uppsala, Sweden

ABSTRACT

We have developed a method for fabricating almost any type of optical surfaces in diamond. The method consists of the following steps: First, a polymer film, spun onto diamond substrates of optical quality, is patterned by lithographic processes. Next, the surface relief is transferred into the underlying diamond by use of inductively coupled plasma dry etching in an oxygen/argon chemistry. Using this technique, we have successfully demonstrated the fabrication of diamond spherical microlenses, blazed gratings, Fresnel lenses, subwavelength gratings and diffractive fan-out elements. The spherical microlenses had apertures of 90 µm and f-number of 4. The phase error, measured with a Twyman-Green interferometer at 633 nm, was found to be less than 31 nm. The diffraction efficiency for the blazed grating was measured to be 68% at 400 nm, with a theoretical maximum of 71%. The subwavelength grating was designed for reducing surface reflections at a wavelength of 10.6 µm. Spectrophotometric results show that the optical transmission was increased from 70%, using a non-structured diamond substrate, to 97%, using our subwavelength structured diamond. Finally, the fan-out element has been tested with a 6 kW carbon-dioxide laser, to microstructure pieces of PMMA. The results are excellent, showing diffraction limited spots.

Keywords: CVD diamond, diffractive optics, high power lasers, plasma etching, antireflection.

INTRODUCTION

Diamond is a very interesting material for optical purposes. There are several reasons for this; diamond is the hardest material found in Nature, diamond has a wide optical transparency window (220 nm and above), it is resistant against chemicals and has the highest thermal conductivity of all solids known. It is therefore attractive to fabricate diffractive or refractive optical elements in diamond for e.g. high power laser applications. Interesting areas of micro-optical elements in diamond is for beam shaping of CO₂-lasers, Nd:YAG lasers or diode laser arrays. Today ZnSe is chosen as the optical material for CO₂-lasers (to focus the laser beam or as an optical window). However, diamond has the potential to replace ZnSe as the optical material for use with CO₂-lasers because of its unique optical properties. For instance, thermal lensing, which is due to heating of a material leading to a localized change in refractive index and thus a lensing effect, for a diamond window can be more than 200 times less severe than in ZnSe (ref. 1).

Binary structures in diamond have been demonstrated using excimer laser ablation (ref. 2) and ion beam milling (ref. 3). Due to the stepped approximation, binary elements suffer however from lower diffraction efficiency than true analogue structures and both of the above mentioned processes are rather slow and not suitable for more than laboratory demonstration. In this paper we present an overview of the different diamond micro-optical structures (both analogue and binary) fabricated by our group (refs. 4 to 6). The manufacturing technology uses electron-beam lithography, replication by hot embossing or photolithography followed by plasma etching in an inductively coupled plasma (ICP) system.

MICRO-OPTICS FABRICATION

The substrates used in all experiments were polycrystalline CVD diamond grown in microwave plasma, with the first seeding material removed. The surfaces are polished to a root-mean-square (RMS) roughness below 15 nm. The material is commercially available from Drukker International B.V., The Netherlands, and was specially made for optical components that require a high transmission from the ultraviolet to the far infrared.

Continuous blazed gratings and diffractive Fresnel lenses

Fabrication of the diffractive optical elements (DOEs) was done with direct-write electron-beam lithography (system: JEOL JBX-5DII), which allows continuous-relief elements to be exposed. The DOE pattern was written in electron sensitive resist (PMGI SF15, MicroChem Corp., USA) spun onto CVD diamond substrates (300 μ m thickness, diameter 10 mm, flatness < 2.5 fringe at λ =633 nm). Both blazed gratings and diffractive lenses of Fresnel type were exposed. Feature sizes of the blazed grating were period of 45 μ m and grating depth 3 μ m.

Refractive microlenses

Fabrication of refractive microlenses was done with standard photolithography followed by thermal reflow of photoresist. The microlenses was fabricated in Shipley 5740 photoresist spun onto diamond substrates (300 μ m thickness, diameter 5 mm, flatness < 1 fringe at λ =633 nm). The thickness of the resist layer was 7 μ m and the diameter of the exposed pillars between 10 and 100 μ m. By heating the substrate at 150 degrees for 15 minutes the pillars melt and form almost perfect spherical microlenses with a height of 13 μ m.

Subwavelength gratings and diffractive fan-out elements

The fabrication of the subwavelength grating was done with direct-write electron-beam lithography (system: Philips FEG-ESEM). A thin layer of aluminum was first deposited onto the diamond substrates diamond having the same material properties as described above, followed by spin-coating of poly(methylmetacrylate) (PMMA). After the resist layer had been exposed and developed the naked metal areas were removed by dry etching, the remaining areas functioned as etch stop during the subsequent dry etching in an inductively coupled plasma (ICP) etching system. The grating period of the two-dimensional subwavelength grating was 4 μ m. For the fabrication of the diffractive fan-out element photolithography was used to mask the aluminum, since the smallest feature size is about 10 μ m.

PLASMA ETCHING OF THE DIAMOND MICRO-OPTICAL STRUCTURES

To fabricate the micro-optical structures in diamond a home built ICP etching system was employed. In the few publications on etching of diamond that exist, pure O_2 or O_2 /Ar have been used as etch gases. Studies have been done with reactive ion etching, which generates slow etch rates (10-60 nm/min) (ref. 7). However, with electron cyclotron resonance (ECR) etch rates of up to 300 nm/min has been reported (ref. 8). ICP-etching (used in our experiment) is also, as ECR, a high density system which therefore usually gives similar etch results. In our experiment electronic grade O_2 and Ar were used as etch gases. Etch conditions were gas flows of 7 sccm O_2 , 8 sccm Ar, chamber pressure 2.5 mTorr, 500 W ICP power, -140 V bias, which gave etch rates of 1900 nm/min, 1200 nm/min and 190 nm/min in e-beam resist, photoresist and diamond, respectively. The selectivity between the etch rate in e-beam resist and the etch rate in diamond is 0.1, which means that the height of the structure will be compressed.

OPTICAL AND TOPOGRAPHICAL MEASUREMENTS

Continuous blazed gratings and diffractive Fresnel lenses

Fig. 1 shows an interferometer picture of a blazed grating (period $45~\mu m$, depth 300~nm) and a diffractive Fresnel lens (focal length 10~mm, f-number 20, at a wavelength of 400~nm) etched into diamond. One can notice that the surface roughness of the etched element is fairly good. The measured diffraction efficiency of the $45~\mu m$ period blazed grating in the first order was 68.2% at 400~nm wavelength. No AR-coating was provided. The reason why the diffraction efficiency does not reach the theoretical maximum is mainly due to deviation of the optimal relief depth and the fact that the relief structure in e-beam resist is not perfect. By using atomic force microscope (AFM) data from the original structure we simulated an optimum diffraction efficiency in the first order of 71.5% for the e-beam exposed structure, therefore we cannot expect a much higher value after etching.

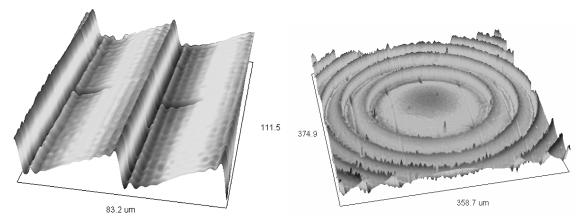


Figure 1. (left) Interferometer picture of a blazed diamond grating (45µm period, depth 300 nm). The ripple along the grating originates from the 16 different e-beam exposure doses used. (right) Interferometer picture of a Fresnel lens in diamond.

Refractive microlenses

Fig. 2 shows a surface scan of a diamond microlens. One can notice that the surface of the etched elements is very good. The diamond microlenses was examined with an optical interferometer to measure the lens properties and the surface roughness.

The examined microlens has a diameter of 90 μ m and a height of 2 μ m. The radius of curvature is 511 μ m, focal length is 365 μ m, and the f-number is 4. To measure deviations from a perfect spherical lens we subtracted a sphere with a curvature of 511 μ m from the interferometer data of our diamond lens. The deviation from a perfect lens was measured over > 90% of the lens area, and was calculated to be 6.7 nm (RMS). The phase error, measured with a Twyman-Green interferometer at λ =633 nm, was found to be less than 31 nm (λ /20).

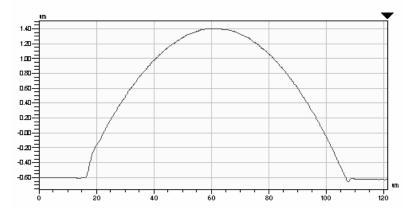


Figure 2. Interferometer picture of a surface scan over a microlens fabricated in diamond (diameter 90 μm, height 2 μm).

Subwavelength gratings and diffractive fan-out elements

The subwavelength grating was designed for reducing surface reflections at a wavelength of 10.6 micrometer. Since diamond has a high refractive index, 2.4 at λ =10.6 μ m, 29% of the incoming light will be lost due to Fresnel reflection from both surfaces. To reduce the surface reflection the surface can be coated with one or several layers of suitable thin film materials. However, it would be beneficial to avoid introducing another material. For instance, if diamond is chosen because of its resistance in harsh environments the whole idea will fall if another material also has to be introduced. Fig. 3 shows an SEM picture of the two-dimensional subwavelength grating, having a period of 4 μ m. The AR-grating was optically evaluated with a spectrophotometer and showed that the transmission was increased from 71% to almost 97%, see Fig. 4. Theoretical maximum is about 99%.

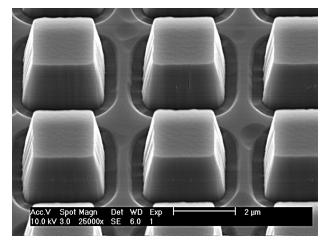


Figure 3. Scanning electron microscope picture of a diamond subwavelength grating designed for reducing surface reflections at a wavelength of 10.6 μm. The grating period is 4 μm and the grating depth is 1.8 μm.

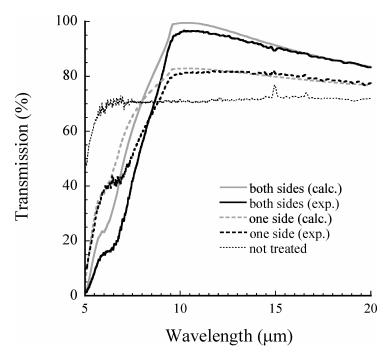
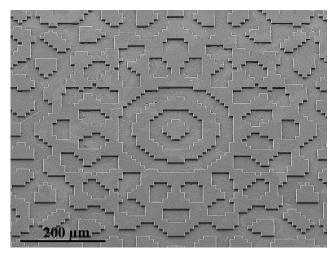


Figure 4. Transmission spectra measured with a spectrophotometer of blank diamond, diamond with subwavelength grating on one side and double-side treated diamond. The transmission has been increased from 71% to 97%. The calculated transmission values are also shown.

One of the DOEs is a binary fan-out element designed to generate 16 spots forming a ring pattern. The fan-out element is optimized for the wavelength of a CO_2 laser, λ =10.6 µm. CO_2 lasers are widely used in the industry for cutting and drilling metal as well as in the medical industry. The fan-out was fabricated in two versions, one for use with a CO_2 -laser and the other for use with a HeNe laser (λ =632.8 nm). The DOE was carefully optically evaluated with a HeNe laser and showed excellent performance. The measured diffraction efficiency was 64.5% for red light, which is compared with the calculated value of 65.7%. The fan-out element, designed for a wavelength of 10.6 µm, was used to drill holes in a thick PMMA plate by placing the DOE in the CO_2 laser beam. Fig. 5 shows a SEM picture of the fabricated fan-out element in diamond and PMMA microstructured with the CO_2/DOE combination.



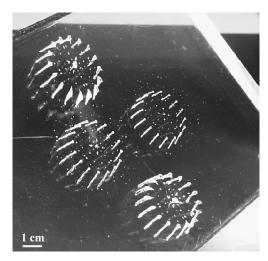


Figure 5. (left) SEM picture of the plasma etched diamond DOE (etch depth 3.84 μ m). (right) Picture of a PMMA sample microstructured with a CO2-laser together with a diamond fan-out element. The picture shows four different exposures (exposure time 0.5 s).

CONCLUSION

In conclusion, we have studied the transfer of diffractive structures and refractive microlenses into diamond using ICP etching. An O₂/Ar chemistry has been found to give satisfying results. The transfer process produced smooth surfaces. The outstanding properties of diamond and a decrease in the production cost of synthetic diamond, combined with a rapid and accurate micromachining method, will allow the commercialization of diamond optics. We believe that diamond optics, in the future, will be found in high-power laser applications and applications where the environmental conditions are extreme such as high temperature, corrosive gases, high aero-dynamic load, etc.

REFERENCES

- 1. Brierley, C.J., et al.: The potential of CVD diamond as a replacement for ZnSe in CO₂ laser optics. Diamond and Related Mater., vol. 8, no. 9, 1999, 1759-1764.
- 2. Gloor, V., et al.: Antireflection structures written by excimer laser on CVD diamond. Appl. Phys. A, vol. 70, no. 5, 2000, 547-550.
- 3. Tarutani, M., Takai, Y. and Shimizu, R.: Application of the focused-ion-beam technique for preparing the cross-sectional sample of chemical vapor deposition diamond thin film for high-resolution transmission electron microscope observation. Jap. J. Appl. Phys., vol. 31, no. 9A, 1992, 1305-1308.
- 4. Karlsson, M., Hjort, K. and Nikolajeff, F.: Transfer of continuous-relief diffractive structures into diamond by use of inductively coupled plasma dry etching. Opt. Lett., vol. 26, no. 22, 2001, 1752-1754.
- Karlsson, M. and Nikolajeff, F.: Fabrication and evaluation of a diamond diffractive fan-out element for high power lasers. Opt. Express, vol. 11, no. 3, 2003, 191-198. http://www.opticsexpress.org/abstract.cfm?URI=OPEX-11-3-191
- 6. Karlsson, M. and Nikolajeff, F.: Diamond micro-optics: microlenses and antireflection structured surfaces for the infrared spectral region. Opt. Express, vol. 11, no. 5, 2003, 502-507. http://www.opticsexpress.org/abstract.cfm?URI=OPEX-11-5-502
- 7. Dorsch, O., Werner M. and Obermeier, E.: Dry etching of undoped and boron doped polycrystalline diamond films. Diamond and Related Mater., vol. 4, no. 4,1995, 456-459.
- 8. Kiyohara, S., Yagi, Y. and Mori, K.: Plasma etching of CVD diamond films using an ECR-type oxygen source. Nanotechnology, vol. 10, no. 4, 1999, 385-388.

DIAMOND MICRODOSIMETERS AND MICRODETECTORS

C. Manfredotti, E. Vittone, F. Fizzotti, A. Lo Giudice, C. Paolini and P. Olivero

Experimental Physics Dept., University of Torino, Italy and INFM, National Institute for Matter Physics, UdR To-University, Italy

ABSTRACT

Diamond displays many attractive properties which make it an ideal material both for nuclear particle detection and for X-ray dosimetry in medical fields. In fact diamond is radiation hard, tissue equivalent and compatible, and by using CVD (Chemical Vapour Deposition) it can be deposited on different substrates and in different shapes. We have fabricated CVD diamond microdosimeters by depositing thin diamond films (< 20 um thick) on tungsten wires and tips with diameters ranging from 50 um to 30 um. Tips shape can be easily controlled by electrochemical etching the W wire, from emispherical to almost conical one. The electrodes are arranged in a coaxial geometry. These devices can both detect alpha particles, protons and ions with a reasonable energy resolution and with bias voltages of the order of 50 V and can be used as X-ray microdosimeters in small field radiotherapy planning, with an extremely good spatial resolution. We have recorded the performances and the homogeneity of the response of these detectors with proton and alpha particles microbeams by IBICC (Ion Beam Induced Charge Collection) and we have measured the exact dose rate profile of small X-ray beams with an unprecedented spatial resolution.

Keywords: CVD diamond, microdosimeter, microdetector, X-rays, tips.

INTRODUCTION

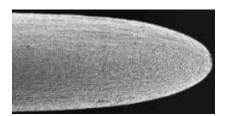
Diamond is generally assumed to be an ideal material as radiation detector for bio-medical applications (ref. 1). The attractiveness of diamond essentially stems from its radiation hardness, chemical stability against all the body fluids and its absolute no-toxicity. Moreover, diamond is to be considered a "tissue equivalent" material since its atomic number (Z=6) is close to the effective atomic number of soft tissue ($Z_{\rm eff}$ =5.92 for fat and $Z_{\rm eff}$ =7.4 for muscle) (ref. 2). This fact is particularly important to measure the absorbed dose in biological tissue where the energy deposited by low energy gamma or X-ray (< 150 keV) is highly dependent on the atomic number of the material. Improved diamond synthesizing techniques have generated new optimism about the possibility of applying diamond in radiation detection, overcoming the difficulties (high cost and poor reproducibility), which limit the widespread application of natural diamond in this field. In particular, the Chemical Vapour Deposition (CVD) technique has proven to be able to produce low cost "detector grade" diamond films suitable for application in radiation dosimetry (ref. 3). Besides obvious advantages of this technique (low cost, high impurity control, good reproducibility), it should be emphasised that it is able to synthesize both large area detectors, as required for medical imaging, and miniaturised detectors. The latter feature is particularly appreciated in radiation oncology units where detectors with excellent spatial resolution and high sensitivity are required for radiotherapic treatments (brachytherapy or stereoactic radiosurgery).

Since 1995, our group has been involved in the fabrication of position sensitive and needle shaped detectors for in-vivo dose monitoring and for photon and charge particle beam profiling (ref. 3). A thin diamond film (10-15 μ m) is deposited on a tungsten tip which base diameter is below 300 μ m. The performance of such detectors is described in previous papers (ref. 3 and references therein) and can be considered for in vivo dose measurements. As a matter of fact, their small dimensions make them suitable for dose measurements in small radiation fields such as in stereotactic radiosurgical beams where ion chambers are inappropriate because of their poor spatial resolution and their sensitivity to lateral electronic disequilibrium (ref. 4).

However, the unusual geometry of the substrate makes it difficult to obtain a perfect reproducibility of the diamond deposition. As a consequence, an accurate characterisation of the electronic performance of such devices is an unavoidable step before their application under radiotherapy x-ray beams.

EXPERIMENTAL

The HFCVD apparatus used to deposit diamond tips is described in previous publications (ref. 6). Diamond film (10-15 μ m thick) was grown on 50-300 μ m wide tungsten tips. The shape of the tips was obtained by means of the same electrochemical technique as used to obtain sharp tips for Scanning Tunnelling Microscopy.



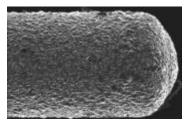


Figure 1. SEM micrographs of CVD diamond tips realized on a tungsten substrate (left) and on a SiC substrate (right). The thickness of diamond film is 10μ m, the internal diameter is 200μ m.

After deposition the samples were annealed in air or in oxygen atmosphere to remove the hydrogenated and/or graphitic layer present on the diamond surface. Then, a Ti (40 nm) + Au (100 nm) electrode was evaporated on the top of the diamond tip. By applying a bias voltage at the top electrode and earthing the W substrate (which acts as a counter electrode) a solid state ionisation chamber is then made. It is worth noticing that the current flowing under a bias voltage of 100 V is about 50 pA. This fact allowed us to set a very low electronic threshold level of the acquisition chain.

Fig. 1 shows two different samples of CVD diamond tips deposited on a tungsten wire suitably etched (left) and an a SiC wire (right) with a different terminal shape. A miniaturised diamond solid state chamber was then fabricated by using the diamond as the sensitive region, the tungsten substrate and a thin titanium/gold evaporated layer as electrodes. The detector was then sealed in cylindrical polystyrene housing of 20 mm diameter.

The current/voltage characteristics for all the samples were measured both in dark and under both a X-ray radiological beam (maximum energy 120 keV) with or without a Cu filter and with the X-ray beam of a Siemens MD Class MEVATRON 615 MeV accelerator for radiotherapy. The profiles of the X-ray beam reported here refer only to the radiological beam with very narrow field. In this case, pulse charge integration was carried out in order to improve the S/N ratio. The current pulses were recorded and digitized by means of an ADC acquisition card. An example of the pulses is reported in Fig. 2: while fluctuations were present in the pulse shape, the results confirmed a very good stability of the radiological apparatus, which is an obvious requirement for beam profile step-by-step measurements.

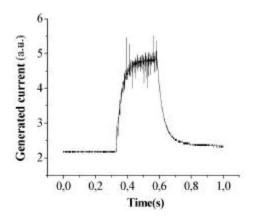


Figure 2. Time evolution of the current pulse (in arbitrary units) generated by X-ray in the tip CVD diamond detector

In order to test the performances of the tips as particle detectors, which could be of some interest because of the good space resolution of this detector, IBIC (Ion Beam Induced Charge) measurements were carried out by irradiating with a proton microbeam (nominal spot diameter 1 μ m) the top electrode in parallel geometry, i.e. with the beam parallel to the tip axis. A standard charge sensitive electronic chain was used to shape and amplify the signal induced by charge carriers generated by a 2.4 MeV proton beam with a rate of less than 1000 p/s.

RESULTS AND DISCUSSION

The current/voltage curves under high energy (6 MeV, dose rate $35\mu Gy/s$) and under low energy (X-ray tube voltage 150~kV, dose rate= $60~\mu Gy/s$) X-ray irradiation revealed in some cases a photocurrent increase with respect to dark of the order of 10^3 , when dark current of the tip was very low ($10^{-12}~A$). The sensitivity has been calculated from the linear behaviour of the electrical response of the tips operating at a bias voltage of 100~V under the X-ray source irradiation at fixed peak energy of 150~keV and different X-ray tube currents. The slopes of the linear fits are of the order of 7~nC/Gy for diamond tips in this case.

The linearity of the response (integrated charge) with respect to the absorbed dose is of paramount importance in radiological and radiotherapic dosimetry. The tips proved to be extremely linear at each maximum energy of X-ray over a suitable range of doses. One example is shown in Fig.3, which reports the behaviour of the collected and integrated charge as a function of exposition X-ray dose as measured by a standard ionization chamber.

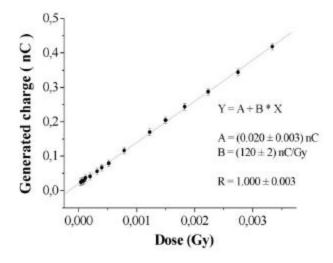


Figure 3. Linearity of signal of a CVD diamond tip at a bias voltage of 100 V with respect to dose of X-rays with a maximum energy of 40 KeV.

The sensitivity of the response of the tips, in terms of collected charge over the exposition dose, is depending on the maximum energy of the X-ray beam, because the range of photoproduced electrons is of the order of the thickness of CVD diamond film. This happens almost exactly at 80 keV, which corresponds to an effective energy of 40 keV, where the range of electrons is equal to the thickness of the film and the charge collection efficiency is the largest one. Above 80 keV the sensitivity decreases, because the stopping power of electrons decreases, while below 80 keV the sensitivity increases almost linearly with energy (see Fig. 4).

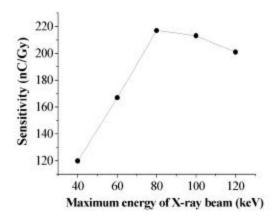


Figure 4. Sensitivity of a CVD diamond tip as a function of the maximum energy of the X-ray beam.

In the case of a filtered or hardened X-ray beam (2 mm Cu) one observes almost the same behaviour. In conclusion, in the energy range, which is quite common for radiological investigations (70 - 120 keV), for any filtering thickness, the maximum fluctuation of sensitivity is of the order of 10%.

The time response of the dosimeters is also very important and it is reported in Fig. 5 in the case of a 6 MeV therapeutic X-ray beam: apart from the initial peak, due to the accelerator beam autocalibration, and from a tail (which is reported in some detail in the insert), the conclusion is that the time response is compatible with common times used in radiotherapy planning.

The time response in the case of radiological apparatuses is also very important and the tip presents very good time responses for standard cases, as it will be shown in the next two figures. Fig. 6 reports the pulses as recorded from a mammography apparatus at increasing energies, from 24 to 34 keV, and taken progressively in time: it is very clear that the no-pulse line is constant ant that no memory is kept of previous pulses. Fig. 7 shows the pulse shapes from a standard radiological apparatus for the same maximum energy (80 keV) and at increasing mAs (from 1 mAs, corresponding to a time duration of 0.013 s up to 100 mAs, corresponding to 1.3 s): the time behaviour is exactly what is expected. Also in this case the pulses were recorded sequentially and no memory of the previous pulses was observed.

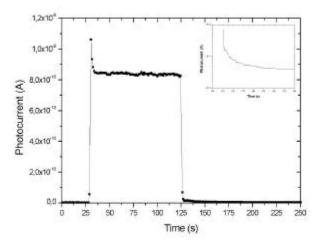


Figure 5. Time response of tungsten-CVD diamond tip to 6 MeV X-rays. A detail of the tailing part of the response is shown in the insert.

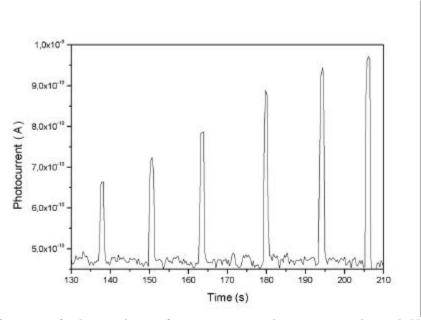


Figure 6. Sequence of pulses coming out from a mammography apparatus and recorded by the tip: the maximum energy of the X-ray beam was sequentially increased from 24 to 34 keV.

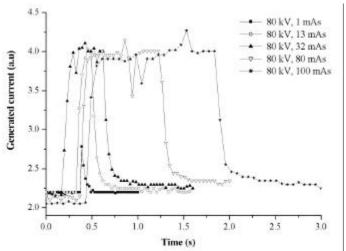


Figure 7. Digitized pulses as recorded at 80 keV of maximum X-ray energy for increasing current x time products (mAs) of the radiological apparatus, from 1 mAs to 100 mAs (time duration is from 0.013 s up to 1.3 s).

For a good performance of a X-ray dosimeter, the reproducibility is very important, of course. Taken into account that no memory of previous pulses is affecting the measure under observation, statistical and systematic possible errors were checked by recording 100 subsequent pulses all taken at 80 keV and with 13 mAs of charge. The result is shown in Fig. 8, together with a gaussian fit. The symmetry of the peak is very clear about the absence of systematic errors, while from the fit, which is very good, a standard deviation of 0.02 nC is derived, which, compared with the measured collected charge of 0.32 nC, gives a statistical error of 6.2%, which, in turn, is completely comparable with the precision of the apparatus itself, which is expected to be 5%. A precision of the order of very few percent is really an extraordinary result for this prototype of tip dosimeter.

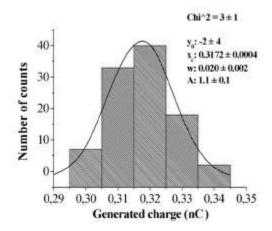


Figure 8. Test of the reproducibility of the measured charge (0.32 nC) recorded by the tip dosimeter for 100 subsequent pulses at 80 keV, 13 mAs, together with a gaussian fit. The standard deviation is 6.2% if the central value.

The spatial resolution is, in principle, a highly expected property for a dosimeter which, as observed from the front, has an intrinsic dimension of 300 μ m, which could be easily reduced down to 50 μ m or less. In order to check the resolution capability, a very narrow X-ray beam has been microscopically scanned by the tip dosimeter and the results were recorded. The tip was in axial (or frontal position) with its axis parallel to the X-ray beam as much as possible, at a distance from X-ray source of 6 cm. The source was focused by lead collimators at 7 x 7 mm², at a maximum energy of 80 keV with 13 mAs of charge. The tip was biased only at 20 V in this case. The results are shown in Fig. 9: by microscopic stage, the measurements were taken in step of only 0.5 mm by covering 50 points over a range of 2.5 cm, formerly in one direction and after backwards, always in order to check the reproducibility. Apart from the asymmetry of the profile, which is due to the non-exact centering of the tip, and from the non ideal shape of the profile, reasonably due to the machine, the results are impressive: the results forth and back are always within the experimental errors. Obviously, there is no possibility of comparison with other results, since the spatial resolution of the tip is better than any one quoted

in literature. The linearity of the response at 80 keV, and the relative constancy of the sensitivity around the same energy allow us to directly translate this signal or charge profile in a real dose profile.

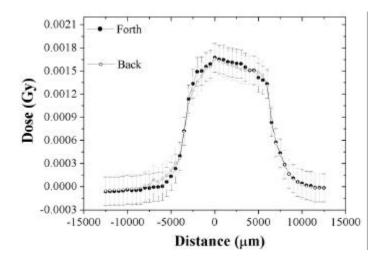


Figure 9. Profile of a 80 keV X-ray beam with a field of view 7mm x 7 mm, 13 mAs, as recorded by the tip dosimeter at a distance of 6 cm. Grey points refer to the same profile as taken backwards. Top recorded dose is 1.6 mSv. Measurement errors are indicated.

The X-ray beam profile could be measured also in the "transverse" position of the tip, i.e. with its axis perpendicular to the X-ray beam, but in this case the are two drawbacks: the former is that the signal is lower (by a factor of 2.5 in this case) since half of the dosimeter is "covering" the other half. The latter one is that in this case the mounting of the tip is much more affecting the spatial resolution. The profile, in other words, is lower and wider or not as sharp as previously.

For a good dosimeter, the threshold dose or the Lower Detection Limit (LDL) could be important in radiation protection applications. Defined as the dose capable of giving a charge signal three times the standard deviation over the noise, the LDL can be easily calculated as a dose value and it varies from 1 μ Gy at 40 keV to 0.5 μ Gy at 120 keV. These values are quite surprising for such a small dosimeter (its volume should correspond to an equivalent air volume of few mm³ of a really very small ionisation chamber) and they could be questionable. As a matter of fact, dose values down to few tens of a μ Gy were measured in several occasions.

A comparison with other dosimeters is outside of the scope of this paper (a short comparison is presented in ref. 4) but a comparison with the well known natural diamond dosimeters (ref. 7) or with the "bulk" CVD diamond dosimeters could be shortly quoted. In fact, the sensitivity as expressed in nC/Gy is of course of practical use, but compares two different quantities, since the dose is referring to the mass. By referring also the collected charge to the mass, one gets a more "comparable" sensitivity in terms of nC/J, since Gy refers to a deposited energy of 1 J in a mass of 1 Kg. In this case, the sensitivity of our tip is of the order of 10 C/J, to be compared with a value of 0.3 C/J, measured by us on a bulk CVD dosimeter.

Finally, we report some results obtained by IBIC which are quite relevant to the arguments discussed so far and could also represent some kind of further application of tips dosimeters as particle detectors. CVD diamond films are in fact proposed as nuclear detectors, but, with very few exceptions, only for tracking applications (ref. 8, 9) since the energy resolution is generally insufficient for spectroscopy. CVD diamond films, being polycrystalline, are very inhomogeneous and the energy resolution is strongly affected by inhomogeneous broadening of full energy peaks and possibly other effects such as detrapping (ref.10, 11). In our opinion, when grains are relatively small, morphological uniformity is better and with it also the uniformity of the electrical response, which is defined by charge collection efficiency and by charge collection distance. In fact, this could be appreciated from Fig. 10, which shows IBIC charge collection efficiency maps as obtained by a proton microbeam at 2.4 MeV, for an "axial" irradiation at a rate of no more than 1000 p/s, in order to avoid space-charge build up and possibly radiation damage of the sample. The maps, taken at a bias voltage of 100 and 150 V are reasonably homogeneous, even if the geometry is not a planar one. Moreover, the sample does not show polarization effects, which are due to space charge accumulation due to the non-collected charge. Polarization effects are quite strong in cases when the charge collection distance is lower or much lower than the sample thickness, as observed by IBIC.

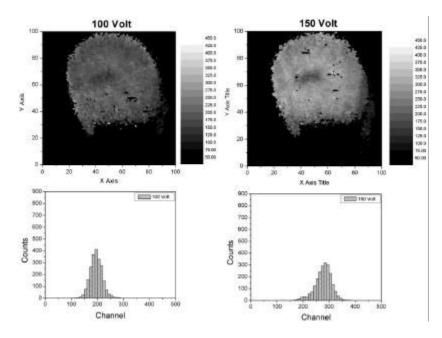


Figure 10. IBIC maps of charge collection efficiency obtained at 100 and 150 V of bias voltage, with a proton microbeam of 2.4 MeV of 1 μ m nominal spot diameter, together with the relevant multichannel spectra.

In our case, we can estimate that the total charge collection length (i.e. the sum of the collection lengths of electrons and holes) is comparable with the sample thickness (about $10~\mu m$) and therefore the not collected charge is not that important and it does not give rise to space charge polarization effects. This is also the reason why we observed a good reproducibility of the measurements and no memory effect, fast response times, time or dose dependent behaviours, such as those which are necessary for "bulk" natural or CVD diamond dosimeters in order to get them "stabilized", etc.

CONCLUSIONS

It has been clearly demonstrated that CVD diamond tips can be profitably and suitably used as "microdosimeters" in the radiological and radiotherapeutic field with no problem of "priming", with a good precision and repeatability. Their sensitivity is definitely better than commercial natural diamond dosimeters and their spatial resolution is unprecedented by any other kind of solid-state active dosimeter. Applications in fields such as stereotaxis or any kind of radiological field in which superior spatial resolution is required are not only possible, but highly desirable. Moreover, also nuclear particle spectroscopy applications (particularly alpha particles because of the range in diamond) could be envisaged, presently with modest energy resolution (20 % in the MeV range). Dosimeters and detectors with small thickness and a good morphological homogeneity could be a real breakthrough for CVD diamond applications without requiring efforts such as those for homoepitaxy or for samples with very long charge collection distance. Tissue equivalence for tips dosimeters realized on W wires could be questionable, particularly at lower energies, but the use of "lighter" substrates such as SiC is quite possible and it could solve this problem. In the MeV X-ray range, CVD diamond tips on SiC wires could achieve both tissue equivalence, stability and repeatability, together with a very strong radiation hardness.

REFERENCES

- 1. B.Planskoy, Phys. Med. Biol. 25, 3 (1980) 519-532.
- 2. F.Attix, W.C.Roesch, E.Tochilin, "Radiation Dosimetry", Vol.1, 2^d edition, Academic Press, New York (1968).
- 3. E.Vittone, F.Fizzotti, A.Lo Giudice, P.Polesello, C.Manfredotti, Nucl. Instr. and Meth. A 428 (1999) 118.
- 4. M.Heydarian, P.W.Hoban, A.H.Beddoe, Phys. Med. Biol. 41 (1996) 93-110.

- 5. D.Bollini, F.Cervellera, G.P.Egeni, P.Mazzoldi, G.Moschini, P.Rossi, V.Rudello, Nucl. Instr. and Meth. in Phys. Res. B, 109/110 (1996), 94.
- 6. C.Manfredotti, F.Fizzotti, A.Lo Giudice, G.Mucera, P.Polesello, E.Vittone, Y.Mankelevich, N.V.Suetin, Diamond. Related. Mater. 6 (1997) 1051-1056.
- 7. W. U. Laub, T. W. Kailich and F. Nuessling, Phys. Med. Biol. 44 (1999) 2183.
- 8. C.Manfredotti, F.Fizzotti, A.Lo Giudice, C.Paolini, E.Vittone and R.Lu, Nucl. Instr. Meth in Phys. Res. B 187 (2002) 566.
- 9. W.Adam et al., IEEE Trans. Nucl. Sci. 49 (2002) 1857.
- 10. C.Manfredotti, F.Fizzotti, E.Vittone, M.Boero, P.Polesello, S.Galassini, M.Jaksic, S.Fazinic and I.Bogdanovic, Nucl. Instr. Meth. in Phys. Res. B100 (1995) 133.
- 11. C.Manfredotti, E.Vittone, F. Fizzotti, A.Lo Giudice and C.Paolini, Diamond and Rel. Mat. 11 (2002) 446.

Electrochemical Advanced Oxidation Process for Water Treatment Applications

Matthias Fryda, Thorsten Matth, Shane Mulcahy

CONDIAS GmbH

fryda@condias.de

Lothar Scher, Markus Ger, Inga Tter

Fraunhofer IST

Abstract

The unique electrochemical properties exhibited by boron doped diamond films are such that new and improved electrochemical processes may now be explored both at laboratory and industrial scale. The coating of a conventional electrode material with a boron doped diamond film results in the realisation of an electrode which not only is extremely chemically stable but one which opens up the widest known electrochemical window before water decomposition takes place. The stability of DiaChem electrodes has been proven through the loading of the electrodes with increasing current densities of up to several A/cm2 in sulfuric acid.

The electrochemical generation of oxidants used for the recovery or treatment of wastewaters from industrial plants by electrochemical oxidation processes is playing an ever increasing role due to their reliable operating conditions and ease of handling. For example decomposition of cooling fluid in water has been investigated. It has been clearly shown that within the boundary of measurement accuracy it is possible to completely mineralize any organic carbon present. Long chain organic molecules such as cooling fluid may be mineralized from hydroxyl radicals without the development of intermediate products.

EAOP pilot cells as shown in fig. 3 are presently in use in a number of applications from the industrial waste water treatment to water recycling for the optics industry. These tests have displayed excellent results with regards to energy efficiency and effectiveness. It has been demonstrated that it is possible to achieve COD reduction for water flow rates of up to 2001/hour.

HIGH-DENSITY ELECTRON EMISSION FROM ION-IMPLANTATED DIAMOND

Tadashi Sakai^{1,2}, Tomio Ono^{1,2}, Mariko Suzuki^{1,2}, Naoshi Sakuma^{1,2}, Hiroaki Yoshida¹,

¹FCT Project / JFCC, Japan

²Advanced Discrete Semiconductor Technology Lab., Toshiba Corp. 1, Komukai Toshiba-cho, Saiwai-ku, Kawasaki, 212-8582, Japan

e-mail: tad.sakai@toshiba.co.jp

Masataka Hasegawa, Hideyo Okushi, Yoshinori Koga

³Research Center for Advanced Carbon Materials, AIST Tsukuba Central 5, Tsukuba 305-8565, Japan

ABSTRACT

We report high-density electron emission characteristics from ion-implanted homo-epitaxial diamond.

At the previous this conference, we had reported over 100mA/cm² electron emission from a sulfur-ion implanted homo-epitaxial diamond. To find best ion-species and implant-conditions, three types of ions such as phosphor, boron and sulfur have been implanted and their characteristics were evaluated. Among the above species, the phosphor-ion implanted sample showed highest electron emission density over 1A/cm² with emission area of 300µm in diameter. We believe that this is one of the largest emission density values for carbon-based materials under a large emission area measurement.

From the measurement of electron emission, maximum emission densities of individual samples were found to exclusively obey to their surface conductivity rather than the implanted ion-species. Also, a graphitized defect was observed at the surfaces of well emitting samples. These results and emission characteristics indicated that high-density electron emission is strongly related to the conductive carbon structure together with the semiconducting diamond matrix. Detailed emission characteristics and emission models will be discussed.

ACKNOWLEDGEMENT

This work has been performed as a part of FCT project, which is supported by METI through NEDO.

Keywords: ion implantation, homoepitaxial diamond, electron emission

ULTRAVIOLET SENSORS USING HIGHLY-ORIENTED DIAMOND FILMS

Kazushi Hayashi, Takeshi Tachibana, Yoshihiro Yokota, Koji Kobashi

Kobe Steel, Ltd., Electronics Research Laboratory 1-5-5, Takatsuka-dai, Nishi-ku, Kobe 651-2271, Japan e-mail: diamond@rd.kcrl.kobelco.co.jp

Jocelyn Achard, Alix Gicquel

LIMHP-CNRS, Université Paris-Nord 93430, Villetaneuse, France

Charles Olivero, Marie-Claude Castex

LPL-CNRS, Université Paris-Nord 93430, Villetaneuse, France

Alexey Treshchalov

Institute of Physics, University of Tartu 51014, Tartu, Estonia

ABSTRACT

Ultraviolet sensors were fabricated using undoped, highly oriented diamond (HOD) films. The sensors have a pair of interdigited electrodes of Pt or Al with the gap length of 5, 10 and, 15 µm on the HOD surfaces. Both stationary and temporal responses to irradiations of ultraviolet (UV) lights from a deuterium lamp and an ArF excimer laser (193 nm) were measured. It was found that the sensors possessed "solar-blind" property. Namely, the output signal due to a dye laser irradiation (313 nm) was only 1 % of that of the ArF laser irradiation. It was also found that the output signal due to the ArF laser irradiation well followed the incident laser pulse shape within a few nano-seconds. It was thus demonstrated that UV sensors made of HOD films can be practically used as solar-blind, robust UV laser power monitors.

Keywords: Highly oriented diamond film, UV sensor.

1. INTRODUCTION

An attention to sensors utilized for vacuum ultraviolet (UV) region has rapidly increased over the last several years. Recent technologies in the semiconductor industry require more precise measurement of exposure with UV light sources such as ArF (193 nm) and F_2 (157 nm) excimer lasers in the photolithography processes. A demand of Xe excimer lamps (172 nm) is increasing for sterilization, surface modification, and dry cleaning of various electronic materials. Due to its harsh nature of the UV light, however, conventional UV sensors consisting of Sibased devices frequently face serious difficulties in their performance, especially in the lifetime.

Diamond is known to be a typical wide bandgap (5.5 eV) semiconducting material having excellent chemical inertness and radiation hardness. Further, it has a high breakdown voltage (10^7 V/cm) and a high saturation carrier velocity ($1.5 \times 10^7 \text{ cm/s}$) (ref. 1), incomparable to Si, GaAs, and SiC. Hence, diamond is considered to be a suitable material for solar-blind, high-speed optoelectronic switches and UV sensors that can withstand high power laser irradiations. Many studies have been carried out to establish practical UV sensors with a high sensitivity and a fast response (refs. 2 to 9).

Among various sorts of diamond, highly oriented diamond (HOD) films, grown by chemical vapor deposition (CVD) combined with the bias-enhanced nucleation (BEN) technique (refs. 10 and 11), are considered to be most suitable for UV applications. The HOD films, consisting of azimuthally oriented (001) facets, contain a lower density of grain boundaries than polycrystalline diamond films does. In addition, they are economically more viable than single crystal diamond. In the present study, we have fabricated UV sensors using HOD films, which have a pair of interdigited electrodes on the surfaces. Both stationary and temporal responses to irradiation of UV lights from a deuterium lamp and an ArF excimer laser were measured. The irradiation using a dye laser (313 nm) was also conducted for comparison.

2. EXPERIMENTAL

2.1 Device fabrication

HOD films were deposited on high-resistivity Si (001) substrates using microwave plasma CVD apparatus capable of BEN treatment (ref. 12). After a carburization of Si (001) surfaces, the BEN treatment, in which negatively biased substrates to the counter electrodes were subjected to the plasma, was applied in the initial stage of the deposition in order to form epitaxial nuclei on the surface. Next, a textured growth process was carried out to grow out epitaxially nucleated diamond crystals. Consequently, the surface of the films consisted of (001) facets of several μm^2 , while the typical film thickness was approximately 5 μ m. The films were cleaned in a saturated solution of CrO₃ in H₂SO₄ to remove graphitic components and the surface conducting layer (ref. 13), and successively rinsed in a solution of aqua regia and H₂SO₄. Interdigited Pt or Al electrodes were then fabricated on the HOD film surfaces by photolithography (lift-off technique), followed by magnetron sputtering of metal elements. The thickness of the electrodes was 180 nm, while the separation between the interdigited electrodes (gap length) was 5, 10, or 15 μ m. The area covered by the interdigited electrodes was 2 × 2 mm², and the total size of the sensors was 3 × 4 mm². Figure 1 shows an optical microscope image of UV sensors. The electrode pattern fabricated on the HOD surface can be clearly seen. The sensor was finally mounted and wire-bonded on a hermetic seal (industry standard TO5 type package) in nitrogen atmosphere. For some sensors, a glass window whose transmittance was about 60 % at 200 nm, was attached. Packaged diamond UV sensors are shown in Fig. 2.

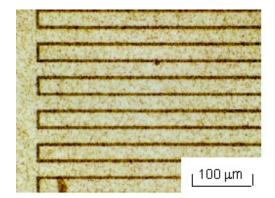


Figure 1. Optical microscope image of interdigited electrodes on diamond UV sensor.



Figure 2. Diamond UV sensors mounted in industry standard packages.

2.2 Device characterization

Stationary characteristics of UV sensors were examined using the following monochromated light sources. A deuterium lamp of 30 W output power was used for characterization in the range between 170 and 270 nm, while a 100W-halogen lamp in the range between 270 and 870 nm. The photocurrents generated by the irradiation of both light sources were measured using a Keithley 617 electrometer with a bias voltage of 40 V between the electrodes of the sensors. The dark currents of the sensors were less than 100 pA, typically 10-20 pA when the bias voltage of 40 V was applied. The responsivity of the sensors was estimated by dividing the measured photocurrent by output power of the light source at each wavelength. Note that discontinuity observed at 270 nm (shown by dotted line) is due to exchange of the light sources.

The signal of UV sensors by a pulsed irradiation of an ArF excimer laser (λ = 193 nm, pulse width = 5 ns) and a dye laser (λ = 313 nm, pulse width = 7 ns) was measured under a bias voltage of either 80 or 100 V between the electrodes. The experimental setup for the measurements and the driving circuit are described elsewhere (ref. 7). The pulse energy of the ArF laser was 4 mJ, but reduced to 25 μ J at the sensor. The dye laser also had the same energy. The entire area covered by the electrodes of the sensors was irradiated by the laser light in this experiment in order to reduce influence of localized charge distribution to the response (ref. 14). The signal from the sensors was measured as a voltage output across the 50 Ω resistor in the driving circuit. The data sampling speed was 1 GHz.

3. RESULTS AND DISCUSSION

Typical responsivities of HOD sensors as a function of irradiated wavelength are shown in Fig. 3. The bias voltage was fixed at 40 V, while distances between the electrodes were 5, 10, and 15 μ m, respectively. It is seen that sharp cut-off in the response of the sensors is observed at around 220 nm, which corresponds to a band gap energy of diamond (5.5 eV). A decrease in the response observed in the wavelength shorter than 180 nm is attributed to the absorption by the window glass used. The sensor having a 5- μ m gap length had the highest responsivity among the sensors in the UV region below 225 nm, while an apparent response was also observed at visible light region. On the other hand, the current levels for the sensors with 10 and 15 μ m gap length at visible light region are almost the same as detection limit of measurement system. The ratio between the responsivity below 225 nm and that of the visible light region is more than 10^2 , indicating excellent solar blind property of the present HOD UV sensors.

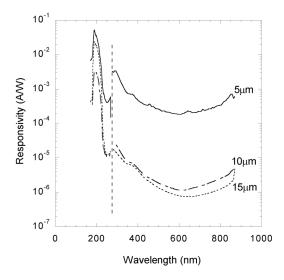


Figure 3. Spectral response of diamond UV sensors. The distances between the electrodes were 5, 10, and 15 μ m, respectively.

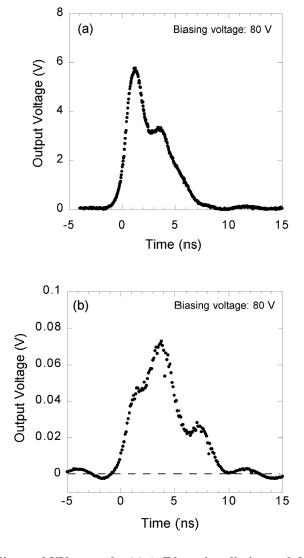


Figure 4. Response of diamond UV sensor by (a) ArF laser irradiation and (b) dye laser irradiation.

Figure 4(a) shows a typical output signal from a UV sensor by an ArF laser pulse irradiation. The sensor consisted of Pt electrodes with a 15 µm gap length, and was biased at 80 V. It was found that the signal was composed of two peaks; a main peak at 1.1 ns, and a second peak at 3.8 ns. The pulse width at (FWHM) for the incident laser was around 5 ns, which was in good agreement with that estimated from the main peak. The second peak was frequently observed in the sensors evaluated in the present study, and the output voltage of the second peak was almost half of that of the main one. Sensors with Al electrodes exhibited similar characteristics. The response of a UV sensor (Al electrodes with a 15 µm gap length) to a dye laser pulse irradiation is shown in Fig. 4(b). The sensor was measured with a biasing voltage of 80 V. In this case, the laser energy is below the band gap energy, and the signal consisted of three different peaks at 1.5, 3.8, and 7.2 ns. The intensity of the second peak was higher than that of the first peak. It is emphasized that the output signal due to the dye laser irradiation was as low as 0.1 V, and compared with the result of Fig. 4(a), the output signal by the dye laser irradiation was weaker by a factor of 10². It proves again the excellent solar blind property of the present HOD UV sensors. Judging from the peak positions, the peaks at 1.5 and 3.8 ns in Fig. 4(b) seem to result from the same processes as the corresponding peaks at 1.1 and 3.8 ns in Fig 4(a), although the peak intensities are different between these data.

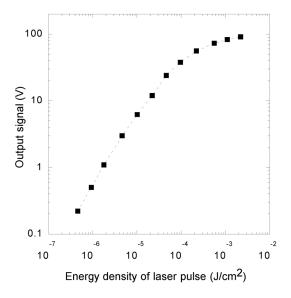


Figure 5. Pulse energy dependence on response of UV sensor by ArF laser irradiation.

Contrary to band gap excitation due to ArF laser, the irradiation below band gap energy mainly results in the formation of photocurrent originated from the defect located in the band gap. Hence, the output signal due to the dye laser irradiation strongly reflects the crystallinity of the materials. It is concluded that the present HOD films possess high quality in terms of electronic transport. As for appearance of sub peaks, Glinski et al. (ref. 14) observed a second peak in their voltage output signal when the area in the vicinity of an electrode was irradiated by a 222-nm laser, and concluded that the space charging effect was responsible for the second peak. However, it is not certain at the present stage if the same mechanism is responsible for the appearance of the second peak in Figs 4. These peaks might be due to a carrier emission from bandgap states at grain boundaries.

The output voltage of UV sensors to the ArF laser irradiation increases linearly with applied bias voltage. Figure 5 shows the output signal of the sensors as a function of energy density of incident ArF laser pulse. The sensor was biased at 100 V. In this figure, the peak voltage of each signal was plotted. It is clearly seen that the response was linear from below $\mu J/cm^2$ to mJ/cm^2 range. It means that the HOD sensors have sufficient properties for practical laser power monitoring. The signal tends to be saturated at higher energy irradiation. It however occurred only when the output signal becomes close to the biasing voltage, probably due to the measurement circuit.

4. CONCLUSION

We have fabricated UV sensors using HOD films. Stationary characteristics of the sensors were examined in the range between 170 and 870 nm. Sharp cut-off in the response was found to be observed at around 220 nm, which corresponds to a band gap energy of diamond (5.5 eV). The ratio between the responsivity below 225 nm and that at visible light region is more than 10^2 . Temporal response of UV sensors was also measured by pulsed irradiation of the ArF excimer laser and the dye laser. For the case of the ArF laser irradiation, the signal has the main peak at 1.1 ns and a second peak at about 3.8 ns. It was speculated that the second peak is due to carrier emission from gap states at grain boundaries. In the case of the dye laser irradiation, there were three peaks at 1.5, 3.8, and 7.2 ns, and the peak intensities were weaker by more than a factor of 10^2 than the case of the ArF laser irradiation. The present work indicated that UV sensors made of HOD films could be put to practical use as power monitors for ArF and F_2 excimer lasers.

REFERENCES

- 1. Pan, L.S. and Kania D.R, Eds.: Diamond: Electronic Properties and Applications, Boston, MA, 1995.
- 2. Polyakov, V.I., et al.: Photodetectors with CVD diamond films: electrical and photoelectrical properties photoconductive and photodiode structures. Diamond and Related Materials, vol. 7, no. 2–5, Feb 1998, 821.
- 3. Marinelli M., et al.: Methane-induced texturing of chemical vapor deposition diamond films and correlation with UV photoresponse. Diamond and Related Materials, vol. 7, no.7, Jul 1998, 1039.
- 4. Pace, E.; Benedetto, R.D.; and Scuderi, S.: Fast stable visible-blind and highly sensitive CVD diamond UV photodetectors for laboratory and space applications. Diamond and Related Materials, vol. 9, no. 3–6, Apr/May 2000, 987.
- 5. Whitfirld, M.D., et al.: Diamond photodetectors for next generation 157-nm deep-UV photolithography tools. Diamond and Related Materials, vol. 10, no. 3–7, Mar/Jul 2001, 693.
- 6. Whitfirld, M.D., et al.: Diamond photoconductors: operational lifetime and radiation hardness under deep-UV excimer laser irradiation. Diamond and Related Materials, vol. 10, no. 3–7, Mar/Jul 2001, 715.
- 7. Hayashi, K., et al.: Temporal response of UV sensors made of highly oriented diamond films by 193 and 313 nm laser pulses. Diamond and Related Materials, vol. 10, no. 9–10, Sep/Aug 2001, 1794.
- 8. Achard, J., et al.: Photoconductivity of highly oriented and randomly oriented diamond films for the detection of fast UV laser pulse. Diamond and Related Materials, vol. 11, no. 3–6, Mar/Jan 2002, 423.
- 9. Salvatori, S., et al.: Optimised contact-structures for metal-diamond-metal UV-detectors. Diamond and Related Materials, vol. 11, no. 3–6, Mar/Jan 2002, 458.
- 10. Yugo, S., et al.: Generation of diamond nuclei by electric field in plasma chemical vapor deposition. Appl. Phys. Lett., vol. 58, no. 10, Mar 1991, 1036.
- 11. Stoner, B.R and Glass, J.T.: Textured diamond growth on (100) β-SiC via maicrowave plasma chemical vapor deposition. Appl. Phys. Lett., vol. 60, no. 6, Feb 1992, 698.
- 12. Tachibana, T; Hayashi, K; and Kobashi, K.:Azimuthal rotation of diamond crystals epitaxially nucleated on Silicon {001}. Appl. Phys. Lett., vol. 68, no. 11, Mar 1996, 1491.
- 13. Hayashi, K., et al.: Investigation of the effect of hydrogen on electrical and optical properties in chemical-vapor-deposited homoepitaxial diamond films. J. Appl. Phys., vol. 81, no. 2, Jan 1997, 744.
- 14. Glinski, J., et al.: Space-charge-induced optoelectronic switching in IIa diamond. App. Phys. Lett., vol. 45, no. 3, Aug 1984, 260.

BI-STABLE THERMAL MICROACTUATORS BASED ON CVD DIAMOND

R. Müller, P. Schmid, A. Munding, F.J. Hernandez-Gullien, E. Kohn

Department of Electron Devices and Circuits, University of Ulm, 89069 Ulm, Germany Tel: +49-731-5026187, Fax: +49-731-5026155, e-mail: rmueller@ebs.e-technik.uni-ulm.de)

ABSTRACT

In this work, two examples of thermally driven MEMS devices based on polycrystalline diamond films are presented. These are a bi-stable diamond microswitch and a diamond micropump. By employing the classical bi-metal effect and using diamond as a multi-purpose material (i.e. mechanical carrier, heater element, bi-metal element) the device layout can be rather simple.

Device working principles, layouts, technology and first results on device operation are given.

Keywords: CVD-Diamond, MEMS, Microswitch, Micropump.

INTRODUCTION

The outstanding material properties of diamond predestine the material for the use in heavy duty micro electro mechanical systems. Its excellent thermal power handling capability has been used for the realization of thermally driven micro actuators. The thermal actuation principle employed is the classical bi-metal effect. Applied to microsystems it can produce very high deflection forces at low driving voltages, which overcomes some of the main drawbacks of other driving concepts, like electrostatic or piezoelectric actuation.

A thermal actuator needs permanent heating to remain in the deflected state, representing a static power loss, which is highly undesirable. This disadvantage may be overcome by a bi-stable design, which may be based on a stressed material leading to a stable deflection already present in the quiescent state. This feature is inherently present in (polycrystalline) diamond CVD films, which show an intrinsic compressive stress of about 100-200 MPa due to the CVD growth mechanism used on a foreign substrate like Si.

Based on this evaluation, two different microdevices, a bi-stable microswitch and a membrane micropump with integrated passive valves, have been investigated. Thermal, mechanical and fluidic simulations have been performed to optimize the design.

DEVICE PRINCIPLE AND TECHNOLOGY

The device principle employed is a bi-metal actuator consisting of a free standing diamond beam or membrane on which a metal is placed. The differences in thermal expansion of diamond and the metal lead to a bending of the structures when heated. Since its material properties (high coefficient of thermal expansion together with a high Young's modulus) are optimal in this respect, Nickel has been chosen. The required thickness to produce a sufficient bending moment is in the order of several micrometers, thus the Nickel layer has been deposited by an electroless plating process. The technology for the realization of the free standing diamond structures consists of the deposition of diamond on a sacrificial layer, dry etching to define the device structures and removal of the sacrificial layer to release the structures. Details on the technology can be found in ref. 1.

Since diamond can be doped with boron resulting in a moderate conductivity, it is also a nearly ideal material for heater elements. Therefore the diamond layer itself has been used as a heater. By proper placement of the electrical supply lines, a local heating of the appropriate regions is possible.

In *Figure 1*, the realization of a simple switching structure based on the above described principle is shown. The device consists of the single-anchored beam covered with Nickel and actuated by a current flowing through the diamond layer. The bending of the switches in the "up"-position is due to a stress in the Nickel layer, which is deposited at elevated temperatures. The actuation voltage for closing the switch is only 1.3 Volt.



Figure 1: Switching of diamond bi-metal switch (middle: "down" position, top/bottom: "up" position), the middle structure is actuated by a current flow.

THE BI-STABLE MICROSWITCH

In the simple configuration shown above, a static power is needed to hold the thermal switches in their "down"-position. For the switches shown, this power is approx. 100 mW. Such a static power loss is highly undesirable. Therefore a bi-stable configuration has been designed by which this disadvantage can be overcome.

Realization

The basic structure for the bi-stable configuration is a double-anchored beam as shown in *Figure 2*. Due to the intrinsic stress caused by the diamond growth process, such a beam buckles into one of two stable states. Switching between these states is possible by using the bi-metal effect creating bending moments at appropriate positions, which is shown in *Figure 3*. The localized heating can be achieved by a proper placement of the metalization, that delivers the current for the heating regions in the diamond layer.

These considerations lead to a device layout as shown in *Figure 4*. The supply lines consist of a Cr/Au metalization, which is rather thin compared to the Ni metalization creating the bi-metal effect. These lines have been realized by sputtering and lift-off. The optimum placement of the supply metalization and the bi-metal regions has been determined by electrical, thermal and mechanical FEM simulations.

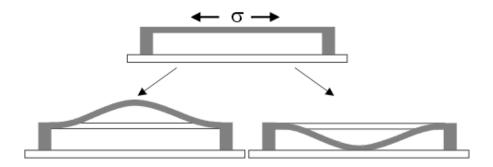


Figure 2: Deflection of a cantilever anchored at both ends due to intrinsic stress.



Figure 3: Switching by local heating of the microswitch

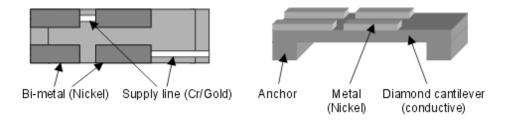


Figure 4: Layout of bistable microswitch

Results

Based on the basic layout shown above and on the optimum values for the geometric parameters obtained from simulations, switches have been realized. The two stable states could be observed and a reproducible switching from up to down and vice versa has been possible. For initiating the switching events, only short pulses of the actuating voltage were necessary, switching from up to down was achieved by applying a voltage of 4 V for 90 μ s, switching from down to up by applying 3.3 V for 70 μ s.

Figure 5 shows the microswitch in its "up" and "down" position respectively. In the "down"-position, the beam doesn't touch the bottom contact exactly in its middle but rather in the right third, because the stress in the Nickel layer (as mentioned above) leads to a non-ideal bending line of the beam. However, a reproducible contact can be observed.

Switch-on and switch-off times have also been measured. The switch-on time was approx. $220 \,\mu s$, consisting of the heating time of approx. $100 \,\mu s$ and the switching time, which is mainly limited by air damping. The switch-off time was approx. $80 \,\mu s$. Both are dependent on the actuating power and decrease with increasing heating power.

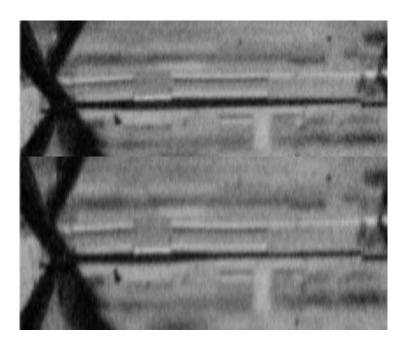


Figure 5: Bistable microswitch in "up" position (top) and "down" position (bottom)

THE MICROPUMP

Realization

To fabricate the micropump a two part technology was chosen, splitting up the device into the actuated diamond membrane in the top part, which is glue-bonded on the capillary system in the bottom part (see *Figure 6 a*).

For the top part, a 3 μ m thick, boron-doped diamond layer was grown on a silicon substrate using bias enhanced nucleation and MWCVD. Next the silicon was patterned and etched from the backside using KOH to form a membrane and the fluidic connections. As explained above, the diamond layer suffers residual stress from growth resulting in a buckling of the membrane. Employing identical processing technologies as for the microswitch, the bimetal actuators (Ni) and the Cr / Au contact metalization were fabricated last (see *Figure 6 b*).

The bottom part was realized using a photosensitive expoxy (SU-8). This part contains the fluidic channels, the input, the output and the pumping chamber and the passive valves. The passive valves are particularly shaped channels which put up different flow resistance depending on the fluid direction. In other words, they act like a non-ideal check-valve to direct the fluidic flow (see ref. 2).

In the last step, both parts were bonded together using a thinned photoresist as glue. They had to be adjusted that the membrane was placed exactly over the pumping chamber and that the inlet and outlet holes in the top part were situated over the input and output chambers This could be achieved using a flip-chip bonder.

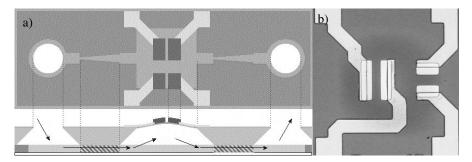


Figure 6: a) Layout and b) micrograph of diamond micropump.

To find the right parameters for the design of the device, two different sets of finite-element simulation have been performed with ANSYS.

In the first set, the membrane was simulated mechanically and thermally to find the right parameters for the position and the size of the nickel actuators. Next the membrane movement was simulated using the parameters from the first simulation (see *Figure 7 a, b*) to find the switching temperature from up to down position and vice-versa. This finally led to the heating power of the actuators.

In the second set the fluid movement in the passive valve structures was simulated. This was necessary to find the optimum opening angle and length of the valves. As a result several variations seemed possible. Depending on their size and angle, the valves could either operate as diffuser, allowing for a preferred flow in the direction with the wider opening or as a nozzle with a preferred flow in the other direction.

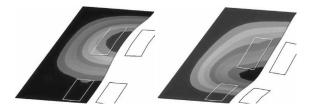


Figure 7: ANSYS simulation of a) deflected membrane up and b) down

Mode of Operation

From theory, applying a voltage pulse to either the up- or the down-actuator, the buckled membrane could be deflected to its stable up- or down-position respectively. This changes the volume of the chamber underneath and induces a fluid flow. Since inlet and outlet are connected to the chamber via the passive valves, the flow experiences a preferred direction resulting in a net fluidic flow in one direction. By powering the up- and down-actuators alternatively with a certain frequency, a pumping effect is expected to happen.

Results

For a first test, the top part of the membrane was successfully operated. The maximum deflection of $d = 15 \mu m$ for the 500 μm size membrane was measured for heating power of P = 4W (see *Figure 8*). It could also be shown, that an oscillating movement of the membrane was possible up to a frequency of 100Hz. Although higher frequencies have not been tested yes, it is believed that the device will work up to several kHz oscillating frequency.

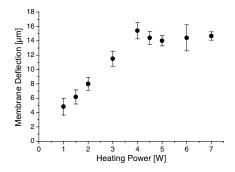


Figure 8: Measured membrane deflection depending on heating power

REFERENCES

- M. Adamschik, S. Ertl, P. Schmid, P. Gluche, A. Flöter, E. Kohn: Electrostatic Diamond Micro Switch Proc. Transducers '99, 1284-1297 (1999)
- 2. Gerlach; Torsten: Microdiffusers as dynamic passive valves for micropump applications. Sensors and Actuators A, 69 (1998), 181–191

CAPACITANCE-VOLTAGE-FREQUENCY CHARACTERISTICS OF NI/DIAMOND SCHOTTKY DIODES ON OXIDIZED BORON-DOPED HOMOEPITAXIAL DIAMOND FILM

Y.G. Chen a, b, M. Ogura a, b, H. Okushi a, b

Diamond Research Center, National Institute of Advanced Industrial Science and Technology (AIST), 1-1-1 Higashi, Tsukuba, Ibaraki 305-8565, Japan
 CREST, Japan Science and Technology Corporation (JST), Japan

ABSTRACT

The electrical properties of Ni/diamond Schottky diodes fabricated on oxidized boron-doped homoepitaxial diamond film have been studied in order to investigate the electrical behaviors of diamond-based electronic devices. The current-voltage (I-V) characteristics of the Ni-Schottky contacts to the boron-doped homoepitaxial diamond film show excellent rectification properties. The capacitance-voltage (C-V) features of the Ni/diamond Schottky diodes were characterized in the frequency range from 10^{-3} Hz to 2×10^{5} Hz. The C-V measurements indicate that the space charge density (N_I) and the diffusion potential (V_d) values are about 6.5×10^{16} cm⁻³ and 1.25 V, respectively, and have weak frequency dependence in the range from 10^{-3} Hz to 10^4 Hz. The capacitance-frequency measurement at zero bias indicated that the degrading capacitance at high frequency ($>10^4$ Hz) is primarily due to the high series resistance of the homoepitaxial diamond film. The sudden drop in capacitance with increasing forward bias (V_F) observed in Ni/diamond Schottky diodes is an interesting feature which can be explained by the model proposed by A.J. Snell et al.

Keywords: Diamond films; Boron doping; Capacitance-voltage characteristic; Schottky diode

INTRODUCTION

Due to the attractive physical and electrical properties such as wide band gap, high breakdown voltage, high thermal conductively, low dielectric constant, chemical inertness and excellent radiation hardness, diamond has been recognized as a promising material for producing electronic devices which can be operated at high power, high frequency, high temperature and in chemically harsh environments [1-4]. In order to realize the reliable application of diamond in semiconductor industry, some fundamental material-related issues in diamond film deposition must be solved in advance. One of the pre-condition is to obtain the high-quality (device grade) diamond films with a low density of defects and residual impurities. The second one is to develop a technique for the p- or n-type doping control. In recent years, the group in AIST Japan has successfully synthesized high quality undoped homoepitaxial diamond films with flat surface on atomic scale, by applying the microwave-plasma chemical vapor deposition (CVD) technique [5-8]. The investigation of cathodoluminescence (CL) has shown a strong free excitonic emission at 5.27 eV even at room temperature (RT) [7-9]. Based on the growth method of the undoped homoepitaxial diamond films, device-grade boron (B)-doped (p-type) homoepitaxial diamond films have also been successfully synthesized by using trimethylboron [B(CH₃)₃, TMB] gas as a boron doping source [10]. Some junction properties of metal/B-doped films (Schottky junctions) have been investigated by Hayashi [11] and Yamanaka [10, 12]. Their reports and the authors' present experimental data [13] indicated that thermionic emission was dominant for surface oxidized B-doped homoepitaxial diamond films at room temperature. The activation energy of the hole concentration for the B-doped films has been measured to be around 0.36 eV [10, 14].

It is well-known in the semiconductor devices field that many of the useful properties of a p-n junction can be achieved by simply forming an appropriate metal-semiconductor contact. This approach is obviously attractive because of its simplicity of fabrication; also, metal-semiconductor junctions are particularly useful when high-speed rectification is required. From the literature, there are a number of reports about the electrical property measurements on rectifying metal/polycrystalline (or natural) diamond Schottky diodes [15-19]. From the point of view of the authors, at present stage, the best way to show the potential of diamond in electronic applications or the nature of diamond is to fabricate some simple devices by applying high quality (device grade) homoepitaxial diamond film so as to exclude the effects of defect, impurity, etc. Accordingly, in this work, the nickel (Ni)/B-doped homoepitaxial

diamond Schottky diodes are fabricated and the electrical properties of the diodes are studied using current-voltage (I-V) measurement and capacitance-voltage (C-V) measurement in a broad frequency range (10^{-3} Hz $\sim 2 \times 10^{5}$ Hz).

EXPERIMENTS

B-doped homoepitaxial diamond films were deposited on HPHT synthetic Ib diamond substrates with dimensions of 4 mm \times 4 mm \times 0.3 mm using microwave plasma-enhanced CVD apparatus. The surface was (001) with a misorientation angle of around 2°. Source gas was 0.3% CH₄ diluted with H₂. Doping with B was carried out using trimethylboron [B(CH₃)₃, TMB] which was also diluted with H₂. The TMB/CH₄ ratio in the source gas was 50 ppm. The gas pressure, total gas flow rate, microwave power were 50 Torr, 400 sccm and 750 W, respectively. The substrate temperature was kept at 800°C, measured by a thermocouple attached to the backside of a susceptor.

Before the performance of any electrical measurements, an acid-mixture of H_2SO_4 and HNO_3 at 200°C for 15 min was used for oxidization of the B-doped diamond film to remove the hydrogen-terminated surface layer. Ohmic contacts were fabricated on the diamond surface by evaporating Ti followed by Pt and Au to prevent the oxidization of Ti electrode and then annealed at 400°C for 30 min in Argon environment in order to achieve good ohmic properties. Hall-effect measurements were performed at room temperature to determine the Hall mobility and hole concentration, which were determined to be 1280 cm²/Vs and 2.67×10^{14} cm⁻³, respectively. To fabricate the metal/diamond Schottky diodes, Ni with a diameter of 200 μ m was evaporated onto the surfaces of the above-treated diamond films. Current-voltage (*I-V*) measurements of the Ni/diamond Schottky diodes were carried out using a Hewlett Packard 4140B pico-ampere meter. Capacitance-voltage (*C-V*) measurements of the diodes were performed using LCR (300-2×10⁵Hz) and Triangle-wave (0.005-0.02 Hz) measurements, respectively.

RESULTS AND DISCUSSIONS

Figure 1 shows the typical I-V characterization of a Ni/diamond Schottky diode fabricated on B-doped diamond film measured at room temperature (298K). As evident in Fig. 1, the high series resistance of the diamond film limits the forward current and causes departures from linearity over much of the forward region. In order to determine I_0 and n accurately, the effect of the series resistance should be considered, which has been observed to dominate current conduction processes in some other wide band gap semiconductors. Applying the method proposed in the reference [15], a series resistance of a Schottky diode was calculated to be 1.85×10^5 ohm, which is at the same order of the total resistance of the diode at forward bias 2V, i.e. 4×10^5 ohm. Accordingly, the series resistance from the diamond film can not be omitted and the ideality factor n of the diode was determined to be 1.1 at 298K, indicating that the diode was nearly ideal.

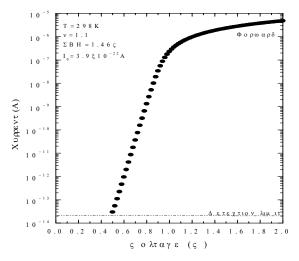


Fig. 1. Typical current-voltage characteristic of a Ni/diamond Schottky diode fabricated on B-doped diamond film at 298K.

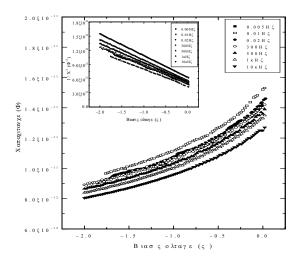


Fig. 2. Reverse bias C-V-F characteristics of a Ni/diamond Schottky diode at 298K. Insert: Mott-Schottky plots of C²-V curves.

Figure 2 shows the capacitance-voltage relations from the Ni/diamond Schottky diode in a broad frequency range in the reverse bias region. The C-V curves corresponding to low frequencies (0.005 Hz, 0.01 Hz and 0.02 Hz) and relative high frequencies (300 Hz -10^4 Hz) were measured by applying triangle-wave measurements and LCR measurements, respectively. The insert in Fig. 2 is the Mott-Schottky plots [20] of I/C^2 -V from the C-V data of the Ni/diamond Schottky diode at 298K. The space charge densities (N_I) and the built-in potentials (V_d) calculated from the I/C^2 -V relations are plotted in Fig. 3, which show a weak frequency dependence, and the space charge densities are around $5.7 \times 10^{16} \text{cm}^{-3}$. Based on the data in Fig. 3, the width of the depletion layer is evaluated about 110 nm. The Schottky barrier height (SBH) deduced from built-in potential is about 1.6 eV which is similar to the SBH determined from I-V measurement, 1.46 eV.

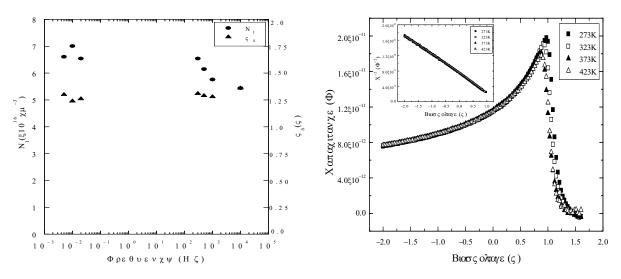


Fig. 3. Frequency dependence of space charge densities (N_{I}) and built-in potentials (V_{d}) at 298K.

Fig. 4. Temperature dependence of *C-V* characteristics in reverse and forward bias ranges.

Figure 4 shows the capacitance-voltage relations from the Ni/diamond Schottky diode at 1kHz in different temperatures in both reverse and forward bias regions. From the figure, we can see that in reverse and small forward bias ranges, the barrier capacitance-voltage curves show the general trend normally found with crystalline barriers, which can be explained well by the proposed model from Roberts and Crowell [21]. With increasing forward bias, the sudden drop in capacitance is observed, which can not be explained by purely electronic model [21]. The sudden drop phenomena in capacitance can be explained well by the proposed model of A.J. Snell et al. [22], which was proposed to study the capacitance and conductance at metal-amorphous silicon barriers. According to the model, the metal/semiconductor Schottky diode can be considered as an equivalent circuit which is composed of two series sections: (1) the depletion layer of width W, having a capacitance C_1 and a conductivity σ_1 (corresponding to resistance R_1), and (2) the bulk of the specimen, thickness d-W, characterized by C_2 and σ_2 (corresponding to resistance R_2). On the basis of the above model, the capacitance C and conductance G measured between the specimen electrodes can be expressed in terms of the quantities in the equivalent circuit and as a function of the angular frequency ω of the bridge shown as follows.

$$C = \frac{R_1^2 C_1 + R_2^2 C_2 + \omega R_1^2 R_2^2 C_1 C_2 (C_1 + C_2)}{(R_1 + R_2)^2 + \omega^2 R_1^2 R_2^2 (C_1 + C_2)^2}$$
(1)

$$G = \frac{R_1 + R_2 + \omega^2 R_1 R_2 (R_1 C_1^2 + R_2 C_2^2)}{(R_1 + R_2)^2 + \omega^2 R_1^2 R_2^2 (C_1 + C_2)^2}.$$
 (2)

In the above equations, the effect of contact resistance has been neglected in the frequency range of interest by assuming the good contacts. As shown in Fig. 2, the capacitance-voltage curves have weak frequency-dependence in reverse bias range and the frequency-dependent terms in equations (1) and (2) can be negligible as compared to the other terms for the applied frequency less than 1 kHz. Accordingly, in reverse and small forward bias ranges, $R_1 >> R_2$ which results in $C \approx C_1$ and $G \approx 1/R_1$. The measurements should thus lead to the relevant barrier quantities. However,

with increasing forward bias, the condition $R_1 << R_2$ will be approached and then C will tend towards C_2 and C_3 towards C_4 . Figure 4 also show the weak temperature-dependence on the C-C characteristics of Ni/diamond Schottky diodes, which is due to the wide-band-gap of diamond and the deep location of dopant in the band gap.

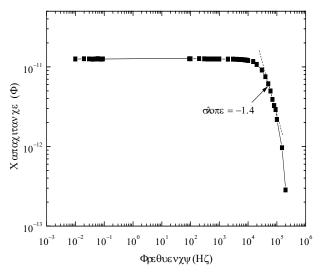


Fig. 5. Zero bias *C-F* plot of Ni/B-doped homoepitaxial diamond Schottky diode at room temperature.

Figure 5 shows a capacitance-frequency (C-F) plot of the Ni/B-doped homoepitaxial diamond Schottky diode at zero bias voltage. From the figure, we can see that in the broad frequency range of 0.005Hz-10⁴Hz, the capacitance is weak dependent on the frequency which is compatible to the results shown in Fig. 4. When the frequency applied is increased to higher than 10⁴ Hz, the capacitance has strong frequency dependence and tends to decrease faster. Generally, the measured capacitance of a Schottky diode is dependent on the reverse bias voltage and frequency. The voltage and frequency dependence is due to the factors of a Schottky barrier, boron-doped impurity levels, and high series resistance and so on. At low frequency the measured capacitance is dominated by the depletion capacitance of the Schottky diode which is bias dependent and frequency independent. As the frequency is increased, the total diode capacitance is affected not only by the depletion capacitance but also by the bulk resistance and the dispersion capacitance, which is frequency dependent and associated with hole emission from slowly responding deep impurity levels [23, 24]. Because of these effects, the capacitance-bias dependence becomes less pronounced or disappears. The C-F dependency shown in Fig. 5 can be explained qualitatively by the above model proposed by A.J. Snell [22]. In this study, we would like to apply a theoretical model taking the effect of series resistance into consideration developed by Glover [25] to analysis the C-F characteristic quantitatively. It was found that the junction capacitance could be represented by a series equivalent circuit consisting of capacitors C_d and C_f and resistance R_f and R_s , described by the following equation [25]:

$$C_m(V, \omega, T) = C_T / [1 + (\omega R_T C_T)^2],$$
 (3)

where $1/C_T = 1/C_d(V) + 1/C_f(\omega, T)$, and $R_T = R_f(\omega, T) + R_s(T)$. C_m is the measured capacitance. C_d is the depletion capacitance which is voltage dependent, but frequency and temperature independent. C_f (which is proportional to $\omega^{-1/2}$) is the capacitance due to the additional junction length required at higher frequencies for hole emission from the slowly responding deep levels. The dissipative loss due to the phase shift is represented by R_f , and R_s is the series resistance of the diamond film. According to the model, Glover [25] concluded that at low frequency C_m became simply C_d , so that the barrier height and doping concentration might be obtained in spite of the effect of the series resistance R_s , and at higher frequencies or low temperatures $C_T \rightarrow C_f$. One can then distinguish two cases, depending on the value of R_s . When R_s =0, $\omega C_T R_T = 1$ so that $C_m = C_f/2$, and the measured capacitance C_m falls off with frequency as $\omega^{-1/2}$. When R_s >> R_f , however, the second term in denominator of Eq. (1) dominates, so that C_m depends on frequency as $\omega^{-3/2}$. The plot shown in Fig. 5 confirms the limiting case of the high series resistance effect on the C-F characteristics of the Ni/B-doped homoepitaxial diamond Schottky diode. At

high frequencies (>10⁴ Hz), the capacitance of the diode with high series resistance begins to decline with a slope of -1.4 (i.e. showing $C_m \propto$ frequency ^{-1.4}). The slope is due to the high series resistance of the device. The characteristic slope of -1.4 at high frequency is in agreement with the theoretical prediction described by Glover [25] on synthetic crystalline diamond. Our experimental data has confirmed the characteristic feature of this dependence.

CONCLUSION

In this work, the electrical properties, including the I-V and C-V characterizations of the Ni/B-doped diamond Schottky diodes were studied carefully. The I-V measurements show that the Ni/B-doped diamond Schottky diodes have excellent rectification properties. The C-V-F measurements indicate the measured capacitance varies with applied bias and frequency. The sudden drop in capacitance in forward bias range can be explained well by the proposed model of A.J. Snell. At low frequency range 10^{-3} Hz to 10^4 Hz, the C-V characteristic was inert to the frequency. At high frequencies, the Schottky diodes with high series resistance had declining capacitance with increasing frequency. The C-F characteristics of the Ni/B-doped homoepitaxial are in good agreement with the prediction of the model developed by Glover.

ACKNOWLEDGEMENT

The authors wish to thank Drs. S. Ri, M. Hasegawa and H. Watanabe in the same research team in AIST for partial skillful technical assistances. Special thanks are due to Dr. S. Yamanaka of Sumitomo Chemical Co., Ltd. for his previous work in AIST.

REFERENCES

- 1. Collins, A.T., et al.: Properties of Diamond, edited by J.E. Field (Academic, San Diego, CA, 1979).
- 2. Shenai, K., et al.: Optimum semiconductors for high-power electronics. IEEE Trans. Electron. Devices ED-36 (1989) 1811.
- 3. Geis, M.W.: Diamond transistor performance and fabrication. Proc. IEEE 79 (1991) 669.
- 4. Trew, R.J., et al.: The potential of diamond and SiC electronic devices for microwave and millimeter-wave power applications. Proc. IEEE 79 (1991) 598.
- 5. Hayashi, K., et al.: High Quality Homoepitaxial Diamond Films Grown in End-Launch Type Reactors. Mater. Res. Soc. Symp. Proc. 416 (1996) 217.
- 6. Hayashi, K., et al.: Homoepitaxial diamond films with large terraces. Appl. Phys. Lett. 68 (1996) 1220.
- 7. Okushi, H., et al.: Diamond films epitaxially grown by step-flow mode. J. Cryst. Growth 183 (1998) 338.
- 8. Hayashi, K., et al.: Stepped growth and etching of (001) diamond. Diamond Relat. Mater. 5 (1996) 1002.
- 9. Watanabe, H., et al.: Strong excitonic recombination radiation from homoepitaxial diamond thin films at room temperature. Appl. Phys. Lett. 73 (1998) 981.
- 10. Yamanaka, S.: High-quality B-doped homoepitaxial diamond films using trimethylboron. Jpn. J. Appl. Phys. 37 (1998) L1129.
- 11. Hayashi, K., et al.: Investigation of the effect of hydrogen on electrical and optical properties in chemical vapor deposited homoepitaxial diamond films. J. Appl. Phys. 81 (1997) 744.
- 12. Yamanaka, S., et al.: Low-compensated boron-doped homoepitaxial diamond films. Diamond Relat. Mater. 9 (2000) 956.
- 13. Chen, Y.G., et al.: Temperature dependence on current-voltage characteristics of nickel/diamond Schottky diodes on high quality boron-doped homoepitaxial diamond film. Appl. Phys. Lett. (submitted).
- 14. Yamanaka, S., et al.: Low-compensated boron-doped homoepitaxial diamond films using trimethylboron. phys. stat. sol.(a) 174 (1999) 59.
- 15. Venkatesan, V., et al.: Effect of back contact impedance on frequency dependence of capacitance-voltage measurements on metal/diamond diodes. Appl. Phys. Lett. 63 (1993) 1065.
- 16. Kang, W.P., et al.: Temperature dependence and effect of series resistance on the electrical characteristics of a polycrystalline diamond metal-insulator-semiconductor diode. J. Appl. Phys. 78 (1995) 1101.
- 17. Rodrigues, A.M., et al.: Interface Properties and Capacitance-Voltage Behaviour of Diamond Devices Prepared by Microwave-Assisted CVD. phys. stat. sol. (a) 174 (1999) 165.

- 18. De Cesare, G., et al.: On the electrical properties of polycrystalline diamond films on silicon. Diamond Relat. Mater. 4 (1995) 628.
- 19. Pereira, L., et al.: Electrical AC behavior of MPCVD diamond Schottky diodes. Diamond Relat. Mater. 10(2001) 615.
- 20. Sze, S.M.: Physics of Semiconductor Devices (second edition, Wiley, New York, 1996).
- 21. Roberts, G.I. and Crowell, C.R.: Capacitance energy level spectroscopy of deep-lying semiconductor impurities using Schottky barriers. J. Appl. Phys. 41 (1970) 1767.
- 22. Snell, A.J., et al.: The interpretation of capacitance and conductance measurements on metal-amorphous silicon barriers. Phil. Mag. B 33 (1976) 935.
- 23. Rhoderick, E.H. and Williams, R.H.: Metal-Semiconductor Contacts (Clarendon, Oxford, 1988).
- 24. Crowell, C.R. and Nakano, K.: Deep level impurity effects on the frequency dependence of Schottky barrier capacitance. Solid-State Electron. 15 (1972) 605.
- 25. Glover, G.H.: The C-V characteristics of Schottky barriers on laboratory grown semiconducting diamonds. Solid-State Electron. 16 (1973) 973.

HOLE MOBILITY IN BORON-DOPED HOMOEPITAXIAL CVD DIAMOND THIN FILMS

Kunio Tsukioka and Hisashi Ogawa

Department of Electronic Engineering, Faculty of Engineering, Tamagawa University 6-1-1 Tamagawa Gakuen, Machida, Tokyo 194-8610, Japan E-mail: tsukioka@eng.tamagawa.ac.jp
Fax: +81-42-739-8858, Phone: +81-42-739-8397

Hideyo Okushi

Research Center for Advanced Carbon Materials National Institute of Advanced Industrial Science and Technology Tsukuba Central 5, 1-1, Higashi-1, Tsukuba, Ibaraki 305-8565, Japan

ABSTRACT

The electric conductivity and Hall effect of boron-doped homoepitaxial CVD diamond thin films have been measured in the temperature range from 150K to 900 K. The temperature dependence of Hall mobility is analyzed by using an iterative technique assuming the scattering by ionized impurities, acoustic deformation potential and nonpolar optical phonons. The acoustic deformation potential constant E_1 , the coupling constant of nonpolar optical phonons $D_{\rm npo}$ and the donor concentration $N_{\rm D}$ are used as fitting parameters. We take into account the band nonparabolicity through the hyperbolic band model. The density of state mass $m_{\rm d}$, the conduction mass $m_{\rm c}$ and the nonparabolicity parameter α are estimated from a LAPW band calculation. The temperature dependence of hole concentration is also numerically analyzed on the basis of the electric neutrality and the hyperbolic band model with fitting parameters of the acceptor concentration $N_{\rm A}$, the donor concentration $N_{\rm D}$, and the acceptor ionization energy $E_{\rm A}$. For all the samples, best fits between experimental and theoretical values are obtained when $E_{\rm 1} \sim 16.0$ eV, $D_{\rm npo} \sim 1.2 \times 10^{12}$ eV/m and $E_{\rm A} \sim 0.365$ eV. Some indications of the impurity conduction were seen in the low temperature range.

Keywords: CVD diamond thin films, Hall mobility, scattering mechanisms, impurity conduction

INTRODUCTION

Diamond, which has a very wide band gap (5.5 eV) and extraordinary thermal conductivity, has attracted remarkable attention as a material for semiconductors in the next generation. The synthesis technique of diamond thin films has advanced considerably in the last decade. It has been already reported that device-grade thin films of Boron doped diamond were successfully prepared by microwave plasma CVD method (refs.. 1,2). Furthermore, Isberg et al (ref. 3) has reported, last September, very high mobility values (0.45 m²/V.s for electrons, 0.38 m²/V.s for holes) in a high-purity single-crystal CVD thin film. In this situation, an interest is growing in detailed studies on electric properties of CVD diamond thin films.

In this work, we report the results of electric conductivity and Hall effects measurements in boron-doped homoepitaxial CVD diamond thin films over the temperature range from 150K to 900 K. The analyses of the experimental data give us the information about the impurity levels, the donor and acceptor concentrations and the carrier scattering mechanisms in the diamond crystal.

EXPERIMENT

Samples studied in this work are B-doped homoepitaxial diamond thin films grown with microwave plasma CVD method (refs.. 1,2) on the substrates of Ib synthetic diamond with the size of $4\times4\times0.3~\text{mm}^3$. A sample list is shown in table 1, where CH₄ (%) and TMB (ppm) represent CH4/H₂ ratio and TMB(trimethylboron)/ CH₄ ratio in the source gas, respectively. Ohmic contacts were fabricated on the diamond surface in the van der Pauw configuration by evaporating Ti followed by Au to prevent oxidization of the Ti electrode.

Table 1. Sample list.

Sample name	B1	B2	B4	B23	B36	B37	B42	B93
CH ₄ (%)	0.3	0.3	0.3	0.3	0.3	0.3	1	0.1
TMB(ppm)	100	100	500	50	30	40	15	25
Thickness (µm)	1.1	1.1	1	0.8	2.7	3.2	2.2	2

The magnitude of magnetic flux density is $0.5 \sim 1$ T. The samples are mounted on a sapphire plate attached on a ceramic heater. The heater is put on a block of machinable ceramics. The sapphire plate, the ceramic heater and the machinable ceramic block were joined together with the alumina cement. The sample holder is put in the inner Dewar of a double Dewar cryostat made of stainless steal. Above room temperature, the samples are heated with the ceramic heater in a vacuum about 10^{-6} Torr. Below room temperature, the sample temperature is regulated by adjusting the balance between cooling by liq. N_2 injected into the outer Dewar and heating by the ceramic heater. In both cases, the sample temperature is regulated with a PID controller using a platinum thermometer. As the sample resistance becomes very high at low temperatures, voltages are measured using an electrometer with an input impedance of more than $2 \times 10^{15} \Omega$ and a handmade scanner with an isolation resistance of more than $10^{14} \Omega$.

CALCULATION MODEL

A simplified model is applied to for the valence band of diamond. We assume a single equivalent isotropic band, instead of the heavy and the light hole bands (ref. 4). The band nonparabolicity is taken into account through the hyperbolic band model,

$$\frac{\hbar^2 k^2}{2m_{\rm d}^*} = \varepsilon \left(1 + \alpha \varepsilon\right). \tag{1}$$

The values of the density-of-state mass m_d and the nonparabolicity parameter α are obtained in such a way that the density-of-states calculated using the hyperbolic band model fit those calculated by an LAPW method (ref. 5). The value of the conduction mass m_c is estimated by using the theoretical mass parameter values of the LAPW band calculation.

The experimental data of hole concentration is analyzed assuming that there are a donor level and an acceptor level (the single donor-single acceptor model). The values of hole concentration are calculated from the condition of electric neutrality,

$$p + N_D^+ = n + N_A^-, (2)$$

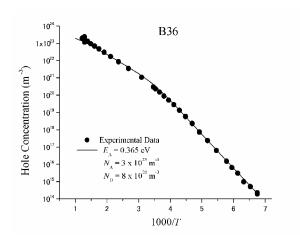
where p, $N_{\rm D}^+$, n, and $N_{\rm A}^-$ are concentrations of holes, ionized donors, electrons and ionized acceptors, respectively. As the samples are compensated p-type semiconductors in the freeze-out region over the whole temperature range studied, the donor atoms are completely ionized and there is very few electrons. This means n = 0 and $N_{\rm D}^+ = N_{\rm D}$. The hole concentration p at a given temperature is calculated by numerically solving the equation (2). The values of $N_{\rm A}$, $N_{\rm D}$ and the activation energy of the acceptors $E_{\rm A}$ are determined in such a way to obtain a best fit between the experimental and the calculated values of hole concentration in the whole temperature range studied.

The temperature dependence of hole mobility is analyzed with an iterative method (refs. 6,7), considering the scattering by ionized impurities, acoustic deformation potential and nonpolar optical phonons. The iterative method can correctly handle the inelasticity of the nonpolar optical phonon-scattering. The total concentration of ionized impurities N_i which contribute to the carrier scattering is,

$$N_{\rm i} = N_{\rm D}^+ + N_{\rm A}^- = 2N_{\rm D} + p. \tag{3}$$

For the hole concentration p in the equation (3), the best-fit data obtained in the hole concentration analyses are used. The acoustic deformation potential constant E_1 , the coupling constant of nonpolar optical phonons $D_{\rm npo}$ and the donor concentration $N_{\rm D}$ are used as fitting parameters to obtain a best fit between the experimental and the calculated values of hole mobility in the whole temperature range studied.

The Hall factor $\gamma_{\rm H}$ is assumed to be unity, thus, the hole concentration p and Hall mobility $\mu_{\rm H}$ are calculated from the relation, p = 1/eR and $\mu_{\rm H} = \sigma R$, where R is Hall coefficient.



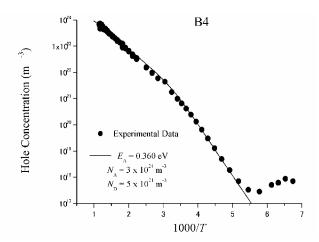


Figure 1. Hole concentration of B36 as a function of 10³/T.

Figure 2. Hole concentration of B4 as a function of $10^3/T$.

RESULTS AND DISCUSSION

The temperature dependence of the hole concentration and the Hall mobility are analyzed for the samples listed in table 1. The hole concentrations of B36 and B4 are illustrated as functions of 1000/T in Fig. 1 and Fig. 2, respectively. Closed circles represent the experimental values and solid lines are theoretical fitting curves calculated on the basis of the equation (2). For B36 which has the highest mobility in the samples studied in this work, the temperature dependence of p is well described by the simple model described above. A best fit between the experimental data and the theoretical values is obtained for $N_A = 3.0 \times 10^{23}$ m⁻³, $N_D = 8.0 \times 10^{20}$ m⁻³ and $E_A = 0.365$ eV. The hole concentration of B4 with the highest doping level (TMB 500 ppm) decreases along a best fit curve ($N_A = 3.0 \times 10^{24}$ m⁻³, $N_D = 5.0 \times 10^{21}$ m⁻³ and $E_A = 0.360$ eV) down to 190 K, but it increases with the decreasing temperature below 170 K. The results of analyses for all the samples are summarized in table 2. The values of E_A estimated from the p vs 1000/T graphs are about 0.365 eV, which are in good agreement with those in the literature. The estimated values of N_A and N_D range from 8×10^{22} m⁻³ to 3×10^{24} m⁻³ and from 8×10^{20} m⁻³ to 6×10^{21} m⁻³, respectively. The N_A values are compatible with those values from SIMS and C-V characteristic of a Schottky junction.(ref. 1). From the values of N_A and N_D the compensation ratios are calculated. The samples used in this work are found to be slightly compensated ($N_D/N_A = 0.1\% \sim 3\%$).

The hole mobilities of B36 and B4 are illustrated as functions of T in Fig. 3 and Fig. 4, respectively. Closed

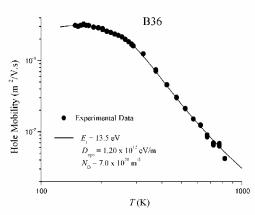


Figure 3. Temperature dependence of hole mobility in B36.

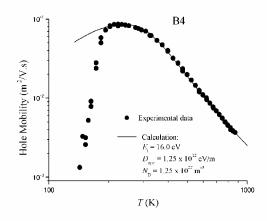


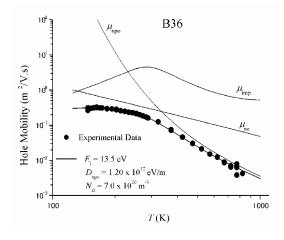
Figure 4. Temperature dependence of hole mobility in B4.

Table 2. Results of analyses.

Sample name	B1	B2	B4	B23	B36	B37	B42	B93
E_l (eV)	16.0	16.0	16.0	14.0	13.5	16.0	16.0	16.5
$D_{\rm npo} ({\rm x} \ 10^{12} {\rm eV/m})$	1.20	1.00	1.25	1.25	1.20	1.20	1.20	1.30
$N_{\rm D} ({\rm x} 10^{21} {\rm m}^{-3}) ({\rm from} \mu_{\rm H})$	1.50	2.00	12.5	5.50	0.70	2.00	25.0	2.50
$N_{\rm A} ({\rm x} 10^{23} {\rm m}^{-3})$	0.80	2.00	30.0	4.50	3.00	2.50	20.0	4.50
$N_{\rm D}$ (x 10 ²¹ m ⁻³) (from p)	2.50	2.50	5.00	6.00	0.80	1.00	3.00	6.00
$E_{\rm A}({ m eV})$	0.365	0.365	0.360	0.365	0.365	0.365	0.365	0.365

circles show the experimental values and solid lines represent theoretical fitting curves calculated with the iteration method. For B36 a best fit between experimental data and theoretical values is obtained when $E_1 = 13.5$ eV, $D_{npo} =$ 1.2×10^{12} eV/m and $N_D = 7 \times 10^{20}$ m⁻³ over the whole temperature range studied. There is little difference between the experimental values and the theoretical curve even at low temperatures. A best fit for B4 is obtained when $E_1 = 16.0$ eV, $D_{\rm npo} = 1.25 \times 10^{12}$ eV/m and $N_{\rm D} = 1.25 \times 10^{22}$ m⁻³ above 200 K. However, the experimental hole mobility is steeply reduced below 200 K and the difference between the experimental data and the fitting curve rapidly increases with decreasing temperature. Similar discrepancies in $\mu_{\rm H}$ values at low temperatures are seen in every other sample studied in this work except B36. The results of analyses for all the samples are collected in table 2. The estimated E_1 values ranges from 13.5 eV to 16.5 eV, which are comparable with the value of E_1 for a natural diamond, 14.5 eV(refs.. 4,8). The $D_{\rm npo}$ values are from 1.0×10^{12} eV/m to 1.3×10^{12} eV/m, which are about twice as large as that of the natural diamond (refs., 4,8). This discrepancy could be attributed to some scattering mechanisms particular to thin-film samples and/or the difference in the measurement method (Hall effect or time of flight). However, there is so far no reasonable interpretation for this problem. Figures 5 and 6 show the calculated hole mobilities for each scattering mechanism in B36 and B4, respectively. Solid circles indicate the experimental data. In B36 the hole mobility is controlled by the nonpolar optical phonon-scattering above 350 K and by the acoustic phonon scattering from 350 K to 130 K. The scattering by ionized impurities becomes dominant below 130 K. In B4 with the highest doping level, on the other hand, the ionized impurity scattering becomes predominant below 240 K. Below 200 K the temperature dependence of mobility can not be interpreted in terms of an ordinary band conduction model at all.

There are a couple of signs which suggest the contribution of impurity conduction at low temperatures: In all the samples except B36, a steep decrease in hole mobility is observed below 200 K and well defined peaks appear in the temperature dependence of Hall coefficients at low temperatures in a few samples. As seen from table 2, the values of N_D estimated from mobility data do not agree with those values from the hole concentration data. This could also be due to an influence of the impurity conduction.



 $D_{\text{npp}} = 1.25 \times 10^{12} \text{ eV/m}$ $N_{\text{D}} = 1.25 \times 10^{12} \text{ eV/m}$ $N_{\text{D}} = 1.25 \times 10^{12} \text{ m}^{3}$ μ_{imp} T(K)

B4

Experimental data

Figure 5. Calculated hole mobility of B36 for each scattering mechanism.

Figure 6. Calculated hole mobility of B4 for each scattering mechanism.

CONCLUSION

The electric conductivity and Hall effect have been measured from 150K to 900 K for eight samples of boron-doped homoepitaxial CVD diamond thin film. The hole concentration data were numerically analyzed on the basis of the single donor-single acceptor model and the condition of electric neutrality with fitting parameters of the acceptor concentration $N_{\rm A}$, the donor concentration $N_{\rm D}$, and the acceptor ionization energy $E_{\rm A}$. These analyses yields $E_{\rm A}$ values of about 0.365 eV, which is in good agreement with those in the literature. The temperature dependence of hole mobility was analyzed with an iterative technique assuming the scattering by ionized impurities, acoustic deformation potential and nonpolar optical phonons using the acoustic deformation potential constant $E_{\rm 1}$, the coupling constant of nonpolar optical phonons $D_{\rm npo}$ and the donor concentration $N_{\rm D}$ as fitting parameters. Best fits between the experimental and the theoretical values are obtained when $E_{\rm 1} = 13.5$ eV ~ 16.0 eV, and $D_{\rm npo} \sim 1.2 \times 10^{12}$ eV/m. The $E_{\rm 1}$ values are compatible with the value of 14.5 eV in a natural diamond, but the values of $D_{\rm npo}$ is about twice as large as that of the natural diamond. Some indications suggesting the impurity conduction are seen in most of the samples at low temperatures.

ACKNOWLEDGEMENT

We are grateful to Sadanori Yamanaka (Sumitomo Chemical company, Limited) for preparing the samples of CDV diamond thin film. We wish to thank Hiroshi Sakurada (AMANO Corporation) for his cooperation and support in this work.

REFERENCES

- 1. Yamanaka, S., et al.: High-Quality B-Doped Homoepitaxial Diamond Films using Trimethylboron. Jpn. J. Appl. Phys. Vol. 37, Part2, No. 10A, Oct. 1998, L1129.
- 2. Yamanaka, S., et al.: Low-Compensated Boron-Doped Homoepitaxial Diamond Films Using Trimethylboron. phys. stat. sol., vol. (a) 174, 1999, 59.
- 3. Isberg, J., et al.: High Carrier Mobility in Single-Crystal Plasma-Deposited Diamond. Science, Vol. 297, Sept. 2002, 1670.
- Tsukioka, K.: Scattering Mechanisms of Carriers in Natural Diamond. Jpn. J. Appl. Phys. Vol. 40, Part1, No.5A, May 2001, 3108.
- 5. Fong, C. Y. and Klein, B. M.: Diamond: Electronic Properties and Applications, eds. Pan, L. S. and Kania, D. R., Kluwer, Boston, MA, 1995, Chap. 1.
- 6. Rode, D. L.: Semiconductors and Semimetals. Academic, New York, NY, 1975, Vol. 10, Chap. 1.
- Nag, B. R.: Electron Transport in Compound Semiconductors. Springer-Verlag, Berlin, Heidelberg, 1980, 153 and 185.
- 8. Nava, F., et al.: Transport Properties of Natural Diamond Used as Nuclear Particle Detector for a Wide Temperature Range. IEEE Trans. Nucl. Sci. Vol. NS-26, No. 1, Feb. 1979, 308.

Electrical effect of vacuum-evaporated α-NPD on Oxygen-terminated Boron-doped

Chemical-Vapor-Deposited Homoepitaxial Diamond Films

Min-seung Chun, Tokuyuki Teraji and Toshimichi Ito

Department of Electrical Engineering, Graduate School of Engineering, Osaka University, 2-1 Yamada-oka, Suita, Osaka 565-0871, Japan

ABSTRACT

Electrical properties of chemical-vapor-deposited (CVD) homoepitaxial diamond layers, based upon Hall effect measurements in the temperature range from 100 K to 300 K, have been investigated when an organic material, N,N'-diphenyl-N,N'- bis(1-naphthyl)- 1,1'biphenyl- 4,4''diamine (α -NPD), was thermally deposited on them. In cases of O-terminated B-doped (p-type) diamond films with different carrier densities, substantial reductions in the electric conductivity due to hole density reductions were observed in the temperature range from 170 K to 200 K, where the Hall coefficients significantly changed. At temperatures higher than \approx 200 K, however, it is found that the sheet conductivity of the substrate diamond layer was increased after the α -NPD deposition to values larger than those measured before the α -NPD deposition. These results indicate that a substantial amount of holes can be transferred from the CVD diamond film to the overlayered α -NPD film when an appropriate interface was formed between the α -NPD and diamond films. The possibility will be discussed that CVD diamond films can be applicable as a transparent anode material and a hole transport material with a extremely high thermal conductivity and a strong chemical inertness for organic light-emitting diodes.

The corresponding author; Min-Seung Chun.

mschun@daiyan.pwr.eng.osaka-u.ac.jp Tel) +81-6-6879-7723 Fax) +81-6-6879-7704

Keywords: α-NPD, diamond, hall measurement, carrier concentration, Hall coefficient

M. Murakawa, M. Miyoshi, Y. Koga, L. Schäfer, and Y. Tzeng (Editors)

Preparation of Diamond Coated Electrodes and the Application to Wastewater

Treatment

XC He, XQ Yang, HS Shen, RB Li,YL Wang, JP Jia

State Key Lab of MMSM's

Dept. Of Materials Science

Shanghai Jiao Tong Univ., Shanghai 200030

Abstract

B-doped diamond coated electrodes were grown on silicon and graphite substrates respectively by hot

filament chemical vapor deposition (HFCVD) method. Detailed researches have been done to check out

the influence of the growth parameters on film structure, surface morphology as well as the electrical and

electrochemical properties of CVD diamond films. The textile wastewater treatment with diamond

electrodes had a remarkable execution.

The simulative and actual textile wastewater treatment with B-doped diamond coated electrodes on Si

substrate had a remarkable execution. After 2 hours, the COD of the simulative and actual wastewater was

reduced by 82.14% and 86.28% respectively. And the chromaticity color of the simulative and actual

wastewater was reduced by 99% and 60.45% respectively.

XC He

Professor

State Key Lab of MMCM's

Dept. of Materials Science

Shanghai Jiao Tong University

Shanghai, China 200030

Tel.: 86-21-62933163

FIELD EMISSION PROPERTIES OF DIAMOND PARTICLES: ELECTRON INJECTION INTO THE CONDUCTION BAND BY TUNNELING AT THIN INSULATING INTERFACE LAYER

Akihiko Watanabe A) and Makoto Kitabatake A), B)

A) Frontier Carbon Technology Project/JFCC,
Center for Advanced Research Projects, 6F, Osaka University, 2-1 Yamada-oka, Suita, Osaka, 565-0871, Japan
E-mail: nave@cam.hi-ho.ne.jp
B) Advanced Technology Research Laboratories, Matsushita Electric Industrial Co., Ltd.,
Hikaridai 3-4, Seika, Soraku, Kyoto, 619-0237, Japan

ABSTRACT

Mechanisms of the field emission from diamond particles (DP) with an insulating layer between the DP and the electrode was studied. The SiO_2 thin layer was formed on metal substrate, and then the DPs were dispersed by the spin-coat technique. The chemical vapor deposited diamond films were formed on the DP to obtain well-defined DP surfaces. Energy positions of Fermi level (E_F), valence band maximum (E_{VBM}) and conduction band minimum (E_{CBM}) of the DP surface were measured by ultraviolet photoemission spectroscopy (UPS). UPS spectra suggested that the surface of these specimens exhibited negative electron affinity (NEA). The field emission electron spectroscopy (FEES) spectra were measured using a stainless-steel grid electrode placed <1mm above the specimen with an extraction voltage (V_{ex}). The FEES spectra exhibit peaks, which show energy shift (V_s) toward the lower energy below E_F with increasing V_{ex} . V_s is considered to be derived by the field enhancement at the insulating layer. Intensity of the field emission current (I_{fe}) shows close relation with the V_s . The linearity of the Fowler-Nordheim (F-N) plot between I_{fe} and V_s was observed while the relationship between I_{fe} and V_{ex} show ambiguous characteristics. These results suggest that the field emission from the DP is mainly affected by field enhancement at insulating layer (between the DP and the electrode) rather than that at diamond surface (between the DP and vacuum).

This work was supported by the FCT Project, which was consigned to JFCC by NEDO.

Keywords: Diamond, Field emission, Negative electron affinity, Electron spectroscopy, Electron injection.

EXPERIMENTAL COMPARISON OF DIAMOND COATED ELECTRODE WITH RELATED MATERIALS IN ATMOSPHERIC BIPOLAR CORONA DISCHARGE

Tetsuya Akitsu and Kayoko Iwamura

University of Yamanashi, Department of Electrical Engineering, Takeda 4-chome 3-11 Kofu Yamanashi 400-8511 Japan

Akimitsu Hatta

Kochi University of Technology, Department of Electronics Tosa-yamada, Koumi-gun, Kochi 782-8502 Japan

Shuji Takaishi

YGK Corporation, Kuruwada, Kushigata-chou Nakakoma-gun Yamanashi 400-0311 Japan

ABSTRACT

The plasma CVD diamond coating on tungsten needles have been studied aiming an application in the static charge eliminator, using the bipolar corona discharge at the atmospheric pressure. The surface of the tungsten needle was coated by diamond coating and ion emission, the neutralization time as well as the long term stability of the ion emission have been examined.

Keywords: Diamond coating, Plasma CVD, Bipolar corona discharge, Atmospheric plasma

INTRODUCTION

ESD (electrostatic discharge) is a significant cause of precise electronic device failures at all stages of production and field use. Much effort has been expended toward developing treatment for materials to speed up charge recombination. Most of commercial ionizers depend upon electrical corona to produce bipolar ionization. The corona discharge is a type of discharge phenomenon driven by the localized self breakdown in the vicinity of the high voltage induced electrodes, in wire or needle shape made of metallic materials such as Nickel-Chromium and Tungsten. In the AC corona devices, the discharge is driven with alternating potential at line frequency, 50 Hz or with a train of positive and negative pulse through a capacitor. In the Double DC ionizers, in continuously operating DC corona of each polarity also use sharp edge of metallic electrode to initiate atmospheric discharge.

Most static charge elimination is performed in the open-air environment. The problem is that the sharp needle of bare tungsten will be rounded in time because of erosion by the oxidation. In the present work, we developed diamond-coated tungsten needle electrodes using the microwave plasma CVD. The performance of static charge elimination and the discharge characteristics were compared in an asymmetric gap between needles and grounded grid and wall. It is very interesting how the negative electron affinity works in the atmospheric corona discharge. Diamond has the largest thermal conductivity among the available industrial materials. Thus, thin layer of diamond releases the Joule or electron bombardment heating localized in the vicinity of the tip. Thus, the diamond coating can protects the material keeping the temperature below the threshold of the oxidation or not?

EXPERIMENTAL APPARATUS

The Atmospheric bipolar corona discharge

The bipolar ionization in the AC corona can produce the automatic balance between the positive and negative ions, better performance of the static eliminator. On the other hand, the amount of positive and negative ions should be precisely balanced. In the open air, positive ions are formed by stripping electrons from atomic and molecular species, such as H^+ and negative ions by electron attachment, such as O_2^- .in gases containing oxygen, carbon dioxide and water vapor

In Fig. 1, one can find the schematic capture of the apparatus, the AC corona static charge eliminator consists of one or plural arrays of asymmetric gaps between needle and ground plane excited with alternating high voltage, at the line frequency.

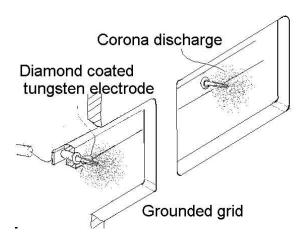


Figure 1 Asymmetric needle to plane electrode used in the experiment.

Plasma CVD growth of diamond crystals on tungsten needles

The thin diamond crystal was grown on the surface of tungsten needles in plasma. In Fig. 2, one can find SEM images showing nucleation of diamond crystals along the scratch on the tungsten needles, (a) the growth of diamond crystals comprising in arrays along the scratch on the lateral surface of the needle, (b) similar textures observed at the tip. In Fig 2, (c) one can find high density and in (d) rather sparse growth of diamond particles. The unintentional variation of the scratch pattern possibly influences the discharge characteristics of each needle. The effect should be review in the future experiment .

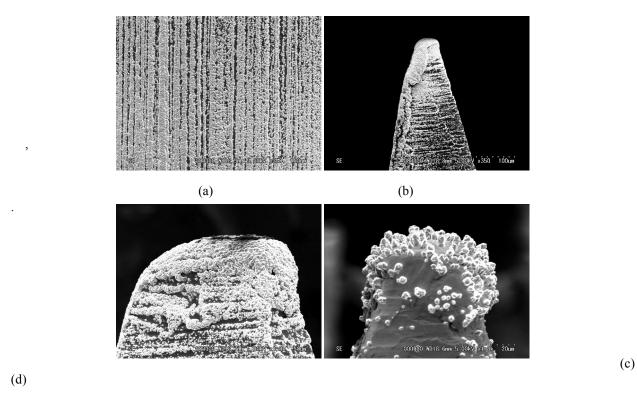


Figure 2. Typical examples for the diamond crystals observed on the tungsten needles.
(a) The lateral surface of a needle showing the nucleation of diamond crystals along the scratch formed during the lapping, (b) the tip of a needle also showing the diamond crystals nucleation along the trace of scratch, (c) high density and (d) rather sparse growth of diamond crystals on the tip.

The plasma CVD deposition was carried out by ASTEX, AX-6300 Plasma CVD device excited by microwave, 2.45GHz, 1kW, in hydrogen 95sccm, methane 4sccm, oxygen 1sccm mixture, at the total pressure 6.6kPa. one hour deposition time. The tip of the tungsten needles, 0.6 m in diameter and 8 mm in length average, was sharpened at an angle of 10 degrees or sharper. The needles were supported using an instrument made of aluminum disc; 50 mm in diameter, with 52 holes separated in equal distances each other. Small spring was inserted into each hole to fix the end of needles. Tungsten needles were fixed just like a pincushion with the sharpened tip facing the plasma. The present deposition condition was lower than the normal operational conditions of the device, 15 kPa and 5 kW microwave power. because the tungsten needles melted in the full operational conditions.

EXPERIMENTAL RESLTS

The bipolar ion emission and the performance of the static elimination

The efficiency of the bipolar ion emission was measured with an ion counter settled 30 cm apart facing the neutralizer. Figure 3 shows the dependence of the positive and negative ion emission as functions of the excitation voltage. The ion current was compared between two diamond coated tungsten electrodes and four uncoated tungsten electrodes giving comparable ion flux, as shown in Fig. 3. The horizontal axis of Figure 3 shows the RMS voltage measured at the primary windings of the high voltage transformer. The full scale 100 % stands for 4,200 V RMS. One can observe gradual rise of the ion flux at 60 to 70 %. Figure 4 shows the variation of neutralization time as functions of the primary voltage. The neutralization time is determined as the duration of time needed for the decay of the voltage of the static charge stored by an electrode facing the ion flux. One can find that the neutralization time becomes shorter when the ion flux is supplied by the neutralizer, at certain voltage.

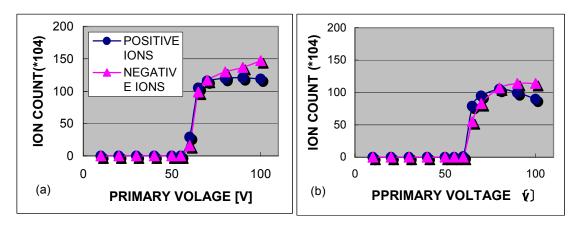


Figure 3 Variation of the bipolar ions emission as functions of the excitation voltage.

(a) Diamond-coated tungsten electrodes and (b) uncoated tungsten needles.

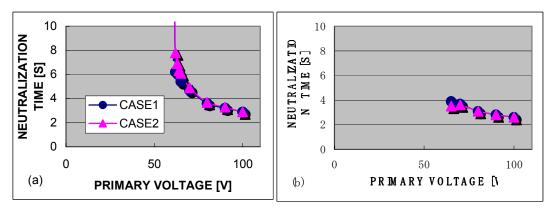


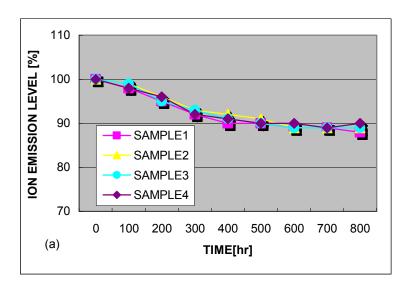
Figure 4 Variation of the charge neutralization time as functions of the excitation voltage.

(a) Diamond-coated tungsten needles and (b) uncoated tungsten needles,

The life time of the electrode: the long term decay of the bipolar ion flux

The ion current was monitored in continuous DC discharge at higher discharge current called streamer region. Figure 5 shows the long term observation of the ion emission level. In Fig. 5 (a), the diamond coated tungsten electrodes, one can find that the decay rate of the ion emission saturates at 90 % of the initial emission level. In Fig. 5(b), the ion emission level of uncoated tungsten electrodes continues to decay.

The result of the present experiment clearly indicated that the diamond coating is capable to extend the life time of bipolar corona electrodes in the atmospheric environment.



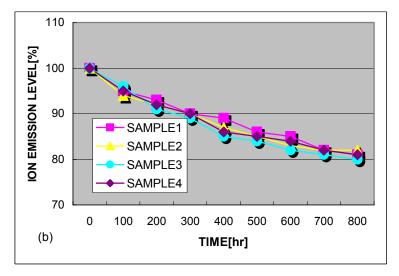


Figure 5 Long term decay of the bipolar ion emission
(a) Diamond-coated tungsten needles and (b) Uncoated tungsten.

CONCLUSION

The corona discharge can produce amount of bipolar ion flux sufficient for the static charge eliminator meeting the industrial standard, without generating heat or reactive species that corrodes the surface of the work pieces. The result of the present research showed that the diamond coating successfully extended the life time and the capacity of the electrode in atmospheric discharges and decrease in the amount of contamination produced by the static charge eliminator.

MICROWAVE POWER PERFORMANCE OF DIAMOND SURFACE-CHANNEL FETS USING HIGH-QUALITY HOMOEPITAXIAL LAYERS

M. Kasu^{1,2}, M. Kubovic¹, A. Aleksov¹, I. Kallfass¹, U. Spitzberg¹, N. Kobayashi², T. Makimoto², H. Schumacher¹, and E. Kohn¹

¹ Department of Electron Devices and Circuits, University of Ulm Albert-Einstein Allee 45, D-89081 Ulm, Germany <u>kasu@nttbrl.jp</u>

² NTT Basic Research Laboratories, NTT Corporation 3-1 Morinosato-Wakamiya, Atsugi, 243-0198, Japan

ABSTRACT

High-quality homoepitaxial diamond layers were used to fabricate surface-channel short-gate FETs. RF measurements of FETs with 0.2- μ m-long gate yielded f_T of 20 GHz, f_{maxMAG} of 50 GHz, f_{maxU} of 58 GHz. FETs with 0.4- μ m-long gate exhibited a maximum output power level (P_{out}) at 1 GHz of 0.35 W/mm.

Keywords: homoepitaxial layer, CVD, H-termination, FET.

INTRODUCTION

Diamond intrinsically exhibits a high carrier saturation velocity (1x10⁷ cm/s), high electric breakdown field (>10 MV/cm), and high thermal conductivity (20 W/cm K). These properties promise high performance high speed / high power devices (ref. 1). High microwave performance of surface-channel MES field-effect transistors (FETs) and MIS FETs has been reported (ref. 2,3). In their FET fabrication, H surface termination was used as a p-type doping method (ref. 4). Recently Kasu and Kobayashi reported high quality homoepitaxial diamond layers (ref. 5). The high quality of our layers was shown by free exciton luminescence at room temperature (RT) and very narrow diamond-related Raman peak. In this presentation, we report on microwave power performance of surface-channel FETs using the high quality diamond layers.

EXPERIMENTAL

Homoepitaxial diamond layers were grown on high-pressure, high-temperature (HPHT)-synthesized Ib-type diamond (001) substrates (size: $3x3x0.5 \text{ mm}^3$) by microwave plasma chemical vapor deposition (CVD). The details of the growth procedure were reported previously (ref. 5). After the growth the surface was exposed again to the H plasma to ensure the hole conduction on the H-termination. In secondary ion-mass spectroscopy (SIMS), the H, B, N concentrations inside the layer were below the background concentration. In Raman measurements, the full width at half maximum (FWHM) of a diamond-related peak (1332 cm⁻¹) was as low as 2.35 cm⁻¹ (ref. 5).

Figure 1 shows schematic illustration of FET structure. The H-terminated surface exhibits the p-type conduction and is used as a p-type conductive layer. For the isolation between devices, the H-terminated surface was oxidized, because on the oxidized surface, surface Fermi level pins at 1.7 eV above the valence band. The ohmic contacts as a source and a drain were formed using Au evaporation on the H-terminated surface. The Schottky contact as a gate was formed using Al evaporation on the H-terminated surface. The Schottky barrier height is approximately 0.8 eV. The submicron long T-shaped gates (gate length; L_G =0.2 to 0.8 μ m) were formed using a three-layer resist, electron-beam lithography, lift-off, and evaporation. The gate width, W_G , was changed from 25 to 200 μ m. The details of FET fabrication were reported previously (ref. 2).

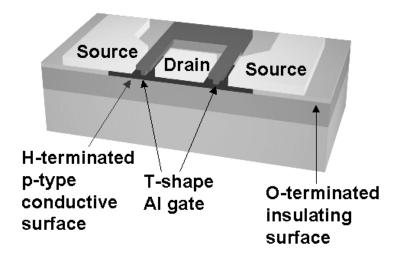


Figure 1. Schematic illustration of diamond surface-channel straight-gate-type FET.

RESULTS AND DISCUSSIONS

DC characteristics

Figure 2 shows DC output characteristics and transfer characteristics (L_G =0.2 μm and W_G = 200 μm). From the transport characteristics of this device at V_G =-8V, we extrapolated the maximum transconductance (g_m) of 100 mS/mm.

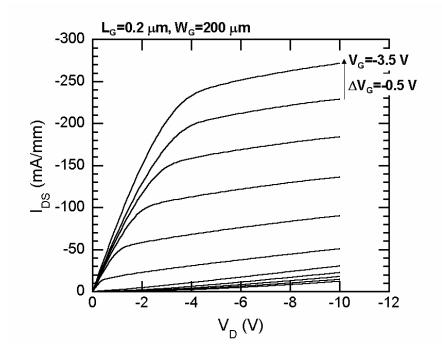


Figure. 2. DC characteristics.

RF characteristics

Figure 3 shows the frequency dependence of h_{21} , maximum available gain (MAG), and Mason's unilateral gain (U) at V_G =-0.3 V and V_D =-10 V. They yielded f_T =20 GHz, f_{maxMAG} =50 GHz, and f_{maxU} =58 GHz. These f_T , f_{maxMAG} and f_{maxU} values are the highest values in diamond electronic devices at present.

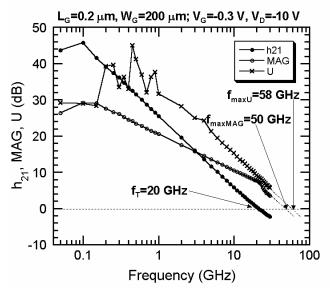


Figure 3. Frequency dependence of h_{21} , MAG, U at V_G =-0.3 V, V_D =-10 V and extracted values for f_T (20 GHz), f_{maxMAG} (50 GHz), and f_{maxU} (58 GHz).

RF power characteristics

Figure 4 shows RF power characteristics (L_G = 0.4 μ m, W_G = 550 μ m). The condition is that V_D = -20 V, V_G = -2 V, and the frequency was 1 GHz. The gain was constant at 13 dB in the range Pin< 0 dBm. The maximum power reached 0.35 W/mm. This value is higher than one previously reported of 0.2 W/mm. This measured maximum power value is still limited by impedance mismatch between the device output and the measurement system.

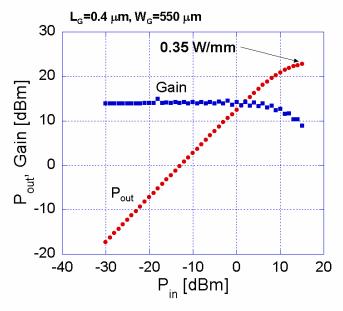


Figure 4. Output power, P_{out} (dBm) and gain (dB) as a function of input power, P_{in} (dBm), for the 0.2 μ m-gate FET of sample B (a class-A bias point: V_D =-20 V and V_G =-2 V at 1 GHz). The maximum P_{out} is 0.35 W/mm.

CONCLUSIONS

The s parameter measurements resulted in cut-off frequencies of the 0.2 μm gate length device of f_T =20 GHz, $f_{max}(MAG)$ =50 GHz and $f_{max}(U)$ =58 GHz are the highest values for diamond FETs. The output power of 0.35 W/mm was still limited by the load impedance in the measurements.

ACKNOWLEGEMENT

One of the authors (MK) expresses many thanks to Drs. Yoshiro Hirayama, and Sunao Ishihara (NTT) for their encouragement and support. MK thanks Drs. Wolfgang Ebert and Andrej Denisenko (University of Ulm) for fruitful discussions.

REFERENCES

- Kohn, E.; Ebert, W.: Low-Pressure Synthetic Diamond, Manufacturing and Applications, Springer, Berlin, 1998, 331.
- 2. Aleksov, A., et al.: Microwave Performance of Diamond Surface-Channel FETs, IEEE Electron Device Lett., vol. 23, 2002, 483.
- 3. Umezawa, H., et al.: RF Performance of Diamond MISFETs, IEEE Electron Device Lett. vol. 23, 2002, 121.
- 4. Kawarada, H., et al.: Characterization of Hydrogen-Terminated CVD Diamond Surfaces and Their Contact Properties, Diamond and Related Materials, vol. 3, 1994, 961.
- 5. Kasu, M.; Kobayashi, N.: High Mobility and High Crystalline-Quality Chemical-Vapor-Deposition Grown Homoepitaxial Diamond, to be published in Diamond and Related Materials, 2003.

CHARACTERIZATION OF THE CONTACT LAYER FORMED BY AR ION IMPLANTATION INTO HOMOEPITAXIAL DIAMOND FILM

H. Yoshida¹, M. Suzuki^{1, 2}, N. Sakuma^{1, 2} and T. Sakai^{1, 2}

¹FCT project / JFCC, FCT Lab., Tsukuba Central 5, 1-1-1 Higashi, Tsukuba, Ibaraki, 305-8565, Japan ²Advanced Discrete Semiconductor Technology Lab., Toshiba Corp. 1, Komukai Toshiba-cho, Saiwai-ku, Kawasaki, 212-8582, Japan

e-mail: hiro-yoshida@aist.go.jp

³M. Ogura, K. Yamamoto H. Okushi

³Research Center for Advanced Carbon Materials, AIST Tsukuba Central 5, Tsukuba 305-8565, Japan

ABSTRACT

In this study, we characterized the contact layer formed by Ar ion implantation into homoepitaxial diamond films by applying X-ray photoelectron spectroscopy (XPS), and determined specific contact resistances between the layers and pad metal by the transmission line model (TLM) techniques for the first time. The resulting specific contact resistance value of 10⁻⁴ohm cm² indicates capability of the layer as a practical device contact.

The diamond thin film was grown homoepitaxially on high-pressure and high-temperature (HPHT) synthetic Ib diamond (100) substrate by microwave-plasma CVD method. 40keV Ar ions were irradiated at doses of 1×10^{14} , 1×10^{15} and 1×10^{16} ions/cm² under room-temperature. Then, Au/Pt/Ti were evaporated and patterned to make the TLM metal pads. The resulting contact resistances showed a strong dependence on the amount of Ar dose even at the higher dose region. The lowest contact resistance value of 10^{-4} ohm cm² was obtained in the case of 1×10^{16} ions/cm² doses after $400\Box$ annealing in nitrogen atmosphere.

Farther, applying this metal / ion implanted layer structure as an ohmic contact, planer type Schottky barrier diodes were fabricated on high homo-epitaxial diamond films. Their current - voltage characteristics especially at a high temperature are also introduced and discussed.

ACKNOWREDGEMENT

This work was supported by the Frontier Carbon Technology (FCT) project that was consigned to the Japan Fine Ceramics Center by NEDO.

Keywords: Diamond properties & applications, Ion implantation, Contact layer, Ohmic contact

ELECTRICAL PROPERTIES OF DOPED AND UNDOPED HOMOEPITAXIAL DIAMOND LAYERS GROWN BY MICROWAVE PLASMA CVD

Suzuki Mariko

FCT/JFCC, Toshiba Corporation

mariko.suzuki@toshiba.co.jp

Hiroaki Yoshida

FCT/JFCC

Naoshi Sakuma, Tomio Ono, Tadashi Sakai

FCT/JFCC, Toshiba Corporation

Masahiko Ogura, Hideyo Okushi

AIST

Abstract

The electrical properties of homoepitaxial diamond layers have been investigated by I-V, C-V and frequency-dependent capacitance measurements. Undoped and B-doped diamond layers were grown by microwave plasma CVD on Ib (100) diamond substrates. Lateral Schottky barrier diodes were fabricated on these diamond layers. Individual Schottky contact (Au/Ni dot electrode) was surrounded by the ohmic contact (Au/Pt/Ti) with 20um gap. The contact pads have three kinds of area, which were 7.5×10-4cm2, 3.4×10-4cm2 and 2.0×10-4cm2, respectively. The ohmic contact area was greater than 150 times that of the largest dot. B, N, H, and O concentrations were determined by SIMS measurements.

The ideality factor n and barrier height for the Schottky junctions were typically found to be in 1.2~1.3 and to be ~1.1eV, respectively, from the results of I-V measurements. The results of frequency-dependent capacitance measurements, with a frequency ranging from 10 Hz to 1 MHz, have shown the well-known dispersion effect, which occurs when a deep level is unable to follow the high-frequency voltage modulation and contribute to the net space charge in the depletion region. Net acceptor concentrations in the B-doped diamond layers were found to be 1-6×1017cm-3. The correlation between net acceptor concentration and B concentration was revealed.

OPTICAL AND ELECTRIC PROPERTIES OF (111)-ORIENTED DIAMOND HOMOEPITAXIAL LAYER

M. Kasu^{1,2}, A. Aleksov², N. Teofilov³, M. Kubovic², Y. Taniyasu¹, R. Sauer³, E. Kohn², T. Makimoto¹, and N. Kobayashi¹

NTT Basic Research Laboratories, NTT Corporation
 3-1 Morinosato-Wakamiya, Atsugi, 243-0198, Japan <u>kasu@nttbrl.jp</u>

² Department of Electron Devices and Circuits, University of Ulm Albert-Einstein Allee 45, D-89081 Ulm, Germany

³ Department of Semiconductor Physics, University of Ulm Albert-Einstein Allee 45, D-89081 Ulm, Germany

ABSTRACT

We have obtained high-quality (111)-oriented homoepitaxial layers with a low density of stacking faults. From the (111)-oriented layers, we observed well-resolved free-exciton transitions in cathodoluminescence at 13 K. In Raman scattering spectrum the line width of diamond-related peak was as low as 1.9 cm⁻¹. A field-effect transistor with an 11 µm-long gate exhibited maximum normalized current of 24 mA/mm.

Keywords: homoepitaxial layer, CVD, cathodoluminescence, Raman, FET.

INTRODUCTION

High performance of high-frequency high-power electronic devices using diamond is expected (ref. 1), diamond exhibits intrinsically a high hole saturation velocity $(1x10^7 \text{ cm/s})$, a high electric breakdown field (>10 MV/cm), and a high thermal conductivity (20 W/cmK) (ref. 2). Recently, Kasu and Kobayashi obtained (001)-oriented homoepitaxial diamond layers of high quality by decreasing the unepitaxial-crystalline density (ref. 3). Using these layers, we fabricated metal-semiconductor (MES) field-effect transistors (FETs) that exhibited high performance of radio-frequency (RF) characteristics (transit frequency, f_T , of 20 GHz and maximum frequency of oscillation via the maximum available gain, f_{maxMAG} , of 50 GHz) (ref. 4).

Most of reports on chemical-vapor-deposition (CVD) growth of homoepitaxial diamond layers use (001) orientation (refs. 3,5). However, there are only few on the (111) orientation (refs. 6,7), because (111)-oriented homoepitaxial layers have many stacking faults compared with (001)-oriented layers and that (111)-oriented highly crystalline layers are much more difficult to grow (ref. 7). Recently, we clarified the formation mechanism of stacking faults in (111)-oriented homoepitaxial layers (ref. 8). We found that the surface with a higher density of stacking faults exhibits a lower conductivity and obtained high quality homoepitaxial layer with a low density of stacking faults.

In this presentation, we describe electrical and optical properties of (111)-oriented homoepitaxial diamond layers of high quality. From these layers, we observed well-resolved free-exciton transitions in cathodoluminescence (CL), and a sharp peak in Raman scattering. Using the layers, we fabricated FETs for the first time using (111)-orientation.

EXPERIMENTAL

The (111)-orientated homoepitaxial diamond layers were grown on (111)-oriented HPHT Ib-type diamond substrates (2.5 x 2.5 x 0.5 mm³) by microwave plasma CVD. The homoepitaxial layers were undoped. As-grown surfaces were terminated with H atoms and exhibited surface hole conduction (ref. 9). The microwave power and frequency were 1.3 kW and 2.54 GHz, respectively. The sources were highly pure (6N) CH₄ gas and purified (better

NASA/CP—2003-212319 165 August 18, 2003

than 6N) H_2 . The flow rates were 3 and 300 sccm, respectively. The typical growth temperature was 660° C. The growth rate at a growth temperature of 660° C was 0.13 μ m/h.

In Raman measurements, the excitation wavelength was 532.23 nm. The excitation light was focused onto the surface to obtain information for the homoepitaxial layer near the surface only. The spectra were taken across the entire surface. For CL measurements, the sample was mounted in a cold Cu finger of a continuous flow liquid He cryostat and was excited by electrons of 6-keV energy. The luminescence signals were dispersed by a monochromator (1-m focal length, grating with 1200 lines/mm blazed at λ = 250 nm) and detected by a liquid-nitrogen-cooled ultraviolet charge-coupled device optimized for 200-nm wavelength. In Hall-effect measurements, the hole sheet concentration and mobility of the H-terminated layers were measured at room temperature (RT) in air at a magnetic field of 0.324 T using a van-der-Pauw geometry. The polarity of the Hall coefficient invariably exhibited p-type conduction. The FET fabrication process was the same as in our previous report (ref. 4) except for the gate formation. The Al gate was formed by optical lithography.

RESULTS AND DISCUSSION

Raman measurements

Figure 1 shows Raman spectra of a 1.5-µm-thick diamond homoepitaxial layer grown at 687° C. There is a very sharp diamond-related peak, which is related to the sp³-hybridized C, at 1332 cm⁻¹. The full-width at half maximum (FWHM) of the peak is as low as 1.90 cm⁻¹, as shown in Fig. 1(b). This FWHM value is lower than both our lowest FWHM value for (001)-oriented layers, 2.35 cm⁻¹ (ref. 3), and the value for natural diamond, 2.0 cm⁻¹ (ref. 10). The FWHM value corresponds to the degree of atomic ordering of the sp³-hybridized C on the atomic scale. The growth condition for the sharp Raman peak is different from that used to obtain a low density of stacking faults. On (111)-oriented layers, there are more stacking faults, which relax the residual strain induced by a HPHT substrate, than on (001)-oriented layers. Furthermore, similar to the spectrum of the (001)-oriented layer which we had obtained previously (ref. 3), the spectrum for the (111)-oriented layer shows no features of a graphite phase (around 1500 cm⁻¹) and no luminescence of the neutral N-vacancy complexes (around 2100 cm⁻¹, corresponding to the photon energy of 575 nm). This indicates no residual N in the layer.

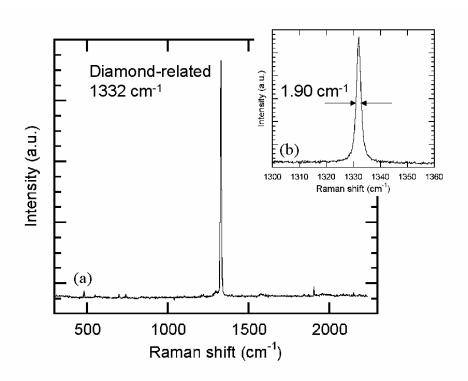


Figure 1. Raman spectra of a (111)-oriented homoepitaxial diamond layer.

Cathodoluminescence

Figure 2 shows a CL spectrum of a (111)-oriented homoepitaxial layer taken at 13 K. The sample was grown at 650° C and the homoepitaxial layer thickness was 6.2 μ m. One can clearly see a strong transverse-optical (TO)-phonon assisted free exciton (FE) recombination line at a photon energy of 5.275 eV (235.0 nm) and well-resolved transverse-optical plus zone center optical (TO+O^{Γ})- and transverse-acoustic (TA)-phonon assisted FE transitions at the positions known from the literature. This is the first time that well-resolved FE transitions have been observed in (111)-oriented homoepitaxial layers. The observation of well-resolved FE transitions proves that the carrier lifetime is long enough for the carriers to recombine radiatively in the high-quality layer. Further, we observed boron-bound exciton (BE) recombinations as the TO- and $(TO+O^{\Gamma})$ -phonon assisted transitions, although a boron source was never used in our growth system. Thus, at present, the origin of the residual boron is not clear.

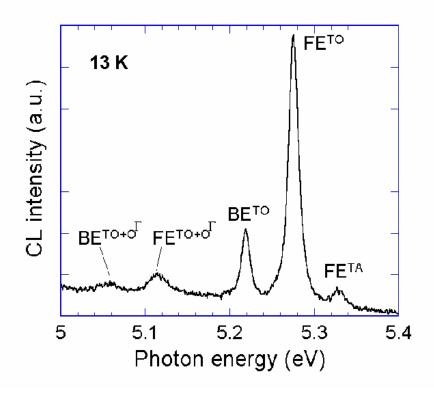


Figure 2. CL spectrum of a (111)-oriented homoepitaxial layer at 13 K.

Hall measurements

Figure 3 shows the hole mobility and sheet concentration measured in air at RT for different growth temperatures. The thickness was fixed to about 1 μ m. The holes are generated by the H surface termination (ref. 9). The surface conductivity due to the H-termination was estimated to be approximately $5x10^2$ times higher than the bulk conductivity due to the residual impurities in the layer. Therefore, the measured mobility and the conductivity originated from the surface conductivity due to the H-termination. In the figure, for samples whose resistivity was too high to be measured, mobility and conductivity were assumed to be zero. As the growth temperature increased, both mobility and sheet concentration decreased. One possible reason for this is that the stacking-fault density increased as the growth temperature increased. As we will report elsewhere (ref. 8), we found that the surface conductivity in regions with stacking faults is lower than in the other regions. Therefore, we expected that stacking faults in the layer are responsible for the degradation in surface conductivity. At the growth temperature of 660° C, we obtained a layer with the minimum stacking-fault density, and its mobility reached 74 cm²/Vs at a surface hole sheet concentration of $1.7x10^{13}$ cm².

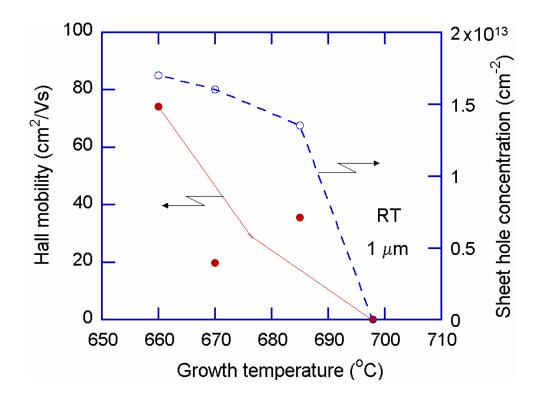


Figure 3. Hall mobility and sheet hole concentration at RT for various growth temperatures.

The holes are generated by H termination.

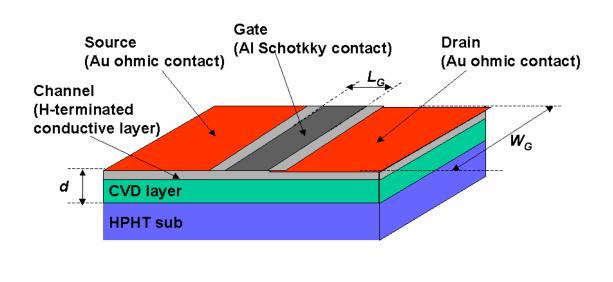


Figure 4. MES FET structure.

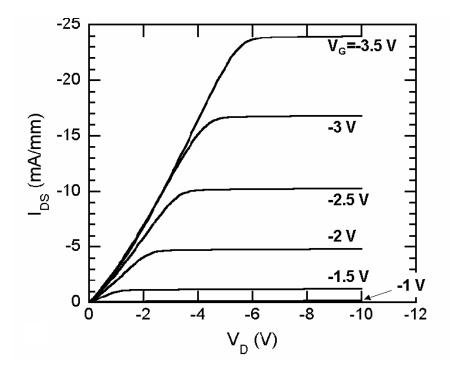


Figure 5. Output characteristics of a MES FET (L_G ; 11 μ m, W_G ; 100 μ m) using a (111)-oriented layer. The maximum normalized current is 24 mA/mm and the maximum transconductance, g_m , is 14 mS/mm.

Characteristics of FET

Using a (111)-oriented high-crystalline-quality layer with 0.5- μ m thickness, we fabricated a MES FET structure (Fig. 4). The surface conductance of the channel was controlled by an Al Schottky gate. The gate length (L_G) was 11 μ m and the width (W_G) was 100 μ m.

Figure 5 shows its output characteristics, i.e., the normalized drain-source current, I_{DS} , as a function of the drain voltage, V_D , for different gate voltages, V_G . The drain saturation current seems almost constant in a wide drain voltage range. There were neither gate-current leakage nor drain-current leakage. The maximum normalized current was 24 mA/mm. The maximum transconductance, g_m , was 14 mS/mm. At the same gate length, these values are comparable with those obtained for (001)-oriented diamond layers.

CONCLUSIONS

We have obtained a (111)-oriented high-quality diamond homoepitaxial layer by decreasing the stacking fault density. We observed well-resolved free-exciton transitions in low-temperature cathodoluminescence, and a sharp diamond Raman-peak (linewidth; 1.9 cm⁻¹). The surface exhibited a maximum mobility of 74 cm²/(Vs) at a sheet concentration of 1.7x10¹³ cm⁻³ at room temperature. A field-effect transistor with a 11-µm-long gate exhibited a maximum normalized current of 24 mA/mm. These results confirm that the crystalline quality of the (111)-oriented layers is approaching that of (001)-oriented layers.

ACKNOWLEGEMENT

One of the authors (MK) expresses many thanks to Drs. Yoshiro Hirayama and Sunao Ishihara (NTT) for their encouragement and support. MK thanks Gako Araki, Seiichiro Mizuno, Akio Takano (NTT Advanced Technology) for measurements, and Drs. Wolfgang Ebert and Andrej Denisenko (University of Ulm) for fruitful discussions.

REFERENCES

- 1. Kohn, E.; Ebert, W.: Low-Pressure Synthetic Diamond, Manufacturing and Applications, Springer, Berlin, 1998, 331.
- Dreifus, D.L.; Fox, B.A.: Handbook of Industrial Diamonds and Diamond Films, Marcel Dekker Inc., New York, 1998, 1043.
- 3. Kasu, M.; Kobayashi, N.: High Mobility and High Crystalline-Quality Chemical-Vapor-Deposition Grown Homoepitaxial Diamond, to be published in Diamond and Related Materials, 2003.
- 4. Kasu, M., et al.: Microwave Power Performance of Diamond Surface-Channel FETs using High-Quality Homoepitaxial Layers, Proceedings 7th Applied Diamond Conference.
- 5. For example, Watanabe, H., et al.: Homoepitaxial Diamond Film with an Atomically Flat Surface Over a Large Area, Diamond and Related Materials, vol. 8, 1999, 1272.
- 6. Koizumi, S., et al.: Growth and Characterization of Phosphorous Doped {111} Homoepitaxial Diamond Thin Films, Appl. Phys. Lett., vol. 71, 1997, 1065.
- 7. Sakaguchi, I., et al.: Homoepitaxial Growth and Hydrogen Incorporation on the Chemical Vapor Deosited (111) Diamond, J. Appl. Phys., vol. 86, 1999, 1306.
- 8. Kasu, M., et al.: Atomic Model of Stacking Faults with Microtwins in (111)-Oriented Homoepitaxial Diamond Layer Grown by Chemical Vapor Deposition, to be published elsewhere.
- 9. Kawarada, H., et al.: Characterization of Hydrogen-Terminated CVD Diamond Surfaces and Their Contact Properties, Diamond and Related Materials, vol. 3, 1994, 961.
- 10. Bachmann, P. K.; Wiechert, D. U.: Optical Characterization of Diamond, Diamond and Related Materials, vol. 1, 1992, 422.

PROPERTIES AND APPLICATIONS OF DIAMOND

Characterization and Applications of Single Crystal CVD Diamond

Patrick J. Doering

Apollo Diamond, Inc.
PO Box 328, Sherborn, MA 01770 USA doeringp@apollodiamond.com

ABSTRACT

Recent developments in growth of single crystal diamond by the CVD process has shown that this technique is capable of producing diamond with the highest purity and crystalline perfection on a consistent basis. Further, CVD can produce large single crystals in a cost effective manner. In addition, the CVD technique is suitable for introduction of dopant impurities into the diamond in a controlled manner. This combination of properties indicate that single crystal CVD diamond will enable advanced applications of diamond in the areas of optics and microelectronics, as well as in some of the more traditional applications of diamond. Recent progress in single crystal CVD diamond technology has demonstrated diamond with properties meeting or exceeding the theoretical promise which diamond has presented for the past several decades. In this presentation, we will discuss some of the demonstrated properties of single crystal CVD diamond as well as some of the applications which these properties enable, including new technology areas such as quantum computing.

Keywords: CVD Diamond, Single Crystal Diamond, Semiconductors, Optics

DIAMOND FIELD EFFECT TRANSISTORS FOR MICROWAVE DEVICES AND BIOSENSING APPLICATIONS

H.Kawarada, H.Umezawa, S.Miyamoto, H.Matsudaira, and K-S.Song

School of Science and Engineering, Waseda University, Shinjuku-ku, Tokyo 169-8555, Japan CREST, Japan Science and Technology Cooperation

ABSTRACT

Due to its extreme properties, diamond is expected to be the ultimate semiconductor device. However, its progress as an active device has been slow because there has been no doping technology developed to realize its high electrical conductance. We focused on a highly conductive p-type layer appearing on a hydrogen terminated diamond surface and developed surface channel field effect transistors (FETs). In this study, we demonstrate that this type of FET is applicable in high-frequency devices operating at high power and biosensors in electrolyte solution.

Keywords: Field Effect Transistors, Microwave Devices, Biosensors, Hydrogen Termination

INTRODUCTION

Among wide band gap semiconductors, diamond has large band gap (5.5 eV). The breakdown field is 2-3 times as large as that of SiC or GaN. Due to its strong covalent bonds, it exhibits the highest thermal conductivity, 4 times as large as that of SiC. The figures of merit for high power, high frequency, and integrated devices calculated from these physical properties far exceed those of other semiconductors. Although p-type carrier control can be done by boron, the acceptor level is so deep (0.37ev) that the carrier concentration at room temperature is very low resulting in low transconductance less than 1mS/mm in conventional FETs.

Compared with the boron doped layer, the surface conductive layer of hydrogen-terminated (H-terminated) diamond has suitable properties for FETs, because high surface carrier concentration (10¹³ cm⁻²) is obtained with shallow carrier profiles where 90 % carriers exist less than 10 nm from the surface. Moreover, ohmic contacts can be obtained because of the low Schottky barrier heights at the H-terminated surfaces. These advantages are summarized in Fig.1. Up to now relative high transconductances of 50-150mS/mm have been obtained in metal-semiconductor (MES) FETs or metal-insulator-semiconductor (MIS) FETs using the H-terminated diamond surfaces (refs 1 to 3).

On the other hand, conductive polycrystalline diamonds doped with high density (10¹⁹cm⁻³) boron are normally used for the electrochemical electrodes which attract attentions because of wide potential windows of 3.0-3.5 eV more than 1eV wider than glassy carbon or Pt used as normal electrochemical electrode. The p-type surface conductive layer can be also used this purpose, because the surface of diamond is chemically inert and biocompatible. Within the potential window, the FET operation with the electrolyte solution as gate can be expected.

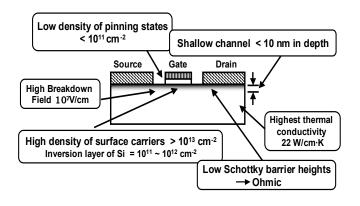
In the present paper we are going to show the two types of application from the point of RF operation and biosensing of surface channel diamond FETs which exhibit high transconductance and operations in electrolyte solution.

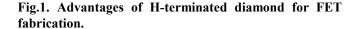
RF OPERATION OF DIAMOND FETS

RF operations of diamond FETs have been recently obtained with the gate length of 2.0- $0.2\mu m$. f_T of 11 GHz and f_{max} of 18 GHz in the 0.6 μm gate-length MISFETs (ref.2) and f_T of 11GHz and f_{max} of 30 GHz in the $0.2\mu m$ gate-length MESFETs (ref.3) are reported. A small signal current gain and power gain of a recent MISFET with 0.4 μm gate-length shows maximum f_T of 15 GHz and f_{max} of 20 GHz is shown in Fig.2.

Figure 3 summarizes the f_T of diamond MISFETs and MESFETs as a function of reciprocal gate length. The MISFETs exhibit better performances compared with those of MESFETs at equivalent gate length. The gate insulator of the MISFETs is CaF_2 which is deposited on H-terminated surface with 20-30 nm in thickness without damaging the surface C-H bonds. The surface states caused by dangling bonds are scarcely observed. One reason for the higher f_T was explained by the reduction of the gate capacitance in the MISFETs compared with those of MESFETs.

NASA/CP—2003-212319 174 August 18, 2003





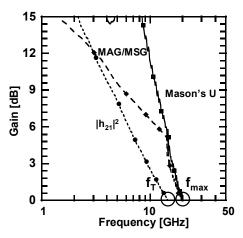


Fig.2. Small signal current gain and power gain of a recent MISFET with 0.4 µm gate-length.

Another reason is explained by the mobility increase in the CaF_2 passivated diamond surface. Figure 4 shows the sheet carrier density and the carrier mobility of CaF_2 passivated and unpassivated diamond surfaces. The dotted lines correspond to sheet resistances, 5-20 k Ω /sq. After CaF_2 passivation, the plots cross the dotted lines and move toward the lower resistance region. The carrier mobility of the diamond MIS interface increases by 2.5 to 3 times, although carrier density decreases to 2/3. The increase in mobility results in low sheet resistance. When the H-terminated surface is passivated by CaF_2 , the hole scattering by ionized acceptors decreases and the carrier mobility increases.

Since the source-gate and gate-drain spacings become crucial in the series resistance of short channel FETs with 0.1-0.2 μm gate length. Accordingly the extrinsic g_m is saturated because of the relatively high resistance of surface conductive layer (5-10 k Ω /sq. as shown in Fig.4). The removal of the parasitic resistances at the source-gate and gate-drain spacings should be take into consideration for the further advance of surface channel diamond FETs.

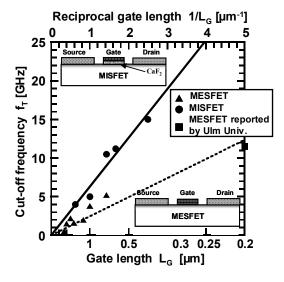


Fig.3. f_T of diamond MISFETs and MESFETs as a function of reciprocal gate length.

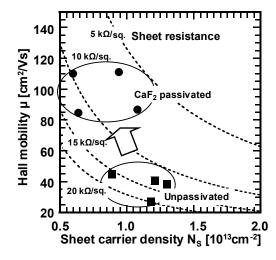


Fig.4. Sheet carrier density and carrier mobility of CaF₂ passivated and unpassivated diamond surfaces.

ELECTROLYTE SOLUTION GATE FETS FOR BIOSENSING

The electrolyte solution gate diamond is shown in Fig.5(a), where the metal gate of MESFET or MISFET is replaced by electrolyte solution. This FET is similar to the ion sensitive FET (ISFET) normally fabricated on Si technology used for pH sensing or biosensing . The silicon ISFET shown in Fig. 5(b) needs passivation layers such as Si_3N_4 to protect gate oxide layer which is the most delicate part of Si MOSFETs. On the other hand, the surface channel (sensing region) is exposed to electrolyte solution in the case of diamond FETs. It is very advantageous for sensing very subtle change of surface potential. This new type FET is named as solution gate (SG) FETs.

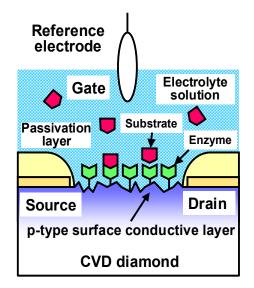
The SGFET characteristics show perfect pinch-off and saturation behavior. In the bare H-terminated diamond surfaces exposed directly to electrolyte solution, these characteristics have been reproducibly obtained in pH 1-13. Considering that the surface of polycrystalline diamond is very rough, the I_{DS} - V_{DS} is unexpectedly good. The operation is based on the electric double layer between the electrolyte and H-terminated surface.

So far, we have reported that the threshold voltage of the H-terminated diamond surface is insensitive to pH solutions (ref.4). Otherwise the H-terminated diamond surface is sensitive to chloride (Cl⁻) ions (ref.5). The threshold voltages of SGFETs shifts about 30 mV/decade as a function of Cl⁻ or Br⁻ ion's concentration (Fig.6). This means that the upper band bending of H-terminated diamond surface is enhanced in the Cl⁻ ionic solutions. And it leads to the increase of the surface carrier density. One of the attractive biomedical applications for the Cl⁻ sensitive SGFETs is the detection of chloride density in blood or in sweat especially in the case of cystic fibrosis. The sensitivities of Cl⁻ and Br⁻ ions have been lost on the partially O-terminated diamond surface as shown in Fig.6. These phenomena can be explained by the change of surface polarity on the H-terminated and the O-terminated surface.

The as-grown CVD diamond surface terminated by hydrogen exhibits the surface p-type conductivity, which is used in p-channel SGFET. The surface channel properties can be changed by chemical modification of the surface lead to the enzyme immobilization for molecule recognition (Fig.5(a)). Since the diamond surface is more modifiable than Si based material such as Si, SiO_2 , or Si_3N_4 , a new type of biosensor can be developed. One of the examples as urea sensor is shown as follows. The H-terminated diamond surface layer is modified chemically to become pH sensitive (ref.7). Urease is immobilized partially on the diamond surface channel of the SGFETs, which is sensitive to pH values. The diamond SGFETs of urea sensor have a structure where urease immobilized surface channel is directly exposed to urea solution and drain/source electrodes are covered with epoxy resin as shown in Fig.5(a).

Urea sensitive diamond SGFETs are based on the biocatalyzed decomposition of urea by urease. Although the two decomposition products affect oppositely the pH at the surface channel, the dissociation of NH₄⁺OH⁻ is higher than that of carbonic acid, resulting in the pH increase.

$$(NH_2)_2CO \text{ (urease)} + 2H_2O + H^+ \longrightarrow 2NH_4^+ + HCO_3^-$$



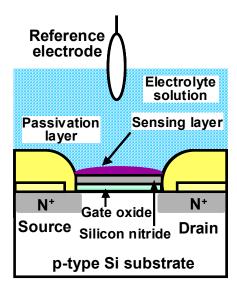
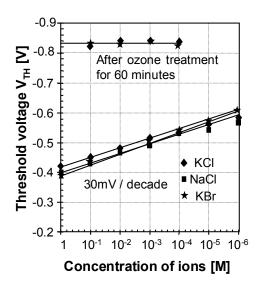


Fig. 5. (a) solution gate FET on diamond. (b) ion sensitive FET based SiMOS technology.



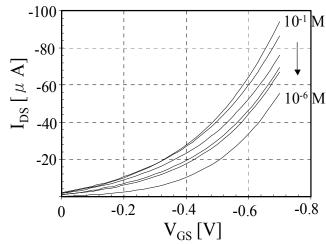


Fig.6. Threshold voltages shift on Hterminated diamond surface in KCl, NaCl and KBr solutions. The shifting of the threshold voltages disappears after ozone

Fig.7. I_{DS} - V_{GS} characteristics of diamond SGFET with pH sensitivity as a function urea density. The change of threshold voltages is about 30 mV/decade.

We have checked the change in the drain-source current and the threshold voltage of SGFETs to examine the sensitivity of urea on the diamond surface channel. As urea density increases, the absolute value of the drain-source current increases at about 5μ A/decade and the threshold voltage decreases at about 30 mV/decade in a FET with 500 μ m gate length as shown in Fig.7.

It is expected that the sensitivity of urea on polycrystalline diamond surface can be increased by the miniaturization of gate length, because the $5\mu m$ gate SGFETs exhibit more sensitivity by 50 times in the chloride ion detection of the $500\mu m$ gate SGFET.

FUTURE APPLICATION

DNAs are also immobilized covalently on diamond surface at the density of 10^{11-12} cm⁻² which is two orders of magnitude higher than on glass plate. It is very advantageous for fully electrical DNA chips based on the addressability at the nanometer scale.

Nano scale modification of diamond surface by AFM has been also developed to change H-terminated surface to oxygen-terminated surface where the oxidation stops at monolayer level. The formation of nanodevices has been also made based on the different electric properties between H-terminated surface (p-type semiconducting) and O-terminated surface (insulating). As a nano electron device, single electron transistors two tunneling junctions and one side gated (or in-plane gate) FET have been successfully made (ref.8). These recent results are combined with diamond transistor operated in GHz or electrolyte solution to develop a new type of electron device in the future.

REFERENCES

- 1. H.Taniuchi, H.Umezawa, H.Kawarada et al. IEEE Electron Device Lett. EDL 22 (2001) 390.
- 2. H.Umezawa, H.Kawarada et al. IEEE Electron Device Lett. **EDL 23** (2002) 121.
- 3. A.Aleksov, E.Kohn et al. IEEE Electron Device Lett. EDL 23 (2002) 488.
- 4. H.Kawarada, et al., Phys. Status Solidi A 185 (2001) 79.
- 5. T. Sakai, H. Kawarada, et al. Jpn. J. Appl. Phys. 48 (2002) 2595.
- 6. K-S.Song, H. Kawarada et al. Biosensors and Bioelectronics (2003) (in press)
- 7. K-S.Song, H. Kawarada et al (submitted)
- 8. M.Tachiki, H. Kawarada et al. Appl. Phys. Lett. **81** (2002) 2854.

DIAMOND ELECTROCHEMISTRY

John Foord, James McEvoy, Arnab Chatterjee and Richard Compton

University of Oxford, Physical and Theoretical Chemistry Laboratory, South Parks Road, Oxford OX1 3QZ, United Kingdom

Frank Marken

University of Loughborough, Department of Chemistry, Loughborough, LE11, 3TU, United Kingdom

ABSTRACT

Diamond electrodes have attracted great interest in electrochemistry since they offer many advantages over other competitive electrode materials such as glassy carbon. In particular, the high mechanical strength, chemical inertness and biocompatibility of diamond enables its use in hostile conditions or in "bio-media" which prohibit the use of other electrode materials. A resistance to electrode fouling, low background currents, optical transparency and selective reaction kinetics for particular classes of electrochemical reaction are other important advantages. As a result diamond electrodes are currently being explored for chemical processes such as electrochemical synthesis, and destruction of pollutants, as well as for chemical sensors.

The purpose of the present talk will be to describe our work on a range of electrochemical problems using diamond electrodes. Topics to be addressed will include the influence which the nature of the diamond film exerts on the electrochemistry observed, the variations which occur as a result of changes in the surface condition of the diamond electrode, and recent developments in diamond electrochemistry for bio-sensing applications.

Key words: diamond, electrochemistry, surface chemistry, sensors

Corresponding author: Prof. JS Foord, Univ. of Oxford, Physical and Theoretical Chemistry Laboratory, South Parks Road, Oxford, OX1 3QZ, United Kingdom.

Tel: +44 1865 275967

email: john.foord@chem.ox.ac.uk

SCANNING PROBE MICROSCOPY OF CARBON-NANOPARTICLE-BASED EMITTERS

V.D. Frolov, A.V. Karabutov, V.I. Konov, S.M. Pimenov General Physics Institute, Vavilov str. 38, 119991 Moscow, Russia

P.Ya. Detkov, V.V. Ovsyakov

Russian Federal Nuclear Center-Institute of Technical Physics, ul. Vasilieva 13, 456770 Snezhinsk, P.O.245, Russia

E.N. Loubnin

Institute of Physical Chemistry, Leninsky prospekt 31, 117915, Moscow, Russia

ABSTRACT

The techniques of scanning tunneling microscopy/spectroscopy (STM/STS) and atomic force microscopy/spectroscopy (AFM/AFS) with conductive cantilevers are applied to study electronic properties of the emission sites in field electron emitters based on carbon nanoparticles (nanodiamonds, carbon nanotubes). The emitters are produced by (i) electrochemical codeposition of metals with nanodiamond, (ii) electrophoretic deposition of single-wall carbon nanotubes, and (iii) shock-wave compacting/implantation of carbon nanoparticles into metal layers.

STM analysis of the emitter surface allows to get mapping of the surface relief, field emission, surface electron potential, and local electroconductivity. It is generally found that the position of the emission sites is coincident with high-conducting regions where the surface electron potential is lowered. In addition, the STS/AFS data showed different character of local conductivity in nm-sized surface regions of the nanodiamond- and nanotube-based emitters. The obtained data provide further support for the field emission model based on the analysis of the field-enhanced emissivity of low-dimensional regions due to the quantum well effect, which has been previously proposed to account for the low-field electron emission from nanocrystalline diamond and nitride films.

Keywords: scanning probe microscopy/spectroscopy, nanodiamond, carbon nanotubes, field emission

INTRODUCTION

During recent years, various aspects of field electron emission from carbon materials have being attracted increasing attention of researchers over the world, that was caused by exciting results on low-field electron emission from carbon nanostructured materials (nanocrystalline diamond/graphite films, DLC films, carbon nanotubes, etc.) and highly promising applications of carbon-based emitters (refs. 1-3). The issues concerning the mechanism of the low-field emission phenomenon are of great interest, and for a deep insight into the mechanism the need of studying the electron emission from an 'individual' emission center with high spatial resolution is evident. One of advanced techniques used for these purposes is a method of field emission microscopy (refs. 1,2), which was demonstrated to be very successful for imaging the emitting structures on the tips of carbon nanotubes (refs. 4). Another approach is based on the application of scanning tunneling microscopy (STM) to field electron emission studies (refs. 5-7). This technique, called as the scanning tunneling-field emission microscopy (STFEM), provides mapping of surface relief, field emission intensity, surface electron potential, and local conductivity with spatial resolution of few nanometers, and gives valuable information on the position and electronic properties of the emission sites. Using STFEM, extensive studies of the emission site properties have been carried out for nanocrystalline diamond films and related materials (refs. 7-14). The results of these studies contributed to better understanding of the emission processes and evidenced that the quantum-size effects can play an important role in the emission mechanism (refs. 9,10,13,14). In addition to STM, other scanning probe microscopy (SPM) techniques based on AFM with conductive cantilevers are efficiently used for examination of nanoscale electronic properties of low-field emitting carbon films (refs. 15,16). In this paper, we present experimental results of complex microscopic investigations of carbon-nanoparticle-based emitters using various SPM techniques (STFEM, STM/STS, AFM/AFS). The emitters are produced by different methods, including electrochemical codeposition of metals with nanodiamond, electrophoretic deposition of singlewall carbon nanotubes onto conducting substrates, shock-wave compacting of metal powders with carbon nanotubes, and shock-wave implantation of carbon nanoparticles into metal substrates.

EXPERIMENTAL DETAILS

Three types of carbon nanoparticles were used as a 'building' nanomaterial in constructing the emitting carbon nanostructures on substrate surfaces. These nanoparticles are i) ultradisperse diamond (UDD, particle size of about 5 nm) produced by explosions (ref. 17 and refs. therein), ii) single-wall carbon nanotubes (SWNT) synthesized by a dc arc discharge technique (ref. 18), and iii) graphite-like particles of 80-150 nm size. Brief description of the samples of carbon-nanoparticle-based emitters and methods of their fabrication is given in Table 1.

Sample #	Method of fabrication
1	Codeposition of nickel with ultradisperse diamond particles from electroplating solutions Samples: Cu substrates electroplated with Ni-UDD composite coating of 5 µm thickness Post-deposition treatment: heat treatment in hydrogen at 750 C
2	Electrophoretic deposition of single-wall carbon nanotubes from alcohol suspensions onto Ni substrates
3	Shock-wave compacting of metal powders with single-wall carbon nanotubes Substrate: metal substrate coated with electroplated silver layer Compacted surface layer: powder mixture of silver nanoparticles with single-wall carbon nanotubes

Shock-wave implantation of graphite-like nanoparticles into the surface layer of copper substrates

Table 1. Samples of carbon-nanoparticle-based emitters

Two SPM devices were used for characterization of the emitter surface. The first setup is a high-vacuum scanning tunneling-field emission microscope (STFEM), which is used to determine correlations between microscopic distributions of four surface parameters – surface relief, field emission intensity, surface electron potential, and local electroconductivity, measured with the resolution of ~ 2 nm in vacuum of 10^{-6} Torr (refs. 6,7).

The second device is a scanning probe microscope 'Solver P47' (NT-MDT Co., Russia), which provides complex investigations of the surface properties with spatial resolution of ~ 0.1 nm in air by means of STM/STS and AFM/AFS (ref. 16). This SPM setup enables to measure: (i) the surface relief with AFM in the contact mode and resonant semi-contact mode and with STM in the constant tunneling current regime; (ii) the surface electron states with AFM in the resonant non-contact mode; (iii) the differential electroconductivity in the STS regime; (iv) the work function by the Kelvin method (SKM) in the resonant non-contact mode; (v) the local current-voltage (I-V) characteristics over a scanned area, along a given line and in a certain point with AFM (the contact mode) as well as with STM. The I-V data obtained over the scanned area (64×64 points) are presented in the form of four-dimensional space with coordinates {X,Y,I,V} which cross-sections at given values of V allow to draw a series of spreading resistance images (SRI) of the surface and to analyze a fine structure of the conductivity. The I-V data obtained along a given line are presented in the form of three-dimensional space with coordinates {X,I,V} which cross-sections at certain values of V are used to determine precise sizes of both conducting and insulating regions.

For the AFM measurements, special cantilevers containing tips coated with different conducting layers (W₂C, TiN, Pt) are used. STM probes are fabricated from the W or Pt-Ir alloy wires.

Macroscopic characterization of the field emission properties of the samples was carried out by means of 'microprobe' and 'flat luminescent screen' methods, as described elsewhere (refs. 8,12).

RESULTS AND DISCUSSION

Field emitters based on metal-nanodiamond composite coatings

Figure 1a compares the I-E characteristics (measured with a 'microprobe' setup) of two samples with Ni-UDD composite coating, demonstrating a significant improvement in the emission behaviour after the heat treatment in hydrogen at 750° C. The as-deposited sample exhibited no emission current at the applied fields of up to 200 V/ μ m, whereas after hydrogen treatment the Ni-UDD composite coating was characterized by 50 V/ μ m threshold fields and 'smooth' (i.e., without activation) current-on-field behaviour. Testing the hydrogen-treated sample with a 'flat screen' technique showed a very low threshold field of 0.6 V/ μ m which increased to 2.5 V/ μ m after the 1-hour training at current of 400 μ A (Figure 1b). Emission centers, visualized with the luminescent screen, were placed predominantly around the center of the sample (Figure 1c), and the surface density of the centers after the training was significantly improved. The difference in the emission thresholds, measured by the 'microprobe' and 'flat

screen' setups, might be due to a geometrical factor ('true' distance between the microprobe and emission centers is larger than that normally to the surface) and/or nonuniform distribution of the emission centers on the surface. The Ni-UDD sample after hydrogen treatment was further studied with SPM methods.

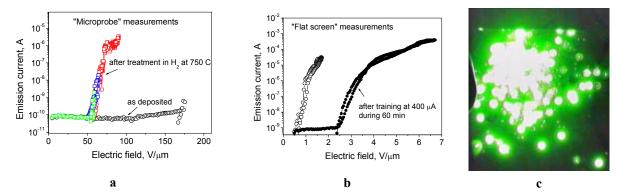


Figure 1. Field electron emission from the Ni-UDD composite coatings: (a) I-E characteristics of as-deposited and hydrogen-treated samples measured with a 'microprobe' setup; (b) I-E curves (after hydrogen treatment) measured with a 'flat screen' setup; (c) field emission image at E=10 V/μm and current 470 μA.

Figure 2a displays the results of the STFEM mapping of the hydrogen-treated Ni-UDD coating, which are presented in the form of the profiles of the surface relief, field electron emission, surface electron potential and local electroresistivity (the data of the last parameter are resulted from measurements in the "bias spectrum" regime). The sample surface is characterized by a grain-like morphology with the grain height of about 1 μ m and the grain size of 0.3-1 μ m. The grain conductivity is $G \sim 0.6~G\Omega^{-1}$, and the grain boundary regions are more conducting (G=10-15 $G\Omega^{-1}$ at the bias voltage U= -1 V, voltage polarity corresponds to electron flow from the probe). Emission centers (EC) with a lateral size of 0.1-0.3 μ m are located near the grain boundary regions. The EC position correlates with a lowered surface electron potential. The value of the characteristic field at the EC is F_c =15-30 V/ μ m. In addition, poorly conducting inclusions (G<0.5 $G\Omega^{-1}$) with a lateral size of 100-200 nm are found; they are located on the grain slopes and the density of such inclusions is low (\sim 10⁵ cm⁻²). It should be noted that these experimental data are obtained at the bias voltage $|U| \le 4V$, because at |U| > 4V some regions (they, as a rule, are associated with a lowered electron potential) show an extremely high magnitude of the "Z-spectrum" mode signal.

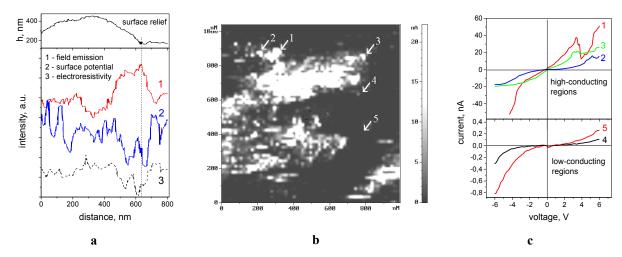


Figure 2. (a) STFEM 'profiles' of surface relief, field emission intensity, surface electron potential, and resistivity along the same line scan on the surface of the hydrogen-treated Ni-UDD composite; (b) AFM-SRI obtained at the applied voltage U= -2 V, and (c) I-V characteristics of high-conducting and low-conducting regions marked by arrows in Figure 2b (the voltage is applied to the AFM probe).

The electroconductivity distribution on the Ni-UDD sample surface was investigated using AFM with Pt-coated cantilever in the contact mode. A reason to apply the AFM contact mode was to exclude the current instabilities caused by modulation of the gap between the probe and the sample. Figure 2b shows an AFM-spreading resistance image (SRI) of the emitter surface, where the regions of higher brightness correspond to higher conductivity. The AFM-SRI examination with higher resolution revealed the presence of high-conducting inclusions ($G \approx 10~G\Omega^{-1}$) with a lateral size of 5-10 nm on the sample surface. The I-V characteristics of such high-conducting inclusions are presented in Figure 2c in comparison with the I-V curves of low-conduction regions. It is important, that most of the I-V characteristics of high-conducting regions have a section of negative differential resistance in the voltage range from 4 V to 6 V. As discussed above, a rapid increase of Z-spectrum" mode signal was observed in the same voltage range. The obtained AFM-SRI results are in agreement with the previously reported data for ultrananocrystalline diamond films (ref. 16) and confirm our supposition that the field electron emission from the high-conducting regions is accompanied by resonant tunneling of electrons through local surface energy states (refs. 9,10).

Carbon nanotube-based emitters

The emitters fabricated by electrophoretic deposition of single-wall carbon nanotubes onto Ni substrates (sample #2 in Table 1) exhibited very low threshold fields of \leq 1 V/ μ m for the 'flat screen' measurements and high emission stability at high currents, but moderate surface density of the emission sites.

The STFEM mapping showed the surface protrusions with a height of up to 3 μ m. However, more detailed investigations of the surface were found to be impracticable because of extremely high current noise under both the tunneling and field electron emission conditions. In order to study the sample microstructure, we developed STM measurements in air using a scanning probe microscope 'Solver P47'. It was found that the sample mapping could be sufficiently realized in the tunneling regime under the electron current being held near the 0.1 nA level (the STFEM feedback system is capable to hold the current $I \ge 0.5$ nA). Figure 3a displays the surface relief map of the $0.98 \times 1.02~\mu\text{m}^2$ area; it is seen that there is a region with a characteristic lateral size of about $0.5~\mu$ m on the surface, and protrusions at this place look like wrinkles with a height of the order of 10 nm. Being scanned with a higher resolution (≤ 0.1 nm), this surface area shows formations with a width of 2-3 nm and length of ~ 50 nm (Figure 3b). Such nm-sized regions can be associated with single-wall carbon nanotubes lying on the substrate. It is distinctive that the surface electron potential of the 'nanotube' regions is higher than for the neighboring regions (Figure 3c). Also, it should be noted that the electron current instability becomes higher with increasing voltage, and it reaches a giant level under the emission measuring conditions. The results of Figures 3b and 3c seems to be important for understanding the emission process from SWNT-based cathodes, therefore more detailed STM study of the electronic structure of SWNT is required.

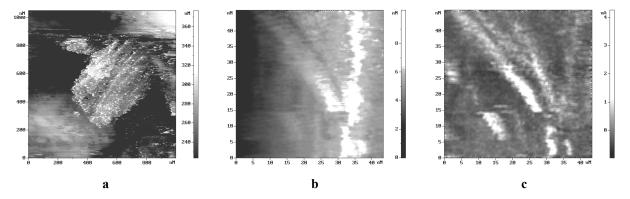


Figure 3. STM images of the sample surface of electrophoretically-deposited single-wall carbon nanotubes on Ni substrate: (a) 2D map of the surface relief, the scanned area is 0.98×1.02 µm²; (b,c) comparative 2D maps of the surface relief (b) and surface electron potential (c), the scanned area is 43×47 nm².

The sample produced by shock-wave compacting of a powder mixture of silver nanoparticles with single-wall carbon nanotubes (sample #3 in Table 1) showed the threshold field of 2-3 V/µm for the 'flat screen' measurements. Most of the emission sites were located in the surface areas near the edges of the sample, where the emission site density was relatively high. Raman spectra of the sample evidenced that the structure of the 'compacted' carbon nanotubes was more defective than that of the original nanotube material. The Raman spectrum of the shock-wave

loaded nanotubes is presented in Figure 4a in comparison with the spectrum of the electrophoretically-deposited nanotubes (excitation wavelength 514.5 nm).

During STFEM mapping it was found that, if the bias voltage between the probe and the sample was U> 1 V (electron flow from the sample), the probe scanning was accompanying with 'lifting' the surface. In general, the process developed reversibly, i.e., after scanning the most of the surface area relaxed to the initial state, as was confirmed by mapping the surface at U< 1 V. Such effect did not allow us to obtain correct data on emission center properties for the most of the sample surface. For the 'stable' regions, the emission center position was found to coincide with the high-conducting regions, and the surface electron potential at the EC is lowered. The characteristic emission field at such ECs was found to be $F_c = 10-20 \text{ V/}\mu\text{m}$. For the most of the sample surface areas the conductivity was $G > 10 \text{ G}\Omega^{-1}$. In addition, local I-V characteristics were measured. The I-V characterization revealed the 1-2 nm sized inclusions clustered on the sample surface as shown in STM-SRI in Figure 4b. A typical I-V characteristic measured inside the inclusion is shown in Figure 4c. The inclusion conductivity is $G \approx 100 \text{ G}\Omega^{-1}$, and it can be associated with nanotubes placed normally to the surface.

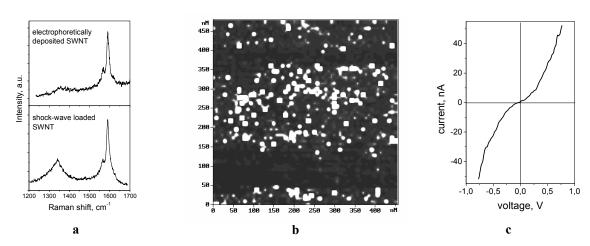


Figure 4. (a) Raman spectra of the samples #2 and #3; (b) STM-SRI of the sample #3 measured at U=-0.7 V, and (c) typical I-V characteristic of the high-conducting inclusion (the voltage is applied to the STM probe).

Emitters fabricated by shock-wave implantation of carbon nanoparticles into metal layers The sample #4, obtained by shock-wave implantation of graphite-like particles (mixed with UDD particles) into electroplated copper layer on copper substrates, showed the threshold emission fields of 8-10 $V/\mu m$ for the 'microprobe' measurements, but, as a rule, an initial emission activation was observed at higher fields.

STFEM mapping showed that the sample surface was characterized by grain-like morphology with the typical grain size of 1-2 μ m and the grain height of 0.5 – 1 μ m (Figure 5a). Effective emission centers were found to locate on the grain slope regions where the surface electron potential was lowered (Figs. 5b,c). It should be noted that the most part of the sample surface showed high electroresistance, R> 5 G Ω . Emission centers were associated with the high conducting regions (R< 0.2 G Ω). The characteristic emission field at the emission centers was about 5 V/ μ m.

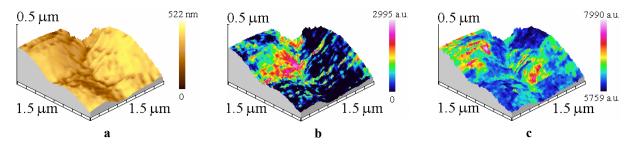


Figure 5. Sample #4: 3D map of the surface relief (a), and STFEM images of field electron emission (b) and surface electron potential (c) superimposed onto the surface relief map.

CONCLUSIONS

The obtained results demonstrate that the scanning probe microscopy/spectroscopy techniques provide unique opportunities for investigations of the nature and nanoscale electronic properties of the emission centers in carbon-based field emitters. For the emitters studied, it is found that the position of the emission sites coincides with high-conducting regions where the surface electron potential is lowered, that, along with the previously reported data for nanocrystalline diamond and nitride films, allows this fact to attribute to a 'fundamental property' of the emission center in low-field emitting materials. The data on the specific conductivity behaviour in nm-sized regions give supporting evidence that the quantum-sized effects play an important role in the low-field emission phenomena.

ACKNOWLEDGEMENTS

The authors are thankful to A.S. Pozharov for the synthesis of single-wall carbon nanotubes, and to I.I. Vlasov and E.D. Obraztsova for Raman characterization of the carbon-based emitters. The work was supported by ISTC Project #1400.

REFERENCES

- 1. Sheshin, E.P.: Surface structure and field emission properties of carbon materials. Publishing House of MIPT, Moscow, 2001 (in Russian).
- 2. Saito, Y., Uemura, S.: Field emission from carbon nanotubes and its application to electron sources. Carbon, 38, 2000, 169-182.
- 3. Lee, N.S., et al.: Application of carbon nanotubes to field emission displays. Diamond Relat. Mater., 10, 2001, 265-270.
- 4. Saito, Y., Hata, K., and Murata, T.: Field emission patterns originating from pentagons at the tip of a carbon nanotube. Jpn. J. Appl. Phys., 39, 2000, L271-L272.
- 5. Frolov, V.D., et al.: Scanning field electron emission microscope for diamond cold cathodes studies. Abstracts of Diamond 1996, Sept. 8-13, 1996, Tours, France, p. 11.111.
- 6. Frolov, V.D., et al.: Scanning tunneling microscopy: application to field electron emission studies. J. Phys. D: Applied Physics, 32, 1999, 815-819.
- 7. Frolov, V.D., et al.: Application of scanning tunneling-field emission microscopy for investigations of field electron emission from nanoscale diamond films. Ultramicroscopy, 79, 1999, 209-215.
- 8. Karabutov, A.V., et al.: Grain boundary field electron emission from CVD diamond films. Diamond Relat. Mater., 8, 1999, 763-767.
- 9. Frolov, V.D., et al.: Electronic properties of the emission sites of low-field emitting diamond films. Diamond Relat. Mater., 9, 2000, 1196-1200.
- 10. Frolov, V.D., et al.: Similarity in field electron emission from nanocrystalline diamond and related materials. Diamond Relat. Mater., 10, 2001, 1719-1726.
- 11. Krauss, A.R., et al.: Electron field emission from ultrananocrystalline diamond films. J. Applied Physics, 89, 2001, 2958-2967.
- 12. Karabutov, A.V., et al.: Low-field electron emission of diamond/pyrocarbon composites. J. Vac. Sci. Technol. B, 19, 2001, 965-970.
- 13. Karabutov, A.V., Frolov, V.D., Konov, V.I.: Diamond/sp²-bonded carbon structures: quantum well field electron emission?. Diamond Relat. Mater., 10, 2001, 840-846.
- 14. Frolov, V.D., et al.: Field electron emission and nanostructural correlations for diamond and related materials. Ultramicroscopy, 95, 2003, 99-105.
- 15. Zhang, L., et al.: A combination study of conductivity and contact potential in low-field-emission carbon films by conductive scanning probe microscopy. New Diamond Front. Carbon Technol., 9, 1999, 53-61.
- 16. Frolov, V.D., et al.: Electronic properties of low-field emitting ultrananocrystalline diamond films. Ultramicroscopy, 2003, in press.
- 17. Loubnin, E.N., et al.: Electroplating of gold-nanodiamond composite coatings. New Diamond Front. Carbon Technol., 9, 1999, 273-282.
- 18. Obraztsova, E.D., et al.: Structural measurements for single-wall carbon nanotubes by Raman scattering technique. NanoStructured Materials, 12, 1999, 567-572.

FABRICATION OF 3-D SHAPED MICRO BODY STRUCTURES OF DIAMOND BY USE OF FOCUSED ION BEAM

Masao Murakawa, Hiroyuki Noguchi and Sadao Takeuchi

Nippon Institute of Technology 4-1 Gakuendai, Miyashiro, Saitama 345-8501 Japan E-mail address: mura@nit.ac.jp Fax: 81-480-33-7645

Phone: 81-480-33-7618

ABSTRACT

Diamond is believed to be a suitable candidate material for micro- and nanotechnology due to its extreme hardness. However, this very property of diamond also makes its processing very difficult. More specifically, the processing of diamond by grinding with a fine powder of diamond itself is indeed possible if the grinding shape is a planar one, but the processing of diamond into a 3-D shape by grinding is very difficult. Furthermore, in the case of diamond processing by means of ion milling, the shape is limited to a 2.5-D one and the processing speed is very low as well. The use of a focused ion beam (FIB) device could be an alternative means for processing diamond. It has been generally used as a means for preparing specimen materials for electron microscopy by sectional cutting along a certain area of the material or slicing the material into very thin flakes ranging from 100 nm to 50 nm in thickness. Although FIB device technology has been advancing in that the devices can now deal with nanometer sizes due to the very fine diameter of the ion beam, generally speaking, it is not very suitable for precision processing of 3-D shapes. Accordingly, the purpose of this paper is to introduce a FIB device which has been designed to enable the precision processing of diamond into 3-D body shapes. This has been made possible by the introduction of various additional features of the device for precision 3-D processing of any kind of specimen including even the hardest material, diamond. The features of the device include: a U-centric mechanism whereby we can retain the focused point on the specimen even when the specimen is inclined; processing capability of any configuration on a plane; processing using bit map data; controllability of irradiation period of each single beam. These combined features render the device optimally suitable for use as a tool for fabrication, e.g., micromachines of any 3-D shape fabricated of any material including diamond. In this work we introduce several fancy demonstrations of diamond single crystal or very thick DLC having a 3-D configuration, which are made possible for the first time by the use of this sophisticated FIB device.

Keywords: FIB, focused ion beam, diamond, 3-D shapes, nanotechnology

INTRODUCTION

Considering the conditions of the use of micromachines, their materials are required to have a small coefficient of friction and little wear under no-lubricant condition. Diamond is expected to be an appropriate material for micromachines, because it has good tribological characteristics and chemical resistance. However, the hardness of diamond makes it extremely difficult to process into the desired shape, especially a 3-D shape.

The Lithograph Galvanformung und Abformug (LIGA) process which is based on semiconductor processing technology is a well-known microprocessing method. In LIGA, first, a mask is fabricated, then, via etching using the mask, the mask shape with a deeper depth is processed; using the thus-obtained object as a model, a mold is fabricated by electrocasting. Therefore, the final workpiece is not directly processed in LIGA and the shape is limited to a 2.5-D one. In addition, it is impossible to process diamond using LIGA.

In contrast to LIGA, when a focused ion beam (FIB) processing is used, a workpiece is directly irradiated by an ion beam without a mask, and 3-D processing is possible by repeated processing at the same location. Furthermore, it is possible to fabricate the workpiece by inclining it during the processing. We report the fabrication of diamond using FIB.

NASA/CP—2003-212319 185 August 18, 2003

EXPERIMENTAL APPARATUS

Table 1 shows the specifications of the FIB device used for processing. The feature of this device is that it enables removal processing at a high speed, due to a very high acceleration voltage, 40 keV, and a high maximum beam current, 37 nA. Moreover, the image resolution of this device is capable of 6 nm; it is suitable for microprocessing. It is possible to fabricate the desired shapes, such as rectangles, circular arcs, free curves, polygons, lines, and circles; in addition, the processing using bit map data as image data is possible. We may combine these desired shapes for various applications.

Table 1	FIB processing	annaratus and	nrocessing	conditions
I abic I	TID processing	apparatus anu	processing	comunitions

FIB processing apparatus	Hitachi High-Technologies Corporation FB-2100		
Processing voltage	40keV		
Beam current	37 nA – 0.01 nA		
Ion source	Ga liquid metal		
Resolving power	6 nm		
Assist gas	Not used		
Processing rate	$0.9 \times 10^9 \text{nm}^3 / \text{min}$		
Coating for conductive surface process	Au : 10nm-100 nm		

Example of 2.5-D processing of synthesized diamond single crystal

Figure 1 shows that a relatively high-intensity beam, 1.8 nA, irradiates the surface of a synthesized diamond single crystal and processes it at a high speed. Figure 1(a) demonstrates a specimen fabricated by a removal process at a high speed of 24 s per one unit. Figure 1(b) demonstrates that 16 identical specimens are copied and processed in 7 min. Thus, the processing of multiple uniform shapes is possible by producing a single shape data.

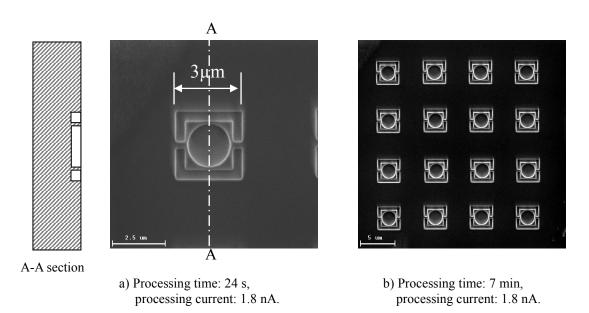
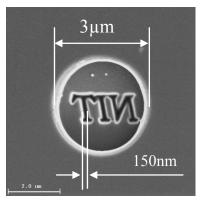
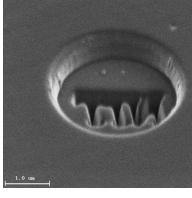


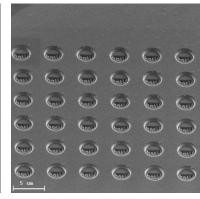
Figure 1. Example of 2.5-D processing of synthesized diamond single crystal.

Example of 3-D processing of synthesized diamond single crystal

Figure 2 shows an example of the processing of a synthesized diamond single crystal; a 0.4 nA beam which is weaker than 1.8 nA used in Fig.1 was irradiated in order to increase the processing accuracy onto its surface to fabricate a circular shape, following which mirror-image characters of "NIT" were carved on the same place. processing time per unit was 3 min, which is fairly long, but the processing width of the characters is 150 nm, showing that sub-micron-level removal processing was achieved for diamond. In this case, 36 models were copied and the processing of a uniform shape was carried out; the total processing time was 108 min.







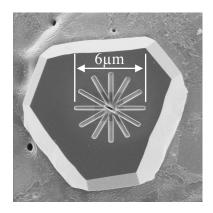
- a) Processing time: 3 min, processing current: 0.4 nA.
- b) The image of a) observed from diagonally upward direction.
- c) Processing time: 108 min, processing current: 0.4 nA.

Example of 3-D processing of diamond. Figure 2.

Example of 2.5-D processing of flat diamond

Figures 3, 4 and 5 show a flat diamond platelet sample synthesized on a copper substrate(refs. 1 to 3). The diamond sample has a hexagonal micro-flat-plate shape and is convenient for use as a material for micromachining. Namely, after processing of the diamond sample on the copper substrate, the fabricated diamond sample can be removed by etching of the substrate. Figure 3 shows the processing of a single rectangular shape 3 µm long and 0.3 µm wide on the flat diamond sample. This rectangular image was then rotated by 30 degrees 11 times and the same processing steps were repeated, without rotating the workpiece itself.

Figures 4 and 5 show the processing of a gear with external dimensions of 10 µm on the same flat diamond sample; after 60 min of processing, the same shape was processed onto the copper substrate together with the diamond.



flat diamond by rotation of image data.

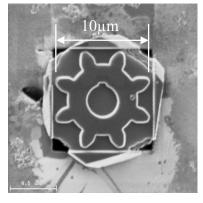


Figure 3. Example of processing of Figure 4. Example of processing of gear shape on a flat diamond sample (processing time: 30 min, processing current: 0.4 nA).

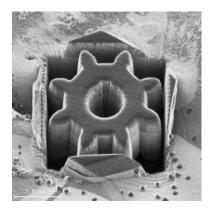


Figure 5. Example of processing of gear shape on a flat diamond sample (after completion of the processing, processing time: 60 min).

Example of 3-D processing of flat diamond

The U-centric function enables easy inclination of a specimen, because the position of the specimen is not changed on the display even when the specimen in the FIB device is inclined. Using this U-centric function, we inclined a flat diamond sample at 45°, and fabricated a blade of turbine shape; Figs. 6, 7 and 8 show the fabrication process. In Fig. 6, to retain a circular shape with a 15 µm diameter from the diamond flat plate, the unnecessary part outside the circle is removed. In this processing, an electric current of 8.2 nA and a processing time of 2 h were required due to the large volume to be removed. The subsequent processing conditions are shown in Fig. 7; the workpiece is inclined at 45° and the blades are fabricated one by one. The processing time for one blade was 7 min. Then, the workpiece was rotated by 45° around the central axis and identical processing was repeated 8 times; the blade section shown in Fig. 8 was obtained.

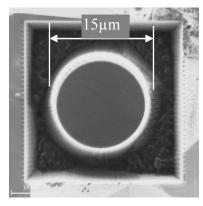


Figure 6. Example of processing of turbine shape on a flat diamond sample (cutting of circle) (processing time: 120 min, processing current: 8.2 nA).

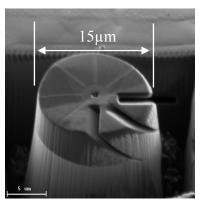


Figure 7. Example of processing of turbine shape on a flat diamond sample (processing time: 7 min/one blade, processing current: 1.8 nA).

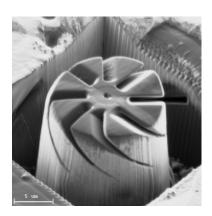
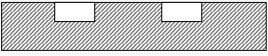


Figure. 8. Example of processing of turbine shape on a flat diamond sample (processing time: 60 min for 8 blades, processing current: 1.8 nA).

Example of 2.5-D processing and lithography of silicon

Although diamond has an excellent friction-resistant characteristic, its efficiency in the case of removal processing is lower than that of silicon. Here, examples of processing of silicon, and the lithographic formation of the processed microshape onto plastic are shown. Figure 9 shows the processing at a beam current of 0.36 nA; a gear with a 10 μ m external diameter was obtained with a 10 min processing time. Figure 10 shows the processing of a total of 10 gears with a 100 min processing time, carried out as follows: the shape data obtained in Fig. 9 was copied, and the data values were decreased or increased to make two sets of 5 shapes with outer diameters of 8 μ m, 9 μ m, 10 μ m, 11 μ m, and 12 μ m used for processing. As shown here, after the production of a single set of shape data, processing of various shapes can be realized by reduction, enlargement, and deformation by one-directional magnification.

Using this silicon mold, we attempted the lithographic processing of shapes on plastic, with the aim of achieving the mass production of microcomponents. To fill resin in the cavity of a mold, first a photocuring resin was dropped onto the surface of the silicon mold in vacuum, then the silicon mold was exposed to air so that the photocuring resin completely filled into the microcavity due to the atmospheric pressure. Subsequently, the photocuring resin was solidified by light irradiation. The solidified filmlike component was removed from the silicon mold, and the condition of the lithographed shapes was examined; Figs. 11 and 12 show the results. In these figures, microshapes are well-lithographed. A mold-removal agent which may degrade the accuracy of lithography was not used during the processing. In this forming method, almost no external forces are applied to the mold, and a large number of microshapes can be lithographed simultaneously.



A-A section

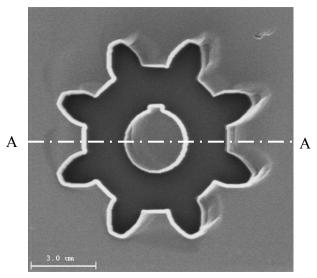


Figure 9. Example of processing of gear-shaped cavity (processing time: 10 min, processing current: 0.36 nA, workpiece: silicon).

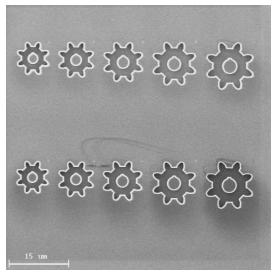


Figure 10. Example of processing of multiple gear-shaped cavities (processing time: 100 min, processing current: 0.36 nA, workpiece: silicon, processed dimensions: minimum 8 μm and maximum 12 μm, the number of units processed: 10).

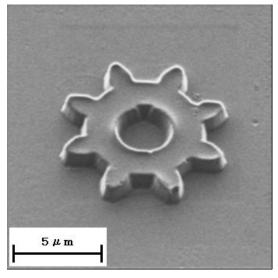


Figure 11. Example of lithography of gear shape (resin used: photocuring resin).

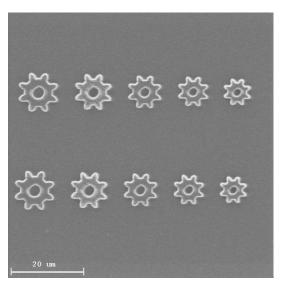


Figure 12. Example of lithography of gear shapes (resin used: photocuring resin).

SUMMARY

To fabricate micromachining components with a 3-D shape, we provided examples of processing using a FIB device. The results demonstrated that accurate and high-speed processing of a multiple number of cavities is possible for diamond. With the FIB, a workpiece can be processed directly without using a mask, and the shape data for processing can be arbitrarily produced; bit-map data which is a kind of image data can be used as processing data.

In the example of processing of silicon, we processed a gear with an external size of $10 \mu m$, and demonstrated the possibility of mass production of microcomponents applying lithographic processing using photocuring resin.

REFERENCES

- 1. K. Hirabayashi, S. Amanuma and Y. Hirose: Appl.Phys. Lett., 60, p.574(1992)
- 2. K. Hirabayashi, T. Kimura and Y. Hirose: Appl. Phys. Lett., **62**, p.354(1993)
- 3. K. Hirabayashi, and Y. Hirose: J. Cryst. Growth, **142**, p.140 (1994)

TRIBOLOGICAL BEHAVIOR OF CVD DIAMOND TOOLS

E. Uhlmann, M. Brücher

Institute for Machine Tools and Factory Management, Technical University of Berlin, Berlin, Germany

ABSTRACT

Diamond cutting tools are often the only choice for the machining of high-strength and highly abrasive non-ferrous alloys. During machining, a complex interaction of different wear mechanisms takes place on the tools. This interaction considerably hinders a purposeful detection of specific wear mechanisms. Therefore, the objective is to systematically analyze the wear processes that occur when machining a hypereutectic aluminum silicon alloy with CVD-diamond tools. The main wear mechanisms are identified and the limits for the use of various CVD-diamond tools are indicated. The findings gained will serve in the further development of these high-performance cutting materials.

Keywords: Cutting, Diamond coating, Wear

INTRODUCTION

Metal cutting operations on difficult-to-machine workpiece materials can often only be performed by using extremely hard polycrystalline cutting materials. For the manufacture of components made of highly abrasive, high-strength non-ferrous alloys in particular, there is no alternative to diamond-based cutting materials. However, an alternative process to diamond synthesis is becoming more and more established in the form of chemical vapor deposition (CVD), which opens up new possibilities in the field of high-performance tools (refs. 1 to 3).

Metal cutting processes involve a complex interaction of several wear mechanisms. These include abrasion, adhesion, tribo-oxidation, as well as surface damage. This complex interplay of the load variables occurring in the metal cutting process makes it considerably more difficult to purposefully detect specific wear mechanisms (ref. 3).

Tests on metal cutting of abrasive aluminum alloys using CVD-diamond tools have shown that in particular abrasive and adhesive wear, as well as tribo-oxidation, lead to tool failure (refs. 3 to 6). Therefore, analogy tests were conducted to provide a differentiated view of the wear mechanisms occurring in the metal cutting process with CVD-diamond. The results achieved in model tests were subsequently verified in tests carried out during actual metal cutting operations.

CVD-diamond thick-film and CVD-diamond thin-film tools were used in the tests. The CVD-diamond thick-films soldered onto cemented carbide substrate with a coating thickness of $s_D = 500 \,\mu\text{m}$ were deployed as electrically non-conducting and as boron-doped electrically conducting material. The CVD-diamond thin-films were deposited directly by means of a hot-filament CVD-process on two different substrate materials with a coating thickness of $s_D = 6 \,\mu\text{m}$ and $s_D = 28 \,\mu\text{m}$. A cemented carbide with the ISO specification K10 and a silicon nitride ceramic (Si₃N₄) were used as substrates. The sintered polycrystalline diamond with binder phase (PCD) and an average grain size of 10 $\,\mu\text{m}$, which has been on the market for about 30 years, was used as reference material.

The findings shall serve to identify the main wear mechanisms and to indicate the limits of the use of various CVD-diamond tools, as well as to provide information for the further development of these cutting materials.

ADHESION

To examine the adhesive wear behavior of different diamond-based cutting materials, a ball-disc tribometer was used. The ball was made of the workpiece material GD-AlSi17Cu4Mg and had a diameter of $D_{ball} = 10$ mm. The disc was made of the diamond cutting materials to be investigated. The normal force $F_N = 25$ N, the frequency $f_R = 15$ Hz, and the amplitude $A_R = 1$ mm were kept constant during all tests, which were performed in a constant atmosphere with a relative air humidity of H = 40 % and an ambient temperature of T = 22.5 °C. The friction time t was varied between 100 and 700 s.

After the adhesive loading of the two CVD-diamond thick-film cutting materials and of the PCD by the alloy GD-AlSi17Cu4Mg, no material deposits were found on the cutting material surfaces. The reason for this is that the cutting material surface exhibits only a very slight roughness. When the cutting material surface is examined after adhesive loading, however, distinct scratches can be seen on the surfaces (Figure 1). Because of its very low hardness, aluminum cannot cause such wear on extremely hard diamond. Therefore, other effects must have occurred.

Particularly the silicon crystals present in the workpiece material represent a possible cause of the scratches. Measurements using an electron beam microprobe, however, proved that aluminum oxide (Al_2O_3) had formed on the surface. The very hard Al_2O_3 particles that are partially present on the surface may be responsible for the scratches on the surface (Figure 1). The coefficient of friction of the material couple CVD-diamond thick-film/GD-AlSi17Cu4Mg was 0.1; for the couple PCD/GD-AlSi17Cu4Mg it was 0.2.

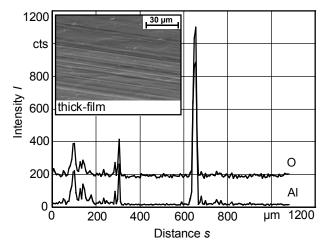


Figure 1. Elementary analysis to verify the formation of Al₂O₃ on the surfaces of CVD-diamond thick-film coatings.

As a result of the pronounced surface roughness of CVD-diamond thin-films, large areas of the cutting material surface are covered with material deposits due to the friction tests with GD-AlSi17Cu4Mg. The intensity of the material deposits mainly depends on the roughness of the surface, which is influenced in particular by the coating thickness. The coefficients of friction are factor 3 to 4 higher than with CVD-diamond thick-film coatings.

At the tips of the diamond crystals of the thin-films, the relative movement between the frictional partners causes material to be removed from the workpiece material. The aluminum particles settle in the spaces between the crystals and, as the frictional process continues, smear the surface of the diamond coating (Figure 2). The material deposits are particularly pronounced on diamond coatings with a film thickness of $s_D = 28 \mu m$. In contrast, on diamond coatings with a film thickness of 6 μm , only isolated material particles of the workpiece material are found. The material deposits on the surface are removed from the cutting material surface and are built up anew periodically in the repeated process of frictional movement. The resulting material deposits have various degrees of thickness and are distinctly rough.

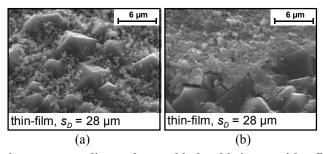


Figure 2. Adhesive wear on a diamond-coated indexable insert with a film thickness of $s_D = 28 \mu m$ after t = 200 s (a) and t = 500 s (b).

ABRASION

A modified sandblasting unit was used for the abrasion tests. The blasting angle was $\alpha = 30$ ° and the distance between the nozzle and the samples was a = 20 mm. Silicon carbide (SiC) with a grain size of 0.5 mm was used. The indexable inserts were sandblasted for a duration of t = 600 s unless the coatings failed earlier.

The CVD-diamond thin-films showed the lowest resistance to abrasion. They failed as a result of large coating areas chipping after just a few minutes of abrasive loading, which can be attributed to the coating/substrate interface

being damaged by the impact pulses (Figure 3). The diamond in this coating system, however, remains undamaged. Laser-acoustic surface measurements proved that after abrasive loading the coating adhesion had weakened. Conclusions can be drawn about the coating adhesion from the proliferation behavior of the surface waves in the material. Figure 3 shows the phase velocity c of the waves as a function of the frequency f. From the rise in the curve in the high frequency range the modulus of elasticity of a CVD-diamond coating can be calculated. The modulus of elasticity of an ideally adhered CVD-diamond coating is approximately 1100 GPa. The curves shown in Figure 3 of a diamond-coated ceramic with a film thickness of $s_D = 6 \mu m$ show a decrease in the modulus of elasticity as a function of the duration of sandblasting. Conclusions concerning the consequently not ideal and thus reduced coating adhesion can be drawn from the significantly lower moduli of elasticity after abrasive loading. Drawing quantitative conclusions about what happens to the coating adhesion is difficult with the laser-acoustic method because even slight changes in the film thickness result in major changes of the modulus of elasticity.

The weakening of the coating adhesion as an effect of the abrasive loading can be explained with the occurrence of microcracks in the substrate material. This finding is backed up by the fact that, because of its brittleness, the diamond coating is not able to reduce the pulse energy of the blasting particles but conducts it directly to the substrate. As a result, damage occurs at the exposed points in the substrate, and in particular at points in the coating/substrate transition at which the pulses of the abrasion medium impact attain their greatest effect. This is the case in particular for points of high stress and cavities. The greater number of cavities and the higher level of inherent stresses in diamond-coated cemented carbides as compared with the ceramic substrate material are the reason for their earlier failure as a result of chipping. Also, the resistance to chipping is higher for diamond coatings of greater film thickness.

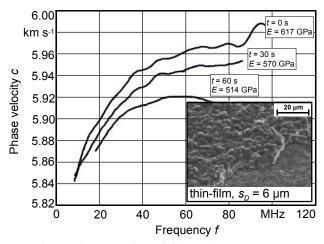


Figure 3. Changes in coating adhesion of CVD-diamond under abrasive loading.

In the tests, the CVD-diamond thick-film coating materials showed the highest resistance to abrasion. This mainly reflects the fact that the samples used were freestanding coatings and thus there was no interface to a substrate which represented the weak point for the CVD-diamond thin films. The diamond itself was not subject to any abrasive wear. In addition, there was no recognizable difference in wear resistance between the doped and the undoped material.

The sintered polycrystalline diamond with binder exhibited lower resistance to abrasion than the CVD-diamond thick-film coating materials. In particular the soft cobalt binder matrix is damaged by SiC, which causes complete diamond crystals to break out of the composite cutting material.

TRIBO-OXIDATION

Oxidation tests were carried out with heating times of t = 4 and 8 min and temperatures of T = 500 to 900 °C in an air atmosphere.

A characteristic feature of the oxidation process on diamond is the occurrence of crater structures, a roughening of the crystal surfaces and a reduction of the material's mass. The oxidation process takes place as a result of the direct reaction between diamond and oxygen. Subjected to the same loading, diamond single crystals are more temperature-stable than CVD-diamond. The reason for the lower temperature stability of the CVD-diamond compared with the single crystal lies in the higher defect concentration in the crystals and in a higher proportion of sp²-bound

carbon on the grain boundaries (ref. 7). The defect concentration is significantly determined by the speed of growth. The {111} lattice levels are the most reactive levels and they oxidize most strongly. They exhibit the highest defect concentration, which results from the high growth rate in this direction when the CVD-diamond is produced.

At a temperature below T = 800 °C and a heating time of t = 4 min, the CVD-diamond thick-film cutting materials exhibit no changes or damage to the surface of the nucleation side of the material. Nor are any differences with respect to the surface structure recognizable between the cutting materials with and without boron doping up to a temperature of T = 800 °C. The surfaces possess slight roughness and, as in the initial polished condition, no grain structure is visible. Only at a temperature of about 800 °C and after a heating time of t = 4 min does damage occur to the surface of both cutting materials. This damage differs in extent between the two materials, however.

An increase in temperature to T = 900 °C with a heating time of t = 4 min leads to complete destruction of the undoped cutting material. Its surface is badly jagged and covered with deep grooves (Figure 4a). Oxidation begins at the grain boundaries and defect areas of the material. Locally there is an increased proportion of sp²-bound carbon, which promotes the oxidation process. On the cutting material doped with boron, an oxidation front forms on the surface (Figure 4b). Here, damage also takes the form of a roughening of the surfaces.

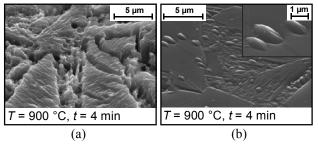


Figure 4. Oxidative wear on the undoped (a) and doped (b) CVD-diamond thick-film cutting material.

This differing behavior can be attributed to the boron doping of the one cutting material. As the content of boron increases, the fault density in the lattice levels decreases. As already described above, under thermal loading damage first occurs at these fault points. In earlier tests with CVD-diamond doped with boron, a decrease in the damage rate of the {111} lattice levels by up to 50 % was found compared with CVD-diamond that had not been doped. Boron doping of CVD-diamond therefore not only brings about electrical conductivity, but also improves the resistance to damage by thermal stresses (ref. 7).

On the thin-film cutting materials, from a thermal loading of T = 800 °C on, the corners and edges of the diamond crystals start to become rounded, which becomes even more distinct at still higher temperatures. In addition, the formation of crater-like structures is characteristic for wear by oxidation (Figure 5a). With a film thickness of $s_D = 6 \mu m$, the damage caused by oxidation starts at an earlier stage than on the 28 μm thick CVD diamond coating due to the larger number of grain boundaries. The substrate material was not observed to have any influence on the resistance to oxidation wear.

In the case of the PCD cutting material, the cobalt binder is a solvent for carbon. It dissolves diamond below the diamond melting point, which causes graphite to form at the diamond grain boundaries of the PCD material. Another problem results from the different coefficients of thermal expansion of diamond and cobalt. The varying levels of expansion lead to the formation of stress cracks (ref. 8). In contrast to the CVD-diamond cutting materials, the damage on PCD starts at a heating time of t = 4 min and a temperature of T = 600 °C as a result of the cobalt binder discharging from the surface (Figure 5b).

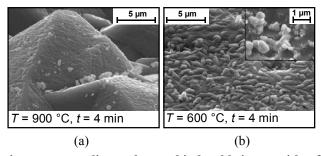


Figure 5. Oxidative wear on a diamond-coated indexable insert with a film thickness of $s_D = 28 \mu m$ (a) and PCD (b).

METAL CUTTING TESTS

To verify the model tests, the results were compared with those from metal cutting tests conducted in external longitudinal/cylindrical turning with a cutting speed of $v_c = 1200$ m/min, a feed of f = 0.1 mm, and a cutting depth of $a_p = 0.5$ mm.

The indexable inserts were of the ISO shape SPUN 120304. As wear criterion, the attainment of a width of wear land of VB = 0.2 mm was selected along with equally sized chippings of the diamond film on the coated substrates. In addition, quality deficiencies on the workpiece, such as changes in the surface finish, were taken into account when assessing the cutting ability.

Both CVD-diamond thick-film cutting materials exhibit high resistance to abrasion. This is illustrated by the only slight rounding of the cutting edge in Figure 6a. With the parameter settings presented above, a tool life of 7 min was achieved with this cutting material modification. Adhesion represented the dominating wear mechanism. In the metal cutting tests it was observed that aluminum is deposited on the flank. These aluminum agglutinations form periodically and are steadily separated from the flank of the cutting material by the continuously moving work-piece material. This effect was evidenced both by the occurrence of pronounced changes in the cutting forces and a change in the appearance of the surface. The periodically formed build-up edge on the flank causes diamond particles to become dislodged from the flank of the cutting material (Figure 6a). Significant adhesive deposits on the face or oxidation wear were not detected. There was no recognizable difference between the doped and undoped cutting material as far as tool life and the prevailing wear mechanisms were concerned.

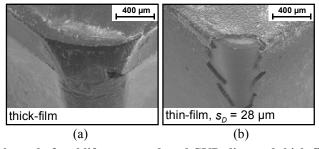


Figure 6. Signs of wear at the end of tool life on an undoped CVD-diamond thick-film indexable insert (a) and a diamond-coated ceramic indexable insert (b).

In contrast to the CVD-diamond thick-film cutting material and in addition to the same type of adhesive wear, wear resulting from oxidation and abrasion was found on the flank of the PCD material. The discharging of the cobalt binder from the cutting material surface as a result of excessive thermal loading was significant. Also, the abrasive effect of the silicon crystals in the workpiece material causes the metallic binder in the cutting material to separate. As a result, the diamond crystals lose their binding in the cutting material matrix and break out. These processes lead to a lower tool life of PCD of 5 min, compared with the CVD-diamond thick-films.

It was not possible to conduct tool life tests on cemented carbide and ceramic with CVD-diamond thin-film coatings due to the occurrence of chipping on all coating systems after cutting times of 30 s. Figure 6b shows the wear on one corner of a diamond-coated ceramic indexable insert with a film thickness of $s_D = 28 \mu m$. In addition to chipping of the coating over a large area, the material deposits occurring after just a few seconds on the face and flank are characteristic of the wear behavior exhibited by CVD-diamond thin-film coatings. Another significant disadvantage of this cutting material modification is the considerable rounding of the cutting edge as a consequence of the coating as illustrated in Figure 6b.

CONCLUSION

The results provided by the metal cutting tests confirm the findings of the model tests: A high resistance to abrasive wear and thermal loading was verified in the case of the CVD-diamond thick-film cutting materials. Like the ball-disc test, the metal cutting tests showed no significant build-up edge on the face. Adhesive material deposits on the flank, however, were found to be characteristic. To reduce these deposits it is necessary to increase the working clearance angle from the previously selected $\gamma = 6$ °. In doing so it must be taken into account that the indexable inserts may fracture as a result of the smaller wedge angle. In addition, it was found that boron doping does not have

a negative effect on the wear behavior of a CVD-diamond thick-film cutting material, but that in fact the property profile improves because of the higher resistance to thermal loading.

The polycrystalline diamond with metallic binder does not possess the performance capacity of the CVD-diamond thick-film cutting material. The model tests and also the metal cutting tests showed that PCD is inferior to the binder-free material regarding resistance to abrasion and thermal loading. The reason for this is to be found in the soft cobalt binder matrix which cannot withstand abrasive loading and high temperatures.

The main problem for the CVD-diamond thin-film coatings is the adhesion of the coating. Both in the model tests and in the metal cutting tests, none of the coating systems investigated was able to achieve satisfactory results. Moreover, the pronounced roughness of the coating and the increased rounding of the cutting edge represent a further problematic area in thin-film technology. In the future, it will be possible to help solve these problems e.g. by applying coatings which promote adhesion and by using laser post-processing techniques to impart smoothness to the coating and to reduce rounding of the cutting edge.

In particular the CVD-diamond thick-film cutting material has considerable potential to be used in the machining of high-strength and highly abrasive non-ferrous alloys thanks to its polished surface, its high resistance to abrasive and thermal loadings, and the absence of problems connected with coating adhesion.

ACKNOWLEDGMENTS

The authors express their thanks to Dr. J. Gäbler and Dr. L. Schäfer (Fraunhofer Institute for Surface Engineering and Thin Films, Germany) and H. Rabe (DeBeers Industrial Diamonds, South Africa) for providing the sample material.

REFERENCES

- 1. Hintermann, H. E.; and Chattopadhyay, A. K.: Low Pressure Synthesis of Diamond Coatings, Annals of CIRP, 1993, 42/2:769-772.
- 2. Olson, J. M.; and Windischmann, H.: The Development of High-Perfomance CVD Diamond Coated Cutting Tool Inserts, Diamond Films and Technology, 1998, 8/2:105-124.
- 3. Uhlmann, E.; Lachmund, U.; Brücher, M.: Wear behavior of HFCVD-diamond coated carbide and ceramic tools, Surface and Coatings Technology, 2000, 131:395-399.
- 4. Klocke, F.; and Krieg, T.: Coated Tools for Metal Cutting Features and Applications, Annals of CIRP, 1999, 48/2:1-11.
- 5. Yoshikawa, H.; and Nishiyama, A.: CVD Diamond Coated Inserts for Machining High Silicon Aluminum Alloys, Diamond and Related Materials, 1999, 8:1527-1530.
- 6. Tomac, N.; Tonnessen, K.; and Rasch, F. O.: Machinability of Particulate Aluminum Matrix Composites, Annals of CIRP, 1992, 41/1:55-58.
- 7. Miyata, K.; and Kobashi, K.: Air Oxidation of Undoped and B-doped Polycrystalline Diamond Films at High Temperature, J. Mater. Res., 1996, 11/2:296-304.
- 8. Bex, P. A.; and Shafto, G. R.: The Influence of Temperature and Heating Time on PCD Performance, Ind. Diamond Rev., 1984, 3:128-132.

EVALUATION OF MECHANICAL PROPERTIES OF HIGH-TOUGHNESS MULTILAYERED DIAMOND FILMS

S. Takeuchi

Nippon Institute of Technology 4-1 Gakuendai, Miyashiro, Saitama 345-8501 Japan

M. Kojima, M. Murakawa

Nippon Institute of Technology 4-1 Gakuendai, Miyashiro, Saitama 345-8501 Japan

ABSTRACT

When diamond is used as a wear-resistant material for tools, its unique wear resistance cannot be fully exploited due to the possibility of brittle fracture. In general, diamond films synthesized by the vapor phase method are polycrystalline and exhibit columnar crystal growth. In the polycrystalline structure, once cracks occur on the surface of the film, they tend to propagate through the columnar particles, leading to decreased toughness. The authors succeeded in synthesizing multilayered diamond films by repeated application of the bias-enhanced hot filament method. The multilayered films were superior in surface roughness, and the bending strength of the film was approximately 30% higher than that of a conventionally produced diamond film. In this study, we synthesized multilayered diamond film by the hot filament method using a WC-Co alloy substrate, and evaluated the adhesion strength for use in anti-wear parts.

Keywords: diamond film, multilayer, toughness, adhesion strength

INTRODUCTION

In various tools coated with diamond, the wear resistance of diamond is exploited. As the substrate for such diamond-coated tools, WC-Co alloy substrates are generally used. Since a temperature of approximately 1073 K or higher is required for the synthesis of diamond films, adhesion of the film to the substrate is decreased due to thermal stress resulting from the difference in the thermal expansion coefficient between the diamond film and the substrate. We synthesized a multilayered diamond film, in which diamond films with different crystallinities were laminated, and clarified that the toughness (bending strength) of the obtained film is approximately 30% higher than that of the diamond films obtained by the conventional method (ref. 1).

In this study, multilayered diamond films were synthesized on an WC-Co alloy substrate with variation of the substrate temperature during synthesis, and the increase of the adhesion strength of the diamond film depending on the substrate temperature was examined.

EXPERIMENTAL METHOD

Synthesis of diamond film

A hot-filament chemical vapor deposition system, as shown in Figure 1, which utilizes ethanol as the precursor was used to produce the diamond films.

Table 1 summarizes the synthesis conditions. A WC-Co alloy containing 6 wt% Co, used as the substrate, was electroetched to coarse its surface. The temperature of the substrate was controlled by a CA thermocouple in contact with the back surface of the substrate. The substrate temperature was controlled as follows (Fig. 2): nucleation stage of 1073 K, and film growth stage of 1053 K, 1063 K or 1073 K.

In order to obtain a multilayered film, approximately 50 mA bias current was turned on and off intermittently. The target coating thickness was 10 um.

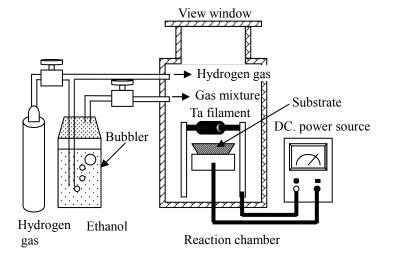


Table 1. Conditions for synthesizing diamond

Filament temperature (K)	2573 - 2673
Reaction pressure (kPa)	6.65
Flow rate of hydrogen (cm ³ min ⁻¹)	150
Concentration of ethanol in H ₂	1 – 1.5
(vol. %)	
Substrate temperature (K)	1053 - 1073
Bias current (mA)	50
Bias voltage (V)	250
Bias treatment on/off time (min)	5/60

Figure 1. Schematic view of the hot-filament chemical vapor deposition system.

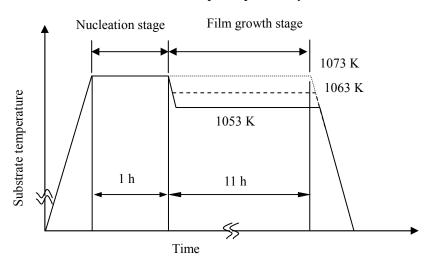


Figure 2. Substrate temperature for diamond synthesis

Table 2. Measurement conditions for X-ray diffraction

Measurement system	Iso-inclination method
Target	Cu
Voltage	30 kV
Current	8 mA
Diffraction angle	140.8 deg.
Psi angle	0, 18, 27, 33, 39, 45 deg.
Stress constant	-2589.5 MPa

Evaluation of various properties of diamond films

The residual stress of the diamond film coated on a WC-Co substrate was measured by the X-ray diffraction method. Table 2 summarizes the conditions for X-ray diffraction. For Young's modulus (E) and Poisson's ratio (ν) used to determine the X-ray stress constant, actual measured values for polycrystalline diamond, i.e., E = 1050 GPa and ν = 0.2, were used (ref. 2).

The thermal expansion coefficient of a diamond film was measured in the temperature range from room temperature to 1173 K using a free-standing diamond film of $2 \times 10 \times 0.2$ (t) mm in size. The temperature was increased by 5 K/min.

Adhesion of the film was evaluated by an indentation test using a Rockwell C-scale indenter with a tip radius of 0.2 mm. The indentation load was increased from 400 N in steps of 100 N until the diamond film broke.

RESULTS AND DISCUSSION

Figure 3 shows the SEM micrograph of a polished cross section of the multilayered diamond film. The expected multilayered structure was obtained.

Table 3 summarizes the residual stress of a single-layered film and a multilayered film, both of which were coated on WC-Co alloy substrates. The substrate temperature during film growth was 1073 K for both films. The residual stress of the single-layered film was -1925 \pm 215 MPa, while that of the multilayered film was -1665 \pm 185 MPa, which is approximately 8% lower than that of the single-layered film.



Table 3. Measured residual stress in the coated diamond films on WC-Co alloy substrate (with the scattering of stress values being treated with a statistical method)

Film structure	Residual stress	Film thickness
	(MPa)	(um)
Single layer	-1925±215	11.5
Multilayer	-1665±185	9.5

Figure 3. SEM micrograph of a polished cross section of the multilayered diamond film

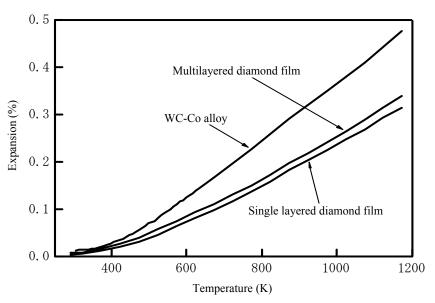


Figure 4. Measurement results of thermal expansion of various free-standing diamond films

Figure 4 shows the thermal expansion of single-layered and multilayered diamond films and WC-Co alloy. Diamond films as well as WC-Co alloy expand linearly in proportion to temperature. The average thermal expansion coefficients of WC-Co alloy, single-layered film and multilayered film in the temperature range 298 K to 1173 K are 5.626 x 10⁻⁶/K, 3.558 x 10⁻⁶/K and 3.807 x 10⁻⁶/K, respectively. In other words, the average thermal expansion coefficient of the multilayered film was approximately 7% larger than that of single-layered film. Based on this finding, the mismatch of the thermal expansion coefficients between the substrate and the diamond film, which leads

to decreased adhesion strength of the diamond film, is suppressed in the multilayered diamond film compared to the case of the single-layered film.

Figure 5 shows the results of the indentation test of the single-layered and multilayered diamond films synthesized on WC-Co substrates at the three film growth temperatures described above. With decreasing film growth temperature, both single-layered and multilayered diamond films could tolerate higher indentation load. Namely, with decreasing film growth temperature, the adhesion strength of the film increases. The following is considered as an explanation. With decreasing film growth temperature, the residual stress of the film decreases. Furthermore, when the difference in the film structure is focused on, the indentation load at which the multilayered diamond film breaks is approximately 40% higher than that in the single-layered film. The fact that the bending strength of the multilayered film is approximately 30% higher than that of the single-layered film may explain the large indentation load required for the multilayered diamond film.

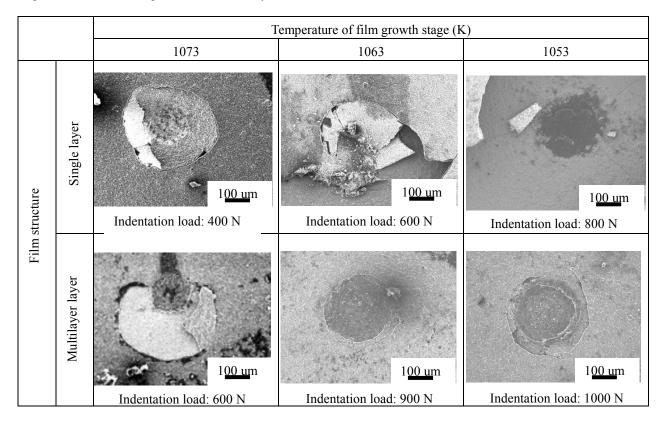


Figure 4. Results of indentation test of various diamond films

CONCLUSION

The dependence of the adhesion strength of diamond film and WC-Co substrate on the type of film structure was examined. The result indicates that when multilayered diamond film is prepared under a low film growth temperature, the adhesion strength of the diamond film increases significantly.

REFERENCES

- 1 S. Takeuchi, S. Oda, M. Murakawa: Synthesis of multilayer diamond film and evaluation of its mechanical properties, Thin Solid Films 398-399, 2001, pp238-243.
- 2 C.A.Clein, G.F. Cardiale: Young's modulus and Poisson's ratio of CVD diamond, Diamond Related Materials, 2, 1993, pp918-922.

PROCESSING OF DIAMONDS BY SHORT PULSE LASERS

H. Miyazawa and S. Takeuchi

Nippon Institute of Technology 4-1 Gakuendai, Miyashiro-machi, Minamisaitama-gun, Saitama 345-8501, Japan

> K. Shihoyama HOYA PHOTONICS CORP. 3-5-24 Hikawacho, Toda-shi, Saitama 335-0027, Japan

ABSTRACT

A study on the processing of diamonds using two kinds of short pulse lasers was conducted. Diamonds used are single crystals synthesized at high temperature and high pressure, and platelet single crystal synthesized by the chamber-flame CVD method. Polycrystalline diamond film synthesized by the CVD method was also used. ArF excimer laser with pulse width of 20 nanoseconds, and a Ti-sapphire laser with pulse width of 150 femtoseconds were used. A laser beam was introduced to focus on the surface of the specimen in air. Results obtained are summarized as follows. In excimer laser processing, (1) only a slight difference the grooving properties is observed for various single-crystal diamonds, and (2) polycrystalline diamond is processed more easily than single-crystal diamonds. In the processing using the femtosecond laser, (1) combinations of high output energy and low beam scan speed produce a high-quality groove with straight wall and sharp edge, (2) other combinations of the parameters produce grooves having defects such as crack formation and/or attachment of by-product both in and outside of the groove, or having a narrow neck on the upper portion of the groove, and (3) controlled processing conditions can realize clean processing with no heat-affected zones on the surface of the groove.

Keywords: laser processing, single-crystal diamond, polycrystalline diamond, excimer laser, femtosecond laser

INTRODUCTION

The superior characteristics of diamond in mechanical, electrical, chemical and thermal properties make it an ideal material for applications in many industrial fields. The excellent characteristics, however, make it difficult to process by conventional techniques, such as mechanical, electrical and/or chemical methods, in terms of both flexibility and productivity. However, it has been demonstrated by many researchers that the laser technique can solve most of the problems concerned (refs. 1-2). Ralchenco et al. (ref. 3) well surveyed and introduced laser processing performances of various kinds of lasers, mainly for chemical vapor deposited (CVD) diamond film. On the other hand, the improvement of the CVD technique has resulted in, for example, the successful synthesis of platelet single-crystal diamond (ref. 4) which might be used as the material for a micromachine element. Laser technology is also making progress toward producing a commercially available femtosecond (fs) laser machine. It has been reported that this laser can realize the clean processing of diamond (refs. 5-6), but details are still unknown.

This paper consists of two sections. The first section deals with ArF excimer laser processing performances of diamonds. The second section deals with grooving properties of diamonds processed using a femtosecond laser.

EXPERIMENTALS

A variety of diamonds synthesized by various methods were used as the material to be processed. They are commercially available single-crystal diamonds of facets (111), (110) and (100) synthesized by the high-temperature and high-pressure (HTHP) method, and platelet single-crystal diamond and polycrystalline diamond film both synthesized in laboratory by the chamber-flame method using acetylene as a precursor. An ArF excimer laser of 193

nm wavelength and a Ti-Sapphire laser of 775 nm wavelength were focused to irradiate the surface of diamonds in air. Experimental conditions are summarized in Table 1.

Table 1 Experimental conditions.

	Lasers used		
	ArF excimer laser	Ti-Sapphire fs laser	
Wavelength	193 nm	775 nm	
Pulse width	10 ns	150 fs	
Repetition rate	1 ~ 100 Hz	1 kHz	
Energy density (approx.)	$15, 25 \text{ J/cm}^2$	3, 6, 25, 100 J/cm ²	
Beam spot size (approx.)	3.6 μ m	$10~\mu$ m	
Beam irradiation	Raster mode	1, 5, 20, 50 μ m/s	
	(10-150 shots/spot)		
Processing atmosphere	in air	in air	
	Diamond specimen		
	Single-crystal diamonds synth	esized at high temp.& high press.	
	(111), (110), (100) (100)		
	 Polycrystalline diamond 	film synthesized by	
	chamber-flame CVD met	hod (thickness: 300 μ m)	
	Platelet single-crystal		
	diamond synthesized by		
	chamber-flame CVD method		
		•	

The morphologies of the processed surface such as the shape of the groove, presence of contaminants and/or heat-affected zone were detected and evaluated using a scanning electron microscope (SEM) and a Raman spectral analyzer.

RESULTS AND DISCUSSION

Processing of diamonds by ArF excimer laser

Figure 1 shows the effects of beam shot number N and energy density E on the grooving properties of single-crystal diamonds synthesized by the HTHP method. As shown in figure (a), the groove width differs in accordance with the facet of the diamond. The width strongly depends on E but only slightly on N. The values at $E=25 \text{ J/cm}^2$, for example, in the range from 2.7 um for (110) and (100) to 3.2 um for (111), are all smaller than the spot size of the laser beam. On the other hand, as shown in figure (b), the depth of the groove increases almost proportionally to N, during approximately the first 100 shots, and then the rate decreases gradually or approaches the values of a small range, for example, the range from 1.5 um for (110) to 1.9 um for (111) at $E=25 \text{ J/cm}^2$.

Figure 2 shows the effects of beam shot number N and energy density E on the grooving properties of various diamonds, polycrystalline film and platelet single crystal, synthesized by the chamber-flame CVD method. As shown in figure (a), the values of both N and E do not significantly influence the width of the groove processed on the surface of diamonds concerned. However, the higher E produces wider grooves, and the values obtained for polycrystalline diamond are larger than those obtained for platelet single-crystal diamond. All the values obtained are in a small range from 3.0 um to 4.3 um. Regarding the depth of the groove processed on the platelet single-crystal diamond, the increase of N does not always increase the depth particularly in the case of low E of 15 J/cm². In the case of polycrystalline diamond, however, it was found that the depth increases almost proportionally to the number of beam shots N.

Figure 3 compares the depths of the grooves processed on various diamonds. As shown in the figure, for the diamond processed at low E of 15 J/cm², the values of the groove depth for single-crystal diamonds of different facets and for platelet single crystal differ in the range of $0.6 \sim 1.5$ um. However, the figure also shows that a higher E of 25 J/cm² produces deeper grooves of approximately 1.8 um (± 0.3 um). These values are far smaller than those obtained for polycrystalline diamond, which were 3.8 um at E=15 J/cm² and 4.2 um at E=25 J/cm². The results indicate that the polycrystalline diamond can be processed more easily than single-crystal diamonds. The reason is

considered to be that the increase of laser beam absorption at grain boundaries of the polycrystalline diamond makes it easier to process than single-crystal diamonds with no grain boundary.

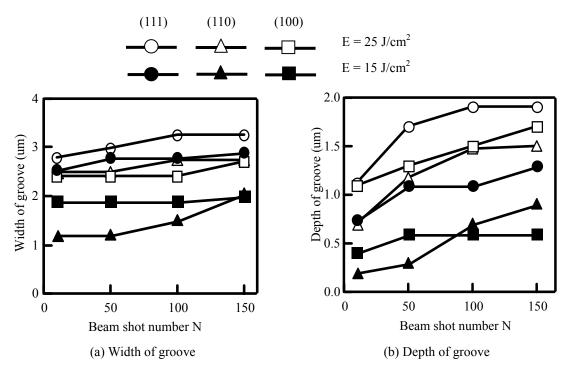


Figure 1. Effects of beam shot number and energy density on the grooving properties of single-crystal diamonds synthesized at high temperature and high pressure.

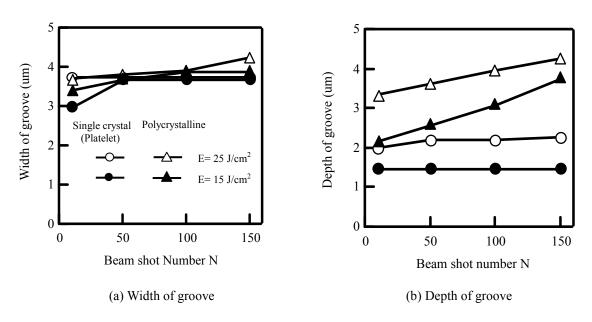


Figure 2. Effects of beam shot number and energy density on the grooving properties of various diamonds

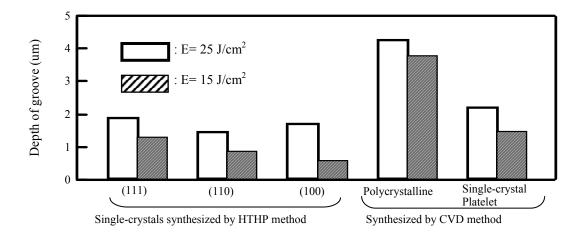


Figure 3. Comparison of the depths of the grooves processed on various diamonds (N=150).

Although not shown, Raman spectra of processed surfaces revealed the presence of a graphitic layer, as has been reported elsewhere (ref.7). Clean processing with no heat-affected zone was not possible throughout the experiment conducted.

Processing of diamonds by Ti-Sapphire fs laser

Morphology of the processed groove

Figure 4 shows typical morphologies of the groove processed on a single-crystal diamond. Processing conditions are also shown in the figure.

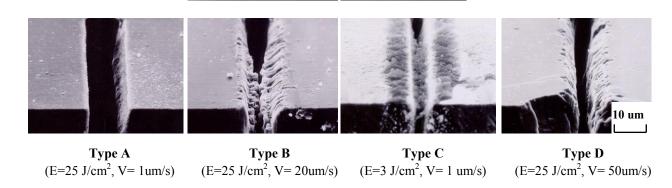


Figure 4. Typical morphologies of the groove processed on a single-crystal diamond.

As shown, the groove morphology is classified into four types, A, B, C and D. Type A is a high-quality groove with straight wall and sharp edge. Type B is a nail-shaped groove having a narrow neck on the upper portion of the groove. Type C is a narrow groove with the attachment of by-product both inside and outside of the groove. Type D is a groove with cracking along the upper groove edge.

Table 2 summarizes the influences of energy density E and beam scan speed V on the morphology of the grooves processed. In the table, Type (A) indicates that the quality of the groove is slightly inferior to Type A.

Table 2 Influences of energy density and beam scan speed on the morphology of the processed grooves.

100	A	(A)	(A)	D
25	A	В	В	D
6	(A)	В	В	D
3	C	В	D	D
E (J/cm ²) V (um/s)	1	5	20	50

As shown in the table, high-quality grooves of Type A are obtained under the conditions of high E combined with low V. Type B grooves are obtained under the conditions of E lower than 25 J/cm^2 combined with V of approximately 5 – 20 um/s. The low E combined with low V condition yields Type C grooves. A beam scan speed as high as 50 um/s always produces a Type D groove. For the processing of polycrystalline diamond, the morphologies of the groove prepared are almost the same as those obtained for single-crystal diamond but never have cracks. The reason why polycrystalline diamond never yields cracks is considered to be that the grain boundaries of the diamond interrupt the propagation of microcracks yielded at the surface processed.

Grooving property

Figure 5 shows the grooving properties of single-crystal diamond processed by fs laser.

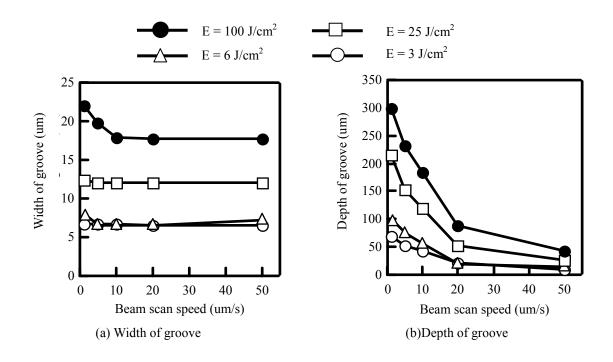


Figure 5. Grooving properties of single-crystal diamond processed by fs laser.

Figure (a) shows that the width of the groove strongly depends on the energy density E. The width differs from 6 to 22 um according to the change of the value of E from 3 to 100 J/cm². The effect of beam scan speed on the width is so small that it only changes it it from 18 to 22 um even at the highest E of 100 J/cm². On the other hand, as shown in figure (b), the depth of the groove is affected by the values of both E and V. In the case of E=100 J/cm², for example, a 42-um-deep groove is processed at V=50 um/s, and a 300-um-thick specimen is cut at V= 1 um/s.

Although not shown, the overall tendency of grooving performance of polycrystalline diamond was nearly the same as that observed for single-crystal diamond.

Results of Raman spectral analysis

As shown in Figure 4, a Type C groove as narrow as 6.5 um involves by-products both inside and outside of the groove. The Raman spectral analysis results of the by-product proved that it is amorphous carbon. However, for the grooves other than Type C, a sharp peak was detected at wave number 1333 cm⁻¹ at all surfaces of the bottom and/or wall of the groove, indicating that there are no heat-affected zones on the surfaces concerned. The reason why Type C grooves yield contamination of amorphous carbon is considered as follows. When the fs laser is focused to irradiate the surface of a diamond, a high-temperature plasma plume is generated. When the groove processed is wide and/or shallow, the generated plume is released easily from the inside of the groove which results in the processing with no heat-affected zones. On the other hand, when the groove is narrow and deep, the generated plume is restricted within the groove to heat the wall which results in the generation of amorphous carbon in and around the processed groove.

CONCLUSIONS

A study on the processing of diamonds by the usage of short pulse lasers, ArF excimer laser and Ti-Sapphire femtosecond laser, was conducted. Diamonds mainly used are single-crystal diamonds synthesized by the HTTP method, and polycrystalline diamond film synthesized by the CVD method. Results obtained are summarized as follows. In excimer laser processing, it was found that there are only slight differences in the grooving properties for various single-crystal diamonds, and that polycrystalline diamond is processed more easily than single-crystal diamond. In the processing using femtosecond laser, it was found that the combination of high output energy and low beam scan speed produces a high-quality groove with straight wall and sharp edge. Other combinations of the parameters than those described produce grooves having problems such as crack formation and/or attachment of byproduct in and outside of the groove, or having a narrow neck on the upper portion of the groove. However, there is no problem of cracking for polycrystalline diamond. It was also found that only the use of a femtosecond laser can realize processing with no heat-affected zones on the processed surfaces of diamonds.

REFERENCES

- 1. R. E. Wanger: Laser Drilling Mechanics, J. Appl. Phys., 45, 1974, 4631-4637.
- 2. H. Miyazawa, S. Miyake, et al.: Laser-Assisted Thermochemical Processing of Diamond, Appl. Phys. Lett., 64, 1994, 387-389.
- 3. V. G. Ralchenco and S. M. Pimenov: Laser Processing of Diamond Films, Diamond Films and Technology, Vol.7, No.1, MYU, Tokyo, 1997, 15-40.
- 4. K. Hirabayashi, T. Kimura and Y. Hirose: Morphology of flattened diamond crystals synthesized by the oxyacetylene flame method, Appl. Phys. Lett. 62, 1993, 354-356
- 5. P. A. Molian, R. Windholz, et al.: Femtosecond Laser Processing of CVD-Diamond, Applications of Diamond Films and Related Materials, 1995, 275-278.
- 6. M. Shirk, P. Molian, et al.: Ultra-Short Pulsed Laser Microstructuring of Diamond, Applications of Diamond Films and Related Materials, Proc. SPIE, Vol.4088, 2000, 98-101.
- 7. S. M. Pimenov, V. I. Konov, et al.: Effects of Excimer Laser Polishing on Surface Properties and Tribological Performance of Diamond Films, Diamond Films and Technology, Vol.7, No.1, MYU, Tokyo, 1997, 61-78.

A SYSTEM MADE OF DIAMOND FOR ASSEMBLING MICROELEMENTS

Yuichi NAKAZATO, Akiyoshi SEKINE, Goro SEKINE, Hajime MIYAZAWA and Sadao TAKEUCHI

Nippon Institute of Technology Miyashiro-machi, Minamisaitama-gun, Saitama Pref., 345-8501 JAPAN

ABSTRACT

Diamond is a high performance material in many ways, i.e., having mechanically the highest hardness, thermally the highest thermal conductivity, chemically high stability in various atmospheres at ordinary temperatures, and electrically high insulation. The goal of this study is to fabricate a maintenance-free micromachine system equipped with diamond elements that can work under severe conditions, in human body for example, for a long period.

As the first step of this study, the authors made a micromanipulator having diamond end effector that can handle micro elements, as small as several to several ten micrometers, made of diamond. The shape of end effector was first designed and the distribution of stress caused during its operation was simulated by the FEM method to avoid possible harmful stress concentration. Then, a homemade thick CVD diamond film was cut by YAG laser to define the final configuration of the effector. Then a coil made of a thin shape memory alloy wire, superior to electrostatic and / or piezoelectric devices in power-weight ratio and acceptable drive range, was used for the actuator. The manipulator produced worked satisfactorily to grip and locate diamond micro elements of the size described.

Keywords: CVD Diamond, YAG laser, Shape Memory Alloy, Manipulator, Assembling Microelements.

INTRODUCTION

A micromanipulator with a diamond end effector was manufactured and is reported in this paper. It is well known that many kinds of research studies related to micromachines have been conducted since the mid-1980s when semiconductor-manufacturing techniques enabled the manufacture of such devices as minute gears and motors at micrometer scale on silicon substrates (refs.1, 2). However, these manufacturing methods, which adopt a photofabrication technique, have a disadvantage in that they can create only planar machines through two-dimensional processes. Thus, the development of a system which can be applied to the construction of three-dimensional micromachine has been urgently requested.

To solve the above-mentioned problem, the authors fabricated a micromanipulator that can handle microelements of micromachine systems. After discussing the basic design of the manipulator, i.e., designs of the gripping style, mechanism for operation, and materials for the end effector and actuator, a micromanipulation system having a diamond end effector actuated by a shape-memory alloy coil was constructed. The performance of the system was evaluated through the measurement of the frequency of the open-close operation and gripping force, and based on the ease of actual operation.

BASIC DESIGN OF MICROMANIPULATOR

Gripping style

The present status of the technique for handling a minute element is as follows. In the electronics industry, in the arrangement of IC components for cellular phone units for example, major change was required not for the handling system, but for the end effector, because the size of the components is bigger than several hundred micrometers. Then, a system which is designed to handle components of centimeter or ten-centimeter size can be modified by installing an end effector which can deal with smaller elements of the size described (ref.3). A typical end effector used in the system is the vacuum gripper which hold and arrange components by vacuum suction (ref.4). In the medical and molecular biological fields, cells and/or cell nuclei of various sizes from submicrons to several hundred microns are the objects to be handled. In this case, a thin glass tube with negative pressure achieved

by the usage of a syringe is employed to aspirate the target matter together with liquid and insert it to the position required.

These manipulation systems using suction techniques have disadvantages such as difficulty in the control of the holding force and holding position, which are required for the construction of micromachine systems, and the area required for the system is large. In this study, to overcome the problems described above, a mechanical gripping system with small fingertips which allow arrangement, connection and/or insertion of microelements for the construction of micromachine systems is fabricated.

Mechanism for operation

A mechanical end effector requires a link mechanism composed of revolving pairs and sliding pairs. However, the decrease in the size of the system cause an increase of friction and surface tension, resulting ultimately in the decrease of the performance of the system. To overcome this problem, some researchers have introduced link mechanisms with elastic hinges that do not contain revolving or sliding pairs (ref.5). These mechanisms, however, have problems in the amount of displacement, buckling due to load, and lifetime of the system. However, when such mechanism is applied to micromachines, the size effect decreases the influences of gravity and inertia, making these problems negligible. Thus, in this study, we decided to develop an end effector composed of a single elastic hinge mechanism that does not involve any revolving or sliding pairs.

Material for end effector

Silicon and its compounds are generally used as the materials for micromachine systems mainly because of their ease of manufacturing. However, it is important to understand that after the micromachine system is constructed, it is difficult, or sometimes even impossible, to disassemble it and replace parts in the system because of its small size. Therefore, the system must be maintenance free. From this point of view, selection of the material used is important. The material should have high mechanical strength and hardness with a low friction coefficient, and high chemical stability. We have selected diamond as the most suitable material for micromachine systems (ref.6). However, the hardness of diamond elements precludes the use of end effectors made of materials other than diamond for a long period. Hence, we decided to use diamond film as the end effector material.

Actuator for end effector

For the actuation of the end effector, such methods as the use of electrostatic force (ref.7) or piezoelectric elements (ref.8) have been studied. Since an end effector with electrostatic force is similar to the vacuum gripper in its gripping style, it is not suitable for assembling elements of various sizes. Piezoelectric elements have a limited holding area and the size acceptable to grip. To overcome these problems, in this study, SMA (shape-memory alloy) was selected as the actuator material of the end effector. The material can be controlled flexibly, making it easier to control the gripping force. Regarding the slow speed of action, which is regarded as the greatest disadvantage of this material, the scale effect, i.e., minimizing the size of the end effector, increases the cooling efficiency, which will result in the improvement of the performance. The manuscript elements have been formatted using the "styles" capability of Microsoft Word. To use the styles, select the text to which you wish to apply a style, then go to the style box on the toolbar. Click once on the downward pointing arrow to the right, and select the appropriate style.

MICRO-MANIPULATOR SYSTEM BASIC DESIGN OF MICROMANIPULATOR

Overview of the system

The system consists of $\hat{\imath}$) an end effector to grip micro elements, $\hat{\imath}$) a SMA coil actuator used to open and close the fingers of the end effector, $\hat{\imath}$) an electromotive drive unit for rough positioning of the end effector, $\hat{\imath}$) a hydrostatic drive unit for precise positioning of the end effector, and $\hat{\imath}$) an optical telescopic microscope to observe the relative positions of the element to be gripped and the fingertips of the end effector, and the gripping operation.

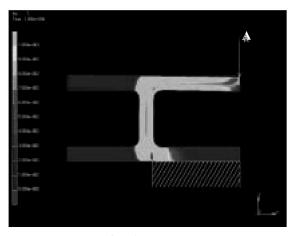
Design of end effector

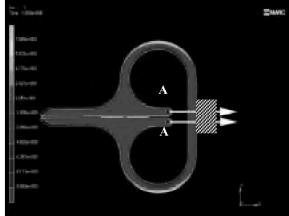
While diamond has many superior characteristics, as described above, because of its high/low ductility, stress concentration should be avoided as much as possible when it is subjected to large elastic deformation. Therefore, we calculated the elastic deformation and stress concentration using the finite element method (FEM) and determined the final shape and sizes. Figure 1 shows the results of the elastic analysis. In the FEM analysis, parameters listed in Table 1 were used, and the hatched area in Fig. 1 was constrained as boundary conditions; the

stress and amount of displacement when an identical force was applied to point A are shown. For the FEM analysis, we used the analytical software "Marc" (Analyze Co.). As shown in Figure. 1 (a), high stress concentration occurs in the hinge of the simple "H" shaped end effector. This shape does not accommodate a large amount of displacement of the fingers. On the other hand, as shown in Figure. 1 (b), no stress concentration is observed in this shape, indicating that this shape allows a larger amount of displacement of the hinge made of diamond film

Table 1 Parameters used in FEM analyses of stress distribution and deformation of end effector

Young's modulus	1050[GPa]
Poisson's ratio	0.25
Thickness	50[f m]
Temperature	25[•]





(a)Before improvement

(b) After improvement

Fig. 1 Results of FEM analysis

Preparation of end effector

Figure 2 shows the end effector made of diamond film according to the shape design described shove. The small hole "B" seen in the photograph is used to connect the end effector to the actuator with a thin wire. A 100- μ m-thick CVD (chemical vapor deposition) diamond film made by us was used as the material for the end effector. A Qsw-YAG laser machine was used to contour-cut the film into the designed shape. The detail of the techniques for synthesizing CVD diamond film and laser cutting of the film are reported elsewhere (refs.9,10).

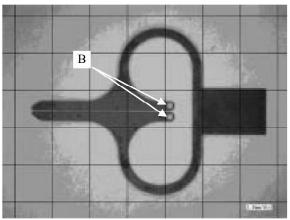


Fig.2 End effector made of diamond film

Design of actuator

Table 2 shows the specifications of the SMA actuator. We selected Nitinol (Ti-Ni system) wire out of approximately ten types of SMA materials because it has excellent mechanical characteristics as well as chemical stability. Coils of this material are commercially available. The diameter of the wire is 75 μ m and the memorized shape is set to be a coil of outer diameter 300 μ m. The direction of memory is one way and the shape recovery temperature (Af temperature) is 60 $^{\bullet}$. Figure 3 shows (a) the schematic illustration and (b) a photograph of the arrangement of the end effector and actuator. The end effector is fixed at the end of a hold bar and is connected to the actuator, also fixed at the bar, via a thin stainless steel wire. The original position of the actuator is controlled and set precisely by using an adjust screw. Since the shape-memory effect of the actuator is one directional, the contracting force of the actuator is used for the closing operation, while the elasticity of the diamond film is used for the opening operation of the end effector. Although not shown in the figure, the actuator is connected to an electric power supply unit which generates PWM (pulse width modulation) voltage to heat the actuator or SMA coil. The holding power of the end effector is controlled by the amount of Joule heat generated at the actuator.

SMA wire

Material:Nitinol(Ti:50,Ni:50[at%])
Diameter:50 µm

Memory shape
Linear

Memory direction
Shape recovery
temperature
(Af temperature)

Material:Nitinol(Ti:50,Ni:50[at%])
Diameter:50 µm

Linear

60 [c]

Table 2 Specifications of SMA actuator

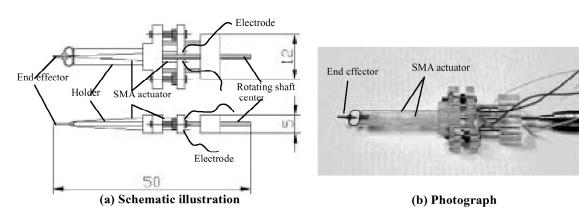


Fig.3 End effector system

PERFORMANCE TEST

Experimental apparatus and conditions

In order to evaluate the performance of the end effector quantitatively, the following measurements were conducted: i) measurement of gripping force, ii) measurement of action speed, and iii) measurement of possible holding area. Figure 4 shows the system for the measurement of gripping force. One of the fingers of the end effector was connected, through a small hole "B" shown in Figure. 3, to a load cell using a stainless steel wire as thin as $50~\mu m$. A PWM modulated electric voltage was supplied to the SMA actuator to drive the end effector, and the data obtained were sent to the load tester.

Experimental results

Table 3 shows the performance of the end effector fabricated. It was found that the frequency of the open-close operation is as slow as 1 to 1.2 Hz. However, the range of grippable size is as wide as 10 to 50 μ m, which is wider

than the range of any other microactuator described in Section 1. Furthermore, a gripping force as high as 100 mN, a large value considering the small size of the end effector, was obtained.

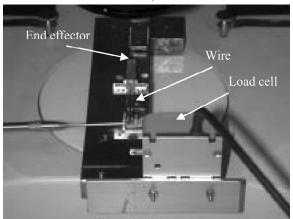


Fig.4 Experimental apparatus to measure the gripping force

Table 3 Performance of the end effector fabricated

Frequency of open-close operation at room temperature	1~1.2 [Hz]
Gripping force [max]	100~300 [mN]
Size acceptable to grip	10~40 [μm]

In order to evaluate the performance of the fabricated micromanipulator system through actual performance, we attempted to arrange many micro-diamond grains. Here, the size of diamond grains were 10 to 40µm in diameter. Figure 5 shows the diamond grains arranged using the end effector system shown in Figure. 3 (b). The system worked very smoothly to grip, carry and position the grains of diamond as shown in the figure.



Fig.5 Diamond grains arranged using fabricated micromanipulator system

CONCLUSION

A micromanipulation system having an end effector made of thick diamond film combined with an actuator made of SMA coil was constructed. The shape of the end effector was first designed and the distribution of stress during its operation was simulated by the FEM method to avoid possible stress concentration, followed by Qsw-YAG laser contour-cutting of a thick CVD diamond film to define the final configuration of the effector. Then the performance of the system was evaluated quantitatively. The system functioned satisfactorily to grip and position diamond grains from 10 to $40~\mu m$ in diameter.

ACKNOWLEDGMENTS

We appreciate the support provided by High-Tech. Research Project from the Ministry of Education, Culture, Sports, Science and Technology.

REFERENCES

- 1. L.S.Fan, Y.C.Tai and R.S.Muller, 1988, "IC-processed Electrostatic Micro-motors," 1988 IEEE Int. Electr. Devices. Meeting, pp.666-669.
- 2. M.Mehregany, S.F.Bart, L.H.Lang, S.D.Senturia and M.F.Schecht, 1989, "A Study of Three Microfabriated Variable-capacitance Motoers, Transducers'89, B5.3.
- 3. Horie Mikio, Ikegami K. and Wittenburg J., 1996, "New Micromachine Elements "Super-Elastic Hinge" and its Application to Three-Dimensional Micromeshanisms," Proc. Of International Conference of Machine Design and Deveropment, Miskolc, Hungary, pp.120-121.
- 4 K.Sato, "In Vitro Fertilization of Hamster Eggs by Miacroinjection of Rabbit Apermatozoa," J. Mamm. Ova Res., vol.16, No.2, pp.89.
- 5. Howell L. L. and Midha A., 1996, "A Loop-Closure Theory for The Analysis and Synthesis of Compliant Mechanisms," ASME, J. of Mechanical Design, pp.121-131.
- 6. Sadao Takeuchi, Hajime Miyazawa and Masao Murakawa, 2000, Synthesis of Flat Diamond for Micromachine System," Proc. of Autumn Meeting of the Japan Society for Precision Engineering, p.473.(in Japanese).
- 7. K. Furuta, 1999, "Experimental Processing and Assembling System (Microfactory)," The fifth International Micromachine Symposium, pp.173-177.
- 8. S.Takahashi, 1985, "Multilayer Piezoelectric Ceramic Actuators and Their Applications," Jpn. J. Appl. Phys. Vol.24, Suppl. 24-2,pp.41-45.
- 9. M. Murakawa and S. Takeuchi, 1993, "Fabrication of Diamond Coated Cutting Insert Using an Improved Atmospheric Chamber Flame Method, Diamond Films and Technology," vol.2, No.4, pp.189-199.
- 10. Hajime Miyazawa, Shojiro Miyake, Shuichi Watanabe, Sadao Takeuchi, Toshiyuki Miyazaki and Masao M Murakawa, 1995, "Laser Microcontouring of Diamonds," Proc. of ICALEO'95, pp.381-390.

MICROCUTTING OF DURALUMIN USING FOCUSED-ION-BEAM-PROCESSED PROFILE CUTTING DIAMOND BITES

Hiroyuki Noguchi, Sadao Takeuchi and Masao Murakawa

Nippon Institute of Technology 4-1 Gakuendai, Miyashiro, Saitama 345-8501 Japan FAX: +81-0480-33-7592 PHONE: +81-0480-33-7592

E-mail: hnoguchi@nit.ac.jp

ABSTRACT

Single-crystal diamond bites can be used for ultrahigh-precision cutting of noniron metal materials because diamond has high hardness, stiffness and wear resistance. However, the diamond bite itself is processed using microdiamond particles, thus the shapes of the bite are limited to those using straight lines and simple circular arcs. In recent years, since the spot diameter of the iron beam of focused ion beam (FIB) devices has been reduced substantially, nanosize processing of various materials has become possible. In microcutting, it is possible to manufacture fine axes by sharpening blade edges and reducing cutting resistance. On the basis of this observation, we applied FIB to the finishing and shaping of the cutting edge of diamond bites. Using FIB-processed diamond bites, we manufactured a microshaft of 5 µm diameter by lathe turning of duralumin. Furthermore, using a diamond tool whose edge had been sharpened by FIB, we succeeded in producing a highly accurate notch with 3 µm depth in the microshaft.

Keywords: FIB, Focused Ion Beam, Diamond bite, 3-D shapes, nano technology

INTRODUCTION

Diamond has been widely used as a material of microcutting tools used for nonferrous metal. However, the tool tip radii of commercially available diamond lathe cutting tools are too large to machine fine shaft to microsize (microshaft, hereafter). In this study, we carried out micromachining of diamond micro tool and notch cutting of diamond using a FIB device with which the micromachining of diamond is possible. In this experiment, commercially available diamond bites, the cutting edges of which have been subjected to finishing, were compared with unfinished bites in order to confirm the efficacy of FIB devices.

EXPERIMENTAL METHOD AND EXPERIMENTAL APPARATUS

In the machining of the microshaft, first, the tip of the commercially available diamond needle with a small tip radius was machined into a flat bite to suppress bending of the material due to cutting resistance by decreasing the area of the contact point. Figures 1 and 2 show the images of a FIB-processed diamond needle and the shape of the machined needle tip, respectively. The length of the cutting face is 4 µm and the clearance angle is 20°.

Next, two types of bite were prepared. The first bite was obtained as follows: The cutting edge of a commercially available diamond bite was sharpened from the back surface of the bite by FIB. The second bite had the same shape as the first one but was obtained without any sharpening processes. Using the two bites, microaxes and micronotches were produced and their accuracies were determined. The FIB process was carried out from the back surface of the diamond bite to prevent the shear droop of the edge of the diamond bite due to beam scattering.

An FIB device (Hitachi High Technologies, FB-2100) was used for machining and observation of the bites, and extra super duralumin A7075 was used as a work material.

Figure 3 shows a diamond bite with a sharpened edge, Fig. 4 a conceptual diagram of edge sharpening, and Fig. 5 a prototype lathe cutting apparatus.

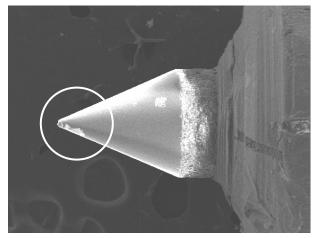


Figure 1 FIB-processed diamond needle

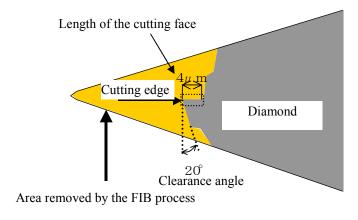


Figure 2 Shape of the machined tip of the diamond needle

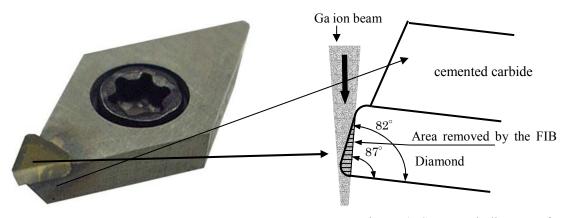


Figure 3 Diamond bite with sharpened cutting edge

Figure 4 Conceptual diagram of cutting-edge sharpening

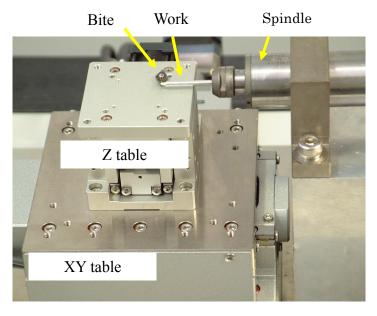


Figure 5 Exterior appearance of a machining apparatus using a diamond bite with a sharpened cutting edge

EXPERIMENTAL RESULTS

Figure 6 shows an example of a microshaft machined using a commercially available diamond bite with a tip radius of 30 μ m. The machining limit that can be applied to the microshaft was a diameter of 10 μ m. As shown in Fig. 6, when the microshaft was machined using a bite with a tip radius of 30 μ m, the area of the cut point was large, and the rotational frequency of the principal axis was 45,000 min. Under these conditions, the cutting speed was extremely low (1.4 m/min), therefore the work material bent and broke during machining.

On the other hand, when the diamond needle with a sharpened cutting edge was used (the radius of the cutting edge was approximately zero μ m), a microshaft with a tip diameter of 5.2 μ m was obtained (Fig. 7). Since the cutting speed was low (0.7 m/min), it was impossible to obtain an axis with a smaller diameter.

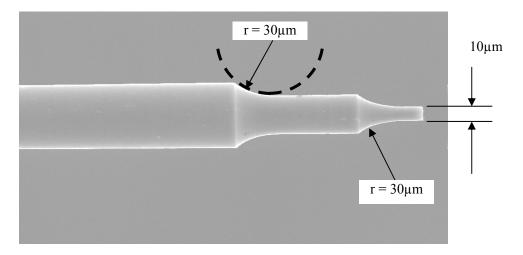


Figure 6 Example of a microshaft of 10 μm diameter that was machined using a commercially available diamond bite with a tip radius of 30 μm

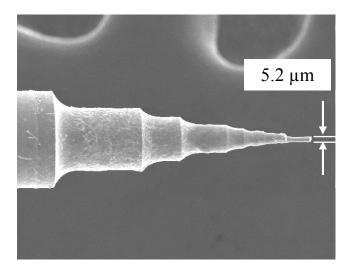
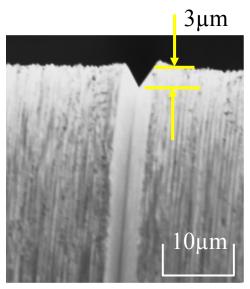
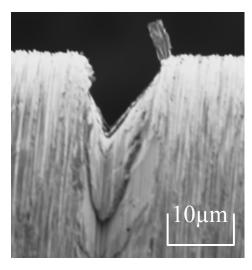


Figure 7 Example of a microshaft of 5.2 μm diameter that was machined using a bite obtained by FIB processing of a diamond needle

Figure 8 shows a comparison of the notches obtained using (a) a diamond bite with an included angle of 60° and a FIB-sharpened cutting edge, and (b) a commercially available diamond bite without a sharpened cutting edge. In the notch cutting of an axis with 100 μ m diameter using a diamond bite with a FIB-sharpened cutting edge, a highly accurate notch with 3 μ m depth was obtained; also, the surface morphology of the notched surface was good. However, when a commercially available diamond bite was used, it was impossible to obtain an accurate notch with 3 μ m depth; rather, a much deeper notch was obtained during a subsequent notch cutting process. Also, the surface morphology of the notch was inferior to that of the notch obtained using the bite with a sharpened edge. Based on these findings, we confirmed that there is a significant difference in depth accuracy between the notches obtained using the two bites.



a) Notch obtained using a diamond bite with a FIB-sharpened edge



b) Notch obtained using a commercially available diamond bite

Figure 8 Comparison of notches (workpiece: duralumin)

Next, an experiment in which notch cutting and sharpening of the cutting edge using a FIB-processed diamond bite with a 90° included angle was carried out for a duralumin axis of $15~\mu m$ diameter obtained by fine-axis machining. Figure 9 shows a schematic diagram of the duralumin axis subjected to sharpening of the cutting edge and notch cutting and Fig. 10 shows an image of the obtained axis. Since the cutting speed is low (2 m/min), sufficient machining was not possible even when the FIB-processed diamond bite was used.

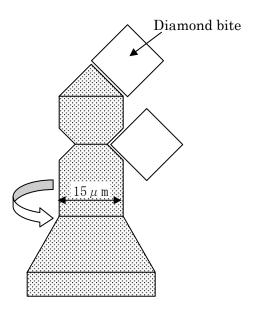


Figure 9 Schematic diagram of the duralumin microshaft subjected to edge sharpening and notch cutting

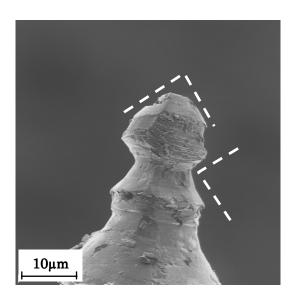


Figure 10 Comparison of the results of cutting experiments (workpiece : duralumin)

CONCLUSIONS

Diamond tools have been widely used as microcutting tools. We considered that the cutting performance of diamond lathe cutting tools can be improved by reducing cutting resistance through (1) prevention of shear droop by polishing the cutting edge using the FIB process and (2) decreasing the area of the cut point. Comparative experiments were carried out. Results indicated that we succeeded in machining microaxes of $5.2 \mu m$ diameter. Furthermore, it was possible to obtain a highly accurate notch with a depth as small as $3 \mu m$. In the future, we are planning another experiment in which cutting is performed while the cutting tools are subjected to ultrasonic vibration in order to obtain a more accurately cut surface.

FORMATION OF FLAT POLYCRYSTALLINE DIAMOND SURFACE BY ION BEAM ETCHING

Takatoshi Yamada

Institute of Multidisciplinary Research for Advanced Materials, Tohoku University,

2-1-1, Katahira, Aoba-ku, Sendai, Miyagi 980-8577, Japan

Atsuhito Sawabe

Department of Electrical Engineering and Electronics, Aoyama Gakuin University,

6-16-1, Chitosedai, Setagaya, Tokyo 157-8572, Japan

ABSTRACT

CVD polycrystalline diamond thin film was etched by Ar ion beam in order to form flat diamond surface.

Beam incident angle and etching time were used as parameters. The etched surface was characterized by SEM

and by 3-D morphological measurement system. It was found although the etching time of 50h was needed, the

relatively flat surface was obtained.

KEY WORDS: flat surface, Ar ion beam etching, polycrystalline diamond surface

1. INTRODUCTION

Although flat diamond surface is required in order to use CVD diamond films for practical devices,

as-deposited CVD diamond surface obtained by conventional CVD method was rough due to polycrystallinity.

Ion beam etching (IBE) is expected to be one of the most appropriate techniques to form the flat diamond

surface, since IBE enables to perform the uniform and the anisotropic etching for broad area (ref 1). Geis et al.

reported that high etching rate (280nm/min) of single crystal diamond using ion beam assist etching where NO₂

was used as reactive gas (ref. 2). However, it was reported that the grain boundaries and non-diamond carbon

components were etched faster than diamond where etching gas contained O (ref. 3). Therefore, it seems to be

not appropriate for gas containing O to use etching of CVD polycrystalline diamond. In this paper, Ar ion beam

is used to form flat polycrystalline diamond surface, and beam incident angle and etching time are used as

parameters.

2. EXPERIMENTAL

CVD polycrystalline diamond films were etched by Ar ion beam, and Kaufman type ion source was used in this study. The etching conditions were as follows; Ar pressure was $3.2 \times 10^{-2} \text{Pa}$, the beam current density was 2.0mA/cm^2 , the accelerated voltage was 500V, the sample temperature was kept at 10 °C. The sample was rotated (2rpm). The beam incident angles from normal to diamond surface were 0 and 80deg. The etching time was used as a parameter.

CVD diamond (3x3mm²) deposited on Si substrate by dc plasma CVD method was used (ref. 4). The obtained film was identified polycrystalline diamond by means of RHEED, XRD and Raman spectroscopy. The film thickness of CVD diamond was estimated to be 20 µm from SEM observation.

The surface morphologies before and after etching were observed by SEM. The average surface roughness (Ra) and maximum difference in height (Rz) were calculated by 3D morphological characterization system (Sanyu Denshi) which is interlocked with SEM. Au thin film in 10nm thickness was coated on diamond surface in order to characterize Ra and Rz. The measurement area was $20x20\mu m^2$.

3. RESULTS AND DISCUSSION

The changes in Ra, Rz and surface morphology for the beam incident angles of 80 and 0deg. are shown in Fig. 1 and 2. It is found from Fig. 1 that both Ra and Rz decrease with increasing the etching time, and that .the surface morphology after the etching of 50h [Fig. 1(d)] shows the relatively flat surface

As for the beam incident angle of 0deg. (Fig. 2), the smallest Ra and Rz are obtained after 10h etching. It was reported that grain boundaries were selectively etched using O plasma (ref. 3). In SEM images, such selective etching is not observed. However, craters are observed in Fig. 2 (c). The etching mechanism of polycrystalline diamond has not clarified, it is considered that the formation of craters is due to defects in CVD diamond.

It took longer time to form flat polycrystalline CVD diamond surface under the condition of beam incident angle of 80deg. However, decreasing of the etching time to obtain small Ra and Rz is expected by controlling the etching time and beam incident angle from the results of Ra and Rz measurements. It is found that IBE is one of the most appropriate techniques to form flat polycrystalline diamond surface.

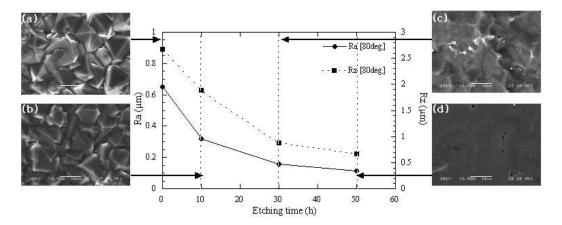


Fig. 1. The changes in Ra, Rz and the surface morphology for the beam incident angle of 80deg.

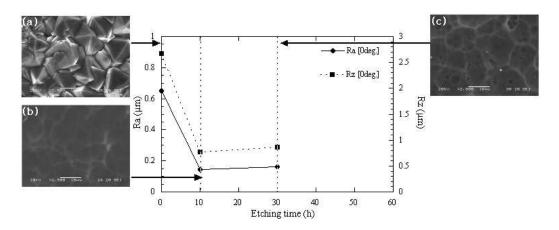


Fig. 2. The changes in Ra, Rz and the surface morphology for the beam incident angle of 0deg.

4. SUMMARY

IBE was used to form flat polycrystalline CVD diamond surface. Ra, Rz and the surface morphology strongly depended on the beam incident angle and etching time. Under the etching conditions of beam incident angle of 80 for 50h, the smallest Ra and Rz were obtained, and the relatively flat surface was formed

REFERENCES

- 1. C. J. Mogab, in VLDI technology, Ed. S. M. Sze, McGraw-Hill (1983).
- 2. N. N. Efremow, M. W. Geis, D. C. Flanders, G. A. Lincoin and N. P. Ecoomou, J. Vac. Sci. Tecnol. B3, (1985), pp. 416-418.
- 3. M. Hata, M. Kamo and Y. Sato, New Diamond 12 (1996) pp.12-17 [Japanese].
- 4. K. Suzuki, A. Sawabe and T. Inuzuka, Appl. Phys. Lett. 53 (1987) pp. 1818-1820.

ELECTRICAL DISCHARGE MACHINING USING ELECTRICALLY CONDUCTIVE CVD DIAMOND AS AN ELECTRODE

Kiyoshi Suzuki¹, Manabu Iwai², Anurag Sharma¹, Tetsutaro Uematsu², Kazuo Shoda¹, Masanori Kunieda³

¹ Department of Systems Engineering, Nippon Institute of Technology Miyashiro, Saitama 345-8501, Japan

² Department of Mechanical Systems Engineering, Toyama Prefectural University Kosugi, Toyama 939-0398, Japan

³ Department of Mechanical Systems Engineering, Tokyo University of Agriculture & Technology Koganei, Tokyo 184-8588, Japan

ABSTRACT

In order to improve EDM operation efficiency and accuracy along with the possibility of realizing a good quality EDMed surface, electrically conductive thick CVD diamond film was employed for the very first time as an electrode in die sinking EDM operation. This CVD diamond film of 0.5mm thickness, having a very high coefficient of thermal diffusivity and a low specific resistance suitable for carrying out EDM operation, has recently become commercially available. Die sinking EDM on high speed steel (SKH51, HRC63) was performed using this electrically conductive CVD diamond film as an electrode.

Significantly high stock removal rate can be achieved along with virtually no wear of the CVD diamond electrode using kerosene oil as working fluid for various pulse durations at reversed polarity (workpiece: negative). The EDM can be performed at high current densities (~10A/mm²), which are impossible with copper and graphite electrodes. Significantly high stock removal rate of 0.11mm³/min along with an insignificant amount of electrode wear shows an excellent possibility of successful application of the CVD diamond electrode at reversed polarity. On the other hand, when this electrically conductive CVD diamond is used as a workpiece in EDM with the diamond or copper electrode, an excellent shape control along with insignificant amount of electrode wear can be achieved. From the overall results of the experiments it can be concluded that the electrically conductive CVD diamond film has a great future potential application as an electrode material in micro EDM.

Keywords: EDM, electrically conductive CVD diamond, electrically conductive CVD diamond electrode

1. INTRODUCTION

General demands for electrical discharge machining (EDM) are (1) improvement of efficiency, (2) improvement of accuracy, (3) improvement of surface integrity, (4) reduction of electrode wear, (5) ability of EDM on large areas, (6) correspondence to complicated shapes, (7) correspondence to micro processing and (8) EDM of hard-to-work materials. In order to cope with above demands, various countermeasures have been adopted. With respect to EDM machines, the typical countermeasures are improvement of response by adopting high response CNC systems, improvement of electrical discharging ability and stiffness by adopting engineering ceramic material in construction of parts of EDM machines, and adoption of high frequency electric power source. With respect to working fluid for EDM, improvement of insulating property of both oil and water, development of special oil mixed with electrically conductive particles for quasi-mirror surface finishing and others have been realized. Regarding electrode materials, however, copper, graphite, Cu-W and Ag-W materials still prevail, and proposal for new electrode materials is very scarce (ref. 1).

One of the authors pointed out that the ideal electrode material should possess high electrical and thermal diffusivity along with a high melting point (ref. 2). In this research, the authors have focused their attention on electrically conductive CVD diamond, which possesses superior thermal diffusivity, and they have investigated the electrical discharging ability of the electrically conductive CVD diamond when used as an electrode in EDM.

2. Potential of electrically conductive CVD diamond as an electrode material

2.1 Commercially available electrically conductive CVD diamond

Thick CVD diamond film possessing sufficient electrical conductivity was manufactured recently by doping boron during CVD process and it is commercially available from Element Six (ref. 3). This new type of diamond film can be cut to desired shapes using a wire cut EDM process by users themselves. The diamond film cut with a wire cut EDM has been mainly used up till now as a cutting tool tip possessing very high anti-wear property. However, in this research an attempt is made to use this CVD diamond film as an electrode for electrical discharge machining.

2.2 Features of the electrically conductive CVD diamond film

The properties of the electrically conductive CVD diamond film used for the experiment are listed in **Table 1**. The electrically conductive thick CVD diamond film shows a rather low specific resistance of $\rho \le 0.4 \sim 1 \times 10^{-3} \Omega \cdot m$. This low resistance opens a possibility of its application as an electrode in EDM. Along with this, a very high thermal diffusivity of the order of $k=0.23\sim0.28\times10^{-3} \text{m}^2/\text{s}$ may be of great advantage in dissipating the heat generated in the working zone during EDM within a very short time. Moreover, the electrically conductive diamond electrode can be formed to almost any desired shape by using simple EDM such as wire-cut EDM, whereas normal diamond shapes can be formed only by using diamond grits. Also, this diamond electrode possesses a very high hardness, which is thought to be advantageous in the case of ED dressing of super-abrasive metal bonded wheels.

	•		
Material	Electrically conductive CVD diamond	Copper	Graphite
Specific resistance (Ω·m)	$\approx 0.4 \sim 1 \times 10^{-3}$	17×10 ⁻⁹	14×10 ⁻³
Specific gravity	≈ 3.5	9.0	1.8
Young's modulus (N/m ²)	$\approx 1000 \sim 1100 \times 10^9$	1054×10 ⁹	-
Thermal conductivity (W/m·K)	≈ 400 ~ 500	400	75
Coefficient of thermal expansion	$\approx 0.9 \sim 1.1 \times 10^{-6}$	17×10 ⁻⁶	-
Thermal diffusivity (m ² /s)	$\approx 0.23 \sim 0.28 \times 10^{-3}$	0.12×10 ⁻³	0.15×10^{-3}

Table 1. Properties of electrically conductive CVD diamond.

3. EDM experiments using a diamond electrode

3.1 Experimental setup and parameters

An electrically conductive thick CVD diamond film segment of 5mm×6mm×0.5mm is mounted on the head of a die sinking EDM machine by means of a jig as shown in **Fig. 1**. The workpiece material is high speed steel (SKH51, HRC63, JIS G4403) and a special kind of kerosene (Vitol 2, Sodick) is used as working fluid for the EDM process. **Table 2** lists the experimental conditions.

3.2 Comparison of EDM properties under recommended conditions with existing electrode materials Copper and graphite electrodes were used to collect equivalent data for comparison with the results of the CVD diamond electrode. EDM conditions recommended for a copper electrode and a graphite electrode in EDM on a

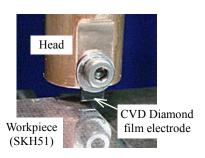


Figure 1. Experimental setup on EDM machine.

Table 2. Experimental conditions.

EDM machine	Die sinking EDM machine (A35R, Sodick)		
EDIVI IIIaciiiiic	<u> </u>		
Working fluid	Oil (Vitol 2, Sodick)		
	Electrically conductive CVD diamond film		
Electrode	(CVDITE-CDE, 5×6×0.5mm, Element Six)		
Electione	2. Copper (10×10×0.5mm)		
	3. Graphite (5×6×0.5mm)		
Workpiece	High speed steel (SKH51-JIS G4403, HRC63)		
	$u_i = 90, 120V$		
	$i_e = 1.5, 2, 3, 4, 6, 8, 16A$		
EDM conditions	$t_e/t_o = 2/4\mu s$, $6/6\mu s$, $6/50\mu s$, $12/7\mu s$, $12/10\mu s$,		
	20/15µs, 20/20µs, 30/30µs, 60/60µs		
	EDM time = 10 minutes		

working area of $3\text{mm}\times0.5\text{mm}$ without electrode wear were applied. EDM conditions recommended for a copper electrode are open circuit voltage of u_i =90V, discharge current of i_e =1.5A, discharge duration of t_e =20 μ s, pulse interval time of t_o =15 μ s (long pulse) and reversed polarity (workpiece: nagative). EDM conditions recommended for a graphite electrode are u_i =90V, i_e =1.5A, t_e/t_o =12/7 μ s and reversed polarity. EDM was continued for 10 minutes in all cases. The performance of the diamond electrode was compared under the above-recommended conditions for copper and graphite electrodes respectively.

The results are shown in **Fig.2**. Under the conditions recommended for the copper or graphite electrode, the material removal rate in the case of the diamond electrode is nearly half comparing with the copper or graphite electrode, but the shape and quality of EDMed groove are superior in the case of the diamond electrode. Electrode wear is almost nil in the case of the copper and diamond electrodes, but in the case of the graphite electrode, electrode wear of $56\mu m$ is observed for the EDMed depth of $270\mu m$.

	Condition recommended for copper electrode (90V/1.5A, t _e /t _o =20/15µs, 10min.)		Condition recommended for graphite electrode (90V/3A, t _c /t _o =12/7μs, 10min.)	
	Diamond electrode	Copper electrode	Diamond electrode	Graphite electrode
EDMed workpiece surface (SKH51)	500μm EDMed depth: 350μm	EDMed depth: 630μm	EDMed depth:135μm	EDMed depth: 270μm
Electrode surface after EDM	lmm Wear: nearly zero	Wear: nearly zero	Wear: nearly zero	Wear: 56µm

Figure 2. Comparison of CVD diamond electrode with copper and graphite electrodes. (t_e: discharge duration, t_o: pulse interval time, Working area: 3mm×0.5mm, Reserved polarity, EDM time: 10min.)

3.3 Comparison under short pulse condition

An experiment for comparing the effect of short current pulse on the EDM efficiency was performed. It is quite well known that the use of short pulse improves the EDMed surface quality. The EDM conditions used are u_i =120V, i_e =4A, t_e/t_o =6/50 μ s, reversed polarity and machining time of 10 minutes. The electrode materials used for comparison are copper, graphite and CVD diamond. The results of this experiment are shown in **Fig.3**. In the case of the diamond electrode a very high EDMed depth of 600 μ m can be observed along with a very small amount of wear of the electrode. On the contrary, in the case of both copper and graphite electrodes, a very small depth less than 85 μ m can be EDMed along with a lot of wear of the electrode.

3.4 Performance of diamond electrode under various current and pulse conditions

EDM experiments were performed to study the effect of varying current densities and pulse conditions for the diamond electrode on the EDM efficiency. The first experiment was performed under the current values of 3, 6, 9, 12 and 15A. The second experiment was performed under the different pulse conditions of $t_c/t_o=6/6$, 12/10, 20/15, 20/20, 30/30, 60/60µs. The results of the experiments are shown in **Figs.4** (a) and (b). It is observed that the EDM efficiency increases along with the increase in current density and also that a significantly high amount of current density ($\sim 10 \text{A/mm}^2$) can be given to the diamond electrode. The efficiency of diamond electrode, however, remains nearly constant for the different pulse conditions. This is quite different from the behavior of generally used electrodes. For example, EDM using a copper electrode shows a very large variations in efficiency with changes in pulse times, i.e the efficiency deteriorates to a very large extent when a short pulse condition of $t_c/t_o=6/50\mu s$ is used as shown in Fig.3. **Figure 5** shows a comparison of the EDM efficiency between the diamond and copper electrodes until the EDMed depth of 0.2mm at $t_i=90V$, $t_e=3A$, $t_e/t_o=6/6$, 20/20µs, reserved polarity.

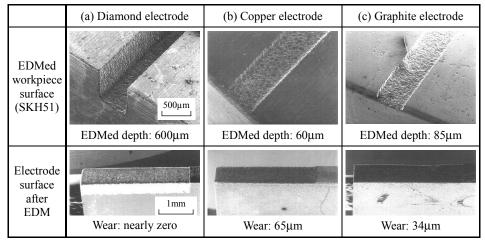


Figure 3. Comparison of EDM efficiency among electrode materials under short pulse condition. (u_i=120V, i_e=4A, t_e/t_o=6/50μs, Working area: 3mm×0.5mm, Reversed polarity, EDM time: 10min.)

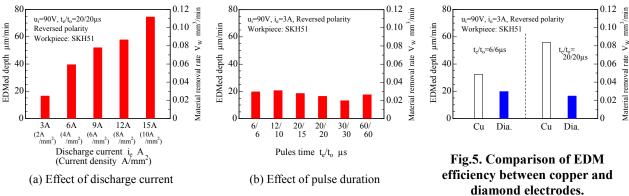


Fig.4. Performance of diamond electrode under various EDM conditions.

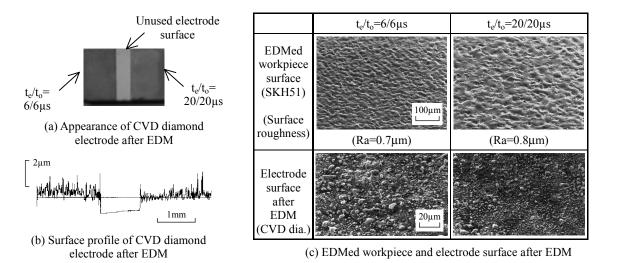


Figure 6. EDM on a large surface area. (u_i=120V, i_e=4A, t_e/t_o=6/50μs, Working area: 5mm×2.5mm, Reversed polarity)

3.5 EDM on a large surface area

EDM was performed on a large surface area (5mm×2.5mm) of high speed steel using the electrically conductive CVD diamond as an electrode. EDM was performed under two pulse conditions, the first condition was a short pulse of t_e/t_o =6/6µs and the second condition was a long pulse of t_e/t_o =20/20µs. Reversed polarity was used. **Figure 6** shows the results of this experiment. The surface of the electrode after EDM in the case of the short pulse condition appears to be coarser than the surface in the case of the long pulse condition. But the craters on the EDMed workpiece surface appear to be smaller in size for the short pulse condition compared to the long pulse condition. On close observation of the CVD diamond electrode surfaces, small globular particles appear to be attached to the surfaces. These particles appearently appear to be the debris of the workpiece getting attached to the electrode surface during EDM.

4. EDM of electrically conductive CVD diamond

Experiments for investigating the effect of EDM on the electrically conductive CVD diamond as a workpiece were performed. Two electrode materials, copper and electrically conductive CVD diamond, were used for the experiments. Two experiments were performed under the conditions of u_i=90V, i_e=1.5, 3A, t_e/t_o=6/6, 20/15μs, reversed polarity and machining time of 10 minutes. In the first case, a channel shape was EDMed on the CVD diamond workpiece as shown in **Fig.7**. The results are shown in **Figs.8** and **9**. In the case of the diamond electrode, negligibly small amount of wear is observed, whereas in the case of the copper electrode a comparatively high amount of wear is observed. The EDM efficiency of the CVD diamond electrode is slightly higher in the three cases as shown in Fig.8. In the second case, stepped shapes with depth of each step of 0.1mm were EDMed on the CVD diamond workpiece. The results of this experiment are shown in **Fig.10**. The electrode wear in the case of the copper electrode is about 10μm for each step, whereas in the case of the diamond electrode almost no wear is observed. In another case, micro holes (φ 0.3mm) were EDMed on the CVD diamond workpiece using a copper electrode. The results are shown in **Fig.11**. In this case it is observed that a very good shape control of the EDMed holes is maintained. The low amount of wear of the CVD diamond electrode is a very important property while performing micro EDM operations in which the wear of the electrode leads to a considerable amount of dimensional error.

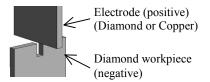


Figure 7. Schematic illustration of experiment.

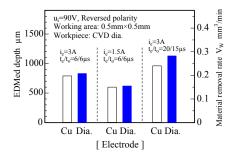


Figure 8. EDM efficiency of copper and diamond electrodes on EDM of CVD diamond workpiece.

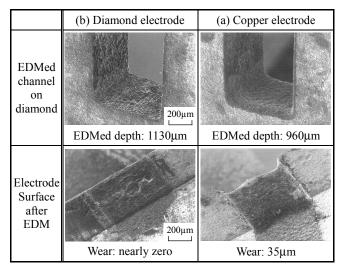


Figure 9. Channel shape EDM of CVD diamond workpiece. $(u_i=90V, i_e=3A, t_e/\tau_o=20/15\mu s, Working area: 0.5mm×0.5mm, Reversed polarity, EDM time: 10min.)$

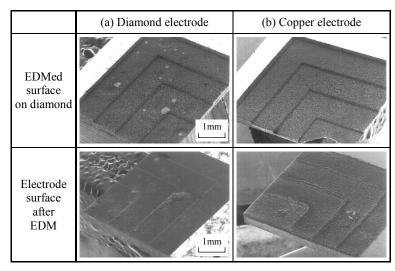
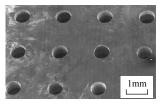


Figure 10. EDM of stepped shape on CVD diamond workpiece. $(u_i=90\text{V}, i_e=3\text{A}, t_e/t_o=20/15\mu\text{s}$, depth of step=0.1mm, reversed polarity)



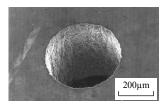


Figure 11. Micro hole EDM of CVD diamond.

(Cu electrode (φ 0.3mm), u_i=90V, i_e=1.5A, t_e/t_o=20/20μs)

5. Conclusions

- 1. The first attempt to perform EDM operation using a recently developed electrically conductive thick CVD diamond film as an electrode was successfully made.
- 2. Significantly high stock removal rate of the order of 0.11mm³/min can be achieved along with nearly zero electrode wear in EDM of high speed steel at a reversed polarity (workpiece: negative) under short pulse and high current density conditions.
- 3. Very low amount of wear of the CVD diamond electrode is observed on comparison with copper and graphite electrodes under their respective recommended EDM conditions. This low electrode wear can prove very useful especially in manufacturing micro parts.
- 4. A very high current density of the order of 10A/mm² which is impossible in the case of copper and graphite electrodes can be applied to the electrically conductive CVD diamond electrode.
- 5. EDM efficiency does not change significantly with pulse condition, which is quite different from conventional electrode materials like copper and graphite.
- 6. The electrically conductive CVD diamond, when used as a workpiece in EDM, can be machined to give a high degree of dimensional control, which indicates a possibility of manufacturing CVD diamond electrodes of different shapes for micro EDM.
- 7. Overall conclusion is that the electrically conductive thick CVD diamond film has a great potential for use as an EDM electrode material in the near future.

The authors would like to express their heartfelt thanks to Element Six Limited and Sodick Co., Ltd. for their kind cooperation.

REFERENCES

- 1. K.Masui, H.Minami, H.Tsukahara, H.Hagino, M.Ishibashi, T.Yamamoto: EDM Machinability of Zn-alloy for Die Making, Journal of Electrical-Machining Technology, Vol.23, No.75 (1999) pp.25-28. (in Japanese)
- 2. Heng Xia, M.Kunieda, N.Nishiwaki: Simulation of Electrode Surface Temperature in Die-Sinking EDM Process, International Journal of Electrical Machining (IJEM), No.4 (1999) pp.13-18.
- 3. Element Six Limited, Catalog

WEAR BEHAVIOR OF THIN CVD DIAMOND FILMS DURING THE INTERRUPTED CUT

Eckart Uhlmann, Rouven Kott

Technical University Berlin, Institute for Machine Tools and Factory Management Pascalstrasse 8-9, D-10587 Berlin, Germany

ABSTRACT

CVD diamond films are often used as wear protection for cutting tools. During the machining of non-ferrous metal alloys nano- and microcrystalline CVD diamond films reduce abrasive wear due to their inherent hardness. In many applications this coating technology has the potential to replace conventional polycrystalline diamond (PCD) with binder as cutting material. As opposed to PCD, CVD diamond not only offers outstanding properties but also has a high geometrical flexibility regarding the tools to be coated when deposited as a thin film. However, in the past adhesion problems of CVD diamond films have limited their application range. This becomes especially evident during machining in the interrupted cut. Recent developments in the tool coating industry such as customized pre-treatment methods of the substrate have led to CVD diamond films with improved film adhesion. Hence this paper discusses the wear behavior of newly developed CVD diamond films during face milling of the aluminum cast alloy G-AlSi7Cu4Mg. In addition to the cutting experiments to separately investigate the adhesive and abrasive wear behavior of the films model tests were performed.

Keywords: Production process, tool coating, CVD diamond, face milling.

INTRODUCTION

The machining of high quality components, which mostly consist of difficult-to-machine materials, is characterized by the fact that essential operation times normally determine the manufacturing costs. This means that great potential for an economic manufacture is to be found in the advancement of the machining processes, the machines and especially the tools and hence the cutting materials. Due to its outstanding characteristics in many applications, diamond as a coating on the edge of machining tools offers the chance for a considerable increase of tool lives. The extreme hardness of diamond as a cutting material is required for the machining of highly abrasive non-ferrous materials such as hypereutectic aluminum silicon alloys. CVD diamond as a thin film enables the manufacture of diamond tools with an outstanding geometrical flexibility. Despite its potential, this CVD technology has been rarely applied in industry so far. However, CVD diamond coated tools have been tested in the past for numerous machining operations of highly abrasive materials (ref. 1). Frequently, tool failure due to poor coating adhesion was observed (ref. 2). To overcome this problem extensive research has been carried out to develop suitable pre-treatment methods for the substrate (ref. 3). This paper discusses the wear behavior of different industrially available CVD diamond films which were deposited on indexable inserts by two job coaters. The diamond coated tools differ with respect to coating thickness and diamond morphology. In the following the cutting tool materials are characterized and classified by means of wear model tests and machining of G-AlSi17Cu4Mg in the interrupted cut.

CUTTING TOOL MATERIALS

Three CVD diamond coatings deposited by two job coaters A and B with a film thickness s_D of 8 µm, 15 µm (A) and 20 µm (B) were tested. In all cases the substrates used were indexable inserts of the geometry SEHT 1204 AFN according to ISO 1832 as depicted in fig. 1a and were made of carbide grade K10. In the following the diamond coated tools are referred to as CVD 8, CVD 15 and CVD 20 with respect to their film thickness. The uncoated tools were labeled as K10 according to the carbide grade. The cutting edge roundness r_{β} was measured by means of a light microscope at cross-sections prepared by electrical discharge machining. The results listed in fig. 1a indicate that the cutting edge roundness is governed by the film thickness. The sum of the initial cutting edge roundness r_{β} , of the substrate and the film thickness s_D roughly gives the cutting edge roundness r_{β} .

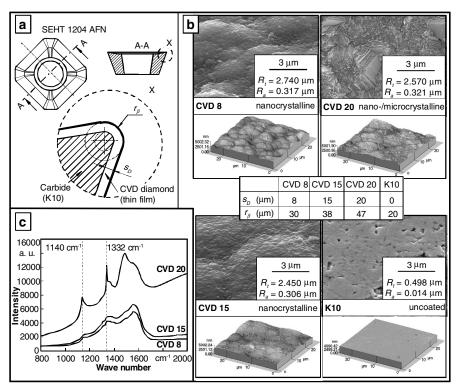


Figure 1. (a) Tool geometry, (b) cutting edge roundness, surface roughness of the CVD diamond coated tools and (c) Raman spectra of the diamond films.

The CVD diamond films differ regarding their surface topography as depicted in fig. 1b taken by means of a scanning electron microscope (SEM). CVD 8 and CVD 15 show typical features of nanocrystalline CVD diamond whereas CVD 20 shows both nano- and microcrystalline structures on the surface. The polished surface of the uncoated carbide K10 is depicted for comparison. Raman spectroscopy is a common method to determine the structure of carbon films (ref. 4). For this, the Raman spectra of the different CVD diamond films were measured using a laser with a wave length of 488.12 nm. The Raman spectra in fig. 1c reveal the typical feature for nanocrystalline diamond which is a peak at a wave number of 1140 cm⁻¹ (ref. 4). In the case of CVD 20 the characteristic diamond peak at 1332 cm⁻¹ could be observed. This peak was less distinct but still visible for CVD 8 and CVD 15. Atomic force measurements (AFM) were conducted to evaluate the surface roughness values R_t and R_a which are given in fig. 1b. Despite the differences in the optical appearance of the coated tools CVD 8, CVD 15 and CVD 20 the surface roughness was found to be similar with R_t and R_a of about 2.5 μ m and 0.3 μ m whereas the uncoated tool has a much smoother surface with R_t lower than 0.5 μ m and R_a of 0.014 μ m.

MODEL WEAR TESTS

The planning of manufacturing processes can be efficiently assisted by means of computational methods to predict the tool's performance such as thermal and mechanical tool loads. The finite element method has become a useful tool to simulate cutting processes (ref. 5). However, this method requires material data of the cutting tool material to allow a realistic estimation of tool loads and tool life. For this, the knowledge about predominant wear mechanisms of the cutting tool material as well as contact conditions in the tool/work piece contact zone are essential. During the machining of hypereutectic aluminum silicon alloys the cutting tool is subjected to a combination of adhesive and abrasive wear. In order to separately investigate the adhesive and abrasive wear resistance of the uncoated and different CVD diamond coated carbide tools friction and sand blasting tests were conducted.

Friction tests

The adhesive wear resistance of CVD diamond films can be evaluated by means of friction tests. The frictional partners are either ball and disk (ref. 6) or pin and disk (ref. 7 and 8). The disk performs either an oscillatory or a rotary motion during the test. The ball or pin shaped counterpart is pressed against the disk with a normal force F_N . In this study friction tests were performed using a ball-on-disk tribometer. The disks were made of the cutting tool materials CVD 8, CVD 15, CVD 20 and K10, whereas the ball material was the hypereutectic aluminum silicon alloy G-AlSi17Cu4Mg. During the tests the frictional force F_R was measured by means of a dynamometer that uses the piezo-electrical principle. The coefficient of friction (COF) was calculated as the ratio of the frictional force F_R and the normal force F_N . The total friction time t_f for each experiment was 5 min. The final state of the cutting tool surface was documented by means of SEM images.

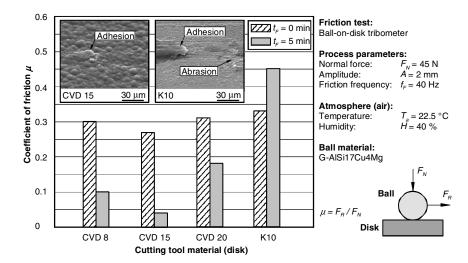


Figure 2. Results and conditions of the friction tests with respect to the coefficient of friction.

The test conditions and the results for all cutting tool materials at the beginning and the end of the tests are given in fig. 2. In all cases the initial COF at $t_f = 0$ min was between 0.27 and 0.33. However, a variation of the COF over time could be observed. For all CVD diamond films a decrease in COF was characteristic. CVD 15 reached a COF of less than 0.05 after a friction time of about 4 min. The measured coefficients of friction agree well with the observations made by means of SEM, where only little adhesive wear in the form of ball material depositions could be detected for the diamond coated surfaces. In the case of the uncoated carbide K10 the COF reached 0.45 for $t_f = 5$ min. The surface of K10 showed adhesive as well as abrasive wear scars.

Sand blasting tests

The abrasive wear resistance of CVD diamond films is often evaluated by means of sand blasting tests (ref. 9). In some cases grinding wheels are used in combination with bound (ref. 10) or unbound (ref. 11) abrasive media.

The process parameters for the sand blasting tests are the abrasive medium, the nozzle diameter d_N , the angle of impingement α_s , the working distance l_N and the air pressure p_S . In the case of thin CVD diamond films the abrasive particles often cause severe damage to the diamond/substrate interface during impact leading to a sudden chipping of the coating. This becomes especially evident for blasting at large angles of impingement, in which case the test results reflect the quality of the interface or film adhesion rather than the abrasive wear resistance. In this study a precision sand blasting device with a nozzle diameter d_N of 1mm was used. The abrasive was SiC with a particle size ranging from 63 μ m to 106 μ m. The air pressure before the nozzle p_S was 6 bar. The nozzle was positioned above the specimen with a working distance l_N of 2 mm at an angle α_S of 30 °.

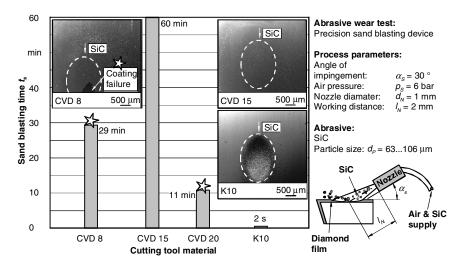


Figure 3. Results and conditions of the sand blasting tests.

The mass loss over sand blasting time t_s is a common evaluation criterion for the abrasive wear resistance of a material (ref. 9). However, the small quantity of abraded material under the testing conditions used did not allow this procedure. Therefore, the abrasive wear resistance was evaluated by the sand blasting time t_s until a failure of the diamond film occurred. Smoothing of the diamond film was observed as the characteristic wear behavior for CVD 8, CVD 15 and CVD 20. Fig. 3 shows the final state of the abraded surfaces of CVD 8 and CVD 15 for comparison of K10 after $t_s = 2$ s. The SEM images reveal an instant damage of the uncoated carbide, whereas the diamond coated surfaces offer enhanced resistance against the abrasive particles. However, coating failure as depicted in fig. 3 occurred for CVD 8 and CVD 20 after a blasting time of 29 min and 11 min, respectively. CVD 15 outperformed CVD 8 as well as CVD 20 since no exposure of the substrate material was visible after $t_s = 60$ min. This leads to the conclusion that the abrasive wear resistance is influenced by the coating thickness as well as the morphology of the CVD diamond. The nanocrystalline CVD 8 and CVD 15 show stronger abrasive wear resistance than the micro- to nanocrystalline morphology of CVD 20.

CUTTING EXPERIMENTS

Face milling tests according to ISO 8688-1 were performed to evaluate the tool life during dry machining of the hypereutectic aluminum silicon alloy. Also, the characteristic wear behavior of CVD diamond coated tools was documented by means of SEM. The work piece material G-AlSi17Cu4Mg existed as rectangular test bars of $150 \times 30 \times 70 \text{ mm}^3$. The machining parameters and the experimental set-up are given in detail in fig. 4. The machining condition chosen represents a typical roughing operation which strongly stresses the tool due to the high abrasiveness of the work piece material on the one hand and the high dynamical stresses caused by the interrupted cut on the other hand. The tool life criterion for the diamond coated tools was defined as the point of time where the first coating chippings occurred. For the uncoated tools a width of wear land of VB = 0.2 mm was chosen as the tool life criterion. The tools were examined at intervals of 0.15 m for the total machined length L by

means of an optical microscope in order to detect chippings of the diamond films or to measure the width of wear land VB. The experimental results for the different cutting tools in fig. 4 show that the mean values of tool life for the diamond coated tools are significantly higher than for the uncoated tool. Also, a large scatter in L values for CVD 20 is noticeable. CVD 15 showed the best performance with an average L of 2.7 m and a comparably low standard deviation of 0.38 m as opposed to 2.14 m for CVD 20.

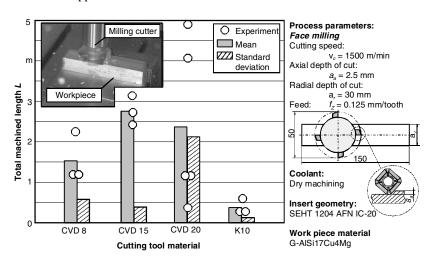


Figure 4. Results and machining conditions of the sand blasting test with respect to the tool life.

Fig. 5a to 5d show the typical wear patterns observed for the cutting tool materials during the machining tests. The main cutting edge of CVD 8 is shown for a total machined length of L = 1.2 m in fig. 5a. The tool life criterion was reached as the diamond film was continuously abraded and the substrate surface was exposed. A smooth transition between the exposed substrate and the intact diamond film could be observed. In the case of CVD 15 the coating as well as the substrate failed after machining L = 2.7 m as depicted in fig. 5b. Fatigue failure of the substrate underneath the diamond film was probably caused by the high dynamical loads during the interrupted cut. In the case of CVD 20 the diamond film locally chipped off the substrate. The wear pattern shown in fig. 5c for L = 4.1 m indicates that high dynamical loads weakened the interface diamond/substrate which then led to large area chippings of the diamond film on the tool's rake face. The cutting edge of the uncoated carbide K10 was instantly attacked by the abrasive Si particles of the work piece material. The loss of geometrical integrity was reached after a machining length of L = 0.3 m.

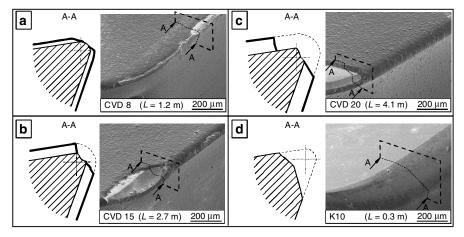


Figure 5. SEM images of the worn cutting edges for (a) CVD 8, (b) CVD 15, (c) CVD 20 and (d) K10.

CONCLUSIONS

Three CVD diamond films deposited on carbide indexable inserts have been subjected to wear model tests and face milling of G-AlSi17Cu4Mg. The wear mechanisms leading to a failure of the coating were found to vary for different coating thickness and diamond morphology.

The frictional behavior of the cutting tool materials against G-AlSi17Cu4Mg was tested by means of a ball-on-disk tribometer. The coefficient of friction was found to be similar for all cutting tool materials in the early stage of the test. However, due to different adhesive wear mechanisms on the tool surface the contact conditions changed leading to a variation in the coefficient of friction over time. A decrease in the coefficient of friction for the diamond coatings was caused by abrasive wear and therefore flattening of the ball. The degree of adhesion of ball material on the disk surface governs the resulting coefficient of friction. The adhesive wear of the diamond films was negligible which led to a reduction of the coefficient of friction over testing time.

No large area chippings of the CVD 8 and CVD 20 films occurred during sand blasting. This indicates good adhesion properties of the diamond films to the substrate. It could be observed that the larger coating thickness of CVD 15 compared to CVD 8 positively affected the abrasive wear resistance. Despite the coating thickness of 20 μ m the abrasive wear resistance of CVD 20 was found to be the lowest of all diamond films tested. This can be attributed to the microcrystalline morphology of CVD 20. Coarser diamond crystals promote the propagation of cracks initiated by the abrasive particles towards the interface diamond/substrate. In the case of nanocrystalline diamond structures of CVD 8 and CVD 15 the surface was smoothened in the early stage hindering further crack propagation (ref. 12).

The results of the cutting experiments were in good agreement with the results of the wear model tests. A large scatter in the tool life for CVD 20 might be attributed either to weak adhesion properties of the diamond film or to a lower fatigue strength of the microcrystalline diamond structure.

REFERENCES

- 1. Uhlmann, E., Lachmund, U., Brücher, M.: Wear behavior of HFCVD-diamond coated carbide and ceramic tools, Surface and Coatings Technology, vol. 131, 2000, pages 395-399.
- Fernandes, A.; Neves, A.; Silva, R. F.; et al.: Evaluation of MPCVD Diamond Film Adhesion on Hard Metal Substrates by Micro Raman Spectroscopy. Diamond and Related Materials, vol. 6, 1997, pages 769-773
- 3. Tönshoff, H. K.; Mohlfeld, A.; Gey, C.; et al.: Mechanical Pretreatment for Improved Adhesion of Diamond Coatings. Surface and Coatings Technology, vol. 116-119, 1999, pages 440-446.
- 4. Hollmann, P.: Micro- and Nanocrystalline Diamond Coatings with Extreme Wear Resistance and Ultra Low Friction. Acta Universitatis Upsaliensis, Comprehensive Summaries of Uppsala Dissertations from the Faculty of Science and Technology 325, 1997.
- 5. Yen, E.; Söhner, J.; Altan, T..; et al.: Estimation of tool wear in metal cutting with the finite element method. CIRP Workshop on Modelling, Purdue, USA, 2002.
- 6. Bhushan, B.; Subramaniam, V.V.; Malshe, A.; et al. :Tribological properties of polished diamond films. J. of Applied Physics, vol. 15, 1993, pages 4174-4180.
- 7. Niedzielski, P.; Miklaszewski, S.; Beer, P.; et al.: Tribological properties of NCD coated cemented carbides in contact with wood. Diamond and Related Materials, vol. 10, 2001, pages 1-6.
- 8. De Barros, M.I.; Vandenbulcke, L.; Bléchet, J.J.: Influence of diamond characteristics on the tribological behaviour of metals against diamond-coated Ti-6Al-4V alloy. Wear, vol. 249, 2001, pages 68-78.
- 9. Amirhaghi, S.; Reehal, H.S.; Plappert, E.; et al.: Growth and erosive wear performance of diamond coatings on WC substrates. Diamond and Related Materials, vol. 8, 1999, pages 845-849.
- 10. Gahlin, R.; Alahelisten, A.; Jacobson, S.: The effects of compressive stresses on the abrasion of diamond coatings. Wear, vol. 196, 1996, pages 226-233.
- 11. Alahelisten, A.: Abrasion of hot flame-deposited diamond coatings. Wear, vol. 185, 1995, pages 213-224.
- 12. Gunnars, J.; Alahelisten, A.: Thermal stresses in diamond coatings and their influence on coating wear and failure. Surface and Coatings Technology, vol. 80, 1996, pages 303-312.

New Diamond Coated Carbide Dental Bur in Operation

Htet Sein 1, Wagar Ahmed *1, Mark Jackson 2, Ricardo Polini 3

¹Department of Chemistry and Materials, Manchester Metropolitan University, Chester Street, Manchester M1 5GD, UNITED KINGDOM

²Department of Mechanical Engineering, Tennessee Technological University, P.O box.5014, Cookeville, TN 38505, UNITED STATES of AMERICA

³Dipartimento di Scienze e Tecnologie Chimiche, Universita' di Roma "Tor Vergata" Via Della Ricerca Scientifica, 00133 Roma, ITLY

> *¹Corresponding author: <u>w.ahmed@mmu.ac.uk</u> Tel: +44-161-247-1423, Fax: +44-161-247-6357

Abstract

Depositions of hot filament chemical vapour deposited (HFCVD) diamond on cobalt-cemented tungsten carbide (WC-Co) rotary cutting dental burs are presented. Conventional dental tools made of sintered polycrystalline diamond (PCD) have a number of problems associated with heterogeneity of the crystallite, decreased cutting efficiency and short life. A preferential (111) faceted diamond has been obtained after 15 hours deposition at a growth rate of 1.1µm/hr. Diamond coated WC-Co dental burs and conventional sintered burs are mainly used in turning, milling and drilling operation for machining metal ceramic hard alloys such as cobalt-chrome, composite teeth and aluminum alloy in dental laboratory. The influence of structure, mechanical characteristics of both diamond grains and hard alloys on the wear behaviour as well as the regime of grinding on diamond wear are considered. Erosion wear properties are also investigated under air-sand erosion testing method. After machining with excessive cutting performance, calculations can be made on flank and crater wears areas. Diamond coated WC-Co dental bur offered significantly better erosion and wear resistance compared to uncoated WC-Co tools and sintered burs.

Keywords: Wear, Diamond, HFCVD, Cutting tools

1. Introduction

Diamond films are of interest for tribological applications because of their high hardness, low friction coefficient, high wear resistance and chemical inertness [1]. Diamond coatings are used in cutting tools and biomedical applications. At the present time, the most widely used dental diamond burs are manufactured by imbedding diamond particles onto a metal matrix using a suitable binder containing nickel ions. Those burs have several limitations mainly due to the heterogeneity of diamond crystallites, contamination of oral tissue and variation in the product performance. There is no universal specification of the diamond particles sizes imbedded into the binder matrix in order to ensure repeatable and consistent cutting performance. Recently, CVD has been used for the fabrication of new dental burs [2] with continuous diamond film offering improvement in cutting efficiency and longer life. Much of the work on the CVD of diamond has been carried out on flat substrates. Although, cutting tools such as drills and inserts have been successfully coated with diamond-based coatings; there are only a few reports of diamond deposition onto rotary cutting tools, such as cylindrical abrasive pencils and small spiral drills [3]. In this study, we report the deposition of uniform diamond films onto the cutting edges of Co cemented WC-Co dental burs used in dental laboratory and clinical surgery using a modified hot-filament chemical vapour deposition (HFCVD) system. The filament is mounted in a vertical arrangement with the dental bur held concentrically in between the filament coils, as opposed to the horizontal position commonly used in the HFCVD system configurations. This new vertical filament arrangement used in the modified HFCVD system enhances the thermal distribution and ensures uniform diamond coating [4].

In this paper we report the results of our investigation on diamond films deposited on WC-Co dental burs and micro tools using a HFCVD system and subsequent machining results on extracted human teeth, Cobalt-Chromium hard metal alloy, borosilicate glass and porcelain teeth. The Co cemented dental burs operate at extremely high cutting speeds in the range between 10,000 to 300,000 r.pm [5]. Such high operating speeds impose stringent demands on the cutting surfaces and the coating deposited. The coating deposited is required to be tough, adherent, hard and wear resistant in order to enhance overall tool performance and lifetime.

2. Experimental

2.1 Substrate Preparation

The (WC- 6 wt.% Co) dental bur used were 20-30 mm in length and 1-1.5 mm in diameter. Prior to diamond deposition the dental burs were ultrasonically cleaned in acetone for 10 minutes to remove any surface impurities. The poor adhesion of deposited diamond films onto cemented tungsten carbide surfaces can lead to catastrophic film failure in metal cutting due to presence of Co binder [6]. The Co binder suppresses diamond nucleation and causes deterioration of diamond film adhesion [7]. To eliminate this problem, it is usual to pre-treat the WC-Co dental bur surface prior to CVD diamond deposition. The WC surface has etched away with Murakami solution and surface Co has removed by acid etching followed by ultrasonically washed in distilled water [8].

2.2 CVD diamond deposition

Diamond synthesis was performed in a stainless steel HFCVD chamber of internal diameter of 200 mm. The gas phase mixture of hydrogen (purity, 99.99%) and methane (purity, 99.99%) with CH_4/H_2 volume ratio fixed at 1.0% (1.0 % CH_4 with excess hydrogen) was activated by tantalum filament (0.5 mm in diameter) wound in a 10 mm internal diameter spiral. The dental bur was positioned centrally and coaxially within the spiral vertical filament at 5 mm distance. The filament temperature (1800-2100°C) was monitored by a two-colour pyrometer. The substrate temperature was measured at between 800-950 °C. The total pressure of the gas mixture in reactor was 2.66 kPa (20 torr) and flow rate was 200 sccm. The diamond deposition was carried out for 15 hrs with single used filament. The deposited diamond films were analysed by scanning electron microscopy (Jeol JSM-5600LU) and micro Raman spectroscopy measurements were performed in back-scattering geometry at room temperature by using a Dilor XY triple spectrometer equipped with a liquid nitrogen cooled charge coupled device detector and an adapted Olympus microscope.

2.3. Diamond film erosion test

Erosion tests were carried out in a high velocity air-sand erosion facility capable of attaining impact velocities of up to 360 m s⁻¹. In the sand-blasting rig, sand was injected into an air stream and accelerated down to a 10 mm diameter stainless steel tube, 0.8 meter in length, into the erosion chamber where it strikes the diamond deposited substrate. The sand used was a blend of dental laboratory grade. The broad size distribution in the range $100\text{-}400\,\mu\text{m}$ and average diameter of sand was $250\,\mu\text{m}$. Sand feed rate of $5.9\,\text{kg}$ m⁻² s⁻¹ was employed for test. The nozzle to stand off distance was 40 mm and test on the substrate area was average 10mm in diameter. All tests were conducted using air-sand jet impact angle of 90° as the erosion of brittle materials is at normal impingement. The diamond-coated bur has to be rotated 120° at a time for three intervals. The tests were interrupted every $10\,\text{min}$ in order to monitor the diamond coating [9].

2.4 Dental bur machining: drilling and turning tests

The machining unit was specifically constructed with a water-cooling system so that maximum spindle speed of 250,000 revolutions per minute (r.p.m), feed rates of between $5-20 \mu m$ per revolution and cutting speeds in the range 100 to 200 m/min for cutting human teeth with clinical bur. Separate set up for laboratory bur was used to operate at 20,000-30,000 r.p.m with a feed rate of 0.2-0.5 mm/rev without water-cooling.

The flank wear of the burs was estimated by SEM analysis at pre-selected time interval of one minute. Prior to SEM analysis diamond coated burs were ultrasonically washed with 6M H₂SO₄ solutions to remove any unwanted machining material, which eroded onto surface of CVD diamond coated bur. For comparison, conventional PCD (polycrystalline diamond) sintered bur with different geometry were also tested on the same substrates materials.

3. Results and discussions

The diamond coatings deposited by HFCVD on dental burs, whose surface was roughened by murkami's reagent prior to deposition. EDS spectra confirmed the removal of the Co binder from the surface. Surface morphology of predominately (111) faceted octahedral shape diamond films was obtained after deposition for 15 hrs. The SEM micrograph of $17\mu m$ thick diamond is shown in figure. 1.

Results of the erosion tests on diamond coated dental bur were compared with the untested diamond coated bur [figure. 2 (a), (b)]. The coating failure occurred, the only surface features observed were minor amounts of micro or sub-micro chipping of the crystal. Diamond has greatest resistance to plastic deformation of any material and damage is always of a wholly elastic nature, with no traces of plastic deformation [10].

Figure.3 shows a SEM micrograph of a CVD diamond coated laboratory dental bur at the cutting edge. The film is homogeneous with uniform diamond crystal sizes, typically the crystal sizes are in the range of 6-10 µm. As expected the surface morphology is rough making the dental burs extremely desirable for abrasive cutting applications. In contrast, figure. 4 (a) is a close up view from SEM micrograph of a conventional PCD sintered bur. The diamond particles are imbedded onto surface with a suitable binder matrix material such as nickel (Ni²+). Typically the surface is inhomogeneous and sizes of particles ranging from 50-200 µm causing considerable variation in the cutting performance of the tool. Figure. 4 (b) shows the morphology of a sintered diamond bur after being tested on borosilicate glass at a cutting speed of 30,000 rpm for 5 minutes with an interval at every 30 sec. It is clearly evident that there is significant removal of diamond particles from the surface of the tool after 500 holes. As expected there is the deterioration of the abrasive performance of the PCD sintered diamond dental burs. Borges et al [2] also reported significant loss of diamond particles occurred during cutting with the commercial sintered diamond bur. In addition, the metallic nickel (Ni²+) binder shows major defects generated by pulled-out particles.

Figure. 5 and 6 show an SEM image of CVD diamond coated laboratory bur after machining tests on borosilicate glass and porcelain teeth respectively, for 5 mins at a cutting speed of 30,000 r.p.m. It is clearly indicated that the diamond films are still intact on the pre-treated WC substrate and diamond coating displayed good adhesion also there is no indication of diffusion wear after the initial test for 500 holes. However, the machining materials such as glass pieces are eroded onto cutting edge of diamond coated dental bur as adhesive wear were

observed [Figure. 5]. After testing on porcelain teeth the mechanism of wear probably involves adhesion as well as abrasion. Figure. 6 shows that inorganic fillers from porcelain teeth adhered to the cutting tool surface in localised areas when increased rate of abrasion was used [11].

Fig. 7 shows that the SEM image of uncoated WC-Co dental bur tested on the borosilicate glass using the same machining conditions. The uncoated WC-Co bur displayed flank wear along the cutting edge of the bur. The areas of flank wear were investigated at the cutting edge of the dental bur. Fig. 8 shows that the area of flank wear is plotted against function of time after tested on borosilicate glass. It is evident that a longer duty cycle of machining could cause higher rate of flank wear on the cutting edge of tool. Therefore, the cutting edge of WC-Co dental bur should have significant thickness of CVD diamond, which will enhance not only quality of cutting but also prolong the tool life [12]. The diamond coated laboratory dental bur has machined on the cobalt-chrome (Co-Cr hardest metal alloy used in dental technology) for over 80,000 holes. After excessive cutting duty significant flank wear has been observed along the cutting edge of dental bur. Figure. 9 show that not only the delamination of diamond but also the wear of WC surface at the interface between diamond and WC.

Natural human teeth were cut using a diamond coated clinical bur. The cuts were made in the central groove of the teeth. This permitted cutting three grooves in each tooth. Figure. 10 show a SEM image of diamond coated clinical WC-Co dental bur after testing on extracted teeth. It is evident from the SEM shown that the tooth materials such as dentine clog up the bur surface reducing its abrasive performance.

Raman analysis was performed in order to evaluate the quality and stress imparted in CVD diamond films. The Raman spectrum shown in fig. 11 shows that at the tip, centre and end of cutting tool a single sharp peak at 1336, 1337 and 1337 cm⁻¹ respectively was observed for different positions. The result of Raman analysis on WC-Co substrates at several different locations on the tool has shown indications of compressive stress in the coating [13].

4. Conclusions

Etching treatment of surface of the substrate in order to remove the surface cobalt resulted in much better adhesion. Erosion tests show that adherent diamond films offer significantly better erosion resistance. Therefore deposition of diamond on metal surface offers protective coating on uncoated substrate. The PCD sintered diamond bur lose significant proportions of imbedded diamond particles during the abrasive machining procedure where CVD diamond coated diamond bur remain intact with potential of prolong tool life. Thicker coating of CVD diamond at the cutting edges expected to give tool longer life and better quality of machining. The performance and lifetime of CVD coated dental bur is much superior to the sintered bur and uncoated WC-Co bur. An excessive cutting performance caused the delamination of diamond film as well as wear off WC surface. Further works is required to study the effects of diamond film adhesion related to quality of cutting and thickness at the cutting edge based on the performance of tool.

Acknowledgments

H.Sein is grateful to the Faculty of Science and Engineering at Manchester Metropolitan University for providing facility, support and the studentship. We are also in dept to Tennessee Technology University (USA) and University of Rome (Tor Vergata, Italy) for discussions and providing experimental results.

References

- 1. W.Ahmed, C.A Rego, R.Cherry, A. Afzal, N. Ali, I.U. Hassan, Vacuum, 56 (2000) 153-159
- C.M. Borges, P.Mange, M.Dent, E.Pfender, D.Ring, J.Heberlein, J. of Prosthetic dentistry July (1999) 73-79
- 3. J. Gabler, L. Schafer, H. Westermann, Diamond and Related materials, 9 (2000) 921-924
- 4. H. Sein, W. Ahmed, C. A Rego, Diamond and Related Materials, 11 (2002) 731-735
- 5. M.S. Pines, A. Schulman, JADA, Vol 99, November (1979) 831-833
- M.B.Gusev, V.G. Babaev, V.V.Khvostov, G.M.Lopez Ludena, A.Yu.Brebadze, I. Y. Koyashin, A.E.Alexenko, Diamond and Related Materials, 6 (1997) 89-94
- 7. I.Endler, K.Bartsch, A. Leonhardt, H. J. Scheibe, H. Ziegele, I. Fuchs, Ch. Raatz, Diamond and Related Materials, 8 (1999) 834-839
- 8. S. Kamiya, H. Takahashi, R. Polini, E. Traversa, Diamond and Related Materials, 9 (2000)
- S.Amirhaghi, H.S.Reehal, R.J.K.Wood, D.W.Wheeler, Surface and Coatings technology, 135 (2001) 126-138
- S.Amirhaghi, H.S.Reehal, E. Plappert, Z. Bajic, R.J.K.Wood. D.W.Wheeler, Diamond and Related Materials, 8 (1999) 845-849
- 11. A. Inspector, E.J Oles and C.E. Bauer, Int.J.Refract; Metal Hard Materials, 15 (1997) 49.
- H. Sein, W. Ahmed, M. Jackson, N. Ali, and J. Gracio, Surf. Coat. Technol, 163-164 (2003) 196.
- 13. W. Tang, Q. Wang, S. Wang and F. Lu, Diamond and Related Materials, 10 (2001) 1700.

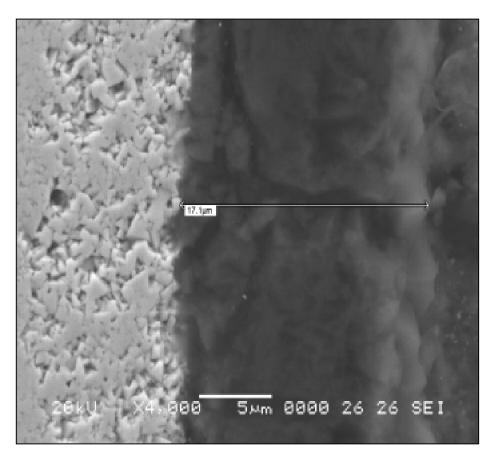


Figure 1. Cross section of diamond film on coated dental bur.

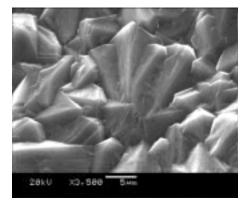


Figure 2. (a) Diamond film before erosion test

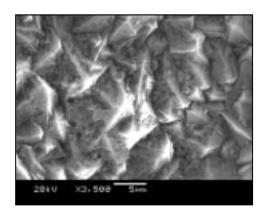


Figure 2 (b) Diamond Film after erosion test

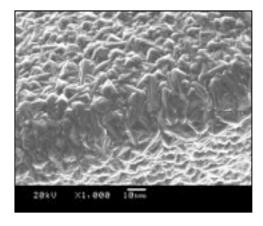


Figure 3. Cutting edge of diamond coated dental bur.

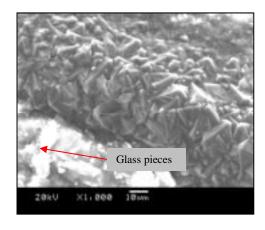


Figure. 5 Cutting edge of diamond coated bur after testing with glass.

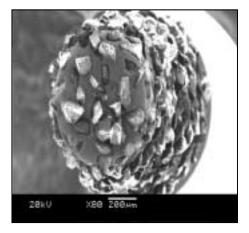


Figure. 4 (a) Inhomogeneous surface of PCD diamond sintered bur.

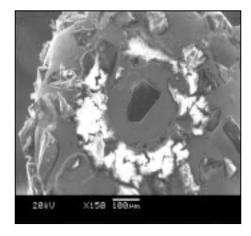


Figure. 4 (b) PCD diamond sintered bur after testing with glass.

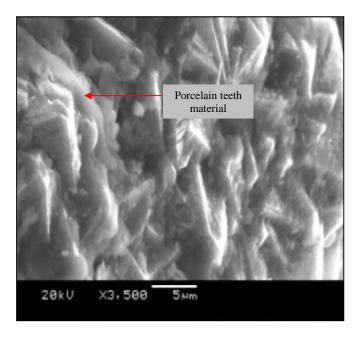


Figure. 6 Close view of diamond coated bur after testing with porcelain teeth.

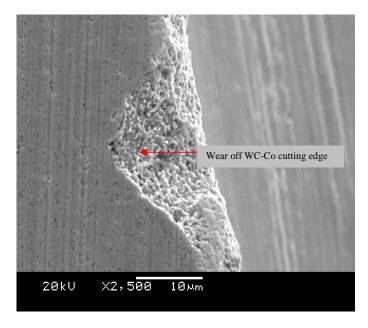


Figure. 7 Cutting edge of uncoated WC-Co dental bur after machining with glass.

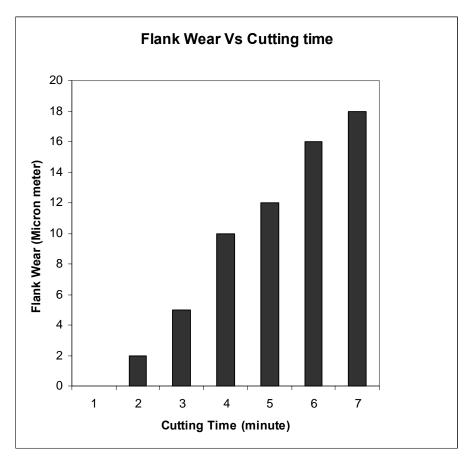


Figure. 8 Flank Wear (μm) against Function of Time (min).

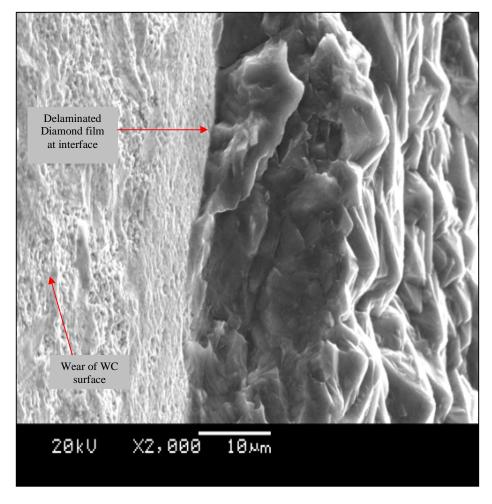


Figure. 9 Delaminated diamond film at interface between diamond and wear of WC.

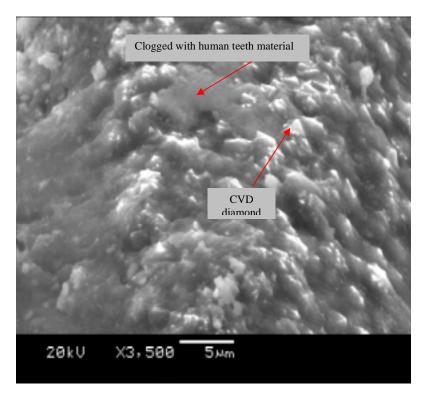


Figure. 10 diamond coated clinical bur after testing on human teeth.

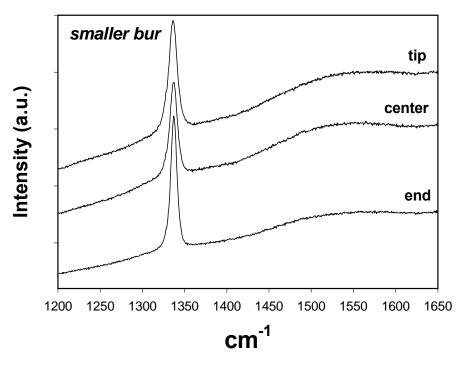


Figure. 11 Raman spectrum of diamond films.

AURORA PLD GROWTH OF CaF₂ THIN FILM AND APPLICATION TO IMPROVED CaF₂/DIAMOND MIS INTERFACE FORMATION

Shigeto Honda, Shinsuke Komatsu and Takeshi Kobayashi

Department of Physical Science, Graduate school of Engineering Science, Osaka University
1-3 Machikaneyama, Toyonaka, Osaka 560-8531, Japan
Phone: +81-6-6850-6311,Fax: +81-6-6850-6341
*e-mail: honda@sup.ee,es,osaka-u.ac.jp
CREST, Japan Science and Technology Corporation (JST), Japan

ABSTRACT

For the realization of a high quality diamond MIS device, we so far proposed to utilize CaF_2 as the non-oxide gate insulator. CaF_2 has been long prepared by the evaporation method. Recently, we introduced the pulsed laser deposition (PLD) method and fabricated diamond MIS diodes by PLD. To look at more improvement of the CaF_2 /diamond MIS interface, we started to study the aurora PLD (using the magnetic field) for CaF_2 film formation in addition to the conventional PLD. Aurora method is characterized by the enhanced ionization and/or activation of ablated particles during transport from the target to substrate through interaction between the particles and applied magnetic fields and expected to obtain better quality of film. Plume emission spectroscopic measurements have revealed that the aurora PLD plume emission admirably increased more than 30 times higher than conventional one. Time-resolved plume image analyses have closely been done.

Keywords: diamond, CaF₂, PLD, MIS, diode, FET, ablation, plume, gate

INTRODUCTION

Semiconducting diamond has many unique properties such as high thermal conductivity, large break down voltage, wide bandgap, NEA and so on. Therefore, diamond has been expected to be a promising material suitable for high-temperature, electro-optic device applications (refs.1 to 2). However, for the realization of the diamond electronic devices, the electrical stabilization is naturally required. According to our previous research, it was found that oxygen adsorption on the diamond surface induced a lot of surface states, which degraded the electrical properties of metal-insulator-semiconductor (MIS) interface to a great extent (refs.3). To overcome this problem, nonoxide CaF_2 gate insulator has been utilized and made diamond surface stable to a certain extent. We succeeded in getting the greatly improved electrical properties of the diamond metal-insulator-semiconductor field effect transistor (MISFET) by ultrahigh vacuum process, whose observed effective mobility (μ_{eff}) was $400 \text{cm}^2/\text{V} \cdot \text{s}$ at room temperature (refs.4). Kawarada et al. (refs.5) fabricated a 0.7- μ m-gate-length diamond MISFET and the maximum transconductance of 100 mS/mm was obtained by DC measurement. Although diamond electronics progressed markedly to date as stated above, there still remain problems including the MIS interface states that are far from the silicon technology, and therefore, further stabilization has been desired.

The PLD method is widely used by thin film growth of various materials, for example superconductors, and has many properties different from other familiar methods, such as the separation of the heat source from the chamber, the capability of deposition under a wide ambient gas pressure range and little difference between the target and the thin film composition. However, the conventional PLD method has a drawback that many droplets fly directly to the substrate resulting in the formation of pinhole defects, which prevents from the application of the obtained films to electronic devices. Though many methods to reduce the droplets have been suggested by many groups, (refs.6) the eclipse method is considered to be the most convenient and effective solution for eliminating droplets completely. By using the eclipse method, high-quality oxide superconductor, dielectric and oxide magnetic thin films with no droplets are now available (refs.7). Actually, however, CaF₂ PLD faced another kind of serious problem other than

the droplets. Namely, a grown CaF_2 film was entirely covered with a number of fragments (differed from droplets) even when the eclipse method was employed. Fragment was a tough obstacle, being hard to solve. We recently succeeded in obtaining a good CaF_2 film without any fragments by the Stand Still Target (SST) method (refs.8) and applied the obtained CaF_2 film to diamond MIS diode. Unfortunately, however, the C-V characteristic was hardly different from conventional diamond MIS diode (CaF_2 was deposited by evaporation method). The reason for this is thought as that not only the droplets but also a large proportion of the activated growth species and radicals were also shielded by the shadow mask. As the result, the advantages of the PLD method might be lost.

In this study, we started researching CaF₂ thin film deposition by the "aurora PLD method" by aiming its use to high quality diamond MIS devices. The aurora PLD works under application of the magnetic field from the substrate side and characterized by the enhanced ionization and/or activation of ablated particles during transport from the target to substrate through interaction between the particles and applied magnetic fields (refs.9).

EXPERIMENTAL

An ArF excimer laser (λ =193nm, laser fluence \sim 3J/cm²) and a CaF₂ single crystal target were used for the PLD experiments. The schematic configuration of components is shown in Fig.1. A permanent magnet was placed at the substrate position. A diameter of the permanent magnet was 10mm.

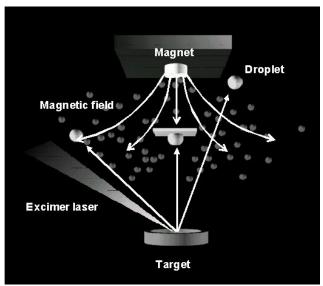


Fig. 1. Schematic drawing of the aurora PLD Method. [9]

A framing streak camera (Hamamatsu Photonics, C4187) was used to take time-resolved two-dimensional (2D) images of the plume. Fast-intensified and continuous 2D images can be obtained using this streak camera with a gate microchannel plate (MCP) and a cooled charge-coupled-device (CCD) system with a minimum exposure time of 50ns. We also obtained spectroscopic measurements (near time-averaged) using a multichannel spectrometer (Hamamatsu Photonics, PMA-11). To distinguish between the light emissions from the atoms and ions, we also used interference filters.

RESULTS AND DISCUSSION

Figure 2 shows the images of the CaF_2 plume observed under 1.6Pa argon pressure. Each image shows the plume at 1, 4, and 7μ s after laser irradiation. The emission intensity is indexed by the grey-tone indicated below the images. In the conventional PLD, the plume simply expands with reducing the emission intensity as time goes. A series of plume-image changes is shown in Fig. 2(a). Contrasting with this, the plume images of the aurora PLD show dynamics, being substantially different from the conventional ones. That is a shinning emission from the plume is

growing bigger and bigger as the plume leading-edge is getting closer to the magnet. These images imply that a lot of active species could be still maintained near the substrate position in the aurora PLD method. In other words, the "Aurora Effect" surely seem to blossom in the case of CaF₂.

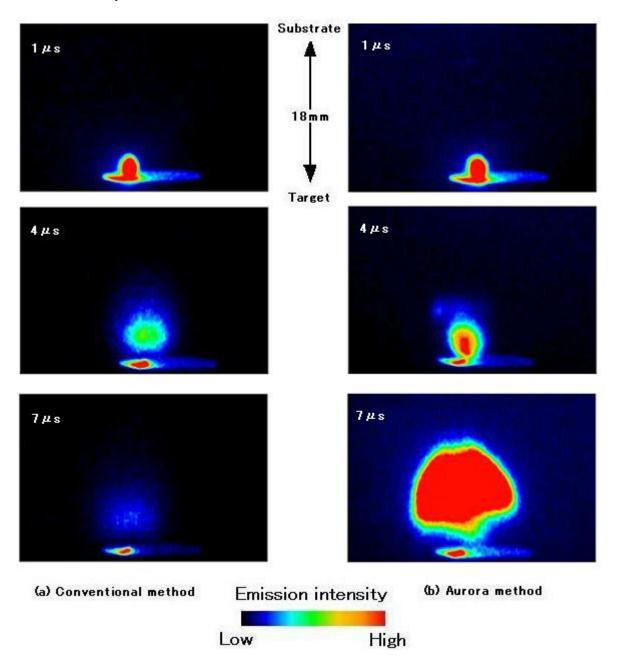


Fig. 2. Time-resolved images of the CaF₂ plume under a 1.6Pa ambient argon pressure. (a) conventional method, and (b) aurora method.

Plume spectroscopic measurements were carried out near the substrate (location of the magnet) using CaF₂ target by the aurora and conventional PLD methods. The results are shown in Fig. 3. (Pay caution to the ordinate scale of

(b), which is 50 times higher than that of the (b)). Both measurements were done at almost same position. Notice that spectra peaks of 393nm, 397nm and 423nm among many are significantly increasing after the onset of the aurora PLD. Especially the peak of 393nm is increasing more than 35 times higher. The peak of 393nm is related with calcium ion, so these results seem to show that the magnetic field enhances the ionization of the particle in the plume and plasma density. Contrary to this, peaks other than those remained almost unchanged.

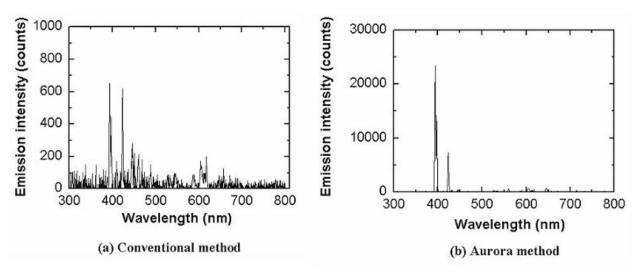


Fig. 3. Plume Emission spectra near the substrate side. CaF₂ target. (a) Aurora method, and (b) conventional method

Figure 4 shows the time- and wavelength-resolved images of the CaF_2 plume in both the conventional (a) and aurora (b) PLD (1.6Pa Ar) methods. The wavelength-resolved measurement was done by using the interference filter. The center wavelength of the filter was selected to transmit the emission line at near 400nm. From comparison of Figs. 2(b) and 4(b), there is no obvious difference in the plume images between them. In consequence, one can conclude that the shinning emission of the aurora PLD method is arising from peaks of near 400nm. At least at present, it is hard to definitely assign the emission at 400nm. So other measurements such as time-of-flight (TOF) are needed. Whatever the shinning species might be, these activated particles in the aurora PLD will affect the quality of the CaF_2 film and the CaF_2 /diamond interface.

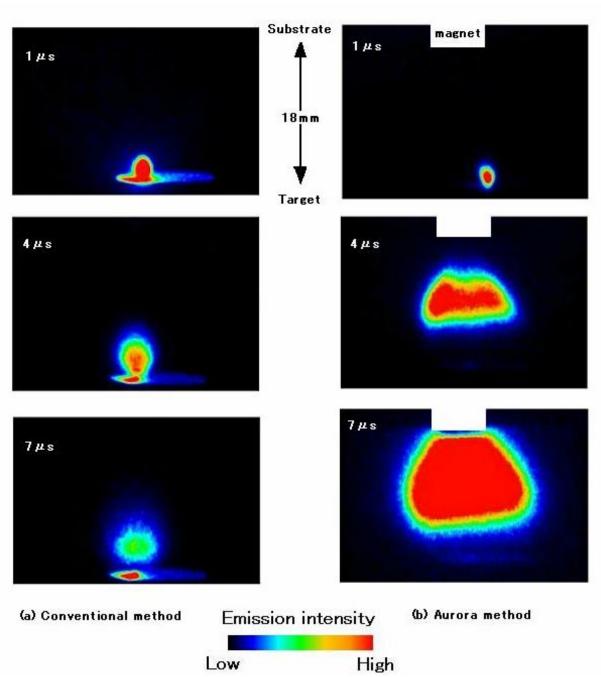


Fig. 4. Time-resolved images of the CaF₂ plumes. 1.6Pa argone ambient. The interference filter (The center wavelength was 400nm) was used in the measurements.

(a) conventional PLD method, and (b) aurora PLD method.

CONCLUSIONS

In this study, we deposit CaF₂ thin films by the conventional and aurora PLD methods, in latter of which magnetic field was applied to the traveling particles. It is found that a magnetic field from a permanent magnet enhances the ionization or excitation of the species in the plume from the CaF₂ target. The plume emission peak at the wavelength of 400nm was growing up to 37 times as high as that of the conventional PLD.

REFERENCES

- 1. G. Sh. Gildenblat, S. A. Grot, C.W. Hatfield and A. R. Badzian: High-Temperature Thin-Film Diamond Field-Effect Transistor Fabricated Using a Selective Growth Method. IEEE Electron Device Lett. 12, 1991, 37.
- 2. C.R. Zeisse, C. A. Hewett, R. Nguyen, J.R Zeidler and R. G. Wilson: An Ion Implanted Diamond Metal-Insulator-Semiconductor Field Effect Transistor. IEEE Electron Device Lett. 12, 1991, 602.
- 3. Y. Yun, T.Maki and T.Kobayashi: Surface state density distribution of semiconducting diamond films measured from the Al/CaF₂/i-diamond metal-insulator-semiconductor diodes and transistors. J.Appl.Phys. 82, 1997, 3422.
- 4. Y. Yun, T. Maki, H. Tanaka, Y. Shirakawa and T. Kobayashi: Electrical Properties of Al/CaF₂/i-Diamond Metal-Insulator-Semiconductor Field-Effect-Transistor Fabricated by Ultrahigh Vacuum Process. J.Appl.Phys. 37, 1998, 1293.
- 5. H. Ishizuyka, H. Umezawa, H. Taniuchi, T. Arima, N. Fujihara, M. Tachiki, H. Kawarada: DC and RF characteristics of 0.7-µm-gate-length diamond metal-insulator-semiconductor field effect transistor Diamond Relat. Mater. 11, 2002 ,378.
- 6. K.Kinoshita, H.Ishibashi, and T.Kobayashi: Improved Surface Smoothness of YBa₂Cu₃O _y Films and Related Multilayers by ArF Excimer Laser Deposition with Shadow Mask "Eclipse Method". J Appl.Phys. 33, 1994, L417.
- 7. T.Kudo, M.Tachiki, T.Kashiwai and T.Kobayashi: Band Diagram of Metal-Insulator-Magnetic Semiconductor (La_{0.85}Sr_{0.1}5Mn_{0.3}) Structure at Room Temperature. J.Appl.Phys. 37, 1998, L999.
- 8. T.Maki, K.Okamoto, M.Sugiura, T.Hosomi, T.Kobayashi: The great improvement of surface smoothness of CaF2 in pulsed laser deposition even under the two-photon absorption process. Appl. Surface. Science 197-198, 2002, 448 9. M.Tachiki, T.Kobayashi: Manipulation of Laser Ablation Plume by Magnetic Field Application. J.Appl.Phys. 38, 1999, 3642.

THERMODYNAMICALLY PREDICTED C-H-O PHASE DIAGRAM

Takahiro Tsutsumoto and Akira Yamamoto

Western Industrial Research Institute of Hiroshima 2-10-1 Aaga-minami, Kure, Hiroshima 737-0004, Japan

ABSTRACT

A C-H-O diagram for carbon deposition from gas phase was thermodynamically calculated from free energies of formation of the limited chemical species, CH_4 , C_2H_2 , CO and CO_2 , and C-H-O gas composition for diamond deposition was discussed. The feasible area of diamond deposition is in the vicinity of carbon solubility limit in the diagram. Solubility limit of carbon to hydrogen is much lower than that of carbon to oxygen, because the formation free energies of C_2H_2 and CH_4 in C-H system are much higher than those of CO and CO_2 in C-O system. The necessity of low C/H ratio in gas composition for diamond deposition comes from the low solubility limit of carbon to hydrogen. CO becomes extremely stable at higher temperatures. Therefore carbon is soluble up to C/O=1, which appears as the solubility line, called the "CO line", in the C-H-O diagram. The vicinity of this solubility line shows a good agreement with C-H-O gas composition for diamond deposition.

Keywords: C-H-O phase diagram, diamond deposition, thermodynamic prediction,

1. INTRODUCTION

Since Matsumoto reported diamond synthesis from methane and hydrogen gas mixture with a reproducible method (ref. 1), over 20 years have passed. During that time, various methods have been developed (refs. 2 to 5), and reaction processes of diamond deposition have been investigated with the measurements of chemical species in the gas phase (refs. 6 to 7). However, the essential problem of why diamond synthesis from the low-pressure gas phase is possible still remains.

Spityin et al. have pointed out that the atomic hydrogen in the gas phase has a selective etching effect on graphite (ref. 8). However, there is no clear explanation about the apparent contradiction of the deposition and the etching of carbon occurring at the same time. Since Hirose et al. successfully deposited diamond using alcohol (ref. 10) and oxyacetylene (ref. 4), it has become popular to use gas containing oxygen for diamond deposition. Bachman et al. showed a clear composition domain for diamond deposition in C-H-O composition diagram as diamond domain (ref. 11). In the diagram, diamond can deposit in the very vicinity of the hydrogen axis in the C-H system and near the strait line between the hydrogen axis and the point of CO (C/O=1) in the C-H-O system, the "CO line". However, there has been no simple and clear theoretical explanation about these phenomena.

In this paper a simple prediction of C-H-O phase diagram is proposed using thermodynamic data for limited gas species, CH₄, C₂H₂, CO₂ and CO, and the diamond domain and diamond deposition mechanism are discussed.

2. CALCULATION METHOD

In order to estimate carbon solubility limit to hydrogen or oxygen, free energies of formation of gas species, CH₄, C₂H₂, CO₂ and CO were used. The notations of these free energies, ΔG_{fn} , and corresponding reaction equations follow, and the data are shown in figure 1.

$$C(s) + 2H_2(g) = CH_4(g)$$
 ΔG_{fl} (1)
 $2C(s) + H_2(g) = C_2H_2(g)$ ΔG_{fl} (2)

$$2C(s) + H_2(g) = C_2H_2(g) \quad \Delta G_{f2}$$
 (2)

$$2C(s) + O_2(g) = 2CO(g) \quad \Delta G_{f3}$$
 (3)

$$C(s) + O_2(g) = CO_2(g) \qquad \Delta G_{f4}$$
 (4)

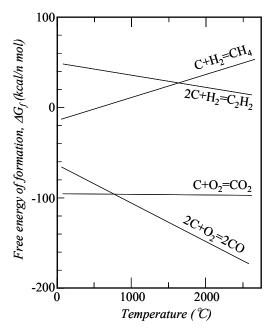


Figure 1 Free energies of formation of chemical species CH₄, C₂H₂, CO and CO2 used for calculation of carbon deposition.

In these equations "(s)" means solid state, "(g)" means gas state, and solid carbon here is graphite. From the equations (1) and (2), two equilibrium constants can be determined in C-H system as follows,

$$K_{I} = \frac{P_{CH_{4}}}{a_{c} \cdot (P_{H_{2}})^{2}} = exp\{-\Delta G_{fI} / (R \cdot T)\}$$
(4)

where
$$a_c$$
, P_{H_2} , P_{CH_4} and $P_{C_2H_2}$ are carbon activity, partial pressure of H_2 , CH_4 and C_2H_2 , respectively. In the C-

 $K_1 = \frac{P_{CH_4}}{a_c \cdot (P_{H_2})^2} = exp\{-\Delta G_{f1}/(R \cdot T)\}$ (5)

where a_c , P_{H_2} , P_{CH_4} and $P_{C_2H_2}$ are carbon activity, partial pressure of H_2 , CH_4 and C_2H_2 , respectively. In the C-

 $C_1 = \frac{P_{CH_4}}{a_c \cdot P_{H_2}}$ are carbon activity, partial pressure of H_2 , CH_4 and C_2H_2 , respectively. In the C-

 $C_2 = \frac{P_{CH_4}}{a_c \cdot P_{H_2}}$ and $P_{C_2H_2}$ are carbon activity, partial pressure of H_2 , CH_4 and C_2H_2 , respectively.

H system total pressures, P_t , are given for reaction (1) and (2), respectively, as follows,

$$P_t = P_{H_2} + P_{CH_A} \tag{6}$$

$$P_t = P_{H_2} + P_{C_2 H_2} \tag{7}$$

Thus the solubility limit of carbon to hydrogen can be determined from equations (4) and (6), or equations (5) and (7), respectively, by substitution of a_c = unity (for existence of solid carbon).

In C-O system, the famous reaction of carbon deposition in the field of metal refining, the "Boudouard reaction", and its free energy change can be derived from equations (3) and (4) as follows,

$$2CO = C + CO_2 \qquad \Delta G_{f4} - \Delta G_{f3} \tag{8}$$

Therefore the carbon solubility in oxygen is determined from the following equations in the same manner,

$$K_3 = \frac{a_c \cdot P_{CO_2}}{(P_{CO})^2} = \exp\{-(\Delta G_{f4} - \Delta G_{f3})/(R \cdot T)\}$$
(9)

$$P_t = P_{CO_2} + P_{CO} \tag{10}$$

Carbon to hydrogen ratio and carbon to oxygen ratio, C/H and C/O, are determined as follows,

$$C/(C + H) = P_{CH_4}/(5P_{CH_4} + 2P_{H_2}) \text{ or } 2P_{C_2H_2}/(4P_{C_2H_2} + 2P_{H_2})$$
(11)

$$C/(C+O) = (P_{CO} + P_{CO_2})/(2P_{CO} + 3P_{CO_2})$$
(12)

3. RESULTS AND DISCUSSION

3. 1. C-H system

Figure 2 shows the solubility limit of carbon in hydrogen as the forms of CH_4 and C_2H_2 in gas phase. This figure quantitatively agrees well with the previous works (refs. 12 to 14). This result implies that the carbon solubility limit is virtually determined by only two chemical species, CH_4 and C_2H_2 , in lower and higher temperature regions, respectively. Because of the no volume change of the C_2H_2 formation reaction, the solubility limit at higher temperature range is independent from the gas pressure. On the other hand the solubility limit increased with increasing gas pressure because the formation of CH_4 is expansion reaction.

In the diamond deposition using C-H gas system, C₂H₂ forms at high temperature for gas activation. On the substrate surface, C₂H₂ is quenched and decomposes because of lower stability at the lower temperature range with depositing solid carbon. However, the solid carbon can evaporate in the form of CH₄ at the substrate temperature because CH₄ becomes stable at that temperature. These processes enable the simultaneous deposition and evaporation (or etching) of carbon on the substrate surface with the aid of atomic hydrogen. These simultaneous reactions are believed to be key processes for diamond deposition.

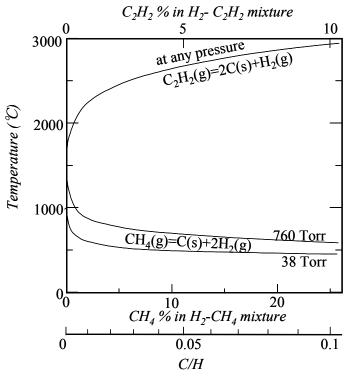


Figure 2 Solubility limit of carbon in hydrogen as CH₄ and C₂H₂.

3.2. C-O system

Figure 3 shows the solubility of carbon in oxygen as the forms of CO or CO₂ in gas phase. This reaction of solid carbon deposition is well known in the field of metal refining as "Boudouard reaction". Compared with the C-H system, oxygen shows an extremely high affinity to carbon, and oxygen molecules cannot exist in the presence of solid carbon. Therefore no etching effect of oxygen molecule or atomic oxygen is expected in the diamond deposition, because solid carbon, diamond, exists in the process. This reaction is also affected from the pressure of reaction gas, because volume changes through the reaction.

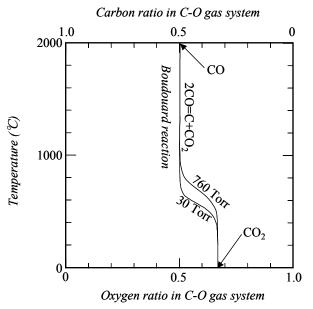


Figure 3 Solubility limit of carbon to oxygen estimated by "Boudouard reaction" (2CO=C+CO₂).

3.2. C-H-O system

The importance of CO for understanding the diamond deposition process using a reaction gas in C-H-O system should be pointed out. CO becomes extremely stable at higher temperatures such as the temperature for gas activation. This is obvious from fig. 1. Therefore if the oxygen were added to the C-H system at higher temperature of gas activation for diamond deposition, firstly the oxygen combines with carbon and forms CO, and excess carbon resolves in hydrogen in the form of C_2H_2 . Through these considerations, and combining C-H and C-O phase diagrams with C-H-O composition diagram, C-H-O phase diagram is obtained, as shown in figure 4.

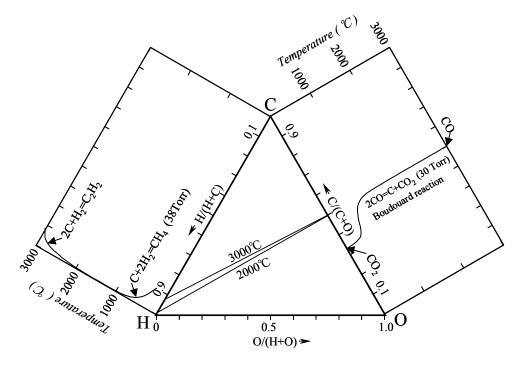


Figure 4 C-H-O phase diagram of carbon deposition.

4. CONCLUSIONS

In order to understand diamond deposition using C-H-O reaction gas, C-H, C-O and C-H-O phase diagram are predicted from the thermodynamic data for limited chemical species, CH₄, C₂H₂, CO and CO₂, and the following conclusions are obtained.

- 1. Solubility limit of carbon to hydrogen or C-H phase diagram is mainly determined by CH₄ and C₂H₂.
- 2. Low carbon concentration for preferable for diamond deposition with C-H gas comes from low stability of CH₄ and C₂H₂, that is, high free energies of formation of them.
- 3. C-H-O phase diagram can be determined from the thermodynamic data of the limited chemical species, CH₄, C₂H₂, CO and CO₂.
- 4. "CO line" for diamond deposition in C-H-O diagram is caused by the extremely high stability of carbon mono-oxide, CO, at high temperature.

Simultaneous reactions of deposition and evaporation of carbon should be a key process for deposition of metastable diamond that is believed to come from the fact that the stable gas phases exchange between high and low temperature.

REFERENCES

- 1) S. Matsumoto, et al.: J. Mater. Sci., 17, 1982, p.3106.
- 2) M. Kamo, Y. Sato and N. Setaka: J. Cryst. Growth, 62, 1983, p.642.
- 3) K. Suzuki, et al.: J. Appl. Phys., 50, 1987, p.728
- 4) Y. Hirose and S. Amanuma: "Denshizairyou (electric materials)", August, 1989, p.45. (in Japanese)
- 5) S. Matsumoto, et al.: Appl. Phys. Lett., 22, 1987, p.737
- 6) H. Komiyama, et al.:NEW DIAMOND, vol.7, No. 3, 1991, p.14. (in Japanese)
- 7) S. Ohta and N. Fujimori: NEW DIAMOND, Vol. 11, No. 1, 1995, p.28. (in Japanese)
- 8) B. V. Spityn, and L. L. Bouilob and B. V. Derjaguin: J. Crystal Growth, 52, 1981, p.219
- 9) T. Tsutsumoto : Proc. of 2nd Int. Conf. on the Applications of Diamond Films and Related Mater. MYU, 1993, p.521
- 10) Y. Hirose and Y. Terasawa: NEW DIAMOND, Vol.2, No. 2, 1986, p.34. (in Japanese)
- 11) P. K. Bachman, D. Leers and H. Lydtin: Diamond and Related Materials, 1, 1991, p.1.
- 12)B. Lersmacher, et al., Carbon, 5, 1967, p. 207.
- 13) Sommer and F. W. Smith: J. Mater. Res., 5, 1990, p. 2433.
- 15) W. Piekarczyk, et al.: J. Crystal growth, 106, 1990, p. 281

PIEZORESISTIVE PROPERTY OF CVD DIAMOND FILMS

Akira Yamamoto, Takahiro Tsutsumoto

Western Industrial Research Institute of Hiroshima Prefecture 2-10-1 Agaminami, Kure, Hiroshima 737 0004, Japan E-Mail: aki@seibu-kg.pref.hiroshima.jp

ABSTRACT

Piezoresistive properties of chemical vapor-deposited boron-doped p-type polycrystalline diamond films were investigated. The p-type polycrystalline diamond films of about 2 µm thickness were grown on SiO₂/Si substrate using a hot-filament reactor. Effective carbon concentration, defined as (C-O)/H, was varied from 2.2 to 5.5 %, and boron to carbon ratio was kept constant. Gauge factor for the p-type diamond piezoresister decreased with carbon to hydrogen ratio. The quality of the diamond films were examined by using a scanning electron microscope (SEM), Raman spectroscopy and X-ray diffraction. The diamond films were degraded with the (C-O)/H.

Keywords: Piezoresistive effect; Gauge factor; Hot filament CVD; P-type diamond films;.

1. INTRODUCTION

Boron-doped diamond shows piezoresistive effect [1]. Sensors using diamond strain gauge can be used in harsh environments [2]. The typical gauge factor was reported to be over 2000 for single crystalline diamond and under 100 for poly-crystalline diamond [3]. To produce diamond sensors for pressure or acceleration measurement, manufacturing technology of low cost diamond film with enough piezoresistive effect for the sensors is important. Polycrystalline diamond film is superior to single crystalline diamond in terms of production cost, but the gauge factor of the polycrystalline diamond film must be improved at least to 100, which is a comparable value of Si. Polycrystalline diamond piezoresister fabricated on a polished polycrystalline diamond wafer [4] and an intra-grain poly-diamond piezoresistor [3] was reported to show high gauge factors of 1000 and 4000, respectively. However, those techniques can not be used widely, because of the cost and special technique required. In this report, with a view to improving the gauge factor of the polycrystalline diamond film, the effect of the carbon concentration of reaction gas to the gauge factor was investigated.

The relationship between boron concentration and gauge factor has been investigated, but the effect of another parameter, (C-O)/H, on the gauge factor was not been adequately investigated, well.

2. EXPERIMENTAL

Boron-doped diamond films were deposited on thermally oxidized Si substrates, $10\times10\times0.4$ mm³. The thickness of the thermal SiO₂ layer was 1µm and the boron-doped film was 2 µm. The Si substrate was scratched with diamond powder 1-5 µm in diameter by ultrasonic cleaner for 60 minutes. The deposition was carried out in a hot-filament chemical vapor deposition (CVD) reactor under the conditions shown in Table 1. The growth parameters used are largely standard growth conditions for CVD diamond films. The Si substrate was heated to 900 °C at 30 Torr varying (C-O)/H from 2.2 to 5.5 % with a constant 290 ppm boron concentration in liquid solution. In this experiment, the carbon to hydrogen ratio was varied in order to improve the quality of the diamond film. Hydrogen was introduced through two lines. One of them was used for evaporation of liquid solution. The boron was doped during the deposition with reaction gas using a solution of H₃BO₃ to methanol (CH₃OH) which was diluted to 1/3 with acetone ((CH₃)₂CO), and vaporized by hydrogen bubbling. Effective carbon concentration was defined as (C-O)/H and calculated by

$$\frac{C-O}{H} = \frac{2Q^3}{2(Q_1 + Q_2) + 6Q^3}$$

Where Q1 is hydrogen gas flow rate, Q2 is bubbling hydrogen gas flow rate and Q3 is acetone gas flow rate. Morphology and structure of the diamond films were examined using a scanning electron microscope (SEM), Raman spectroscopy and X-ray diffraction. Ohmic contact to diamond was made with a silver based epoxy adhesive. Piezoresistive effect measurements were carried out using a lever structure, as shown in Figure 1, which applied tensile strain to the film [5].

C 1 / / /	1000 00
Substrate temperature	900 ℃
Filament temperature	2500 ℃
Filament-substrate distance	5 mm
*(C-O)/H	2.2~5.5%
Pressure	30 Torr
Time	60 min.
Hydrogen flow rate	300 sccm(main)
	30~106 sccm(bubbling)

^{*} Evaporation of methanol was neglected.

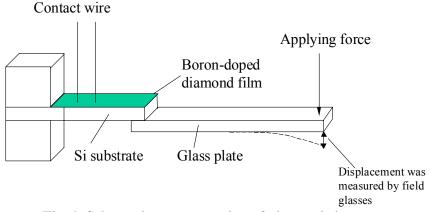


Fig. 1. Schematic representation of piezoresistive effect measurement

3. RESULTS AND DISCUSSION

Figure 2 shows the relationship between (C-O)/H and gauge factor. Gauge factor increased with decreasing the carbon to hydrogen ratio, from 33 to 3. The gauge factor is determined from strain and resistance change of the film.

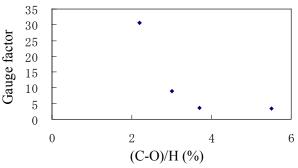


Fig. 2. Gauge factor vs. (C-O)/H

Table 2 Resistivity of diamond films

Sample No.	(C-O)/H	Resistivity
2023	5.5%	$0.44~\Omega$ · cm
2040	4.4%	0.08 Ω · cm
2048	3.0%	2.96 Ω · cm
2050	2.2%	3.15 Ω · cm

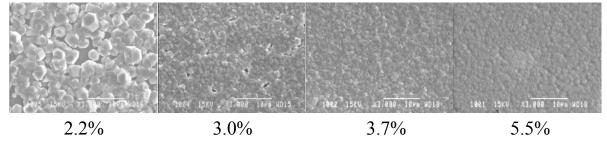


Fig. 3. Morphologies of the diamond film with various (C-O)/H.

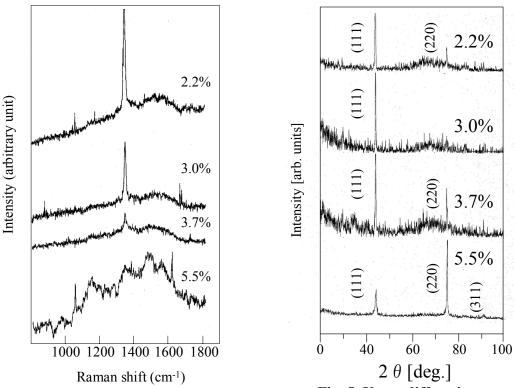


Fig. 4. Raman spectra of diamond films.

Fig. 5. X-ray diffraction pattern of diamond films

Table 2 shows resistivity of the diamond films. Each sample was deposited with the same boron concentration in the liquid solution, but resistivity greatly changed with (C-O)/H.

Figure 3 shows SEM photos of the diamond films. The morphology of the diamond films changed with (C-O)/H. In the 5.5% sample, diamond facets are not seen, and become smooth surface. However, diamond facets appear and become more clear with decreasing (C-O)/H.

Figure 4 shows the Raman spectroscopy of the diamond films. In the 2.2% sample, diamond peek in 1333cm⁻¹ is observed clearly, but it becomes lower with increasing (C-O)/H and finally disappears in the 5.5% sample. A broad G peak at approximately 1580cm⁻¹ is observed in all the samples, and the quality of the diamond film is improved with decreasing (C-O)/H. From these results, diamond is detected in the 2.2%, 3.0% and 3.7% samples but could not be identified in the 5.5% sample.

Figure 5 shows XRD patterns of the diamond films. Diamond peaks are observed in all the samples, the intensity of the (111) peak is stronger than that of (220) peak in the 2.2%, 3.0% and 3.7% samples but in the 5.5% sample, (220) becomes main. The texture of the diamond film change from (111) to (220) with (C-O)/H.

From these results, the quality of the diamond film is improved by decreasing (C-O)/H, as is its gauge factor. As improving the quality of the diamond film, graphitic carbon in grain boundary would decrease which enables carrier

to move easily. In the 5.5% sample, diamond peak is observed by XRD, but the film has no diamond Raman peak, and the morphology shows no diamond facets. This would be caused by the formation of a nano crystalline diamond.

4. CONCLUSION

Piezoresistive properties of chemical vapor-deposited boron-doped p-type polycrystalline diamond films were investigated. The p-type polycrystalline diamond films of about 2 μ m thickness were grown on SiO₂/Si substrate using a hot-filament reactor under (C-O)/H was varying from 2.2 to 5.5% and boron-to-carbon ratio kept at 290 ppm. Gauge factor for the p-type diamond piezoresister reached 33 in the 2.2% sample. The quality of the diamond films strongly affects the piezoresistive effect of polycrystalline diamond.

REFERENCES

- 1. M.Aslam, I.Taher, and A. Masood, Appl. Phys. Lett. 60 (1992) 2923.
- 2. J.L.Davidson, D.R.Wur, W.P.Kang, et al., Diamond and related Materials, 5 (1996) 86.
- 3. S. Sahli, D.M. Aslam, Sens. Actuators A71 (1998) 193.
- 4. M. Deguchi, N. Hase, M. Kitabatake, et al., Diamond and related Materials, 6 (1997) 367.
- 5. M.Aslam, I.Taher, Transducers 1993 (1993) 718.

SCANNING TUNNELING MICROSCOPY STUDIES OF HYDROGENATED AND OXYGENATED CVD DIAMOND (100) SURFACES

J. Nakamura, T. Teraji and T. Ito

Department of Electrical Engineering, Graduate School of Engineering, Osaka University, 2-1 Yamada-oka, Suita, Osaka 565-0871, Japan

ABSTRACT

We have investigated surface atomic structures of microwave-plasma chemical-vapor-deposited (CVD) homoepitaxial diamond (100) using a scanning tunneling microscope (STM) in ultra-high vacuum. The STM images were taken from H-terminated B-doped diamond (100):H 2×1 structure at plus and minus sample biases. At a plus sample bias, the images related to empty states of the surface atoms were featured by a row separation of 0.50 nm. At a minus sample bias, however, the images corresponding to occupied states were featured by a row separation of 0.25 nm. These STM images are considered to reflect anti-bonding and bonding orbitals of the surface C-H bonds related to the 2×1 structure, respectively. We also observed STM images of O-terminated B-doped diamond (100) surfaces. The STM images taken from an O-terminated surface showed a regular structure reflecting the 2×1 structure that had formed before the oxidization. This indicates that a moderate oxidization can keep the surface atomic regularity of the 2×1-structured H-terminated diamond (100). Furthermore, from these observations, possible oxygen sites bonded to the diamond (100):H 2×1 surface are discussed in relation to the amount of hydrogen in the CVD diamond surface.

Keywords: CVD diamond, surface structure, STM, hydrogen, oxygen

J. Nakamura

2-1 Yamada-oka, Suita, Osaka 565-0871, Japan

Phone: +81-6-6879-7723 Fax: +81-6-6879-7704

E-mail: nakamura@daiyan.pwr.eng.osaka-u.ac.jp

THEORETICAL ANALYSIS ON PIEZORESISTIVE EFFECT OF DIAMOND FILMS

BY CHEMICAL VAPOR DEPOSITION

K. J. Liao, W. L. Wang, C. Y. Kong, S. X. Wang, Q. Feng, Y. Ma

Department of Applied Physics, Chongqing University, Chongqing 400044 P. R. China

ABSTRACT

The piezoresistive effect in p-type heteroepitaxial diamond films was investigated. The diamond films were

prepared on Si (100) by microwave plasma chemical vapor deposition. The films were boron doped by the cold

implantation and rapid annealing technique. The experimental results showed that the gauge factor for the diamond

films at 100 microstrain was about 1200 at room temperature. Based on the Fuchs and Sondheimer thin film theory

and valence band split-off model, a theoretical calculation of the piezoresistive effect in diamond films was

presented by Solving Boltzmanm transport equation in the relaxation time approximation and using the parallel

connection resistance model. The analysis results were in good agreement with the experimental data.

Keywords: Diamond films, Piezoresistive effect, Valence band split-off, CVD

INTRODUCTION

Recently, it was found that both the p-type single and polycrystalline diamond films prepared by chemical vapor

deposition have a very significant piezoresistive effect (ref. 1 to 2). Diamond has a unique combination of

mechanical, electronic and chemical properties. Therefore, there is a tremendous potential for diamond

piezoresistive sensors with a performance much better than that of similar Si or SiC, especially in chemical harsh,

strong radiation and high temperature (ref. 3 to 6). In this work, the piezoresistive effect in p-type diamond thin

films was investigated. The origin of the piezoresistive effect in diamond films was theoretical analyzed.

EXPERIMENTAL DETAILS

The diamond films were grown on Si (100) by microwave plasma CVD system. The chamber was evacuated to

10⁻³ Torr. The reactive gases were a mixture of H₂ and CH₄. The Total pressure was about 18 mbar and the flow rate

was 300sccm. The substrate temperature was set at 850 °C. The microwave power and frequency were 800W and

NASA/CP-2003-212319 260 August 18, 2003 2.45GH₂, respectively. The substrates were treated with a hydrogen plasma for 20min, then, a bias of -250V relative to the microwave plasma was applied to the substrate for 20min. CH₄/H₂ was about 2%. Subsequently, the bias voltage was turned off, but all the process conditions, remained unchanged except for CH₄/H 0.5% and substrate temperature 750°C. The growth time was 12h. X-ray and Raman spectroscopy measurements showed that the films were in the orientation growth with diam (100) //Si (100) and diam <110> // Si <110> (ref. 7 to 8). The diamond films were boron-doped by the cold implantation and rapid amealing technique (ref. 9).

The strain gauge of p-type diamond films were prepared by etching the boron-doped diamond layers on the undoped diamond films using oxygen plasma in a reactive ion etching system. The diamond strain gauge on diamond / silicon diaphragm was set in a seated test vessel to measure the piezoresistive effect. Ar gas was introduced into the vessel and a tensile stress was created by the gas pressure. The strain can be measured by Raman spectroscopy (ref. 10). The resistance of the films was determined by electrical four-point measurements.

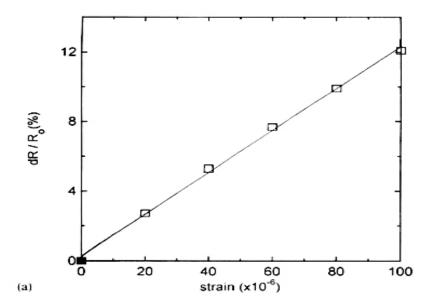


Fig.1. Relationship between the relative resistance changes and the tensile strain at room temperature.

Fig. 1. Shows the relative changes in resistance ($\Delta R/R_0$) with strain at room temperature for p-type heteroepitaxial diamond films. The gauge factor can be obtained from the curve. It was found that the gauge factor is about 1200 at 100 microstrain, greatly exceeding that of polycrystalline diamond films and crystalline silicon (ref. 11 to 12).

THEORITICAL ANALYSIS

The origin of piezoresistive effect in p-type diamond films was ascribed to strain-induced splitting or shift of the boron acceptor level relative to the valence band (ref. 2). The effect can be studied by solving the Boltzmann

equation in the relaxation time approximation. Considering an electric field \bar{E} , the Boltzmann equation can be written as

$$\vec{v} \cdot \nabla f - \frac{e}{\hbar} \vec{E} \cdot \nabla_{\vec{k}} f = -\frac{f - f_0}{\tau} \tag{1}$$

where \bar{v} is the velocity of hole, $f(\bar{v},\bar{r})$ and $f_0(\bar{v})$ are the distribution and equilibrium distribution function, respectively, \bar{r} is the plate vector of the hole, τ and \hbar are the relaxation time and the plank constant, respectively. $\nabla_{\bar{k}}$ is the gradient of wave vector \bar{k} . The general solution of eq. (1) can be obtained by the Fucks-Sondheimer thin film model (ref. 13) in the form

$$f = f_0 - \vec{v} \cdot \vec{D} \frac{\partial f_0}{\partial \varepsilon} \left[1 + F(\vec{v}) \exp(-z/\tau v_z) \right]$$
 (2)

where $\vec{D} = -e\tau A\vec{E}$, $A = 1 + F(\vec{v}) \exp(-z/\tau v_z)$, ε is hole energy and $F(\vec{v})$ can be defined as $F^{\pm}(\vec{v})$ for $v_z > 0(+)$ and $v_z < 0(-)$ from Fucks boundary conditions (ref. 13),

$$F^{+}(\vec{v}) = -\frac{1 - S}{1 - S \cdot \exp(-d/v_z)} \qquad v_z > 0$$
 (3)

$$F^{-}(\vec{v}) = -\frac{1 - S}{1 - S \cdot \exp(-d/v_z)} \cdot \exp(d/v_z) \qquad v_z < 0$$

$$\tag{4}$$

where S is the coefficient of surface scattering. Then, the current density and conductivity can be written as

$$\vec{J} = \frac{2e}{(2\pi)^3} \int \vec{v} (f - f_0) d^3 \vec{k} = \frac{3e^2}{(2\pi)^3} \int \tau A \vec{v} \vec{v} \cdot \vec{E} \frac{\partial f_0}{\partial \varepsilon} d^3 k$$
 (5)

$$\sigma_{ij} = \frac{2e^2}{(2\pi)^3} \int \tau A v_i v_j \frac{\partial f_0}{\partial \varepsilon} d^3k \tag{6}$$

The conductivity components for the stripe sample can be written as

$$\sigma_{xx} = \frac{e^2 p}{m^* \sqrt{\pi}} \int_0^\infty \tau A \alpha^{\frac{3}{2}} e^{-\alpha} \cdot \sin^3 \theta d\alpha d\theta \tag{7}$$

in which $\alpha = (E_v - \varepsilon)/kT$, P is hole density. For the cases of the spherical energy surface and the mixed scattering by lattice vibration and ionized impurities, the relaxation time can be become as (ref. 14),

$$\tau = \frac{3\sqrt{\pi}m^*\mu_L}{4e} \cdot \frac{\alpha^{\frac{3}{2}}}{\beta + \alpha^2} \tag{8}$$

where μ_L is the mobility of hole and β is a slowly varying function of energy. Substituting eq. (8) into (7), then conductivity is given by

$$\sigma_{xx} = Pe\mu_L \varphi(t)k(\beta) \tag{9}$$

in which

$$\varphi(t) = 1 - \frac{3}{8t}(1 - S) \tag{10}$$

$$K(\beta) = \int_0^\infty \frac{\alpha^3 e^{-\alpha}}{\alpha^2 + \beta} d\alpha \tag{11}$$

where $t = \frac{d}{\lambda}$, d is film thickness, λ is the mean free path of the hole.

The valence bands of semiconducting diamond are consisted of the light-hole band, the heavy-hole band and the split-off band. The energy interval between the heavy-hole band and split-off band is about 0.006eV without strain. The light-hole and heavy-hole bands are degenerate. Considering a parallel connection resistance model for the light, heavy and split-off bands, the conductivity under certain strain can be given by

$$S_{xx}(\Delta \varepsilon) = \sum_{i=1}^{3} \sigma_{xx}(i)$$
 (12)

where $\sigma_{xx}(i)$ (i = 1,2,3) is the conductivity of light, heavy and split-off hole bands, respectively. Thus, piezoresistivity of the films under the certain strain can be written as

$$\frac{\Delta \rho}{\rho_0} = \frac{S(0)}{S(\varepsilon)} - 1 = \frac{A(0)}{A(\Delta \varepsilon)} - 1 \tag{13}$$

in which

$$A(\Delta \varepsilon) = \sum_{i=1}^{3} P_{i2}(\Delta \varepsilon) \cdot \mu_{i2} \cdot \varphi(t_i) \cdot K(\beta_i)$$
(14)

where $P_{i2}(\Delta\varepsilon) = \frac{P_i}{p_2}$ (i = 1,2,3), and $\mu_{i2} = \frac{\mu_{Li}}{\mu_{L2}}$, $\Delta\varepsilon$ is the energy level interval between light-hole band and heavy-hole band.

Fig. 2. Shows the numerical calculation results of piezoresistive effect for p-type heteroepitaxial diamond films under a uniaxial stress according to eq. (13). From Fig. 2, it can be seen that the relative changes in the resistivity with $\Delta\varepsilon$ are much likely that with strain as shown in Fig. 1. The relative change in resistivity is approx 0.12 at 100 microstrain at room temperature. There are also the same values when $\Delta\varepsilon$ is about $0.56 \times 10^{-3} \text{eV}$. These imply that the light-hole band shifts to $0.56 \times 10^{-3} \text{eV}$ downward under a tensile stress, which was caused by 100 microstrain. These suggested that the piezoresistive effect in p-type diamond films is responsible in terms of the light-hole band split-off under the stress.

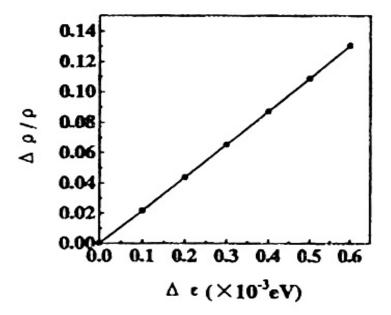


Fig. 2. The calculation results of the Piezoresistive effect for p-type heteroepreaxial diamond films under a uniaxial stress.

CONCLUSION

The experimental results have showed that there was a very large piezoresistive effect in the p-type heteroepitaxial diamond films. The gauge factor for the films at 100 microstrain was found to be 1200 at room temperature, greatly exceeding that of crystalline silicon. The origin of piezoresistive effect in diamond films can be explained by a valence band split-off model. Theoretical calculation was in good agreement with experimental results.

ACKNOWLEDGMENTS

This work was supported by the National Nature Science Foundation of China under grand No.50005027.

- Wang W. L, Jiang X, Taube K et al., Piezoresistive effect of polycrystalline p-type diamond films of various doping levels at different temperature, J. Appl. Phys. Vol. 82, No. 2, 1997, 729~732
- 2. Aslam M, Taber I, Masood A, Piezorsistivity in vapor deposited diamond films, Appl. Phys. Lett, No. 60, 1992, 2923~2925

- 3. Zhu W, Stoner B. R, Williams B. E, et al., Growth and characterization of diamond films on nondiamond substrate for electronic applications, Proc of IEEE. Vol. 79, No. 5, 1991, 627~645
- 4. Gildenblat G. Sh, Grot S. A, Badzian A, The electrical properties and device applications of homoepitaxial and polycrystalline diamond films, Proc. of IEEE, Vol. 79, No. 5, 1991, 647~668
- 5. Deguchi M, Kitabatake M, Hirao T et al., Piezoresistive properties of chemical-vapor-deposited p-type diamond strain-gauges fabricated on diaphragm structure, Diamond Ralat. Mater. 1996, 5, 728~731
- 6. Fang L, Wang W. L, Ding P. D, et al., Study on the piezoresistive effect of crystalline and polycrystalline diamond under uniaxial strain, J. Appl. Phys, 1999, Vol. 86, No. 9, 5158~5193
- 7. Jing X, Klages C. –P, Zachai R, et al., Epitaxial diamond thin films on (100) silicon substrate, Appl. Phys. Lett. 1993, Vol. 62, No. 26, 3438~3440
- 8. Wang W. L, Liao K. J, Feng B, et al., Piezoresistity of p-type heteroepieaxial diamond films on Si (100), Diamond Relat. Mater, 1998, 7, 528~532
- 9. Wang W. L, Liao K. J, Wang B. B, Enhanced transverse magnetoresistive effect in semianducting diamond films, Chin. Phys. Lett, 2000, Vol. 17, No. 5, 370~372
- 10. Ager III J. W, Drong M. D, Quantitative measurement of residual biaxial stress by Raman spectroscopy in diamond grown on a Ti alloy by chemical vapor deposition, Phys. Rev. B, 1993, Vol. 48, No. 4, 2601~2607
- 11. Fang L, Wang W. L, Ding P. D, et al., Study on Piezoresistive effect in p-type polycrystalline diamond, Science in China, 1999, Vol. 47, No. 7, 769~778
- 12. Wang W. L, Jiang X, Klages C. –P, Piezoresistive studies of diamond films, Chin. Sci. Bull. 1995, Vol. 40, No. 3, 209~212
- 13. Fuchs K, Wills H. H, The conductivity of thin metallic films according to the electron theory of metals, Proc. Camb. Phil. Soc. 1938, 34, 100~108
- 14. Beer A. C, Willardson R. K, Hall and transverse magnetoresistive effects for warped band and mixed scattering, Phys. Rev. 1958, 110, 1286~1294

IDENTIFICATION OF THE CHEMICAL STATE OF CARBON ATOMS ON NANODIAMOND POUDER SURFACES

A. P. Dementjev, K. I. Maslakov

RRC "Kurchatov Institute", 1, Kurchatov sq., Moscow 123182, Russia, e-mail: A.Dem@ru.net

ABSTRACT

The chemical state of carbon atoms on surface of nanodiamond particles is not known. In order to identify the chemical state the N(E) CKVV Auger spectroscopy with X-ray excitation of Auger emission have been used. According to the CKVV data on the surfaces of nanodiamond particles the carbon atoms have the same electron configuration as in graphite: $\sigma_s^{\ 1}\sigma_p^{\ 2}\pi^1$, but opposite to graphite the $\pi*\pi$ transitions do not take place. The phenomenon is evidence of absence of overlapping π -levels. The same chemical state takes place on surface of natural diamond (110) after H-treatment. The chemical state is inactive to environment.

Keywords: AES, Nanodiamond, Surface chemical state.

INTRODUCTION

It is well known that the CVD diamond growth on non-diamond substrates begins after long time treatment of the surfaces. Nano size diamond powder considerably reduces this time (ref. 1,2). This fact allows to assume, that on a surface of ND particles there is a chemical state (C_d) of carbon atoms, which is responsible for diamond nucleation and growth. The Nano size diamond powder is designed as Nanodiamond (ND) or Ultra dispersion diamond (UDD). In order to identify the chemical state of carbon atoms on (ND or UDD) surfaces the N(E) CKVV Auger spectroscopy with X-ray excitation of Auger emission have been used.

EXPERIMENTAL

XPS and X-ray excited Auger electron spectra (XAES) were obtained using the MK II VG Scientific spectrometer with nonmonochromatized Al K α X-ray source (1486.6 eV). The base pressure both in main and preparation chambers was equal to $5*10^{-10}$ mbar. All spectra were calibrated relative to the reference C1s XPS peak (284.8 eV). The position of C1s was determined with respect to Ar2p_{3/2} XPS peak at 241.3 eV after implantation of a small dose of Ar $^+$ into UDD.

UDD powders (3-5 nm) were received from the Kiev Institute of Superhard Materials, Snejinsk and from Krasnoyarsk. The UDD powder was deposited on a Si plate with native oxide by mean an alcohol suspension in an ultrasonic bath. Si2p XPS peak was used to measure surface coverage. W hot-filament (2300 K) was used for decomposition of H₂ The temperature of W- filament was measured by a pyrometer. Distance between the hot-filament and sample is equal to 10 mm. The temperature of diamond, UDD and silicon samples was measured by thermocouple that was deposited side by side. Apparently, such a method of temperature measurement underestimates its real value on the surface due to the temperature gradient in the surface layer. The surfaces of UDD and natural diamond were analyzed before and after H treatment at 10⁻⁶ mbar in the preparation chamber of the spectrometer. After that the sample was transferred in to analysis chamber. The crystal plane (110) of a natural diamond of size 6*5 mm and 1.5 mm thickness was mechanically polished by means of a cast iron wheel. The roughness was equal to about 1 nm. An ultrasonic rinse in acetone and then in alcohol was performed prior to the mounting sample in the vacuum chamber.

RESULTS

Fig. 1 shows comparison of UDD CKVV Auger spectrum with Auger spectra of carbon atoms in sp² and sp³ references forms. The slopes of the right parts spectra of HOPG and fullerine coincide. Hence the same process takes place in the case of fullerine. The shift of the CKVV Auger spectra fullerene can be attributable to the more deep

NASA/CP—2003-212319 266 August 18, 2003

position of its π - band in comparison with that of graphite as was shown by Swami et al (ref.3). The Auger spectra of UDD differ from that of fullerene, polyethylene and HOPG. The slope of the right part of polyethylene and UDD spectra coincides but differs in the kinetic energy position.

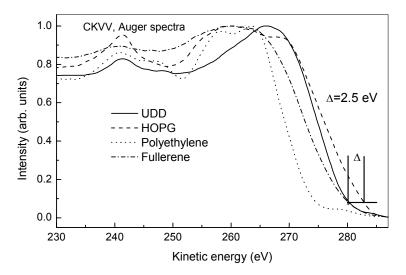


Figure 1. Comparison of experimental Auger spectra.

In order to determine the chemical state of C-atoms on a surface of UDD and diamond after H-treatment we must identify CKVV Auger spectra. Earlier we showed (ref. 4) that the Auger spectra of these states are the same.

The comparison of UDD and HOPG spectra with the self-convolution of DOS (the last one is taken from Murday *et al* (ref. 5, 6) is represented in Fig. 2. It can be seen that in the UDD case $\pi^*\pi$ and $\sigma_s^*\pi$ transitions are not realized. The contribution of $\sigma_p^*\pi$ take place in the spectra and consequently there are π -bonds on the surface. So, this implies that on UDD surfaces the carbon atoms have the same electron configuration as in graphite: $\sigma_s^1 \sigma_p^2 \pi^1$ but opposite to graphite the $\pi^*\pi$ transitions do not realized.

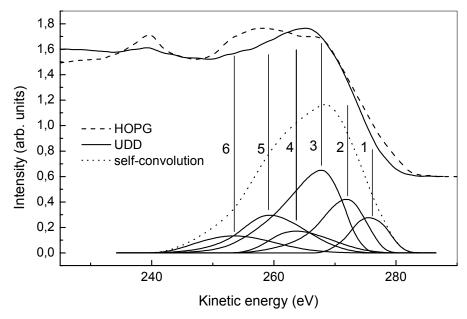


Figure 2. Comparison of the experimental Auger spectra of HOPG and UDD with the self-convolution of graphite: $1 - \pi * \pi$; $2 - \sigma p * \pi$; $3 - \sigma p * \sigma p$; $4 - \pi * \sigma s$; $5 - \sigma p * \sigma s$; $6 - \sigma s * \sigma s$.

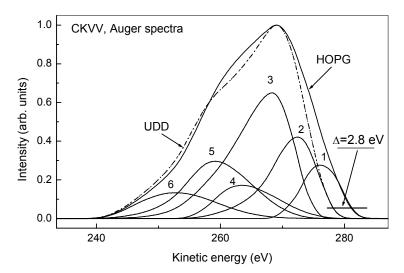


Figure 3. Comparison of the self-convolution for 1 – 6 transitions (denoted as HOPG) with that for UDD without 1 and 4 transitions. The components of the self-convolution for UDD do not show.

The right part of the theoretical spectra on Fig. 3 agree with the experimental spectra on Fig. 1,2 on the slope and on the Δ as well as. The results support our supposition about absence of the $\pi^*\pi$ and $\sigma s^*\pi$ transitions.

The slope of the right part of polyethylene and UDD spectra (Fig. 1) coincides but differs in the kinetic energy position. The right part CKVV spectrum of polyethylene is the self-convolution of the σp valence band (ref. 7). The σp - band occupation is equal to 3 electrons. The coincidence of the right part slope of the spectra is evidence of the same number of electrons taking part in the Auger decay in the both cases. For better visualization of these ideas we shall consider a scheme of Auger decay for graphite, UUD and polyethylene:

$$\begin{array}{c} \text{Graphite} \\ \text{C1s}^2 \, \sigma_s^1 \sigma_p^2 \pi^1(\text{VB}) + \text{X-ray} \rightarrow \text{C1s}^1 \sigma_s^1 \sigma_p^2 \pi^1(\text{VB}) + \text{e (photoelectron)} \\ \text{C1s}^1 \sigma_s^1 \sigma_p^2 \pi^1(\text{VB}) \rightarrow \text{C1s}^2 \sigma_s^1 \sigma_p^2 \pi^0(\text{VB}) + \text{hv (inner X-ray)} \\ \text{C1s}^2 \sigma_s^1 \sigma_p^2 \pi^0(\text{VB}) \rightarrow \text{C1s}^2 \sigma_s^1 \sigma_p^2 \pi^1(\text{VB}^{-1}) \\ \text{C1s}^2 \sigma_s^1 \sigma_p^2 \pi^1(\text{VB}^{-1}) + \text{hv (inner X-ray)} \rightarrow \text{C1s}^2 \sigma_s^1 \sigma_p^2 \pi^0(\text{VB}^{-1}) + \text{e (Auger electron)} \\ \text{UDD} \\ \text{C1s}^2 \sigma_s^1 \sigma_p^2 \pi^1(\text{VB}) + \text{X-ray} \rightarrow \text{C1s}^1 \sigma_s^1 \sigma_p^2 \pi^1(\text{VB}) + \text{e (photoelectron)} \\ \text{C1s}^1 \sigma_s^1 \sigma_p^2 \pi^1(\text{VB}) \rightarrow \text{C1s}^2 \sigma_s^1 \sigma_p^2 \pi^0(\text{VB}) + \text{hv (inner X-ray)} \\ \text{C1s}^2 \sigma_s^1 \sigma_p^2 \pi^0(\text{VB}) + \text{hv (inner X-ray)} \rightarrow \text{C1s}^2 \sigma_s^1 \sigma_p^1 \pi^0(\text{VB}) + \text{e (Auger electron)} \\ \text{C1s}^2 \sigma_s^1 \sigma_p^3 + \text{X-ray} \rightarrow \text{C1s}^1 \sigma_s^1 \sigma_p^3 + \text{e (photoelectron)} \\ \text{C1s}^1 \sigma_s^1 \sigma_p^3 \rightarrow \text{C1s}^2 \sigma_s^1 \sigma_p^2 + \text{hv (inner X-ray)} \\ \text{C1s}^2 \sigma_s^1 \sigma_p^3 + \text{X-ray} \rightarrow \text{C1s}^1 \sigma_s^1 \sigma_p^3 + \text{e (photoelectron)} \\ \text{C1s}^2 \sigma_s^1 \sigma_p^3 + \text{X-ray} \rightarrow \text{C1s}^2 \sigma_s^1 \sigma_p^3 + \text{e (photoelectron)} \\ \text{C1s}^2 \sigma_s^1 \sigma_p^3 + \text{X-ray} \rightarrow \text{C1s}^2 \sigma_s^1 \sigma_p^3 + \text{e (photoelectron)} \\ \text{C1s}^2 \sigma_s^1 \sigma_p^3 + \text{V-ray} \rightarrow \text{C1s}^2 \sigma_s^1 \sigma_p^3 + \text{e (photoelectron)} \\ \text{C1s}^2 \sigma_s^1 \sigma_p^3 + \text{V-ray} \rightarrow \text{C1s}^2 \sigma_s^1 \sigma_p^3 + \text{e (photoelectron)} \\ \text{C1s}^2 \sigma_s^1 \sigma_p^3 + \text{V-ray} \rightarrow \text{C1s}^2 \sigma_s^1 \sigma_p^3 + \text{e (photoelectron)} \\ \text{C1s}^2 \sigma_s^1 \sigma_p^3 + \text{V-ray} \rightarrow \text{C1s}^2 \sigma_s^1 \sigma_p^3 + \text{e (photoelectron)} \\ \text{C1s}^2 \sigma_s^1 \sigma_p^3 + \text{V-ray} \rightarrow \text{C1s}^2 \sigma_s^1 \sigma_p^3 + \text{e (photoelectron)} \\ \text{C1s}^2 \sigma_s^1 \sigma_p^3 + \text{V-ray} \rightarrow \text{C1s}^2 \sigma_s^1 \sigma_p^3 + \text{e (photoelectron)} \\ \text{C1s}^2 \sigma_s^1 \sigma_p^3 + \text{V-ray} \rightarrow \text{C1s}^2 \sigma_s^1 \sigma_p^3 + \text{e (photoelectron)} \\ \text{C1s}^2 \sigma_s^1 \sigma_p^3 + \text{V-ray} \rightarrow \text{C1s}^2 \sigma_s^1 \sigma_p^3 + \text{e (photoelectron)} \\ \text{C1s}^2 \sigma_s^1 \sigma_p^3 + \text{V-ray} \rightarrow \text{C1s}^2 \sigma_s^1 \sigma_p^3 + \text{e (photoelectron)} \\ \text{C1s}^2 \sigma_s^1 \sigma_p^3 + \text{V-ray} \rightarrow \text{C1s}^2 \sigma_s^1 \sigma_p^3 + \text{e (photoelectron)} \\ \text{C1s}^2 \sigma_s^1 \sigma_p^3 + \text{V-ray} \rightarrow \text{C1s}^2 \sigma_s^1 \sigma_p^3 + \text{e (photoelectron)} \\ \text{C1s}^2 \sigma_s^1 \sigma_p^3 + \text{V-ray} \rightarrow \text{C1s}^2 \sigma_s^1 \sigma_$$

The VB is a valance band formed by π - electrons of graphite. The process (2a) show $\pi 0$ -hole infill by valence band (VB) electrons as results of which the Auger decay go through the π - electrons. The (1) - (3) equations show processes for right part of Auger spectra. The (2*), (3*) and (2**), (3**) processes one should introduce in order to understand the coincidence of the slope of the experimental Auger spectra UDD and polyethylene. In the Auger decay takes part three electrons: $\sigma p^2 \pi^1$ (UDD) and σp^3 (polyethylene). These hypothetical schemes are supported by results in Figures 2, 3. So, this implies that on UDD surfaces the carbon atoms have the same electron configuration that in graphite: $\sigma s^1 \sigma p^2 \pi^1$, but opposite to graphite the $\pi * \pi$ transitions are absent. In principle the $\pi * \pi$ transitions it is impossible in graphite because of one electron on the π^1 - level. But the $\pi * \pi$ transitions in graphite take place due to the fact of π - holes delocalization in graphite (2a process). We use the CKVV Auger spectrum of polyethylene as standard of sp³ – bonds because a preparation of diamond surface with the sp³ - bonds are difficult if not impossible to realize. We received UDD-like state on diamond surfaces as result of a standard polishing process.

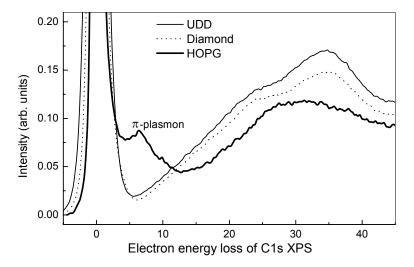


Figure 4. EEL of C1s XPS spectra.

Fig. 4 shows coincidence of EEL spectra UDD and diamond. This implies the same chemical states in both cases but differ from that of HOPG. The depth information of the CKVV Auger emission, Electron energy loss of C1s and valence band XPS is equal to about 2, 7 and 10 monolayers respectively according to our estimation on base Powell and Jablonski formulas (ref. 8). So, the combination of the techniques allow to study chemical bonds in the range of $2 \div 10$ monolayers. It is very important since the growth of CVD diamond go through layer by layer deposition. The EEL of C1s XPS spectra opposite to CKVV Auger show diamond state on the nanodiamond particles. This is because of the difference in the depth information. The absence of π-plasmon feature in EEL spectrum of UDD is evidence of very thin layers with the $\sigma s^1 \sigma p^2 \pi^1$ surface state. The Electron energy loss of C1s spectra are informative about C = C bonds through the π -plasmon excitation (ref. 9,10).

DISCUSSION

Our results show that on the surfaces of nanodiamond powder and natural diamond after *in-situ* or *ex-situ* H-treatment take place the same chemical state of carbon atoms (ref. 4). Obviously, Pate's (ref. 11) experimental data allow to gain insight into the chemical state of carbon atoms that was observed by the CKVV Auger spectra. Pate (ref. 11) found that valence band and core level spectra of diamond (111) undergo reversible changes due to cycles of hydrogen adsorption and desorption. After desorption of hydrogen the PES spectrum shows the presence of a feature in spectrum similar to that of the π - bands of graphite. The analogous state was observed by Himpsel et al (ref. 12). The angle-integrated data were very similar to the behavior of the π bands of graphite. However, the angle resolved data show that the surface state has not the same momentum distribution as the π -bands of graphite. It is very likely that, the N(E) CKVV Auger spectra are conditioned by the same surface state that was observed by Pate (ref. 11) and Himpsel *et al* (ref. 12). Probably, the CKVV Auger spectra allow work out in detail of π - bonded chain model of Pandey (ref. 13). For example, the CKVV Auger spectra is evidence of absence the π -levels overlapping. The same data did not follow from PES measurements (ref. 11,12).

The $\pi*\pi$ transitions in CKVV Auger decay are virtual only under delocalization of π -holes. The $\pi*\pi$ transitions are inherent for standard chemical compounds with sp^2 – bonds. The absence of the transitions allow to suppose that we deal with a new surface chemical state of carbon atoms. Along with that the chemical states of carbon atoms may be classified by CKVV Auger spectra as: sp^2 - $,sp^3$ –bonds and Nanodiamond-like chemical state (NDLCS). We suppose the NDLCS is originality chemical state of carbon atoms on base of the next measurements:

- a volume of Nanodiamond samples as received and after *in-situ* H-treatment and heating up to 1100 K;
- natural diamond (110) after *in-situ* H-treatment at 1000 K;
- natural diamond (110) after *ex-situ* H-treatment during 8 minutes at 1100 K in ASTeX-PDS19 techniques at conditions of CVD growth without CH₄;

- after interruption of ex-situ CVD diamond growth in ASTeX-PDS19 techniques;
- after standard mechanical polishing.

In every of the measurements the CKVV Auger spectra were practically equiform. The results are evidence of a inertness of the NDLCS and powerful of the Auger emission with X-ray excitation for study of CVD growth *insitu* and *ex-situ* as well as.

CONCLUSIONS

According to the CKVV data on the surfaces of the nanosized particles the carbon atoms have the same electron configuration that in graphite: $\sigma_s^1\sigma_p^2\pi^1$ but opposite to graphite without overlapping of π -levels because the $\pi*\pi$ transitions are absent. The chemical state of the nanosized particles is inactive to environment. The Auger spectra of the nanosized particles have original shape and differ from that for standard chemical compounds with $sp^2-or sp^3-bonds$. It seems plausible that the NDLCS is responsible for diamond nucleation and growth.

- 1. A.A. Smolin, V.G. Ralchenko et al, Appl. Phys. Lett. 62 (1993) 3449.
- 2. V.I. Konov, A.A. Smolin, V.G. Ralchenko et al., Diamond and Related Materials, 4 (1995) 1073.
- 3. N. Swami, Hong He, B. E. Koel, Phys. Rev. B59 (1999) 8283
- 4. A.Dementjev, K. I. Maslakov el at New Diamond and Frontier Carbon Technology, Vol. 12, No. 1 (2002) 15.
- 5. J. S. Murday, B. J. Danlap, F. L. Hutson, P. Oelhafen, Phys. Rev. B24 (1981) 4764.
- 6. J. E. Houston, J. W. Rogers, Jr., and R. R. Rye, F. L. Hutson and D. E. Ramaker, Phys. Rev. B34 (1986) 1215.
- 7. J.A. Kelber, R.R. Rye, G.C. Nelson and J.E. Houston, Surf. Sci. 166 (1982) 148.
- 8. C. J. Powell and A. Jablonski, NIST Electron Inelastic-Mean-Free-Path Database-Version 1.1 National Institute of Standards and Technology, Gaithersburg, MD (2000).
- 9. McFeely F.R., Kowalczyk S.P., Ley L. et. al.: Phys. Rev., B9 (1974) 5268.
- 10. G. Beamson and D. Briggs High Resolution XPS of Organic Polymers. The Scienta ESCA300 Database, John Wiley and Sons Ltd. West Sussex PO19 1UD, England 1992.
- 11. B.B. Pate: Surf. Sci. 165 (1986) 83.
- 12. F. J. Himpsel, D. E. Eastman, P. Heimann, and J. F. Van der Veen: Phys. Rev. B 24 (1981) 7270.
- 13. K.C. Pandey, Phys. Rev.B25 (4338) 1982.

CHEMICAL MODIFICATION OF DIAMOND POWDER USING PHOTOLYSIS OF PERFLUOROAZOOCTANE

T. Nakamura, M. Ishihara, T. Ohana and Y. Koga

National Institute of Advanced Industrial Science and Technology Central 5, 1-1-1 Higashi, Tsukuba, Ibaraki 305-8565, Japan E-mail: takako-nakamura@aist.go.jp; Fax: +81-29-851-5425; Tel: +81-29-861-9307

ABSTRACT

Photolysis of perfluoroazooctane with diamond powders led to the chemical modification of the diamond surfaces under mild conditions to introduce perfluorooctyl ester and ether functional groups, confirming by means of FT-IR, XPS and ¹⁹F NMR measurements.

Keywords: Perfluoroalkylation, Photolysis, Diamond powder, Surface modification

INTRODUCTION

Diamond is a material, which has been widely investigated because of its various unique properties such as electrical, thermal and mechanical properties (ref. 1). Chemical modifications of the diamond surfaces have been expected to lead improvement of its original behaviors (ref. 2 to 4). We can find recent studies on introduction of organic functional groups such as benzoyloxy (ref. 5), cyano (ref. 6) and alkyl substitutents (ref. 7) on the surface of diamond films and powders terminated with hydrogen or oxygen by using photo- and thermochemical methods.

On the other hand, perfluoroalkyl-containing organic compounds have attracted much attention in the field of medicinal chemistry and material science because of their unique properties derived from the presence of fluorine atoms, namely biological activities and water/oil repellent properties (ref. 8). Previously we reported that photolysis of perfluoroazooctane (1) gave perfluorooctyl radicals effectively in solutions under mild conditions for perfluoroalkylation of organic compounds (ref. 9). Introductions of substituents containing fluorine atom would result in improvement of the behavior of diamond surfaces, which is enhanced lubricity and stability under extreme conditions (ref. 10). To date, fluorination of diamond surfaces has been studied by use of F₂ gas (ref. 11), CF₄ plasma (ref. 12) and X-ray irradiation (ref. 13). These methods would make problems about handling of the reactions and make it necessary to use special vessels. In this paper, we report on an useful method for chemical modification of diamond powders with perfluoroalkyl substituent by using photolysis of 1 under mild condition.

EXPERIMENTAL

A typical experiment is described as follows. Azo compound 1 (3.7 mg) in perfluorohexane (4 ml), prepared according to the literature (ref. 14), was irradiated with a low-pressure mercury lamp for 8 h at room temperature in the presence of diamond powders (10 mg) purchased from Tomei diamond industry Co., Ltd. (MD500, 500 nm) and an argon atmosphere with stirring. After removal of the perfluorohexane solution from the reaction mixture, the residual powders were washed with perfluorohexane and hexane. The washed powders were analyzed with a microscopic FT-IR, X-ray photoelectron and solid-state ¹⁹F NMR spectrometers.

RESULS AND DISCUSSION

Figure. 1a, b shows FT-IR spectra of the diamond powders before and after treatment of irradiation with 1. The sample after the photoreaction indicates observations of a new peak at 1196 cm⁻¹ with C-F stretching bands and of a red shift of carbonyl stretching vibration from 1792 to 1751 cm⁻¹. It is known that the surface of untreated diamond powders has carbonyl groups such as carboxylic acid and cyclic ketone (ref. 2 and 12). These results suggest that perfluorooctyl radical generated by photolysis of 1, abstracted hydrogen from carboxylic acid, and then the reaction

NASA/CP—2003-212319 271 August 18, 2003

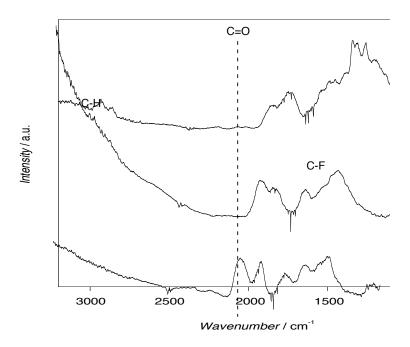


Figure 1. FT-IR spectra of (a) untreated diamond powders, (b) diamond powders after treatment of perfluorooctylation and (c) hydrolyzed fluorinated powders.

of another C₈F₁₇ radical with carboxylic radical to give perfluorooctyl ester on the surface of diamond powders (Scheme 1).

In order to confirm the formation of perfluorooctyl ester functionality on diamond surface, the fluorinated material was treated under hydrolysis condition in aqueous NaOH. An FT-IR spectrum of the hydrolyzed material showed that the ester group reverted to carboxylic acid with a peak due to carbonyl group of the untreated diamond powders as shown in Figure. 1c. However, C-F stretching bands remained around 1200 cm⁻¹ region and peaks of 2930 and 2856 cm⁻¹ were observed in the region of C-H stretching bands after hydrolysis. It was found that these results reveal perfluorooctylation and hydrogenation of cyclic ketone on the surface of diamond powders occurred to

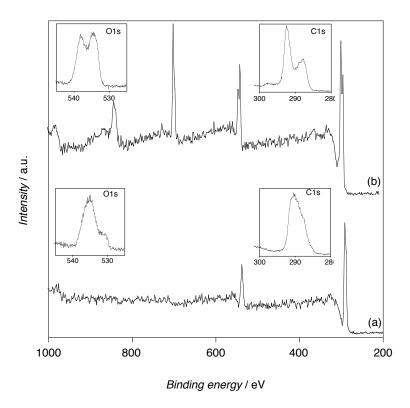


Figure 2. XPS spectra of diamond powders (a) before and (b) after irradiation with perfluoroazooctane (1). The inset is carbon 1s and oxygen 1s spectra of untreated and fluorinated diamond powders.

form perfluorooctyl ether group which could remain unaltered under hydrolysis condition, accompanied with esterification of the diamond powders as shown in Scheme 1.

As shown in Figure 2, XPS spectra of the diamond powders were measured before and after treatment of perfluorooctylation, showing that a new peak at 694.4 eV of fluorine 1s was observed after irradiation. In the carbon 1s region, a strong peak at 293.1 eV with higher binding energies ascribed to carbon atom bound to fluorine atom,



Figure 3. ¹⁹F NMR spectrum of fluorinated diamond powders.

compared with the untreated diamond powders. Additionally, binding energies of 534.6 and 538.0 eV of oxygen 1s were also observed due to C=O and C-O, respectively.

Moreover, the presence of the fluorinated surfaces on diamond powders was characterized with a solid-state ¹⁹F NMR for further confirmation. The spectrum shown in Figure 3 exhibited signals at ☐ ☐79.2 ppm (-OCF₂-) together with signals at ☐ -119.2 ppm (-CF₂-). No observation of signals due to −NCF₂- moiety shows that introduction of perfluorooctyl group on diamond surfaces occurred, not physical adsorption of 1.

CONCLUSION

Photolysis of azo compound 1 with diamond powders led a chemical modification of the surface to form perfluorooctyl ester and ether functional groups. The introduction of the perfluoroalkyl substituents was confirmed by FT-IR, XPS and ¹⁹F NMR measurements. Application of this method to diamond and its related materials thin films as a lubricant is under investigation.

- 1. Wei, J.; Yates Jr., J.T.: Diamond surface chemistry. 1. A review, Crit. Rev. Surf. Chem., vol. 5, 1995, 1.
- Miller, J.B.; Brown, D.W.: Photochemical modification of diamond surfaces, Langmuir, vol. 12, 1996, 5809.
- 3. Ando, T., et al.: Chemical modification of diamond surfaces using a chlorinated surface as an intermediate state, Diamond Relat. Mater., vol. 5, 1996, 1136.
- 4. Ikeda, Y., et al.: Halogenation and butylation of diamond surfaces by reactions in organic solvents, Diamond Relat. Mater., vol. 7, 1998, 830.
- 5. Tsubota, T., et al.: Chemical modification of hydrogenated diamond surface using benzoyl peroxides, Phys. Chem. Chem. Phys., vol. 4, 2002, 806.
- 6. Tsubota, T., et al.: Chemical modification of diamond surface using a diacyl peroxide as radical initiator and CN group-containing compounds for the introduction of the CN group, Phys. Chem. Chem. Phys., vol. 4, 2002, 3881.
- 7. Strother, T., et al.: Photochemical functionalization of diamond films, Langmuir, vol. 18, 2002, 968.
- 8. Banks, R.E.: Organofluorine Chemicals and their Industrial Applications, Ellis Horwood, London, 1979.
- 9. Nakamura, T.; A. Yabe: A Direct Introduction of Perfluorooctyl Group into Cycloalkanes using the Photolysis of Perfluoroazooctane upon 185 nm Irradiation, J. Chem. Soc., Chem. Commun., 1995, 2027.
- 10. Molian, P.A.; Janvrin, B.; Molian, A.M.: Laser Chemical-Vapor Deposition of Fluorinated Diamond Thin-Films for Solid Lubrication, Wear, vol. 165, 1993, 133.
- 11. Kealey, C.P., et al.: Fluorination of polycrystalline diamond films and powders. An investigation using FTIR spectroscopy, SEM, energy-filtered TEM, XPS and fluorine-18 radiotracer methods, J. Mater. Chem., vol. 11, 2001, 879.
- Ando, T., et al.: Diffuse-Reflectance Fourier-Transform Infrared Study of The Plasma-Fluorination of Diamond Surfaces using a Microwave- Discharge in CF₄, J. Chem. Soc., Faraday Trans., vol. 89, 1993, 3105
- 13. Smentkowski, V.S.; Yates, J.T.: Fluorination of diamond surfaces by irradiation of perfluorinated alkyl iodides, Science, vol. 271, 1996, 193.
- 14. Chambers, W.J.; Tullock, C.W.; Coffman, D.D.: The Synthesis and Chemistry of Fluoroazoalkanes, J. Am. Chem. Soc., vol. 84, 1962, 2337.

OXIDATION EFFECTS ON POLYCRYSTALLINE DIAMOND FILM SURFACE

Jingqi Li*, Qing Zhang, S. F. Yoon, J. Ahn

Microelectronics center, School of Electrical and Electronic Engineering, Nanyang Technological University, Singapore 639798. E-mail: p144703764@ntu.edu.sg

ABSTRACT

Polycrystalline diamond films deposited by Hot Filament CVD technique are oxidized in both Thermogravimetric Analyser (TGA) and Lindberg furnace at temperature from 500° C to 800° C. TGA result shows that the onset oxidation temperature is about 700° C and the activation energy is 175kJ/mol. SEM images indicate that $\{111\}$ facets are preferentially oxidized, $\{100\}$ is the least reactive facets. On $\{111\}$ facts, the oxidation is not randomly but regularly oriented, with some thin and long 'ridges' parallel to <110> direction, which has not been reported before. After oxidation at 700° C and 800° C, slight graphitization on diamond surface is indicated by Raman spectra.

Keywords: CVD diamond, Oxidation, TGA, Activation energy.

INTRODUCTION

Oxygen play a very important role both in improving diamond film quality by oxygen addition into reactive gas (refs. 1 to 2) and in modifying surface properties, such as electron emission (ref. 3), negative electron affinity (ref. 4), and electrical conductivity (ref.5), et al. Therefore, investigation of interaction of oxygen with diamond surface is of great importance.

In this study, polycrystalline CVD diamond films were prepared using HFCVD technique. Thermogravimetric analyzer (TGA) and Lindberg furnace were used for measuring the on-set oxidation temperature and diamond surface etching, respectively. The oxidation effects on diamond surface are discussed in detail.

EXPERIMENTAL DETAIL

CVD diamond films used in this study were deposited on Si (100) substrate using HFCVD technique, the substrate pretreatment and deposition conditions are the same as our previous paper (ref.6).

For the thermogravimetric analysis (TGA) study, free-standing diamond films were prepared by dissolving the silicon substrate in an HF solution and then analyzed using thermogravimetric technique which was performed on a PEKIN ELMER TGA7 Thermogravimetric analyzer. The oxidation of diamond films was conducted between room temperature and $1000~^{0}$ C at a heating rate of 5^{0} C/min in the atmosphere. The gas flowing rate in the furnace was 30ml/min.

In order to study the oxidation properties, diamond films on silicon were oxidized in Lindberg furnace at temperatures of 500, 600 and 800°C for 10 min, and at 700°C for 2min and 10min. A flow of 1000sccm oxygen was used as oxidation source. During the temperature ascending and descending procedure, a flow of 1000sccm nitrogen, instead of oxygen, was fed into the furnace to protect the sample from oxidation.

RESULT AND DISCUSSION

Before oxidation, diamond film surface was examined by scanning electron microscopy (SEM) images, as shown in Fig.1. The as-grown surface is a mixture of (111) and (100) facets, but dominated by (111) ones with average grain size of about $8\mu m$. X-ray diffraction pattern and Raman spectroscopy result suggest that diamond films have high quality, no impurities are detectable by both of them.

Weight loss of the diamond films as a function of temperature is shown in Fig.2. It is found that the oxidation began at about 700° C, the weight of free-standing diamond films lost slowly from 700° C to 835° C. After 835° C, the weight dropped quickly until all the diamonds were burned out at 970° C. The starting temperature for oxidation is in the range of reported value of $500\sim800^{\circ}$ C (ref.7 to 11), and is slight higher than that of natural diamond. The different results in the publications maybe caused by the quality of the diamond in the study, such as film thickness, grain size and defect number. Zhu *et al* (ref.7) has compared the starting oxidation temperature of diamond films

with diamond powders and found that the diamond powder started oxidation at a lower temperature. The smaller the powder grains, the lower the starting temperature.

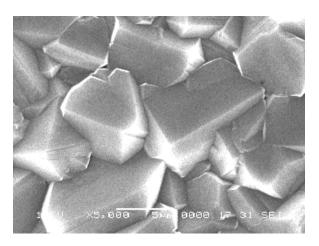


Figure 1. SEM image of as-grown diamond surface

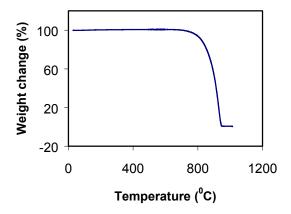


Figure 2. Diamond weight loss as a function of temperature

Oxidation rates at different temperatures are deduced from the TGA curve, and then are used to calculate the activation energy of diamond oxidation by Arrhenius plots. In our experiment, the activation energy is 175kJ/mol. This value is less than the reported experimental and theoretical values for oxidation of pure {100} face, which is in the range of 183~230kJ/mol (refs.11 to 14). Because the sample surface is dominated by {111} face, this activation energy value indicates that {111} is oxidized more easily than {100} face.

The morphology change of diamond films due to oxidation was observed by SEM. No oxidation phenomenon was found at 500 and 600° C. At 700° C, the oxidation effect was apparent. After 10min oxidation, the diamond grains have been etched seriously, but some {100} facets are still unchanged, as seen in Fig.2a, which demonstrates that {100} is the least reactive facet to oxidation. All the facets are oxidized at 800° C for 10min. Figure 2b is an image of a facet after oxidation at 700° C for 2min. It is interesting to notice that the surface is composed of many thin and long 'ridges' in parallel with one of the longer sides of this irregular hexogen. The formation of 'ridges' on

the oxidation surface indicates that the oxidation prefers a definite direction, along which the oxidation occurs much easily. According to Clausing's cubo-octahegral crystal evolution model (ref. 15), this facet is a {111} facet, and the preferred oxidation direction can be attributed to <110>.

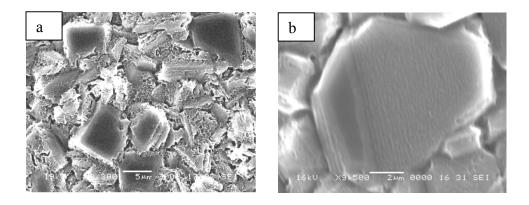


Figure 4. Diamond surface after oxidation at 700°C. The oxidation time for a and b are 10mins and 2mins, respectively.

Diamond films oxidized at different temperature are analyzed by Raman spectra. There is no substantial change for diamond peak at 1332cm^{-1} , but the broad peak at about 1580cm^{-1} increase slightly as the temperature, as shown in Fig.3, which is an indication of surface graphitization. This is in agreement with Zhu et al's result[7]. After oxidation, there are a large amount of dangling bonds on diamond surface which cause high surface energy. Such carbon atoms tend to form C=C bond clusters to decrease the dangling bond number in the same mechanism as the formation of Pandy π -bonded chain (ref. 16) on diamond surface. We suggest that these C=C bond clusters are responsible for the graphitization.

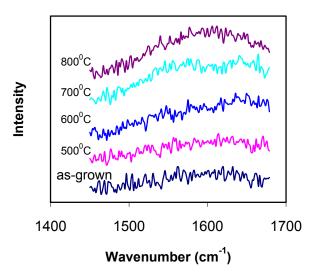


Figure 5. Raman spectra of diamond films after oxidation at different temperature.

CONCLUSION

Oxidation of polycrystalline CVD diamond is investigated using TGA and Lindberg furnace, which give oxidation activation energy and etched diamond surface, respectively. Both activation energy and oxidation observation on diamond surface indicate that {111} facet is more reactive than {100}. The oxidation on {111} surface is not randomly, but prefers along <110> direction. The slight graphitization of diamond surface after oxidation is due to the formation of C=C bond clusters.

- 1. I. Sakaguchi, M. Nishitani-Gamo, K. P. Loh, et al: Suppression of surface cracks on (111) homoepitaxial diamond through impurity limitation by oxygen addition. Appl. Phys. lett. Vol.73, 1998, 2675.
- 2. Y. S. Han, Y. K. Kim, J. Y. lee: Effects of argon and oxygen addition to the CH₄-H₂ feed gas on diamond synthesis by microwave plasma enhanced chemical vapor deposition", Thin Solid Films, vol.310, 1997, 39.
- 3. A. Shih, J. Yater, P. Perhrsson, et al: Secondary electron emission from diamond surfaces. J. Appl. Phys. vol.82, 1997, 1860.
- 4. N. Eimori, Y. Mori, A. Hatta, et al: Electron affinity of single-crystalline chemical-vapor-deposited diamond studied by ultraviolet synchrotron radiation. Jpn. J. Appl. Phys. Part1, vol. 33, 1994, 6312.
- 5. Y. Mori, H. Kawarada, A. Hiraki: Properties of metal/diamond interfaces and effects of oxygen adsorbed onto diamond surface. Appl. Phys. Lett., vol.58, 1991, 940.
- 6. J. Li, Q. Zhang, S. F. Yoon, et al: Reaction of diamond thin films with atomic oxygen simulated as low-earth-orbit environment. J. Appl. Phys., vol.92, no.10, 2002, 6275.
- 7. W. Zhu, X. H. Wang, A. R. Badzian and R. Messier: An investigation of the oxidation behavior of CVD diamond films. Proceeding of the second international conference, New Diamond Science and Technology, 1990, p821.
- 8. K. Tankala and T. Debroy: Etching of HFCVD diamond films in air, nitrous oxide and Argon. Proceeding of the second international conference, New Diamond Science and Technology, 1990, p827.
- 9. C. Q. Sun, H. Xie, W. Zhang, et al: Preferential oxidation of diamond {111}. J.Phys. D: Appl. Phys., vol.33 2000, 2196.
- 10. J. Y. Howe, L. E. Jone, D. W. Coffey: The evolution of microstructure of CVD diamond by oxidation. Carbon, vol.38, 2000, 929.
- 11. P. John, N. Polwart, C. E. Trope, J. I. B. Wilson: The oxidation of (100) textured diamond. Diamond Relat. Mater., vol.11, 2002, 861.
- 12. F. K. de Thejie, N. J. van der Laag, M. Plomp, W. J. P. van Enckevort: A surface topographic investigation of {001} diamond surfaces etched in oxygen. Phil. Mag. A, vol.80, 1999, 725.
- 13. T. Evan, C. Phaal: The kinetics of the diamond-oxygen reaction. Proc of the 5th conf. on Carbon, Pergamon Press, 1962, p.147-53.
- 14. M. Frenklach, D. Huang, R. E. Thomas, et al: Activation energy and mechanism of CO desorption from (100) diamond surface. Appl. Phys. Lett., vol.63, 1993, 3090.
- 15. R. E. Clausing, L. Heatherly, E. D. Specht, and K. L. More: Texture development in diamond films grown by hot filament CVD process. Proceeding of the second international conference, New Diamond Science and Technology, 1990, p575.
- 16. K. C. Pandy: New dimerized-chain model for the reconstruction of the diamond (111)-(2X1) surface. Phys. Rev. B, vol.25, 1982, 4338.

CHEMICAL REACTIONS OF C-ATOMS WITH NANODIAMOND AND DIAMOND SURFACES

A. P. Dementjev, K. I. Maslakov

RRC "Kurchatov Institute", 1, Kurchatov sq., Moscow 123182, Russia, e-mail: A.Dem@ru.net

ABSTRACT

The deposition of carbon atoms on surfaces of: a) silicon substrate; b) ultra dispersion diamond (UDD) and natural diamond (110) after H-treatment (ND-H-t) has been studied in-situ by N(E) CKVV AES with x-ray excitation combined with C1s and valence band XPS techniques. The chemical state (C_d) of carbon atoms on the surfaces of ND-H-t is identical to that in UDD. According to the CKVV Auger spectra the C_d state is conditioned by π -band different from that of graphite. The carbon atoms were prepared by decomposition of CH₄ on W hot-filament at 2300 K. In case a) the carbon atoms formed a graphite-like structure. In case b) the CKVV Auger spectra did not show any modification of initial chemical state on UDD or ND-H-t surfaces up to about 4 monolayers. The results point to incorporation of carbon atoms into diamond structure.

Keywords: AES, Nanodiamond, Surface chemical reactions.

INTRODUCTION

The growth mechanism of CVD diamond films is a continuing subject of debate (ref. 1, 2). The theoretical models (ref. 2) of CVD diamond growth consist from more then hundred of elementary chemical reactions for both gas-phase and surface. While the gas-phase reaction mechanism is based on the known rate coefficient of elementary chemical reactions and experimental measurements, the surface reaction mechanism brings up a few problems. The main of them is the identification of chemical state of carbon atoms on a growth surface. The data (ref.3,4) imply the existence of two chemical states of carbon atoms C_dH (sp³) and C_d (sp²) on diamond surface after H-treatment.

In the present paper we are reporting our results on identification of the chemical interaction C_d + C-atoms by N(E) CKVV Auger spectra, electron energy loss of C1s and valence band XPS. These techniques allow to determine chemical state of carbon atoms in depth from 2 to 10 mono layers. It is very important because the growth on surface go through layer by layer deposition.

EXPERIMENTAL

The surfaces of UDD and natural diamond were analyzed before and after H or CH_4 —treatment at 10^{-6} mbar in the preparation chamber of the spectrometer after that the sample was transferred in to analysis chamber. The carbon atoms were prepared by decomposition of CH_4 on W hot-filament at 2300 K. The temperature of substrate is equal about 700 K. The experimental condition were the same as in (ref. 5). The crystal plane (110) of a natural diamond of size 6*5 mm and 1.5 mm thickness was mechanically polished by means of a cast iron wheel. The roughness was equal to about 1 nm. An ultrasonic rinse in acetone and then in alcohol was performed prior to the mounting of the sample in the vacuum chamber.

RESULTS

First of all we determine products of CH₄ decomposition by theirs deposition on silicon wafer with native oxide. Fig. 1- 4'show the wide, Si2p XPS, CKVV and Electron energy loss of C1s XPS spectra before and after carbon deposition on Si substrate. The deposition speed of carbon atoms on silicon substrate was determined by effective attenuation of intensity Si2p and O1s spectra using Powell and Jablonski data (ref. 6). The speed is equal to about one monolayers/minute. The Si2p XPS spectra (Fig. 6) show weak chemical interaction of carbon atoms silicon and oxygen because there are not considerable changes in the Si2p spectrum in Fig. 2. The CKVV Auger spectra (Fig. 3)

NASA/CP—2003-212319 279 August 18, 2003

and EEL of C1s XPS (Fig. 4) show the growth of a thin layers of graphite. Carbon atoms have been deposited on Sisubstrate after Ar etching as well. In this case SiC was formed (Fig. 5).

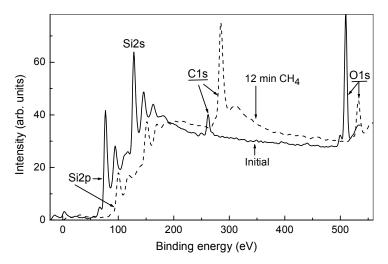


Figure 1. Wide spectra before and after C-atoms deposition on Si substrate.

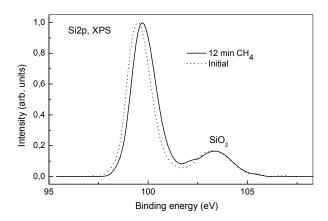


Figure 2. Si2p before and after C-atoms deposition

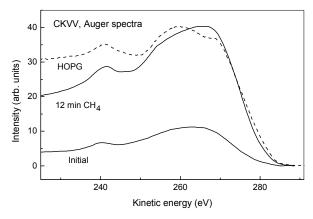


Figure 3. CKVV before and after C-atoms deposition on Si substrate (Initial is carbon contamination).

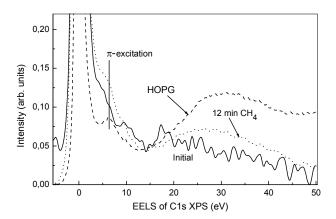


Figure 4. EEL before and after C-atoms deposition on Si substrate.

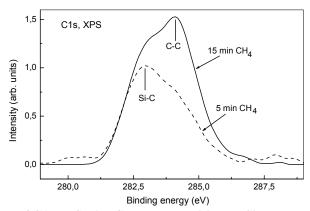


Figure 5. Evolution of C1s XPS with C-atoms deposition on Si-substrate after Ar-etching.

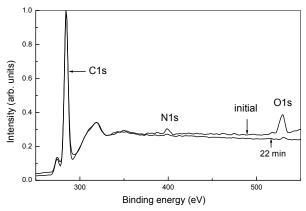


Figure 6. Wide spectra before and after C-atoms deposition on UDD substrate.

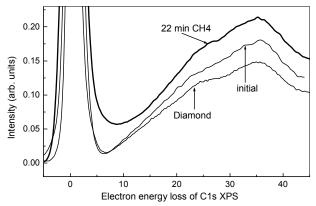


Figure 7. Evolution EEL of C1s XPS with C-atoms deposition on Diamond (Initial is UDD).

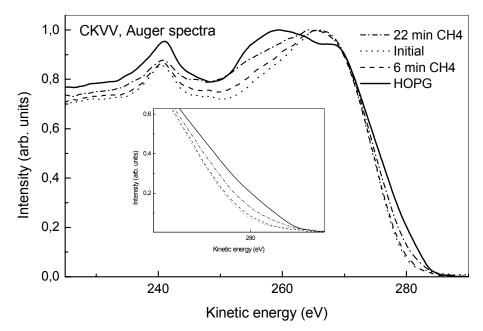


Figure 8 Evolution of CKVV spectra with C-atoms deposition on UDD and ND-H-t.

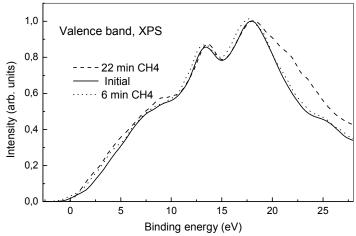


Figure 9. Evolution of Valence band XPS with C-atoms deposition on Diamond.

DISCUSSION

The understanding of the chemical states and chemical interaction on diamond surfaces is important for further technological advances in the growth of smooth diamond films by the chemical vapor deposition method. In this connections we tried to study a peculiarities of C-atoms chemistry on diamond surface.

Graphite growth takes place under deposition of C-atoms on Si- substrate with native oxide. This conclusion follows from spectra on fig. 1, 3, 4. The Si2p XPS spectrum (Fig. 2) shows the absence of chemical interaction of C-atoms with substrate in this case. As result of chemical interaction of C- atoms with clean Si-substrate the growth SiC take place (Fig. 5) and diffusion of C- atoms in to deeper layers.

The Wide, CKVV, EEL and valence band spectra (Fig. 6-9) demonstrate another chemical interaction under deposition of C-atoms on natural diamond and UDD in comparison with that on Si-substrate with native oxide. Depth information (DI) of CKVV Auger emission, EEL of C1s XPS and Valence band is equal 2, 7 and 10 monolayers, respectively. As is easy to see on Fig. 6-9 there is not sharp modification of the spectra. It is expected that the modification of all spectra would be stronger. There are a few explanations for this modification:

- 1) C-atoms did not interact with diamond and UDD surfaces;
- 2) C-atoms incorporated in to structure of the deeper layers;
- 3) Strong diffusion and dilution of the C-atoms during deposition take place.

Obviously, the case 1) has low probability, because the deposition of C-atoms on Si-O substrate take place without interaction. We have not answer on the cases 2) and 3) at present time.

Fig. 8 shows modification of the Auger spectra with C-atom deposition. In view of our data (ref. 5) the modification results in increase of $\pi^*\pi$ contribution. The noticeable changes of the CKVV spectra occurred only after 22 minutes of the C-treatment. This spectrum can be synthesized as 0.5 CKVV (UDD) + 0.5 CKVV (HOPG). This phenomenon can be considered either as the absence of adsorption on diamond surface or as the incorporation of adsorbed C-atoms into structure of the substrate without its modification. But the attenuation intensity of N1s XPS is evidence of C-atoms adsorption (Fig. 6). Consequently, the incorporation of C-atoms into structure of the substrate without its modification up to some monolayers should be supposed. The following reaction could take place in our experiment:

$$\begin{array}{ll} D_p + H \rightarrow D \backslash C_d H & (1) \\ D \backslash C_d H + X \text{-ray (or thermo-des.)} \rightarrow D \backslash C_d + m H & (2) \\ D \backslash C_d + C \rightarrow D \backslash C_d C & (3) \\ D \backslash C_d C \rightarrow (D + n D) \backslash C_d & (4) \end{array}$$

where, D_p – the chemical state on native diamond surface after polishing (sometimes this state represents the sp^2/sp^3 mix sometimes it is UDD-like), D – diamond structure under top layers. The H-treatment of the D_p in preparation chamber creates the C_dH –site on the diamond surface (ref. 1). As the result of thermodesorption during H-treatment or the Auger decay induced in main chamber the desorption of H-atoms and formation of the C_d – site on D takes place (ref. 2). In the preparation chamber C -atoms interact with the C_d –sites on the surface, as the result of this process the nD – diamond layers grow up to some monolayers. The supposition of the nD – diamond layers is based on absent of the graphite inherent peculiarities in CKVV Auger spectra and XPS.

CONCLUSIONS

We have tried to show that by using the N(E) CKVV Auger spectroscopy in combination with electron energy loss of C1s and valence band XPS it should be possible to probe *in situ* C-atoms interaction with the diamond surfaces. The techniques allow to determine the chemical state of carbon atoms in the depth from 2 to 10 monolayers. It is very important because the growth on surface goes through layer by layer deposition.

Obviously, we observed the incorporation of C-atoms in to diamond structure.

- 1. D. G. Goodwin and J. E. Butler: Ch. 11 in Handbook of industrial diamond and diamond films, Ed. M. A. Prelas, G. Popovici and L. K. Bigelow, (Marcel Dekker, New York, 1998).
- 2. M. Frenklach and Hai Wang: Phys. Rev. B 43 (1991) 1520.
- 3. B.B. Pate: Surf. Sci. 165 (1986) 83.
- 4. F. J. Himpsel, D. E. Eastman, P. Heimann, and J. F. Van der Veen: Phys. Rev. B 24 (1981) 7270.
- 5. A. P. Dementjev, K. I. Maslakov, Identification of the chemical state of carbon atoms on naanodiamond powder, this ADC/FCT 03, transaction.
- 6. C. J. Powell and A. Jablonski, NIST Electron Effective-Attenuation-Length Database-Version 1.0 National Institute of Standards and Technology, Gaithersburg, MD (2001)

Electron emission from nano-structured diamond films deposited on ion

implanted Si substrates

Changzhi Gu

State Key Laboratory of Surface Physics, Institute of Physics

czgu@aphy.iphy.ac.cn

Abstract

Electron emission from diamond surface can occur due to its low or even negative electron affinities.

Diamond films can show a planar electron emission property at low electric field and be manufactured cheaply.

Although a considerable research effort on diamond field emission has been made in decade, there are no obvious

mechanisms by which electrons can be transported through the bulk diamond film to the surface and how to obtain

stable electron emission.

Nano-structured diamond film is one of the most promising materials for active display device because the high

grain boundary density in film can submit more emit sites. In this paper we reported that the enhanced and stable

electron emission at low applied fields is obtained from nano-structured diamond films deposited on Si substrates

implanted by high concentration boron (B) and phosphor (P) ion.

3 μ m-thickness nano-structured diamond films were grown on B and P ion implanted Si wafers by a microwave

plasma enhanced chemical vapor deposition (MPECVD) process. The average grain size for films deposited on high

concentration B and P implanted substrates is 30-200 nm. The electron emission properties from the films on

implanted substrates were studies, an enhanced emission property from high concentration implanted samples were

concluded. The results show that the high concentration implanted samples have an obvious decreasing in threshold

and increasing in current density, particular to the high concentration P implanted sample. This can be attributed to

the higher grain boundary density induced by small grain size of nano-structured diamond films deposited on

implanted substrates, which permit more emit sites.

NASA/CP—2003-212319 284 August 18, 2003

CHARGE-BASED DEEP LEVEL TRANSIENT SPECTROSCOPY OF DEFECTS IN ELECTRON-IRRADIATED AND ANNEALED CVD DIAMONDS

V.I. Polyakov, A.I. Rukovishnikov, N.M. Rossukanyi

Institute of Radio Engineering & Electronics, RAS, 11 Mohovaya str., Moscow 103907, Russia

V.G. Ralchenko, I.I. Vlasov

General Physical Institute, 38 Vavilova str., Moscow 119991, Russia

ABSTRACT

Electrically active defects in undoped and moderately boron-doped microwave plasma CVD diamond films subjected to electron-irradiation and/or vacuum annealing to high, up to 1625° C, temperatures were studied with Charge-based Deep Level Transient Spectroscopy. Concentration, activation energy E_A , and capture cross-section of native and boron-related defects are determined. The undoped samples before the treatments displayed the acceptor defects with a continuous energy spectrum, while the B-doped samples showed two discrete levels with E_A of 0.37 and 0.25 eV. The electron irradiation (2 MeV, dose 5×10^{18} cm⁻²) changes the parameters of boron-induced levels, reduces the concentration of the defects with the continuous energy spectrum, and strongly, by four orders of magnitude, reduces electrical conductivity. After annealing only one B-related level with E_A = 0.37 eV (boron in substitutional position) remains, but simultaneously an increase in abundance of acceptor defects with low activation energy was observed.

Keywords: diamond film, electron irradiation; annealing; boron doping, DLTS

INTRODUCTION

Defects result in efficient recombination centers or carrier traps, and determine carrier concentration, mobility and other electrical properties, which are important for diamond electronic application. Besides the defects formed during diamond growth specific defects can be created by ionising radiation. In case of electron irradiation the changes in electrical properties of boron-doped single-crystal diamond is interpreted in terms of radiation-induced donors, i.e. the introduction of donor defect levels into forbidden gap (refs. 1 to 4). In particular, the electrical resistivity of diamond increases, as was observed for single-crystals and homoepitaxial diamond films after light ion (H, He) irradiation (refs. 5,6), and for neutron-irradiated polycrystalline CVD diamond (ref. 7). It was found, mainly from optical measurements on electron damaged p-type boron-doped single-crystal diamonds, that the electron-induced defects are vacancies (refs. 1 to 4), which can act as compensating donors reducing the electrical conductivity in p-type diamond (ref. 4,5). Furthermore, the electron-induced defects can decrease the carrier mobility that also would reduce the conductivity (ref.6). The concentration of electron-induced defects and their interaction with other native and impurity-related defects depend on the type of diamond and post-growth treatment, such as annealing (refs, 1 to 4, 8).

For unambiguous determination of the type of the defect-related conductivity, as a rule the Hall effect measurements are used. This technique, however, is difficult to use for diamond in view of its high resistivity (ref. 6). In the present work the isothermal Charge based Deep Level Transient Spectroscopy (Q-DLTS) (refs. 9 to 13) was applied to measure the concentration, activation energy, and capture cross-section of uncompensated electrically active defects in CVD diamond.

In our previous work (ref. 11) it was found that as-grown B-doped polycrystalline diamond films show a continuous Q-DLTS spectrum with two (for some samples, three) boron-induced peaks corresponding to discrete acceptor energy levels. In contrast, only one boron-induced level with activation energy 0.37 eV is displayed in B-doped homoepitaxial diamond films and single-crystal diamonds (ref.12). Here we characterise, using primarily Q-DLTS technique, undoped and boron-doped microwave plasma CVD polycrystalline diamond films subjected to electron irradiation and/or annealing at high temperatures.

EXPERIMENTAL DETAILS

Sample preparation

The samples of undoped (electrical resistivity $\rho = 10^{12}$ - $10^{13}\,\Omega$ cm at the room temperature) and moderately boron-doped ($\rho \sim 10^5\,\Omega$ cm) polycrystalline diamond films were examined. The diamond films of 0.4 mm thickness have been grown on Si substrates in a microwave plasma-enhanced CVD system ASTeX-PDS19 (ref. 11,14). The films were chemically separated from the substrate, and cut by a laser to smaller plates (samples) for characterization. The surface conductive layer (if any) on the surfaces of as-grown samples was removed by annealing in air at 800 K for 20 min.

Several undoped and B-doped samples were irradiated with 2 MeV electrons at a dose 5×10^{18} cm⁻², and annealed at 1625^{0} C in vacuum of 10^{15} torr for 1 hour. A sandwich contact configuration was used for the electrical measurements. Low resistivity Ohmic contacts on diamond were prepared by a deposition of Ti/Au bilayer, and its subsequent annealing at 400^{0} C. For making Schottky contacts Ni films were deposited by magnetron sputtering.

Isothermal Charge-based Deep Level Transient Spectroscopy (Q-DLTS)

The isothermal Q-DLTS technique used to characterise the electrically active defects (acceptors in our case) differs from well-known C-DLTS method (ref. 15) in that the parameters of trapped charge ΔQ , rather than capacitance ΔC , transient process is measured in the Q-DLTS method after voltage pulse application. In C-DLTS algorithm the time period of ΔC measurement $\Delta t = t_2 - t_1$, where t_1 and t_2 are the times counted from the beginning of the discharge, is kept fixed while the sample temperature T is scanned to obtain the DLTS spectrum. The algorithm used in Q-DLTS obtains the spectrum by scanning the rate window $\tau_m = (t_2 - t_1)/\ln(t_2/t_1)$ while keeping fixed the sample temperature. Assuming the charge emission from the traps to vary exponentially with time, and keeping the ratio t_2/t_1 constant, the functional dependence $\Delta Q(\tau_m)$, that is Q-DLTS spectrum, has a maximum ΔQ_{max} , that can be used to determine the trapping center parameters (refs. 9 to 13). The t_2/t_1 ratio in the present measurements was equal to 2. In this case the hole emission rate e_p of the acceptor level is obtained from the Q-DLTS spectrum as $e_p = \tau_m^{-1} = \ln 2/t_1$, where τ_m is the value measured at $\Delta Q(\tau_m) = \Delta Q_{max}$. The activation energy E_A and capture cross-section σ_S are derived from Arrhenius plot $\ln(\tau_m^{-1} \times T^{-2})$ vs T^{-1} where $\tau_m \sim \sigma_S^{-1} T^{-2} \exp(E_A/kT)$ and where k is the Boltzmann's constant.

Using a Q-DLTS spectrum at a selected temperature the concentration N_t of uncompensated acceptors related to the observed peak in the Q-DLTS spectrum is obtained as $N_t \cong 4\Delta Q_{max} \, w/Aq\Delta w^2$, where A is the electrode area, q is the electron charge, Δw is the depth of subsurface layer from which emission of the trapped charge occurs, or the change of the depletion layer width (w) caused by charging pulse of bias voltage. The Q-DLTS measurements were performed in the temperature range of 85 to 520 K, the time τ_m varied from 10^{-6} to 10 s. The Q-DLTS spectra were obtained using an ASEC-03 system with charge sensitivity $\Delta Q_{min} = 10^{-16}$ Coulomb and deep level concentration sensitivity $N_t/N = 10^{-7}$ (N – concentration of free carriers).

RESULTS AND DISCUSSION

Conductivity

The undoped as-grown diamond samples showed p-type conductivity with value in the range of $\sigma = 10^{-12} - 10^{-13} \,\Omega^{-1} \mathrm{cm}^{-1}$ at room temperature. The conductivity decreased with temperatures down to $\sigma = 10^{-7} - 10^{-8} \,\Omega^{-1} \mathrm{cm}^{-1}$ at 500K. Arrhenius plots of the conductivity for an undoped sample before and after electron irradiation are displayed in Fig. 1a. The activation energy of the conductivity is $E_a = 0.72 \, \mathrm{eV}$ in as-grown film. As a result of electron irradiation E_a did not change, but a strong decrease, by four orders of magnitude, in the conductivity is observed (Fig.1a). A similar effect of e-irradiation takes place also for a B-doped sample (Fig. 1b). Its conductivity decreased by two orders of magnitude, activation energy slightly increasing from initial $E_a = 0.3 \, \mathrm{eV}$ to $E_a = 0.37 \, \mathrm{eV}$ after irradiation, the latter value being well established activation energy of substitutional boron acceptor.

Kalish et al. (ref. 5) reported the reduction in conductivity of B-implanted single-crystal diamond subjected to ion irradiation, that was ascribed to boron compensation by vacancies created by the stopping ions. The vacancy concentration created by e-irradiation in our case, about $3x10^{17}$ cm⁻³, is comparable with B concentration, a few ppm (ref. 11), in the film, therefore a substantial part of boron atoms are compensated, and the conductivity strongly decreases.

We note that a certain fraction of all vacancies could be spent for compensation of the defects (acceptors) other than boron. In particular, in polycrystalline diamond structural acceptor defects localized in bulk as well as on grain boundaries can interact with the radiation defects. Vacancies are immobile in the analyzed temperature range T < 500 K (refs. 7,8), but are supposed to be able to migrate along grain boundaries. Our Q-DLTS spectra show continuous energy components (see below), which typically belong to disordered regions and grain boundaries. The observed radiation-stimulated spectra modifications may indicate the grain boundary-enhanced defect diffusion.

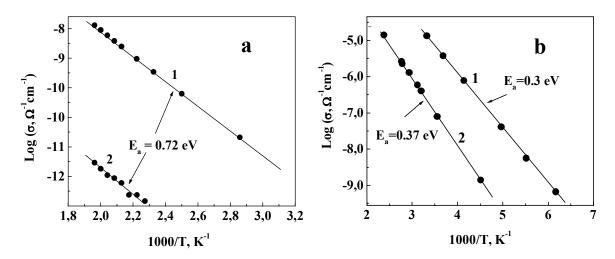


Figure 1. Temperature dependence of conductivity σ for undoped (a) and boron-doped (b) diamond films: 1 - as-grown; 2 - after electron irradiation. E_a is the activation energy of conductivity.

Q-DLTS spectra

Activation energies of conductivity found from Arrhenius plots for undoped film (Fig. 1) seems to not correspond to any definite type of defect, rather they are some effective values several different defects (or continuous spectrum of them) are present. More details on the defects were obtained with Q-DLTS measurements.

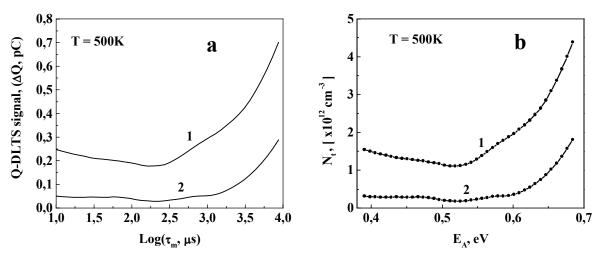


Figure 2. Energy spectra of defects in undoped diamond film: (a) experimental Q-DLTS spectrum taken at 500K, (b) absolute defect concentration N_t estimation from Q-DLTS data: 1 – as-grown; 2 – after electron irradiation.

The Q-DLTS spectra at 500K for as-grown and electron irradiated samples are shown in Fig. 2a. No clear peaks are seen in the spectra, most probably the electrically active defects with the continuous energy spectrum are

localized at the grain boundaries. The p-type of the defects was evidenced by the sign of ΔQ signal. The DLTS spectra can be transformed to defect concentration N_t as a function of the activation energy E_A if capture cross-section $\sigma_S = 10^{-18}$ cm², a reasonable value for defects in CVD diamond (see for example, ref. 7), is assumed. We find that the e-irradiation reduces by a factor of 2 to 4 the concentration N_t of the native defects in the E_A range of 0.4-0.7 eV (Fig.2b), and this is in line with the conductivity decrease. However, it was not possible to examine lower activation energies, which could give a major contribution to conductivity, because of too sample high resistance.

The Q-DLTS spectra of the as-grown and electron-irradiated B-doped diamond sample are shown in Fig. 3a. As revealed by Q-DLTS in our earlier work (refs. 11,12) in as-grown B-doped CVD diamond the incorporated boron atoms produce two or three electrically active defects. The acceptor levels (peaks A, B) have activation energies E_A = 0.36 and E_A = 0.25eV, and capture cross-sections of σ_S = 1.3 x 10⁻¹³ and σ_S = 4.5 x 10⁻¹⁹ cm², respectively. The former level with E_A = 0.36eV is probably induced by boron atoms in substitutional sites in the grain bulk, while latter level with lower energy may be due to another position of incorporated boron. The grain boundaries with high density of defects can act as sinks for impurity atoms (refs. 16,17), so an enhanced boron concentration can be expected there, not necessarily in stable substitutional sites. This results in more complex DLTS spectra with peaks of different activation energies and capture cross-section. As a consequence, the measured activation energy of the conductivity E_a = 0.3 eV in as-grown sample is noticeably less than in B-doped monocrystalline diamond (0.37eV).

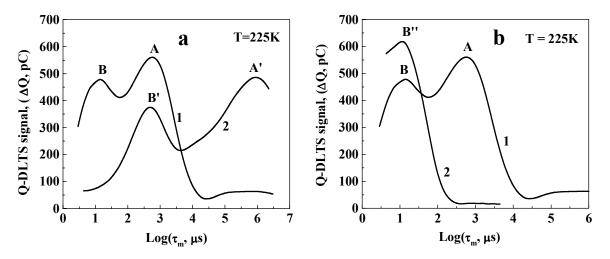


Figure 3. Q-DLTS spectra of B-doped diamond film at T=225 K: (a) 1 – as-grown sample; 2 – after electron irradiation; (b) 1 – as-grown sample; 2 – after annealing at 1625°C.

The concentration of boron-induced acceptors is reduced by electron irradiation as seen from the decrease of the ΔQ signal magnitude (Fig. 3a). The calculated values of E_A , σ_S , and N_t are summarized in Table 1. The impact of radiation on concentration of the two boron-related acceptors (reduction in N_t is about 20% for peaks A and B) is much less compared to the case of undoped sample (see Fig. 2). This may be due to lower content of native acceptors in the as-grown undoped film, so the compensation degree at the given irradiation dose should be higher for the undoped sample.

Table 1. The parameters of boron-induced defects in B-doped diamond film before and after electron irradiation and annealing, as determined from Q-DLTS spectra

Samples		E _A , eV	$\sigma_{\rm S}$, cm ²	N_t , cm ⁻³
As-grown	Peak A	0.25	4.5 10 ⁻¹⁹	$3 \cdot 10^{16}$
	Peak B	0.36	$1.3 \ 10^{-13}$	$2.4 \cdot 10^{16}$
After electron	Peak A'	0.26	5 10 ⁻²¹	$2.4 \cdot 10^{16}$
irradiation	Peak B'	0.37	10 ⁻¹⁴	$2 \cdot 10^{16}$
After annealing	Peak B''	0.37	3 10 ⁻¹³	$3 \cdot 10^{16}$

Annealing effect

The parameters of defects in diamond may strongly vary by annealing (see for example, refs. 6,18). The B-doped diamond sample showed significant changes in Q-DLTS spectra after annealing at 1625°C (Figs. 3b). For the annealed film the 0.25eV peak in the spectrum disappeared while the 0.37eV peak somewhat increased (see Fig. 3b, and Table 1), the spectrum becomes typical for monocrystaline films.

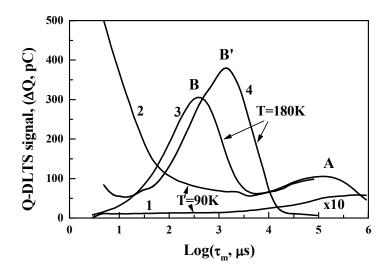


Figure 4. Q-DLTS spectra (low energy defects) of B-doped diamond film measured at 180 and 90K: 1 and 3 – as-grown sample; 2 and 4 – after annealing at 1625°C.

The high enough conductivity of B-doped samples made it possible to perform DLTS measurements at low temperatures to obtain information about defects with lower (>0.01eV) activation energies (Fig. 4). It is seen again the absence of the 0.25eV deep level (A peak) after annealing (spectrum at 180K), but at T=90K a signal from some acceptors with continuous energy spectrum rises steeply towards very low activation energies (Fig.4, compare curves 1 and 2). What kind of defect modification in the polycrystalline diamonds occurs upon the annealing is not clear enough, however, we note that at the very high annealing temperature used at the present work a graphitization of grain boundaries and darkening of the sample took place (ref.19). Leaving the possible conductivity through the graphitic channels along the grain boundaries out of the consideration, the resulting conductivity of heat-treated diamond would be determined by interplay of reduction in free-carriers concentration supplied by annealed-out 0.25eV defect, and enhanced content of the carriers with continuous spectrum at lower energies.

CONCLUSIONS

Native and boron-related acceptor defects in free-standing undoped and boron-doped MPCVD polycrystalline diamond films have been examined by Q-DLTS technique. A considerable (up to four orders of magnitude) decrease in electrical conductivity and reduction in native acceptors concentration is found in electron-irradiated undoped diamond films, this being ascribed to the radiation-created defects which act as compensating donors for native acceptors. Qualitatively similar, but weaker effect was observed for samples moderately doped (few ppm) with boron. Vacuum annealing at 1625°C lives in the DLTS spectrum only one peak with activation energy 0.37 eV, known for substitutional boron in single crystal diamond, other defects (0.25 eV) initially presented being cured. In addition, defects with very low energy (~0.01 eV) forming a continuous spectrum appears upon that high-temperature treatment.

ACKNOWLEDGEMENTS

This work was supported by the Russian Foundation for Basic Research Grant No 01-02-16046 and Grant INTAS-01-2173.

- Davies G., Lawson S.C., Collins A.T., et al: Vacancy-related centers in diamond. Phys.Rev. B 46, 1992, 13157-13170.
- 2. Field J.E., The Properties of Diamond, Academic Press, New York, 1979.
- 3. Field J.E., The Properties of Natural and Synthetic Diamond, Academic Press, New York, 1992.
- 4. Palmer D.W., in: Davies G. (Ed.), Properties and Growth of Diamond, EMIS, Datareviews Series No 9 INSPEC, London, UK, 1994.
- 5. Kalish R., Uzan-Saguy C., Philosoph B., et al: Loss electrical conductivity in boron-doped diamond due to ion-induced damage. Appl. Phys. Lett., 70, 1997, 999-1001.
- 6. Reznik A., Uzan-Saguy C., Kalish R.: Effects of point defects on the electrical properties of doped diamond. Diamond and Related Materials, 9, 2000, 1051-1056.
- 7. Bruzzi M., Bucciolini M., Lagomarsino S., et al: Deep levels in CVD diamond and Their influence on the electronic properties of diamond-based radiation sensors. Phys. Stat. Sol. (a), No.3, 2002, 563-571.
- 8. Prins J.: Vacancy diffusion and trapping in electron-irradiated type IaA diamonds. Diamond and Related Materials, 10, 2001, 87-93.
- 9. Polyakov V.I., Perov P.I., Ermakova O.N., et al: Kinetics of the photoresponse and spectra determined by the Q-DLTS method for heterostructures made by the MOCVD hydride method and containing an insulating AlGaAs layer. Sov. Phys. Semicond., 23, 1989, 76-79.
- 10. Polyakov V.I., Rossukanyi N.M., Rukovishnikov A.I., et al: Effects of post-growth treatment and coating with ultrathin metal layers on the band bending and field electron emission of diamond films. J. Appl. Phys., 84, 1998, 2882-2889.
- 11. Polyakov V.I., Rukovishnikov A.I., Rossukanyi N.M., et al: Electrical properties of thick boron and nitrogrn contained CVD diamond films. Diamond and Related Materials, 10, 2001, 593-600.
- 12. Polyakov V.I., Rukovishnikov A.I., Varnin V.P., et al: Charge-sensitive deep level transient spectroscopy of boron-doped and gamma-irradiated mono- and polycrystalline diamond. Diamond and Related Materials, 12, 2003, in press.
- 13. Gaudin O., Whitfild M.D., Foord J.S., et al: Deep level transient spectroscopy of CVD diamond: the observation of defect states in hydrogenated films. Diamond and Related Materials, 10, 2001, 610-614
- 14. Ralchenko V.G., Smolin A.A., Konov V.I., et al., Large-area diamond deposition by microwave plasma, Diamond and Related Materials., 6, 1997, 417-421.
- 15. Lang D.V.: Deep-level transient spectroscopy: a new method to characterize traps in semiconductors. J.Appl. Phys., 45, 1974, 3023-3041.
- 16. von Windheim J.A., Venkatesan V., Malta D.M., et al: Comparison of the electrical properties of single-crystal and polycrystalline diamond by Hall effect and capacitance-voltage measurements. Diamond and Related Materials, 2, 1993, 841-846.
- 17. Malta D.M., von Windheim J.A., Wynands H.A., et al: Comparison of the electrical properties of simultaneously deposited homoepitaxial and polycrystalline diamond films. J. Appl. Phys., 77(4), 1995, 1536-1545.
- 18. Chen Chia-Fu, Chen S.H.: Electrical properties of boron-doped diamond films after annialing treatment. Diamond and Related Materials, 4, 1995, 451-455.
- 19. Khomich, A.V., Ralchenko, V.G., Vlasov, A.V., et al., Effect of high temperature annealing on optical and thermal properties of CVD diamond, Diamond and Related Materials, 10, 2001, 546-551.

HYDROGEN IMPLANTED CVD BORON DOPED MONOCRYSTALLINE DIAMOND

D. Ballutaud¹, F. Jomard¹ and E. Rzepka¹,

¹Laboratoire de Physique des Solides et de Cristallogénèse, CNRS, 1 Place A. Briand 92195 Meudon cedex (France)

A. Boutry-Forveille²

²Laboratoire de Magnétisme et d'Optique de Versailles, Université deVersailles-Saint-Quentin, 45 Avenue des Etats-Unis, 78035 Versailles cedex (France)

ABSTRACT

Boron doped ($[B]=5x10^{18}$ cm⁻³) monocrystalline [100] diamond films grown by chemical vapour deposition have been implanted with D⁺ and D₂⁺ ions at room temperature, with an energy of 50 and 100 keV respectively, and the same atomic deuterium dose of $5x10^{16}$ cm⁻². The implanted samples were submitted to successive thermal annealings under ultra-high vacuum. The deuterium profiles were analysed after deuterium implantation and after thermal annealing by Secondary Ion Mass Spectrometry (SIMS). The structural modifications of the buried implanted layer in the diamond film have been analysed by confocal micro-Raman scattering and by Scanning Electron Microscopy. In the case of a deuterium molecular ion implantation, a graphitised and amorphous buried layer may be detected after a 1050 °C thermal annealing. While no deuterium diffusion from the implantation buried layer is detected in the film, the SIMS deuterium profile exhibits a depletion at the implantation peak maximum. A blistering of the diamond layer occurs during a 1350°C thermal annealing. This effect is not observed for D⁺ ionic implantation. In this case, some deuterium diffusion is observed in the film after a 1050°C thermal annealing.

INTRODUCTION

The hydrogen diffusion and the complex formation between dopant and hydrogen have been investigated previously in CVD boron doped monocrystalline diamond by introducing hydrogen (deuterium) from a radio-frequency or a microwave plasma. It has been shown that deuterium may diffuse in boron doped diamond, and that the boron-deuterium complexes are not stable above 750°C (refs. 1 and 2).

On the other hand, unlike silicon, there is little detailed information about hydrogen implanted layers in diamond (ref. 3). Due to metastability of diamond (the stable phase being graphite under ambient conditions), ion implantation may lead to graphitisation and/or amorphisation if the implantation dose reaches the threshold of amorphisation. The formation of ion beam induced buried layers is of interest for processing the lift-off technique (ref. 4), or for producing buried graphitised layer for applications.

This work deals with high dose hydrogen (deuterium) implanted diamond films and their evolution when submitted to thermal annealing. Deuterium is used generally as a tracer for hydrogen analysis by Secondary Ion Mass Spectrometry (SIMS) or for deuterium effusion experiments. Two different ions have been implanted, D_2^+ and D_2^+ , as they are liable to induce different implantation defects and to present different diffusivities.

EXPERIMENTAL

Boron doped ([B]= $6x10^{18}$ cm⁻³) monocrystalline diamond films, grown by chemical vapour deposition on [100] diamond substrates, have been implanted with a D_2^+ dose of $2.5x10^{16}$ cm⁻² with an energy of 100 keV

for the first sample (sample A), and a D^+ dose of $5x10^{16}$ cm⁻² with an energy of 50 keV for the second sample (sample B).

The implanted samples were submitted to successive thermal annealings under ultra-high vacuum (pressure $<10^{-4}$ Pa) during 30 minutes at 950 °C, 1050 °C and 1350 °C. The deuterium profiles were analysed after deuterium implantation, and after annealing, by Secondary Ion Mass Spectrometry (SIMS) using a CAMECA IMS4F equipment and a Cs⁺ primary beam. The SIMS crater depths were measured with a TENCOR profilometer. The structural modifications of the implanted layer in the diamond films were followed by confocal micro-Raman analysis and Scanning Electron Microscopy. Raman scattering measurements were performed in backscattering configuration with a Dilor Jobin-Yvon HR800 spectrometer and a resolution of 0.2cm^{-1} on the FWHM of the diamond line. The excitation was made using the 633 line of an He-Ne laser. For the used conditions of measurement, the spot size is approximately $0.6~\mu m$ and the depth resolution about $0.5~\mu m$.

RESULTS

Sample A

Figure 1 (curve a) shows the deuterium profile obtained in the sample A after D_2^+ implantation. This profile exhibits a deuterium concentration maximum at 570 nm deep. The deuterium profile is not modified after annealing at 950 °C. After an annealing at 1050 °C, the film which was originally transparent has become dark green, and the deuterium concentration profile presents a depletion at a depth of 570 nm, previous position of the deuterium maximum (figure 1, curve b), which could be due to cavity formation in the bulk, or a change of the bulk phase in the implanted buried layer as graphitisation or amorphisation. After a 1300 °C annealing, a blistering of the layer has appeared, as revealed by SEM (figure 2). The deuterium concentration profile (figure 1, curve c) then evidences the blistering phenomenon. This phenomenon has been observed previously by Gippius et al, after implantation of an hydrogen dose of 10^{17} cm⁻² (ref. 3), and by Locher et al, after oxygen implantation (ref. 4).

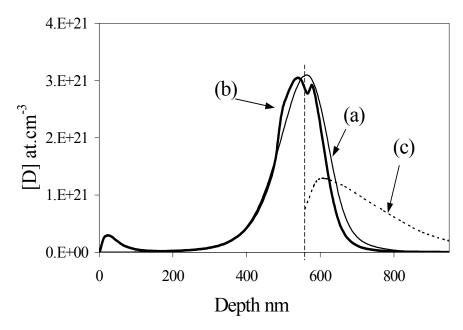


Figure 1. Deuterium concentration profiles in sample A, implanted with D_2^+ . Curve (a): as implanted; curve (b): after annealing at 1050 °C; curve (c): after annealing at 1350 °C. The dotted vertical line shows the surface level after blistering.

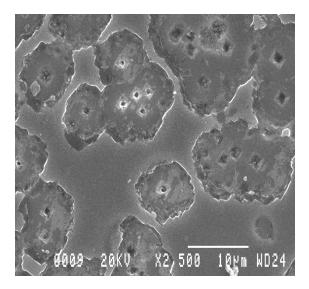


Figure 2. SEM micrography of the sample A surface blistered after a thermal annealing at 1350 $^{\circ}\mathrm{C}$

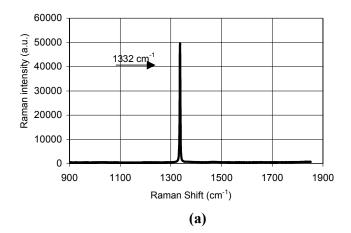
Figure 3a and 3b shows the Raman spectra obtained respectively on the as-grown sample A (figure 3a), after deuterium implantation (figure 3b), and after the thermal annealing at 1050 °C (figure 3c), using focalization at 0.5 µm under the surface of the sample. In the last case, it appears two bands at approximately 1580 and 1360 cm⁻¹ in addition to the diamond line at 1332 cm⁻¹. These bands are characteristic of amorphous carbon films and are usually referred as G (graphitic) and D (disordered) bands, respectively (ref. 5). The micro-Raman analysis of the surface obtained by blistering (figure 4) shows an increase of the G band compared to the D band which could indicate that some more graphitisation occurs before blistering.

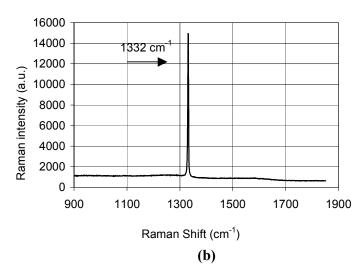
Sample B

The sample B implanted by D^+ ions has been submitted to the same treatments as sample A. Figure 5 shows the modifications of the implanted deuterium profile (figure 5a) after a thermal annealing at 1050 °C (figure 5b). Some deuterium has diffused in the diamond bulk. After a 1350 °C thermal annealing, no deuterium can be detected in the film. The blistering phenomenon is not observed.

CONCLUSION

It seems that a graphitisation process (ref. 3) is at the origin of the blistering which is observed on the D_2^+ implanted sample. The difference of behaviour between sample A and sample B may be explained by the radiation damages induced by the implanted ion. They may be different depending on implantation of D^+ or D_2^+ . It has been shown previously that D^+ diffuses from a deuterium plasma in B-doped diamond (ref. 1). The diffusivities of D^+ and D_2^+ ions are also different. If D_2^+ is present in the diamond bulk, the onset of dissociation of the molecule is at about 700°C, and consequently the diffusion occurs at higher temperature than for D^+ . It has been shown previously that D^+ can diffuse from a deuterium plasma in B-doped diamond (ref. 1) and that D-boron complexes are dissociated in diamond at temperatures higher than 700 °C (ref. 1). But even in these conditions, deuterium can be trapped on structural defects (ref. 6). The brutal release of deuterium at high temperature in the case of D_2^+ implantation may explain the blistering observed in sample A.





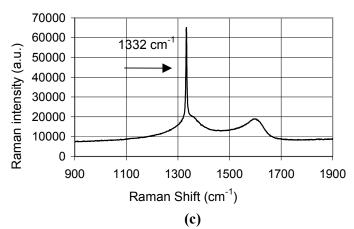


Figure 3. Raman spectrum obtained on the as-grown sample A (a), after deuterium implantation (b) and after the thermal annealing at 1050° C (c), at $0.5~\mu m$ under the sample surface.

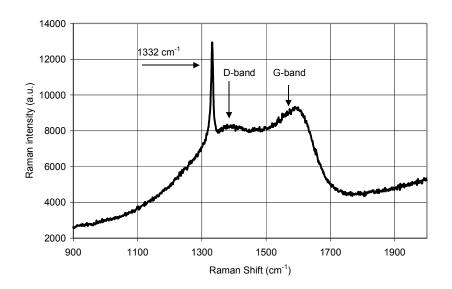


Figure 4. Micro-Raman analysis of the surface obtained by blistering on sample A.

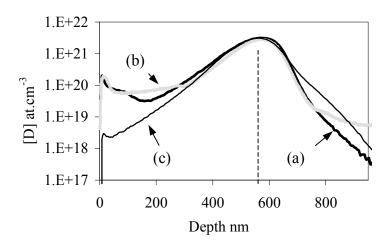


Figure 5. SIMS deuterium D^+ profiles in sample B. As-implanted (a); after a 1050° C thermal annealing (b); the implanted D_2^+ profile of sample A (figure 1a) has been reported on the figure.

- 1. Chevallier, J., Lusson, A., Ballutaud, D. et al,: *Hydrogen-acceptor interactions in diamond*. Diamond and Related Materials 10 (3-7), 2001, 399.
- 2. Chevallier, J., Jomard, F., Teukam, Z. et al,: *Hydrogen diffusion in n-type diamond*. Diamond and Related Materials 11(8), 2002, 1566.
- 3. Gippius, A., Khmelnitsky R., Dravin, V. et al, : *Defect induced graphitisation in diamond implanted with light ions*. Physica B 308-310, 2001, 573-576.
- 4. Locher, R., Behr, D., Güllich, H. et al: Lift-off technique of homoepitaxial CVD diamond films by deep implantation and selective etching. Diamond and Related Materials 6, 1997, 654-657.
- 5. Artamonov, V., Klyui, N., Melnik, V. et al, : Microraman and microhardness study of nitrogen implanted diamond-like-carbon films. Carbon 36 (5-6), 1998, 791-794, 1998.
- 6. Teukam, Z., Ballutaud, D., Jomard, F. et al: *Trap limited diffusion of hydrogen in boron-doped diamond*, Diamond and Related Materials, to be published.

Dielectric losses in CVD diamonds at frequencies 1 kHz - 200 GHz and temperatures 70 - 800 K

B.M. Garin, M.P. Parkhomenko

Institute of Radio Engineering and Electronics of Russian Academy of Sciences, 1, Vvedensky Sq., Fryazino, Moscow Region 141190, Russia; E-mail: garin@ms.ire.rssi.ru; Fax: +7(095)702-95-72; Tel.: +7(095)526-9266

V.V. Parshin, S.E. Myasnikova

Institute of Applied Physics of Russian Academy of Sciences, 46, Ulyanov St., 603950 Nizhny Novgorod, Russia

R. Heidinger, I. Danilov

Forschungszentrum Karlsruhe, Association FZK-Euratom, Institute for Materials Research I, P.O.Box 3640, D-76021, Karlsruhe, Germany

J. Molla

Association Euratom-CIEMAT, av. Complutense 22, E 28040 Madrid, Spain

V.G. Ralchenko

Natural Science Centre of General Physics Institute of Russian Academy of Sciences, 38 Vavilova St., 117942 Moscow, Russia

V.N. Derkach, S.I. Tarapov

Institute of Radiophysics and Electronics NAS of Ukraine, 12 Ac. Proskura St., 61085 Kharkov, Ukraine

ABSTRACT

The low loss materials for output windows still remains to be a weak point in megawatt millimeter waves gyrotrons for controlled plasma heating in fusion reactor. CVD diamond is considered currently as the most promising material for such windows. We determined its dielectric properties in extremely broad frequency and temperature ranges and compared with theory. The combinations of data on dielectric losses in broad frequency and temperature ranges give most information on the loss mechanisms.

To measure the loss tangent from 1 kHz up to 200 GHz and temperatures 70 - 800 K different types of resonator technique were used. The diamond wafers were prepared by different producers using a microwave plasma CVD technique. The record breaking low values of loss tangent were observed $(\tan \delta \sim 4.5 \cdot 10^{-6} \text{ at } T = 300 \text{ K}, f = 170 \text{ GHz})$. However they are still one order of magnitude higher than the theoretical lower loss limit for diamond.

Frequency and temperature dependencies of loss tangent in other materials with diamond-like lattice (Au-doped Si, compensated GaP, InP, GaAs, and Au-doped Si) were measured and analyzed for better understanding of the loss mechanisms. In addition, a semiconducting boron-doped CVD diamond has been also measured as a model material.

The dielectric loss mechanisms and application to gyrotron windows are discussed.

Key words: diamond, diamond-like materials, dielectric loss, loss mechanisms, gyrotrons.

1. INTRODUCTION

Development of megawatt millimeter (MM) waves gyrotrons for plasma heating is one of the key elements of the future fusion reactor technology. The low loss material for the output window, still remains to be a weak point in powerful gyrotrons. Due to its unique properties CVD diamond is considered as the most promising material.

At present the investigations of dielectric loss (absorption) in CVD diamonds in the MM range [1-9] are carried out quite actively. As it follows from the theory of the "intrinsic" lattice loss (ILL) corresponding to the two-phonon absorption processes in ideal crystal [10,11], the diamond-type crystals (including diamond and silicon) have the least theoretical lower loss limits determined by the ILL [11,12]. Moreover, the minimum theoretical estimation of ILL corresponds to diamond [5,7,8]. On the other hand, the progress in the technology of diamond synthesis [1,3-8,13]

led to manufacturing of polycrystalline CVD diamonds with very low losses at room temperature. In some specimens the losses reach the extremely low values $(\tan\delta \sim 8\cdot10^{-6} \text{ at } 170 \text{ GHz } [5,7,8])$ and approach the record breaking low loss among various materials at room temperature $(\tan\delta \sim 310^{-6})$ observed for gold-doped silicon Si:Au [14] and corresponding to the lower loss limit for silicon at this temperature [11,12]. The issue on the loss mechanisms in real CVD diamond of high quality is very significant, particularly for revealing the perspectives for a further loss reducing.

The A^{III}B^V compounds (such as GaAs, GaP, InP) have analogous type of crystal lattice (zinc blend type). According to theoretic estimations [11] the ILL in such crystals is approximately two orders of magnitude higher than in the diamond type crystals. The lattice loss in such crystals practically was not studied (except [12a], where the losses were measured at fixed temperature and frequency). The evaluation of loss in these materials as model systems would provide the possibility for verification of existing knowledge on lattice loss mechanisms.

The comparison of the loss frequency and temperature dependencies to theory may allow to identify the loss mechanisms. The experimental data in very broad frequency and temperature ranges give most information on loss mechanisms. At the present work the data on loss $\tan\delta$ measurements in CVD diamonds and related materials at extremely broad frequency and temperature ranges are presented and compared to theory. The dielectric loss mechanisms and application to gyrotron windows are discussed.

2. EXPERIMENTAL DATA AND COMPARISON TO THEORY

Measurement techniques

Dielectric properties were measured at frequencies f = 45 - 200 GHz by an improved open resonator technique at temperatures T = 300-800 K [9,15] and T = 70-300 K [6]. The technique used provides the opportunity to separate the bulk and the surface losses in the total loss in a sample [9]. The measurements in the frequency range between 1 kHz and 100 MHz were performed with a resonant circuit, and at 15 GHz with a resonant cavity [16].

Experimental data

Losses in CVD diamonds.

In the Table 1 the data on the bulk dielectric losses in very low loss CVD diamonds are presented. The CVD diamond plates were produced by microwave plasma chemical vapor deposition (MPCVD) in DeBeers company (specimens 1-4, 6-9) and at the General Physics Institute, Moscow (specimen 5, [see 13]). Some of the samples were used in real gyrotron windows. The samples in the Tabl.1 are presented in the order of loss tangent decrease (so the lowest loss samples are at the end). The record breaking low loss in CVD diamond was observed ($\tan \delta \sim 4.5 \cdot 10^{-6}$).

In Fig.1 the loss tangent temperature dependence for specimen 5 at 170 GHz and at temperatures up to 500 C is presented (curve 1). This specimen, described in [5,7,8], is interesting as it contains relatively few defects (non-diamond inclusions) and impurities.

At low temperatures T = 70 - 260 K in a CVD diamond (the specimen of diameter d = 50mm and thickness t = 0.4 mm, grown by the ellipsoidal reactor at FhG/IAF, Freiburg, Germany), a flat loss dependence was observed within the measurement uncertainties in this 'thin' specimen [17].

In Fig.2 the loss frequency dependencies at t = 20 °C for specimens 1 and 2 with relatively high concentrations of defects are presented (for the contribution due to bulk absorption). At f < 140 GHz the dependence, which can be approximated by $\tan \delta \sim 1/f$, was found. A similar relationship was observed earlier also in other CVD-diamonds and was assigned to the loss due to electric conductance in non-diamond inclusions [7,8]. However, at higher frequencies, f > 140 GHz, a deviation of frequency dependence upwards was observed.

At f = 1 kHz - 15 GHz the loss frequency dependencies are rather week [18], see below.

A boron-doped ("blue") CVD diamond as a model system was examined. The wafer was of 35 mm diameter and 0.36 mm thickness with resistivity $\rho \sim 10^5 \,\Omega \cdot \text{cm}$ ($T = 300 \,\text{K}$). The measured loss at $f = 181.257 \,\text{GHz}$ is $\tan \delta = 4.2 \cdot 10^{-3}$. Also the loss was measured at $T = 80 - 260 \,\text{K}$ and $f \sim 145 \,\text{GHz}$ (Fig.3). A slow loss decrease with temperature increase at $T = 80 - 200 \,\text{K}$ changes with a sharp loss increase at $T > 230 \,\text{K}$.

Losses in gold doped silicon.

In Fig.4 the loss frequency dependencies at room temperature in gold doped silicon Si:Au are presented for two specimens (d = 100 mm, t = 3.11 and 3.12 mm for the specimens 1 and 2, respectively) with different resistivities.

Dielectric properties of compensated GaAs, GaP, and InP crystals.

In Fig.5 the frequency dependencies in GaP and GaAs are presented for very broad frequency range $10^3 - 10^{11}$ Hz at room temperature. In InP an increase of refractive index n is revealed at f = 50 - 200 GHz.

In Fig.6 loss temperature dependencies at 70 - 260 K and f = 145 GHz in compensated (semi-insulating) GaAs, GaP, and InP crystals are presented.

Table.1. Bulk loss tangent $\tan \delta$ (surface losses are excluded) for selected CVD diamonds with lowest losses (specimens numbers 1–9, t and d are the thickness and diameter of specimens) at T = 300 K.

(specimens numbers 1–9, t and a are the				
Frequency [GHz]	$tan\delta [10^{-5}]$			
1. "ITER-1", <i>t</i> = 2.22 m				
56.585	5			
84.867	3.5			
113.153	3.0			
141.432	2.45			
169.710	2.45			
197.990	2.5			
2. "ITER-2", <i>t</i> = 1.523 t	mm, $d = 106 \text{ mm}$			
82.622	1.84			
123.920	1.71			
165.220	1.65			
206.925	~1.6			
3. "ITER-3", $t = 1.86$ m	nm, d = 104 mm			
67.846	2.3			
101.741	2.0			
135.645	1.7			
169.549	1.4			
203.448	1.35			
4. 22DB6, <i>t</i> = 1.86 mm, <i>d</i> = 106 mm				
68.276	2.2			
102.393	1.9			
136.514	1.6			
170.630	1.4			
204.747	1.3			

Frequency [GHz] $tan\delta [10^{-5}]$ 5. Diagascrown-113, $t \sim 0.74$ mm, $d = 55$ mm 170.0 0.8 6. 53DB1, $t = 1.798$ mm, $d = 106$ mm 70.182 1.05 105.257 1.0 140.332 ~ 0.8 175.407 ~ 0.6 7. "India", $t = 1.489$ mm, $d = 106$ mm 84.652 ~ 1				
5. Diagascrown-113, $t \sim 0.74$ mm, $d = 55$ mm 170.0 0.8 6. 53DB1, $t = 1.798$ mm, $d = 106$ mm 70.182 1.05 105.257 1.0 140.332 ~ 0.8 175.407 ~ 0.6 7. "India", $t = 1.489$ mm, $d = 106$ mm				
6. 53DB1, $t = 1.798$ mm, $d = 106$ mm 70.182 1.05 105.257 1.0 140.332 ~0.8 175.407 ~0.6 7. "India", $t = 1.489$ mm, $d = 106$ mm				
70.182 1.05 105.257 1.0 140.332 ~0.8 175.407 ~0.6 7. "India", t = 1.489 mm, d = 106 mm				
105.257 1.0 140.332 ~0.8 175.407 ~0.6 7. "India", t = 1.489 mm, d = 106 mm				
140.332 ~0.8 175.407 ~0.6 7. "India", t = 1.489 mm, d = 106 mm				
175.407 ~0.6 7. "India", t = 1.489 mm, d = 106 mm				
7. "India", <i>t</i> = 1.489 mm, <i>d</i> = 106 mm				
84,652 ~1				
•				
126.958 ~0.7				
169.261 ~0.55				
8. "India-Barrier", $t = 1.533$ mm, $d = 106$ mm				
81.866 ~1				
122.777 ~0.6				
163.698 ~0.5				
9. 52DB1, $t = 1.795$ mm, $d = 106$ mm				
140.428 ~0.5				
175.523 ~0.45				

Comparison to theory and discussion

As it can be seen from Fig.1 (curve 1), at the temperatures < 400 °C there is a negligible increase of the loss tangent value. At lower temperatures T = 70 - 260 K «flat» dependence was observed in CVD diamond [17]. This can be explained by predomination of the loss caused by electric conductance in some non-diamond inclusions (see [7,8]). At T > 400 °C the significant increase of loss tangent was observed. It can be attributed to switch-on of some other mechanism characterized by strong loss temperature dependence. According to theory [10], ILL also is characterized by rather strong temperature dependence. From analysis based on the theory, the main contribution to the ILL in diamond type crystals is connected with "difference" two-phonon absorption processes where absorption of electromagnetic quantum is accompanied by the excitation of optical phonon and absorption of acoustic phonon. For diamond the "low temperature" limit ($T << T_D$) is applicable at T < 900 K for ILL temperature dependence [10]:

$$\tan \delta \sim T^{-1} \exp(-T_{\rm D}/T) \text{ at } T < T_{\rm D}/2 \tag{1}$$

where T is the absolute temperature, T_D is Debye temperature ($T_D \approx 670$ K and 1900 K in the silicon and diamond, respectively). In Fig.1 the ILL theoretical dependence (1), fixed to the measured loss at T = 420 °C, is presented .(curve 2). The experimentally observed loss increase at T > 420 °C is in disagreement with the ILL mechanism. The slope is considerably larger in comparison with (1), it corresponds to activation energy 0.56 eV, that is much higher than the "activation" energy $kT_D \sim 0.17$ eV in the dependence (1) which describes the phonon excitation in the ILL

process. So the loss observed at T > 420 °C should be due to another mechanism, for instance, the excitation of charge carriers from deep level in the band gap, or some Debye-type dipole relaxation mechanism. Even for high

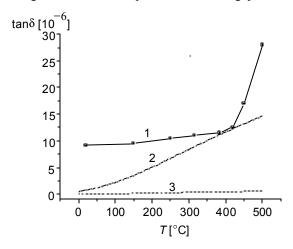


Fig.1. Loss $\tan\delta$ temperature dependencies: 1 are the experimental data at f = 170 GHz in the CVD diamond specimen 5 [5,7,8]; 2 is ILL theoretical dependence (1) fixed to the experimental point at T = 420 °C; 3 is the estimation of the ILL absolute value in diamond [4,7].

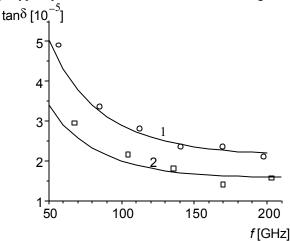


Fig.2. Loss tan δ frequency dependencies in CVD diamonds at T = 20 °C: 1 – the specimen 1; 2 – the specimen 3. Points are the experimental data, lines are the theoretical approximations (3).

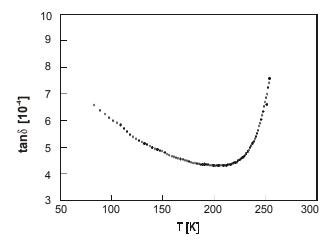


Fig.3. Temperature dependence of loss tangent $tan\delta[10^{-4}]$ in boron-doped CVD diamond at low temperatures.

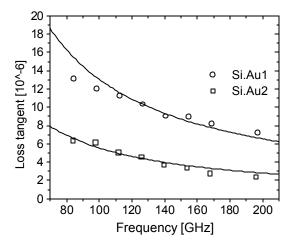


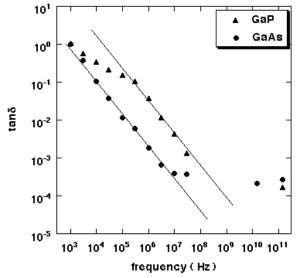
Fig.4. Loss frequency dependencies in gold-doped silicon: points O and are the measured data for specimens 1 and 2, respectively at room temperature; lines are fits tanδ ~1/f.

quality specimen 5 the observed loss is not due to the ILL at high temperatures ($T \sim 500$ °C).

The ILL absolute value estimation in diamond is presented in Fig.1 by the curve 3 assuming $\tan \delta \sim 3.10^{-8}$ at $T = 20^{\circ}$ C and the temperature dependence according to (1). The curve 2 in Fig.1 gives the ILL upper estimate at 170 GHz and T = 20 - 500 °C. Particularly at T = 20 °C for ILL $\tan \delta < 7.10^{-7}$ [19] that is at least one order of magnitude lower than the lowest observed loss in CVD diamonds (see Table 1). The ILL, which is extremely low in diamond, remains to be not revealed experimentally, the same being true for other diamond-type crystals, including Si [12,14].

The deviation of frequency dependence at f > 140 GHz upwards from the dependence $\tan \delta \sim 1/f$ (Fig.2) can be explained by contribution of non-intrinsic lattice loss (NLL) mechanism connected with one-phonon excitation of acoustic lattice vibrations owing to presence of a lattice disorder (including defects and impurities) [20]. Taking into

account the influence of the microscopic internal field effect expressed by the factor $[(\epsilon'+2)/3]^2$, where ϵ' is the real part of dielectric permittivity, at shorter MM wavelengths and at higher frequencies the expression for the NLL due



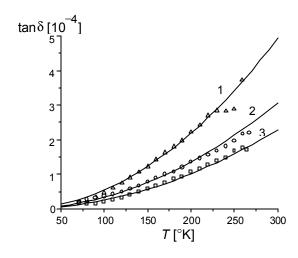


Fig.5. Loss frequency dependencies in compensated GaP and GaAs at low frequencies.

Fig. 6. Loss temperature dependencies in compensated $A^{III}B^V$ crystals: InP (1), GaAs (2), GaP (3); points are experimental data, lines are fits $\tan \delta \sim T^2$.

to the charged defects or impurities [20], can be written in the form:

$$\tan\delta \cong \frac{2(\varepsilon + 2)^2 nz^2 e^2 \omega}{27\varepsilon \mu v_t^3}$$
 (2)

(where n and z are the concentration and effective charge of defects, e is the elementary charge), μ and v_1 are the density and transverse sound velocity in medium. As it is shown in [21], for the estimations of the one-phonon NLL due to the interatomic dangling bonds with the concentration n, the expression (2) at z = 1 is applicable. According to (2), the one-phonon NLL $\tan \delta \sim f$, and is practically independent on temperature [20].

The observed loss frequency dependence in the specimens 2 and 3 (Fig.2) can be well described (within the measurement errors) by a simple approximation:

$$\tan \delta = (a/f + bf) \cdot 10^{-5},$$
 (3)

where a,b = const, f in GHz). The first term corresponds to the loss due the electric conductance in non-diamond inclusions [7,8], and the second term bf corresponds to one-phonon nonintrinsic lattice loss according to (2).

The dependencies, measured for CVD diamonds at much lower frequencies $10^3 - 10^{10}$ Hz differ (are very weak) from the relation (3) and are due to other loss mechanisms, such as hopping conduction mechanism [18].

In the B-doped diamond the loss temperature dependence (Fig.3) has a minimum and differs from the one for the free charge carriers dc conductivity [22]. The loss is more than two order higher than that calculated from dc resistivity $\rho \sim 10^5 \,\Omega \cdot \text{cm}$ ($T=300 \,\text{K}$) according to known relation $\tan \delta = (\epsilon' \epsilon_0 \,\omega \rho)^{-1}$ (4) (ρ and ϵ' are the resistivity and dielectric permittivity of medium, ϵ_0 is the electric constant). The much higher relaxation rates could arise from non-diamond inclusions, or disordered diamond (primarily at grain boundaries), or some boron precipitates. From sharp loss increase at 230–260 K the activation energy $E_a \sim 0.15 \,\text{eV}$ was estimated. It differs from $E_a = 0.3 \,\text{eV}$ for boron donors in the diamond lattice, evaluated from dc conductivity at room and higher temperatures [22]. The loss dependence at $T < 200 \,\text{K}$ (Fig.3) is analogous to the one observed in silicon [23].

In single crystals Si:Au the loss dependence $\tan \delta \sim 1/f$ is observed (Fig.4). In this case the concentration of defects is low, and the loss due to free charge carriers dominates. In compensated crystals GaP and GaAs this type of the loss dominates only at very low frequencies 10^3-10^8 Hz (Fig.5). At higher frequencies $(10^8-10^{10}$ Hz) the loss mechanism changes. It might be related to hopping conductivity with a frequency dependence f^{-m} (m=0.1), and is analogous to the mechanisms observed and considered in CVD diamonds [18] at $f < 10^{10}$ Hz. At higher frequency f = 145 GHz the temperature dependency $\tan \delta \sim T^2$ was observed (Fig.6). It corresponds to the theoretical dependence for the two-phonon ILL mechanism in such materials (cubic crystals without center of symmetry) [24].

CONCLUSIONS

The detailed comparison of experimental temperature and frequency dependencies of dielectric losses in CVD diamonds and related materials with theory at very broad temperature and frequency ranges was made here. The loss nature in these materials at various temperatures and frequencies at the MM range are revealed.

The record breaking low loss in CVD diamond was observed ($\tan \delta \sim 4.5 \cdot 10^{-6}$ at $f \sim 170$ GHz, T = 300 K). It is confirmed that the intrinsic lattice loss in diamond (determining the theoretical lower loss limit) is extremely low, particularly at room temperature being at least one order of magnitude lower than the lowest measured loss. So, as it follows from estimations, there is a principle opportunity to create diamond windows for gyrotrons with the power >> 1 MW at CW operation if the quality of CVD diamond would be improved.

AKNOWLEDGEMENTS

The work was supported by INTAS (project No. 01-2173); Russian State Program "Development of super high resolution SubMM wave spectroscopy methods" (project No. 40.020.1.1.1160.)

REFERENCES

- [1] Sussmann R.S., Brandon J.R., Scarsbrook G.A., et al., Diam. Relat. Mater. 3 (1994) 303.
- [2] Heidinger R., Digest of the 19th Int. Conf. on Infrared and Millimeter Waves, Sendai, Japan (1994) 277-278.
- [3] Heidinger R., Sporl R., Thumm M., Brandon J.R., Sussmann R.S., Dodge C.N., Digest of 23rd Int. Conf. on Infrared & Millimeter Waves. Colchester, England (1998) 223-224
- [4] Garin B.M., Kopnin A.N., Parkhomenko M.P., Ralchenko V.G., Konov V.I., Chigryai E.E., ibid., p.230.
- [5] Parshin .V.V., Ralchenko V.G., Konov V.I., ibid., p.232-233.
- [6] Sporl R., Schwab R., Heidinger R., Parshin V.V., Digest of ITG Conf. "Displays and Vacuum Electronics", Garmisch-Patenkirchen, Germany (1998) 369-374.
- [7] Garin B.M., Parshin V.V., Ralchenko V.G., et al., Proc. of III Int. Kharkov Symp. "Physics and Technology of Millimeter and Submillimeter Waves", Kharkov, Ukraine, Vol.1 (1998) 278-280.
- [8] Garin B.M., Parshin V.V., Ralchenko V.G., et al., Technical Phys. Lett. 25, No.4 (1999).
- [9] Koposova E.V., Myasnikova S.E., Parshin V.V. and Vlasov S.N., The absorption investigation in CVD-diamond plates and windows at 50–200 GHz, Diam. Relat. Mater. 11 (2002) 1485-1490.
- [10] Galdetskii A.V., Garin B.M., Preprint No.17(320), Inst. of Radio Engineering and Electronics of the USSR Acad. of Sci., Moscow (1981); Garin B.M., Digest of 18th Int. Conf. on IR & Millimetre Waves, Colchester, England, Vol.1 (1993) 509-510.
- [11] Garin B.M., Proc. of Third Int. Conf. on Millimeter-Wave and Far-Infrared Sci. and Technol., Guangzhou, China (1994) 275-277.
- [12] Garin B.M., Kopnin A.N., Parkhomenko M.P., et al., 21st Int. Conf. on IR & MM Waves, Berlin, Germany (1996) paper CT15; Garin B.M., Kopnin A.N., Parkhomenko M.P., et al., Technical Phys. Lett. 20 (1994) 878-879.
- [13] Ralchenko V.G., Smolin A.A., Konov V.I., et al, Diam. Relat. Mater. 6 (1997) 417.
- [14] Heidinger R., Molla J., Parshin V.V., Digest of 21st Int. Conf. on IR & Millimeter Waves, Berlin, Germany (1996) paper AW8.
- [15] Krupnov A.F., Tretyakov M.Yu., Parshin V.V., Shanin V.N., Myasnikova S.E., J. Mol. Spectr. 202 (2000)107.
- [16] Molla J., Ibarra A., Margineda J.A., Zamarro J.M., Hernandez A., IEEE Trans. Instrum. Meas. 42 (1993) 817.
- [17] Spoerl R., Heidinger R., Wild C., et al., Dielectric properties of CVD diamond for radiofrequency applications, Advances in Science and Technology 21: Diamond Films/ P. Vincenzini (Ed.), Publisher: Techna (Florence) (1999).
- [18] Molla J., Ibarra A., Maffiotte C., Diam. Relat. Mater. 9 (2000) 1071-1075.
- [19] Garin B.M., Parshin V.V., Myasnikova S.E., Ralchenko V.G., 8th Int. Conf. "New Diamond Science and Technology 2002", Digest, Melbourne, Australia, July 2002, p.64.
- [20] Garin B.M., Sov. Phys. Solid State, 32 (1990) 1917-1920.
- [21] Garin B.M., SPIE Proc. Vol.2211b (1994) 606-614.
- [22] Polyakov V.I., Rukovishnikov A.I., Rossukanyi N.M., et al.: Charge based deep level transient spectroscopy of defects in electron-irradiated and annealed CVD diamonds, to be presented at ADC/FCT Conf., Japan (2003).
- [23] Heidinger R., Kumlin A., 16th Int. Conf. on IR and MM waves, SPIE Vol.1576 (1991) 450-451.
- [24] Gurevich V.L., Sov. Phys. Solid State 21 (1979) 1993.

EXCIMER LASER ANNEALING OF DIAMONDS IMPLANTED WITH LIGHT IONS

S.M. Pimenov, V.V. Kononenko, T.V. Kononenko, V.I. Konov

General Physics Institute, Vavilov str. 38, 119991 Moscow, Russia (tel.: +7-095-132 8315, fax: +7-095-232 3862, e-mail: pimenov@nsc.gpi.ru)

P. Fischer, V. Romano, H.P. Weber

Institute of Applied Physics, University of Bern, Sidlerstrasse 5, CH-3012 Bern, Switzerland

A.V. Khomich

Institute of Radio Engineering & Electronics, Vvedenskogo square 1, 141190 Fryazino, Russia

R.A. Khmelnitskiy

P.N. Lebedev Physical Institute, Leninsky avenue 53, 117924 Moscow, Russia

ABSTRACT

In this paper the results of studies on annealing/graphitization/ablation processes induced in ion-implanted diamond layers by nanosecond pulse irradiation with KrF excimer laser (λ =248 nm, τ =15 ns) are reported. The deeply buried damaged layers in diamond single crystals are produced by implantation with hydrogen, deuterium, and helium ions of 350 keV energy. It is shown that the non-linear depth distribution of radiation defects is a factor which strongly influences the character of laser-induced processes in the ion-implanted layers. Particularly, the annealing/graphitization behavior is found to be very different for irradiation conditions when a laser beam is incident on the ion-implanted surface with low defect density or, passing through diamond, onto the buried layer with high defect density. In the latter case, the annealing of radiation damage is much more efficient and graphitization in the deeply buried layers is inhibited. Based on white-light-interferometry examination of laser-irradiated surface (with sub-nanometer resolution) and optical transmission in laser spots, peculiarities of laser annealing and graphitization in diamonds implanted to different doses are demonstrated and discussed.

Keywords: diamond, laser irradiation, ion implantation, annealing, graphitization

INTRODUCTION

The technique of ion implantation, widely used for doping of diamond (refs. 1-3) and producing of diamondgraphite heterostructures for various electrical and optical applications (refs. 3-5), involves high-temperature annealing as a post-implantation step needed to repair the radiation damage and activate the dopants or to produce buried graphitic layers in diamond. It is generally accepted that there is a critical damage level (critical implantation dose) related to a certain defect density, and, depending on whether the diamond is implanted to a dose below or higher than the critical level, the high-temperature treatment results in either annealing (i.e. recovery of the damaged structure) or graphitization of the ion-implanted layers (refs. 6-9). Among the post-implantation processing techniques, laser irradiation of ion-implanted diamonds by visible-light nanosecond pulses was reported to be possible (refs. 10,11). As distinct from conventional thermal annealing, the use of laser pulsed irradiation enables one to modify the structure of ion-damaged diamond layers with high spatial selectivity and to create patterns with variable properties - from insulating (annealed) to highly-conducting (graphitized). In addition, a deeply buried damaged layer in diamond, in which high internal stresses are produced by ion implantation and which can be locally heated by laser radiation, can be considered as an effective high-pressure cell, that gives a unique opportunity to study various structure transformations of carbon during short laser pulse action (ref. 10). Based on this, we employed nanosecond pulse radiation of UV excimer lasers to study laser-induced annealing and graphitization processes in diamonds, implanted with light ions (H⁺, D⁺, He⁺) to doses both lower and higher than the critical value. The choice of the light ions was made because of they produce minimum radiation damage and deeply buried layers in diamond (ref. 9), that is important for device applications. Particular attention in the research was paid to the influence of non-linear defect density distribution in a near surface layer on the laser-induced annealing/graphitization behavior in the ion-implanted diamonds.

EXPERIMENTAL DETAILS

The samples of diamond IIa type or intermediate IIa/Ia type single crystals were implanted with 350-keV ions of helium (He^+), deuterium (D^+), and hydrogen (H^+) at room temperature (refs.4,9). Data on the ion implantation doses (D) used for each sample, as well as the critical dose (D_{cr}) for the implanted ions are presented in Table 1.

N	Diamond	Ion implantation conditions	Critical dose (D _{cr})	Projected range (R _p)
#18	(110) IIa type	He ⁺ ions, 350 keV	$2.8 \times 10^{16} \text{ cm}^{-2}$	0.77 μm
		$10^{15} \text{cm}^{-2} \text{ and } 10^{16} \text{cm}^{-2}$		
#119	(110) Ia type	D ⁺ ions, 350 keV	$5x10^{16} \text{ cm}^{-2}$	1.58 μm
		2, 4, 6, 8, 10, 12x10 ¹⁶ cm ⁻²		·
#130	(110) IIa type	H ⁺ ions, 350 keV	$8x10^{16} \text{ cm}^{-2}$	1.75 μm
		4, 8, 12, 16, 20, 24x10 ¹⁵ cm ⁻²		·

Table 1. Samples of ion-implanted diamonds

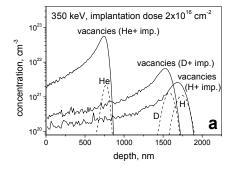
Two KrF excimer lasers (Lambda Physik, EMG 1003i and LPX 300) emitting pulses of 15-20 ns duration at the wavelength λ =248 nm were used. Laser spot size was 50-100 μ m; intensity distribution over the spots was uniform.

Optical transmission of the ion-implanted diamond before and after laser irradiation was measured at the wavelength of λ =532 nm with a transmission optical microscope equipped with a CCD array without gamma-correction. A surface profiler "Zygo" (model New View 5000) based on phase-shifting interferometry was used to examine the topology of original and laser-irradiated surface. The technique of white-light-interferometry (WLI) microscopy provides measurements (with sub-nm resolution) of the surface profile changes in laser spots resulting from the "diamond-to-graphite" or reverse transitions due to the difference in the specific volume of the materials.

RESULTS AND DISCUSSION

Ion implantation leads to the formation of radiation defects among which vacancies and interstitials are the main defects (refs. 7,8,12). Figure 1a shows the defect density distribution (calculated by Monte Carlo simulation (refs. 4,9)) created by H^+ , D^+ and He^+ ions of the same energy and implantation dose. An important feature is that the maximum density of defects is produced at a certain depth below the surface – at about the depth of the maximum of the implanted ion distribution referred to as the projected range, R_p (the R_p values for different ions are given in Table 1). We call this region with the high concentration of radiation defects as a buried damage layer. It is seen from Fig. 1a that implantation with lighter ions produce deeper damage layers in the bulk of diamond.

It is known that the ion-implanted diamond exhibits a volume expansion (pronounced in the surface swelling) due to the formation of vacancies and other structural defects (ref. 13), and the radiation defects are responsible for the GR (general radiation) optical absorption bands in the visible-UV spectral range (refs. 5,9). This gives obvious criteria for experimental observation of laser annealing and graphitization, namely: during laser annealing both the material compaction and increase in the optical transmission must ensue, whereas for laser graphitization the 'extra' surface swelling and loss in transmission must be observed.



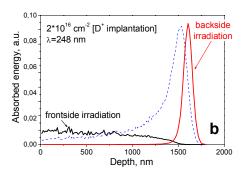


Figure 1. (a) Data of Monte Carlo calculations of the depth distributions of the implanted ions and radiations defects (vacancies) in diamond implanted with 350-keV ions of hydrogen, deuterium and helium (Ref. 9); and (b) calculated depth profiles of absorbed laser energy in the D⁺ ion-implanted diamond for 'frontside' and 'backside' irradiation regimes with KrF laser; dash line is the vacancy density distribution after ion implantation at dose D=2x10¹⁶ cm⁻².

Because of the non-linear defect density distribution (shown in Fig. 1a), it was assumed that the laser-induced annealing/graphitization behavior could be different if a laser beam were incident either on the ion-implanted surface with low defect density or, passing through diamond, onto the buried layer with the high defect density (we call these irradiation regimes as 'frontside' and 'backside' irradiation, respectively). This assumption was supported by calculations of the absorbed laser energy profiles for both these irradiation conditions; the results are shown in Fig. 1b and described in more detail in reference 14. In the experiments we applied the 'frontside' and 'backside' regimes of irradiation of the ion-implanted diamond plates.

KrF laser irradiation of He⁺ ion-implanted diamond

Main features of UV laser-induced processes in He⁺ ion-implanted diamond (with lowest R_p value, see Table 1) are shown in Figs. 2 and 3. During 'frontside' irradiation, a sharp transition from annealing to graphitization of He⁺ ion-implanted layers is observed at $E\approx1.7$ J/cm² (Fig. 2a), and at fluences $E\geq3$ J/cm², surface graphitization is accompanied by material ablation. The WLI images and surface profiles of laser spots, corresponding to these successive stages (annealing, graphitization, graphitization+ablation), are presented in Figs. 2b-2e.

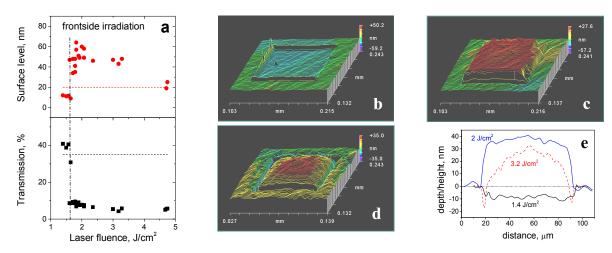


Figure 2. (a) Changes in the optical transmission (at λ=532 nm) and surface level of laser spots produced in He⁺ ion-implanted diamond (D=10¹⁶ ions/cm²<D_{cr}) under 'frontside' irradiation with single pulses. Dash lines show the original values of the transmission and surface level of the ion-implanted regions; (b)-(e) WLI images of laser spots produced at E=1.4 J/cm² (b), E=2 J/cm² (c), and E=3.2 J/cm² (d), and WLI surface profiles across these spots (e).

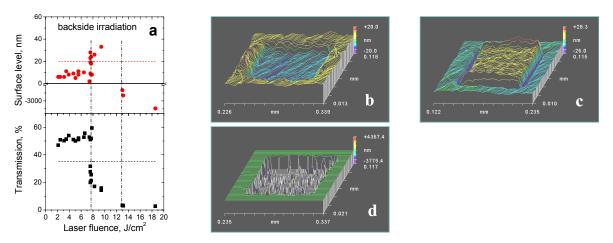


Figure 3. (a) Changes in the optical transmission (at λ =532 nm) and surface level of laser spots produced in He⁺ ionimplanted diamond (D=10¹⁶ cm⁻²<D_{cr}) under 'backside' irradiation with single KrF laser pulses. Dash lines show the values of the transmission and surface level of as-implanted regions; (b)-(d) WLI images of laser spots obtained as a result of annealing at E=7.4 J/cm² (b), graphitization at E=9.4 J/cm² (c), and explosive ablation at E=13 J/cm² (d).

In case of 'backside' irradiation, efficient annealing takes place at fluences of up to E=7.5 J/cm², extending to much higher fluences compared with the 'frontside' irradiation regime. Graphitization of the buried layer is observed in the fluence range $7.5 \le E < 13 \text{ J/cm}^2$, followed by the transition to the explosive ablation regime at $E \approx 13 \text{ J/cm}^2$. The depth of laser spots produced by explosive ablation at $E \approx 13 \text{ J/cm}^2$ is $2.3-2.6 \mu m$, which is considerably larger than the value of $R_p \approx 0.77 \mu m$. WLI microscopy images of laser spots, corresponding to the annealing, graphitization, and explosive ablation in the He⁺ ion-implanted diamond, are shown in Figs. 3b-3d.

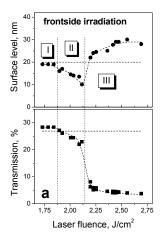
KrF laser irradiation of D⁺ ion-implanted diamond

Figure 4 shows the changes in optical transmission and surface level in laser spots after the action of single laser pulses under 'frontside' and 'backside' irradiation. After 'frontside' irradiation at low intensities of up to E=1.9 J/cm² (region I, Fig. 4a), the annealing is observed but the effect is weak as the transmission increases by only 1-2% and the surface level decreases by $1\div 2$ nm. In the range E=1.9-2.1 J/cm² (region II, Fig. 4a), further reduction in the surface level is observed, however, along with the material compaction a progressing decrease in the transmission is also observed which indicates the developing graphitization process to take place. It is therefore supposed that the observed effects is a result of 'competition' of the annealing and graphitization processes. For $E \ge 2.1$ J/cm² (region III, Fig. 4a) graphitization occurs, resulting in a sharp decrease in the transmission and 'extra' surface swelling.

Under 'backside' irradiation, the behavior of the ion-implanted diamond is changed dramatically (Fig. 4b). The laser fluence range, within which the laser annealing occurs, extends to high fluences of up to 14 J/cm^2 (region I in Fig. 4b). Taking the intrinsic absorption in diamond (at λ =248 nm) into account, the "true" value of the incident fluence is 9 J/cm^2 . The annealing efficiency (the transmission increase of up to 20% after the single pulse action) is much higher than that after the single pulse action during 'frontside' irradiation (the transmission increase of 1-2%).

For the fluences $E > 14 \text{ J/cm}^2$ (region II, Fig. 4b) a sharp transition from the annealing to explosive-like ablation of μ m-thick layer is observed, the evidence to which is the formation of a crater of $\sim 3.5 \mu m$ depth. The crater depth is much larger than the R_p value of $\approx 1.58 \mu m$. The data of Fig. 4b indicate that the graphitization process in the buried layer is inhibited, however simple estimations of the laser energy absorbed in the buried layer give the value of about $\epsilon_{abs} = 510 \text{ kJ/cm}^3$ which exceeds the vaporization energy of diamond ($\epsilon_v = 210 \text{ kJ/cm}^3$ (ref.15)). Although such estimation is rather rough, it allows us to suggest that various HPHT processes can develop in the buried layer during laser pulse action in accordance with the P-T phase diagram (ref.16), e.g. spontaneous diamond-to-graphite transition in the range of pressures P=5-10 GPa and temperature around 4000 K or melting of carbon at higher temperatures. Once laser heating stimulates graphitization in the region of the high defect density, the graphitization front moves both into the bulk of diamond and to the surface until high internal pressure inside the growing graphite-like layer exceeds the mechanical damage threshold of diamond, afterwards the explosive ablation occurs.

It is worth noting that during 'backside' irradiation of diamond implanted to the above-critical doses (D \geq 6x10¹⁶ cm⁻²) the annealing stage was never possible. For D=8x10¹⁶ cm⁻², graphitization began at low fluences of E=1.4 J/cm² ("true" value is 0.9 J/cm²) and was observed at fluences of up to E=7.6 J/cm². At E=10.5 J/cm², explosive ablation also occurred, but the depth of the crater formed was \approx 1.71 μ m, being in agreement with the $R_p \approx$ 1.58 μ m.



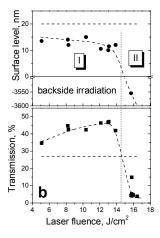
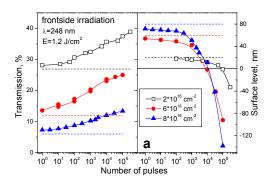


Figure 4. Changes in optical transmission (at λ =532 nm) and surface level of laser spots produced in D⁺-implanted diamond (D=2x10¹⁶ cm⁻² < D_{cr}) under 'frontside' (a) and 'backside' (b) irradiation with single KrF laser pulses. Dash lines show the original values of the transmission and surface level of the ion-implanted regions.

Figure 5a shows the results of multipulse 'frontside' irradiation of different regions implanted to doses below and higher than D_{cr} . For the multipulse regime one can see the progressive annealing with number of shots but the complete annealing is not achieved as the transmission is much less than that of the unimplanted diamond. It is found that not only annealing occurs but also does the etching of diamond, as soon as the surface level in laser spots becomes below the unimplanted diamond surface. The observed laser etching of diamond takes place in the absence of apparent surface graphitization, and the etching rates are very low – from 10^{-4} to 10^{-3} nm/pulse.

Figure 5b shows that during multipulse 'backside' irradiation the optical transmission and material compaction (material density) are further increased, enhancing the annealing effect.



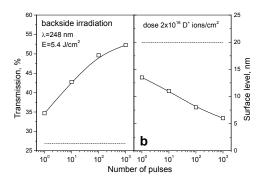


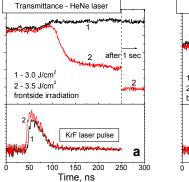
Figure 5. Changes in the optical transmission (at λ =532 nm) and surface level of laser spots in the D⁺ ion-implanted diamond during multipulse 'frontside' (a) and 'backside' (b) irradiation with KrF excimer laser. Dash lines show the original values of the optical transmission and surface level of the surface regions implanted to different doses.

KrF laser irradiation of H⁺ ion-implanted diamond

Similar to the D^+ ion-implanted diamonds, laser irradiation of H^+ ion-implanted diamond (for $D < D_{cr}$) resulted in identical annealing/graphitization behaviour. During 'frontside' irradiation, 'weak' annealing of the ion-implanted layers occurred at $E < 3.5 \text{ J/cm}^2$, and at $E \ge 3.5 \text{ J/cm}^2$ a sharp transition to graphitization of the ion-implanted layer was observed. Under 'backside' irradiation, we observed effective annealing during the action of single laser pulses at fluences of up to $E < 14 \text{ J/cm}^2$ and 'suppression' of the graphitization process in the buried layer. If the energy density exceeded the value $E \ge 14 \text{ J/cm}^2$, explosive ablation of a surface layer of $\sim 3-3.5 \text{ }\mu\text{m}$ thick took place.

Contrary to the 'suppression' of graphitization in the D^+ and H^+ ion-implanted diamonds, the presence of the graphitization stage during 'backside' irradiation of the He⁺ implanted diamond (see, Fig. 3a) is likely to result from the difference in the R_p values, evidencing that the thickness of the constraining diamond cap may strongly affects the evolution of laser-induced HPHT processes in the buried layers.

For time-resolved optical transmission measurements the radiation of a HeNe laser (λ =630 nm) was used as a probe beam. The intensity of a HeNe laser beam was detected by an avalanche diode with the rise time of < 500 ps; the diode signals were recorded with a fast oscilloscope (Tektronix, 5GS/s). A typical character of the time-dependent transmission during and after the laser irradiation of the H⁺ ion-implanted diamond is shown in Fig. 6.



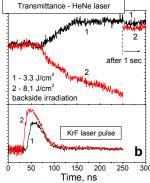


Fig. 6. Transmission of a probe beam of a He-Ne laser through H⁺ ion-implanted diamond (dose D=1.2x10¹⁶ cm⁻², D<D_{cr}) during and after the KrF laser pulse action: a) 'frontside' irradiation, and b) 'backside' irradiation.

The transmission signals were measured i) during and after the pulse action in the time interval 0-250 ns, and ii) in about 1 sec after the pulse end. One can see that the annealing and graphitization start on the tail of a laser pulse, when the temperature is close to the maximum value, evidencing the thermal character of the laser-induced processes in the ion-implanted diamond. At the same time, the graphitization process during 'frontside' irradiation continues for a 'long time' after the end of the laser pulse (Fig. 6a). Even more surprising is a recovery of the transmission under 'backside' irradiation (Fig. 6b). The curve "2" in Fig. 6b, as well as the curve "1", is related to the annealing stage, however the transmission signal slowly decreases for the time period up to 250 ns, and then, after 1 sec, 'jumps' to the value exceeding the initial transmission value.

CONCLUSIONS

A non-linear defect density distribution in a near surface layer was found to be a major factor affecting the UV laser-induced annealing/graphitization behavior in diamonds implanted with light ions.

During 'frontside' irradiation, multipulse laser action at fluences lower than the graphitization thresholds resulted in partial annealing of diamond layers implanted to the doses both $D < D_{cr}$ and $D > D_{cr}$, indicating that the annealing occured in near-surface layers (not in the buried layer with the high defect density). Competing with the annealing process, laser etching of the ion-implanted diamond was observed at very low rates of 10^{-4} - 10^{-3} nm/pulse.

During 'backside' irradiation, the annealing efficiency was much higher than for 'frontside' irradiation and the annealing occurred in the buried layer (for $D < D_{cr}$). For the H^+ and D^+ implanted diamond, the graphitization in the buried layer was inhibited and a sharp transition to explosive-like ablation of few micron thick layers was observed. At $D > D_{cr}$, the annealing stage was never possible and graphitization was induced in buried layers at low fluences.

ACKNOWLEDGEMENTS

The work is supported by Swiss National Science Foundation under the Projects 7SUPJ062184 and 7IP62635.

REFERENCES

- 1. Vavilov, V.S.: Possibilities and limitations of ion implantation in diamond, and comparison with other doping methods. Physics-Uspekhi, 37, 1994, 407-411.
- 2. Prins, J.F.: The Properties of Natural and Synthetic Diamond. Academic Press, London, 1992, 301-341.
- 3. Kalish, R.; and Prawer, S.: Handbook of Industrial Diamonds and Diamond Films. Marcel Dekker, Inc., New York, 1998, 945-982.
- 4. Khmelnitskiy, R.A., et al.: Optical characterization of graphitized layers in ion-implanted diamond. Lasers in Synthesis, Characterization, and Processing of Diamond, Proceedings of SPIE, 3484, 1997, 204-211.
- 5. Kalbitzer, S.: Diamond for high-density optical recording, Appl. Phys. A, 72, 2001, 639-670.
- 6. Uzan-Saguy, C., et al.: Damage threshold for ion-beam induced graphitization of diamond. Appl. Phys. Lett., 67, 1995, 1194-1196.
- 7. Kalish, R., et al.: The nature of damage in ion-implanted and annealed diamond. Nucl. Instrum. Meth. Phys. Res. B, 148, 1999, 626-633.
- 8. Prins, J.F.; Derry, T.E.: Radiation defects and their annealing behaviour in ion-implanted diamonds. Nucl. Instrum. Meth. Phys. Res. B, 166-167, 2000, 364-373.
- 9. Gippius, A.A., et al.: Defect-induced graphitisation in diamond implanted with light ions. Physica B, 308-310, 2001, 573-576.
- 10. Prawer, S.; Jamieson, D.N.; Kalish, R.: Investigation of carbon near the graphite-diamond-liquid triple point. Phys. Rev. Lett., 69, 1992, 2991-2994.
- 11. Allen, M.G., et al.: Pulsed laser annealing of P-implanted diamond. Appl. Phys. Lett., 63, 1993, 2062-2064.
- 12. Gippius, A.A.: Luminescent characterization of radiation damage and impurities in ion-implanted natural diamond. Diamond Relat. Mater., 2, 1993, 640-645.
- 13. Prins, J.F.; Derry, T.E.; and Sellschop, J.P.F.: Volume expansion of diamond during ion implantation. Phys. Rev. B, 34, 1986, 8870-8874.
- 14. Kononenko, V.V., et al.: Laser-induced phase transitions in ion-implanted diamond. Diamond Relat. Mater., 2003, in press.
- 15. Evans, T.: The Properties of Natural and Synthetic Diamond. Academic Press, London, 1979, 403-424.
- 16. Bundy, F.P.: Pressure-temperature phase diagram of elemental carbon. Physica A, 156, 1989, 169-178.

MEASUREMENTS OF THERMAL CONDUCTIVITY OF UNDOPED AND BORON-DOPED CVD DIAMOND BY TRANSIENT GRATING AND LASER FLASH TECHNIQUES

V.G. Ralchenko, A.V. Vlasov

General Physics Institute, Russian Academy of Sciences, 38 Vavilov str., 119991 Moscow, Russia Tel: +7-095-1328229; Fax: +7-095-1357672; E-mail: ralchenko@nsc.gpi.ru

E.V. Ivakin, A.V. Sukhadolau

Institute of Physics, Academy of Sciences of Belarus, 70 Skaryna Ave., 220072 Minsk, Belarus

A.V. Khomich

Institute of RadioEngineering & Electronics, 1 Vvedenskogo sq., 141190 Fryazino, Russia

ABSTRACT

In-plane (k_{\parallel}) and perpendicular (k_{\perp}) thermal conductivity of high quality polycrystalline diamond films have been measured using a transient thermal grating (TG) and a laser flash (LFT) techniques, respectively. Undoped and boron-doped films have been grown by microwave plasma CVD. The TG were excited in bulk by Nd:YAG laser pulses at 1064 and 266 nm, while in LFT 1064 nm radiation was used. The in-plane values k_{\parallel} , averaged over the film thickness (0.3-0.5 mm), fall in the range of 15-20 W/cmK at room temperature. The anisotropy of 10-20% in thermal conductivity ($k_{\parallel} < k_{\perp}$) caused by specific columnar growth of diamond grains is revealed. In the temperature range T = 25 – 200°C the thermal conductivity follows the relationship $k \sim T^{-1}$ typical for dielectrics at high T. Using a quasi-surface TG excitation in VUV spectral range (213 nm wavelength) k_{\parallel} values of thin sub-surface layers were measured, and the depth nonhomogeneity of thermal conductivity was estimated. A strong, up to 2.7 times, variation in k_{\parallel} across the film thickness is revealed for some specimens. Thermal conductivity as high as 22.4 W/cmK is measured at the growth (coarse-grained) surface of a B-doped film.

Keywords: CVD diamond, B-doped diamond, thermal conductivity, transient thermal gratings

INTRODUCTION

The record high thermal conductivity of diamond among other substances at room temperature makes it the ideal material for many applications in which the thermal properties (combined with low electromagnetic absorption, high strength, and other valuable parameters of diamond) play a key role. Selected examples of advanced CVD diamond applications include heat spreaders for semiconductors lasers, microwave transistors and multichip modules (ref. 1), optics for CO_2 lasers (refs. 2,3), windows for powerful gyrotrons (refs. 4,5), multiplayer cutting tools (ref. 6). While the thin (a few microns) polycrystalline diamond films typically have the thermal conductivity, k, up to 10 W/cmK at best (ref. 7), thick (a few hundred microns) undoped CVD diamond wafers show k values approaching to those known for the most pure type IIa single crystal natural diamonds, k = 20 - 24 W/cmK (ref. 8). High thermal conductivity has been found also for natural (ref. 9) and synthetic HPHT (ref. 10) boron-doped diamonds, however, much less is known on thermal properties of B-doped CVD films.

Commonly the polycrystalline CVD diamond exhibits a depth inhomogeneity of thermal conductivity, since the grain dimensions gradually increase in the process of layer growth. In addition, k displays an anisotropy because the grains have columnar shape with their axes directed perpendicular to surface. Perpendicular diffusivity D_{\perp} and conductivity k_{\perp} are typically larger than the in-plane values $D_{\rm II}$ and $k_{\rm II}$, and the thermal anisotropy can be as high as 50% (ref. 11). In the present paper we used the method of transient thermal gratings, TG (ref.12) and a laser flash-technique, LFT (ref.13) to measure in-plane and perpendicular thermal diffusivity and conductivity of thick undoped and B-doped diamond films grown in a microwave plasma CVD reactor. Both techniques determine diffusivity D, from which the conductivity $k = D\rho C$ is calculated, where ρ and C are the density and specific heat of diamond, respectively.

EXPERIMENTAL

Transient Thermal Grating Technique

The TG method is based on transient thermal grating recording in the sample by two interfering laser beams, and monitoring the thermal decay of the grating with a probe beam diffracting on the TG (Fig. 1). The D_{II} can be determined from the relation $D_{II} = \Lambda^2/8\pi^2\tau_D$ (ref. 14), where the time constant τ_D of the exponential decay of diffraction signal and the grating spacing Λ are two experimentally measured parameters. For excitation laser wavelength longer than the fundamental absorption edge ($\lambda_{ex} > 225$ nm), the CVD diamond is almost transparent and the thermal gratings are formed in the bulk (Fig. 1a). Thus the diffusivity data averaged over the slab thickness are obtained. For shorter wavelengths, because of a strong light absorption, the TG is formed only in a thin subsurface layer. Actually a layer with thickness of the order of Λ/π (ref. 14), thicker than the optical absorption depth, is involved in dissipation process in this case (Fig. 1b). This makes possible to tune the spatial scale of heat transfer by variation of grating period Λ , and perform the thermal characterisation of depth inhomogeneity of gradient materials.

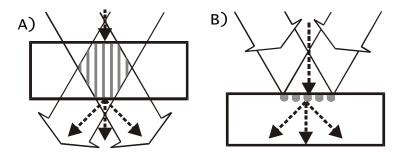


Fig. 1. Geometry of bulk (A) and subsurface (B) thermal gratings formed with pulsed laser excitation at wavelength $\lambda_{ex} > 225$ nm (low optical absorption) and $\lambda_{ex} < 225$ nm (high absorption). The probe beam of a He-Ne laser (dashed lines) diffracts on the gratings.

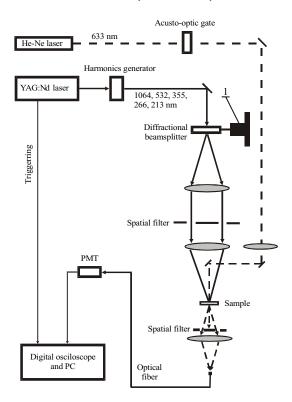


Fig. 2. Set-up for $D_{\rm II}$ measurement using thermal grating technique.

Figure 2 represents the TG-based laser system to measure $D_{\rm II}$. The thermal grating is formed by 9 ns pulses of a Nd:YAG laser equipped with DKDP crystal for higher harmonics generation. Two interfering beams were created using a quartz glass diffraction grating, that transformed almost 80% of incident energy to -1st and +1st orders, the zeroth order being absent. The pulse energy on the sample surface was in the range of 1-3 mJ. The two beams formed a periodic pattern on area less than 1 mm² on sample surface. The period of thermal grating could be varied in the range of 30-120 μ m. The temporal evolution of intensity of a He-Ne laser probe beam passing through the sample and diffracting on the TG is recorded by PMT. The diffraction signal decay time is determined by exponential fitting procedure. The stationary temperature of the sample can be varied in the range from room temperature to 200°C. Phase sensitive detection of diffraction signal allows to reduce the error in the measured diffusivity down to $\pm 3\%$. More details on the measuring methodology can be found in (refs. 12,15).

Laser Flash Technique

The LFT method is based on measurement of travelling time of the thermal wave excited by a laser pulse, from one side of the plate to another (Fig. 3). In this case the diffusivity D_{\perp} in the direction perpendicular to the sample surface is determined, the D_{\perp} value, by definition, being averaged over the sample thickness.

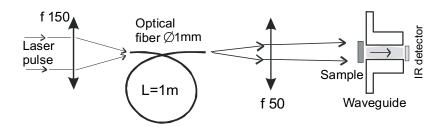


Fig. 3. Schematics of laser flash technique.

A pulsed YAG:Nd laser (wavelength 1.06 µm, pulse width 8 ns) was used for sample surface heating. Highly uniform intensity distribution within irradiation spot is achieved by passing the beam through a silica optical fiber (1 mm diameter, 1 m long). Both sides of the samples were covered with a thin titanium film to provide surface absorption and enhance thermal radiation emissivity. Propagation time of the thermal wave through the sample thickness was determined by measuring the temperature rise kinetics at the rear side of the sample by a HgCdTe detector with 300 ns resolution. Between the sample and detector a metallic tube (waveguide) with reflecting inner surface is placed to confine the thermal radiation and direct the maximum flux to the detector. The temperature rise on the rear side did not exceed 3°C, thus the thermal transport data obtained refer to room temperature. The temperature kinetics induced by a large number of laser pulses (usually 200 pulses were accumulated) were averaged with a PC to improve the measurement accuracy, which typically is in the range of 5-8%.

Samples

Diamond films have been grown on silicon substrates of 63 mm diameter in CH_4/H_2 gas mixtures in a microwave plasma assisted CVD reactor (ASTeX PDS19 model, 5 kW power, 2.45 GHz frequency) as described elsewhere (ref. 16). The undoped 0.3-0.5 mm thick samples of different qualities were produced at the following deposition parameters: methane content of 2.0-2.5% in hydrogen, gas flow rate 300 - 1000 sccm, pressure 100 Torr. The samples were translucent, their resistivity at room temperature (R.T.) was in the range of $10^{12} - 10^{14}$ Ohm·cm. Concentration of substitutional nitrogen impurity varied between 0.8 and 8.5 ppm, while hydrogen content was in the range of 80-350 ppm, as determined from IR absorption spectra.

One sample (#125, "blue diamond") was moderately doped with boron (N_A - $N_D \approx 4ppm$) in the course of deposition process (ref. 17), its R.T. resisitivity was about 10^3 Ohm·cm. The only feature observed in Raman spectra of all samples was a strong and narrow (ca. 3 cm⁻¹) diamond line at 1332 cm⁻¹ wavenumber, no traces of other carbon phases was found. The diamond films were chemically separated from the substrate, the mother diamond wafers were laser cut to the sizes of 4 to 48 mm², and mechanically polished to the roughness less than 10 nm (as measured with AFM) to minimize the light scattering. On some samples the highly defective fine-grained layer of 20-30 μ m thickness at the nucleation side has been mechanically removed.

RESULTS

Thickness-averaged thermal conductivity

In-plane and perpendicular thermal conductivity of three representative samples are given in Table I. The $k_{\rm II}$ values have been obtained by TG method at 266 and 1064 nm excitation wavelengths. The thermal conductivity was found according to relation $k_{\rm II} = D_{\rm II}\rho C$, where ρ =2.51 g/cm³ is the density and C=0.5 J/gK is the specific heat of diamond. Due to low absorption at laser wavelengths used the gratings were formed almost uniformly through the film thickness. The k_{\perp} values fall within 17-20 W/cmK range, being systematically larger by 10-20% than the inplane $k_{\rm II}$ values, the result typical for polycrystalline films (ref. 11). The anisotropy is due to columnar structure of CVD diamond (the columnar grains are directed normally to the film plane, increasing in diameter roughly proportionally to the film thickness). Also impurities and defects are concentrated mostly nearby the grains boundaries. Therefore, the in-plane thermal flux meets higher thermal resistance than that in perpendicular direction (along the columns).

Table I. H and N impurity concentrations, thermal conductivities k_{II} and k_{\perp} averaged over the
film thickness, excitation wavelength and period of thermal gratings in TG measurements

	Hydrogen	Nitrogen	Excitation	Thermal	Thermal	Thermal
	conc.	conc.	wavelength,	grating period,	conductivity k_{\perp}	conductivity $k_{\rm II}$,
Sample #	ppm	ppm	nm	μm	W/cmK	W/cmK
112	100	2.1	266	78,5	17.4	15.0
111	80	3.7	266	120	20.5	17.8
125*	150	<1	1064	131	20.0	18.0

^{*} B-doped diamond

The thermal conductivity is controlled by phonon scattering rate on various defects. Since hydrogen has a tendency to decorate the defects the hydrogen impurity concentration can be a good indicator of imperfections in CVD diamond. An inverse correlation of thermal conductivity and bonded hydrogen (C-H) content in CVD diamond has been previously reported by other authors (refs. 8,18). Here we show (Fig. 4, full squares) the k_{\perp} versus hydrogen content plot for a broad selection of our thick (0.2 – 1.0 mm) films. The k_{\perp} value decreases from 21 to 4.5 W/cmK with H concentration increase from 70 to 4500 ppm. Interestingly, that the present data are in a good agreement with the results obtained with LFT by Coe and Sussmann (ref. 18) for MPCVD films produced by De Beers, in spite of possible difference in diamond deposition technologies. Their data, recalculated by us from integrated C-H absorption intensity (in cm⁻²) to H concentration (in ppm) using a relation 1 cm⁻² = 1.7 ppm, are shown in Fig. 4 (open squares).

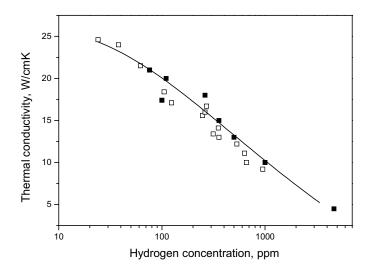


Fig. 4. Thermal conductivity k_{\perp} versus H concentration in diamond films (full squares). For comparison the data for MPCVD films taken from (ref. 18) are shown (open squares).

Depth inhomogeneity of in-plane thermal conductivity

Two sides of the free-standing diamond films show different structures. The nucleation side displays small, of the order of 1 μ m, grains, while the growth side shows larger grains, typically of 20-100 μ m size. To reveal an inhomogeneity of $k_{\rm II}$ in the film cross-section the thermal gratings with spacing 92 μ m were excited by VUV radiation at 213 nm wavelength on each side of the sample. The TG is formed in a thin (about 3 μ m) subsurface layer. In addition to the TG decay via in-plane heat dissipation the heat flux also penetrates in perpendicular direction to the depth $\Lambda/\pi \approx 30~\mu$ m, which is still much smaller than the sample thickness (Fig. 1). This allows to probe the different sides, and measure a local thermal conductivity rather than to get an averaged $k_{\rm II}$ value. The results summarized in Table II show the higher $k_{\rm II}$ on growth side, as might be expected. The difference in $k_{\rm II}$ on two sides for the samples #112 and 125 is rather small, less than 30%, because the most defective fine-grained layer (ca. 30 microns thick) on nucleation side was polished away. In contrast, the $k_{\rm II}$ on the two sides differ by a factor of 2.7 for sample (#86) with unpolished bottom side. For the B-doped sample #125 a very high value $k_{\rm II}$ =22.4 W/cmK, approaching to those for most pure type IIa diamonds, is determined on growth side.

Table II. Thermal conductivity $k_{\rm II}$ measured with TG excited at 213 nm wavelength on nucleation and growth sides of diamond films (* nucleation side unpolished).

	Film thickness,	$k_{\rm II}$ (nucleation side)	$k_{\rm II}$ (growth side)
Sample #	μm	W/cmK	W/cmK
112	330	14.8	18.0
125	330	16.3	22.4
86*	450	7.4	20.0

Thermal conductivity at elevated temperatures

Temperature dependencies of thermal conductivity $k_{\rm II}$ were calculated from the measured diffusivity $D_{\rm II}({\rm T})$ using the data on specific heat $C({\rm T})$ tabulated in (ref. 19). The specific heat significantly, by a factor of 2, varies in the measured temperature range of 25-200°C. The $k_{\rm II}$ vs T plot for two samples, undoped and B-doped, are represented in Fig. 5. The results for type IIa diamonds (ref. 20) are also shown for comparison. The decrease of thermal conductivity with T (mostly due to phonon-phonon scattering mechanism) is well fitted with the relationship $k \sim T^{-n}$. We found for our CVD samples n=0.99±0.07, and n = 1.29 for type IIa crystals (Fig. 5), the latter being in a good agreements with the value n=1.26 at T=320-450 K reported for IIa type diamonds by Burgemeister (ref. 9).

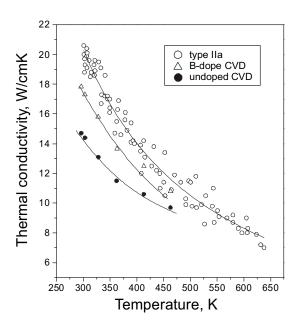


Fig. 5. Thermal conductivity $k_{\rm II}$ versus temperature for undoped diamond film (#112, closed circles) and B-doped film (#125, triangles). The data for type IIa single crystal diamonds taken from (ref. 20) are shown for comparison (open circles). Solid lines are fitting $k \sim T^{-n}$.

CONCLUSIONS

Transient thermal grating technique and laser flash techniques have been used to measure in-plane ($k_{\rm II}$) and perpendicular (k_{\perp}) thermal conductivity of thick MPCVD diamond films. The k values, averaged through the film thickness, approach 20 W/cmK. Anisotropy in thermal conductivity (k_{\perp} - $k_{\rm II}$)/ k_{\perp} less than 20% is found. A strong, up to 2.7 times, difference between $k_{\rm II}$ on nucleation side and growth side of the films is revealed. For a B-doped diamond film very high value $k_{\rm II}$ =22.4 W/cmK approaching to those for type IIa diamonds is determined on the growth side. Thermal conductivity inversely correlates with hydrogen concentration in diamond. At temperatures T=25-200°C the thermal conductivity of the high quality CVD diamond follows a relationship $k \sim T^{-n}$ with $n \approx 1.0$.

ACKNOWLEDGEMENTS

This work was supported in a part by the State Science and Technology Committee of Belarus, grant No. M-20, RFBF grant No. 03-03-32396 and INTAS grant No. 01-2173.

REFERENCES

- 1. Eden, R.C., Application of diamond substrates for advanced high density packaging, Diamond Relat. Mater. 2 (1993) 1051-1058.
- 2. Brierley C.J., Beck C.M., Kennedy G.R., et al., The potential of CVD diamond as a replacement to ZnSe in CO₂ laser optics, Diamond Relat. Mater. 8 (1999) 1759-1764.
- 3. Kononenko, V.V., Konov, V.I., Pimenov, S.M., et al, CVD diamond transmissive diffraction optics for CO₂ lasers, New Diamond and Frontier Carbon Technology, 10 (2000) 97-107.
- 4. Thumm, M., MPACVD-diamond windows for high-power and long-pulse millimeter wave transmission, Diamond Relat. Mater. 10 (2001) 1692-1699.
- 5. Parshin, V., Ralchenko, V., and Konov, V., Diamonds for high-power gyrotron window, 23rd Int. Conf. on Infrared and Millimeter Waves, Colchester, UK, Conference Digest, (1998), 232-233.
- 6. Nedelik, J., Kremser, W., and Lux, B., Low-pressure diamond coatings used as heat spreaders on heavy-duty metal cutting tools, Diamond Films and Technology, 8 (1998) 37-50.
- 7. Graebner, J.E., Ralchenko, V.G., Smolin, A.A., et al., Thermal conductivity of thin diamond films grown from d.c. discharge, Diamond Relat. Mater., 5 (1996) 693-698.
- 8. Twitchen D.J., Pickles C.S.J., Coe S.E., et al., Thermal conductivity measurements on CVD diamond, Diamond Relat. Mater. 10 (2001) 731-735.
- 9. Burgemeister E.A., Thermal conductivity of natural diamond between 320 and 450 K, Physica B, 93 (1978) 165-179
- 10. Nakamura, K., Horiuch, K., Yamashita, S., et al., Thermal conductivity of boron-doped ¹²C diamonds, Diamond Films and Technology, 7 (1997) 339-341.
- 11. Graebner, J.E., Jin, S., Kammlott, G.W., et al., Anisotropic thermal conductivity in chemical vapor deposition diamond, J. Appl. Phys. 71 (1992) 5353-5356.
- 12. Ivakin, E.V. and Rubanov, A.S., Thermal diffusivity measurement of high-conducting solids by the method of transient gratings, Analytical Sciences, 17 (2000) 126-128.
- 13. Vlasov, A., Ralchenko, V., Gordeev, S., et al., Thermal properties of diamond/carbon composites, Diamond Relat. Mater., 9 (2000) 1104-1109.
- 14. Eichler, H.J., Gunter, P. and Pohl, D.W., Laser-induced dynamic gratings, Springer, Berlin, 1986.
- 15. Ivakin, E.V., Sukhodolov, A.V., Ralchenko, V.G., et al., Measurement of thermal conductivity of polycrystalline CVD diamond by laser-induced transient grating technique, Quantum Electronics (Moscow), 32 (2002) 367-372.
- 16. Ralchenko V.G., Smolin A.A., Konov V.I., et al., Large-area diamond deposition by microwave plasma, Diamond Relat. Mater., 6 (1997) 417-421.
- 17. Polyakov V.I., Rukovishnikov A.I., Rossukanyi N.M., et al., Electrical properties of thick boron and nitrogen contained CVD diamond films, Diamond Relat. Mater., 10 (2001) 593-600.
- 18. Coe, S.E., Sussmann, R.S., Optical, thermal and mechanical properties of CVD diamond, Diamond Relat. Mater., 9 (2000) 1726-1729.
- 19. Nepsha V.I. Heat capacity, conductivity and the thermal coefficient of expansion, in Handbook of Industrial Diamonds and Diamond Films, ed. by M. A. Prelas et al. N.Y., Marcel Dekker, 1997, pp.147-192.
- 20. Ositinskaya T.D. Superhard Materials (Kiev), No. 4 (1980) 13 (in Russian).

X-RAY THREE-BEAM DIFFRACTION BY DIAMOND SINGLE CRYSTALS

V.N. Tkach ¹, I.M. Fodchuk ², M.D. Borcha ²

We have studied the effect of the real structure of diamond single crystals on variations of the intensity profiles of the Kossel lines at the intersection of them. The intensity profile of intersecting lines characterizes an anomalous X-ray transmission and is not a simple sum of individual lines. The revealed effect is most sharply defined for type 1b diamond crystals (having a nitrogen impurity in the lattice). The experimental data on the X-ray diffraction by diamond single crystals qualitatively fit the theoretical calculations of the X-ray diffraction by a single crystal of the cubic syngony in the three-beam region when an ultrasonic wave passes through the crystal. The anomalous distribution of the intensity over the three-beam region is attributed to the periodic deformation of the diamond lattice caused by a selective absorption of a nitrogen (boron) isomorphic impurity by a growing crystal.

1. INTRODUCTION

The fullest volume of the reliable information about the lattice distorting in single crystals is given by X-ray diffraction methods [1], based on the dynamic theory of the radiation scattering. Unfortunately, the area of their usage is limited. So, for example, the usage of double crystal and furthermore three-crystal spectrometer when studying the fine structure of diamond lattice is hindered by a low intensity of an analytical signal due to small sizes of real crystals. For this reason the development of new or improving the existing precision techniques for studying the fine structure of real crystals is actual. The Kossel method can be related to such techniques. The advantages of this highly informative method are as follows:

the X-ray pattern simultaneously exhibits several reflections from equivalent $\{hkl\}$ lattice planes;

- the precision determination of the lattice constants [2] is possible from diffraction line displacements;
- the study the fine structure of the real crystals is possible from a change in the intensity of the line profile.

When the wide divergent X-ray beam diffraction is used, the multi-beam regions are the intersection of Kossel's lines. As is shown in [3, 4], the multi-beam diffraction is extremely sensitive to deformations. Therefore, of interest is to study the influence of one-dimensional equidistant bending of atomic planes on the X-ray scattering in two-beam regions and on anomalous multi-beam X-ray transmission in single crystals with a diamond lattice.

¹V.N. Bakul Institute for Superhard Materials of the National Academy of Sciences of Ukraine, Kiev, Ukraine

² Yu. Fedkovich Chernovtsy State University, Chernovtsy, Ukraine

In the present work we have made calculations using the dynamic theory of X-ray scattering by perfect crystals with one-dimensional strains and experimental measurements of Kossel's lines intensity for single crystals of synthetic diamonds.

2. MULTI-BEAM DIFFRACTION

According to the dynamic theory, the interaction between the incident and scattering X-rays causes a change of the velocity of the resultant wave transmitted through a crystal. When the diffraction conditions are simultaneously met for three and more planes, the enhancement of X-ray scattering by lattice defects is observed.

The authors of [5] offered the general approach to the calculation of *N*-wave Borrmann diffraction parameters: coordinates of excitation points on dispersion surfaces, coefficients of absorption and excitation of wave vector modes, X-ray transmission and scattering intensity. This approach was used for the calculation of four-beam diffraction parameters in a Ge perfect crystal. The authors of Ref. [6] showed that with multi-beam diffraction the transmitted wave is adsorbed much weaker, that means the enhancement of anomalous wave transmission as compared to the two-beam Borrmann effect.

2.1. THREE-BEAM DIFFRACTION BY DIAMOND CRYSTALS

The physical interpretation of the phenomenon of anomalous X-ray transmission is as follows. During the propagation of radiation in the crystal the standing waves with nodes, which coincide with atomic planes, develop. If the electric field intensity in the nodes approaches zero, the absorption of the radiation is a minimum. In this case, only thermal vibrations of the lattice are the main reason for the minor scattering.

The distribution of the intensity of the regions of the Kossel line intersections is calculated using the Takagi equations. Unfortunately, there is no algorithm of their solution in a general form for a $\vec{U}(\vec{r})$ strain field. It is caused first of all by the fact that in a general case, it is not possible to separate σ and π polarization, and because no less than three coplanar nodes of the reciprocal lattice take part in multi-beam diffraction [7].

The multi-beam symmetric X-ray diffraction by a crystal with one-dimensional strain field is described by the system of differential equations, which in the matrix form [3] look like:

$$\frac{d\hat{E}}{dz} = (\hat{A} - \hat{\alpha}(z))\hat{E}(z) , \qquad (1)$$

where the boundary conditions for Laue *N*-diffraction are given by:

$$\hat{E}(0) = \hat{E}_a \quad . \tag{2}$$

Matrix $\hat{\alpha}$ is the angular local disorientation of atomic planes. Matrix $\hat{\alpha}$ elements are determined as:

$$\alpha_m(z) = \alpha_m^0 - 2\pi \frac{d}{dz} (\vec{H}_m \vec{U}(z)) = \alpha_m^{(0)} - \alpha_m',$$
 (3)

where $\vec{U}(\vec{r}) = (U_x, 0, 0)$, $U_x = B \cdot z^2$, B is the deformation parameter. For the three-beam diffraction:

$$\alpha_H = \alpha_H^0 - p_H \cdot z$$
; $\alpha_K = \alpha_K^0 - p_K z$,

where:

$$p_H = p\cos(\alpha) , \qquad p_K = p\cos(\alpha - \varphi) ,$$

$$p = 2B\lambda^2 \gamma_0^2 \left| \vec{H}_m \right| .$$

Here: $\alpha_m^0 = 2\lambda \cdot \left[(\vec{H}_m \cdot \vec{e}_1) \Delta \phi + (\vec{H}_m \vec{e}_2) \Delta \theta \right]$, $\vec{e}_1 = \lambda \left[\vec{K}_0 \times \vec{n} \right]$, $\vec{e}_2 = \left[\vec{e}_1 \times \vec{K}_0 \right]$, \vec{K}_0 - wave vector, which satisfies the condition of exact reflection position, angles $\Delta \theta$ and $\Delta \phi$ characterize the crystal deviation from \vec{K}_0 along \vec{e}_1 and \vec{e}_2 vectors, and α is the angle between $|\vec{H}_H|$ and $|\vec{H}_K|$ diffraction vectors.

Calculations were made for the case of three—beam ($\bar{1}11,111/200$) and ($111,\bar{1}\bar{1}1/220$) diffraction, Fe K_{α} -radiation with $\mu t \approx 10$, where t is the crystal thickness, μ is the normal absorption coefficient.

The results of the Kossel pattern calculation for a perfect diamond crystal are given in Fig. 1a. Figure 1b shows the theoretical profile of three-beam intersection intensity in the direction indicated in the pattern.

The results of the theoretical modeling of the anomalous X-ray scattering region providing the equidistant bending of atomic planes in the crystal with the orientation of displacement vector in the direction perpendicular to the binding plane $\vec{U} \perp \vec{H}_{220}$ are given in Fig. 2. As indicated in [3], with such a choice of orientation \vec{U} , the highest sensitivity of the X-ray diffraction to the lattice strain is achieved.

The comparison of computing results (Fig.2) demonstrates that under deformations with the *B* parameter a decrease in the intensity and the transformation of three-beam scattering region are observed.

Figures.3a and 3b show the experimental Kossel pattern from a crystal synthesized in the Ni-Mn-C system and the intensity profile of the three-beam intersection. The intensity distribution curve of the anomalous scattering exhibits a qualitative agreement between theoretical modeling and experiment.

As the modeling of the process for the three-beam region of the X-ray anomalous scattering was carried out for a case of the equidistant bending of planes, it is possible to state that it is precisely these bendings that are present in real diamond single crystals. We think that, the occurrence of a strain field in real diamond single crystals is caused by an impurity sublattice.

The main problem in the modeling of the radiation intensity in the anomalous scattering region, as follows from an experimental diamond pattern (Fig. 4), is in the correct choice of the shape of a lattice strain field with allowance made for its anisotropy caused by the selective absorption of impurities during the crystal growth. It is just this that explains the different natures of the two-beam reflections of the $CoK_{\alpha1,2}$ -radiation in different equivalent crystallographic directions (111) and (1 $\overline{1}$ 1).

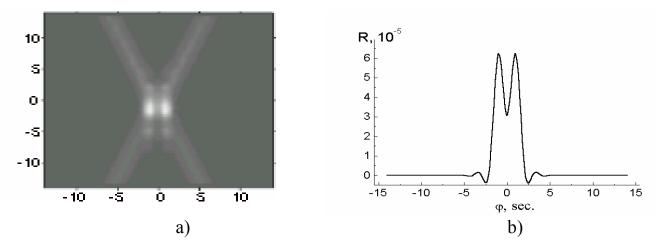


Fig.1. Perfect crystal, $t = 336 \mu m$, $(111, \overline{1} \, \overline{1} \, 1/220)$ -diffraction. a) $R_o(\Delta \varphi, \Delta \theta)$; b) intensity distribution in the direction perpendicular to binding reflection (220).

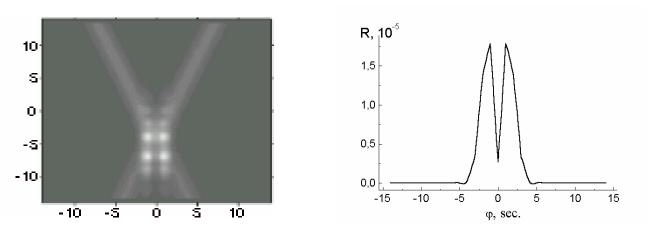


Fig.2. Influence of one-dimensional deformation on the three-beam region. $U(z)=Bz^2$, B=10.

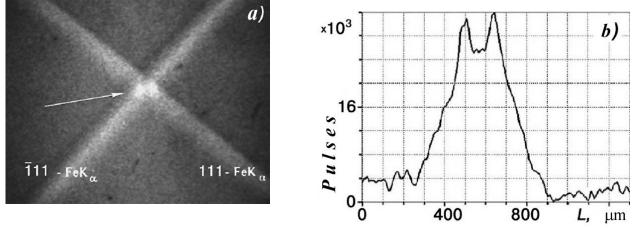


Fig.3. Experimental pattern for the diamond synthesized in the system Ni-Mn-C. Fe $K_{\alpha 1,2}$ -radiation, <001> crystal orientation. a) three-beam scattering region; b) distribution of the intensity in the direction indicated by an arrow.

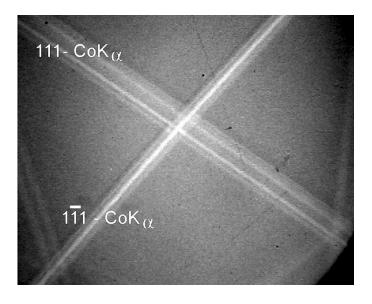


Fig.4. (111,1 $\overline{1}$ 1/020) -diffraction of the Co $K_{\alpha 1,2}$ -radiation in a synthetic diamond single crystal.

REFERENCES

- 1. L.I. Datsenko, V. B. Molodkin, and M. E. Osinovsky, Dynamic X-ray Scattering by Real Crystals in Russian], Naukova Dumka, Kiev, 1988.
- 2. A.S. Vishnevsky and V.N. Tkach, «Precision determination of the diamond lattice parameters by Kossel's method,» Sverkhtverdye Materialy, no. 4, pp. 22-24, 1982.
- 3. N.D. Raransky, M.B. Ostapovich, I.M. Fodchuk, and V.N. Ostapovich, «Three-beam pendulum oscilations rystals with equidistantly bended reflecting planes,» Ukrainsky Fizichesky Zhurnal, vol. 31, no. 7, pp. 1080-1088, 1986.
- 4. N.D. Raransky, I.M. Fodchuk, Ya.M. Struk, and S.N. Novikov, «Three-beam (111,111) X-ray diffraction by a Ge crystal with a periodic displacement field,» Metallofizika, vol. 10, no. 5, pp. 59-63, 1988.
- 5. Ben Post, S.-L.Chang and T.C.Huang, «Simultaneous Four-Beam Borrmann Diffraction,» Acta Cryst., A33, pp. 90-97, 1977.
- 6. G. Borrmann and W. Hartwig, « Die Absorbtion der Rontgenstrahlen im Dreistrahlfall der Interferenz,» Z. Krystallogr., Bd. 121, no. 6,pp. 401-409, 1965.
- 7. Sh. Chen, Multi-Beam X-Ray Diffraction by Crystals [in Russian], Mir, Moscow, 1987.

M. Murakawa, M. Miyoshi, Y. Koga, L. Schäfer, and Y. Tzeng (Editors)

Molecular dynamics simulation of boron implanted into diamond

Rongbin Li, Yongbin Dai, Xiaojun Hu, Heshen Sheng, Xianchang He

State Key Lab of MMCM "s, Shanghai Jiaotong University, Shanghai 200030, P. R. China

rble@sjtu.edu.cn

ABSTRACT

Molecular dynamic simulations, utilizing the Tersoff many-body potential, are used to investigate the

microscopic processes of a single boron atom with energy of 500eV implanted into the diamond (001)2 1

reconstruction surface. We investigate the variations of the coordination number with time required for it to relax

during and short after the B bombarding event with energy of 500 eV. We find from the number of threefold

coordinated atoms that rearrangements of the atoms occurred while the temperature of the sample falls within the

range 5000~1000K. The time spent in this temperature range is defined to be thermal spike life, which is estimated to

be 0.18 ps. The lattice relaxations in the diamond (001) 2.1 reconstruction surface or near surface of simulated have

been discussed. It shows that, the outermost layer atoms tend to move inward, and the other atoms move outward.

The interplanar distance between the outermost layer and the second layer has been shortened by 15% compared

with its starting interplanar distance. According to our simulation, we find that the implanted boron could exit in

diamond stably and form <110> split-interstitial. Stress distribution in the calculated diamond configuration is

inhomogeneous. After B implanted into diamond with energy of 500 eV, there is an excess of compressively stressed

atoms in the lattice, which induces the total stress in the diamond lattice being compressive.

Keywords: molecular dynamics simulation, ion implantation, diamond

DIAMONDLIKE CARBON AND CUBIC BORON NITRIDE

TRIBOLOGICAL PROPERTIES OF GRAPHITE LIKE AND DIAMOND LIKE CARBON COATINGS

D. G. Teer

Teer Coatings Ltd., 290 Hartlebury Trading Estate, Hartlebury, Worcs DY10 4JB. UK.

Two carbon based coatings with exceptional tribological properties have been developed. One is a Graphite Like Carbon known as Graphit-iC TM and the other is a hydrogenated Diamond Like Carbon known as Dymon-iCTM.

The Graphit-iC is deposited by magnetron sputter ion plating from carbon targets using unbalanced magnetrons in a closed field arrangement. The resultant high plasma density produces a dense, non crystalline, electrically conducting carbon coating with sp2 bonding. The hardness is dependant on the deposition parameters but can be over 40Gpa. Using a chromium interlayer excellent adhesion is achieved. The coefficient of friction is dependant on the load but is generally below 0.1. In pin on disc tests under dry conditions at low and moderate loads, up to 45N with a 5mm pin, the wear rate was about 10^{-17} m³/Nm but at higher loads the wear rate was much higher resulting in premature failure. By adding chromium to the coating the hardness was reduced and wear rates of 10^{-17} m³/Nm were obtained at loads up to 140N on a 5mm pin in the pin on disc test. The carbon-chromium composite coating had the same low friction as the pure carbon.

The Dymon-iC is also deposited using a closed field unbalanced magnetron sputter ion plating system but the process is one of Plasma Enhanced CVD using a hydrocarbon gas. The bias voltage applied to the substrates is Pulsed DC but the plasma is further enhanced by additional RF electrodes. This type of system means that upscaling to large production systems is easy and also the bias voltage and ion current to the samples can be independently controlled so that the deposition parameters can be optimised to control the coating properties. Again a chromium layer is used to give good adhesion to the substrate. The coating is an amorphous metal free hydrogenated carbon coating with a significant proportion of sp3 bonds. It is electrically insulating. The coefficient of friction is slightly less than that of Graphit-iC and the wear rate in dry pin on disc tests using a 5mm ball up to a load of 100N is 10^{-17} m³/Nm similar to that of the Graphit-iC.

There are some important differences between the two coatings. The Graphit-iC has excellent properties under water with wear rates better than 10^{-19} m³/Nm but it has poor properties in vacuum. This is consistent with its graphite like properties.

Dymon-iC has poor properties under water and early tests indicate that the properties in vacuum are good but more tests are needed.

Both coatings have excellent tribological properties with oil under boundary lubrication conditions. In long term testing comparing Graphit-iC and Dymon-iC with a hard CrN coating no wear could be detected for any of the coatings but the bearing steel counterface had significant wear against the CrN coating with little wear against the carbon coatings.

The mechanism of low friction for the Graphit-iCTM has been studied in some detail and the results will be presented and discussed. The differences between the coatings lead to different types of application and some of these are presented.

ELECTRONIC POWER SYSTEM APPLICATION OF DIAMOND-LIKE CARBON FILMS

Richard L.C. Wu* and H. Kosai

K Systems Corporation, 1522 Marsetta Drive, Beavercreek, Ohio 45432, USA E-mail: <u>rlwu@aol.com</u>, Tel (937) 429-5151, Fax (937) 429-1122

S. Fries-Carr and J. Weimer

Air Force Research Laboratory, Wright-Patterson AFB, OH 45433, USA

M. Freeman

DARPA TACTICAL Technology 3701 North Fairfax Drive Arlington, VA, USA

G.E. Schwarze

NASA/Glenn Research Center, 21000 Brookpark Rd, Cleveland, OH 44135 USA

ABSTRACT

A prototype manufacturing technology for producing high volume efficiency and high energy density diamond-like carbon (DLC) capacitors has been developed. Unique dual ion-beam deposition and web-handling systems have been designed and constructed to deposit high quality DLC films simultaneously on both sides of capacitor grade aluminum foil and aluminum-coated polymer films. An optimized process, using inductively coupled RF ion sources, has been used to synthesize electrically robust DLC films. DLC films are amorphous and highly flexible, making them suitable for the production of wound capacitors. DLC capacitors are reliable and stable over a wide range of AC frequencies from 20 Hz to 1 MHz, and over a temperature range from –50° C to 300° C. The compact DLC capacitors offer at least a 50% decrease in weight and volume and a greater than 50% increase in temperature handling capability over equal value capacitors built with existing technologies. The DLC capacitors will be suitable for high temperature, high voltage, pulsed power and filter applications

Keywords: Diamond-like carbon, capacitor, high energy density, high volume efficiency

1.0 INTRODUCTION

Capacitors are a pervasive technology in every military and commercial application. Millions are used in electronic power systems and are considered to be a critical link to a common area of failure. Capacitors often fail under raised temperature conditions which may be due to lowering of the voltage breakdown strength, increase in dissipation factor and problems associated with drift of the dielectric constant. Diamond-like carbon (DLC) possesses unique properties of high dielectric strength, high resistivity, low loss, high decomposition temperature, chemical inertness and radiation hardness. It has been demonstrated that very thin (0.5 µm) DLC films can be deposited directly onto smooth aluminum surfaces with good adhesion and that amorphous DLC films are highly flexible, making them suitable for the production of wound capacitors. Increased performance and reduction of capacitor size have been the main goals of our research in diamond-like carbon (DLC) dielectrics [1-2].

2.0 DEVELOPMENT OF DIAMOND-LIKE CARBON FILM CAPACITORS

2.1 Dual Ion-Beam Deposition of DLC Films

A unique dual ion-beam deposition system was used for the deposition of high quality DLC films on both sides of capacitor grade aluminum foil and metallized polymer films in a continuous feed mode inside a class 100 clean room environment [3]. Highly reactive hydrocarbon ions were generated by two 6 cm x 22 cm linear inductively coupled RF (13.56 MHz) ion guns. The DLC films were produced by the impact of these ions onto the

aluminum foil surface or metallized polymer films. A quadruple mass spectrometer was used to monitor the plasma ion compositions during the deposition for quality control.

The dual ion-beam deposition system consisted of two 370-liter (61 cm in diameter by 102 cm long) stainless steel chambers that were bolted together; each was fitted with an ion source to coat one side of the aluminum foil. Each chamber was pumped by two Varian 1000 liter/sec. turbo pumps and backed by three Varian 600 l/min tri-scroll roughing pumps. A 70 liters/sec turbo booster pump was installed in one of the chambers for pumping the quadruple mass spectrometer. The background and deposition pressures of the system were 10⁻⁵ and 10⁻² Pa, respectively. The web-handling system was housed in a stainless steel chamber (36 cm in diameter by 183 cm long), which connected the two ion source chambers together. A computer data acquisition and control system furnished with LabView software was implemented for the complete automation of the entire dual ion-beam deposition system.

The gases used were methane and hydrogen. An in situ quadrupole mass spectrometer was used to monitor the ionic species during the deposition. The predominant ion in the plasma was CH_3^+ . The ion beam energy was varied over the range of 50 eV to 1000 eV, and films of varying thicknesses over the range from 0.3 to 0.8 μ m were deposited.

The chemical composition of DLC films was measured by Rutherford back-scattering (RBS) and hydrogen forward scattering. The film thickness of the DLC films was measured by a step profilometer (DekTak III) and by ellipsometry. The surface morphology and pin hole distribution were characterized by optical spectroscopy and atomic force microscopy.

2.2 Fabrication of DLC Test Capacitor

A method was developed for the fabrication of parallel-plate test capacitors on silicon wafers, on glass and on quartz substrates using two levels of metal electrodes, which were deposited through shadow masks. The parallel plate capacitors were produced by the deposition of aluminum dots through a shadow mask after the DLC film was deposited on the metallized substrates or aluminum foil.

2.3 DLC Test Capacitor Measurement

Electrical connections to the test capacitors were made with two probes on a standard probe station, in such a way that the probes touched the lower and upper aluminum electrodes of the capacitor. The electrical properties of the DLC films were determined by performing three sets of measurements: (a) capacitance as a function of frequency, (b) leakage current as a function of applied voltage, and (c) capacitance and leakage as functions of environmental conditions.

From the knowledge of the area of the capacitor, the DLC film thickness and the capacitance value, the electrical properties of the films such as dielectric constant, D.C resistivity and breakdown strength were obtained.

2.4 Electrical Quality of DLC Films

The deposited DLC films were amorphous and flexible, and had optically smooth surfaces. The electrical properties of capacitor grade DLC films were determined to be: dielectric constant of 3.3, breakdown strength of 7 MV/cm, and D.C. resistivity of $> 10^{15}$ ohm-cm. The chemical composition of the films was found to be 55.2 at. % C, 43.3 at. % H, 1.4 at. % Ar, and trace levels of metals of ~ 0.014 at. %.

2.5 Temperature Dependence of DLC Film Capacitors

The DLC capacitors were tested as various temperatures from -50° C to 400° C over the frequency region of 20 Hz to 1 MHz. Using a high temperature test station, the temperature characteristics of DLC film coatings on aluminum foil were also studied. For the high temperature tests, the measurements were conducted under vacuum (10^{-3} torr) . The frequency dependence of the capacitances and dissipation factors of the DLC capacitors was

measured from 25°C to 400°C. Figures 1 shows an example of capacitance variation for various temperatures. This figure indicates that the capacitors do not lose their initial characteristics up to 400 °C.

For low temperature testing, sample capacitors (DLC158_S1_AL_C39) were placed inside a chamber maintained at -50 0 C and LCR measurements were performed. The DLC film capacitance at -50 0 C was found to be the same as the room temperature value within measurement error over the frequency range of 20 Hz to 1 MHz. At the low temperature of -50 0 C, the dissipation factor was almost constant around 5E-3, whereas at room temperature the value was higher (1E-2 \sim 5E-3). This result indicates that DLC film capacitors can work at low temperatures as well as (or better than) at normal room temperature.

In this way it was established that the DLC capacitors can be operated from -50° C to 300° C.

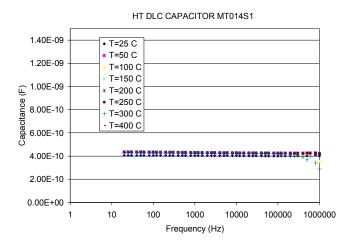


Figure 1 DLC capacitance as a function of frequency for various temperatures

2.6 Storage Life of DLC film Capacitor

In order to test the effects of ambient air on DLC capacitors, three DLC parallel plate capacitors were fabricated and measured in July 1996. These capacitors were stored in ordinary ambient air for two years. The electrical characteristics of the DLC films were measured again on March 26, 1998. After two years in ambient air, the properties of these DLC capacitors had not changed with time. Subsequently, the capacitance was measured at various temperatures in the range of 25 to 100°C, and found to remain essentially constant.

Another DLC capacitor was tested after five years of storage in air. No special storage conditions were used. The frequency dependence of the capacitance before and after five years was found to be the same. These results generally show that DLC electrical properties do not change appreciably over a 20-60 month period.

2.7 Effects of Oil on DLC film Capacitors

Some type of oil is always used in conventional capacitor manufacturing processes in order to remove air gaps from between the different layers in the capacitor. Air gaps may exist in the tightly wound DLC capacitors, and result in reduced capacitance value, as well as decreased breakdown strength. In order to study the DLC behavior with oil, DLC deposited aluminum foils were immersed in four different kinds of oil for more than a day. The oils used were mineral oil, vegetable oil, castor oil and canola oil. It was found that these oils did not cause the DLC to peel from the aluminum foil surface nor damage the DLC film. It also demonstrated that capacitance, insulation resistance and breakdown voltage of DLC capacitors did not change with or without the oils.

3.0 MANUFACTURING TECHNOLOGY

A compact capacitor winding system, consisting of a motorized film winder and two film supporting posts, was used to produce short-length DLC capacitors for testing. Several DLC capacitors were produced by rolling a pair of DLC coated aluminum foils. The capacitors were tested for capacitance and power dissipation factors. The capacitance values remained steady with variation of the AC signal frequency over the range 20 Hz to 1 MHz. Also the power dissipation factors were found to be quite low.

4.0 CONCLUSIONS

A prototype manufacturing technology for producing high energy density DLC film capacitors has been designed, constructed and verified. DLC is an amorphous, flexible film that can be deposited at a low temperature on both sides of capacitor grade aluminum foils or aluminum coated polymer films. DLC films possess low dissipation factor, high resistivity, high breakdown strength, and chemical inertness. These properties make DLC films suitable for producing high energy density pulse power capacitors. Conventional film capacitor manufacturing technology can be adapted for producing high energy density DLC capacitors. Moreover, DLC capacitors are reliable and stable over a wide range of AC frequency from 20 Hz to 1 MHz, and over the temperatures range from -50° C to 300° C. The compact DLC capacitors offer a 50% decrease in weight and volume, and a greater than 50% increase in temperature handling capability over equal value capacitors built with existing technologies. The tubular capacitor form lends itself easily to large-scale, low-cost manufacturing. The DLC capacitors will be suitable for high temperature, high voltage and pulsed power applications.

5. 0 ACKNOWLEDGEMENT

This research was conducted under K Systems Contract No. F33615-98-C-2818, sponsored by Air Force Research Laboratory, Power Division, Wright Patterson AFB, OH under SBIR Phase II Program, and was partially supported by the NASA Glenn Research Center and the Army Research Laboratory.

6.0 REFERENCES

- [1] S. Fries-Carr, R.L.C. Wu and P.B. Kosel, "Capacitor Structures with Dielectric Coated Conductive Substrates", U.S. Patent No. 5,844,770, Dec. 1, 1998.
- [2] R.L.C. Wu, J. Wrbanek, W. Lanter, P.B. Kosel, S. Fries-Carr and J.A. Weimer, "A New Manufacturing Technology for Producing High Energy Density Diamond-like Carbon Capacitors, in Proc. 20th CARTS, pp 69-75, 2000.
- [3] R.L.C. Wu, H. Kosai, M. Freeman, G.E. Schwarze, S. Fries-Carr, and J. Weimer, Proceeding of Twenty-Five International Power Modulator Symposium and High Voltage Work Shop, pp 282-285 (2002).

APPLICATION OF DIAMOND LIKE CARBON FILMS TO GAS BARRIER FOR HYDROGEN FUEL CELL TECHNOLOGY

Akimitsu Hatta, Haruka Matsuhisa, Tetsuya Kaneko and Michio Watamori

Department of Ele. & Photo. Systems Engineering, Kochi Univ. Technol. 185 Miyanokuchi, Tosayamada-cho, Kami-gun, Kochi 782-8502, Japan hatta.akimitsu@kochi-tech.ac.jp

Yoshinori Koga

Research Center for Advanced Carbon Materials, National Institute of AIST Central 5, 1-1, Higashi-1, Tsukuba 305-8565, Japan

Hironobu Inagaki, Kenzo Fukuda

WE-NET Center, The Institute of Applied Energy 14-2, Nishishinbashi 1-chome, Minato-ku, Tokyo 105-0003, Japan

ABSTRACT

We propose application of diamond like carbon films to Hydrogen fuel cell technology. The Hydrogen fuel cell has been developed for a new style of clean energy. The Hydrogen storage system is one of important issues especially for the vehicles. The leakage of Hydrogen through the tank wall cannot be disregarded at such a high pressure of 40-70 MPa. The brittle fracture by Hydrogen is a serious problem for safety. For such the small molecule as hydrogen, the lighter elements such as Beryllium, Boron, Carbon, Nitrogen, etc, will perform better barrier from diffusion into the material. DLC film is a promising barrier to prevent Hydrogen diffusion into the substrate.

The Hydrogen leakage through DLC films deposited on polymer sheets has been investigated for the purpose of evaluation of hydrogen barrier by the DLC film. Without the DLC film, Hydrogen can easily pass through such the sheet of polyethylene terephthalate (PET) widely used for bottling drink. With a thin DLC film deposited by an RF plasma CVD method, the leakage rate through the sheet is decreased by more than 30%. Even by a thin film of a few 10 nm, the Hydrogen diffusion was partly stopped. It is necessary to optimize fabrication condition to improve the barrier performance.

Keywords

DLC, Hydrogen, Fuel Cell, Gas Barrier, PET

Acknowledgement

This study has been carried out as a part of the WE-NET Project administrated through New Energy and Industrial Technology Development Organization (NEDO). The authors thank to NEDO for its financial support.

CUBIC BORON NITRIDE AND BORON BASED TOOL COATINGS – MECHANICAL AND TRIBOLOGICAL PROPERTIES

Martin Keunecke, Klaus Bewilogua

Fraunhofer-Institute for Surface Engineering and Thin Film (IST), Bienroder Weg 54E, 38108 Braunschweig, Germany, e-mail: keunecke@ist.fhg.de

Abstract

Due to their broad range of mechanical properties, from very soft e.g. hexagonal boron nitride, to very hard, e.g. titanium diboride or especially cubic boron nitride (cBN), boron based coatings can be applied in a wide range of cutting operations. The soft coatings can be used as a dry lubricant for cutting operations. The very hard modifications are suitable for wear resistant coatings on cutting tools for highly abrasive machining operations.

After a short overview of the relevance of cBN in production engineering and future trends we will present in detail the current status of development of cBN coatings. Different ways for cBN deposition will be discussed, including the research results of the Fraunhofer IST. Using a modified sputter technique and a special B-C-N gradient interlayer, an essential adhesion improvement of the cBN top layer has been achieved. Our new process allows to prepare cBN films thicker than 2 µm on silicon and nearly 1 µm on cemented carbide cutting inserts. Measurements of mechanical properties like hardness and Young's modulus reveal that the properties of the cBN films are nearly identical to those of cBN bulk material. Results of cutting and machining tests for cBN and other boron based tool coatings will be presented.

FROM MOLECULES TO MATERIALS: HARD AND SOFT BORON NITRIDE PHASES OF TECHNOLOGICAL IMPORTANCE

Hermann Sachdev*, Institut für Anorganische Chemie FR 8.11, Universität des Saarlandes, Postfach 151150, D-66041 Saarbrücken,

e-mail: h.sachdev@mx.uni-saarland.de

Abstract

Boron Nitride (BN) displays several phases of industrial importance, e.g. phases with threefold coordinated atoms (h-BN, r-BN, o-BN) display high thermal resitance, low friction and good insulating properties, whereas phases with tetracoordinated atoms (c-BN, w-BN) exhibit extreme hardness and can be used as wear resistant coatings. Due to these interesting thermal, electrical and tribological features, films and layers of these materials are of specific interest^{1,2}. In order to enhance a growth of hard phases (c-BN, w-BN) from the gas phase or at ambient pressure, it is important to understand the nucleation and growth mechanisms and avoid the formation of sp²- type BN 3,4,5. Due to the outstanding material properities of the individual BN phases, there is a huge interest in the specific synthesis of the individual modifications, and in general mainly infrared spectroscopy is used to determine the formation of c-BN films and nanoscale powders^{2,6,7}. A critical analysis of the characterization of the individual BN phases with IR- and Raman-spectroscopy is presented and their use and limitations are discussed⁸. In the case of c-BN, polytypism was oberved for the first time with raman spectroscopy in analogy to silicon carbide (SiC)⁹, and the formation of boron nitride phases by chemical vapor deposition (fig. 1) and by thermal decomposition of suitable precursors is presented. Amorphous boron nitride was obtained at temperatures below 400°C (fig. 2), which does not show recrystallisation by heating up to 1500°C. SEM, XRD- and IR- spectra indicate the formation of sp²- type boron nitride and display a new source for the selective formation of BN based nanoscale materials. By CVD of borazines, a selective formation of monoatomic layers of h-BN was achieved. Furthermore, the syntheses of boron nitride nanotubes and boron nitride based ceramic composites are presented. These investigations and studies are of principle interest for the understanding of the nucleation and growth of the distinct crystalline phases of BN.

Fig. 1: Gas phase nucleation of h-BN on c-BN (textured, epitaxial growth)

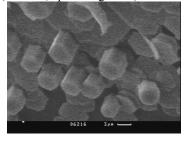
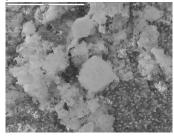


Fig. 2: Amorphous boron nitride (containing BN nanotubes)



Literature: [1] Properities of Group III Nitrides, J. Edgar (Ed.), INSPEC, London 1994. [2] P. B. Mirikami, K. F. McCarthy, D. Medlin Mater Sci. Eng. 1997 R21 (2) 47; [3] H. Sachdev, M. Strauß, Diamond Related Mater. 8 (1999) 319; [4] H. Sachdev, M. Strauß, Diamond Related Mater. 9 (2000) 614; [5] V. Sholozhenko, V. Turkevich, J. Therm. Analysis 38 (1992) 1181; [6] L. Rao, R. B. Kaner, Inorg. Chem. 1994, 33, 3210; [7] D. L. Cui et al. Chem. Mater. 2002 (13) 2457; [8] H. Sachdev, Chem. Mater. 2002 (14) 3615; [9] H. Sachdev, Diamond Related Mater. (2003) in press.

INTRINSIC ABSORPTION-EDGE SPECTRUM AND INDIRECT EXCITON RELATED LUMINESCENCE OF CUBIC BORON NITRIDE

Kenji Watanabe, Takashi Taniguchi, Isao Sakaguchi, and Hisao Kanda Advanced Materials Laboratory, National Institute for Materials Science Namiki 1-1, Tsukuba, Ibaraki, 305-0044, Japan

ABSTRACT

We have observed direct experimental evidence describing the indirect band gap nature of cubic boron nitride (cBN) by means of absorption and cathodoluminescence spectroscopy. Samples were prepared by the temperature gradient method under high pressure and high temperature conditions. The pure, colorless crystals were successfully synthesized using a barium-BN catalyst and taking special care in protecting the materials for cBN growth from oxygen contamination. Those high quality samples show a series of cathodoluminescence bands which is readily assigned to the indirect bound and free exciton luminescence assisted by zone-boundary phonons of point X. In addition, the absorption bands to represent the indirect exciton and band absorption nature is also observed near the indirect exciton energy being the respective phonon energies apart. As a result, an exciton gap energy of 6.35 eV and a band gap energy of 6.42 eV are consistently estimated from both the absorption and luminescence spectra.

Keywords: cubic boron nitride (cBN), indirect exciton, indirect band gap, absorption, cathodoluminescence

INTRODUCTION

Owing to chemical stability and theoretically predicted superior electronic properties, cubic boron nitride (cBN) is one of the materials expected as the possible next generation of electronic devices having high reliability under extreme conditions. Extensive studies of the luminescence properties of cubic boron nitride single crystals have been made since the first report on synthesis of cBN under high temperature and high pressure conditions. ^{1,2} However, the indirect band gap nature including an accurate indirect band gap energy remains not well understood. This is mainly because quality of samples is not so high that indirect exciton related luminescence spectra has not been measurable. In general, the indirect band gap is determined by an indirect exciton or indirect band absorption spectrum near the band edge, ³ though such a spectrum has never been reported in samples so far.

In this work, we used carefully purified materials for the temperature-gradient method under high pressure and high temperature employing a barium catalyst system, then successfully obtained colorless transparent samples which showed both cathodoluminescence (CL) and absorption spectra related to indirect exciton. Each spectral structure can be consistently assigned to phonon-assisted transitions between the valence band maximum Γ and the conduction band minimum X using theoretically calculated phonon energies.

EXPERIMENT

Single crystals of cBN were grown by temperature gradient method at pressure of 5.5 Gpa and temperature of 1500-1700 °C for 20-80 hours. The solvent and source of deoxidized hexagonal BN were packed into a molybdenum (Mo) sample chamber under a nitrogen atmosphere. Morphology of grown crystals was strongly affected by the growth temperature and solvent, such as compounds of alkali-earth metal and BN. The solvent used affected the colors of the grown crystals. Amber color crystals were obtained by using lithium boron nitride solvent, while colorless crystals were obtained by using barium boron nitride.

Although the barium boron nitride solvent system for the temperature-gradient method is very effective for synthesizing pure, colorless samples, a growth cell containing BN source materials tends to be contaminated by oxygen during a synthesis process and the oxygen contamination tints crystals amber color. Thus, we took special care in preventing the growth materials from being contaminated by oxygen, then obtained colorless transparent crystals in which the concentration of oxygen was one order of magnitude less than that for typical amber colored crystals synthesized by means of a conventional method.⁵

The absorption spectra were calculated from transmission spectra obtained by using monochromatic ultraviolet light from a monochromator and a deuterium lamp, and a Si photodiode detector. CL was measured with using a

scanning electron microscopy system as an electron beam source, and a spectrograph with a CCD detector.

RESULTS AND DISCUSSION

Figure 1 shows an example of the absorption spectrum near band gap energy from a sample having 100 um thickness, while the inset is the spectrum taken from a sample having 300 µm thickness. The circles and the line are results for the experiment and a theoretical fitting, respectively. The equations ($\hbar\omega$ - $E_{\rm th}$)^{1/2} for threshold energy $E_{\rm th}$ = 6.204, 6.233, and 6.252 eV and $(\hbar\omega - E_{\rm th})^{3/2}$ for $E_{\rm th}$ of 6.272 eV, respectively, show good agreement with the experimental result. Therefore, the threshold energies between 6.204 and 6.252 eV can be assigned to phonon-assisted exciton absorption and the energy of 6.272 eV to phonon-assisted band absorption. Assuming an indirect band gap of cBN, namely, the valence band maximum and conduction band minimum positioning at Γ and X point in momentum space, respectively, the phonons concerning those absorption belong to the ones at the boundary of X point. Theoretically calculated energies of 0.143, 0.112, 0.127 and 0.088 eV are used for longitudinal optic (LOx), transverse optic (TOx), longitudinal acoustic (LAx) and transverse acoustic (TAx) phonons at X point, respectively, in our assignment.⁴ As summarized in Table I, those threshold energies are readily assigned to phonon absorbed indirect exciton and band transitions. As a result, the indirect exciton energy gap and indirect band gap are obtained as 6.35±0.01eV 6.42±0.01 eV, respectively. Then the exciton binding energy is estimated to 6.42-6.35 = 0.07 eV.

Concerning the samples we have examined, several CL bands appeared near the band edge as shown in Fig. 2. These luminescence bands having a shortest wavelength among luminescence bands which have ever been reported within band gap energy from cBN, have been measured for the first time. A series of the luminescence bands from 6.050 to 6.089 eV among those is reasonably assigned to the bound exciton luminescence as summarized in Table I. The activation energy of 0.172 eV was obtained from the fitting for the temperature dependence of the intensity for the 6.068 eV band by solving the rate equation between radiative and non-radiative transitions; this energy corresponds to the localized energy for the bound exciton (not shown).

As increasing the sample temperature, the broad weak band appeared at the energy of 6.25 eV. It is

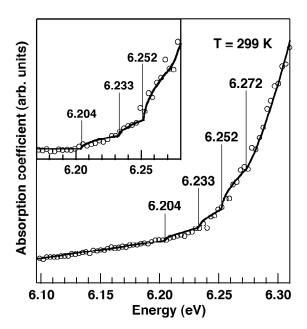


Fig.1 An absorption spectrum near the band edge in cBN

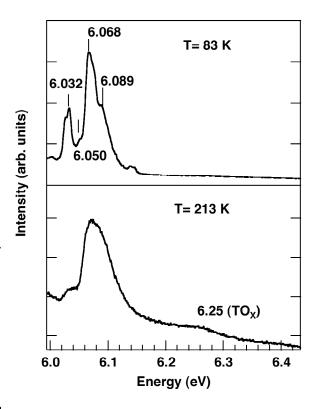


Fig.2 The CL spectra near band edge in cBN

possible to assign to the indirect free exciton luminescence with creation of the TOx phonon (Table I). The temperature at which the 6.25 eV band appears, corresponded to the one at the intensity of 6.068 eV bound exciton

TABLE I: Summary of absorption and cathodoluminescence measurements.

Threshold or peak (eV)			Band gap (eV)
Absorption			
6.204	0.143 (LOx)	6.347	
6.233	0.112 (TOx)	6.345	
6.252	0.088 (TAx)	6.340	
6.272 0.143 (LOx)			6.415
Free exciton luminescence			
6.25 0.112 (TOx)		6.362	
Bound exciton luminescence	e (localized energy 0.172 eV)		
6.050	0.127 (LAx)	6.349	
6.068	0.112 (TOx)	6.352	
6.089	0.088 (TAx)	6.349	

luminescence decreasing. This phenomena can be attributed to an increase of the number of free exciton due to the thermal release of the bound exciton from defects.

The defect for the bound exciton as well as the origin of the 6.032 eV band, which shows the different activation energy from the 6.068 eV band, is not clear at present. This might be caused by residual impurities (carbon, oxygen, or beryllium) or nitrogen vacancy.

CONCLUSION

The indirect band nature of cBN single crystals grown by temperature gradient method under high pressure and high temperature was observed by means of cathodoluminescence and absorption spectroscopy. The exciton gap energy of 6.35 eV and the indirect band gap energy of 6.42 eV were determined by analyzing the indirect exciton related structures appearing in the luminescence and absorption spectra with the appropriate phonon energies apart.

REFERENCES

- [1] J. R. H. Wentorf, J. Chem. Phys. 26, 422(1957).
- [2] O. Mishima and K. Era, in Electric Refractory Materials, edited by Y. Kumashiro (Marcel Dekker, Inc., New York, 2000), pp.495-556.
- [3] R. J. Elliott, Phys. Rev. 108, 1384 (1957).
- [4] K. Karch and F. Bechstedt, Phys. Rev. B56, 7404 (1997).
- [5]T. Taniguchi, and S. Yamaoka, J. Cryst. Growth 222, 549(2001).

DLC FILM GROWTH ON THE SURFACE OF MONOCRYSTALLINE Si AND $\alpha\text{-}AL_2O_3$ WITH THE USAGE OF ION SOURCE

Zh. Panosyan, S. Voskanyan, Y. Yengibaryan, A. Stepanyan

State Engineering University of Armenia
105 Teryan Street, Yerevan 375009, Republic of Armenia
Phone: (3741) 521792, (3741) 272202, Fax: (3741) 545843, E-mail: joseph@seua.am

ABSTRACT

The technology of diamond-like carbon (DLC) film deposition, that allows to vary the composition and structure of the film giving an opportunity to modify the properties of the obtained samples, has been developed.

In the present work the special gas-mixer was utilized, with the help of which the gas mixtures of C_7H_8 or C_6H_{12} , Ar and N_2 were supplied between the anode and cathode of the ion source. By varying the electrical parameters of ion source and concentration of gas mixture and by shaping the plasma geometry, it is possible to modify the average kinetic energy of ions that have reached the substrate. This feature has permitted to grow DLC films on the surfaces of monocrystalline Si (c-Si), Al_2O_3 and other substrates over a 100 cm² area with non-uniformity of characteristics less than 5%. The density ρ of the obtained films has been increased up to 2.5 g/cm³, and the microhardness HV - up to 3100 kgf/mm². The DLC films are stable to chemically hostile environment, to radiation impacts, as well as to thermal influences up to 400 0 C. By altering the film deposition conditions it is possible to vary the electrical, optical and mechanical properties of DLC films in a wide range.

Keywords: DLC film, technology, uniformity, microhardness, density

INTRODUCTION

Today, one of the unsolved problems existing in the field of solar energy conversion is obtaining of thin-film protective and enlightenment coatings that will not only have necessary mechanical, electrical and optical characteristics but will also be reliable and stable to long-term environmental impacts, such as moisture ingress, temperature, ultraviolet and particular radiations, etc. at the process of operation. Application of diamond and DLC films as an encapsulating layer in solid-state electronics including photovoltaic (PV) cell industry is at the centre of attention (ref. 1). There are a lot of technologies for DLC film obtaining (ref. 2), but in most cases the film growth is realized by complicated technological systems with the usage of ultrahigh and radio frequencies at high process temperature, so it is aimless to use these systems in PV cell production. In view of this fact, the development of inexpensive, uncomplicated and low-temperature technologies of DLC film deposition is of great importance. Such technology, based on the DC plasma-enhanced chemical vapour deposition method, using radial ion source and gas mixture of cyclohexane (C_6H_{12}) or toluene (C_7H_8) for Si and Al_2O_5 surface encapsulation, has been developed (ref. 3).

EXPERIMENTALS

As a result of carried out experimental work, the influence of some process variables on structure, mechanical, electrical and optical properties of growing films has been determined. The main factors are concentrations of nitrogen (N_2) and hydrocarbon vapours in the gas mixture of argon, and the average magnitude of kinetic energy (E_k) of ions forming plasma, as with increase of E_k of ions the changing of the process of decomposition and ionization in ion system, as well as the changing of processes of absorption and desorption of particles on the surface of substrate takes place. Having determining the available ranges of variation of these parameters, it was possible to optimize the deposition conditions for achieving particular properties of the DLC films. Several characteristics of the deposition process as well as some DLC film parameters on c-Si substrates are presented in Table 1 $(U_{ac}$ – the voltage between anode and cathode of ion source, U_b – the bias voltage, applied on substrate holder and electrodes, I_p - the plasma current density, n- the refractive index of the film, d- the thickness of the film, HV– the microhardness of the film).

Depending on appropriate deposition condition of DLC film, the required magnitudes of E_k of ions in the plasma and I_p on the substrate surface was set. Thus, by controlling these parameters, it is possible to obtain DLC films with appropriate adhesion strength, microhardness, density, internal defects and stress, friction coefficient, and refractive index.

Table 1.	The process	s variables o	f the DI	∠C film d	eposition ar	nd film _l	parameters on c-Si substrates.
----------	-------------	---------------	----------	-----------	--------------	----------------------	--------------------------------

#	№ Si sample	U _{ac} , kV	I _p , mA/cm ²	U _b ,	P, Pascal	С ₇ Н ₈ , %	d, nm	n	HV kg·f/mm ²
1	SK11	2.6	0.25	-350	$6x10^{-3}$	28	250	2.00	2750
2	SK23	2.8	0.30	-400	8x10 ⁻³	24	290	2.10	2700
3	SK28	2.2	0.60	-250	9x10 ⁻³	18	185	2.40	3000
4	SK31	2.4	0.80	-350	3x10 ⁻²	15	200	2.35	3100
5	SK75	1.8	0.40	-50	5x10 ⁻²	8	192	2.60	2850

In order to obtain DLC films on the surfaces of Si, Al₂O₃ and other substrates over a 100 cm² area with a non-uniformity less than 10%, a new system of diaphragm and ion-acceleration electrodes has been developed and installed between the ion source and substrate. The direct-current radial ion source is introduced into the vacuum chamber at a pressure level of 10⁻³ Pa. A voltage U_{ac} in the range of 1÷3 kV is supplied between the anode and cylindrical cathode where plasma is produced and has a shape of truncated cone. By using an electrode-diaphragm with a slit of "concave-lens" configuration, the ions spread out at an angle of over 30° relative to the plasma axis. Gauze with a size of 0.3÷0.5 mm mesh is also installed on the electrode-diaphragm. With the help of bias voltage from the power module, this gauze allows adjusting the average magnitude of kinetic energy of the ions, which is in the range of 20÷50 eV, that reach the substrate surface. As a result, the plasma density distribution reshapes to a

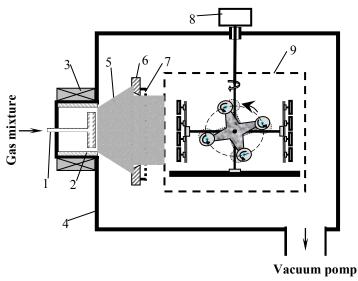


Fig. 1. Schematic view of the equipment for DLC film deposition: 1- anode, 2- cathode, 3- solenoid, 4- vacuum chamber, 5- plasma stream, 6- diaphragm electrode, 7- ion-acceleration electrode, 8- engine, 9-rotaiting system.

cylinder form with a non-uniformity less than 10%. Inside the plasma, the non-uniformity of the average kinetic energy of ions of C^+ , H^+ , N^+ and Ar^+ , does not exceed 10%. The concentration ratios of these ions vary according to the initial vapour concentrations of C_6H_{12} or C_7H_8 , and $Ar-N_2$ mixture supplied to the ion source.

Multifarious optical and electrical properties of DLC films have been achieved by introduction into ion source of various ratios of hydrocarbon vapours and gases forming monoenergetic ions of C⁺, H⁺, O⁺, N⁺, Ar⁺ etc., simultaneously changing space distribution and magnitude of applied electrical and magnetic fields.

In order to reduce the optical and mechanical non-uniformity of the DLC films to less than 5% and to decrease the film deposition temperature, a rotating system of substrate holders was designed with combination of aforementioned electrode-diaphragm (fig. 1). The rotating system is in planetary motion with a combination of additional gyration of the substrate holders, and it provides a neces-

sary trajectory of the substrate motion, i.e., passing of the substrates through all possible zones of the plasma stream. Therefore, better uniformity of deposited DLC film is achieved. It is possible to vary the gyration rates of the substrate holders. This feature is also important for control of the ratio of substrate's stay duration within plasma zone and out of it, providing the necessary cooling of the substrates. This method allows the DLC to be deposited in the range of 30÷80 °C with good temperature stability, reduced internal mechanical stresses, and improved adhesion quality, microhardness and optical properties.

Results of Raman spectroscopic analysis for the DLC films deposited at different growth conditions with thickness varying from 60 nm to 900 nm show that the majority of the carbon in the films is more in sp³ bonding as for diamond than in sp² as for graphite.

RESULTS AND DISCUSSIONS

Some samples of DLC films with thickness of $60 \div 900$ nm were made by the aforementioned technology. Specific surface resistance (ρ_s) of the films has been determined by the four-probe method according to the following expression:

$$\rho_s = 4.53 \cdot \frac{U_{2-3}}{I_{1-4}} \text{ [Ohm/\square]}, \tag{1}$$

where U_{2-3} – voltage between 1 and 2 probes.

And resistance (ρ_v) relates to ρ_s in the following proportion:

$$\rho_{v} = \rho_{s} \cdot d \text{ [Ohm-cm]}, \tag{2}$$

where d – the thickness of the DLC film that has been measured by interference microscope.

It has been defined that specific surface resistance of DLC film depends on its density which is set by appropri-

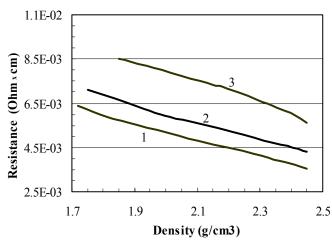


Fig. 2. Dependence of resistance of DLC films upon their density, grown at various deposition conditions: 1- C₇H₈:N₂:Ar=17:28:55, and accordingly, 2-27:18:55, and 3-37:8:55.

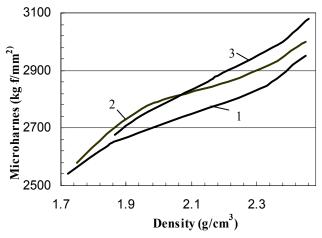


Fig. 3. Dependence of microhardness of DLC films upon their density, grown at various deposition conditions, similar to conditions of growth of samples, presented on fig. 2 (curves 1-3, accordingly).

ate process variables, particularly by concentrations of gases in the working mixture. Fig. 2 shows the dependences of resistance (ρ_v) of DLC films upon their density (ρ). The films have been grown at various concentrations of N₂ in gas mixture and at constant concentration of Ar: curve 1 - C₇H₈:N₂:Ar=17:28:55, and accordingly, curve 2 - 27:18:55, and curve 3 - 37:8:55. It could be inferred from curves that the increase of N₂ concentration in gas mixture leads to decrease of the value of resistance of growing film in the range of (8.5÷3.5)x10⁻³ Ohm·cm.

Microhardness of the DLC films has been measured for investigation of their mechanical characteristics. Vickers' technique does not allow to measure microhardness of such thin films, as at pressing of tip in the form of pyramid the penetration depth (h) is more than the thickness (d) of the film (h>>d). Therefore, the modified Vickers' technique has been used. The main point of modification is the following: the tip in the form of pyramid made of diamond has been replaced with a tip in the form of a globe made of hard alloy and with radius (r). At fixed applied force (P) the globe was rotated with a steady angular rate (ω) on the surface of DLC film. Determining the period (t) of multifold passing of the globe, when total wearing of the film takes place and the globe reaches the surface of substrate (h=d), it is possible to calculate the penetration depth of globe for per revolution. Whereupon, the average diameter of track (D), left by trip, for per revolution has been determined. By means of the following expression the microhardness of DLC film has been estimated:

$$HV = K \frac{\mu \cdot P \cdot \omega \cdot t}{8r \cdot d} \text{ [kg·f/mm}^2\text{]}, (3)$$

where μ - friction coefficient, P – applied force (kg·f), ω - angular rate of globe rotation (revo), t – period of globe rotation (min), r – radius of globe (mm), K – definite constant coefficient.

Fig. 3 (curves 1-3) illustrates the dependences of microhardness of DLC film samples upon their density. The samples have been made at the same deposition conditions that correspond to conditions of growth of samples for which the curves 1-3 (fig. 2) are presented. The measurement results have shown that the increase of N₂ concentra-

Fig. 4. Reflectance spectra of DLC film on various zones of the c-Si substrate surface; film has been grown in the equal width regions of plasma, given in the picture attached above.

tion in gas mixture leads to decrease of the absolute value of film microhardness.

The measurements of optical reflectance spectra (R) were held both for the DLC samples grown on the surface of c-Si, and on the surfaces of Al₂O₃ and sintered quartz. The measurement results of the samples c-Si with DLC film have shown that the curves have identical shape and almost the same value of R on all the zones of the surface with area over 100 cm² (fig. 4). There were also carried out the measurements of the film density (p) with the help of weighing method on the same zones of the substrate surface, which had identical values within the limit of accuracy of measurement. Depending on the magnitude of negative bias voltage, the film density varied from 1.7 to 2.5 g/cm². Comparing the results of numerous experiments, it can be concluded that the DLC films grown by aforementioned technology on the surface of c-Si, Al₂O₃ and sintered quartz have a non-uniformity of parameters less than 5%.

The possibility to vary the magnitudes of re-

fractive index and width of band gap depending on deposition conditions allows growing both one- (fig. 5) and bilayer (fig. 6) enlightening and protecting structures in one technological process for substrate encapsulation.

Fig. 5 illustrates the reflectance spectra of polished c-Si without coating (curve 1), and of two samples of c-Si with one-layer DLC film (curve 2, sample SK11 and curve 3, sample SK28, see Table 1). And fig. 6 shows the reflectance spectra of two DLC samples of bi-later film, grown in one technological process with changing of deposition conditions in order to chose the proper values of refractive index (curve 1: n_1 =2.0, n_2 = 2.4, curve 2: n_1 =1.8, n_2 =2.35). As it can be inferred from fig. 6, bi-layer DLC coating with the proper values of refractive index provides the coefficient of reflection less than 5% in the photosensitive range of Si.

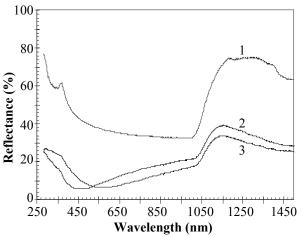


Fig. 5. Reflectance spectra of: 1 - c-Si without any film, 2 - DLC film on c-Si (SK11) and 3 - DLC film on c-Si (SK28).

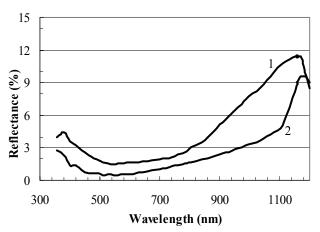


Fig. 6. Reflectance spectra of bi-layer DLC films on c-Si substrate with various values of refractive index: $1 - n_1 = 2.0$, $n_2 = 2.4$ and $2 - n_1 = 1.8$, $n_2 = 2.35$).

Fig. 7 shows the transmittance spectra (T) of DLC films grown at various deposition conditions on the surface of Al_2O_3 . Depending on technological parameters there was a significant alteration of film coefficient T in the range of $\lambda = 200 \div 600$ nm, and in the range of $\lambda = 600 \div 1100$ nm was not any alteration of T. The increase of atomic-weight

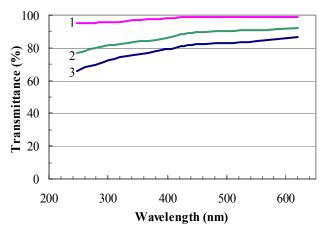


Fig. 7. Transmittance spectra of the DLC films on Al₂O₃ substrates, grown at various deposition conditions: 1- n=2.4, d=185nm; 2- n=2.57, d=185nm; 3- n=1.48, d=240nm.

ratio of hydrocarbon vapours in gas mixture leads to increase of coefficient T (curve 1 for sample SK11, curve 2 for sample SK28, and curve 3 for sample SK75).

The obtained DLC films on the substrate of c-Si and Al₂O₃ have shown high stability to external influences. These samples grown at various deposition conditions kept their properties up to 400 °C thermal exposures. They were also subjected to moisture, to chemically hostile environment and to ultraviolet radiation impacts, and any changes of the film parameters were been observed. The tests were conducted by the following methodology:

- 1. Moisture impact the sample were kept in chamber at relative humidity of 90% and at temperature of 25 °C within 20 hours;
- Chemically hostile environment impact at 25 °C the sample were kept: (1) in the concentrated acids of H₂SO₄ and HNO₃ within 30 min, (2) in the 1% solutions of the same acids within

1 hour, and (3) in the fat solution of NaCl (sea-fog simulation) within 40 min.

Because of the abovementioned properties and such high stability of DLC films on the surface of Si, they have been applied in production of PV cells of new generation (ref. 4). The obtained PV cells have also been subjected to the listed impacts by the same methodology. The efficiency, as well as the mechanical and optical properties of encapsulated PV cells have been measured before and after of each test. The visual inspection by microscope of substrate surface has also been conducted. The test results presented in Table 2 prove the high stability of protective properties of DLC films.

These test samples have also been subjected to ultraviolet radiation within ~400 hours. Comparison of the measurement results of PV cell efficiency after such long-term exposure has shown that the film stability to some extent depends on gas mixture composition during deposition process. At high nitrogen concentration the films have less stability to ultraviolet.

Table 2	2. The te	st results on stability of the DLC films to various environmental impacts.
		TAM A ARTY 11 (SA RES) A/

	N ₂ , %	Efficiency of PV cell (Si+DLC), %					
№			After impacts				
PV cell		Before impacts	Moisture	Chemically hostile environment	~400 hours ultraviolet		
30	35	9.87	9.85	9.78	8.31		
45	33	8.82	8.90	8.80	7.57		
43	25	9.27	9.23	9.28	8.44		
41	23	9.71	9.75	9.58	8.62		
44	15	9.11	9.18	9.14	8.77		
42	13	8.90	8.93	8.78	8.52		

CONCLUSIONS

Thus, the DLC films grown by the developed technology have required optical, electrical and mechanical properties with non-uniformity less than 5%. Optically, the DLC film with a thickness of 180 nm has a coefficient of transmittance T \geq 95%, coefficient of reflection R<5% in the range of λ =300÷1100 nm. The value of refractive index varies n=1.6÷2.7 and, accordingly, a energy of band gap E_g of 3.5÷4 eV, depending on deposition conditions. This feature will allow good sunlight transmission of λ >350 nm without any considerable absorption by the coating itself. The microhardness of DLC films has been increased up to 2700÷3100 kg·f/mm². These film mechanical characteris-

tics shall provide a relatively high mechanical stability to the substrate surface. The DLC films are also stable to various environmental impacts and can be applied successfully in optics, microelectronics, as well as in PV cell production as an encapsulation coating.

REFERENCES

- Zh. Panosyan, S. Voskanyan, Y. Yengibaryan, and A. Stepanyan. "Obtaining and Investigation of the Thin-Film Encapsulating Diamond-Like Carbon Films for Photovoltaic Converters". Proceedings of 15th International Symposium "Thin Films in Optics and Electronics", Kharkov, Ukraine, April 21-26, 2003, to be published.
- Proceedings of the Sixth Applied Diamond Conference/Second Frontier Carbon (ADC/FCT2001), Technology Joint Conference, Y. Tzeng, K. Miyoshi, M. Murakawa, Y. Koga, K. Kobashi, and G.A.J. Amaratuga, editors Auburn, Alabama, USA, 2001, p. 837.
- 3. K. Kassabian, Zh. Panosyan, A. Stepanyan, G. Torosyan, Y. Yengibaryan. Low-Temperature Technology of Obtaining the Protecting Layer from Diamond-Like Film, Proceedings of the Sixth ADC/SFC Technology Joint Conference, Auburn, Alabama, USA, 2001, p. 431-435.
- 4. Zh. Panosyan, Y. Yengibaryan, A. Stepanyan, and S. Voskanyan. Design and Manufacturing of Photovoltaic Module for Production of the Ecologically Pure and Safe Electric Power. Vestnik of International Academy of Science of Ecology and Safe Human Activity, v.7, №6 (54), Saint-Petersburg, 2002, p.47-50.

PREPARATION AND PROPERTIES OF DIAMOND-LIKE CARBON FILMS FROM CH₄, C₂H₄, AND C₂H₂ WITH PLASMA SOURCE ION IMPLANTATION

K. Baba and R. Hatada, Materials Science Section, Industrial Technology Center of Nagasaki 2-1303-8, Ikeda, Omura, Nagasaki 856-0026, Japan

S. Miyagawa, National Institute of Advanced Industrial Science and Technology (AIST) 2266-98 Anagahora, Moriyama-ku, Nagoya 463-8560, Japan

ABSTRACT

Diamond-like carbon (DLC) films were prepared on silicon wafer substrates by plasma source ion implantation (PSII) with superposed negative pulse. Methane, ethylene and acetylene gases were used as working gases for plasma. A negative DC voltage and a negative pulse voltage were superposed and applied to the substrate holder. The DC voltage was changed in the range from 0 to -4 kV and the pulse voltage was changed from 0 to -18 kV. The surface of DLC films was very smooth. The deposition rate of DLC films increased with increasing in superposed DC bias voltage. I_D/I_G ratios of Raman spectroscopy were around 1.5 independent on pulse voltage. The hydrogen concentration estimated by an elastic recoil detection (ERD) analysis was in the range from 20 at% to 28 at% depending on the source gas and the deposition condition. The hardness of around 10-20 GPa was derived for the film prepared with high DC and high pulse voltage. The friction coefficient estimated by a ball-on-disc test was around 0.1 for almost films. The residual stress was smaller than 1GPa (compressive) for all films and there was no clear dependence on working gas.

Keywords: DLC, PSII, ERD, hardness, tribology

INTRODUCTION

Diamond-like carbon (DLC) coatings exhibit a number of attractive mechanical and tribological properties such as low friction, high wear resistance, and high hardness. Much of work has been carried out on DLC films by a variety of methods, including physical vapor deposition (PVD) (refs. 1, 2) and chemical vapor deposition (CVD) (refs. 3, 4). Plasma source ion implantation (PSII) and related methods have possibility to give high adhesion and good surface coverage for DLC films.

In this paper, we report the results of DLC films deposition by a PSII without additional plasma sources. High negative pulse voltage superposed on negative DC voltage was applied to the substrate to generate plasma (ref. 5). This method has some advantages such as, simple construction, easy to scale-up and good coverage. DLC films were prepared by using this method from CH_4 , C_2H_4 and C_2H_2 plasma. All samples are subsequently characterized by scanning electron microscopy (SEM) and Raman spectroscopy. Hardness and wear properties were estimated by an indentation method and ball-on disc tests.

EXPERIMENTAL

The plasma source ion implantation apparatus used in this study is described in detail elsewhere (ref. 5). Methane (CH₄), ethylene (C_2H_4) and acetylene (C_2H_2) gases were used as source gases for DLC films. In this study plasma was generated by the application of superposed bias voltage of DC and pulse to substrate without additional plasma source. Silicon wafer (100) was used as a substrate. CH₄, C_2H_4 and C_2H_2 gases were introduced into the vacuum chamber. The DC bias voltage was in the range of 0 to -4 kV, the pulse voltage was changed from 0 to - 18 kV with the pulse frequency of 100 Hz and the pulse width of 100 μ s. The vacuum pressure during deposition was 2.5 Pa for all source gases. The thickness of the coatings measured by cross-sectional scanning electron microscope (SEM) was about 400 nm for all films. The surface morphology of the films was observed by SEM and atomic force microscope (AFM). The film structure was characterized by Raman spectroscopy. The hydrogen concentration was estimated by an elastic recoil detection (ERD) analysis with He⁺ at 2.8 MeV. The internal residual stress of the DLC films deposited on silicon wafers was estimated quantitatively by the bending beam method from the Stoney equation.

The hardness of DLC films was evaluated by an indentation method with the maximum load of $200 \mu N$. Furthermore, a ball-on-disc test was employed to obtain information about the friction coefficient and wear resistance of the films in dry air. 6 mm in diameter tungsten carbide ball was used as the ball. The sliding speed was 100 mm/sec and the normal load was 2N.

RESULTS AND DISCUSSION

The surface of the films was very smooth and the average roughness Ra estimated by AFM was smaller than 0.44 nm.

The effect of the source gases and the substrate superposed DC bias voltage on the deposition rate is shown in Fig. 1. The films were prepared with a superposition of a peak pulse bias voltage of -18 kV and different DC bias voltage. It is clearly seen that the deposition rate increase significantly with increasing DC bias voltage for all source gases. And the deposition rate of the films grown in C_2H_2 plasma was higher than other source gases. In this study, plasma was generated by the application of pulse and DC voltage to the substrate directly, and then higher plasma density was obtained by the application of higher DC voltage with the constant pulse voltage. As the result, higher deposition rate is obtained at higher DC voltage.

Fig. 2 shows the hydrogen content in the DLC films estimated by an ERD analysis. The hydrogen content was in the range from 20 to 28 at%, and there is no clear dependence on the DC voltage and the source gas species.

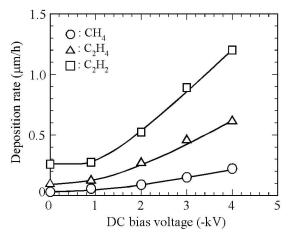


Figure 1. Deposition rate of the DLC films prepared at various DC bias voltage. Total bias voltage is -18kV.

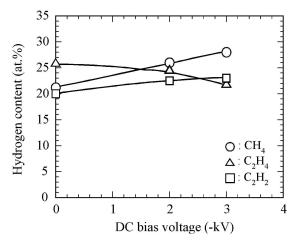


Figure 2. Hydrogen content changes of the DLC films prepared at various DC bias voltage. Total bias voltage is -18kV.

Fig. 3 shows the Raman spectra of the DLC films prepared from CH_4 , C_2H_4 and C_2H_2 plasmas at -16 kV pulse and -2 kV DC bias voltage. The spectral profile is fitted by two Gaussian profiles centered at around 1400 cm⁻¹ corresponding to the D-line and centered at around 1560 cm⁻¹ corresponding to the G-line (refs. 6, 7). The integrated intensity ratio I_D/I_G is correlated to the sp^3/sp^2 bonding ratio and the graphite particle size (ref. 7). The I_D/I_G ratios were in the range from 1.21 to 1.38 for the films except for the films deposited at -4 kV DC from C_2H_2 plasma. These values are common values for DLC films (ref. 8). For the film deposited at -4 kV from C_2H_2 plasma, I_D/I_G value was 1.63.

Load-displacement curve measurements by an indentation method were used to estimate the hardness of the films. The hardness of the films prepared from CH_4 and C_2H_4 plasma were in the range from 9 to 13 GPa. On the other hand, the hardness of the films prepared from C_2H_2 plasma increased with DC voltage, and the hardness of 20 GPa was derived at -4 kV DC.

Fig. 4 shows the stress of the films as a function of DC voltage. Small compressive values around 0.5 GPa, compared with other deposition methods, were derived for all films. There is no clear dependence on DC voltage and source gas species.

Tribological property of DLC films is one of the important properties of DLC films. Fig. 5 shows the friction coefficient of DLC films prepared from C_2H_4 estimated by a ball-on-disc test as a function of rotation cycles. Low friction coefficient around 0.1 was derived for all deposition conditions, and the lowest value was derived for the film prepared with DC voltage of -2kV. For the films prepared from CH_4 and C_2H_2 showed similar friction coefficient as C_2H_4 . After 10000 rotations the friction coefficient became 0.13 - 0.15.

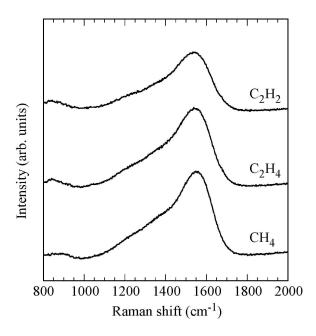


Figure 3. Raman spectra of DLC films prepared from CH_4 , C_2H_4 and C_2H_2 plasma at -16kV pulse and -2kV DC.

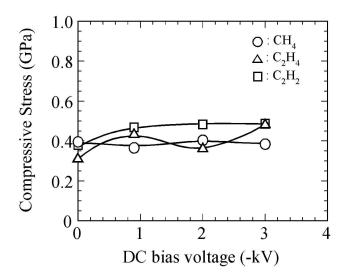


Figure 4. Compresive stress of the DLC films prepared at various DC bias voltage. Total bias voltage was -18kV.

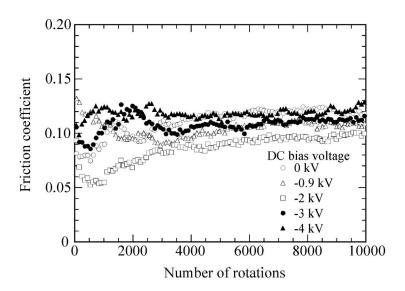


Figure 5. Friction coefficient changes as a function of the number of rotations in the ball-on-disc tests for the DLC films prepared from C_2H_4 . Total bias voltage was -18kV.

CONCLUSIONS

The DLC films were prepared from CH_4 , C_2H_4 and C_2H_2 plasma by PSII with superposed bias voltage. The surface morphology and film thickness were observed by SEM and AFM. The structure was evaluated by ERD and Raman analysis. The internal residual stress of the DLC films deposited on silicon wafers was estimated quantitatively by the bending beam method. The mechanical properties were estimated by an indentation method and a ball on disc tests. The most important results can be summarized as follows:

- (1) DLC film can be derived by the application of superposed bias voltage to substrate without additional plasma source.
- (2) The deposition rate for C₂H₂ plasma was higher than other source gases at the same deposition condition.
- (3) Application of superposed DC bias voltage for the pulse voltage is effective to increase the deposition rate of DLC films.
- (4) The hydrogen contents in the films were in the range of 20-28 at%.
- (5) Intensity ratio I_D/I_G of Gaussian profiles of Raman spectra was around 1.5, and there was no clear dependence on DC voltage.
- (6) Hardness of the DLC films was 10 20 GPa, and there was no dependence on DC bias voltage.
- (7) Friction coefficient were 0.10 0.15 after 10,000 rotations.

ACKNOWLEDGEMENTS

The authors would like to acknowledge Dr. S. Nakao and Dr. Y. Miyagawa, National Institute of Advanced Industrial Science and Technology for ERD analysis.

REFERENCES

- 1. N-H. Cho, et al.: Chemical structure and physical properties of diamond-like amorphous carbon films prepared by magnetron sputtering. J. Mater. Res., **5** (1990) 2543.
- 2. B. F. Coll and M. Chhowalla: Amorphous diamond film by enhanced arc deposition. Surf. Coat. Technol., **79** (1996) 76.
- 3. A. A. Benmassaoud and R. W. Paynter: Influence of the power and pressure on the growth rate and refractive index of a-C:H thin films deposited by r.f. plasma-enhanced chemical vapour deposition. Thin Solid Films, 287 (1996) 125.
- 4. B. Druz et al.: Ion beam deposition of diamond-like carbon from an r.f. inductively coupled CH₄-plasma. Surf. Coat. Technol., **86-87** (1996) 708.
- 5. K. Baba and R. Hatada: Deposition of diamond-like carbon films by plasma source ion implantation with superposed pulse. Nucl. Inst. Meth. Phys. Res. B, in press
- 6. R. O. Dillon, J. A. Woollam, V. Katkanant: Use of Raman scattering to investigate disorder and crystallite formation in as-deposited and annealed carbon films. Phys., Rev. **B29** (1984) 3482.
- 7. M. Ramsteiner and J. Wagner: Resonant Raman scattering of hydrogenated amorphous carbon: Evidence for bonded carbon clusters. Appl. Phys. Lett., **51** (1987) 1355.
- 8. H. Tsai and D. B. Bogy: Characterization of diamondlike carbon films and their application as overcoats on thin-film media for magnetic recording. J. Vac. Sci. Technol. **A5** (1987) 3287.
- 9. M. A. Tamor and W. C. Vassell: Raman "fingerprinting" of amorphous carbon films. J. Appl. Phys., **76** (1994) 3823.

IDENTIFICATION OF CHEMICAL BONDS ON UPPER LAYERS OF DLC USING AUGER SPECTROSCOPY AND XPS

A. P. Dementjev, K. I. Maslakov

RRC "Kurchatov Institute", 1, Kurchatov sq., Moscow 123182, Russia, e-mail: A.Dem@ru.net

Kensuke Uemura

ITAC Ltd. Company, 2-24-7, Kita-Otsuka, Toshima-ku, Tokyo 170-0004, Japan

I.Sh.Trakhtenberg, A.P.Rubshtein, S.A.Plotnikov, A.B.Vladimirov, V.A.Yugov Metal Physics Institute Ural Branch RAS, 18, S. Kovalevskaya St., 620219 Ekaterinburg, Russia.

ABSTRACT

Hydrogen free DLC were deposited by solid carbon arc sputtering system. The DLC samples have been examined by N(E)CKVV Auger spectroscopy and Electron energy loss spectra of C1s XPS (EEL of C1s). According to the CKVV data, concentration of the sp³ bonds averages 60% - 70%. The EEL of C1s XPS spectra have not π -plasmon feature that is the inherent peculiarity of C=C bonds. Obviously, these data are showing the evidence of absence of the sp²-bonds in traditional understanding. The DLC samples were heated *in-situ* up to 800K or Ar ion etched. The CKVV showed the transformation of sp³ bonds from 70% to 0% but EEL of C1s XPS did not show the π -plasmon formation. The results are showing the evidence of DLC decomposition only on upper layers.

Keywords: DLC, sp²- sp³-bonds, ion etching.

INTRODUCTION

The diamond like carbon films are important and interesting materials for industrial applications. It is thought the DLC films consist of a mixture sp^2 - and sp^3 - bonds and that the chemical bonding determine their mechanical properties (ref.1). The Electron energy loss spectroscopy with E_p =100-200 keV (EELS) and X-ray absorption near edge spectroscopy (XANES) are main techniques for identification of the chemical bonds in DLC. The near edge structures at $1s \to \pi^*$ and $1s \to \sigma^*$ transitions of sp^2 - and the $1s \to \sigma^*$ transition of sp^3 bonds differ significantly and are easy to identify on base standard samples, where π^* and σ^* are empty states. Detailed description of XANES and EELS results have been done in (ref. 1). According the techniques the sp^3 - bonds is averaged about 60 –70 %. The depth information (DI) of the techniques is equal about tenth nm.

In order to study the occupied chemical bonds on uppermost layers we used N(E)CKVV Auger spectroscopy, (sp^2-, sp^3-bond) sensitivity, DI is equal to about 2 monolayers) and electron energy loss spectra of C1s XPS (EEL of C1s). The loss spectra have inherent structures (ref. 2) at 7 eV for sp^2 - bonds with DI about 7 monolayers. The analysis of the Database spectra of polymers (ref. 3) shows that this feature of C1s is inherent to all polymers with C=C bonds.

EXPERIMENTAL

Hydrogen free DLC were deposited by 1 Hz arc-pulse sputtering of graphite on tool steel at 10^{-3} Pa. The substrate temperature during deposition did not exceed 120° C (ref. 4). The DLC microhardness was measured using three different devices and methods was 70-80 GPa (the load was changed from 2N to 20 mN). The thickness of DLC was 1.5 μ m. After DLC deposition the two samples (N5, N6) were subjected to the ion bombardment (reactive inert argon or oxygen). The conditions of ion etching were as follows: $P = 4x10^{-2}$ Pa, E = 3.0 keV. The DLC film was etched to 100 nm depth.

XPS and X-ray excited Auger electron spectroscopy (XAES) data were obtained by a MK II VG Scientific spectrometer. The experimental conditions were the same as previously described in detail (ref. 5). The sample heating and Ar etching were carried out *in-situ*. The temperature variation was realized by the change of distance between a sample and the tungsten filament. The Ar beam parameters were 1 keV and 5 μA. The four (N1-N4)

samples were investigated after the *in-situ* heating and ion etching and the other three samples – after the *ex-situ* ion treatment.

RESULTS

It was shown (ref. 4) that the CKVV spectra have inherent features to sp^3 -, sp^2 - bonds and as well as to the mixture of sp^2/sp^3 -bonds. The different of experimental CKVV spectra from that of the standards suggests the presence of atoms with different bonds. To determine sp^2/sp^3 ratio, a synthesis of the original spectra with the sp^3 and sp^2 standards must be done. Fig. 1 shows the synthesis of CKVV Auger spectra of the sample N1. The polyethylene is standard of sp^3 -bonds and fullerene is standard of nanocarbon with sp^2 —bonds. Results of the synthesis for all samples are given in Table 1.

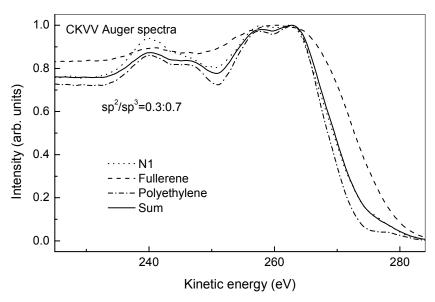


Figure 1. Synthesis of the CKVV Auger spectra by that of fullerine and polyethylene.

Table 1. The results of the analysis of DLC by CKVV Auger spectra and EEL of C1s XPS

	Type of treatment	Chemical state			
		CKVV Auger data	EEL of C1s XPS data		
1- 4	Ex-situ deposited DLC	$sp^3 \sim 70 \%$	$sp^2 \approx 0$		
3	<i>in-situ</i> annealing	sp ² nanocarbon-like	$sp^2 \approx 0$		
	(T = 800 K, t = 2 min)				
4	in-situ Ar etching	sp ² graphite-like	$sp^2 \approx 0$		
	(E = 1 kev, t = 4 min)		_		
5	ex-situ Ar ion etching	$sp^{3} \sim 60 \%$	$sp^2 \approx 0$		
	(E = 3 kev, t = 60 min)				
6	ex-situ O ion etching	$sp^{3} \sim 60 \%$	$sp^2 \approx 0$		
	(E = 3 kev, t = 45 min)		_		
HOPG	in-situ Ar etching	$sp^2 = 100\%$	$sp^2 \approx 0$		
	(E = 1 kev, t = 2 min)		_		

HOPG was used for study a modification of sp²-bonds under Ar ion etching.

Thus the Auger analysis showed the presence of 70% of sp³ on the DLC surface. The specimen heating leads to nanocarbon formation with sp² bonds and the ion etching – to graphite (Fig. 2).

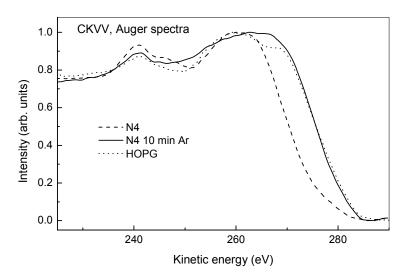


Figure 2. Modification of the CKVV Auger on upper layers of DLC after in-situ Ar etching.

Fig. 3 shows comparison of C1s XPS spectra of DLC before and after in –situ Ar etching with that of HOPG and PcI - poly(cis-isoprene). The EEL of C1s feature of DLC have not π -plasmon. There is only a magnification of intensity spectra over the range 2 - 10 eV. But the CKVV spectra showed the C = C –bonds formation. The right part of CKVV spectra (Fig. 2) coincidences with that of HOPG. This implies the decomposition of DLC on upper layers and the formation of graphite.

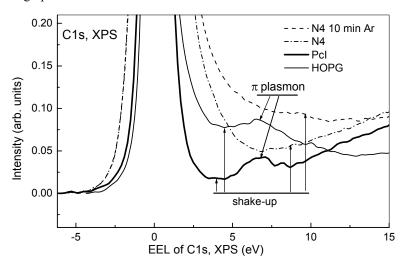


Figure 3. Comparison EEL of C1s XPS spectra before and after Ar etching with that of HOPG and PcI -poly(cis-isoprene) -(-CH2 - CH = C - CH2 -)nCH3

One should suppose that the right part of C1s XPS spectra (Fig. 3) over the range 1-10 eV are the sum of the next processes: I – inelastic extrinsic scattering (ref. 6); II – HOMO \rightarrow LUMO shake-up transition (ref. 7); III - π -plasmon (ref. 2,7). Obviously, only the I and II processes are plausible reason of the intensity spectra of DLC over the range 2 - 10 eV.

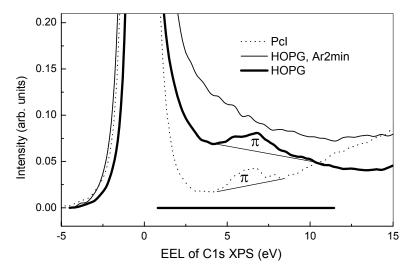


Figure 4. EEL of C1s XPS spectra of HOPG before and after in-situ Ar etching.

The modification of chemical bonds after Ar etching of HOPG has been studied (Fig. 4). The disappearance of the π -plasmon after the ion etching is an unexpected phenomenon because some amount of C=C bonds should be formed after graphite decay in a certain region of ion influence. On the other hand, the CKVV spectra are not changed which show the evidence of the C=C bonds on the top two monolayers. It is possible that the primary Ar ion could give its energy to carbon atoms and the resulting in change of condition corresponds to that of the DLC deposition, but only under top layers. High sensitivity of the C1s XPS to the π -plasmon is illustrated on poly(cisisoprene) spectrum. There is only 20% of C=C bonds in poly(cis-isoprene) but the π -plasmon has a significant intensity.

Fig. 5 and Fig. 6 show EEL of C1s and CKVV Auger spectra of DLC samples after *ex-situ* Ar-, O- ion etching. The last conditions of etching differ from that of *in-situ* etching by current strength. The spectra is showing evidence of π - plasmon absent as results of the etching.

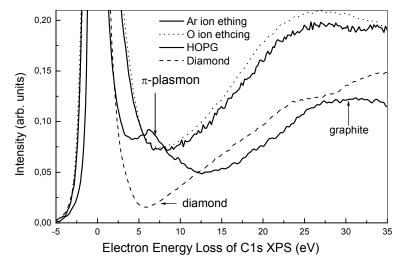


Figure 5. EEL of C1s spectra of DLC after ex-situ Ar-, O- ion etching.

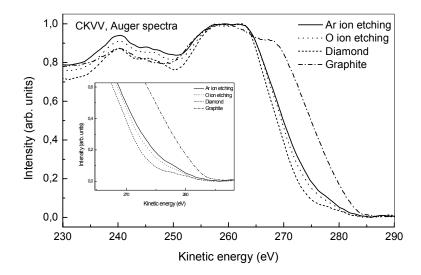


Figure 6. CKVV Auger spectra of DLC after ex-situ Ar-, O- ion etching.

DISCUSSION

Our results are on the contrary to the XANES and EELS data (ref. 1) on C=C bonds in DLC. The difference in the mechanism of EEL of C1s spectrum formation from that of XANES and EELS should be noted. The π -plasmon is the main identifier of C=C bonds. It forms at the excitation of π -electrons and therefore is directly connected with the presence of C=C bonds (ref. 2,7). The Database (ref. 3) represents numerous experimental data that prove the π -plasmon to be the inherent feature of the C = C bonds whereas XANES and EELS are formed by the excitation of C1s-electron to π or σ empty state. At present we can not explain the reason of this discrepancy. Obviously a combined XANES and XPS investigations could reveal this reason. Diaz et al. (ref. 8) carried out the combined investigation of DLC but unfortunately they analyzed only the main C1s XPS line with no EEL of C1s XPS.

CONCLUSIONS

- 1. CKVV Auger data (DI \approx 2 monolayers):
 - sp³ bonds average to 60-70% on the surfaces of *ex-situ* prepared DLC;
 - the *in-situ* DLC ion etching and heating lead to 100% of sp² graphite-like state and sp² nanocarbon-like state respectively only in top-most layers.
 - the *in-situ* Ar etching of HOPG leads to the formation of amorphous graphite.
- 2. EEL of C1s XPS data (DI \approx 7 monolayers):
 - the spectra of *ex-situ* prepared DLC have not the π -plasmon that is inherent to C=C bonds;
 - the *in-situ* Ar ion etching and heating do not lead to the formation of C=C bonds;
 - the ex-situ ion etching by Ar or O do not change significantly the chemical state of carbon atoms;
 - the *in-situ* Ar etching of HOPG leads to the disappearance of the π -plasmon.
- 3. The obtained data on the absence of C=C bonds in DLC conflict with the XANES and EELS data.
- 4. Obviously, our data are showing the evidence of absence of the sp²-bonds in traditional understanding.

REFERENCES

- 1. Y. Lifshitz, Diamond Relat. Mater. 8 (1999) 1659.
- 2. McFeely F.R., Kowalczyk S.P., Lev L. et. al.: Phys. Rev., B9 (1974) 5268.
- 3. G. Beamson and D. Briggs High Resolution XPS of Organic Polymers. The Scienta ESCA300 Database, John Wiley and Sons Ltd. West Sussex PO19 1UD, England 1992.
- 4. I.Sh.Trakhtenberg, S.A.Plotnikov, et al, Diamond and Related Materials 5 (1996) 943.
- 5. A. Dementjev, New Diamond and Frontier Carbon Technology, 11(2001) 35
- 6. S. Tougaard Phys. Rev. B34 (1986) 6779.
- 7. S. Krummacher et al Phys. Rev. B48 (1993) 8424.
- 8. J. Diaz, S. Anders et al, J. Electr. Spectr. Relat. Phenom. 101-103 (1999) 545.

DIAMOND-LIKE CARBON FILMS DEPOSITED BY PLASMA-BASED ION IMPLANTATION METHOD

Masatou Ishihara, Takako Nakamura, Akihiro Tanaka and Yoshinori Koga

Research Center for Advanced Carbon Materials, National Institute of Advanced Industrial Science and Technology, AIST Central 5, 1-1-1 Higashi, Tsukuba, Ibaraki 305-8565, Japan

Masahiro Suzuki, Toshiya Watanabe and Osamu Tsuda,

Joint Research Consortium of Frontier Carbon Technology, JFCC, c/o AIST Central 5, 1-1-1 Higashi, Tsukuba, Ibaraki 305-8565, Japan

ABSTRACT

Diamond-like carbon (DLC) films were deposited on Si substrates and high-carbon chromium bearing steel (SUJ2) substrates by a plasma-based ion implantation method using an electron cyclotron resonance (ECR) plasma source with a mirror field and a power supply to apply negative high-voltage pulses and a negative DC bias to the substrate. CH₄ gas was used as a carbon source. The plasma was produced from CH₄ gas with an ECR power supplier. Before the deposition process of DLC films, carbon ions were implanted into the substrate surface by applying the high-voltage pulses of -10 kV for the formation of a carbon mixing layer. The DLC films with a smooth surface and a low friction coefficient could be formed by applying the negative high-voltage pulses of -2 kV to a substrate with a low duty ratio of 1%. The wear resistance of the DLC films was improved by the formation of the carbon mixing layer. The effect of the mixing layer formed at the interface between the DLC films and the substrate will be discussed in this presentation.

Keywords: DLC, Plasma-based ion implantation; ECR plasma with a mirror field, Mixing layer, Tribological property

Corresponding author

Masatou Ishihara Research Center for Advanced Carbon Materials National Institute of Advanced Industrial Science and Technology AIST Central 5, 1-1-1 Higashi, Tsukuba, Ibaraki 305-8565, Japan e-mail: m.ishihara@aist.go.jp

Tel: (+81) 29-861-4699 Fax: (+81) 29-861-4474

Synthesis of Carbon Materials Using Abnormal DC Glow Discharge Plasma CVD

Hiromichi Yoshikawa

FCT Research Laboratory, Japan Fine Ceramics Center 1-1-1 Higashi, Tsukuba, Ibaraki, Japan yoshi@os.rim.or.jp / h-yoshikawa@aist.go.jp

Yoshinori Koga

National Institute of Advanced Industrial Science and Technology, 1-1-1 Higashi, Tsukuba, Ibaraki, Japan

ABSTRACT

Diamond is a valuable material for the industry because of useful properties including extreme hardness, wide-band optical transparency, and high thermal conductivity. Especially thick and large-scale diamond films can be used in various industrial applications. However, its practical use has been limited due its relatively high cost and scarcity. Microwave plasma CVD using 915MHz is one of the most commonly used methods for synthesizing diamond films. Recently, the plasma transition state from glow discharge to arc discharge has been used for the synthesis of diamond. This system has a greater potential for upward scalability because of its multiple cathode structure [1]. The abnormal glow discharge plasma has the additional advantage of requiring only a very simple plasma generation system using direct current supply units, which results in a lower equipment cost. In the present study, we report the relationship between the obtained carbon materials and the results of optical emission spectroscopy (OES), including images of the first atomic hydrogen Balmer line and the C2(0,0) Swan band.

This work has been supported by the New Energy and Industrial Technology Development Organization (NEDO).

[1] J. Lee, K. Eun, Y. Baik, H. Cheon, J. Rhyu, T. Shin, J. Park, Diamond Relat. Mater. 11 (2002) 463

DEPOSITION OF BC/TA-C MULTILAYER THIN FILMS BY LASER ABLATION

Manabu Taniwaki* and Masahiro Suzuki

FCT Project/JFCC, c/o AIST, Tsukuba Central 5, 1-1-1 Higashi, Tsukuba, Ibaraki 305-8565, Japan

Masatou Ishihara and Yoshinori Koga

Research Center for Advanced Carbon Materials, AIST, 1-1-1 Higashi, Tsukuba, Ibaraki 305-8565, Japan

Fumio Kokai

Department of Chemistry for Materials, Faculty of Engineering, Mie University, 1515 Kamihama-cho, Tsu, Mie 514-8507, Japan

ABSTRACT

We deposited amorphous multilayer thin films of boron carbide (BC) and tetrahedral amorphous carbon (ta-C) by pulsed laser deposition (PLD) using B_4C and graphite targets at room temperature. The laser beam (266 nm, 4-5 ns pulse width) from a Q-switchd Nd:YAG laser was used to irradiate the targets at a constant laser fluence of 4 J/cm². The multilayer films consisted of bilayer structures with a bilayer period λ in the nanometric range (1-128 nm). The hardness of BC/ta-C multilayer thin films measured by a nanoindentation technique were between 38 and 48 GPa, dependent on the thickness of the layer ($\tau = \lambda/2$). The highest hardness value was obtained for $\tau = 8$ nm. The coefficient of friction was in the range 0.1-0.27, which is lower than that of BC single-layer films (>1.0). We also deposited amorphous multilayer thin films of boron nitride (BN) and ta-C to compare with BC/ta-C multilayer thin films.

Keywords: Boron carbide, Amorphous carbon, Multilayer, Pulsed laser deposition, Hardness

*Corresponding author:

E-mail: m.taniwaki@aist.go.jp, Fax: +81-29-861-4796, and Tel: +81-29-861-9982

SEMICONDUCTING TETRAHEDRAL CARBONS TRANSFORMED TO SEMIMETAL NANOCOMPOSITE MATERIALS BY ION IMPLANTATION

O. Kutsay, I. Bello*, Y. Lifshitz, W.Y. Luk, C.W. Lam, S.T. Lee, X.M. Meng

Center of Super-Diamond and Advanced Films (COSDAF) and Department of Physics and Material Science, City University of Hong Kong, Hong Kong SAR, China

ABSTRACT

The transformation of the semiconductor tetrahedral carbon (ta-C) films to semimetal nanostructures induced by ion beam implantation at high doses has been studied. The structural analysis shows that originally abundant sp³ carbon atomic bonding of ta-C is gradually converted to a graphitic phase during the course of ion bombardment. The atomic scale analysis of implanted amorphous films shows the formation of structure with the higher degree of order. The graphitic basal planes are formed preferably along the ion tracks. Studying the mechanism of the ion-beam structuring shows that the critical damage for the transformation onset is 0.24 atomic displacements per an incident ion. The displacement and subplantation of carbon atoms are tools of nanostructuring and driving forces for the conversion of short ordered sp³ bonding configuration to the higher degree of an ordered structure when proper ion energies and doses are applied. As a result the resistivity can be altered from the original resistivity of 10¹⁰ to 10⁻⁴ ohm-cm at highest doses. The modification in resistivity is consistent with the change from interband to intraband absorption due to band overlapping which suggests the transformation from semiconductor to semimetal. Interesting is that the implanted structure with remaining sp³ bonding retains its high harness which is about 20 GPa.

Keywords: tetrahedral carbon, nanostructuring, implantation, amorphous phase transformation

*Corresponding author's e-mail address: apibello@cityu.edu.hk

NANO-GRAPHITE DEPOSITION BY ELECTRON CYCLOTRON RESONANCE PLASMAS PUTTERING METHOD

T. Ohana, T. Nakamura, A. Tanaka, Y. Koga

Research Center for Advanced Carbon Materials, AIST Tsukuba Central 5, 1-1-1 Higashi, Tsukuba, Ibaraki 305-8565, JAPAN E-mail: t.ohana@aist.go.jp, Fax: +81-29-861-4474, Tel: +81-29-861-4572

K. Tsugawa

Joint Research Consortium of Frontier Carbon Technology, JFCC c/o AIST Tsukuba Central 5, 1-1-1 Higashi, Tsukuba, Ibaraki 305-8565, JAPAN

ABSTRACT

The diamond-like carbon (DLC) films are of interest in connection with protective materials. Previously, we reported the deposition of DLC and carbon nitride films using an electron cyclotron resonance (ECR) plasma sputtering method. The deposited DLC film at low-pressure atmosphere showed low friction. In this paper, we investigated the deposition of carbon films under the condition of high plasma density and high-pressure atmosphere using ECR plasma sputtering. High density of plasma with low electron temperature was obtained in the neighborhood of the substrate by the control of the magnetic flux density. The nanocrystal graphite in size about few nm was deposited on the Si (1 0 0) substrates by the sputtering of graphite target in argon atmosphere at room temperature. The nanocrystal graphite films deposited at the high plasma density (5.0 x 10^{11} cm⁻³) showed good tribological properties. New Raman peaks of G band were obtained. From the analysis of XPS, the nanocrystal graphite gives C1s binding energy of 284.8 eV. The electrical resistivity of the films was 10^{-2} cm.

Keywords: Carbon nanocrystal, ECR plasma, Raman, Tribology

INTRODUCTION

Electron cyclotron resonance (ECR) plasma can give the stable plasma at low pressure and the high plasma density easily (ref. 1 and 2). Previously, we investigated deposition of amorphous carbon film by using ECR sputtering methods (ref. 3). We found that the deposited film showed low-friction. Recently, Hirono et al. reported conductive carbon nanocrystallite using ECR sputtering method (ref. 4). In this paper, the deposition of nanocrystal films of graphite with the low-friction coefficient and low wear rate on Si substrates using ECR sputtering method was investigated. The properties of films were investigated on the basis of Raman spectra, XPS and tribological analyses.

EXPERIMENTAL

Plasma analyses were carried out by Langmuir probe (ref. 5). The schematic diagram of the experimental setup is shown in Figure 1. The probe was placed on the center of the ECR plasma and an applied voltage was scanned from -200 V to +200V. The plasma density, plasma potential and electron temperature were calculated from the I-V characteristics.

Films were deposited on Si (1 0 0) substrates by ECR plasma sputtering from a graphite target (Toyo Tanso, 99.99 %) in argon (Nippon Sanso, purity 99.9999 %) atmosphere. Microwave (2.45 GHz) was introduced into a plasma chamber and a negative bias was applied to a carbon target with DC power supply. The typical deposition conditions were as follows, pressure; $5.4 \times 10^{-2} - 2.2 \times 10^{-1}$ Pa, target bias; -300 V, microwave power; 400 W, substrate temperature; room temperature, deposition time; 15 min, and substrate bias; self-bias. The substrate was washed with acetone, ethanol and water in ultrasonic bath for 5 min, and then the surface was pre-sputtered by argon plasma for 10 min before deposition.

NASA/CP—2003-212319 354 August 18, 2003

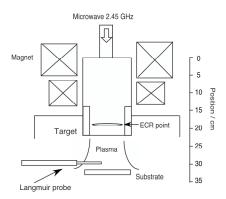


Figure 1. The schematic diagram of the plasma analyses setup.

Films obtained by ECR plasma sputtering were characterized by Raman spectrometry. Raman analyses were performed using JASCO NRS-1100 system with 532 nm excited laser at 100 mW. The carbon configuration and chemical composition of films were determined using X-ray photoelectron scanning surface analysis system (XPS). These measurements were performed using ULVAC, model PHI 5600 and the valence band energy spectra were measured with an Al K \square x-ray source operation at 100 W at pass energy 23.5 eV. The tribological properties of the films were investigated by means of ball-on-disk method. The friction measurements were conducted under humid air (30 – 40 %) at room temperature against SiC ball. The sliding speed was 100 rpm, and diameters was 3 – 5 mm. The ball was contacted with films at a load 0.1 – 0.2 N. The wear tracks were observed by AFM system (SEIKO Inst. Inc., Nanopics 1000). The electrical resistivity of films was measured by 4-point probe method (Mitsubishi Chem. Corp., MCP-T600).

RESULTS AND DISCUSSION

Films deposited in a high plasma density of $3.5 - 5 \times 10^{11}$ cm⁻³ were investigated. The deposition rate was 4.5 - 6.3 nm/min. As shown in Table 1, low potential gaps (12 - 22 V) between plasma potential (Vp) and floating potential (Vf) were observed and the etching effect during the film deposition is low (ref. 6). Figure 2 shows SEM micrographs of the obtained films. Nano-particles of a size less than 60 nm on the surface of films were observed.

Table 1. Deposition rate, plasma density, and Vp-Vf, at (a) 5.4x10⁻² Pa (b) at 1.2x10⁻¹Pa, and (c) at 2.2x10⁻¹ Pa.

	(a) 5.4 x 10 ⁻² Pa	(b) 1.2 x 10 ⁻¹ Pa	(c) $2.2 \times 10^{-1} \text{ Pa}$
Deposition rate (nm/min)	6.3	6.7	4.5
plasma density (x10 ¹¹ cm ⁻³)	3.5	4.9	5.0
Vp -Vf (V)	22	15	12

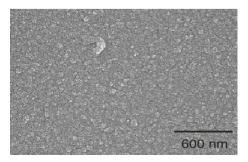


Figure 2. SEM image of deposited film deposited at 1.2 x 10⁻² Pa.

The characterization of these films was investigated by means of XPS and Raman spectroscopies. The C1s XPS spectra were shown in Figure 3. The binding energy of three films appeared at the same position at 284.8 eV. The film has mainly sp² bonding component, because the binding energy of graphite is 284.5 eV (ref. 7). These films include a small mount of oxygen that came from absorbed water on the surface of plasma camber and carbon target.

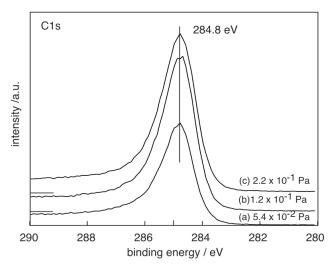


Figure 3. XPS spectra in the carbon 1s region of deposited films, (a) deposited at 5.4 x 10^{-2} Pa, (b) at 1.2 x 10^{-1} Pa, and (c) at 2.2 x 10^{-1} Pa.

In Raman spectra of the film deposited at 2.2×10^{-1} Pa, fine structures of 1614, 1602, 1572, and 1522 cm⁻¹ at the G-band region were observed as shown in Figure 4. The assignment of these peaks is not clear. Robertson et al. reviewed the interpretation of Raman spectra of disordered and amorphous carbon (ref. 8). They indicated that the G band of nanocrystal graphite appeared at 1600 cm⁻¹. Furthermore, the I(D)/I(G) ratio depended on La (cluster diameter or in-plane correlation length). The estimated La from the I(D)/I(G) ratio of these films corresponds with the cluster diameter of 2-3 nm (ref. 8), although the fine structures appeared at the G-band region could not be explained. Therefore, it is considered that the obtained films have a nanocrystal graphite phase.

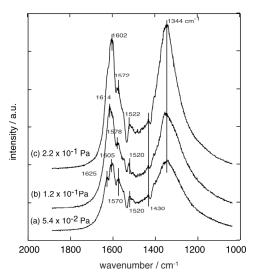


Figure 4. Raman spectra of deposited films, (a) deposited at 5.4 x 10^{-2} Pa, (b) at 1.2 x 10^{-1} Pa, and (c) at 2.2 x 10^{-1} Pa.

The electrical resistivity of these films was about $10^{-2} \square$ cm. These results were consistent with the film having a nanocrystal graphite structure.

The result of ball-on-disk friction test is shown in Figure 5. The friction coefficient of the deposited film at 1.2 x 10^{-1} Pa kept less than 0.1 during friction test. The wear rates were estimated by AFM measurement of wear track. The wear rates are 2 x 10^{-5} mm³/N·m, 3.0 x 10^{-7} mm³/N·m and 3.0 x 10^{-6} mm³/N·m for the film deposited at 5.4 x 10^{-2} Pa, 1.2×10^{-1} Pa and 2.2×10^{-1} Pa, respectively. The film deposited at 1.2×10^{-1} Pa showed lower friction coefficient and wear rate compared with the values of glassy carbon (the friction coefficient of 0.15-0.2 and wear rate $10^{-6} - 10^{-7}$ mm³/ N·m (ref. 9 and 10)). It is considered that the good tribological properties were due to nanocrystal structure. Because of the reduction of the layer structure, the film's wear resistance increased (ref. 6). The relationship between the film structure and plasma properties is not clear. However, in the previous work at lower plasma density (ref. 3), the nanocrystal graphite structure could not be obtained. Therefore, it is concluded that the film obtained at high plasma density of ECR plasma has nanocrystal structure and good tribological properties.

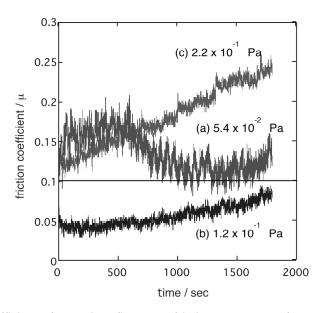


Figure 5. Friction coefficient of deposited films. the friction test was performed at 5.2 cm/s and 0.1 N.

CONCLUSION

ECR plasma density and electron temperature were controlled by magnet power, microwave power and pressure. The high plasma density $(10^{11}-10^{12}~\text{cm}^{-3})$ and low electron temperature (2-2.5~eV) were obtained. The carbon films deposited on the Si substrate were nanocrystal graphite which gives a new Raman spectrum at 1600 cm⁻¹ reagion. The film deposited at 1.2×10^{-1} Pa showed the low friction coefficient of 0.05 and the lowest wear rate of 3 x $10^{-7}~\text{mm}^3/\text{N}\cdot\text{m}$. It is concluded that the nanocrystal graphite film show good tribological property.

REFERENCES

- 1. Ono, T., et al.: Electron-Cyclotron Resonance Plasma Deposition Technique using Raw-material Supply by Sputtering: Jpn. J. Appl. Phys., vol. 23, no. 8, 1984, L534.
- 2. Matsuoka, M.; and Ono, K.: Ion energy analysis for sputtering-type electron-cyclotron-resonance microwave plasma: J. Appl. Phys., vol. 64, no. 10, 1998, 5179.
- 3. Ohana, T., et al.: The structure and tribological property of amorphous carbon and carbon nitride films prepared by ECR plasma sputtering method: Diamond and Related Materials, vol. 10, no. 3-7, 2001, 1093.
- Hirono, H., et al.: Superhard conductive carbon nanocrystallite films: App. Phys. Lett., vol. 80, no. 3, 2002, 425
- 5. Uhm, H.S., et al.: A Study Of Density In Electron-Cyclotron-Resonance Plasma: IEEE Trans, Plasma Sci., vol. 23, no. 4, 1995, 628.

- 6. Hirono, S., et al.: High wear durability of ECR-sputtered carbon films: IEEE Trans. Magn., vol. 34, no. 4, 1998, 1729.
- 7. Moulder, J.F., et al.: Handbook of X-ray Photoelectron Spectroscopy, Perkin-Elmer, Prairie, MN, 1992, 40.
- 8. Ferrari, A.C.; and Robertson, J.: Interpretation of Raman spectra of disordered and amorphous carbon: Phys. Rev. B, vol. 61, no. 20, 2000, 14095.
- 9. Hokao, M., et al.: Friction and wear properties of graphite/glassy carbon composites: Wear, vol. 237, no. 1, 2000, 54.
- 10. Chen, J.S., et al.: Structural and tribological properties of hard carbon film synthesized by heat-treatment of a polymer on graphite substrate: Thin Solid Films, vol 389, no. 1-2, 2001, 161.

CN_X FILMS PREPARED ALTERNATIVE IRRADIATION OF ¹²C⁺ AND ¹⁴N⁺ ION BEAMS

Kazuhiro Yamamoto and Yoshinori Koga

National Institute of Advanced Industrial Science and Technology (AIST) Higashi 1-1-1, Tsukuba, Ibaraki, 305-8565 JAPAN

Toshiya Watanabe and Koichiro Wazumi

Joint Research Consortium of Frontier Carbon Technology, JFCC c/o AIST, Higashi 1-1-1, Tsukuba, Ibaraki, 305-8565 JAPAN

ABSTRACT

Carbon nitride(CN_x) films were deposited on Si(100) wafers by means of alternative irradiation of mass-separated low energy $^{12}C^+$ and $^{14}N^+$ ion beams at the ultra-high vacuum pressure 10^{-7} Pa. The influence of substrate temperature during deposition on the structure, composition, and chemical bonds of the films was investigated. The ion energy of both ion species was 50 eV. The Si substrate was kept at room temperature (RT), 460, 800, or 1130 K during deposition. The films were characterized by transmission electron microscopy (TEM), X-ray diffraction (XRD), electron energy-loss spectroscopy (EELS), and X-ray photoelectron spectroscopy (XPS). The carbon and CNx film prepared at rt was amorphous. The amorphous carbon films changed to a graphite-like one with the random crystal orientations when the substrate temperature is increased. The amorphous CN film prepared at rt consisted of sp 2 C—N, sp 3 C—N, sp 2 C—C, and sp 3 C—C bonds, whose bond angles were distorted. This distortion of the chemical bonds decreased, and the structure of the CNx film changed to a graphite-like one on increasing the growth temperature. The graphite-like CNx film has a highly preferential crystal orientation, and the c-axis of the graphite basal plane is parallel to the film growth surface. The basal plane is also curved and interlinked because of the presence of in-plane sp 2 C—N and three-dimensional sp 3 C—N bonds.

Keywords: CN film, chemical bond, structure, MSIBD

INTRODUCTION

The existence of superhard materials formed from carbon and nitrogen, which have a similar structure to \Box -Si₃N₄, was theoretically predicted in 1989 (ref. 1). According to their calculation, this metastable compound β -C₃N₄ could have hardness, thermal conductivity, and thermal stability properties superior to those of diamond. Other phases of C₃N₄ have recently been reported, such as a α -phase of trigonal structure (ref. 2), a defect zinc-blend structure (ref. 3), and a rhombohedral structure (ref. 4). Recently, there have been many reports of attempts to form a carbon nitride solid; however, most of the CN_x films obtained were amorphous with some types of bonds between the carbon and nitrogen atoms. Amorphous carbon films with a disordered network of sp²- and sp³- bonded carbon atoms have also attracted much attention. The physical and chemical properties of films with high sp³ bond fraction are similar to those of diamond. Hence, they are called diamond-like carbon (DLC) films. These films are characterized by extreme hardness, high electrical resistivity, optical transparency and high thermal conductivity, all of which are very attractive for a variety of applications.

Mass-separated ion-beam deposition (MSIBD) is the most suitable method for studying thin-film growth, because it can provide monoenergetic ion species, and because the deposition parameters are independently controllable. We have developed an MSIBD system with an ion current density greater than 0.20 mA/cm^2 , and an ultra-high vacuum (UHV) of less than 8×10^{-7} Pa. This system permits deposition without damage to the films from impact of high-speed neutral carbon species, which are produced by inelastic collisions of the fast carbon ions with residual gas molecules. We believe that such collisions are the cause of degradation of the sp³-bonded fraction (ref. 5). In a previous paper, we have reported that a carbon film prepared at an ion energy of 100 eV on a room-temperature substrate had an sp³ bond fraction of more than 80%, a hardness of 80 GPa, and extreme tribological properties (ref. 6). In this paper, we report the preparation of carbon nitride films by the alternative irradiation of mass-separated low

NASA/CP—2003-212319 359 August 18, 2003

energy $^{12}C^+$ and $^{14}N^+$ ion beams. We also report an investigation of the effects of the substrate temperature on the structure of the films, and on the chemical bonds formed in the films.

EXPERIMENTAL

Carbon nitride films were prepared on the Si substrate by using mass-separated ion beams of $^{12}C^+$ and $^{14}N^+$. Our MSIBD system consisted of an ion source, a mass-separation magnet, a transport tube with magnetic lenses, a deflection magnet, deceleration electrodes, and a deposition chamber with a sample-exchange transporter. Details of the system have been given elsewhere (ref. 5). A mixture of CO_2 and N_2 was used as the source gas for the carbon and nitrogen ions. Alternating irradiation of $^{12}C^+$ and $^{14}N^+$ ions was accomplished by switching the extracted voltage of the ions. The ion energy of both ion species was 50 eV. The transport ratio of carbon ions to nitrogen ions at the substrate was 1. The Si(100) substrate, which had been cleaned with a solution of HF and HNO₃, was introduced into the UHV deposition chamber, in which the substrate temperature was kept at room temperature (RT), 600 K, 800 K, or 1130 K during deposition. The base pressure in the deposition chamber was 1.0×10^{-8} Pa, and the pressure during deposition was 6×10^{-7} Pa. The current density of the carbon and nitrogen ions was 0.10 mA/cm^2 .

The structures of the films were investigated by grazing-incidence X-ray diffraction (GI-XRD), with a copper K \Box X-ray source and a parallel-beam optical system. The incidence angle was 0.5°. The micro-structural characterization of in-plane view specimens was carried out with an energy-filtering transmission electron microscope (EF-TEM) (Leo, EM-922). The microscope was equipped with an OMEGA-type energy filter, which allows the selection of electrons undergoing certain energy losses during their transmission through the sample. The electron acceleration voltage was 200 kV. The specimens for TEM observation were prepared by a conventional mechanical grinding and dimpling process, and were thinned by ion milling with Ar ions at an energy of 5 keV. The incident angle of the ions was 4° to the surface, which prevented the specimen from being damaged by ion irradiation. The composition and chemical bonds of the carbon nitride films were determined by using ex-situ XPS with monochromated Al K α X-ray radiation and EELS. EEL spectra were obtained by EF-TEM mentioned above. The spectrometer was calibrated by using Au (4f_{7/2}) = 84.0 eV, Ag (4d_{5/2}) = 368.3 eV, and Cu (2p_{3/2}) = 932.7 eV. Before XPS measurements were made, a sample surface was cleaned by Ar-ion etching. The energy of the Ar ion was 500 eV, and the etching time was 5 s, to prevent surface damage of the films.

RESULTS AND DISCUSSION

Structure

GI-XRD was used to investigate the structure of the obtained films. XRD patterns of the carbon nitride films deposited at the substrate temperature of RT and 1130 K are shown in Fig. 1. There was no difference between the two XRD patterns, and only a broad peak at 55° was observed. The peak position from the (004) reflection of graphite is 54.6°, but the (002) peak of graphite at 26.4 deg., which is usually observed as the strongest line for the graphite-like structure, was not observed. A possible explanation is that this broad peak is not the (004) line of graphite, but represents the contribution from the hybridization of sp²- and sp³-bonded carbon and nitrogen, with a short-range ordering. These XRD patterns suggest that the structure of the films is amorphous, or that the films have a strongly preferential crystal orientation. This is discussed further in the section below on TEM measurements.

The structures of the films produced were also examined with TEM. The high-resolution TEM images of the inplane view of the CN_x films deposited at RT and 1130 K are presented in Figure 2(a) and (b), respectively, along with the SAD patterns of the film. CN_x film prepared at RT exhibited a typical amorphous structure, and crystalline grain was not observed. The selected-area electron diffraction (SAD) pattern of this specimen showed broad rings, in agreement with the result from XRD analysis. For CN_x films deposited at 1130 K, layered structures, which were curved and interlinked, were clearly observed. A bright ring was apparent in the SAD pattern of this film, and was identified as the (002) reflection of graphite. Another ring, identified as the (004) ring of graphite, was also observed. As the other reflection of graphite was not observed in the SAD pattern, the c-axis of the graphite-like structure is parallel to the film surface, in agreement well with the results of XRD, which suggest that the film has a highly preferential crystal orientation. The curved basal plane contains the carbon and nitrogen atoms according to the EELS analysis, as discussed below.

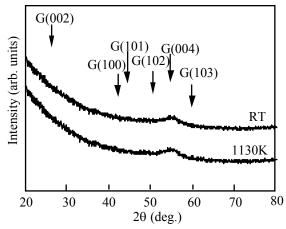


Figure 1. XRD patterns of CN films prepared at RT and 1130 K.

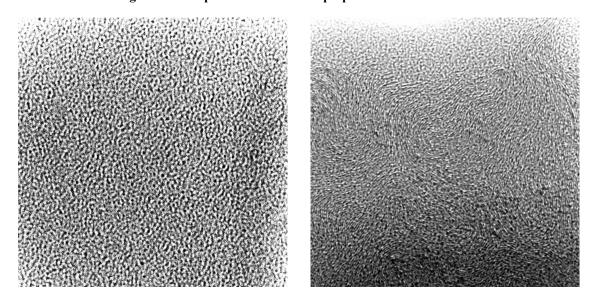


Figure 2. High-resolution TEM images of CN films prepared at (a) RT and (b) 1130 K.

Composition

The film composition was determined by ex-situ XPS after Ar⁺ ion etching. The compositions of the films prepared at various substrate temperatures are given in Fig.3. The oxygen content of all the films was less than 1 at. %. The CN films in this study were prepared from only two components, carbon and nitrogen ions, under ultra-high vacuum conditions. Therefore, the oxygen content is due to the presence of adsorbed molecules on the film surface, which were not be removed by the ion etching, because of the weak etching necessary to prevent surface damage.

The nitrogen content was 26.5 at. % for films formed at RT, and decreased slightly with increasing substrate temperature during deposition. The nitrogen content of the film prepared at 1130 K was 19.6 at. %. Note that the N content decreased rapidly, to below 10 at. %, at a substrate temperature of above 870 K in CN_x films deposited by reactive magnetron sputter deposition (ref. 7) or plasma-assisted laser deposition (ref. 8). In this study, the N content remained at about 20 at. % for substrate temperatures of up to 1130 K. It is well known that there is a threshold for physical sputtering for many materials, below which there will be no sputtering, and above which the sputtering process can increase markedly. It is thought that impact between ions and the growing CN film was prevented because an ion energy of 50 eV—a value close to the threshold for physical sputtering—was used for the film preparation.

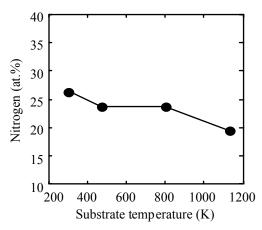


Fig. 3 Dependence of nitrogen content in CN films on substrate temperature during deposition.

Chemical bond

The C1s and N1s XPS spectra of CN thin films prepared at substrate temperatures of RT, 470 K, 800 K, and 1130 K are presented in Figure 1. The binding energy (BE) of graphite, which consists of 100% sp²-bonds, is 284.5 eV (ref. 9), and that of a polycrystalline diamond film after Ar⁺ ion etching is 285.3 eV (ref. 10). The BE of carbon in the C—N bond is 287.7 eV for sp³-hybridization, and 286.1 eV for sp²-hybridization (ref. 11). These values were determined with amorphous CN films. The peak position of the C1s spectrum of the film prepared at rt was 285.5 eV. This position shifted towards the lower-energy region with increasing substrate temperature. As the nitrogen content in the CN films prepared at 1130 K was about 20 at. %, it appears that there are two contributions—from the sp² C—C at 284.5 eV and from the sp² C—N at 286.1 eV—which vary with increasing substrate temperature.

Two main contributions were visible in the N1s spectra. The first, at 398.3 eV, corresponds to the sp³ C—N bond. The second, at 400 eV, is associated with the sp² C—N bond [11]. These values have also been previously found for amorphous CN films. Two main peaks at 398.3 eV and 400 eV were shifted to lower and higher regions, respectively, with increasing substrate temperature. The full width at half-maximum (FWHM) of each peak also narrowed with increasing substrate temperature. Therefore, it seems that the bond distance and bond angle between carbon and nitrogen shift in a manner corresponding to increased stability. In particular, we believe that the bonding of sp² C—N changes to the in-plane configuration, so that the peak position of the sp² C—N shifts from 400 eV to 400.9 eV.

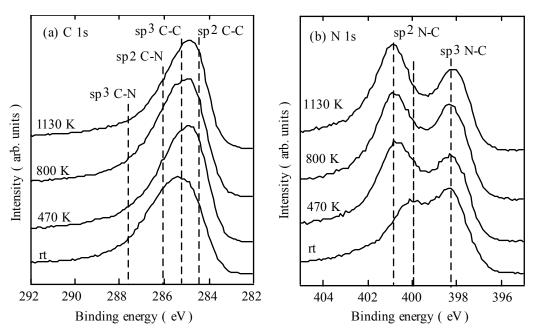


Fig. 4 XPS in the carbon 1s region (a) and the nitrogen 1s region (b) of the prepared CN films, depending on the substrate temperature.

EELS analyses were performed for CN_x films prepared at RT and 1130 K. EELS spectra of both films in the carbon K-edge are reproduced in Figure 3(a). The peak at 292 eV can be attributed to the transition from 1s to the σ^* state, and the shoulder at 284 eV is related to the transition from 1s to the π^* state. The presence of the π^* peak indicates the existence of carbon sp² or sp bonds in the structure. The σ^* peak is broad for the film prepared at RT, because of its amorphous structure. Sub-peaks at 300 and 325 eV appear in the spectrum of the film prepared at 1130 K. The sub-peak at 300 eV is due to changes in the distances and the bond angles between carbon atoms. The broad peak at 325 eV indicates the near-edge structure of carbon. The presence of these peaks clearly indicates that the carbon atoms are ordered in a graphite-like manner. The agreement between this result and the results of the TEM and SAD analyses reveals that the structure of the films becomes graphite-like with a preferential orientation, at a substrate temperature of 1130 K.

EELS spectra in nitrogen K-edge are presented in Figure 3(b). The peak at 398 eV is attributed to the transition from 1s to the π^* state, and the peak at 405 eV arises from the transition from 1s to the σ^* state. The peak at 405 eV of the film prepared at RT is broad, owing to their amorphous structure. The FWHM of this peak narrows, and a new sub-peak at 400 eV appears in the film prepared at 1130 K. We believe that the film prepared at 1130 K has two kinds of configurations of the sp²-nitrogen: as pentagonal and hexagonal rings of a graphite-like structure.

The carbon K-edge EELS spectra of films prepared at the ion energies of 50 as the function of he substrate temperature during deposition are shown in Figure 4. In our previous work, it has been clarified that the fraction of sp³ bond in the film prepared at 50 eV and RT was 76%, which was calculated from EELS spectra.[5] These value are consistent with the results from a SAD, which reveals that the film prepared at 50 eV and RT has the diamond-like configuration of carbon atoms. The intensity of π^* peak at 285 eV increases with increasing the substrate temperature during deposition, and the sp³ bond fraction decreases. The σ^* peak of the film prepared at RT is broad due to the amorphous structure. The sub-peaks at 300 and 325 eV are appeared for the films prepared under substrate heating. These clarify that the carbon atoms are ordered like graphite in the short range. This is in agreement with TEM and SAD analyses, which reveals that the structure of films changes to graphite-like one due to the substrate heating during deposition.

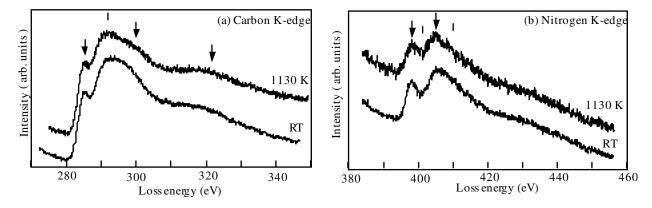


Figure 5. EELS spectra in (a) the carbon K-edge region and (b) the nitrogen K-edge region of CN films prepared at RT and 1130 K.

CONCLUSIONS

Carbon nitride films were prepared by alternating irradiation with mass-separated ion beams of $^{12}C^+$ and $^{14}N^+$ at various deposition temperatures. CN films prepared at rt have an amorphous structure containing 27 at. % nitrogen. The amorphous CN film consists of sp^2 C—N, sp^3 C—N, sp^2 C—C, and sp^3 C—C bonds, all of which have distorted bond angles. This distortion of the chemical bonds diminished, and the structure of CN film changed to a graphite-like one with increasing growth temperature. The graphite-like CN film has highly preferential crystal orientation, and the c-axis of the graphite basal plane is parallel to the film surface. The basal plane is also curved and interlinked because of the presence of in-plane sp^2 C—N bonds and three-dimensional sp^3 C—N bonds.

REFERENCES

- [1] A. Y. Liu and M. L. Cohen, Prediction of new low compressibility solids, Science 245 (1989) 841.
- [2] Y. Guo and W. A. Goddard III, Is carbon nitride harder than diamond? No, but its girth increases when stretched (negative Poisson ratio), Chem. Phys. Lett. 237 (1995) 72.
- [3] A. Y. Liu and R. M. Wentzcovitch, Stability of carbon nitride solids, Phys. Rev. B50 (1994) 10362.
- [4] J. Ortega and O. F. Sankey, Relative stability of hexagonal and planar structures of hypothetical C_3N_4 solids, Phys. Rev. B51 (1995) 2624.
- [5] K. Yamamoto, T. Watanabe, K. Wazumi, F. Kokai Y. Koga, and S. Fujiwara, The sp3 bond fraction in carbon films prepared by mass-separated ion beam deposition, Diamond Relat. Mater. 10 (2001) 895.
- [6] K. Yamamoto, K. Wazumi, T. Watanabe, Y. Koga, and S. Iijima, Tribological properties of diamond-like carbon films prepared by mass-separated ion beam deposition, Diamond Relat. Mater. 11 (2002) 1130.
- [7] H. Sjöström, I. Ivanov, M. Johansson, L. Hultman, J.-E. Sundgren, S.V. Hainsworth, T.F. Page, and L.R. Wallenberg, Reactive magnetron sputter deposition of CNx films on Si(001) substrates: film growth, microstructure and mechanical properties, Thin Solid Films, 246 (1994) 103.
- [8] M. Tabbal, P. Merel, S. Moisa, M. Chaker, A. Ricard, and M. Moisan, X-ray photoelectron spectroscopy of carbon nitride films deposited by graphite laser ablation in a nitrogen postdischarge, Appl. Phys. Lett. 69 (1996) 1698
- [9] J. F. Moulder, W. F. Stickle, P. E. Sobol, and K. D. Bomben, Handbook of X-ray Photoelectron Spectroscopy (Perkin-Elmer, Eden Prairie, MN, USA), (1992) 40.
- [10] K. Yamamoto, F Kokai, Y. Koga, and S. Fujiwara, Electron energy loss spectroscopy studies of amorphous carbon films prepared by pulsed laser deposition, New Diamond Front. Carbon Technol. 9 (1999) 289.
- [11] K. Yamamoto, Y. Koga, and S. Fujiwara, Binding energies of amorphous CN and SiCN films on X-ray photoelectron spectroscopy, Jpn. J. Appl. Phys. 40 (2001) L123.

Calculation of the electronic structure of SiCN crystal by LAPW method*

X.L. Zhu^{1,2}, X.B. Niu^{1,2}, Y. Liao^{1,2}, L. Yu^{1,2}, Q.X. Yu², G.Z. Wang^{1,2}, R.C. Fang²

Structure Research Laboratory, ²Department of Physics,

University of Science and Technology of China, Hefei, 230026, P.R.China

ABSTRACT

The excellent character and broad potential for application of Silicon Carbon Nitride Film have attracted many researchers in the fields of both condensed matter physics and materials science and engineering, etc. However, most of work concentrates on the preparation of SiCN. Scientists have prepared various SiCN materials, such as SiCN crystal [1], nanocrystalline[2], ceramics[3], etc. Thus we investigate the electronic properties of SiCN crystal using LAPW (linearized Augmented Plane Wave) method in order to give proper interpretation of its characteristic.

The LAPW method is among the most accurate methods for performing electronic structure calculations for crystals. It is based on the density functional theory. Because the structure of SiCN crystal is similar to that of $_Si_3N_4$ [4], in the course of calculation, we calculate the $_Si_3N_4$ firstly, then substitute C atom for Si. We could vary the Si:C:N ratio, and compare the electronic structures in the different ratios of Si:C:N. (In experiment, the average [N] for the crystalline phase is about 50 at %, only slightly than the theoretical value for the C_3N_4 or Si_3N_4 . the C:Si ratio varies between 5:1 and 1:1 with a mean value around 2:1.[1]). This method is used to investigate the intact crystal.

We also use supercells, which include several cells of $_Si_3N_4$ (or $_C_3N_4$) and substitute a Si (or C) atom in it with a C (or Si) as a defect atom. In this method SiCN is considered as a doped system. We use the GGA (Generalized Gradient Approximation) to do the exchange-correlation potential.

Reference

- [1] L.C. Chen, K.H. Chen, S.L. Wei P.D. Kichambare, J.J. Wu, T.R. Lu, C.T. Kuo, Thin Solid Films 355-356 (1999) 112, 114
- [2] K. Szulzewsky', Ch. Olschewski, L Kosche, H.-D. Klotz, R. Mach, NanoStructured Materials, Vol. 6, pp. 325–1995
- [3] GuÈ nter Thurn, Je roà me Canel, Joachim Bill and Fritz Aldinger, Journal of the European Ceramic Society 19 (1999) 2317
- [4] Chao Chang, Paper for Doctor's degree (6/2001) P78

^{*} Supported by National Natural Science Foundation of China and Anhui Province Natural Science Foundation.

^{**} Corresponding author: E-mail: liaoyuan@ustc.edu.cn; Tel.: +86-551-3607142.

Synthesis of B-C-N films by electron beam excited plasma-assisted rf magnetron sputtering

Takeshi Hasegawa*)

FCT research department

Japan Fine Ceramics Center,

FCT Lab., AIST Tsukuba Central 5, 1-1-1 Higashi, Tsukuba, Ibaraki 305-8565, Japan

Kazuhiro Yamamoto and Yozo Kakudate

Research Center for Advanced Carbon Materials

National Institute of Advanced Industrial Science and Technology,

AIST Tsukuba Central 5, 1-1-1 Higashi, Tsukuba, Ibaraki 305-8565, Japan

*) Corresponding author under temporary transfer from Kawasaki Heavy Industries, Ltd.

Phone: +81-29-861-9982

Fax: +81-29-861-4796

E-mail: t.hasegawa@aist.go.jp

Abstract

Boron-carbon-nitrogen (B-C-N) thin films have been synthesized using electron beam excited plasma (EBEP)-assisted rf magnetron sputtering system with boron nitride and graphite target. Compositions of the films were varied by controlling the rf power for the graphite target and determined by X-ray photoelectron spectroscopy. We obtained $B_x C_y N$ films, x=1.0-1.1 and y=0.03-0.25. The composition dependence of infrared transmission spectra showed that structure of the film was very sensitive to carbon content; a cubic phase was found only in a carbon-poor region and disappeared abruptly with increasing carbon content. Results of transmission electron microscope, electron diffraction, and electron energy loss spectroscopy measurements show that the films involve the cubic phase of carbon-poor B-C-N compound.

This work was supported by the Frontier Carbon Technology (FCT) project, which was consigned to JFCC by NEDO.

Keywords: Nitrides, B-C-N, electron beam excited plasma (EBEP), magnetron sputtering, characterization.

FORMATION OF REFRACTORY COATINGS ON CARBON-BASED MATERIALS BY GAS PHASE TRANSPORT REACTIONS

N.I. Baklanova*, V.N. Kulyukin, T.M. Zima

Institute of Solid State Chemistry and Mechanochemistry of Siberian Branch of Russian Academy of Sciences Kutateladze st.18 Novosibirsk 630128 Russia

*) E-mail: <u>baklanova@solid.nsc.ru</u> Phone: 7 3832 363839 Fax: 7 3832 322847

ABSTRACT

Increased oxidation resistance at high temperatures is one of the critical requirements for high-tech application of carbon materials including carbon and silicon carbide fibers, nanotubes, diamonds. Corrosion resistant coatings such as refractory carbides, nitrides, borides and oxides may improve the oxidation behavior of carbon-based materials. The aim of this work is to study theoretical and experimental aspects of the formation of refractory coatings on different carbon materials under chemical transport through the gas phase.

The formation of coatings composed from the carbides of metals of IV-V groups (V, Nb, Ta, Ti, Zr, Hf, Cr, Si) on carbon and SiC fibers, diamond and graphite substrates are considered. The coatings were examined by X-ray diffraction (XRD), scanning electron microscopy (SEM). The coatings obtained were found to be uniform and adherent to substrates. Under definite conditions the formation of refractory coatings as needles was observed. Oxidation of coated carbon fibers was studied.

Keywords: carbide coatings, RCVD, carbon materials, diamond, oxidation

INTRODUCTION

Carbon-based materials exhibit good mechanical properties, particularity at high temperatures. Despite their numerous advantages such as low density, superior mechanical strength at high temperatures, and excellent friction behavior, they exhibit a fatal drawback, e.g., a very poor oxidation resistance even at temperature as low as 500°C. As a consequence, the most of their applications are limited to nonoxidazing atmospheres, at least for those involving long exposure times. Therefore a reliable antioxidation treatment should be invented to apply to carbon-based materials. Further, carbon-based materials that are often used as reinforced components in composite materials with carbon and metal matrixes are reactive and /or non-wetting with many matrix metals, thus introducing many difficulties in the fabrication and high temperature application of these composite materials [1, 2]

One solution of this problem is to apply a suitable protective coating or diffusion barrier to carbon material. Possible coatings materials are refractory oxides, carbides, nitrides, borides. Carbides, nitrides and borides of refractory metals are oxidized at temperatures below 1000°C, thus exhibiting a not very high resistance to oxidation. However, they form a high melting, nonsoluble water and thermal stable oxides that can hinder to diffusion of oxygen towards to substrate. B-C, Si-B-C, SiC deposits on carbon fiber were fabricated in order to protect interfacial zone from oxidation [3,4]. It was shown that only boron-rich Si-B-C deposits form at interfacial zones a glassy compound that block efficiently carbon oxidation at 600°C. There are also several positive examples for using refractory oxides as promising coatings for carbon-based materials. Alumina and zirconia sol-gel coatings for protective barriers on carbon materials were investigated in refs.5, 6. It was reported problems in achieving a sol that could wet the carbon surface well and develop into a crack free coating. It was noted that the oxidation was delayed to higher temperatures as the coating thickness increased.

The aim of this work is to consider the theoretical (thermodynamic) and experimental aspects of the formation of refractory coatings on carbon materials by means of the gas phase transport reactions. The essence of chemical transport method is that the interaction of a solid with some gas phase substance results in the formation of only gaseous products which then transported into another part of reactor and under the changed equilibrium conditions either decompose with evolution of initial solid or interact with another solid as was shown in ref.7. Chemical

transport through the gas phase (RCVD) is a promising way because of its ability to uniformly coat complex shapes and its high infiltration capability.

EXPERIMENTAL

Initial substances

Different kinds of carbon materials were used in this study. Carbon fibers derived from polyacrylonitrile (PAN) and cellulose, graphite and synthetic diamond powders were used as initial substances. Before deposition process carbon fibers were cleaned by dipping in mixture of acetone/ethanol to remove of sizing agent, drying on an air and heating in furnace at 900°C in argon atmosphere. Cuttings or/and powders of tantalum, vanadium, titanium, zirconium, hafnium, molybdenum, and silicon were used to fabrication coatings on carbon substrates. Halogen and halogen-containing gases were used as transporting agents.

Coating process

Refractory coatings were obtained by RCVD in closed or flow reactor under different conditions (T, P, exposure time, flow rate). A horizontal flow quartz reactor with a length of about 1000 mm was connected to the vacuum system. A tube made of nickel was placed in the reactor to diminish the contamination of coatings by the products formed in the interaction of halogen-containing reagents with the walls of the quartz reactor. Metal cuttings were charged into reactor and packed. Chemically pure argon was used as the carrier gas. The process was carried out at 1200-1300K for 1-50 h, the total pressure in the flow reactor being 10² Pa and in closed reactor being about 10⁵ Pa.

Coating characterization

Microstructural features and phase composition of coatings were studied with help of scanning electron microscopic analysis (SEM, JSM T-20) and X-ray diffraction (DRON-3; CuK_{α} radiation). The mean diameter of initial single filament determined is approximately 7-8 μ m for carbon fiber.

Heat treatment in air

Heat treatment of coated carbon fibers in air was performed in resistant-heated furnace. Samples were placed into preliminary heated at 500-700° C furnace and kept under static conditions for different time.

RESULTS AND DISCUSSION

Thermodynamic approach

Thermodynamic calculation of phase equilibria was performed for the Ta-C-Cl system in detail. The calculation was done within temperature range 300–1500 K and pressure range 1.33– $1.33\cdot10^5$ Pa using self-consisting thermodynamic data. A model of complex chemical equilibrium solid-gas was used in calculation. The model takes into account of the fact that the components present in the gas phase include tantalum chlorides $TaCl_n$, where n=1,2,3,4,5, tantalum, molecular and atomic chlorine, carbon chlorides. According to phase diagram of the Ta-C system $Ta+Ta_2C$ (A), Ta_2C+TaC (B), TaC+C (C) are solid phases that are in equilibrium with gas.

The results of thermodynamic calculations suggest that the total tantalum content in gas phase normalized to chlorine atom at constant pressure and temperature will decrease in the direction $A \rightarrow B \rightarrow C$, while the total carbon content will decrease in reverse direction. It follows from this fact that, first, that transport in closed reactor can be conducted under isothermal conditions, namely at equal temperatures of synthesis zone and source of transport agents. Second, Ta mass transfer will take place in the $A \rightarrow B \rightarrow C$ direction and carbon will occur in the reverse direction. Quantitative characteristics of tantalum and carbon mass transfer strongly different from each other under the same conditions, so chemical transport of carbon through the gas phase can be neglected. The lower chlorides $TaCl_4$, $TaCl_3$, $TaCl_2$ content over A is higher than that over B or C. Thus, under isothermal conditions at constant total pressure tantalum mass transfer to carbon occurs via lower chlorides. It should be noted that these considerations are true only in case when the interaction of tantalum halides with the quartz walls of the reactor is excluded. Abovementioned scheme of process is true for all of the transition metal-chlorine -carbon systems and for halogen agents other than chlorine.

Experimental results of realization of gas phase transport in the metal-halogen-carbon systems

One can see that morphological characteristics of carbide coatings obtained are differ from each other (Fig.1-4). But general observation is that the chosen experimental conditions (time of deposition and total pressure) provide a complete and uniform coating of each separate filament, besides splicing is excluded. The SEM image of coating obtained in the system Ti-C-halogen is represented in Fig.1. One can see that the external surface is rather smooth, homogeneous and dense. It repeats the relief of the initial single filament. The XRD pattern only shows peaks of TiC. The average size of the crystallites is not more than 80 nm. Morphologies of VC coatings are represented in Fig.2. One can see that in dependence on time deposition the external surface becomes rather rough and corn like. The distinct feature of coating obtained in the Mo-C-halogen system is appearance of a porosity. According to XRD data the composition of coating can be represented by Mo and Mo₂C phases. It is important that the specific area in all cases remains high and comparable with those for starting materials (500-600 m²/g).

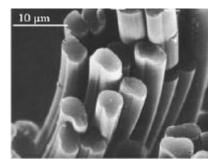


Figure 1. TiC coating on carbon fibers.

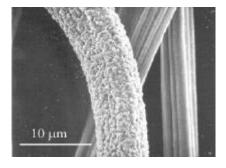
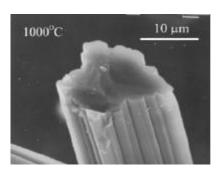


Figure 2. VC coating on carbon fibers.



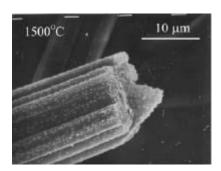
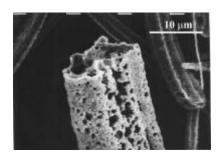


Figure 3. SiC-Si₃N₄ coating on carbon fibers heat-treated at different temperatures.



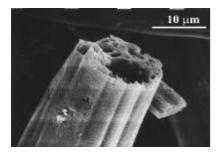
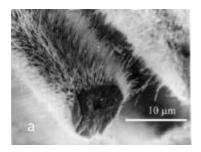
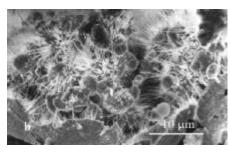


Figure 4. Molybdenum carbide coatings.

The appearance of secondary porosity for Mo_2C coating appear to be due to interaction of gaseous molybdenum oxyhalogenides with carbon support. Besides, molybdenum can act as an active catalyst of carbon and oxygen reaction. The formation of secondary porosity is a special interest for catalytic applications of modified fibers. We studied the catalytic activity of molybdenum carbide coated carbon fibers. As a test reaction the liquid phase oxidation of c-hexane in c-hexanol in the presence of phosphormolybdenic heteropolyacide has been chosen. The conventional Pt on support catalysts were used as references. From the results obtained it follows that the catalytic activity of Mo_2C -coated carbon fiber catalyst is more than 5 times higher than that of conventional catalysts under the same gas capacity of the both catalysts.

When the RCVD process in the system Me-C-halogen was carried out in closed reactor at total pressure 10⁵ Pa and at 1000°C we observed some interesting features of carbide coatings on different carbon materials (Fig.5a, b, c). The tantalum carbide layer starts to grow in the very first minutes of exposure. The layer is a fine-grained coating. At the first time TaC is predominant phase. Starting from one hour and a half, the formation of Ta₂C phase as thin needles becomes noticeable. One of the reasons of the appearance of Ta₂C as needles seems to be the ordering of carbon vacancies of nonstoichiometric tantalum carbide, as was noted in ref. 8.





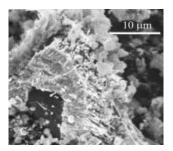
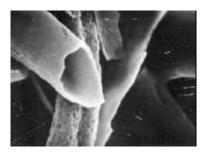


Figure 5. Tantalum carbide coatings as needles on carbon based materials: (a) carbon fiber, (b) graphite, (c) diamond powder

Oxidation resistance of refractory carbide coated carbon materials

The study of oxidation resistance of refractory carbide coated fibers showed that these deposits are not efficient to protect carbon. A rapid mass loss is observed at the beginning of oxidation tests. Mass gain due to MeO_n (where M=Ti, Zr, Hf, V,) formation is lower than mass loss due to CO_2 evolution. After oxidation, a hole is formed between the fiber and coating.



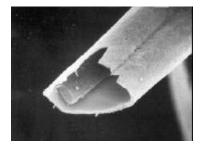
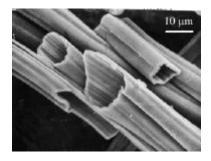


Figure 6. The different stages of oxidation of VC-coated carbon fibers.

SEM observation carried out at the end of the oxidation test on the ZrC-, HfC-, TiC-, VC-coated carbon fibers shows the formation of hollow tubes (Fig.7). The formation of hollow tubes was observed also for SiC-coated carbon fibers in ref. 3. According to XRD data the walls of tubes are composed of corresponding of oxides. The surface of tubes is very smooth and thickness is constant along their whole cross-section. No formation of hollow

tubes for the Mo₂C-coated carbon fibers was observed because of high vapor pressure molybdenum oxides at this temperatures. The most oxidation resistant among coatings under investigated by us is SiC-Si₃N₄ one.



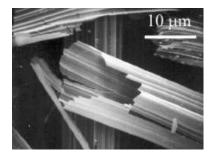


Figure 7. TiO₂ and HfO₂ hollow tubes derived from coated carbon fibers.

CONCLUSIONS

Chemical transport of metals of the IV-V groups through the gas phase in the form of halogenides leads to the formation of carbide coatings on carbon materials. Carbide coatings are uniform in the thickness and possess a high adhesion to the carbon supports. Under definite conditions the formation of refractory coatings as needles was observed. Oxidation of coated carbon fibers was studied. The coatings are oxidized slower than the carbon and oxidation progresses between the fiber and the coatings. The most oxidation resistant among coatings investigated is $SiC-Si_3N_4$ one.

ACKNOWLEDGEMENT

This work was supported by NATO SfP grant # 973472. Authors are grateful to Dr. N. Kuznetsova (BIC SB RAS) for studies of catalytic activities of coated carbon materials.

REFERENCES

- 1. Strife, J.R., Sheehan, J.E. "Ceramic Coatings for Carbon-Carbon Composites" Am.Ceram.Soc.Bull., 67, #2, 1988, 369-374.
- 2. Himbeault, D.D., Varin, R.A., Pikarski, K. "Carbon fibers coated with titanium carbide using the liquid metal transfer agent technique". J.Mater.Sci. 24, 1989, 2446-2750.
- 3. Labruquere, S., et al. "Enhancement of the oxidation resistance of interfacial area in C/C composites. Part.I: oxidation resistance of B-C, SiB-C and SiC coated carbon fibers". J.Eur.Ceram.Soc. 22, #7, 2002, 1001-1009.
- 4. Labruquere, S., et al. "Internal protection of C/C composites by boron-based compounds. J.Eur.Ceram.Soc., 22, #7, 2002, 987-999.
- 5. Sim, S.M., et al. "Sol-Gel Coatings on Carbon/Carbon Composites". Mater.Res.Soc.Sym.Proc., 73, 1990, pp. 647-652.
- 6. Deslandes, Y., and sabir, F.N. "Inhibition of Oxidation of Carbon Fibers by Sol-Gel Coatings". J.Mater.Sci.Lett., 9, #1, 1990, 200-202.
- 7. Schafer H., in Preparative Methods in Solid State Chemistry, P.Hagenmuller, ed. Academic Press, New York and London, 1972, pp.277-364.
- 8. Markhasev B.I., et al. "Ordering in Nonstoichiometric Niobium and Tantalum Carbides". Inorg..Mater., 21, #10, 1985, 1697-1699 (in Russian).

DEPOSITION OF CUBIC BORON NITRIDE FILMS BY PLASMA BASED ION IMPLANTATION

Osamu Tsuda, Toshiya Watanabe, Masahiro Suzuki

Japan Fine Ceramics Center, Joint Research Consortium of Frontier Carbon Technology, c/o Research Center for Advanced Carbon Materials, AIST Tsukuba Central 5, 1-1-1 Higashi, Tsukuba, Ibaraki 305-8565, Japan (oz.tsuda@aist.go.jp)

Masatou Ishihara, Akihiro Tanaka and Yoshinori Koga

Research Center for Advanced Carbon Materials, AIST Tsukuba Central 5, 1-1-1 Higashi, Tsukuba, Ibaraki 305-8565, Japan

ABSTRACT

Cubic Boron Nitride (cBN) film depositions were performed by a radio frequency (RF) bias sputtering with a plasma based ion implantation (PBII). Effects of PBII conditions, such as pulse bias voltage and duty ratio, on the nature of the deposited BN films were investigated systematically. It is revealed that the high voltage pulse bias is detrimental to cBN nucleation while cBN growth can proceed with the high voltage pulse biasing. Effects of PBII conditions were also investigated on the compressive stress and the adhesion strength of the deposited films using the two step depositions methods.

Keywords: cubic boron nitride, plasma based ion implantation, two step deposition, stress, adhesion

INTRODUCTION

There have been many deposition techniques utilized for the synthesis of cubic boron nitride (cBN) (refs. 1 to 6), which is a promising material for a variety of coating applications due to its excellent properties, such as high hardness, chemical inertness and thermal conductivity. However, cBN films deposited by such methods have highly compressive stress (refs. 7 and 8) as well as insufficient adhesion strength, which results in adhesion failure at thickness above a few hundreds nm. This is one of the most serious problems which prevent the industrial applications of cBN film coatings. Many methods have been proposed and performed for the stress reduction and the adhesion improvement, such as high temperature annealing (ref. 9), buffer layer insertion (refs. 10 and 11), high temperature deposition (ref. 12) etc.

Stress reduction by high energy ion bombardment during deposition (ref. 13) or post implantation with 350 keV Kr ions (ref. 14), or 1 MeV N ions (ref. 15) has also been effectively demonstrated. Boyen et al. has reported that the alternative irradiation with assisting ions during deposition and high energy ions (300 keV Ar⁺) results in low stress cBN films (ref. 16). Moreover, Fitz et al. has successfully deposited low stress (1 GPa) cBN films by simultaneous irradiation with 35 keV N⁺ or 70 keV Ar⁺ ions and 500 eV assisting ions (ref. 17). In addition to the stress relaxation effect, high energy ion implantation results in atomic mixing at the interface between the film and the substrate, which leads to adhesion improvement (ref. 18).

These high energy ion bombardment techniques have been performed by conventional ion beam methods. Recently, as a new technique of ion implantation, plasma based ion implantation technique (PBII) has widely been studied for film depositions such as DLC (ref. 19) and TiN (ref. 20), and surface modification (ref. 21) etc. This technique has some advantages superior to the conventional line-of-sight ion beam methods: ability for three-dimensional coatings on complex shaped objects, high current density, and process time independent of area etc.

Thus we have employed the plasma based ion implantation for cBN deposition. Our goal is on the deposition of cBN films thick enough and durable for tribological applications. In this article, as a first step to adopt the PBII to cBN deposition, the purpose is focused on the survey of the optimal PBII conditions, such as pulsed high bias voltage, duty ratio, pulse duration and radio frequency self bias voltage simultaneously applied.

EXPERIMENTAL

The apparatus used was basically an unbalanced RF magnetron sputtering system with an RF substrate biasing (ref. 3), equipped with a high voltage pulse generator (fig. 1). The substrate electrode was immersed in the plasma diffusing from the target electrode by the unbalanced magnetic field. The pulsed negative high voltage was applied to the substrate electrode by the high voltage pulse generator (fig. 2(a)). RF bias voltage was also applied simultaneously to the substrate electrode through an inductor which suppresses interference from the RF bias source to the high voltage pulse bias generator (fig. 2(b)). The ϕ 4" target used was a sintered hBN (99.7%). 30 mm x 30 mm Si (100) wafers were used as substrates and mounted on a ϕ 90mm stainless holder. Substrates were heated during depositions only by irradiation from the plasma or the target or by ion/electron bombardment. The distance between the target and the substrate was approximately 110 mm, which is larger enough to hold the plasma between the target and the substrate than the Child law sheath thickness formed during the high voltage pulse duration. The working pressure was chosen so that the sheath was collisionless. When the chamber was evacuated below the pressure of $1x10^{-4}$ Pa, depositions were made with the target power (P) of 1200 W at a pressure of 0.13 Pa in a discharge of 95% argon and 5% nitrogen after sputter-cleaning of the target and substrate surfaces for 30 minutes. The pulsed negative

bias voltage ($V_{\rm pulse}$), the duty ratio (Rd), and the high voltage pulse duration (T_{pulse}) were varied from 0 kV to 20 kV, 0% to 10 %, 6 μ s to 300 μ s, respectively (fig.2(a)). The negative self bias voltage applied (V_s) simultaneously with $V_{\rm pulse}$ was 200 V in the experiments using the biasing in the fig. 2(b).

The deposited films were analyzed by fourier transform infrared spectroscopy, Xray photoelectron spectroscopy, and scanning electron microscopy. The internal stress was evaluated from the curvature of the specimen measured by a surface profilometer using Stoney's equation.

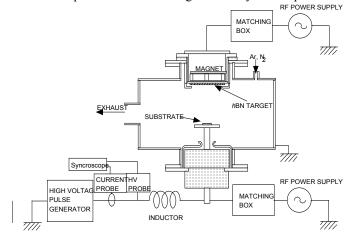


Fig. 1 Schematic illustration of the sputter-PBII system

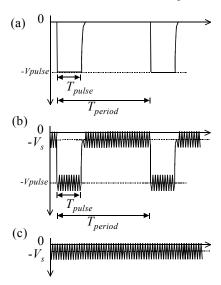


Fig.2 Substrate biasing used for PBII. (a) high voltage pulse biasing, (b) high voltage pulse biasing superimposed with RF self biasing. T_{pulse} : duration of the high voltage pulse, T_{period} : period of the repetition of the pulse, V_{pulse} : negative pulse bias voltage, V_s : RF negative self bias voltage, (c): conventional RF self biasing

RESULTS AND DISCUSSIONS

Figures 3(a) and 3(b) show the IR spectra of the deposited films with the pulse biasing in fig.2(a). The depositions were performed with a variety of V_{pulse} and $R_d = 1$ % (fig. 3(a)), and with a variety of R_d and $V_{pulse} = 10$ kV (fig. 4(b)). The condition of $V_{pulse} = 0$ kV or $R_d = 0$ % denotes the case without the biasing. In all cases, the spectra exhibited only the absorption peaks at around 1380 cm⁻¹ and 800 cm⁻¹, which correspond to sp^2 stretching vibration mode and sp^2 bending vibration mode, respectively. No cBN TO absorption peak was observed in those spectra. The peak around 1380 cm⁻¹ shifted to the lower wave number with the increased R_d , which resulted from amorphous or disordered sp^2 BN formed by high energy ion bombardment (ref. 22). Figures 4(a) and 4(b) show dependence of nitrogen-to-boron atomic ratio and deposition rate on V_{pulse} and R_d , respectively. The nitrogen-to-boron atomic ratio was almost constant irrespective to the pulse bias conditions, though it decreased slightly with an increase in V_{pulse} or

 R_d . The atomic ratio for all the cases was smaller than that of a cBN film deposited with $V_s = 200$ V, of which nitrogen-to-boron atomic ratio is also shown in figs. 4(a) and 4(b) (open circle). It has been widely recognized that stoichiometry is one of the necessities for cBN formation (ref. 23). Accordingly, nitrogen deficiency is one of the possible reasons for the inhibition of cBN formation. It is required for cBN formation to avoid the nitrogen deficiency by some methods, such as nitrogen addition with higher concentration. The deposition rate also decreased slightly with an increase in V_{pulse} or R_d owing to enhanced re-sputtering.

Since the PBII conditions adopted above led to the destructive effects on cBN formation, BN film depositions using the simultaneous biasing (fig. 2(b)) were made with reduced R_d (0.2%), $V_{pulse} = 10 \text{kV}$ and $V_s = 200 \text{ V}$ for the purpose of survey of optimal PBII conditions. From the results previously obtained in the other series of deposition experiments using the conventional RF biasing (fig.2(c)), it was clear that cBN films were able to be deposited with V_s above 100 V and that almost pure cBN films with sp2 bonded initial layers adjacent to the substrates were able to be formed with Vs = 200 V and the deposition time of 600 s. Figure 4(a) shows the IR spectrum of the BN films deposited with the simultaneous biasing. Only sp^2 BN absorption peaks were observed in the spectrum. It is surprisingly that R_d as low as 0.2 % resulted in the inhibition of cBN formation. In reference 17, the current density of high energy ions (35 keV N⁺, 70 keV Ar⁺) used for stress reduction is lower than the critical current density above which cubic-to- sp^2 phase transformation is induced, and is 10 % as large as that of assisting ions with low energy (500eV Ar⁺, N₂⁺). The R_d of 0.2 % is much smaller than that in the reference by two orders of magnitude. It should be noted that these results cannot be attributed to nitrogen deficiency because the nitrogen-to-boron ratio of the film was 0.88, which is as high as those of cBN films (0.87-0.94).

Figure 5(b) shows the IR spectrum of the cBN film deposited by the two step deposition technique shown in fig. 5(a). In the first step, a cBN template layer was deposited with the conventional RF biasing (fig. 2(c)), and then in the second step the pulsed high voltage was applied simultaneously with the RF self bias voltage. The dashed line in fig. 5(b) shows the IR spectrum of the cBN template layer. The bias conditions used for each step are as follow: 1^{st} step: $V_s = 200 \text{ V}$ for 600 s, 2^{nd} step: $V_{pulse} = 10 \text{ kV}$, $R_d = 0.2 \%$, $V_s = 200 \text{ V}$ for 600 s. The difference in the IR absorbance shows the contribution of the BN film deposited in the second step. Clearly the IR absorption corresponding to cBN TO (1080cm⁻¹) increased in the second step. This result shows that the high voltage biasing is detrimental for cBN nucleation while cBN growth can proceed even with such a high voltage biasing once cBN nucleates. In the present study, therfore, it is revealed that the cBN growth window expands into the higher energy side (at least up to 10 keV) as well as the lower side than the cBN nucleation window as reported in the literature (ref. 24). Unfortunately, the absorption peaks at 1390 cm⁻¹ and 790 cm⁻¹ corresponding to sp^2 BN bond vibrations were also enhanced in the second step. This indicates that a mixture of cubic and sp^2 phases was formed in the second step. To investigate effects of PBII on cBN growth and internal stress, the two step deposition method mentioned above was performed. The conditions are as follows: 1^{st} step: $V_s = 200$ V, deposition time 300 s, 2^{nd} step: $V_s = 200$ V, $V_{\text{pulse}} = 10 \text{ kV}, 20 \text{ kV}, T_{\text{pulse}} = 6 \text{ } \mu\text{s} - 300 \text{ } \mu\text{s}, R_d = 0.02 \% - 0.5 \%, deposition time 600 s. Figures 6(a), 6(b) and 6(c)$ show changes in the compressive stress and the IR absorbances of sp^2 bonding vibrations and cBN TO of the deposited flims with R_d . The compressive stress decreased with an icrease of R_d in all cases, showing that the high energy ion bombardment reduced the compressive stress. However, the IR absorbance of cBN also decreased while those of sp^2 BN increased with an increase of R_d for all T_{pulse} conditions. Figure 7 shows a relationship between the curvature of the deposited films and the IR absorbace of cBN TO. The curvature of the cBN films monotonically increased with an increase of the IR absorbance of cBN TO, and all the marks lie in an identified master curve. In addition, the mixture of cBN and sp^2 BN, which was deposited with the conventional RF biasing (fig. 2(c), $V_s = 100$ V, closed circles), also obeyed the relationship. Since the curvature is proportional to a product of the compressive stress and the film thickness, these results mean that the stress reduction by PBII with the two step deposition method is attributed to the phase transformation of cBN with a large compressive stress to sp^2 BN with a low stress, and that PBII didn't affect stress reduction in cBN phase, in contrast with the case reported in reference 17 using spontaneous irradiation of high and low energy ion guns. Though the reason for the discrepancy is not clear, that might be due to the difference in the substrate temperature or the ionic species.

To utilize the interface mixing by PBII for the improvement of the adhesion strength, BN film depositions were performed with the pulse biasing ($V_{\text{pulse}} = 10 \text{ kV}$, $T_{\text{pulse}} = 60 \text{ µs}$, $R_d = 10 \text{ %}$) for 1200 s in a discharge of 95% Ar and 5% CH₄ in the first step (mixing step), and then with the conventional RF biasing (Vs = 200V) for 2000 s in the Ar-5%N₂ discharge in the second step (growth step). Though the film was delaminated just after the exposure to the air, the delamination behavior was quite different with the cBN films deposited without the mixing procedure. For the case with the pulse biasing the delamination traces were directed vertically and horizontally (fig. 8), while the cBN films deposited without the mixing procedure were delaminated uniformly. The directions of the traces correspond to the cleavages of the silicon substrate. Evidently the delamination occurred in the silicon substrate, not at the interface,

resulting from the adhesion improvement by the interface mixing. The cBN film with the mixing procedure with Ar- $5\%N_2$ showed almost the same delamination behavior as the cBN films without the mixing. Consequently, PBII can be effectively utilized for the purpose of the adhesion improvement with the insertion of the "glue layer" which enhances the interface mixing with the substrate and the film. However, what to extent the pulse biasing improves the adhesion strength, or what materials could be used for the "glue" buffer layers for various substrate materials should be clarified in the further study.

CONCLUSIONS

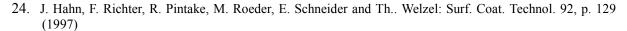
Cubic Boron Nitride (cBN) film depositions were performed by a radio frequency (RF) bias sputtering with a plasma based ion implantation. High voltage pulse biasing was detrimental for cBN nucleation even if the deposited film was almost stoichiometric. In contrast, once cBN nucleation occurred, the mixed phases of cBN and sp^2 bonded BN were able to be formed even with high voltage pulse biasing. The stress reduction of the cBN films deposited by the two step deposition procedure using PBII is attributed to the cubic-to- sp^2 phase transformation due to the high energy ion bombardment. The adhesion was improved by the interface mixing using PBII when the "glue" layer was inserted at the interface which enhanced the mixing.

ACKNOWLEDGEMENTS

This work is supported by the Frontier Carbon Technology (FCT) project, which is consigned to Japan Fine Ceramics Center (JFCC) by New Energy and Industrial Technology Development Organization (NEDO).

REFERENCES

- 1. N. Tanabe and T. Hayashi: Diamond Relat. Mater., 1(1992) 151
- 2. D. J.Kester and R. Messer: J.Appl.Phys., 72(1992) 504
- 3. O. Tsuda, Y. Yamada, T. Fujii, and T. Yoshida: J. Vac. Sci. Tech., A13(1993) 2843
- 4. D. L. Medlin, T. A. Friedmann, P. B. Mirkarimi, M. J. Mills, and K. F. MacCarty: Phys. Rev. B50(1994) 7884
- 5. H. Hofsass, C. Ronning, U. Griesmeier, M. Gross, S. Reinke, and M. Kuhr: Appl. Phys. Lett., 67(1995) 46
- 6. T. Ichiki and T. Yoshida: Appl. Phys. Lett., 64(1994) 851
- 7. S. Ulich, J. Scherer, J. Schwan, I. Barzen, K. Jung, H. Ehrhardt: Diamond and Related Mater., 4(1995) 288
- 8. W. Dworschak, K. Jung, and H. Ehrhardt: Diamond and Related Mater., 3 (1994) 337
- 9. M. Murakawa, S. Watanabe, S. Miyake: Mater. Sci. Eng., A140, p. 753 (1991)
- 10. T. Ikeda, Y. Kawate, Y. Hirai: J. Vac. Sci. Technol., A8, p. 3168 (1990)
- 11. M. Murakawa and S. Watanabe: Surf. Coat. Technol., 43/44, p. 145 (1990)
- 12. D. Litvinov, C. A. Tayler II, R. Clarke: Dia. Relat. Mater., 7 p. 360 (1998)
- 13. S. Reinke, M. Kuhr and W. Kulisch: Dia. Relat. Mater., 5, p. 508 (1996)
- 14. P. Widmayer, P. Ziemann, S. Ulrich and H. Ehrhardt: Dia. Relat. Mater., 6, p.621 (1997)
- 15. J. Ullmann, A. J. Kellock and J. E. E. Baglin: Thin Solid Films, 341, p. 238 (1999)
- 16. H. -G. Boyen, P. Widmayer, D. Schwertberger, N. Deyneka and P. Ziemann: Appl. Phys. Lett., 76, p. 709 (2000)
- 17. C. Fitz, A. Kolitsch and W. Moeller: Appl. Phys. Lett., 80 (2002) 55
- 18. M. Murakawa, S. Watanabe, S. Miyake: Dia. Film Technol., 5, p. 353 (1995) (52)
- 19. T. Watanabe, K. Yamamoto, O. Tsuda, A. Tanaka and Y. Koga, Surf. Coat. Technol., 156 (2002) 317
- 20. S. Schoser, J. Forget and K. Kohlhof, Surf. Coat. Technol., 93 (1997) 339
- 21. E. Richter, R. Guenzel, S. Parasacandola, T. Telbizova, O. Kruse and W. Moeller, Surf. Coat. Technol., 128/129 (2000) 21
- 22. C. Ronning, E. Dreher, H. Feldermann, M. Gross, M. Sebastian, H. Hofsaess, Diamond Relat. Mater., 6 (1997) 1129
- 23. P. B. Mirkarimi, K. F. McCarty, D. L. Medlin, Mater. Sci. Eng., R21 (1997) 47



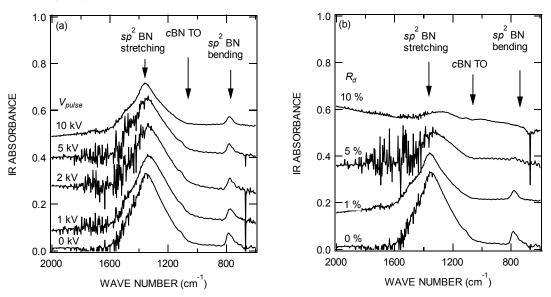


Fig. 3 IR spectra of BN films deposited by PBII : (a) with $R_d = 1\%$ and various V_{pulse} , (b) with $V_{pulse} = 10$ kV and various R_d .

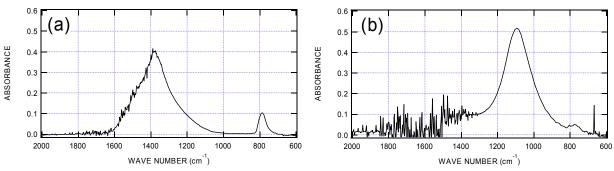


Fig.4 IR spectra of BN films deposited by sputter-PBII for 1200s. (a): with high voltage biasing superimposed with RF self biasing (fig. 2(b)), $V_{pulse} = 10 \text{ kV}$, $V_s = 200 \text{ V}$ and $R_d = 0.2 \%$. (b):conventional RF bias sputtering: $V_s = 200 \text{ V}$ and without high voltage pulse biasing (fig. 2(c)).

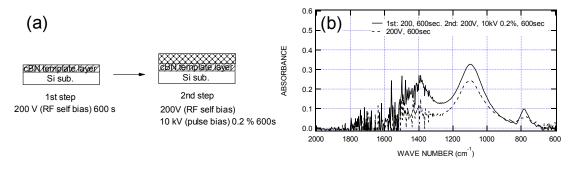


Fig. 5 cBN film deposition by the two step deposition method. (a) deposition procedure of the two step deposition, (b) IR spectrum of the cBN film. The conditions of the steps are as follow: 1^{st} : $V_s = 200 \text{ V}$ for 600 s, 2^{nd} : $V_{pulse} = 10 \text{ V}$ and $V_s = 200 \text{ V}$ for 600 s. The dashed line shows the IR spectrum of the template cBN film deposited with the condition of the 1^{st} step.

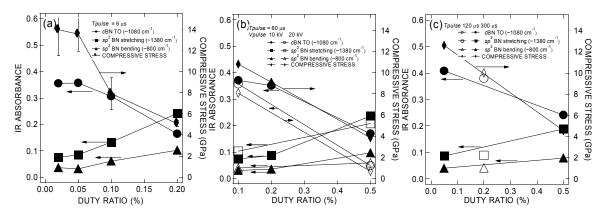


Fig. 6 Changes in the absorbances and the internal compressive stress of BN films deposited by two with the two step deposition. 1^{st} :, 2^{nd} with the duty ratio. (a) T_{pulse} =6 μ s,(b) T_{pulse} =60 μ s, V_{pulse} =10kV, 20kV, (c) T_{pulse} =120 μ s, 300 μ s.

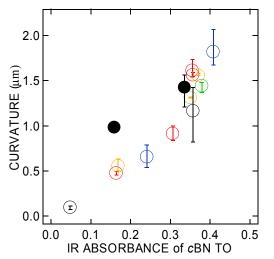


Fig. 7 Relationship between IR absorbance of cBN TO and the curvature of the films deposited by PBII.

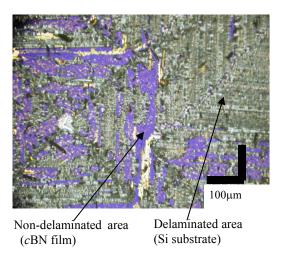


Fig. 8 Surface photograph of the cBN films deposited with the interface mixing by PBII.

NUCLEATION MECHANISM OF CUBIC BORON NITRIDE IN VAPOR PHASE DEPOSITION

Hangsheng Yang, Chihiro Iwamoto, and Toyonobu Yoshida

Department of Materials Engineering, School of Engineering, The University of Tokyo, Hongo 7-3-1,

Bunkyo-ku, Tokyo 113-8656, Japan

ABSTRACT

Cubic boron nitride (cBN) thin films were deposited on ultrathin Si flake substrates by inductively coupled plasma-enhanced chemical vapor deposition. The prepared films were sufficiently thin for direct HRTEM observation without inducing damage in the cBN films. Isolated cBN nuclei as small as 1 nm layer were observed on the textured tBN. The surface of cBN films was pure cubic phase without sp2-bonded BN, contrary to the so-called subsurface growth mechanisms. The chemical species responsible for cBN growth were analyzed by quadrupole mass analysis with ion energy analyzer (QMA-EA). QMA-IE analyses revealed that the boron source, B2H6, was totally ionized under the deposition conditions, while N2 was only partly ionized. The existence of neutral species such as N2 molecules inhibited cBN nucleation and growth. The introduction of Ar into the deposition system increased the N2 ionization yield markedly, which reduced the sp2-bonded BN formation from neutral N2 molecules on the growth surface and promoted cBN growth.

In summary, both damage-free HRTEM observations and QMA-IE analyses suggest that cBN nucleates at a top surface rather than in subsurface region in vapor phase deposition.

Keywords: Cubic boron nitride, CVD, HRTEM, QMA-EA, mechanism

A NANOINDENTATION STUDY OF THICK CUBIC BORON NITRIDE FILMS PREPARED BY CHEMICAL VAPOR DEPOSITION

C. Y. Chan, W. J. Zhang, K.M. Chan, I. Bello*, S. T. Lee

Center of Super Diamond and Advanced Films (COSDAF) and Department of Physics and Materials Science, City University of Hong Kong, Hong Kong SAR, P.R. China

S. Matsumoto

Advanced Materials Laboratory, National Institute for Materials Science, 1-1 Namiki, Tsukuba, Ibaraki 305-0044, Japan

ABSTRACT

The mechanical properties of high-quality cubic boron nitride (cBN) films deposited using fluorine chemistry were systematically investigated by nano-indentation measurements performed in both cross-sectional and plan-view directions. The large film thickness (\sim 5 μ m) allows the effective suppression of both substrate and indenter size effects. The hardness and elastic modulus values were found to be 70 and 800 GPa, respectively, which are the highest values ever obtained on cBN films deposited by either PVD or CVD methods so far (comparable to those reported for cBN crystals synthesized by high-pressure high-temperature methods). The variation of hardness across the cBN film thickness was investigated using a cross sectional configuration. In conjunction with the transmission electron microscopic observations, the relationship of the hardness measured with the crystallinity and crystal size/grain boundaries was discussed.

Keywords: cubic boron nitride, chemical vapor deposition, nano-indentation, hardness, elastic modulus

* Corresponding author: apibello@cityu.edu.hk

Influence of Impurities on the Morphology and the Raman Spectra of cubic Boron Nitride

Hermann Sachdev

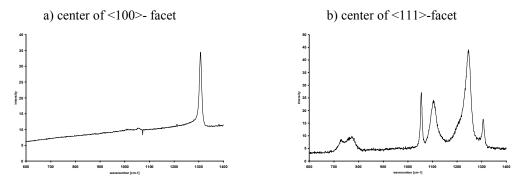
Institut für Anorganische Chemie FR 8.11, Universität des Saarlandes, Postfach 151150, D- 66041 Saarbrücken, e-mail: h.sachdev@mx.uni-saarland.de

Abstract

It is still a challenging problem to understand the growth mechanisms of cubic boron nitride (c-BN) in the high pressure high temperature (HPHT) synthesis as well as to develop film deposition techniques (CVD- or PVD-methods) of microcrystalline c-BN layers for protective or abrasive applications. It is possible to grow cm- seized diamond single crystals by HPHT- methods and to achieve microcrystalline diamond films by CVD- or PVD-methods with good mechanical properties¹, but regarding c-BN, even in the HPHT- process it is not possible to obtain well grown, large single crystals² and up to now, film deposition methods lead only to the formation of nanocrystalline c-BN layers of weak quality. The structural analogy between carbon- and boron nitride sp²-and sp³-phases is only valid regarding their physical and mechanical properties, but there is a significant difference in their syntheses^{3,4}. In order to enhance and modify c-BN growth, the understanding of the growth mechanism is of significant importance⁵.

A detailed Raman spectroscopic characterization of HPHT- c-BN samples with distinct morphology and facettation indicates a correlation between crystal impurities and the resulting morphology. The results reveal a strong anisotropy of <100>- and <111>- growth directions of c-BN, which are affected by crystal impurities and their nature will be discussed (fig. 1). The presented study reveal significant information to modify c-BN growth and to realize the growth of microcrystalline films of cubic boron nitride.

Fig. 1: Micro- Raman measurement of individual facets of a c-BN crystal



Literature: [1] B. Stritzker, M. Schreck, Diamond Related Mater. 5 (1996) 266 - 271; [2] E. Rapoport, Ann.Chim. Fr. 10 (1985) 607 - 638; [3] H. Sachdev, M. Strauß, Diamond Related Mater. 8 (1999) 319 - 324; [4] H. Sachdev, M. Strauß, Diamond Related Mater. 9 (2000) 614 - 619; [5] H. Sachdev, Diamond Related Mater. 10 (2001), 1390 - 1397.

NASA/CP—2003-212319 380 August 18, 2003

Persistence of graphite phase in G-ball under high pressure showing metallic behavior

Atsuko Nakayama -

Research Center for Advanced Carbon Materials, National Institute of Advanced Industrial Science and Technology (AIST)

atsuko-nakayama@aist.go.jp

Katsuya Shimizu, Takehiro Matsuoka

Grad. School of Engi. Sci., Osaka Univ.

Fumio Kokai

Faculty of Engi., Mie Univ.

Yoshinori Koga, Sumio Iijima

AIST

Abstract

Graphitic-carbon polyhedrons "G-balls" are supposed to have a closed-shell framework of graphite according to TEM image. It is expected that high-pressure structural-change of G-balls is topologically different from that of graphite. High-pressure x-ray powder-diffraction measurements of G-balls has been carried out at room temperature. In addition, the temperature dependences of electrical resistances were obtained in order to investigate the relationship between structures and electronic properties. The graphite phase in G-balls is very stable and does not have the phase transition even if the pressure is higher than 40 GPa. The volume reduces by 29 % at 43 GPa. The value of bulk modulus, B0, is determined to be B0=41.5 GPa. G-balls are geometrically difficult to cause the side-splitting between graphene sheets in comparison with graphite, resulting in absence the phase transition. Electrical resistance measurements exhibit the metallic behavior of G-ball at the pressure above 20 GPa at room temperature. The c-axis length shortens by 18 % at 20 GPa, which means the extraordinary overlapping between carbon pi-orbitals.

CUBIC BN SINGLE CRYSTALS AND SINTERED BODIES SYNTHESIZED AT HIGH PRESSURE

Takashi Taniguchi National Institute for Materials Science 1-1 Namiki Tsukuba Ibaraki 305-0044 Japan

ABSTRACT

Single crystals and sintered bodies of cBN were synthesized under high pressure and high temperature. For the growth of single crystals, temperature gradient method was applied at 5GPa and 1600 °C for 20-100 hrs. Be doped crystals exhibit p-type semiconducting properties and S-doped and unintentionally doped crystals exhibit n-type properties, as characterized by Hall measurements. Although the origin of the donor level is not qualified yet in the unintentionally doped crystals, oxygen, carbon, or nitrogen vacancy may be the candidate for the donor. It was found that additive of Be atoms were localized as acceptor in particular growth sectors of the crystals. Consequently, self-organized p-n domains were realized in the Be-doped crystals showing ultra-violet light emission by inducing current across the sector boundaries. Some advancement has also been achieved to obtain colorless crystal, which has very high electrical resistivity and exhibiting band edge nature in optical properties.

In view to practical application of cBN, improvement of the mechanical properties of the sintered body is important. It can be seen that optimization of sintering conditions, such as pressure, temperature, and initial grain size will allow us to fabricate binder-less bodies with fine-grained structure. Recent progress of synthesis of fine-grained cBN sintered body without binder will be also described.

Key Word: cBN, Single crystal, Semiconductor, Binderless sintered body, High pressure.

Corresponding author: T.Taniguchi National Institute for Materials Sciences, 1-1 Namiki Tsukuba Ibaraki 305-0044 Japan TEL:029-851-3354 ext:563 FAX:029-858-5654 TANIGUCHI.takashi@nims.go.jp

CHEMICAL SYNTHESIS OF GRAPHITE-LIKE B/C/N MATERIALS LEADING TO THE SHOCK SYNTHESIS OF THE HETERODIAMOND

TAMIKUNI KOMATSU

2-24-4 Sakura, Tsukuba-shi, Ibaraki 305-0003, Japan Tel: +81-029-857-7325, Fax: +81-029-857-7325, E-mail: <u>BRA01367@nifty.ne.jp</u>

ABSTRACT

Graphite-like B/C/N materials, g-BC_xN, are chemically prepared in very high yields using a polymer pyrolysis system of boron trichloride and commercially available N-containing materials such as tetracyanoethylene and polyacrylonitrile. Using the g-BC_xN materials, a series of new diamond materials, B/C/N heterodiamond, are shock-synthesized.

amine, nitrile, cyanamides, etc. $\frac{BCl_3$, ambient temp polymerization $\frac{N_2 \ 1000^{\circ}\text{C}}{\text{carbonization}} \xrightarrow{\text{heat-treatment}} \frac{g\text{-CN}_x(BN)_y}{\text{heat-treatment}}$

The Lewis acid-base reaction initially occurs between BCl_3 gas and the basic organic compounds, is followed by polymerization, carbonization and heat-treatment. The g- BC_xN materials over the almost entire range of compositions can be prepared: the g- BC_3N material is obtained in ca. 75 % yield from polyacrylonitrile, and the g- BC_4N is in nearly 100 % yield from tetracyanoethylene. The materials have a miscible blend (hybrid) structure consisting of CN_x and $(BN)_y$ segments and have turbostatic hexagonal structures similar to the structure of the chemical vapor deposition g- BC_2N . The g- BC_xN materials obtained are explosively shock-compressed and successfully phase-transformed into their almost allotropic heterodiamond materials. Keywords: polymer pyrolysis, carbonization, shock-compression, boron carbide nitride, heterodiamond

INTRODUCTION

Over the past two decades, the new carbon-based BC_xN and CN_x materials combined with graphite-like sp² and diamond-like sp³ bonds have been prepared for the purpose of their unknown high potentials as hard materials and high temperature semiconductors. Many researchers have prepared a variety of graphite-like BC_xN (g-BC_xN) materials by solid-gas reaction (ref.1 and 2), precursor pyrolysis (ref. 3 to 5) and mainly by chemical vapor deposition (CVD) (ref. 6 to 9). A few g-BC_xN materials prepared by CVD have been transformed into cubic BCN (ref. 10) and cubic BN/C mixed crystals (ref. 11) under static high pressure and high temperature conditions. In 1993, we prepared for the first time a single phase of diamond-structured BC_{2.5}N material (heterodiamond) by explosive shock compression of the CVD-synthesized g-BC₂N. It was confirmed that the shock-synthesized heterodiamond exists as polycrystalline nanoparticles and possesses desirable characteristics of both diamond and cubic BN, i.e., a good high thermal oxidation resistance superior to diamond, the highest bulk modulus next to diamond and very small thermal expansion (ref. 12 to 14). In particular, the heterodiamond sinter has all of the ideal properties for steel-cutting tools (ref. 15).

For the purpose of industrial uses of the heterodiamond materials, bulk synthesis of their precursors, g-BC_xN, is essential and chemical synthetic methods must be most effective for this purpose. However, useful methods were almost unknown. Recently, we developed a series of C₃N₄-like polymers composed of heptaazaphenalene nuclei (ref. 16 to 18). The polymers were found to react with boron halides and change into new g-BC_xN materials of high BN contents. This reaction system was further extended to various organic Lewis bases such as amines and nitriles (ref. 19). The chemically synthesized g-BC_xN materials were investigated in terms of appropriateness as the precursors of the heterodiamond. In this conference, the bulk synthesis of the g-BC_xN materials and shock-synthesis of the heterodiamond are reported.

EXPERIMENTAL

Preparation of the g-BC_xN materials

Commercially available materials such as melamine, melamine-formaldehyde resin, urea-formaldehyde resin, hexamethylenetetramine (hexamine), acetonitrile, adiponitrile, malononitrile, acrylonitrile (AN), tetracyanoethylene (TCNE), polyacrylonitrile (PAN), diaminomaleonitrile and dicyanodiamide were used as the N-containing starting materials. Boron trichloride (BCl₃) was used as B-source. The B/C/N samples were prepared according to the synthetic procedure reported previously (ref. 19). The initial reaction between the

starting material and BCl₃ and successive polymerization of the initial product were carried out in a three-necked separable quartz flask equipped with a gas-admitting tube, mechanical quartz stirrer and vent tube and a furnace. Gaseous BCl₃ from a pressure bomb was directly introduced into the apparatus containing the starting material. From acetonitrile, malononitrile, acrylonitrile and tetracyanoethylene (TCNE), white adducts sensitive to moisture were initially formed at room temperature. The adducts underwent autocatalytic polymerization at ambient temperatures below 373 K. The polymeric intermediates were carbonized at 1273 K under an inert atmosphere until all volatile products were expelled, and followed by heat treatment at 1773 K in a stream of N₂ gas. Bulky and brittle black solids were obtained.

Preparation of the BC_xN heterodiamond materials

The above bulky solids were mechanically crushed into fine powders. The fine powders (12 g) were mixed with copper powders (188 g), pressed into disks of the apparent density of 5.6-5.8 g cm⁻³, followed by shock compressed. Fig. 1 shows a cylindrical shock compression apparatus used in the experiment. The apparatus was constructed with an inner steel cylinder filled with the disks and an outer steel flyer surrounded by an explosive on the outside. A TNT-mixed explosive (2 kg) with a detonation velocity of 5.0-5.5 km s⁻¹ was used. The incident shock pressure and temperature on the sample were estimated to be 35 GPa and 3500 K, respectively. The recovered sample was machined, immersed in conc. HNO₃ to dissolve copper matrix, boiled in an acid mixture of conc. H₂SO₄ (70 parts) and conc. HNO₃ (30 parts) to decompose an unreacted material, boiled in a 30 % NaOH solution to dissolve trace amounts of contaminants, washed with distilled water and dried at 473 K. Bluish black fine powders were obtained.

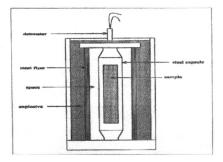


Fig. 1 Cross section of the cylindrical shock-compression apparatus.

Characterization

The chemical compositions of the samples were determined by CHN elemental analysis and ICP-mass analysis for boron contents. The analysis was carried out three times and the results were averaged. Trace amounts of metallic contaminants were detected by an electron probe X-ray microanalyser. The structures of the materials were investigated by IR, Raman scattering, X-ray photoelectron spectroscopy (XPS), X-ray powder diffraction (XRD), high-resolution transmission electron microscopy (HRTEM) equipped with parallel electron energy-loss spectroscopy (PEELS) and electron diffraction (ED), and field emission scanning electron microscopy (FE-SEM). The heat resistance to oxidation in a stream of air was investigated by thermogravimetry (TG) in the range 300-1573 K at a heating rate of 20K min⁻¹.

RESULTS AND DISCUSSION

Bulk synthesis of the g-BC_xN materials

All the B/C/N samples contained large amounts of carbon, nitrogen and boron. The contents of hydrogen were below 0.1 %, a detection limit of the CHN analyzer. IR spectroscopy measured no NH stretching bands. Chemical compositions and yields of the BC_xN materials greatly depended on the starting materials as shown in Table 1. The materials are described with a formula of CN_x(BN)_y and CB_x(BN)_y consisting of a large portion of BN pairs and slight excesses of N or B elements. The B/N atomic ratio to carbon is widely ranging from 1 to 10. The aromatic amines such as melamine and its derivatives that are resistive to nitrogen evolution during carbonization produced small amounts of B/C/N materials exhibiting very high B/N content. On the other hand, the aliphatic N-rich amines and nitriles gave low B/N content. Nitriles such as AN, TCNE, PAN and malononitrile that are easily polymerized (or cyclopolymerized) gave them in very high yields.

Table 1. Compositions and yields of the chemically synthesized BC_xN materials.

Starting materials	Reaction	BCl ₃	B/C/N	Yield
	systems	Temp(K)	Composition	(%)
Melamine	Solid-gas	473	$CB_{0.97}N_{1.01}$	10
Melamine resin	Solid-gas	673	$CB_{0.49}N_{0.60}$	19
Urea resin	Solid-gas	473	$CB_{0.27}N_{0.28}$	15
Hexamine	Solution-gas	RT	$CB_{0.22}N_{0.27}$	35
Acetonitrile	Liquid-gas	RT	$CB_{0.50}N_{0.50}$	30
Adiponitrile	Liquid-gas	RT	$CB_{0.19}N_{0.18}$	50
Malononitrile	Liquid-gas	323	$CB_{0.33}N_{0.25}$	60
AN	Liquid-gas	RT	$CB_{0.32}N_{0.32}$	70
TCNE	Solution-gas	RT	$CB_{0.19}N_{0.22}$	98
PAN	Solution-gas	473	$CB_{0.21}N_{0.22}$	75
Diaminomaleonitrile	Solution-gas	RT	$CB_{0.28}N_{0.29}$	70
Dicyanodiamide	Solution-gas	RT	$CB_{0.19}N_{0.18}$	10

IR spectra of all the B/C/N materials were similar in appearance to the spectrum of a mixture of carbonaceous CN_x and boron nitride as shown in Fig.2. The B-N bonds at 1400 cm⁻¹ are, however, shifted 27 cm⁻¹ to higher wavenumber from the peak of h-BN. This shift is much larger than those arising from fine carbon particles present in h-BN. The large shift indicates chemical bonds between the CN_x and BN segments. X-ray powder diffraction patterns of the B/C/N materials are similar to those of turbostatic hexagonal carbon-based materials such as g-BCN, g-BC₃N and g-CN_x. A half width of the (002) peak was 4-5 degrees similar to that of the CVD-synthesized BC₃N.

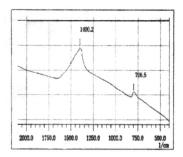


Fig. 2 IR spectrum of the chemically synthesized BC₂N.

Shock-synthesis of the heterodiamond

The chemical compositions of the purified materials obtained by shock compression of the starting BC_2N and BC_3N samples were $BC_{2.5}N$ and $BC_{3.5}N$, respectively. Little amounts of carbon, boron and nitrogen elements probably volatile during passing of shock-wave. The purified materials were assigned to the heterodiamond materials by XRD and IR measurements. Table 2 shows the compositions and yields of the shock-synthesized materials. The yield of the heterodiamond having large B/N content was a little lower in comparison to the yield of the shock diamond.

Table 2. Compositions and yields of the shock-synthesized materials.

Starting samples	Shock-synthesized materials	Yield
Composition	Composition	(%)
BCN	BC _{1.4} N	5
BC ₂ N	BC _{2.5} N	7
BC ₃ N	BC _{3.5} N	7
BC ₅ N	BC _{6.0} N	10
Control: Graphite	С	10

Fig. 3 shows the XRD pattern of the shock-synthesized material of composition $BC_{2.5}N$. This pattern is assigned to a cubic crystal system. The (100), (200), (222) and (420) reflections are absent similar to the pattern of the diamond structure obeying the extinction rule. The lattice constant estimated from the (111) peak position was $a_0 = 0.3611$ nm between those of diamond and cubic BN and close to the value of cubic BN rather than that of diamond. Fig. 4 shows the IR spectrum of the same material. The material indicates a very broad peak due to sp³ bonds at 1088 cm⁻¹ that is shifted 12 cm⁻¹ lower wavenumber from the peak of diamond. The peak position of the heterodiamond materials tends to approach more and more closely to the position of diamond with decreasing B/N content, however, is much lower than that of cubic BN.

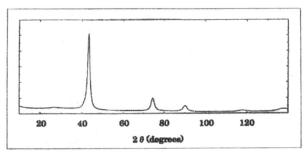


Fig. 3 XRD pattern of the shock-synthesized material of composition BC_{2.5}N.

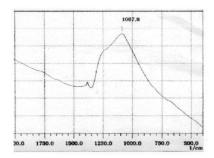


Fig. 4 IR spectrum of the shock-synthesized material of composition BC_{2.5}N.

REFERENCES

- 1. T. Y. Kosolapova, et al., Poroshk. Metall. (Kiev), 1 (1971) 27.
- 2. M. Kawaguchi and T. Kawashima, J. Chem. Soc., Chem. Commun., 1993, 1133.
- 3. L. Maya and L. A. Harris, J. Am. Ceram. Soc., 73 (1990) 2498.
- 4. J. Bill, M. Friess and R. Riedel, Eur. J. Solid State Inorg. Chem., 29 (1992) 195.
- 5. Y. Goto, et al., J. Eur. Ceram. Soc., 19 (1999) 2695.
- 6. A. R. Badzian, et al., Khim. Svyaz. Poluprovodn. Polumet., 1972, 362.
- 7. R. B. Karner, et al., *Mater. Res. Bull.*, 22 (1987) 399.
- 8. J. Kouvetakis, et al., Synth. Met., 34 (1989) 1.
- 9. M. Kawaguchi, T. Kawashima and T. Nakajima, Chem. Mater., 8 (1996) 1197.
- De Beers Industrial Diamond Division Ltd., Ger. Pat., 2806070, 1979; R. J. Wedlake and A. L. Penny, Chem. Abstr., 90 (1979) 42865Z.
- 11. A. R. Badzian, Mater. Res. Bull., 16 (1981) 1385.
- 12. T. Komatsu, et al., J. Mater. Chem., 6 (1996) 1799.
- 13. T. Komatsu, Y. Kakudate and S. Fujiwara, J. Chem. Soc., Faraday Trans., 92 (1996) 5067.
- 14. T. Komatsu, J. Chem. Soc., Faraday Trans., 94 (1998) 101.
- 15. T. Komatsu, et al., J. Mater. Chem., 11 (2001) 1781.
- 16. T. Komatsu and T. Nakamura, J. Mater. Chem., 11 (2001) 474.
- 17. T. Komatsu, J. Mater. Chem., 11 (2001) 799.
- 18. T. Komatsu, J. Mater. Chem., 11 (2001) 802.
- 19. T. Komatsu, J. Mater. Chem., 12 (2002) 1288.

PROPERTIES AND APPLICATIONS OF DLC

Resonant Raman spectra of Carbon Systems

J. Robertson and A.C. Ferrari

Department of Engineering, University of Cambridge, Cambridge, CB2 1PZ, UK

Abstract

Raman spectroscopy is a non-destructive means to characterise many carbon systems, including diamond, graphite, nano-diamond, carbon nanotubes, diamond-like carbon and carbon nitride alloys. Raman at a single wavelength excitation gives only limited information. We review here how multi-wavelength Raman gives much more information on these phases, because it uses the resonant Raman condition.

Introduction

Raman is the inelastic scattering of light by phonons in a crystal, or equivalently, the differential change in the dielectric constant by a Raman active vibrational mode. A perfect crystal of diamond has a single Raman active mode at 1332 cm⁻¹. This peak has been used for 15 years as the key indicator of the quality of diamond in polycrystalline diamond grown by chemical vapour deposition (CVD). The width of the peak is used as an indicator of the diamond quality and the shift of the peak indicates the presence of stress.

CVD diamond can also have two or three other modes, centred on 1590 cm⁻¹, 1350 cm⁻¹ and sometimes 1140 cm⁻¹. These are from sp² bonded carbon. Graphite consists of hexagonal sp² bonded sheets and is a zero band gap semiconductor. A single layer of graphite has one Raman active mode at 1580 cm⁻¹ due to in-plane vibrations of E_2 symmetry, labelled 'G'. The Raman spectrum of microcrystalline graphite has another peak, called 'D', at about 1350 cm⁻¹. Diamond-like carbon (DLC) and its alloys contain both sp³ and sp² bonded carbon. The Raman scattering efficiency of sp² sites is 50-260 times higher than sp³ sites. This means that even those types of DLC containing the maximum sp³ content of ~90%, their Raman spectrum is dominated by the sp² bonding features, the G and D peaks.

Resonant Raman

The Raman scattered intensity is given by [1]

$$C = \left| \frac{<0 \mid H_{eR}(\omega_i) \mid a >< a \mid H_{e-ion} \mid a >< a \mid H_{eR}(\omega_s) \mid 0 >}{(E_a - \hbar \omega_i)(E_a - \hbar \omega_s)} \right|^2$$

where $|0\rangle$ is the initial state, H_{eR} is the electronic interaction at constant atom position R $H_{e\text{-ion}}$ is the electron-lattice interaction, $|a\rangle$ is an intermediate state, ω_i is the incident photon energy and ω_s is the scattered photon energy. Resonance occurs when the intermediate state $|a\rangle$ corresponds to an actual electronic state. There can be a single resonance or a double resonance.

First order Raman scattering in systems such as silicon [2,3] are relatively independent of excitation energy because the excitation is over the band gap into a continuum of states, so there is resonance but with no particular enhancement. There is a different situation in diamond. The excitation (unless for photons over 5.5 eV) is from the valence band to a virtual state in the gap, so there is no resonance. In contrast, in sp² systems, the excitation energy can always resonate with a particular band gap, because graphite is a zero gap semiconductor. This realisation finally led to a proper understanding of the origin of the D peak in graphite [4].

Graphite

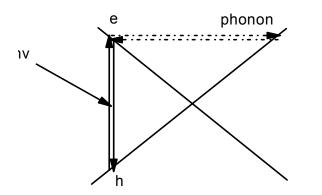
The D mode in graphite is a symmetric breathing mode of A₁ symmetry of the hexagonal arrays of carbon atoms [5,6]. It corresponds to a mode at the K zone-boundary and only appears with disorder. An unusual feature of the D peak is that its wavenumber disperses with laser energy [7,8].

Fig 1 shows the band structure of graphite which has a zero gap at the K point of the Brillouin zone, with valence and conduction bands that vary linearly away from K. This means that constant energy surfaces are circles around K in the 2D zone. An incident photon of a given energy will always find a direct transition from the valence to the conduction band. The electron of wavevector k can now be scattered by a phonon to the band at -k. It can then be scattered back to the left, by a defect. The electron then recombines with the hole to emit the outgoing Raman photon. The condition for this process is that the electron wave-vector, k, is related to that of the phonon, q, by [4]

Thus, as the excitation energy increases, the phonon wavenumber moves away from K at twice the rate of the electron wavenumber, and this increases the phonon wavenumber at a rate of about 55 cm⁻¹/eV, the observed dispersion [7,8].

It is slightly more complicated than this because k and q are measured from the K point, not the zone centre Γ . When this factor is included, it is realised that in principle all Raman transitions in graphite could be a double resonance, not just the D modes [9]. This can be used to map out the phonon dispersion curves of graphite.

This ties up most of the Raman questions in graphite. However, there remains the question of which mode is the D mode. It should have A_1 symmetry [5,10]. But the above assignments take a mode of E symmetry at K [11]. There are no experimental data from neutron scattering or energy loss to settle this point. It is not clear if the calculated phonon dispersion curves (Fig 2)[12] can take an A_1 mode at the required wavenumber of 1350 cm⁻¹.



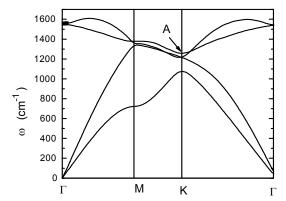


Fig. 1. Schematic band structure of graphite showing Fig. 2. Phonon dispersion curves for graphite [14]. double resonance condition [5].

Carbon nanotubes

Carbon nanotubes are rolled sheets of graphite, either single walled or multi-walled. In single walled nanotubes (SWNTs), the wrapping vector or chirality determines their structure [13]. The wrapping vector is expressed as a pair of integers (n,m) times the graphite bond length, a. Raman has been extremely valuable in determining the properties of nanotubes [13-15]. This is because their one-dimensionality creates large van-Hove singularities in the electronic density of states (DOS), which in addition to resonance, enhances the Raman cross-section. A single CNT can in fact be observed [16,17]. The Raman of SWNTs shows three main features, a 'radial breathing mode' (RBM) at around 200 cm⁻¹, the D peak, if it has defects, and the G tangential modes. The RBM is very valuable because its wavenumber varies inversely with tube diameter [15],

$$\omega = A/d$$

where $A = 222 \text{ nm/cm}^{-1}$.

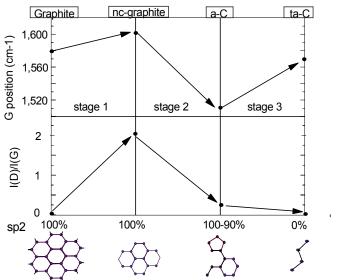
As the π electron states of a SWNT are derived from graphite's by zone folding, the energy difference of the van Hove singularities in the DOS also varies inversely with tube diameter. Raman is at resonance when the photon energy matches these transitions. The resonance conditions on the G modes can be used to determine the (n,m) values [17]. This is a much simpler process that the alternative of using scanning tunnelling microscopy.

There are still some questions about mode assignments in SWNTs. The G peak of tangential modes is split into a pair. The upper mode was attributed modes along the tube axis and the lower mode to circumferential modes. Warping is expected to lower the stiffness of bonds around the tube [12]. However, Raman active modes in a long thin shape must have A not E symmetry, and a different assignment is then given [15].

Diamond-like Carbon

Diamond-like carbon is a metastable form of amorphous carbon (a-C) or hydrogenated amorphous carbon (a-C:H) containing a significant fraction of sp³ bonds [18,19]. Raman is also a very popular characterisation

method of DLC. This follows the ability to understand the trends in the behaviour of the G and D peaks with degree of amorphous character, along the so-called amorphisation trajectory of 3 stages, from single crystal graphite to fully sp³ bonded DLC [11](Fig 3). Recall that the Raman spectrum will only depend on how the sp² component of the bonds varies along this trajectory, so it can be described in terms of the correlation length of the sp² bonding, L_a.



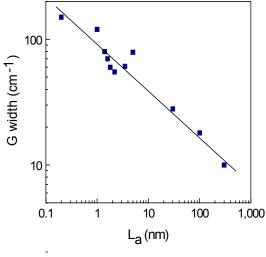


Fig. 3. Amorphisation trajectory for carbon [10].

Fig. 4. Width of G band versus disorder [20].

Stage 1 is the disordering of single crystal graphite into micro-crystalline graphite, but retaining the hexagonal sheets of atoms. L_a decreases from infinity to about 1 nm. Stage 2 is the topological disordering of hexagonal sheets of graphene to give sp^2 bonded amorphous C. L_a decreases from 1 nm to 0.2 nm. Stage 3 corresponds to the transformation of sp^2 a-C to sp^3 a-C, during which the configuration of the sp^2 sites changes from aromatic to olefinic. L_a remains at 0.2 nm. The first thing to notice is that the peak widths (eg of the G peak) vary inversely with L_a [20], see Fig 4. This factor can be used to check which stage you are in.

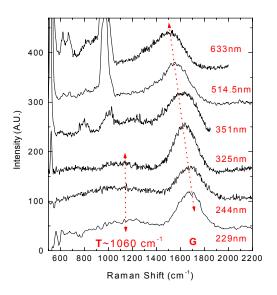
Fig 3 shows the variation of G position and D to G intensity ratio I(D)/I(G) through these stages [10]. The G peak moves up slightly through stage 1, due to phonon confinement, and to the upward phonon dispersion curve of graphite away from Γ . I(D)/I(G) increases to a maximum following the Tuinstra-Koenig relationship, $I(D)/I(G) = k/L_a$. In stage 2, the G peak moves down, as the bonds on average get weaker with the introduction of disorder. I(D)/I(G) decreases to zero following the relationship $I(D)/I(G) = k'(L_a)^2$. In stage 3, the G peak becomes much broader and asymmetric. When fitted by a Breit-Wigner-Fano line shape, not a Gaussian, the peak position moves up towards 1580 cm⁻¹. This is its graphite position, but the mode is not like in graphite, it is localised on a pair of sp² carbon atoms. The D peak remains at zero intensity.

Raman only measures the sp² configuration. We have so far assumed a unique relationship between the sp² configuration and sp³ fraction. However, this need not always hold. For example, annealing or deposition at high temperatures causes sp² sites to cluster, while the sp³ fraction is like that at lower temperatures. This non-uniqueness has been called hysteresis [10]. It is not possible to resolve this question using Raman at a single wavelength.

There are many interesting features to the excitation of Raman of DLC over a range of photon energies [21]. Fig. 5 shows the multi-wavelength Raman spectra of tetrahedral amorphous carbon (ta-C), a highly sp³ bonded version of a-C. Firstly, a new mode appears around 1040 cm⁻¹ when the photon excitation exceeds about 4.5 eV or 300 nm. This 'T' peak is due to sp³ bonded sites, which are now directly excited by excitation of the σ states [22,23]. Second, the G and D peaks, both due to sp² sites, both show dispersion. The G dispersion is shown in Fig 6. In this case, the rate of dispersion increases with the amount of disorder [21]. There is no dispersion for graphite and microcrystalline graphite, some dispersion in sp² bonded a-C, and a very large dispersion in ta-C.

The second point is that the electronic states and vibrational modes of sp² aromatic clusters map onto a graphite lattice by folding the Brillouin zone [10]. Thus, similar resonance effects are expected in the amorphous carbons and graphite. The G peak dispersion arises because the photon energy resonates with the band gap of a particular sp² bonded cluster. For aromatic clusters, the band gap varies inversely with the size of the cluster [18]. The G mode frequency varies with the cluster size, and increases strongly when the bonding moves from aromatic to

olefinic. This causes the very large G peak dispersion seen in ta-C, as infra-red photons resonate with the few large aromatic clusters while the UV photons will resonate with C=C bonded pairs with the highest vibrational frequency [21]. The D peak behaves differently. The D peak disperses in perfect graphite, as we noted above. Interestingly, the frequency dispersion of the D peak gets *less* as the disorder increases.



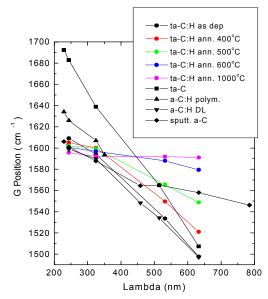
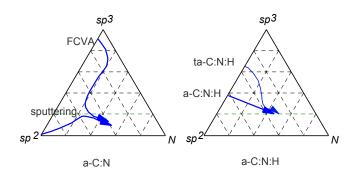


Fig. 5. Raman spectra of ta-C excited at different wavelengths.

Fig. 6. Dispersion of G peak in various carbons, as function of disorder.

Carbon Nitride Alloys

The original objective of research in carbon nitride was to synthesise crystalline C_3N_4 , which is predicted to have a hardness comparable to diamond. However, this has not happened. There is nevertheless considerable interest in the amorphous phases $a-CN_x$ and $a-CN_x$:H because they can show different mechanical properties than simple nitrogen-free DLC. An example is their use as a protective coating of magnetic storage disks.



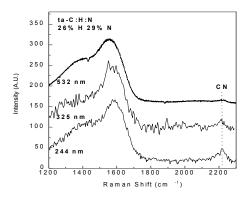


Fig. 7. Ternary phase diagrams of a-C:N and a-C:N:H [24].

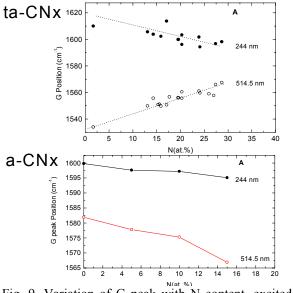
Fig. 8. Raman spectra of ta-C:N:H

We have recently classified the bonding in carbon nitride alloys into four categories, high sp² and high sp³ unhydrogenated alloys and high sp² and high sp³ hydrogenated alloys [24]. Their compositions follow the ternary phase diagrams shown in Fig 7.

There has been considerable effort to use Raman to determine the bonding in carbon nitride systems. The addition of N promotes the appearance of a vibrational mode around 2200 cm⁻¹, which is due to the -C≡N group, seen for example in the spectra of a ta-C:N:H sample in Fig. 8. Otherwise, we believe that no unique features in the IR or Raman spectra in the 500-2000 cm⁻¹ range can be attributed to specific C-N bonding. This is because the C-N

vibrational modes are not localised, and therefore they are mixed with the other C-C modes. In this way, the vibrational features of the 500-2000 cm⁻¹ range can be interpreted using the same framework as that used for N-free diamond-like carbon.

The main features are the G and the D peak. The dispersion of the G peak is very useful in showing the type of carbon nitride under study. Let us assume that it is known if the carbon nitride does or does not contain hydrogen, from the IR spectrum in the 3000-3300 cm⁻¹ range. The question is then whether it is sp²-rich or sp³-rich. The behaviour of nitrogen is opposite in the two cases. If N is added to sp²-rich a-C or a-C:H, for example formed by sputtering, then N tends to increase the C sp³ bonding [25], by encouraging the network to cross-link. The network also becomes less graphitic with more topological disorder, so the sp² bonded units which dominate the Raman scattering become smaller. On the other hand, if N is added to sp³-rich a-C, for example formed by cathodic arc, the N tends to reduce the amount of sp³ bonding, and to make the sp² sites more graphitic [26].



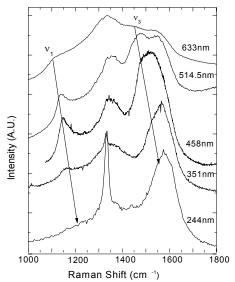


Fig. 9. Variation of G peak with N content, excited at 244 nm and 514 nm.

Fig. 10. Raman spectrum of typical nanocrystalline diamond excited at different wavelengths.

These trends are clear in the multi-wavelength Raman spectra, which thereby become the simplest method to observe this [24]. Fig 9(a) shows that the variation of G peak wavenumber with N addition for the high sp³ ta-C:N. The G peak lies at 1620 cm⁻¹ for 244 nm excitation and at 1540 cm⁻¹ for 514 nm excitation, as expected for ta-C. It moves to 1600 and 1560 cm⁻¹ respectively for 30% added nitrogen. This decrease in dispersion with added N indicates that the bonding has become more sp² and graphitic, if one compares with Fig 8. In contrast, Fig 9(b) shows that the G peak in low sp³ a-C:N lies at 1600 and 1582 cm⁻¹ for 244 nm and 514 nm excitation. It moves to 1595 and 1567 cm⁻¹ respectively, when 15% of N is added. This increase in dispersion with added N indicates that the aromatic character of the sp² bonding has decreased, probably because of an increase in the sp³ content.

The final thing about Raman and carbon nitride is that it could be used to prove that a sample was C_3N_4 . Crystalline C_3N_4 is difficult to make probably because the competing phases are more stable. It differs from the competing phase because it is fully σ bonded, whereas the competing phases are sp^2 and π bonded. In fact, nitrogen is known in chemistry to promote sp^2 bonding of the adjacent carbons. The presence of empty π^* states can be determined by Electron energy loss spectroscopy or equivalent methods like XANES [27]. The other problem is that the presence of Si from the substrate can stabilise the β - C_3N_4 structure, as in β - Si_3N_4 . Now, Raman from π bonds will always show dispersion, whereas Raman vibrations of σ bonds will not. Thus, the proof of the existence of C_3N_4 is that it should not contain Si and that none of the Raman modes should show dispersion.

Nano-crystalline diamond

Poor growth conditions during CVD diamond lead to the production of 'nano-crystalline' diamond. However, this material is now of interest in its own right, as it is a form of polycrystalline diamond with a smooth

surface. The formation of nano-crystalline diamond coincided with the appearance of a Raman peak at 1150 cm⁻¹ as in Fig. 13. Raman scattering in small crystals leads to the participation of phonon modes away from the zone centre. Ultimately, there is the loss of k selection, all phonon modes become allowed, and the Raman spectrum will become the vibrational density of states. It was natural to assign this peak to nano-crystalline diamond [28] because the peak intensity seemed to correlate with the fraction of nanocrystalline diamond and because the wavenumber 1150 cm⁻¹ corresponds roughly to the peak in the vibrational density of states (VDOS) of diamond.

This assignment was questioned on two main grounds [29]. First, although it is called nanocrystalline diamond, the grain size is actually 100 nm or more, not 1 nm. Thus, there is little phonon confinement and little loss of k-selection. Second, the 1150 cm⁻¹ mode is found to disperse with laser excitation energy, as seen in Fig 4. A VDOS feature cannot disperse. On the other hand, this is just as expected for a mode from sp² bonded sites, for example in a grain boundary.

Interestingly, by subtracting the G and D peaks from the Raman spectrum, the underlying spectrum was recovered, and it was found to fit that of trans-polyacetylene (trans-PA)[29]. The peak's dispersion also fitted. Thus, the 1150 cm⁻¹ is attributed to intensified scattering from an sp²-like grain boundary phase. However, the assignment to trans-PA was not fully accepted for two reasons. First, the correlation between the 1150 cm⁻¹ peak and the nanocrystalline fraction is observed, and it is unclear why this should relate to the intergranular phase. Second, trans-PA contains hydrogen and it decomposes at about 400C. Nevertheless, the assignment has been verified because (a) the 1150 cm⁻¹ peak is removed by thermal annealing in vacuum at 800-900C [30], as expected for a H-related peak (but at much higher temperature than for external trans-PA), and (b) the mode is found to be red-shifted in deuterium substituted samples [31].

References

- 1. P Y Yu and M Cardona, 'Fundamentals of Semiconductors', Springer (1999) p390
- 2. J. B. Renucci, R. N. Tyte and M. Cardona, Phys, Rev. B, 11, 3885 (1975)
- 3. M Cardona, P B Allen, Helv Phys Acta 58 307 (1985)
- 4. C. Thomsen, S. Reich, Phys. Rev. Lett. 85, 5214 (2000).
- 5. F. Tuinstra and J. L. Koenig, J. Chem. Phys. **53**, 1126 (1970)
- 6. C. Mapelli, C. Castiglioni, F Negri, G. Zerbi, J Chem Phys 114, 963 (2001) and preprint
- 7. R. P. Vidano, D. B. Fishbach, L. J. Willis, T. M. Loehr, Solid. State Comm. 39, 341 (1981)
- 8. I. Pocsik, M. Hundhausen, M. Koos, L. Ley, J. Non-Cryst. Solids **227-230**, 1083 (1998)
- 9. R Saito, A Jorio, A G Souza-Filho, G Dresselhaus, M D Dresselhaus, Phys Rev Lett 88 027401 (2001)
- 10. A C. Ferrari, J. Robertson, Phys. Rev. B, **61**, 14095 (2000)
- 11. R. A. Jishi, L. Venkantaraman, M. S. Dresselhaus and G. Dresselhaus, Chem. Phys. Lett. 209, 77 (1993)
- 12. O Dubay, G Kresse, Phys Rev B 67 035401 (2003)
- 13. M S Dresselhaus, P C Eklund, Adv Phys 49 705 (2000)
- 14. A Jorio, R Saito, J H Hafner, C M Lieber, T McClure, M S Dresselhaus, Phys Rev Lett 86 1118 (2001)
- 15. J Maultzsch, S Reich, C Thomsen, Phys Rev B 65 233402 (2002)
- 16. G S Duesburg, I Loa, M Burghard, K Syassen, S Roth, Phys Rev Lett 85 5436 (2000)
- 17. A Hartschuh, E J Sanchez, X S Xie, L Novotny, Phys Rev Lett 90 099503 (2003)
- 18. J. Robertson, Adv. Phys., **35**, 317 (1986)
- 19. J. Robertson, Mat. Sci. Eng. Rep. **37** 129 (2002)
- 20. D. S. Knight and W. B. White, J. Mater. Res. 4, 385 (1989)
- 21. A. C. Ferrari, J. Robertson, Phys. Rev. B, **64**, 075414 (2001)
- 22. K. W. K. Gilkes, H. S. Sands, D. N. Batchelder, J. Robertson, W. I. Milne, Appl. Phys. Lett. 70, 1980 (1997)
- 23. M Profeta, F Mauri, Phys Rev B 63 24515 (2001)
- 24. A C Ferrari, S E Rodil, J Robertson, Phys Rev B, to be published (2003)
- 25. N. Hellgren, M. P. Johansson, E. Broitman, L. Hultman, and J. E. Sundgren, Phys. Rev. B 59, 5162 (1999)
- 26. S. E. Rodil, W. I. Milne, J. Robertson, L.M. Brown, Appl. Phys. Lett. 77, 1458 (2000)
- 27. N Hellgren, et al, App Phys Lett 79 4348 (2001)
- 28. R. J. Nemanich, J. T. Glass, G. Lucovsky, R. E. Shroder, J. Vac. Sci. Technol. A6, 1783 (1988)
- 29. A.C. Ferrari, J. Robertson, Phys. Rev. B **63** 121405 (2001)
- 30. R Pfeiffer, H Kuzmany, Diamond Related Mats (2003)
- 31. R Pfeiffer, H Kuzmany, submitted to App Phys Lett (2003)

AN OVERVIEW OF DLC COATINGS FOR BIOLOGICAL APPLICATIONS

R. Hauert

Swiss Federal Laboratories for Materials Testing and Research (EMPA) Überlandstrasse 129, CH-8600 Dübendorf (Switzerland)

ABSTRACT

This paper gives an overview on diamond-like carbon (DLC) coatings in biomedical research and applications. DLC is a class of materials with shows an excellent biocompatibility as well as very good tribological properties. By the incorporation of additional elements into the DLC all of these properties can be changed within a certain range. The amount of different proteins adsorbed on the surface can be influenced by the concentration of additional elements in the DLC film. These adsorbed proteins will then subsequently influence cell attachment, cell proliferation and cell differentiation. Certain toxic elements such as Cu, Ag, V, embedded in the DLC will, when exposed to a biological media, be released and cause toxic reactions. This allows the preparation of surfaces with a tunable antibacterial effect. Concerning the wear of UHMWPE cups operated against DLC coated hip joint balls, depending on the experimental setup, different results are found in the literature. Especially, the proteins adsorbed on the joint surfaces strongly influenced the wear results obtained. DLC coatings have an excellent haemocompatibility, which is expressed in a decreased thrombus formation. DLC coated cardiovascular implants such as artificial heart valves, blood pumps and stents are already commercially available.

Keywords: DLC, biomaterials, biomedical applications, hip joint, haemocompatibility.

INTRODUCTION

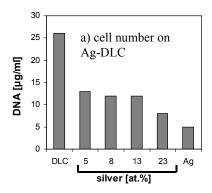
The implantation of biomaterials into the human body allows it to re-establish biological and mechanical functions and therefore to increase the quality of life. The load bearing properties of the implants are mainly controlled by the bulk properties of the implant whereas the interaction with the surrounding tissue is governed by the implant surface. The implant surface influences in particular the interaction and adsorption of different proteins which, in turn, control the cell adhesion and behavior. However, the overall reaction of the body on an implant is a system property that includes many different aspects, such as surface chemistry and texture, implant movement, biodegradation and surgical aspects. The highly corrosive environment and the low tolerance of the body to some dissolution products restrict the materials to be used for implants. These are alloys based on titanium, iron (surgical steel), cobalt, chromium, nickel (may cause allergies), zirconium, tantalum, the noble metals and carbon in its different forms, as well as ceramics such as alumina and zirconia. Additionally different polymers such as PTFE (Teflon), PEEK (polyetheretherketone) and polyethylene are also used for implants. For an introduction to biological process at surface see the overview articles by Castner and Ratner [1] and by Kasemo [2]. To create a surface for desired bioreactions, a promising approach is to start from an existing biocompatible coating (to prevent inflammatory reaction or repulsion) and to alloy it with adequate elements. Additionally, it has to be considered that the bioreactions and the in-vivo behavior of an implant are influenced also by the surface texture as described by Boyan [3]. Due to its bio- and haemocompatible nature [4.5], there is a growing interest in the application of DLC on orthopedic and other implants [6]. Additionally, DLC is an excellent base coating to be alloyed with different elements. The amorphous nature of DLC opens the possibility to introduce certain amounts of additional elements, such as Si, F, N, O, W, V, Co, Mo, Ti, and their combinations, into the film and still maintain the amorphous phase of the coating. By this technique, different film properties such as tribological properties, electrical conductivity, surface energy and biological reactions of cells in contact with the surface can be continuously adapted to a desired value. Today two main fields of biological applications of DLC can be seen. The application of DLC in blood contacting implants such as heart valves and stents and the use of DLC to reduce wear in load bearing joints. However, whereas DLC coated heart valves and stents are already commercially available, the situation for DLC coated load bearing implants is contradicting. For an introduction to DLC see the review articles by Robertson [7-9] and Butter and Lettington [10,11].

CELLS IN CONTACT WITH DLC AND ALLOYED DLC

Several research groups confirmed the biocompatibility of DLC by growing different cell types in-vitro on DLC and studying the cell response. Macrophages, fibroblasts, human myeloblastic ML-1 and other cell types have been grown on DLC under different conditions and cell responses such as proliferation rate, viability, cell adhesion, differentiation, cell morphology and cytoskeletal architecture have been monitored [12-14]. In-vitro experiments as well as the in-vivo reaction of DLC coated CoCr cylinders, implanted for 90 days in the lateral femoral cortex of sheep, showed that the DLC coated surfaces are well tolerated by the body [15]. Mohanty et al. [16] confirmed the biocompatibility on DLC coated Ti samples which stayed in the skeletal muscle of rabbits for up to one year. An overview on the reaction of different cells on DLC can be found in review articles [10,17,18].

Bioreactions can be tuned by tuning the surface chemistry of an implant to create a specific surface yielding a defined biological response. This can be done by alloying or by surface treatments, for example plasma exposure, ion implantation or chemical attachment of specific molecules. DLC as a biocompatible base material can be easily alloyed with other biocompatible materials such as titanium as well as with toxic materials such as silver, copper and vanadium. By varying alloy element concentration, it should be possible to tailor the bioreactions to any desired point between the bio-properties of DLC and those of the added element. In the last years only a few papers present experiments where bioreactions on DLC have been changed by alloying [19-25]. In [19] the addition of SiO_x to DLC reduced the induction of inflammatory reactions, as described below in the section "blood contacting applications". Similarly, some companies (Sulzer CarboMedics and St. Jude Medical) use silicon-alloyed pyrolytic carbons (Pyrolite®), a material that proved to be resistant to clotting, also indicating an improved biocompatibility by the addition of Si. Dorner-Reisel et al. [20] demonstrated that the addition of Ca-O to DLC decreased the film hardness, the wetting angle and the fraction of sp³/sp² bonded carbon. Cell tests with mouse fibroblast showed, with respect to the pure DLC, a increased number of cells and an improved cell viability for the Ca-O-DLC films. Which one of the changed film properties had the main contribution for the improved cell behavior was not determined. A correlation of the number of adhering blood platelets, which influences the blood compatibility of a surface, with the ratio of the Raman D/G band signals, which depends on the fraction of sp³/sp² bonded carbon, is shown in [26].

For applications where no cells or bacteria should attach to a surface, such as catheters, sensors and temporary implants, surfaces that inhibit cell proliferation and differentiation are required. DLC films containing different amounts of the cytotoxic elements silver, copper or vanadium can be made by standard DLC deposition and simultaneously magnetron sputtering. When such films are exposed to biological media, the metallic element is, within days or weeks, slowly released out of the film causing adverse reactions in the cells attached to the surface. By this approach, cytotoxic reaction as well as cell differentiation can be continuously tuned between the bioreactions on the pure metals and the biocompatible behavior of DLC. Above the surface a sufficient concentration of the toxic element has to be obtained to prevent cell growth. The toxic elements will then usually be distributed in the body and the total amount of the toxic element released has to be well tolerated by the body. As an example, the total number of cells, taking the total amount of DNA in BMC (bone marrow cells) cultures after 14 days in-vitro as an index, is displayed in figure 1a [25]. With increasing silver content an increasing tendency of BMC cells to differentiate into osteoclast (bone resorbing cells) cells was determined by the TRAP (tartrate resistant acid phosphatase)/DNA ratio as can be seen in figure 1b. Similar effects were also obtained by copper containing DLC



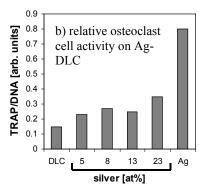


Figure 1: a) number of BMC cells monitored by the total amount of DNA and b) relative osteoclast activity after 14 days in-vitro for Ag-DLC films containing different amounts of silver. Data from [25].

[25] and vanadium containing DLC [22].

Ti-DLC Films have been produced to obtain a biocompatible surface which is enhancing bone ingrowth and in addition is harder than titanium to prevent abrasion and scratching. The Ti-DLC films containing different amounts of titanium (Ti-DLC) films were produced using a PACVD deposition system and simultaneously running a titanium magnetron sputter process [22]. When Ti-DLC is exposed to a biological environment, the adsorption of different proteins was

altered as a function of the Ti content in the DLC film [23,25]. The chemical composition of the Ti-DLC films exposed to air were determined by XPS at the surfaces. A pure Ti film after air exposure consisted of only 23 at.% of Ti on the surface and the balance was oxygen and adventitious carbon. The surface of different Ti-DLC films was covered with human plasma, the proteins were allowed to adsorb for 30 minutes and where then separated according to their size by SDS-polyacrylamide (sodium dodecylsulfate) gel electrophoresis. As an illustration, fig. 2 compares the protein adsorption on various Ti-DLC films on cpTi and glass. Certain protein bands. marked by arrows. were missing, enhanced or diminished depending on the surfaces subjected to protein adsorption tests. Commercially pure titanium and DLC surfaces showed a different protein pattern. By increasing titanium concentration in the carbon matrix, the band pattern of proteins eluted DLC shifted towards that of cpTi eluates.

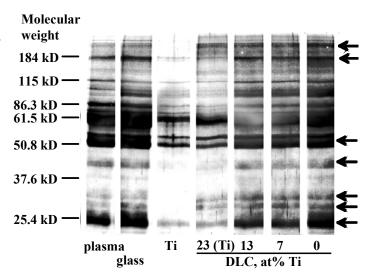


Fig. 2. Adsorption of human plasma proteins on glass, cpTi, Ti-DLC. The molecular weight marker is indicated on the left side. Arrows point to the bands where density differs according to different surfaces. Data from [23, 25].

Since cells interact with the adsorbed proteins, differences in protein adsorption are expected to result in differences in cell attachment, cell proliferation and cell differentiation, Bone marrow cells can, depending on the environment, differentiate into osteoblast (bone producing cells), or into osteoclast (bone resorbing cells). Since

osteoclast cells resorb bone material their presence disturbs the ingrowth of implants. The relative number of bone marrow cells which differentiated into osteoblasts was determined for the different surfaces by the ratio of ALP (a marker for the osteoblast activity) to the relative cell number (amount of DNA present) and is shown in figure 3a [21,22]. The cells on the Ti-DLC films showed no significant difference to the glass reference sample and a slightly higher differentiation of osteoblasts was only observed on the titanium film (23 at% Ti). The relative activity of bone resorbing cells, i.e. osteoclasts, on the different surfaces was determined by the ratio of TRAP (a marker for the osteoclast activity) relative to the total number of cells (amount of DNA) and is shown in figure 3b. The differentiation of bone marrow cells into resorbing cells, i.e. osteoclasts, on the other hand was, with reference to the glass sample, inhibited on all Ti-DLC films especially the Ti-DLC (7 at%) film and similarly on the titanium film (23 at% Ti). The differentiation of bone marrow cells into bone resorbing cells, i.e. osteoclasts, is inhibited by the addition of Ti into the DLC, making Ti-DLC a valuable coating for implants requiring a hard surface and an improved fixation by improved osseointegration [21,22].

When introducing a coating into the body, the beneficial properties of the coating have to be weighted in against the unknown long-term behavior and danger of delamination. Materials that are well tolerated in bulk form are able to induce toxic reactions if present in particulate form. To investigate the bioreactions induced

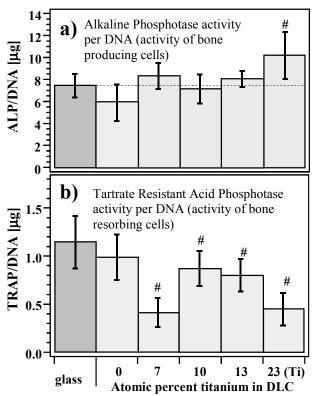


Figure 3: a) The ALP and b) TRAP activity (per DNA) of bone marrow cell on Ti-DLC films after 14 days in culture. The # denotes a significant difference from the plain DLC sample. Data from [21,22].

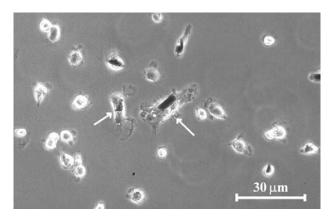


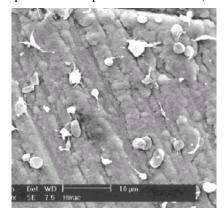
Fig. 4. Phase contrast microscopy image of bone marrow cells exposed to DLC fragments obtained from a delaminated 300 nm thick film. Arrows point at internalized particles. Picture from [25].

by DLC particles, bone marrow cell cultures have been incubated in-vitro with particles from a deliberately delaminated ca. 300 nm thick DLC film. The cells were able to internalize most of the particles within a few days (see figure 4) and the appearance of the cells was after seven days not different from the control cultures with no particles. Furthermore, the addition of particles did not have any effect on the lysosomal activity of the cells nor on the proliferation or differentiation, indicating that no toxic or inflammatory reaction of the body to delaminated DLC particles may be expected [25,27].

BLOOD CONTACTING APPLICATIONS

For implants in direct contact with blood, a key issue is the ability of the implant surface to prevent thrombus formation. The reactions of the body to a

blood contacting implant crucially depends on the surface of the implant, especially the chemical situation present at the surface, the surface texture, the local flow conditions as well as other factors. It is generally known, that increased platelet adhesion, activation and aggregation on implant surfaces exposed to blood precede the formation of a thrombus. Therefore in-vitro analysis of these properties is usually performed as a first test of the haemocompatibility of a surface. Additionally, the platelet morphology (circularity and area) can be taken as an indication of the ability of the surface to support thrombus formation. A high ratio of the proteins albumin/fibrinogen, adsorbed on a implant surface prior to cell or platelet attachment, can be correlated with a low number of adhering platelets and therefore with low tendency of thrombus formation. However, some materials may show contradicting results between the in-vitro experiments described above and the in-vivo behavior, as shown in [28] for polyurethane and parylene. Several papers of in-vitro essays on DLC surfaces indicate that this material may have the ability to suppress thrombus formation similar or even better than glassy carbon, a material widely used for heart valves. For illustration, in figure 5 in vitro experiments of blood platelets attached to DLC and Formvar (polyvinyl formal) are displayed. On the DLC surface no platelet activation or aggregation can be observed [29]. Blood platelets on Formvar show a aggregation of the activated blood platelets, a behavior which is usually preceding thrombus formation [30]. An introduction to DLC coatings and plasma surface treatment of mechanical heart valves is given in the review article by Tran et al. [31]. Using whole human blood and a parallel plate flow chamber, Krishnan et al. [32] showed that the adherence of platelets depends on the shear rates that the material is exposed to. Compared to a Ti surface, the platelet adhesion is reduced on DLC. In-vitro experiments by Jones et al.



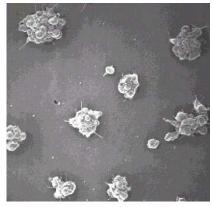


Figure 5: SEM pictures of human blood platelets on, left: DLC, right: Formvar (polyvinyl formal). The aggregation of activated blood platelets on the right picture is preceding thrombus formation. Pictures from M. I. Jones at al [29] and S. L. Goodman [30].

[29,33] showed that the DLC surfaces expressed a decreased area coverage of platelets compared to titanium, TiN and TiC. Whereas on the Ti containing surface platelet activation, clotting of platelets and thrombus formation was observed, no such reaction took place on the DLC surface.

A higher ratio of albumin/fibrinogen adsorption was observed on the DLC surfaces, compared to Ti, TiN and TiC which is an indication of the ability of DLC to prevent thrombus formation [29]. A higher albumin/fibrinogen ratio was also observed on DLC

compared to silicone (a polymer widely used for implants) by Dion et al. [34]. Cui and Li state in their review article [17] a good tissue- and blood-compatibility for DLC and amorphous CN films from in-vitro experiments, with DLC also showing a high albumin/fibrinogen ratio. The albumin/fibrinogen ratios from the different research groups are summarized in figure 6. It can be seen that DLC has the best albumin/fibrinogen ratio among all the materials tested.

Gutensohn et al. [35] analyzed the intensity of the platelet activation antigens CD62p and CD63. In their invitro experiment they showed that the DLC coating of a 316L stainless steel coronary artery stents resulted in a decrease of the CD62p and CD63 antigens indicating a low platelet activation on DLC and therefore a low tendency for thrombus formation. Additionally, they showed the metal ion release from the stainless steel stents, which may negatively influence the haemocompatibility of a surface, could be suppressed by the DLC coating. Similarly, the ability of DLC to have a low percentage of platelets adhering to the surface was shown by Alanazi et al. [36] in an in-vitro experiment using a flow chamber and whole human blood. However, the results obtained varied with the deposition conditions used for the DLC production. Analogous results can be found in many other papers, confirming that DLC and also ta-C have a good biocompatibility and lower number of adhering platelets compared to pyrolytic carbon, Ti, 316L stainless steel and other implant materials [10,37-39].

Only a few papers present in-vivo results of DLC coated implants. Scheerder et al. [19] report on DLC and DLN or DylynTM (diamond like nanocomposite) coated stainless steel stents, which were implanted into pigs for six weeks. The DLN or DylynTM coatings were produced by Bekeart, Belgium from siloxane precursors. In [40], DylynTM is described as a Si:O containing DLC where the Si atoms are present as SiO_x in different oxidation states and also as SiC. Their histopathologycal observation on the explanted stents showed a decreased thrombus formation for the DLC and the DLN coated stents compared to the uncoated stents. However, the inflammatory reactions, monitored by the number of inflammatory cells on the stent surface, were significantly higher on DLC than on DLN [19]. If the addition of Si:O to DLC generally results in a reduced inflammatory reaction and therefore an increased biocompatibility of DLC should be further investigated. In his Ph.D. thesis [41] Yang studied the haemocompatibility of different surfaces implanted for two hours into the intrathoracic venae cavae of Swedish native sheep. The results showed that there was significantly more thrombus on pyrolytic carbon and methylated titanium than on titanium, cobalt-chromium [42] and DLC [41]. The lowest coverage of thrombus was obtained for a TiN coated sample [41]. The diamond like coating center in UK reports on their home-page on DLC coatings in a blood flow accelerator. They showed, by in-vivo experiments, that on an uncoated device significant thrombus deposits occur, both on the accelerator device and artery wall, whereas an inhibition of thrombus formation and platelet deposition was observed in the DLC coated device. A DLC coated centrifugal ventricular blood pump device (made by SunMedical Technology Research Corporation, Nagano, JAPAN) coated with DLC was implanted in calves and, even without post-operative anticoagulation, only minor evidence of thrombosis was found on the DLC coated surfaces after explantation [43,44].

Due to the good haemocompatibility of DLC a few companies have DLC coated implants already commercially

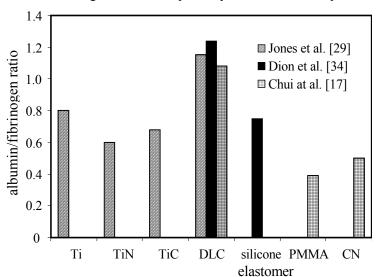


Figure 6: Albumin/fibrinogen ratio for different surfaces. Data from [17,29,34].

available or in the state of development. The Cardio Carbon Company Limited states that it has the following two DLC coated titanium implants under development or in clinical trials. An "Angelini Lamina-flo" mechanical heart valve (displayed in figure 7) and an "Angelini Valvuloplasty" ring which is used for heart valve repairs. The ring is sutured round the valve orifice to reshape it and to retain the natural functions and structure of the valve. The company Sorin Biomedica produces heart valves and stents which are coated by a ca. 0.5 µm thick CarbofilmTM. This coating is produced by PVD from a carbon target and the company states that CarbofilmTM has a turbostratic structure equivalent to that of pyrolytic carbon. However, deposition by PVD from a carbon target usually results in a-C (amorphous carbon) coatings. A clinical study on coated

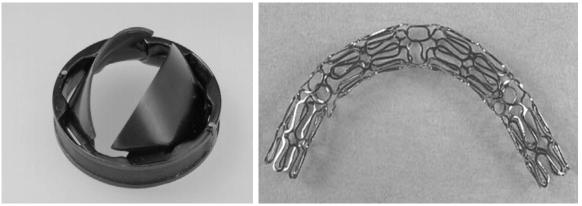


Figure 7: Left: a DLC coated titanium mechanical heart valve which is under development from the company Carbon Company Limited. Right: DLC coated stent from the company PHYTIS.

stents, implanted in 122 patients, resulted in a low restenosis rate of 11% after six month [45]. The company *PHYTIS* sells DLC coated stents (displayed in figure 7) on which they report a reduced rate of restenosis due to the DLC coating and that target revascularisation has been necessary in only 3.27% of the lesions treated. Probably, none of the worldwide key players in commercial production of heart valves and stents is selling DLC coated implants up to now. However, in recent years, drug-eluting polymer coating on stents have become the main area of interest and showed a large potential in preventing restenosis in the time after implantation, see for example the overview article by Garas et al. [46]. Therefore, a excellent implant surface may be obtained by coating with DLC to obtain a good long term behavior, in combination with a additional biodegradable drug eluting polymer to prevent restenosis during healing time after implantation. However, this combination is already patented by Herbst and Klein (PCT Patent WO 02/080996 A1).

HIP JOINTS AND LOAD BEARING IMPLANTS

In prosthetic hip replacements, polyethylene wear debris is identified as the main factor limiting the lifetime of the implants. Especially debris from the joint can induce tissue reactions and bone resorption that may lead to the implant loosening. An overview of different materials and surface-treatments used in bearing surfaces in human joint replacements was published in 1999 by Dearnley [47].

It is known that DLC shows a low wear and also low friction coefficients between 0.05 and 0.2 in atmosphere against most materials except some polymers. DLC, in some cases also modified by alloying with different elements, has, due to its outstanding properties, been studied extensively as a tribological coating as described in the review articles by Grill, Donnet and Gangopadhyay [48-51] and is also established in several industrial applications [52-55]. Under tribological conditions, usually the softer of the two materials will be worn. In the case of DLC the situation may be different since the wear of DLC, which has a graphitic nature, can be deposited onto the partner surface forming the so-called transfer layer. Then DLC slides against its own transfer layer and, although it is the harder surface, only DLC is worn at a very low wear rate, whereas the softer partner surface will not be worn. However, it is questionable if this situation is also present in an in-vivo joint where body fluids are capable of removing the wear products out of the tribological contact area. Due to it's excellent biocompatibility and it's low wear and friction, DLC was a promising candidate, tested as a coating in orthopedic applications by several research groups.

There are many papers reporting on experiments using a hip simulator to determine friction and wear of DLC coated hip joint balls sliding against UHMWPE (ultra high molecular weight polyethylene) or of metal/metal joints with both sides coated with DLC. Tiainen [56] as well as Lappalainen et al. [57] reports that hydrogen free DLC, also named tetrahedral amorphous carbon (ta-C), coated metal hip joint balls tested in 1wt% NaCl water by pin-on-disk and in a hip joint simulator reduce the wear of the UHMWPE cup by a factor of 10-100. In the case of a metal /metal joint with both sides coated, the wear could be reduced by a factor of 10⁵. Additionally, an increase in the corrosion resistance of the metallic material was obtained by the coating [56]. Tested in a knee wear simulator using distilled water as a lubricant, Oñate et al. [58] obtained a decrease of a factor of five in wear of the UHMWPE by coating the cobalt chromium counter face with DLC. Dong et al. [59] tested different coatings in a pin-on-disk tester, also using distilled water as a lubricant, and obtained a large decrease in UHMWPE wear with all the

coatings. However, the thermally oxidized Ti6Al4V coating still performed about eight times better than the DLC coating. Analogously, Dowling et al. [6] coated a stainless steel femoral head with DLC and determined the wear of the UHMWPE cups in a hip joint simulator using distilled water. They obtained a decrease of wear by a factor of six due to the DLC coating. The same low wear of the UHMWPE was also obtained when using a zirconia femoral head under the same test conditions.

Sheeja et al. [60] prepared multilayer ta-C (tetrahedral amorphous carbon) films by the filtered cathodic arc method from pure C targets. The wear tests of the CoCrMo/UHMWPE and DLC/UHMWPE sliding pairs have been made in water and simulated body fluid on a pin-on-disk apparatus and, in contradiction to the results presented above, no significant difference in wear could be measured between the coated and the uncoated samples [61].

Saikko et al. [62] compared the wear of UHMWPE cups operated against CoCr, alumina and DLC coated CoCr hip joint balls in a biaxial hip wear simulator in the presence of diluted calf serum. For all three combinations tested, they obtained wear rates of the UHMWPE cups between 48 and 57 mg per one million cycles. This is no significant difference in the wear due to the DLC coating and all wear values obtained are in the range known from clinical observations with CoCr and alumina hip joint balls. Similar results have been obtained also by Affatato et al. [63]. Femoral heads made from 316L stainless steel, alumina, CoCrMo and DLC coated TiAlV have been tested in a hip joint simulator using bovine calf serum as a lubricant. They obtained wear rates of the UHMWPE cups between 25 and 37 mg per million cycles for all four material combinations tested.

From the results shown above it can be seen that apparently contradicting results on the wear of DLC coated joints are obtained. There are several issues presented below which may explain these differences found in the literature. The liquid lubricant used in a tribological test has a crucial influence on the friction and wear values obtained as well as on the type of wear particles produced [64-66]. It was suggested that when bovine serum or synovial fluid was used as a lubricant, the different proteins, especially phospholipids, adsorbed on the surfaces, strongly influences the tribological behavior in the joints [64,66]. Also, the surface texture has a decisive influence on the wear behavior of a joint. It was shown that even single scratches, which may not be detected by an average surface roughness measurement, are capable of increasing the wear rate of UHMWPE by a factor of 30-70 [67]. As a summary, it can be stated that wear tests on load bearing implants should be made in an adequate implant joint simulator. As a lubricant, a supply of synovial fluid (or any other fluid containing an adequate distribution of proteins) has to be maintained to compensate for the proteins decomposed due to high pressures between contact spots of the bearing [68]. Additionally, the surface texture of the areas involved in the tribological process must be characterized carefully.

From the literature presented above, it can be said that the superior properties, which DLC shows in air or vacuum, can probably not be easily transferred to hip joints and other load bearing implants. The build up of a transfer layer does not seem to take place, and the UHMWPE counterpart still shows wear. Perhaps DLC coated load bearing implants sliding against ceramics or against DLC coated counterparts may show good "ceramic like" tribological properties, but it is questionable if a real improvement in wear against the existing ceramic/ceramic or metal/ceramic bearings can be obtained.

Dearnley [47] states in his review article, published in 1999, that he is unaware of any commercially available DLC coated bearing surfaces for joint replacements. To my knowledge, to date, only the French company "M.I.L. SA (Matériels Implants du Limousin SA)" commercially offers DLC coated titanium shoulder-joint balls and anklejoints with both parts (the tibial and the talar component) made from a nitrided AISI Z5 CNMD 21 steel and coated with DLC.

CONCLUSIONS

Two main fields of biological applications of DLC can be found in the literature. The application of DLC in blood contacting implants such as heart valves and stents and the use of DLC to reduce wear in load bearing joints. Additionally, it is possible to tune the biological properties of DLC by alloying with different elements. DLC coatings can also be used to reduce the release of metal ions (especially nickel, which is the most common contact allergen) from metallic implants.

For blood contacting applications of DLC, the different in-vitro and in-vivo experiments showed a high albumin/fibrinogen ratio, a low number of platelets adhering to the surface, a decreased platelet activation and a decreased tendency of thrombus formation for DLC surfaces confirming the excellent haemocompatibility of DLC. Additionally, the reported decrease in inflammatory reactions by the addition of Si:O into the DLC matrix [19,40] has to be further examined. Since it is possible to add different elements into the DLC matrix and to continuously

adjust the different biological properties, it should be possible to improve the excellent blood compatibility of DLC even further.

For DLC coated load bearing implants, the different in-vitro experiments showed contradicting results, due to the different experimental setups (pin-on disk, hip or knee simulator, different surface roughness) and the different liquids used as lubricants. The low wear properties known from the tribological behavior of DLC in air could not be adapted to load bearing joints operated in a biological fluid. No in-vivo experiments on DLC coated load bearing implants could be found in the literature.

REFERENCES

- [1] D.G. Castner and B.D. Ratner, Surface Science 500 (2002) 28.
- [2] B. Kasemo, Surface Science 500 (2002) 656.
- [3] B.D. Boyan, T.W. Hummert, D.D. Dean, Z. Schwartz, Biomaterials 17/2 (1996)137.
- [4] M. Allen, F. Law, R. Rushton, Clin. Mater. 17/1 (1994) 1-10.
- [5] R. Butter, M. Allen, L. Chandra, A. H. Lettington, R. Rushton, Diamond Relat. Mater. 4 (1995) 857.
- [6] D. P. Dowling, P. V. Kola, K. Donelly T. C. Kelly, K. Brumitt, L. Lloyd, R. Eloy, M. Therin and N. Weill, Diamond Relat. Mater. 6 (1997) 390.
- [7] J. Robertson, Prog. Solid State Chem. 21 (1991) 199.
- [8] J. Robertson, Surf. Coat. Technol. 50 (1992) 185.
- [9] J. Robertson, Mat. Sci. Eng. R 37 (2002) 129-281
- [10] R.S. Butter and A.H. Lettington, J. chem. Vapor Deposition 3 (1995) 182.
- [11] A.H. Lettington, Carbon 36/5-6 (1998) 555-560.
- [12] L.A. Thomson, F.C. Law, N. Rushton, J. Franks, Biomaterials 12 (1991) 37
- [13] L. Lu, M.W. Jones, R.L.C. Wu, Bio-Medical Materials and Engineering 3/4 (1993) 223.
- [14] S. Linder, W. Pinkowski and M. Aepfelbacher, Biomaterials 23 (2002) 767-773.
- [15] M. Allen, B. Myer, N. Rushton, Journal of Biomedical Materials Research 58/3 (2000) 319-328.
- [16] M. Mohanty, T. V. Anilkumar, P. V. Mohanan, C. V. Muraleedharan, G. S. Bhuvaneshwar, F. Derangere, Y. Sampeur and R. Suryanarayanan, Biomolecular Engineering 19, (2002) 125-128.
- [17] F.Z. Cui, D.J. Li, Surf. Coat. Technol. 131 (2000) 481-487.
- [18] R.A. Freitas Jr., Foresight Update 39, Nanomedicine: Is diamond biocompatible with living cells?, Forsight Institute, Palo Alto, Ca, USA, (1999).
- [19] I. De Scheerder, M. Szilard, H. Yanming, X.B. Ping, E. Verbeken, D. Neerinck, E. Demeyere, W. Coppens, F. Van de Werf, The Journal of Invasive Cardiology 12/8 (2000) 389-394.
- [20] A. Dorner-Reisel, C. Schürer, C. Nischan, O. Seidel and E. Müller, Thin Solid Films, 420-421 (2002) 263-268.
- [21] A. Schroeder, G. Francz, A. Bruinink, R. Hauert, J. Mayer, E. Wintermantel, Biomaterials 21 (2000) 449-456.
- [22] G. Francz, A. Schroeder and R. Hauert, Surf. Interface Anal. 28 (1999) 3.
- [23] R. Hauert, L. Knoblauch-Meyer, G. Francz, A. Schroeder and E. Wintermantel, Surface and Coatings Technology 120-121 (1999) 291-296.
- [24] R. Hauert, U. Müller, G. Francz, F. Birchler, A. Schroeder, J. Mayer and E. Wintermantel, Thin Solid Films, 308-309/1-4 (1997) 191-194.
- [25] Annick Schroeder, Ph.D. Thesis, Dissertation Nr. 13079 at ETH Zürich (1999).
- [26] J. Y. Chen, L. P. Wang, K. Y. Fu, N. Huang, Y. Leng, Y. X. Leng, P. Yang, J. Wang, G. J. Wan, H. Sun, X.B. Tian, P.K. Chu, Surf. Coat. Techno. 156 (2002) 289-294.
- [27] A. Schroeder, G. Francz, A. Bruinink, R. Hauert, J. Mayer, E. Wintermantel, Biomaterials (accepted) (2003).
- [28] B. A. Weisenberg, D.L. Mooradian, Journal of Biomedical Materials Research 60/2 (2002) 283-291.
- [29] M. I. Jones, I. R. McColl, D. M. Grant, K. G. Parker, T. L. Parker, Journal of Biomedical Materials Research, 52/2 (2000) 413-421.
- [30] S. L. Goodman, Journal of Biomedical Materials Research: 45/3 (1999) 240-250.
- [31] H.S. Tran, M.M. Puc, C.W. Hewitt, D.B. Soll, S.W. Marra, V.A. Simonetti, J.H. Cilley, A.J. DelRossi, Journal of Investigative Surgery 12/3, (1999) 133-140.
- [32] L. K. Krishnan, N. Varghese, C. V. Muraleedharan, G. S. Bhuvaneshwar, F. Derangère, Y. Sampeur and R. Suryanarayanan, Biomolecular Engineering 19 (2002) 251-253.
- [33] M. I. Jones, I. R. McColl, D. M. Grant, K. G. Parker, T. L. Parker, Diamond Relat. Materials 8 (1999) 457-462.

- [34] Dion, I; Roques, X; Baquey, C; Baudet, E; Basse Cathalinat, B; More, N ,Bio-Medical Materials and Engineering 3/1 (1993) 51-55.
- [35] K. Gutensohn; C. Beythien; J. Bau; T. Fenner; P. Grewe; R. Koester; K. Padmanaban, P. Kuehnl, Thrombosis Research 99/6 (2000) 577-585.
- [36] A. Alanazi, C. Nojiri, T. Noguchi, T. Kido, Y. Komatsu, K. Hirakuri, A. Funakubo, K. Sakai, and Y. Fukui, ASAIO Journal 46 (2000) 440-443.
- [37] P.K. Chu, B.Y. Tang, L.P. Wang, X.F. Wang, S.Y. Wang, N. Huang, Rev. Sci. Instrum. 72/3 (2001) 1660-1665
- [38] L. J. Yu, X. Wang, X. H. Wang, X. H. Liu, Surf. Coat. Techno. 128-129, (2000) 484-488.
- [39] Ralf Max Beck, Ph.D. Thesis, University Tübingen, Germany (2001).
- [40] D. Neerinck, P. Persoone, M. Sercu, A. Goel, C. Venkatraman, D. Kester, C. Halter, P. Swab and D. Bray ,Thin Solid Films 317/1-2 (1998) 402-404.
- [41] Yanqi Yang , Linköping University Medical Dissertation No 539, Department of Cardiothoracic Surgery, Linköping University, Linköping, Sweden., ISBN 91-7219-084-1 ISSN 0345-0082 Linköping (1997).
- [42] Y. Yang, S.F. Franzen, C.L. Olin, The Journal of Heart Valve Disease 5/5 (1996) 532-537.
- [43] T.A. Snyder S. Kihara, K. Litwak, K. Yamazaki, W.R. Wagner, Proceedings: Society for Biomaterials, 28th annual meeting transactions (2002) 8.
- [44] K. Yamazaki, P. Litwak, O. Tagusari, T. Mori, K. Kono, M. Kameneva, M. Watach, L. Gordon, M. Miyagishima, J. Tomioka, M. Umezu, E. Outa, J.F. Antaki, R.L. Kormos, H. Koyanagi, B.P. Griffith, Artificial Organs 22/6 (1998) 466-474.
- [45] D. Antoniucci, A. Bartorelli, R. Valenti, P. Montorsi, G. M. Santoro, F. Fabbiocchi, L. Bolognese, A. Loaldi, M. Trapani, D. Trabattoni, G. Moschi, S. Galli, The American Journal of Cardiology 85/7 (2000) 821-825.
- [46] S. M. Garas, P. Huber, N. A. Scott, Pharmacology & Therapeutics 92 (2001) 165-178.
- [47] P. A. Dearnley, Proceedings of the Institution of Mechanical Engineers. Part H, Journal of Engineering in Medicine 213/2 (1999) 107-135.
- [48] A. Grill, Surf. Coat. Techno. 94-95 (1997) 507.
- [49] C. Donnet, Surf. Coat. Technol. 100-101 (1998) 180.
- [50] A. Gangopadhyay, Tribology Letters 5 (1998) 25.
- [51] A. Grill, Diamond Relat. Mater. 8 (1999) 428.
- [52] R. Hauert, U. Müller and M. Tobler, conference proceeding of the 17th international SAMPE EURPE Conference, 28-30. Mai 1996, Basel, Switzerland, Ed: U. Meier (1996) 367.
- [53] E.C. Cutiongco, D. Li, Y.W. Chung and C. S. Bhatia, Trans. ASME 118 (1996) 543.
- [54] K.-R. Lee K. Y. Eun, Mater. Sci. and Engin. A 209 (1996) 264.
- [55] J. Güttler, J. Reschke, Surf. Coat. Technol. 60 (1993) 531.
- [56] V-M. Tiainen, Diamond Relat. Materials 10 (2001) 153.
- [57] R. Lappalainen, H. Heinonen and A. Anttila, S. Santavirta, Diamond and Related Materials 7/2-5 (1998) 482.
- [58] J. I. Oñate, M. Comin, I. Braceras, A. Garcia, J. L. Viviente, M. Brizuela, N. Garagorri, J. L. Peris and J. I. Alava. Surface and Coatings Technology 142-144 (2001) 1056-1062.
- [59] H. Dong, W. Shi and T. Bell, Wear 225-229/1 (1999) 146-153.
- [60] D. Sheeja, B. K. Tay, X. Shi, S. P. Lau, C. Daniel, S. M. Krishnan and L. N. Nung, Diamond and Related Materials 10/3-7 (2001) 1043-1048.
- [61] D. Sheeja, B. K. Tay, S. P. Lau and L. N. Nung, Surface and Coatings Technology 146-147 (2001) 410-416.
- [62] V. Saikko, T. Ahlroos, O. Calonius and J. Keränen, Biomaterials 22/12, (2001) 1507-1514.
- [63] S. Affatato, M. Frigo, A. Toni, Journal of Biomedical Materials Research 53/3 (2000) 221-226.
- [64] S.C. Scholes, A. Unsworth, A.A.J. Goldsmith, Phys. Med. Biol. 45 (2000) 3721-3735.
- [65] T. Ahlroos, V. Saikko, Wear 211 (1997) 113-119.
- [66] V. Saikko, T. Ahlroos, Wear 207, (1997) 86-91.
- [67] J. Fisher, P. Firkins, E.A. Reeves, J.L. Hailey, G.H. Isaac, Proceedings of the Institution of Mechanical Engineers. Part H, Journal of Engineering in Medicine 209/4 (1995) 263-264.
- [68] M.A. Wimmer, J. Loos, R. Nassutt, M. Heitkemper, A. Fischer, Wear 250 (2001) 129-139.

CARBON-BASED WEAR COATINGS: PROPERTIES AND APPLICATIONS

Kazuhisa Miyoshi

National Aeronautics and Space Administration Glenn Research Center Cleveland, Ohio 44135 USA

Keywords: Wear coatings, CVD diamond, DLC, Surface systems, and Tribology

EXTENDED ABSTRACT

The technical function of numerous engineering systems—such as vehicles, machines, and instruments—depends on the processes of motion and on the surface systems (ref. 1). Many processes in nature and technology depend on the motion and dynamic behavior of solids, liquids, and gases. Smart surface systems are essential because of the recent technological push toward higher speeds, loads, and operating temperatures; longer life; lighter weight and smaller size (including nanotechnology); and harsh environments in mechanical, mechatronic, and biomechanical systems (ref. 2). If proper attention is not given to surface systems, then vehicles, machines, instruments, and other technical systems could have short lives, consume excessive energy, experience breakdowns, result in liabilities, and fail to accomplish their missions. Surface systems strongly affect our national economy and our lifestyles. At the NASA Glenn Research Center, we believe that proper attention to surface systems, especially in education, research, and application, could lead to economic savings of between 1.3 and 1.6 percent of the gross domestic product (ref. 1).

Wear coatings and surface systems continue to experience rapid growth as new coating and surface engineering technologies are discovered, more cost-effective coating and surface engineering solutions are developed, and marketers aggressively pursue, uncover, and exploit new applications for engineered surface systems in cutting tools and wear components (ref. 3). Wear coatings and smart surface systems have been used widely in industrial, consumer, automotive, aerospace, and biomedical applications (refs. 3 and 4). This presentation expresses the author's views of and insights into smart surface systems in wear coatings (refs. 2 and 5 to 10).

A revolution is taking place in carbon science and technology (ref. 11). Diamond, an allotrope of carbon, joins graphite, fullerenes, and nanotubes as its major pure carbon structures. It has a unique combination of extreme properties: hardness and abrasion resistance; adhesion and friction; thermal conductivity; chemical and thermal inertness; corrosion and wear resistance; radiation resistance and biocompatibility; electronic, acoustic, and electrochemical characteristics; and environmental compatibility. These properties make diamond attractive for a wide range of diverse applications. In particular, chemical-vapor-deposited (CVD) diamond coatings offer a broad potential, since size and cost are not as limiting. The production of large, superhard diamond films or sheets at low cost make designer materials possible (ref. 2).

This presentation is divided into two sections: properties and applications of hard coatings. The first section is concerned with the fundamental properties of the surfaces of CVD diamonds and related materials. The surface properties of hard coatings with favorable coefficients of friction (\leq 0.1) and dimensional wear coefficients (\leq 10⁻⁶ mm³/N·m) in specific environments are discussed. The second section is devoted to applications. Examples of actual, successful applications and of potential challenging applications of the coatings—such as CVD diamond, diamondlike carbon, and cubic boron nitride—are described. Cutting tools coated with CVD diamond are of immediate commercial interest. Other applications, such as microelectromechanical systems (MEMS), valves, and bearings of CVD diamond, are being developed, but at a slow pace. There is a continually growing interest in commercializing

diamondlike carbon for wear parts applications, such as biomedical parts and implants, forming dies, transport guides, magnetic tapes and disks, valves, and gears. Cubic boron nitride films are receiving attention because they can be used on tools to machine ferrous materials or on wear parts in sliding contact with ferrous materials.

REFERENCES

- 1. H.P. Jost, Tribology—Origin and Future, Wear, vol. 136 (1990) pp. 1–17.
- K. Miyoshi, Solid Lubrication: Fundamentals and Applications, Marcel Dekker, New York, NY, 2001
- 3. R.D. Bollier, R. Horsfall, and A. Inspekter (conference chairs), World Markets and Technology for Advanced Coatings and Surface Systems for Cutting Tools & Wear Parts, Organized by Gorham Conferences, Gorham, ME, 2002.
- 4. R. Hay, R. Horsfall, and Z. Yaniv (conference chairs), World Markets, New Applications, and Technology for Wear and Superhard Coatings, Organized by Gorham Advanced Materials, Inc., Gorham, ME, 1998.
- K. Miyoshi, J.J. Pouch, and S.A. Alterovitz, Plasma-Deposited Amorphous Hydrogenated Carbon Films and Their Tribological Properties, Materials Science Forum, vols. 52 and 53, Trans Tech, Switzerland (1989) pp. 645–656.
- 6. K. Miyoshi, Fundamental Tribological Properties of Ion-Beam-Deposited Boron Nitride Thin Films, Materials Science Forum, vols. 54 and 55, Trans Tech, Switzerland (1990) pp. 375–398.
- 7. R.L.C. Wu, A.K. Rai, A. Garscadden, P. Kee, H.D. Desai, and K. Miyoshi, Synthesis and Characterization of Fine Grain Diamond Films, J. Appl. Phys., vol. 72, no. 1, 1 July (1992) pp. 110–116.
- 8. K. Miyoshi, R.L.C. Wu, A. Garscadden, P. N. Barnes, and H.E. Jackson, Friction and Wear of Plasma-Deposited Diamond Films, J. Appl. Phys., vol. 74, no. 7, 1 October (1993) pp. 4446–4454.
- 9. K. Miyoshi, Lubrication by Diamond and Diamondlike Carbon Coatings, J. Tribology, vol. 120, ASME (1998) pp. 379–384.
- K. Miyoshi, M. Murakawa, S. Watanabe, S. Takeuchi, S. Miyake, and R.L.C. Wu, CVD Diamond, DLC, and c-BN Coatings for Solid Film Lubrication, Tribology Letters, vol. 5, (1998) pp. 123– 129.
- 11. H.O. Pierson, Handbook of Carbon, Graphite, Diamond, and Fullerenes: Properties, Processing, and Applications, Noyes Publications, Park Ridge, NJ, 1993.

Tribological Characteristics of Novel Superhard Carbon Compacts for Self-Lubricating Applications

M. Y. Chen, S. T. Korfhagen

Air Force Research Laboratory, AFRL/MLBT, Wright-Patterson AFB OH 45433-7750; O. A. Voronov, Diamond Materials, Inc., 120 Centennial Ave., Suite 104, Piscataway, NJ 08854

Abstract

Tribological performance of a recently developed hard carbon material (DiamoniteTM) was evaluated. The samples of new carbon ceramic were sintered from fullerene C_{60} under high pressure. Pin-on-disc experiments were performed without lubrication between 440C stainless steel balls and the superhard carbon disc samples at 200-400 rpm, with loads of 0.25 N, 0.5 N and 1.00 N. The testing environments include humid air (40 % RH) and dry nitrogen atmospheres. Microstructural analysis of the as-sintered carbon ceramic, wear scar analysis on the carbon discs, and material transfer to the steel balls were examined using a scanning electron microscope. The coefficients of friction obtained were 0.15-0.17 in lab air. In dry testing condition, the material showed surprisingly low coefficients of friction (0.05-0.12). Raman analysis was used to determine the chemical bonding of the as-polished materials and the changes in sp³ to sp² ratio of carbon bonding before and after wear tests. Comparisons of the tribological performance of new carbon ceramic with diamond ceramic will be presented. The results demonstrated the feasibility of using this fullerene-derived carbon material with a low coefficient of friction for self-lubricating antifriction applications.

Keywords: friction, self lubricating, diamond, fullerenes, Diamonite[™], carbon ceramic. *Corresponding Author: Tel.+1-937-255-9099; fax +1-937-255-2176; E-mail: ming.chen@wpafb.af.mil

Ming Y. Chen AFRL/MLBT Bldg 654, 2941 P Street Wright Patterson AFB OH, 45433-7750 USA

Tel:937-255-9099 Fax:937-255-2176 ming.chen@wpafb.af.mil

S. T. Korfhagen AFRL/MLBT Bldg 654, 2941 P Street Wright Patterson AFB OH, 45433-7750 USA Tel:937-255-3234 Fax:937-255-2176

O. A. Voronov Diamond Materials, Inc. 120 Centennial Ave., Suite 104 Piscataway, NJ 08854 USA

Tel:732-885-0805 Fax:732-885-5910 ovoronov@aol.com

VARIOUS APPLICATIONS OF DLC INCLUDING FLEXIBLE DLC-COATED RUBBER COMPONENTS

Hisanori Ohara, Takahiro Nakahigashi

Nippon ITF Inc. 575 Kuzetonoshiro-cho, Minami-ku, Kyoto-shi, Kyoto, 601-8205 Japan

ABSTRACT

DLC (Diamond-Like Carbon), a kind of the hard carbon film, has such features as the lowest friction coefficient among various ceramic coating materials, high hardness, and less damage in the counterparts. Because of these features, many developments regarding application for various kinds of sliding parts are in progress. However, people now call other films DLC, too, even though they are different from those defined in '80s. Moreover, new manufacturing methods such as sputtering and cathodic arc ion-plating are now used in addition to the conventional ones such as the radio frequency (rf) plasma assisted chemical vapor deposition (PACVD) and the ion beam deposition. It is required to use these DLCs properly for each usage. Another topic in these days is a flexible DLC film that uses rubber as the substrate material instead of the generally used substrate materials such as metals and ceramics. This new DLC film is applied to the rubber seal ring (O-ring) for zoom lens system of 35 mm compact cameras

This paper reviews the technological trend of various applications of the recent DLC films including flexible DLC films coated on rubber components.

Keywords: DLC, application, rubber, flexible-DLC, O-ring

INTRODUCTION

Among various thin film coating materials, DLC (Diamond-Like Carbon) has such features as the lowest friction coefficient, high hardness, superior wear resistance, and less damage in the counterparts. Because of these features, many types of DLCs have been developed and easily available in the global market.

Historically, in the early 70's, amorphous pure carbon film deposited using ion beam deposition was the first DLC, which was called "i-C" (ref. 1). After that, hydrogen-containing (hydrogenated) amorphous carbon film deposited using ionized beam of hydrocarbon gas was developed in the late 70's (ref. 2). Radio frequency plasma assisted chemical vapor deposition (RF-PCVD) was also developed for hydrogenated amorphous carbon film. Non-hydrogenated amorphous carbon film is also deposited using cathodic arc physical vapor deposition (CA-PVD), cathode sputtering or laser ablation. In the middle 80's, metal containing amorphous carbon film was developed using simultaneous sputtering of metal and carbon targets (ref. 3). In the 90's, plasma immersion ion implantation and deposition (PIII&D) method was developed for hydrogenated amorphous carbon film.

Thus, many types of amorphous carbon, which are classified as DLC, have been developed and have been put in practical use. However, each DLC shows different characteristics such as friction coefficient, electric conductivity, and the degree of transparency, and so on, according to the hydrogen and/or metal content and sp3/sp2 ratio. Hence, today's DLC market is, so to speak, in a state of confusion. Generally, film properties are strongly depended on the film contents. Also, film contents are strongly depended on the source material and the principle of deposition process. So, we must use each DLC properly taking the essential information written above into consideration.

TYPICAL PROPERTIES OF DLC AND IT'S TENDENSIES

As generally said, among the various thin film materials, DLC has superior friction properties such as low friction coefficient, superior wear resistance, less damage in the counterparts, and good non-sticking properties against the counterparts. In dry (no lubricant) sliding condition, these characteristics can not be obtained in the case when more popular ceramic coating films such as titanium nitride (TiN) and chromium nitride (CrN) are applied.

Many researchers have tried to clarify why DLC shows such low friction coefficient and good tribological properties. In the early stage of such researches, it was reported that graphitization of DLC could have been the reason (ref. 4). Graphite itself is a solid lubricant material. During friction, DLC is thought to be transformed or decomposed to generate thin graphite layer at the sliding surface of DLC. Recently, it was found that the highly hydrogenated DLC showed extremely low friction coefficient in ultra-high vacuum or in dry nitrogen (ref. 5, 6, 7). These results indicate that hydrogen, which is contained in DLC, plays an important roll during friction (ref. 8, 9). Fukui and his co-workers investigated the surface of DLC (a-C:H) after friction test in ambient air using the time-of-flight secondary ion mass spectroscopy, and they found the evidence of hydrocarbon material which was generated during friction (ref. 10). This "friction polymer" or "transferred layer" is thought to act as the lubricant material during friction. Hydrogen in the DLC film also affects the film hardness and so on.

The content of diamond-like (sp3) C-C bonding state is also the essential parameter of DLC (ref. 11). The higher the sp3/sp2 ratio in the DLC, the higher the hardness and transparency of DLC. Using CA-PVD, relatively high sp3/sp2 ratio can be obtained, and such DLC is called tetrahedral amorphous carbon (ta-C). On the other hand, graphite-like carbon film with relatively low sp3/sp2 ratio, which is called amorphous carbon (a-C), is obtained using conventional cathode sputtering.

Recently, unbalanced magnetron sputtering (UBMS) has been widely used to deposit DLC (ref. 12). Generally, graphite cathode and inert gas, such as argon, are used to deposit the a-C film. But, in many cases, some kind of hydrocarbon gas, such as acetylene, is simultaneously used to deposit the a-C:H film. Furthermore, metal carbide cathode, inert gas and hydrocarbon gas are used to deposit the metal containing a-C:H film. Therefore, UBMS is a useful technique to obtain the various kinds of DLCs including multi-layered or composite structured DLCs.

Some kinds of metallic or non-metallic additives produce unique properties. Silicon containing a-C:H shows very low friction coefficient under dry (no-oil) condition (ref. 13). Tungsten containing DLC, such as WC/C, shows lower internal stress, hence thick coating more than 3 μ m can be obtained. But, also the film hardness is generally low, it is possible that the wear resistance property tends to fall down.

Hence, deposition methods and source materials are determined by the film properties. We must use proper DLC for each usage taking the required characteristics and the properties of DLC into consideration. Other requirements than the triblogical properties, such as reliability and low cost, are simultaneously needed recently.

From the viewpoint of the general friction parts such as automobile engine parts, oil-based lubricant is usually used. In such conditions, low friction coefficient of DLC, it is the biggest advantage of DLC, disappears. Figure 1 shows interesting results of friction coefficients for many kinds of bulk or thin film materials with and without engine oil lubrication (ref. 14). DLC shows low friction coefficient without lubricant. But, under oil lubrication, all other materials show almost same friction coefficient as that of DLC. This is thought to be the reason why the DLCs' market has not expanded explosively in spite of its excellent properties. If the friction coefficient of DLC decreases remarkably even under the oil lubrications, huge market will be expected.

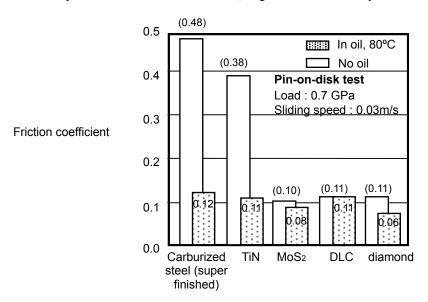


Figure 1. Friction coefficients of various materials with and without oil lubrication (ref. 14).

TYPICAL APPLICATIONS

Figure 2 shows various characteristics and applications of DLC. These features enable DLC film to apply to friction parts, cutting tools, molds, jigs, and various kinds of protection films for many uses.

Acoustic diaphragms for loudspeakers, which utilize the high elastic modulus of DLC, were our first commercial mass-production in late 80's. In 90's, DLC coated valve seats for single lever faucet were developed (ref. 15). Many other machine parts were also produced for automobile engine, semiconductor processing apparatus, and so on.

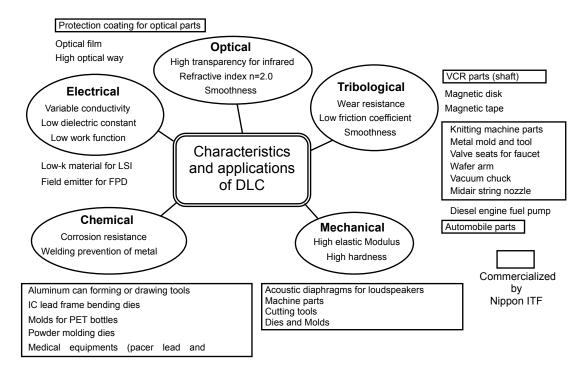


Figure 2. Characteristics and applications of DLC.

In the early stage of DLC production, adhesion strength of DLC film was not so high. On the other hand, from the viewpoint of substrate material, polymer or rubber material, which is not enough to endure the DLC coating process temperature, could not be coated with DLC. Therefore, we developed two new DLCs for each requirement.

HIGH ADHESIVE DLC FOR HEAVY DUTY USE

In order to enhance the reliability of DLC, new PVD process was developed. We call this DLC as "HA-DLC (high adhesive DLC)".

Figure 3 shows the comparison of Rockwell C scale indents for conventional DLC and HA-DLC. There is no delamination around the edge of indent for HA-DLC (figure 3, (b)), while large delamination is observed for conventional DLC (figure 3, (a)). Using other evaluation test, too, we concluded that the adhesion strength of HA-DLC is a few times higher than that of conventional DLC. HA-DLC does not contain hydrogen. The hardness of HA-DLC is higher than that of conventional DLC, and is up to 45 GPa. Superior wear resistance can be obtained due to its high hardness and high adhesion strength. Heat resistance is also better than the hydrogenated DLC (a-C:H). HA-DLC can be used up to 773 K in ambient air and 873 K in nitrogen environment. HA-DLC shows interference color, because of its good transparency.

HA-DLC is most suitable for heavy-duty use, such as cutting tools for aluminum machining, molds, machine parts, and so on. Especially, HA-DLC coated cemented carbide and high-speed steel cutting tools show superior performance for aluminum dry machining.

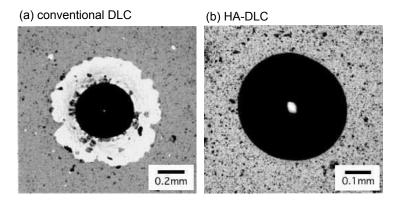


Figure 3. Optical microphotographs of Rockwell C scale indents for (a) conventional DLC and (b) HA-DLC. Substrate material is carburized steel (AISI 4115, HRC58). Film thickness is 0.8 µm for both cases. Film hardness is Hv 15 GPa for conventional DLC and Hv 32 GPa for HA-DLC.

FLEXIBLE DLC FOR RUBBER PARTS

Generally, in order to improve the surface lubricity and to mix up with carbon black, oil is so far added to polymer materials such as rubber. When oil runs dry, however, drawbacks such as gradual increase in the friction coefficient arise. For instance, windshield wipers of the automobile become noisy in a half year or so. Components and products made of rubber also tend to cling to the other materials used together therein. We wondered if we could eliminate such oily additives that could cause such bad effects. We have proceeded to coat onto the polymer materials such as rubber and resin while making the best use of the features of DLC.

We thought that three issues have to be resolved. (1) Low heat resistance of the polymer materials such as rubber and resin, (2) pollution of the polymer material surface by oil, resin, and oxidation prevention agents, etc., and (3) easy deformation of the polymer materials. To resolve these possible problems: (1) We have developed a processing method using the amplitude-modulated RF plasma CVD method which enables coating at lower temperature (below 333 K) and does not allow the processing temperature to rise any higher. (2) To prevent the pollution, we need to clean the polymer surface without solvent. However, lengthy washing using organic solvent causes dissolving out of the oily additives that are contained in rubber. Cleaning in a short time cannot sufficiently remove the pollution. We have therefore decided to clean the polymer surface by hydrogen plasma. (3) To prevent the detachment of thin hard film in the transformation of soft substrate, the film should be flexible enough to follow the polymer material transformation. We have modified the DLC film structure to permit both expansion and contraction. Hardness of this film is lower than that of usual DLC films (Hv 15 GPa or higher). Because of the above mentioned characteristics of this film, we have named it "Flexible DLC (A trade mark in Japan)."

The details of this "Flexible DLC (F-DLC)" have been reported in other papers (ref. 16, 17). Consequently, we established the mass-production apparatus for this F-DLC. Major features of F-DLC are as follows: (1) Low friction coefficient (0.25), (2) better wear resistance, (3) no detachment of thin DLC film even after the soft substrate is deformed, (4) no deterioration of rubber and polymer substrate due to the extreme low process temperature of 333 K or less, (5) good water repellent effect, and (6) good gas barrier effect. Using these unique features, extensive marketing activities have been carried out.

One of the typical applications of F-DLC is that to the rubber seal ring (so called "O-ring"). F-DLC coated O-ring was successfully applied to the sealing parts of zoom lens system of 35mm compact film cameras (ref. 18).

F-DLC coated O-ring for compact zoom camera

This type of compact cameras has special feature of waterproof against a splash (all weather design), and is equipped with 4.5x zoom lens system. Therefore, this zoom lens system requires the sealing system to protect from both water and light. Figure 4 shows the schematics of the zoom lens system. Each O-ring (lip seal) is fixed at the inside edge of zoom sleeve, and touches with the outside of inner sleeve. If the friction coefficient of rubber lip against the zoom sleeve (painted) is high, large power consumption arises during zooming action to shorten the battery life.

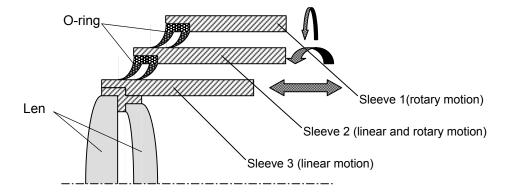


Figure 4. Schematics of zoom lens system for 35mm compact camera (ref. 18).

Before applying the F-DLC to the O-rings, polytetrafluoroethylene (PTFE) coating was used to provide the slippery characteristics. However, since PTFE coating was carried out using spray, it was difficult to control the film thickness and to obtain the non-coated area precisely. Furthermore, the elastic property of PTFE film is not enough, PTFE film is occasionally broken during assembling the camera. These phenomena lead to the inferior of assembled camera.

In order to reduce such troubles, F-DLC coating was applied to the O-ring. It was confirmed by the preparatory test that there was no negative effect, and the expected performances were realized. This camera equipped with F-DLC coated O-ring was put into commercial production in March 2001. After the production of 400,000 cameras in a year, it became clear that there was no inferior which was caused by the trouble of the F-DLC coated O-ring.

SUMMARY

Today's situation of DLC was summarized as above. There are various types of DLCs available in the global market. But it is required for us to use each DLC for each application considering the film properties, which are strongly depended on the film contents and the deposition process.

Our HA-DLC, whose adhesion strength is remarkably improved compared to the conventional DLCs, is developed for heavy-duty use. HA-DLC coated cutting tools show superior performance for the aluminum dry machining.

Our F-DLC is specially designed for rubber and resin components using very low temperature deposition process. The F-DLC coated O-ring was successfully applied to the sealing parts of zoom lens system of the 35mm compact film camera in the commercial production. As a result, F-DLC contributed to reducing the occurrence of inferior product.

REFERENCES

- 1. Aisenberg, S.; Chabot, R.: Physics of ion plating and ion beam deposition. Journal of Applied Physics, vol. 42, no.7, 1971, 2953-2958.
- 2. Weissmantel, C.; Reisse, G., et al.: Preparation of hard coatings by ion beam methods. Thin Solid Films, vol. 63, 1979, 315-325.
- 3. Dimigen, H.; Hübsch, H., et al.: Tribological and electrical properties of metal-containing hydrogenated carbon films. Applied Physics Letter, vol. 50, 1987, 1056-1058.
- 4. Liu, Y.; Erdemir, A., et al.: An investigation of the relationship between graphitization and frictional behavior of DLC coatings. Surface and Coating Technology, vol. 86-87, 1996, 564-568.
- 5. Donnet, C.; Fontaine, J., et al.: Diamond-like carbon-based functionally gradient coatings for space tribology. Surface and Coating Technology, vol. 120-121, 1999, 548-554.
- 6. Erdemir, A.; Eryilmaz, O.L., et al.: Synthesis of diamondlike carbon films with superlow friction and wear properties. Journal of Vacuum Science and Technology, vol. A 18, no. 4, 2000, 1987-1992.
- 7. Erdemir, A.; Eryilmaz, O.L., et al.: Synthesis of superlow-friction carbon films from highly hydrogenated methane plasmas. Surface and Coating Technology, vol. 133-134, 2000, 448-454.

- 8. Fontaine, J.; C. Donnet, C., et al.: Tribochemistry between hydrogen and diamond-like carbon films. Surface and Coating Technology, vol. 146-147, 2001, 286-291.
- 9. Erdemir, A.: The role of hydrogen in tribological properties of diamond-like carbon films. Surface and Coating Technology, vol. 146-147, 2001, 292-297.
- 10. Fukui, H.; Irie, M., et al.: An investigation of the wear track on DLC (a-C:H) film by time-of-flight secondary ion mass spectroscopy. Surface and Coating Technology, vol. 146-147, 2001, 378-383.
- 11. Ferrari, A.C.; Robertson, J.: Interpretation of Raman spectra of disordered and amorphous carbon. Physical Review B, vol. 61, no. 20, 2000, 14095-14107.
- 12. Monaghan, D.P., Teer, D.G., et al.: Deposition of wear resistant coatings based on diamond like carbon by unbalanced magnetron sputtering. Surface and Coating Technology, vol. 60, 1993, 525-530.
- 13. Sugimoto, I.; Miyake, S.: Oriented hydrocarbons transferred from a high performance lubricative amorphous C:H:Si film during sliding in a vacuum. Applied Physics Letters, vol. 56, no. 19, 1990, 1868-1870.
- 14. Kanou, M.: Application of DLC Coating to Sliding Parts in Engine. Journal of Japanese Society of Tribologists (in Japanese), vol. 47, no. 11, 2002, 815-820
- 15. Kuwayama, K.:Friction of DLC/a-SiC Coated Alumina in Water. Synopses of International Tribology Conference, Nagasaki, 2000, 216
- 16. Sasaki, S.; Nakahigashi, T.: Evaluation of tribological properties of DLC coated on rubbers using nano-indentation and nano-scratch testing. Synopses of International Tribology Conference, Nagasaki, 2000, 435
- 17. Nakahigashi, T.; Miyake, K., et al.: Properties of flexible DLC film deposited by amplitude-modulated RF p-CVD. (Presented in the 27th Annual International Conference & Exposition on Advanced Ceramics & Composites, Cocoa Beach Florida, January 2003. To be published in Journal of American Ceramics Society)
- 18. Nakahigashi, T.; Iura, S., et al.: Application of flexible DLC coating to O-ring for zoom camera (in Japanese). Proceedings of JAST tribology conference Tokyo, May 2002, 2002, 109-110

DEVELOPMENT OF HARD CARBON FILMS AND THEIR TRIBOLOGICAL PROPERTIES FOR THE FRONTIER CARBON TECHNOLOGY PROJECT

Akihiro TANAKA

Research Center for Advanced Carbon Materials, National Institute of Advanced Industrial Science and Technology AIST Tsukuba Central 5, Tsukuba 305-8565, Japan e-mail: a-tanaka@aist.go.jp, Fax: +81-29-851-5425, Phone: +81-29-861-7069

ABSTRACT

In Japan, a national project called the "Frontier Carbon Technology (FCT)" project has been in existence from 1998 with a five-year plan for development. This project included Research and Development of processing technologies with materials that had highly desirable mechanical properties such as low friction, high wear resistance, and high adhesion. Diamond-Like Carbon (DLC) films with excellent friction and wear properties were prepared using thermal electron excited plasma Chemical Vapor Deposition (CVD) system. This system was characterized by a pulse-bias technique. The DLC film deposited under the appropriate conditions exhibited low friction coefficients (0.03 to 0.07), and a small specific wear rate of 3*10⁻⁹-mm³/Nm; these values were superior to the desired targets of the FCT project. Adhesion of DLC film to the substrate was improved using a process consisting of Electron Cyclotron Resonance (ECR) plasma-enhanced CVD combined with high-energy ion implantation. The DLC film deposited by this system exhibited stability (i.e., without peeling) under severe sliding conditions that included a 100-N load (maximum contact pressure of 2.6-GPa). DLC films were synthesized on complex-shape substrates by a plasma-based ion implantation (PBII) system developed for the FCT project. The thickness uniformity of the DLC film deposited on a substrate which simulated a complex-shape was within a distribution of ±10 %. A journal bearing unit was coated by a CVD diamond-film. The bearing unit, which was accurately finished by high speed grinding, demonstrated very low friction.

Keywords: DLC film, Diamond film, Tribology, Friction, Wear, Adhesion, Bearing

INTRODUCTION

In Japan, a national project on highly functional carbon and related material technology, "Frontier Carbon Technology (FCT)" has been conducted since 1998, following a five-year plan. The FCT project consisted of two

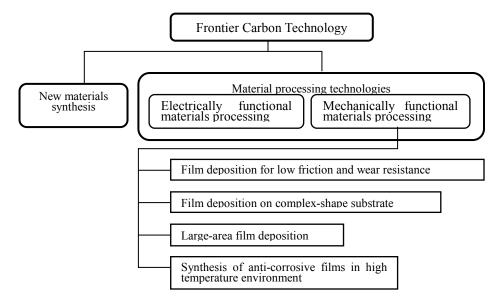


Fig. 1 FCT project

types of R&D, i.e., new materials synthesis technologies and material processing technologies. R&D on material processing technologies included two processing technologies for electrically and mechanically functional materials (Fig. 1)., Synthesis technologies for materials with excellent tribological properties or corrosion resistance at high temperatures were developed as part of the R&D effort on mechanically functional materials processing. Film deposition technologies were also developed on complex-shape substrates and large-area substrates. This paper details the results of this R&D effort on mechanically functional materials processing, focusing on those results with excellent tribological properties.

DLC FILMS WITH BOTH LOW FRICTION AND HIGH WEAR RESISTANCE AND EXCELLENT ADHESION $^{(1,\,2)}$

DLC films with low friction and high wear resistance

DLC films were prepared using a thermal electron excited plasma CVD system, characterized by a pulse bias technique (Fig. 2). The material gas used was benzene and the substrate was a silicon wafer and an alloy steel. The

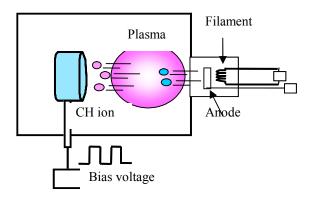


Fig.2 Thermal electron excited plasma CVD

films were deposited using the following pulse bias conditions; a frequency of 1-kHz, a bias voltage from -0.5 to -3-kV, and a duty ratio from 1 to 100 %. The duty ratio is the ratio of the time when the voltage was turned-on to the total time of one cycle. The film thickness varied from 0.6 to 1.7-µm

Friction and wear properties of the films were examined using a ball-on-disk friction tester consisting of a SiC ball in dry air. Fig. 3 shows the friction and wear of DLC films on silicon wafers, evaluated under 2-N load. The

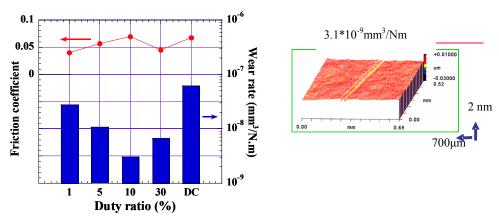


Fig. 3 Friction and wear of DLC films deposited by a pulse-bias technique

friction coefficient exhibited very low values of between 0.03 and 0.07, independent of the duty ratio. The specific wear rate, however, depended substantially on the duty ratioe and exhibited a minimum value of 3*10⁻⁹-mm³/Nm at a duty ratioe of 10 %; the wear depth was extremely shallow as shown in Fig. 3. These values of friction and wear were superior to the targets of the FCT project; a friction coefficient of < 0.1 and a specific wear rate of 10⁻⁸-mm³/Nm. Analysis of DLC films showed that the hydrogen content increased and the internal stress decreased with a decreasing duty ratio. A decrease in internal stress generally brings an increase in adhesion between the film and substrate. When the DLC film was deposited, using the pulse bias technique, however, the decrease in internal stress seemed to affect wear as well as adhesion. The excessive hydrogen content must produce a polymer-like carbon film with a lower wear resistance, although the internal stress decreases.

Another approach was conducted to develop a DLC film with superior friction and wear properties. DLC multilayer films, consisting of alternating sub-layers of soft and hard DLC films, were deposited using the same plasma CVD system. A soft DLC sub-layer, which had a relatively low hardness, good adhesion and low internal stress, was deposited on a substrate with a relatively high dc bias voltage, along with argon incorporation in the first layer. A second hard DLC film with relatively high hardness and high internal stress was deposited with a low bias voltage and without argon incorporation. The soft and hard sub-layers were alternately laminated by sequential deposition. The outmost sub-layer was formed with the hard DLC sub-layer.

The tribological properties of DLC multilayer films were investigated using a ball-on-disk friction tester, using a SiC ball. Fig. 4 shows the friction-and-wear behavior of the DLC multiplayer with both a four-layer and single layer films under a 2-N load in different environments (dry air, O_2 , and vacuum). The friction coefficient was controlled by the environment. The multilayer structure had little influence on the friction coefficient of the DLC films. Compared to the DLC single layer film, there was only small increase in the friction coefficient with the DLC multilayer film. However, the wear of the DLC single layer film was obviously influenced by the environment. The specific wear rate of the DLC single layer film was very high, in the range of 10^{-7} -mm³/Nm when sliding in O_2 and air. The specific wear rate of the multilayer films under different environments, on the other hand, was almost the same, and exhibited a low and stable value of $\sim 1*10^{-8}$ -mm³/Nm for all three environments. The DLC multiplayer film with a further improvement in the deposition process showed excellent tribological properties and good adhesion even under a high load of 20-N.

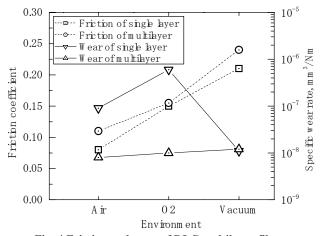


Fig. 4 Friction and wear of DLC multilayer films

DLC films with excellent adhesion

DLC film adhesion to a substrate was improved using an apparatus consisting of ECR plasma-enhanced CVD,

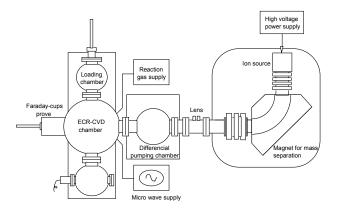


Fig. 5 ECR plasma CVD apparatus combined with an ion implantation system

combined with high-energy ion implantation (Fig. 5). The advantage of this apparatus is that it can CVD-coat and ion-implant simultaneously. The substrates chosen were practical materials such as alloyed steel and a nickel-based alloy. An interlayer of C-Si was first deposited on a substrate using implanted carbon ions and then a gradated DLC film.

Fig. 6 shows the friction behavior of DLC films on an alloy steel substrate that was measured with a ball-ondisk friction tester consisting of a SiC ball under a heavy load of 100-N. This is equivalent to a maximum contact pressure of 2.6-GPa. The DLC film with both an interlayer deposition and ion implantation, maintained a low friction coefficient of < 0.05 until more than 41,000 revolutions were achieved. The DLC film with interlayer only

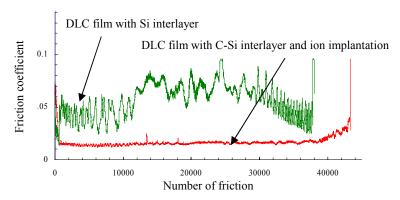


Fig. 6 Friction behaviors of DLC films with and without IP under 100-N

ruptured at a lower revolution count. These results suggest that both interlayer and ion implantation together is very effective method to improve film adhesion.

DLC FILMS DEPOSITED ON COMPLEX- SHAPE SUBSTRATES (3)

DLC films were synthesized on complex-shaped substrates using a plasma-based ion implantation (PBII) method developed for the FCT project (Fig. 7). ECR plasma with a mirror field was used to generate a high-density plasma. A negative DC and high-voltage pulse-bias were simultaneously supplied to the substrate. DLC films were deposited to substrates placed on the surface of a concave or a convex holder, which simulated a complex-shape, machine part.

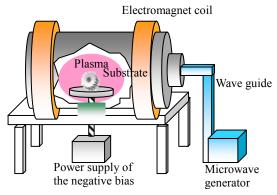


Fig. 7 Plasma-base ion implantation system developed for FCT project

The normalized thickness of DLC films deposited on convex and concave holder substrates is shown in Fig. 8. The film thickness formed on a convex face (microwave incident angle > 0) was almost constant, and independent of the deposition conditions. The DLC films with both DC and a 5- μ s pulse-bias, had a good thickness uniformity even on the substrates held the concave holder (microwave angle < 0). The thickness uniformity of DLC films deposited on the substrate for both holders was within a distribution of ± 10 %. This result suggests that all substrates were immersed in a uniform plasma density. The DLC films with both DC and a 5- μ s pulse-bias showed a low and constant friction coefficient of 0.02 under a high load of 20-N, and irrespective of the microwave incident angle.

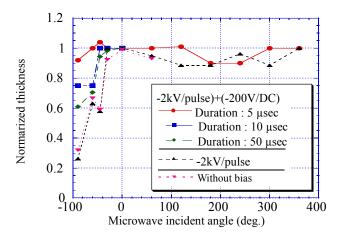


Fig. 8 Film thickness of DLC films deposited by PBII method

PRESISION MACHINING OF DIAMOND COATED BEARING (4)

A precise, diamond-coated bearing unit was developed. Diamond films were deposited on the outer surface of the shaft and the inner surface of a journal bearing composed of Si₃N₄, using a hot filament-CVD method. The size of shaft was 8-mm in diameter and 30-mm in length, the size of bearing was 8-mm in bore and 9-mm in length. Film thickness on both shaft and bearing was 25 to 30-μm and 7 to 10-μm, respectively. The surface roughness and cylindrical accuracy after deposition were over acceptable limits. The application of a high speed grinding technique to the diamond coated bearing unit gave a smooth surface and an accurate cylindrical shape. After grinding, the roundness, cylindrical accuracy, and maximum surface roughness of the shaft were 1.2, 1.5, and 0.5-μm, respectively.

With the journal bearing, a high speed grinding gave a roundness and maximum surface roughness of 1.9 and 0.1- μ m, respectively. This finishing was acceptable for the quality expected of a journal bearing unit. The friction test of this bearing unit gave a friction coefficient < 0.01, although it was fairly high at the early stage of test.

ACKNOWLEDGEMENTS

This work was been supported by the New Energy and Industrial Science and Technology Development Organization of Japan, as a part of the FCT project of the Ministry of Economy, Trade and Industry of Japan.

REFERENCES

- 1) K. Wazumi, A. Fuchigami, Tanaka, and Y. Koga, Proc. ADC/FCT 2003, (2003).
- 2) W. Zhang, A. Tanaka, K. Wazumi, and Y. Koga, Proc. JAST Tribology Conf., (2003).
- 3) T. Watanabe, O. Tsuda, M. Suzuki, K. Yamamoto, Y. Koga, and A. Tanaka, Proc. ADC/FCT 2003, (2003).
- 4) T. Imai and Y. Seki, Proc. 3rd Symp. on FCT, (2003) 110, (in Japanese).

FRICTIONAL BEHAVIOR OF NANO-UNDULATED SURFACE OF DIAMOND-LIKE CARBON FILMS

S. J. Park, C. S. Lee, T. Y. Kim and K.-R. Lee

Future Technology Division, Korea Institute of Science and Technology, P.O Box 131, Cheongryang Seoul 130-650 Korea

D.-H. Ko

Department of Ceramic Engineering Yonsei University Seoul 120-701 Korea

ABSTRACT

Frictional behavior of nano-undulated diamond-like carbon (DLC) films deposited by plasma assisted chemical vapor deposition (PACVD) process was investigated. In order to prepare the nano-undulated DLC film, a Si wafer with nano-sized Ni dots was prepared by rapid thermal annealing of Ni thin films. Since the structure of DLC film deposited by PACVD was independent of the substrate materials and that the size of Ni nano dots could be controlled in a systematic way by changing the thickness of the Ni film, we could investigated the effect of nano-scale surface roughness on the tribological behavior of DLC films. The friction coefficient between steel ball and undulated DLC films of the roughness varying from 0.6 to 13.7 nm was measured by using a ball-on-disk type wear rig in ambient environment. The friction coefficients were in the range from 0.15 to 0.2, independent of the surface roughness. Wear of the steel ball was much enhanced with higher content of Fe in the debris as the roughness increased. However, the size of the debris decreased with increasing roughness. Raman spectrum analysis revealed that the chemical bond structure of the debris is significantly dependent on the surface roughness. The friction behavior was discussed in terms of the chemical compositions and the agglomeration behavior of debris.

Keywords: Nano-undulated surface, Friction behavior, Diamond-like carbon film

INTRODUCTION

Surface roughness of materials has been considered to affect significantly on their tribological behaviors (ref. 1). In macro-scale tribology, it was reported that the surface roughness could reduce the friction coefficient by suppressing the wear particle generation, removing the wear particle from sliding interface or/and preventing the wear particle agglomeration (refs. 2 and 3). This artificial rough surface has the potential for artificial joint because of the low friction coefficient and the suppression of the wear particle generation (refs. 4 and 5). However, systematic investigation on the dependence of the tribological behaviors on the surface roughness in nano-scale was yet to be reported.

Recently, we suggested a method to manipulate the microstructure of tetrahedral amorphous carbon (ta-C) films deposited by filtered vacuum arc process (ref. 6). By incorporating the nano-sized Ni dots on the substrate surface, we could obtain nano-sized graphitic phases grown from the Ni dots to the surface. In addition to the possibility of nano-scale manipulation of the ta-C films, this method can also be used to control the surface roughness in nano-scale by adjusting the size of Ni dots. In contrast to the filtered vacuum arc process, PACVD deposition resulted in the homogeneous microstructures of carbon regardless of the substrate materials. By employing PACVD method for carbon deposition, nano-scale undulated surface of the DLC film could be obtained. In the present work, the DLC film of nano-scale undulated surface was used to investigate the tribological behaviors for various values of surface roughness. In the present range of the surface roughness (from 0.5 to 14 nm), the tribological behavior was independent of the roughness presumably due to the smaller size of debris and suppressed tribo-chemical reactions in rough surface.

EXPRIMENTAL PROCEDURE

Nano-sized Ni dots on Si substrate were prepared by annealing Ni thin films of thickness ranging from 3 to 14 nm. The Ni thin film was deposited on the 600- μ m-thick Si (100) wafers by DC magnetron sputtering method. In order to change the deposited Ni film to nano dots, the specimen was annealed in a rapid thermal process (RTP) at 800° C for 15 min in hydrogen environment. Hydrogen pressure during the annealing was kept at 1 Torr by adjusting the flow rate of hydrogen. Ni dots of diameter ranging from 15 to 90 nm were uniformly distributed on the substrate. The average size of nano Ni dots monotonically increased with the thickness of the Ni film.

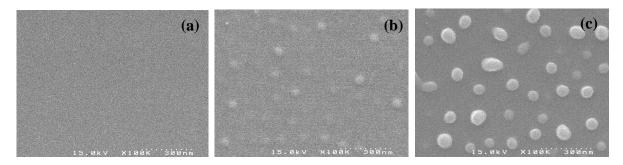
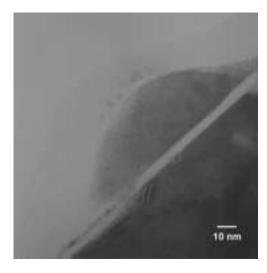
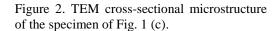


Figure 1. SEM microstructure of DLC films surface. (a) rms=0.6nm (b) rms = 5.1 nm (c) 13.7 nm

DLC film was deposited by radio frequency plasma assisted chemical vapor deposition (r.f.-PACVD) using methane as precursor gas. The film was deposited at the negative bias voltage –150V and deposition pressure 1.33 Pa. Thickness of the film was fixed at 100 nm in all samples. Roughness of the film measured by an atomic force microscope ranged from 0.6 to 13.7 nm depending on the thickness of the Ni films. SEM microstructure of the surface was shown in Fig. 1. Tribological properties were characterized by using ball-on-disk type wear rig using steel ball (AISI 52100) of diameter of 6 mm as the counter face materials. Normal load was fixed at 4 N (0.53GPa) and the sliding speed 17.3 cm/s. The test environment was in ambient air at room temperature. After the tribological characterization, SEM, Auger electron spectroscopy and Raman spectroscopy were employed to analyze the morphologies and chemical bond structure of the debris and the wear track.

RESULTS AND DISCUSSION





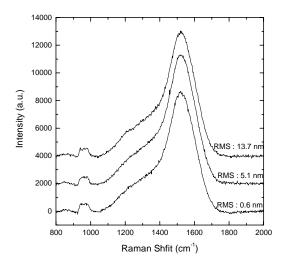


Figure 3. Raman spectra of DLC films for various surface roughness.

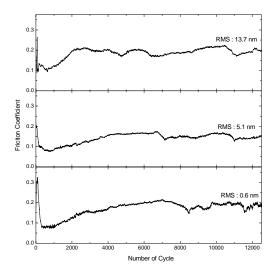


Figure 4. Evolution of friction coefficient for various values of surface roughness.

Microstructure of the DLC films and the interface was investigated by cross sectional TEM microscope. Figure 2 shows the TEM microstructure of the sample of Fig. 1 (c). In contrast to the case of ta-C films, growth of second phase on Ni catalyst could not be observed in the present work. Instead, amorphous layer was uniformly covered both Si substrate surface and Ni nano dots. EDS analysis showed that the composition of the deposited film was pure carbon. Homogenous single phase of carbon film deposition could also be confirmed by Raman spectroscopy. Figure 3 shows the Raman spectra of the films. All the spectra were essentially same regardless of the thickness of Ni film, i.e. the size of Ni dots. No significant change in wetting angle of pure water, electrical resistivity and residual compressive stress could be observed. These results thus showed that the homogeneous DLC films of different surface roughness could be prepared by the present method.

Figure 4 is the evolution of friction coefficient with increasing the number of contact cycle. After the initial

transient period, steady state of the friction occurs after 2,000 cycles. Even if the increase in the friction coefficient to the steady state coefficient occurred earlier in the roughest film, the steady state friction coefficients were independent of the surface roughness. However, the roughness of the surface significantly enhanced the wear of the steel ball. The wear rate of the ball increased from 3.8×10^{-10} to 1.8×10^{-9} mm³/cycle as the roughness increased from 0.6 to 13.7 nm. Composition analysis by Auger electron spectroscopy also showed that the amount of Fe in the debris increased with the surface roughness.

SEM microstructures of the debris near wear track were shown in Fig. 5. The SEM microstructure showed that the debris agglomeration was suppressed with the surface roughness. Raman spectra of the debris shown in Fig. 6 revealed a significant difference in the chemical bond structures of the debris. Raman peak near 700 cm⁻¹ is the characteristic line of Fe oxide. D and G peak, centered at 1300 and 1550 cm⁻¹ respectively, composed the carbon Raman peak. As the roughness increased, intensity of Fe oxide peak decreased. This result implies that the tribochemical reaction to oxidize Fe originated from the wear of steel ball was considerably suppressed in rough surface. Another significant observation in Raman spectra would be the changes in carbon Raman peak. The shape of carbon peak changed from that of typical DLC films to graphitic one with decreasing the surface roughness. This observation also confirmed that the tribo-chemical reaction was suppressed in the case of rough surface.

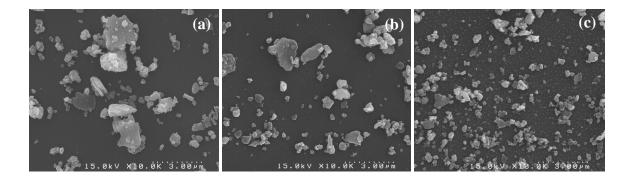


Figure 5. SEM microstructures of the debris near the wear track. (a) rms=0.6nm (b) rms = 5.1 nm (c) 13.7 nm

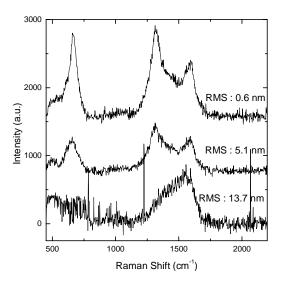


Figure 6. Raman spectra of the worn scar debris on the steel balls

It was reported by the present authors that the debris composition and their agglomeration during sliding play an important role to determine their tribological behaviors (ref. 7). The humidity dependence of the friction between DLC film and steel ball was shown to be due to the Fe oxide debris and their agglomeration. In high humid environment, Fe oxide debris dominates in the sliding environment, resulting in higher friction coefficient. The present observation can be understood based on the same conjectures. Increasing surface roughness can resist the sliding as can be deduced from the increased wear of the ball. However, smaller debris of DLC structure might have an opposite effect on the friction coefficient. Furthermore, reducing amount of Fe oxide with increased surface roughness could decrease the friction coefficient. These two opposite effects seem to result in the friction behavior independent of the surface roughness.

CONCLUSIONS

Nano-scale undulated DLC films prepared by PACVD using Ni nano dots on the Si substrate made it possible to investigate the friction behavior of DLC films for various surface roughness in nano-scale. Although the friction coefficient appeared independent of the surface roughness, the tribo-chemical reactions such as debris shape, composition and chemical bond were intimately related with the surface roughness. Surface roughness enhanced the wear of counter face materials, which might increase the friction coefficient. However, oxidation of Fe and graphitization of the debris were suppressed by the surface roughness, which would suppress the agglomeration of the debris. These changes in the case of rough surface might reduce the friction coefficient. These two opposite effects seem to be balanced in the present experimental condition resulting in the friction behavior independent of the surface roughness. More elaborate experimental work is in progress to separate the opposite effects.

ACKNOWLEDGEMENTS

This research was performed by the financial support of 'Center for Nanostructured Materials Technology' under '21st Century Frontier R&D Programs' of the Ministry of Science and Technology, Korea.

REFERENCES

- 1. Rabinowicz, E.: Friction and wear of materials. John Wiley & Sons, New York, N. Y., 1995, 179
- 2. Oktay, S. T. and Suh, N. P.: Wear Debris Formation and Agglomeration. J. Tribol., 114, 1992, 379
- 3. Suh, N. P., et al.: Control of Friction. Wear, 175, 1994, 151
- 4. Nishimura, I., et al.: Modification of the Frictional Surface of Artificial Joint. ASAIO Journal, 1993, 762
- 5. Young, S. K., et al.: Friction reduction in total joint arthroplasty. Wear, 222, 1998, 29
- 6. Lee, C.-S., et al: Nanoscale Manipulation of Tetrahedral Amorphous Carbon Film, submitted to Thin Solid Films, 2003.
- 7. Park, S. J., et al.: Humidity Dependence of the Tribological Behavior of Diamond-like Carbon Films against Steel Ball. Submitted to Diam. Rel. Mater, 2002.

TRIBOLOGICAL PROPERTIES OF SEGMENT-STRUCTURED DIAMOND-LIKE CARBON FILMS

*Yuichi AOKI and Naoto OHTAKE

Department of Mechanical Science and Engineering, Tokyo Institute of Technology 2-12-1, O-okayama, Meguro-ku, Tokyo 152-8552, Japan *e-mail: yuuichi@stu.mech.titech.ac.jp, TEL: +81-3-5734-2418, FAX: +81-3-5734-2824

ABSTRACT

Diamond-like carbon (DLC) have been widely recognized as a tribo-coating material with a high wear resistant solid lubricant with a low friction coefficient. The tribological behavior of DLC films depends on the environmental conditions, the nature of the coating, and mechanical properties of a substrate. Particularly, when the DLC films are distorted with the deformation of the soft substrate, it is apparent that fragile DLC films are strongly damaged. In this study DLC films have been deposited by RF-plasma CVD with a methane gas on the soft material substrates, such as a rubber and aluminum, and the friction and wear tests were conducted using a ball-on-disk test. In the case of rubber substrate, DLC films show relatively low friction coefficient from 0.2 to 0.3, despite of large substrate deformation. Observation results of the surface of the rubber substrates suggest that the DLC film forms a "segment structure" automatically, then "segment structure coating" was applied to aluminum substrate. Ball-on-disk test results revealed that wear resistance of the segment-structured DLC film was about two-fold higher than that of a conventional continuous DLC coating.

Keywords: Diamond-like carbon, soft substrate, Tribology, Friction, Deformation, segment-structure

INTRODUCTION

The tribological properties of diamond-like carbon films have been widely studied (refs. 1 to 3). Their high hardness, low friction coefficient and high chemical stability have made them great candidates for wear-resistant coatings for many applications (refs. 4 to 5). In order to enlarge the application field of DLC films, there are many technical requirements. For example, optimization of internal stress to improve in adhesion, preparation of thick films, deposition on the substrate which has three-dimension complicated shapes, are mentioned. Especially improvement of adhesion is important problem (refs. 6 to 8). When DLC films deposited on the steel substrate which is well used in industry, fabrication of Si interlayer between substrate and DLC is effective in improvement of adhesion. Furthermore the addition of Si or Ti into the coatings reduces internal stress of DLC films and the DLC film has good adhesion to a substrate (ref.9). Internal stress improves film hardness, however it makes the DLC film brittle (ref.10). When substrate is a soft material such as rubber, DLC film is distorted with the deformation of substrate, and then DLC film is damaged. At this time DLC coatings are successfully applied to hard materials. If DLC coating can be applied to a soft substrate, the application field of DLC will be enlarged.

The purpose of this paper is to present a new coating method which can be applied to soft material substrates. First, first, tribological property of DLC films prepared on a rubber substrate by RF-plasma CVD are discussed using a ball-on-disk test. Observation results of the substrate led us idea that segment structure is formed automatically. Based on these results, a new coating method: "segment-structured DLC coating" is proposed. Segment-structured DLC films are prepared on a soft Al (purity 99.6%) substrate. Tribological properties are discussed comparing with conventional continuous DLC films.

EXPERIMENTAL

Figure 1 shows a schematic of a RF-plasma CVD apparatus used for preparation of DLC films. The apparatus consist of a magnetron electrode, a substrate holder and a vacuum chamber. The magnetron electrode and the substrate holder can be applied RF power and they are water-cooled. Methane was used as a source gas. By applying RF (13.56 MHz) power, the substrate holder or the magnetron cathode is negatively charged. Maximum RF power supply was 500 W. The substrate biasing voltage $V_{\rm dc}$ by self-biasing was varied from 0 to -500V. Si interlayer can be prepared by RF-magnetron sputtering before deposition if necessary. Si target of 60 mm in

NASA/CP—2003-212319 423 August 18, 2003

diameter was placed on the magnetron cathode. Substrate was rinsed in acetone and mounted on the substrate holder. After substrate introduction, the chamber was pumped to the base pressure of 10⁻³ Pa. Then, argon plasma was initiated at the substrate holder to remove contaminated layer at the surface of the substrate. The standard condition of argon flow introduced into the chamber was about 10 cm³/min. After the substrate pretreatment, the argon gas valve was closed and methane gas with a standard condition flow rate about 5.5 cm³/min was then introduced into the chamber regulated to 10 Pa. Subsequently, glow discharge was generated to prepare DLC films on the substrate.

Figure 2 shows a schematic drawing of wear test. Friction and wear properties were evaluated in dry sliding tests using a conventional rotational ball-on-disc (BoD) apparatus. The specimen was mounted on the rotational table and mirror-polished steel balls 6mm in diameter were slid against the DLC films deposited on a substrate with no additional lubrication. A sliding speed of about 0.1 m/s and normal load range of 0.5-5 N were used. Friction coefficient was calculated from the normal load and the frictional force measured by load cells.

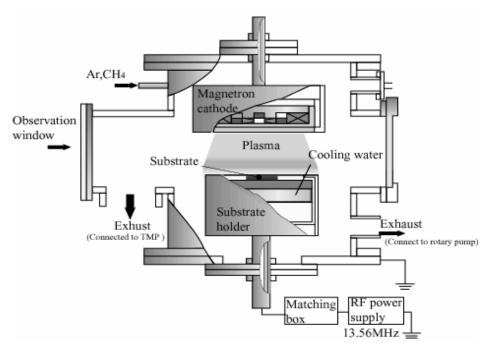


Fig.1 Schematic illustration of RF plasma CVD apparatus

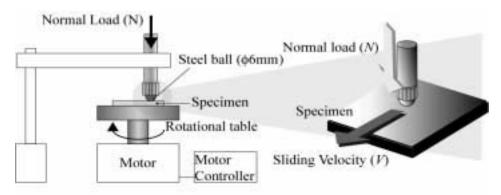


Fig.2 Schematic illustration of friction and wear test using a rotational ball-on-disc (BoD) apparatus

RESULTS AND DISCUSSION

Preparation of DLC films on a rubber substrate and its tribological property

Deposition parameters of DLC films on a rubber substrate are shown in Table 1. The butyl rubber substrate used in this study was about $15x50x1mm^3$. RF-power was 100 W and self-biasing voltage was 300V. Under this condition, the deposition rate was estimated to be about 50 nm/min and DLC films were about 0.8 μ m thick after 15min. deposition.

Typical Raman spectrum of the DLC films grown at the rubber substrate is shown in Fig.3. It can be seen that the spectrum is consisting of a G peak and a D peak, indicating that this is DLC films. The lower line is the Raman spectrum of the rubber substrate.

Figure 4 (a) shows the effect of the load on the friction coefficient between the stainless steel ball and a rubber coated with DLC films. Normal load was varied from 0.98N to 4.9N. The friction coefficient of films is approximately constant (from 0.1 to 0.2) during 9,000 cycles at the load of 0.98, 1.96N. However, At the load of 2.94, 4.90, high coefficient is observed and then friction coefficient is increase suddenly at around 200cycles because the rubber substrate was fatally damaged due to the high load rather than DLC films peeled off. Secondly wear test was performed under adding the large strain to the substrate. Figure 4 (b) shows the effect of the substrate deformation on the friction coefficient. The normal load was kept at 0.49N and a tensile strain added to the substrate was H0.25,0.5. Although the result indicate the friction coefficient of each films is slightly increase from 0.15 to 0.25 during 25,000 cycles, low friction coefficient is maintained. It should be noted that the fiction coefficient of DLC films on the rubber substrate does not depend on the tensile strain. It is generally believed that DLC film is damaged if large strain is added, nevertheless the friction coefficient is constant in this experiment. This means that DLC films prepared in this study have a certain degree of plasticity and moreover do not completely peeled off from the substrate even if large tensile strain is added. Thickness of DLC films was about 1 μ m, which is almost the same as the surface roughness of a rubber substrate. It is likely that by adding the tensile strain, DLC films are fractured at the concave parts of the substrate and remain at the convex part. This schematic illustration is shown in Fig.5.

Table 1 Deposition condition

Substrate	Butyl rubber	CH ₄ flow	5.5 cm ³ /min
RF power	100 W	Pressure	10 Pa
frequency	13.56 MHz	Deposition time	15 min.
Self biasing	300 V	Film thickness	about 0.8 µm

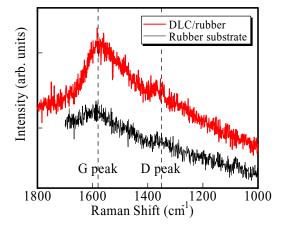


Fig.3 Raman spectrum of DLC films on a rubber substrate

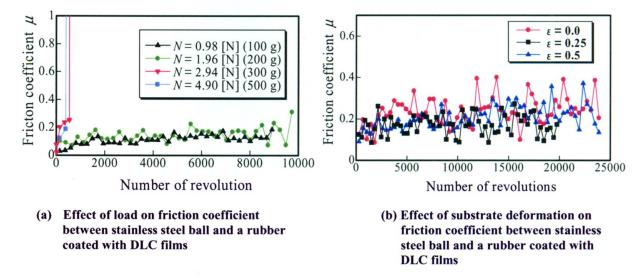


Fig.4 Friction coefficient vs. rotation number in a ball-on-disc test for different conditions

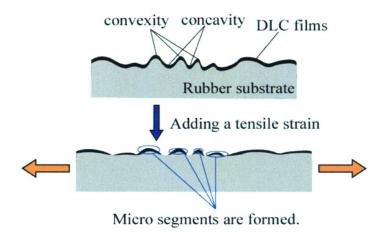


Fig. 5 Schematic illustration of micro segment model

Preparation of segment-structured DLC films on an Al substrate and its tribological property

Segment structure

Figure 6 illustrates the concept of segment structure. DLC films are intentionally separated into contiguous small segments shown in the right-hand figure. When a substrate is deformed, continuous DLC films are ordinarily damaged by the strain (ε), shown in the left-hand figure. On the other hand, it is expected that segment-structured DLC films cope flexibly with the deformation of a substrate even if large strain is applied to the film. This structure is expected to reduce the strain of DLC films.

Figure 7 (a) shows the preparation method of segment-structured DLC films. Tungsten mesh wire was set above the substrate for masking as a grid-like structure. Tungsten wire of 0.1mm in diameter was used and grid interval was 1mm. DLC films with the segment size of 1x1mm² and interval of 0.1mm between segments was obtained. Figure 7(b) shows the optical microscopic view of the segment-structured DLC film prepared.

Preparation of segment-structured DLC films

Tungsten mesh wire was set above the substrate after the substrate was placed on the substrate holder. After the sputter etching with argon plasma, Si interlayer was prepared on the substrate by RF-magnetron sputtering to

increase the adhesion. Si interlayer was about 100 nm in thickness. Then, segment-structured DLC films were prepared. Deposition parameters were about the same in the case of a rubber substrate shown in Table 1. The Al substrate used in this study was 99.6% purity and its surface roughness was about 50-200 nm. The Young's modulus of the substrate is 70 GPa. RF-power applied was 110 W and self-biasing was about -400 V. Under this condition, the deposition rate was estimated to be about 50 nm/min and DLC films were about $1.0 \text{ }\mu\text{m}$ thick after 20 min. deposition.

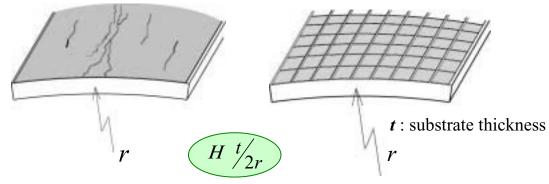


Fig.6 Schematic illustration of segment-structured DLC films

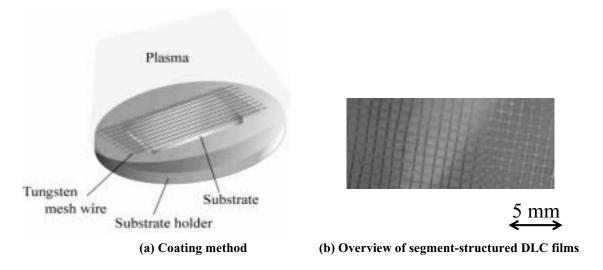


Fig.7 Coating method of segment-structured DLC films and the overview of "segment-structured DLC films"

Tribological property of segment-structured DLC films

Properties of segment-structured DLC films with Si interlayer (a), continuous DLC films with Si interlayer (b) and continuous DLC films without Si interlayer (c) were compared in order to investigate the effect of segment-structure and Si interlayer.

Raman spectra of the DLC films are shown in Fig.8 (i). Each spectrum is consisting of a G peak and D peak, indicating that these films are DLC films. The shape of the three spectra are similar, indicating that the difference in the quality of these DLC films is negligible.

Toribological properties were investigated by the BoD test. A mirror-polished stainless steel balls 6mm in diameter were slid against the DLC films at the normal load of 0.7N. The results are shown in Fig.8 (ii). In this test DLC films without Si interlayer (c) were peeled off immediately after starting the test, and so it was tested again with reduced normal load of 0.16N. On the other hand DLC films with Si interlayer (b) shows low fiction coefficient at the normal load of 0.7N until 6,000 cycles. This result shows that the adhesion between DLC and the substrate is improved by Si interlayer. Furthermore, segment-structured DLC film (a) shows low friction coefficient until 12,000 cycles, which is two-fold longer than (b). This result led us to the conclusion that the fracture of the DLC film can be successfully avoided by applying the segment structure. Additionally, abrasive wear seems to be

decreased because the debris were grabbed into the space between segments, and fracture of the film is stopped at the gap between segments.

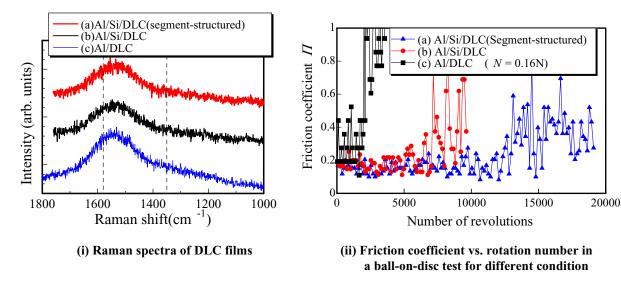


Fig.8 Tribological properties of DLC films prepared under different condition

CONCLUSION

Deposition of DLC films on the relatively soft substrate by RF-plasma CVD was carried out. The friction and wear test were performed using a ball-on-disk test. In the case of a rubber substrate, good tribological property was obtained under the large deformation of substrate, and micro segment model is suggested. In the case of an Al substrate, segment-structured DLC films were prepared with Si interlayer by a new coating method. In this test low friction coefficient was observed and the wear resistant was significantly improved in comparison with the conventional continuous DLC.

REFERENCES

- (1) C. Donnet, A. Grill: Friction control of diamond-like carbon coatings, *Surface and Coating Technol.*, vol94-95, October 1997, p456
- (2) A.Grill: Tribology of diamondlike carbon and related materials: an updated review, *Surface and Coating Technol.*, vol94-95, October 1997, p507
- (3) J.S. Wang, Y. Sugimura, et al.: The mechanical performance of DLC films on steel substrates, *Thin Solid Films*, vol.325, July 1998, p163
- (4) H. Nakaue, T. Mitani, et al.: Applications of diamond-like carbon films to electronic components, *Thin Solid Films*, vol.212, May 1992, p240
- (5) K.R. Lee, K.Y. Eun, et al.: Application of diamond-like carbon films for anti-abrasion and low friction properties of VCR head drums, *Surface and Coating Technol.*, vol76-77, December 1995, p786
- (6) K.C. Walter, M. Nastasi, and C. Munson: Adherent diamond-like carbon coating on metals via plasma source ion implantation, *Surface and Coating Technol.*, vol93, September 1997, p287
- (7) C. Donnet, J. Fontaine, et al.: Diamond-like carbon-based functionally gradient coatings for space tribology, *Surface and Coating Technol.*, vol120-121, November 1999, p548
- (8) K. Bewilogua, U, C.V. Cooper: Erratum to: "Effect of target material on deposition and properties of metal-containing DLC Me-DLC coatings", *Surface and Coating Technol.*, vol32, October 2000, p275
- (9) J.C. Damasceno, S.S. Camargo, and M. Cremona: Deposition and evaluation of DLC-Si protective coatings for polycarbonate materials, *Thin Solid Films*, vol.420-421, December 2002, p195
- (10) M.R. Begley, A.G. Evans, et al: Spherical impression of thin elastic films on elastic-plastic substrates, *International Journal of Solids and Structures*, vol.36, June 1999, p2773

Tribological properties of a-C:H thin films formed by the simultaneous application of pulse and DC bias

Toshiya WATANABE, Osamu TSUDA, Masahiro SUZUKI

Japan Fine Ceramics Center, Joint Research Consortium of Frontier Carbon Technology,
c/o Research Center for Advanced Carbon Materials, AIST Tsukuba Central 5

1-1-1 Higashi, Tsukuba, Ibaraki 305-8565, JAPAN

TEL: +81-29-861-9982 FAX: +81-29-861-4796

E-mail address: watanabe-t@aist.go.jp

Kazuhiro YAMAMOTO, Yoshinori KOGA and Akihiro TANAKA

Research Center for Advanced Carbon Materials, AIST Tsukuba Central 5

1-1-1 Higashi, Tsukuba, Ibaraki 305-8565, JAPAN

ABSTRACT

Ion-beam-assisted deposition is an efficient technique to synthesize metastable hard materials. However, it is difficult to apply this technique to surface modification of three-dimensional or complex shaped objects because of the line-of-sight process of ion beams. A new surface modification technique called "Plasma Based Ion Implantation (PBII)," is currently being studied. This is a surface modification technique that applies negative high voltage pulses to the object immersed in a plasma, and ions in a plasma are able to irradiate in any direction to the object. In this study, carbon films were formed by the application of pulse and DC bias. The relationship between the deposition conditions, such as voltage and duty ratio, and the tribological properties of carbon films were investigated.

DLC films with a low friction coefficient (0.02) and a low wear rate (6x10⁻⁸mm³/Nm) under high conducted load (20 N) could be formed by the simultaneous application of the pulse (-2kV) of duty ratio (1%) and the DC bias (-200V) for the surface of convex and concave faces with high uniformity. The uniformity of the film thickness, structure and the mechanical property was much improved over the conventional deposition technique that uses an ion beam.

Keywords: plasma based ion implantation, ECR plasma with a mirror field, DLC film, tribological property

THE TRIBOLOGICAL PROPERTIES OF DLC FILMS DEPOSITED BY HOT FILAMENT PLASMA CVD TECHNIQUE

Masahiro SUZUKI and Toshiya WATANABE

Japan Fine Ceramics Center, Joint Research Consortium of Frontier Carbon Technology c/o Research Center for Advanced Carbon Materials, AIST Tsukuba Central 5, 1-1-1 Higashi, Tsukuba, Ibaraki 305-8565, Japan

Akihiro TANAKA and Yoshinori KOGA

Research Center of Advanced Carbon Materials National Institute of Advanced Industrial Science and Technology (AIST) AIST Tsukuba Central 5, 1-1-1 Higashi, Tsukuba, Ibaraki 305-8565, Japan

ABSTRACT

Diamond-like carbon (DLC) films have good tribological properties such as a low friction coefficient and high wear resistance. However, the tribological properties of DLC films are significantly affected by other factors, such as the deposition technique, deposition conditions, and sliding conditions (velocity, normal load, and atmosphere). In this work, DLC films were deposited by a hot filament plasma Chemical Vapor Deposition (CVD) technique onto silicon wafers using a variety of source gases. The tribological properties of DLC films were investigated using a reciprocating friction tester under different sliding conditions in dry air, and the effects of test conditions, mating materials and source gases on the tribological properties of the DLC films were investigated. The tribological properties of DLC films were relatively unaffected by velocity and normal load, while mating materials had a considerable effect. The transfer layers formed on the mating material surfaces seems to play a significant role on the resulting tribological properties.

Keywords: DLC, Friction, Wear, Mating materials, Velocity, Normal load

INTRODUCTION

In most studies of DLC film properties, desirable properties have been noted, such as low friction, high wear resistance, high hardness, and high corrosion resistance (refs. 1, 2). It is known, that tribological properties are strongly affected by various factors such as deposition technique, deposition conditions, and test conditions (velocity, normal load, and atmosphere) (refs. 3 to 5). However, the study that the detailed tribological properties of DLC films have been examined widely changing the effecting factors such as deposition conditions and sliding conditions have been insufficient.

In this study, DLC films were prepared with a hot filament plasma CVD system with different source gases. The tribological properties of these films were examined, using a ball-on-plate reciprocating friction tester in dry air while under a wide variety of test conditions. To determine the mechanism of good tribological properties, the friction surfaces were examined using optical microscopy and micro-laser Raman spectroscopy. Comparative studies were also conducted of films prepared by RF plasma-CVD and ECR plasma-CVD coupled with the PBII technique.

EXPERIMENTAL

DLC film deposition

DLC films were deposited on silicon wafers by a hot filament plasma CVD technique. The carbon source gas was CH_4 in most cases, but C_6H_6 and C_7H_8 also were used for a comparison. In addition, DLC films were prepared by RF plasma-CVD and ECR plasma-CVD coupled with PBII. Film thickness was measured by a surface profilometer. Film hardness was measured by a nanoindenter. The film structural analysis was done with laser Raman spectroscopy (Ar ion laser, λ =514 nm). Hydrogen content of the DLC film was analyzed with an elastic

NASA/CP—2003-212319 430 August 18, 2003

recoil detection analysis (ERDA). The deposition conditions and some resulting mechanical properties are summarized in Table 1.

Tribological tests

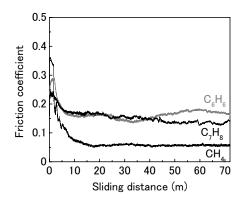
All tribological tests were conducted using a ball-on-plate reciprocating friction tester. Friction force was monitored using a strain gage. The plate specimen was a DLC film and the mating ball specimen was either a steel or ceramic ball, 4.76 mm in diameter. Prior to testing, specimens were cleaned with petroleum benzine and acetone in an ultrasonic cleaner, and then dried in desiccators.

Tests were conducted under a load of 0.6 to 4 N (Hertzian maximum stress, 0.6 to 1.2 GPa) and at reciprocation speeds of 30 to 120 cycles per minute and at a stroke length of 5 mm (linear velocity, 5 to 20 mm/s). The environment was dry air (humidity < 20%) and the total sliding distance was 72 m. The mating balls used were AISI 440C in most cases. For some tests, Al_2O_3 , Si_3N_4 and AISI 52100 balls were also used. The wear scar morphology of DLC films and mating balls were observed using optical microscopy. Transfer materials on the wear scar of the mating ball and on the wear tracks of DLC films were analyzed using micro-laser Raman spectroscopy.

RESULTS AND DISCUSSION

Effect of source gas

Figure 1 shows the effect of source gas chemistry on friction and wear properties. The CH_4 -grown DLC films exhibited a low friction coefficient and relatively high wear rates. On the other hand, DLC films deposited using C_6H_6 and C_7H_8 showed a relatively high friction coefficient and low wear rates. In all cases, the transfer was observed with mating balls, but the amount of transfer differed. These results suggest that DLC films with moderate



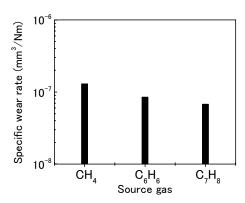


Fig. 1 Friction coefficient and specific wear rate of DLC films, prepared by different source gases

Table 1. Deposition conditions and some mechanical properties

	HF-DLC			PBII-DLC	RF-DLC	
Deposition techniques	Hot filament CVD			ECR plasma CVD in conjunction with PBII	RF plasma CVD	
Source gases	CH ₄	C_6H_6	C_7H_8	CH ₄	CH ₄	
Substrate	Si wafer					
Bias	DC:-1500V			V _{self} :-200V V _{pulse} :-2000V (duty: 1%)	DC:-700V	
Hardness (GPa)	11	28	27	10	18	
Thickness (nm)	300	450	500	300	400	
Hydrogen content (at. %)	29	23	24	37	31	

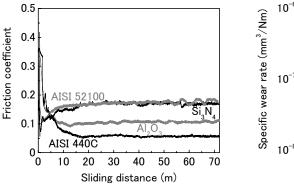
hardness show good tribological properties. For DLC films with higher hardness, the transfer amount is insufficient because of the low DLC wear rate. Therefore, the lubrication effect is insufficient. On the other hand, the wear-resistance of DLC films with lower hardness is poor.

Effects of mating materials

The effect of mating materials on friction and wear properties of DLC films is shown in Fig. 2. With all cases, the friction coefficient began with a high value of > 0.3. The friction coefficient when sliding against AISI440C and Al₂O₃, rapidly decreased to values of 0.05 and 0.1, respectively. For AISI52100 and Si₃N₄, however, the friction sharply decreased to < 0.1; in a short time, it increased gradually, and then stabilized to ~ 0.18 . Large differences were not observed among the specific wear rate of DLC films against Al₂O₃, Si₃N₄ and AISI52100 balls, and the specific wear rate value was $1-3\times10^{-7}$ mm³/Nm in all cases. On the wear surface of AISI 440C and Al₂O₃ balls, transfer materials were observed. For AISI 52100 and Si₃N₄ balls, on the other hand, no transfer material was observed. These transfer materials seem to be a key factor and are the subject of the next section.

Effects of normal load and sliding speed

The effect of normal load on friction and wear properties is shown in Fig. 3. With the exception of a light load (0.6 N), DLC films showed a low friction coefficient. At a light load of 0.6 N, the friction coefficient was always high (μ =0.35-0.4). The friction decreased monotonously with increasing sliding distance at first, and then attained a steady-state value. The specific wear rate of DLC film under a light load, on the other hand, was too small to be detected. For loads of > 2 N, the specific wear rate of DLC films were hardly affected by normal load and it was 1×10^{-7} mm³/Nm. The specific wear rate of the mating ball was difficult to determine due to the transfer from the DLC film.



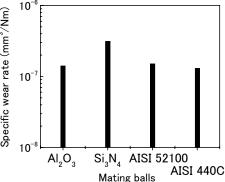
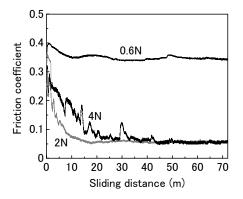


Fig. 2 Friction coefficient and specific wear rate of DLC films, sliding against different mating balls



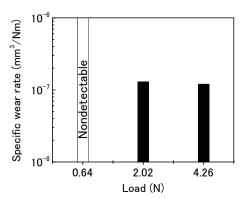


Fig.3 Friction coefficient and specific wear rate of DLC films versus normal load

The effect of sliding speed on friction and wear properties of DLC films is shown in Fig. 4. A steady-state friction coefficient was hardly affected by sliding speed. Frictional behavior was similar to those shown in Fig. 3. The specific wear rate slightly increased when increasing the sliding speed.

Figure 5 shows wear scars of ball and DLC specimens observed with an optical microscopy. With loads of 2 N, some portions of wear scars appeared to be covered by transferred materials; in this case, the friction coefficient was low. With high friction (0.6 N), however, the transferred materials were not found in the center of the ball specimen wear scars. This suggests that transferred materials on the ball wear scars caused a low friction coefficient. With the wear scar of DLC films, the obvious difference was observed between films under 0.6 N and 2 N. The film wear clearly occurred with loads of 2 N, although the film wear was hardly recognized with loads < 0.6 N. The observation of a friction surface suggests that the transfer materials on the ball surface came from the wear debris of the DLC film.

To verify this observation, we analyzed the wear scar using a Raman instrument (Fig. 6). Under a light load, no clear peak was recognized in the wear scar of the mating ball. For a load of 2 N, on the other hand, the Raman

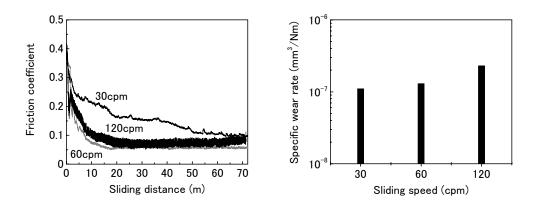


Fig.4 Friction coefficient and specific wear rate of DLC films versus sliding velocity

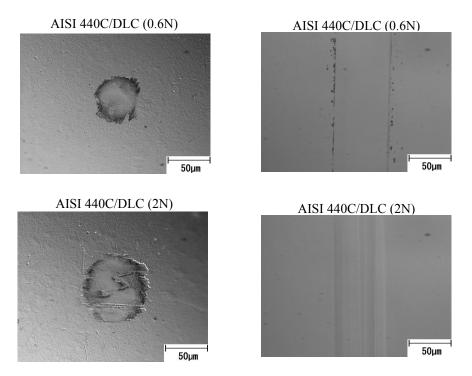


Fig.5 Wear surface of AISI 440C and DLC films after the tests

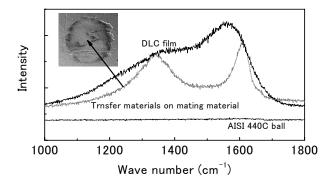
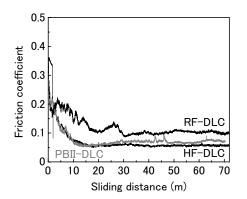


Fig.6 The micro-laser Raman spectra of transferred materials on AISI 440C



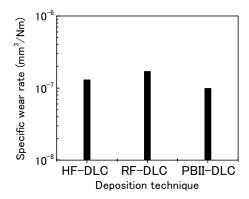


Fig. 7 The effect of deposition methods on friction and wear properties of DLC films

spectra of transferred materials on the mating ball were clearly different from those of the DLC film. The spectrum analysis showed that the structure of transfer materials changed from DLC to other structures. This suggested that the transferred materials on the mating ball strongly affected the friction and wear behavior of DLC films. The friction coefficient must be high when the transfer materials on the mating surface are negligible at the early stage of friction. With progress of friction, the transfer materials accumulate on the mating ball and then graphitization occurs. The graphitization lowers the friction and wear of DLC films.

Tribological properties of DLC films deposited using different methods

Figure 7 shows the friction and wear of three types of DLC films. In each case, a low friction coefficient (under 0.1) and a good wear-resistance (1×10^{-7} mm³/Nm) were obtained. Optical micrographs of wear scars of DLC films and mating balls resembled each other. The wear scars of DLC films appeared flat and the transferred film existed on the wear scar of mating materials. These facts again suggest that the transfer materials are the key factor controlling the tribological properties of these films and are independent of the deposition technique. However, further investigation will be necessary to understand the lubrication mechanisms of transfer materials.

CONCLUSIONS

DLC films were prepared by a hot filament plasma CVD technique and their tribological properties were determined using a ball-on-plate reciprocating friction tester in dry air under various conditions. For AISI 440C and Al₂O₃ balls, the friction coefficient was low, but the friction for AISI 52100 and Si₃N₄ had relatively high values. From the dependence of the tribological properties on the source gas, it is thought that there is adequate film

hardness for good tribological properties. When the normal load and sliding speed was changed, desirable tribological properties were obtained, except under a light load. DLC films deposited using the three different techniques showed good tribological properties, irrespective of the deposition technique. The results of optical microscopy and micro-laser Raman spectroscopy suggested that both the transfer of DLC to the mating ball and the structural change of transferred materials are necessary to achieve excellent tribological properties.

ACKNOWLEDGMENTS

This work was supported by the Frontier Carbon Technology (FCT) project, which was consigned to the Japan Fine Ceramics Center (JFCC) by the New Energy and Industrial Technology Development Organization (NEDO), Japan.

REFERENCES

- 1. A. Grill: Review of the tribology of diamond-like carbon, Wear, vol.168, 1993, 143-153
- 2. A. Grill: Tribology of diamond like carbon and related materials: an updated review, Surface and coating technology, vol.94-95, 1997, 507-513
- 3. A. Erdemit, et al.: Effect of source gas chemistry on tribological performance of diamond-like carbon films, Diamond and Related Materials, Vol.9, 2000, 632-637
- 4. K. Vercammen, et al.: A comparative of state-of-the-art diamond-like carbon films, Surface and Coating Technology, Vol.133-134, 2000, 466-472
- 5. A. Tanaka, et al.: Tribological study on DLC films depending on the hardness of mating materials and applying loads, Proceedings of 2nd World Tribology Congress, The Austrian Tribology Society, 2001

TRIBOLOGICAL PROPERTIES OF PULSE-BIASED HYDROGENATED AMORPHOUS CARBON FILMS

Koichiro Wazumi

FCT Joint research consortium
Ishikawajima-Harima Heavy industries Co.,Ltd

1 Sinakaharachou, Isogo-ku, yokohama, Kanagawa 235-8501, JAPAN
TEL+81-45-759-2819, FAX+81-45-759-2206
e-mail;kouichirou wazumi@ihi.co.jp

Kenji Fuchigami

Ishikawajima-Harima Heavy industries Co.,Ltd 1 Sinakaharachou, Isogo-ku, yokohama, Kanagawa 235-8501, JAPAN

Akihiro Tanaka and Yoshinori Koga

Research Center for Advanced carbon Materials AIST Tsukuba Central 5, 1-1 Higashi, Tsukuba, Ibaraki 305-8565, JAPAN

ABSTRACT

Hydrogenated amorphous carbon films have been prepared on Si substrates in plasma CVD system by using pulse bias techniques. ERDA analysis showed that pulse-biased film prepared at a duty ratio of 10% included large amount of hydrogen compared to the dc-biased films prepared at the same bias voltage of –1kV. Mechanical properties showed that the density, hardness and internal stress of pulse-biased films decreased compared to the dc-biased films. The film hardness decreased from 33 Gpa of dc-biased one to 15.5 Gpa in pulse-biased one. Film stress decreased from 2.9 Gpa for dc-biased one to 0.5 Gpa for pulse-biased one. Tribological properties by a ball-on-disk friction tester in the dry air condition showed that friction coefficient of dc-biased film with a counterpart of SiC ball was 0.06 and that of pulse-biased films was 0.045, which did not show clear difference. However the specific wear rate had a much difference between these two films. The wear rate of dc-biased films was 6 x 10⁻⁸ mm³/Nm and that of pulse one is 5 x 10⁻⁹ mm³/Nm showing the extremely low wear in dry air condition. The reason was thought to be due to the decrease of internal stress of the films because of the increase of hydrogen content and the existence of mixed structures of hydrocarbon bonding.

Keywords: Hydrogenated amorphous carbon, plasma CVD, pulse bias, tribology.

INTRODUCTION

Amorphous carbon films showing the high hardness and low frictional properties are currently of great interest for wear protection and friction reduction to the various mechanical applications. Pulse-biased technique during the deposition of these films are well known as a plasma source ion implantation (PSII) techniques and much attention have been paid to coating studies for complicated shape materials. However tribological properties of the amorphous carbon films by this technique also show the attractive characteristics. Baba showed the adhesive properties of the pulse-biased films in RF plasma CVD system and the structure change of pulse-biased films at different bias voltage (ref.1, 2). Los Alamos group prepared the pulse-biased amorphous carbon films from C₂H₂ and Ar gas in RF plasma CVD. They showed the structural and mechanical changes of the films with different gas mix ratio and different duty ratio from 30 % to 0 %, optical properties changes with different bias voltage, and wear rate of pulse biased films was 6.1x10⁻¹¹ mm³/Nm in dry air condition (ref.3, 4, 5). Through these studies, however it has not still been clarified the mechanism of superior tribological properties of pulse-biased films compared to the dc-biased carbon films. In order to clarify these points, we prepared pulse biased films at different duty ratio of 100 %(dc), 30 % and 10 % at the same bias voltage of -1 kV, and measured the tribological properties. As a result we found that pulse biased amorphous carbon films showed very low wear rate due to its low internal stress attributed to high hydrogen content and the mixed structure of hydro-carbon molecules accumulated at pulse-on time and pulse-off time. In this article

we argue the difference of dc-biased films and pulse biased films showing the relation of mechanical properties, chemical properties and tribological properties.



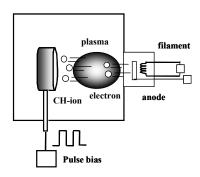


Figure 1. Deposition chamber.

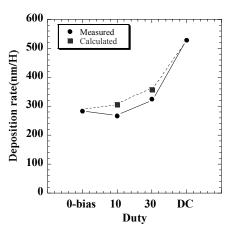
Figure 2. Schematic diagram of CVD system

EXPERIMENTAL

Deposition of amorphous carbon films was carried out on a Si (100) wafer in thermal electron excited dc plasma CVD system, which included an ion source gun comprising a hot filament and anode. Prior to the deposition, silicon wafer was sputter-cleaned by Ar plasma applying the negative bias voltage of 2kV to the wafer for 15 minutes. After that procedure C₆H₆ gas was introduced into the chamber at constant flow rate of 5sccm to produce hydrocarbon plasma. The deposition was executed by applying pulse bias voltage to the substrate with fixed pulse voltage of -1 kV and fixed frequency of 1 kHz for 3 hours. Four kinds of films were prepared at different duty ratio of 100 %(dc), 30 %, 10% and 0%(no bias). Substrate temperature was about 150 C. The chemical bonding state of the carbon atoms was analyzed by Ar laser used RAMAN. And the hydrogen content and film density was calculated from the results of elastic recoil detection analysis (ERDA) measurements for hydrogen atoms and Rutherford backscattering spectrometry (RBS) measurement for carbon atoms. The film hardness was measured by a Nanoindentor at a constant stiffness mode from the surface of the films to the 300nm depth. The internal stress was calculated by Stoney's equation from the curvature of the deposited substrate measured by an optical interferometer.

RESULTS AND DISCUSIONS

Fig.3 shows the comparison of a measured deposition rate and calculated deposition rate of the pulse biased films. The calculation was done by the simple summation of the deposition rate at pulse-off time and pulse-on time in accordance with the pulse duty ratio. Although measured deposition rate is slightly smaller than calculated one, both deposition rate showed almost same curves demonstrating that the pulse-biased deposition process was basically done by the repetition of the pulse-on deposition and pulse-off deposition. The slight difference of these two curves however indicates that certain amounts of molecules accumulated at non-bias time were sputtered out by the energized ions impinging during pulse-on time. Fig.4 shows the RAMAN spectra of dc-biased film, pulse-biased films and non-biased film respectively. The spectrum of non-bias film shows the broad band spectrum with highly intensive background which is attributed to the polymer structure of hydrocarbon molecules. On the other hand dcbiased film shows the two peaks, which consists of broad G (1544 cm⁻¹) and D (1343 cm⁻¹) band. The spectra of pulse-biased films also show convoluted line of broad G (1560 cm⁻¹) and D (1382 cm⁻¹) band. The intensity of spectra is lager than that of dc-biased film. Although pulse-biased films are thought to include the mixed structure of dc-biased hydrocarbon and non-biased hydrocarbon bonding, these results indicate that their structures are rather similar to that of dc-biased film. RBS and ERDA measurements were done to estimate the hydrogen content in each films based on the comparison of the number of carbon atoms measured by RBS and that of hydrogen atoms by ERDA system. Fig. 5 shows the amount of the hydrogen content at different pulse duty ratio. The hydrogen content increased from 26 at.% to 33 at.% by decreasing the duty ratio from 100 %(dc) to 10 %. Non-biased film included



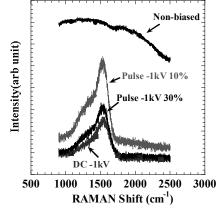
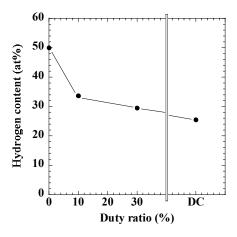


Figure 3. Deposition rate

Figure 4. RAMAN spectra of pulse-biased films

50 at.% of hydrogen. These data indicate that the structure of non-biased film is different from the dc -biased and pulse- biased films. RAMAN results support this idea since spectrum of non-biased film is different from other ones. Fig.6 shows the hardness of each film. The hardness decreased from 33 GPa to 15.5 GPa by reducing the pulse-duty ratio from 100 % to 10 %. The hardness of the non-biased film could not be measured since it was easily removed during the measurement. Generally the hardness of ta-C, a-C and a-C:H films depend on the sp³/sp² ratio of carbon structure and the amount of hydrogen content (ref.6). The sp³/sp² ratio of carbon bonding significantly changed in terms of the bias voltage and ion energy (ref.7). In our case dc-biased and pulse-biased films were prepared at the same bias voltage. Therefore it is assumed that hardness difference of pulse-biased films and dc-biased films was mainly attributed to the hydrogen content shown in Fig. 5. The residual stress was estimated from the curvature of the coated Si wafer. Every film shows the compressive stress and it decreased from 2.9 GPa to 0.5 GPa by reducing the duty ratio from 100 %(dc) to 10 %. The residual stress of the non-biased film was 0.01 Gpa. It is obvious that the stress of pulse-biased film is quite low compared to the dc-biased films. Since the stress was also affected by the amount of hydrogen content, these low stress values of pulse-biased films was attributed to the high hydrogen content. However other factor also should be considered. When dc-biased film was deposited at the bias voltage of – 150 V, hardness of that film shows 15.5 Gpa, almost same value as pulse-biased films of 10% duty ratio. Hydrogen content reached to 42.5 at.% and compressive stress was 1.26 Gpa. Therefore it is clear that the stress of the pulsebiased film is low compared to the dc-biased film at the same hardness level. The reason was assumed that mix structure of hydrocarbon molecules has the effect to release the high compressive stress of dc-biased structure. The density of films decreased from 2.0 g/cm³ to 1.6 g/cm³ by reducing the duty ratio from 100 %(dc) to 10 %. The density of the non-biased film is 1.1 g/cm³. The tendency of the density variation has related to the hardness and stress variations.



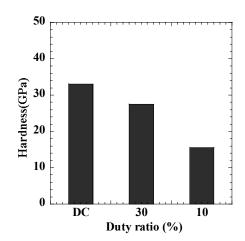
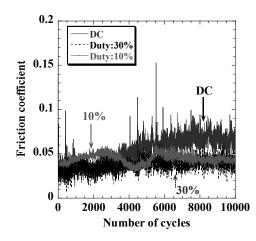


Figure 5. Hydrogen content of pulse-biased films

Figure 6. Hardness of pulse-biased films



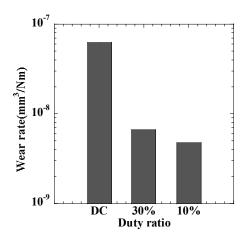


Figure 7. Friction coefficients of pulse-biased films

Figure 8. Wear rate of pulse-biased films

Friction coefficient has been measured in ball-on-disk tribology tester using SiC ball in dry-air condition. Fig.7 shows the friction coefficient of dc-biased and pulse-biased films at the 2 N load during the test of 10000 cycles. In dc-biased film friction behavior was unstable compared to that of pulse-biased films. Friction coefficients were 0.065, 0.045 and 0.045 for the dc-film, pulse-biased film of 30 % and film of 10%, respectively. Since the friction coefficient value has certain fluctuations in each experiment. It is difficult to point out the difference of friction coefficient between dc-biased films and pulse-biased films. On the other hand the specific wear rate shows clear difference between the two kinds of films shown in Fig.8. The wear rate of dc-biased film was 6 x 10⁻⁸ mm³/Nm and that of pulse one was 5 x 10⁻⁹ mm³/Nm showing the extremely low wear in dry air condition. The depths of wear track were 40 nm in dc-biased films and 2 nm in pulse-biased of duty ratio of 10 %. As shown in Fig.7, friction coefficient of dc-biased films shows unstable movement. Therefore it was speculated that dc-biased film had small destruction at inside the films during the friction test. In our experiments these kind phenomena can be observed in the film, which has high compressive stress. Therefore it can be concluded that relatively high hydrogen contests and the mixture of C-H bonding in pulse-biased films leads to the quite low stress, which contributes to the significantly low wear value.

CONCLUSIONS

Hydrogenated amorphous carbon films have been prepared on Si substrates in plasma CVD system by using the pulse bias techniques. Pulse-biased films prepared on the duty ratio of 10% include much hydrogen compared to the dc-biased films and film density, hardness and internal stress of pulse-biased ones decrease compared to the dc-biased films. Although friction coefficient of dc-biased film and that of pulse-biased films did not show much difference, specific wear rate shows complete difference in these films. Wear rate of dc-biased films was 6×10^{-8} mm³/Nm and that of pulse one is 5×10^{-9} mm³/Nm showing the extremely low wear in dry air condition. The reason was thought to be due to the decrease of internal stress of the pulse-biased films attributed to the increase of hydrogen content and mixed structure of hydrocarbon bonding. This work was supported by FCT (Frontier Carbon Technology) project of Japanese government, which was consigned to Japan Fine Ceramics Center by NEDO

REFERENCES

- (1) K.Baba and R.Hatada; Surface and coating Technology, 103-104(1998) 235
- (2) K.Baba and R.Hatada; New Diamond and Frontier Carbon Technology, 9,6(1999) 417
- (3) X.M.He, K.C.Walter, M.Nastasi, S.-T.Lee and X.S.Sun, Thin Solid Films, 355-356 (1999) 167
- (4) X.M.He, K.C.Walter, M.Nastasi, S.-T.Lee and M.K.Fung, J.Vac.Sci.Technol. A18 (2000) 2143
- (5) X.M.He, J.F.Bardeau, D.H.Lee, K.C.Walter, M.Tuszewski and M.Nastasi; J.Vac.Sci.Technol. B17(2)(1999) 822
- (6) A.Grill; Diam. Relat. Mater, 8 (1999) 428
- (7) E.G.Lacerda, F.C.Marques, F.L.Freire Jr, Diam. Relat. Mater, 8 (1999) 495

VISCO-ELASTIC PROPERTIES OF REACTOR ON DIAMOND-LIKE CARBON FILMS IN BOUNDARY LUBRICATION

T. Saitoh, S. Miyake and S. Watanabe

Nippon Institute of Technology, 4-1 Gakuendai, Miyashiro-machi, Minamisaitama-gun, Saitama, JAPAN

Y. Yasuda and Y. Okamoto

Nissan motor Co. Ltd., JAPAN, 1 Nastushima-machi, Yokosuka-shi, Kanagawa, JAPAN

Corresponding author:

Tadashi Saitoh, Systems Engineering Major, Graduate school, Nippon Institute of Technology, 4-1 Gakuendai, Miyashiro-machi, Minamisaitama-gun, Saitama, 345-8501, JAPAN, e-mail: s954234@stu.nit.ac.jp, TEL: +81-(0)480-34-4111 (EXT.345), FAX: +81-(0)480-33-7745

ABSTRACT

To improve the lubrication properties of DLC (Diamond-like Carbon) films, DLC films were deposited by adding additive materials such as titanium (Ti), iron (Fe), molybdenum (Mo) and titanium dioxide (TiO₂) with using by magnetron sputtering, and its friction properties were evaluated by oscillation type scratch tester, and ball-on-disk type tribometer in oil lubricant. In the scratch test, it is found that the critical loads of ferrous and titanium containing DLC films were larger than DLC film without metal. Friction coefficient of DLC film without metal is nearly 0.10 when using oil lubrication containing MoDTC (molybdenum dithocarbamates). On the other hand, all materials containing DLC films show lower friction than DLC film without metal does. Especially, DLC film deposited with adding appropriate quantity of titanium exhibits a low friction coefficient μ = 0.03. In order to know mechanism of lower friction of titanium contained DLC film, the viscoelastic properties of sliding and no-sliding areas were evaluated by force modulation method of AFM (Atomic Force Microscopy). The viscoelastic properties of sliding areas increased as comparing with that of no-sliding areas. It is thought that reactor of lower friction have been formed in sliding track of titanium containing DLC films in oil lubrication containing MoDTC.

Keywords: lubrication properties, containing DLC, scratch test, molybdenum dithocarbamates, reactor

INTRODUCTION

Recently, with the progress of science and technology, the environments in which mechanical parts are used are rapidly expanding. Therefore, ensuring the reliability of mechanical parts, which are used under extreme conditions of high speed, high load, extreme temperature and radioactive and reactive atmospheres, is becoming important (ref. 1). As surface films, diamond-like carbon (DLC) films are expected to withstand the above-mentioned severe environments. By coating a DLC film on metal and other materials, it is also possible to lower the wear of opposing surfaces due to the low friction of DLC films (ref. 2). Even though DLC films have displayed many such excellent tribological properties depending on their application fields, there are many insufficiency points such as their film strength, lubrication property and adhesion to substrates. It has been proposed to fabricate DLC films containing metal elements at on the interface between substrate and films (ref. 3 to 5).

In this work, the boundary lubrication properties of DLC films with other additive materials were investigated in friction test as adding the extreme-pressure additives in oils and their viscoelastic properties of sliding parts were evaluated.

EXPERIMENTAL METHOD

Deposition Method of DLC Films

DLC films containing other materials were deposited by using radio frequency (RF) magnetron sputtering with argon gas and a graphite target. To coat DLC films containing other materials, fan-shaped targets such as titanium (Ti), molybdenum (Mo), ferrous (Fe), and titanium dioxide (TiO₂) were used and they were singly set up on a graphite target. The size of the fan-shaped target is varied at an area ratio under 1/8, 1/16 and 1/32 to control the

additive quantity of metals. The substrate is mirror finishing silicon wafer (Si(100)). The films thickness of various materials containing DLC is about 200 nm.

Scratch and Lubrication Properties Evaluation Method

Adhesion and strength of film were evaluated in an oscillation type scratch test with acoustic emission (AE). A diamond stylus was moved across the film by phonograph under progressively increasing load. A low-frequency transverse swing is superposed on the stylus. This swing width corresponds to the friction property. And, to evaluate the adhesion strength of various materials containing DLC films, AE detection points was inspected to know a critical load of film.

A ball-on-disk type tribometer was used to investigate lubrication properties by rotating the sample with the application of a certain load on an AISI440C (SUS440C) ball indenter. To investigate the boundary lubrication properties of DLC films, lubricant-containing with extreme-pressure additives, such as molybdenum dithiocarbamates (Mo-DTC) were used. Lubrication properties of DLC films were evaluated under conditions of a load 5.0 N, rotating speed 100 rpm, sliding speed 31.4 mm/s and 6000 total reciprocation cycles.

RESULT AND DISCUSSION

Scratch Properties of Metal Containing DLC Films

The friction properties and critical loads of metal containing DLC and DLC without metal films are displayed in Figure 1. The slope of curves gives the coefficients of friction. The *Wc* in Figure 1 (a) shows critical loads by AE detection. The critical load of DLC film without metal is 65 mN higher than that of ferrous and titanium containing DLC films. And, the friction coefficient of titanium containing DLC film and DLC film without metal were obtained stable friction. The ferrous and titanium containing DLC films show the increasing critical loads as shown in Figure 1(b). Especially, the critical load of titanium contained DLC film deposited by using a target of 1/16 is nearly two times larger than that of DLC film without metal. And, ferrous and molybdenum containing DLC films show the

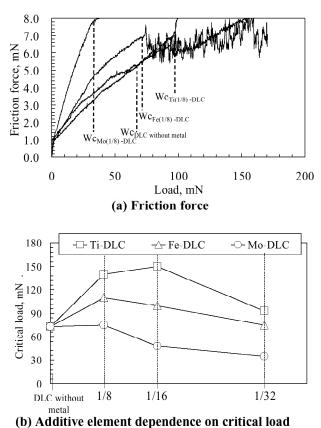


Figure 1 Friction properties and critical loads of metal containing DLC and DLC without metal films

highest critical load, when they were deposited using a target of 1/32. The metal containing DLC film shows maximum adhesion strength with addition of an appropriate metal

Lubrication properties of various material containing DLC films

Result of lubrication properties of various materials containing DLC films is show in Figure 2. For both SCM415 and silicon wafer, friction coefficients are 0.15. The friction coefficient of DLC film without metal shows 0.2, it is higher than those of silicon wafer and SCM415. In this case, the lubrication effect of Mo-DTC containing oil is negligible in DLC films without metal. In comparison, the friction coefficient of ferrous containing DLC films is actually high initially but it diminishes to 0.07 with boundary lubrication. And, TiO_2 -containing DLC film shows decreasing friction from 2,000 rotating, that becomes to μ = 0.07. Under the same conditions, it is shown that titanium containing DLC film has the lowest friction coefficient, μ = 0.05. The friction coefficients of metal-containing DLC films such as Ti, Ti0 additive tend to decrease slowly even though their values are initially high. These results are considered to be due to the other materials containing DLC films having active sites that react with extreme-pressure additives under friction.

Figure 3 shows the dependence of friction coefficients in the case of boundary lubrication of titanium containing DLC films on metal target size. The friction coefficient becomes markedly low, μ = 0.03, when titanium target area ratio is 1/32. Therefore, the mechanism of the low friction coefficient of titanium containing DLC film is deduced to be lower friction reactant with addition of an appropriate metal. These results are corresponding to the adhesion strength by scratch test.

The viscoelastic characteristics of sliding areas were evaluated by AFM force modulation (ref. 6). We measured 5 points of sliding track (A-E) and a point of no-sliding area (F). Viscoelastic properties such as phase lag of sliding

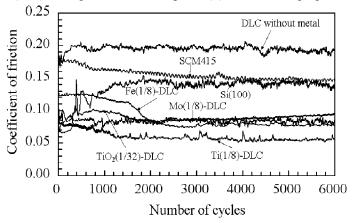


Figure 2 Variation in friction coefficient of Lubrication properties of specimens under boundary lubrication.

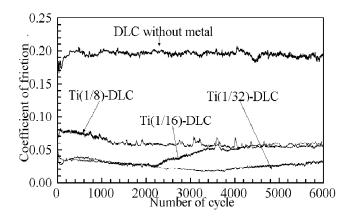


Figure 3 Lubrication properties of titanium containing DLC films

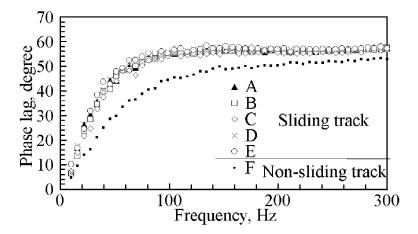


Figure 4 Phase lag of sliding track and non-sliding track.

track (A-E) and no-sliding track were shown in Figure 4. There are large difference in phase lag between sliding tracks and no-sliding area as shown in Figure 4. Phase lag was about 55 degree in sliding tracks A-E and about 45degree in no-sliding area, when frequency is 100 Hz. This result indicates that the viscoelastic characteristic of a sliding track differs greatly from that of the no-sliding area. It is considered that the reactant was formed on the track by friction under boundary lubrication with Mo-DTC containing lubricant.

CONCLUSION

The boundary lubrication properties of DLC films with other additive materials were investigated in friction test as with Mo-DTC containing lubricant and their viscoelastic properties of sliding parts were evaluated. The main results are as following.

- [1] The metal containing DLC film shows maximum adhesion strength with additive of an appropriate metal
- [2] The low friction coefficient of titanium containing DLC film is deduced to be lower friction reactant produced by sliding.
- [3] Reactant was formed on the track by friction under boundary lubrication with Mo-DTC containing lubricant.

ACKNOWLEDGMENT

This work was partially supported by a Grant-in-Aid to the Science Research Foundation from the Ministry of Education, Culture, Sports, Science and Technology (B12450069).

REFERENCE

- 1. Enomoto, Y.; Miyake, S.: Tribology of Thin Films, University of Tokyo Press, Tokyo, JP, 1994 [in Japanese]
- 2. Miyake, S.; Takahashi, S.; et al.: Friction and Wear Behavior of Hard Carbon Films. ASLE Trans., vol. 30, 1987, pp. 121-127.
- 3. Saitoh, T.; Miyake, S.; Watanabe, S.: Scratch Properties of Metal Contained Diamond Like Carbon (DLC) Films. Hyomen Gijutsu (Surface Finishing Society of Japan), vol. 53, no. 9, 2002, pp. 606-611. [in Japanese]
- 4. Miyake, S.: Tribological Improvement of Carbon Films by Material Additions. Jour. of Japa. Soci. of Trib., vol .41, no. 9, 1996, pp.754-759. [in Japanese]
- Donet, C.: Recent Progress on the Tribology of doped Diamond-like and Carbon Alloy Coatings. Surf. And Coat. Tech., vol. 100-101, 1998, pp.180-186.
- 6. Asif, S., A., Syed; Wahl, K., J.; Colton, R., J.: Nanoindentation and Contact Stiffness Measurement Using Force Modulation with a Capacitive Load-displacement Transducer. Rev. of Sci. Inst., vol. 70, 1999, pp. 2408-2413.

SOLID LUBRICANT PROPERTIES OF CARBON NANOMAERIALS AND THEIR POLYMERIC COMPOSITE COATINGS,

M. Y. Chen, S. T. Korfhagen

Air Force Research Laboratory, AFRL/MLBT, Wright-Patterson AFB, OH 45433-7750, USA, Z. Bai and S. C. Tan, Wright Materials Research Co., 1187 Richfield Center, Beavercreek OH 45430, USA.

Abstract

Co-continuous alumina/aluminum based composites with excellent physical and mechanical properties offer great potentials for lightweight, wear resistant, and high temperature applications. The development of suitable coating materials will provide low coefficient of friction to extend life under different environments for aerospace applications. In this study, carbon powders containing diamond clusters or fullerene were burnished on to the surface of alumina/aluminum substrates. These powders and c-nanofiber materials were also incorporated in polymer matrices and were spin coated onto the alumina/aluminum composites. Performance of a newly developed aerospace thermoplastic material and two currently used aircraft canopy materials were chosen as the matrix materials for comparison. Tribological evaluation of alumina/aluminum composites with and without coatings was performed against 440C stainless steel balls using pin-on-disc wear tests at 0.2 m/s sliding velocity, 0.25 N, and 0.75 N normal load. The morphology and wear tracks on the composite discs and material transfer to the steel balls were examined using a scanning electron microscope. Raman analysis was performed to determine the chemical bonding of the as-burnished materials and the changes after wear tests. The effects of reinforcement or lubricant material, polymer matrix material and test environment on the friction behavior will be presented.

Ming Y. Chen AFRL/MLBT
Bldg 654, 2941 P Street Wright Patterson AFB OH, 45433-7750 USA
Tel:937-255-9099 Fax:937-255-2176 ming.chen@wpafb.af.mil

S. T. Korfhagen AFRL/MLBT Bldg 654, 2941 P Street Wright Patterson AFB OH, 45433-7750 USA Tel:937-255-3234 Fax: 937-255-2176

Z. Bai and S. C. Tan Wright Materials Research Co. 1187 Richfield Center Beavercreek OH 45430 USA Tel:937-431-8811 Fax:937-429-4101

Tribological properties of Ti-DLC films on various polymers

T. HASHIZUME 1, S. MIYAKE 2, S. WATANABE 2 and M. SATO 1

¹Oiles corporation 4 Kirihara-cho, Fujisawa-shi, Kanagawa 252-0811, JAPAN ²Nippon Institute of Technology 4-1 Gakuendai, Miyashiro-Machi, Minamisaitama-gun, Saitama 345-8501, JAPAN

Our study is to search for tribological properties of diamond-like carbon (DLC) film known as anti-wear hard thin film on various polymers. This report discusses the deposition of DLC films on various polymer substrates in vacuum by magnetron radio frequency (RF) sputtering method with using argon plasma and graphite, titanium target. The properties of friction and wear were measured using a ball-on-disk wear -testing machine. The properties of friction and wear were remarkably improved by DLC coating. Furthermore, the composition of DLC film was been analyzed by using auger electron spectroscopy (AES). The wear rate of titaniumcontaining DLC film was lower than that of no-metal-containing DLC film.

Keywords: Diamond-like Carbon, DLC, Ti-DLC, Thin film, Coating

1. INTRODUCTION

Since the polymer material has the outstanding tribological characteristic, it is used in various fields such as tribo-material [1], [2]. However, with the constant demands for the improved performance such as hardness, heat resistance and wear resistance, development and application of the latest technology is the must. Research of hard coating, such as a DLC film was done in order to solve this problem [4,5]. Moreover, examination of metal-doped DLC film was also performed for the purpose of improving the characteristic of DLC film [6,7]. This research is focused on studying and investigating the tribological characteristics of various Ti-DLC film [8,9] coated polymer materials and their influences on the improvement of requested performance.

2. EXPERIMENTAL METHODS

2.1 Polymer substrates

Polyimide (PI) and Polyamide6 (PA6) were used as substrate.

Magnetron RF sputtering equipment was used in forming a DLC film on a polymer material and its schematic illustration is shown in Fig.1. Graphite (C) was used as a target in this research. RF electric

power (13.56MHz) was exerted on both substrate and target sides. DLC film was deposited by the magnetron radio frequency (RF) sputtering with forming Ar plasma in vacuum under conditions RF electric power 200W on target side and 0 ~50W on substrate side, vacuum pressure 10Pa, and depositing time 60 minutes. A fan-shaped piece of titanium was placed on the graphite target to deposit titanium-included film [4] on polymer substrate. Proportion of titanium in DLC film can be changed by increasing or decreasing the size of titanium placed on the graphite target.

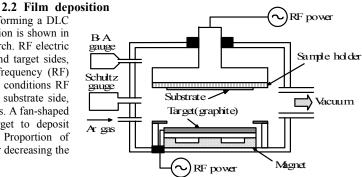


Fig.1 Schematic illustration of magnetron RF sputtering

2.3 Friction and wear test

In order to determine the friction characteristic of DLC film coated polymer, the friction examination was carried out using a ballon disk type wear-testing machine in a dry environment under following conditions the ball size, the material, and testing conditions were; SUS440C (φ6mm) indenter, load 1.0 N, rotation rate 100 rpm, turning-radius 3 mm, rotation 6000 times. A speed is 31.4 mm/s as a result of calculating from the above conditions. In order to determine a wear characteristics of the piece of a substrate, and indentation ball were observed by differential interference microscope.

2.4 Characterization of film

The formation of DLC film was analyzed using Auger Electron Microscopy (AES), and its hardness was measured by nanoindentation method using Atomic Force Microscopy (AFM). Using the silicon wafer as the substrate, the deflection of films was measured by measurement equipment. Based on the following Storney formula (1), the internal stress in the DLC film was computed.

$$\sigma = 4Es \ ds2 \ \delta/3(1-vs) \ 12 \ df$$
 ----- (1)

3.RESULTS AND DISCUSSIONS

Fig.2 shows a relationship between friction coefficient and number of cycles. In DLC film, in the beginning of the test, friction coefficient shows a high value of approximately μ =0.8, and it is keep to the high friction coefficient till the end of test. In Ti-DLC (1/32) film, after the start immediately, its friction coefficient approximately μ =0.6 were shown and Ti-DLC(1/32) also shows a low

value as compared with DLC film. Actually, the friction coefficient of Ti-DLC(1/32) becomes close to that of DLC film when increasing the number of cycles more than 1000 times. On the other hand, in Ti-DLC(1/16) film, its friction coefficient shows a low value of μ =0.5 in the beginning of test. Although the friction coefficient of Ti-DLC(1/16) film rose a little with increasing the number of cycles, the friction coefficient showed a low value as compared with DLC film and Ti-DLC(1/32) film. A damage of DLC film on surface is as observing the wear track after friction test, the damage of DLC film is large, but those of Ti-DLC(1/32) and Ti-DLC(1/16) are remarkably reduced differently due to the addition amount of Ti as measuring the transfer film formation on the indentation ball. This transfer film is considered to by one of the causes of friction coefficient reduction.

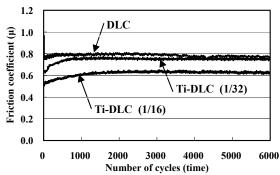
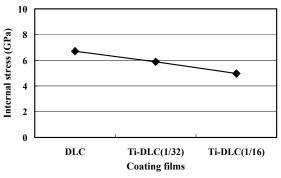


Fig.2 Friction properties dependence on number of cycles

The formation of the DLC film added titanium is investigated to strengthen the adhesion of a DLC film on Si-wafer and mechanical intensity. It was confirmed that the quantity of titanium contained in DLC film increased along with increasing piece size titanium used as target by the analysis of AES. Furthermore, it was known that addition titanium is uniformly distributed on the DLC film. With the measurement equipment and the Storney formula (1), the internal stress of a film was calculated. As increasing the size of titanium, the internal stress of the film decreased (as shown Fig.3). When the proportion of titanium in the target was 1/16, the internal stress decreased approximately 30% compared to that of DLC film without titanium addition, which was 7GPa.



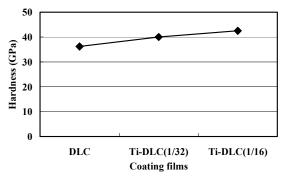


Fig.3 Internal-Stress dependence of coating films

Fig.4 Hardness dependence of coating films

Moreover, as shown in Fig.4, with nano-indentation method, the nano-indent hardness of the DLC film was approximately 35GPa. With the hardness of film with addition of titanium increased to 43 GPa when the proportion of titanium target is 1/16. It is considered that the combination of titanium and carbon can terminate dangling bond of DLC film in the molecular level. The quantity of TiC contained in Ti-DLC film with the increase in the area of Ti target by this increases, and it is thought that hardness improved. Moreover, that the hardness of Ti-DLC became high because of the TiC with increasing the size of Ti target [9].

4. CONCLUSIONS

The tribology characteristics, such as friction coefficient and wear-resistance were improved by forming a DLC film on a polymer material. Farther it was confirmed that by adding titanium in a DLC film, the internal stress of a surface film can be decreased and hardness is improved.

5. REFERENCES

- [1] S. Miyake, "Lubrication," JAST, Vol.30, No.5, 1985, pp. 371
- [2] I. Sekiguchi, "Tribologist," JAST, Vol. 45, No.1, 2000, pp. 12
- [3] Y. Enomoto, "Tribology of Thin Films," University of Tokyo Press, 1994, pp. 43
- [4] K. Suzuki, T. Saito, SFJ, 103, 2001, pp. 249
- [5] T. Hashizume, S. Miyake, et al, JSME, No.02-1 V, 2001, pp. 109-110
- [6] S. Kijima, T. Saito, S. Watanabe, et al, SFJ, 103, 2001, pp. 247-248
- [7] T. Saito, S. Miyake, S. Watanabe, JAST, 2001-11, 2001, pp. 159-160
- [8] T. Hashizume, S. Miyake, S. Watanabe, et al, JAST, 2002-10, 2002, pp. 231-232
- [9] N. Chaoin, A. Ando, M. Okui, et al, SFJ, 107, 2003, pp. 267

TRIBOLOGICAL PERFORMANCE OF Cr-CONTAINING DLC FILMS

Katsuyuki Kotake, Shojiro Miyake and Shuichi Watanabe

Nippon Institute of Technology 4-1 Gakuendai, Miyashiro, Saitama 345-8501, Japan

ABSTRACT

Diamond-Like-Carbon films have been widely recognized as being a wear-resistant solid lubricant with a low friction coefficient. Recently, there have been many attempts to improve the tribological behavior of DLC films by the addition of various metals. In this study, in order to apply for severe sliding conditions, for example, for auto-motive parts, etc., tribological performance of Cr-containing DLC films has been investigated. Cr-containing DLC films were deposited by means of an ion-plating having electrical resist-heating unit for Cr vaporization. The reactive evaporation between C vapor using electron-beam and Cr vapor has been carried out under various plasma-gas conditions. DLC films were also prepared using same ion-plating for comparison. Tribological performances of the films were demonstrated by means of a ball-on-disk tribometer under various lubricating environments. Friction coefficient of Cr-DLC film is lower than that of DLC film under oil lubrication with appropriate additives.

Keywords: Cr-containing DLC films, Reactive ion-plating, Tribological performance, Oil lubrication

INTRODUCTION

Diamond-Like-Carbon (DLC) films have been widely recognized as being a wear-resistant solid lubricant with a low friction coefficient (ref. 1). Therefore, it is considered that DLC films are very useful for tribological coating on various industrial substrates. As an application development, it is promoted as a purpose of the tribological characteristic improvement to mechanism element, etc. However, according to industrial circumstances, we have many experiences that the enough performance is not shown, so that the development of a film is desired in such cases. Therefore, some improvements of mechanical properties of the film such as toughness improvement, etc., have been obtained from metal-containing DLC film (ref. 2). In addition, it has also been clarified that the excellent sliding characteristic have been shown by tribo-reaction in the friction surface under the oil environment including some various additives. Recently, there have been many attempts to improve the tribological behavior of DLC films by the addition of various metals. In this study, for the purpose of the further improvement on coated members, the result of formation of Cr-containing DLC films and their frictional property evaluation have been described.

EXPERIMENTAL

In the formation of Cr-containing DLC film, an ion plating equipment with the dual vapor source which consisted of resist heating evaporator for Cr layer formation and electron beam evaporator for C layer formation, have been used. Pure Cr metal (99.99%) and Gr (99.999%) were used as evaporation materials. Cr-containing DLC films were formed by controlling Cr content which respectively changed the evaporation boat temperature of Cr for 1100, 1150 and 1200 °C, during vapor deposition of C by constant electron beam (electron beam electric power: 10~kV, 100~mA). In making to be an intermediate layer with the purpose of the adhesion force improvement, it has been formed at the thickness of Cr layer about 50nm. The thickness of formed film was made to be all samples being constant for 200nm. Si wafer (100) was used as a substrate. The deposition was carried out under Ar gas atmosphere at a pressure of $2.0~x~10^{-1}$ Pa. Deposition conditions are shown in Table 1.

RESULTS AND DISCUSSION

Chemical composition of deposited films was analyzed by AES. Figure 1 shows AES spectra of the films. The spectra shown in this figure are given after etching by Ar ion (1kV, 2min) in respect of the film surface. From the figure, it was proven that Cr content for a film differed by changing the evaporation temperature of Cr, as intended. Cr content increased with increasing evaporation temperature. Though it was also found that N was also included in a film, the reason is uncertain at present. Other elements have not been detected.

The internal stress was obtained from the bend quantity of the substrate after film formation by the equation of Stony. Figure 2 shows the result of measured internal stress. The internal stress of the film also changes by difference between the Cr content, and their stress values of the films formed at evaporation temperature of 1100 and 1150 °C show lower than that of C film which does not contain Cr.

Table 1 Deposition conditions.

Sample		C Film	C-Cr Film (1100°C)	C-Cr Film (1150°C)	C-Cr Film (1 2 00°C)
Substrate		Si (100)	Si (100)	Si (100)	Si (100)
Film Structure		С	C-Cr/Cr	C-Cr/Cr	C-Cr/Cr
Evaporation Ten	nperature	-	1100℃	1150℃	1200℃
Deposition Time	Cr	-	41	30	22
(min)	C-Cr	60	50	30	27
Electron Beam Current (mA at 10 kV)		100	100	100	100
Bias (-kV)		1	1	1	1
Filament Current (A)		10	10	10	10
Bombardment (kV)		0.35	0.35	0.35	0.35

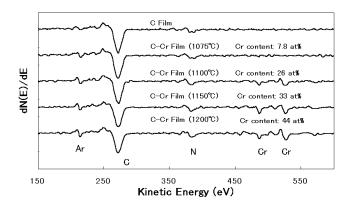


Fig. 1 AES spectra of the films.

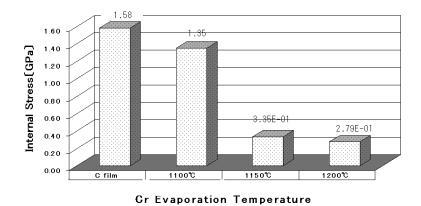


Fig. 2 Internal stress values of the films.

Tribological properties of various films have been evaluated by means of ball-on-disk type tribometer. Friction tests were performed at room temperature and under dry condition and various oil lubrications (base oil: SAE #30, additives: MoDTC, ZnDTP and Ca sulfonate). The stainless steel ball indenter (SUS440C, 6 mm in diameter) was used for the experiment. Applied load and disk rotation speed were 1 N and 100 rpm, respectively. Figure 3 shows friction coefficients and specific wear rates for the films under dry condition. Friction coefficient of the film formed at a temperature of 1200 °C was same as that of DLC film, showing low values of about 0.05. However, the friction coefficients of the films deposited under other conditions showed high values. The wear rate increased with the increase in friction coefficient. Figures 4, 5 and 6 show friction coefficients and specific wear rates for the films under various oil lubricants. Fig. 4 shows these properties of the individual films under oil with ZnDTP additive. The friction coefficients were almost same of about 0.2 for all films in this case. Fig. 5 also shows these properties under oil with MoDTC additive. From this figure, it was observed that the friction coefficient showed low value under 0.1 for all films, and these values were lower than those under dry condition. The effect of the frictional improvement remarkably appeared in this case. Figure 6 shows friction coefficients and specific wear rates for the films under oil lubrication with containing all additives. The friction coefficient showed very low value of under 0.05 for all films. Especially, the wear rate of the Cr-containing film formed at 1150 °C showed lower value than that of DLC film.

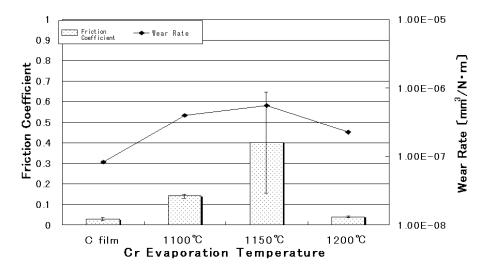


Fig. 3 Friction coefficients and wear rates of the films under dry condition.

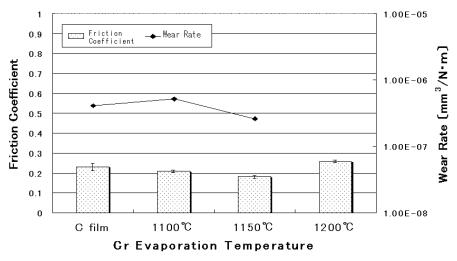


Fig. 4 Friction coefficients and wear rates of the films under oil lubrication (ZnDTP).

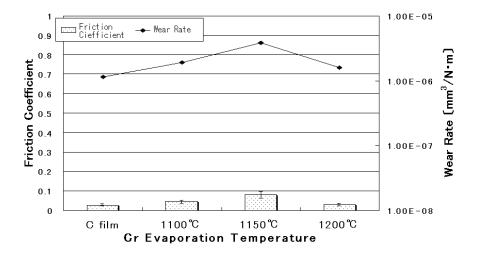


Fig. 5 Friction coefficients and wear rates of the films under oil lubrication (MoDTC).

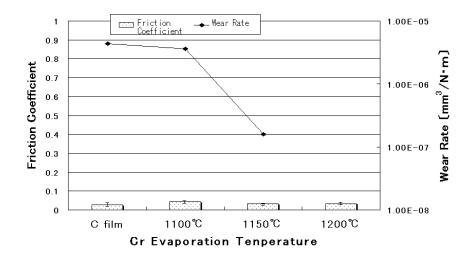


Fig. 6 Friction coefficients and wear rates of the films under oil lubrication (ZnDTP + MoDTC + Ca sulfonate).

CONCLUSIONS

The obtained results are summarized as follows:

- (1) By changing the evaporation temperature of Cr, it was possible to control Cr content for a film.
- (2) Internal stress of formed film depended on the Cr content.
- (3) Friction coefficient and wear rate of the film was affected by adding Cr.
- (4) Tribological properties of the films were improved when the film was deposited under Ar atmosphere.
- (5) Tribological properties of the films were influenced by oil additives, due to tribo-reaction effects.

REFERENCES

- 1. A. Grill; Wear, 168 (1993) 143.
- 2. A. Matthews and S. S. Eskildsen; Diamond and Related Materials, 3 (1994) 902.

FLUORINATED AMORPHOUS DIAMOND LIKE CARBON FILMS BY PECVD

G. Q. Yu*, B. K. Tay, Z.Sun, S. P. Lau

School of Electrical and Electronic Engineering, Nanyang Technological University, Nanyang Avenue, Singapore 639798

ABSTRACT

Fluorinated amorphous diamond-like carbon films (a-C:F) were prepared on room-temperature (100) Si substrates using radio frequency plasma enhance chemical vapor deposition (rf PECVD) by varying the ratio of carbon tetrafluoride and methane (CF₄:CH₄). The films formed were investigated in terms of the surface morphology, chemical composition, microstructure, mechanical properties, and surface free energy by means of atomic force microscopy (AFM), x-ray photoelectron spectrum (XPS), micro-scratch test, nano-indenter test and contact angle measurement. It was observed that with increasing CF₄:CH₄, the roughness and F content of the a-C:F films increased while the hardness, Young's modulus and surface energy decreased. The microstructure of the films also changed from diamond-like to graphite-like. The reduction of the film surface energy with varying F content is believed to be mainly due to the change of bonds in the film, i.e., the decrease of -C-CF bond and corresponding increase of -CF, -CF₂, as evidenced by XPS results.

Keywords: Fluorinated amorphous diamond-like carbon films; x-ray photoelectron spectrum; surface free energy

* Corresponding author: egqyu@ntu.edu.sg

1. INTRODUCTION

Diamond-like carbon (DLC) films are known for their high hardness, wear resistance, chemical inertness, and low friction coefficients [1]. The properties of DLC may be modified by incorporation of dopants [2], such as silicon, fluorine, nitrogen, oxygen and various metals. It has been reported that incorporation of fluorine into DLC film will greatly reduce its surface free energy but almost keep DLC-behavior [3]. The non-wetting behavior combined with DLC superior properties allows numerous practical applications in nonstick kitchenware and protective coatings for optics. The surface free energy of materials is a characteristic factor, which affects the surface properties and interfacial interactions such as adsorption, wetting and adhesion, etc. In addition, fluorinated amorphous carbon films have been intensively investigated as a possible candidate due to its low-dielectric constant.

In this work, radio frequency plasma enhanced chemical vapor deposition (rf PECVD) was employed to prepare fluorinated amorphous DLC film (thereafter denoted as a-C:F) using carbon tetrafluoride (CH₄) and methane (CF₄) as precursors. The deposition was performed as a function of CF₄/CH₄ ratio at rf power of 60 W. The films properties were investigated by means of contact angle measurement, atomic force microscopy (AFM), x-ray photoelectron spectroscopy (XPS), Raman spectroscopy, scratch test and nano-indenter. The emphasis studied was placed to investigate the factors affecting the film surface energy.

2. EXPERIMENTAL DETAILS

2.1 Film preparation

The experimental setup, capacitively coupled radio frequency (13.56MHz) plasma enhanced chemical vapor deposition (rf PECVD) is asymmetrical in its configuration. Self-bias will be produced on substrate cathode during the deposition. This self-bias originates from the large difference of motion speed between electrons and ions in plasma [4], and depends on process parameters such as rf power applied, as shown in figure 1. After being ultrasonically cleaned in acetone, methanol and de-ionized water in sequence, (100) Si substrates were placed on the cathode electrode kept at room temperature by cooling water. The base vacuum in the chamber is $\sim 3 \times 10^{-4}$ Pa. Before deposition, the substrates were *in-situ* sputter cleaned for 10 min in argon plasma operated at 100 W. High-purity CH₄ and CF₄ were led into chamber as gas precursors. A very thin carbon interlayer was first deposited to improve the overall adhesion, and then a-C:F films were deposited at varying CF₄/CH₄ flow rate ratio (referred to as CF₄:CH₄) and 60 W power. A DLC film deposited by the same setup was used as a reference sample (DLC Ref.). During deposition, the process pressure was fixed at ~ 6.5 Pa.

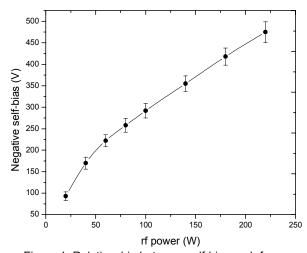


Figure 1. Relationship between self-bias and rf power.

2.2 Surface energy calculation

The surface free energy of the samples is generally obtained from measuring contact angle formed when liquid drops on the sample surface. The relationship between surface energy of the sample (γ_S) and the contact angle (θ) is universally described by the Young equation [5],

$$\gamma_{\rm S} = \gamma_{\rm L} \cos \theta + \gamma_{\rm LS}$$

where γ_L is the known surface energy of the testing liquid, γ_{LS} is the unknown interfacial energy of the film/liquid. To eliminate γ_{LS} from the equation, many methods have been developed based on consideration of the intermolecular forces. Among all, three methods [6-8] are often used, namely the harmonic mean equation (a), the geometric mean equation (b) and acid-base equation (c). They are expressed respectively as follows,

$$\gamma_{LS} = \gamma_S + \gamma_L - 4 \left(\frac{\gamma_S^d \gamma_L^d}{\gamma_S^d \gamma_L^d} + \frac{\gamma_S^p \gamma_L^p}{\gamma_S^p \gamma_L^p} \right)$$

$$\gamma_L = \gamma_S + \gamma_L - 2 \left(\sqrt{\gamma_S^d \gamma_L^d} + \sqrt{\gamma_S^p \gamma_L^p} \right)$$
(a)
$$\gamma_{LS} = \gamma_S + \gamma_L - 2 \left(\sqrt{\gamma_S^d \gamma_L^d} + \sqrt{\gamma_S^p \gamma_L^p} \right)$$
(b)

$$\gamma_{LS} = \gamma_S + \gamma_L - 2\left(\sqrt{\gamma_S} \gamma_L + \sqrt{\gamma_S} \gamma_L\right)$$

$$\gamma_{LS} = \gamma_S + \gamma_L - 2\left(\sqrt{\gamma_S} \gamma_L + \sqrt{\gamma_S} \gamma_L\right) + \sqrt{\gamma_S} \gamma_L + \sqrt{\gamma_S} \gamma_L\right)$$
(c)

where γ with superscript d and p means a dispersion component and a polar component, γ with superscript LW, + and - stands for a Lifshitz-van der Waals component, Lewis acid component and Lewis base component. Three liquids with different polarity, de-ionized water, methylene iodide (CH₂I₂) and formamide, were applied for the measurement. The contact angle was averaged over four data obtained from different spots on the samples for each liquid. Comparison was also made on the surface energy calculated from the above methods.

It should be pointed out that another surface energy - critical surface energy (γ_c) is often mentioned elsewhere. This critical surface energy is introduced by Zisman [9], and is the surface energy of a reference liquid which fully wets the sample surface, i.e., $\gamma_c = \gamma_L = \gamma_S$ at $\theta = 90^\circ$. In this work, this value was not given.

2.3 Other characterizations

The surface morphology of the films was observed over 1 μ m \times 1 μ m by a scanning atomic force microscope (AFM, Nanoscope IIIa) with a tapping mode. The chemical composition and bonding states of the films were characterized by x-ray photoelectron spectroscopy (XPS) with Al K α line (1486.6 eV) as the exciting source. In this characterization, the system was calibrated by the binding energy (\sim 284.7 eV) of C1s and all samples were analyzed without surface etching. A micro-Raman spectroscopy (Renishaw 1000) with 514.5 nm Ar⁺ laser was used to study the film microstructure, where the laser output power used was \sim 2 mW. The adhesion property was analyzed by micro-scratch test. Scratch test parameters used were as follows: progressive type, a maximum load of 25N, loading rate of 4N/min, the scratch length of 5mm Rockwell-type diamond indenter with 200 μ m radius. The hardness (H) and Young's modulus (E) were characterized by a nanoinderter (Nanoindenter II, Nano Instruments), where the continuous stiffness option was used and the maximum load was 10 mN.

3. RESULTS

3.1 Surface morphology

Figure 2 gave a typical AFM image of the a-C:F films. The films deposited were all uniform and smooth. Compared with DLC reference sample (0.17nm), the a-C:F films exhibited more rougher surface. The surface roughness also increased with CF₄:CH₄, from 0.23 nm at 1:4 to 0.28 nm at 4:1, as shown in figure 3. The increase was possibly caused by fluorine preferential etching of the films since the films were not ideally isotropic. In addition, the variation of the roughness with the ratio seemed not monotonous.

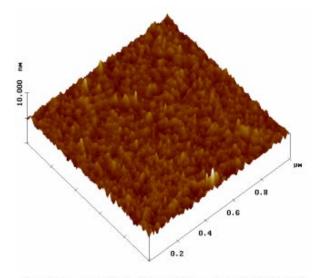


Figure 2. A typical AFM image of the film (1:1).

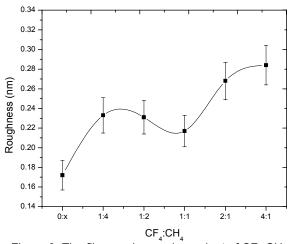


Figure 3. The film roughness dependent of CF₄:CH₄.

3.2 Chemical compositions and bonding states

Figure 4 showed the C1s local XPS spectrum for the film deposited at 1:1. It was well decomposed into four peaks, which centered at ~284.9, ~287.4, ~289.8 eV and ~292.3 eV), respectively. Due to surface contamination and charging effect during XPS analysis, it is very complex and also still controversial to identify these peaks. According to H. Touhara et al [10], the peak at 285 eV was assigned to the carbon atoms with the mixed bonded structures of sp² and sp³ configurations, and the peak at 287 eV was due to the carbon atoms bonded to oxygen. In addition, the peaks with 289 and 291 eV were ascribed to CF bonds and CF₂ bonds, respectively. The peak at ~292 eV was not reported. In other references [11-14], assignment was made between binding energy and structural unit as: -C-CH (284.6 eV), -C-CF (287.4 eV), -CF (289.5 eV), -CF₂ (292 eV), -CF₃ (294 eV). Based on the above data and the fact that a small amount of oxygen occurs on the films surface and hydrogen always occurs in the PECVD-deposited films as reflected in the Raman spectrum below, assignment is done as follows: -C-C and -C-CH (284.9 eV), -C-CF and -C=O (287.4 eV), -CF (289.8 eV) and -CF₂ (292.3 eV), where the fraction of -C-CH and -C=O should be much lower than that of -C-C and -C-CF, respectively. On the other hand, F atomic concentration can be obtained following the equation,

$$at.\% = \frac{(A_i/S_i)}{\sum_{i} (A_i/S_i)}$$

where subscript is film element, A and S is the peak area and sensitivity factor of the element (S = 0.78, 1.00 for C1s and F1s [10]). Similarly, the bond concentration was also done according to the relevant peak area divided by the sum of all the peaks area. Their concentrations were presented in figure 5, with varying CF_4 : CH_4 . It was observed that F was incorporated into the films with addition of CF_4 , and then increased correspondingly with CF_4 : CH_4 . At CF_4 : CH_4 of 1:4, F incorporated existed primarily in the form of CF bond state (-C-CF and -CF). The amount of -C-CF was greater than that of -CF. As CF_4 : CH_4 increased up to 4:1, the former content decreased while the latter concentration increased relatively slightly. What's more, when CF_4 : CH_4 increased to 1:1, another bonding state, CF_4 appeared in the films. Afterwards, CF_2 content gradually increased with increasing CF_4 : CH_4 .

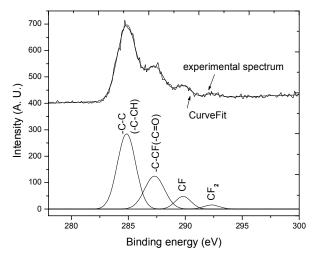


Figure 4. C1s XPS spectrum of the film (1:1).

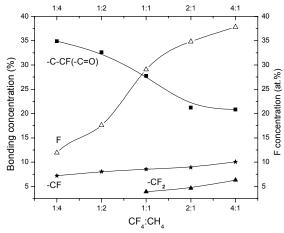


Figure 5. Concentrations of F and bonds of films at different $CF_a:CH_a$.

3.3 Microstructure

The microstructure of the a-C:F film was very similar to that of DLC (not shown), where G-band ("graphite", ~1540cm⁻¹) and D-band ("disorder", ~1340cm⁻¹) were obviously observed after fitting. The G band originates from the symmetric E2g vibrational mode in graphite-like materials, while the D band arises from the limitations in the graphite domain size induced by grain boundaries or imperfections [15], e.g., sp³ carbon, or other impurities. Quantitative analysis (figure 6) revealed that the intensity ratio of D- and G- band (I_D/I_G) increased, and G-band shifted upward with increasing CF₄:CH₄, which were due to an increased number of sp² bonds and the formation of sp² clusters in the amorphous network, i.e., rings or chains [16]. This result indicated the films became more graphitic with the increase in F content. It was also found that photoluminescence (PL) background appeared in

Raman spectra, and decreased with more addition of CF₄. The PL is generally believed to originate from hydrogen (H) or be due to that film is polymer-like as confirmed in carbon nitride film [17-19]. In our case, the films deposited are diamond–like carbon as disclosed below. It is therefore concluded the PL here is ascribed to H atoms in the films, where some hydrogen atoms are replaced by F atoms due to F incorporation and the PL intensity is reduced correspondingly.

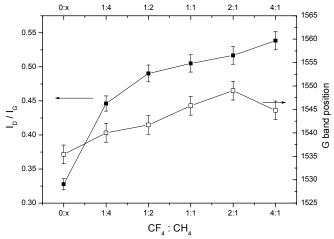


Figure 6. Dependence of I_D/I_G and G-band peak position on CF₄:CH₄.

3.4 Mechanical properties

Scratch test disclosed the a-C:F films were all well adhesive to the substrate (not shown). The hardness (H) and Young's modulus (E) can be calculated from the indentation load-displacement data [20]. It was drawn that the film hardness and modulus both decreased with increasing CF_4 : CH_4 (figure 7). As shown, with the introduction of CF_4 gas, the film hardness and modulus slightly dropped compared with that of DLC reference sample. When CF_4 : CH_4 increased, they further decreased. The lowest hardness was ~ 16 GPa larger than that of Si substrate (~ 12 GPa). This hardness feature of the films is guaranteed by the above-mentioned self-bias produced on the substrate, which increases the bombarding energy of deposited species and therefore results in the formation of DLC films [21]. The decrease in the film hardness is believed to be partly due to change in the microstructure as concluded from Raman analysis, i.e., more graphitized with more incorporation of F into the films. Another cause is possibly the reduction in the internal stress of the films induced by F incorporation into the films.

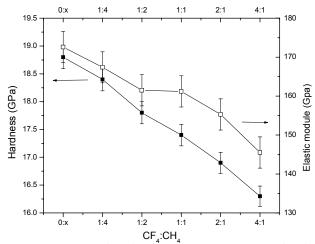


Figure 7. Dependence of the film hardness and modulus on CF₄:CH₄.

3.5 Surface free energy

Figure 8 showed the variation of the film surface energy with varying CF₄:CH₄. From (a), after introduction of CF₄ at 1:4, the surface energy was sharply reduced compared with that of DLC reference sample, suggesting that something like chemical composition altered in the films. The reduction extent calculated from the geometric mean method was more than those from the other two. On the other hand, the reduction rate did not vary until CF₄:CH₄ reached 1:2. After that, the reduction rate increased. As CF₄:CH₄ c increased to 2:1, the surface energy seemed to drop most quickly. The change in the reduction rate was very similar for all the methods. From (b), (c) and (c), it was also concluded that the reduction in the surface energy was largely ascribed to the decrease in the dispersion component, which was not dependent on the calculation approaches.

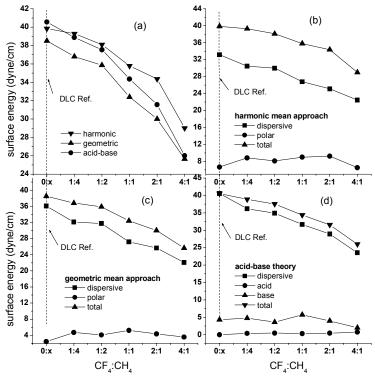


Figure 8. Surface energy of the films deposited at the different CF,:CH,.

4. DISCUSSION

In general, the surface roughness affects the measured contact angle and therefore the surface energy. According to Neumann [22], a model similar to that for heterogeneous solid surface can be developed in order to account for surface irregularities, being given by Wenzel's equation,

$$\cos\theta = r \cos\theta_0$$

where θ is the measured contact angle, θ_0 is the thermodynamical value for the smooth surface, and r quantifies the surface roughness (ratio of the real area of the surface to the apparent area of the geometrical interface). Clearly, more rougher the contact surface (larger r) is, more smaller is the observed contact angle (larger surface energy). However, as concluded from the AFM test (figure 2) and the contact angle measurement (figure 8), with increasing CF₄:CH₄, the film surface roughness increased while the surface energy decreased. Therefore, the relationship between the roughness and the measured contact angle does not follow the above equation. As such, it is concluded that the roughness plays a negligible role on the surface energy. This may be ascribed to the fact the surface roughness is so small. A similar result for other materials was reported elsewhere [23-25].

The effect of F content in the films on the surface energy is very noticeable (figure 5 and figure 8). As pointed out above, besides a small fraction of -C-CH and -C=O bonds, there are -C-C, -C-CF, -CF and -CF₂ bonds in the films, where -C-C bond is the backbone of DLC film. The bonding states and their contents changed with increasing F content. With increasing F content up to ~37%, -C-CF bond content decreased and -CF increased, while the

surface energy decreased. Especially, at F content of ~ 30 at.%, $\cdot \text{CF}_2$ appeared and thereafter also increased with F content. The bonds associated with F have a corresponding trend as the surface energy does with increasing F content. It is thus concluded that the reduction in the surface energy is mainly caused by the decrease of $\cdot \text{C-CF}$ bond and the increase of $\cdot \text{CF}_2$ and $\cdot \text{CF}_2$ bonds. The introduction and increase of $\cdot \text{CF}_2$ is maybe responsible for the accelerating decrease in the surface energy since $\cdot \text{CF}_2$ is a basic unit of PTFE, which is a simple linear C-C backbone with two F atoms on each C atom and possesses the lowest surface energy.

The effect of the film microstructure on the surface energy was very negligible. The film became more graphitized as more F was incorporated. This graphitization should not account for the reduction of the surface energy.

It is well known that surface energy originates from the unbalance of the force between atoms or molecules inside and interface. Generally, the polar component results from three different intermolecular forces due to permanent and induced dipoles and hydrogen bonds, whereas the dispersion component arises from instantaneous dipole moments [23]. So, the variation of -C-CF, -CF and -CF₂ bonds mainly lowered the dispersion component, and therefore reduced the surface energy of the film significantly.

5. CONCLUSIONS

Fluorinated amorphous diamond-like carbon films (a-C:F) were prepared on room-temperature (100) Si substrates by rf PECVD. The films were investigated in terms of the surface morphology, chemical composition, microstructure, mechanical properties, and surface free energy by means of atomic force microscopy (AFM), x-ray photoelectron spectrum (XPS), micro-scratch test, nano-indenter test and contact angle measurement. It was observed that with increasing CF₄:CH₄, the roughness, F content of the a-C:F films increased while the hardness, Young's modulus and surface energy decreased. The films also became more graphitized. The reduction of the surface energy with varying F content is believed to be mainly due to the change of bonds in the film, i.e., -C-CF bond decreased and -CF, -CF₂ increased. The roughness and the microstructure played negligible roles in affecting the film surface energy.

References:

- 1. A. Grill, Diamond Relat. Mater. 8, (1999) 428.
- 2. M. Grischke, K. Bewilogua, K. Trojan, H. Dimigen, Surf. Coat. Technol. 74-75, (1995) 739.
- 3. R. Memming, Thin Solid Films 143, (1986) 279.
- 4. B. Chapman, Glow Discharge Processes: sputtering and plasma etching, New York: Wiley, 1980.
- 5. T. Young, Philos. Trans. R. Soc. London 9, (1805) 255.
- 6. S. Wu, J. Polym, Sci . Part C 34 (1971) 19.
- 7. D. K. Owens, R. C. Wendt, J. Appl. Polym. Sci. 13 (1969) 1741.
- 8. F. M. Fowkes, J. Adhes. Sci. Technol. 1 (1987) 7.
- 9. W. A. Zisman, Ind. Eng. Chem. 55 (1963) 19.
- 10. H. Touhara, F. Okino, Carbon 38 (2000) 241.
- 11. A. Dilks, in: C.R. Brundle, A.D. Baker (Eds.), Electron Spectroscopy, Academic Press, London, 1981.
- 12. D.T. Clark, in: D. Briggs (Ed.), Hand Book of x-ray Photoelectron Spectroscopy, Heyden, London, 1978.
- 13. A. Dilks, E. Kay, Macromolecules 14 (1980) 855.
- 14. J. L. He, W. Z. Li, L. D. Wang, J. Wang, H. D. Li, Nucl Instr & Meth. in Phys. Res. B 135 (1998) 512
- 15. N. Hellgren, M.P. Johansson, E. Broitman, I. Hultman, J.E. Sundren, Phys. Rev. B 59 (1999) 5162.
- 16. A. C. Ferrari, J. Robertson, Phys. Rev. B 61, (2000) 14095.
- 17. G. Q. Yu, S. H. Lee, J. J. Lee, Diamond Relat. Mater. 11 (2002) 1633.
- 18. N. Mutsukura, Diamond Relat. Mater. 10 (2001) 1152.
- 19. G. Q. Yu, S. H. Lee, D. G. Lee, H. D. Na, H. S. Park, J. J. Lee, Surf. Coat. Technol. 154 (2002) 68.
- 20. W. C. Oliver and G. M. Pharr, J. Mater. Res. 7, (1992) 1564.
- 21. C. A. Davis, G. A. J. Amaratunga, K. M. Knowles, Phys. Rev. Lett. 15 (1998) 3280.
- 22. A. W. Neumann, Adv. Colloid Interface Sci. 4 (1974) 328.
- 23. J. S. Chen, S. P. Lau, B. K. Tay, G. Y. Chen, Z. Sun, Y. Y. Tan, G. Tan, J. W. Chai, J. Appl. Phys. 89 (2001) 7814.
- 24. H. J. Busscher, A. W. J. van Pelt, P. de Boer, H. P. de Jong, J. Arends, Collids. Surf. 9 (1984) 319.
- 25. N. Sprang, D. Theirich, J. Engemann, Surf. Coat. Technol. 74-75 (1995) 689.

DEPOSITON OF C-F THIN FILMS BY SUPUTTERING AND THEIR MICRO-MECHANICAL PROERTIES

M. Wang, S. Watanabe and S. Miyake

Nippon Institute of Technology, 4-1 Gakuendai, Miyashiro-machi, Minamisaitama-gun, Saitama, 345-8501, JAPAN

ABSTRACT

Deposition of carbon fluorinated (C-F) and Graphite/PTFE films using RF magnetron sputtering is reported in this article. The films fabricated with forming argon plasma and laying several millimeter size of poly-tetra-fluoroethylene (PTFE) up graphite as targets are characterized using fourier transform infrared spectroscopy, automatic contact angle meter, surface free energy analyzer and surface profile measuring system. Results indicate that there have been C-F bonding and Carbon amorphous structure existing in modified surfaces, the water-repellence of surface modified under different conditions has been increased, and their surface free energy shows lower as comparing with silicon substrate essentially due to C-F bonding existing. In addition, in order to understand the micro-mechanical characteristics of the films in detail, the viscoelastic properties of surface deposited films were studied with atomic force microscope (AFM). Tan δ of PTFE film is low around 0.1. It could be confirmed that viscoelastic properties of surface are able to be changed and improved by surface modification method.

Keywords: C-F bonding, AFM, viscoelasticity, PTFE.

INTRODUCTION

Surface modification by Physical Vapor Deposition (PVD) has been greatly paid attention and applied in recent years. For silicon applied extensively in many fields, it is quite difficult to realize silicon processing because the adhesion and friction of its surface is so large. Graphite/PTFE and carbon fluorinated films are well known for advanced tribological, mechanical properties, and their many applications in high technology areas. It has been reported that deposition of PTFE on silicon wafers was successfully performed to improve its self-lubrication and water-repellence due to weak interaction of C-F combination between their superficial molecules [1].

In this article, we attempt to fabricate Graphite/PTFE films on silicon wafers for the propose of improving friction, water-repellence, mechanical and viscoelastic properties by radio frequency (RF) magnetron sputtering with argon plasma using target PTFE and graphite as targets. The surface conditions of modified silicon were characterized and films deposited with different targets and deposition times were compared. Their viscoelastic properties also were evaluated in this paper.

EXPERIMENTAL METHOD

Fig. 1 shows the schematic illustration of RF magnetron sputtering equipment. Silicon (100) wafer was used as substrate. Firstly, Graphite-PTFE films were synthesized on silicon in a sputter deposition chamber with argon plasma and dual PTFE/Graphite targets by adjusting the size of target PTFE and deposition time shown in Table. 1. Secondly, deposition of Graphite films was finished using only graphite as a target under deposition conditions shown in Table. 2. In order to evaluate tribological properties of C-F films on silicon substrate, C-F films deposited under different conditions were examined by some analytical techniques for investigating C-F binding, thickness value, self-lubrication, and water-repellence. Contact angle measurement was performed using refined water and Iodine methane to measure surface free energy. With a Fourier transform infrared spectroscopy (FT-IR), the chemical bonding features of C-F films were investigated. Furthermore, viscoelastic properties such as storage modulus, loss modulus and Tan δ were evaluated by means of atomic force microscope (AFM) [2]. These

properties of C-F films were compared with those of untreated silicon and PTFE films reported in our previous paper [3] to clarify the effect of modification due to different deposition conditions.

Table 1. Graphite-PTFE films deposition condition

Apparatus	Radio frequency (RF) sputtering
	equipment
Gas pressure (torr)	Argon, 3.4×10^{-2}
Target (mm ²)	Graphite, PTFE (7×7)
RF power (kW)	0.2~0.5
Deposition time (min)	20

Table 2. Graphite films deposition condition

Apparatus	Radio frequency (RF) sputtering		
	equipment		
Gas pressure (torr)	Argon, 3.4×10^{-2}		
Target (mm ²)	Graphite		
RF power (kW)	0.2~0.5		
Deposition time (min)	15		

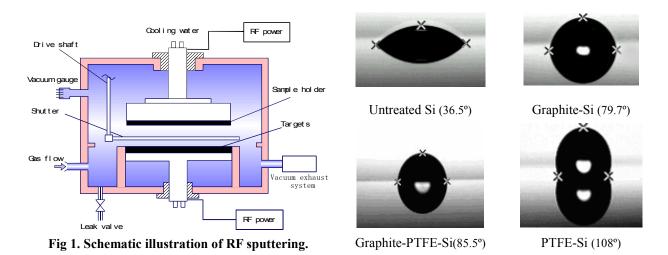


Fig 2. Refined water drop profiles of untreated, Graphite and Graphite/PTFE deposited on Silicon.

RESULT AND DISCUSSION

Measurement of surface free energy

To know the surface conditions of depositing Graphite/PTFE and Graphite films on silicon and compare with PTFE deposited film. Surface free energy of various film deposited silicon was evaluated using a water drop. Fig. 2 shows drop profiles of film deposited silicon wafer. As comparing with a drop contact angle 36.5 degree of refined water on untreated specimen, Graphite, Graphite/PTFE and PTFE deposited films respectively increase to 79.7 degree, 85.5 degree and 108 degree and it indicates that the surface tension of deposited specimens decrease due to surface modification [4].

Fig. 3 shows the contact angles measured with three kind liquids such as refined water, etc. and surface energy was displayed in Fig. 4. According to Extended Fowkes's theory of 3, surface free energy (γ s) is the sum of

dispersion force (γ sd), dipole force (γ sp), and hydrogen bond (γ sh) as following equation,

$$\gamma s = \gamma sd + \gamma sp + \gamma sh$$

It is considered that surface free energy of silicon is reduced from 71.5mN/m to 40.2mN/m and 17mN/m because C-F bond were formed on silicon with Graphite and PTFE sputtering treatment.

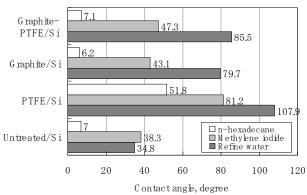


Fig 3. Contact angle values of the films and the Si substrate.

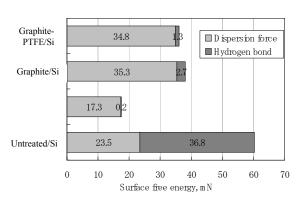


Fig 4. Surface free energy of the films and the Si substrate.

FT-IR measurement of C-F bonding

IR is a common characterization tool for C-F compounds as C-F bond shows a distinct feature. A distinct absorption band assigned to a C-F stretching is noted around the wave number of 1200 cm⁻¹ [5]. As shown in Fig. 5, it is seen that there is a peak near 1200 cm⁻¹ in PTFE target because PTFE possesses a typical C-F combination. Graphite-PTFE and PTFE films display an obvious peak around 1200 cm⁻¹. However, there is not the absorption to appear in carbon film. On the basis of this result, the characteristic bonds of C-F appear indicating that the C-F combination is formed when depositing the PTFE and carbon/PTFE films using PTFE as a target.

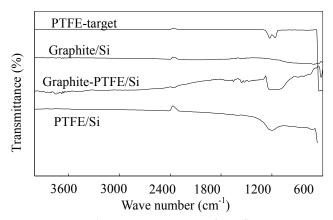


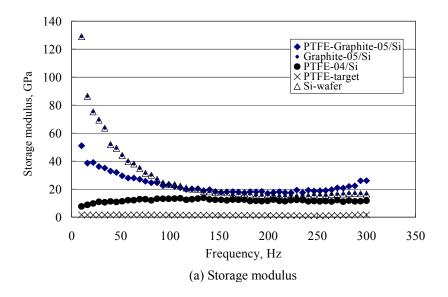
Fig 5. FT-IR spectra of the films.

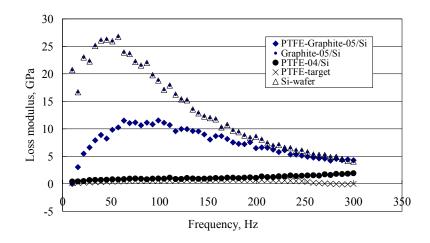
Evaluation of viscoelastic properties

As comparing viscoelastic properties of carbon fluorinate and carbon film deposited on silicon with untreated silicon, it is found that their viscoelastic properties are different due to used targets and deposition time. As shown in Fig. 6 (a), PTFE itself employed as a target displays a typical storage modulus which is smaller than 10 GPa. Simultaneously, it could be found that storage modulus of PTFE and PTFE-Graphite exhibit a low storage modulus

under 20 GPa when loading frequency is below 100 Hz. It is inferred that storage modulus decrease due to C-F bonding existing. This result is corresponding to that of FT-IR measurement, whereas storage modulus of untreated substrate and Graphite film shows a high value over 20 GPa. With load frequency increasing to 150-300Hz, all storage modulus tend to being about 20 GPa.

Observing Fig. 6 (b), loss modulus of untreated silicon is approximately similar to that of Graphite deposited silicon. As the film was deposited under PTFE and graphite, its loss modulus was decreased under 15 GPa. On other hand, it is very obvious that loss modulus is extensively changed close to small value which is the same as loss modulus of PTFE target. It is confirmed that loss modulus could be remarkably lowered due to weak interaction of C-F bonding formed in films. Fig. 7 indicates that Tan δ of PTFE film deposited is under 0.1 at a range of loading frequency from 0 from 220Hz. As observing Fig. 6, it is easily found that viscoelastic properties of Graphite/PTFE films deposited silicon are situated between those of Graphite and PTFE film deposited on silicon.





(b) Loss modulus

Fig 6. Viscoelastic properties of the films.

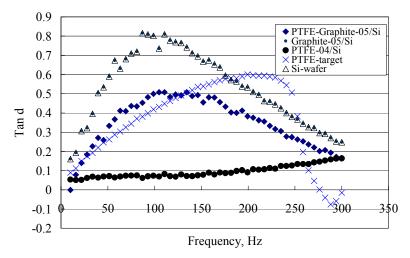


Fig 7. Viscoelastic property of Tan δ of the films.

CONCLUSION

PTFE, PTFE-Graphite, Graphite films were deposited on silicon substrates by means of magnetic sputtering using PTFE target and dual PTFE and Graphite targets. The surface structure conditions, water-repellence and tribological properties were studied. Based on PTFE target, surface free energy of PTFE and PTFE-Graphite films were lowered and their viscoelastic properties were obviously changed. It is confirmed that surface structure and tribological properties of modified silicon substrate were improved due to weak interaction of C-F combination. Tan δ of PTFE film deposited on silicon is shown very lower. As observed Graphite film, its storage modulus, loss modulus and Tan δ is basically the same as those of untreated silicon. It is clarified that the effect of deposited film on mechanical properties is different depending on using target, and tribological properties of PTFE and PTFE-Graphite films were remarkably improved due to C-F combination.

REFERENCES

- 1. Y. Enomoto.; and S. Miyake: Tribology of Thin Films. University of Tokyo Press, 1994 [in Japanese]
- 2. S. A. Syed Asif.; K. J. Wahl.; and R. J. Colton.: Rev. of Sci. Inst. 70, 5 (1999) 2408.
- 3. N. Shimizu.; S. Watanabe.; and S. Miyake.: Surface Modification of CF₄ Plasma Treatment. Proceeding of Mechanical Congress, Japan, vol. II, 8, 2000, pp. 395.
- 4. N. Shimizu, S. Watanabe, M. Wang and S. Miyake: Deposition of PTFE Film by means of Sputtering. Proceeding of 105th Meeting of the Surf. Fin. Soc. Of Jap. 179 (2002), pp. 4.
- 5. HORIGUTI HIROSI, Total figure explanation of light absorb by infrared ray, in 1997

WEAR RESISTANT BEHAVIOR OF AMORPHOUS CARBON AND CARBON NITRIDE FILMS PREPARED BY SHIELDED ARC ION PLATING

Kyung Hwang LEE, Riichiro OHTA, Hiroyuki SUGIMURA

Department of Materials Processing Engineering, Graduate School of Engineering, Nagoya University, Nagoya 464-8603, JAPAN TEL: +81-52-789-2796 FAX: +82-52-789-3260 E-mail address: ioncorr@plasma.numse.nagoya-u.ac.jp

Yasushi INOUE

Research Center for Nuclear Materials Recycle, Nagoya University, Nagoya University, Nagoya 464-8603, JAPAN

Osamu TAKAI

Center for Integrated Research in Science and Engineering, Nagoya University, Nagoya 464-8603, JAPAN

ABSTRACT

Amorphous carbon (a-C) and carbon nitride (a-CNx) films are promising for many industrial applications owing to their high hardness, wear resistance and solid lubricity. Nowadays, the films attract much attention as biomedical, since the films have chemical and mechanical durabilities in vivo. A CNx frequently shows excellent wear resistance, even though its hardness is not so high in comparison with a-C. Tribological properties of such films have been intensively studied in relation to chemical structures of the films. However, those are not sufficiently elucidated.

In this study, a-C and a-CNx films are deposited by shielded arc ion plating (SAIP) with arc current of 60 A, bias voltage in the range from 0 to 500 V and gas pressure of 1 Pa. Mechanical properties of the films including hardness, elastic modulus, recovery, contact stiffness and plastic and elastic deformation energies were measured by a nanoindenter interfaced with an atomic force microscopy (AFM) using a diamond tip (Berkovich type: 65.3° of half angle). Wear resistant behavior of the films was studied by a ball-on-disc tribotester with a load of 5 N and a sliding speed of 100 mm/s. The nanoindenter was also applied to evaluate wear resistant behavior of the films in nm scale. To study chemical structures, the films were analyzed by X-ray photoelectron spectroscopy (XPS) and Raman spectroscopy. We will mainly discuss on the wear resistant behavior in relation to other mechanical properties of a-C and a-CNx films measured based on nanoindentation, as well as the relation of the chemical structures to the tribological properties of the films.

Keywords: a-C film, a-CN film, shielded arc ion plating (SAIP), tribology, nanoindentation

ANTI-WEAR CHARACTERISTICS OF CARBON NITRIDE THIN FILMS

Shuichi Watanabe, Shojiro Miyake, Mieko Sutoh and Masao Murakawa Nippon Institute of Technology 4-1 Gakuendai, Miyashiro, Saitama 345-8501, Japan

ABSTRACT

The carbon nitride has been proposed theoretically with a possible structure of β -C₃N₄ which have replaced Si of β -Si₃N₄ with C, by Liu and Cohen in 1989. It was announced that β -C₃N₄ had a higher bulk-modulus value than that of diamond. The research in forming C-N compounds has been actively done. Recently, it has been reported that carbon nitride film has showed a unique property, such as a high elastic recovery compared with DLC film, even if a structure of this film was amorphous. In this study, carbon nitride films have been deposited by means of the magnetically enhanced plasma ion-plating equipment. The following two methods of the deposition were investigated. One is the reactive ion-plating which is a reactive evaporation between carbon vapor and nitrogen plasma. The second is a method of an ionized evaporation caused by mixed gas plasma using hydrocarbon and nitrogen gases. Wear performance and deformation energy evaluation of the films were examined by the micro-wear and nano-indentation tests using AFM device having a peculiar transformer head added to the measuring units. Moreover, crystal structure and chemical composition of the film have been analyzed using FT-IR and XPS, respectively. The film formed with the ionized evaporation using C₂H₂-Ar-N₂ gas plasma showed that the hardness becomes harder than that of the film formed with the reactive ion-plating, due to the confirmation of C-N bonding structure from the result of FT-IR and XPS. When the film is formed under CH₄-N₂ gas plasma, it has been observed that no micro-wear of the film was occurred, resulting in showing good wear resistance. This is understood that the film shows large elastic recovery from the result of the deformation energy evaluation.

Keywords: Carbon nitride film, Ion-plating, Ionized evaporation, Micro-wear, Deformation energy evaluation

INTRODUCTION

The possibility with the bulk modulus over the diamond has been theoretically proposed by Liu & Cohen (ref. 1). The research on the synthesis of a crystalline carbon nitride thin film has been actively carried out. In particular, carbon nitride films show some excellent mechanical properties such as low friction and high wear resistance like DLC (refs. 2 to 7). Therefore, it is considered that the films are very useful for tribological coating on various industrial substrates. Although there have been some achievements in synthesizing very fine crystalline carbon nitride film (ref. 8), most such films were amorphous. The development of a method capable of generating consistent crystalline thin films is therefore eagerly awaited. Authors have also researched on the synthesis of carbon nitride thin films using the reactive ion-plating between C vapor by the electron beam and Ar-N₂ and C₂H₂-Ar-N₂ gas plasmas. The results have been found that it has not come to it in the synthesis of a film of the theoretical stoichiometry, though the carbon nitride film having a composition ratio N/C value of about 0.6 was possible. In present state, although there is some uneven profile in the film surface, but the film structure shows an amorphous state, so that it is difficult to synthesize a film with the high density. Therefore, a synthetic film does not show excellent tribological characteristic (low friction, high friction durability, etc.).

Since these situations were considered, the synthesis of the carbon nitride film was tried by means of an ionized evaporation in gas plasma formed using the same equipment. The C_2H_2 -Ar- N_2 mixed gas was used in the formation of the gas plasma. In addition, the synthesis of a film was tried under the CH_4 - N_2 mixed gas system in order to increase the content of nitrogen in the film. In this report, the tribological characteristic of carbon nitride film synthesized by ionized evaporation using above-mentioned C_2H_2 -Ar- N_2 mixed gas, was compared with it of the film formed by ion plating. In addition, the similar evaluation was also carried out on the film formed by the CH_4 - N_2 mixed gas.

EXPERIMENTAL

The Magnetically Enhanced Plasma Ion Plating (MEP-IP) (ref. 9) was used for this experiment. Schematic illustration of the equipment is shown in Fig. 1. Carbon nitride films have been deposited by means of ionized evaporation technique using C_2H_2 -Ar- N_2 and CH_4 - N_2 gas plasmas. The deposition conditions are shown in Table 1. Total gas pressure in the chamber during deposition was fixed at 6.6×10^{-2} Pa, gas flow ratio of C_2H_2 :Ar: N_2 =

1:1:1, and $CH_4:N_2=1:1$. RF bias applied to the substrate was variously changed. Ionization potential and ionizing current are fixed at 60 V and 16 A, respectively. Si wafer (100) was used for the substrate, and it took 30 min in the film formation time. Carbon nitride films produced by the reactive ion plating have been also carried out the similar evaluation for the comparison purpose. The film structure and composition are analyzed by means of FT-IR and XPS. In order to evaluate an intrinsic mechanical property of the film, the micro-mechanical properties of the films were examined by utilizing an atomic force microscope (AFM) in the nano-indentation test. In this test, the load applied to the indenter was set at 100, 200, or 300 μ N with a constant loading rate of 50 μ N/sec. A pyramidal diamond tip (Berkovich-type) was used as the indenter.

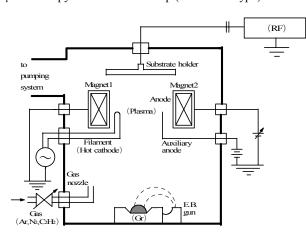


Table 1 Deposition conditions.

Substrate	Si wafer (100)
Total gas pressure	6.6 × 10 ⁻² Pa
G as flow ratio	$C_2H_2:Ar:N_2 = 1:1:1$ $CH_4:N_2 = 1:1$
D ischarge potential	60 V
D ischarge current	16 A
Substrate bias (RF): V dc	-10 ∼ -205 V

Fig. 1 Schematic illustration of ion-plating used for this experiment.

RESULTS AND DISCUSSION

Figure 2 shows the IR absorption spectra of the films measured using FT-IR. In this figure, data obtained from the films deposited by ionized evaporation (C_2H_2 -Ar- N_2) under two cases of Vdc values of -25 - -30V and -85 - -90V. There is a strong absorption corresponding to the C-N combination, at wave number of around 1200 cm-1. The result of the film formed by ion plating for the comparison at the equal substrate bias value is also shown in the figure. It is clear that the absorption of ion-plated film is smaller than that of ionized-evaporated film

Figure 3 shows the hardness of the film deposited by the ionized evaporation (C_2H_2 -Ar- N_2), measured by nano-indentation test by means of AFM. The value of hardness is soft of around 5GPa for the film deposited under a low Vdc of -25 - -30V. In the case of higher Vdc of around -200 - -205V, the hardness indicated much higher value of about 30 GPa in the case of indentation load of 300 μ N. It is found that the film deposited under a higher Vdc value shows the higher hardness. It was proven that these values were higher than a film

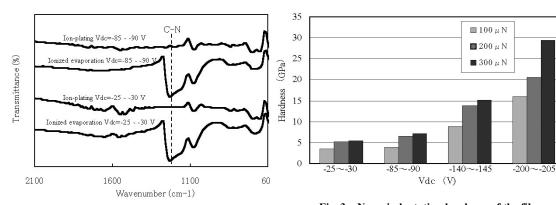


Fig. 2 FT-IR spectra of the films deposited by ion-plating and ionized evaporation.

Fig. 3 Nano-indentation hardness of the films deposited by ionized evaporation (C_2H_2 -Ar- N_2) under various Vdc values.

deposited by the ion plating. In addition, measured hardness increased with increasing of the indentation load. In general, the value of measured hardness increases as indentation load is smaller, however, in this case, the reverse tendency is shown. It seems to base on being big in respect to elastic recovery of the carbon nitride film.

Figure 4 shows worn surface profiles after the micro wear test for the films formed in CH_4 - N_2 gas plasma. It is found that the surface shapes of the films formed under Vdc values of -10 and -40 V are uneven, and the others show comparatively flat. From this figure, the wear mark can be confirmed for the films formed under Vdc value of -40, and -120, and the depth values have been measured about 40nm in both cases. However, no wear marks could be almost confirmed for the films under Vdc value of -10V at -80V, in spite of the same wear condition.

Figure 5 shows worn surface profiles after the micro wear test for the films formed in C_2H_2 -Ar- N_2 gas plasma. It has been observed that wear depth became smaller with increasing the Vdc value. However, for the film formed under Vdc value of -200V no wear could observe, because it was hard with 30GPa.

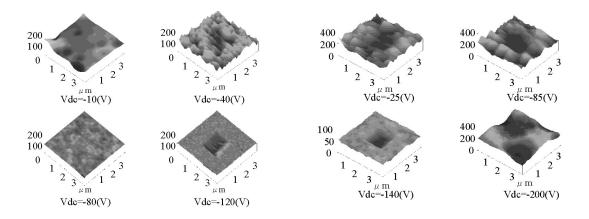


Fig. 4 Surface profiles showing micro wears for the films deposited by ionized evaporation (CH_4-N_2) .

Fig. 5 Surface profiles showing micro wears for the films deposited by ionized evaporation (C_2H_2 -Ar- N_2).

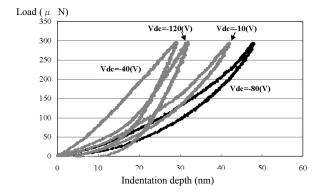
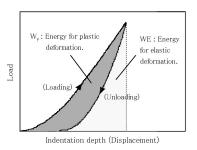


Fig. 6 Nano-indentation curves of the films deposited by ionized evaporation (CH₄-N₂).



Total deformation energy (Applied energy): $W_T = W_P + W_E$ Plastic deformation rate : $R_P = W_P/W_T$

Fig. 7 Schematic representation of indentation curve showing the areas for W_P and W_E .

Figure 6 shows a force curve (at a load of 300 μN) obtained by nano-indentation test for the film formed under the CH₄-N₂ system. In the case of the film formed under Vdc value of – 80 V, although no wear observed from the result of Fig. 4, the hardness value was lower than that of silicon substrate. However, it was observed that the films exhibited a large amount of elastic recovery on unloading, even if the films did not have any resistance for penetration on loading as shown in Fig. 6. To clarify the degree of elastic recovery phenomenon, we have defined the plastic deformation rate (R_p) of the film by means of an energy analysis for the indentation curve. The idea about this energy analysis is based on the existing literature (ref. 10). Figure 7 shows the schematic representation of indentation curve showing the areas for W_P (energy for plastic deformation) and W_E (energy for elastic deformation). This figure also shows the definitions of W_T (total deformation energy; W_T = $W_P + W_E$) and $R_P (R_P = W_P / W_T)$. Fig. 8 shows the results of deformation energy analysis from nano-indentation curves for the individual films as well as Si substrate when the applied load was 300 µN. As observing in this figure, it can be found that the film formed under Vdc value of - 80 V, clearly display a smaller plastic deformation rate (the value is about 20 %) as compared with that of the film formed under Vdc of – 120 V (about 60 %). In the case of Si, Si is one of the materials showing the nature of brittleness, the R_P value was about 60 % in spite of indicating a higher hardness value. Thus, it has been confirmed that the film formed under suitable condition exhibited a low plastic deformation rate, that is, indicates large elastic recovery, although the film hardness was not so high. It is assumed that the film can play excellent tribological properties because of the large elastic recovery, and resulting in no wear.

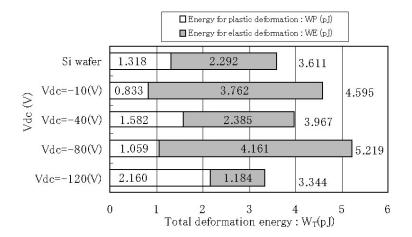


Fig. 8 Results of deformation energy analysis from nano-indentation curves for the films deposited by ionized evaporation (CH $_4$ -N $_2$) and the Si substrate.

Composition and structure analysis of the film was performed by XPS. Fig. 9 shows the XPS spectra for the films formed under Vdc values of -80 V (showing high wear resistance) and -40 V (observing wear mark). From this figure, it was found that there were clear differences in the structure of the films in both spectra of C1s and N1s. In the both spectra, larger peak heights of sp^2CN and spCN combinations in the case of the film formed under Vdc of -80 V, were observed in comparison with those of the film formed under -40 V. Therefore, the value of Vdc strongly affected the film structure, and then this fact seems to originate for the small of the plastic deformation rate.

CONCLUSIONS

We compared and examined mechanical properties of the carbon nitride films formed by ion plating and ionized evaporation. The obtained results are summarized as follows.

1) It was confirmed that carbon nitride film formed by the ionized evaporation by C_2H_2 -Ar- N_2 gas plasma showed higher hardness than that of the film formed by the ion plating, due to the confirmation of C-N bonding structure from the result of XPS.

- 2) It was found that there was stronger IR absorption of C-N stretching at a wave number of 1200⁻¹ for the film formed by the ionized evaporation in compared with the film formed by the ion plating.
- 3) The hardness value of the film formed by CH_4 - N_2 gas plasma showed comparatively low value, however, it has been observed that no micro-wear of the film was occurred, resulting in showing good wear resistance. This is understood that the film shows large elastic recovery from the result of the deformation energy evaluation.

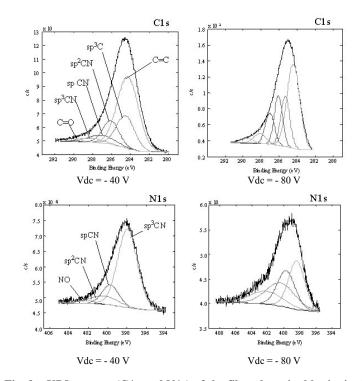


Fig. 9 XPS spectra (C1s and N1s) of the films deposited by ionized evaporation (CH₄-N₂) at Vdc values of -40 and -80 V.

REFERENCES

- 1. A. Y. Liu and M. L. Cohen: Science, 245 (1989) 841.
- 2. S. Muller: Sensors and Actuators, A21/A23 (1990) 1.
- 3. T. A. Yeh, C. L. Lin, J. M. Sivertsen and J. H. Judy: J. Magnetism Magnetic Materials, 120 (1993) 314.
- 4. E. C. Cutiongco, D. Li, Y. W. Chung and C. S. Bhatis: Trans. ASME, 118 (1996) 543.
- 5. S. Miyake, S. Watanabe, H. Miyazawa, M. Murakawa, R. Kaneko and T. Miyamoto: Appl. Phys. Lett., 65 (1994) 3206.
- A. Czyzniewski, W. Precht, M. Pancielejko, P. Myslinsli and W. Walkowiak: Thin Solid Films, 317 (1998) 384.
- 7. S. Watanabe, S. Miyake and M. Murakawa: Proc. 6th Applied Diamond Conf./2nd Frontier Carbon Tech. (ADC/FCT2001), (July 2001) 599.
- 8. S. L. Sung, T. G. Tasi, K. P. Huang, J. H. Huang, and H. C. Shih: Jpn. J. Appl. Phys., 37 (1998) L148.
- 9. M. Murakawa and S. Watanabe: Surf. Coat. Technol., 43/44 (1990) 128.
- 10. Y. Sawahira, A. Sato, N. Kikuchi, E. Kusano, H. Nanto and A. Kinbara: J. The Vacuum Society of Japan, 42 (1999) 652. (in Japanese)

MECHANICAL PROPERTIES OF ta-C FILMS DEPOSITED ON POLYETHYLENE AND METALLIC SUBSTRATES

Carlos J. M. Siqueira

Federal University of Parana, Department of Mechanics, Polytechnic Centre, C.P. 19011, Curitiba, Parana, Brazil

Wanderley Veiga

Federal University of Parana, Department of Physics, Polytechnic Centre, C.P. 19011, Curitiba, Parana, Brazil

Vladimir P. Poliakov

Federal University of Parana, Department of Mechanics, Polytechnic Centre, C.P. 19011, Curitiba, Parana, Brazil

Ivo A Hümmelgen

Federal University of Parana, Department of Physics, Polytechnic Centre, C.P. 19011, Curitiba, Parana, Brazil

Gregory G. Kirpilenko

Patinor Coatings Ltd, NIIMV, Zelenograd, 130460, Russia

ABSTRACT

Research in the area of advanced materials application in artificial prosthetics with a view to minimize the biochemical and mechanical complications of implanted materials is carried out. In this paper the results of physical chemical characterization, mechanical properties (nano-hardness, elastic modulus) and tribological testes of ta-C films deposited on ultra high molecular weight polyethylene (UHMWPE) and metallic substrates (Ti, Co-Cr- Mo, stainless steel 138F, hard alloy) are presented. These films were obtained by pulsed arc plasma method (physical vapour deposition, PVD) using a carbon source accelerator in a vacuum of 2 x 10⁻⁴ Pa. Physical chemical characterization of ta-C films had been carried out by different methods. The nano-hardness and elastic modulus of ta-C films (~250 nm) deposited on the metallic and UHMWPE substrates were measured by nanoindentation method. It was determined that the nano-hardness and elastic modulus are larger for ta-C deposited on the metallic substrates than that deposited on UHMWPE. Wear resistance and the coefficient of friction of ta-C film were measured by different methods.

Keywords: ta-C, nano-hardness, elastic modulus, wear, biomaterials.

The corresponding author: Vladimir P. Poliakov

Federal University of Parana, Department of Mechanic, Polytechnic Centre, C.P. 19011, Curitiba, Parana, Brazil

e-mail: vladimir@demec.ufpr.br

tel: 55-41-361-3125; fax: 55-41-361-3129

EFFECT OF TEMPERATURE AND ION BOMBARDMENT ON DLC RELIEF GENERATION AND MODIFICATION

A.P.Rubshtein, I.Sh.Trakhtenberg, V.A.Yugov, S.A.Plotnikov, Yu.S.Ponosov, A.B.Vladimirov, Metal Physics Institute Ural Branch RAS, 18 S.Kovalevskaya St., 620219 Ekaterinburg, Russia, e-mail: rubshtein@imp.uran.ru

Kensuke Uemura

ITAC Ltd., 2-24-7, Kita-otsuka, Toshima-Ku, Tokyo 170-004, Japan

ABSTRACT

DLC were deposited by arc-pulse sputtering of graphite. Raman spectroscopy was used for determination of $\rm sp^3/sp^2$ ratio. DLC deposition temperature was varied by change of pulse frequency. After deposition DLC were etched by argon or oxygen ions (E = 3 keV). Study of DLC surface relief were carried out by means of atomic-force and laser microscopes. It is shown that DLC surface has domain-like structure with ranges of peaks along boundaries. Separate protrusions are observed on DLC surface. Their height is comparable to coating thickness. Generation of DLC relief strongly depends on intensity of diffusion process taking place on the growing film surface. Increase of deposition temperature leads to growth of rough relief (agglomerations of protrusions). DLC relief modification by ion bombardment depends on chemical type of ions. There are peculiarities of DLC relief modification by reactive oxygen and inert argon. The peculiarities are related with changing of different components of DLC relief by oxygen and argon. Argon bombardment lowers the height of peaks and partially removes them from DLC surface without noticeable change of protrusions and areas of inside domains. Oxygen etching (physical and chemical) smoothes areas of inside domains, decreases height of protrusions and makes the hollows near peaks deeper.

Keywords: DLC, arc-pulse sputtering, relief, ion bombardment

INTRODUCTION

Hydrogen-free diamond-like carbon coatings (DLC) are very attractive materials for practical applications due to their good practical properties [1,2]. There exist several methods of DLC deposition which allow to vary coating properties such as sp³/sp² ratio, hardness, intrinsic stress, friction coefficient, surface roughness and etc. [1-5]. But the deposition of smooth DLC with high hardness, high sp³/sp² ratio and strong adhesion is not always possible. For example, hard and smooth DLC as a rule are stressed. This fact adversely affect to adhesion [2-4]. If the decrease of intrinsic stress is achieved by diminution of sp³ bounded carbon atoms, the DLC roughness grows [3]. That is why the post deposition treatment of DLC surface is the important part of the technology to improve the DLC tribological properties [5,6]. The main tendency in a now-a-days DLC properties characterization is a comprehensive approach including the examination of post deposition modification (particularly ion bombardment). This comprehensive approach not only serves to extend knowledge about DLC growth mechanism, but gives the useful information for DLC technology also.

The main goal of a present work is to examine the effect of temperature on DLC properties. This examination is straight directed to solve the important technological task. It is well known that difference between thermal expansion coefficients of DLC and substrate can lead to the deterioration of adhesion. That is why it is necessary to choose such average temperature of coating-substrate system at which tensile stress on DLC-substrate interface would be small.

EXPERIMENTAL DETAILS

DLC were deposited by arc-pulse sputtering of graphite [7]. The temperature of deposition was varied by change of graphite sputtering frequency f. The frequency of pulses mainly affects on the temperature of DLC surface. Variation of the average temperature of DLC-substrate system in one deposition cycle was made by use of heat-eliminating and heat-insulating substrates. In first case a substrate was directly connected to a copper holder, in second case - through a ceramic plate. Besides, two samples were received in condition of identical average inflow of heat to DLC by the use of relevant pause during deposition at high frequency. An average temperature of DLC, deposited at f = 5 Hz, does not exceed 120° C. An increase of frequency (f > 10 Hz) elevates temperature up to 200° C. DLC deposition conditions are shown in Table 1.

After deposition DLC were subjected to argon or oxygen bombardment (E = 3 keV). Thickness of a deleted layer was 100 nm.. The etching depths were calculated in accordance to calibrated sputtering rate for each type

Table 1. Conditions of DLC deposition

No	Conditions of DLC deposition		
sample	Substrate	Frequency (f)	
1	heat-eliminating substrate	5 min 20 Hz + 15 min pause (average f = 1 Hz)	
2	heat insulating substrate	5 min 20 Hz + 15 min pause (average f = 1 Hz)	
3	heat-eliminating substrate	5 Hz (uninterrupted deposition)	
4	heat insulating substrate	5 Hz (uninterrupted deposition)	

of ion.

DLC microhardness was calculated by extrapolation of microhardness vs pyramid depth dependence [8]. Study of DLC surface relief was carried out by means of atomic-force microscope "Nanopics" and laser microscope VK-8500 "Keyence" with the following statistical data processing.

Raman spectroscopy (Ar-ion laser, λ = 514.5 nm) was used to measure sp^3/sp^2 ratio of DLC [9]. Depth of information is ~ 10 nm, beam diameter is about 2 μ . Fifteen measuring points on DLC surface were selected randomly to calculate sp^3/sp^2 average value.

RESULTS

1. Microhardness

Table 2 includes microhardness of DLC deposited at different frequency of graphite target sputtering f. As can see from Table 2, the increase of frequency by a factor of more than order lowers the microhardness.

Table 2. Microhardness of DLC, deposited onto HSS at different frequency of graphite target sputtering

f,	DLC thickness,	H _v , GPa
Hz	μm	GPa
1	~ 1.0	80
1	~ 1.4	100
20	~ 1.0	55
20	~ 1.0	60

2. Raman spectroscopy

 Sp^3/sp^2 ratio of DLC was determined using Raman spectrums (Table 3) [9]. Etching by both oxygen and argon leads to diminution of sp^3/sp^2 within upper layer. The distinction between sp^3/sp^2 for O_2 and Ar can be related with difference between Raman depth of information (RDI) and depths of ion penetration (IDP) (Fig. 1). IDP s were calculated by TRIM (3.5 nm for argon and 5.5 nm for oxygen) [10]. Whereas RDI in 2-3 times exceeds IDR, actually diminution of sp^3/sp^2 on length path of ions in a film is greater.

Table 3. Results of Raman spectroscopy study

Sample	I_D / I_G	$\mathrm{Sp}^3/\mathrm{sp}^2$
As deposited DLC	0.26	(70-80)%
After Ar etching	0.37	(60-70)%
After O ₂ etching	0.44	(50-60)%

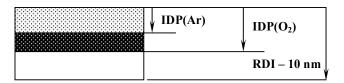


Figure 1. Magnitude comparison of depths of ion penetration (IDR) and Raman information (RDI).

3. Study of DLC relief

As deposited DLC has domain-like structure with ranges of peaks along boundaries. Separate protrusions are observed on DLC surface (Fig. 2). Their height is comparable to a coating thickness. High surface temperature during DLC growth facilitates the forming of rough relief (Fig. 3a). The increase of average temperature of DLC-substrate system by diminution of heat outflow from a substrate promotes appearance of considerable quantity of protrusions (Fig. 3b). Deposition at low frequency is not accompanied by roughening of relief (Fig. 3c). Increase of average temperature during deposition at low frequency by means of heat-insulating substrate does not lead to visible changes of relief (Fig. 3d).

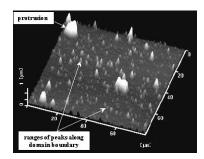


Figure 2. AFM image of DLC

There are peculiarities of DLC relief modification by reactive oxygen and inert argon. The peculiarities are related with changing of different components of DLC surface relief: inside domain, peak ranges and protrusions (Figs. 2, 4a, 5a). Oxygen bombardment smoothes areas of inside domain, lowers height of protrusions and etches the hollows located near peaks (Figs. 5b, 6b). Argon bombardment decreases the height of peaks and partially deletes them from a surface without noticeable change of protrusions and areas of inside domain (Fig. 5c)

DISCUSSION

Generation of DLC surface relief strongly depends on an intensity of diffusion process taking place on the growing film surface. Defect areas are inevitably created on film during deposition. These defect areas are the preferable places for more fast growth of the coating. First of all, such areas are formed when large graphite particles from unfiltered carbon beam fall to the growing surface. Particle impacts lead to a local overheat and creation of the low mobility sp² fragments [11]. The protrusions start to grow on these fragments. Secondary, accumulation of intrinsic stress with growth of film thickness stimulates the generating of peaks also. The pyramidal islands start to grow when certain critical coating thickness is exceeded [12]. The growth of intrinsic stress leads to formation of domain-like structure with ranges of peaks along boundaries. More rapid growth of defect areas is accompanied by outflow of nearest carbon atoms. One can see on area roughness profile of asdeposited DLC (Fig.6a), that there are deep hollows near locations of peaks. This fact is an evidence of peaks building by outflow of carbon atoms from nearest areas. The diffusion growth mechanism of relief takes place. Intensification of diffusion process by increase of surface temperature during DLC deposition reinforces the carbon atoms migration all along growing structure and consequently leads to roughening of DLC. Oxygen lowers the height of peaks and etches nearest areas. Above all, chemical etching by oxygen occurs on areas with weak bounded carbon atoms. That is why reasonably to make an assumption that the defect areas are the preferable places for growth of sp² clusters. Decrease of DLC microhardness in consequence of generation of rough relief at high frequency confirms this assumption.

RESUME

The increase of deposition temperature leads to the growth of rough relief. That is why, the decrease of graphite sputtering frequency (i.e. temperature) is one of the possible ways for deposition of smooth and hard DLC by nonfiltered carbon beam. Etching of DLC by oxygen mainly takes place owing to a chemical interaction. This process is accompanied by more rapid removal of sp² fragments. Long time of oxygen etching can drastically change the practical useful properties of DLC in consequence of increase of roughness and decrease of sp³/sp² in upper layer (about 6 nm). Bombardment by argon is more preferable for DLC smoothening. Grafitization of upper layer of DLC by ion bombardment can improve tribological properties owing to the decrease of friction coefficient.

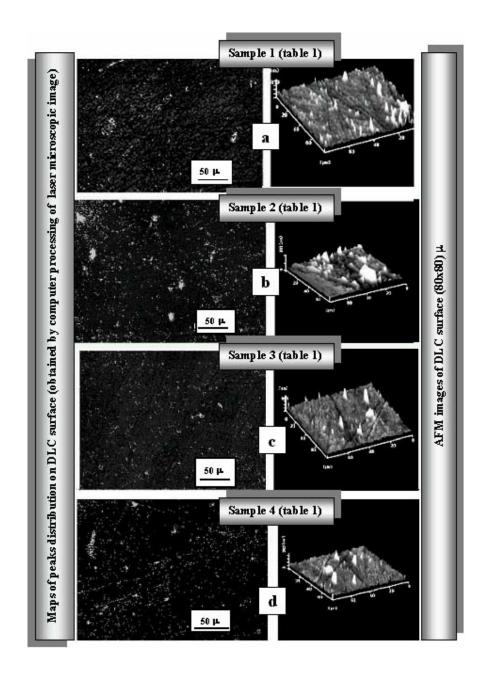


Figure 3. Maps of peaks distribution on DLC (left column) and AFM images (right column) of DLC deposited at different temperature.

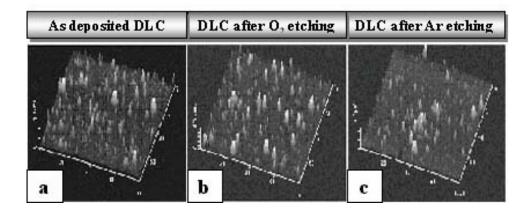


Figure 4. AFM images of as deposited DLC (a) and after oxygen (b) and argon (c) bombardment.

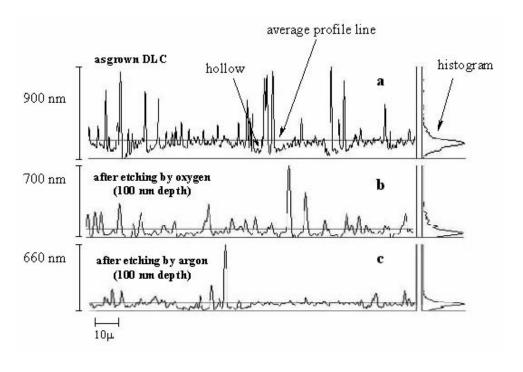


Figure 5. Area roughness profile of as deposited DLC (a), DLC after etching by oxygen (b) and argon (c)

REFERENCES

- Aksenov I.I., Strel'nitsky V.E. Synthesis of hydrogen-free diamond-like coatings. ISFTE-12, Kharkov, Ukraine, 2001, 96 – 103.
- 2. Sanders D.M., Anders A. Rewiew of cathodic arc deposition technology at the start of the new millenium. Surface and Coating Technology 133-134 (2000) 78-90
- 3. Lifshits Y. Diamond-like carbon present status. Diamond and related materials 8 (1999) 1659-1676
- 4. Chen Z.Y., Zhao J.P., at al. Influence of ion energy on the surface morpfology of tetraherral amorphous carbon films. Journal of Materials Science Letters 17 (1998) 335-337
- 5. Vladimirov A.B., Trakhtenberg I.Sh., at al. The effect of substrate and DLC morphology on the coating tribological properties coatings. Diamond and Related Materials 9 (2000) 838-842
- Logothetidis S., Lioutas Ch.B., Gioti M. Post-growth modification of amorphous carbon films under ion beam bombardment: grain size dependence on the film thickness. Diamond and Related Materials 7 (1998) 449-453
- 7. Vladimirov A.B., I.Sh.Trakhtenberg, at al. Modification of amorphous DLC films by low energy ion bombardment. Diamond and Related Materials 5 (1996) 943-946
- 8. Tolmachev Yu.N., at al. Some peculiarities of microhardness testing of thin DLC films deposited on soft substrates. Proceedings of ISDF4, Kharkov, Ukraina, 1999, p.207-208.
- 9. Ferrari F.C. Determination of bonding in diamond-like carbon by Raman spectroscopy. Diamond and Related Materials 11 (2002) 1053-1061
- J.F. Ziegler, J.P.Biersack, U.Littmark. The Stopping and Range of Ions in Solids, Pergamon Press. New York, 1985
- 11. Milani P., at al. Cluster assembling of nanostructured carbon films. Diamond and Related Materials 10 (2000) 240-247
- 12. Dvurechenskii A.V., Zinoviev V.A. at al. Proceeding of 11-th Int. Conf. on Radiation Physics and Chemistry of Cond. Mat., Tomsk, Russia, 2000, p.238-242

APPLICATION OF DLC COATED DIES TO VARIABLE SHAPE EXTRUSION OF ALUMINUM SQUARE PIPES

Naoto OHTAKE, Ko-ichi HORITA, Akira YAMAGATA

Department of Mechanical Engineering and Science, Tokyo Institute of Technology, 2-12-1 O-okayama, Meguro-ku, Tokyo, Japan

Kaoru HARA*

Department of Manufacturing Technologists, Institute of Technologists, 333 Maeya, Gyoda-shi, Saitama, Japan

ABSTRACT

An aluminum space frame is one of the candidates to be applied to a structure of car bodies in near future because of its lightweight as well as high strength. To omit the secondary forming process in the production of an aluminum space frame, a variable shape extrusion apparatus with either a taper mandrel or a step mandrel and four movable dies was developed, and experiments to investigate the characteristics of hot extrusion were conducted by using the apparatus. Results from the experiments suggest that the step mandrel provides good dimensional accuracy due to its bearings parallel to the extruding direction. On the other hand, it was also found that pick-up occurred easily on the surface of extrusion when the step mandrel was used. Dies were coated with diamond-like carbon (DLC) around their bearings to prevent the dies from sticking of aluminum, and it was confirmed that the DLC coating has a significant effect to improve the conditions of the surface of extruded pipes.

Keywords: Extrusion, Aluminum, Variable shape, Square pipe, DLC coating

INTRODUCTION

Recently, the automobile industry has faced strong requests to give consideration to environmental issues, such as global warming and energy consumption issues. In order to solve these issues, weight reduction of body parts, which contribute to 20% through 25% of the car weight, is considered to be essential (refs. 1 to 2). The aluminum space frame technique has been developed as a method of the weight reduction for car bodies. However, it is necessary to carry out the extensive secondary forming process for aluminum square pipes with a uniform cross section at the body assembly. To omit the secondary processing, the variable shape extrusion has been proposed.

The authors have developed the variable shape extrusion apparatus that enables the extrusion of a square pipe with continuously varying inner and outer diameters. We conducted experiments using plasticine and lead billets. From the experiments, we found that the extrusion apparatus was able to form square pipes in variable shapes. Results from the experiments also showed that the inner and outer diameters of the extruded square pipes became smaller than the setting values.

Following a series of previous studies, we conducted experiments on hot extrusion of aluminum square pipes at 673K in temperature with the variable shape extrusion apparatus in this study. We investigated the effect of the shape of the mandrel or die on dimensional accuracy of extruded pipes. Furthermore, the DCL coating was applied to the periphery of the die bearings so that the surface quality of extruded pipes could be improved.

EXPERIMENTAL

The way to vary the dimension of a square pipe

Figure 1 illustrates the developed process to vary the shape of a square pipe. A square pipe is formed from the material extruded between movable dies and the mandrel. Products with variable outer diameters are obtained by sliding four movable dies to the adjacent dies. The inner diameter of a product can be varied by moving the mandrel along the extrusion direction. Also, the inner and outer diameters of a square pipes can be set independently by operating the movable dies and moving the mandrel along the extrusion direction.

Variable shape extrusion apparatus

The variable shape extrusion apparatus is schematically shown in Fig.2. Six heaters (300W a heater) are located

*Corresponding author: e-mail: hara@iot.ac.jp

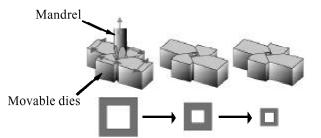


Fig.1 The developed process to vary outer and inner shape of a square pipe

Table 1 Extrusion condition

Billet material	A1050
Temperature of billet	673K
Ram speed	0.3 - 3mm/min
Lubrication	None
Inner diameter	4 - 8mm
Outer diameter	10 - 14mm
Extrusion ratio	2.6 - 6.5

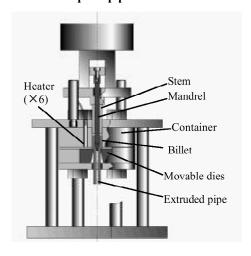


Fig.2. Schematic drawing of the variable shape extrusion apparatus

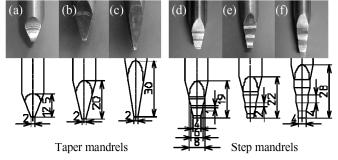


Fig.3 Tip shapes of mandrels used

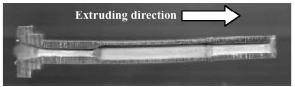


Fig.4 Overview of extruded pipe

around the billet. In addition, in order to keep the entire apparatus at a uniform temperature, the whole apparatus is covered with a heat insulating material. The tip shapes of mandrels used are shown in Fig.3. Taper mandrels (a) through (c) have tips processed into tapered straight shapes (tip inclination angles: about 10, 15 and 20°). Step mandrels (d) through (f) have tips processed into tapered step shapes (bearing (step) lengths: 1, 2 and 4 mm). Products obtained in the experiments were cut in half lengthwise and their inner and outer diameters were measured directly at intervals of 2.5 mm from the top. An aluminum square pipe (billet: A1050) formed with the extrusion apparatus is shown in Fig. 4 as an example.

In the experiments, three types of tapered mandrels and three types of step mandrels were used. Hot extrusion at 673K was carried out with square pipes of various inner and outer diameters and the effect of differences in mandrel tip shapes on dimensional accuracy of the extrusions was investigated. Its extrusion condition is listed in Table 1. In addition, the DLC coating was applied to the die surface by the RF plasma CVD method to prevent sticking and improve the surface quality of extrusions.

RESULTS AND DISCUSSION

Influence of differences in mandrel tip shapes

Figure 5 shows a result from the comparison of inner and outer diameters of the extruded square pipes. The square pipes were formed with a step mandrel containing a bearing of 2 mm in length and tapered mandrels of 10° and 20°. The outer diameter setting was kept constant at 12 mm and the inner diameter setting was varied sequentially from 6, 8 to 4 mm. In addition, the bearing length of the die was set constant to 2 mm. This figure shows that the outer and inner diameters of the products were reduced compared with the setting values. The smallest dimensional error for the outer and inner diameters was observed when a step mandrel with a bearing, parallel to the extrusion direction, was used. Also, the dimensional errors tended to be larger as the tip inclination angle of a taper mandrel increased. The inner diameter decreased remarkably due to longitudinal dents measuring about 0.1 through

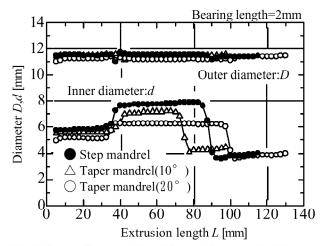


Table 2 Dimensional accuracy of extruded square pipe

(Die bearing length:2mm)		D	d		
		12mm	6mm	8mm	4mm
10°taper mandrel	D_m , d_m	4.2	6.15	10.5	6.92
	$\sigma_{\rm D}$, $s_{\rm d}$	0.01	0.01	0.05	0.02
20°taper mandrel	D_m , d_m	6	14	21.9	4.53
	$\sigma_{\rm D}$, $s_{\rm d}$	0.02	0.03	0.02	0.1
Step mandrel (Bearing length:2mm)	D_m , d_m	4.1	2.69	2.6	5.29
	σ _D , s _d	0.02	0.04	0.07	0.11

Fig.5 Outer diameter:D and inner diameter:d of the pipes extruded by using three kinds of mandrels

0.8 mm deep in the center section on the side of the products. The width and depth of the dents increased along with an increase in the inclination angle and a decrease in product thickness. In every mandrel, a product dimension was remarkably disordered when its dimension setting was changed. However, the disorder is expected to be improved when the setting value is gradually changed during extrusion since it is caused by temporarily interrupted extrusion that occurs with changes in the setting.

In order to understand quantitatively the effect of the extrusion conditions on the accuracy of a product, the dimensional accuracy of the product was evaluated by using the standard deviation (σ_D, σ_d) and the relative average of dimensional error (the ratio of the average error to the setting value) defined by the following equation.

$$(D_{\scriptscriptstyle m},d_{\scriptscriptstyle m}) = \frac{\sum \left| \left(D^*,d^*\right) - \left(D,d^*\right) \right|}{N} \cdot \frac{1}{\left(D^*,d^*\right)} \cdot 100 \left[\%\right]$$

here, D_m , d_m : the relative average of the dimensional error of D and d,

 D^*, d^* : setting values of D and d,

D, d: actual values of outer and inner diameters,

N: number of data.

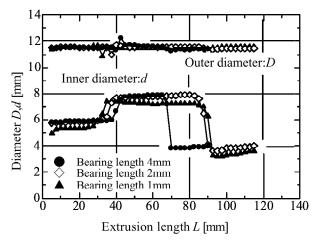
The measured values for computation were chosen from the region where the state of extrusion was fully stable. Table 2 summarizes results from the experiments shown in Fig. 5. The dimensional error was the least with a step mandrel. These results show that the standard deviation is small enough for every mandrel, and extruded square pipes with a sufficiently small error can be obtained when stable and steady extrusion is performed.

Influence of bearing length

Dimensional accuracy for step mandrels with varied bearing lengths was investigated next. The dimensional accuracy of extrusion was measured for three types of step mandrels with different bearing lengths. The result is shown in Fig. 6. The length of the die bearing was set identically to that of the step mandrel employed. This figure shows that the dimensional accuracy tended to improve as the bearing length increases and the dimensional error of the 1mm step mandrel was comparable to that of a 15° taper mandrel. On the other hand, in step mandrels with bearing lengths of 2 mm and 4 mm, when the extrusion ratio was large, sticking of aluminum was observed on the bearing surface of the die. Pick-up, which was regarded as the result of sticking, occurred on the surface of extruded square pipes in these cases. Little difference was observed in the dimensional accuracy for 2-mm-long and 4-mm-long bearings. Taking it into consideration, it is supposed that 2 mm or about 3 mm bearing length is suitable, as is generally claimed in the case of extrusion of aluminum alloys (ref.3).

The difference of metal flow between a taper mandrel and a step mandrel

The die bearing was observed immediately after extrusion to examine the contact state of the billet and a die during extrusion. Figure 7 shows the pictures of the die bearing immediately after extrusion. The bearings of the die and the step mandrel in (a) were 4 mm long respectively, and the die bearing in (b) was 2 mm long. As seen in the



Bearing

(Bearing length: 4mm)

(a) Step mandrel

(Bearing length: 2mm)

Fig. 7 Observation of the surface of a die after extrusion

Fig.6 Influence of bearing length on outer diameter:D and inner diameter:d

pictures, the metal sticks to the whole surface of the bearing of the step mandrel. This indirectly proves that the direction of metal flow was corrected in the bearing section of a mandrel. On the other hand, little sticking of the metal was observed in the case of the taper mandrel. This result indicates that the billet is extruded with very slight or no contact with a die bearing when a taper mandrel is used, as the metal flows along the taper surface of the mandrel. This may explains why the outer and inner dimensions become smaller than the setting value with a taper mandrel.

Metal flow around the dies was analyzed with the finite element method to explain the generation of the shrinkage and the dents on the side of a product. "SUNDY BASIC", high-viscosity fluid three-dimensional-analysis software by PLAMEDIA Corp., was used for analysis and the material was approximated as a high-viscosity Newtonian fluid. Although variable shape extrusion, in which cross-sectional configuration varies continuously, is an unsteady phenomenon, the measurement results of the products showed that metal flow around the dies is

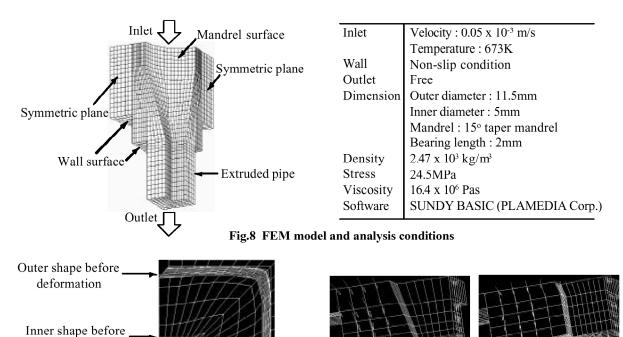


Fig.9 Deformation of extruded pipe by computation

deformation

Fig.10 Comparison of metal flow between a taper mandrel and a step mandrel

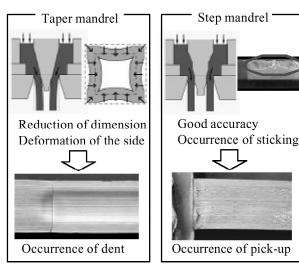


Fig.11 Problems to be caused by metal flow

Table 3 Deposition condition of DLC film

Process gas	CH_{4}
Substrate biasing voltage	- 450V
RF-sputtering frequency	13.56MHz
Deposition time	10min.
CH ₄ gas flow	10sccm
Substrate temperature	Room temperature

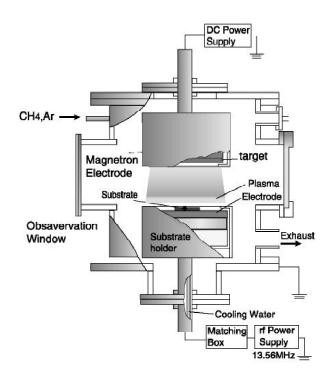


Fig.12 Schematic drawing of the RF plasma CVD apparatus

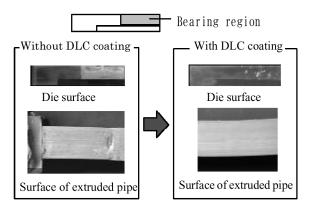
steady under constant extrusion conditions. Therefore, in this study, a steady analysis was conducted with the assumption of a sufficiently stable state in which the material is supplied at a constant rate into the container.

Figure 8 shows a FEM model and analysis conditions. A square pipe was extruded with a taper mandrel, a flow guide, and movable dies from a tubular container. The 1/4 analytic model was used in consideration of the axial-symmetry of a square pipe. Inlet velocity to a fluid range was set as the ram speed. The slip condition was set only on the bearing section of a die from the experimental results, and the non-slip condition was set on the other solid wall. Figure 9 shows the cross-sectional configuration of the product obtained by computation. Results from the computation, which showed that a dent occurred on the side and the inner and outer diameters shrunk from the setting value, coincide with ones from the extrusion experiments. Figure 10 shows a comparison of metal flows in the bearing section between a taper mandrel and a step mandrel. While the metal flow in a taper mandrel directs inward along the inclined surface of a mandrel, the flow in a step mandrel is corrected along the extrusion direction by the bearing of a mandrel.

Problems caused by metal flows with taper mandrels and step mandrels were summarized in Fig.11. In case of the taper mandrels, since a metal flow along the inclined surface of the mandrel tip remained after a die passage, the inner and outer diameters shrunk remarkably from the setting value. Since extrusion was carried out maintaining the cross-sectional area in a die, the center of the side with low stiffness was curved inward, thus forming a longitudinal dent there. Therefore, it can be effective to make the inclination angle at a tip small in order to reduce forming defects as well as to improve accuracy in variable shape extrusion with a taper mandrel. In case of the step mandrels, since the step part at the tip functioned as a bearing in the step mandrel and the metal flow direction was corrected, the dimensional accuracy exceeded that of the taper mandrels. On the other hand, when extrusion ratio was large, sticking of aluminum occurred easily on the bearing surface of the die.

DLC coating of dies

For reducing the friction coefficient to prevent the pick-up, it was presumed effective to coat the die surface (refs. 4 to 5). Accordingly, a DLC film was deposited by the RF plasma CVD method on the top surface and bearing surface of a die with a bearing of 4 mm in length. Extrusion experiments were carried out to investigate the effect of the coating in this case. The RF plasma CVD apparatus used for the DLC coating of dies is shown in Fig.12. As for



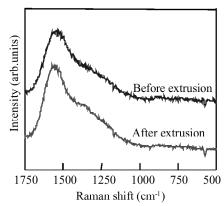


Fig.13 Effect of DLC coating on surface conditions of extruded pipes

Fig.14 Raman spectra of DLC film

the coating, first the surface of a die put on the lower electrode was cleaned by Ar sputtering, and then Si was sputtered as the middle layer by the magnetron electrode. Finally, the DLC film was deposited over the middle layer. Its deposition condition is shown in Table 3. All of the processes were carried out continuously under a vacuum state.

Figure 13 shows the comparisons of the bearing surface of the die and the surfaces of extruded pipes in terms of their surface qualities as well as the comparisons before and after coating. The result demonstrates that the surface quality of an extruded pipe has been improved remarkably as a result of reduced sticking of aluminum to the die bearing. The direct effect of the DLC coating accounts for this result. Furthermore, to investigate the structural change of the DLC film before and after extrusion, the Raman spectra analysis of the DLC films before and after extrusion are shown in Fig. 14. In spite of hot-extrusion of 673K, the quality of DLC film was maintained. These results lead us to the conclusion that DLC coating has outstanding effect for reducing the sticking of aluminum alloy on the steel dies in hot-extrusion process. DLC coating contributes to realize the variable shape extrusion with high surface quality.

CONCLUSIONS

Variable shape extrusion of aluminum alloy was performed. Dimensional accuracy and surface quality were investigated. The results obtained are as follows:

- 1. Step mandrels improve dimensional accuracy
- 2. Reduction of aluminum sticking to the die bearing is essential to improve surface quality of extrusions.
- 3. Employing a DLC coated die in variable shape extrusion (hot extrusion at 673K) of aluminum reduces aluminum sticking and improves surface quality of extruded square pipes.

ACKNOWLEDGMENTS

The authors would like to thank Dr. Toshiyuki Yasuhara and Mr. Yu-ichi AOKI of Tokyo Institute of Technology for their valuable assistance and support. The authors also thank Mr.Kenji Ebara and Mr.ShinichiroTanifuji of PLAMEDIA CORPORATION for their close support.

REFERENCES

- 1. Daniel Carle and Golden Blount: The suitability of aluminum as an alternative material for car bodies, Materials & Design, 20(1999), 267-272.
- 2. Masaaki SAITO, Shuuichiro Iwatsuki, et al.: Development of aluminum body for the most fuel efficient vehicle, JSAE Review, Vol.21, Issue 4, Oct. 2000, 121-127.
- 3. JSTP(editing): Extrusion-from fundamentals to up-to-date techniques-, CORONA PUBLISHING CO. LTD., Tokyo, JPN., 1998,90-91.
- 4. Syojiro MIYAKE: Tribology and applications of DLC and cBN films, Journal of JSPE, Vol.66, No.4, Apr. 2000, 539-543.
- 5. Osamu IMAI: Characteristics and application of DLC film, NEW DIAMOND, Vol.16, No.1, Jan. 2000, 9-15.

THE CHARACTERISTICS OF PHOTO-CVD SiO₂ AND ITS APPLICATION IN GaN MIS PHOTODETECTOR

Bohr-Ran Huang, Tien-Kun Lin

Institute of Electronics and Information Engineering, National Yun-lin University of Science and Technology, 123, University Road, Section 3, Touliu, Yunlin, 640 Taiwan, R.O.C.

Yan-Kuin Su, Shoou-Jinn Chang, Yu-Zung Chiou

Institute of Microelectronics and Department of Electrical Engineering, National Cheng Kung University, No1.Ta-Hsueh Road, Tainan City, 701, Taiwan, R.O.C.

ABSTRACT

SiO₂ insulating layers were deposited onto GaN by photo chemical vapor deposition (photo-CVD) technique using deuterium (D₂) lamp as the excitation source. Physical, chemical and electrical characteristics of the Al/SiO₂/GaN metal-insulator-semiconductor (MIS) capacitors were investigated. Furthermore, the SiO₂/GaN interface trap density, D_{lt}, was estimated to be $8.4 \times 10^{11} \text{ cm}^{-2} \text{ eV}^{-1}$ for the photo-CVD SiO₂ layers prepared at 300°C from high frequency capacitance method. With an applied field of 4 MV/cm, the oxide leakage current density was found to be only $6.6 \times 10^{-7} \text{A/cm}^2$. Finally the GaN MIS photodetector was fabricated by using photo-SiO₂ as insulating layer. The peak responsivity of GaN MIS photodetectors was about 0.12 A/W at 3V bias. At low frequency, the noise exhibits the $1/f^{2.5}$ type noise. For our $200 \times 200 \,\mu\text{m}^2$ device, at bandwidth of 500 Hz, the corresponding noise equivalent power density (NEP) and normalized detectivity (D*) are calculated to be $2.19 \times 10^{9} \,\text{W}$ and $2.03 \times 10^{8} \,\text{cmHz}^{0.5} \,\text{W}^{-1}$, respectively.

KEYWORDS: GaN, photo-CVD, SiO₂, metal-insulator-semiconductor, photodetector.

INTRODUCTION

The excellent physical and electrical properties of GaN have made it a good candidate in high-temperature, high-power and high frequency applications [1]. High quality III-V ternaries such as Al_xGa_{1-x}N and In_yGa_{1-x}N [2] were also demonstrated for heterojunction field effect transistors (HFETs), heterojunction bipolar transistors (HBTs) and light-emitting diodes (LEDs) β]-[4]. Nitride-based blue and green LEDs [5]-[6] are already commercially available. Recently, many researches were focused on the fabrication of GaN-based metal-insulator-semiconductor (MIS) capacitors with SiO2 as the insulating material. It has been reported that SiO₂ layers can be deposited onto GaN by remote plasma-enhanced chemical vapor deposition, low-pressure chemical vapor deposition and liquid phase deposition [7]. Recently, it has been shown that photo chemical vapor deposition (photo-CVD) can also be used to grow high quality SiO₂ layers [8]-[11] on various semiconductor substrates. In using photo-CVD to grow thin films, selecting proper light source with a radiation spectrum matching the absorption spectra of the reactance gases is very important. In this study, we used a deuterium (D₂) lamp as the excitation source. It is known that D₂ lamp emits strong ultra violet (UV) and vacuum ultra violet (VUV), which can effectively decompose SiH₄ and O₂, since O₂ could absorb photons in the wavelength region from 133 nm to 175 nm and SiH₄ could absorb photons in the wavelength region below 147 nm [8]-[12]. Thus, energy can be directly transferred from D₂ lamp to excited SiH₄ and O₂. In addition, such a photo-CVD system offers better control in the oxide region and selective growth is possible. It has been reported that the quality of oxide layers grown by such a photo-CVD system is close to that grown by thermal oxidation and the electrical properties of the photo-CVD grown oxide are acceptable for device applications [8]-[11].

In additional, the increasing demand for low cost and low noise ultraviolet (UV) photodetectors has led to the development of wide-bandgap semiconductor photodetectors. It is well known that part of noise contribution in GaN MSM photodetectors is related to the dark current (shot noise), mostly due to the enhanced tunnel transport at dislocation. Another noise component is related to the carriers trapping by surface state density and dislocations in planar device such as MSM photodetectors. To achieve low noise GaN photodetectors, efforts have been made to reduce the density of dislocation by epitaxial lateral overgrown (ELOG) GaN and passivate the surface state density. In this paper, we realized the deposition of SiO₂ layers to passivate the GaN surface and suppress the dark current. Furthermore, the characterized Al/SiO₂/GaN MIS capacitors and ITO/SiO₂/GaN MIS photodetectors using photo-SiO₂ films as insulator were also discussed.

NASA/CP—2003-212319 484 August 18, 2003

EXPERIMENTS

Prior to the deposition of SiO₂ layers, an n-type GaN epitaxial layer was grown on (0001) sapphire substrates by metal-organic chemical vapor deposition (MOCVD). The electron concentration of the n-type GaN epitaxial layer was about 5×10¹⁷ cm⁻³. The 50 nmthick SiO₂ films were subsequently deposited onto the GaN epitaxial layer by 150 Watt D₂ lamp under different process pressures and different substrate temperatures. The gas ratio was fixed at SiH₄/O₂=0.055 [8]-[11]. Atomic force microscopy (AFM) and X-ray photoelectron spectrum (XPS) were then used to characterize the surface and chemical properties of deposited SiO₂ films. Al/SiO₂/GaN MIS capacitors were subsequently prepared by etching and metal evaporation. Finally the ITO/10 nm photo-SiO₂/GaN MIS photodetector was fabricated by sputtered ITO films onto photo-SiO₂/GaN. The active region of MIS photodetectors was 200×200 μm², with 10 μm width and space of finger electrode. The capacitance-voltage (C-V) and current-voltage (I-V) characteristics of these fabricated MIS capacitors were then measured by an HP 4284B LCR meter and an HP 4155B semiconductor parameter analyzer, respectively. During photo current measurement, a 150 Watt deuterium lamp illuminated from the front side of the photodetectors was used as the UV light source (wavelength from 120 nm to 300 nm). A 1 kW xenon arc lamp was used as the light source for spectral responsivity measurements, and a standard synchronous detection scheme was employed to measure the front-side illuminated detector signal. At low frequency measurement, the ac signal of the device was coupled to an EG&G PARC 113 preamplifier. Then an HP3562A spectrum analyzer is used to display the output of EG&G preamplifier.

RESULTS AND DISCUSSION

A. The Characteristics of Photo CVD SiO₂ Layer

Figure 1 shows the growth rate of SiO_2 as a function of process pressure for the photo-CVD SiO_2 layers grown at different substrate temperatures.

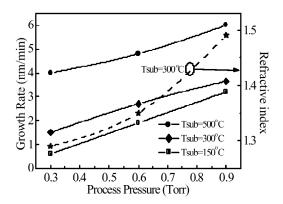


Fig 1. The growth rate of SiO₂. The refractive index of the SiO₂ layer grown at 300°C was also shown.

It was found that the SiO₂ growth rate increases as the substrate temperature increases. The growth rate of SiO₂ increases linearly as the process pressure increases. Such a linear increase suggests that the limiting factor for the growth rate is the amount of SiH₄ and O₂ molecules available to provide excited Si and O atoms. At higher process pressure, the number of excited Si and O atoms will increase so as to result in a higher SiO₂ growth rate. The refractive index of the photo-CVD SiO₂ layer grown at 300°C and prepared at different process pressure was also shown in Fig. 1. The refractive index also increases as the process pressure increases. Such an observation is probably due to the fact that the SiO₂ layer prepared at high process pressure is more condense again due to the increased number of excited Si and O atoms. It should be noted that the refractive index of the 300°C photo-CVD grown SiO₂ layer prepared at 0.9 Torr is very close to that of the thermally grown SiO₂ layer prepared on the top of Si substrates. Figures 2(a) and 2(b) show the AFM pictures of bare GaN without SiO₂ and photo-CVD SiO₂ grown at 300°C, respectively. It was found that the root mean square roughness was 0.251 nm and 0.304 nm for bare GaN without SiO₂ and photo-CVD SiO₂ grown at 300°C on GaN, respectively. Such a smooth surface of the photo-CVD SiO₂ film provides a uniform electrical field in the capacitor.

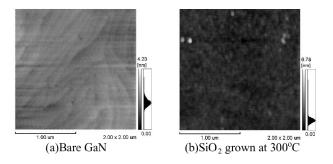


Fig 2. AFM images of SiO₂ films prepared by photo-CVD

A detail study of chemical nature of the photo-CVD SiO_2 film was characterized by XPS (X-ray Photoelectron Spectrum). As shown in Fig. 3, the blind energy for XPS Si_{2p} and O_{1s} are 103.4 eV and 532.9 eV, respectively. According to the XPS handbook, it can be found that the silicon and oxygen chemical bounding energy are the same as that of observed in thermal SiO_2 on Silicon.

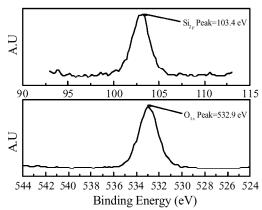


Fig 3. The XPS spectrum of Si_{2p} and O_{1s} for photo-CVD SiO₂ on GaN

The C-V characteristics of the photo-CVD SiO_2 grown at different temperatures were shown in Fig. 4. The ideal simulated C-V curve was also plotted in the same figure.

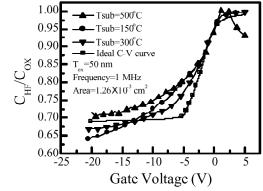


Fig 4. High frequency C-V characteristics of Al/SiO₂/GaN MIS capacitors at different substrate temperature.

No significant hysteretic curve was observed as the gate voltage varied from +5 to -20V and then backs to +5V for all three samples even at an elevated temperature of 70° C. The lack of hysteresis in these C-V curves indicated that the number of mobile ions in SiO₂ layer is negligibly small. The interface state density, D_{it}, of these MIS capacitors can also be determined from these curves by high frequency capacitance method [12]. It was found that the D_{it} are estimated to be 1.2×10^{12} cm⁻²eV⁻¹ and 8.4×10^{11} cm⁻²eV⁻¹ for photo-CVD SiO₂ layers on

GaN prepared at 150° C and 300° C, respectively. The smaller D_{t} for the photo-CVD SiO₂ layer deposited at 300° C could be attributed to the fact that a higher substrate temperature can significantly improve the SiO₂/GaN interfacial properties probably through supplying thermal energy to the Si and O atoms. Compare to Ga_2O_3 on GaN reported by Fu et al.[13], the D_{it} of our photo-CVD SiO₂ prepared at 300° C on GaN was one order smaller. The D_{it} observed from our photo-CVD SiO₂ /n-GaN interface was also comparable to those observed from PECVD SiO₂ /n-GaN interfaces reported by Arulkumaran et al. [14] However, D_{it} was increased to 6.4×10^{12} cm⁻²eV⁻¹ when the substrate temperature was increased to 500° C. The exact reason for the increase in D_{it} is not clear yet. Possible reasons for such degradation in oxide quality include faster oxide growth rate and/or some interface reactions, which occur at high temperatures. Figure 5 shows the LV characteristics of the three fabricated Al/SiO₂/GaN MIS capacitors. All capacitors were biased in the accumulation region. It was found that photo-CVD SiO₂ deposited at 300° C exhibits the smallest leakage current among the three samples. Such a result also agrees well with the C-V data shown in Fig. 4. With an applied field of 4 MV/cm, the leakage current was only 6.6×10^{-7} A/cm² for the photo-CVD SiO₂ layer deposited at 300° C, as shown in Fig. 5.

B. The Responsivity and Noise Characteristics of GaN MIS Photodetectors

Finally the ITO/10-nm photo-SiO₂/GaN MIS photodetectors was fabricated and characterized. As shown in Fig. 6, it can be found that the photo-SiO₂ film is a good candidate to suppress the dark current in the application of photodetectors.

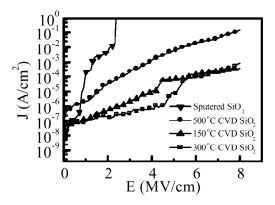


Fig 5. The I-V characteristics of the Al/SiO2/GaN MIS capacitors.

Furthermore, the GaN MIS photodetectors has a seven orders improvement in dark current and the photo current/dark current ratio was about 1.51×10^3 at 4 V bias for ITO/10 nm photo-SiO₂/GaN MIS photodetectors. We believe that we could adjust the thickness of SiO₂ films to optimize the photo current/dark current ratio in the future works. As shown in Figure. 6, the spectral responsivity decreased rapidly from 0.11 A/W at 338 nm to 4.9×10^{-4} A/W at 400 nm with a 3 V bias. Such a rapid decrease in spectral responsivity across the cutoff region again suggests that the quality of our samples is reasonably good. However, high fluctuation was observed below the cutoff wavelength, it is related to the impurity, defect and doping level in such a high band gap material.

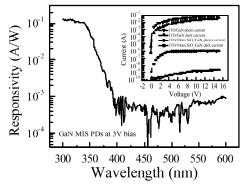


Fig 6. The responsivity spectrum of GaN MIS photodetectors (The I-V curve is shown in the insert)

The noise characteristics of GaN MIS photodiodes was measured in the frequency range of 10 Hz~100 kHz using a low noise current preamplifier and a fast Fourier transform (FFT) spectrum analyzer. The bias was varied from 16.515 V to 18.571 V and sample temperature was kept at room temperature. As shown in Fig. 7, the low-frequency noise in GaN MIS photodiodes is not commonly 1/f-type noise. Also the measured noise spectrum can be expressed by the following relation:

$$S_n(f) = \frac{S_0}{f^{\gamma}} \tag{1}$$

where

 S_n : the spectral density of the noise power,

 S_0 : noise value at 1 Hz;

f: frequency;

?: the fitting parameter;

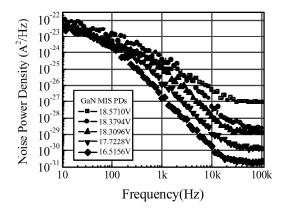


Fig 7. The low-frequency noise spectra at various bias condition with fitting curves.

By using fitting curve, the ? was estimated to be ~2.5. It implies the noise of device at low frequency is not exactly 1/f-type noise. For a bandwidth of B, the total square noise current can be estimated by integrating the $S_n(f)$ over the frequency range from zero to bandwidth B.

$$\langle i_n \rangle^2 = \int_0^B S_n(f) df$$

$$= \int_0^1 S_n(1) df + \int_1^B S_n(f) df = S_0 + \int_1^B S_0 / f^{2.5} df$$
(2)

where the $S_n(f)$ in the bandwidth range from 0 to 1 was assumed to be the same and equals to $S_n(f)$ at 1 Hz. The noise equivalent power (NEP) is given by

$$NEP = \frac{\sqrt{\langle i_n \rangle^2}}{R} \tag{3}$$

Where R is the responsivity of photodiodes. And the normalized detectivity (D*) is given by

$$D^* = \frac{\sqrt{A}\sqrt{B}}{NEP} \tag{4}$$

where A is the area of photodiode in square centimeters and B is the bandwidth in Hertz.

For our device, with area of $200\times200~\mu\text{m}^2$, given bias of ~16 V, the responsivity was assumed to be 0.12 A/W (for ?=330 nm). The $S_0(f=1,~V=16~V)=4.17\times10^{-20}~A^2/Hz$. For a given bandwidth of 500 Hz, the corresponding noise equivalent power (NEP) and normalized detectivity D* are calculated to be $2.19\times0^{-9}~W$ and $2.03\times10^8~cmHz^{0.5}W^{-1}$. The NEP of our GaN MIS photodetector was slightly less than the NEP of Schottky barrier detectors reported by Q. Chen et al.[15] Such a low NEP indicated that the photo-CVD SiO₂ can effectively passivate the GaN surface and result in a low NEP and high detectivity.

SUMMARY

In summary, high quality SiO_2 insulating layers were successfully deposited onto GaN by photo-CVD technique using deuterium (D_2) lamp as the excitation source. It was found that the limiting factor for the SiO_2 growth rate is the amount of SiH_4 and O_2 molecules available to provide excited Si and O atoms. The interface trap density, D_{it} , was estimated to be 8.4×10^{11} cm⁻²eV⁻¹ for the photo-CVD SiO_2 layers prepared at 300° C. Furthermore, the leakage current was only 6.6×10^{-7} A/cm⁻² with an applied field of 4 MV/cm for the 300° C photo-CVD grown $Al/SiO_2/GaN$ MIS capacitor. Finally the photo-CVD SiO_2 was used as the insulator to suppress dark current and passivate GaN surface in the application of GaN MIS photodetectors. The designed photodetectors exhibit a peak responsivity of 0.12 A/W at 330 nm. For a given bandwidth of 500 Hz, the corresponding noise equivalent power (NEP) and normalized detectivity D* of GaN MIS photodetectors are first reported to be 2.19×10^{-9} W and 2.03×10^{8} cmHz^{0.5}W⁻¹.

ACKNOWLEDGEMENT

This work was supported partially by National Science Council, Taiwan under the grant NSC-91-2623-7-006-006.

REFERENCE

- [1] M. Khan, M. S. Shur, J. N. Kuznia, Q. Chen, J. Burn and W. Schaff, "Temperature activated conductance in GaN/AlGaN heterostructure field effect transistors operating at temperatures up to 300 °C," Appl. Phy. Lett., (1995), pp.1083
- [2] T. Mukai, M. Yamada and S. Nakamura," Characteristics of InGaN-based UV/blue/green/amber /red light-emitting diodes," *Jpn. J. Appl. Phys.*, (1999), pp3976
- [3] T. Mukai, M. Yamada and S. Nakamura," Current and temperature dependences of electroluminescence of InGaN-based UV/blue/green light-emitting-diodes," Jpn. J. Appl. Phys., (1998), pp1358
- [4] S. Nakamura and M. Senoh, "Superbright Green InGaN Single-Quantum-Well-Structure Light-Emitting Diodes," *Jpn. J. Appl. Phys.*, (1995), pp1332
- [5] S. Nakamura, T. Mukai, and M. Senoh," Candela -class high-brightness InGaN/AlGaN double heterostructure blue-light-emitting diodes," *Appl. Phys. Lett.*, (1994), pp1687
- [6] J. K. Sheu, j. M. Tsai, S. C. Shei, W. C. Lai, Y. K. Su, S. J. Chang and G. C. Chi, "Low-operation voltage of InGaN-GaN light-emitting diodes with Si-doped In_{0.3}Ga_{0.7}N/GaN short-period superlattice tunneling contact layer," *IEEE Electron Device Letters*, (2001), pp. 460-462
- [7] H. C. Casey, Jr., G. G. Fountain and R. G. Alley, B. P. Keller and Steven P. DenBaars, "Low interface trap density for remote plasma deposited SiO₂ on n-type GaN," *Appl. Phys. Lett.*, (1996), pp 1850
- [8] C. J. Huang and Y. K. Su, "Effect of substrate temperature on the properties of SiO₂/InP structure prepared by photochemical vapor deposition," *Journal of Applied Physical*, (1990), pp3350
- [9] S. J. Chang, Y. K. Su, F. S. Juang, C. T. Lin, C. D. Chiang and Y. T. Cherng, "Photo-enhanced native oxidation process for Hg_{0.8}Cd_{0.2}Tc photoconductors," *IEEE J. Quantum Electron.*, (2000), pp583.
- [10] C. T. Lin, Y. K. Su, S. J. Chang, H. T. Huang, S. M. Chang and T. P. Sun, "Effects of passivation and extraction surface trap density on the 1/f noise of HgCdTe photoconductive detector," *IEEE Photo. Technol. Lett.*, (1997), pp232.
- [11] C. T. Lin, Y. K. Su, H. T. Huang, S. J. Chang, G. S. Chen, T. P. Sun and J. J. Luo, "Electrical properties of the stacked ZnS/photo-enhanced native oxide passivation for long wavelength HgCdTe photodiodes," *IEEE Photo. Technol. Lett.*, (1996), pp676.
- [12] E. H. Nicollian and J. R. Brews, MOS (Metal Oxide Semiconductor) physics and technology, New Jersey: Artech House, (1982)., chapter 8
- [13] D. J. Fu, Y. H. Kwon, T. W. Kang, C. J. Park, K. H. Baek, H. Y. Cho, D. H. Shin, C. H. Lee, and K. S. Chung, "GaN metal--oxide--semiconductor structures using Ga-oxide dielectrics formed by photoelectrochemical oxidation," *Appl. Phys. Lett.*, (2002), pp446
- [14] S. Arulkumaran, T. Egawa, H. Ishikawa, T. Jimbo, and M. Umeno," Investigations of SiO₂/n-GaN and Si₃N₄/n-GaN insulator-semiconductor interfaces with low interface state density," *Appl. Phys. Lett.*, (1998), pp 809
- [15] Q. Chen, J. W. Yang, A. Osinsky, S. Gangopadhyay, B. Lim, M. Z. Anwar and M. Asif Khan, "Schottky barrier detectors on GaN for visible--blind ultraviolet detection," *Appl. Phys. Lett.*, (1997), pp2277

FABRICATION OF DIAMOND-LIKE CARBON FILM

Wataru Ohashi , Hiroaki Yoshimura, Haruka Matsuhisa, Yusuke Aoki, Akimitsu Hatta

Department of Electronic and Photonic Systems Engineering, Kochi University of Technology 065016z@gs.kochi-tech.ac.jp

Abstract

We are developing an electron emitter device of a polycrystalline diamond film for cathode and a diamond-like carbon film for insulator. The insulation of the DLC films used for the previous devices was not sufficient. The purpose is to improve the insulation of DLC films. A required performance for the device is below 0.15mA/cm2 at more than 50V.

Diamond-Like Carbon films are fabricated by a high frequency plasma CVD method, and the insulation of the films was evaluated. Materials gas of benzene (C6H6) was flowed into a chamber, pressure was 5Pa, HF power was 100W (13.56MHz), and deposition duration was 10 - 60 seconds, the substrates were n-type silicon wafer.

The thickness of DLC films was 50nm - 170nm. A coating of gold electrode is vacuum evaporated over both the DLC film and silicon wafer. The current-voltage characteristic between the electrodes was measured. The shottkey characteristic can be ascertained from the I-V curve. The insulation at low voltage was sufficient, however, the leak current increased up to 2.7mA/cm2 at 40V. It is necessary to improve the insulation at the high voltage.

Electron emission and Raman investigation of hydrogenated diamond like carbon prepared by pulsed laser deposition

Lin Yu, Qihong Wu, Yuan Liao, Qingxuan Yu, Guanzhong Wang, Rongchuan Fang Department of physics, USTC, Hefei, Anhui 230026 P.R.China

ABTRACT

The structure and the electron-field emission behavior of hydrogenated diamond-like carbon prepared by pulsed laser deposition are investigated. The diamond-like carbon films contain a mixture of sp³-bonds and sp²-bonds, possessing a large electron-field-emission current density[J_e =368 μ A/cm² at 14V/ μ m], a low turn-on field [E_0 =6V/ μ m] and a low effective work function[ϕ e=0.0399eV]. The superior electron-field-emission properties of DLC films, as compared with those of diamonds, are ascribed to their nanostructured grains and surface groups such as C-H, which can produce large changes in electron affinity. From Raman spectra, the DLC films possess a diffused D-band resonance peak at 1350cm⁻¹ and a diffused G-band resonance peak near 1580cm⁻¹. Breit-Wigner-Fano and Lorentzian line shape simulations are used to fit the spectra. After the emission, the Raman peak position is shifted due to the presence of nanostructure.

Keywords: electron emission, Raman, diamond like carbon

E-mail: yulin@mail.ustc.edu.cn

Proceedings of the Seventh Applied Diamond Conference/ Third Frontier Carbon Technology Joint Conference (ADC/FCT 2003) M. Murakawa, M. Miyoshi, Y. Koga, L. Schäfer, and Y. Tzeng (Editors)

The effect of annealing on the field emission properties of amorphous CN_x films

J. J. Li ^{1, 2}, Z. S. Jin ^{1 #}, W. T. Zheng ¹, X.Y. Lu ¹

1. National Key Laboratory of Superhard Materials and Department of Materials Science, Jilin University,

Changchun 130021, P. R. China;

2. College of Science and Engineering, Yanbian University, Yanji 133002, P. R. China

Abstract:

The carbon nitride films deposited by r.f magnetron sputtering in pure N2 discharge were annealed in

vacuum up to 900 °C. The chemical composition and bonding structure of the films were studied using X-ray

photoelectron spectroscopy (XPS), Fourier Transformation Infrared (FTIR). The effects of the thermal annealing

on bonding structure and the electron field emission characteristics of CN_x films were investigated. It is found

that the sp² carbon bonds and N content in CN_x films are closely related to field emission of CN_x films. The

results show that thermal annealing treatment cause a great loss of N content and a larger formation of sp²

carbon bonds in CN_x films, which would enhance significantly the field emission properties for the CN_x films.

The CN_x films annealed at temperature of 750 °C show the optimal electron emission properties. In addition, the

correlation between the change in concentration of sp² carbon bonds in the films induced by annealing and

electron emission properties for the CN_x films was discussed.

Keywords: Carbon nitride films; chemical bonding; annealing temperature; electron field emission, magnetron

sputter.

#Corresponding author, Tel: +86-431-5168884

Fax: +86-431-5168884, E-mail address: diamond@jlu.edu.cn or up li@yahoo.com.cn

NASA/CP-2003-212319 492 August 18, 2003 Proceedings of the Seventh Applied Diamond Conference/ Third Frontier Carbon Technology Joint Conference (ADC/FCT 2003) M. Murakawa, M. Miyoshi, Y. Koga, L. Schäfer, and Y. Tzeng (Editors)

Influence of the DC substrate bias on the filed emission of amorphous carbon nitride

films deposited on Silicon tips arrays

J. J. Li a, b, Z. S. Jin , W. T. Zheng, X.Y. Lu

National Key Laboratory of Superhard Materials, Jilin University, Changchun 130021,

P. R. China;

Z.K.Li, Z.Jin, L.Sun

b. College of Science and Engineering, Yanbian University, Yanji 133002, P. R. China

Abstract

Amorphous carbon nitride films were deposited on silicon tip arrays by rf magnetron sputtering in pure

nitrogen atmosphere. Effect of DC substrate negative bias on electron filed emission properties of

as-deposited carbon nitride films was investigated. The field emission property of carbon nitride films on

tips was compared with that on silicon wafer. The result shows carbon nitride films deposited on tips

possess a stable field emission with lower threshold field, which is more excellent than that on wafer. This

result has relation to the change of the local curvature and geometry of the films surface. But DC substrate

bias will reduce the filed emission property of carbon nitride films on silicon tips during deposition, which

can explained that the bias causes a blunter silicon tips due to the damage by high-energy ions

bombardment during increasing substrate bias. On the other hand, the effective work function of the films

is increased with DC substrate bias, which indicates the decrease of electron field emission of the films.

Keywords: Carbon nitride films; substrate bias; electron field emission, magnetron sputter; silicon tips

arrays.

*Corresponding author, Tel: +86-431-5168884

Fax: +86-431-5168884, E-mail adress: diamond@jlu.edu.cn or up li@yahoo.com.cn

Proceedings of the Seventh Applied Diamond Conference/ Third Frontier Carbon Technology Joint Conference (ADC/FCT 2003) M. Murakawa, M. Miyoshi, Y. Koga, L. Schäfer, and Y. Tzeng (Editors)

Investigation of structure and field emission characteristics of diamond-like films

prepared by high power excime laser

H. Y. Peng a,b , Z. S. Jin , J. J. Li, H.Ji

a. National Laboratory of Superhard Materials, Changchun 130021, China

H. Shen, L. X. Zhao, J. J. Shen

b. Institute of Optical-electric Technology of Heilongjiang Province, Mudanjiang 15700, China

Abstract

Diamond-like films have been prepared using high power and high frequency XeCl excime laser under

high vacuum H₂ and N₂ gas environment, respectively. The bonding structure of the films was studied by

Raman spectrum and electron diffraction method. The results show that the films have typical

characteristics of DLC contained nano-diamond grains. The measurement result of field emission show

that the threshold electric filed is reduced with increasing laser power at $10^8 \text{ W/cm}^2 \sim 10^{10} \text{ W/cm}^2$, and 300

HZ. The threshold electric filed is 2 V/ μ m when 10 10 W/cm² laser power is applied in the experiment.

Keywords: bonding structure, filed emission, diamond-like films, high power excime laser.

Corresponding author, Tel: +86-431-5168884

Fax: +86-431-5168884, E-mail address: diamond@jlu.edu.cn

MULTI-SENSOR DURABILITY CHARACTERIZATION OF THIN DIAMOND-LIKE FILMS

Dr. N. V. Gitis, J. Xiao, M. VinogradovCenter for Tribology, Inc., 1715 Dell Ave., Campbell, CA 95008, USA, www.cetr.com

ABSTRACT

A number of durability tests have been performed on the precision micro-tribometer UMT, using various upper tools like hard ceramic balls, pins, blades and diamond stylus, in such testing modes as uni-directional or reciprocating linear and rotational motions. Multiple test parameters were monitored simultaneously, including servo-controlled vertical load, lateral friction force, high-frequency contact acoustic emission, contact or surface electrical resistance, digital video of the testing zone. The multi-sensing technology allowed for repeatable and comprehensive characterization of the durability of both thick (microns) and thin (nanometers) diamond-like films.

Keywords: durability tests, films, multiple sensors.

INTRODUCTION

There are numerous techniques known for durability testing of films and coatings, some of the most common being a tape test, stud-pull test, scratch test and an indentation test. In the tape test, a tape is pulled off the surface containing a scratch, which provides the failure initiation. In the stud pull test, a stud held with thermosetting epoxy is pulled off the film surface. The indentation test, wherein a ball is pressed into the surface, is used for hard coatings, and the failure pattern indicates acceptable behavior. In the scratch test, where an indenter moves in both vertical (loading) and horizontal (sliding) directions, and an acoustic emission sensor allows for detection of the initiation of fracture, while the scratch pattern indicates the type of failure.

The UMT series Micro-Tribometer has been developed to perform all the variety of the common adhesion tests. During any of them, it can simultaneously measure contact or surface electrical resistance, displacement or deformation or depth of penetration, contact acoustic emission, temperature, forces in all three directions and digital video of the contact area. This report covers evaluation of the coating durability by the scratch test.

INSTRUMENTATION

The fully computerized Micro-Tribometer mod. UMT-2M provides a combination of precision linear and rotational motions, including reciprocating and unidirectional, with programmable speeds ranging from 0.5 μ m/s to 50 m/s. A load is applied via a closed-loop servo-mechanism and is programmed to be kept constant or linearly increasing, ranging from 0.1 mN to 1 kN. The environmental temperature and pressure can also be controlled. Friction force (F_x), normal load (F_z), electrical contact resistance (ECR), and contact acoustic emission (AE) are all measured at a total sampling rate of 20 kHz, displayed in real time and recorded for further analysis.

Specimens in a wide variety of shapes (servo-control of normal load allows for its control with user-specified tolerances even on uneven and wavy surfaces) and dimensions (up to 150 mm) can be accommodated. For scratch tests various tool geometries and materials can be used, metal or ceramic balls, needles, cylinders, diamond stylus or patented micro-blade.

NASA/CP—2003-212319 495 August 18, 2003

EXPERIMENTAL

Two types of coatings were tested in this work, several-micron thick carbon coatings used on sheet glass for automotive windows and few-nanometer thin hard diamond-like coatings used on hard magnetic disks and heads. These two types have been chosen as being very different in both hardness and thickness, thus covering a wide spectrum of practical applications.

The effects of scratching tools were studied on three types of tools, 1.6-mm balls from stainless steel and tungsten carbide, 10-micron sharp diamond stylus and a novel tungsten carbide micro-blade, which is as sharp as the stylus (10 micron), but very wide (0.8 mm).

To achieve effective results, the multi-sensor technology was utilized, with the simultaneous F_{z_i} , F_{x_i} ECR and AE measurements.

RESULTS ON THICK COATINGS

Neither steel nor tungsten carbide balls produced useful delamination data. The sharp diamond stylus scratched the coating, but did not delaminate it. The micro-blade produced repeatable both scratch-resistance and delamination/adhesion results.

The micro-blade test consisted of linearly increasing the applied load from 1 cN to 100 cN, while slowly sliding the micro-blade at 1 mm/s, with continuous multi-sensor process monitoring.

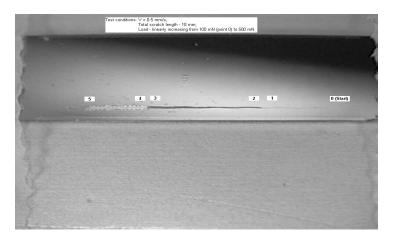


Figure 1. Coating Tested With Micro-Blade

The optical photo of the tested surface is shown in Figure 1 above, the corresponding friction force plot is presented in Figure 2 on the next page. One can clearly see three zones, namely: deformation with no debris formation at very low loads (right part of Fig. 1, left part of Fig. 2), micro-scratching with production of a lot of micro-debris (middle parts of Fig.s 1 and 2), followed by delamination with chunks of debris formed at higher loads (left part of Fig. 1, right part of Fig. 2). The critical loads (or times) of scratching (on the borderline of the deformation and micro-scratching zones) and delamination (on the borderline of the scratching and delamination zones) can be found easily fro these tests, and tend to be repeatable.

Though both the optical and force plots show all the three zones, the borderlines between them, defining the critical loads (times) or micro-scratching and delamination, can be determined with higher accuracy by utilizing additional electrical and acoustic measurements.

If a coating is non-conductive and a substrate is conductive, then electrical contact resistance is measured. If a coating is conductive, the electrical surface resistance is monitored. In either case, the electrical measurements typically show both critical thresholds of the onset of scratching (when electrical

resistance begins to change) and breaking through the coating (when electrical resistance reaches the level of the substrate resistance). An example of a sharp threshold is given in Figure 3.

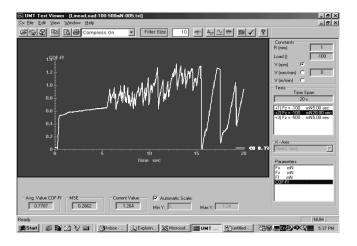


Figure 2. Friction Force in Test With Micro-Blade

The high-frequency contact acoustic emission reflects the scratching and delamination processes of solid coatings when their structure is relatively ordered and they are relatively hard. For instance, most metal and ceramic coatings emit substantial acoustic waves during such tests, while most soft polymers do not emit measurable acoustics. The acoustic emission resolution in terms of surface defects is defined by its frequency. For example, to detect a 10-nm scratch or delamination defect in the coating at a test speed of 1 cm/s (taking into account that 1 cm = 10,000 nm and a signal has to be several times higher than the process), one needs the signal frequency of at least 5 kHz. In fact, we use the range of up to 5 MHz, which allows for detection of the very beginning of the tiniest micro-scratches and micro-delamination.

The effective use of the contact acoustic emission signal is illustrated in Figure 3 below. In this example, the critical threshold of breaking through the coating can be determined by the sharp drop in

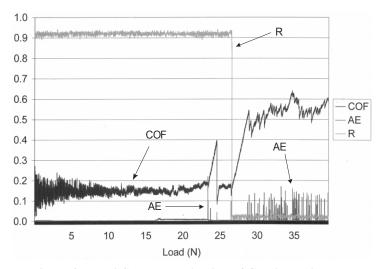


Figure 3. Multi-Sensor Monitoring of Coating Failure

electrical resistance, and is fully supported by the sharp increases in friction and acoustic signals. It is interesting that both friction and acoustic show a substantial pre-failure rise at the same lower load,

corresponding to the beginning of coating damage. Moreover, the ultra-sensitive acoustic emission started even earlier, which reflected the onset of tiny coating damage, undetectable yet by the electrical and force signals.

Results on Thin DLC Coatings

DLC, or diamond-like carbon coatings, are used in various industries. Their deposition technologies and so properties vary from application to application. For example, we have observed in numerous tests that the durability of very thin DLC coatings on hard magnetic disks and heads is the highest, while the durability of the DLC coatings on window glass and razor blades is much lower. Correspondingly, the scratch adhesion test procedure should be different.

Soft copper or gold-plated 4-mm or 6-mm balls have produced the most repeatable test data on the softest DLC coatings. Hard 1.6-mm tungsten carbide balls produced quite repeatable results on mid-range DLC coatings. Sharp diamond styluses scratched the coating, but did not delaminate it. Also, the sharp stylus data had limited repeatability due to the surface morphology differences from one scratch to another. The tungsten carbide micro-blade, averaging the scratch data over their substantial width, produced the most repeatable results for the hardest and thinnest coatings. Again, in all these tests the critical thresholds were determined by simultaneous measurements of forces, electrical and acoustic signals (se Fig. 3), though the latter ones were not informative for very thin coating films. The electrical resistance of DLC coatings was always measurable, though the harder and more diamond-like was a coating, the less conductive it was.

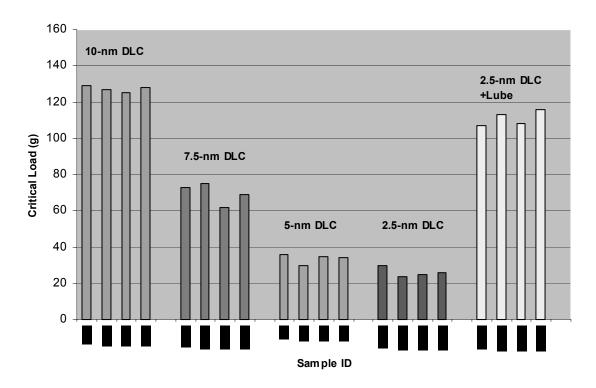


Figure 4. Micro-Scratch Test Data for Thin DLC Films

The thinnest coating tested was a 1.5-nm DLC film on a magnetic head wafer, the durability of which was found to be dependent on the rate of deposition. The Figure 4 above includes some of the results for

thin hard DLC coatings on magnetic disks. For each DLC thickness four disks were tested, and the high data repeatability between them is obvious from this figure. Reduction in film thickness by a factor of 4, from 10 nm to 2.5 nm, decreased the critical load by a factor of 5, from 125 to 25 cN. Lubricating the disk with a thin 2-nm layer of a topical Fomblin lubricant, common for the magnetic disks, increased the critical load by a factor of 4.5 for the thin 2.5-nm coating.

CONCLUSIONS

- 1. The multi-sensing technology, based on simultaneous high-resolution force, electrical and acoustic (when possible) measurements, allows for very accurate determination of both delamination/adhesion and scratch/wear resistance of both thin and thick diamond-like coatings. Using the test tools with larger contact area or length, like micro-blade or ball, may allow for more repeatable results than those obtained with sharp styluses.
- 2. The micro-tribometer mod. UMT-2 provides a useful platform for all common types of scratch/wear and adhesion/delamination tests, with the complete utilization of all the advantages of the multi-sensing technology

CALIBRATION OF THE MEASUREMENT OF SP²-TYPE BONDING IN CARBON USING EELS IN AN ELECTRON MICROSCOPE

V. Stolojan* and M. J. Goringe

School of Engineering, University of Surrey, Guildford, GU2 7XH, UK.

J. H. B. Deane

School of Electronics, Mathematics and Computing, University of Surrey, Guildford, GU2 7XH, UK

S. Ravi P. Silva

Advanced Technology Institute, University of Surrey, Guildford, GU2 7XH, UK.

*Corresponding author: tel.: +44 (0)1483 686299, fax: +44 (0)1483 686291, email: V.Stolojan@surrey.ac.uk

ABSTRACT

Electron Energy Loss Spectroscopy (EELS) in an electron microscope is an accurate method for the measurement of the sp²-type bonding in carbon, due to the presence of a clearly defined sharp peak in the specific carbon K spectral edge, whose area is directly proportional to the number of π empty states in the local density of states. However, an absolute measurement of sp² bonds requires to be scaled to the total number of sp² and sp³ bonded atoms and then normalized to a 100% sp²-bonded standard. Usually, pure graphite is used as a 100% sp²-bonded standard. However, this normalizing value is affected by the anisotropy of the π empty states, as their excitation probability depends on the amount of momentum that is transferred by the incident electron beam in the direction of the π empty states, which is orientation dependent. Here we review the theoretical prediction of a magic angle for an electron microscope, when sp² measurements are independent of the experimental conditions and support it with experimental verification. Furthermore, we analyze the implications of anisotropy on the measurements of the sp²-type bonding in amorphous carbon samples and in carbon nanotubes.

Keywords: EELS, sp² measurement, magic angle, TEM, carbon.

INTRODUCTION

Many of the properties of amorphous carbon films are directly related to the amount of sp²-bonded carbon atoms present in the film (ref. 1 to 3). One way of measuring the sp²-type bond concentration is to use the carbon K-edge in Electron Energy Loss spectra obtained in transmission with an electron microscope, representing the energy lost by the incident electron through atomic transitions from the 1s core level to empty states in the 2p Localized Density of States (LDOS). For this particular case (high energy loss), we can use the dipole transition approximation, which results in the spectrum being proportional to the imaginary part of the dielectric function.

For sp²-bonded carbon, the 2p empty LDOS is split into π^* and σ^* anti-bonding states, whilst there are no π^* states in sp³-bonded carbon. As the great majority of π^* states are separated from the σ^* states by around 6eV, there is a peak present in the carbon K-edge whose area is a direct measure of the number of sp²-bonded atoms in the sample. For comparison purposes, the area under this peak is normalized to an area of the carbon K-edge that is a measure of the total number of carbon atoms in the sample, and then further normalized to the equivalent ratio in a sample with 100% sp²-bonded carbon. This method is applicable for samples with very little (<5%) sp-hybridized carbon (ref. 5, 6).

However, the probability for energy loss depends not only on the amount of energy lost by the incident beam (i.e. the number of empty states in the 2p LDOS), but also on the magnitude and direction of momentum transferred. Therefore, for an anisotropic 2p LDOS (an sp^2 -hybridized carbon atom), the carbon K-edge will depend also on the orientation of the atom with respect to the direction of the transferred momentum, so that it will depend on the particular experimental conditions in the microscope, defined by the incident energy and convergence and collection angles. In particular, the probability for the excitation of the π^* states will depend on how these anisotropic states are oriented with respect to the optic axis of the microscope, which afflicts, in the first instance, the use of graphite

as a 100% sp²-bonded material norm. Furthermore, the counting of each the sp²-bonded carbon atoms in a given carbon-containing sample is weighted by the particular orientation of that atom.

Previous authors (ref 6) have identified a particular set-up in the electron microscope, called the magic angle, where the counting of the sp²-bonded atoms is independent of the orientation of the π^* states, but there is disagreement both in the theoretical and experimental value of this condition.

Here, we show the reasons for the disagreement of the theoretical derivations of the magic angle (ref. 6 to 8). We also apply the calculations developed by Souche et al. (ref 7) to study the effect of anisotropy of the π^* states on the measurement, from the carbon K-edge, of the sp²-bonded carbon in amorphous carbons and for single-walled carbon nanotubes. We also test experimentally the sp²-concentration predicted for carbon nantoubes.

ANISOTROPY OF THE EELS SCATTERING CROSS-SECTION FOR THE CARBON K-EDGE

The geometry of the interaction of the incident electron beam with the sample, referred to as the experimental set-up (Fig. 1), is defined with respect to the optic axis by an incidence semi-angle α , a scattering semi-angle β , the angle γ of orientation of the anisotropy axis (i.e. the orientation of the sp² bond) and a characteristic angle θ_E , given by:

$$\theta_{\rm E} \simeq \frac{\Delta \rm E}{2 E_0} \tag{1}$$

where E_0 is the incident electron energy and ΔE is the energy lost (i.e. ~285eV for the carbon K-edge). The characteristic angle represents the decrease in the wavelength of the scattered electron that has lost energy to a transition between from 1s to empty states in the 2p energy levels of carbon (the C K-edge). For a TEM with parallel illumination, the incidence semi-angle is zero, whilst in a general case for a convergent probe, α is limited by an objective aperture. Similarly, the collector aperture at the entrance into the spectrometer usually defines the collection semi-angle.

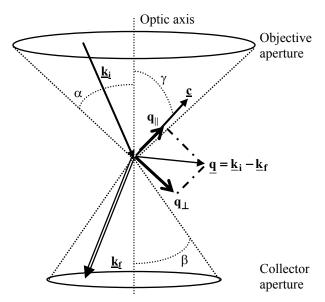


Figure 1. Scattering geometry in a TEM in a general case, defined by incidence and collection semi-angles α and β respectively. The axis of anisotropy \underline{c} is oriented at an angle γ from the optic axis. For a given incident electron momentum $\underline{k}_{\underline{i}}$ and a given scattered momentum $\underline{k}_{\underline{f}}$, the momentum transferred to the sample \underline{q} can be expressed in terms of components of momenta exchanged with the sample parallel (q_{\parallel}) and

perpendicular (q_{\perp}) to the axis of anisotropy.

Using the dielectric function to describe the response of the sample to the incident electron, the probability for the energy loss is derived from considering the retardation effects on the electric field of the fast electron traversing the sample (ref. 9):

$$\frac{d\sigma}{dE} \propto \int E^2 \operatorname{Im} \left[\frac{-1}{\sum_{i,j} q_i \varepsilon^{ij} q_j} \right] d^3 \mathbf{q}$$
 (2)

where i and j refer to the parallel and perpendicular components of the transferred momentum, with the corresponding component of the dielectric response of the material ϵ^{ij} . The integration is performed over the whole range of the exchanged momenta \mathbf{q} .

One of the important points in the evaluation of this integral is to realize that, for a given incident momentum, the scattered momenta can have directions anywhere within the cone defined by the point of incidence of the electron on the sample and the collector aperture (Fig. 1). This means that when one expresses equation 2 in either spherical or cylindrical coordinates, two independent polar angles are required to describe the incident and scattered momenta independently. This was done accurately in reference 7, but not in reference 6, with the result that reference 6 predicts the same magic angle as reference 7 for parallel illumination($\beta \approx 4\theta_E$), but a different magic angle as soon as the incident semi-angle is non-zero (Figure 2).

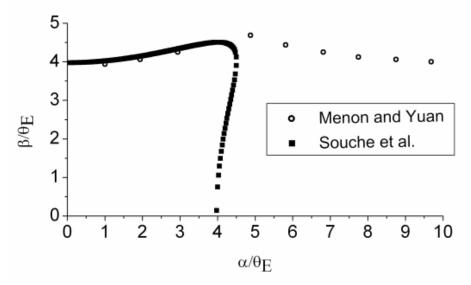


Figure 2. Comparison of the magic angle condition predicted using the calculations of reference 7 and reference 6 for the scattering cross section. At the magic angle, the scattering cross-section for a uniaxially anisotropic material does not depend on its orientation with respect to the optic axis. Note that the magic angle curve predicted using Souche et al. is symmetric about the reduced incidence and scattering angles.

We note that the magic angle curve predicted using the calculations of Souche et al in Figure 2 is symmetric about the line $\alpha' = \beta'$, where $\alpha' = \alpha/\theta_E$ and $\beta' = \beta/\theta_E$ are the reduced incidence and scattering semiangle. As a dedicated STEM is usually described as an 'upside-down' TEM, this shows that the two are geometrically equivalent if the respective apertures are also 'upside-down'.

On the other hand, the curve predicted using the calculations of reference 6 is asymmetric because, when using only one polar angle to describe both the incident and scattered momenta, one integrates over the surface of the scattered electrons cone (see Fig. 1) rather than over its' volume. The asymmetric result of reference 6 has lead to the conclusion that the measurement of the sp²-bonded carbon in amorphous carbon films is dependent on the experimental set-up of the microscope (ref. 10). As proved further on in this work, this is not the case if the reference 7 symmetric result for the integral in equation 2 is used.

When integrating over the transferred momenta \mathbf{q} in equation 2, we obtain the following general expressions for the EEL scattering cross-sections for transitions to π^* and σ^* empty states respectively:

$$\frac{d\sigma_{\pi^*}}{dE} \propto A + (B-A)\cos 2\gamma$$

$$\frac{d\sigma_{\sigma^*}}{dE} \propto (3A-B) + (A-B)\cos 2\gamma$$
(3)

where A and B are parameters that depend only on α ' and β ', the reduced semi-angles. The proportionality factors are identical for both scattering cross-sections.

For a general case where α is non-zero, A and B are given by:

$$A = \alpha'^{2} \ln \left[\frac{1 + \beta'^{2} - \alpha'^{2} + \sqrt{\left(1 + \alpha'^{2} + \beta'^{2}\right)^{2} - 4\alpha'^{2}\beta'^{2}}}{2} \right] + \beta'^{2} \ln \left[\frac{1 - \beta'^{2} + \alpha'^{2} + \sqrt{\left(1 + \alpha'^{2} + \beta'^{2}\right)^{2} - 4\alpha'^{2}\beta'^{2}}}{2} \right]$$

$$B = 2 \left(1 + \alpha'^{2} + \beta'^{2} - \sqrt{\left(1 + \alpha'^{2} + \beta'^{2}\right)^{2} - 4\alpha'^{2}\beta'^{2}} \right)$$

$$(4)$$

For parallel illumination, equation 4 is no longer applicable and equation 2 integrates to:

$$A = \frac{\beta'^{2}}{1+\beta'^{2}} + \ln(1+\beta'^{2})$$

$$B = 4\frac{\beta'^{2}}{1+\beta'^{2}}$$
(5)

The definition of the concentration of sp²-type bonds is:

$$sp^{2}(\alpha',\beta',\gamma)[\%] = \frac{\frac{d\sigma_{\pi^{*}}}{dE}}{\frac{d\sigma_{\pi^{*}}}{dE} + \frac{d\sigma_{\sigma^{*}}}{dE}}$$
(6)

Using the definitions in equation 3, it can be easily seen that the denominator in equation 6 is isotropic and hence is a good measure of the total number of carbon atoms in the sample, as used in the experimental measurement of the sp^2 content (ref. 5, 11).

In terms of Equation 3, the condition for the magic angle is the particular experimental set-up where A=B, and the pairs of reduced incidence and scattering semi-angles for which this condition is established are given in Figure 2

In the case of parallel illumination, the magic angle condition applied to equation 5 has a solution for $\beta \approx 3.97$, which is approximately thrice the value calculated in reference 8 of 1.36. It can be shown that the value for the reduced scattering angle at the magic angle condition of reference 8 was calculated wrongly, as the authors omitted to integrate over the whole scattering angles before equating the terms in equation 5. If that is done, then the magic angle condition at parallel illumination predicted using their approach is identical to that of reference 7.

PREDICTIONS FOR THE MEASUREMENT OF THE C-K EDGE IN PLANAR GRAPHITE, AMORPHOUS CARBONS AND CARBON NANOTUBES

Planar Graphite

The measured C-K edge for planar graphite is simply described by equation 3. It can be seen that, at the magic angle, equation 6 reduces simply to:

$$\operatorname{sp}^{2}\left[\%\right] = \frac{1}{3} \tag{7}$$

This is perhaps not surprising, as it is equivalent to the sum rule, describing the fact that in a 100% sp²-bonded carbon sample, there is one π state out of a total of three 2p states. It also means that, due to anisotropy, the sum rule, as deduced from the method of measurement from the C-K edge is only obeyed at the magic angle condition.

Away from it, certain geometric corrections must be applied. This proves that the method currently used for the determination of the sp²-content is sufficiently reliable, as it calculates experimental values of 0.31 (ref. 5) and 0.33 (ref 11) for the 100% sp²-bonded carbon normalization factor.

Amorphous carbons

For a 100% sp²-bonded amorphous carbon film, with no preferential orientation of the carbon sp²-bonds, the effect of anisotropy is calculated by integrating equation 3 over all possible orientations of the sp²-bonded carbon atoms and then substituting in equation 6. This is because there is no physical equivalence with the substitution of equation 3 into equation 6 prior to integration, as equation 6 refers here to the average values for the individual cross sections (i.e. integration prior to substitution):

$$sp_{\text{amorphous}}^{2} \left[\%\right] = \frac{\frac{1}{2} \int_{0}^{\pi} \frac{d\sigma_{\pi^{*}}}{dE} \sin \gamma \, d\gamma}{\frac{1}{2} \int_{0}^{\pi} \frac{d\sigma_{\pi^{*}}}{dE} \sin \gamma \, d\gamma + \frac{1}{2} \int_{0}^{\pi} \frac{d\sigma_{\sigma^{*}}}{dE} \sin \gamma \, d\gamma} = \frac{1}{3}$$
(8)

Equation 8 demonstrates that the measurement of the sp² content from amorphous carbon is independent of the experimental condition, and it always is a direct measure of the sum rule for the 2p density of states.

Carbon Nanotubes

The theoretical derivation here is applicable to both single-walled and multi-walled nanotubes, as it does not consider any effects due to interference between the several concentric single walled tubes that make up multi-walled nanotubes. For a carbon nanotubes whose axis is oriented an angle δ with respect to the optic axis, equation 6 becomes, in terms of the parameters defined in equations 4 and 5:

$$sp^{2}(\alpha',\beta',\delta)[\%] = \frac{A}{4A-B} - \frac{B-A}{2(4A-B)} \frac{\sin 2\delta}{\delta}$$
(9)

As in the case of planar graphite, it can be seen that at the magic angle condition, equation 9 again represents the sum rule. Equation 9 also shows that, unless the magic angle condition is achieved in the microscope, the measurement of the carbon K-edge from carbon nanotubes depends on their orientation with respect to the optic axis of the microscope.

EXPERIMENTAL VERIFICATION OF THE ANISOTROPY THEORY FOR A CARBON NANOTUBE

The magic angle condition was tested previously in reference 12, using highly oriented pyrolytic graphite in a TEM with parallel illumination. The measured reduced scattering angle at which the magic angle condition is established was ~2. In order to further test the discrepancy between the theoretical value and the experimental one, we measured the sp² content using a single-walled carbon nanotube at two different orientations, for different collection angles. The measurements were performed using a Philips CM200 TEM with a LaB₆ filament, equipped with a GIF2000 Gatan Imaging Filter. The spectrometer was operated in image-coupled mode, and the scattering angle was varied by changing the camera length of the microscope. The collection angle was calibrated from the diffraction pattern of the amorphous carbon film that supported the carbon nanotube sample. Care was taken to accurately centre the collector aperture onto the optic axis of the microscope for each of the collection angles. Each spectrum was processed in the usual way, by removing the pre-edge background and correcting for multiplescattering using Fourier ratio deconvolution. The sp²-content was measured, for a set of collection angles, for two orientations of the carbon nanotube ($\delta \cong 90^{\circ}$ and $\delta \cong 60^{\circ}$), using a 3-Gaussian method for modeling the π^* peak of the carbon K-edge (ref. 11, 13.). Figure 3 is a comparison of the simulated (equation 9) and measured sp² contents of the carbon nanotube, showing that the reduced collection angle at the magic angle condition is close to 4. The different result of reference 12 could be due to the method of modeling the π^* peak, as well as the much lower signal (and hence the much higher noise) of the data points at low collection angle. Confidence is gained here (Figure 3) as the data is well represented by equation 9.

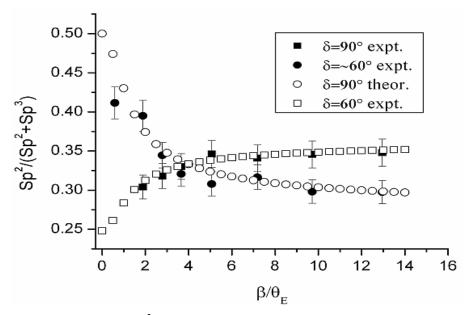


Figure 3. Measured and simulated sp²-content for a single-walled carbon nanotube, viewed with its axis at ~60° and 90° to the optic axis of the microscope respectively. The good fit of the theoretical model suggests that the reduced collection angle at the magic angle condition is ~4.

ACKNOWLEDGEMENTS

The authors are grateful to the EPSRC for financial support (multi-disciplinary project grant GR/N36073/01).

REFERENCES

- 1. Silva, S.R.P., et al.: Handbook of Thin Film Materials, Academic Press, 2002, vol. 4, pp. 403-505.
- 2. McKenzie, D.R., Bruley, J. and Smith, G.B.: Electron Energy-Loss Study of Bonding in Amorphous Silicon-Carbon Alloy-Films Prepared With Hydrogen Dilution, Appl. Phys. Lett., vol. 53, 1988, 2284.
- 3. Ferrari, A.C. et al.: Density, sp(3) Fraction, and Cross-Sectional Structure of Amorphous Carbon Films Determined by X-Ray Reflectivity and EELS, Phys. Rev. B, vol. 62, 2000, 11089.
- 4. Berger, S.D., McKenzie, D.R. and Smith, G.B.: EELS Analysis of Vacuum Arc-Deposited Diamond-Like Films, Phil. Mag. Lett., vol. 57,1988, 285.
- 5. Fallon, P.J.: Microscopy and Spectroscopy of CVD Diamond, Diamond-Like Carbon and Similar Materials, PhD thesis University of Cambridge, 1992, pp. 74-75.
- 6. Menon, N.K. and Yuan, J.: Quantitative Analysis of the Effect of Probe Convergence on Electron Energy Loss Spectra of Anisotropic Materials, Ultramicroscopy, vol. 74, 1998, 83.
- 7. Souche, C. et al.: Orientation Sensitive EELS-Analysis of Boron Nitride Nanometric Hollow Spheres, Micron, vol. 29, 1998, 219.
- 8. Paxton, A.T. et al.: The Near-Edge Structure in Energy-Loss Spectroscopy: Many-Electron and Magnetic Effects in Transition Metal Nitrides and Carbides, J. Phys. Cond. Mat., vol. 12, 2000, 729.
- 9. Inokuti, M.: Inelastic Collisions of Fast Charged Particles with Atoms and Molecules --- The Bethe Theory Revisited, Rev. Mod. Phys., vol. 43, 1971, 297.
- 10. Stolojan, V. et al.: Comparative study of properties of DLC films by Electron Energy Loss Spectroscopy and X-ray reflectivity, Electron Microscopy and Analysis 2001, IOP Conf. Ser., vol. 161, 1999, 361.
- 11. Stolojan, V.: Properties of Amorphous Carbon: INSPEC Series, IEE, London, 2003, 83.
- 12. Daniels, H.R. et al.: Electron Energy Loss Spectroscopy (EELS) at the Magic Angle, Electron Microscopy and Analysis 2001, IOP Conf. Ser., vol. 161, 1999, 97.
- 13. Papworth, A.J. et al., EELS Characterisation of the sp² Bonding Fraction Within Carbon Thin Films, Phys. Rev. B, vol. 62, 2000, 12628.

Study of High Transparency Diamond Like Carbon Film on Quartz Substrate Growth by Hot-Filament Chemical Vapor Deposition

Niu Xiaobin, Liao Yuan, Shi Hualiang

229-418, USTC, Hefei, Anhui, 230026, P.R. China

xbniu@mail.ustc.edu.cn

Abstract

By using the mixed methane and hydrogen gas, we successfully synthesized Diamond Like Carbon (DLC) films on quartz substrate in Hot-Filament Chemical Vapor Deposition (HFCVD) system. The prepared films were proved to be the DLC films by investigating the Raman Spectroscopy and have both very high hardness and high transparency (>80%) from 400nm to the whole infrared band, which can be used as shields of optical windows. We also did a series of experiments to study relations between the growth of the film and the Substrate temperature, Flament temperature, the time of growth and the consistency of methane and hydrogen.

NANO NI DOT EFFECT ON THE STRUCTURE OF TETRAHEDRAL AMORPHOUS CARBON FILMS

Churl Seung Lee, Tae-Young Kim, Kwang Ryeol Lee

Future Technology Research Division, Korea Institute of Science and Technology, P. O. Box 131, Cheongryang, Seoul, 130-650, Korea

Ki Hyun Yoon

Department of Ceramic Engineering, Yonsei University, Seoul, 120-749, KOREA

ABSTRACT

Nano-scale manipulation of thin film structure has attracted much attention, owing to their possibilities to obtain novel properties associated with the nano-scale microstructure. A great effort is also focusing on the nano-scale manipulation of tetrahedral amorphous carbon (ta-C) films. Multilayer structures composed of ta-C films of different properties are the most widely investigated structure. In the present work, we demonstrated that nano-sized graphitic columns embedded in hard amorphous ta-C matrix could be prepared by using nano-sized Ni dots on the substrate surface. The Ni dots were prepared by annealing Ni thin film of thickness ranging from 3 to 13 nm. The ta-C film was then deposited by filtered vacuum arc process. Microstructure analysis and electrical resistivity measurement showed that nano-scale columns of highly conducting graphitic phase grew at the Ni dots. Size of Ni dot has significant effects on the nano-scale structure evolution, and thus mechanical and electrical properties. The growth of the graphitic phase was discussed in terms of the catalyst effect of Ni for the transformation of carbon materials into stable graphitic phase.

Keywords: nano-scale structural manipulation, tetrahedral amorphous carbon, filtered vacuum arc process, Nano-sized Ni dots, catalyst effect

INTRODUCTION

Novel properties associated with nano-structures have been widely reported (ref.1). For example, nano-sized powder materials, nano-composite, or nano-scale multiplayer thin films frequently exhibit novel properties that cannot be implemented in the materials of conventional microstructures. A great effort is also focusing on the nano-scale manipulation of tetrahedral amorphous carbon (ta-C) films. Although ta-C film has a unique combination of high hardness, chemical stability and optical transparency, high residual compressive stress and poor adhesion has limited their applications (ref.2). Nano-composite films or nano-scale multilayer structures of the films of different properties is being widely investigated to resolve these drawbacks (refs.3 to 4). Search for novel properties of nano-structured ta-C film would also be the motivation of these investigations.

In the presented work, we developed a method to obtain nano-scale structural manipulation of ta-C film deposited by filtered vacuum arc process. By incorporating nano-sized Ni dots on the substrate surface, we could obtain highly conducting graphitic phase grown from the Ni dots to the surface of ta-C film. Since the catalyst effect of Ni for the transform to more stable graphitic phase, this method resulted in nano-composite materials in lateral dimension, i.e. nano-sized graphitic columns embedded in hard amorphous ta-C matrix. The reduction of mechanical properties and electrical resistivity with increasing size of the Ni dots could be understood in the viewpoint of the local increase of sp² bonds in hard ta-C matrix.

EXPERIMENTAL PROCEDURE

Nano-sized Ni dots on Si substrate were prepared by annealing Ni thin films of thickness ranging from 3 to 13 nm. The Ni thin film was deposited on the 600-µm-thick Si (100) wafers by DC magnetron sputtering method. In

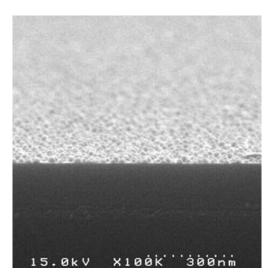


Figure 1. SEM microstructure of Ni dots formed by annealing of sputter deposited Ni film of thickness 3.4 nm

order to change the deposited Ni film to nano dots, the specimen was annealed in a rapid thermal process (RTP) at 800°C for 15 min in hydrogen environment. Hydrogen pressure during the annealing was kept at 1 Torr by adjusting the flow rate of hydrogen. Figure 1 is typical SEM microstructure of Ni dots obtained by the present annealing process. Ni dots of diameter ranging from 15 to 90 nm were uniformly distributed on the substrate. The average size of nano Ni dots monotonically increased with the thickness of the Ni film.

After Ni dot pretreatment, 100-nm-thick ta-C films were deposited by using filtered vacuum arc process. Details of the deposition equipment have been described elsewhere (ref.3). Prior to deposition, the substrate was pre-cleaned by carbon arc plasma beam mixed with Ar ions at the negative bias voltage of -800 V. The Si (100) strips with thickness of 100±5 µm, with and without Ni dot, were also used as the substrate to measure the residual stress of the film. The structure of the film was analyzed by employing transmission electron microscopy (TEM). The electrical resistivity of the film was measured by a four-point probe method. The residual stress of the film was

obtained from curvature of film/substrate composite using Stoney equation (ref.5). Nanoindentation in continuous stiffness measurement (CSM) mode was used to characterize the hardness and the plane strain modulus of the film. Atomic-bond structure was analyzed by using a Raman spectroscopy. Raman spectra were obtained by a triple-Raman spectroscope in the range from 800 to 2000 cm⁻¹, using an Ar ion laser of wavelength 514.5 nm.

RESULTS AND DISCUSSION

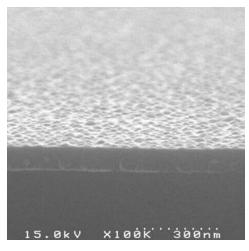


Figure 2. SEM microstructure of ta-C film deposited on the substrate of Fig. 1.

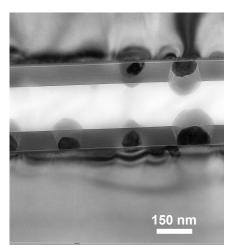


Figure 3. TEM cross-section of the ta-C film deposited on the substrate of Fig. 1.

Figure 2 shows the typical SEM microstructure of ta-C coated surface on the substrate shown in Fig. 1. Composition of the film analyzed by Auger spectroscopy was pure carbon without any impurities of Ni or Si on the film surface. The morphology of the nano-sized Ni dots on the substrate remained on the deposited surface. The rms

roughness of the surface measured by an atomic force microscope increased from 2.07 to 25.1 nm as the thickness of the Ni film increased from 3.4 to 13.1 nm. Figure 3 shows TEM cross-section of the ta-C film with nano-sized Ni dot on the substrate. The microstructure showed that a nano-scale second phase was grown on the nano-sized Ni dots. The second phase could be clearly distinguishable not only from Ni dots but from the amorphous carbon matrix. The size of the second phase is closely related with those of Ni dots. In the case of the smallest Ni dots prepared from the thinnest Ni film of 3.4 nm, the second phase was so small that could not reach to the film surface. However, the size of second phase increased as that of Ni dots increased.

The content of the second phase is proportional to the size of Ni dots that is in turn proportional to the thickness of Ni film. Therefore, the properties of the film were analyzed as a function of thickness of Ni film to understand the characteristics of the second phase. Figure 4 shows the dependence of electrical resistivity and the Raman spectra on the thickness of Ni films. The resistivity gradually decreased until thickness of deposited Ni film was 3.4 nm. However, the resistivity dropped by approximately 5 orders of magnitude when the thickness was larger than 3.4 nm. This behavior is in parallel with the structural evolution that the growth of the second phase reached to the surface only when the thickness of Ni film is larger than 3.4 nm. Hence, the present observation showing that the conducting path was formed in the insulating ta-C matrix as the size of Ni dot increased, would suggest that the second phase grown from the Ni dots is highly conducting.

Raman spectroscopy has been extensively used to study the structural variation in amorphous carbon materials such as hydrogenated amorphous carbon (a-C:H) or tetrahedral amorphous carbon (ta-C) films in addition to diamond or graphite (ref.6). Raman spectroscopy can reveal two aspects of the film properties. Intensity of the peak near 980 cm⁻¹, the second order Raman excitation of Si, is a measure of the optical transparency of the film. Raman spectra of Fig. 4 (b) show that the intensity significantly decreased when the thickness of Ni was larger than 3.4 nm, which implies that the optical transparency of the film was degraded with increasing content of the second phase. On the other hand, intensity of the peak at 1550 cm⁻¹ (also referred to as G peak) increased as the thickness of Ni film increased. It is well known that the G peak originates from E_{2g} phonons among the zone center modes of graphite sheet (ref.7). Since the film thickness was kept at 100 nm in all cases, this result suggests the increase of sp² bonds in ta-C matrix. Combined with electrical resistivity measurement, these observations show that the second phase grown at the Ni dots is sp²-rich graphitic phase which is electrically conducting and optically less transparent.

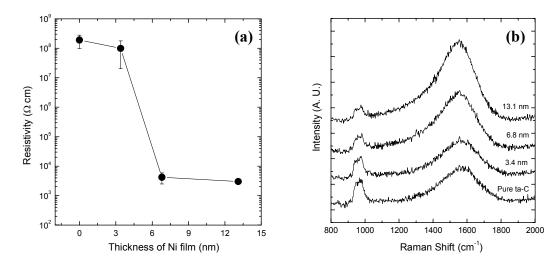


Figure 4. (a) The change of electrical resistivity of the film as the thickness of the Ni film and (b) Raman spectra for various values of thicknesses of the Ni film.

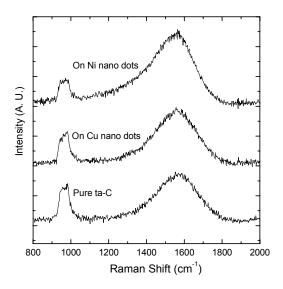


Figure 5. Raman spectra of the film for various cases of metal dots on Si substrate.

Fig. 5 shows the Raman spectra when using Cu nanodots instead of Ni dots. For comparison, Raman spectra of homogeneous pure ta-C film deposited without metal dots and the film with Ni nano dots of the same were also presented. In contrast to the case of using Ni dots, the Raman spectrum was essentially identical to that of pure ta-C film when using Cu nano dots. Transition metals such as Ni, Co are well known to be the catalyst for the transformation of amorphous carbon to more stable graphite. Lamber et al. reported that Ni catalyzed effectively the conversion of amorphous carbon to graphitic carbon at temperature as low as 730 °K (ref.8). It can be thus said that the catalyst effect of Ni for enhancing the transformation to stable graphitic phase played a major role for the structural evolution of the present work. Thermal activation for the phase transformation seems to be provided by the high energy ion bombardment on the growing surface or high flux of electrons from the arc plasma.

CONCLUSIONS

Nano-scale structural modification in lateral dimension was possible by filtered vacuum arc deposition of carbon using Ni nano dots on the Si substrate. Structural analysis and electrical resistivity measurement revealed that highly conducting graphitic phase was grown on the nano-sized Ni dots, which resulted in the nano-scale conducting phase embedded in amorphous ta-C matrix. The structural manipulation was due to the catalyst effect of Ni for the transformation of carbon to the more stable graphitic phase.

ACKNOWLEDGEMENTS

TEM analysis by Mr. Hyun Ruh at KRISS and judicious discussion with Dr. Wook Seong Lee is gratefully acknowledged. This research was performed by the financial support of 'Center for Nanostructured Materials Technology' under '21st Century Frontier R&D Programs' of the Ministry of Science and Technology, Korea.

REFERENCES

- 1. R. Hauert, J. Patscheider, L. Knoblauch, et al.: New Coating by Nanostructuring, Advanced Mater., vol. 11, 1999, 175-177.
- 2. P. J. Fallon, V. S. Veerasamy, C. A. Davis, et al.: Properties of filtered-ion-beam-deposited diamondlike carbon as a function of ion energy, Phys. Rev. B, vol. 48, 1993, 4777-4782.
- 3. C. S. Lee, K.-R. Lee, K. Y. Eun, et al.: Structure and properties of Si incorporated tetrahedral amorphous carbon films prepared by hybrid filtered vacuum arc process, Diamond Rel. Mater., vol. 11, 2002, 198-203.
- 4. S. Anders, D. L. Callahan, G. M. Pharr, et al.: Multilayers of amorphous carbon prepared by cathodic arc deposition, Surf. Coat. Technol., vol. 94-95, 1997, 189-194.
- 5. S. A. Brenner and S. Senderoff: Calculation of stress in electrodeposits from the curvature of a plated strip, J. Res. Natl. Bur. Stand., vol. 42, 1949, 105-121.
- 6. J. Schwan, S. Ulrich, V. Batori, H. Ehrhardt: Raman spectroscopy on amorphous carbon films, J. Appl. Phys., vol. 80, 1996, 440-447.
- 7. M. Yoshikawa, G. Katagiri, H. Ishida: Raman spectra of diamondlike amorphous carbon films, J. Appl. Phys., vol. 64, 1988, 6464-6468.
- 8. R. Lamber, N. Jaeger, and G. Schulz-Ekloff: Electron microscopy study of the interaction of Ni, Pd and Pt with carbon, Surf. Sci., vol. 197, 1988, 402-414.

SELECTIVE NANO COPPER DOT FORMATION ON DIAMOND-LIKE CARBON FILM

Tae-Young Kim, Churl-Seung Lee, Seung-Cheol Lee, Kwang-Ryeol Lee

Thin Film Technology Research Center, Korea Institute of Science and Technology, P.O.Box 131, Cheongryang, Seoul, 130-650, Korea assun@kist.re.kr (South Korea, Seoul)

Kyu-Hwan Oh

School of Materials Science and Engineering, College of Engineering, Seoul 151-744, Korea Seoul National University

Kyuhwan@snu.ac.kr (South Korea, Seoul)

ABSTRACT

We selectively formed nano-scale copper dots on a structure-modulated Diamond-Like Carbon (DLC) films that was obtained by filtered vacuum arc (FVA) process using Si (100) substrate with nano-sized nickel dots on the surface. The structure modulated DLC film has nano-scale graphitic phases embedded in hard DLC matrix. The film exhibits significantly different surface properties that can be used for the selective copper dot formation on the surface. Copper thin film deposited on the structure-modulated film was thermally treated in hydrogen environment. Nano-sized copper dot could be obtained only on the nano-scale graphitic phase. Mechanism of the selective Cu dot formation will be discussed in terms of surface energy and morphology of the surface.

Keywords: DLC(Diamond like Carbon), FVA, Nickel, graphitic phase, copper dot

Corresponding author: Kwang-Ryeol Lee

e-mail: krlee@kist.re.kr

address: Thin Film Technology Research Center, Korea Institute of Science and Technology,

P.O.Box 131, Cheongryang, Seoul, 130-650, Korea

Phone: +82-2-958-5494 FAX: +82-2-958-5509

THE MICROSTRUCTURE AND PROPERTIES OF TETRAHEDRAL AMORPHOUS CARBON FILMS DEPOSITED BY FILTERED ARC ACCELERATED AT DIFFERENT ENERGETIC GRADES

Zhu Jiaqi* Han Jiecai Meng Songhe Li Qiang

(Center of Composite Materials, Harbin Institute of Technology, Post-box 1247, Xidazhi Street 92, Nangang District, Harbin, P.C. 150001, China,)

Zheng Weitao

(Department of Materials Science, Jilin University, Jiefang Road 119 Changchun, P.C.130023, China)

ABSTRACT

Tetrahedral amorphous carbon films were deposited on single crystalline silicon substrate by the species with the different impinging energetic grades produced by the static-electricity pulse negative bias from 0 to 2000 V. The microstructure of the ta-C films is the amorphous sp³ hybridization skeleton enchased with sp² clusters whose inplane correlation length is less than 1 nm in light of visible Raman spectroscopic measurement. At the low energetic grade, the sp³-rich energetic window, and the sub-high energetic grade, the more is the content of sp³ in the films, the smoother is the surface of the films. The dependence between the impinging energy of the species and the surface morphology can be illustrated perfectly according to subimplantation growth mechanism. Nevertheless at the high energetic grade, the impinging ions with appropriate energy and angle can sputter and smoothen the surface, the roughness is even lower than the one of the films with the richest sp³. The hardness and Young's modulus of the films deposited at the high energetic grade (-2000 V) are higher than those of the films prepared at the floating conditions. Simultaneously, the critical scratching load of the films deposited with the substrate bias of 2000 V is even larger than the one of the sp³-rich films.

Keywords: tetrahedral amorphous carbon (ta-C); filtered cathodic vacuum arc (FCVA); Raman spectroscopy; Surface morphology; Mechanical properties

1. INTRODUCTION

Tetrahedral amorphous carbon (ta-C) films being rich of sp³ hybridization resemble much diamond and have the expansive applications in the electronic, mechanical, mechanical, defensive fields because of the superexcellent properties, such as high hardness, high modulus, high conductivity, high resistivity, high infrared transparency, and high biologic compatibility, and so on. Ta-C films are deposited generally by an ion beam with the lower energy. [1-3] Their microstructure and properties are controllable in a wide scale by modulating the impinging energy and other process parameters, i.e. the content of sp³ bonding atoms from 50% up to 90% [4], correspondingly hardness from 20 GPa to 80 GPa [5], Young's modulus from 200 GPa to 760 GPa [5,6], optical gap from 2.0 eV to 4.0 eV [7], etc. But up to the present, the majority of the relative research works has been focused on how to prepare sp³-rich amorphous carbon films with low energetic species and establish the optimal process, for example P.J. Fallon changed substrate bias from 0 to –450 V to substantiate the growth mechanism of diamond-like carbon films [8], X. Shi, et al., accommodated the ion energy from 0 to 200 eV to clarify the connection between structure and mechanical properties of the films [9], J. Salo, et. al., produced the plasma with 0~140 eV and measured the ion energy by the electro-optical time-of-flight method [10], D. Chen, et al., altered the substrate bias from 20 V to –100 V to research the optical properties and surface morphology of the films [11], and so forth. There are also a great deal of literatures majoring in deposition with lower energy from 0 to 500 eV [11][12~16], but there are short of deep and careful research on ta-C films deposited at high energetic grade exceeding 1000 eV, even then some mistakes appeared, for instance the connections between the sp³ component and surface morphology.

NASA/CP—2003-212319 512 August 18, 2003

^{*} Corresponding author. Tel.+86-451-6417970; Fax.: +86-451-6412512; E-mail: zjqhit@yahoo.com.cn (Zhu Jiaqi).

On the other hand, considerable thickness and the good adhesion between the substrates and the ta-C films are necessary to fulfill the specific applications in the different fields. But one of the primary restraining factors is the remained compressive stress on a high level in the films, which restricts the maximum thickness of 100~200 nm. [1][17] In order to strengthen the adhesive intensity between the substrate and the films and reduce the intrinsic stress, the different groups respectively applied a graded layer design [16], the multilayers alteration [18,19], and the combinative deposition with low energy and implantation with high energy [20~22], and other measures. The third method is that the layer on service is deposited with lower impinging energy after the admixture zone of several or tens of nanometers has been produced at the high energetic grade [20-22]. The second method means that hard and soft alterative layers are prepared by the diversification of the key process parameters to diminish the stress and aggrandize the thickness [18,19]. The first method denotes that a graded zone of microstructure and properties is formed in the boundary area between the films and the substrate by gradual change of impinging energy to decrease the stress concentration [16]. For whichever method, the character that the microstructure and properties can be modulated at the different energetic grades is taken full advantage of. But there are deficient of all-round and indepth understandings, even some deviations, especially about the ta-C films deposited at the high energetic grade, for example the correlation between the hardness and the critical scratching load, the comparison of hardness and modulus at the different energetic grades, and so forth. Accordingly, in this work the microstructure, surface morphology, and mechanical properties of the ta-C films prepared at the different energetic grades (the sp³-rich energy window denoting 80~150 eV [8,9][23], the low energetic grade being less than this energy window, the sub-high energetic grade that is in excess of the sp³-rich energy window but less than 1000 eV, and the high energetic grade that is more than 1000 eV) will be investigated.

2. EXPERIMENTS

2.1 Sample preparation

The samples were prepared by the filtered cathodic vacuum arc technology whose working theory and system conditions were consulted to reference [23]. The carbon plasma beam was produced from the vacuum arc on the high pure (99.999%) graphite target ignited by a retractable anode arm. After macroparticles and neutral species were separated from the plasma beam, the pure C^+ ions were deposited on the substrate fixed on the rotating chuck. The necessary impinging energy was achieved by means of static acceleration engendered by the direct current pulse substrate negative bias from 0 to 2000 V (pulse frequency: 1500 Hz, pulse width: 14 μ s). A series of samples were prepared with 100 nm thickness on the P(100) polished single crystal silicon wafers. Before deposition, the bare substrates were rinsed with acetone in a supersonic bath for 15 min and then were etched for 5 min by Ar⁺ ions produced by Kaufman gun whose working gas flux was setup as 8 sccm. During etching, the voltage of the ion beam power unit (BPU) was 750 V, the current of BPU was 100 mA, and the voltage of the accelerator power unit (APU) was 350 V. Consequently, the final etching energy of Ar⁺ ions was 1100 eV. The base vacuum pressure was 3.0×10^{-6} Torr, and the pressure would climb up to 6.0×10^{-5} Torr during deposition due to outgassing of the cathode. The arc current was 60 A and the magnetic field intensity of the filtered duct was 40 mT. The arc was ignited by the striker assemble once every fifteen seconds. The deposition rate was kept at 0.7 nm/s in the area of Φ 250 mm. The velocity of the substrate chuck was remained at 33 r/min to ensure the uniformity of deposition and etching.

2.2 Films characterization

The microstructure of ta-C films was measured by Ranishaw RM1000 Raman spectroscopy whose excited light source was Ar⁺ ion laser with 514.5 nm wavelength. In order to undamage the microstructure of the films and acquire clearly the characteristic signals, the input power was kept as 25 mW, the measurement step was 1.4 cm⁻¹, and the sampling duration was setup as 100 s in the scale from 800 to 2000 cm⁻¹. Hardness and Young's modulus were examined by MTS XP-type nano-indenter with Berkvovich three-sided pyramid diamond indenter, which stepped continuously into the 150 nm deep from the surface. The measurement precision of load and displacement was respectively 75 nN and 0.1 nm. Each sample was measured for ten times in the different locations at room temperature and relative humidity 30%. The adhesive property was assessed by the nano-scratching accessory. The pyramid side of the indenter was placed forward and was preindented with 1.5 mN force. The maximum indention load was 30 mN and the scratching distance was 500µm. The critical scratching load was determined by means of inspecting the friction coefficient and the side friction force. Five scratches were measured in the different areas of

each sample. The Digital Instruments Dimension 3100 atomic force microscope (AFM) was used to examine the surface roughness. For every sample the root-mean-square (RMS) surface roughness was inspected five times in tapping mode in different given area $(1\times1\mu\text{m}^2)$ and the atomic force probe was replaced every $3\sim5$ measurement.

3. RESULTS AND DISCUSSION

3.1 Raman measurements

Raman spectroscopy is a popular and undestructive tool wide utilized to characterize the microstructure of diamond and its related materials. The details about bonding hybridization of tetrahedral amorphous carbon films can be manifested by Raman spectra. Raman scattering is connected with the polarizability of bonds and in fact the spectra peak at a certain wavenumber reflects the resonant process that is produced due to the mutual actions between the impinging photons and the certain hybridization [24][27]. The bonds whose band gap matches with the energy of photons will preferentially be excited. Amorphous carbon consists of the carbon atoms with three hybridizations, i.e. sp¹, sp², and sp³, whose band gap overcast from 0 to 5.5 eV. Therefore, in order to respectively acquire the characteristic signals the researchers from the different countries have taken advantage of Raman laser with the wavelength from 244 nm to 785 nm [24-26]. But the most common and the steadiest is the 514.5 nm green Raman spectroscopy. Raman shift reflecting the microstructure details of ta-C films concentrates in the scale of from 800 to 2000 cm⁻¹, hereby, in this paper the spectra only in the range mentioned above are illustrated in the Fig.1. The Raman spectra of all the films demonstrate an asymmetric broad peak concentrating about on 1580 cm⁻¹ in the scale of from 1300 to 1700 cm⁻¹. Additionally, the small square topped peak at about 950 cm⁻¹ is produced from the second-order Raman spectra of the underlying silicon substrate [28]. There is no evident "peak shoulder" for D peak reflecting the breathing mode of those annular sp² sites during the Raman shift of 1300~1400 cm⁻¹ like the Raman spectra of other diamondlike carbon films.

The band gap of π bonds (sp² hybridization) is 2.25 eV [29], which matches the impinging energy (2.36 eV) of laser photons excited by 514.5 nm Ar⁺ ions. But the band gap of σ bonds (sp³ hybridization) is 5.50 eV [24] that differentiates in great disparity from the energy of visible photons. Hence, the Raman crossed section of sp² hybridization is larger 50~230 times than the one of sp³ hybridization [30]. Even though ultraviolet Raman (244 nm wavelength) is adopted, the characteristic signals of sp³ sites are feebler than the ones of sp² sites because of the long range polarisability of π bonds [25,26]. In light of above analysis, the asymmetric broad peak in the Fig.1, which can be taken approximately as G peak that is correlated with the stretching vibration of catenulate π bonds and the E_{2g} symmetry of crystalline graphite [2][24], represents virtually the earmarks of sp² sites and is characterized as the Raman "fingerprint" of amorphous carbon [31,32].

S. Prawer et al. ^[28] found that sp²:sp³ composition could be assessed quantitatively as a function of the skewness of the broad peak when they measured the Raman spectra of the diamondlike carbon films deposited by the mass-selected-ion-beam technology by Raman spectroscopy. Consequently, in this work the asymmetric broad peak whose skewness was indicated with the coupling coefficient (Q) in the Fig.2 was fitted with a single skew Lorentzian lineshape described by the Breit-Wigner-Fano function ^[23]. When Q⁻¹ approaches to zero, the symmetric true Lerentzian lineshape is resumed and simultaneously the content of sp³ is the maximal. In reference to the results examined by electron energy loss spectroscopy (EELS) ^{[8,9][28]}, the sp³ component of the film is more than 80% if the parameter Q is less than about –20. From the Fig.2, we can see that the coupling coefficients of the films deposited under the different substrate bias are all less than –20 and there is an obvious regularity that the coupling coefficient is minimum as the negative bias is 80 V and the coupling coefficients increase respectively as the negative bias enhances or lowers. It is worth noticing that the value of parameter Q is maximal under the floating conditions and the Q value (–28.48) is still in the better situations at the high energetic grade (-2000 V).

The full width at half maximum (FWHM) of G peak as a function of impinging energy confirms to the coupling coefficient as a function of the substrate negative bias. It has been shown in the Fig.3 that the FWHM of the films deposited under the floating conditions at low energetic grade is a little larger than the one of the films prepared at high energetic grade (-2000 V). Tamor and Vassell [31] researched the Raman spectra of more than a hundred amorphous carbon samples from the five different laboratories and found that the in-plane correlation length of sp² sites (La) is less than 1 nm when the FWHM of G peak is more than 50 cm⁻¹. The FWHM of the films prepared in this work obviously exceeds this numerical value. Hence, the microstructure of the films could be regarded as the amorphous skeleton of tetrahedral σ bonds beset with tiny sp² clusters (La<1 nm). It is different from the other experimental results that the position of G peak is almost unchanged with the shift of energetic grade because of the tiny difference of the sp³ content in the films.

3.2 Surface morphology of the films

Atomic force microscope (AFM) has become an effective tool by which the surface morphology of amorphous carbon can be measured accurately. Y. Lifshitz [1] validated successfully the subimplantation growth mechanism of diamondlike carbon films by AFM. Whereafter the other researchers [4][11][13][33] illustrated the phenomena that the surface morphology of ta-C films changed with ion energy or substrate temperature and coincidently considered that the surface roughness of ta-C films was correlated closely with the content of sp³ hybridization, i.e. the more were tetrahedral bonds in the films, the smoother was the surface of the films.

Under the experimental conditions in this work, the sp³-rich energy window is around -80 V [23] that is equivalent to the impinging energy of 100 eV. The C⁺ ions with the above appropriate impinging energy will breach the bondage of the substrate surface and will implant several atom layers under the surface. Subsequently, the energetic ions produce a process of "atomic peening" and cause ions to be incorporated into spaces in the growing film which are much smaller than the general volume of the ions [34]. Thereby the subimplantation process engenders the high local compressive stress that is even more than 10 GPa. According to the pressure-temperature phase diagram for carbon [12], the growth conditions of sp³ hybridization are provided. An AFM image of the ta-C films with the smooth surface and the most sp³ components is shown in the Fig.4(b). The C⁺ ions at low energetic grade can't hurdle the astriction of the substrate surface and are entrapped in the surface layer. Since the phase of sp² hybridization is stable thermodynamically at the ambient temperature and pressure, the films [Fig.4(a)] with less sp³ component and the rougher surface are formed under the floating conditions. At the sub-high energetic grade, for example under -200 V bias, the superfluous energy leads to prolonging the "thermalization stage" and impels the partial ions having been implanted into shallow surface layers to transfer and congregate again back to the surface. Correspondingly, the surface roughness increases again, the sp³ component decreases, and the Raman coupling coefficient hoists too. From Fig.4(c), we can find that there are some hunch ridges on the surface. But it is worth noticing that the surface of the films deposited at the high energetic grade (for instance with -2000 V substrate bias) and containing the less sp³ component is even smoother than the surface of the sp³-rich films [Fig.4(d)].

To enforce the measurement results, the root mean square (RMS) surface roughness was calculated with the digital process software package annexed with the AFM system. It has been shown in the Fig.5 that the RMS roughness of the films deposited at the low energetic grade is the maximal, and decreases with the enhancement of the impinging energy till the sp³-rich energy window and then increases again with the hoisted energetic grade.But the RMS surface roughness of the films prepared at the high energetic grade (-2000 V substrate bias) is the lowest. This phenomenon is owing to the dynamic balance of surface growth and surface damage during deposition process. While the energetic species act with the surface layers of the substrate each other, there are not only the collisions between the impinging ions and the atoms in the surface and the entrapments of the deposited ions in the surface layers, but also thermal vibrations, thermal dissipations, and thermal transferences of the impinging ions under the effects of the "thermal spikes". Besides the above surface growing process, there are sputtering, replacements, formation of point defects, and the other damage process in the surface layers. When the energetic grades are lower, the actions of sputtering are slender because of the lower impinging energy thereby the deposition process mainly is exhibited as surface growth. The gradual changes of surface morphology can be perfectly illuminated in light of the subimplantation growth mechanism. But at the high energetic grade, the impinging ions with higher energy can implant into the deeper layers under the surface and may be entrapped into the spaces being less than the volume of deposited ions among the atoms of the growing films so that they can't transfer back to the surface and the original smooth surface can be remained. On the other hand, the sputtering action will become more prominent due to the higher impinging energy and the tiny tubercles will be sputtered preferentially so as to smoothen the surface. It has been shown in the Fig.4(d). But if the impinging energy is so high (for example -20 keV [1][22]) that a great deal of vacancies and cavities have been produced, the actions of surface damage will play a main role and the surface of the films become rougher once again [1]. Surpassing the sp³-rich energetic window, the content of sp³ hybridization becomes less and less with the increase of impinging energy. But if the ion energy is appropriate, the surface of the films may become smoother owing to the sputtering actions, which has been neglected before.

3.3 Mechanical properties of the films

The nano-indenter is generally adopted to assess the mechanical properties of the thin films, such as hardness, Young's modulus, and critical scratching load. In order to guarantee the accuracy and the reproducibility of the experimental results, the area function of the three-sided pyramid diamond indenter had been rectified with the standard copper bulk and the ambient temperature was held at $24 \, \Box$ to avoid the thermal drift during measurement. The films deposited at the four different energetic grades were examined and the results were shown in the Fig.6.

When the impinging energy of the ions is situated in the sp³-rich energy window, e.g. 80 V substrate negative bias, the hardness and Young's modulus of the films are respectively maximal, i.e. 51.49 GPa and 512.39 GPa. At the low energetic grade, namely under the floating conditions, the hardness and Young's modulus are respectively minimal, i.e. 31.17 GPa and 325.16 GPa. It means that the adjustable scopes of hardness and Young's modulus are correspondingly close to 20 GPa and 200 GPa by the modulation of the impinging energy. In addition, when the ions energy surpasses the sp³-rich energy window, both hardness and Young's modulus gently decline. Even if the substrate negative is -2000 V at high energetic grade, Young's modulus still approaches to the one of the films deposited at the sub-high energetic grade. Hardness of the films prepared at the high energetic grade (-2000 V) is kept on the higher level, i.e. 39.72 GPa, and is distinctively more than the one of the films deposited under the floating conditions. The experimental results are contrary neither more nor less than to the viewpoints of D. Sheeja et al. [19]. To cushion the compressive stress and prepare ta-C thick films of 1 μm, they applied a design that soft layers and hard layers were alternated and every layer was prepared with the process restraining the proportion of sp³ hybridization. They believed that the harder layer about with the thickness of 100 nm could be deposited on the floating conditions and the softer layer about with the thickness of 20 nm could be prepared with the negative substrate bias of 2500 V. The reason for the divarications might be due to the differences of the pulse width and frequency of the direct current pulse bias. But it should be much more attributed to the facts that there are devoid of all-sided and veracious understanding about the mechanical properties of the films deposited at the different energetic grades, especially for the films prepared at the high energetic grade.

From the Fig.6, we can also find that the dependence of hardness or Young's modulus and impinging energy consists just with the one of the critical scratching load and impinging ion energy at the low energetic grade, the sp³-rich energy window, and the sub-high energetic grade. Namely, the higher are hardness and Young's modulus, the greater is the critical scratching load. But at high energetic grade, hardness and Young's modulus are much lower than those of the films deposited at –80 V substrate bias, whereas the critical scratching load is the highest. Hence, the adhesive property is remarkably enhanced as the grading implantation layer with the ingredients of the films has been formed between the substrate and the films at the high energetic grade. Obviously, the combinative application of the different energetic grades is able not only to guarantee the necessary content of sp³ hybridization in the films, but also to insure the excellent cohesive property.

4. INCLUSIONS

- (1) Ta-C thin films have been prepared with the filtered cathodic vacuum arc technology. The Raman spectra of the films, which can be fitted well with a single skew Lonretzian lineshape described by Breit-Wigner-Fano function, are an asymmetric broad peak centering at 1580 cm⁻¹. The optimal deposition process of sp³-rich films can be confirmed in light of the changing correlation between the coupling coefficients or full-width at half-maximum and the substrate negative bias. The microstructure of ta-C films is that the amorphous sp³ skeleton beset with sp² clusters whose in-plane correlation length is less than 1 nm.
- (2) At the low energetic grade, the sp³-rich energy window, and the sub-high energetic grade, the surface roughness is closely connected with the content of sp³ in the films. The more is sp³ component; the smoother is the surface of the films. This phenomenon may be illustrated on the foundation of the subimplantation growth mechanism of DLC films. However at the high energetic grade, the films whose root mean square surface roughness is even lower than the one of the films deposited in the sp³-rich energy window since the surface has been smoothened as a result of the sputtering action of the impinging ions.
- (3) The hardness and Young's modulus of the films deposited at the high energetic grade, e.g. the substrate bias of -2000 V, are obviously higher than those of the films prepared at the low energetic grade, e.g. under the floating conditions. The implantation at the high energetic grade is able to improve prominently the anti-scratching property of the films. The combinative application of the different energetic grades is able not only to guarantee the necessary content of sp^3 hybridization in the films, but also to insure the excellent cohesive property.

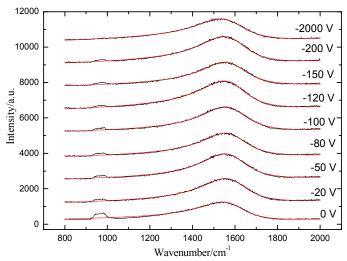


Fig.1 Raman spectra of the ta-C films deposited at different substrate bias

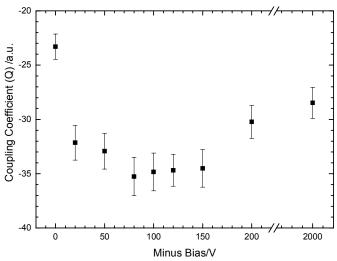


Fig.2 Coupling coefficient as a function of the negative substrate bias

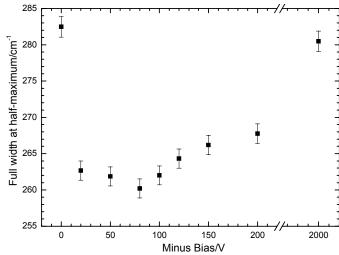


Fig.3 FWHM as a function of the negative bias

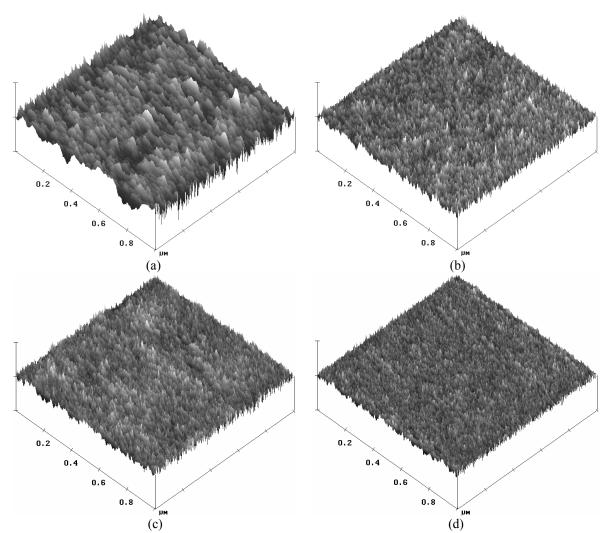


Fig.4 AFM images of the films deposited at the different energetic grades
(a) low energetic grade: under floating conditions, (b) sp³-rich energy window: -80 V,
(c) sub-high energetic grade: -200 V, (d) high energetic grade: -2000 V. 5 nm/div.

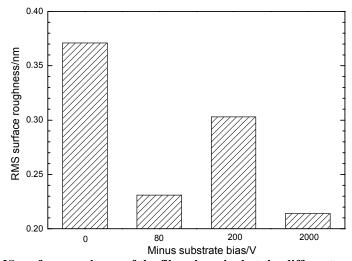


Fig.5 The RMS surface roughness of the films deposited at the different energetic grades

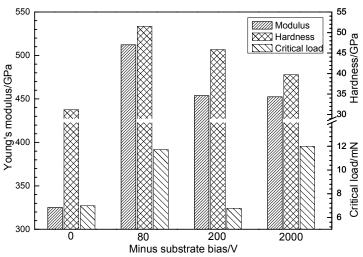


Fig.6 Hardness, Young's modulus, and critical scratching load of the films deposited at the four different energetic grades

REFERENCES

- [1] Y. Lifshitz, Hydrogen-free amorphous carbon films: correlation between growth conditions and properties, *Diamond Relat. Mater.*, 5(1996), 388
- [2] J. Robertson, Diamond-like amorphous carbon, Mater. Sci. Engeer., R37(2002), 129
- [3] Q. Wei and J. Narayan, Superhard diamondlike carbon: preparation, theory, and properties, *Intern. Mater. Rev.*, 45(2000), 135
- [4] X. Shi, L.K. Cheah, J.R. Shi, et al., On the upper limit of sp³ content in tetrahedral amorphous carbon film, *J. Phys.: Condens. Mater.*, 11(1999), 185
- [5] T.A. Friedmann, J.P. Sullivan, J.A. Knapp, et al., Thick stress-free tetrahedral amorphous carbon films with the hardness near that of diamond, *Appl. Phys. Lett.*, 71(1997), 3820
- [6] A.C. Ferrari, J. Robertson, M.G. Beghi, et al., Elastic constants of tetrahedral amorphous carbon films by surface Brillouin scattering, *Appl. Phys. Lett.*, 75(1999), 1893
- [7] A. Wei, D. Chen, S. Peng, et al., Optical and electrical characteristics of amorphous diamond films, *Diamond Relat. Mater.*, 6(1997), 983
- [8] P.J. Fallon, V.S. Veerasamy, C.A. Davis, et al., Properties of filtered-ion-beam-deposited dimondlike carbon as a function of ion energy, *Phys. Rev. B*, 48(1993), 4777
- [9] Shi Xu, D. Flynn, B.K. Tay, et al., Mechanical properties and Raman spectra of tetrahedral amorphous carbon films with high sp³ fraction deposited using a filtered cathodic arc, *Philosophical Magazine B*, 76(1997), 351
- [10] J. Salo, R. Lappalainen, A. Anttila, Energies of carbon plasma beams in the deposition of diamond-like coatings with the pulsed-arc-discharge method, *Appl. Phys. A*, 61(1995), 353
- [11] D. Chen, A. Wei, S.P. Wong, et al., Synthesis and microstructural properties of tetrahedral amorphous carbon films, *J. Non-Crystall. Solids*, 254(1999), 161
- [12] D.R. McKenzie, D. Muller, and B.A. Pailthorpe, Compressive-stress-induced formation of thin-film tetrahedral amorphous carbon, *Phys. Rev. Lett.*, 67(1991), 773
- [13] M. Chhowalla, J. Robertson, C.W. Chen, et al., Influence of ion energy and substrate temperature on the optical and electronic properties of tetrahedral amorphous carbon films, *J. Appl. Phys.*, 81(1997), 139
- [14] B.F. Coll, P. Sathrum, and R. Aharonov, Diamond-like carbon films synthesized by cathodic arc evaporation, *Thin Solid Films*, 209(1992), 165
- [15] S.R.P. Silva, Shi Xu, B.K. Tay, et al., Nanocrystallites in tetrahedral amorphous carbon films, *Appl. Phys. Lett.*, 69(1996), 491
- [16] M. Sütber, S. Ulrich, H. Leiste, et al., Graded layer design for stress-reduced and strongly adherent superhard amorphous carbon films, *Surf. Coat. Technol.*, 116~119(1999), 591
- [17] A. Yu. Belov, H.U. Jäger, Elastic constants of tetrahedral amorphous carbon films: the effect of intrinsic stresses, *Surf. Coat. Technol.*, 151~152(2002), 128

- [18] S. Anders, D.L. Callahan, G.M. Pharr, et al., Multilayers of amorphous carbon prepared by cathodic arc deposition, *Surf. Coat. Technol.*, 94~95(1997), 189
- [19] D. Sheeja, B.K. Tay, S.P. Lau, et al., Structural and tribological characterization of multilayer ta-C films prepared by filtered cathodic vacuum arc with substrate pulse biasing, *Surf. Coat. Technol.*, 132(2000), 228
- [20] E.G. Gerstner, D.R. McKenzie, M.K. Puchert, et al., Adherent carbon film deposition by cathodic arc with implantation, *J. Vac. Sci. Techno.* A, 13(1995), 406
- [21] G.M. Pharr, D.L. Callahan, S.D. McAdams, et al., Hardness, elastic modulus, and structure of very hard carbon films produced by cathodic-arc deposition with substrate pulse biasing, *Appl. Phys. Lett.*, 68(1996), 779
- [22] R.N. Tarrant, C.S. Montross, D.R. McKenzie, Combined deposition and implantation in the cathodic arc for thick film preparation, *Surf. Coat. Technol.*, 136(2001), 188
- [23] Zhu Jiaqi, Han Jiecai, Meng Songhe, Effect of substrate bias on microstructure and properties of tetrahedral amorphous carbon films, *J.Mater. Sci. Technol.*, 2003, to be published
- [24] A.C. Ferrari and J. Robertson, Interpretation of Raman spectra of disordered and amorphous carbon, *Phys. Rev. B*, 61(2000), 14095
- [25] K.W.R. Gilkes, S. Prawer, K.W. Nugent, et al., Direct quantitative detection of the sp³ bonding in diamond-like carbon films using ultraviolet and visible Raman spectroscopy, *J. Appl. Phys.*, 87(2000), 7283
- [26] V.I. Merkulov, J.S. Lannin, C.H. Munro, et al., UV studies of tetrahedral bonding in diamondlike amorphous carbon, *Phys. Rev. Lett.*, 78(1997), 4869
- [27] M. Profeta and F. Mauri, Theory of resonant Raman scattering of tetrahedral amorphous carbon, *Phys. Rev. B*, 63(2001), 245415
- [28] S. Prawer, K.W. Nugent, Y. Lifshitz, et al., Systematic variation of the Raman spectra of DLC films as a function of sp²:sp³ composition, *Diamond Relat. Mater.*, 5(1996), 433
- [29] D. Dasgupta, F. Demichelis, C.F. Pirri, et al., pi bands and gap states from optical absorption and electron-spin-resonance studies on amorphous carbon and amorphous hydrogenated carbon films, *Phys. Rev. B*, 43(1991), 2131
- [30] R.E. Schroder, R.J. Nemanich, J.T. Glass, *Phys. Rev. B*, 41(1990), 3738
- [31] M.A. Tamor, W.C. Vassell, Raman "fingerprinting" of amorphous carbon films, J. Appl. Phys., 76(1994), 3823
- [32] J. Schwan, S. Ulrich, V. Batori, et al., Raman spectroscopy on amorphous carbon films, *J. Appl. Phys.*, 80(1996), 440
- [33] Y.H. Cheng, B.K. Tay, S.P. Lau, et al., Influence of substrate bias on the structure and mechanical properties of ta-C:W films deposited by filtered cathodic vacuum arc, *Surf. Coat. Technol.*, 146~147(2001), 398
- [34] C.A. Davis, A simple model for the formation of formation of compressive stress in thin films by ion bombardment, *Thin Solid Films*, 226(1993), 30

NOVEL SYNTHESIS AND DEPOSITION PROCESSES

SYNTHESIS AND SOME PROPERTIES OF POLYHEDRAL GRAPHITE

Fumio Kokai

Chemistry Department for Materials, Mie University 1515 Kamihama, Tsu, Mie 514-8507, Japan

ABSTRACT

We have applied laser vaporization to grow carbon materials and describe a novel synthesis of polyhedral graphite (PG) particles. This synthesis is based on the condensation of carbon vapor confined by high-pressure Ar gas. We used a CO2 laser (10.6μ m and 5-kW peak power) with a pulse duration of 500 ms. The laser beam was focused onto a graphite target through a ZnSe window in a cylindrical stainless-steel chamber filled with Ar gas at 8 x 105 Pa. The laser spot size and power density on the target were adjusted to 2 mm and 30 kW/cm2, respectively. After laser irradiation of several shots on the fresh surface of a rotating graphite target, the deposits produced on the chamber wall were collected. SEM, TEM, Raman scattering spectroscopy, and powder XRD investigation of the deposited particles demonstrated that this laser vaporization method produces PG with a high yield (> 90%) and without hollow cavities in their centers. Faceted PG particles, ranging in size from 110 to 500 nm, have a turbostatic structure. Studies on the structure and properties, such as electrical resistance, of PG particles during high-pressure compression of the PG particles is underway.

Keywords: laser vaporization, polyhedral graphite, faceted particles

E-mail: kokai@chem.mie-u.ac.jp

THE NOVEL NUCLEATION PROCESS - AN UPDATE: A METHOD IN THE WORKING

Shlomo Rotter

UES Inc. (an AFRL contractor) 1950 Fifth St. Bldg. 18B, Rm. 15 Wright-Patterson AFB, Ohio 45433, USA

ABSTRACT

The novel nucleation process (NNP) was introduced publicly 4 years ago, here in Tsukuba, at the ADC/FCT 1999 meeting and has been in the working since then. The main user was Dr. Jim Butler of the Naval Research Laboratory and recently it made its way to AFRL/WPAFB in Dayton Ohio. A few papers appeared already and more are to come where NNP facilitated the use of diamond thin films for various applications. In this paper we will present data that gives some scientific insight of this method. We will present data on the optical properties of the PT (pre treated) film (using Ellipsometric characterization) and EELS data for the material identification of that carbon film. We will show a range of applications that have been opened up by the NNP method. In particular we will show the use of diamond films as an active passivation layer for high voltage SiC Schottky diodes and the use of diamond as the insulation layer on top of a new family of metal matrix composite (MMC) materials for the packaging of high power devices. It will be obvious to the listener that NNP can be used by anyone involved in diamond CVD and especially to those that didn't think diamond could be used for their particular application. NNP has made diamond an easy material to grow and use in ways and means not accessible before NNP. The more people join in the use of NNP, and the more it will be used by many others for their application it will become more obvious that this is the way to grow diamond in most practical cases.

Keywords: Diamond CVD. NNP, diamond applications

Interrelationships among carbon nanostructures

Michael Sternberg, Dieter M. Gruen, and Peter Zapol Materials Science Division, Argonne National Laboratory, 9700 S. Cass Avenue, Argonne, IL 60439, USA.

Abstract

Carbon nanostructures such as nanotubes, fullerenes, and diamond nanocrystals are receiving increasing attention because of their interest both from fundamental and applied points of view. Interrelationships between the properties of all groups of carbon entities at the nanoscale need to be better understood so that the energetics and conditions under which one form transforms to another can be rationalized.

We present primarily electronic structure calculations showing in detail the growth mechanism of ultrananocrystalline diamond, which results from the reaction of the carbon dimer, C2, with the (110) diamond surface. The evolution of a new monolayer of the diamond lattice is traced from the initial reaction of a single C2 molecule, to the half-monolayer stage to the completed monolayer. Fullerene- and nanotubelike intermediate structural elements appear on the diamond surface during growth. The challenge will be to relate these calculations to studies mentioned below and to gauge the extent to which our current knowledge can lead to an integrated systematics of carbon nanostructures.

Recent calculations by Barnard et al. delineate the stability relationships between diamond clusters, fullerenes and hydrogenated graphite clusters based on size ranges, while the transition of diamond nanocrystals to carbon onions was simulated by Fugaciu and Hermann. Again a comparison of the stability of fullerenes and closed nanotubes was made by Park et al. If the various known members of the nanocarbon family are related to each other by yet to be discovered hierarchical structures, it is possible that insight into the criteria determining the stability of each structure could lead to new, hitherto unknown family members with interesting and useful properties.

Work supported by the U.S. Department of Energy, BES-Materials Sciences, under Contract W-31-109-ENG-38.

HIGHER DIAMONDOIDS: A NEW CLASS of 3-D DIAMOND MOLECULES 1 to 2 NM IN SIZE

J.E. Dahl, S. G. Liu, R.M.K. Carlson, W. Qureshi

Molecular Diamond Technologies, Chevron Texaco Technology Ventures 100 Chevron Way, Richmond, CA 94802

ABSTRACT

Hydrogen-terminated diamonds form a continuous series of molecules ranging in size from macroscopic diamonds, to micron-sized diamonds (including CVD diamonds), to ultra-nanocrystalline diamonds (including ion implant and detonation diamonds as small as 2 to 3 nm), to higher diamondoids (recently isolated for the first time by us, and having sizes from ~1 to 2 nm), finally ending with the lower diamondoids of which, adamantane, consisting of one C₁₀ diamond crystal lattice cage, is the smallest. Except for the higher diamondoids, which have not been available until now, all of these forms have been studied, characterized and used in a variety of applications. We have identified and isolated higher diamondoids (C₂₂ and higher polymantanes) including tetramantanes, pentamantanes, hexamantanes, heptamantanes, octamantanes, nonamantanes, a decamantane and an undecamantane from petroleum. These molecules contain from four to eleven diamond crystal cages face-fused in a variety of ways to give a variety of geometries. Exceptional thermal stability and diverse geometries make possible their isolation from petroleum. Structures were proven by single crystal X-ray crystallography for selected members of three families of higher diamondoids. As members of the H-terminated diamond series, these molecules have great strength and rigidity, but they also show a remarkable variety of 3-dimensional shapes, including resolvable chiral forms (some with unusual primary helical structures, where the helicity is built into the backbone of the molecule, rather than arising from steric effects, such as in the helicenes). Properties of higher diamondoids can be tuned by the attachment of various functional groups, allowing customized mechanical, electronic and biomedical properties. The combination of diamond structure and versatile derivative chemistries, gives these 3-D, 1-2 nm size, chiral/achiral higher diamondoids potential for applications in a wide range of fields, including pharmaceuticals, microelectronics, optics, lubricants, and specialty chemicals. They are useful molecular building blocks that may find applications in nanotechnology and new nanostructured materials. Research quantities of higher diamondoids will be produced this year and larger quantities in the future.

Keywords: Diamondoid, Diamond, Molecular Diamond, Nanotechnology, Nanostructured Material.

CO-DOPING OF DIAMOND WITH BORON AND SULFUR

Sally C. Eaton, (a) Alfred B. Anderson, (b) John C. Angus (a) Dept. of Chemical Engineering (b) Dept. of Chemistry
Case Western Reserve University
Cleveland, OH, USA

ABSTRACT

Characterization of diamond co-doped with boron and sulfur is reported. SIMS analysis shows that the sulfur is concentrated in the near surface region, although increased concentrations of sulfur above background levels appear in the bulk diamond as well. Hall effect and thermoelectric power measurements indicate that the conductivity is n-type in the surface region and can be either n- or p-type in the bulk, depending on the degree of compensation with boron. The co-doped samples are not stable at elevated temperatures and there is an irreversible loss of conductivity when heated above 400 K in air. Electrochemical polarization of the n-type diamond showed blocking at anodic potentials up to +5 V versus the saturated calomel electrode. Two types of p/n junctions using the n-type boron/sulfur co-doped diamond were made: one using boron-doped diamond as the p-type side and the other using the p-type surface conductivity induced by hydrogen termination. The turn-on voltage in both junctions was approximately 0.5 V, which suggests that the Fermi level in the n-type diamond is low in the band gap. The n-type conductivity likely arises from an impurity band. The nature of the centers giving rise to the conductivity is not known.

Keywords: CVD diamond, n-type conductivity, co-doping

INTRODUCTION

Sulfur has been reported to act as a relatively shallow (0.38 eV) donor in diamond. However, other workers have reported that the samples contained boron^{3,4} and were p-type. 3

Albu *et al.*⁵ predicted that substitutional S and BS centers are deep donors, with levels at about 1.5 eV below the conduction band. Miyazaki and Okushi⁶ calculated that substitutional S and the SBS complex are located 1.1 to 1.2 eV and 0.5 eV below the conduction band, respectively.

Eaton *et al.*⁷⁻¹⁰ found that sulfur was incorporated in diamond in measurable concentrations only when boron was present, and n-type conductivity was achieved only at low B/S ratios.

GROWTH EXPERIMENTS

The diamond films were grown in an ASTeX microwave plasma reactor with H_2S as the sulfur source and trimethylboron (TMB) as the boron source. The methane concentration ranged from 0.1 to 1%; the S/C atomic ratio in the source gas varied from 15 to 40,000 ppm. Homoepitaxial films were grown on (111), (110), and (100) diamond substrates. For the (111) and (110) substrates, the gas flow was 200 sccm, the pressure was 25 torr, and the microwave power was 1000 W. The surface temperatures ranged from 700 to 800° C. For the (100) substrates, the gas flow was 200 sccm, the pressure was 35 torr, and the microwave power was 800 W. The surface temperatures ranged from 820 to 840° C.

SECONDARY ION MASS SPECTROSCOPY (SIMS)

Figure 1 shows the SIMS depth profile for diamond films grown on (100) and (111) substrates. Both samples had an n-type thermoelectric effect. The rms surface roughnesses for these samples as determined by atomic force microscopy were 1 nm and 6 nm, respectively.

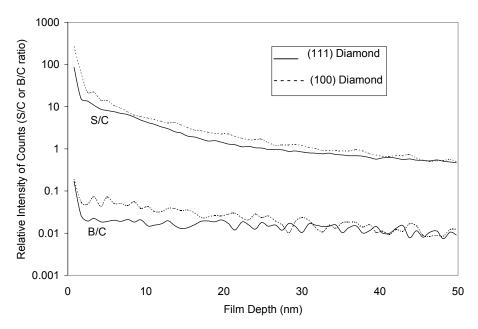


Figure 1. SIMS depth profiles for (100) and (111) diamond samples showing the ratios of the sulfur intensity to the carbon intensity and the boron intensity to the carbon intensity. The analyses probe the first 50 nm of film depth.

ELECTRICAL AND ELECTROCHEMICAL RESULTS

Electrical Results

Hall measurements, which measure the bulk film properties, gave both n-type and p-type results. Thermoelectric measurements, which sample the near-surface region, showed n-type behavior for co-doped diamond films grown at low B/S ratios. All samples tested for the Hall effect had n-type thermoelectric coefficients. These results indicated that in some instances there was an n-type surface layer atop p-type bulk diamond. Values for mobility at room temperature ranged from 1 to 20 cm²/V-s. Thermoelectric and Hall measurements for (100) samples are shown in Table 1.

Table 1. Summary of thermoelectric and Hall measurements on (100) diamond samples co-doped with boron and sulfur. Methane concentration in feed was 1%.

S/C atomic	B/C atomic	Thermoelectric	Sign of Hall	Room temperature Hall
ratio in feed	ratio in feed	coefficient	Measurement	mobility
5000	4	-830 μV/°C (N-type)	N-type	$20-1 \text{ cm}^2/\text{V-s}$
2500	25	-180 μV/°C (N-type)	P-type	$7-4 \text{ cm}^2/\text{V-s}$
5000	25	-100 μV/°C (N-type)	P-type	$17-6 \text{ cm}^2/\text{V-s}$

We also performed scanning tunneling spectroscopy (STS) measurements on the cleaved cross-section of an n-type (110) diamond film to observe conductivity as a function of depth at a high spatial resolution. For the samples tested, we observed n-type conductivity over the entire depth analyzed, but saw a decrease in conductivity by a factor of 4 in the top 600 nm of film depth.

Measurements of electrical conductivity versus temperature were made and are shown in Figure 2. At room temperature and below, the activation energies range from 0.04 to 0.12 eV.

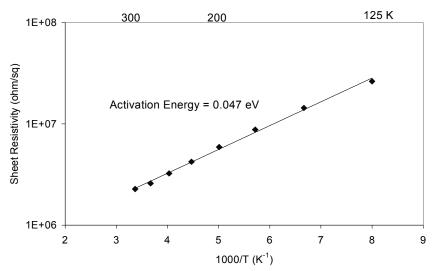


Figure 2. Log of sheet resistance for an n-type (100) diamond at low temperature versus 1000/T. The methane concentration in the source gas was 1%, the S/C ratio was 2500 ppm, and the B/C ratio was 25 ppm.

The excess sulfur in the near-surface region is significantly reduced upon treatment at 800°C with a hydrogen plasma. Also, the samples lose much of their conductivity when heated in air. Above 400 K there is an irreversible loss in conductivity and the activation energy increases to 1 to 1.5 eV. An example of this behavior for one sample is shown in Figure 3.

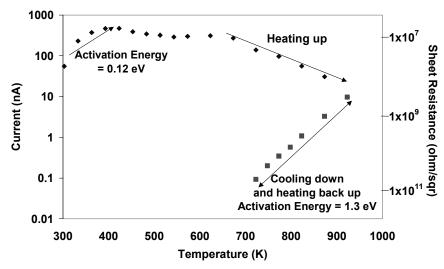


Figure 3. Current versus temperature history for an n-type (111) diamond film exposed to air.

We have cautiously assigned the underlying explanation for this phenomenon to diffusion of hydrogen, which passivates either the donors or acceptors. Experimental evidence obtained by other researchers¹¹ show an n-type activation energy of 1 eV at high temperatures and theoretical estimates place sulfur-related donor levels at about 1 to 1.5 eV beneath the conduction band.⁵ Therefore, we speculate that the high temperature conductivity shown in Figure 4 may arise from activation of electrons into the conduction band.

Electrochemical Results

Due to low conductivity, the co-doped films show noticeable IR drop and the current increases linearly on the anodic sweep of cyclic voltammograms. The window of water stability is approximately the same as boron-doped diamond, ¹² but the background current is higher. Some diamonds could be polarized to +5 V (versus the saturated calomel electrode) without evolving oxygen; hydrogen was evolved on the same sample at -2 V. This behavior is

characteristic of a lightly to moderately doped n-type semiconductor. Other more heavily doped n-type samples did not block anodic current.

FABRICATION OF P-N JUNCTION

A p-n junction was formed on a (111) diamond sample using boron-doped diamond for the p-type layer and sulfur/boron co-doped diamond for the n-type layer. A p-n junction was also formed on a (100) diamond sample using hydrogen-terminated diamond for the p-type layer and sulfur/boron doped diamond for the n-type layer. The S/C feed ratio necessary to achieve n-type diamond on top of p-type diamond is greater than for diamond grown on top of insulating diamond. At S/C ratios of 500 to 1000 ppm, the boron-rich underlayer apparently provided enough boron to the gas phase to compensate the sulfur. Thermoelectric measurements for such samples indicate that the co-doped layer is p-type. N-type layers could only be grown on the boron-doped diamond at S/C ratios of 2000 ppm and higher.

For samples in which p-n junctions were created, the p-type and n-type conductivity of the masked and unmasked sections were confirmed by thermoelectric measurements. For the (111) sample described in Figure 4, a boron-doped layer was first deposited in a hot-filament reactor with feed conditions of 0.5% methane and a B/C ratio in the feed gas of 4000 ppm for 24 hours. Sections of the diamond sample were then masked and an n-type layer was grown in the unmasked region with feed conditions of 0.12% methane, S/C = 6000 ppm, and B/C = 15 ppm for 24 hours growth time. The p-type layer had a sheet resistance of $2.2 \times 10^5 \Omega/\text{sq}$, and the n-type layer had a sheet resistance of $1.3 \times 10^6 \Omega/\text{sq}$.

In Figure 4 the absolute value of the forward and reverse currents is plotted versus the absolute value of the applied voltage. At $\pm 10~V$, the ratio of I_F/I_R is approximately 100 and the turn-on voltage for the p-n junction is approximately 0.5 V. The p-n junction was retested one year after the sample was grown and there was no change in its electrical properties. The p-n junctions with hydrogen-terminated diamond as the p-type layer showed similar rectification properties.

Koizumi et al. 13 give results for a p-n junction with a phosphorus-doped n-type layer. They report a rectification ratio (ratio of forward current to reverse current) of 10^5 at ± 10 V. The turn-on voltage was 4 to 5 V.

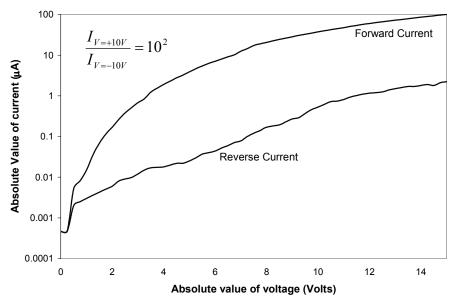


Figure 4. Current-voltage curves for a p-n junction grown on a (111) substrate with boron (p-type) and boron/sulfur (n-type) doped diamond.

RESULTS AND DISCUSSION

Location of Band Edges

The flat-band potential of B/S co-doped diamond is only 1 to 1.5 V more negative on the electrochemical scale than for boron-doped diamond. This implies that the Fermi level is only 1 to 1.5 eV higher (on the vacuum scale) than the Fermi level in boron-doped diamond. There are two possibilities: the surface dipole created by sulfur-termination causes an increase in the electron affinity of approximately + 4 V, *i.e.*, the band edges are severely lowered on the vacuum scale. Alternatively, the band edges are similar in position to those of partially-oxygenated diamond and the Fermi level is low within the band gap. Several pieces of information lead us to conclude that the latter possibility applies to co-doped diamond. From the literature for silicon, sulfur termination causes an increase in the work function of 0.3 eV. For III-V semiconductors, sulfur causes a change in the work function of approximately +/- 0.3 eV, depending on the initial value of the workfunction logical in the workfunction by 0.1 to 0.2 eV compared to hydrogen-terminated diamond. Therefore, the evidence from these sources indicates that the change in work function induced by sulfur is small, and may even be negative. The low turn-on voltage of the p-n junction (Figure 4) suggests that the Fermi levels of the p and n regions are close.

Surface conductivity measurements on sulfur-terminated diamond also support this conclusion. We observed the same conductivity response for both hydrogen and sulfur-terminated diamond. We did not see this pH dependence on oxygen-terminated or fluorine-terminated diamond, ¹⁹ presumably because the band edges for these samples are too low on the vacuum scale for the effect to be present. ²⁰

Conduction Mechanism

Density functional calculations performed by Albu *et al.*⁵ predicted the donor and acceptor excitation energies for several B/S complexes in diamond. Donors and acceptors are located throughout the bandgap and some donor levels are located lower on the vacuum scale than acceptor levels, *e.g.*, the ionized donor, SVS⁺, is approximately 0.2 eV lower than the ionized acceptor, BB⁻, and is approximately 1.5 eV above the calculated level of the substitutional boron acceptor, B⁻. These complexes are noteworthy because they support a possible explanation for n-type conductivity low in the band gap.

If the wavefunctions of the acceptor states overlap, then they can create an acceptor impurity band. Electrons from individual donor states can be excited into this acceptor band and then be free to move. A schematic of this mechanism is shown in Figure 5 below.

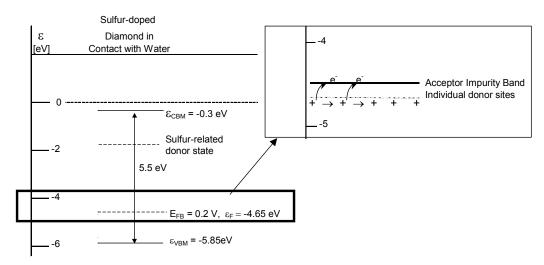


Figure 5. Model of a conduction mechanism low in the bandgap causing n-type conductivity.

ACKNOWLEDGMENTS

Mr. Taishi Fukazawa performed the electrochemical measurements. Useful discussions were held with Yuri Pleskov. The National Science Foundation (Grant CHE98-16345), the Civilian Research and Development Foundation (Grant RC1-2053), and the New Energy and Industrial Technology Development Organization (NEDO) of Japan supported this work.

REFERENCES

- 1. Sakaguchi, I., et al.: Sulfur: a donor dopant for n-type diamond semiconductors. Phys. Rev. B, 60, 1999, R2139-R2141.
- 2. Nishitani-Gamo, M. et al.: Homoepitaxial diamond growth with sulfur-doping by microwave plasma-assisted chemical vapor deposition. Thin Solid Films, 382, 2001, 113-123.
- 3. Kalish, R., et al.: Is sulfur a dopant in diamond? App. Phys. Lett., 76, 2000, 757-759.
- 4. Sternschulte, H.; Schreck, M.; and Stritzker, B.: In situ characterization of CVD diamond growth under H₂S addition by optical emission spectroscopy, mass spectroscopy and laser reflection interferometry. Diam. and Relat. Mater., 11, 2002, 296-300.
- 5. Albu, T.; Anderson, A. B.; and Angus, J. C.: Dopants in diamond nanoparticles and bulk. Density functional study of substitutional B, N, P, SB, S, PN, O, NN and interstitial H. J. Electrochem. Soc. 149 (2002) E143-E147.
- 6. Miyazaki, T.; and Okushi, H.: A theoretical study of a sulfur impurity in diamond. Diam. and Relat. Mater., 10, 2001, 449-452.
- 7. Eaton, S. C. et al.: Electrochemical properties of sulfur-treated diamond. Proc. Sixth Appl. Diam. Conf./Second Frontier Carbon Technology Joint Conf., NASA/CP-2001-210948, 2001, 164-169.
- 8. Eaton, S. C. et al.: Electrochemical properties of sulfur-doped diamond. Diamond Materials VII, PV 2001-25, The Electrochemical Society Proceedings Series, Pennington, NJ, 2001, 139-146.
- 9. Eaton, S. C. et al.: Co-doping of diamond with boron and sulfur. Electrochem. and Solid-State Lett., 5, 2002, G65-G68.
- 10. Eaton, S. C. et al.: Sulfur-doped n-type diamond: Preparation and electrochemical properties. Russ. J. Electrochem. (Transl. of Elektrokhimiya), 39, 2003, 170-176.
- 11. Garrido, J. A. et al.: Electrical and optical measurements of CVD diamond doped with sulfur. Phys. Rev. B, 65, 2002, 165409/1-165409/6.
- 12. Martin, H. B. et al.: Hydrogen and oxygen evolution on boron-doped diamond electrodes. J. Electrochem. Soc., 143, 1996, L133-L136.
- 13. Koizumi, S. et al.: Formation of diamond p-n junction and its optical emission characteristics. Diam. and Relat. Mater., 11, 2002, 307-311.
- 14. Papageorgopoulos, A. Deposition of sulfur on Si(100)2x1: surface restoration. Solid State Comm. 101 (1997) 383-387.
- 15. Bessolov, V. N.; Ivankov, A. F.; and Lebedev, M. K.: Sulfide passivation of III-V semiconductors: The starting electronic structure of a semiconductor as a factor in the interaction between its valence electrons and the sulfur ion. J. Vac. Sci. Tech., 13, 1995, 1018-1023.
- 16. Huang, L. J. et al.: Structure of the SiN_x/GaAs (110) interface modified with ultrathin Si and sulfur passivation. J. Vac. Sci. Tech. B, 14, 1996, 2895-2899.
- 17. Bezryadin, N. N. et al.: Position of the Fermi level on an indium arsenide surface treated in sulfur vapor. Semiconductors, 33, 1999, 1301-1303.
- 18. Miller, J. B.: Amines and thiols on diamond surfaces. Surf. Sci., 439, 1999, 21-33.
- 19. Chakrapani, V.; Eaton, S. C.; and Angus, J. C.: Studies of the conductivity of diamond surfaces. Extended Abstract, ECS Conference, Paris, 2003.
- 20. Maier, F. et al.: Origin of surface conductivity in diamond. Phys. Rev. Lett., 85, 2000, 3472-3475.

FORMATION OF C-N NANOFIBERS IN HIGH ISOSTATIC PRESSURE APPARATUS AND THEIR FIELD EMISSION PROPERTIES

V.D. Blank, D.V. Batov, S.G. Buga, B.A. Kulnitskiy, E.V. Polyakov

Technological Institute for Superhard and Novel Carbon Materials, 7a Centarlnaya St., Troitsk, Moscow Region, 142190 Russia

Sahn Nahm

Divisions of Materials Science and Engineering, Korea University, Seoul, Korea

Yun-Hi Lee

Department of Physics, Korea University, Seoul, Korea

U. Bangert, A.Gutiérrez-Sosa, A. J. Harvey, A. Seepujak, Department of Physics, UMIST, Manchester M60 1QD, UK

Yang-Doo Lee, Duck-Jung Lee and Byeong-Kwon Ju Micro-system Research Center / KIST, Seoul, 136-791, Korea

ABSTRACT

Carbon-nitrogen (CN) nanofibers have been formed in High Isostatic Pressure (HIP) apparatus in 1:1 nitrogen-argon gas mixture at 75 GPa using graphite electrical heater. Bamboo-like, beads-like, corrugated and spring-like nanofibers with the diameter of about 100-150 nm and the length over 10 μ m have been found in a deposit with a low content of amorphous carbon. The nitrogen content up to 8.5 % was found in fibers by EELS analysis. The CN nanofibers were printed on cathode plate and the dode-type flat vacuum lamp with 1 inch diagonal was assembled for the field emission study with the gap between anode and cathode varying in the range of 300 – 900 μ m. The turn-on fields were about 1.3 V/ μ m, the current density was 0.05 mA/cm² at 1.35 V/ μ m. The time reliability and light emission test were carried out for above 100 hours. We suggest that CN nanofibers can be applied to the high brightness flat lamp because of low turn-on field and time reliability.

Keywords: carbon-nitrogen naofibers, high isostatic pressure apparatus, structure, field emission.

INTRODUCTION

The possibility of utilization of carbon nanostructures as electron emitters attracts growing scientific interest (refs. 1to 6). Carbon nanotubes (CNT) and other nanostructures are capable of emitting high currents (up to 1 A/cm^2) at low fields (~ 5 V/im). They already used for producing some cold electron emitter devices (refs. 3 to 6). Despite pure carbon nanostructures CN, SiCN nanostructures attract considerable interest as alternative materials for cold emitters (refs. 7-9). R. Kurt et al. (ref. 7) investigated emissive properties of decorated C/N nanotubes. Plasma enhanced hot filament chemical vapor deposition (PE-HF-CVD) combined with micro-contact printing of catalysts was performed in order to deposit patterned films of nitrogenated carbon (C/N) nanotubes. Each tube was not straight but twisted. The length of a single tube was in the range of 10 - 50 im, the diameter 50 - 1000 nm. Nitrogen concentration in C/N nanotubes was found to be 4.3 %. On catalytic samples the lowest onset, turn – on and threshold fields required to extract a current density of 10 nA/cm², 10 μ A/cm² and 10 mA/cm², respectively, were E_i = 3.8 V/im, E_{to} = 4.7 V/im and E_{thr} = 7.4 V/im. In the case of autocatalytic growth very similar results were obtained, except E_{thr} = 11.5 V/im. Regarding their field emission properties, C/N nanotubes compare quite well with films of pure carbon nanotubes. For arrays of C/N nanotubes thinner than 50 nm an onset field below 3 V/im was observed.

The influence of C-N bonds concentration on the emission properties of films was investigated in reference 8.

The following conclusions have been drawn out. High concentration of tetrahedral C-N bonds lowers the threshold voltage for electron emission. The lower the percentage of double C=N bonds, the higher the emittance.

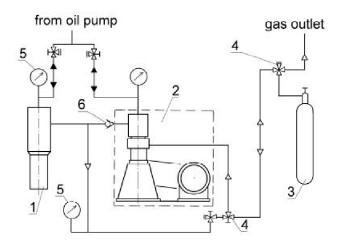
The carbon-nitride nanobells were obtained by G.Y. Zhang et al (ref. 9) with nitrogen content of about 2%. The onset voltage was about 1 V/ im and the threshold field about 10 V/im. They point out that according to *ab initio* calculations, such nanostructures have very high electronic density of states at the open edges.

A method of high isostatic pressure (HIP) growth of carbon nanostructures was designed first by Blank et al (refs. 10,11) and nitrogen concentration up to 13 % have been obtained (ref. 11). Elevated gas pressure promotes desirable chemical reactions due to elevation of chemical potential and diffusion coefficients. This method provides wider range of morphologies of nanostructures and higher nitrogen concentration in C-N nanotubes than CVD techniques.

In this article we investigated structure, nitrogen content and emissive properties of CN nanostructures obtained by HIP apparatus and found that they are competitive with those of pure carbon once for the first time.

EXPERIMENTAL

Nitrogen containing carbon nanostructures were formed in the High Isostatic Pressure (HIP) unit. The block diagram of the unit is shown in Fig. 1. In our experiments we used the HIP apparatus, designed for the maximum pressure value of 350 MPa. Its inner dimensions for mounting heater and screens are the following: diameter 40 mm, height 125 mm. Check valve (6) was used for the better stability of pressure during experiment. High gas pressure was created using the one-stage piston gas compressor (2).



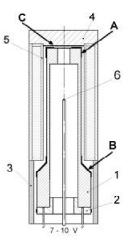


Figure 1. The block diagram of High Isostatic Pressure (HIP) unit (left) and the heating unit (right). In left: 1 - High Isostatic Pressure (HIP) Apparatus; 2 - High pressure Gas Compressor; 3 - Gas-cylinder (or cylinders); 4 - Shutoff valve; 5 - Manometer; 6 - Check valve.

In right: 1 – carbon resistive heater; 2 – copper contacts 3 – supporting ring (graphite); 4 – upper screen; 5 – side screen (graphite); 6 – thermocouple; A, B, C – carbon nanofibers deposition zones.

We used carbon heater as the carbon source. The shape of the graphite heater and heat shielding are shown in Fig. 1(right). The heat shielding is manufactured from graphite, it contains ring 3, plug 4 and cylinder 5. The heating zone with the thickness equal to 0.7 mm was made in the middle part of the heater 1. Carbon deposit was taken from the top part of the heater (zone A). The thermocouple type A insulated by corundum - straw 7 has been used for measurement of temperature. Details of experimental procedure have been presented in (ref. 10). The argon – nitrogen mixture with equal content of gases was prepared in the mixture unit (3) in Fig.1(left). The gaseous pressure was 75 MPa, duration of synthesis 40 min, temperature of the hot zone above 1400°C. Carbon evaporation was carried out by direct resistive electrical heating and improved by presence of nitrogen. We suppose that nitrogen improves carbon evaporating due to formation of C-N clusters on the heater surface and next transfer them into gas phase. Carbon deposit was investigated by transmission (TEM) and scanning

transmission electron (STEM) microscopy, using JEM-200CX, CM20 Philips TEM, VG 601 UX STEM and Hitachi S-4300.

The CN nanofibers were printed on the active area of cathode plate and then the diode-type flat lamp with 1 inch diagonal emitting area was assembled for the field emission study (Fig.2). The cathode electrode lines were formed with metal Cr on cathode glass plate. The green phosphor was printed on ITO coated anode glass. The field emission measurements were performed with the gap between anode and cathode varying in the range of $300 - 900 \, \mu m$ in vacuum chamber at a pressure of 10^{-6} Torr using F.u.G. Elektronik DC Power Supply. The sample temperature during the measurement was $300 \, \text{K}$.

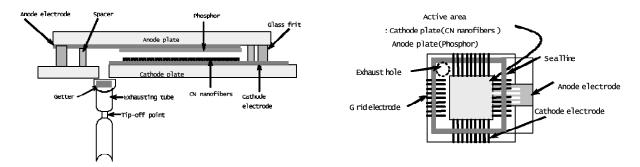


Figure 2. The geometrical structure of vacuum packaged CN nanofibers flat lamp: side view (left) and top view (right).

The green phosphor was printed and the glass frit was dispensed on anode glass plate. And then, it was put on the cathode glass plate with exhausting tube followed by heating to $420 \,\mathrm{C}$ to melt a glass frit in N_2 ambient. A sheet type getter (ST122) was inserted to panel through the tube, as shown in Figure 2. The panel was connected to tip-off system followed by pumping to 10^{-6} Torr.

STRUCTURE

Figure 3 shows SEM images of CN nanofibers formed by HIP. Figure 3a shows a cluster and figure 3b has higher magnification. The CN nanofibers were grown in random with the diameter of about 100-150 nm and the length over 10 μm. Increase of the nitrogen pressure caused increase of the carbon deposit and an appearance of variety of different structures. It can be explained by active gas convection, which caused more active mass transport and fluctuations of temperature. We found bamboo-like nanotubes with equidistant diaphragms, wrinkled bead necklace-like (BdL) tubes with thin walls, nanotubes with thin, not completely formed walls, like corrugated nanofibers (Cor-fibers) and spring-like periodical structure. The examples are shown in Figure 4. All these structures are characterised by curved carbon layers as a result of the presence of included nitrogen atoms. EELS investigations showed presence of nitrogen in tubes. The peak at 401ev of EELS-spectra corresponds to trivalent nitrogen atoms replacing graphite ones in a hexagonal lattice (Fig. 5a). The average nitrogen concentration was calculated to be about 3-4%. The value of nitrogen concentration in BdL tubes was found up to 8.5%.

Although the role of nitrogen for structure formation as well as for modification of material properties is not completely clear, we believe that low value of electron emission onset field found for our nanofibers, can be explained by peculiarities of their structures caused by the presence of nitrogen. At conditions of high argon pressure in HIP apparatus mach smaller amount of nanostructure deposit have been formed and that was mainly cylindrical nanotubes, while relatively big amount of nanofibers of various different configurations were formed at the same pressure-temperature conditions at nitrogen atmosphere. The curved intersected inner C-N layers forming a wavy net-like structure have been observed inside nanofibers (ref. 12). Analogous nanostructure was found in bamboo-like fibres, bead necklace-like fibres and net-fibres with a more complex structure consisting of intersecting graphene layers inside the fibre. The reason for an appearance of curved intersected graphene layers inside the fibre is the presence of nitrogen atoms in graphene layers. It is assumed that nitrogen effectively substitute carbon atoms in the graphitic lattice, resulting in bending of fringes (ref. 13).

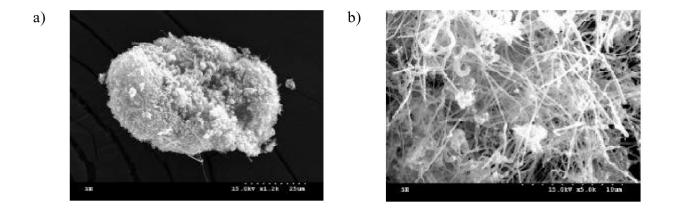


Figure 3. SEM image of carbon-nitrogen (CN) nanofibers formed by HIP; (a) magnification ×1.2k; (b) magnification ×5k.

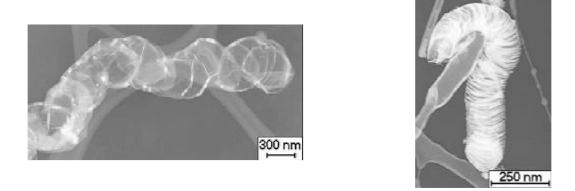


Figure 4. HRTEM image of corrugated (left) and spring-like (right) nanofibers.

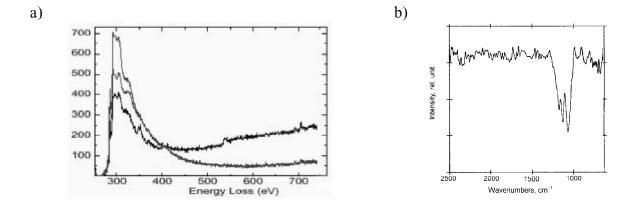


Figure 5. EELS (a) and IR spectra (b) of CN deposit obtained in HIP unit

The corrugated structure was explained in (ref. 14) by formation of pyridine-like bonds between nitrogen and carbon atoms. These bonds are characteristic mostly for edges of graphene layers. The availability of interstitial nitrogen into the graphite layers leads to the distortion and disruption of lattice. Even the small difference between C-C and C-N bond lengths (0.1422 and 0.1429 nm, respectively (ref. 15) causes large inner tensions in the growing layer, giving rise to elastic deformations and the bending of layers. Formation of fullerene-like structures can be considered as another reason for explanation of the structure of the inner layers (ref. 16). The C-N interaction may take place in a form of substitution of carbon atoms by nitrogen ones in (002) graphite planes, but to a greater extent it can create interlayer bonds, cause defects and formation of sp³-bonds. IR-spectroscopy investigations showed that only single C-N bonds present in the nanostructures synthesized (Fig. 5b). The band at 1100 usually is attributed to C-N single bonds vibration frequencies (ref. 17). It is assumed, that namely single C-N bonds are favourable for field emission properties (ref. 8).

FIELD EMISSION

Figure 6 shows the field emission curves of the CN nanofibers and the corresponding Fowler-Nordheim curves. Turn on field at the spacer gap of 300, 500, 700 and 900 μ m was measured 1.56 V/ μ m, 1.48 V/ μ m, 1.2 V/ μ m and 1.44 V/ μ m, respectively. The emission uniformity in the active area was quite good.

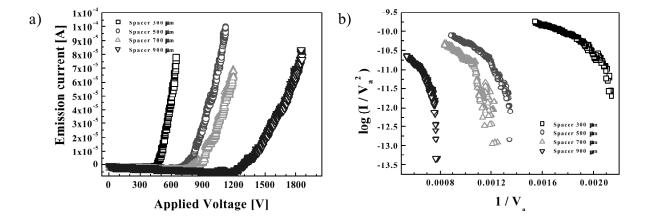


Figure 6. Field emission curves (a) and the corresponding Fowler-Nordheim plot (b) of CN nanofibers.

It is assumed in various studies of the field emission of carbon nanotubes, that electrons are usually emitted from their top tips (ref. 18). But in the case of CN nanofibers, we suppose that besides top tips, electrons can be emitted from nanofiber sides. Substitution of carbon atoms with nitrogen ones in graphene sheet causes its corrugation and appearance of sp^3 carbon sites, favourable for field emission due to the negative electron affinity. Besides that nitrogen atoms may strongly affect on the electron structure of the fibers and supposedly this may also improve emission properties. The Fowler–Nordheim (FN) theory is used to describe field emission behaviour of metallic materials at high applied electric field. According to the theory the plot of $log (I/V^2) vs. I/V$, is expected to be a straight line. However, our FN plots in figure 6 show distinct non-linearity. This deviation from FN theory in field emission probably may be attributed to the geometric structure of the emitters, effect of space charge in the chamber and to a change in the contact resistance between CN nanofiber emitters and the substrate (ref.19).

CONCLUSION

The CN nanofibers were formed by HIP process for the first time. From the field emission measurements CN nanofibers show an excellent characteristics of emitter, better than carbon nanofibers and other known carbon-nitrogen structures. The CN nanofibers flat lamp provides high brightness and uniformity of the light beam. The

CN flat lamp can be applied to automotive, avionics industries, high performance back-lights for liquid crystal displays, view box and so on.

ACKNOWLEDGEMENTS

This research has been supported by the Intelligent Microsystem Center (IMC; http://www.microsystem.re.kr), which carries out one of the 21st century's Frontier R&D Projects sponsored by the Korea Ministry of Science & Technology. A part of the work was also supported by INTAS project No. 00-237

REFERENCES

- 1. Saito Y., Uemura S.: Field Emission from Carbon Nanotubes and its Applications to Electron Sources. Carbon, vol. 38, 2000, pp. 169-182.
- 2. Hoshi F., Tsugawa K., Goto A., et al.: Field Emission and Structure of Aligned Carbon Nanofibers Deposited by ECR-CVD Plasma Method. Diamond and Rel. Mat. vol. 10, 2001, pp. 254-259.
- 3. Satyanarayana B.S., Robertson J. and Milne W.I: Low Threshold Field Emission from Nanoclustered Carbon Grown by Cathodic Arc. J. Appl. Phys., vol. 81, 2000, pp. 3126-3132.
- 4. Obraztsov A.N., Volkov A.PP., Pavlovsky I.: Field Emission from Nanoclustered Carbon Materials. Diamond and Related Mat., vol. 9, 2000, pp. 1190-1195.
- 5. Lee Y.-H., Jang Y.-T., Kim D.-H, et al.: Realization of Gated Field Emittres for Electrophotonic Applications Using Carbon Nanotube Line Emittres Directly Grown into Submicrometer Holes. Adv. Mater., vol. 13, 2001, pp. 479-482.
- 6. Jang Y.-T., Lee Y.-H., Ju B.-K., et al.: Application of Carbon Nanotubes to the Cathode Ray Tube Electron Gun. Vacuum. vol. 68, 2003, pp. 79-85
- 7. Kurt R., Bonard J.M., Karimi A.: Structure and Field Emission Properties of Decorated C/N Nanotubes Tuned by Diameter Variations. Thin Solid Films. vol. 398-399, 2001, pp. 193-198.
- 8. T. Sasaki, Y. Mori, M. Yoshimura, et al.: Effect of Carbon Nitride Bonding Structure on Electron Field Emission. Diamond and Related Materials. vol. 9, 2000, pp.1228-1235.
- 9. Zhang G.Y., Ma X.C., Zhong D.Y., and Wang E.G., Polymerized Carbon Nitride Nanobells. J. Appl. Phys. vol. 91, 2002, pp. 9324-9327.
- 10. Blank V. D., Polyakov E.V., Kulnitskiy B.A., et al.: Nanocarbons Formed in a Hot Isostatic Pressure Apparatus. Thin Solid Films, vol. 346, 1999, pp. 86-92.
- 11. Kiselev N.A., Sloan J., Zakharov D.N., et al.: The Structure of Nanotubes Fabricated by Carbon Evaporation at High Gas Pressure. Carbon, vol. 38, 2000, pp. 1217-1240
- 12. Blank V. D., Polyakov E. V., Batov D.V., et al.: Formation of N-containing C-nanotubes and Nanofibres by Carbon Resistive Heating under High Nitrogen Pressure, Diamond and Rel. Mat., 2003, to be published).
- 13. Hellgren N., Johansson M.PP., Broitman E., et al.: Role of Nitrogen in the Formation of Hard and Elastic CNx Thin Films by Reactive Magnetron Sputtering. Phys.Rev., B vol. 59, 1999, pp. 5162-5165.
- 14. Terrones M., Terrones H., Grobert N., et al.: An Efficient Route to Large Arrays of CNx Nanofibres by Pyrolysis of Ferrocene/Melamine Mixtures Appl. Phys. Lett. vol. 75, 1999, pp. 3932-3936.
- 15. Inagaki M., Tachikawa H., Nakahashi T., et al.: Chemical Bonding State of Nitrogen in K Λpton-derived Carbon Film and Its Effect on the Graphitization Process. Carbon, vol. 36, 1998, pp.1021-1025.
- 16. Sjöström H., Stafström S., Boman M., Sundgren J.E.: Superhard and Elastic Carbon Nitride Thin Films Having Fullerenelike. Microstructure Phys. Rev. Lett., vol. 75, 1995, pp. 1336-1341.
- 17. Zhang Z.J., Fan S., Lieber C.M.: Growth and Composition of Covalent Carbon Nitride Solids. Appl. Phys. Lett., vol. 56, 1995, pp. 3582-3584.
- 18. Jiang N., Koie R.et al., Carbon Nanofibers Synthesized by Decomposition of Alcohol at Atmospheric Pressure. Applied Physics Letters, vol. 81, 2002, pp. 526-528.
- 19. Zhong D. Y., Zhang G.Y., Liu S., et al.: Universal Field-Emission Model for Carbon Nanotubes on a Metal Tipp. Applied Physics Letters, vol. 80, 2002, pp. 506-508.

INVESTIGATION OF LARGE AREA HFCVD-DIAMOND DEPOSITION PROCESSES BY MULTI-FILAMENT TEMPERATURE MEASUREMENTS

Markus Höfer and Lothar Schäfer

Fraunhofer Institute for Surface Engineering and Thin Films, Bienroder Weg 54E, 38108 Braunschweig, Germany, e-mail: hoefer@ist.fhg.de, phone: +49(0)531/2155-620, fax: +49(0)531/2155-900

ABSTRACT

Hot-filament chemical vapor deposition (HFCVD) is a technologically important process for depositing polycrystalline diamond films on large areas or three-dimensional substrates. Growth rate and phase purity of the diamond films are essentially determined by the ability of the hot filaments to produce atomic hydrogen which is affected by the temperature and the state of the filaments with respect to carbon incorporations and carbon coverage, respectively. On the other hand, filament temperature measurements in correlation with deposition parameters give evidence of the state of the filaments and the gas phase activation.

A motor driven optical pyrometer system has been built up for precise and fully automatized filament temperature measurements in multi-filament arrangements. This device allows to investigate how the state of each filament in a given setup is affected by integral parameters like gas composition, heating power, pressure etc. and also by local changes of the boundary conditions, for instance due to the positioning of the substrates or to inhomogeneities of the gas feeding system. The presented results demonstrate that multi-filament temperature measurement is a powerful tool for monitoring, controlling, and optimizing large area HFCVD processes. Thus it enables the systematic improvement of reproducibility, homogeneity, and quality of the deposited diamond films.

Key Words:

polycrystalline diamond, hot-filament CVD, filament temperature measurement, process control

FABRICATION OF VERY-HIGH-ASPECT-RATIO MICROCHANNELS IN CVD DIAMOND BY A MOLDING TECHNIQUE

V.G. Ralchenko

General Physics Institute, 38 Vavilov str., Moscow 119991, Russia; Tel: +7-095-1328229; Fax: +7-095-1357672; E-mail: ralchenko@nsc.gpi.ru

E.I. Givargizov

Institute of Crystallography, Moscow 117333, Russia

ABSTRACT

The growth of diamond films with built-in microchannels (through holes) of a few microns in diameter with aspect ratio up to 50 has been realized using a molding technique and a special template. The method employs the microwave plasma assisted diamond deposition on (111) Si substrate with regular Si whiskers followed by separation of diamond from the substrate to obtain replica of the original pattern. The holes are hexagonal in cross section, and the hole "diameter" is almost constant over the whole depth (ca. 100 µm). The position, diameter and depth of the microchannels can be varied in a broad range. Possible applications of perforated diamond films include membranes, drawing dies, heat spreaders with interconnections for electronic circuits, and novel types of diamond-based composites.

Keywords: CVD diamond; silicon whiskers, molding technique, microchannels

INTRODUCTION

A post-growth processing of CVD diamond films is generally required in most cases to A post-growth processing of CVD diamond films is generally required to employ this material with unique properties for a particular application. Since the mechanical treatment is difficult due to extreme hardness of diamond the laser [1,2] or plasma [1,3] etching techniques are commonly used for diamond film micromachining such as cutting, drilling, surface planarization, fine patterning, etc. Holes of diameter ranged from a few microns to some hundreds microns were produced in CVD diamond by ablation with different types of lasers [2,4,5,], while submicron holes in borondoped diamond for electrochemical applications were etched in oxygen plasma [6]. Yet, the fabrication of deep holes with aspect ratio of the order of 10 or even higher in diamond using a dry etching is still a challenge, especially if strictly parallel and smooth sidewalls of the channel must be obtained. Here we report on growth of diamond film with built-in holes located at predetermined sites using a special silicon template. This method known as the molding technique employs the diamond deposition on a patterned substrate followed by a separation of diamond from the substrate to obtain the replica of the original pattern. Various diamond microstructures such as arrays of pyramids for diamond optics with reduced reflection coefficient [7,8], tips for field electron emitters [9,10], diamond optical lenses [11], optical micro electromechanical systems [12], integrated cantilevers and tips for atomic force microscopy [13], a three-dimensional porous "diamond opal" [14] have been fabricated previously using the molding technique.

EXPERIMENTAL

A sequence of processes to make microholes in polycrystalline CVD diamond is shown schematically in Fig. 1. Silicon whiskers with diameter of 2 and 4 μ m and height in the range of 45 to 110 μ m have been grown on (111) Si wafers by vapor-liquid-solid (VLS) technique [15]. The whiskers directed perpendicularly to the base of the substrate formed a two-dimensional array with a period of 32 μ m on area of 5 mm in diameter (Fig. 2). Since the spontaneous nucleation of diamond on foreign materials has a low probability the nucleation centers must be introduced on the substrate surface before diamond growth. The 10x10x0.3 mm³ substrate was seeded with 5 nm diamond particles in an ultrasonic bath to provide high nucleation density [16]. To produce the exact replica of original pattern after removal of the substrate the diamond nucleation density, N, must be very high in order to provide the conformal coating on microstructured surface. For instance, the replication of a relief with typical 100

nm features would require $N\sim10^{11}$ - 10^{12} particles/cm². The diamond deposition was performed for 24 hours in a microwave plasma CVD reactor (ASTeX PDS19 model) using CH₄-H₂ gas mixtures [17] under the following conditions: methane content of 3%, total flow rate of 1000 sccm, pressure of 80 Torr, microwave power of 3.5 kW, substrate temperature 730°C. The thickness of the film on a flat part of the substrate surface beyond the whisker array was about 50 μ m. Then, the upper part of the diamond film has been removed by grinding till the tips of the Si whiskers appeared on the surface. Finally, the silicon (both whiskers and substrate) has been etched away in hydrofluoric-nitric acid mixture to obtain the free-standing diamond film with through holes replicating the whiskers.

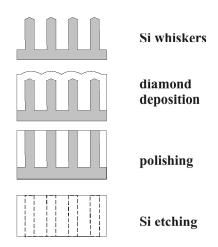


Figure 1. The process of making deep holes in CVD diamond using a template with Si whiskers.

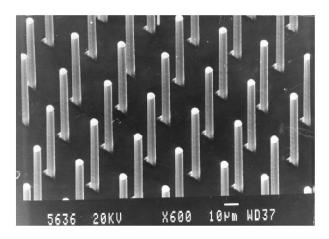


Figure 2. Regular Si whiskers forming a 2D array with period of 32 μm.

RESULTS

Figure 3 shows a SEM picture of as-grown diamond film as viewed from the top. The space between the whiskers has been almost completely filled with diamond as the inspection of sample cross-section revealed. Raman spectra confirmed the diamond to be of good quality, no signatures of amorphous carbon or graphite inclusions was found in the spectra. The diamonds on the very top of the whiskers form a regular array, they look like single crystals (yet, with a significant number of penetration twins on the facets) rather than the polycrystalline material. The size of those top crystals is a factor of two larger compared to the diamond grain size on the flat area. This may be due to a thermal runaway at the whisker apex immersed into the plasma during deposition process because of

restricted heat conduction there, so the nucleation density on the tip could be strongly reduced if the seeds were burnt-off in the hydrogen plasma.

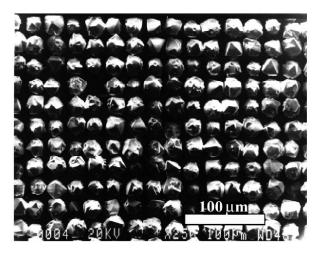
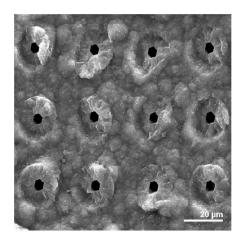


Figure 3. SEM picture of diamond film grown on Si whiskers (top view).

After crude mechanical polishing of diamond film and removal of the silicon an array of six-sided through holes has been produced (Fig. 4). The hexagonal shape of the holes replicates the facets of original Si whiskers. The sidewalls of the holes are very smooth and hole diameter is almost constant over the whole depth, that is the advantages of the method. The diamond film thickness after grinding was somewhat lower but close to the whisker height, so the hole aspect ratio is about 25 in this case. Aspect ratio as high as 50 was achieved was using whiskers of 2 µm diameter. The position, diameter and height of the whiskers and, consequently of the holes, can be varied in a broad range. The holes with much smaller diameter (a few tens nanometres) could be produced in a similar way by diamond growth on Si nanowhiskers as suggested by Dennig et al. [18]. On the other hand, the holes with large diameter (say, hundreds microns) can be produced on template with Si (or other materials, e.g. metals) columns prepared by a technique other than VLS.



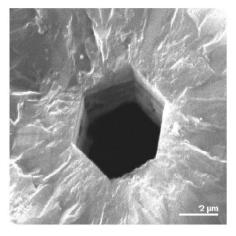


Figure 4. Hexagonal holes in diamond film (a); a single hole at higher magnification (b).

The CVD diamond films (plates) with the through channels could be used as drawing dies and membranes operated in aggressive media. The diamond films with the vias filled with a metal for interconnections can be used as effective heat spreaders in electronic circuits. The diamond with densely packed channels filled with an appropriate material would represent a novel type of composite material with interesting optical (as a photon crystal), thermal and electronic properties.

CONCLUSIONS

The method to fabricate micron-sized holes with very high aspect ratio in diamond films is described. This transfer molding technique involves CVD diamond growth on a template with Si whiskers followed by etching of the template. Regular arrays of parallel holes of 2 and 4 μm were produced. The direct growth of diamond components with built-in microchannels is an example a net-shape technology that allows a minimization of postgrowth diamond treatment.

ACKNOWLEDGEMENTS

The authors are thankful to S. Voronina for assistance in diamond deposition, and S. Lavrischev for SEM work.

REFERENCES

- 1. Ralchenko, V., and Pimenov, S., Processing of diamond, in Handbook of Industrial Diamonds and Diamond Films, ed. by M. Prelas et al., Marcel Dekker, New York, 1997, p. 983-1021.
- 2. Ralchenko, V.G., Pimenov, S.M., Kononenko, T.V., et al. Processing of CVD diamond with UV and green lasers, in Applications of Diamond Films and Related Materials: Third International Conference, ed. by A. Feldman et al., NIST Spec. Publ. 885, 1995, pp. 225-232.
- 3. Shikata, S., Nishibayashi, Y., Tomikawa, T., et al., Microfabrication technique for diamond devices, in M. Yoshikawa et al. (eds), Proc. 2nd Int. Conf. on the Applications of Diamond Films and Related Materials, MYU, Tokyo, 1993, pp. 377-380.
- 4. Migulin, V.V., Ralchenko, V.G., and Baik, Y.-J., Oxygen-assisted laser cutting and drilling of CVD diamond plates, in Lasers in Synthesis, Characterization and Processing of Diamond, V. Konov and V. Ralchenko, Editors, SPIE Proc. Vol. 3484 (1998) 175-179.
- 5. Kononenko, T.V., Kononenko, V.V., Konov, V.I., et al, Formation of antireflective surface structures on diamond films by laser patterning, Appl. Phys. A68 (1999) 99-102.
- 6. Honda, K., Rao, T.N., Tryk, D.A, et al., Electrochemical characterization of the nanoporous honeycomb diamond electrode as an electrical double-layer capacitor, J. Electrochem. Soc. 147 (2000) 659.
- 7. Ralchenko, V.G., Khomich, A.V., Baranov, A.V., et al., Fabrication of CVD diamond optics with antireflective surface structures, Physica Status Solidi (a) 174 (1999) 171-176.
- 8. Ralchenko, V., Khomich, A., Butvina, L., et al. CVD diamond optics with moth-eye antireflective surface structures produced by molding technique, New Diamond and Frontier Carbon Technology, 10 (2000) 109-119.
- 9. Okano, K., Hoshina, K., Ida, M., et al., Fabrication of diamond field emitter array, Appl. Phys. Lett. 64 (1994) 2742-2744.
- 10. Ralchenko, V., Schirone, L., Sotgiu, et al., Direct growth of diamond components, in J.L. Davidson et al. (eds), Proc. of the 6th Int. Symp. on Diamond Materials, The Electrochemical Soc., Pennington, N.J, Vol. 99-32, (2000) pp. 72-79.
- 11. Woerner, E., Wild, C., Mueller-Sebert, W., et al., CVD-diamond optical lenses, Diamond Relat. Mater., 10 (2001) 557-560.
- 12. Bjiorkman, H., Rangsten, P. and Hjort, K. Diamond microstructures for optical micro electromechanical systems, Sensors and Actuators, 78 (1999) 41-47.
- 13. Oesterschulze E., Scholz, W., Mihalcea, et al., Fabrication of small diamond tips for scanning probe microscopy, Appl. Phys. Lett., 70 (1997) 435-437.
- 14. Zakhidov, A.A., Baughman, R.H., Iqbal, Z., et al., Carbon structures with three-dimensional periodicity at optical wavelengths, Science, 282 (1998) 897-901.
- 15. Givargizov, E.I. Ultrasharp tips for field emission applications prepared by the vapor-liquid-solid growth technique, J. Vac. Sci. Technol., B11 (1993) 449-453.
- 16. Konov, V.I., Smolin, A.A., Ralchenko, V.G., et al., D.C. arc plasma deposition of smooth nanocrystalline diamond films, Diamond Relat. Mater., 4 (1995) 1073-1078.
- 17. Ralchenko, V.G., Smolin, A.A., Konov, V.I., et al., Large-area diamond deposition by microwave plasma, Diamond Relat. Mater., 6 (1997) 417-421.
- 18. Dennig, P.A., Liu, H.I., Stevenson, D.A., et al., Growth of single diamond crystallites around nanometer-scale silicon wires, Appl. Phys. Lett. 67 (1995) 909-911.

The growth of diamond films on porous anodic alumina*

Q.T. Wang^{1,2}, X.B. Niu^{1,2}, L. Yu^{1,2}, B. Xu^{1,2}, Y. Liao^{1,2} Q.X. Yu², G.Z. Wang^{1,2}, R.C. Fang²

Structure Research Laboratory, ²Department of Physics,

University of Science and Technology of China, Hefei, 230026, P.R.China

ABSTRACT

Chemical vapor deposition (CVD) diamond and Porous anodic alumina (PAA) are important materials that have been attracting great scientific and technologic interest. This is due mainly to the novel properties of each these materials and to possible applications in several areas. The searches for the improvement of these materials have naturally been made separately. It will evoke great effect on several future applications if such materials can be structured together.

PAA, which is formed by anodization of aluminum in acidic solution, is a typical self-ordered nanohole-array material. Its structure can be described as compact barrier layer directly attaching to aluminum substrate and located over it porous layer, made of a close-packed array of columnar cells, each containing fine, regular, almost cylindrical, parallel-sided, central axial pores.

Diamond is one of the most technologically advanced materials available today. It has a unique combination of excellent physical and chemical properties, which makes it ideal for numerous potential applications.

Diamond deposition on PAA was carried out in a hot filament chemical vapor deposition (HFCVD) system. PAA was used as substrate and tungsten wire as the filament. The conventional gas mixture of methane and hydrogen was used as the reaction source gas. The effects of deposition parameters on PAA are investigated.

The diamond/PAA composite were analyzed by Raman spectroscopy and the morphology was characterized by scanning electron microscopy (SEM), which are commonly used to identify the quality of diamond films. The results indicated that the homogeneous and dense diamond film could be obtained by HFCVD method on PAA.

^{*} Supported by National Natural Science Foundation of China and Anhui Province Natural Science Foundation.

^{**} Corresponding author: E-mail: liaoyuan@ustc.edu.cn; Tel.: +86-551-3607142.

SELF NUCLEATION OF DIAMOND ON ZEOLITE BY CHEMICAL VAPOR DEPOSTION METHOD

E.Titus, P.K.Tyagi, M.K.Singh and D.S.Misra@

Department of Physics, Indian Institute of Technology, Mumbai- 400076, India

A. K. Dua, and Mainak Roy

Novel Materials and Structural Chemistry Division, Bhabha Atomic Research Centre, Mumbai-400085, India

P.N.Joshi and M.V.Kasture

Catalysis Division National Chemical laboratory, Pune - 411 008, India

ABSTRACT

The nucleation stage of diamond in Chemical Vapor Deposition (CVD) is still not properly understood. Several methods were found by trial and error studies to initiate the formation of diamond nuclei on nondiamond substrates, very frequently on single crystal Si wafers. We have obtained first time, diamond nucleation on zeolite substrate with out any pretreatment. Diamond nucleation on zeolite substrate gives some insight into the nucleation mechanism. Depositions were carried out in a hot-filament chemical vapor deposition (HFCVD) apparatus. The HFCVD system was fed with a mixture of methane (0.8%) and balance hydrogen. A series of depositions were done in the pressure range 20-120 torr and at substrate temperature 880°C. The morphologies of the as-deposited films analyzed by scanning electron microscopy (SEM) show isolated diamond grains in the initial nucleation stages, develop into a micro porous films in the next stage and form a continuous film after long time deposition. The grainsizes (20-25microns) were uniform. Raman spectroscopy was used to investigate the crystal morphology, structure and non-diamond impurities in the films deposited at various growth conditions. The Raman spectra taken by focusing laser on single grain showed a single peak of diamond free from other non-diamond features. A single Lorentzian fit to the spectra revealed that the diamond peak is shifted towards higher wave numbers (1335 cm⁻¹) when compared to natural diamond (1332 cm⁻¹). This may be due to the compressive stress of diamond. The FWHM of the Raman peak is also quite high (~10.5 cm⁻¹) when compared to natural diamond (2cm⁻¹). A broad band corresponding to the graphite also appears ~1560 cm⁻¹ in addition to the diamond band in the spectrum taken on large area of the sample. The nature of the hydrogen bonding with sp^3 and sp^2 network and the quantitative analysis were done by Fourier transform infrared (FTIR) spectroscopy. We hope a detailed Transmission Electron Microscopy (TEM) analysis will give more information on nucleation mechanism. A substrate onto which diamond nucleation is not required may enable us to develop the films with uniform grain sizes and it can be used as microfilters. We have used different types of zeolites (HZSM-5, H-β, and NH,-Y) to study the effect of pore size on nucleation. Effect of pore size and Si/Al ratio on microstructure of diamond films will be reported.

@Corresponding author E-mail:nirdesh@phy.iitb.ac.in Tel.No.91 22 25767561 **ELECTRON PARAMAGNETIC RESONANCE · AN AID IN SOLVING TOPICAL**

PROBLEMS OF DIAMONDS

Tamara Artemevna Nachalna, Novikov N.V., Podzyrey G.A., Malogolovets V.G.

Institute for Superhard Materials of NAS of Ukraine

nachmal@ism.kiev.ua

Abstract

We have developed a nondestructive method for identification of diamonds of various origins, which is based

on analysis of the EPR data on impurities, defects, ferromagnetic inclusions, resistance of the

defect-and-impurity states of diamonds to external actions as well as on peculiarities of distribution, interaction,

relaxation and cross-relaxation of paramagnetic centers.

The suggested method allows a practically complete identification of the diamond sample, i.e., it answers the

following questions: is the crystal a natural or a synthetic diamond? Has it formed under static or dynamic

conditions? What is the degree of the development and activity of the sample surface? What ferromagnetic

materials are contained in the growth system (hence, a possible manufacturer)? Has been the test sample

subjected to an additional external action? etc.

We have considered some topical problems, in solving of which the developed method of identification

proved to be efficient (at: synthesis of diamond, exploration and development of new deposits, customs

examination, ascertainment of the authenticity of the museum displays,

sorting of diamonds, etc.)

Keywords: Diamond, EPR, Identification, Impurities, Defects

The corresponding author:

Tamara Artemovna Nachalna

Institute for Superhard Materials of NAS of Ukraine

Ukraine, 04074 Kyiv, Str. Avtozavodskaya, 2

Phone Number: +380 44 4688641

Fax Number: +380 44 4688632

E-mail address: nachmal@ism.kiev.ua

NANOCRYSTALLINE DIAMOND FILMS DEPOSITED BY MICROWAVE PLASMA CVD IN MIXTURES OF ARGON AND METHANE WITH AND WITHOUT HYDROGEN ADDITIVE

Y. K. Liu^{a, b}, Y. Tzeng^a, P.L. Tso^b, and I. N. Lin^c

^aAlabama Microelectronics Science and Technology Center, Auburn University, Alabama, USA ^bPower Mechanical Engineering, National Tsing-Hua University, Hsin-Chu, Taiwan, 300 R.O.C. ^cMaterials Science Center, National Tsing-Hua University, Hsin-Chu, Taiwan, 300 R.O.C.

ABSTRACT

Nanocrystalline diamond films were deposited on silicon by microwave plasmas in gas mixtures of 1% CH₄ + 99% Ar, and 1% CH₄ + 5% H₂ + 94% Ar. Raman scattering, average surface roughness, surface morphology, and electron field emission characteristics were examined and correlated. Nanodiamond films with average roughness of five to fifteen nanometers were deposited. Very smooth nanodiamond films have been deposited. Electron field emission currents from these nanodiamond films were very low even at an applied electric field of $20~V/\mu m$. Nanodiamond films deposited at a high gas pressure of 200~torr without hydrogen additive were found to emit a higher electron current than other nanodiamond specimens deposited at lower gas pressures or deposited in plasmas with hydrogen additive. Surface roughness including micron and submicron sized particles on the surface of the nanodiamond contributed to the higher electron field emission current. Smooth and micron sized particle-free nanodiamond films deposited in hydrogen-poor plasmas exhibited very small electron field emission current.

Keywords: nanodiamond, electron field emission, microwave plasma

INTRODUCTION

Smooth and thin nanocrystalline diamond films with nano-scale diamond grains possess many advantages over polycrystalline CVD diamond films with micron-scale diamond grains. Nanocrystalline diamond has been shown to exhibit good electron field emission characteristics [1-3]. Nanodiamond films incorporated with $\rm sp^2$ carbon and nitrogen dopant have also been shown to enhance electron field emission performance [4-7]. The effects of hydrogen additive and the correlation of Raman scattering characteristics and surface roughness with electron field emission characteristics for nanocrystalline diamond films deposited in gas mixtures of 1% $\rm CH_4$ diluted in argon with and without 5% $\rm H_2$ additive are reported.

EXPERIMENT

Diamond films were grown on <100> silicon substrates using an ASTeX 1.5 kW 2.45GHz microwave CVD reactor. Pre-mixed gases of 1%CH₄+Ar and 1%CH₄+5%H₂+Ar were used for the deposition. Before the nanodiamond growth, silicon was dipped into BOE (buffered hydrofluoric acid etchant) for 10 minutes to remove silicon dioxide. It was then scratched by 1/4 μm diamond paste followed by immersing in nanodiamond/methanol solution in an ultrasonic bath for 1 hour to improve the nucleation density. A dual-band (wavelength of 2.1 and 2.4 μm) optical pyrometer was used to measure the substrate temperature. The as-grown films were examined by Raman spectroscopy using a green laser at the wavelength of 514 nm. The Raman spectra are featured with five main bands and peaks located around 1131-1140, 1332-1333, 1347-1349, 1471-1477, 1545-1549 cm⁻¹, respectively. The band around 1140 cm⁻¹ has been assigned for nanodiamond [8-10], while the peak around 1332 cm⁻¹, and two broad bands centered around 1350 cm⁻¹ and 1550 cm⁻¹ were assigned for the diamond, the D-band and the G-band, respectively. L.C. Nistor and J.V. Landuyt, etc. [11] revealed the peak at 1488 cm⁻¹ and assigned it to disordered sp³ carbon. The signal of the fourth band in the range of 1471-1477cm⁻¹ increases with that for the nanodiamond peak at 1140 cm⁻¹.

Electron field emission was characterized using a diode structure with an anode-cathode spacing of 60μm. The nanodiamond samples served as the cathode and a tungsten rod of 0.2 cm diameter enclosed in a ceramic block was used as the anode. The applied electrical field was calculated by dividing the applied voltage by the gap spacing, i.e., E=V/d, where V is applied voltage and d is 60μm for the experimental setup. The emitted current and applied

voltage were measured and recorded by means of a computer for further analysis. The surface roughness of nanodiamond films were measured by a α -step profiler.

RESULTS AND DISCUSSION

Figure 1 shows the Raman spectra of nanodiamond films deposited at different gas pressures with or without hydrogen additive in 1 % methane diluted by argon. At the same microwave power level, for both cases with and without hydrogen additive, the gas pressure played an important role in affecting the Raman characteristics of the nanodiamond films. The G-band Raman scattering signal for both cases decreased with increasing gas pressure indicating more phase pure diamond films. With the addition of hydrogen, the nanodiamond signal in the range of 1131-1140 cm⁻¹ became stronger under the experimental conditions studied in this work. Because the easiness for the gas mixture of 1%CH₄/Ar without hydrogen additive to have an electrical breakdown by a fixed microwave power, the microwave plasma ball was more difficult to be stabilized around the substrate as compared to that in the gas mixture of 1%CH₄/Ar with 5% hydrogen additive. Hydrogen additive raised the substrate temperature significantly compared to that without hydrogen additive at the same microwave power level. By either increasing the gas pressure or reducing the microwave power the plasma ball for the gas mixture without hydrogen could be lowered inside the reactor chamber and became closer to the substrate. However, without an adequate microwave power or when the gas flow rate was too high for a fixed microwave power, orange-color flame-like plasma was formed close to the edge of the substrate holder resulting in the coating of a lot of soot.

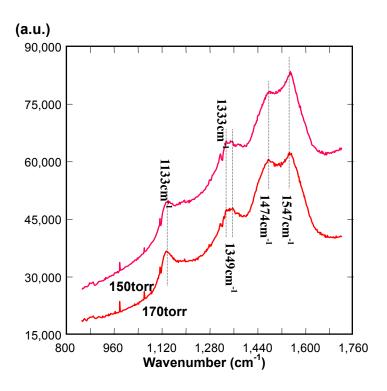
Figure 2 and 3 show the current-electric field (I-E) characteristics of nanodiamond thin films. Nanodiamond films grown at lower pressures at the same microwave power level appeared to exhibit lower turn-on electrical fields for electron field emission. This is correlated with stronger G-band signals shown in the Raman spectra of Figure 1 [4-5]. Nanodiamond films grown with hydrogen additive exhibited a lower electron field emission current than that grown without hydrogen additive. Nanodiamond films grown at high pressures without hydrogen additive showed the best electron field emission current among these specimens.

The average surface roughness for nanodiamond films grown with hydrogen additive was measured to be 11 nm and 14.8 nm for specimens deposited at 150 torr and 170 torr, respectively, at 800 W microwave power. Nanodiamond films grown at a lower pressure at the same microwave power have smoother surfaces. The same trend applies to nanodiamond films grown without hydrogen additive. The average surface roughness for nanodiamond films grown without hydrogen additive was measured to be 5.4 nm and 15.3 nm for specimens deposited at 120 torr and 200 torr, respectively, at 550 W microwave power. Smoother nanodiamond films deposited at lower gas pressures appeared to start to emit electrons at lower electric fields; but, the electron field emission current was lower, too. For example, the smoothest specimen with an average surface roughness of 5.4 nm emitted only 3 x 10^{-9} A at 20 V/ μ m electric field while the specimen deposited at a higher gas pressure with a surface roughness of 15.3 nm emitted 3 x 10^{-6} A at 20 V/ μ m electric field. The average surface roughness, alone, can not explain the differences in electron field emission current because specimens deposited with hydrogen additive also have 11-15 nm average surface roughness while the electron emission currents are only 1 x 10^{-8} A and 1 x 10^{-9} A for specimens deposited at 150 torr and 170 torr, respectively, at 800 W microwave power.

The nanodiamond films have resistance across the film from the surface of the film to the back side of the silicon about 1 $M\Omega$ for a surface area with a diameter of 0.2 cm, which is the diameter of the anode for electron field emission measurements. Although the resistivity of the nanodiamond films deposited in hydrogen-poor plasmas are high, the voltage drop across the nanodiamond film and the substrate contributed to less than 0.1% of the applied voltage. The high resistivity of the nanodiamond films is therefore not the cause of the low electron field emission current measured for these specimens.

With 5% hydrogen additive, the plasma is still hydrogen poor compared to the standard diamond CVD process in 1% methane diluted by 99% hydrogen. Nanodiamond films deposited in hydrogen-poor plasmas do not have hydrogen-terminated surfaces with a negative electron affinity. Although the specimens deposited with hydrogen additive showed stronger nanodiamond Raman signals than that without hydrogen additive, the best performing nanodiamond specimen among these four is the one deposited without hydrogen additive at a high pressure of 200 torr with a surface roughness of 15.3 nm as shown in Figure 3b.

Careful examination of the surface morphology of these four specimens, shown in Figure 4, indicated that the nanodiamond specimen with the highest (but still very small in the micro-amp range) electron field emission current has particles that are visible under 1,000 times magnification by a Normarski phase contrast optical microscope. The nanodiamond specimens with much lower electron field emission currents have no or few particles of the same sizes. The field enhancement provided by these particles is believed to result in the higher electron field emission



(a) $1\% \text{ CH}_4 + 5\% \text{ H}_2 + 94\% \text{ Ar}$

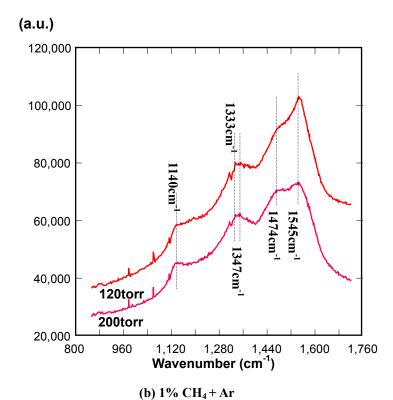


Figure 1. Raman spectra for nanodiamond films. (a) with hydrogen additive, (b) without hydrogen additive.

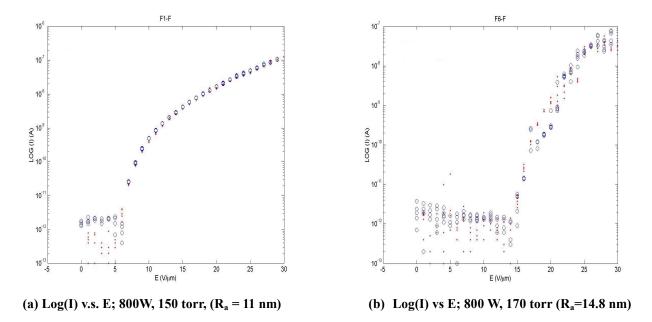


Figure 2. I-E curves for nanodiamond films grown in a gas mixture of 1% CH₄ + 5% H₂ + 94% Ar. The circled curves are for increasing electric field with time while the dotted curves are for decreasing electric field. (a) Power = 800 W, Gas pressure = 150 torr, Gas flow rate = 10 sccm, Substrate temperature = 680° C, Surface Roughness R_a = 11 nm. (b) Power = 800 W, Gas pressure = 170 torr, Gas flow rate = 10 sccm, Substrate temperature = 736° C, Surface roughness R_a = 14.8 nm.

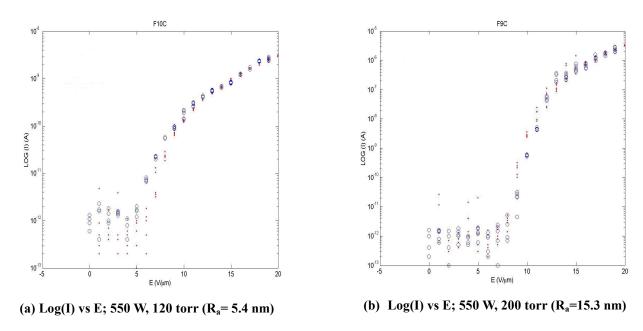


Figure 3. I-E curves for nanodiamond films grown in 1% CH₄+99% Ar. The circled curves are for increasing electric field with time while the dotted curves are for decreasing electric field. (a) Power = 550 W, Gas pressure = 120 torr, Gas flow rate = 5 sccm, Substrate temperature = 550° C, Surface roughness R_a = 5.4 nm. (b) Power = 550 W, Gas pressure = 200 torr, Gas flow rate = 5 sccm, Substrate temperature = 660° C, Surface roughness R_a = 15.3 nm.

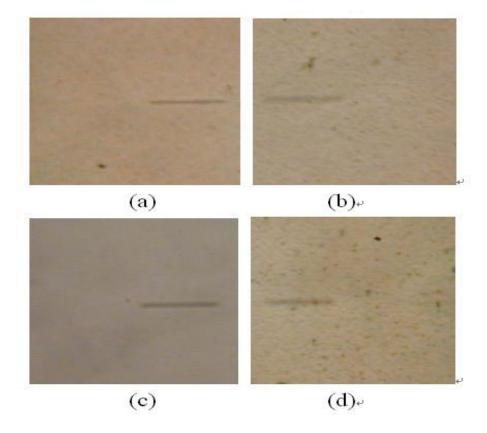


Figure 4. Normarski phase contrast optical microscope images of nanodiamond films. The images (a), (b), (c), and (d) correspond to the nanodiamond films presented in Figure 2 (a), Figure 2 (b), Figure 3 (a), and Figure 3 (b), respectively. The dark markers shown in each image are 10 µm long.

current. These particles were formed under the conditions of a high gas pressure of 200 torr without hydrogen additive. Under these conditions, gas-phase synthesis of non-diamond particles that subsequently get deposited onto the surface of the substrate can not be neglected. This is consistent with the appearance of orange-color flame-like plasma near the edge of the interface between the green plasma ball and the substrate.

CONCLUSIONS

Nanodiamond films deposited by microwave plasmas in gas mixtures of 1% CH₄ + 5%H₂ + 94% Ar and 1% CH₄ + 99% Ar exhibited electron field emission current characteristics that were correlated with Raman spectra, average surface roughness, and surface morphology. Electron field emission current was measured to be very low for our nanodiamond specimens that had smooth surfaces and showed Raman scattering bands and peaks similar to the ones reported in this paper. For each gas mixture and substrate temperature, the microwave power, gas flow rate, and gas pressure were among the most important parameters for determining the surface roughness and electron field emission characteristics of the nanodiamond films. At low gas pressures, the C_2 concentration is low and sp^2 carbon may grow get incorporated into the nanodiamond films. For a fixed microwave power and gas flow rate, when the gas pressure is too high, synthesis of non-diamond particles in the gas phase including soot may occur leading to the appearance of sub-micron-size particles that are embedded in the nanodiamond films. The nanodiamond film grown at a relatively high pressure of 200 torr without hydrogen additive showed the highest (but still very small) electron field emission current among these specimens. The possible formation of non-diamond carbon particles in the gas phase when the nanodiamond films were deposited at high pressures in 1%CH₄+99%Ar without hydrogen additive resulted in non-homogeneous surface roughness that increased local field enhancement in favor of electron field emission.

REFERENCE

- S.G. Wang, Q. Zhang, S.F. Yoon, J. Ahn, Q. Wang, Q.Zhou and D.J. Yang, J. Vac. Sci. Technol. B20(2002), pp. 1982-1986.
- [2] D. Zhou, A.R. Krauss, L.C. Qin, T.G. McCauley and D.M. Gruen, J. Appl. Phys. 82 (1997), pp. 4546-4550.
- [3] D.M. Gruen, Annu. Rev. Mater. Sci. 29 (1999), pp. 211-259.
- [4] K.H. Park, S. Lee, K.H. Song, J.I. Park, K.J. Park, S.Y. Han, S.J. Na, N.Y. Lee and K.H. Koh, J. Vac. Sci. Technol. B16 (1998), pp. 724-728.
- [5] W.P. Kang, A. Wisitsora-at, J. L. Davidson, D.V. Kerns, Q. Li, J.F. Xu and C.K. Kim, J. Vac. Sci. Technol. B16(1998), pp. 684-688.
- [6] K. Wu, E.G. Wang, J. Chen and N. S. Xu, J. Vac. Sci. Technol. B17 (1999), pp. 1059-1063.
- [7] T.D. Corrigan, D.M. Gruen, A.R. Krauss, P. Zapol and R.P.H. Chang, Diamond and Related Materials, 11(2002), pp. 43-48.
- [8] R. B. Jackman, J. Beckman and J. S. Foord, Diamond and Related Materials 4 (1995), pp. 735-739.
- [9] R. E. Shroder, R. J. Nemanich and J. T. Glass, Physical Review B, V.41 No. 6 (1990), pp. 3738-3745.
- [10] S. M. Leeds, T. J. Davis, P. W. May, C. D. O. Pickard and M. N. R. Ashfold, Diamond and Related Materials, 7(1998), pp. 233-237.
- [11] L.C. Nistor, J.V. Landuyt, V.G. Ralchenko, E.D. Obraztsova and A.A. Smolin, Diamond Related Materials, 6 (1997), pp. 159-168.

NOVEL DIAMOND CONE ARRAYS: SINGLE CRYSTALLINE AND NANOCRYSTALLINE

Y. Wu, W.J. Zhang, C.Y. Chan, X.M. Meng, W.K. Wong, I. Bello*, Y. Lifshitz, and S.T. Lee

Center of Super-Diamond and Advanced Films (COSDAF) and Department of Physics and Materials Science, City University of Hong Kong, Hong Kong, P.R.China

ABSTRACT

We have developed a new method for fabricating uniform arrays of single crystal diamond and nanodiamond cones with a very high aspect ratio over large areas using a microwave plasma chemical vapor deposition system. The fabrication of diamond nanocones consists of: i) deposition of diamond films which serve as base materials and ii) subsequent bias-assisted reactive ion etching in hydrogen plasma. In this two-step process [001]—oriented diamond films are converted to very sharp diamond cones with an apical angle of 28° and a tip radius as small as 5 nm. Each cone was identified by TEM as a single crystalline diamond with its [001] axis perpendicular to the substrate surface. Alternatively, when nanodiamond films are used as starting materials for reactive etching by hydrogen plasma, arrays of cones composed of nanodiamond are fabricated. The nanodiamond cones show exceptional electron field emission properties, particularly emission durability and stability compared to single crystalline cones.

Keywords: Single crystal diamond, nanodiamond, CVD deposition, reactive etching

* Corresponding author: apibello@cityu.edu.hk

A DC HF CVD process to grow films of aligned carbon nanotubes. Applications to field emission.

F. LE NORMAND, COJOCARU

CNRS STRASBOURG FRANCE

francois.le-normand@ipcms.u-strasbg.fr

Abstract

A DC HF CVD process to grow films of aligned carbon nanotubes. Applications to field emission. We will describe a new DirectCurrent Hot Filament Catalytic CVD process (DC HF CCVD) that is quite convenient to grow films of aligned carbon nanotubes with a high selectivity. The process is designed in a ultra high vacuum chamber directly connected to a surface analysis chamber provided with XPS AES ELS probes for determination of the carbon nature and surface cleaning and deposition tools (ion beam thermal vacuum evaporation.

CO-DOPING OF DIAMOND WITH BORON AND SULFUR

Li Rongbin, Hu Xiaojun, Shen Hesheng, He Xianchang

State Key Lab of MMCM's, Shanghai Jiaotong University, Shanghai 200030, China

ABSTRACT

Sulfur incorporation in diamond was performed by B-S co-doping method via microwave plasma chemical vapour deposition (MPCVD) technique on undoped Si as substrates. Dimethyl disulfide and boron oxide were the doping sources, which were diluted in acetone. Auger electron spectra (AES) confirmed the presence of sulfur in the films. Scanning electron microscopy (SEM), X-ray diffraction (XRD) as well as Raman scattering spectroscopy were employed to characterize the as-grown films. It was found that limit amounts of boron facilitated sulfur incorporation into diamond. The activation energy of B/S co-doped diamond films is 0.39 eV. SEM observations showed that the crystal quality of these films increases with increasing S incorporation. The observed Fourier transform infrared (FTIR) supported the existence of C, S and B bonding in the films. Even with S incorporation levels of 0.15%, measurements of films resistivity showed that the films had significant high resistance. This might reflect the defects in these polycrystalline films which could act as compensating acceptors, soaking up the donated electrons from the S.

Keywords: co-doping, CVD, diamond, boron, sulfur

NANOCRYSTALLINE DIAMOND FILM ON LARGE AREA GLASS SUBSTRATE

K. Tsugawa, M. Shelby, H. Yoshikawa

Joint Research Consortium of Frontier Carbon Technology (FCT), Japan Fine Ceramics Center (JFCC), c/o Research Center for Advanced Carbon Materials, National Institute of Advanced Science and Technology (AIST) Tsukuba Central 5, 1-1-1 Higashi, Tsukuba, Ibaraki 305-8565, Japan

M. Ishikawa

Graduate School of Science and Engineering, Ibaraki University, 4-12-1 Nakanarusawachyo, Hitachi, Ibaraki 316-8511, Japan

M. Liehr

Applied Films GmbH & Co KG, Siemensstr. 100, D-63755 Alzenau, Germany

Y. Koga

⁵Research Center for Advanced Carbon Materials, AIST Tsukuba Central 5, 1-1-1 Higashi, Tsukuba, Ibaraki 305-8565, Japan

ABSTRACT

A high quality, transparent, smooth nanocrystalline diamond film was successfully grown on a Pyrex glass substrate by the microwave plasma chemical vapor deposition (MWPCVD) method. The deposition was carried out using a CH_4/H_2 plasma maintaining the substrate temperature at as low as 500 °C. The films are smooth and reasonably uniform over an area of 30×30 cm² and exhibit strong adhesion to the glass substrate. UV Raman spectroscopy (244 nm excitation wavelength) shows a high quality diamond film by the sharp peak at 1333 cm⁻¹. X-ray diffraction analysis indicates that the film consists of nanocrystal diamond, i. e., the crystallites ranged in size from 10 to 20 nm. The transmittance for visible light of a film with a thickness of approximately 1 μ m is 55 % at a wavelength of 500 nm and is greater for higher wavelength, reaching 80 % at 766 nm. This high transmittance in the visible light region makes it possible to coat glass windows with diamond film for use in abrasive or other extreme environments, possibly replacing the more expensive materials currently in use.

Keywords: diamond, nanocrystal, glass substrate, microwave plasma CVD

DIAMOND SYNTHESIS IN TEN MINUTES WITH CLOSED REACTION CHAMBER

Kaoru Gyoda , Yuki Tanaka, Kazuhiro Aoki and Yoshiki Takagi

Teikyo University of Science & Technology 2525 Uenohara-cho, Kitatsuru-gun, Yamanashi-pref., JAPAN takagi@ntu.ac.jp

ABSTRACT

Diamond particles were synthesized on Si single crystal substrate in ten minutes reaction time. Reaction chamber was cylindrical shaped with 150mm in diameter and 180mm in height. Our synthesizing method is basically same as conventional hot filament method. Liquid carbon source and hydrogen were introduced to the chamber. Substrate was heated up with tungsten filament radiation to 780 deg C in three minutes. Then temperature was kept for another seven minutes and then cooled down. We got many diamond particles on Si substrate sized from 1 micron up to 10 microns. We tried doping with nickel, phosphorous and boron.

Keywords: liquid carbon source, hot filament, CVD, diamond

INTRODUCTION

For few years, we had been concentrated on a development of completely closed diamond synthesizing system aimed for microgravity experiments. Recently we started the new method with graphite heater as carbon source. With this method, completely closed system is successfully performed. At the same time, we started other new method with liquid carbon sources. With this method, pseudo-closed system is performed. In this paper, experimental results with liquid carbon sources will be presented.

The conventional techniques for depositing diamond at low pressure utilize a flow of a hydrocarbon-hydrogen gas mixture [1] with complicated gas line to introduce reaction gas into a reaction chamber and evacuating reactant gas from it. Beside that, these techniques require a complicated method for generation of atomic hydrogen, such as a plasma [2], hot tungsten filament [3,4], or flame [5]. Therefore, these types of flow systems are considered to be impracticable for mounting on a spacecraft.

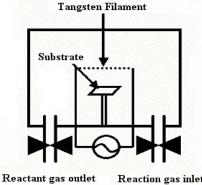
For few years, we had been concentrated on developing completely closed diamond synthesizing system aimed for microgravity conditions [6-9]. Recently we started the new method with graphite heater as carbon source [10,11]. With this method, completely closed system is successfully performed.

In-situ analysis of gaseous species in a reaction chamber by using gas chromatography and possible reaction model is reported elsewhere [12, 13]

EXPERIMENTAL

We used liquid carbon source, such as acetone, methanol and ethanol. One molecule of these three liquid carbon sources has 2, 1 and 2, methyl groups, respectively. So it is expected that diamond will be synthesized with relatively

low activation energy consumption.



eactant gas outlet Reaction gas inlet Fig 1 Reaction apparatus

Reaction apparatus is shown in Fig.1.Tungsten filament was set perpendicular to substrate on the center of the reaction chamber. After air was evacuated from the chamber, liquid carbon source was introduced on the chamber and vaporized to 10 Torr with room temperature, and then hydrogen gas was introduced until reached to 600 Torr in total pressure. After all valves were closed, filament heated up in three minutes then diamond synthesis was started. So this method can be called as a closed system. Temperature of filament was 2200 deg centigrade measured with the two-colored pyrometer (CHINO, Tokyo, Japan, model IR-AQ) through a silica glass window on the chamber. Substrate temperature was 780 deg C measured with K-type thermocouple attached to the substrate. Synthesizing time was seven minutes, distance between substrate and filament was 3.0 mm, and supplied electric power was 200W. Substrates were silicon single

crystal with p-type (100) with 10 x 30 mm² in size. Experimental apparatus, we used for this study, was shown and

explained elsewhere [14]. The chemical agents for second element doping were Ni(OH)₂, H₃BO₃ and H₃PO₄ for nickel, boron and phosphorus, respectively.

RESULTS AND DISCUSSON

Synthesized from acetone

Figure 2 shows SEM photographs of particles synthesized in ten minutes from acetone. The diameters of particles were about 0.5-1 micrometers. The shapes of particles were spherical. (111) planes were not observed on particle surfaces.

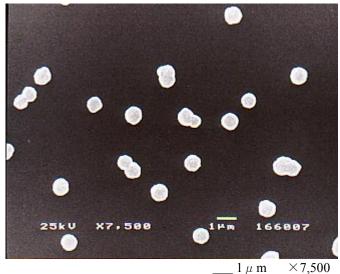


Figure 2. Synthesized from acetone

Synthesized from ethanol

Figure 3 shows SEM photographs of particles synthesized in ten minutes from ethanol. The diameters of particles were about 0.5-1.5 micrometers. (111) planes were observed on many particles.

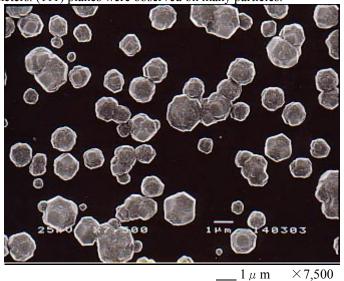


Figure 3. Synthesized from ethanol

Figure 4 shows minima and maxima of particle size. Sizes of particle synthesized from ethanol are larger than that from acetone.

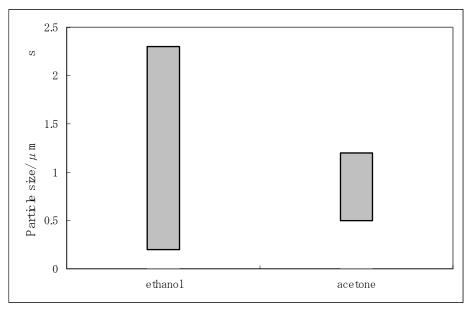


Figure 4. Sizes of particles, Synthesized from acetone and ethanol

Raman spectra

Figure 5 shows the Raman spectra for samples synthesized from acetone and ethanol. With table 1, both peaks had almost same values in $\sim 1333~\rm cm^{-1}$, on the contrary, FWHM for acetone is larger than for ethanol. Broad peaks around 1550 cm-1 from graphite were observed on both spectra.

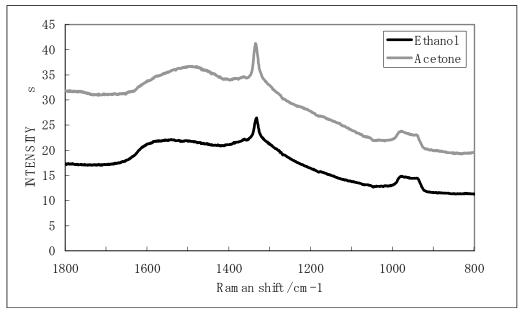


Figure 5.Raman spectra

Table 1.Result of Raman spectra

	Ethanol	Acetone
A peak value/cm ⁻¹	1332	1335
FWHM /cm ⁻¹	11. 13	11. 68
INTENSITY	26. 44	41. 26

With these results, we confirmed that diamond particles were synthesized from ethanol and acetone in ten minutes, successfully. We tried to synthesize diamond from methanol, but failed with some reasons, by now.

We tried doping of the second elements on diamond particles from ethanol.

Nickel doping

Typical diamonds particles obtained on the substrate was shown in figure 6. The diameters of particles were about 1.5-2.5 micrometers. (111) planes were observed on particle surfaces. All particles have diamond shaped clear surfaces.



Figure 6. Nickel doped

Boron doping

Figure 7 shows SEM photographs of particles synthesized from boron doping. The diameters of particles were about 0.1-0.4 micrometers. Particle sizes were too small for confirmation of plane direction. Particles were observed on the small part of the substrate.

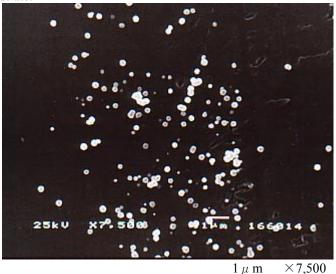


Figure 7. Boron doped

Phosphorus doping

Figure 8 shows SEM photographs of particles synthesized from phosphorus doping. (100) planes were observed on particle surfaces. The diameters of particles were about 0.2-1.8 micrometers.

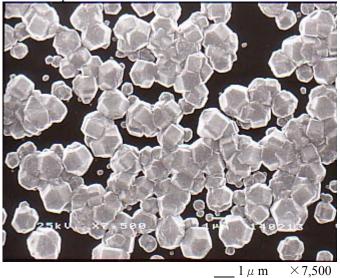


Figure 8. Phosphorus doped

Figure 9 show minima and maxima of particle size. Particle sizes were under the influence of second element doping, positive from nickel, negative from boron and none from phosphorus.

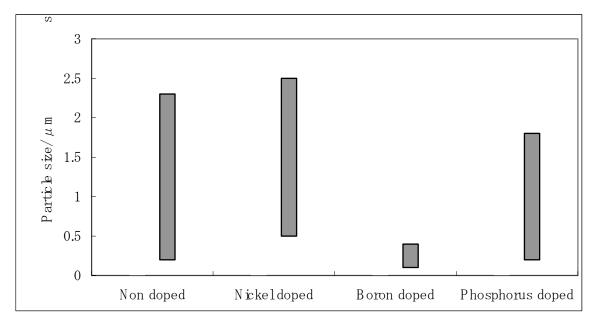


Figure 9. Sizes of particles, Synthesized from non doped, nickel doped, boron doped and phosphorus.

Raman spectra

Figure 10 shows the Raman spectra of samples synthesized from ethanol, non doped, nickel doped, boron doped and phosphorus. With table 2, all four peaks had almost same values in ~1333 cm⁻¹, on the contrary, FWHM for synthesized from phosphorus doping had the larger width compared with others. Broad peaks around 1550 cm⁻¹ from graphite were observed from all four spectra.

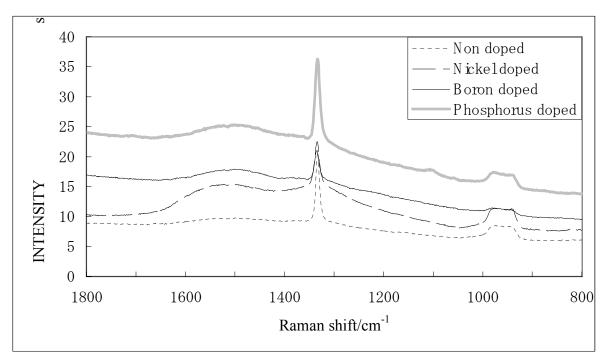


Figure 10.Raman spectra

Table 2.Result of Raman spectra

	Non doped	Nickel doped	Boron doped	Phosphorus doped
A peak value/cm ⁻¹	1332	1335	1335	1334
FWHM /cm ⁻¹	11.13	11.35	10.13	12.56
INTENSITY	26.44	22.49	21.02	36.71

CONCLUSIONS

From the results of experiments, we successfully synthesized diamond with shorter experimental time and lower energy consumption compared with conventional methods.

With the second element doping, we observed the better particle shapes from SEM photographs and stronger peaks from Raman spectra. Especially, with phosphorus doping and nickel doping, higher crystal growth rate and larger coverage were confirmed. More than this, with higher growth rate, graphite phase was synthesized simultaneously with diamond and not decomposed with hydrogen radicals completely. Graphite phase were observed on Raman spectra for doped samples.

REFERENCES

- [1] J. C. Angus, H. A. Will and W. S. Stanko: Journal of Applied Physics 39, 2915 (1968)
- [2] M. Kamo, Y. Sato, S. Matsumoto, H. Setaka: Journal of Crystal Growth 62, 642 (1983)
- [3] S. Matsumoto, Y. Sato, M. Tsutsui, and N. Setaka: Journal of Materials Science. 17, 3106 (1982)
- [4] Y. Hirose and Y. Terasawa: Japanese Journal of Applied Physics. 25, L519 (1986)
- [5] Y. Hirose: Proceeding of 1st International Conference for New Diamond Science and Technology P.51, KTK Terra Publish. (Tokyo, 1988)
- [6] Y. Takagi, S. Sato, K. Kaigawa, A. B. Sawaoka and L. L. Regel: Microgravity Quaterly, 2(1), 39-42 (1992)
- [7] S. Sato, K. Kaigawa, Y. Takagi, Y. Hirose and A. B. Sawaoka: *Journal of the Japan Society of Microgravity Application* **10**(1), 38-45 (1993)
- [8] Y. Tanabe, K. Kaigawa, Y. Takagi and A. B. Sawaoka: *Journal of the Japan Society of Microgravity Application* 11(2), 71-79 (1994)
- [9] Y. Takagi, K. Hibiya and H. Takeuchi: *Journal of the Japan Society of Microgravity Application* 13(4), 225-233 (1996)
- [10] Y. Takagi, L. L. Regel and W. R. Wilcox: *Transaction of the Materials Research Society of Japan* **24**(4), 513-518 (1999)
- [11] Y. Takagi, L. L. Regel and W. R. Wilcox: Journal of the Japan Society of Microgravity Application 15(3), 140-145 (1998)
- [12] Y. Takagi, M. Suzuki, H. Abe and Y. Inatomi: *Journal of the Japan Society of Microgravity Application* 17(3), 159-165 (2000)
- [13] Mayu Uede and Yoshiki Takagi: J. mater. Res., 16,(11) 3069 (2001)
- [14] F. Onishi, R. Hayashi, Y. Takagi, Mat. Res. Soc. Proc. Vol.672 2001 Materials Research Society, O8.13.1

FREQUENCY-DEPENDENCE OF PULSED BIAS-ENHANCED NUCLEATION OF DIAMOND ON (100) SILICON

F. Okuzumi and Z. Sitar

Department of Materials Science and Engineering, North Carolina State University, Raleigh, NC 27695, U.S.A.

S.D. Wolter and J.T. Prater

U.S. Army Research Office, Research Triangle Park, NC 27709-2211, U.S.A.

ABSTRACT

Bias-enhanced nucleation (BEN) is a technique whereby energetic substrate bombardment of ionized species has a profound effect on the promotion of diamond nucleation. Ion subplantation and enhanced surface mobilities of carbonaceous species have been proposed to explain the high nucleation densities as well as epitaxial diamond formed on pristine silicon and SiC.

We have studied pulsed BEN to improve upon earlier results of *dc*-BEN on epitaxial diamond formation and to better understand the dynamics of the plasma sheath region and its effects on bias-enhanced nucleated diamond. Pulsed BEN was performed on (100) silicon substrates using a 17% duty cycle and varying bias frequency in the range of 1 Hz to 2 kHz. We observed a constant proportion of highly oriented diamond of 50% as a function of this relatively low bias frequency range; the transit time of ions through the plasma sheath would be subject to essentially freezing-out only at frequencies on the order of megahertz. A linear increase in bias current with bias frequency, and correspondingly, a linear decrease in the bias duration required to form a quasi-continuous film of diamond was observed.

Keywords: Bias enhanced nucleation, highly oriented diamond, epitaxial diamond, bias frequency

INTRODUCTION

Bias enhanced nucleation has led to significant breakthroughs in diamond thin film research and development efforts. A dramatic enhancement of nucleation density has been observed and argued to be a result of higher energetics of the impinging ions (ref.1) and/or an alteration to gaseous constituents above the substrate (ref. 2). Evidence suggests that these same processes may promote nucleation of highly oriented diamond when a suitable substrate is present. Stoner and Glass (ref. 3) report of textured diamond growth on (100) []-SiC provided evidence that a carbide of sufficient quality must be in existence for this favorable result. In a subsequent work by Wolter *et al.* (ref. 4), it was demonstrated that a carburization process, implemented prior to BEN, also led to highly oriented diamond on (100) silicon.

More recently, BEN studies that have applied an *ac* substrate bias (50-60 Hz) have revealed the feasibility of producing highly oriented diamond on (100) silicon as well (refs. 5 and 6). The *ac*-BEN studies have afforded new insights on the epitaxial nucleation process. This work leads invariably to the question of bias frequency effects on the diamond nucleation enhancement and the epitaxial growth. This paper reports on experimental observations of substrate bias frequency effects employing unipolar, pulsed BEN to nucleate epitaxial diamond on silicon.

EXPERIMENTAL

The (100) silicon substrates used in this investigation were single-side polished. The $2.5 \times 2.5 \text{ cm}^2$ wafers were cleaned in acetone and methanol, and thoroughly rinsed in de-ionized water. The samples were then placed on a molybdenum substrate holder and transferred to the growth chamber through a load-lock entry system. The growth was conducted in a microwave plasma chemical vapor deposition system using a $2.45 \text{ GHz ASTeX}^{TM}$ microwave power supply. Ultra-high purity methane and hydrogen were used as source gases; 5-25 ppm of ultra-high purity nitrogen was added to the source gases to control crystallite morphology.

The substrate holder mounted on a linear transfer rod, that was used to position the substrates within the growth chamber, was isolated from the ground potential to enable the application of a substrate bias. A frequency generator was used to produce square waveforms which were then amplified using a KepcoTM unipolar voltage amplifier. The bias voltage and effective bias current were monitored using an oscilloscope; the effective bias current

was measured as voltage drop across a 10 Ω resistor. Figure 1 shows a schematic representation of this diamond deposition system. Further details of this growth chamber and the substrate biasing set-up may be obtained elsewhere (ref. 6).

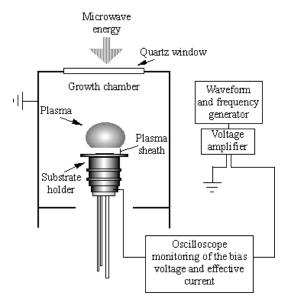


Figure 1. A schematic representation of the diamond deposition system and substrate biasing set-up.

A study was performed to investigate the influence of bias frequency on BEN of highly oriented diamond. In this work, a square waveform with a duty cycle of 17% was employed. A graphic representing 10 Hz and 100 Hz square waveform bias pulses, implementing the 17% duty cycle used in this study, is shown in Figure 2. This graphic exemplifies the differences of the pulse character that occurs with a change of only 1 decade in bias frequency. While the waveforms and total bias ON time of -250 V are identical, an important consideration is the duration of the bias pulses. This duty cycle was chosen after finding that it provided nearly identical results to that of the half- and full-sinusoidal biasing (performed at 50-60 Hz) and resulted in maximizing the percentage of oriented diamond while minimizing total bias duration (ref. 6).

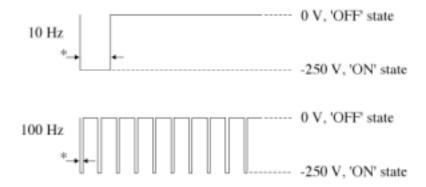


Figure 2. A graphic of the square waveform bias pulses of 10 Hz and 100 Hz at a 17% duty-cycle.

The bias frequencies evaluated in this study were 1, 10, 20, 30, 50, 60, 100, 200, 500, 1000, and 2000 Hz. Significant distortion in the waveform was observed above 2 kHz as a result of the voltage amplifier. Approximately 25 hrs of deposition time was undertaken following the substrate biasing experiments to enable the growth of diamond octahedra and to discern the relative proportion of oriented diamond. See Table I for further information regarding the process conditions used in these experiments.

The percentage of highly oriented diamond and the bias time required to nucleate a quasi-continuous film were the important criteria used to evaluate the effects of bias frequency. The latter criterion was ascertained by visually inspecting the substrate during biasing. From previous observation, the onset of film formation was evidenced by a

darkening of the substrate and was later confirmed by scanning electron microscopy (SEM; JEOL 6400f field emission scanning electron microscope) to be ~90% coalesced. SEM was performed following the nucleation and growth steps to provide a more detailed inspection of the diamond crystallites. A determination of the percentage of oriented crystallites was based on the application of lineal analysis using the SEM micrographs.

RESULTS AND DISCUSSION

It has been observed in previous work in this laboratory, that dc biasing alone (excluding a pre-carburization) is not adequate for the formation of highly oriented diamond on (100) silicon, although significantly enhanced nucleation densities of $\sim 10^{10}$ cm⁻² can be obtained (ref. 4). It was determined that only through the addition of a carburization step prior to the substrate biasing was it possible to obtain highly oriented diamond of an optimized $\sim 50\%$ crystallite density. By comparison, half-sinusoidal and full-sinusoidal substrate biasing has been shown to produce nearly 50% oriented diamond in the absence of a pre-carburization step. The similarities between that of half-wave and full-wave sinusoidal substrate biasing demonstrated that the positive portion of the cyclic waveform was not an important factor in this processing (ref. 7). Nearly identical results were obtained in regard to the overall nucleation density and oriented diamond fraction for both waveforms. This experimental outcome determined that the positive voltage portion of the sinusoidal waveform did not adversely influence this process nor did it enhance it. Consequently, the results obtained in the unipolar bias pulse experiments, used for the study of frequency effects on epitaxial diamond formation, should be directly related to these prior experiments.

Table I. A table of the process parameters for producing highly oriented diamond on (100) silicon using pulsed substrate biasing.

Parameters	Pulsed bias-enhanced nucleation	Diamond deposition
Substrate bias voltage: Pulse ON bias voltage Pulse OFF bias voltage	-250 volts 0 volts	Floating Floating
CH ₄ /H ₂ Pressure Microwave power Substrate temperature	2% 2000 Pa ~1100 Watts ~ 850°C	1% 3300 Pa ~700 Watts 730°C

The distinct differences between dc-BEN and ac-BEN have led the authors to speculate that a modification of the duty cycle would likely have an impact on the diamond nucleation process. Square waveforms of varying duty cycles were the focus of prior work by our group (ref. 7). These studies revealed a transition in waveform from true bias pulse characteristics to conditions similar to those in dc biasing. In all these experiments, the frequency was held constant at 60 Hz using a unipolar bias pulse of -250 V. This data revealed that the bias time required to form a quasi-continuous nucleation layer as well as the oriented diamond fraction were inversely proportional to the substrate bias duty cycle. As the duty cycle was increased, a hyperbolic decrease in bias time to film formation was observed from a duration of ~300 min and oriented diamond fraction of ~50% for a 3% duty cycle to a bias duration of ~20 min for film formation at a duty cycle of 75% with an oriented diamond percentage of only ~10%. Interestingly, the observation of reduced bias times and lower oriented diamond fractions at shorter duty cycles was similar to that observed in this laboratory for dc-BEN (when excluding a pre-carburization step). This indicated that the duty cycles previously studied effectively probed the transition from a dc-like character to attributes of pulsed biasing.

In contrast to the effect of duty cycle, a variation of the bias frequency at a constant duty cycle of 17% had little influence on oriented diamond formation. This is evident in Figure 3 revealing ~50% of the diamond crystallites to be oriented when implementing both 10 Hz and 100 Hz bias frequencies, and otherwise optimized process parameters. A semi-log plot of bias time to film formation as a function of bias frequency from 1 Hz to 2 kHz is shown in Figure 4. This plot represents a collection of data from several separate experiments. A linear decrease in the bias duration to film formation with frequency is evident and correlates with a linear increase in bias current. The plot in Figure 5 indicates the constant highly oriented diamond percentage with bias frequency. The oriented diamond percentage was nominally 45% throughout this entire frequency range.

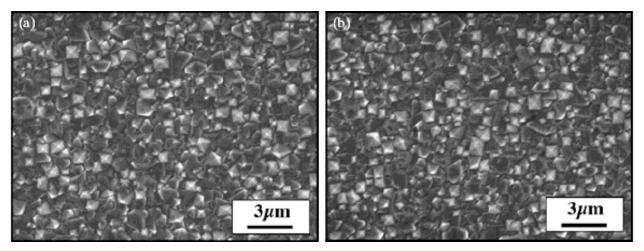


Figure 3. The scanning electron microscopy images of highly oriented diamond on (100) silicon formed from bias-enhanced nucleation using a square waveform bias (17% duty cycle) at (a) 10 Hz and (b) 100 Hz. The diamond was grown for 20 h following the substrate biasing experimentation.

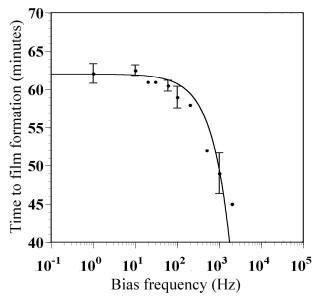


Figure 4. A semi-log plot of bias time to film formation versus duty cycle for bias frequencies of 1 Hz to 2 kHz. The data is fitted linearly and reveals a decrease in this quantity with frequency. (The error bars represent the standard deviation in oriented diamond fraction over different regions of the substrates.)

The lack of influence of bias frequency on epitaxial diamond formation may be anticipated considering the transit time of ions relevant to the nucleation process crossing the plasma sheath to the substrate (ref. 8). For low frequencies, the ions track the changing polarity of the periodic bias potential instantaneously. Even for the highest frequencies used in this study, there was more than enough time for the ionized constituents to traverse the approximately 1 cm thick plasma sheath observed in our growth system during biasing.

Although there was no change in the highly oriented diamond percentage as the frequency was varied from 1 Hz to 2 kHz, a linear decrease in the bias time to film formation was observed. This corresponded to a linear increase in the bias current, which reflects the rate of ionized species arriving at the substrate. The higher bias currents observed with increasing bias frequency translates into a greater flux of positively charged species to the substrate, which may explain the corresponding reduction in bias time to diamond film formation. To explain this observation, an experiment was consequently performed to probe the influence of higher frequency biasing when employing more moderate bias currents to match those of lower frequency biasing. Generally, a bias duration of ~45 min was necessary for diamond film formation performed at a bias frequency of ~2 kHz (as shown in Figure 4); a

corresponding bias current of ~400 mA (at a bias voltage of -250 V) was typically registered. However, when biasing at 2 kHz at a current of ~300 mA (current observed at []100 Hz), the bias duration for film formation was ~60 min, matching the results of the lower frequency biasing. In essence, one could obtain similar results across the entire frequency range of study by involving comparable bias currents.

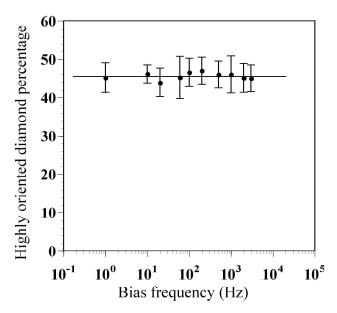


Figure 5. Plot of the percentage of highly oriented diamond versus bias frequency. The error bars represent the standard deviation in the data across different regions of the substrates.

CONCLUSIONS

This investigation indicated an upper limit of \sim 50% for the fraction of oriented diamond with substrate bias frequency in the frequency range of 1 Hz to 2 kHz for pulsed bias-enhanced nucleation. The pulsing action of the square waveform substrate bias (using a 17% duty cycle) was important for the formation of highly oriented diamond in the absence of a pre-carburization treatment. The bias frequency showed very little effect on influencing the formation of epitaxial diamond in this frequency range of study. However, a linear decrease in bias time to diamond film formation was observed with bias frequency.

ACKNOWLEDGEMENTS

We would like to acknowledge the funding for this research which was provided for by the US Army Research Office, grant number DAAG5598D0003.

REFERENCES

- 1. Yugo, S., T. Kanai, T. Kimura, and T. Muto, Appl. Phys. Lett. 58, 1036 (1991).
- 2. Stoner, B.R., G.H. Ma, S.D. Wolter, W. Zhu, Y.-C. Wang, R.F. Davis, and J.T. Glass, Diamond Relat. Mater. 2, 142 (1993).
- 3. Stoner, B.R. and J.T. Glass, Appl. Phys. Lett. 60, 698 (1992).
- Wolter, S.D., B.R. Stoner, J.T. Glass, P.J. Ellis, D.S. Buhaenko, C.E. Jenkins, and P. Southworth, Appl. Phys. Lett. 62, 1215 (1993).
- 5. Wolter, S.D., T.H. Borst, A. Vescan, and E. Kohn, Appl. Phys. Lett. 68, 3558 (1996).
- 6. Wolter, S.D., F. Okuzumi, J.T. Prater, and Z. Sitar, J. Electrochem. Soc. 149, G114 (2002).
- 7. Wolter, S.D., F. Okuzumi, J.T. Prater, and Z. Sitar, accepted for publication in Thin Solid Films.
- 8. Smith, D.L., "Thin-Film Deposition: Principles and Practice", McGraw-Hill, Inc., New York.

ACHIEVEMENT OF 10¹⁴[1/CM²] SURFACE HOLE CARRIER DENSITY ON DIAMOND FILM BY THE SULFUR HEXAFLURIDE INCORPORATED HYDROGEN PLASMA POST-TREATMENT

Go Ota, Takeshi Kobayashi

Department of Physical Science, Graduate school of Engineering Science, Osaka University,
Machikaneyama 1-3, Toyonaka, Osaka 560-8531, Japan.
Phone: +81-6-6850-6311, Fax: +81-6-6850-6341
*e-mail: ota@sup.ee.es.osaka-u.ac.jp
CREST, Japan Science and Technology Corporation (JST), Japan.

Sung-Hoon Kim

Department of Nano Materials Science & Engineering, Silla University, Busan 617-736, Korea

ABSTRACT

This paper deals with manipulation of the surface hole areal density of diamond films by a new treatment method. Our proposal is characterized by a post-treatment of as-grown diamond film surface in (H_2+SF_6) microwave plasma, where SF_6 incorporation was around 0.06 % or less. With increasing the treatment time up to 4 min, the surface resistivity changed from 5×10^5 [/] down to 4×10^2 [/] and, on the other hand, hole areal density increased from 2×10^{13} to $1-2 \times 10^{14}$ [1/cm²]. In addition, these values did not affected at all by the measurement atmospheres. With further increase in the treating-time, however, those electrical properties began to degrade. As to the role of (H_2+SF_6) plasma treatment of diamond film surface, a charge transfer model was given for explanation from chemiphysical point of view.

Keywords: diamond film, chemical vapor deposition, surface conductivity, sulfur hexafluoride, hydrogenation

INTRODUCTION

Since the Landstrass and Lavi's first report in 1989 (ref. 1), researches on the conductive layer induced by hydrogenation on diamond surface grown by CVD method have been widely practiced. It took only a few years to be reported that the career type, its surface density, and its mobility were p-type (ref. 2), around 50 [cm²/Vs], and about 10^{13} [1/cm²] (ref. 3, 4), respectively. This surface conduction is sensitive to a physical and chemical state of the surface. For example, the oxygen-termination deprives conductivity from the diamond surface, and the conductivity is restored when the film surface is exposed to the hydrogen plasma and fully hydrogenated (ref. 5, 6). In addition, this conductivity on hydrogen-terminated diamond film changes at several orders of magnitude in consequence of the change of surrounding gasses (ref. 7, 8). Owing to these unique properties, this surface conductive layer is utilized as MIS devices (ref. 9) or a gas sensor (ref. 10). In spite of these widespread researches, however, the hole density on the conductive layer itself still remains at the order of 10^{13} [cm²].

As we reported before, the deposition of CaF_2 at high temperature on oxygen-terminated diamond regenerates the surface conductivity (ref. 11, 12). This implies the availability of fluorine for the improvement of conductive property on Diamond surface. In this study, we first demonstrated that the surface treatment by the mixture of 0.06% of SF_6 and 99.94% of H_2 gas gave diamond surface more than 10^{14} [1/cm²] holes. This study implies the remarkable effect of an additional SF_6 gas mixture to hydrogen plasma during the terminating process to diamond surface.

EXPERIMENT

Polycrystalline diamond films used for the present experiments were deposited for 2 hours on an p-type silicon wafer by microwave plasma CVD (MPCVD) method under following conditions: 0.8% CH₄ in H₂, 100sccm of gas flow (40 Torr), 2.45GHz, 800W microwave power fed, and 800 substrate temperature. The deposited film was cut into smaller pieces. We here proposed a special treatment method used SF₆ plasma. The as-grown diamond film chips were exposed to the (0.06% SF₆ + 99.94% H₂) plasma generated by 2.45GHz, 400W microwave. The gas flow and total pressure was fixed at around 100sccm, 40Torr, respectively. This fluorination was accomplished in a quartz chamber. After the treatment, we measured the change of resistivity by the four-probe method, hole density and mobility by the hole effect measurement system, and observed surface morphology by the FE-SEM.

RESULT AND DISCUSSION

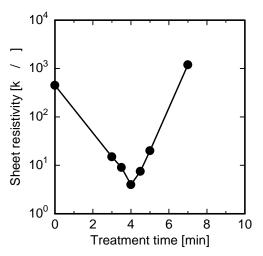
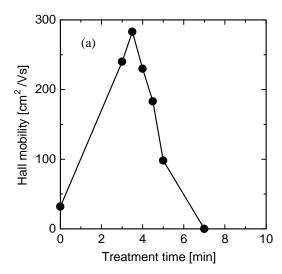


Fig. 1. Change of the sheet resistivity against the treatment time by SF_6+H_2

Figure.1 shows the resistivity of diamond film treated by the (SF₆ and H₂) plasma as a function of the treatment time. The resistivity markedly decreased with increasing treatment time up to 4 min. With further increase in time, the resistivity started to increase, on the contrary. In other words, one can say that SF₆ plasma treatment offers two sorts of surface manipulation. Firstly, a few minutes' treatment elevated the conductivity. With the four minutes treatment, the sheet resistivity decreased from 5×10^5 [/] to 4×10^2 [/]. Secondly, if the treatment lasts longer than 4 minutes, treatment effect appeared completely opposite. For instance, the sheet resistivity of a test specimen with seven minutes' treatment was about 10^6 [/], which is surprisingly larger than that of as-grown one. Moreover, the conductivity was missing in the piece with 13 minutes' treatment.

The decrease in the sheet resistivity is commonly a result of the improvement of either one of or both of carrier density and mobility. The results of Hall effect measurement are shown in Fig. 2. Here the value of sheet carrier density and mobility of



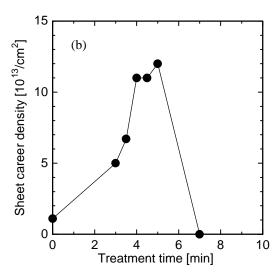


Fig. 2. Change of the sheet career density and Hall mobility against the treatment time by SF_6+H_2 plasma (a) sheet carrier density and (b) Hall mobility.

seven minutes' treated film is expressed as zero, which means the value was so low as to immeasurable and nonsignificant. Figure 2 shows that SF_6+H_2 gas increased both of the carrier density ten times from $1.2 \times 10^{13} [1/\text{cm}^2]$ to $1.2 \times 10^{14} [1/\text{cm}2]$ and mobility 100 times from 32 to 280. These two values also decreased with the more increase of the treatment time.

The surface conductive layer on Diamond film is reported to be sensitive to surrounding atmosphere (ref. 7, 8). For the evaluation of the sensitivity of SF₆+H₂ treated film to air condition, we flow HCl gas to the surface so that we decreased the pH of surrounding air. Nevertheless, the resistance did not change. Furthermore, the value showed no significant decrease after one month's preservation in air. This implies the remarkable stability of the treatment effect.

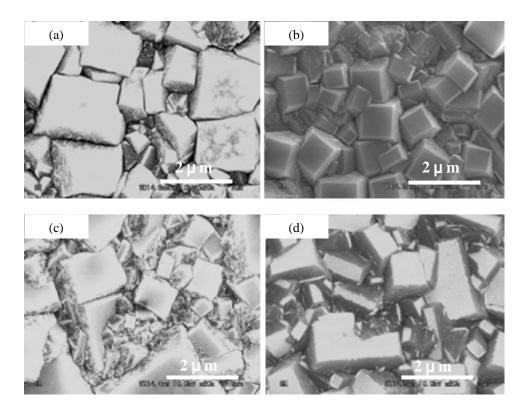


Fig. 3. FE-SEM images of SF_6+H_2 treated diamond surface. Treatment time is (a) 0 (before treatment), (b) 3 min., (c) 5min., and (d) 13min..

To understand why the electrical properties degrade for long time treatment, we observed the successive change of the surface morphology by the SF6 treatment. Figure 3 clearly shows the destruction of the consecutive film structure with grains via a long-term treatment. The square grains seen in Fig. 3(b), which has better sharpness than that in Fig.3 (a), no longer appeared in Fig. 3(d). Instead, rectangle grains broken edges were seen in Fig. 3(d). As Durrent et al. reported about CF₄ plasma treatment on diamond surface (ref. 13), fluorine may cause this change of the surface morphology. This change of morphology may cause the change of mobility shown in Fig. 2(b).

CONCLUSIONS

The effect of (H_2+SF_6) plasma treatment for diamond film surface was investigated. The diamond film resistivity, hole areal density and Hall mobility values showed clearly dependence on (SF_6+H_2) plasma treatment. Particular interest was found on the treatment time: For 0.06% of SF_6 and 400W microwave power, the film reached its minimum resistivity and highest hole density in excess of 10^{14}cm^{-2} at 4 min treatment, and over which it again increased to immeasurable range. The degradation of the morphological film structure by long term SF_6 treatment could be responsible to the increased resistivity.

REFERENCE

- 1 M.I.Landstrass and K.V.Ravi: Resistivity of chemical vapor deposited diamond films, Appl. Phys Lett. vol.55, no. 10, 1989, pp. 975-977
- 2 T.Maki, S.Shikama, et al.: Hydrogenation effect of single-crystal diamond surface, Jpn. Appl. Phys., vol. 31, no. 10A, 1992, pp. L1446-1449
- 3 H.J.Looi, R.B.Jackman, et al.: High carrier mobility in polycrystalline thin film diamond, Appl. Phys. Lett., vol. 72, 1998, pp. 353-355
- 4 N. Jiang and T. Ito: Electrical properties of surface conductive layers of homoepitaxial diamond films, J. Appl. Phys., vol.85, 1999, pp. 8267-8273
- 5 Y.Mori, Y.Show, et al.: Characterization of Surface Conductive Diamond Layer Grown by Microwave Plasma Chemical Vapor Deposition, Jpn. J. Apple. Phys., vol. 32, no.7B, 1992, pp. L987-L989
- 6 S.A.Grot, G.S.Gildenblat, et al: Effect of Surface Treatment on the Electrical Properties of Metal Contacts to Boron-Doped Homoepitaxial Diamond Films, IEEE Electron Device Lett. vol. 11, 1990, pp. 100-102
- 7 Ri S. Gi, T. Mizumasa, et al.: Formation Mechanism of p-Type Surface Conductive Layer on Deposited Diamond Films, Jpn. J. Appl. Phys. vol. 34, no. 10, 1995, pp. 5550-5555
- 8 F. Maier, M. Riedel, et al.: Origin of Surface Conductivity in Diamond, Phys. Rev. Lett. vol. 16, no. 16, 2000, pp. 3472-3475
- 9 Y.Yun, T.Maki, et al. Electrical properties of Al/CaF₂/I-diamond metal-insulator-semiconductor field-effect-transistor fabricated by ultra high vacuum process, Jpn. J. Appl. Phys., vol. 37, no. 11A, 1998, pp. L1293-L1296
- 10 Ri S. Gi, T. Ishikawa, et al: Possibility of Realizing a Gas Sensor Using Surface Conductive Layer on Diamond Films, Jpn. J. Appl. Phys. vol. 36, no. 4A, 1997, pp. 2057-2060
- 11 T. Kobayashi, Y. Yun, et al.: Stabilization of Diamond MIS-Interface by Employing CaF₂ Gate Insulator, Diamond Films and Technology, Vol. 6, 1997, pp. 379-392
- 12 T. Hosomi, K. Tsuji, et al: Surface conduction of diamond films induced by high-temperature CaF₂ deposition, New Diamond and Frontier Carbon Technology, vol. 11, 2001, pp. 325-329
- 13 F. Durrant, V. Baranauskas, et al.: Caracterization of diamond fluorinated by glow discharge plasma treatment, Diam. Rel. Mater. vol.10, 2001, pp .490-495

CHEMICAL VAPOR DEPOSITION OF DIAMOND FILM AT HIGH GAS PRESSURE BY USING PULSED DISCHARGE PLASMA

Mikio NODA

Physics section, Science Education, Aichi University of Education, Kariya, Aichi 448-8542, Japan. E-mail mnoda@auecc.aichi-edu.ac.jp

ABSTRACT

Formation of diamond films at gas pressure (Pg) higher than 300 Torr was succeeded by means of a new method of pulsed discharge plasma chemical vapor deposition (CVD). The pulsed discharge was performed by a pulse power supply fabricated by means of chopping the output of DC power supply with Intelligent Power Module (IPM) and elevating the voltage by a transformer. The switching time of the pulse was shortened to get high discharge beginning voltage, and discharge and non-discharge time in each period of the pulse were adjusted to get stable discharge at high Pg. The deposited films, investigated with scanning electron microscope and Raman spectroscopy, showed that the crystalline quality became superior and the deposition rate increased when Pg increased from 300 to 500 Torr. When a rod-shaped cathode was used against the substrate (anode), the plasma during the deposition was constricted to small diameter with increasing Pg. Emission intensities of H_{α} and H_{β} from the plasma, which were measured with a spectrometer and CCD array sensor, were also increased when Pg increased. By using this method using rod-shaped cathode, the diamond film could be deposited to small area at low substrate temperature.

Keywords: Diamond Film, Plasma CVD, Pulsed Discharge, High Gas Pressure, Low Substrate Temperature

1. INTRODUCTION

Diamond film prepared by plasma chemical vapor deposition (CVD) from vapor phase has excellent properties as well known, and it is desired to deposit the film with high deposition rate at low substrate temperature (Ts). The plasma CVD using intermittent or pulsed discharge instead of usual continuous discharge is an excellent method for improving the crystalline quality of the film and depositing at relatively low Ts. (refs. 1 to 8) The gas pressure (Pg) during the deposition of the diamond film by these CVD methods is usually around 150 or 200 Torr, and it has been reported that the crystalline quality and the deposition rate of the film are extremely improved with increasing Pg. (ref. 9) However, the discharge at Pg higher than about 300 Torr was difficult because the voltage to start the discharge became very high and the discharge came into arc discharge.

In this study, a new method using pulsed discharge was tried to make stable discharge at higher Pg, and deposition of the diamond films at Pg higher than 300 Torr was succeeded. The pulsed discharge was performed by a power supply fabricated by means of chopping the output of the DC power supply with Intelligent Power Module (IPM) and elevating the voltage by a transformer, as reported before. (refs. 3, 5 to 7) In the present experiments, however, the switching time of the pulse was shortened to get high discharge beginning voltage by means of improve the circuit and repair the parts, and the discharge and non-discharge times during each period of the pulse were adjusted to get stable discharge at high Pg.

The deposited films showed that the crystalline quality was improved and the deposition rate of the film increased when Pg increased from 300 to 500 Torr. Furthermore, it was found that the plasma during the deposition was constricted to small diameter with increasing Pg when a rod-shaped cathode was used against the substrate (anode). By using this phenomenon, the diamond film could be deposited to small area at low Ts.

2. EXPERIMENTAL METHOD

In the first, the film was deposited by CVD system using sub-electrode which is almost same as that reported before. (refs. 8 to 9) During this experiment, it was found that the plasma had tendency of constriction to small

diameter when Pg increased. Thereon, the second experiment, where a rod-shaped cathode was used instead of flatshaped cathode, was performed to make clear the phenomenon.

2.1 Sample preparation by CVD system using sub-electrode

Figure 1 shows a schematic diagram of the CVD system, where the sub-electrode is used. The detailed configuration and process were reported before. (ref. 8) After the chamber was pre-evacuated by rotary and turbo molecular pumps, CH_4 - H_2 gas mixture was supplied to the chamber. The gas pressure during the deposition was changed from 300 to 500 Torr, and the gas flow rate was 10 CCM. The CH_4 / $(CH_4$ + H_2) ratio, i.e. methane concentration, was 1%. A Si wafer chip about 5×5 mm in size was used as the substrate. The substrate was mounted on the substrate holder of about 10 mm in diameter after being scrubbed with diamond paste and rinsed with acetone in an ultrasonic cleaner. The substrate was heated so that the substrate temperature (Ts) measured by a radiation thermometer became 700°C. The deposition time of the samples was 2 hours. The distance between the cathode and the sub-electrode (L) was about 15 mm, and the distance between the cathode and the substrate (d) was about 20 mm, in the present experiments.

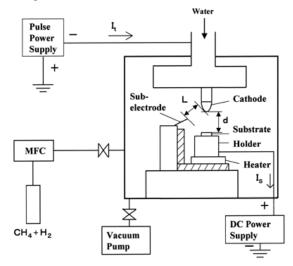


Figure 1. Scheme of pulsed discharge plasma CVD system where sub-electrode is used.

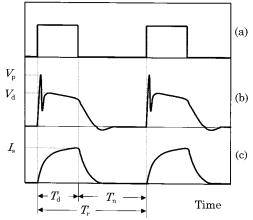


Figure 2. Typical waveforms for discharge voltage (b) and current (c) between cathode and substrate, corresponding to waveform of pulse generator (a).

The pulse power supply was fabricated by means of chopping the output of the DC power supply with Intelligent Power Module (IPM) and elevating the voltage by a transformer, as reported before. (refs. 3, 5 to 7) In the present experiments, however, the switching time of the pulse was shortened to about 20 µs to get high discharge beginning voltage by means of improve the circuit and repair the parts. Figure 2 shows typical waveforms

of the discharge voltage (b) and current (c) between the cathode and the substrate (anode), corresponding to the waveform of PG (a). When IPM comes to ON state by the rise of voltage of PG, the discharge voltage increases to discharge beginning voltage (Vp) by L(dI/dt) in the first, and then decreases to glow discharge voltage (Vd), where L is inductance of the transformer and I the current flowed into the transformer. The current rise time dt was about 20 μ s. The discharge current increases to Is after the beginning of the discharge, and decreases after Td. The shape of the current was corresponding to R-L transient phenomenon. The peak value of Is in the present experiments was kept to 0.6 A to observe the effect of Pg. When Pg was lower than 200 Torr, the deposition of the diamond film was difficult at this low Is.

The discharge conditions were changed widely with the discharge time (Td) and non-discharge time (Tn), denoted in the Fig. 2, and in this experiments, Td and Tn were set to 0.5 and 2 ms, respectively. These discharge conditions were suitable to prevent the decrease of the deposition rate and suppress the arc discharge.

The surface morphology of the deposited films was observed by a scanning electron microscope (SEM). Raman spectra of the samples were measured with the 514.5 nm line of an argon-ion laser.

2.2 Discharge method using rod-shaped cathode

Figure 3 shows a schematic diagram of the CVD system, where rod-shaped cathode fabricated with tungsten wire of 1 mm in diameter is used. The pulsed discharge was performed between the rod-shaped W cathode and the substrate (anode). The discharge and deposition process was almost same as that described above section 2.1. In this experiments, it was found that the diamond film could be deposited at low substrate temperature (Ts), which is impossible to measure with the radiation thermometer, and therefore, Ts was measured with thermo-couple attached near the substrate. Emission spectra from the plasma during the discharge were measured using a spectrometer and CCD array sensor.

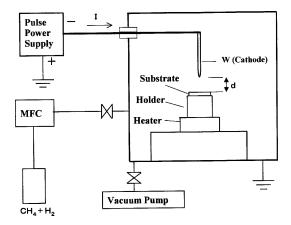


Figure 3. Scheme of pulsed discharge plasma CVD system where needle-shaped cathode is used.

RESULTS AND DICUSSION

3.1 Microstructures of the films deposited by CVD using sub-electrode.

Figure 4 shows scanning electron microscope (SEM) micrographs of the samples deposited by the CVD system shown in Fig. 1. The gas pressure (Pg) during the deposition is changed from 300 to 500 Torr. When Pg is 300 Torr, scattered grains are deposited on the substrate. When Pg is increased to higher than 400 Torr, the size of the grains increases and their crystalline habit becomes clear, showing that the crystalline quality becomes superior and the deposition rate increases with Pg.

Figure 5 shows Raman spectra of the samples shown in Fig. 5. The peak at 1333 cm⁻¹ corresponding to diamond becomes clear when Pg is increased to 400 Torr, in agreement with the results of SEM shown in Fig. 4. Figure 6 shows SEM micrographs of fractured cross sections of the samples deposited at Pg of 400 and 500 Torr. The thickness of the film deposited at 400 Torr is about 1.4 μ m, and increases to about 3 μ m when Pg increases to 500 Torr. Therefore, the deposition rate of the film remarkably increases when Pg increases.

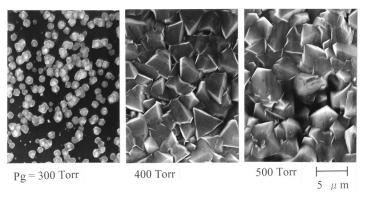


Figure 4. SEM micrographs of the samples when gas pressure (Pg) is changed from 300 to 500 Torr.

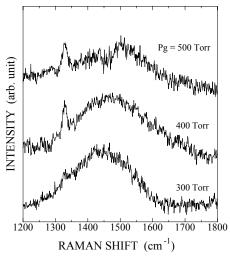


Figure 5. Raman spectra of samples shown in Fig. 5.

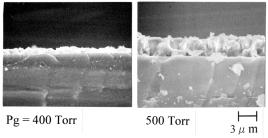


Figure 6. SEM micrographs of fractured cross sections of the samples deposited at Pg of 400 and 500 Torr.

3.2 Discharge and deposition when rod-shaped cathode was used

The results of the above section 3.1 show that the crystalline quality becomes superior and the deposition rate increases when Pg increases. To make clear these results, the phenomena of the pulsed discharge were investigated by more simple CVD method shown in Fig. 3, where the rod-shaped cathode was used. Figure 7 shows the photographs of the glow (plasma) during the discharge by this CVD system. In this experiment, the distance between the rod-shaped cathode and the substrate is about 15 mm, and the peak of the discharge current was 0.3 A. When Pg is increased from 100 to 500 Torr, the glow is constricted to small diameter.

Figure 8 shows emission intensities of H_{α} (a) and H_{β} (b) from the glow shown in Fig. 7. When Pg increases, the emission intensities increase, corresponding to the constriction of the glow. These results show that the plasma

formed by the discharge is constricted and the amount of excited atomic hydrogen increases when Pg increases. As well known, the atomic hydrogen play important role to the growth of the diamond film and remove amorphous component. (ref. 10) Therefore, it can be considered from these results that the increase of Pg is effective to improve the crystalline quality and increase the deposition rate of the film.

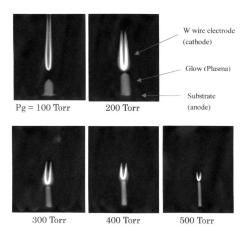


Figure 7. Changes of glow (plasma) when Pg is changed from 100 to 500 Torr.

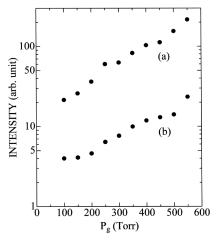


Figure 8. Emission intensities of H_{α} (a) and H_{β} (b) from the glow shown in Fig. 7.

The waveforms of discharge voltage and current in this method were almost same as those shown in Fig. 2. When Pg is increased, Vp and Vd denoted in Fig. 3 were increased corresponding to the results shown in Figs. 7 and 8. The value of Vp and Vd at Pg = 100 Torr were 2,800 and 800 V, and when Pg = 500 Torr, 5,000 and 1,300 V, respectively. The increases of Vp and Vd mean the increase of the input power to the plasma from the power supply. Therefore, it can be considered that the increases of emission intensities of H_{α} and H_{β} shown in Fig. 8 are caused by the input power to the plasma. The input power is also increases when the discharge current increases. However, in this pulsed discharge CVD method, the amount of the current is limited by the capacity of IPM. Therefore, the increase of the Pg to increase the input power is useful for the method using pulse power supply.

These experimental results show that the diamond film can be deposited to small area at low Ts. Figure 9 shows SEM micrographs of the film deposited at low Ts of 500°C by CVD system shown in Fig. 3. In this experiments, the distance between the rod-shaped cathode and the substrate (d) was 5 mm, and the peak of the discharge current (Is) was 0.6 A. The times of Td and Tn were 0.5 and 2 ms, respectively. The gas pressure (Pg) during the deposition is changed from 300 to 500 Torr. When Pg is 300 Torr, crystalline habit of diamond is not clear, and when Pg is increased to higher than 400 Torr, size of the grains increases and their crystalline habit becomes clear. Therefore, the diamond film can be deposited at low Ts of around 500°C by the method using rod-shaped cathode when Pg is increased higher than 400 Torr.

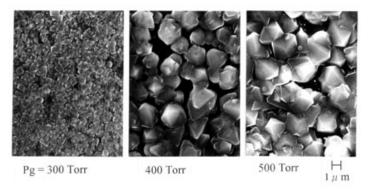


Figure 9. SEM micrographs of the samples deposited at Ts of 500°C by the method using rod-shaped cathode shown in Fig. 3. The gas pressure (Pg) is changed from 300 to 500 Torr.

CONCLUSIONS

Deposition of diamond films at gas pressure (Pg) higher than 300 Torr was succeeded by means of the pulsed discharge plasma CVD. The pulsed discharge could be performed by means of chopping the output of DC power supply with IPM and elevating the voltage by the transformer, where the switching time of the pulse was shortened to get high discharge beginning voltage, and Td and Tn were adjusted to get stable discharge.

When Pg during the deposition was increased from 300 to 500 Torr, the crystalline quality of the film was improved, and the deposition rate of the film increased.

When the rod-shaped cathode was used against the substrate (anode), the plasma during the deposition was constricted to small diameter with increasing Pg, and the emission intensities of H $_{\alpha}$ and H $_{\beta}$ from the plasma increased. By using this method, the diamond film could be deposited to small area at low Ts.

REFERENCES

- 1. Noda, M., et al.: Formation of Diamond Films by Intermittent Discharge Plasma Chemical Vapor Deposition, Jpn. J. Appl. Phys., **33** (1994), 4400-4403.
- 2. Noda, M., et al.: Formation of Diamond Films by Pulsed Discharge Plasma CVD, Advances in New Diamond Science and Technology, MYU, 1994, 73-76.
- 3. Noda, M.,: Formation of diamond films by pulsed discharge plasma chemical vapor deposition, Oyo Buturi, **65** (1996), 1258-1261. [in Japanese]
- 4. Araki, T., Noda, M., Katsuyama, T., : Diamond coating on silicon nitride by intermittent discharge DC plasma chemical vapor deposition, Mater. Sci. Eng., **B48** (1997) 221-225.
- 5. Noda, M., : Formation and Structural Control of Diamond Films by Pulsed Discharge Plasma CVD, Technical Report of IEICE, **SDM97-15** (1997) 15-21. [in Japanese]
- 6. Noda, M., : Formation of Diamond Films by Pulsed Discharge Plasma CVD Using Sub-electrode, Technical Report of IEICE, **SDM99-27** (1999) 81-86. [in Japanese]
- 7. Noda, M., Higaki, T., Araki, T., : Formation of Diamond Films by Pulsed Discharge Plasma Chemical Vapor Deposition using Sub-electrode, Proc. ADC/FCT'99, 402-407.
- 8. Noda, M., : Formation of Diamond Films by Intermittent DC Plasma Chemical Vapor Deposition Using Subelectrode, Jpn. J. Appl. Phys., **33** (1994) 4496-4499.
- 9. Noda, M., Shimizu, H., : Structural Changes due to Gas Pressure of Diamond Films Prepared by Intermittent Plasma Chemical Vapor Deposition, New Diamond and Frontier Carbon Tech., MYU, **12** (2002) 133-136.
- 10. SPEAR, K.E., FRENKLACH, : Mechanism for CVD Diamond Growth, Synthetic Diamond: Emerging CVD Science and Technology, SPEAR K. E. and DISMUKES, J.P. ed. Chap. 8, John Wiley & Sons, 1994, p.243-304.

TWO-STAGE BIAS ENHANCED GROWTH OF NANOCRYSTALLINE DIAMOND FILMS

Tarun Sharda

Research and Development, Seki Technotron Corporation, 5-6-30, Kiba, Koto-ku, Tokyo 135 0042, Japan

Tetsuo Soga

Department of Environmental Technology and Urban Planning, Nagoya Institute of Technology, Gokiso-cho, Showa-ku, Nagoya 466 8555, Japan

ABSTRACT

Biased enhanced growth (BEG) is developed as a process to grow nanocrystalline diamond (NCD) films. In the BEG process the diamond nucleation and growth are obtained in a single stage process. Typical conditions, used in this process, are 5 % CH₄ in H₂ at 30 Torr pressure while heating the substrate in the range of ~ 400 to 700° C. A negative bias of 200 V is applied and the bias current density to the substrate is controlled. The controlled bias current density gives a different set of combination of conditions (bias current density, bias voltage and microwave power) that results in the growth of NCD films composed of grains in the range of 2-30 nm with surface roughness of 20-30 nm at growth rates varying in the range of $0.5 - 2 \mu m/hr$ at 1000 W microwave power.

In the present study, two-stage BEG is reported. In the first stage a bias of 200 V was applied to the substrate for 30 min followed by growth in the second stage at bias voltages varying in the range of 0-320 V. The films were characterized by Raman spectroscopy and atomic force microscopy. Optical properties (thickness and refractive index) of the films were measured by prism-coupling technique using operating wavelengths of 830 and 1300 nm. Hardness of the films was measured by nano-indentor. Hardness increased and roughness decreased with decreasing the bias voltage. Films with average hardness of 75-80 GPa, having stress less than 1 GPa, and rms surface roughness of 15 nm have been obtained. Different regimes of growth were observed, respectively, in the bias range up to 100 V and beyond. A growth mechanism for NCD by BEG process, based on the results, is discussed.

Keywords: nanocrystalline diamond, bias, roughness, hardness, prism-coupling

INTRODUCTION

The high surface roughness of the conventionally grown polycrystalline CVD diamond films prevents their immediate uses in spite of having outstanding properties with their unique combinations suitable for many applications (ref. 1) such as machining and wear applications, optical and thermal management applications. To overcome the problem of surface roughness of diamond films one can opt for either post-polishing or can develop ways to grow smooth diamond films without compromising much with their hardness and other useful properties. Post-polishing is expensive and time consuming (ref. 2,3) and that puts the attention to develop ways for as-grown smooth diamond films (ref. 4,5). One way to reduce the surface roughness during growth is to control of crystalline orientation with (100) facets being parallel to the films place, or by reduction of the grain size, i.e., reduction from grain sizes in micrometers to grain size in nanometers (ref. 4,5). This is the reason that in the last few years efforts in the area of diamond films grown by CVD are diverting from conventional microcrystalline diamond (MCD) films, having grain size of a few hundred of nanometer to several tens of microns, to nanocrystalline diamond (NCD) films, having grain size from 2 nm to a few hundred nanometer.

Recently, we have succeeded in growing very smooth nanocrystalline diamond films on Si substrate by a processing method termed biased enhanced growth (BEG) in microwave plasma chemical vapor deposition (MPCVD) (ref. 6-10). This new method, is an extension to the biased enhanced nucleation (ref. 11) of diamond,

NASA/CP—2003-212319 579 August 18, 2003

offers nucleation and growth in a single process unlike the conventional two or three stages process for the heteroepitaxial growth of diamond. The BEG process is also different than the process that uses carbon dimmer (C_2) as growth species in hydrogen deficient plasmas (CH_4/Ar or C_{60}/Ar) for the growth of NCD films (ref. 4). The NCD film is a layer composed of high concentration of diamond crystals of a few to few tens of nanometer in size with a significant amount of non-diamond carbon decorating the grain boundaries. Here we present some results of two-stage BEG that gives even smother NCD films.

EXPERMINTAL

The NCD films were grown in a 2.45 GHz Seki Technotron Corporation, Japan, (former Applied Science and Technology, USA) made MPCVD system on mirror polished Si(100) substrates using BEG, recently developed by our group (ref. 6,7). Two steps BEG were adopted. In brief, controlled and continuous bias current density (BCD) was provided to the substrates with 5% methane in balance hydrogen at 1000 W of microwave power and 30 Torr pressure. A quartz shield was used to cover the conducting parts of the substrate holder assembly (other than the substrate), while applying negative bias to the substrate throughout the growth to enhance BCD to the substrate at low microwave powers without affecting the microwave plasma. The substrate temperature, which was measured at the bottom of the graphite substrate holder by thermo couple, was kept constant at 600°C. In the first stage a bias of 200 V was applied to the substrate for 30 min followed by growth in the second stage for 60 min at bias voltages varying in the range of 0-320 V. Surface roughness was measured using atomic force microscopy (AFM) and other structural characterizations were carried out by micro-Raman spectroscopy (STR250, Seki Technotron Corporation, Japan) at 514.5 nm. The refractive index and thickness of the films were measured by a Metricon model 2010, USA, analyzer based on the prism coupling technique using operating wavelengths of 830 and 1300 nm. Hardness of the films was measured by nano-indentor.

RESULTS AND DISCUSSION

The prism coupling technique has been described in literature in detail (see ref. 12). In brief, the film thickness and optical constants can be determined together at any point of the sample by observing the wave guiding modes of the sample. The film surface is attached to the base of a right-angle prism by means of a pneumatically operated coupling head as shown in Figure 1(a). This arrangement of holding the sample leaves a small air gap between the film and the prism. A laser beam is sent to the base of the prism and reflection is measured by a photodetector. The guided spectrum of the sample is plotted by measuring the reflected intensity with respect to the angle of incidence of the beam. Dips in the intensity are observed at certain discrete values of the incident angle of the laser beam. At these particular incident angles, the light tunnels through the air gap into the film and enter into guided optical propagation modes resulting in drop in the reflected intensity of the light. The angular location of the modes determine film index, whereas the difference in the angular locations determine the thickness. A typical guided spectrum of an NCD film grown by BEG process is shown in figure 1(b). The vertical lines in the figure exhibit the guided modes observed in the spectra of different films. Operating wavelengths of 830 and 1300 nm were used for all the measurements. The reason for not using the standard wavelength (633 nm) lies in the fact that our NCD films are absorbing for shorter wavelengths (ref. 10, 12). High absorption may lead to higher standard deviation in the measurements. It was also observed that the intensities of the dips at 830 nm decrease with films thickness, obviously because of increase in the optical path length of the guided light in the films. However, it should be mentioned that the guided modes of the MCD films, which has low absorption throughout these regions, can be measured accurately even at lower wavelengths provided that their surfaces are smooth enough not to have high surface scattering losses.

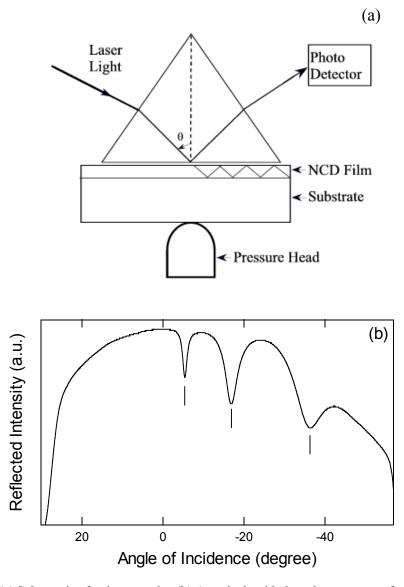


Figure 1(a) Schematic of prism coupler (b) A typical guided mode spectrum of an NCD film

The calculated thickness of the films is plotted as a function of second stage bias voltage in figure 2. The refractive index of the NCD films grown at different second stage bias voltage was found to be 2.33 at 1300 nm and vary with the latter only in the third decimal place. The rms surface roughness of the films, as measured by AFM in an area of 5 X 5 μ m², is also plotted in figure 2 as a function of second stage bias voltage. As observed, thickness and roughness of the samples change with second stage bias voltage almost in a common fashion. The dashed lower and upper lines in the plot respectively indicate the thickness and roughness of the film grown continuously for a total 90 min without changing either the bias voltage or any other condition. Thus, these lines are indicators of what thickness and roughness the samples would be if the first stage bias voltage of 200 V continued as such throughout the growth. The thickness increases with time irrespective of what voltage is applied in the second stage though the growth rate decreases and increases respectively in the second stage at lower and higher voltages than 200 V (first stage bias voltage). The rms roughness varies in the same fashion and interestingly can be as low as 15 nm below a second stage bias voltage of 80 V.

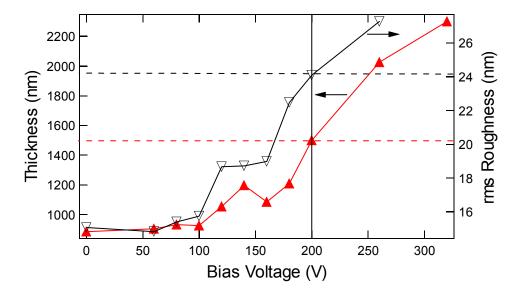


Figure 2. Plots of thickness and rms roughness of NCD films grown at different second stage bias voltages

Different regions of growth are identified from the plot. The thickness and roughness increase gradually up to 100 V with a larger change coming at 100-120 V following a region where the two parameters remain almost constant up to a bias voltage of 160 V. The thickness and roughness start increasing almost linearly and with a faster rate beyond 160 V. As explained in earlier reports (ref. 6,7), the growth of NCD by BEG process could be a result of a combination of surface and subsurface processes. The appearance of different regions of growth may be resulting from the changes in the energy and density of the ions impinging on the growing surface with bias voltage in the second stage of growth. A detail analyses is underway to understand exactly the roles of the two processes at different biasing voltages.

The visible Raman spectra of some of the films grown at different second stage bias voltage are shown in figure 3. In brief, the visible Raman spectra of the films consist of a band near 1150 cm⁻¹, associated to the presence of diamond nano-crystals, along with features near 1350, 1470, and 1580 cm⁻¹. The band near 1470 cm⁻¹ may be related to the disordered sp³ carbon in the films whereas the other bands near 1350 cm⁻¹ and 1580 cm⁻¹, respectively, are well-known graphitic D and G bands. In our films the relative intensity of NCD band (I_n) to the graphitic G band (I_o) is mostly found to have a correlation to structural and mechanical properties of the films and can be understood to represent concentration of NCD in the films (ref. 6-8). The intensity ratio (I_n/I_e) is plotted as a function of second stage bias voltage in figure 4. Clearly from the Raman spectra and the plot of the intensity ratio of I_n/I_g with bias voltage, the NCD concentration appears to be optimizing at moderate second stage bias voltage (80-160 V) that is also correlating to the second region of growth in figure 2. Also plotted in figure 4 is hardness of the films as a function of second stage bias voltage. Interestingly, the hardness increases by decreasing the second stage bias voltage and a hardness of 75 GPa can be achieved at moderate or low bias voltages. Similar to thickness and roughness, shown in figure 2, the hardness of the films also indicate different regions of growth at different second stage bias voltage. However, as mentioned before, a detailed analysis of the results is due and will be published later. Nevertheless, the results suggest that NCD films with a hardness of 75 GPa and rms surface roughness of 15 nm can be grown by two-stage BEG process at a growth rate of 0.5-1 µm/hr at 1 kW microwave power.

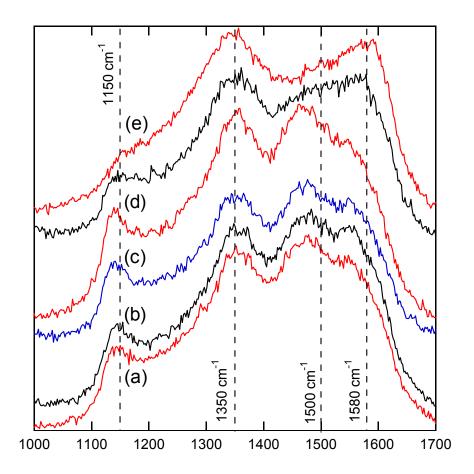


Figure 3. Raman spectra of the NCD films grown at second stage bias voltage (a) 0, (b) 60 V, (c) 120 V, (d) 160 V and (e) 320 V.

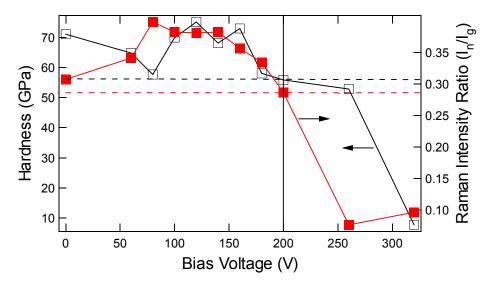


Figure 4. Plots of hardness and Raman intensity ratio I_{n}/I_{g} as a function of second stage bias voltage

It is shown that the surface roughness of NCD films, grown by single stage BEG process, can be further decreased from 24 nm to 15 nm with hardness increasing from 55 GPa to 75 GPa while compromising the growth rate which decreases from 900 nm/hr to approximately 700 nm/hr by applying two stage BEG.

REFERENCES

- 1. Gangopadhyay, A. K. & Tamor, M. A.: Friction and wear behavior of diamond films against steel and ceramics. *Wear* V. 169, 1993, 221.
- 2. Bhusan, B.: Chemical, mechanical and tribological characterization of ultra-thin and hard amorphous carbon coatings as thin as 3.5 nm: recent developments. *Diamond and Relat. Mater.* V. 8, 1999, 1985.
- 3. Erdemir, A., et al.: Tribological properties of nanocrystalline diamond films, *Surf Coat. Technol.* V. 120-121, 1999, 565.
- 4. Gruen, D.M.: Nanocrystalline diamond. Annu. Rev. Mater. Sci., V. 29, 1999, 211.
- 5. Sharda T. and Bhattacharyya S.: Advances in nanocrystalline diamond. *Encyclopedia of Nanoscience and Nanotechnology*, American Scientific Publishers, CA, 2003 (in print).
- 6. Sharda, T., et al.: Growth of nanocrystalline diamond films by biased enhanced microwave plasma chemical vapor deposition: A different regime of growth. *Appl. Phys. Lett.* V. 77, 2000, 4304.
- 7. Sharda, T., et al.: Biased enhanced growth of nanocrystalline diamond films by microwave plasma chemical vapor deposition. *Diamond and Relat. Mater.* V. 9, 2000, 1331.
- 8. Sharda, T., et al.: Strong adhesion in nanocrystalline diamond films on silicon substrates. *J. Appl. Phys.* V. 89, 2001, 4874.
- 9. Sharda, T. et al.: Highly stressed carbon film coatings on silicon: Potential applications. *Appl. Phys. Lett.* V. 80, 2002, 2880.
- 10. Sharda, T. et al.: Structural and Optical Properties of Diamond and Nano-diamond Films Grown by Microwave Plasma Chemical Vapour Deposition. *Diamond and Relat. Mater.* V. 10, 2001, 561.
- 11. Yugo, S., et al.: Generation of diamond nuclei by electric field in plasma chemical vapor deposition. *Appl. Phys. Lett.* V. 58, 1991, 1036.
- 12. Sharda T., Soga T. and Jimbo T.: Optical properties of nanocrystalline diamond films by prism coupling technique. *J. Appl. Phys.* V. 93, 2003, 101.

SYNTHESIZE OF NANNOSTRUCTURE DIAMOND BY MICROWAVE PLASMA CHEMICAL VAPOR DEPOSITION WITH BIASED EMHANCED NUCLEATION AND HYDROGEN-ARGON PLASMA IRRADIATION

Yasuhiko Hayashi, Daisuke Mori, Tetsuo Soga, Takashi Jimbo

Department of Environmental Technology and Urban Planning, Nagoya Institute of Technology, Gokiso-cho, Showa-ku, Nagoya 466-8555, Japan

ABSTRACT

The hard (70GPa) and flat (average roughness of 10nm) nanostructure diamond films were synthesized by the combination of two-step substrate bias growth combined with irradiation of Ar-H₂ plasma after deposition. Ar-H₂ plasma irradiation has been confirmed to increase the hardness and decrease the roughness of films.

Keywords: Nanostructure diamond; 2-step substrate bias method; MPCVD; Hydrogen-argon plasma treatment; Super hard flat

INTRODUCTION

Morphology of diamond film depends on the reactant gases, their mixing ratios, negative substrate bias and the substrate temperature. Chemical vapor deposited (CVD) diamond films are most commonly grown using low partial pressures of methane in hydrogen. As the partial pressure of methane increases, the crystalline morphology disappears, and diamond-like carbon (DLC), which contain both low quality and graphite-like phase is formed. In recent years, it has been found that growing at specific conditions between these two extremes can yield high quality diamond films containing small nanostructure diamond (NSD) in disordered graphite.

Compared with polycrystalline diamond films, the NSD films are very attractive for many industrial applications due to their unique bulk and surface properties such as high optical band gap, high hardness, high thermal conductivity and low electrical conductivity. The smoother surfaces and the wide band gap provide the opportunity to act as ideal transparent protective films on optical components (ref. 1). Moreover, the possibilities of microelectromechanical systems (MEMS) and nanoelectromechanical systems (NEMS) devices have been explored by Gruen (ref. 2).

NSD films with extremely high grain boundary density have been prepared by various methods such as Ar-C₆₀ or Ar-CH₄ precursors with little or without hydrogen using microwave plasma enhanced CVD (MPECVD) (refs. 3 to 7). The former case, C₂ dimmers produced by ion bombardment might provide growth species for NSD. And latter case, NSD is formed by the ion bombardment-induced high frequency secondary nucleation.

It is well known that the grain size is one of the important factor influencing on properties of the NSD film. However, the nucleation mechanism and properties of NSD film remains poorly understood, because of difficulty in locating and controlling the nucleation sites. In this study, we investigate the properties of NSD film grown by microwave plasma enhanced chemical vapor deposition (MPECVD) with two-step substrate bias and hydrogenargon plasma irradiation. We will discuss the effect of substrate temperature at bias enhanced nucleation (BEN) step and hydrogen-argon (H₂-Ar) plasma irradiation after NSD deposition.

EXPERIMENTAL

The NSD films were deposited in a 2.45-GHz MPECVD system with a two-step substrate bias to reduce the residual stress and the surface roughness. The mirror-polished Si(100) substrates, pretreated in an aqueous solution of HF (HF:H2O=1:1 by volume) to remove the oxide, were set on a molybdenum (Mo) holder. Then they were cleaned with H2 plasma for 20 min at 900°C. The CH₄ concentration, microwave power (MP), and total pressure were maintained at 5%, 1000 W, and 30Torr, respectively. The growth time at BEN and BEG steps were 5 and 60 min, respectively. The substrate temperature was varied from 400 to 800° C while keeping substrate bias at BEN of -300 V. After deposition, NSD films were treated by the mixture of Ar-H₂ plasma irradiation with different Ar/(H₂+Ar) ratios at MP of 1000W for 30min.

The surface morphological features of nucleation stage in NSD films were examined using a Seiko Instruments SPI-3800N CAFM system with a Pt probe in a vacuum of 10⁻⁷ Torr. Structural characterizations of the films were carried out by Raman spectra in the back-scattering geometry using the 514.5nm line of an Ar+ ion laser at room temperature in the spectral range from 900 to 1800cm-1 with a resolution of 1.0cm-1, and the signals were separated by a monochromator. The crystallographic structure and crystallinity of NSD films were investigated by X-ray diffraction (XRD) with quite shallow incident X-ray angle using Cu Ka radiation. Hardness of the films was measured by a nanoindentor (UMIS-200) using a Berkovich diamond pyramid. The deposition rate was around 600 - 1800nm/h and, in order to minimize the substrate effect on the hardness measurements, maximum loading force was not exceeded beyond 10mN. Therefore, the indentation depth was kept within the critical depth (maximum penetration depth should not exceed 10% of the film) beyond which there would be sever effect in the hardness measurement of the film from the substrate. Both the UMIS and indenter tip were calibrated using a fused silica standard of known material properties. We also characterize the hydrogen concentration by the technique of elastic recoil detection analysis (ERDA).

RESULTS AND DISCUSSION

Surface morphological features

We first investigated in detail the surface morphology of NSD films. CAFM shows clear morphological change with variation of substrate temperature, as shown in Figs. 1(a), -1(d). For a substrate temperature of 600°C, the large cauliflower-like clusters of 100-130nm in diameter, which are

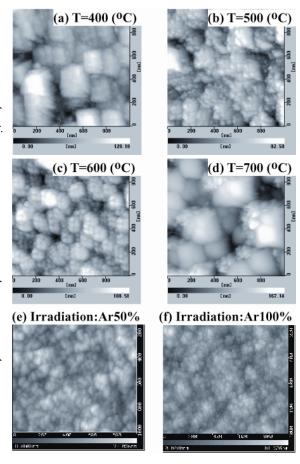


Figure 1. The CAFM surface morphologies of the NSD films deposited at (a) 400 °C, (b) 500 °C, (c) 600 °C and 700°C, and the NSD films irradiated by Ar-H2 plasma with Ar concentrations of 50% and 100% scanned in a 1x1μm².

composed of many 30-50nm in diameter small and uniform grains, were obtained, as shown in Fig. 1(c). The morphology of cluster changes from a cauliflower-like to a columnar above 700°C. The size and shape of cluster strongly depends on the substrate temperature. We clearly find, as shown in Fig. 1(a), the high uniformity of the trapezoidal (columnar) shape clusters composed of small grains, 200nm square and 100nm high, which are connected with each other and enhance the alignment of nuclei below 500°C. In other words, a high density (or coverage) of {100}-oriented, textured grains has been obtained. For a substrate temperature above 700°C, some portion of the small grains coalesces together to form crystallites, while the boundary of crystallite contains individual grains. The current value of the conducting region increased with increase in the substrate temperature. The comparison of CAFM current image of NSD films deposited between 400°C and 700°C revealed that the conductive difference is at least a magnitude of one order. Thus, the surface graphitization of the depositing NSD film might be produced from films deposited above 700°C. The average roughness (Ra) and root mean square (RMS) roughness decreased from 9.8nm and 12.5nm to 9.0nm and 11.3nm, respectively, as the substrate temperature is increased from 400°C to 500°C. However, both Ra and RMS again increase as the substrate temperature is increased above 600°C.

Figures 1(e) and 1(f) show the typical surface morphologies of NSD films irradiated by Ar-H₂ plasma with Ar concentrations of 50% and 100%, respectively. It is clear that the significant morphological change was observed by

Ar-H₂ plasma irradiation compared to the cauliflower-like surface morphology of the NSD film deposited at 500°C, as shown in Fig. 1(b). Moreover, both Ra and RMS of CAFM, which shown in the inset in Fig. 4(b), were almost unchanged and the relation between surface roughness and Ar concentration could not be established. It should be noted that both Ra and RMS slightly decrease and the density of small cluster increases by introduction of Ar-H₂ plasma irradiation after NSD deposition. The uniformity of size and shape of gains improves by Ar-H₂ plasma irradiation. We also observed a significant difference in grain and grain boundary from the NSD film, not shown here, irradiated by only H₂ plasma (Ar=0). The surface roughness of CAFM increased with increase in H₂ plasma exposure time.

XRD characterizations

XRD results reveal that our NSD films were mostly consist of cubic diamond (111), as shown in Fig. 2. Although, both diamond(111) and diamond(220) are reported from the NSD film deposited by continuous BEN method there was no signal at $2\theta=75^{\circ}$ of signature of diamond (220) in our films. It should be noted that the NSD film composed of highly oriented diamond(111) which was achieved by using two-step bias method. During BEN step, high energy carbon ion bombardment might leads to a shallow ion penetration at the subsurface region and a renucleation of diamond on randomly oriented crystallites. It has been accepted that an atomic hydrogen, hydrogen ions and hydrogen radicals are in the plasma. And the etching efficiency of carbon by hydrogen ions is much faster than atomic or radical species. The number of oriented {111}-textured grains and the overall coverage of the film can be increased by NSD growth and hydrogen ion etching simultaneously at BEG step (ref. 8). In our experiment, the BEG step was performed at negative bias of 100V and the ion penetration mechanism was not occurred at this step. The crystallite size was estimated to be approximately 40nm-70nm from the full width at half maximum (FWHM) of the diamond peak and this value is in good agreement with that of CAFM. The maximum intensity and the narrowest FWHM of diamond(111) peak was observed from the NSD film deposited at substrate temperature of 500°C. This may be due to optimal substrate temperature of NSD deposition.

XRD spectra of films irradiated by Ar-H₂ plasma with different Ar concentration show that the absolute intensity of diamond(111) is weaker than those of non-irradiated films, and the diamond(220) observed in all irradiated films. Thus, the NSD film gradually changes from oriented diamond(111) to randomly oriented phase by Ar-H₂ plasma irradiation. The relation between XRD characteristic and Ar concentration during Ar-H₂ plasma irradiation could not be established.

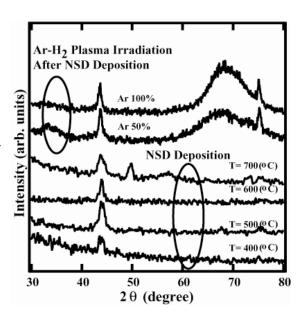


Figure 2. XRD patterns of the NSD films deposited at various substrate and the NSD films irradiated by Ar-H2 plasma with Ar concentrations of 50% and 100%.

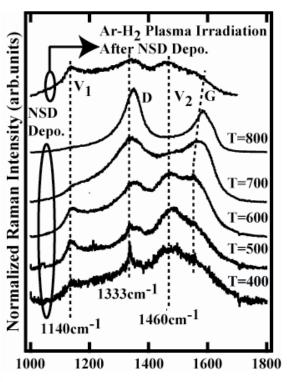


Figure 3. Raman spectra of the NSD films deposited at various substrate temperature and the Raman spectrum of the NSD film irradiated by Ar-H₂ plasma with Ar concentration of 50%.

Raman spectra characterizations

Figure 3 shows Raman spectra of the NSD films deposited with different substrate temperatures and typical Raman spectrum of the NSD film irradiated by Ar-H₂ plasma. The formation of diamond phase is demonstrated by the occurrence of the first order diamond line at 1333cm⁻¹ from films deposited below 600°C. We also observed broad signals near 1140cm⁻¹, 1350cm⁻¹, 1460cm⁻¹ and 1580cm⁻¹. The peaks at 1350 cm⁻¹ and 1550cm⁻¹ (~ 1580 cm⁻¹) are the *D* and *G* modes caused by disordered carbon (ref. 9). The diamond feature at 1333 cm⁻¹ without no peak shift was observed up to a substrate temperature of 700°C and this indicates that almost no residual stress formed in the film. For the substrate temperature at 800°C, Raman spectrum shows amorphous nature of carbon by its prominent G and D peaks. It should be noted that there is some controversy in the interpretation of the peaks at 1140cm⁻¹ and 1460 cm⁻¹ of diamond film.

In comparison with non-irradiated film, although the peak at 1460cm⁻¹ decreases the Ar-H₂ plasma irradiation on NSD films affects no significant change in overall Raman features. On the other hand, however, both 1140cm⁻¹ and 1450cm⁻¹ peaks were disappeared while *G* and *D* bands still remained from the NSD film subjected to only hydrogen plasma (Ar=0).

Lopez-Rios et al. (ref. 10), and later Ferrari and Robertson (ref. 11) have assigned the 1150cm⁻¹ and 1450cm⁻¹ peaks to the sp^2 phase of transpolyacetylen (trans-(CH)_n) by surface enhanced Raman scattering and Raman scattering taken at various laser excitation energies. But, it is very clear that when ever the 1150cm⁻¹ peak has been observed, NSD diamond, either in the cubic form or in the hexagonal form has been observed by both XRD and transmission electron microscope (TEM). Therefore, the possibility of sp^3 diamond phase can not be ruled out at this time. For the case of 1460cm⁻¹ peak, even though the Raman intensity ratio of the 1150cm⁻¹ to this peak ($I_{\text{ratio}} = I_{1150}/I_{1460}$) decrease with increase in Ar concentration during Ar-H2 plasma irradiation, the absolute intensity of I_{1150} was almost constant under same Raman condition. Therefore, only the I_{1460} varies with Ar concentration. This result indicates that the peak at 1460cm⁻¹ is probably related to amorphous sp^2 phase or polymeric chain such as trans-(CH)_n phase which are removed by Ar-H₂ plasma irradiation.

Hardness characterizations

Figure 4 shows the hardness-penetration curves of NSD films with different substrate temperature indented to maximum load of 10mN. The inset in Fig. 4 illustrates the hardness of NSD films as a function of substrate temperature. The data show that the hardness of the NSD film is constant over the 35-60nm penetration depth range and there is almost no influence of the substrate on the measured hardness values.

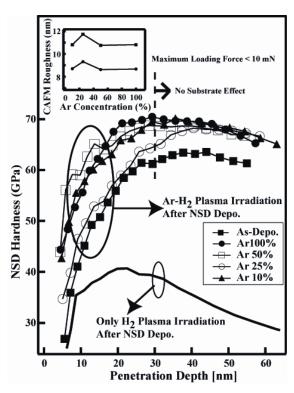


Figure 4. The hardness-penetration curves of NSD films with different substrate temperature indented to maximum load of 10mN. The inset shows the CAFM roughness of NSD films as a function of substrate temperature.

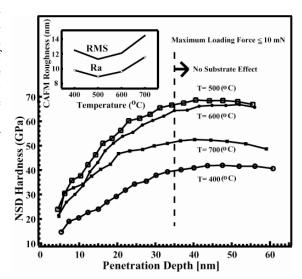


Figure 5. The hardness-penetration curves of NSD films irradiated by Ar-H₂ plasma with different Ar concentrations indented to maximum load of 10mN. The inset shows the CAFM roughness of NSD films as a function of substrate temperature.

The hardness increases with increase in the temperature up to around 600°C and decreases with further increase in temperature. The maximum hardness of 68GPa was obtained from the NSD film deposited at 500°C. The hardest NSD film was obtained where the CAFM values of Ra and RMS were minimum.

Figure 5 shows that the hardness-penetration curves of Ar-H₂ plasma irradiated NSD films with different Ar concentration. The inset in Fig. 5 illustrates the hardness of NSD films as a function of Ar concentration during Ar-H₂ plasma irradiation after NSD deposition. The as-grown NSD film was deposited at substrate temperature of 600°C and the initial hardness of NSD film was 60GPa. It is clear that the film hardness increased from 60GPa to 70GPa with increase in Ar concentration during Ar-H₂ plasma irradiation. Here, it is worth to note that the hardness of the film irradiated by only H₂ plasma (40GPa) decreases significantly as compared to that of the non-irradiated film (60GPa). This result indicates the importance of little or no H₂ during Ar-H₂ plasma irradiation.

Discussion

No clear explanation on origin of high hardness of NSD film and increase of hardness by $Ar-H_2$ plasma irradiation have been reported so far. The question is, therefore, why are the NSD film and the $Ar-H_2$ plasma irradiated NSD film so hard? Based on the substrate temperature dependence of CAFM feature and TEM observations, not shown here, we propose that the hardness of NSD film is attributed to the size of nano-clusters composed of adjacent NSD particles, amount of NSDs embedded in an amorphous tissue as well as surface roughness those are controlled by substrate temperature.

For the case of Ar-H₂ plasma irradiation after NSD deposition, a plasma irradiation introduces a structural change of film. And also, the surface roughness decreases due to decrease of NSD grain boundaries and improve of uniformity of smaller grain size by Ar-H₂ plasma irradiation. We think that some sp^2 amorphous regions change or coalescence together to form sp^3 phase crystallites according to CAFM morphological change. The decrease of 1460cm⁻¹ phase, which is related to sp^2 phase, in Raman spectrum suggests that the NSDs are embedded in an amorphous tissue and both amorphous carbon and NSDs were removed by Ar-H₂ plasma irradiation. The structural change cannot detect clearly by Raman and XRD, however, ERDA indicates that the hydrogen content in the film slightly changes by Ar concentration during Ar-H₂ plasma treatment. It is thought that the hardness can be increased by forming of sp^3 phase crystallites and etching of sp^2 phase, simultaneously, by Ar-H₂ plasma irradiation. On the other hand, however, only H₂ plasma irradiation introduces H-atoms, detected by ERDA, and leads to the increase of sp^2 phase or polymeric chain in a NSD film. The hardness decreases by only H₂ plasma irradiation after NSD deposition due to increase of both sp^2 phase and surface roughness induced by H₂ chemical etching. This result suggests that hydrogen plays a critical role in determining the hardness of NSD film irradiated by Ar-H₂ plasma after NSD deposition.

CONCLUSION

In conclusion, the (111) NSD films mainly composed of diamond(111) were grown by two-step substrate bias method. The maximum hardness of as high as 70GPa with the smallest Ra and RMS of CAFM is obtained at substrate temperature of 500°C with minimum surface roughness. The hardness of film increased by Ar-H₂ plasma irradiation after NSD deposition due to decrease of surface roughness and improvement of uniformity of smaller grain size. The hardness of film irradiated by only H₂ plasma, however, decreased in comparison with non-irradiated film. Thus, we confirm that the introduction of Ar-H₂ plasma after NSD deposition is effective to increase hardness of films. Our results demonstrated that hard NSD films can be produced from Ar-H₂ plasma irradiation after NSD deposition with little or no H₂ using MPECVD.

REFERENCES

- 1. K. Chakrabarti, R. Chakrabarti, K. K. Chattopadhyay, S. Chaudhrui, A. K. Pal, Diamond Relat. Mater. 7 (1998) 845.
- 2. D. Gruen, Annu. Rev. Mater. Sci. **29** (1999) 211.
- 3. D. Gruen, S. Liu, A. R. Krauss, X. Pan, J. Appl. Phys. 75 (1994) 1758.
- 4. D. Gruen, S. Liu, A. R. Krauss, J. Luo, X. Pan, Appl. Phys. Lett. 64 (1994) 1502.

- 5. S. Jiao, A. Sumant, D. M. Gruen, A. R. Krauss, O. Auciello, J. Appl. Phys. 90 (2001) 118.
- 6. C. Z. Gu, X. Jiang, J. Appl. Phys. 88 (2000) 1788.
- 7. X. Jiang, C. L. Jia, Appl. Phys. Lett. 80 (2002) 2269.
- 8. Y. Hayashi, Y. Matsushita, T. Soga, M. Umeno, T. Jimbo, J. Appl. Phys. 91 (2002) 9752.
- 9. D. S. Knigh, W. B. White, J. Mater. Res. 4 (1989) 385.
- 10. T. Lopez-Rios, E. Sandre, S. Leclereq, E. Sauvain, Phys. Rev. Lett. 76 (1996) 4935.
- 11. A. C. Ferrari, J. Robertson, Phys. Rev. B 63 (2001) 121405.

INFLUENCE OF METALS ON DIAMOND TO GRAPHITE PHASE TRANSFORMATION

A.Y Nozhkina

YNDALMAS

Moskow, Russia

Abstract

Transformation of diamond into graphite was investigated in the region of diamond metastability under the action of media chemically active to carbon in the temperature range from 770 K up to 2200 K and pressure range from 10³ Pa up to 3Gpa.

I \mathcal{Y} -III \mathcal{Y} group metals of periodic system and oxygen were used as media chemically active relative to diamond.

Methods of electron diffraction, chemical analyses, emission spectroscopy and X-ray phase analyses were used for determination of the reaction products.

It was found that in the region of diamond metastability the stage of catalytic phase transformation of diamond into graphite took place during the Interaction between diamond and metal. Metals reduce activation energy for transition of diamond into graphite from 109.4kcal/mole to 77.4kcal/mole.

Kinetic of phase transformation of diamond into graphite was investigated.

Pressure does not considerably influence on the rate of phase transformation of diamond into graphite in the presence of transition metals.

It is established that catalytic action of transition metals and silicon considerably increases in the presence of oxygen during into graphite. Action energy is maximal for silicon (40 kcal/mole) and minimal for manganese (13 kcal/mole).

DIAMOND SPONTANEOUS CRYSTALLIZATION FROM Mg-Ni-C SYSTEM AT HPHT

G.S. Bobrovnitchii, A.S. Osipov, A. L.D. Skury

North Fluminense State University, Av Alberto Lamego, 2000, Campos, RJ, Brazil, CEP 28013-600

ABSTRACT

In this work, different Mg-Ni alloys were used as carbon solvents in the synthesization of diamonds at a pressure of 7.7 GPa and temperatures of 1473 to 2073 K. All the alloys were melted by a special treatment at high pressure. The temperature ranges were determined for spontaneous diamond crystallization, using Mg₂Ni, MgNi₂ compounds and two eutectic alloys, according to the Mg-Ni phase diagram. Diamonds were observed to form at temperatures exceeding 1873 K when Mg₂Ni and 0.89at.%Mg+0.11at.%Ni alloys were used as carbon solvents. X-ray diffraction patterns revealed the presence of MgO. Spontaneous diamond crystallization was found to occur above 1573 K, using the MgNi₂ alloy. Cubo-octahedral morphology of diamond crystals were detected at temperatures of 1723-1823 K. Intense spontaneous diamond crystallization was observed at temperatures of 1573 K and upward when the eutectic 0.23at.%Mg+0.77at.%Ni alloy was employed. Unlike the behavior with the MgNi₂ alloy, the rate of spontaneous crystallization increased, as did the number of crystallization centers. The MgNi₂ carbon solvent alloy was found to be preferable for the synthesis of high-quality diamond crystals.

Keywords: High pressure; Diamond crystallization; Mg-Ni alloy; p,T-parameters

INTRODUCTION

The spontaneous crystallization of diamonds under conditions of high pressure and temperature is a well-established process for the Ni-Mn-C, Fe-Ni-C and Fe-Si-C systems (refs.1 to 3). Based on the results of research into these systems, industrial technologies have been developed to synthesize diamond powder. It is worth noting that the lowest pressure and temperature parameters (p,T-parameters) utilized in the process of industrial diamond synthesization are achieved when using Ni-Mn and Fe-Ni alloys, since the carbon they contain displays a high degree of solubility. In most cases, however, the crystals obtained under the abovementioned conditions show a given content of inclusions (ref.4). The presence of inclusions significantly limits the application of these crystals in various types of operations due to the deterioration of the crystals' physical and mechanical properties. On the other hand, natural diamonds with a low content of impurities are known to possess excellent thermal, electrical and optic properties (refs. 5 to 6).

The report (ref.7) assert that crystals with low impurity content and with electrical semiconducting properties can be obtained in the presence of pure Mg. However, in the production of diamonds of the Mg-C system, unlike other types of catalyzers, the p,T-parameters must be maintained under stricter conditions. Therefore, synthesizing diamonds for the production of crystals with semiconductor properties is a complex technical task.

The phase diagrams of the Ni-C (ref.8) and Mg-C (ref.9) systems have already been studied under conditions of high pressure and high temperature. Based on those studies, the pressure and temperature regions in which diamonds can be formed in these systems are well known. Thus, from the scientific standpoint, it is interesting to study the process of diamond formation in the Mg-Ni-C system under high pressure and temperature conditions, aiming to develop an efficient methodology for the production of diamonds with special properties.

EXPERIMENTAL

All the experiments carried out to study the process of spontaneous diamond crystallization in the Mg-Ni alloy and graphite system were conducted under a constant pressure of 7.7GPa and at temperatures varying from 1473 to 2073 K, in 50 K intervals. A high-pressure anvil-type device with toroidal concavity and diameter hole 13.5 mm was used. The reactive volume was set up in the high pressure cell in alternate layers, as illustrated in figure 1.

High pressure capsule used in the synthesis process was made of the block lithographic stone (CaCO₃). The starting materials were supplied with high purity powdered graphite (>99,99%), and the Mg-Ni alloys were produced beforehand under high pressures (1.0 - 2.0 GPa) and high temperatures (1573-1773 K). An anvil-type device with a central concavity of 55 mm was used for the production of the alloys. The compounds of Mg₂Ni,

MgNi₂ and two eutectic alloys of the content 0.89at%Mg-0.11at%Ni and 0.23at%Mg-0.77at%Ni according to the Mg-Ni phase diagram were obtained (ref.10).

The pressure in the reactive volume high pressure cell was measured using the well-known methods to determine the Bi, Tl and PbSe phase transitions at room temperature. The temperature in the cell was measured using a Pt-Pt13%Rh thermocouple in relation to the electric power applied. During the experiments, the temperature was evaluated using devices to measure the electric power applied during heating.

The duration of each process was limited by the time during which it is possible to maintain constant pressure inside the high pressure cell. Hence, each process lasted a maximum of 100 s.

The samples obtained after the thermobaric treatment were analyzed by X-ray diffraction (XRD), optical microscope and scanning electron microscopy (SEM).

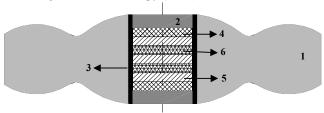


Fig 1. Cross section of the high pressure cell assembly. 1- high pressure capsule; 2-termoinsulation disk (CsCl-40%ZrO₃); 3 – graphite heater; 4- natural graphite disk; 5- powder Mg-Ni alloy and 6 – powder of high purity synthetic graphite.

RESULTS AND DISCUSSION

Table 1 lists the most relevant experimental results obtained from the diamond synthesizing process in the Mg-Ni alloy and graphite system with variable composition, under a pressure of 7.7 GPa.

Table 1. Experimental results of diamonds synthesis in the Mg-Ni-C system at pressure of 7.7Gpa and duration heating of 100 s.

Alloys of Mg-Ni system	Temperature (K)					
	1473	1573	1723	1823	1973	2073
0.89at%Mg+0.11at%Ni	0	0	0	+	+	• 🗆
Mg ₂ Ni	0	0	0	+	+	•
MgNi ₂	0	+	+	•	• 🗆	•
0.23at%Mg+077at%Ni	0	+	•	•	•	•

o: No diamond formation; +: diamond formation with octahedral morphology;

As can be seen, independently of the alloy composition employed, no diamond formation occurred at a temperature of 1473 K. In contrast, the exact opposite occurred from 1873 K upward, i.e., diamonds were present in the samples of all the compositions used in this study. No evident differences were found in the behavior of the alloys with 0.89at%Mg-0.11at%Ni and Mg₂Ni compositions during the diamond crystallization process of the system studied here. Intense formation of diamonds, with the appearance of growing dendrites, was observed at a temperature of 2073 K, with most of the crystals displaying a cubo-octahedral morphology. Figure 2 shows a SEM micrograph of one of the samples obtained in Mg₂Ni-C system. The arrows indicate the presence of a whitish substance in contact with the crystals. An X-ray diffraction of this substance, depicted in figure 3, detected the presence of MgO and Mg(OH)₂.

A possible explanation of the formation of these phases is based on the supposition that, after the diamond formation process and the subsequent reduction of pressure in the high pressure cell, the diamond-graphite-alloy system, the oxygen and the vapor in the air come into contact with each other, thus constituting favorable conditions for the formation of magnesium oxide and hydroxide. The same behavior takes place in the crystallization of diamonds in the Mg-C system under a pressure of 7.7 GPa and temperature of 1973 K, when synthesis of the diamond occurs only from the formation of magnesium carbide (MgC₂) with subsequent fusion and dissolution of the graphite (ref.11). Thus, it is likely that the diamond formation mechanism, using the

^{□:} diamond formation with cubo-octahedral morphology; •: growing polycrystalline diamond.

intermetallic alloy Mg_2Ni or the eutectic alloy 0.89at%Mg-0.11at%Ni as the solvent metal, is similar to the formation mechanism of the Mg-C system.

With regard to the use of the $MgNi_2$ alloy in the diamond synthesis process, spontaneous crystallization was found to occur from a temperature of 1573 K up. The polished surface of the areas of contact between the graphite and the alloy revealed the presence of isolated crystals with a well-defined octahedral morphology, as illustrated in figure 4, with sides of approximately 4.5 μm . At temperatures exceeding 1773 K, crystals were found with a cubo-octahedral morphology, as well as a small amount of cube-shaped crystals with sizes up to 30 μm , as depicted in figure 5. As can be seen, the dentritic growth structure was not significant. The crystals grown with this alloy were generally comed apart, octahedral with blunt-sided.

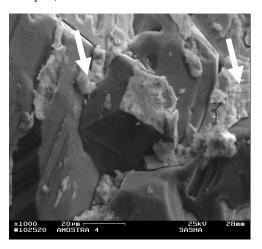


Fig 2. SEM microphotograph of the diamond synthesized from graphite and Mg₂Ni. Substance based on MgO and Mg(OH)₂ indicate by an arrows.

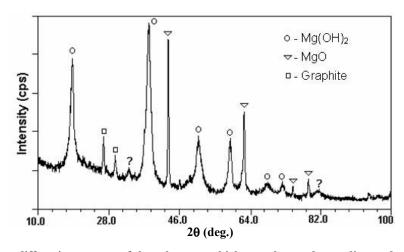


Fig 3. X-ray diffraction pattern of the substance which was observed near diamond crystals (fig.2).

The diamond crystallization process using the 0.23at%Mg-0.77at%Ni alloy displayed intense growth of crystals throughout the reactive volume of the high pressure cell, with crystallization beginning at 1573 K. However, unlike the behavior displayed by the MgNi₂ alloy, higher temperatures hastened the crystals' growth, resulting in the formation of twinned crystals. The same behavior was observed in the synthesis of diamonds of the Ni-C system. Figure 6 contains a micrograph showing twined crystals grown under a pressure of 7.7 GPa and a temperature of 1873 K and a duration of 30 s. The octahedral sides show linear dimensions of about 140 µm. Other regions of the same sample displayed growing polycrystalline diamond, demonstrating the large number of nucleation centers formed under these conditions.

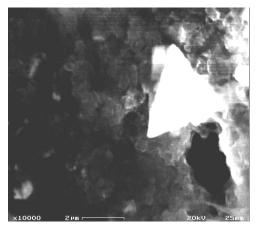


Fig 4. SEM microphotograph of the diamond synthesized from graphite and MgNi $_2$ alloy at 7.7 GPa, 1573 K and 100 s.

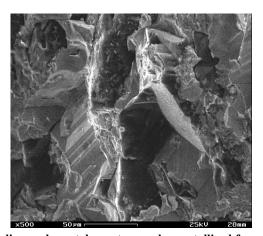


Fig 5. SEM microphotograph of diamond crystal spontaneously crystallized from $MgNi_2$ alloy at 7.7 GPa, 1773 K and 100 s.



Fig 6 - SEM microphotograph of diamond crystals spontaneously crystallized from 0.23 at.% Mg + 0.77 at.% Ni alloy at 7.7 GPa, 1873 K, 30 s.

CONCLUSIONS

The results of the studies reported herein allowed us to determine the minimum temperatures at which diamond crystallization in the Mg-Ni-C system can occur, using the compositions employed in our experiments.

It was established that the diamond formation mechanism using the Mg_2Ni and 0.89at%Mg-0.11at%Ni alloys does not differ significantly from that of the Mg-C system, which requires high temperatures.

In the crystallization of diamonds using the MgNi₂ alloy at temperatures of 1723 to 1823 K, it was found that the crystals generally grew in the shape of octahedrons with blunt and cubic-octahedral faces.

The use of the 0.23at%Mg-0.77at%Ni alloy led to the growth of twinned crystals, with the crystallization process characterized by a large number of crystallization centers and the presence of growing polycrystalline diamonds.

REFERENCES

- 1. Novikov, N.V.; Ivakhnenko, S. A.; and Katsay, M.Ya.: Kinetics of diamond crystals growth at high static pressure. MRS Int.Conf.Proc., 1999, pp.71-80.
- 2. Sugano, T.; et. al. Pressure and temperature region of diamond formation in system graphite and Fe containing alloys. Diam. and Rel. Mat., no 5, 1996, pp.29-33.
- 3. Borimskiy, A. I.; Delevi, V.G.; and Nagorniy, P. A.: Kinetics of formation and growth of diamonds in the Fe-Si-C system. J. Superhard Mat., vol. 21, no 3, 1999, pp. 6-11.
- 4. Champion, F.C.: Electronic properties of diamond. Butterworths, London, 1963, P.130.
- 5. Dean, P.J.: Bound exitons and donor-acceptor pairs in natural and synthetic diamond. Phys. Rev. A., vol. 139, no 2, 1965, pp. 588-602.
- 6. Shimomura, S.; Kanda, H.; and Nakazawa, H.: Observation of micro-inclusions in diamond by scanning X-ray analytical microscope. Diam. amd Rel. Mat., no 6, 1997, pp. 1680-1682.
- 7. Shulzhenko, A.A.; Novikov, N.V.; and Chipenko, G.V.: Peculiarities of diamond growth in the system based on Mg. J. of Superhard Mat., no 3, 1988, pp. 10-11.
- 8. Strong, N.M.; Hanneman R.E.: Crystallization of diamond and graphite. J. Chem. Phis.; vol. 46, no 9, 1967, pp.3668-3676.
- 9. Shulzhenko, A.A.; et. al. State diagram of Mg-C system at 7.7 GPa pressure. J. of Superhard Mat., no 4, 1988, pp. 17-21.
- 10. Massalski, T.B.; et. al. Binary Alloy Phase Diagrams. ASM International, Materials Park, 1990, P. 650.
- 11. Shulzhenko, A.A.; et. al. Peculiarities of diamond synthesis in the system growth contenting Zn and Mg. Kiev, Synthesis, sintering and properties of superhard mat., 2000, pp. 15-22.

POLYMERIC NITROGEN

M. I. Eremets, M. Popov, I. A. Trojan, V. Denisov, P. Dera, R. J. Hemley

Max Planck Inst. für Chemie, Postfach 3060, 55020 Mainz, Germany Geophysical Laboratory, Carnegie Instit. of Washington, Washington DC 20015-1305, USA

Abstract

Common nitrogen consists of diatomic molecule in which atoms hold each other with the strongest triple covalent bonds. However, in principle, nitrogen atoms can be connected with single or double bonds creating a net of atoms similar to polymeric carbon. The non-molecular nitrogen phase has been recently synthesized at very high pressures about 150 GPa, but it can be recovered to atmospheric pressure due to the huge hysteresis of the transformation [Eremets, M.I. et al., Nature 411 (2001) 170]. In the present work in addition to the direct polymerization of N_2 molecules we explore a different approach to the nitrogen polymerization: molecular N_3 anions in the lattice of NaN₃ have been squeezed at pressures up to 160 GPa at temperatures 10-300 K. Raman spectra, X-ray diffraction and electrical conductivity were measured in a diamond anvil cell. As a result of pressurizing to 120-160 GPa sodium azide transforms to new structures completely different from molecular consisted of linear N_3 molecules. These new nonmolecular phases preserve at release pressure to the lowest pressures in diamond anvil cell (< 1 GPa) and some of them can be recovered.

One of these structures (phase I) starts to form at 17 GPa. Raman bands at 1670 - 1850 cm⁻¹ are characteristic for this phase. It appears in the pure form (without signs of molecular ion azide) after pressurizing up to 120-160 GPa (or 80 GPa with subsequent large plastic deformation) and persists in the confined cell to the lowest pressures (0-1 GPa). Probably this phase is formed of strongly coupled azide ions forming new molecules or other clusters.

In the 50 to 160 GPa pressure range the amorphous phase III is formed. The phase III is conductive; it is completely black and opaque. It partly transforms back to the phase I at 50 GPa upon pressure release. This phase is most probably formed by layers of polymeric nitrogen separated by layers of sodium atoms. Other observed phases are formed by different complexes of nitrogen.

Keywords: nitrogen, polymerization, high pressure, Raman spectra.

Formation and analysis of dense boron carbide coatings with a low porosity formed by electromagnetically accelerated plasma spraying

Junya Kitamura

Japan Fine Ceramics Center
i.kitamura@aist.go.ip

Shu Usuba, Yozo Kakudate, Hiroyuki Yokoi, Kazuhiro Yamamoto, Akihiro Tanaka , Shuzo Fujiwara

National Institute of Advanced Industrial Science and Technology

Abstract

Thick coatings, which are necessary for many industrial fields, are easily obtained using thermal spraying compared with other methods such as CVD and PVD. However, the porosity is relatively high in the spray coatings. The ambient gases passing through the many pores in the coating may damage a base substrate material, and the coating would be easily detached. We have obtained thick boron carbide (B4C) coating with a porosity of 3% using electromagnetically accelerated plasma spraying. In this study, by using smaller powder of 2 micron in diameter, dense B4C coatings are formed with a low porosity of less than 1%. The size of the pores is also drastically decreased.

PROPERTIES OF CARBON DEPOSITS FORMED BY PLASMA SPRAYING OF NANODIAMOND

Anna Gubarevich, Osamu Odawara

Department of Materials Science and Engineering, Tokyo Institute of Technology, 4259 Nagatsuta-cho, Midori-ku, Yokohama, 226-8503, JAPAN

Junya Kitamura, Shu Usuba, Hiroyuki Yokoi, Yozo Kakudate, and Akihiro Tanaka Research Center for Advanced Carbon Materials, National Institute of Advanced Industrial Science and Technology AIST Central 5, 1-1-1 Higashi, Tsukuba, Ibaraki 305-8565, JAPAN

ABSTRACT

Deposits of carbon nanoparticles based on an onion-like structure were fabricated by a new one-step method, an electromagnetically accelerated plasma spraying (EMAPS) deposition, from detonation nanodiamond powders on stainless steel substrates. The presence of spherical and polyhedral carbon onion particles was confirmed by transmission electron microscopy (TEM) studies. Carbon bonding in virgin powders and synthesized deposits was studied by two-wavelength Raman spectroscopy under excitation by visible (514 nm) and UV (244 nm) irradiation. The transformation of nanodiamonds to closed curved graphitic nanoparticles was explained by intensive heating and electron irradiation of the spraying powder in plasma. Friction measurement of the deposits showed their availability as solid lubricant films.

Keywords: onion-like carbon, nanodiamond, plasma spray, Raman spectroscopy, solid lubricant

Onion-like carbon (OLC) belongs to the fullerenic or curved-layer carbon structures and consists of closed, concentrically arranged graphitic shells. Many methods have been proposed for OLC synthesis. They can be classified into two groups according to the mechanism of the OLC formation. The first one is the reconstruction of some carbon solid structure under severe conditions: high-temperature treatment of nanodiamond powders (refs. 1 and 2), electron irradiation of graphitic precursors (soot, nanotubes) and diamond crystals (ref. 3), and ball-milling of graphite (ref. 4). The second approach is based on the condensation of OLC from small carbon fragments, such as by the method of implanting high-dose carbon ions into the metal layers (ref. 5), growth by radio-frequency plasmaenhanced chemical vapor deposition (ref. 6), rf-cosputtering (ref. 7), and arc discharge in water (ref. 8). OLC can be obtained as a powder (refs. 1 to 4 and 8), or a film (refs. 5 to 7). OLC possesses attractive properties, and a number of applications are expected to be found. Possible applications are as an optical limiting agent (ref. 9), and as a solid lubricant, especially in space technology (refs. 5 and 10). Due to the strong intrinsic structure of the OLC particles, the near-round shape, and the small size, the particles may decrease the friction coefficient and improve wear protection. To apply the particles as a solid film lubricant, it is necessary to develop an effective way to produce OLC coatings on various substrates. We present here a new method to produce OLC-containing films on steel substrates by plasma spraying of detonation nanodiamond powders.

EXPERIMENTAL METHOD

Spraying of nanodiamonds was conducted by electromagnetically accelerated plasma spraying (EMAPS) (ref. 11), a novel spraying technique which utilizes pulsed high-current arc plasma and is capable of accelerating particles in the velocity range between 1 and 3 km/s, which is not attainable by conventional plasma spraying. Such a high particle velocity is considered to be advantageous in forming a dense spray deposit with high adhesion to the substrate. Another important advantage of EMAPS in this work was its capability of making spray experiments using very small amount of powders The EMAPS process is illustrated in Fig. 1. The apparatus consists of a 3 mF capacitor bank and a coaxial plasma channel combined with a vacuum chamber in which the air pressure is less than 10Pa. Commercially available detonation nanodiamonds 0.05 g in weight were injected with argon into the plasma channel. When the injected nanodiamond particles were dispersed almost all over the plasma channel, a high-current

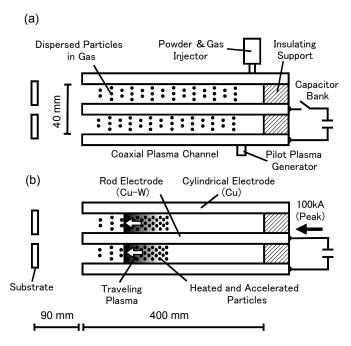


Figure 1. Schematic diagram of EMAPS process. (a) Injection of nanodiamond particles with argon into the plasma channel. (b) Subsequent heating and accelerating of the particles by fast traveling argon plasma caused by pulsed high current arc discharge.

arc discharge of 100kA in peak and 300 ms in duration was initiated at the position of a pilot plasma generator. The transient argon pressure in the plasma channel at the time of arc initiation was approximately 10 kPa. Subsequently, a fast traveling, spatially confined argon plasma was formed by an intense electromagnetic force, i.e., the Lorentz force. The observed traveling velocity, spatial length, and calculated peak pressure of the plasma were 2.5 km/s, 60-100 mm, and 1MPa, respectively. This plasma was considered to be in local thermal equilibrium at a temperature of around 20000K according to the experimental observation of argon positive column plasma (ref. 12), and high-current arc plasma in a railgun-type electromagnetic launcher (ref. 13). The nanodiamond particles were heated and accelerated by the plasma and sprayed on the mirror-polished stainless steel (SUS304) substrate located in the vacuum chamber. The duration of interaction between the nanodiamond particle and the plasma was less than 300 µs.

Deposits on the substrate were detached and dispersed in ethanol by ultrasound for study by transmission electron microscopy (TEM) with a point resolution of 0.19 nm under 200 kV accelerating voltage (Topcon EM-002B). The sample of virgin nanodiamonds was treated by the same method. Carbon bonding in virgin powders and synthesized deposits was studied by Raman spectroscopy under excitation by visible (514 nm, JASCO NRS-2100) and UV (244 nm, JASCO NRS-1000UV) laser irradiation. Friction coefficient of as received carbon deposit on the substrate was measured by ball-on-disk method (CEM TRIBOMETER).

RESULT AND DISCUSSION

Obtained deposits about 1µm in thickness by single deposition procedure were fairly soft and could be detached from the substrate. Fig. 2(a) shows TEM image of diamond nanoparticles less than 10 nm in size used as starting material. The lattice fringes correspond to the {111} crystal planes of diamond, with an interplanar distance consistent with that of bulk diamond (0.206 nm). The shape of the particles is nearly spherical, and some crystals have an octahedral form. Figure 2(b) demonstrates the products of the nanodiamond transformation during the EMAPS process. No original nanodiamond particles can be seen in the picture, only curved graphitic structures: graphite ribbons and carbon onions (spherical and polyhedral). Graphite ribbons consist of 3 or 4 graphitic planes, and their interplanar spacing equals 0.37 nm, exceeding that of graphite (0.3376 nm). The size of carbon onions ranges from several nanometers to 10 nm. The number of graphite shells in the particle can reach 10-12 but is typically 7-8. The average interplanar distance is 0.35 nm.

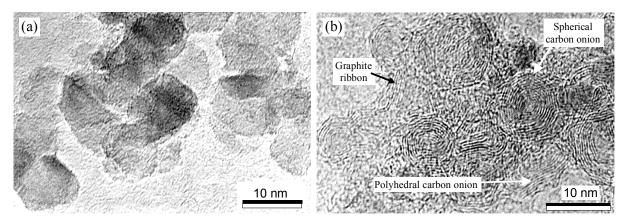


Figure 2. TEM images of (a) nanodiamond particles, (b) products of nanodiamond transformation during EMAPS.

In view of the previously reported data on nanodiamond transformation to OLC under high-temperature treatment (refs. 1 and 2), let us suppose that the structural reformation of the virgin particles occurs under severe plasma conditions during the EMAPS process. A combination of high temperature and high electron concentration favors the formation of curved graphitic structures (ref. 14). However, another concurrent mechanism based on the deeper destruction of virgin particles may be considered. In particular, the nanodiamond particles may undergo evaporation and form a homogeneous cloud (carbon plasma) which, after being under cooling conditions in the chamber, can coagulate in an onion-like structure. Results of the experiments carried out for the spraying of other carbon nanomaterials, not reported here, prove the first assumption since the quality of the coating was found to be strongly dependent on the initial material. Nevertheless, some overlapping of both models should not be ignored. Therefore, an exact simulation of the interaction of nanodiamonds with plasma during the EMAPS process is required.

Figures 3(a) and (b) show the Raman spectra measured from the nanodiamond powder and deposited coatings, respectively. For the carbon materials, especially under UV irradiation, the question of possible damage arises. For

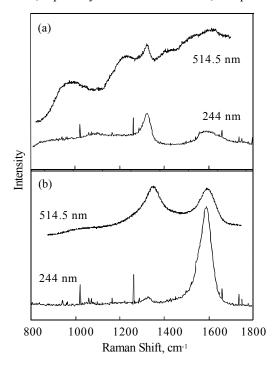


Figure 3. Two-wavelength Raman spectra of (a) nanodiamond, (b) EMAPS carbon coatings.

that reason, in order to collect the representative spectra of the samples, a mapping procedure was applied. The signals from about 50 points, obtained by moving the sample by 20 mm increments in the XY plane, were collected and averaged. This method provides a high signal-to-noise ratio for the short irradiation time of each investigated area. The difference between spectra obtained by visible and UV irradiation is clearly seen. The excited at the 514.5 nm spectrum of nanodiamond, shown in Fig. 3(a), consists of the following main features on a strong photoluminescence background: a characteristic peak of the nanodiamond phase at 1323 cm⁻¹, broad bands around 1090 - 1100 cm⁻¹, 1220 cm⁻¹, and 1600 cm⁻¹ (G mode), shoulders at 1400-1450 cm⁻¹ and at 1500 – 1550 cm⁻¹. The shift of the diamond peak from the 1332 cm⁻¹ position is due to a size effect and was previously well explained by the phonon confinement model (ref. 16). The existing in the nanodiamond powder admixtures of sp² bonded carbon lead to the appearing of the G band at 1600 cm⁻¹. Other spectrum bands and shoulders can not be assigned to densityof-state features of either the sp³-bonded carbon, nor the sp² phase, because they disappear in a UV Raman spectrum of the virgin nanodiamond. This UV spectrum, presented at Fig. 3(a), has the same nanodiamond characteristic peak at 1323 cm^{-1} , a low asymmetric band around $1560 - 1600 \text{ cm}^{-1}$, and a feature near $1060 - 1080 \text{ cm}^{-1}$. The band at 1560 – 1600 cm⁻¹ belongs to the sp²-bonded carbon (G mode). The feature at 1060 – 1080 cm⁻¹, known in literature as a T peak, is due to the resonant enhancement of s-states (ref. 15). The Raman study in the UV region (244 nm, 5.1 eV) gives more reliable information about the presence of sp² and sp³ carbon phases because this energy is sufficient to excite electronic transitions in both structures and the spectra do not emphasize any particular phase. The laser energy of visible light 2.41 eV (514.5 nm) is comparable with the local sp² bonded carbon energy gap, thus the electronic p-p* transition often leads to the dominance of the G and D bands of the other diamond peak.

The spectra of EMAPS carbon coatings are presented in Fig. 3(b). The spectrum excited at 514.5 nm is typical for a large variety of carbon materials. The superposition of the G (~1590 cm⁻¹) and D (~1350 cm⁻¹) bands determines the spectrum shape. As can be seen in Fig. 3(b), the 244 nm spectrum of the carbon coating consists of a strong asymmetric G peak (maximum 1586 cm⁻¹) and a small peak (near 1325 cm⁻¹), but the D peak is absent. The G mode is a sign of the sp² carbon bond stretching and is a characteristic feature of graphite (with the position of pristine graphite at 1582 cm⁻¹). In the presence of disorder, the breakdown of the wave-vector selection rules occurs, and an additional band, the D band, appears in visible spectra. The D peak is caused by the breathing motion of carbon rings, but an exact and complete theory of the nature of this band does not yet exist (ref. 15). The G peak does not disperse with excitation energy in the cases of bulk graphite, nanocrystalline graphite, and glassy carbon. The upward shift occurs only for amorphous networks (ref. 15). The D mode is quite sensitive to the excitation energy, and its intensity decreases when it moves from the visible to the ultraviolet region. The D band disappears at 5.1 eV excitation energy for nanocrystalline graphite but not for amorphous carbons (ref. 15).

Only a few Raman studies have been carried out for OLC. It was shown that a carbon onion possesses a distinctive band in addition to the D and G peaks (ref. 16). The position of this band depends on the quantity of shells. For a particle with seven shells, the band lies at 1572 nm (laser excitation wavelength 457.9 nm). The shift from the characteristic G mode has been explained by the curvature of the graphitic shells (ref. 16). Our spectra

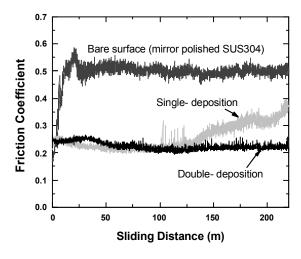


Figure 4. Result of friction measurements in dry air by ball-on-disk method using SiC ball 4.75mm in diameter under the condition of normal force of 1 N and sliding speed of 5cm/s.

excited by 514.5 nm laser did not show this peculiarity, and they are similar to those presented for OLC (ref. 17). We suppose that the splitting of the graphite mode or the shift in the visible Raman spectra can be observed only for well-formed, perfect OLC, but it has been suggested that spherical carbon onions are constructed of imperfect nanodomains with a number of defects, such as dangling bonds (ref. 17). In this case, the spectrum shape and position of the G band in particular seem to be dominated not by closed carbon shells but by some carbon clusters constructed from curved graphitic planes and forming nearly spherical onion-like particles. The data of Obraztsova et al (ref. 16) confirmed that the synthesis of a nearly ideal carbon onion structure from detonation nanodiamond is possible; it is only a question of the experimental conditions. As seen in the TEM pictures (Fig. 2 (b)), the OLC formed by the EMAPS process has a number of defects, which explains the presence in the 514.5 nm spectrum of only the G band near 1590 cm⁻¹. However, the UV Raman spectrum extracts some features of the OLC structure. Line shape analysis performed by fitting of the UV Raman spectrum of OLC with two Gaussians showed that the G peak is a superposition of two bands: 1571 cm⁻¹ and 1592 cm⁻¹. The G band undergoes a high-frequency shift compared with the 514.5 nm spectrum (1590 cm⁻¹), and the shoulder in the G mode, responsible for the OLC, becomes evident. From the comparison between the spectra excited by visible and UV irradiation, particularly (1) the G band shift and splitting and (2) the disappearance of the D band in the UV spectrum, we suppose that the carbon coating consists of organized sp² clusters which form defective graphitic curved structures, including closed shells of OLC (refs. 15 and 16).

Figure 4 shows the friction data of carbon deposits obtained by single- and double EMAPS depositions compared with the friction of bare surface of mirror polished 10 mm x 10 mm square SUS304 substrates. It is demonstrated that the carbon deposit shows apparent lubricating ability whose durability can be improved by increasing the thickness of deposit. Friction measurements in vacuum are now in progress to examine the contribution of OLC particles in the lubricating ability of the deposits.

CONCLUSION

From TEM and Raman studies, it is found that the carbon deposit obtained by EMAPS deposition consists of organized sp² clusters which form defective graphitic curved structures, including closed shells of OLC. The deposit shows apparent lubricating ability whose durability can be improved by increasing the thickness of deposit. Although further effort is necessary to improve the degree of perfection of the OLC structure, the deposition process described here demonstrates a new one-step method to obtain OLC based coatings. This results shows the possibility of using plasma spraying, including EMAPS, to fabricate not only OLC dominant coatings but also the coating of nanodiamond- and OLC-dispersed composite materials, which are promising materials from the standpoint of low friction and high wear resistance in non-oil lubrication (ref. 18).

REFERENCES

- 1. Kuznetsov V.L., Chuvilin A.L., Moroz E.M., et al.: Effect of explosions on the structure of detonation soots: ultradisperse diamond and onion carbon, Carbon, vol. 32, (1994), 873-882.
- 2 Tomita S., Burian A., Dore J. C., et al.: Diamond nanoparticles to carbon onions transformation: X-ray diffraction studies, Carbon, vol. 40, (2002), 1469-1474.
- 3 Lu-Chang Qin and Iijima S.: Onion-like graphitic particles produced from diamond, Chem. Phys. Lett., Vol. 262, (1996), 252-258.
- 4 Chen X.H., Yang H.S., Wu G.T., et al.: Generation of curved or closed-shell carbon nanostructures by ball-milling of graphite, J. Cryst. Growth, vol. 218, (2000), 57-61.
- 5 Cabioc'h T., Thune E., Riviere J.P., et al.: Structure and properties of carbon onion layers deposited onto various substrates, J. Appl. Phys., vol. 91, (2002), 1560-1567.
- 6 Chen X.H., Deng F.M., Wang J.X., et al.: New method of carbon onion growth by radio-frequency plasma-enhanced chemical vapor deposition, Chem. Phys. Lett., vol. 336, (2001), 201-204.
- Mamezaki O., Adachi H., Tomita S., et al.: Thin Films of Carbon Nanocapsules and Onion-Like Graphitic Particles Prepared by the Cosputtering Method, Jpn. J. Appl. Phys., Part 1 vol. 39, (2000), 6680-6683.
- 8 Sano N., Wang H., Alexandrou I., et al.: Properties of carbon onions produced by an arc discharge in water, J. Appl. Phys., vol. 92, (2002), 2783-2788.
- 9 Koudoumas E., Kokkinaki O., Konstantaki M., et al.: Onion-like carbon and diamond nanoparticles for optical limiting, Chem. Phys. Lett., vol. 357, (2002), 336-340.

- Hirata A., Igarashi M., Kaito T.: Solid lubricant properties of carbon onions prepared from diamond clusters and patricles, Proc.6th ADC/SFC Technology Joint Conference (ADC/FCT 2001)/ NASA/CP-2001-210948, (2001), 538-543.
- 11 Kitamura J., Usuba S., Kakudate Y., et al.: Boron Carbide Coating by Electromagnetically Accelerated Plasma Spraying, J. Therm. Spr. Techn., vol. 12, no.1, (2003) 70-76.
- 12 Olsen H.N.: Partition function cutoff and lowering of the ionization potential in an argon plasma, Phys. Rev., vol. 124, (1961), 1703-1708.
- 13 Marshall R.A.: Plasma puffing from a railgun armature, IEEE Trans. Mag., vol. MAG-20, no.2, (1984), 264-266.
- 14 Churilov G.N., Novikov P.V., Tarabanko V.E., et al.: On the mechanism of fullerene formation in a carbon plasma, Carbon, vol. 40, (2002), 891-896.
- 15 Ferrari A.C.: Determination of bonding in diamond-like carbon by Raman spectroscopy, Diam. Rel. Mater., vol. 11, (2002), 1053-1061.
- 16 Obraztsova E.D., Fujii M., Hayashi S., et al.: Raman identification of onion-like carbon, Carbon, vol. 36, (1998), 821-826.
- 17 Tomita S., Sakura T., Ohta H., et al.: Structure and electronic properties of carbon onions, J. Chem. Phys., vol. 114, (2001), 7477-4782.
- 18 Hanada K., Mayuzumi M., Nakayama N., et al.: Processing and characterization of cluster diamond dispersed Al-Si-Cu-Mg composite, J. Mater. Process Technol., vol. 119, (2001), 216-221.

THE JOINING OF DIAMOND TO SIC BY ENERGIZATION PULSE SINTERING METHOD

Jun Tanabe

Nippon Institute of Technology Miyashiro-machi, Minamisaitama-gun, Saitama Pref., 345-8501 JAPAN

Abstract

The application of the energization pulse sintering (EPS) method is comparatively made in low temperature degree and a method of effective diffusion joining between solids in a diamond and the joining of various base materials by a short time. In this study, as materials which were easy to diffuse into diamond and which obtain a bonded SiC was joined with diamond. The junction planes of diamond/SiC confirmed diffusion couple adhesion with all joining conditions by scanning electron microscopy (SEM) and an energy dispersion system (EDS) result after the EPS method. These results showed that grain boundary diffusion and volume diffusion progressed with the volume transport mechanism.

Keywords: diamond, silicon, graphite, : the energization pulse sintering, diffusion bonding, ceramic, non-ferrous metallurgy.

INTRODUCTION

Diamond has the highest strength, tensile strength and compression strength among materials, and it has excellent in physics and chemical property and electrical properties; therefore, there need for cutting tools and gears to which diamond must be applied by joining it to an other circuit substrate material. Possibilities for such joining are brazing method (the liquid phase process) and the CVD and PVD (the vapor phase process). The necessary bond strength is not obtained the brazing method in term of the thermal stress during the cooling. In the meantime, there is a restriction for both the CVD method and the PVD method for film thickness. Therefore, the application of the energization pulse sintering (EPS) method (Figure 1) is comparatively made in low temperature degree and a method of effective diffusion joining between solids in a diamond and the joining of various base materials by a short time.

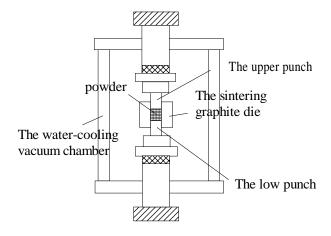


Figure 1 Schematic diagram of the EPS method

In this study, as materials which were easy to diffuse into diamond and which obtain a bonded interface, SiC, were selected. Then, each listed material was joined with diamond and the diffusion mechanism and bond strength were examined.

NASA/CP—2003-212319 605 August 18, 2003

Experimental

A joining experiment

The diamond grains were produced by a high-temperature and high-pressure method, and had a the particle size of about 150 μ m. Figure 2 shows the diamond grains .

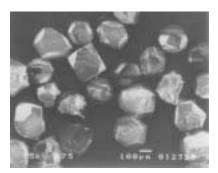


Figure 2 SEM observation of the diamond substrate made by high temperature and pressure method.

A carbon sheet was wound around the inner surface of the graphite die (outer diameter: 30.0mm, a bore: 15.4mm) in order to prevent the reaction, powder (SiC) were placed in the die to 2g, and then 0.2g of diamond grains were placed in the die. The carbon sheet was inserted between the punch and the sample. Figure 2 shows schematic diagram of the die.

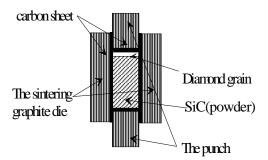


Figure 2 Schematic diagram of the die.

The graphite die with the powder sample was placed in an spark plasma sintering (SPS)² furnace, and the furnace chamber was exhausted to a vacuum (6Pa); then under held for the as welding force of 34MPa, it rapidly changed for temperature conditions of 773K, 973K and 1173K, and maintainers times of 1.2ks, 2.4ks and 3.6ks in the EPS method.

Evaluation method

To evaluate the sample after the processing, the bonded interface was observed by scanning electron microscopy (SEM) and an energy dispersion system (EDS). As a method of evaluating the bond strength of the sample, compression testing was used.

Result and Discussion

Fig. 3 shows by SEM and an EDS result of the junction planes of diamond/SiC after the EPS method.

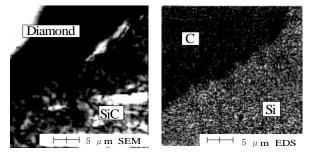


Figure 3 Energy dispersion-type X-ray analysis of SiC/diamond obtained at maintenance temperature:973K, heating time:2.4ks.

The junction planes of diamond/SiC confirmed diffusion couple adhesion with all joining conditions by SEM and an EDS result after the EPS method. These results showed that grain boundary diffusion and volume diffusion progressed with the volume transport mechanism.

I made a truth stress - truth distortion diagram from a result of compression examination as an evaluation method of joining strength of a sample provided by EPS method. Fig.11 shows a truth stress - truth distortion diagram of a SiC/ diamond.

Fig.11 shows a truth stress - truth distortion diagram of a SiC/diamond.

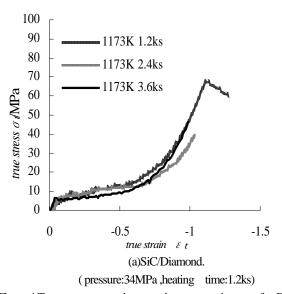


Figure 4 True stress-true strain curves by compression test after EPS method.

The stress in which it was not a plug from the result of compression test committed the bond strength of the sample. And, the bond strength of the sample was deduced from the part in which the curve caused elastic deformation. Though the diffusion is the rate-limiting, and the bond strength seems to increase by extending retention time, and from Fig4, the difference between the strength by the change in the retention time is not almost observed. It can be said that the EPS processing is efficient for this fact and that the joining can quickly do it in the short time of 1.2ks (20 minutes). From the result of this study, compression strength was a condition of the 1173Ks temperature, and it was 10.0MPa. As a result, it can be said that to some extent, adhesion was achieved under all conditions.

CONCLUSION

In this study, joining experiment of SiC/diamond by the EPS method was carried out, and following fact was proven:

- (1) On the joining by the EPS method, grain boundary diffusion and volume diffusion progressed with the volume transport mechanism.
- (2) On the bond strength, they are the welding force and short time, and the joining can possibly call it effective measures from any fact.

. ACKNOWLEDGMENTS

We appreciate the support provided by High-Tech. Research Project from the Ministry of Education, Culture, Sports, Science and Technology.

REFERENCES

- 1. S.Suita and K.Kawamoto: Ceramics Zairyou, Toukyoudaigakusyupannkai, Tokyo, , 1989,25-27 (in Japanese)
- M.Tokita: Houdenn Plasma Shouketu (SPS) System no Genjyou to Syouraisei, Sumitomo Sekitan Kougyou, Kwasaki, 1994,1-10 (in Japanese)

Modeling the deposition of carbon and nitrogen atom/ions on wurtzite AlN (001) surface

R Q Zhang, Dongju Zhang

Center of Super-Diamond and Advanced Films (COSDAF) and Department of Physics and Materials Sciences, City University of Hong Kong, Hong Kong, China aprqz@cityu.edu.hk

Abstract

The bonding behaviors of carbon and nitrogen atom/ions to wurtzite AlN (001) surface have been investigated theoretically using ab initio HF method and the semiempirical AM1 molecular orbital theory. The reactivities of ions were found to be higher on the surface than their neutral atoms based on the frontier molecular orbital theory. The information of the potential energy surfaces calculated for carbon and nitrogen atoms on the AlN substrate suggested that the more ordered and stable Al-N bond can be achieved compared to the Al-C bond. The surface nitride of AlN substrate would improve the quality of the interfacial bonds and hence increase the adhesion between the diamond films and the substrate. Further, the use of the anion beams with an appropriate intensity in ion beam assisted deposition is expected to be more effective for the forming of good ordered interfacial bond than the ionic beam.

Proceedings of the Seventh Applied Diamond Conference/ Third Frontier Carbon Technology Joint Conference (ADC/FCT 2003) M. Murakawa, M. Miyoshi, Y. Koga, L. Schäfer, and Y. Tzeng (Editors)

Room temperature growth of homogeneous ultrathin Co films

on 6H-SiC (0001)-6 $\sqrt{3}\times6\sqrt{3}R30^{\circ}$ surface

Wei Chen^a, Hai Xu^b, A.T.S. Wee^b and Kian Ping LOH^{a,*}

^aDepartment of Chemistry, National University of Singapore, 3 Science Drive 3, Singapore.

^bDepartment of Physics, National University of Singapore, 3 Science Drive 3, Singapore.

Abstract

The effect of a periodic template on the nucleation of cobalt clusters was studied by considering the nucleation phenomena of Co atoms on 6H-SiC (0001)- $6\sqrt{3}\times6\sqrt{3}R30^{\circ}$ surface. The motivation of our study was to see whether the highly "porous" reconstruction allows the Co clusters to form regular-sized, periodic nano-islands. The nucleation process was studied by a combination of UHV-STM, RHEED, LEED and XPS. The 6H-SiC (0001)- $6\sqrt{3}\times6\sqrt{3}R30^{\circ}$ reconstructed surface, which contains homogenous honeycombs (2~3nm in diameter), can confine the Co atoms in the honeycomb and prevent its nucleation into larger clusters during the initial film formation stage at room temperature. The honeycomb layer also acts as a barrier against cobalt silicide formation. XPS results showed that no cobalt silicide was formed even after the sample was annealed to 1100° C. We propose that this can be a novel method to prepare ferromagnetic nano-metal arrays.

*corresponding author: Dr Kian Ping LOH, email: chmlohkp@nus.edu.sg, FAX: +65 6779 1691 Phone (office):65-6874-4778

Key words: room temperature deposition; cobalt; carbide; scanning tunnelimg microscope; 6H-SiC (0001);

AUTHOR INDEX

Achard, J. 130 Ahmed, W. 234 Ahn, J. 95, 275 Akitsu, T. 155 Aleksov, A. 159, 165 Amaratunga, G.A.J. 18, 26, 31 Anderson, A.B. 527 Ando, T. 5 Angus, J.C. 527 Aoki, Y. 423, 490, 557

Baba, K. 340 Bai, Z. 444 Baklanova, N.I. 367 Ballutaud, D. 291 Bangert, U. 533 Batov, D.V. 533 Bello, I. 353, 379, 553 Bewilogua, K. 329 Bhimarasetti, G. 34 Blank, V.D. 533 Bobrovnitchii, G.S. 592 Borcha, M.D. 315 Boskovic, B.O. 59 Boutry-Forveille, A. 291 Brücher, M. 191 Buga, S.G. 533

Carlson, R.M.K. 526 Castex, M.-C. 130 Chan, C.Y. 379, 553 Chan, K.M. 379 Chang, S.-J. 484 Chatterjee, A. 178 Chen, M.Y. 406, 444 Chen, W. 610 Chen, Y.C. 12 Chen, Y.G. 141 Chhowalla, M. 18, 26, 31 Chiou, Y.-Z. 484 Chun, M.-S. 152 Coe, S.E. 111 Cojocaru, C.S. 25 Compton, R. 178

Dahl, J.E. 526 Dai, Y. 320 Danilov, I. 297 Dementjev, A.P. 266, 279, 345 Denisov, V. 597 Dera, P. 597 Derkach, V.N. 297 Detkov, P.Y. 179 Dmitriy, S. 45 Doering, P.J. 173 Dresselhaus, M.S. 19 Dua, A.K. 545

Eaton, S.C. 527 Ebbesen 33 Endo, M. 19 Enomoto, K. 70 Eremets, M.I. 597

Fang, R.C. 365, 491, 544
Feng, Q. 80, 90, 260
Ferrari, A.C. 389
Fischer, P. 303
Fizzotti, F. 120
Fodchuk, I.M. 315
Foord, J. 178
Forrest, R.D. 59
Freeman, M. 324
Fries-Carr, S. 324
Frolov, V.D. 179
Fryda, M. 128
Fuchigami, K. 436
Fujiwara, S. 598
Fukuda, K. 328

Garin, B.M. 297
Ger, M. 128
Gicquel, A. 130
Gitis, N. 495
Givargizov, E.I. 540
Goringe, M.J. 96, 500
Gruen, D.M. 525
Gu, C. 284
Gubarevich, A. 599
Gutiérrez-Sosa, A. 533
Gyoda, K. 557

Han, J. 17
Haq, S. 59
Hara, K. 478
Harvey, A.J. 533
Hasegawa, M. 129
Hasegawa, T. 366
Hashizume, T. 445
Hasko, D.G. 18
Hatada, R. 340
Hatta, A. 155, 328, 490
Hauert, R. 395
Hayashi, K. 130
Hayashi, T. 19
Hayashi, Y. 585

He, X.C. 153, 320, 555 Katagiri, M. 112 Heidinger, R. 297 Kawamura, A. 114 Hemley, R.J. 597 Kawarada, H. 174 Hernandez-Gullien, F.J. 136 Keunecke, M. 329 Hester, J.R. 52 Khmelnitskiv, R.A. 303 Khomich, A.V. 303, 309 Hirata, A. 76 Höfer, M. 539 Kikuchi, T. 26 Högström, H. 115 Kim, S.-H. 569 Honda, S. 244 Kim, T.-Y. 419, 507, 511 Horita, K.I. 478 Kim, Y.A. 19 Horiuchi, K. 114 Kirpilenko, G. 471 Hsu, W.K. 96 Kitabatake, M. 154 Hu, C.G. 53, 80, 90 Kitakata, S. 70 Hu, X. 320, 555 Kitamura, J. 598, 599 Hualiang, S. 506 Kleiman, J. 87 Huang, B.-R. 484 Knorr, M. 32 Hümmelgen, I.A. 471 Ko, D.-H. 419 Kobashi, K. 130 Kobayashi, N. 159, 165 Ide, T. 114 Iijima, S. 381 Kobayashi, T. 244, 569 Iimura, K. 26 Koga, Y. 42, 64, 87, 129, 271, 328, 350, 351, 352, Inagaki, H. 328 354, 359, 381, 429, 430, 436, 556 Inoue, Y. 465 Kohn, E. 136, 159, 165 Isberg, J. 111 Koizumi, S. 112 Kojima, M. 197 Ishihara, M. 271, 350, 352 Ishikawa, M. 556 Kokai, F. 352, 381, 523 Ishikura, T. 114 Komatsu, S. 244 Ito, T. 152, 259 Komatsu, T. 383 Ivakin, E.V. 309 Kong, C.Y. 260 Iwai, M. 222 Kononenko, T.V. 303 Iwamoto, C. 378 Kononenko, V.V. 303 Iwamura, K. 155 Konov, V.I. 179, 303 Korfhagen, S.T. 406, 444 Jackson, M. 234 Kosai, H. 324 Jean, O. 25 Kotake, K. 447 Kott, R. 228 Ji, H. 494 Jia, J.P. 153 Kroto, H.W. 96 Jia, S. 31 Kubovic, M. 159, 165 Jiaqi, Z. 512 Kulnitskiy, B.A. 533 Jiecai, H. 512 Kulyukin, V.N. 367 Jimbo, T. 585 Kunieda, M. 222 Jin, Z.S. 492, 493, 494 Kutsay, O. 353 Jomard, F. 291 Kuwabara, J. 110 Joshi, P.N. 545 Kyotani, M. 42 Ju, B.-K. 533 Lacerda, R. 18 Kakudate, Y. 366, 598, 599 Lam, C.W. 353 Kallfass, I. 159 Lau, S.P. 451 Kanda, H. 46, 112, 331 Laude, T. 46 Kaneko, T. 328 Lee, C.S. 40, 41, 419, 507, 511 Kanki, T. 26 Lee, D.-J. 533 Kanno, S. 109 Lee, K.H. 465 Karabutov, A.V. 179 Lee, K.R. 419, 507, 511 Lee, S.C. 511 Karlsson, M. 115 Lee, S.T. 40, 41, 353, 379, 553 Kasture, M.V. 545 Kasu, M. 159, 165 Lee, S-B. 18

Lee, Y.-D. 533 Lee, Y.-H. 533 Legagneux, P. 18 Li, C.P. 41 Li, J. 275 Li, J.J. 492, 493, 494 Li, J.Q. 95 Li, R.B. 153, 320, 555 Li, X. 34 Li, Z.K. 493 Liao, K.J. 53, 80, 90, 101, 260 Liao, Y. 365, 491, 544 Liehr, M. 556 Lifshitz, Y. 353, 553 Lin, I.N. 88, 547 Lin, T.-K. 484 Litovsky, E. 87 Liu, G.B. 90, 101 Liu, S.G. 526 Liu, Y.K. 12, 547 Lo Giudice, A. 120 Loh, K.P. 610 Loubnin, E.N. 179 Louchev, O.A. 46, 52 Lu, X.Y. 492, 493 Luk, W.Y. 353 Lyshenko, D.A. 89 Ma, Y. 101, 260 Makimoto, T. 159, 165 Malogolovets, V.G. 546 Mane, M. 25 Manfredotti, C. 120 Mani, R.C. 34 Mariko, S. 164 Marken, F. 178

Maslakov, K.I. 266, 279, 345 Matsuda, S. 26 Matsudaira, H. 174 Matsuhisa, H. 328, 490 Matsui, H. 42 Matsumoto, S. 379 Matsuoka, T. 381 Matth, T. 128 McEvoy, J. 178 Meng, F.Y. 65 Meng, X.M. 353, 553 Metzger, T.H. 25 Milne, W.I. 18 Misra, D.S. 545 Miyagawa, S. 340 Miyake, S. 440, 445, 447, 460, 466 Miyamoto, S. 174 Miyamoto, Y. 11 Miyazawa, H. 201, 207 Miyoshi, K. 404

Mori, D. 585 Mulcahy, S. 128 Müller, R. 136 Munding, A. 136 Murakami, H. 70 Murakawa, M. 185, 197, 213, 466 Myasnikova, S.E. 297

Nachalna, T.A. 546 Nahm, S. 533 Naito, M. 26 Nakagawa, K. 5 Nakamura, J. 259 Nakamura, T. 271, 350, 354 Nakayama, A. 381 Nakazato, Y. 207 Nikolajeff, F. 115 Nishitani-Gamo, M. Niu, X.B. 365, 544 Noda, M. 573 Noguchi, H. 185, 213 Normand, F.L. 25, 33, 554 Novikov, N.V. 546 Nozhkina, A.Y. 591

Obraztsov, A.N. 89 Odawara, O. 599 Ogawa, H. 147 Ogura, M. 141, 163, 164 Oh, K.-H. 511 Ohana, T. 271, 354 Ohara, H. 407 Ohashi, W. 490 Ohta, R. 465 Ohtake, N. 70, 423, 478 Okajima, Y. 114 Okamoto, Y. 440 Okamura, H. 110 Okushi, H. 109, 129, 141, 147, 163, 164 Okuzumi, F. 564 Olivero, C. 130 Ono, T. 129, 164 Osipov, A.S. 592 Ota, G. 569 Ovsyakov, V.V. 179

Panosyan, Z. 334 Paolini, C. 120 Park, S.J. 419 Parkhomenko, M.P. 297 Parshin, V.V. 297 Peng, H.Y. 494 Pimenov, S.M. 179, 303 Plotnikov, S.A. 345, 472 Podzyrey, G.A. 546 Poliakov, V.P. 471 Polini, R. 234 Siqueira, C.J.M. 471 Polyakov, E.V. 533 Sitar, Z. 564 Polyakov, V.I. 285 Skury, A.L.D. 592 Ponosov, Y.S. 472 Soga, T. 579, 585 Popov, M. 64, 597 Song, K-S., 174 Prater, J.T. 564 Songhe, M. 512 Pribat, D. 18 Spitzberg, U. 159 Stepanyan, A. 334 Qiang, L. 512 Sternberg, M. 525 Qureshi, W. 526 Stolojan, V. 59, 96, 500 Su, Y.-K. 484 Rajan, K. 34 Sugimura, H. 465 Ralchenko, V.G. 285, 309, 540 Sukhadolau, A.V. 309 Robertson, J. 389 Sun, L. 493 Romano, V. 303 Sun, X.H. 41 Rossukanyi, N.M. 285 Sun, Z. 451 Rotter, S. 524 Sunkara, M.K. 34 Roy, M. 545 Sutoh, M. 466 Rubio, A. 11 Suzuki, K. 110, 222 Rubshtein, A.P. 345, 472 Suzuki, M. 129, 163, 350, 352, 372, 429, 430 Rukovishnikov, A.I. 285 Rzepka, E. 291 Tachibana, T. 130 Tai, N.H. 88 Sachdev, H. 32, 330, 380 Takagi, Y. 557 Takahiro, T. 255 Saitoh, T. 440 Sakaguchi, I. 331 Takai, O. 465 Sakai, T. 129, 163, 164 Takaishi, S. 155 Sakuma, N. 129, 163, 164 Takeuchi, S. 185, 197, 201, 207, 213 Sano, N. 26, 31 Tan, S.C. 444 Sato, M. 445 Tanabe, J. 605 Sato, Y. 46 Tanaka, A. 350, 354, 413, 429, 430, 436, 598, 599 Sauer, R. 165 Tanaka, Y. 557 Sawabe, A. 110, 218 Taniguchi, T. 331, 382 Scarsbrook, G.A. 111 Taniwaki, M. 352 Schäfer, L. 539 Taniyasu, Y. 165 Scher, L. 128 Tarapov, S.I. 297 Schmid, P. 136 Tay, B.K. 451 Schumacher, H. 159 Teer, D.G. 323 Schwarze, G.E. 324 Teo, B.K. 41 Seepujak, A. 533 Teo, K.B.K. 18 Sein, H. 234 Teofilov, N. 165 Sekine, A. 207 Teraji, T. 152, 259 Sekine, G. 207 Tian, J.Z. 95 Sharda, T. 579 Tince, D. 32 Sharma, A. 222 Titus, E. 545 Shelby, M. 556 Tkach, V.N. 315 Shen, H. 494, 555 Tománek, D. 10, 11 Shen, H.S. 153 Trakhtenberg, I.S. 345, 472 Shen, J.J. 494 Treshchalov, A. 130 Sheng, H. 320 Trojan, I.A. 597 Shi, S.-Q. 65 Tsai, T.-Y. 88 Shihoyama, K. 201 Tso, P.L. 547 Shimizu, K. 381 Tsuda, O. 350, 372, 429 Shoda, K. 222 Tsugawa, K. 354, 556 Silva, S.R.P. 59, 96, 500 Tsukioka, K. 147 Singh, M.K. 545 Tsutsumoto, T. 250

Tter, I. 128 Wu, Y. 553 Twitchen, D.J. 111 Wu, Z.H. 101 Tyagi, P.K. 545 Tzeng, Y. 12, 547 Xian, X.H. 53, 90 Xiao, J. 495 Uematsu, T. 222 Xiaobin, N. 506 Xu, B. 544 Uemura, K. 472 Uhlmann, E. 191, 228 Xu, H. 610 Umezawa, H. 174 Ustinov, A.O. 89 Yamada, T. 110, 218 Usuba, S. 598, 599 Yamagata, A. 478 Yamaguchi, C. 42 Yamamoto, A. 250, 255 Vaseashta, A. 106 Veiga, W. 471 Yamamoto, K. 163, 359, 366, 429, 598 Vinogradov, M. 495 Yanagisawa, T. 19 Vittone, E. 120 Yang, D.J. 95 Vladimirov, A.B. 345, 472 Yang, H. 378 Vlasov, A.V. 309 Yang, R. 65 Yang, X.Q. 153 Vlasov, I.I. 285 Volkov, A.P. 89 Yasuda, Y. 440 Voronov, O.A. 406 Yasuhara, T. 70 Voskanyan, S. 334 Yengibaryan, Y. 334 Yokoi, H. 598, 599 Yokota, Y. 130 Walton, D.R.M. 96 Yoon, S.F. 95, 275 Wan, B.Y. 101 Wang, G. 491 Yoon, K.H. 507 Wang, G.Z. 365, 491, 544 Yoshida, H. 129, 163, 164 Wang, H. 26, 31, 53 Yoshida, T. 378 Wang, M. 460 Yoshikawa, H. 351, 556 Wang , Q. 95 Wang , Q.T. 544 Yoshimura, H. 490 Yoshioka, N. 76 Yu, G.Q. 451 Wang, S. 95 Wang, S.X. 260 Yu, L. 365, 491, 544 Wang, W.L. 53, 80, 90, 101, 260 Yu, Q.X. 365, 491, 544 Wang, Y.L. 153 Yuan, L. 506 Watamori, M. 328 Yudasaka, M. 4 Watanabe, A. 154 Yugov, V.A. 345, 472 Watanabe, H. 109 Watanabe, K. 112, 331 Zakhidov, A.A. 89 Watanabe, S. 440, 445, 447, 460, 466 Zapol, P. 525 Watanabe, T. 350, 359, 372, 429, 430 Zeze, D.A. 59 Wazumi, K. 359, 436 Zhang, Q. 95, 275 Weber, H.P. 303 Zhang, D. 609 Zhang, R.Q. 609 Wee, A.T.S. 610 Weimer, J. 324 Zhang, W.J. 379, 553 Weitao, Z. 512 Zhao, L.X. 494 Zheng, W.T. 492, 493 Whitby, R.L.D. 96 Whitehead, A.J. 111 Zhou, Q. 95 Wolter, S.D. 564 Zhou, L.G. 65 Zhou, O. 3 Wong, N.B. 41 Wong, W.K. Zhu, X.L. 365 40, 553 Wort, C. 111 Zhu, Y.B. 80 Zima, T.M. 367 Wu, Q. 491 Wu, R.L.C. 324 Zolotukhin, A.A. 89

REPORT DOCUMENTATION PAGE

Form Approved OMB No. 0704-0188

Public reporting burden for this collection of information is estimated to average 1 hour per response, including the time for reviewing instructions, searching existing data sources, gathering and maintaining the data needed, and completing and reviewing the collection of information. Send comments regarding this burden estimate or any other aspect of this collection of information, including suggestions for reducing this burden, to Washington Headquarters Services, Directorate for Information Operations and Reports, 1215 Jefferson Davis Highway, Suite 1204, Arlington, VA 22202-4302, and to the Office of Management and Budget, Paperwork Reduction Project (0704-0188), Washington, DC 20503.

1. AGENCY USE ONLY (Leave blank)	2. REPORT DATE	3. REPORT TYPE AN	3. REPORT TYPE AND DATES COVERED		
	August 2003	(onference Publication		
4. TITLE AND SUBTITLE	•	5. FUNDING NUMBERS			
Proceedings of the Seventh App Carbon Technology Joint Confe	WDC 22 700 21 14				
6. AUTHOR(S)	WBS-22-708-31-14				
M. Murakawa, K. Miyoshi, Y. K	oga, L. Schäfer, and Y. Tzer	g, editors			
7. PERFORMING ORGANIZATION NAME(S) AND ADDRESS(ES)			8. PERFORMING ORGANIZATION REPORT NUMBER		
National Aeronautics and Space John H. Glenn Research Center Cleveland, Ohio 44135–3191	E-13906				
9. SPONSORING/MONITORING AGENCY NAME(S) AND ADDRESS(ES)			10. SPONSORING/MONITORING AGENCY REPORT NUMBER		
National Aeronautics and Space	Administration				
Washington, DC 20546-0001			NASA CP—2003-212319		
11. SUPPLEMENTARY NOTES					
	l Institute of Advanced Indu ter, Tsukuba, Japan, August	strial Science and Tecl	enter cosponsored by the Nippon hnology, Japan New Diamond Forum, hible person, Kazuhisa Miyoshi,		
12a. DISTRIBUTION/AVAILABILITY STAT	EMENT		12b. DISTRIBUTION CODE		
Unclassified - Unlimited Subject Category: 27	Distrib	ntion: Nonstandard			
Available electronically at http://gltrs	grc.nasa.gov				
This publication is available from the	NASA Center for AeroSpace Inf	ormation, 301–621–0390.			
13. ABSTRACT (Maximum 200 words)					

These are the Proceedings of the Seventh Applied Diamond Conference/Third Frontier Carbon Technology Joint Conference held at Epochal Tsukuba International Conference Center from August 18 to 21, 2003. The diamond CVD process was first reported by Dr. Spitsyn in 1981 and Prof. S. Iijima reported his discovery of carbon nanotubes in 1991. In the past years, both diamond-related materials and novel carbon materials have attracted considerable interest by the scientific, technological, and industrial community. Many practical and commercial products of diamond materials are reported in these proceedings. A broad variety of applications of carbon nanotubes and novel carbons have also been explored and demonstrated. Having more than 175 invited and contributing papers by authors from over 18 countries for presentations at ADC/FCT 2003 clearly demonstrates that these materials, due to the combination of their superior properties, are both scientifically amazing and economically significant.

14.	SUBJECT TERMS			15.	NUMBER OF PAGES
					635
	Chemistry; Materials			16.	PRICE CODE
17.	SECURITY CLASSIFICATION	18. SECURITY CLASSIFICATION	19. SECURITY CLASSIFICATION	20.	LIMITATION OF ABSTRACT
	OF REPORT	OF THIS PAGE	OF ABSTRACT		
	Unclassified	Unclassified	Unclassified		